NATIONAL CENTER FOR EARTHQUAKE ENGINEERING RESEARCH

ISSN 1088-3800

Proceedings of the Fifth U.S.-Japan Workshop on Earthquake Resistant Design of Lifeline Facilities & Countermeasures Against Soil Liquefaction

Edited by T.D. O'Rourke and M. Hamada

Technical Report NCEER-94-0026

November 7, 1994

This Workshop was conducted at the Snowbird Resort and Conference Center, Snowbird, Utah and was supported in whole or in part by the National Science Foundation under grant number BCS 90-25010and the New York State Science and Technology Foundation under Grant No. NEC-91029.

NOTICE

This report was prepared by the National Center for Earthquake Engineering Research (NCEER) through a grant from the National Science Foundation, and other sponsors. Neither NCEER, associates of NCEER, its sponsors, nor any person acting on their behalf:

a. makes any warranty, express or implied, with respect to the use of any information, apparatus, method, or process disclosed in this report or that such use may not infringe upon privately owned rights; or

b. assumes any liabilities of whatsoever kind with respect to the use of, or the damage resulting from the use of, any information, apparatus, method, or process disclosed in this report.

Any opinions, findings, and conclusions or recommendations expressed in this publication are those of the author(s) and do not necessarily reflect the views of NCEER, the National Science Foundation, or other sponsors.

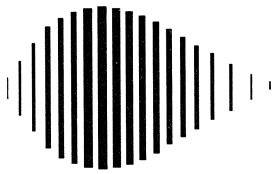

Proceedings from the Fifth U.S.-Japan Workshop on Earthquake Resistant Design of Lifeline Facilities and Countermeasures Against Soil Liquefaction

held at the
Snowbird Resort and Conference Center
Snowbird, Utah
September 29-October 1, 1994

Edited by T.D. O'Rourke[1] and M. Hamada[2]
November 7, 1994

Technical Report NCEER-94-0026

NCEER Task Number 93-2701

NSF Master Contract Number BCS 90-25010
and
NYSSTF Grant Number NEC-91029

1 Professor, School of Civil and Environmental Engineering, Cornell University
2 Professor, Department of Civil Engineering, Waseda University

NATIONAL CENTER FOR EARTHQUAKE ENGINEERING RESEARCH
State University of New York at Buffalo
Red Jacket Quadrangle, Buffalo, NY 14261

PREFACE

The Fifth U.S.-Japan Workshop was held near Salt Lake City, Utah, several kilometers from the Wasatch fault zone. This fault zone is the longest and most active normal-slip fault in North America. Workshop participants were taken on a field trip by the Utah Geological Survey to several trenches crossing the Wasatch fault zone, where evidence of previous surface faulting was preserved in the form of rupture planes and colluvial wedges in the walls of the trenches. This evidence is a striking reminder that the Salt Lake Valley is an active seismic area. Over 80 percent of Utah's 2.3 million residents live and work in the vicinity of the fault zone.

The Fifth U.S.-Japan Workshop was not only an international event, but a forum for engineers and utility personnel in the Salt Lake City area to learn about state-of-the-art developments and to participate in the presentations and discussions as experienced members of a community which must implement seismic resistant design of lifeline facilities and countermeasures for soil liquefaction. It is our hope that research results presented in these proceedings will be applied in engineering decisions and planning, and that the workshop has acted as a catalyst in promoting the transfer of technology from theory to practice.

T.D. O'Rourke
Professor, Cornell University

M. Hamada
Professor, Waseda University

TABLE OF CONTENTS

SECTION	TITLE	PAGE
I	**OBSERVATIONS DURING PAST EARTHQUAKES**	
	Liquefaction-Induced Ground Failures and Displacements Along the Shiribeshi-toshibetsu River Caused by the 1993 Hokkaido Nansei-oki Earthquake *R. Isoyama*	1
	Liquefaction-Induced Ground Surface Disruption *T.L. Youd and C.T. Garris*	27
	Ground Deformations and Their Effects on Structures in Midorigaoka District, Kushiro City, During the Kushiro-oki Earthquake of January 15, 1993 *K. Wakamatsu and N. Yoshida*	41
	Geotechnical Observations at the Van Norman Complex After the 1994 Northridge Earthquake *C.A. Davis and J.P. Bardet*	63
	Observed and Predicted Ground Deformation - Miller Farm Lateral Spread, Watsonville, California *T.L. Holzer, J.C. Tinsley III, M.J. Bennett, and C.S. Mueller*	79
	Characteristics and Damage Investigation of 1993 Hokkaido Nansei-oki Earthquake *T. Iwatate, Y. Sawada, D. Inoue, and Y. Sakamoto*	101
	Liquefaction of Calcareous Sands and Lateral Spreading Experienced in Guam as a Result of the 1993 Guam Earthquake *S. Vahdani, R. Pyke, and U. Siriprusanen*	117
	Effects of Remedial Measures Against Liquefaction at 1993 Kushiro-oki Earthquake *S. Iai, Y. Matsunaga, T. Morita, M. Miyata, H. Sakurai, H. Oishi, H. Ogura, Y. Ando, Y. Tanaka, and M. Kato*	135
	Water Systems Performance: Northridge Earthquake, January 17, 1994 *L. Lund*	153
II	**MECHANISMS OF LIQUEFACTION AND LARGE GROUND DEFORMATION**	
	Construction of Stress-Strain Histories from Recorded Dynamic Response *R. Dobry, M. Gutierrez, M. Zeghal, and A-W. Elgamal*	171
	Behavior of Sand After Liquefaction *N. Yoshida, S. Yasuda, M. Kiku, T. Masuda, and W.D.L. Finn*	181
	Post Liquefaction Deformation of Cohesionless Soil *A.K. Hussein and H.E. Stewart*	199
	A Consideration of the Mechanism for Liquefaction-Related Large Ground Displacement *M. Hamada, H. Sato, and T. Kawakami*	217
	A Comparative Study of Predictive Methods for Liquefaction Induced Embankment Displacements *G.R. Martin and P. Qiu*	233

TABLE OF CONTENTS (Cont'd)

SECTION	TITLE	PAGE
	Torsional Shear and Triaxial Compression Tests on Deformation Characters of Sands Before and After Liquefaction *S. Yasuda, T. Masuda, N. Yoshida, H. Nagase, H. Kiku, S. Itafuji, K. Mine, and K. Sato*	249
	Ground Motion Characteristics and Their Relation to Soil Liquefaction at the Wildlife Liquefaction Array, Imperial Valley, California *R.E. Kayen, J.K. Mitchell, and T.L. Holzer*	267
	Experimental Study on Mechanical Properties of Liquefied Sand *T. Kawakami, N. Suemasa, H. Hamada, H. Sato, and T. Katada*	285
	Review of Energy-Based Liquefaction Research at Case Western Reserve University *J.L. Figueroa, A.S. Saada, and L. Liang*	301
	Post-Liquefaction Ground Flow in Shaking Table Tests *H. Toyota and I. Towhata*	315
	Evaluation of Liquefying Soil through Time Using System Identification *S. Glaser and R. Chung*	331
	Recent Research on Liquefaction of Silts and Silty Sands at Santa Clara University *S. Singh*	347
	CANLEX (Canadian Liquefaction Experiment): A One Year Update *P.K. Robertson, B.R. List, and B.A. Hofmann*	353
III	**LIQUEFACTION AND DYNAMIC RESPONSE OF UNDERGROUND STRUCTURES**	
	Evaluation for Earthquake Ground Motion of Sediment- Filled Basin Under Seismic Observation *K. Sato, T. Iwatate, S. Sasaki, and H. Yajima*	367
	Dynamic Analysis of Lateral Flow of Liquefied Ground *I. Towhata and H. Toyota*	377
	VELACS Project: A Summary of Achievements *M.T. Manzari, K. Arulanandan, and R.F. Scott*	389
	An Experimental Study of Effects of Laterally Flowing Ground on In-Ground Structures *H. Sato, M. Hamada, and M. Doi*	405
	An Assessment of VELACS "Class A" Predictions *J.H. Prevost and R. Popescu*	415
	A New Interpretation Method of Surface Wave Measurements to. Obtain Representative Shear Wave Velocity Profiles of Soils *C.J. Poran, J.A. Rodriguez-Ordonez, T. Satoh, and R. Borden*	425
IV	**MITIGATION OF EARTHQUAKE AND LIQUEFACTION EFFECTS**	
	Experiments on Force Acting on Underground Structures in Liquefaction-Induced Ground Flow *M. Miyajima and M. Kitaura*	445

TABLE OF CONTENTS (Cont'd)

SECTION	TITLE	PAGE
	Evaluation of Pile Response to Liquefaction-Induced Lateral Spread *T.D. O'Rourke, W.D. Meyersohn, Y. Shiba, and D. Chaudhuri*	457
	High Ductility Aseismic Joint Spliced Pile Behavior When Subjected to Liquefaction-Induced Large Ground Displacements *F. Miura, T. Miyasaka, and T. Hirata*	481
	Mitigation of Liquefaction Hazards at Three California Bridge Sites *K. Jackura and A. Abghari*	495
	Assessing Vulnerability of BC Gas Pipelines to Lateral Spread Hazards *D.G. Honegger*	515
	Pipeline Design Against Sand Liquefaction in Isla Del Carmen, Mexico *V. Trueba-López and R. Flores-Berrones*	531
	Preliminary Evaluation of the Use of Compaction Piles for Improvement of the Foundation Soils of the Coastal Dikes of Lake Maracaibo, Venezuela *B. Villegas and J. Murria*	547
V	**LIFELINE PERFORMANCE AND LIQUEFACTION DURING EARTHQUAKES**	
	Minimization of Seismic Damages *K. Kubo*	561
	Estimation of Indirect Losses Caused By Disruption of Lifeline Service: A Pilot Study of the Memphis Light, Gas and Water System *R.T. Eguchi and H.A. Seligson*	565
	Time History Analysis of Seismic Serviceability of a. Water Supply System *I.J. Markov, M.D. Grigoriu, and T.D. O'Rourke*	577
	Troubles People Have to Suffer When Lifelines Fail to Function After Earthquake *H. Hayashi, H. Kameda, and N. Nojima*	593
	Guide to Documenting Earthquake Damage to Power Systems *A.J. Schiff*	601
	Probabilistic Evaluation of Liquefaction Spread for Lifeline Structures *I. Katayama, J.A Pires, and A.H.-S. Ang*	617
	Failure Criterion for Buried Pipe Subject to Longitudinal PGD: Benchmark Case History *M.J. O'Rourke and X. Liu*	639
	Changing Needs for Hazard Information for Pipeline Loss Estimation *D. Ballantyne*	653
	Shaking Table Tests on Floatation of Buried Pipes Due to Liquefaction of Backfill Sands *S. Yasuda, H. Nagase, S. Itafuji, H. Sawada, and K. Mine*	665
	Earthquake Performance of Gas Transmission Pipelines *T.D. O'Rourke and M.C. Palmer*	679
	Magnitude Scaling Factors for Analysis of Liquefaction *T.W. Loertscher and T.L. Youd*	703
	Damage to Water Pipes During the 1994 Northridge Earthquake *M. Hamada, T. Tazoh, T. Iwamoto, N. Suzuki, J. Ejiri, and K. Ohtomo*	717

TABLE OF CONTENTS (Cont'd)

SECTION	TITLE	PAGE
VI	**WORKING GROUP SESSIONS**	
	Report From Working Group No. 1	731
	Report From Working Group No. 2	735
	Report From Working Group No. 3	739
	Report From Working Group No. 4	741
VII	**WORKSHOP PARTICIPANTS**	
	List of Participants	745

U.S.-JAPAN COOPERATIVE RESEARCH PROGRAM AND WORKSHOPS

The U.S.-Japan Research Program on Earthquake Resistant Design of Lifeline Facilities and Countermeasures Against Soil Liquefaction focuses on the earthquake performance of lifelines, with emphasis on liquefaction-induced large ground deformations. Large ground deformations are the principal cause of subsurface structural damage during earthquakes. Currently, there is a growing recognition in the civil and earthquake engineering communities of the importance of large ground deformations. Our understanding of the mechanisms of large ground deformations and their effects on lifeline facilities, and our ability to predict the magnitude and distribution of ground displacements have improved substantially in recent years to provide a rational framework for siting, design, and protective measures. Both Japanese and U.S. researchers have been working on this topic, and it was recognized that considerable benefits will result from their cooperative effort to collect case history data and their recommendations about the most appropriate analytical methods and design procedures.

The program was initiated formally in November, 1988 with the signing of a Memorandum of Understanding between the Japanese and U.S. sides. The document was signed at a ceremony during a workshop in Tokyo, Japan by K. Kubo, Professor Emeritus of Tokyo University, and M. Shinozuka, Sollenberger Professor of Civil Engineering of Princeton University. Professor Kubo signed on behalf of the Association for the Development of Earthquake Prediction (ADEP), the Japanese sponsoring agency. Professor Shinozuka signed on behalf of Robert L. Ketter, the Director of the National Center for Earthquake Engineering Research (NCEER), the U.S. sponsoring agency. A second Memorandum of Understanding was signed in December, 1990 to continue the cooperative program of research. The signatures were K. Kubo, representing ADEP, and M. Shinozuka, the Director of NCEER.

The research program has concentrated on case histories of ground deformations and their effects on lifeline facilities. The case histories were collected in two volumes and published in May, 1992 as a joint Japan-U.S. effort by NCEER. The earthquakes included in the Japanese case histories are: 1923 Kanto, 1948 Fukui, 1964 Niigata, 1983 Nihonkai-Chubu, and 1990 Luzon, Philippines earthquakes. The earthquakes included in the U.S. case histories are: 1906 San Francisco, 1964 Alaska, 1971 San Fernando, 1979 Imperial Valley, and 1989 Loma Prieta earthquakes. The Japanese and U.S. case history studies were coordinated by Professor T.D. O'Rourke of Cornell University and Professor M. Hamada of Waseda University. Case studies are in progress for the 1993 Kushiro, 1993 Hokaido Nansei-oki, and 1994 Northridge earthquakes.

In addition to the publication of the case history volumes, the products of the cooperative research include U.S.-Japan workshops and associated publications of the proceedings covering case history data, analytical modeling, experimental studies and recommendations for improved practices.

The U.S.-Japan Workshop program is a major instrument for collaboration and cooperative exchange. To date, there have been five workshops. The first was held in Tokyo and Niigata, Japan on November 16-19, 1988. The proceedings of this workshop were published by ADEP, and are available from NCEER. The second, third, and fourth workshops were held in Buffalo and Ithaca, NY, on September 26-29, 1989, San Francisco, CA on December 17-19, 1990, and Honolulu, HI on May 27-29, 1992, respectively. The proceedings of these workshops were published by NCEER. The fifth workshop was held at Snowbird, UT on September 29-30 and October 1, 1994. This volume contains the proceedings of the fifth workshop.

Cooperative research between Japanese and U.S. earthquake engineers has resulted in significant new findings about liquefaction and its effects on lifeline facilities, assessment of liquefaction potential, modeling of liquefaction-induced large ground displacements, performance of lifeline facilities and foundations, dynamic response of underground structures, and countermeasures and earthquake resistant design against liquefaction.

It is hoped that the spirit of cooperation fostered by these workshops and research program will contribute to a strong and enduring relationship among U.S. and Japanese engineers. It is believed that the research accomplishments of this collaborative activity will encourage additional joint projects and lead to improved understanding and mastery in the field of earthquake engineering.

M. Hamada
Professor, Waseda University

T.D. O'Rourke
Professor, Cornell University

ACKNOWLEDGMENTS

The organizers of the workshop thank the Association for the Development of Earthquake Prediction (ADEP) and the National Center for Earthquake Engineering Research (NCEER) for sponsoring the research program and workshop activities. In particular, we express our gratitude to M. Shinozuka, Sollenberger Professor of Civil Engineering, Princeton University, and to K. Kubo, Vice President of ADEP and Professor Emeritus of the University of Tokyo, who provided oversight on the cooperative research work and support for the workshop. Our thanks also are extended to G. Lee, Director of NCEER and Dean of the College of Engineering at the State University of New York at Buffalo, for his encouragement and support.

We are grateful for the support of the National Science Foundation (NSF). In particular, we thank Drs. S.C. Liu and C. Astill for their interest and encouragement.

We extend our sincere thanks to the members of NCEER and Cornell University, who helped organize the workshop and assisted in the exchange of information and execution of the program. In particular, we thank Andrea Dargush, Assistant Director of NCEER, and Debbie O'Rourke and Laurie McCall, of NCEER and Cornell University, respectively, for their dedication and outstanding service. We also thank members of the Utah engineering and scientific communities for their active participation. Special recognition in this regard is extended to Professor T.L. Youd of Brigham Young University, S. Musser of the Utah Department of Transportation, and Gary Christianson and Bill Black of the Utah Geological Survey.

T.D. O'Rourke
Professor, Cornell University

M. Hamada
Professor, Waseda University

I OBSERVATIONS DURING PAST EARTHQUAKES

Liquefaction-Induced Ground Failures and Displacements along the Shiribeshi-toshibetsu River Caused by the 1993 Hokkaido Nansei-oki Earthquake
R. Isoyama
Liquefaction-Induced Ground Surface Disruption
T.L. Youd and C.T. Garris
Ground Deformations and Their Effects on Structures in Midorigaoka District, Kushiro City, During the Kushiro-oki Earthquake of January 15, 1993
K. Wakamatsu and N. Yoshida
Geotechnical Observations at the Van Norman Complex after the 1994 Northridge Earthquake
C.A. Davis and J.P. Bardet
Observed and Predicted Ground Deformation - Miller Farm Lateral Spread, Watsonville, California
T.L. Holzer, J.C. Tinsley III, M.J. Bennett, and C.S. Mueller
Characteristics and Damage Investigation of 1993 Hokkaido Nansei-oki Earthquake
T. Iwatate, Y. Sawada, D. Inoue, and Y. Sakamoto
Liquefaction of Calcareous Sands and Lateral Spreading Experienced in Guam as a Result of the 1993 Guam Earthquake
S. Vahdani, R. Pyke, and U. Siriprusanen
Effects of Remedial Measures Against Liquefaction at 1993 Kushiro-oki Earthquake
S. Iai, Y. Matsunaga, T. Morita, M. Miyata, H. Sakurai, H. Oishi, H. Ogura, Y. Ando, Y. Tanaka, and M. Kato
Water Systems Performance: Northridge Earthquake, January 17, 1994
L. Lund

Liquefaction-induced Ground Failures and Displacements along the Shiribeshi-toshibetsu River Caused by the 1993 Hokkaido-nansei-oki Earthquake

Ryoji Isoyama

ABSTRACT

Widespread and large-scale ground failures due to liquefaction occurred along the river valley of the Shiribeshi-toshibetsu River during the 1993 Hokkaido-nansei-oki Earthquake. By using the aerial photographs taken one day after the earthquake along the river, ground failures such as ground fissuring related to lateral spreading, sand boils and associated settlement were investigated, and the ground displacements both horizontal and vertical were measured by comparing the pre- to post- earthquake photographs. Horizontal displacements ranging to 1 to 3m were measured throughout the area that liquefied. The surface ground moved along a very gentle slope toward crescent lake or channel in most cases. Soil surveys were also conducted in the area where the large ground displacement occurred, which showed a fine and very loose sand deposit existing 2 to 5 m in depth below the ground surface.This paper summarizes the preliminary results of the investigation conducted so far for the above mentioned area.

Deputy Director, Earthquake Disaster Mitigation Division, Japan Engineering Consultants, Co. Ltd., Tokyo, Japan.

INTRODUCTION

An earthquake occurred on Monday, July 12, 1993 approximately at 10:17 p.m. (Japan Standard Time) beneath the Sea of Japan off the Oshima Peninsula in Hokkaido, registering the magnitude of 7.8 in JMA Scale. The earthquake was named as the 1993 Hokkaido-nansei-oki Earthquake. This earthquake caused a tsunami which swept the coasts of the Okushiri Island and the Oshima Peninsula on the Sea of Japan causing over 300 dead and missing.

At the same time large scale ground liquefaction occurred in the alluvial lowlands along the coasts of the Sea of Japan and the Pacific Ocean, causing damages to roads, harbors, housing, lifelines and farm lands. The liquefaction can be described as widespread and large scale but did not cause large scale damages to structures despite its scale, due to the lesser degree of urbanization in the area. Major damages of the liquefaction by this earthquake consisted of damages to the Port of Hakodate, and to the fishing harbors along the coast (both reclaimed lands), damages to buildings and lifelines in Oshamanbe and Kamiiso, etc., to the levees of the Shiribetsu and Shiribeshi-toshibetsu Rivers, the road damage on Route 5 mostly between Kunnui and Oshamanbe plus the agricultural damages in the region.

On July 20, 1993 the author investigated the earthquake damages along the Shiribeshi-toshibetsu River in Kitahiyama which is located on the coast of the Sea of Japan. At that moment it had already been reported that the levees and dikes of the Shiribeshi-toshibetsu River had largely been damaged and that liquefaction had occurred in the farming lands. Makeshift repairs on the levees of the Shiribeshi-toshibetsu River was under way in full scale, thus preventing him from seeing the actual damages to the embankments in most sites. Nonetheless, there were large, systematic fissures in the fields and rice paddies with much sand boiling, and it was presumed that large scale liquefaction and accompanying ground deformation, i.e. lateral spreading and ground settlement had set in.

During the Annual Meeting of the Japan Society of Civil Engineers held in September of 1993, a "Meeting on the Update of the 1993 Hokkaido-nansei-oki Earthquake Damages Investigation" was held. During this session Hirano and Shimizu[1)] demonstrated aerial photos of the Shiribeshi-toshibetsu River taken a day following the earthquake and reported on the damages to the levees. The photos demonstrated that large-scale liquefaction and ground deformation had occurred in the surrounding agricultural lands in addition to damages to the levees.

Then the author and Prof.Hamada of Waseda University examined the aerial photographs at the Hokkaido Development Agency and investigated the sites based on this information in September 1993. It became clear that large-scale liquefaction and accompanying ground deformation had

occurred in the river basin. Repair works for the agricultural lands started by borrowing soil immediately after our investigation was conducted, thus erasing ground deformation in most areas.

Ground liquefaction occurred mostly in rice paddies and cultivated fields along the Shiribeshi-toshibetsu River, in contrast to Noshiro City during the 1983 Nihonkai-chubu Earthquake and Niigata City during the 1964 Niigata Earthquake, almost devoid of ground structures to serve as aerial survey marks. On the other hand, sand boils and fissures were photographed visibly on rice paddies and cultivated fields, presumed important future data base for the study of ground deformation patterns and mechanisms.

The present study started under these circumstances involving collection of aerial photos taken before and after the earthquake and aerial photo survey based on them, collection of maps from the past and present, collection of information on boring data of grounds including levees, understanding of ground conditions for areas with marked deformation. This report has been put together with the objective to record the history of the Shiribeshi-toshibetsu River basin and changes in the topography and grounds based on the results of these investigations.

EARTHQUAKE AND EARTHQUAKE GROUND MOTION

Figure 1 shows the epicenter, approximate aftershock zone and the location of the Shiribeshi-toshibetsu River. The hypocenter is situated on the borderline between the Eurasian and North American Plates, on a reverse fault by east-west compression. The earthquake is said to be of a similar type to the 1983 Nihonkai-chubu Earthquake with magnitude 7.7. The aftershock zone encompasses an oval of 200 km north-south and 100 km east-west with the magnitude of 7.8 in JMA scale. The depth of the hypocenter is said to be approximately 30 km.

Figure 1 also shows the maximum horizontal acceleration. These earthquake ground motions were observed by the Japan Meteorological Agency, Hokkaido Development Agency and Railway Technical Research Institute. Based on this data Figure 2 shows the relationship between the maximum horizontal acceleration and the epicentral distance. It demonstrates that the attenuation of maximum acceleration is somewhat fast in comparison with other earthquakes in Japan. Figure 3 shows the records of strong motion by the Railway Technical Research Institute at Oshamanbe and Yakumo near the Shiribeshi-toshibetsu River. Both were recorded on an alluvial plain with the epicentral distance of approximately 100 km while the distance from the fault is approximately 50 to 60 km. It is assumed from these observations that the Shiribeshi-toshibetsu River basin was exposed to ground shaking of at least 200 to 300 cm/sec^2 in acceleration.

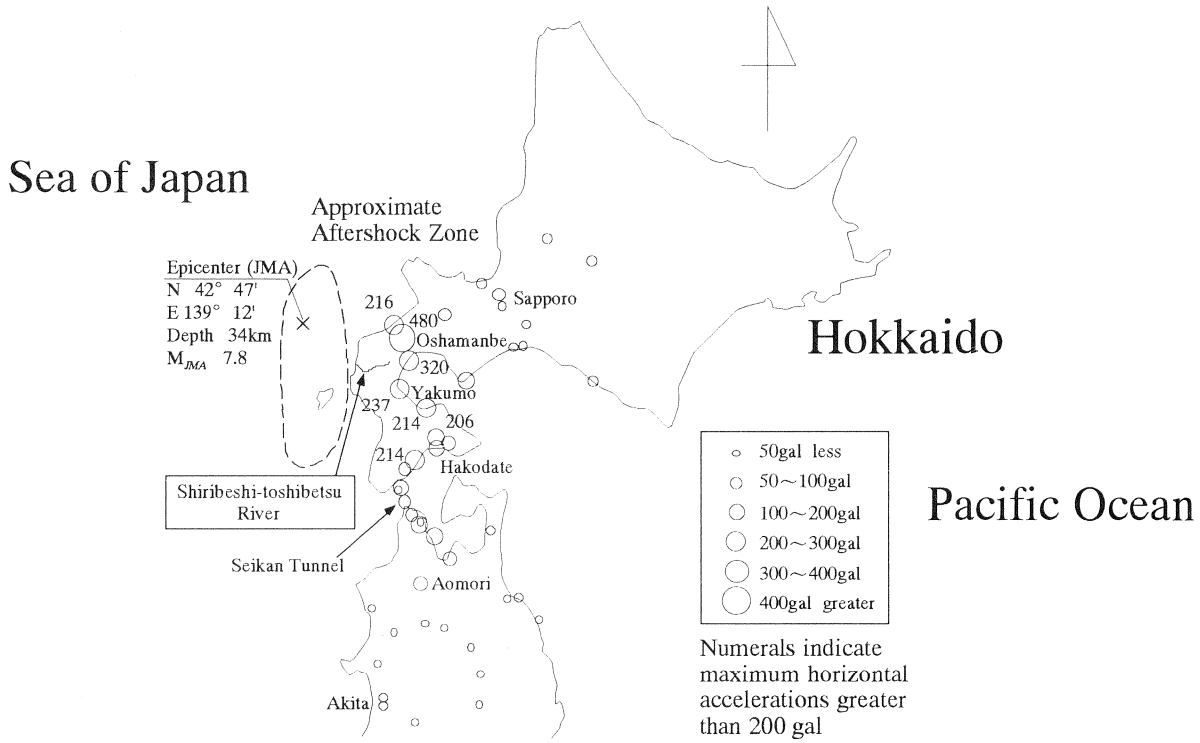

Figure 1 Epicenter of the 1993 Hokkaido-nansei-oki Earthquake, Maximum Horizontal Accelerations Observed[2] and the Location of Shiribeshi-toshibetsu River

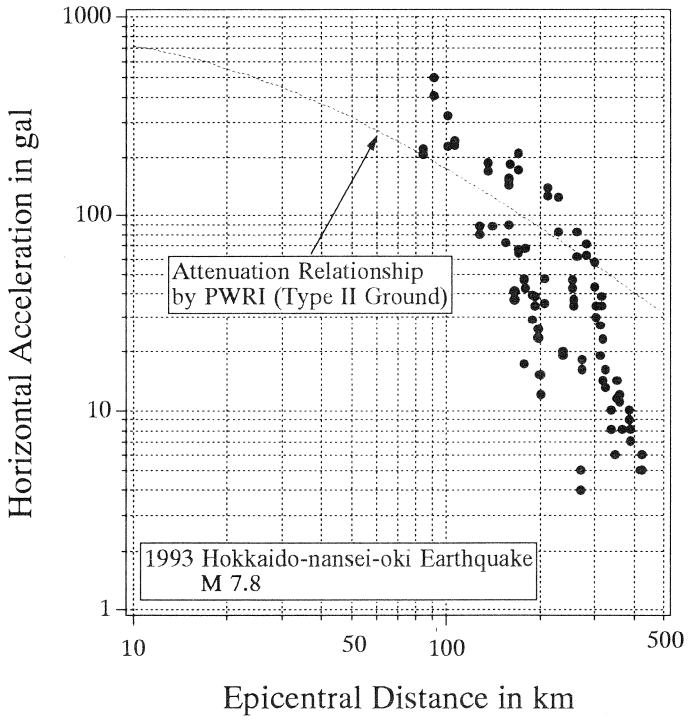

Figure 2 Attenuation Characteristics of Maximum Horizontal Accelerations (A Line in the Figure Indicates an Attenuation Relationship by PWRI[3] for Type II Ground)

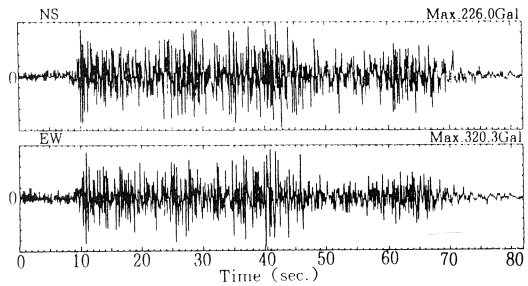

(a) Oshamanbe (Alluvium, Δ = 101 km)

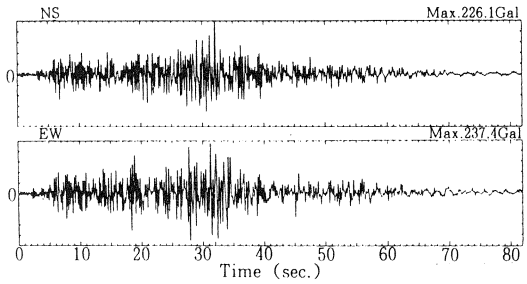

(b) Yakumo (Alluvium, Δ = 106 km)

Figure 3 Strong Motion Records by Railway Technical Research Institute[4] (Δ :Epicentral Distance)

Substantial damages to structures by the ground shaking were very few at Kitahiyama, Setana and Imakane Cities along the Shiribeshi-toshibetsu River. (The authors confirmed that a collapsed house at Kitahiyama had an apparent structural problem.)

OUTLINE OF TOPOGRAPHY AND GROUND CONDITION

Figure 4 shows the topography of the area along the Shiribeshi-toshibetsu River. The Shiribeshi-toshibetsu River originates in the divide between the Sea of Japan and the Pacific Ocean and flows into the former with the course length of approximately 80 km. It meanders down to Imakane in the midstream along a narrow gorge and straightens out to a relatively linear form at Imakane. The straight course from the midstream down is a result of large-scale river improvement work, very popular from the 1950s. The river has levees on both sides from the midstream to the river mouth.

The lowland, along the Shiribeshi-toshibetsu River, is 3 km wide at Imakane and 4 km at Kitahiyama on the midstream, and was presumably formed relatively recently by repeated floods of the Shiribeshi-toshibetsu River. The towns of Imakane and Kitahiyama are built on relatively elevated areas. The ground of the lowland is of thick alluvial ground consisting of sandy soil and clay with the exception of partial peat ground to the south. So-called bedrock with the N value of 50 or more appears at the depth of approximately 70 m from the ground surface and is made of extremely soft and deep alluvial ground. Especially there is an extremely loose sand layer with N value of 1 to 3 at the depth of 1 to 5 meters under the ground surface.

The areas where liquefaction occurred are also shown in Figure 4. As shown in the figure, the topography of the river basin and occurrence of liquefaction are closely related to the meandering of the Shiribeshi-toshibetsu River. Figure 5 shows a topographical change of the area from 1890s to the present based on the topographical chart to the scale of 1/50,000 by the Geographical Survey Institute. It is evident that the river has changed its course considerably over the years. As mentioned earlier, riverine improvements were undertaken after the 1950s, making the river linear from the midstream down. These improvements left the old river bed forming the present crescent lakes and small waterways (see Figure 4). It seems that the old river bed which exists in the current topography roughly corresponds to the river bed of 1917. However, there are many spots where the old river bed have been reclaimed leaving no trace of it in the current topography.

LIQUEFACTION AND GROUND DEFORMATION

Figure 4 shows the area where a ground deformation occurred interpreted by using aerial photos of the investigated area taken after the earthquake. Attention should be paid to the fact that the aerial

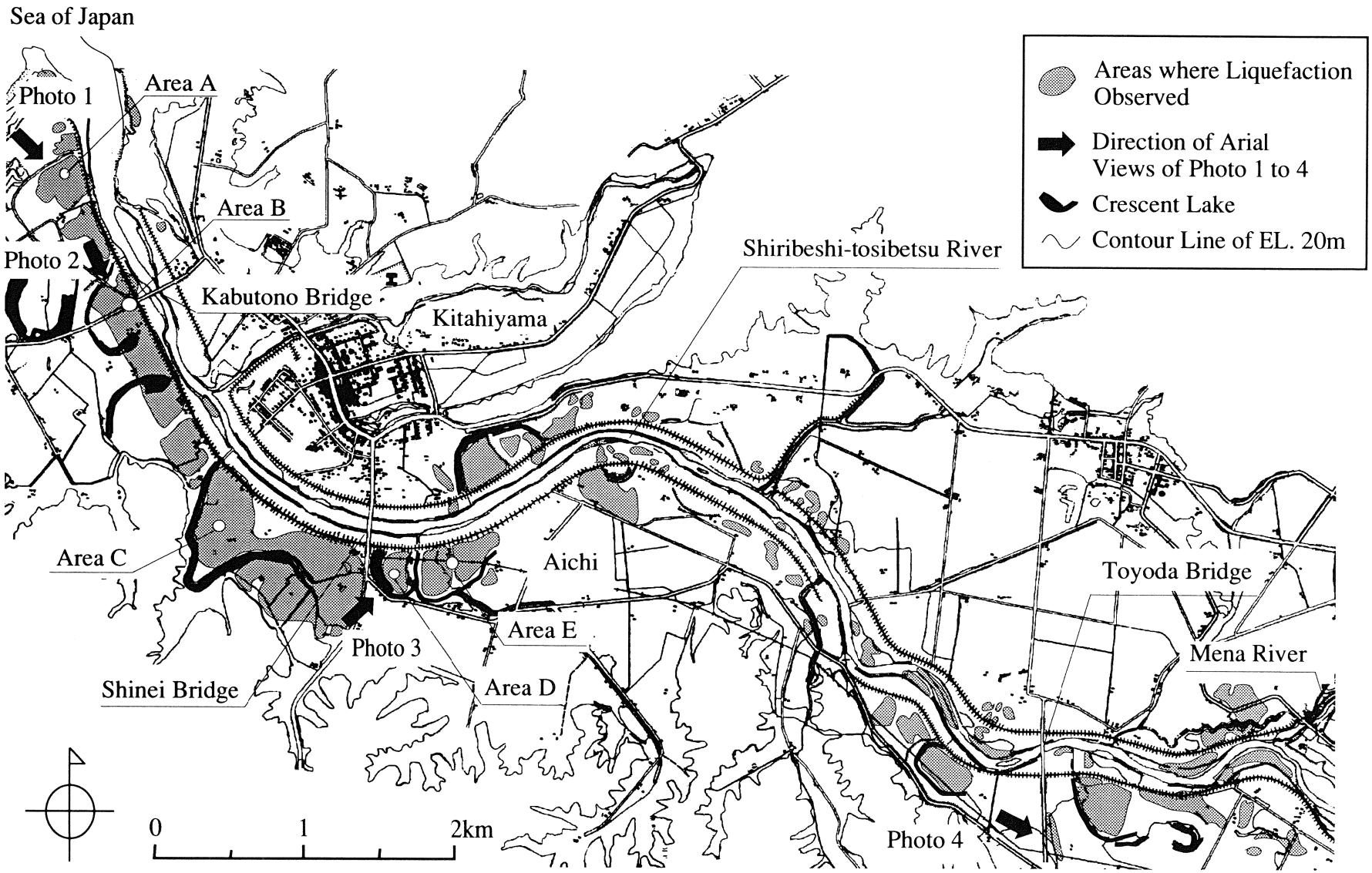

Figure 4 Siribeshi-toshibetsu River and Areas where Liquefaction Observed by Aerial Photograph

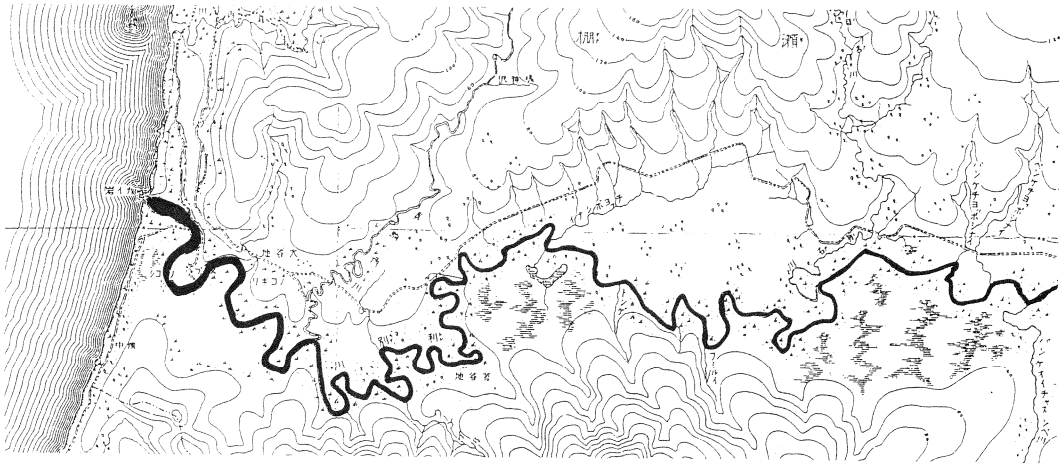

(a) 1896

0 5km

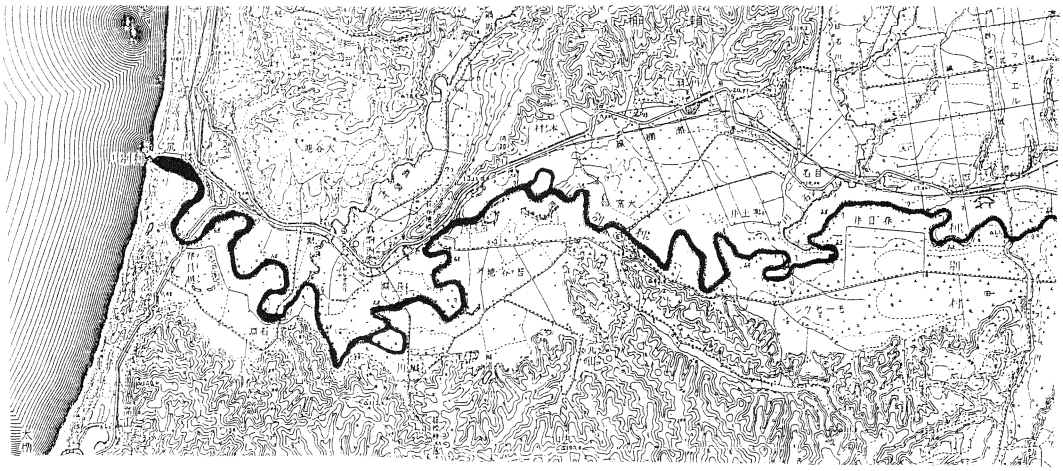

(b) 1917

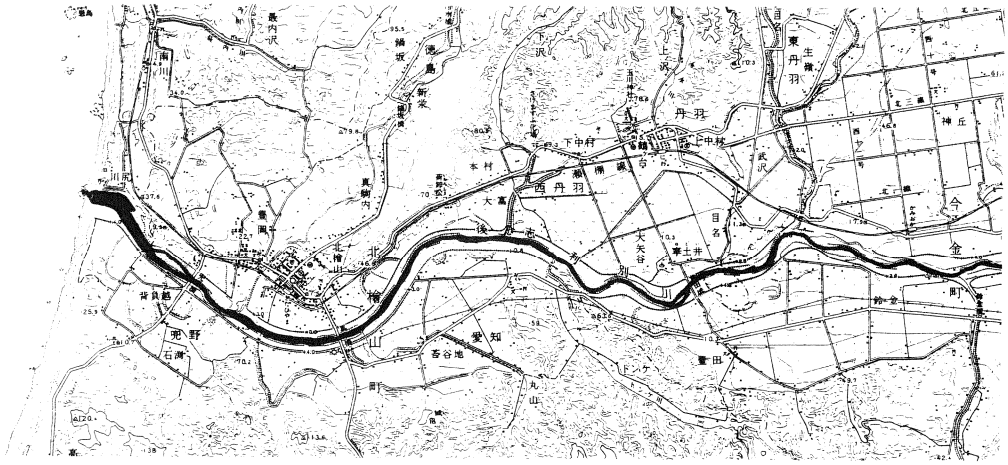

(c)1992

Figure 5 Chronological Change of River Course of the Shiribeshi-toshibetsu River

photos were taken for a damage assessment on the levees and they do not cover all of the surrounding lowland areas. However, most of the areas where severe liquefaction occurred are covered by these photos.

It is evident that the ground deformation occurred from the river-mouth of the Shiribeshi-toshibetsu River up to Suzukane area, approximately 12 km upstream. Liquefaction is prominent on the left bank in the downstream area but occurred on both sides upstream of the Shinei Bridge on Route 229. Deformation is especially prominent on the left bank from the river-mouth to upstream of the Shinei Bridge and in the area from the Toyoda Bridge to the confluence of the tributary Mena River. Typical areas are shown in slanted photographs in Photos 1 to 4. Figure 4 shows overall orientation for these slanted photos.

Interpretation of Deformation

Aerial photos were taken on July 13, 1993, the following day of the earthquake by the Hokkaido Development Agency for assessing damages to the levees. Vertical photos taken were at scales of 1/4,000(altitude 600 meters)and 1/2,000(altitude 300 meters). At the same time, several slanted photos were taken of the river basin(Photos 1 to 4).

Ground deformations were interpreted by experts as ground fissures, sand boiling, water surface (flooded areas) and were plotted on the four topographic charts (1/2,500 scaled) prepared by the Hokkaido Development Agency in 1984.

Aerial Photo Survey

Ground deformations or horizontal and vertical displacements caused by the earthquake were surveyed through comparison of aerial photos taken after the earthquake with those taken before the earthquake. Methods of survey were the same as those employed by the authors at Noshiro and Niigata [5]. The pre-earthquake photos were taken ten years ago in 1984 by the Hokkaido Development Agency.

In order to survey ground deformations by earthquake with aerial photographs taken before and after the earthquake, reference points are required for identification. There were very few such points in the affected area as compared to Noshiro and Niigata. The measurements of displacements must be made for points which are fixed to the ground surface and can be found in both pre- and post-earthquake photos. Ridges between rice paddies, roads, electric poles and roofs of houses, recognizable before and after the earthquake, were used as reference points in this survey.

The accuracy of ground displacement measurements depends on the scales of the pre- and post-

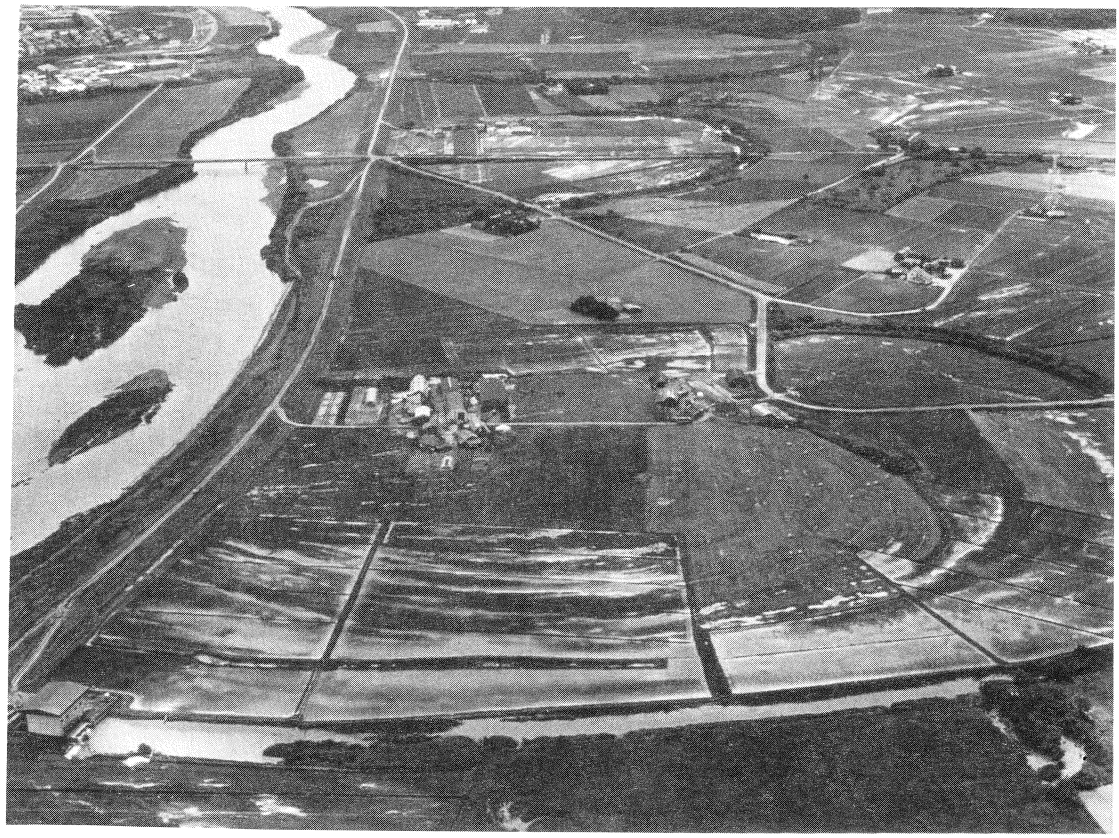

Photo 1 Aerial View from River-mouth (Area A, see Fig. 4)

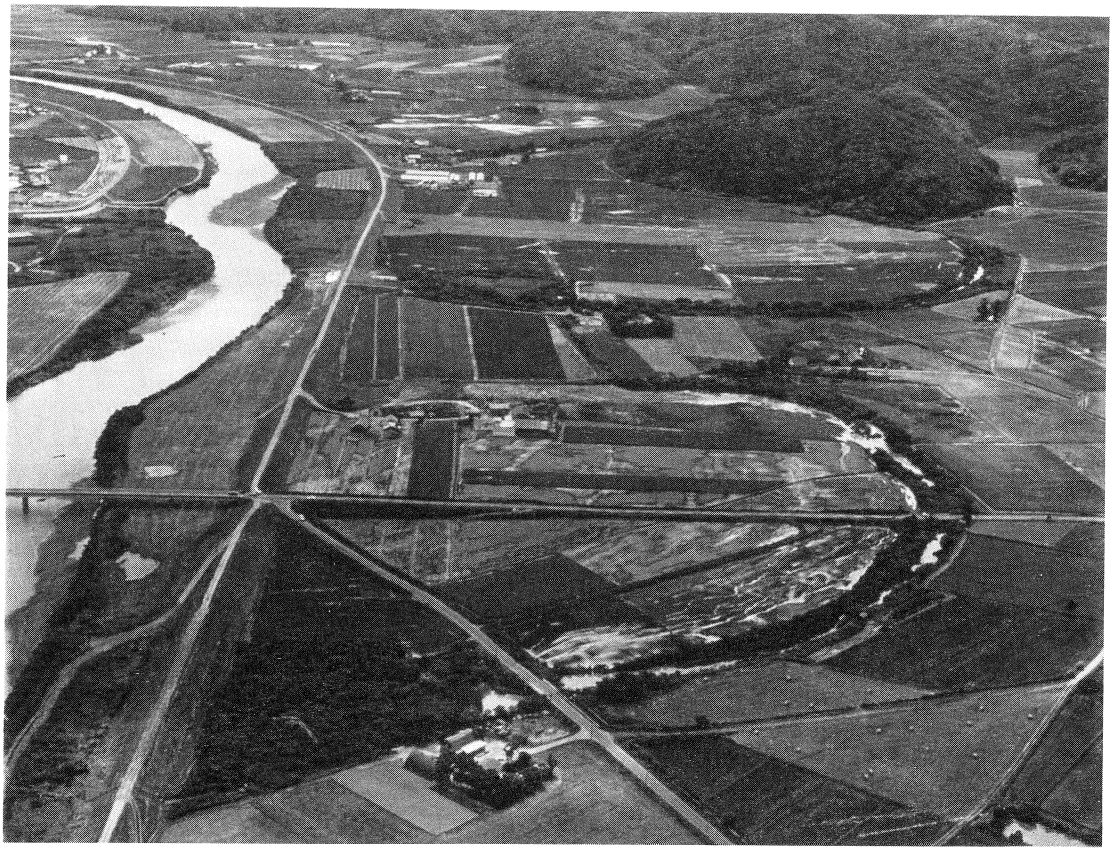

Photo 2 Aerial View of Kabutono Area from Downstream to Upstream (Area B, see Fig.4)

Photo 3 Aerial View of Aichi Area from Downstream of Shinei Bridge (Area D and E, see Fig.4)

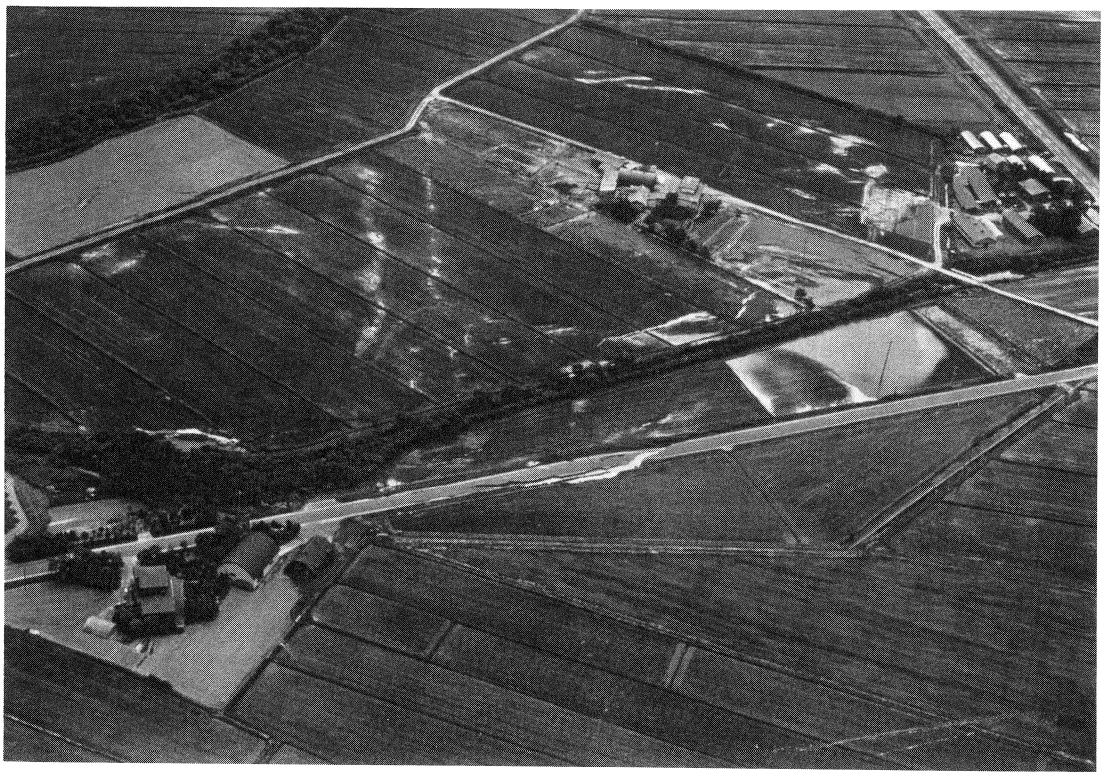

Photo 4 Aerial View of Toyoda Area (see Fig.4)

earthquake aerial photos, human error in reading the coordinates of the measurement points, and other factors. The accuracy was estimated to be ± 22cm horizontally and ± 20cm vertically in this area.

Figures 6 to 9 show the interpretation results of typical ground deformations and results of aerial photo surveys in the areas A, B, C and E . The location of areas A ~ E is shown in Figure 4. Photos 5 to 8 show aerial vertical photos corresponding to Figures 6 to 9 each. Photos 9 to 11 show the ground deformations in the Areas B and E taken by the author. Also Figures 6 to 9 indicate the measured ground displacements. The vectors represent ground displacements in the horizontal direction, each with a number indicating the magnitude of movement in cm. The numbers in parentheses are displacements in the vertical direction in cm, signs + and - show upheaving and settlement of the ground surface respectively. As for Area D on the left bank upstream to the Shinei Bridge (see Fig. 4), it will be discussed in a later section together with the results of the ground investigation.

The following observations can be made from the aerial photo survey and interpretation of the ground deformation above.

- Horizontal ground displacement reached 2 ~ 3 meters in severe cases. Vertical displacements roughly correspond to locations with severe horizontal displacements, resulting in ground settlement ranging 50 to 100 cm. However, it is noted that the level of settlement in some areas is not precise because the water surface has been measured in flooded areas. The actual levels of settlement are thought to be greater in these areas.
- The horizontal ground displacements are generally directed toward the extant crescent lakes on the old riverbed (main stream) or waterways so that the ground fissures and vector direction cross perpendicularly in general. Nonetheless the displacements of the ground are extremely complex in some areas as can be seen in ground fissures.
- Those areas where ground deformation or sand boiling occurred can be clearly distinguished from the areas without them. Such borderlines often correspond to the topographical change points thought to be the old riverbeds.
- As for the points along the levee, the ground displaced mostly outward of the levee by scores of centimeters up to one meter. The displacements apparently show the spreading or flattening of levees.

GROUND DEFORMATION IN AICHI AREA AND SOIL CONDITION

The area of the left bank upstream from the Shinei Bridge (Aichi Area, Area D in Figure 4) was

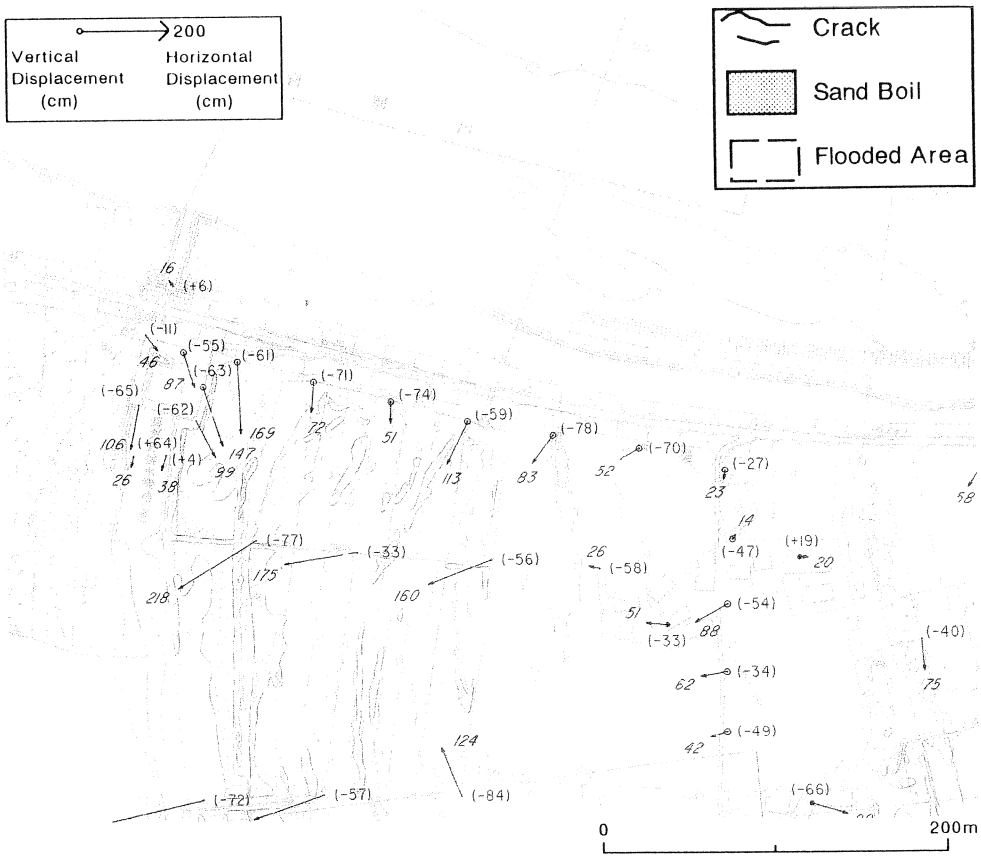

Figure 6 Map Showing Ground Deformations, Cracks and Sand Boils, Area A (About 700 m Upstream from River-mouth, see Fig.4)

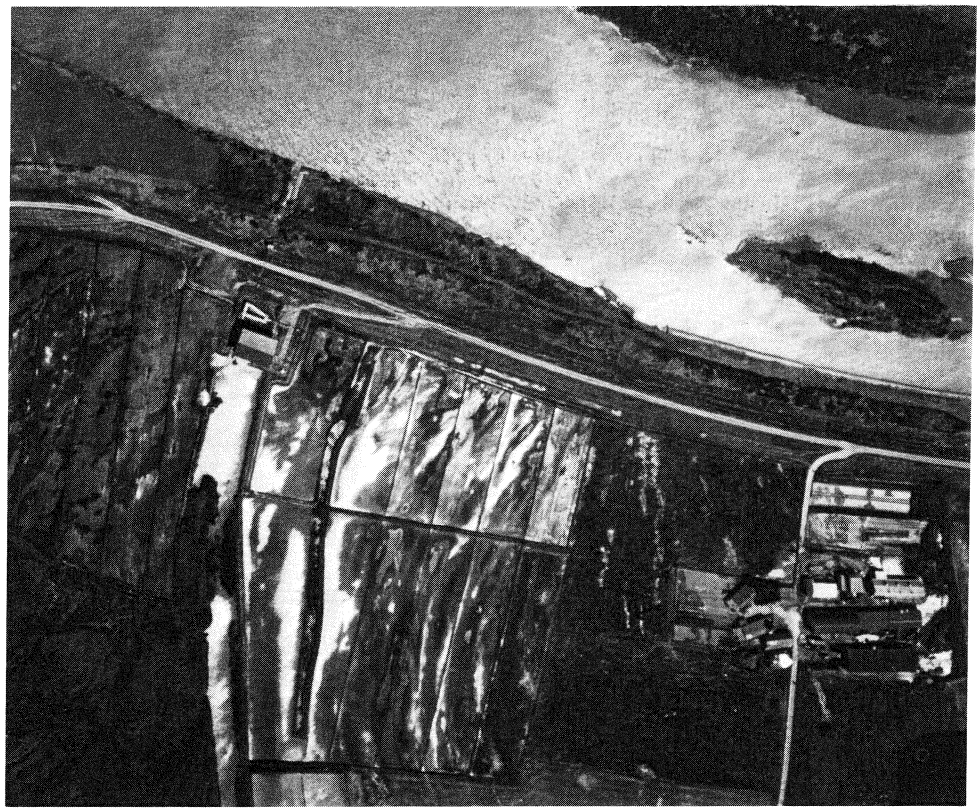

Photo 5 Aerial Photograph of Area A (Same Scale as in Fig.6)

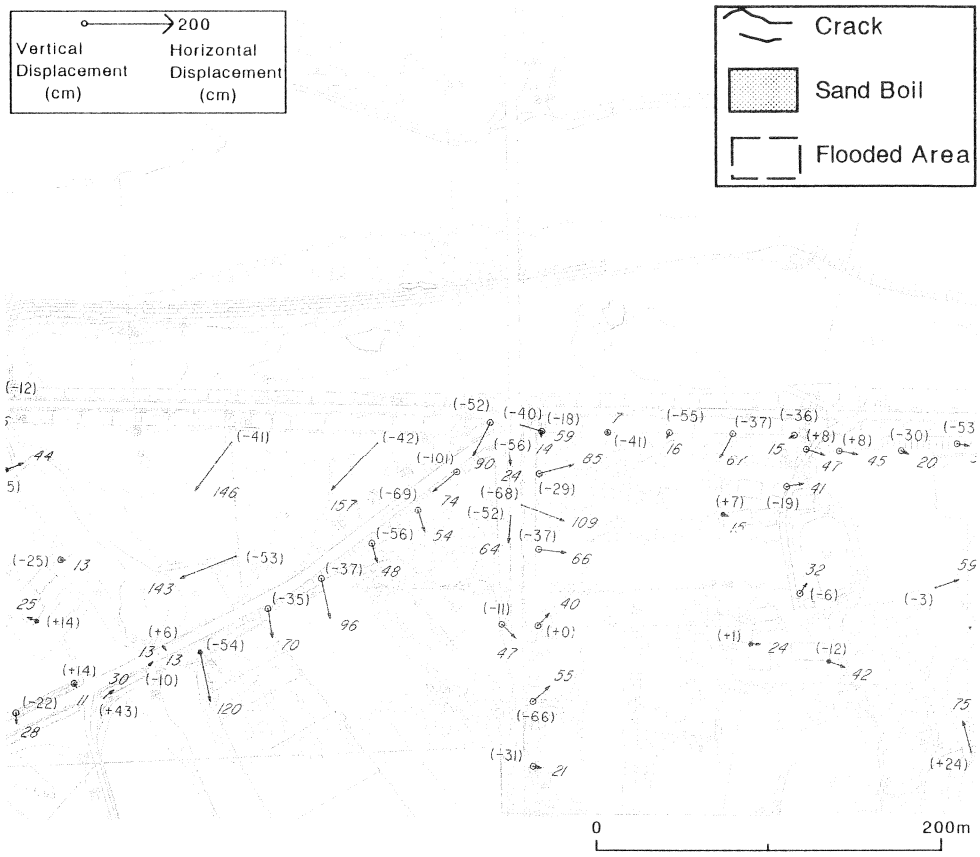

Figure 7 Map Showing Ground Deformations, Cracks and Sand Boils, Kabutono Area (Area B, see Fig. 4)

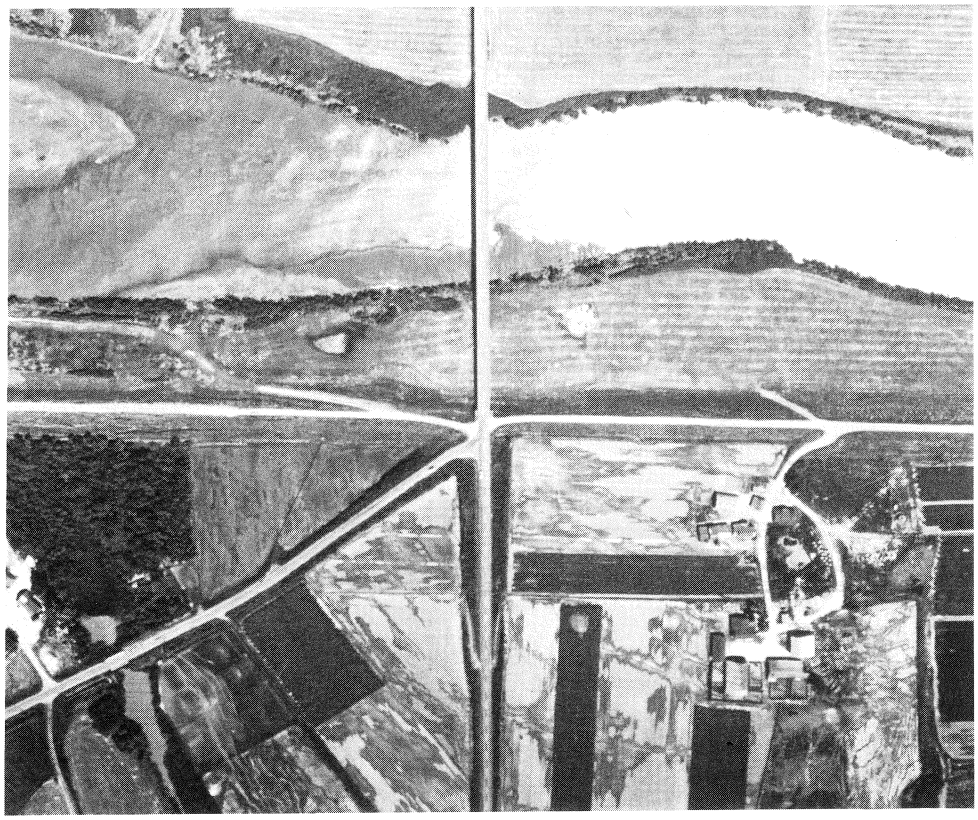

Photo 6 Aerial Photograph of Kabutono Area (Area B, Same Scale as in Fig.7)

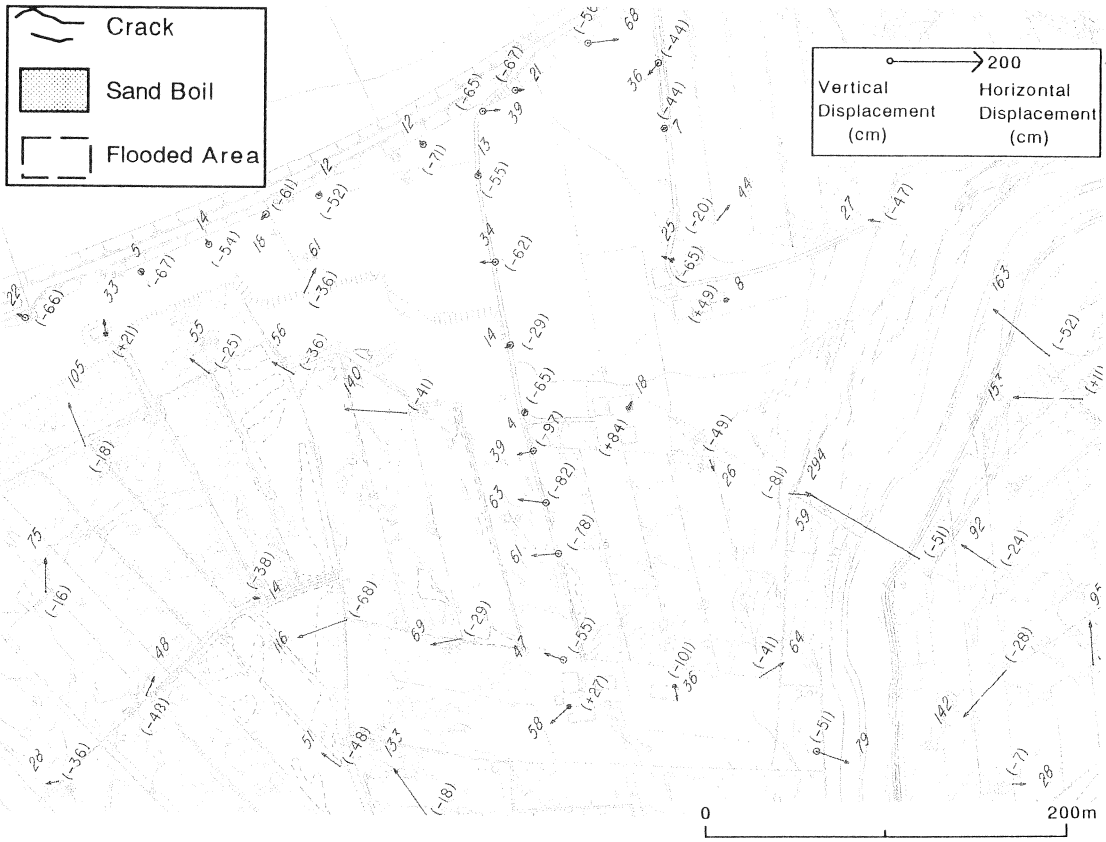

Figure 8 Map Showing Ground Deformations, Cracks and Sand Boils, Area C
(About 800 m Downstream of Shinei Bridge, see Fig. 4)

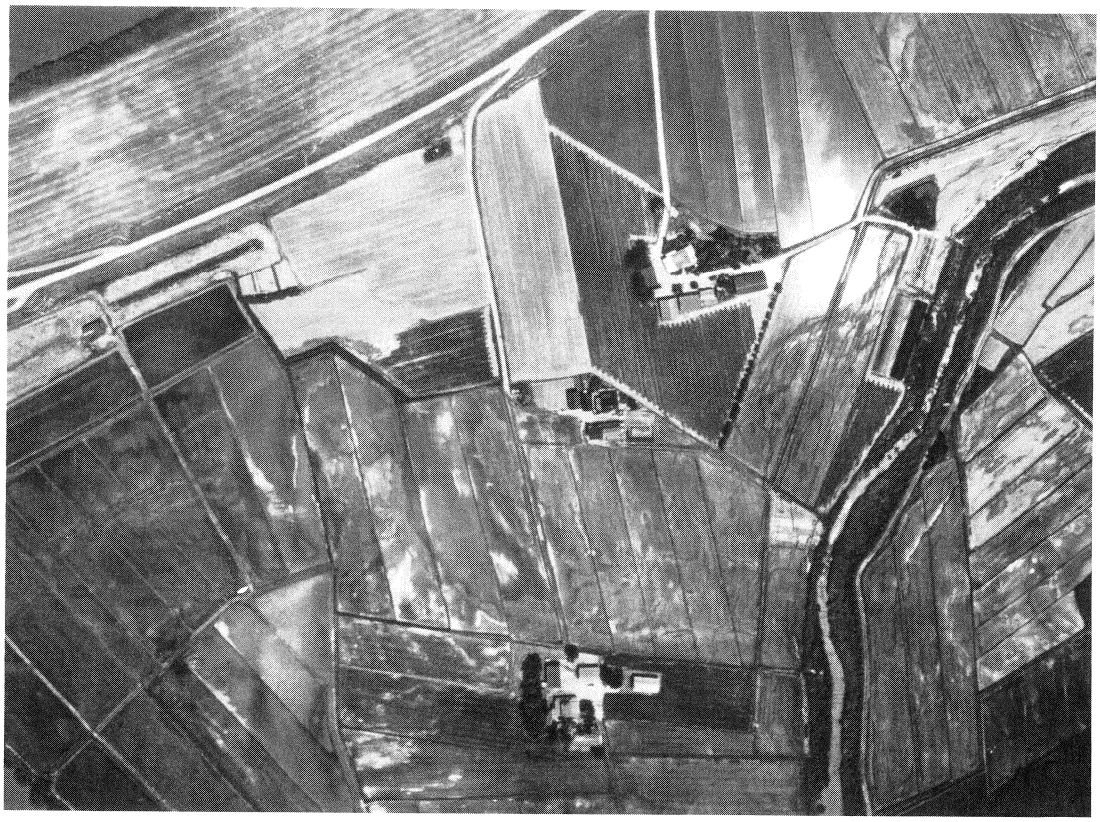

Photo 7 Aerial Photograph of Area C (Same Scale as in Fig.8)

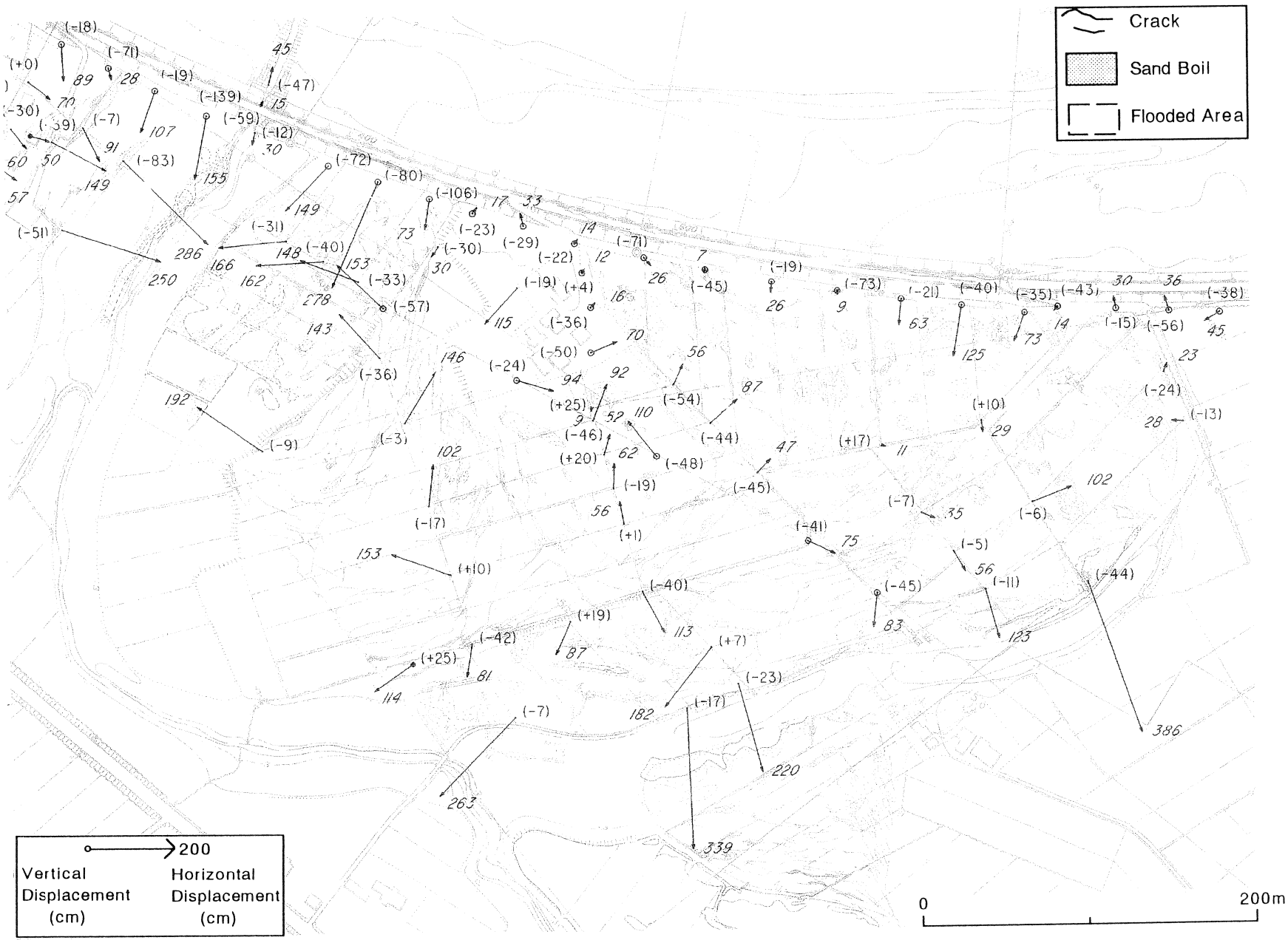

Figure 9 Map Showing Ground Deformations, Cracks and Sand Boils, Aichi Area (Area E, see Fig. 4)

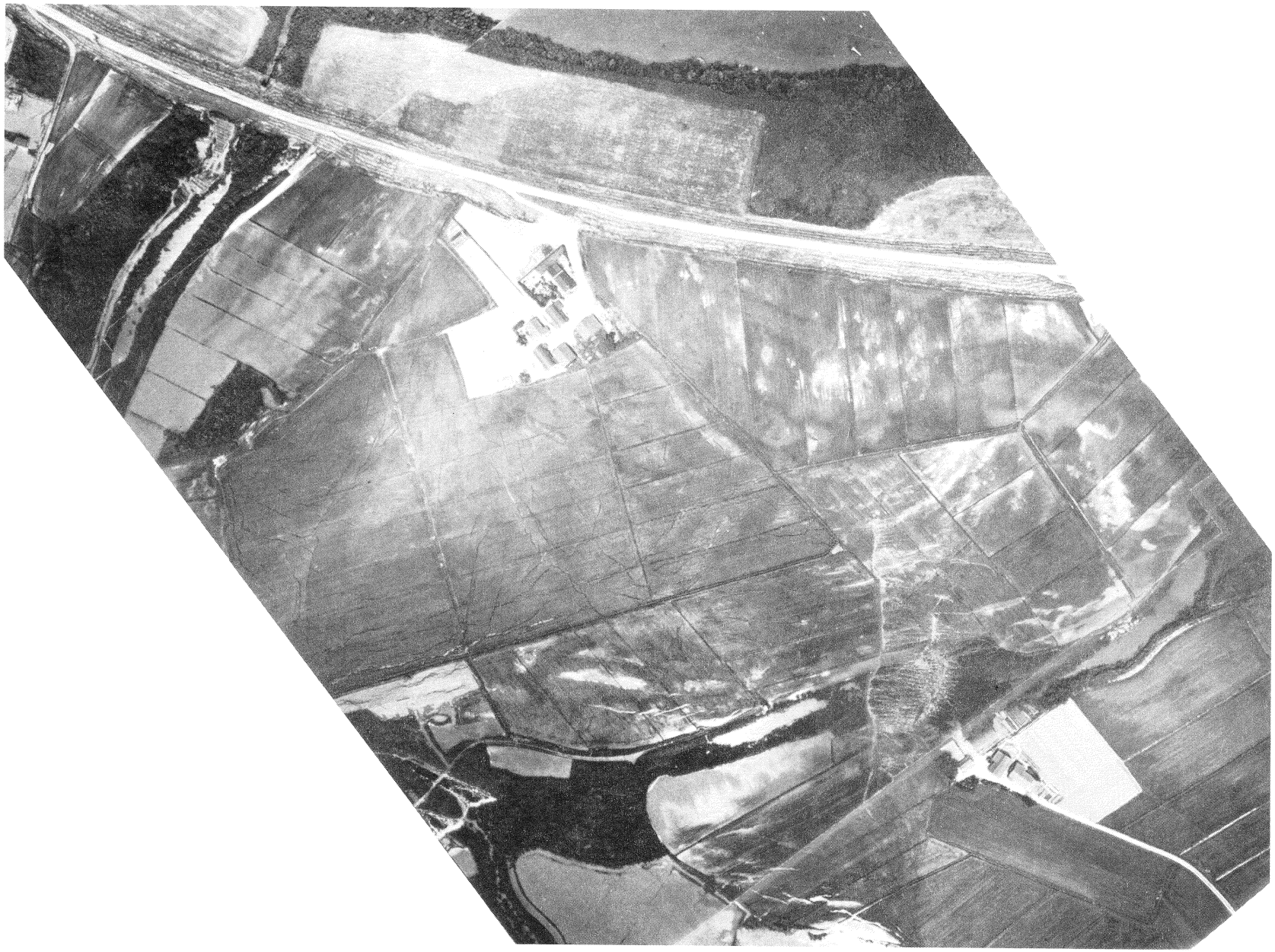

Photo 8 Aerial Photograph of Aichi Area (Area E, Same Scale as in Fig.9)

Photo 9 Fissures and Sharing of Ground Appeared in Kabutono Area
(Area B, see Fig. 4, View to Crescent Lake taken at September 1993)

Photo 10 Fissures Appeared in Kabutono Area (Same Place as in Photo 9,
Taken at July 20, 1993 from right-hand side of Photo 9)

Photo 11 Fissures Appeared in Aichi Area (Area D, see Fig. 4,Edge of Crescent Lake)

selected for its relatively extensive surface change and several ground investigation results already available, where somewhat detailed investigations including soil surveys were undertaken.

Deformation and Damages

The results of the survey and aerial photos of this area are shown in Figure 10 and Photo 12. It is noted that pre-earthquake aerial photos are available only for the portion along the levee (upper half of the Figure). Figure 11 shows the old topography the area upstream of the Shinei Bridge including Area D and E, interpreted by means of stereoscopying of the aerial photos taken by the US Forces in 1948.

In this area the ground displaced toward the old riverbed including crescent lakes and waterways, generating circular fissures along the old river bed, demonstrating the typical pattern of the ground deformation along the Shiribeshi-toshibetsu River. Horizontal displacements were generated right next to the old riverbed toward the lake by approximately 1.5 to 3.0 meters. On the other hand, the displacement is small in the center area of the arc.

Ground surface along the cross section shown in Figure 10 were compared for before and after the earthquake. The result is shown in Figure 12. This shows that the somewhat elevated topography in the center of the arc was depressed toward the old riverbed. The horizontal displacements can be seen from the movement of the ridges of rice paddies. The settlement, which reached approximately 80 cm in the center of the arc and 50 to 80 cm bear the old riverbed, occurred in the entire area. However, the pre-earthquake topography dates back ten years, possibly differing from what immediately preceded the earthquake.

Photos 13 shows fissures, sand boils and damage to the electric poles in this area. For the positioning of the photos, refer to Figure 10. As Photo 13 shows, there were two power transmission pylons; one with four legs (piled foundation) located in the center of the arc had no damage by settlement or tilting despite sand boiling from the foundation (Photo 13 (c)). The other gate-shaped pylon settled, moved toward the waterway and tilted approximately 10 degrees as shown in Figure 13 (b). Electric poles along the levee (Photo 13(a) and (e)) settled and tilted as a result of the settlement of the levee. In this area the levees of the Shiribeshi-toshibetsu River settled in general. Damages to the levees , however, are noteworthy especially somewhat upstream from here while fissures on the levees and settlements here are relatively minor.

Soil Conditions

Four boring tests and 16 Swedish sounding tests were conducted. Soil profiles were prepared along the cross sections shown in Figure 10. Figure 13 shows these soil profiles. The ground surface

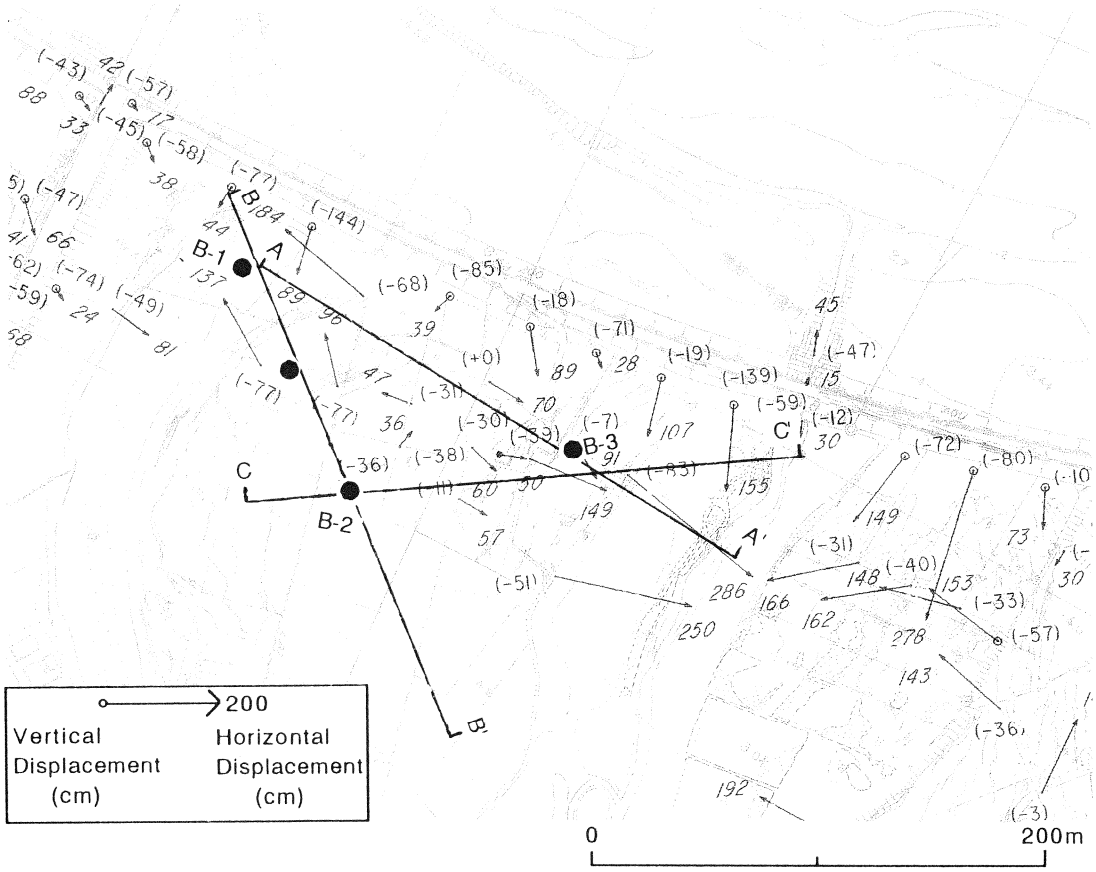

Figure 10 Map Showing Ground Deformations, Cracks and Sand Boils, Aichi Area (Area D, see Fig. 4)

Photo 12 Aerial Photograph of Aichi Area (Area D, Same Scale as in Fig.10)

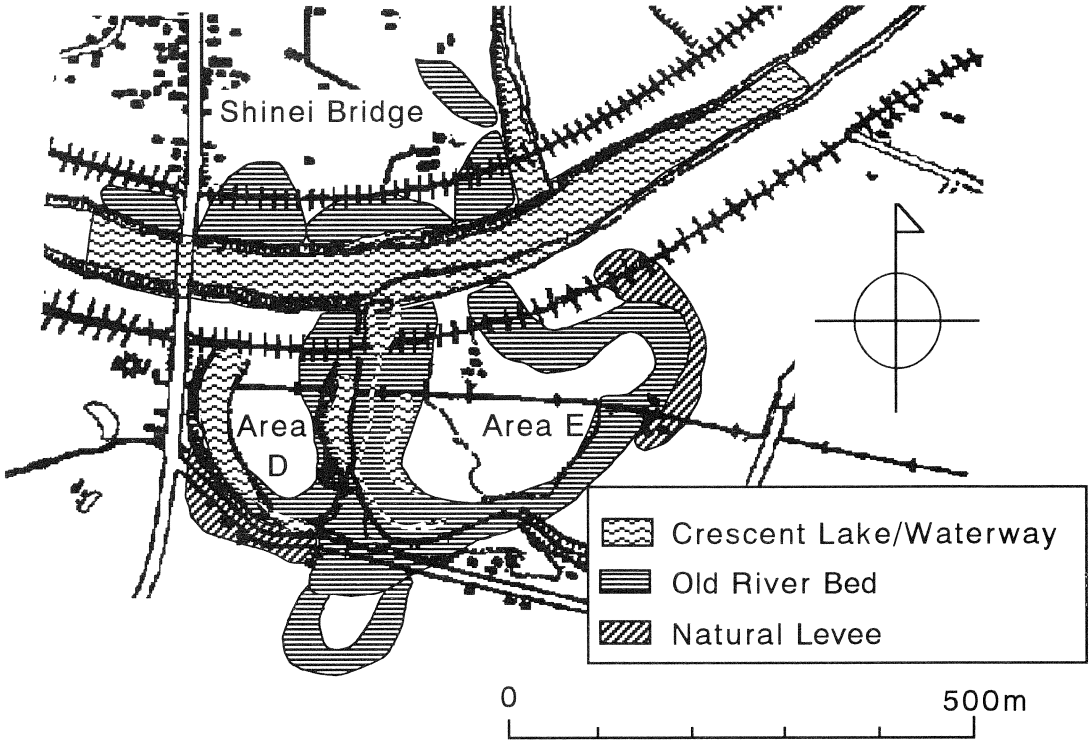

Figure 11 Old and Present River Channels Interpreted by Photograph Taken at 1948 in Aichi Area (Area A and E)

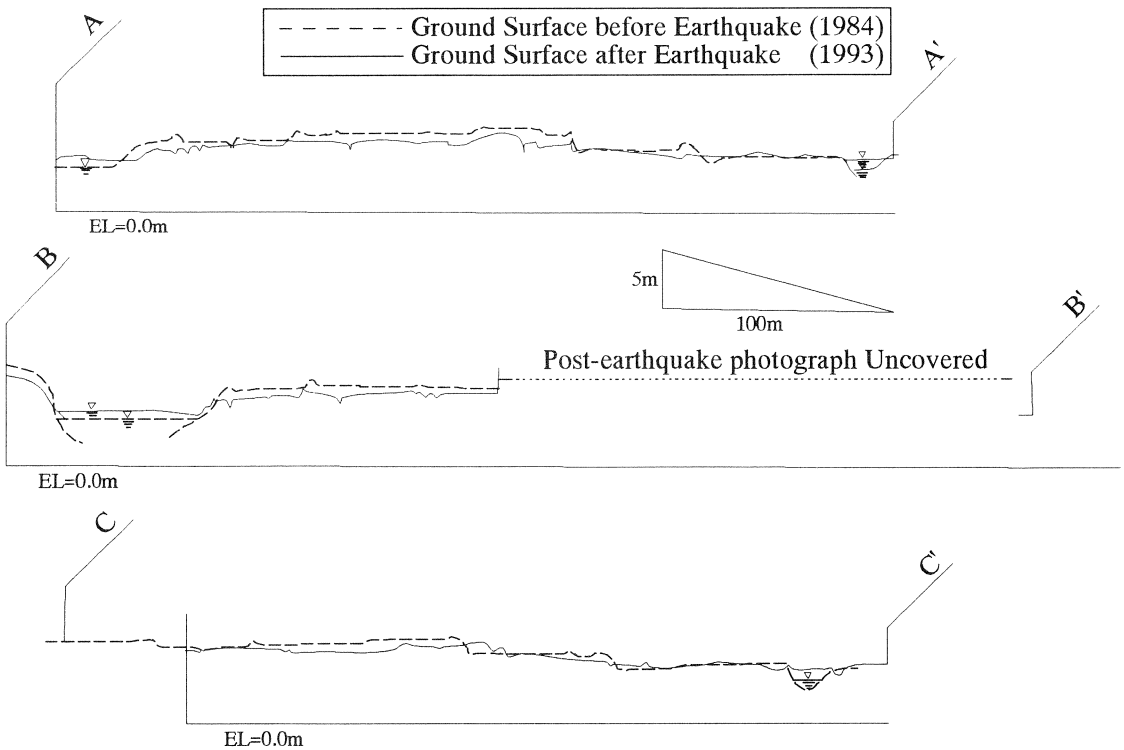

Figure 12 Measured Cross-Sections of Surfaces, Before (1984) and After(1993) the Earthquake (Locations of the Cross-sections are Shown in Fig. 10)

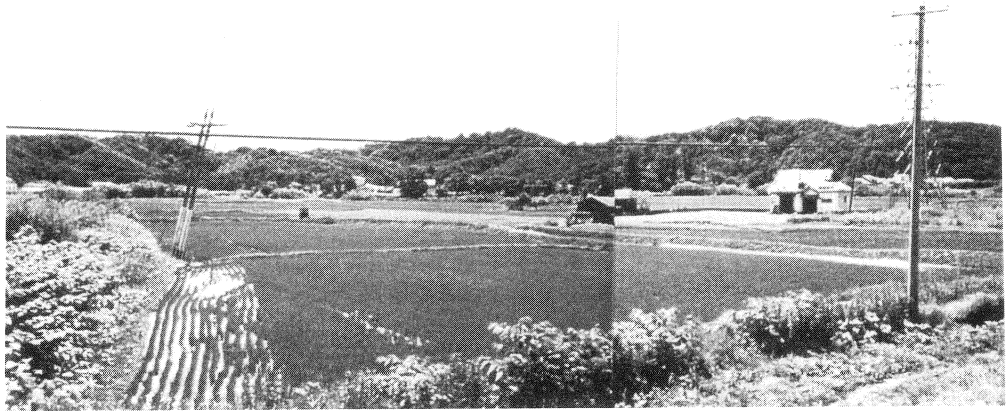

(a) Settlement and Tilting of Electric Pylon (One of Two Pylons, Gate-shaped, Settled and Tiltied in the Center of the Photo)

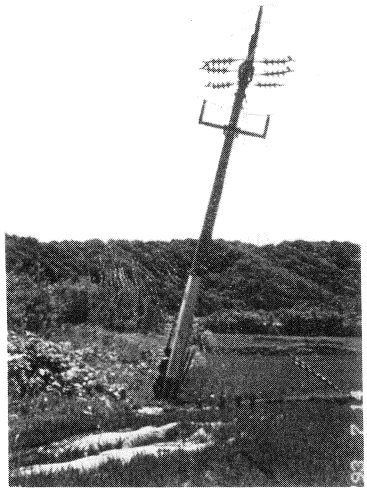

(b) Tilting of Electric Pylon

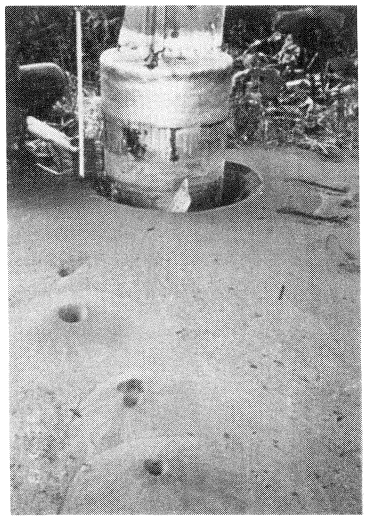

(c) Sand Boil from a Leg of Electric Pylon with four legs

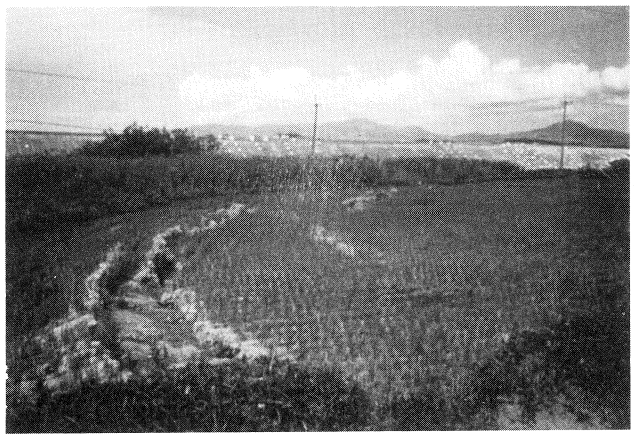

(d) Fissures

(e) Fissures and Sand Boils

Photo 13 Ground Deformations and Damage to Electric Poles in Aichi Area (Area D)

of these profiles follow the surface lines prior to the earthquake shown in Figure 12.

Figure 13 demonstrates that the strata of this area consist mainly of surface soil, upper clay layer, upper sandy soil layer (As-1), lower sandy soil layer (As-2) and lower clay layer. The upper sandy soil layer (As-1) lies underneath the upper clay layer at 1m to 5m from the ground surface and is extremely loose with N value of 1 to 4. The lower sandy layer (As-2) of somewhat hard with N value of approximately 10 appears. Ground water table is approximately 2 meters. (Soil survey was conducted in March 1994 and the water table at the moment of the earthquake could have been different from this.) Properties of the sandy soil layers (As-1 and As-2) are summarized as follows.

The upper sandy soil layer As-1 consists of sandy soil with much varied micro-fine sand, fine sand, and coarse sand with colors of brown-gray whose base is distributed around the sea level (elevation H= 0 m). This much-varied sandy soil is distributed in the entire region of Area D with the layer thickness of 2.0 $\sim$ 4.0 m. Mixtures include silt and small gravel in some spots while mica pieces are mixed in overall in large quantities. N values are very low: N= 1 $\sim$ 4, and average N is 2. Sws values, number of half revolution/m by sounding Nsw 0 $\sim$ 40, and average Nsw=10 $\sim$ 20.

The property values of this layer is summarized in Table 1 with those of As-2. The grain size distribution curves are shown in Figure 14 (a). This soil can be described as clean sandy soil with uniform grain diameter of uniformity coefficient (Uc) 2.5 $\sim$ 4.0 with fine grain content of over 95%. This sandy soil layer underneath the water table is thought to have liquefied completely.

The lower sandy soil layer As-2 is predominantly sandy soil mixed with gravel of dark grey distributed mostly around H= 0 $\sim$ -5.0 m. This layer is distributed 3.0 $\sim$ 5.0 m thick under As-1 layer in the entire area investigated. The grain size distribution curves of this soil are shown in Fig. 14 (b). Gravel is mainly circular/semi circular with diameter ϕ 2 $\sim$ 5 mm, max. ϕ = 10 mm approximately with a higher rate of mixture in top layer and lower rate of mixture in the bottom. The sand diameter varies from small to fine. More silt mixture is found in lower parts, forming silty sand. It is soft sandy soil whose N values are 3 $\sim$ 13, average N $\fallingdotseq$ 7. Nsw is 15 $\sim$ 80, with the average of Nsw $\fallingdotseq$ 50 while Nsw $\fallingdotseq$ 100 is obtained in spots with high gravel content.

Table 1 Property Values of Sandy Soil Layers

Property	As-1	As-2
Density of soil grain ρ_S (g/m^3)	2.70	2.68$\sim$2.73
Natural water content Wn (%)	25 $\sim$ 30	27
Grain soil test fine grains (F)	95% or more	15$\sim$55%
Uniformity coefficient (Uc)	2.6 $\sim$ 3.6	2.7$\sim$17.6

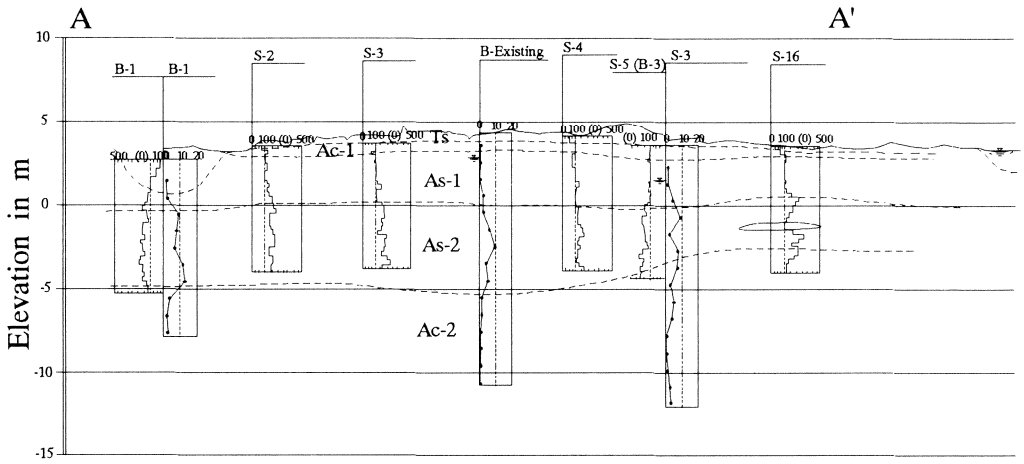

(a) A - A'

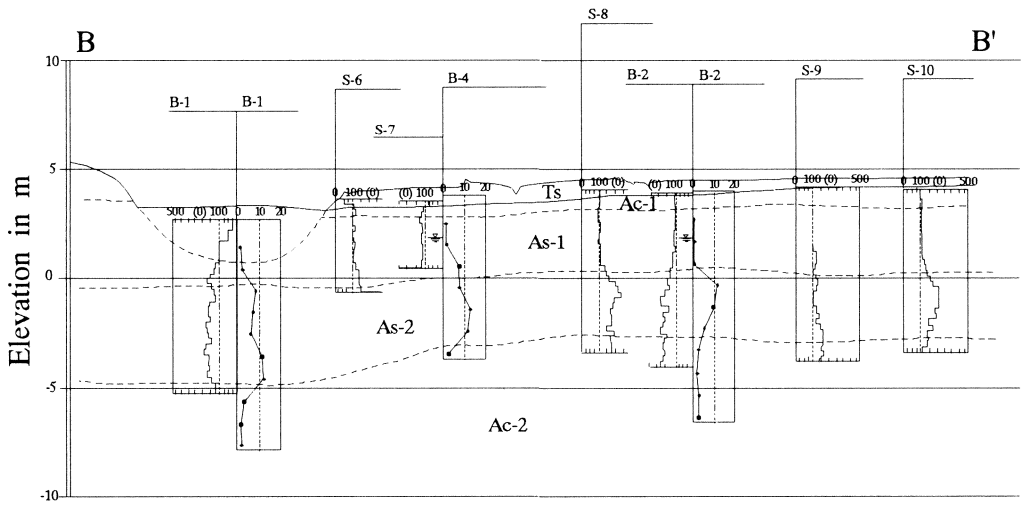

(b) B - B'

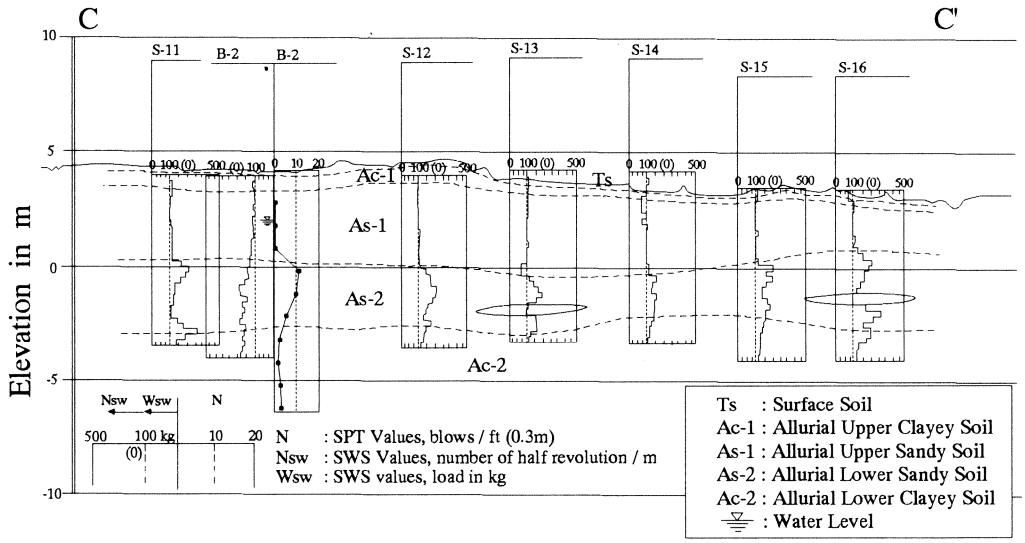

(c) C - C'

Figure 13 Soil Profiles in Aichi Area (Area D) at Cross-sections in Fig.10

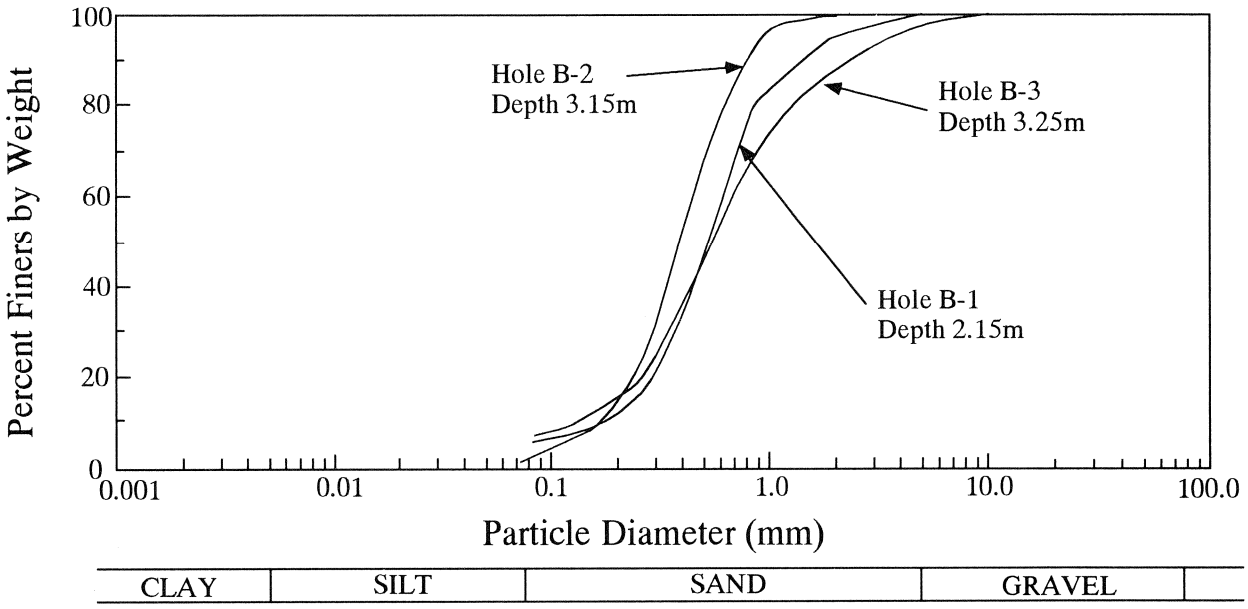

(a) A_{S-1}

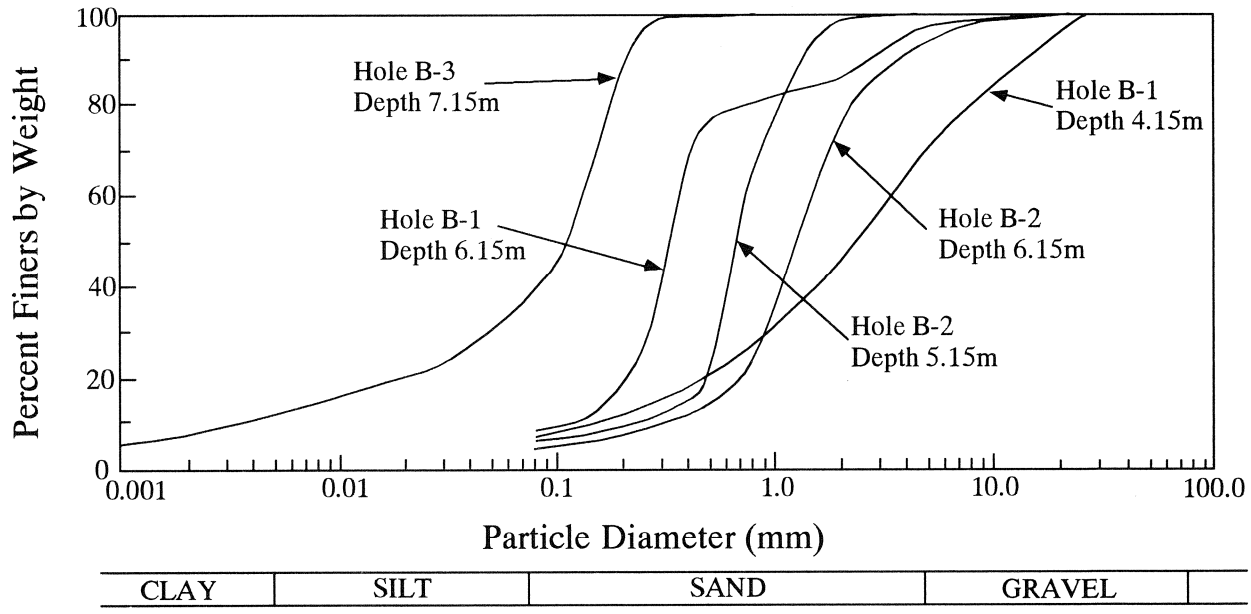

(b) A_{S-2}

Figure 14 Grain Size Distribution Curves from Sand Layers at Aichi Area
(Boring Hole B-1, B-2 and B-3)

CONCLUSION

Identification of ground deformation by means of aerial photos and measurement of ground displacements were undertaken for the basin area of the Shiribeshi-toshibetsu River where liquefaction and accompanying lateral spreading occurred during the 1993 Hokkaido-nansei-oki Earthquake. The result showed that severe liquefaction occurred inside the meandering of the old river beds, still present today as crescent lakes or waterways, while displacements in the horizontal direction was at most 2 to 3 meters toward the crescent lakes or waterways of the old river bed.

Soil investigations were conducted by boring and sounding in the areas where ground deformation is noteworthy. It is presumed from the result that the very loose sandy soil layer existing one meters below the ground surface with thickness of 2 to 4 meters liquefied completely. The lower sandy soil layer distributed under this very loose layer 3 to 5 meters thick contains fine grains and gravel with average N value of 7, and it is not known at the present whether it liquefied or not.

This present article was compiled based on the results obtained from the early stages of the research project of the river basin area of the Shiribeshi-toshibetsu River and the description contained mainly the facts so far discovered. Currently, continued efforts of ground investigation, strength tests of sandy soil layers and the investigation of damages to the farm lands, houses, water pipes and electric power facilities are in progress, and we intend to specify the liquefied layers and study the relationships between the thickness of liquefied layer, permanent ground displacements both horizontal and vertical, as well as the relationship between the ground deformation and the damages to buried pipes and structures.

ACKNOWLEDGMENTS

The author is grateful to Messrs. Yoshida and Shinagawa of Hokkaido Development Agency for providing us aerial photographs, maps and soil data, and to Hokkaido Electric Power Company for providing us photographs of electric facilities. Thanks are due to Messrs. Shibuya and Goto of Waseda University for preparing this manuscript.

REFERENCES

1) Michio Hirano and Yasuyuki Shimizu : Damage to River Embankments, Reconnaissance Report of the Damage Caused by the 1993 Hokkaido-nansei-oki Earthquake (in Japanese), Earthquake Engineering Committee, Japan Society of Civil Engineers, Sept. 1993, 21 - 24.

2) Yutaka Nakamura, Kenji Tomita, Muneyuki Tamogami, Kazutoshi Hidaka, Jun Saita and Shinji Sato : Strong Accelerations and Damage of the 1993 Hokkaido Nansei-Oki Earthquake (QuickReport), JR Earthquake Information No.19b, Railway Technical Research Institute, July 1993.

3) Japan Road Association : Specification for Highway Bridges Part V Earthquake Resistant Design (in Japanese), Feb. 1990.

4) Yutaka Nakamura, Jun Saita and Muneyuki Tamogami : Results of Strong Motion Observation on Kushiro-Oki Earthquake and Hokkaido Nansei-Oki Earthquake by Alarm Seismometers, RTRI Report, Railway Technical Research Institute, Vol. 8, No. 5, May 1994, 1 - 6.

5) Masanori Hamada, Susumu Yasuda, Ryoji Isoyama and Katsutoshi Emoto : Study on Liquefaction Induced Permanent Ground Displacements, Association for the development of Earthquake Prediction, Nov. 1986.

LIQUEFACTION-INDUCED GROUND SURFACE DISRUPTION

T. Leslie Youd
Professor of Civil Engineering
Brigham Young University
Provo, Utah 84602

and

Christopher T. Garris
Senior Staff Engineer
Woodward-Clyde Consultants
Salt Lake City, Utah 84047

ABSTRACT

Although liquefaction is a major cause of earthquake damage, little harm occurs unless liquefaction generates some form of ground surface disruption or ground failure. Thus, ability to accurately predict potential for ground surface disruption is a major concern for geotechnologists charged with safe siting of constructed works. Ishihara presented preliminary empirical criteria for assessing the potential for ground surface disruption at liquefaction sites. Those criteria are based on relationships between the thickness of liquefiable sediment beneath a site and the corresponding thickness of overlying non-liquefiable soil. The purpose of this study is to further evaluate and verify these criteria by testing them against thicknesses calculated from a wide range of earthquake and site conditions. The newly developed data lead to the following conclusions: (1) For sites not susceptible to ground oscillation or lateral spread, the thickness bounds proposed by Ishihara appear to be valid. (2) For sites susceptible to ground oscillation or lateral spread, the bounds suggested by Ishihara are not sufficient for predicting ground surface disruption.

INTRODUCTION

Although liquefaction is a major cause of earthquake damage, little harm occurs unless the liquefied condition leads to some form of ground surface disturbance or ground failure. Thus, ability to accurately predict potential for ground surface disruption is a major concern for geotechnologists charged with safe siting of constructed works.

Ishihara (1985) presented preliminary empirical criteria for assessing the potential for ground surface disruption at liquefaction sites . Those criteria are based on relationships between thicknesses of liquefiable layers beneath a site, and corresponding thicknesses of the overlying non-liquefiable soil (Figures 1 and 2). Ishihara developed these relationships using analyses of field data from sites with or without surface liquefaction effects. He evaluated field reconnaissance and borehole data from three large earthquakes--1964 Niigata, Japan (M=7.5), 1983 Nihonkai Chubu, Japan (M=7.7), and 1976 Tangshan, China (M=7.8). Using borehole logs from sites with or without surface effects of liquefaction, Ishihara calculated thicknesses of liquefiable layers and overlying non-liquefiable layers utilizing criteria published in the Japanese bridge code (Japan Highway Association, 1980). Ishihara plotted those data as shown in Figure 1, and from those data sketched the bounds reproduced in Figure 2. These thickness relationships have been used by many engineers to assess the potential for liquefaction-induced damage to constructed works.

The purpose of this study is to further evaluate and verify Ishihara's criteria by testing the proposed bounds against thicknesses of layers calculated from borehole data taken from field investigations following several additional earthquakes. These investigations cover a wider range of earthquake magnitudes and site conditions than the those considered by Ishihara.

LAYER THICKNESSES FROM SITES OF PAST LIQUEFACTION

To test the bounds published by Ishihara (1985), we calculated layer thicknesses from data on 308 borehole logs taken from sites with or without surface effects of liquefaction shaken by 15 different earthquake ranging in magnitude from 5.3 to 8.0. The sites and the earthquakes that shook them are listed in Table 1. Data from these sites were compiled by Bartlett and Youd (1992) and by Loertscher (1994). Some of the data had been previously collected by Seed and others (1983), Liao (1986), and Ambraseys (1988). Because the "simplified procedure" developed by Seed and his colleagues (Seed and others, 1985) is more widely used in the United States than other procedures to evaluate liquefaction hazard, we utilized the simplified procedure to calculate layer thicknesses. For most sites, the simplified procedure and the procedure given in the Japanese bridge code yield comparable thicknesses.

For the evaluation, we divided surface effects or lack of effects into four categories: (1) no observed surface effects; (2) typical liquefaction effects, including sand boils and small ground fissures, but without noticeable lateral ground displacement; (3) typical liquefaction effects plus effects generated by ground oscillation, such as buckled pavements, curbs, broken pipelines, etc,

but without a consistent pattern of permanent lateral displacements; and (4) surface effects generated by laterals spreads, including a consistent pattern of permanent ground displacements accompanied by ground fissures and usually by sand boils.

Layer thickness combinations from our analyses are plotted on Figures 3 to 10. Figure 3 shows thicknesses for earthquakes with magnitudes ranging from 5.3 to 6.6 and estimated peak accelerations, a_{max}, ranging from 0.13 g to 0.22 g. Although there were only two sites with typical liquefaction effects (sand boils and small fissures) in this data set, the plotted thicknesses agree well with Ishihara's bound for 0.2 g peak acceleration. Most of the data on this plot are from the Marina District in San Francisco which was shaken by the 1957 Daly City (M = 5.3) without generating observed surface effects of liquefaction. This same area was severely disturbed by liquefaction effects during the much larger 1989 Loma Prieta event (M = 6.9).

Figure 4 shows data from several earthquakes in the magnitude 5.9 to 7.0 range with estimated a_{max} ranging from 0.26 g to 0.35 g. The data from sites with surface disruption are correctly predicted by Ishihara's bound with the exception of one badly misclassified datum noted as Vail site, and three points plotted noted as Marina District site where liquefaction-induced ground oscillation occurred during the 1989 Loma Prieta earthquake. The borehole at the Vail site penetrated 4.9 m of non-liquefiable sediment before penetrating only 0.9 m of liquefiable silty sand. Although several sand boils erupted within about 30 m of the drill hole during the 1981 Westmorland, California earthquake, the drill site was near the eastern margin of the disturbed area. Perhaps the liquefiable sediment at the borehole locality was anonymously thin, or perhaps the conduits for the sand boils drifted laterally from nearby thicker liquefiable deposits. In any event, information from field measurements and observations may be expected to contain a small percentage of anomalous or spurious data because of field inhomogeneities. The data from the Marina District indicate that Ishihara's bounds may not be valid for ground oscillation sites.

Figure 5 shows thickness data for earthquakes with magnitudes between 5.9 and 7.0, but with estimated a_{max} between 0.37 and 0.55. Data on this plot come primarily from sites of lateral spreads generated by the 1971 San Fernando and 1979 Imperial Valley earthquakes (M = 6.4 and 6.6, respectively). Many of the data plotted on this figure are poorly predicted by Ishihara's bounds. Most of the points plotting to the right of the bound on this figure are from the Jensen water filtration plant site in Sylmar, California that was badly damaged by a lateral spread during the 1971 San Fernando earthquake. The Jensen facility was constructed on non-liquefiable compacted fill, as thick as 15 m, overlying a 1- to 5-m thick layer of liquefiable alluvial silt and sand. Lateral displacements at the filtration plant ranged from 0.1 m to more than a meter, accompanied by ground fissures and sporadic sand boil eruptions (O'Rourke and others, 1992; Youd 1973). These data indicate that lateral spread can generate disruption to the ground surface for liquefiable layer thicknesses well below the bounds suggested by Ishihara.

Figure 6 shows thickness data for earthquakes with magnitudes between 5.9 and 7.0, but with estimated a_{max} between 0.56 g and 0.78 g. Only one datum on this plot, noted as J.P Castro site, lies well below Ishihara's bound. That datum is from a site of ground oscillation where the thickness of the liquefiable layer was about 0.6 m and the thickness of the surface layer was 6.1 m. Surface effects of liquefaction at the site included sand boils, ground fissures and buckled curbs in close proximity to open fissures (Youd and Keefer, in press). The latter features are

clear indications of ground oscillations, which characteristically buckle rigid linear bodies, such as curbs, due to compressional impacts, while pulling apart adjacent ground and overlying structures during extensional phases of oscillation. The location of this single point below Ishihara's curve on Figure 6 along with the three points from the Marina District plotted on Figure 5 indicate that ground oscillation, as well as lateral spread, can generate disruptions to the ground surface in areas predicted to be free of surface disruption by Ishihara's bounds.

Figures 7 and 8, from the 1964 Niigata and 1988 Nihonkai-Chubu earthquakes, respectively, contain several points that lie beyond Ishihara's bounds. All of these apparently misclassified data are from areas affected by lateral spreads. These data further support the postulate that lateral spreads can produce surface disruptions that are not correctly predicted by Ishihara's bounds.

INTERPRETATIONS FROM RESULTS

Although we compiled a rather large data set, there are some biases in these data. For example, post-earthquake drilling investigations in Noshiro, Japan, were conducted primarily at sites where significant lateral displacement had occurred. Thus, for that locality, few sites were drilled where surface effects were not observed or where liquefaction effects were observed but lateral displacement did not occur. For the smaller magnitude earthquakes ($M<6$), nearly all of the borehole data are from sites where liquefaction was predicted, but surface effects were not evident. Many of these sites are in the Marina District of San Francisco where surface effects of liquefaction occurred during the 1989 Loma Prieta earthquake ($M=6.9$), but did not develop during the smaller 1957 Daly City earthquake ($M=5.3$). Although minor surface effects, primarily small fissures and sand boils, have been observed in the epicentral region of many small earthquakes ($5<M<6$), few of those sites have been drilled and tested. Thus, there are few data from small earthquakes for sites where liquefaction effects were observed. Even with these biases and weaknesses, the data are adequate to support the following general findings:

(1) The data plotted on Figures 3 through 8 indicate that the occurrence or non-occurrence of surface liquefaction effects for sites not affected by lateral spread or ground oscillation generally are correctly predicted by the bounds proposed by Ishihara. Only a few such data points are misclassified according to these bounds. A few misclassified data also occur on the original plots prepared by Ishihara. For example, there are a few misclassified points in Ishihara's data as reproduced in Figure 2. Such infrequent misclassifications are to be expected in any data set based on field observations and tests.

(2) The data plotted on Figures 5 through 8 show that ground surface disturbance at sites with liquefaction-induced ground oscillation or lateral spread are poorly predicted by the bounds propose by Ishihara. From this finding, we infer that localities underlain by sufficiently broad expanses of liquefiable sediment to allow decoupling of the surficial unliquefied layers, from both the underlying and the surrounding solid ground, will lead to a condition of oscillating ground waves over the liquefied layer for flat sites or lateral spread, commonly accompanied by oscillations, for sloping sites or near free faces. These ground failure modes appear to be capable

of disrupting the ground surface even when relatively thin liquefied layers are involved. Conversely, if the lateral extent of a liquefiable deposit is insufficient to allow complete decoupling, as commonly occurs with lenses of liquefiable material such as buried remnants of small fluvial channels, surface effects of liquefaction do not commonly develop for thickness combinations beyond the bounds suggested by Ishihara.

The criteria of Bartlett and Youd (1992) for estimating lateral displacement could be applied to determine the potential for ground surface disruption at liquefiable sites subject to lateral spread. For example, predicted lateral displacements of less than about 0.1 m on sloping sites or near free faces might not be expected to generate significant surface disruption. More study is needed to better define layer thicknesses and extents under which sufficient ground oscillation could be generated to disrupt the surface of flat terrains.

(3) We cursorily examined the data plotted in Figures 3 through 8 to check for magnitude dependence in thickness relationships controlling the development of surface liquefaction effects. The data set is not strong enough, particularly in the smaller magnitude range, however, to clearly discern any influence of magnitude.

CONCLUSIONS

Analyses of the data plotted on Figures 3 through 8 lead to the following conclusions:

1. The thickness bounds proposed by Ishihara (1985) appear to be valid for predicting ground surface disruption at sites that are not susceptible to either ground oscillation or lateral spread.

2. For sites susceptible to ground oscillation or lateral spread, the bounds suggested by Ishihara (Figure 2) are not generally valid for predicting liquefaction-induced ground surface disruption.

REFERENCES

Ambraseys, N.N., 1988, "Engineering Seismology," Earthquake Engineering and Structural Dynamics, Vol. 17, No. 1, p. 1-105.

Bartlett, S.F., and Youd, T.L., 1992, "Empirical prediction of lateral spread displacement," Proceedings, 4th US-Japan Workshop on Earthquake Resistant Design Lifeline Facilities and Countermeasures for Soil Liquefaction, Honolulu, Hawaii, May 1992, NCEER-92-0019, v. 2, p. 351-366.

K. Ishihara, 1985, "Stability of Natural Deposits During Earthquakes," Proceedings, 11th

International Conference on Soil Mechanics and Foundation Engineering, San Francisco. Vol. 1, p. 321-376.

Japan Road Association, 1980, Specifications for Highway Bridges, Part V Earthquake Resistant Design.

Liao, S.S.C., 1986, "Statistical Modeling of Earthquake-Induced Liquefaction," Ph.D. Dissertation, Department of Civil Engineering, Massachusetts Institute of Technology, 470 p.

Loertscher, T.W., 1993, "Magnitude Scaling Factors for Analysis of Liquefaction Hazard," Ph.D. Dissertation, Department of Civil and Environmental Engineering, Brigham Young University, 136 p.

NRC, 1985, Liquefaction of Soils During Earthquakes, National Research Council, National Academy Press, Washington, D.C., 240 p.

O'Rourke, T.D., Roth, B.L., and Hamada, M., 1992, "Large ground deformations and their effects on lifeline facilities: 1971 Sand Fernando earthquake," Case Studies of Liquefaction and Lifeline Performance During Past Earthquakes, Technical Report NCEER-92-0002, p. 3-1 to 3-85.

Seed, H.B., Idriss, I.M., and Aarango, I., 1983, "Evaluation of Liquefaction Potential Using Field Performance Data," Journal of the Geotechnical Engineering Division, ASCE, Vol 102, No. GT4, p. 246-270.

Seed, H.B., Tokimatsu, K., Harder, L.F., and Chung, R.F., 1985, "Influence of SPT Procedures in Soil Liquefaction Resistance Evaluations," Journal of the Geotechnical Engineering Division, ASCE, Vol 111, No. 12, p. 1425-1445.

Youd, T.L., 1973, "Ground movements in Van Norman Lake Vicinity during San Fernando, California, Earthquake of February 9, 1971," San Fernando Earthquake of February 9, 1971, U.S. Department of Commerce, National Oceanographic and Atmospheric Administration, Vol. 3, p. 197-203.

Youd, T.L., and Keefer, D.K., in press, "Liquefaction during the 1977 San Juan Province, Argentina earthquake," Engineering Geology, Elsevier.

Table 1. Earthquakes, sites and Borings Considered in This Study

Earthquake	Magnitude, M_w	Site Name	Number of Borings
1906 SAN FRANCISCO	8.0	SOUTH OF MARKET ZONE	1
		MISSION CREEK ZONE	1
1957 DALY CITY	5.3	MARINA DISTRICT	23
1964 NIIGATA	7.5	MANY LOCALITIES	150
1971 SAN FERNANDO	6.4	JENSEN FILTRATION PLANT	17
		JUVENILE HALL	5
1977 ARGENTINA	7.2	ESCUELA NORMAL	6
		J.P. CASTRO	2
1979 IMPERIAL VALLEY	6.6	HEBER ROAD	3
		MCKIM RANCH	1
		RADIO TOWER	1
1981 WESTMORLAND	6.0	KORNBLOOM	1
		VAIL	1
		WILDLIFE	3
1983 BORAH PEAK	6.9	PENCE RANCH	1
		WHISKEY SPRINGS	3
1983 NIHONKAI-CHUBU	7.7	MANY LOCALITIES	32
1986(JULY) LOTUNG TAIWAN	6.2	LOTUNG	1
1986(NOV.) LOTUNG TAIWAN	6.2	LOTUNG	1
1987 ELMORE RANCH	6.2	KORNBLOOM	1
		WILDLIFE	1
1987 SUPERSTITION HILLS	6.6	HEBER ROAD	2
		KORNBLOOM	1
		MCKIM RANCH	1
		WILDLIFE	1
1987 WHITTIER NARROWS	5.9	17 BRIDGE SITES	21
1989 LOMA PRIETA	7.1	MARINA DISTRICT	28
TOTALS			
15 EARTHQUAKES		**65 SITES**	**309 BORINGS**

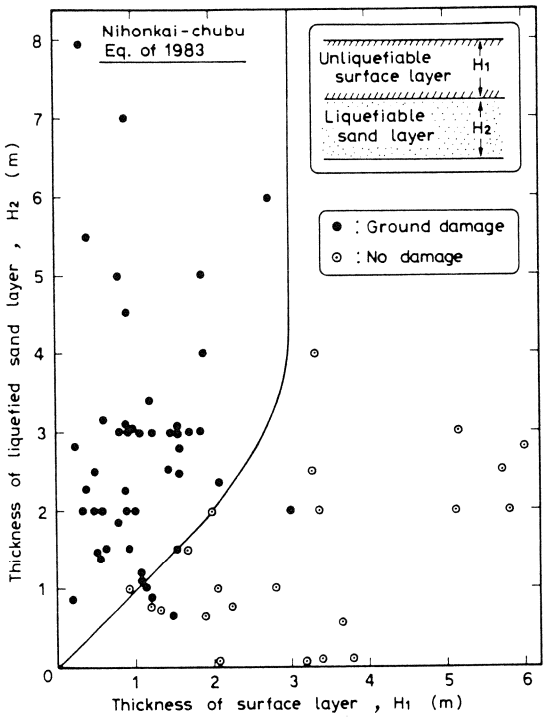

Figure 1. Thicknesses of Liquefied and Overlying Non-liquefied Layers for Discriminating Between Occurrence and Non-occurrence of Surface Effects of Liquefaction (After Ishihara, 1985)

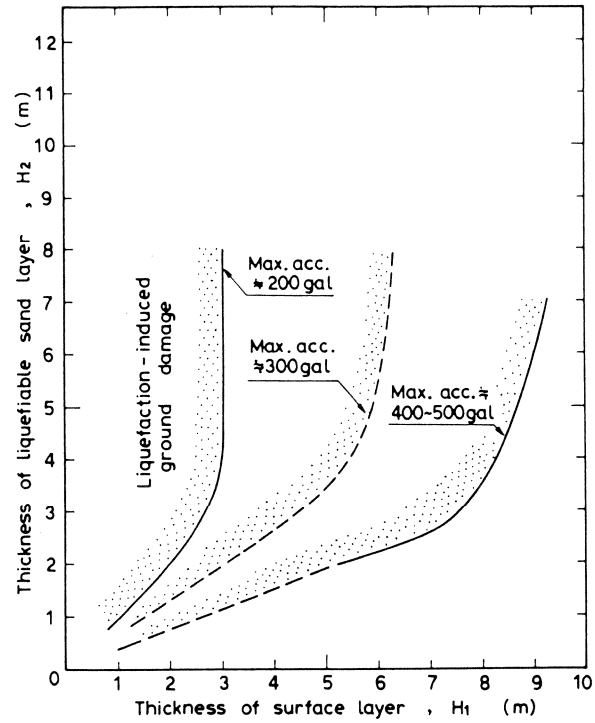

Figure 2. Proposed Boundary Curves for Discriminating Between Occurrence and Non-occurrence of Surface Effects of Liquefaction (After Ishihara, 1985)

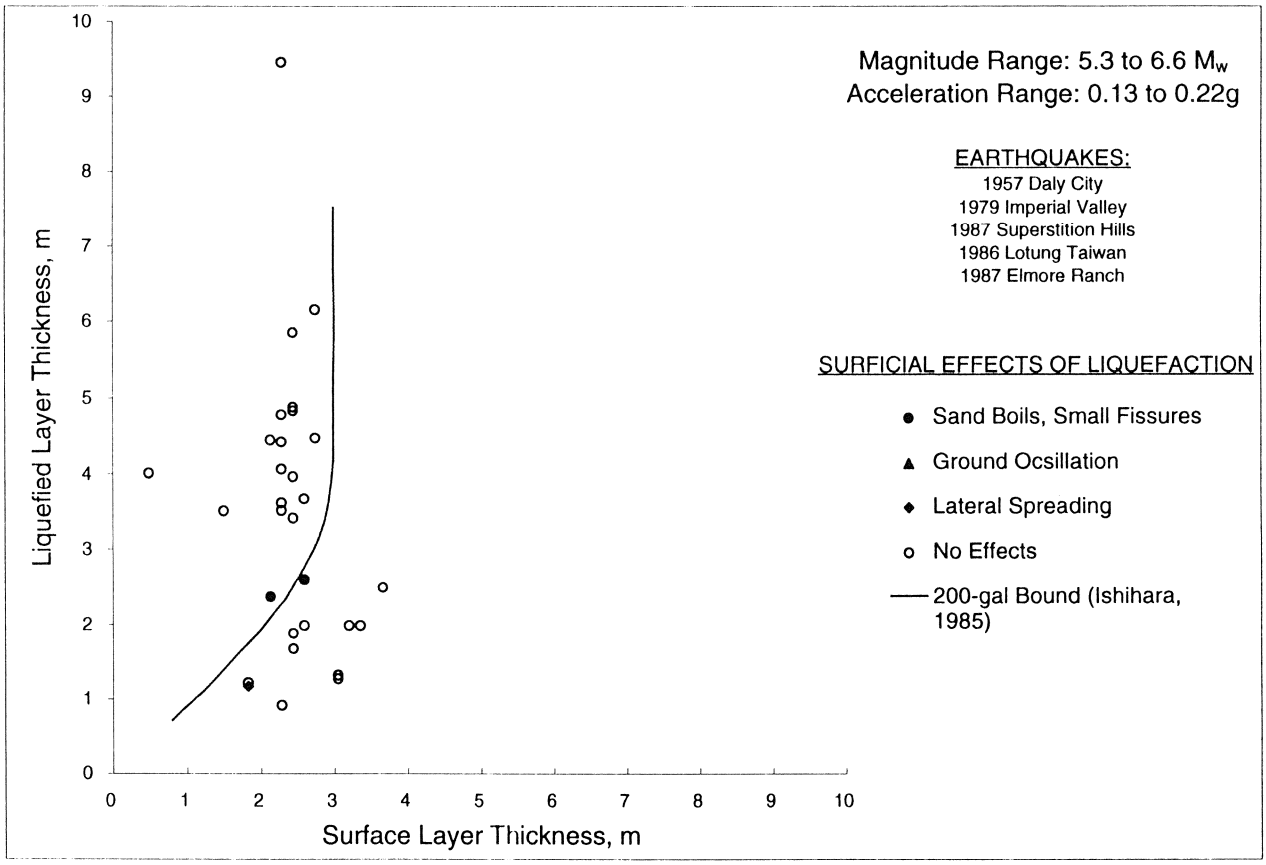

Figure 3. Thicknesses of Liquefied and Overlying Non-liquefied Layers for Various Types of Surface Effects of Liquefaction: Data Compiled in This Study for Magnitude 5.3 to 6.6 Earthquakes.

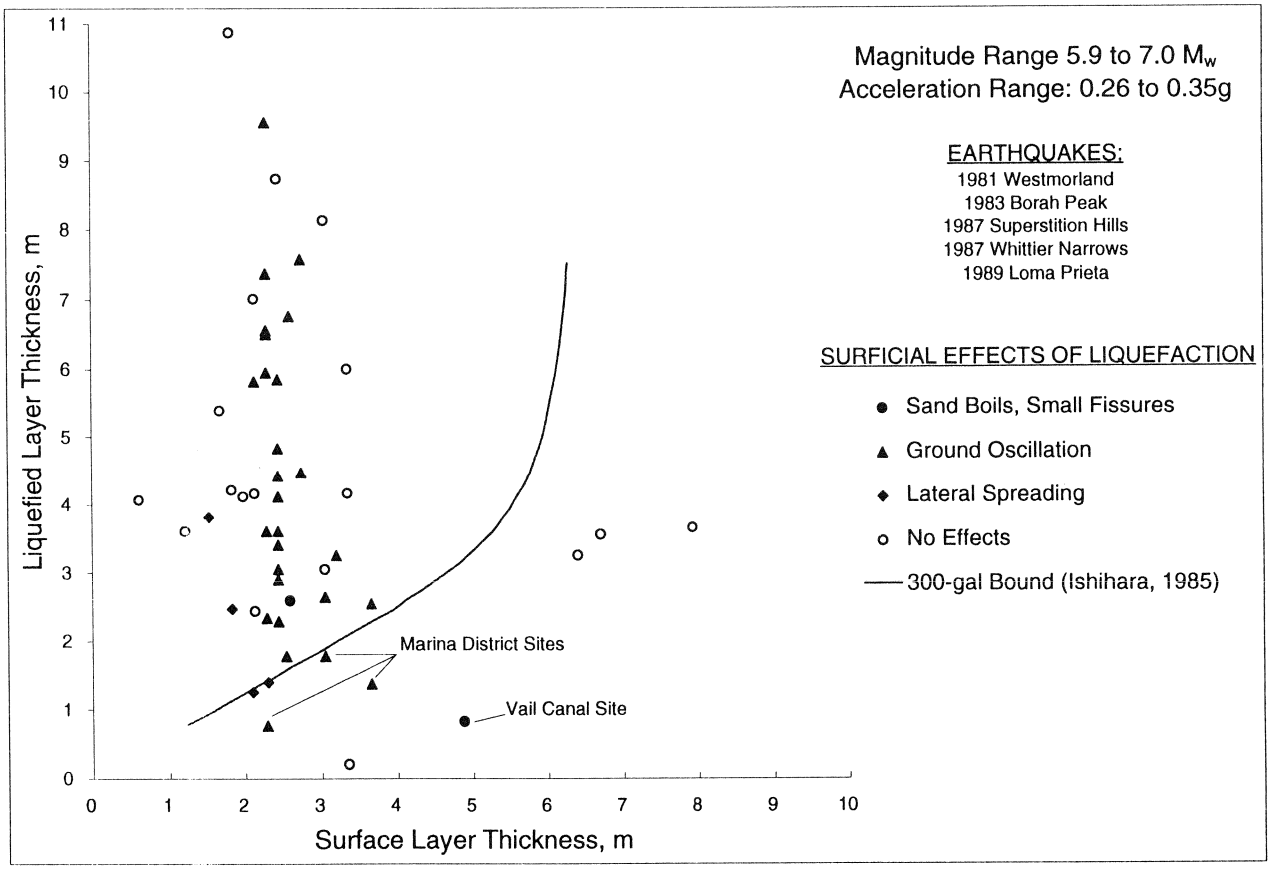

Figure 4. Thicknesses of Liquefied and Overlying Non-liquefied Layers for Various Types of Surface Effects of Liquefaction: Data Compiled in This Study for Magnitude 5.9 to 7.0 Earthquakes.

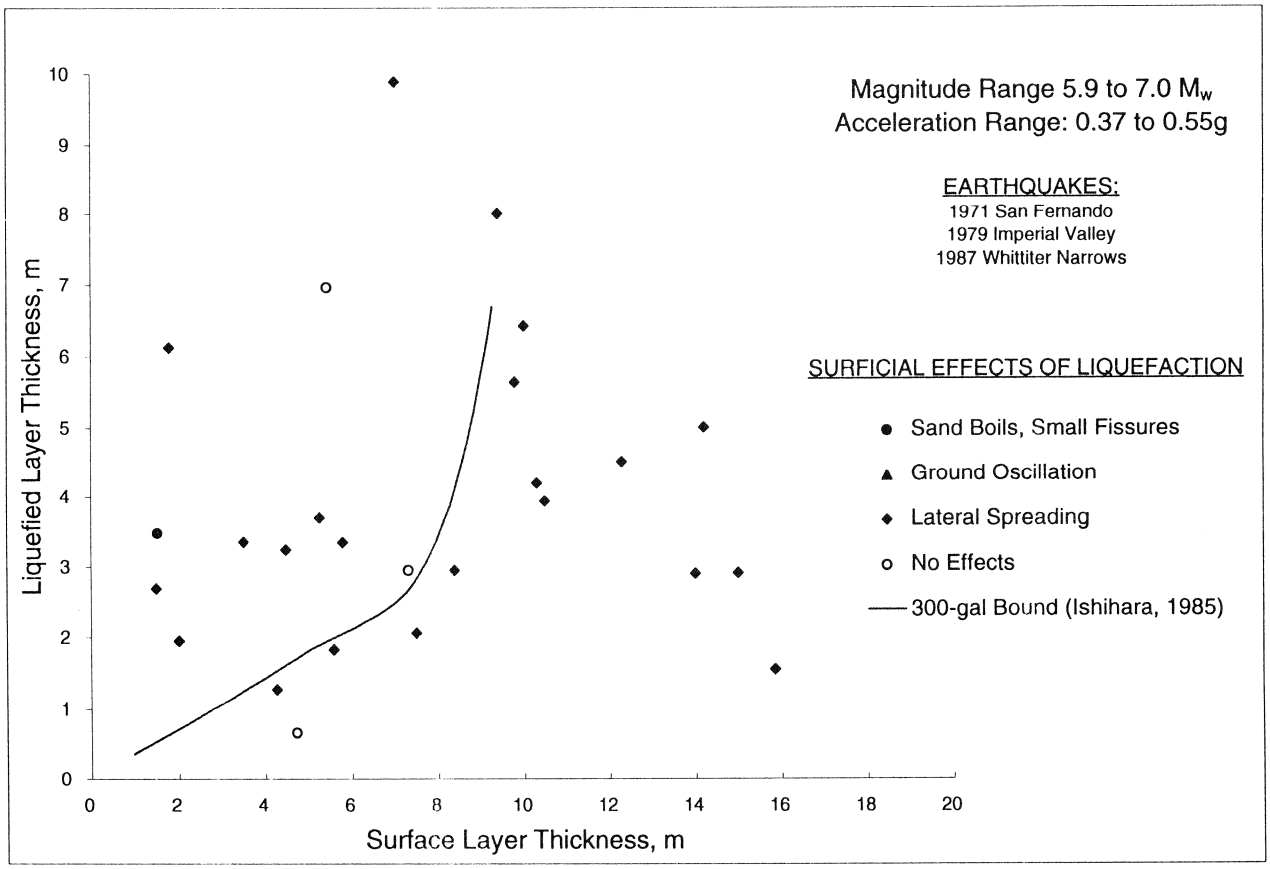

Figure 5. Thicknesses of Liquefied and Overlying Non-liquefied Layers for Various Types of Surface Effects of Liquefaction: Data Compiled in This Study for Magnitude 5.9 to 7.0 Earthquakes.

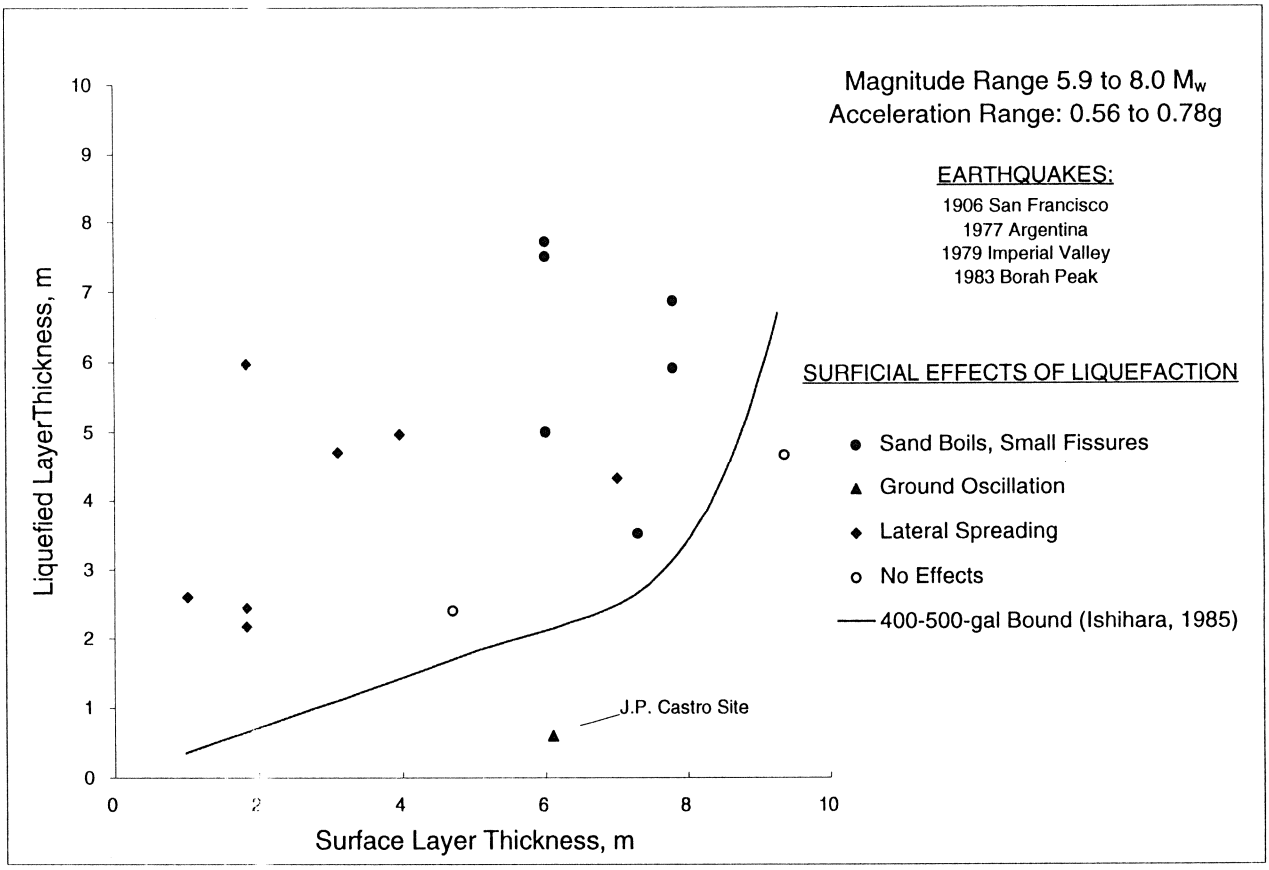

Figure 6. Thicknesses of Liquefied and Overlying Non-liquefied Layers for Various Types of Surface Effects of Liquefaction: Data Compiled in This Study for Magnitude 5.9 to 8.0 Earthquakes.

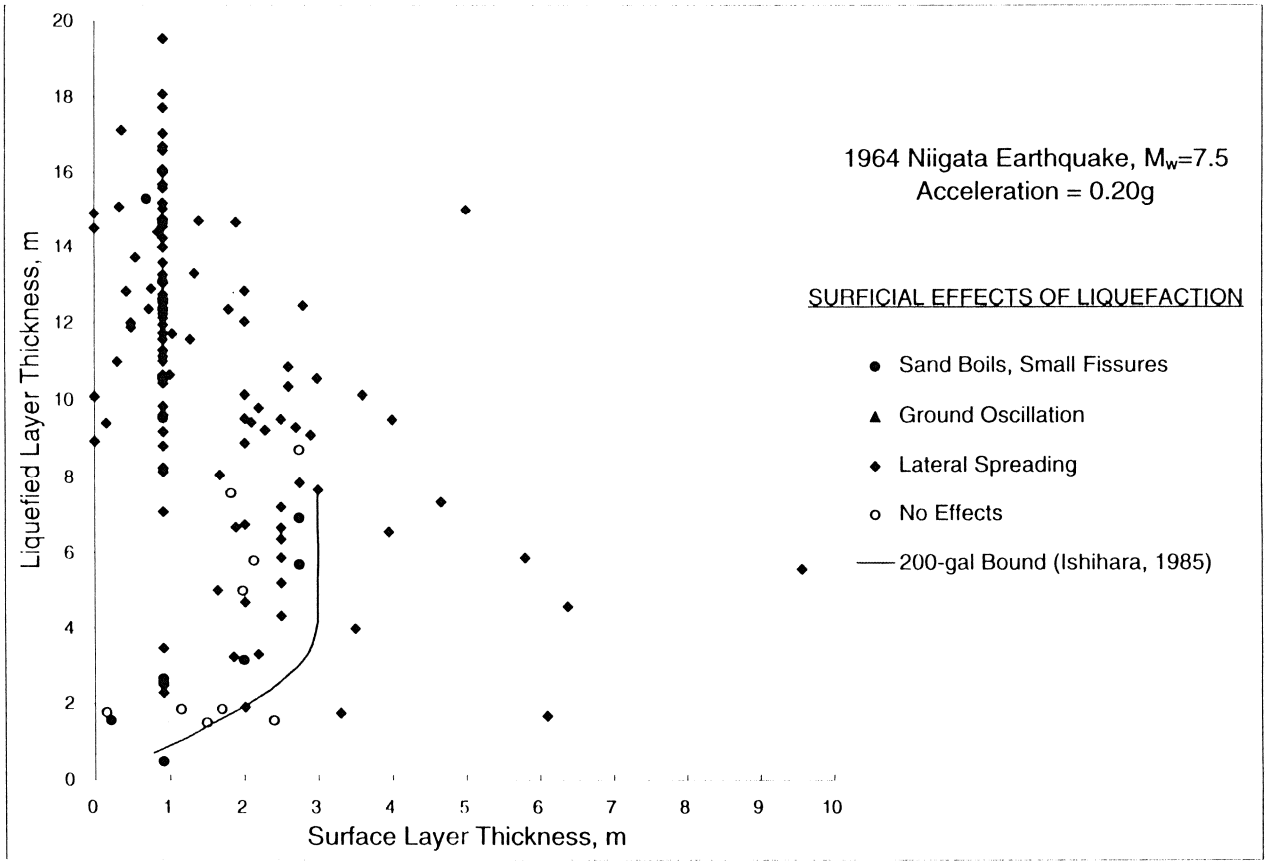

Figure 7. Thicknesses of Liquefied and Overlying Non-liquefied Layers for Various Types of Surface Effects of Liquefaction: Data Compiled in This Study for 1965 Niigata, Japan, Earthquake (M = 7.5)

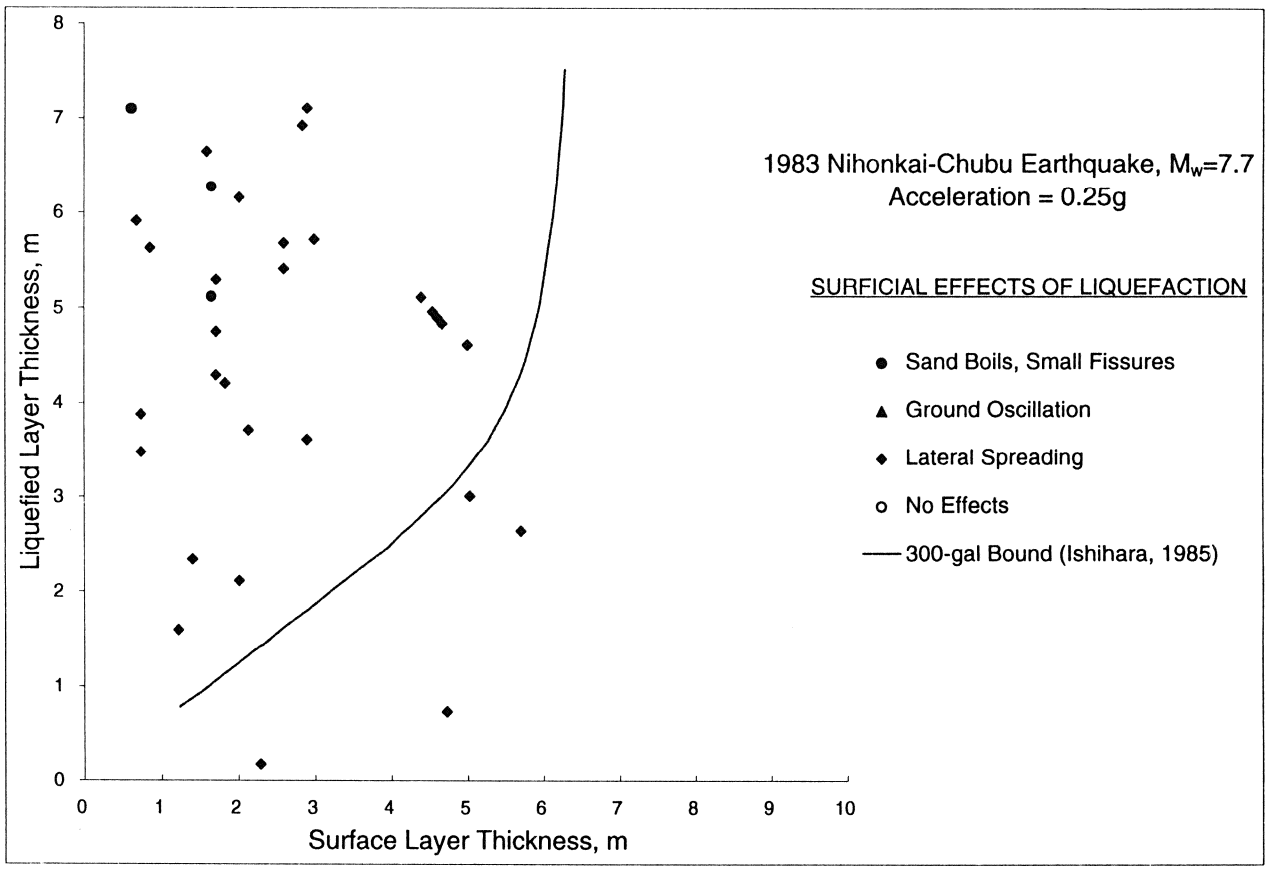

Figure 8. Thicknesses of Liquefied and Overlying Non-liquefied Layers for Various Types of Surface Effects of Liquefaction: Data Compiled in This Study for the 1984 Nihonkai-Chubu Earthquake (M = 7.7)

GROUND DEFORMATIONS AND THEIR EFFECTS ON STRUCTURES IN MIDORIGAOKA DISTRICT, KUSHIRO CITY, DURING THE KUSHIRO-OKI EARTHQUAKE OF JANUARY 15, 1993

by

Kazue Wakamatsu[1] and Nozomu Yoshida[2]

ABSTRACT

Midorigaoka is a residential area situated in Kushiro City, Hokkaido, approximately 900 km northeast of Tokyo. It was developed for housing in 1972–3 by cutting and filling a pleistocene terrace with an maximum elevation of approximately 30 meters above sea level. Following the January 15, 1993, M7.8 Kushiro–oki earthquake, various types of ground failures such as slope failures, ground settlements, ground cracks, sand boils, and lateral movements were evident at many locations in Midorigaoka. Buildings (mostly wooden single family residences) and underground utilities such as water supply, wastewater and natural gas networks were seriously affected by these ground failures. This paper presents the ground failures observed at Midorigaoka during the Kushiro–oki earthquake and examines the relationships within ground deformation patterns, subsurface ground conditions, landform changes, and the performance of wood houses and underground utility lines.

[1] Guest Researcher, Advanced Research Center for Science and Engineering, Waseda University, Tokyo, Japan

[2] Research Head, Engineering Research Institute, Sato Kogyo Co, Ltd, Atsugi, Japan

INTRODUCTION

The Kushiro-oki earthquake struck Hokkaido, a northern island of Japan, at 10:06 PM local time, on January 15, 1993. The magnitude was assessed at 7.8 in the Japan Meteorological Agency (JMA) Magnitude Scale. The epicenter was located 15 km south of Kushiro City and the focal depth was 107 km. The earthquake resulted in 2 deaths and as many as 968 injuries[1]. The damage estimated was 55 billion yen (approximately $550 million) within Hokkaido[1].

Strong motion data were recorded at more than 180 sites through the northern half of Japan. Peak accelerations observed at both free-field sites and the ground floors of structures in the epicentral region are plotted in Fig. 1. A peak horizontal acceleration of nearly 1 g was recorded at Kushiro Meteorological Observatory, 14 km north of the epicenter.

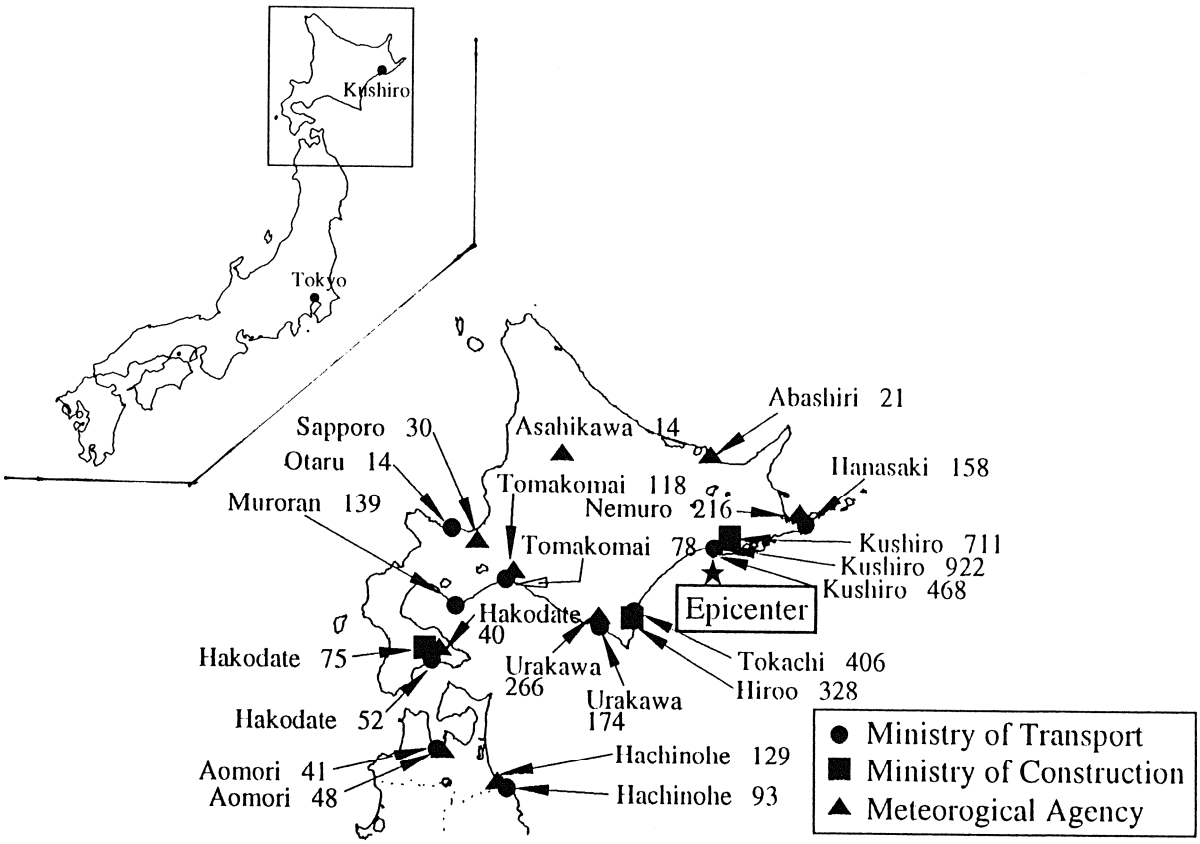

Fig.1 Peak Accelerations in cm/s^2 at Free-field Sites and Ground Floors of Structures during the 1993 Kushiro-oki Earthquake

The earthquake caused ground failures such as land slides, slope failures, and soil liquefaction in the epicentral region. Railways, highways, buildings and underground utilities were affected by these ground failures. The eastern part of Midorigaoka District, a residential area in Kushiro City, was one of the area most seriously affected by the ground failure.

This paper focuses on the damage of the eastern part of Midorigaoka District (simply called Midorigaoka below). At first, a historical review of land reclamation and construction in Midorigaoka is presented. The damage to buried lifeline systems and buildings is evaluated. The lifeline systems include water supply, wastewater and natural gas networks. Geotechnical data were collected and short period microtremor measurements were carried out to determine the subsurface conditions in the area. Photogrammetric analyses were performed to establish the profiles of the landforms before and after the residential development. Furthermore, the effects of changes in landforms, variation in fill thickness and density, subsurface water conditions and intensity of ground motion in concentrating damage in such a local area are evaluated.

GEOLOGY AND HISTORIC DEVELOPMENT OF MIDORIGAOKA

Midorigaoka is located on a pleistocene terrace in the eastern part of Kushiro City, Hokkaido, approximately 900 km northeast of Tokyo. The terrace is comprised of, from upper to lower, volcanic ash known as the Kussharo Pumice Flow Deposit, volcanic sandy soil known as the Otanoshike Formation, and sand, gravel, silt or clay known as the Kushiro Group on a base of Paleogene rock. Photo 1 is an aerial photograph taken in 1947, in which a valley is seen to dissect the terrace around Midorigaoka. The bottom of the valley was underlain by soft and loose soils.

The development of the terrace started from the north-western part of the area around the estuary of Old Kushiro River in the early 1900's and gradually extended toward the north-east. Midorigaoka was developed last, in 1972-73. The area was developed for construction by cutting and levelling the terrace and then filling the valleys with soils from the terrace. Therefore there are two general type of subsurface conditions in Midorigaoka: 1) natural soils associated with the volcanic pumice flow deposit overlying the original or excavated surface of the terrace and 2) fills consisting mainly with the volcanic pumice flow deposit placed on the valleys and hollow parts in the terrace. Typical soil profiles and elastic wave velocities in the terrace and in the valley are shown in Fig.2, respectively. Areas underlain by these different profiles behave differently during the earthquake, as discussed later.

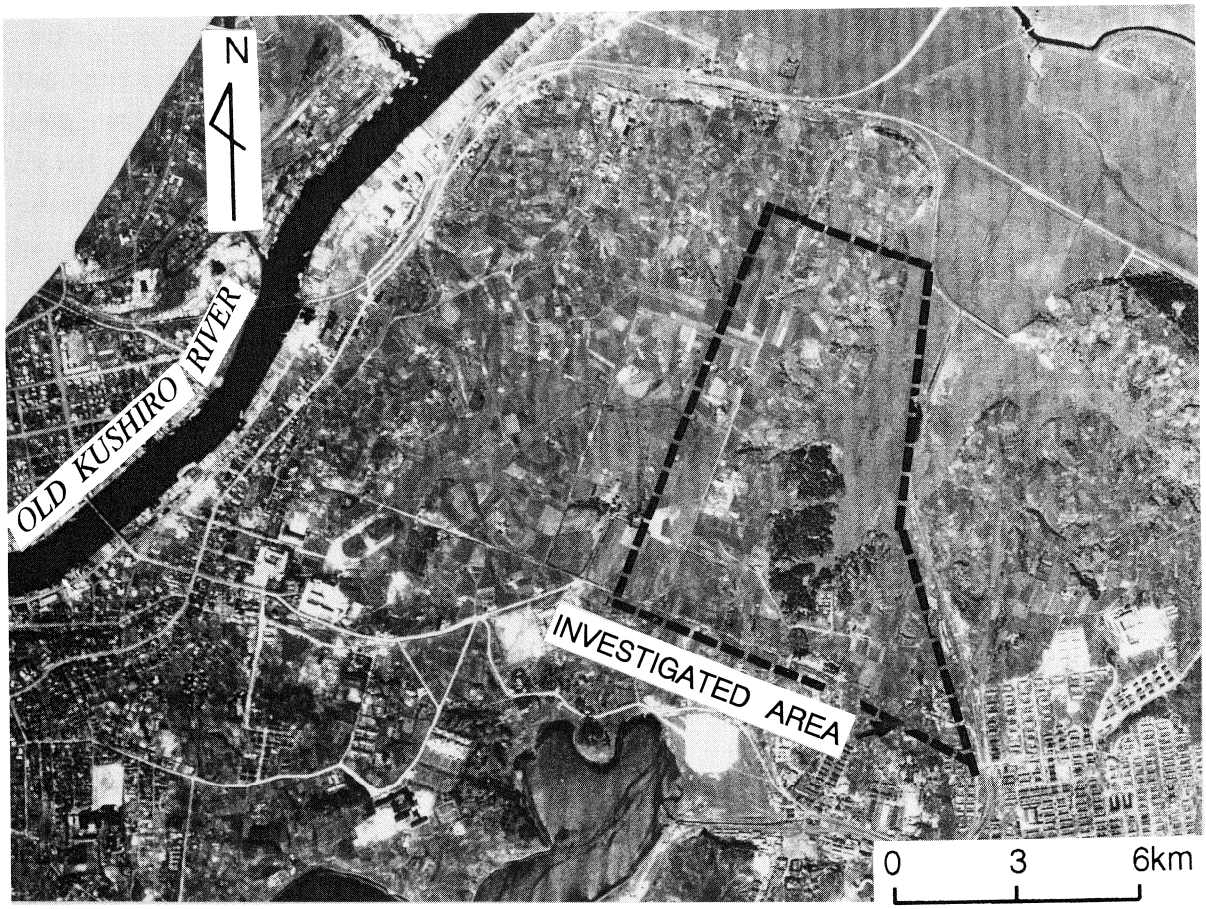

Photo 1 Aerial Photograph of the East of Kushiro City Taken in 1947

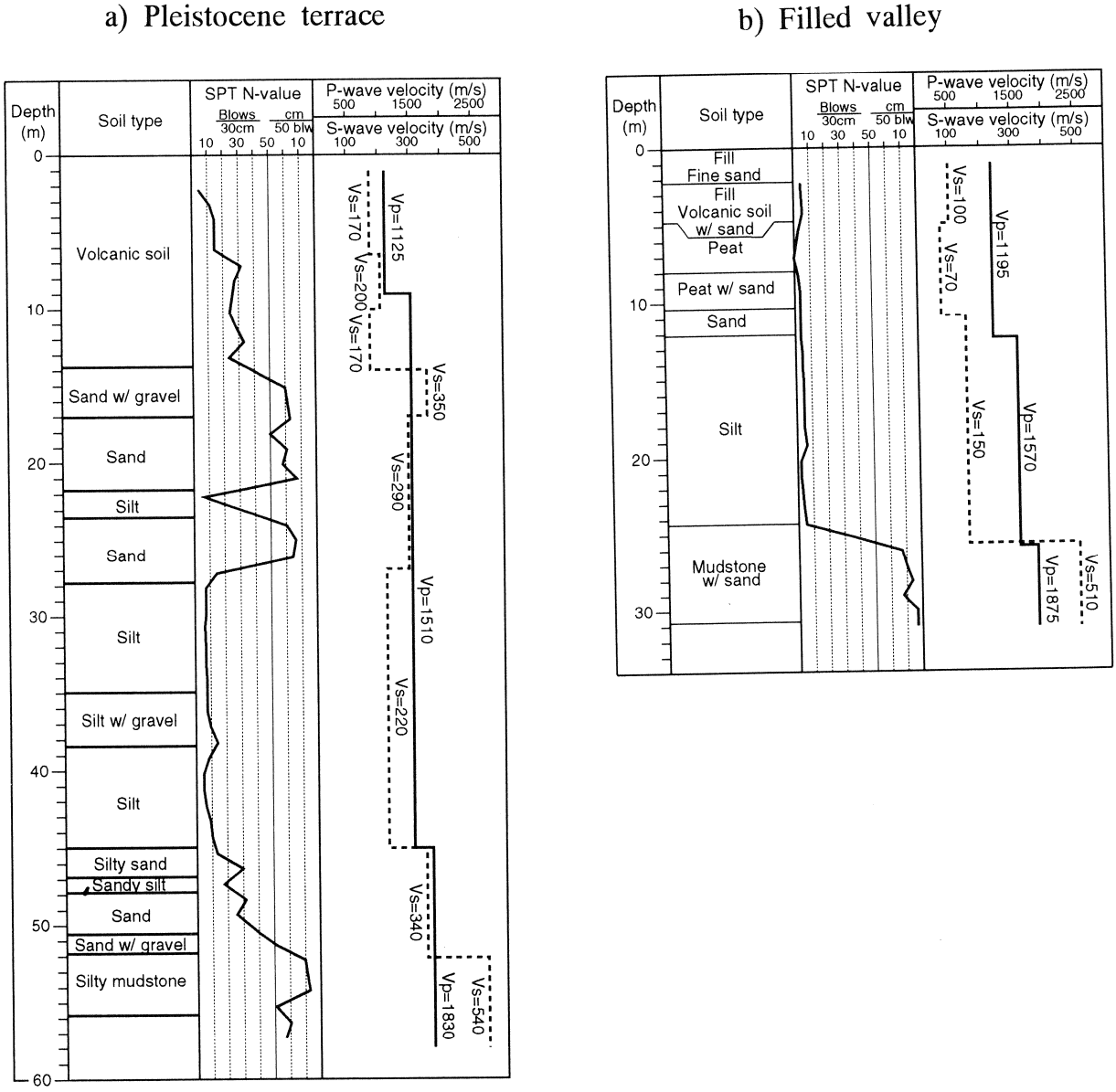

Fig.2 Typical Soil Profiles and Elastic WaveVelocities in Terrace and Valley[2)]

LIQUEFACTION EFFECTS AND OTHER GROUND DEFORMATIONS

Figure 3 shows locations of major ground failures and damage to structures in the eastern part of Kushiro City. The ground failures include slope failures, collapses of retaining walls, ground cracks, ground settlements and sand boils. The locations of damaged structures coincided with these of ground failures, which implies that most of the structural damage was caused by the ground failure. The damage was heavily concentrated in the zone investigated in this paper.

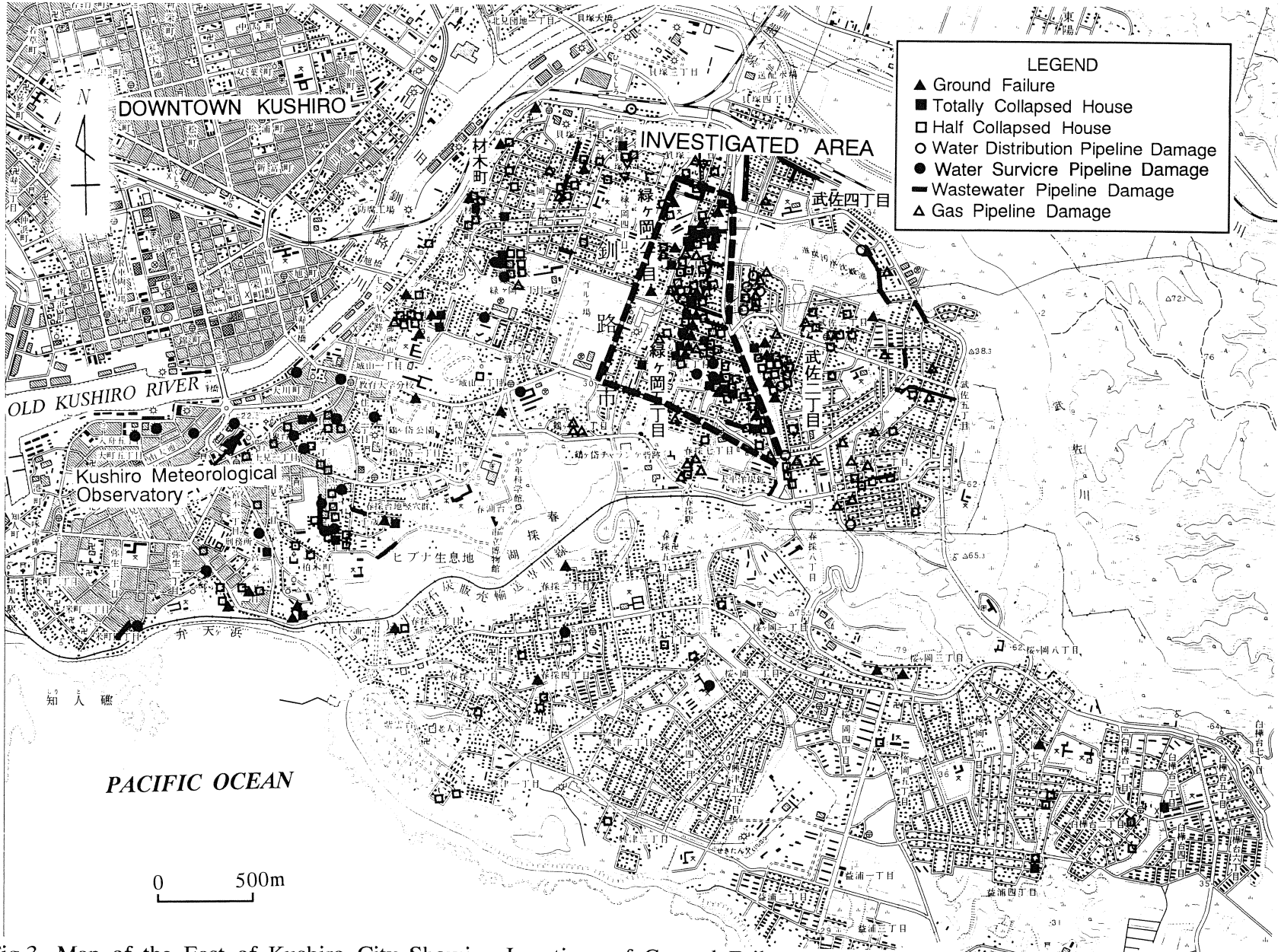

Fig.3 Map of the East of Kushiro City Showing Locations of Ground Failures, Damage to Structures and a Zone Investigated

Strong motions were recorded at the Kushiro Meteorological Observatory which is located about 2.5 km southwest of Midorigaoka and 14 km north of the epicenter (see Fig.3 for location). Figure 4 shows a time record of acceleration. The peak acceleration and velocity are 711 cm/s^2 and 33.5 cm/s, respectively, and the duration of strong shaking is more than 20 seconds. A record with peak acceleration 922 cm/s^2 is also obtained at the ground floor of a building in the same site at a distance of about 20 m from the previous station. This site is located on the pleistocene terrace, which is considered to amplify the earthquake shaking in short period range resulting high peak value.

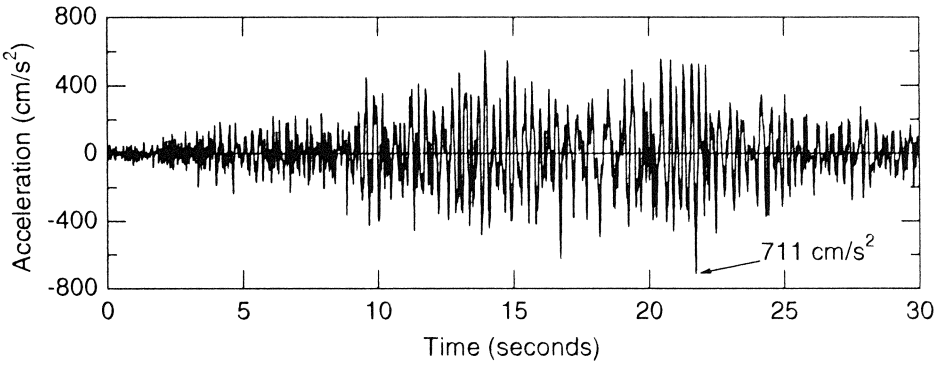

Fig.4 Time Record of Acceleration at Kushiro Meteorological Observatory[3)]

Earthquake records at other stations in Kushiro City did not show such large peak values. The peak acceleration at Kushiro Port was 468 cm/s^2, at the Kushiro River Dike, 320 cm/s^2 and at Otanashike Bridge, 456 cm/s^2. No ground motions were recorded close to Midorigaoka. According to interviews with the residents, seismic intensity in Midorigaoka is estimated to be 5.4 to 5.7 in JMA intensity[3)]

Figure 5 shows distribution of ground failures in Midorigaoka. A slope with a height of 11 m collapsed at site ① in the figure. A wooden house slipped down the slope and two houses were crushed by the collapsed soil as shown in Photo 2. Liquefaction effects such as sand boils and floating up of manholes were observed as well as ground cracks. Manholes floated up 5 to 20 cm at many sites. Sand boils were observed at fewer locations than would be expected because of the frozen layer of ground at the surface estimated to be 50–100 cm thick at the time of the earthquake.

Underground pipelines and foundations of wooden houses settled differentially and were displaced laterally where the ground cracks were abundant. This implies that a large amount of permanent ground deformation occurred in these areas. The magnitudes of the vertical and horizontal ground displacements were estimated to be in the range of approximately 30 to 50 cm on the basis of widths of ground cracks and displacements of pipelines and foundations of the houses.

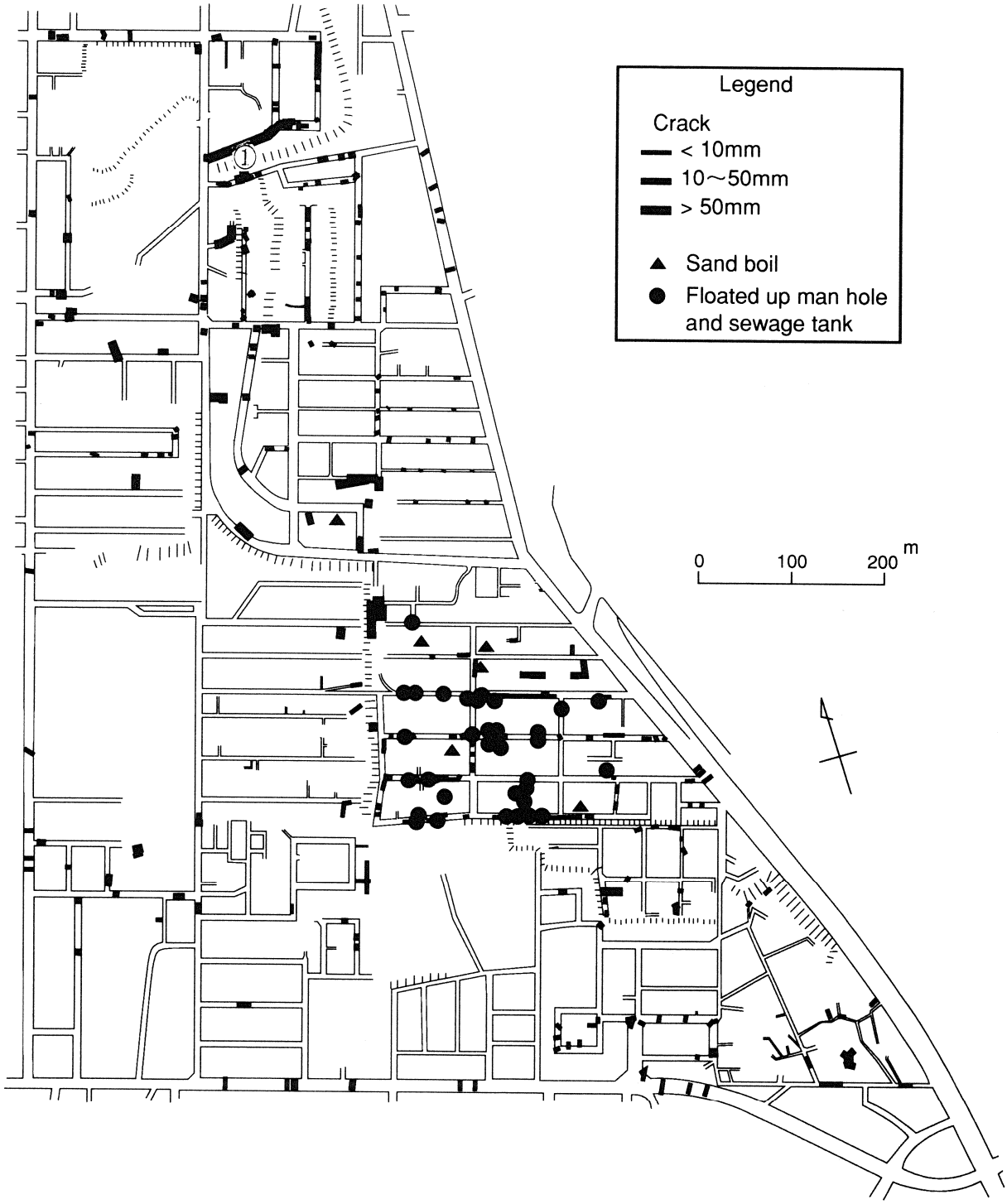

Fig.5 Map of Midorigaoka Showing Locations of Ground Failures and Floated up Manholes[2)]

Figure 6 is a comparison of the grain size distribution curves of sands from sand boil deposits at different locations in Midorigaoka and natural volcanic ash which is generally used as fill material in this area. Both soils have similar grain size characteristics, which implies that volcanic fills were liquefied during the earthquake, and may be natural material.

According to the residents, sand boils and ground cracks were also observed at the time of the 1973 Nemuro-hanto-oki earthquake at the same locations. This indicates reliquefaction at the same sites.

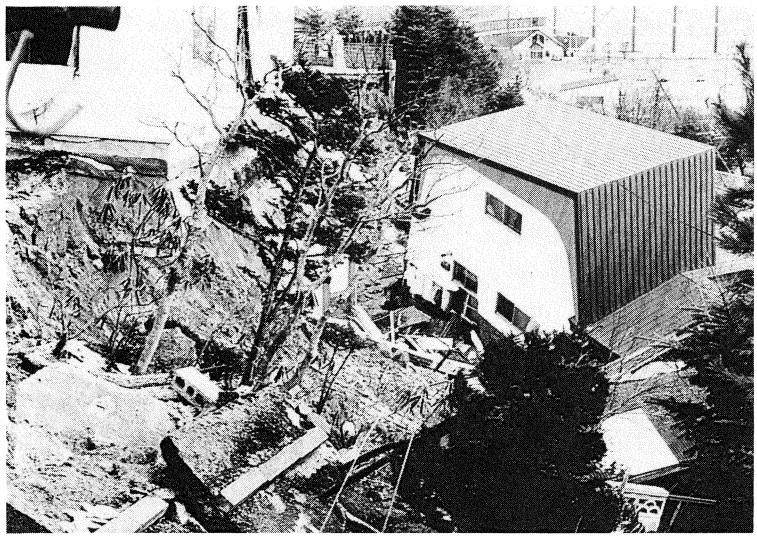

Photo 2 Slipping Down of a Houses due to Slope Failure
(Courtesy of Kiso-jiban Consultants Co.)

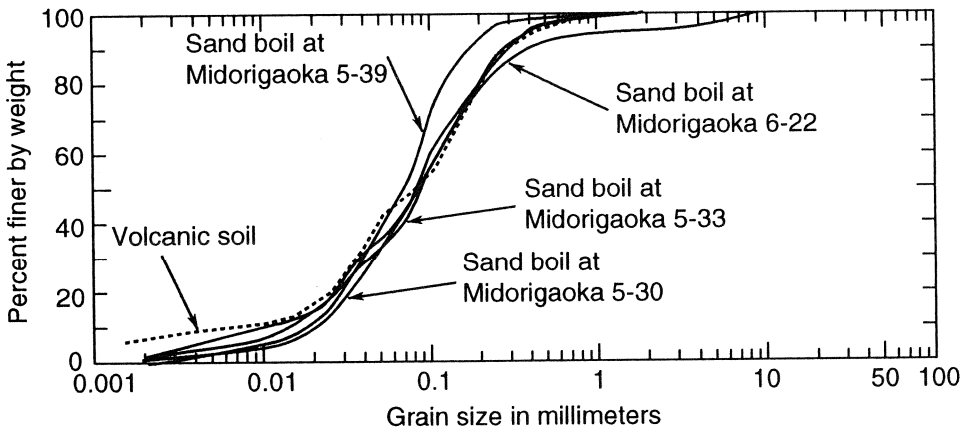

Fig.6 Grain Size Distribution Curves for Volcanic Ash Used as Fill Material[2] and Sands Collected from Sand Boils in Midorigaoka

DAMAGE TO STRUCTURES

Water Supply Lifelines

There are approximately 671,318 m of pipelines in Kushiro City. Main distribution lines are of four types: ductile iron pipe (DIP) with mechanical or push on joints, polyethylene pipe (PP) with coupling joint, gray cast iron pipe (CIP) with socket and spigot joint, and asbestos cement pipe (ACP) with coupling joint. Pipe diameters are 40, 50, 75, 100, 150, 200 and 500 mm. Local service pipes are of three types, PP, CIP and ACP with diameters 13, 20, 25, 50, 75, 100 and 150 mm. All pipelines are buried with a nominal depths of cover greater than 1.6 m.

There was damage at 2 locations in the main water distribution system and at 9 locations in the local service system in Midorigaoka. This is approximately one-third of entire damage in Kushiro City to water supply system. Figure 7 shows the locations, types and diameter of damaged pipes, and damage modes of both main distribution and local pipelines. The pipe and joint damage occurred only in the areas of ground failures shown in Fig.5 in Midorigaoka.

Wastewater Lifelines

There are 947.5 km of wastewater pipelines in Kushiro City ranging in diameter from 200 to 1,000 mm. They consist of vinyl chloride pipes (VCP) and centrifugally compacted reinforced concrete pipes (RCP) with rubber joint. In total 47 sites, 7,744 m of the pipes, were damaged due to the earthquake. Figure 8 shows the locations, types, diameters and lengths of damaged pipes. At the damage locations the pipes buried at a depth of 3.4 m on average and supported by timber piles or macadam. Damage was primarily in the form of floating and settlement of the pipelines due to the displacement of the joints, round cracks of pipes and manholes, pull-out or break of joints, and floating of manholes as shown in Photos 3 and 4. The amount of both floating and settlement of pipelines were ranged from several cm to several ten cm.

Gas Distribution Lifeline

The gas distribution and local service pipelines in Midorigaoka are comprised mostly of steel pipes and some polyethylene pipes, which buried at cover depths of about 1.0 - 1.2 m. Small diameter pipes of 25, 30 and 50 mm were built with threaded joints, whereas large diameter pipes of 100, 150 and 200 mm were built with welded and A-II type mechanical joints. Figure 9 shows the locations of damage to mains and branches of high and low pressure gas distribution lines. All of the damage was occurred at threaded and mechanical joints. No breaks or other damage to pipe with welded joints was reported.

Building

Most buildings in Midorigaoka were single family one- or two- story wooden houses,

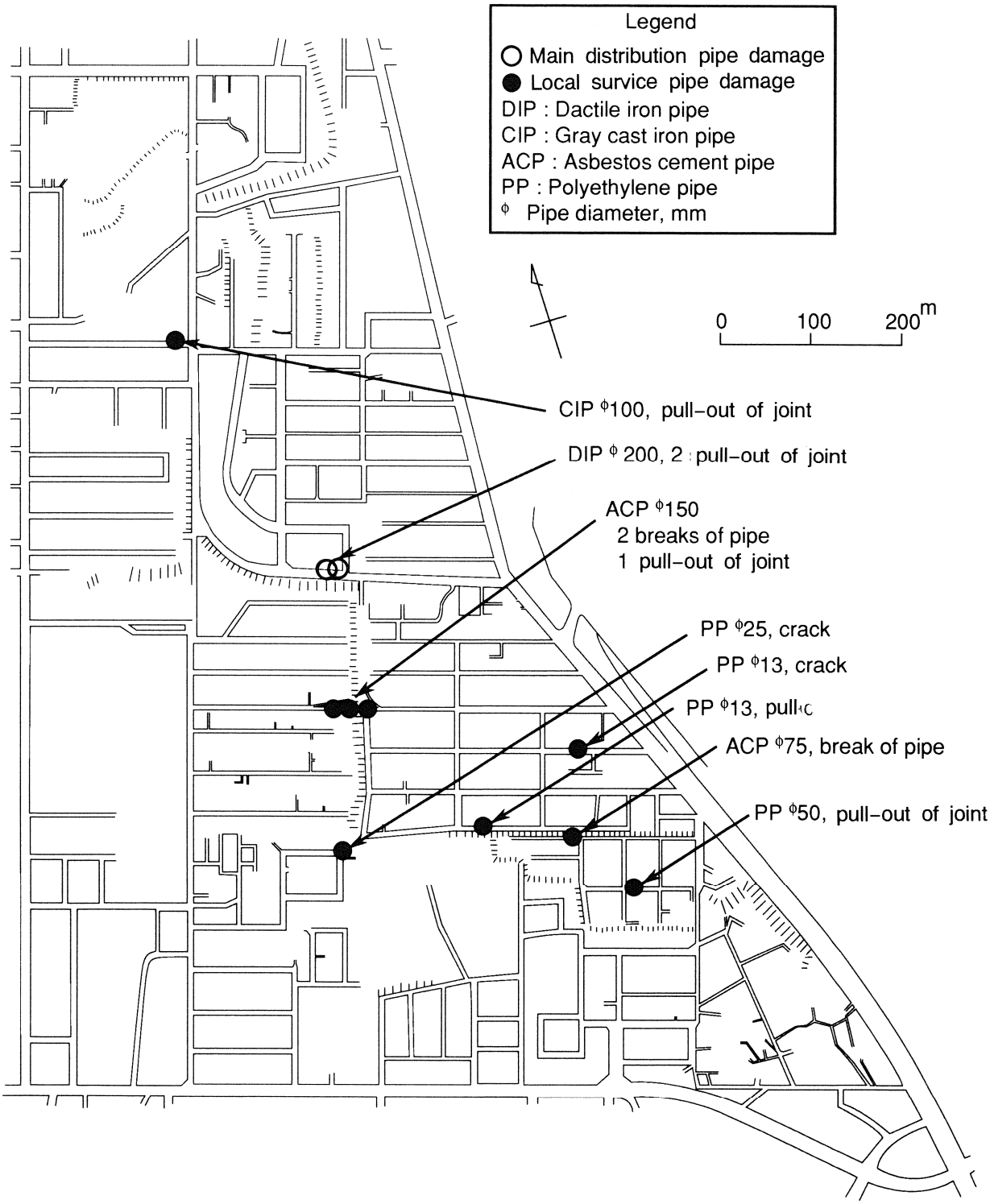

Fig.7 Map of Midorigaoka Showing Locations of Damage to Water Distribution and Survice Pipelines

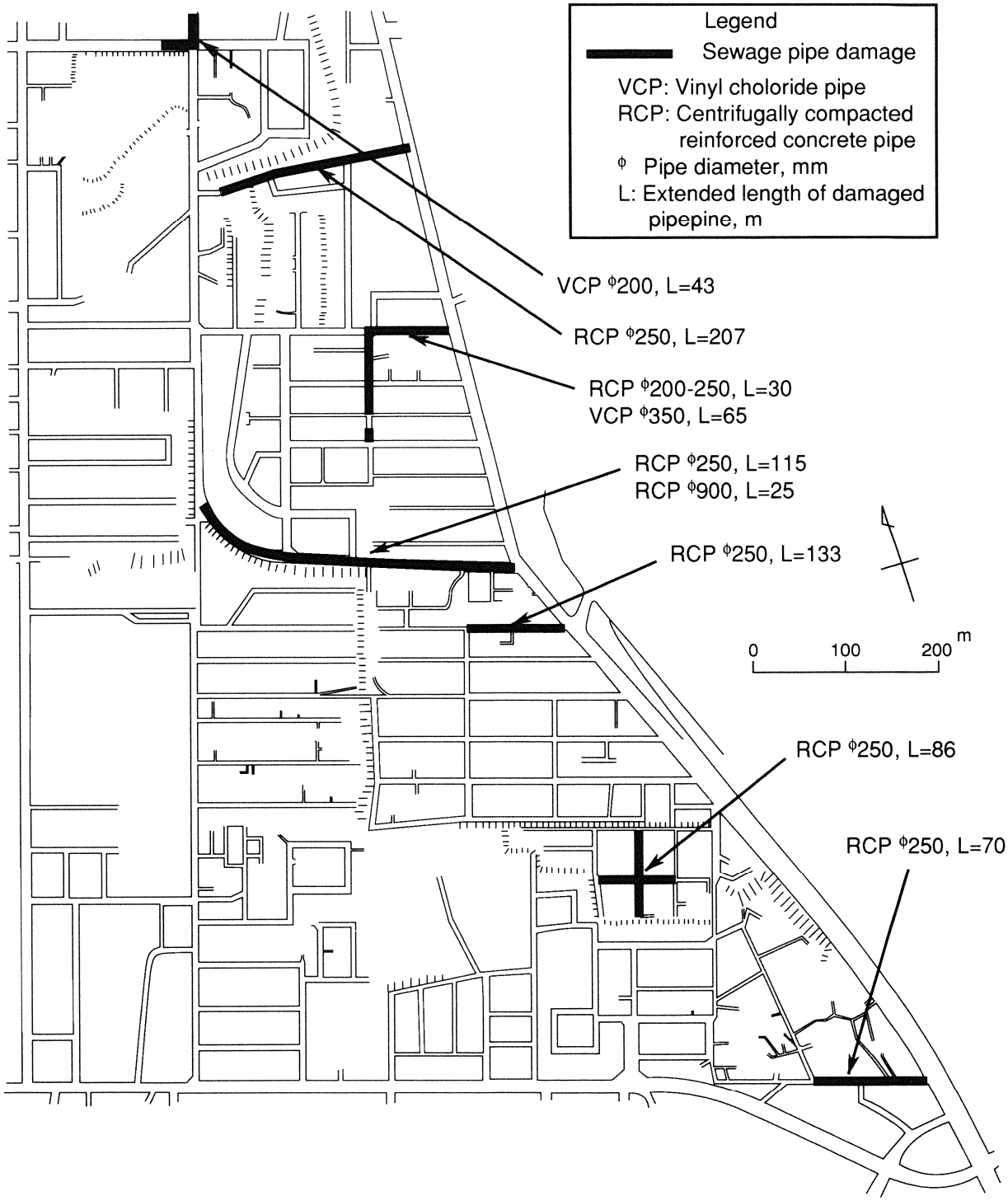

Fig.8 Map of Midorigaoka Showing Locations of Damage to Wastewater Pipelines

Photo 3 Deformation of a Wastewater Pipeline
(Courtesy of Kushiro City Government)

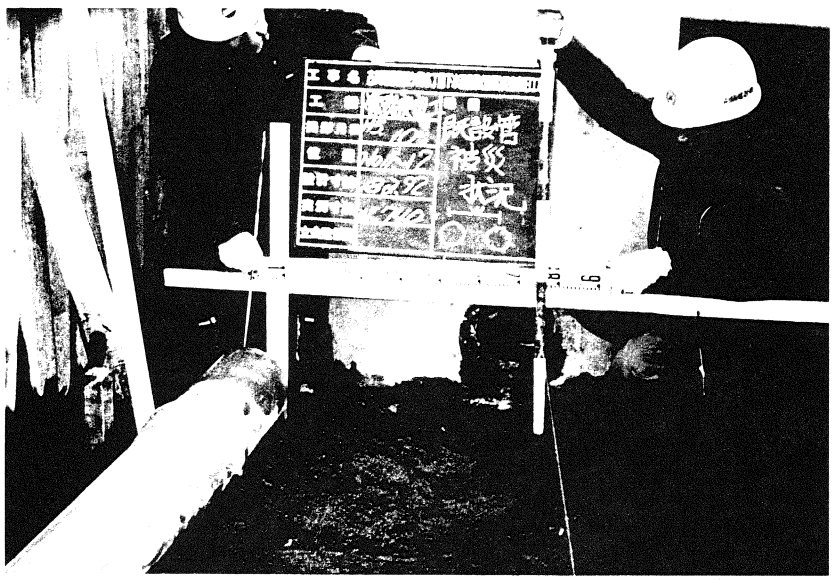

Photo 4 Rupture of Connection between Manhole and Pipe
(Courtesy of Kushiro City Government)

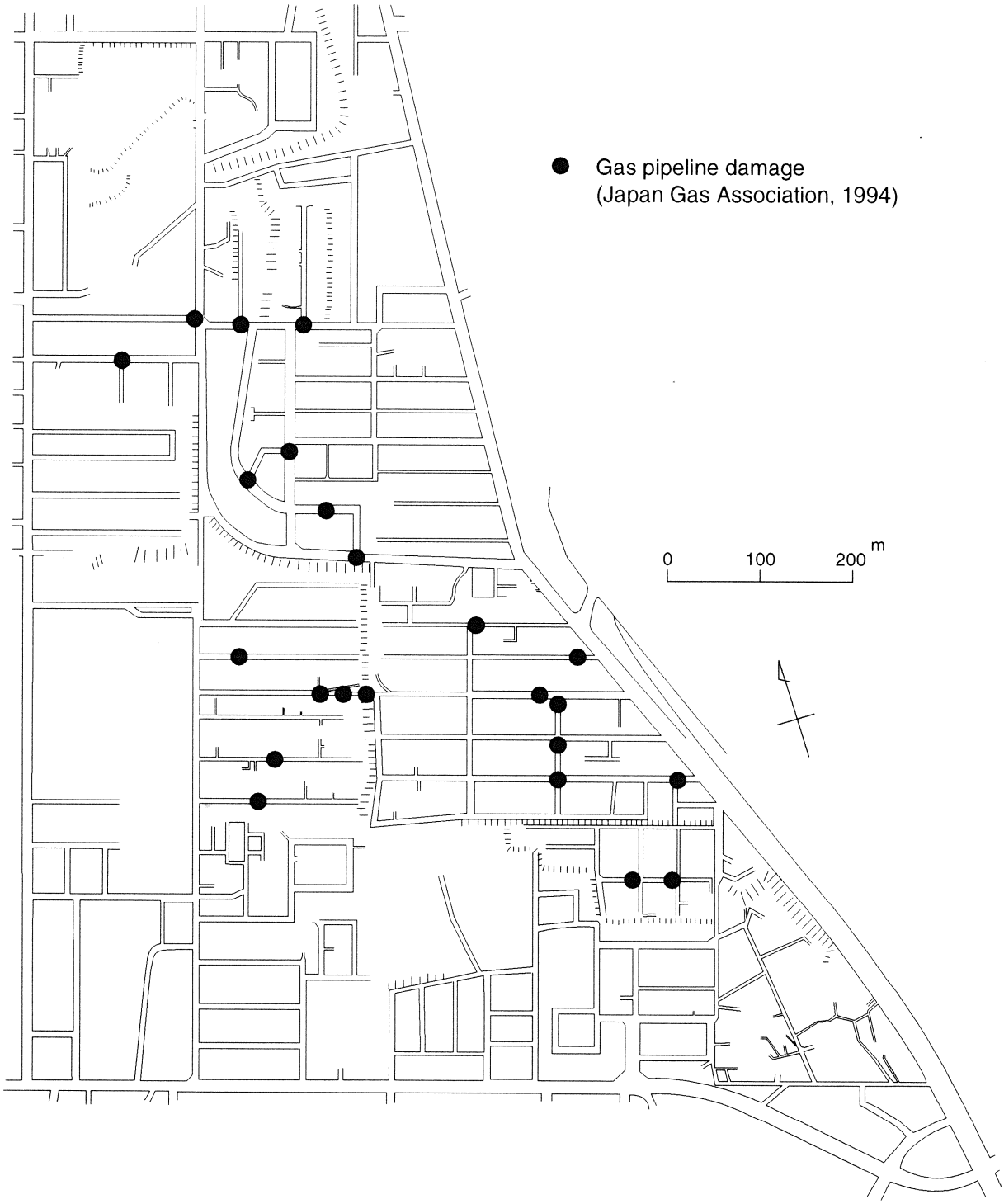

Fig.9 Map of Midorigaoka Showing Locations of Damage to High and Low Pressure Gas Distribution Systems

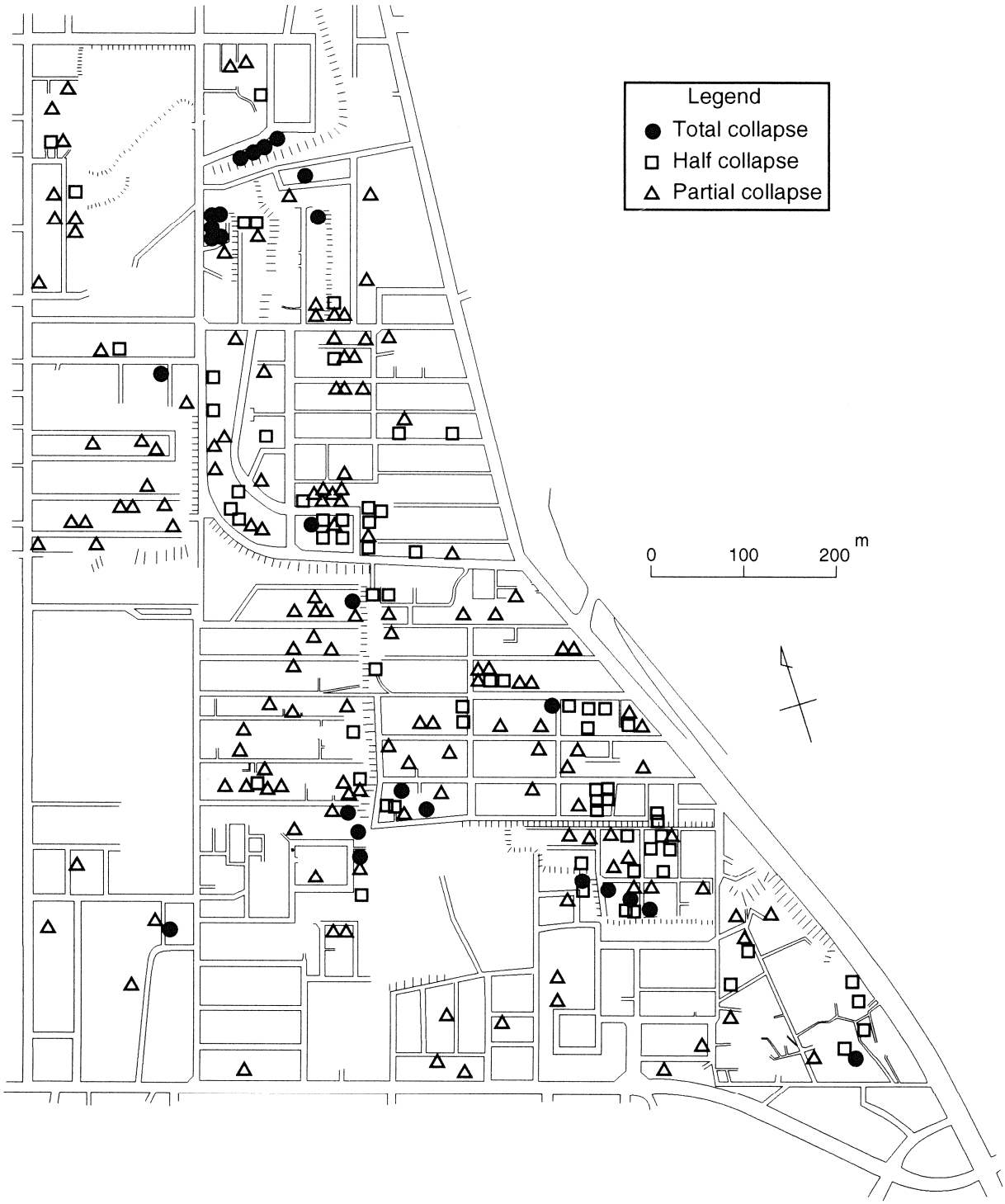

Fig.10 Map of Midorigaoka Showing Locations of Collapsed Houses

which were built in the last twenty years with some engineering design. These houses were significantly affected by the earthquake as shown in Fig. 10. Damage was primarily in the form of cracks of walls and foundation, broken chimneys, differential settlement and horizontal displacement of the foundation. Total collapse indicates damage to main structural members, but does not imply complete collapse of the structure. The most serious instances of damage occurred at site ① in Fig.5 where a slope failure occurred as previously shown in Photo 2.

SUBSURFACE CONDITIONS IN MIDORIGAOKA

Subsurface Soil Conditions

Many boring investigations and standard penetration tests have been performed to clarify the foundation conditions of wastewater utilities in Midorigaoka. On the basis of the boring information, a cross-section oriented in the north-south direction was developed as shown in Fig.11. Loose fill with SPT N-values less than 5 extends along the section with a thickness ranging from 1 to 9 m. The depth of the water table is shallow ranging from 0.3 to 2 m in the valley, whereas in the terrace it is several meters deep. Underlying the fills is very soft peat, which was originally at the bottom of the valley.

The slope failure described before (① in Fig.5) occurred where thickness of fill material is large and the slope is steep, as shown at the left side end of the figure. Sand boils were observed in the gentle slope of valley wall where 1- to 2-m thick fill overlies the water table. Major ground cracks and settlements occurred in the upper part of the slope with sand boils. This pattern of ground deformation implies that lateral movement toward the center of the valley occurred due to the liquefaction of loose fill. This agrees with the fact that grain size characteristics of sand boils was similar to the grain size of the volcanic ash used as fill in Midorigaoka.

Landform Changes due to Development

To examine further the relationships between ground deformation and subsurface conditions, landform changes due to development are investigated by analyzing a pair of aerial photographs taken before and after the development. A total of 13 sections were selected for analysis; 12 sections through Midorigaoka and 1 outside Midorigaoka where few effects of the earthquake were observed. The accuracy of the measurements is about ±1 m in the vertical direction.

The typical examples of the photogrammetric analysis were shown in Fig. 13, in which the locations of streams before development and ground failures and damage to structures are plotted. In the figure, the damaged houses previously shown in Fig.10 are re-classified according to damage mode based on the record by the city government into three types: 1) damage in foundations; 2) damage other than that in foundation such as

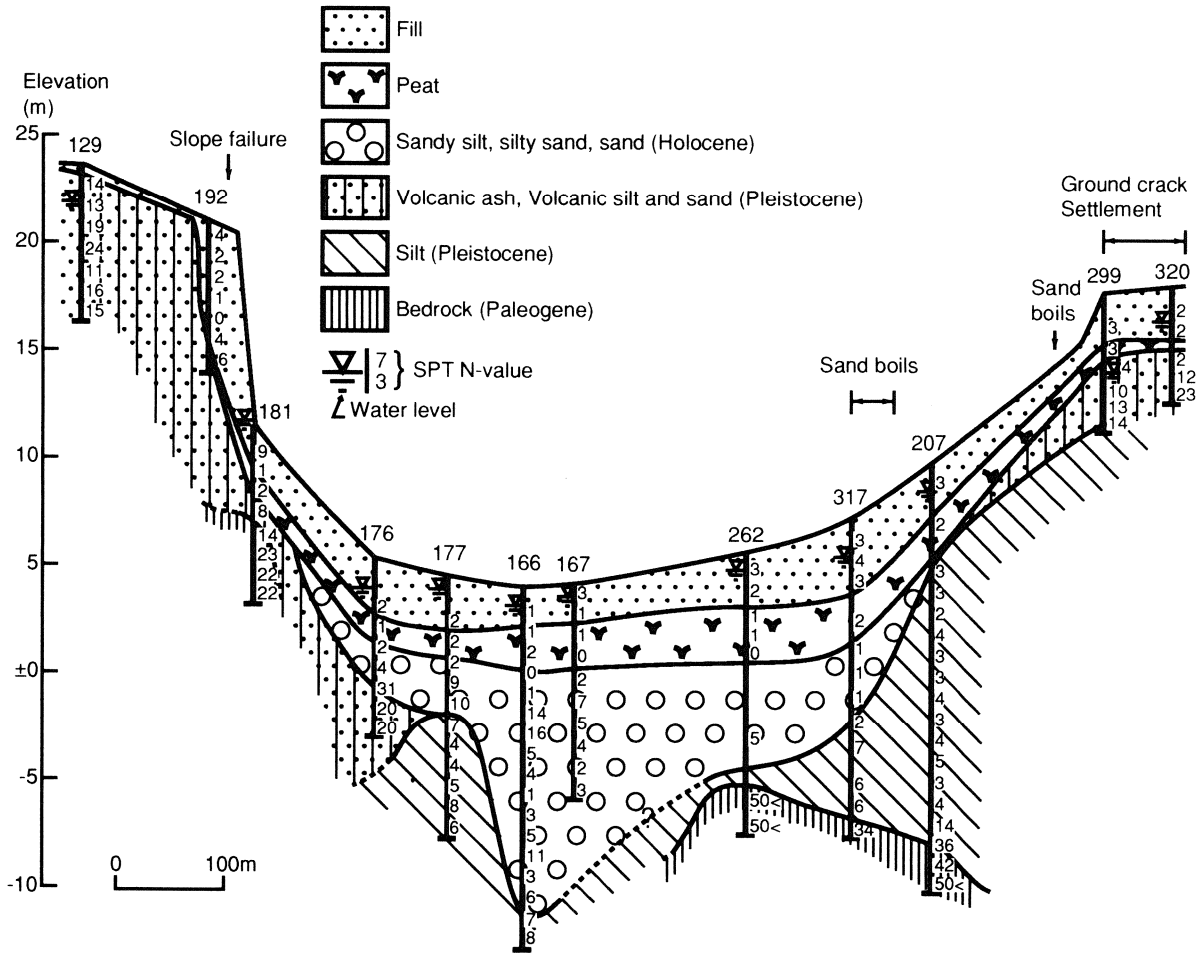

Fig.11 Soil Profile along Cross-Section A-A' in Midorigaoka (see Fig.12 for location)

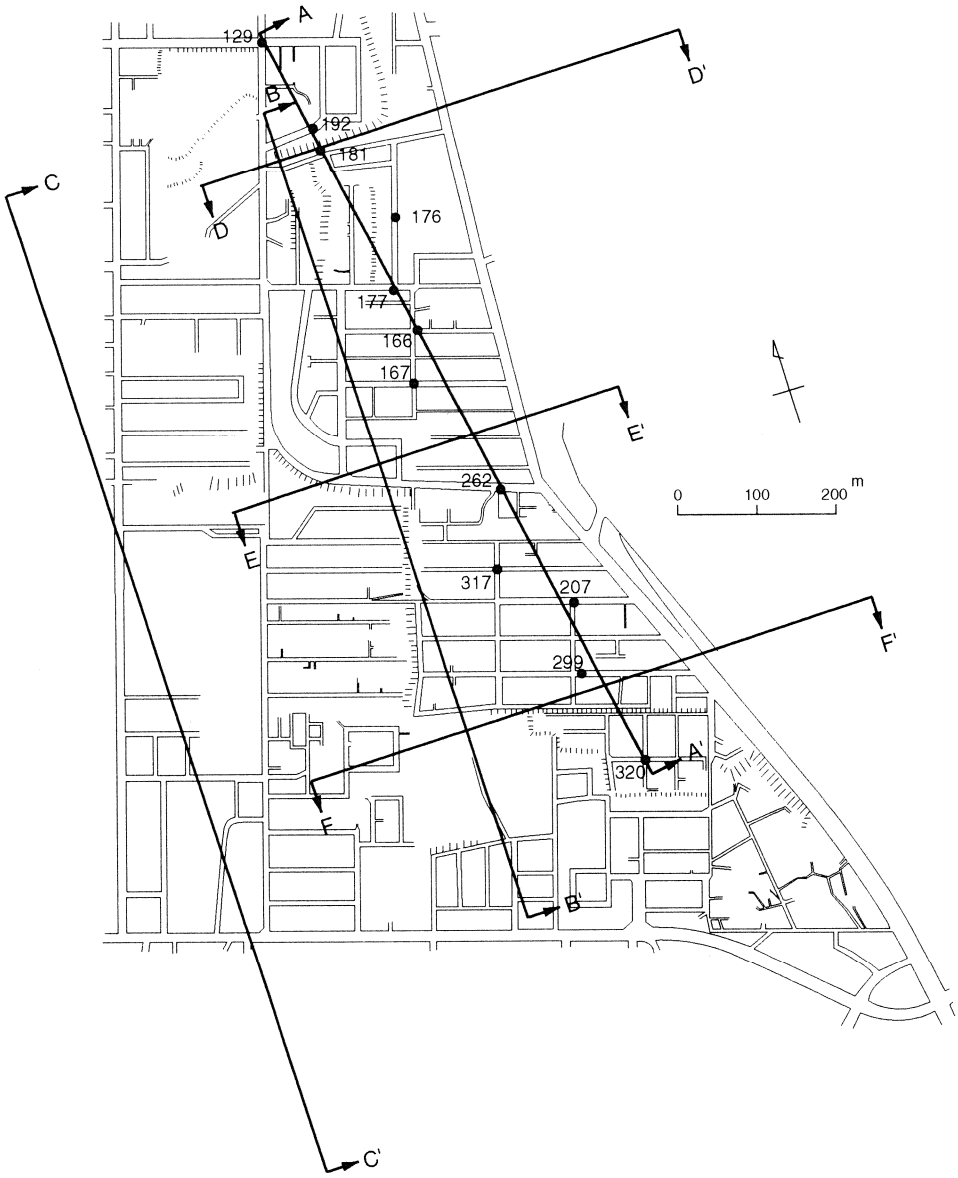

Fig.12 Map of Midorigaoka Showing Locations of Cross-Sections

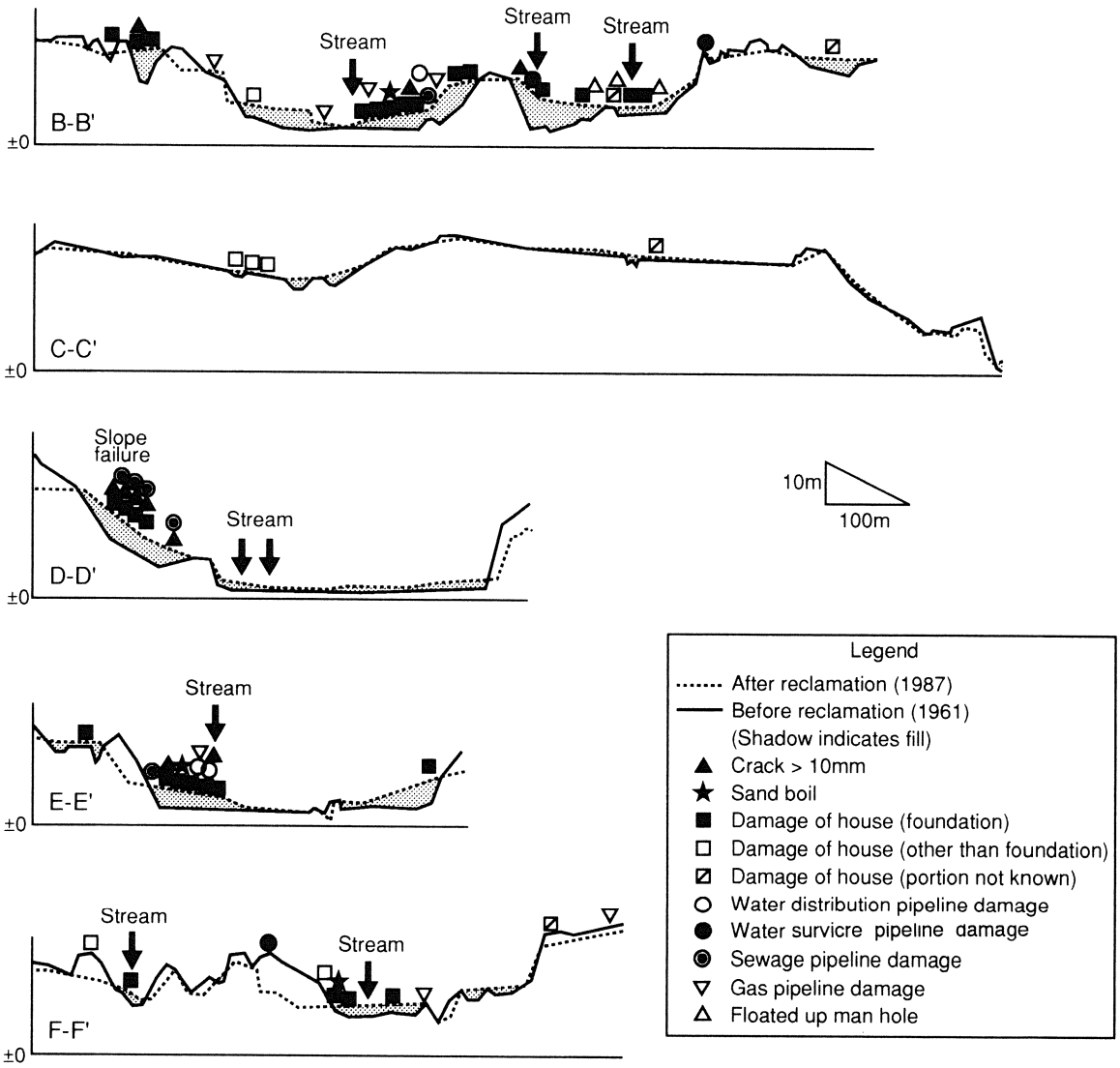

Fig.13 Cross-Sections Showing Landform Changes due to Development (see Fig.12 for locations)

collapsed chimney and cracked exterior wall; and 3) portion of damage not reported. The majority of the damage in Midorigaoka was categorized as the type-1.

It can be seen from the figure that the heaviest concentration of structural damage was observed in the filled area where ground failures such as slope failure, ground cracks and sand boils were concentrated. The slope failure occurred at the boundary between the terrace and the valley where fill is thick and the slope of ground surface is steep as shown in section D-D', whereas liquefaction effects such as sand boils and floated up manholes occurred in the valley where fill is thick, slope is gentle and stream flowed down before the development. Ground cracks also occurred on both steep and gentle slopes in the filled area. Damage to pipelines and foundation of houses occurred in the locations of all ground failures, whereas structural damage was absent in the valley bottom where fills are flat and not so thick, as shown in section D-D'. The data imply that permanent ground deformation and/or movement associated with ground failures was the principal cause of the damage to structures. In contrast, damage other than that in foundation of house such as collapse of chimney and cracks of exterior walls, a few in number, did occur in all part of sections, in both filled and cut areas, which implies that primary cause of the damage was strong ground shaking.

Subsurface Characteristics from Short Period Microtremor Measurement

Microtremor measurements were made in Midorigaoka to determine response characteristics of different sites. Figure 14 shows spectrum ratio H/V, where H and V denote horizontal and vertical Fourier amplitude of microtremors. The solid line denotes the average spectrum and dotted lines at the top and at the bottom are envelops of the measured spectrum. It is noted that large spectral values imply large contrast of stiffness between basin and surface deposit. Therefore, ground shaking is supposed to be larger as H/V value increases.

The predominant period at site A in Fig.14 is about 1 sec., which is the largest period in this area. Probably, there exist of thick silt layer beneath the volcanic ash. At site B, soil profile changes rapidly as seen in Fig.11, which may explain that peat is not absent at site B. Spectrum has clear peak at about 2 Hz at site C, which is 2 times as large as that as site A. It agrees with the observation that bed rock is shallow and impedance ratio between surface layer and bedrock is large here. The same discussion can be made at site E. On the other hand, the location of bedrock is not known and there exists thick and soft silt layer at site D. This explains no clear peak in the spectrum at this site. In summary, the difference in stiffness and thickness of the deposits may control predominant periods. Direct correlation were not seen, however, between the predominant periods and occurrence of ground failures.

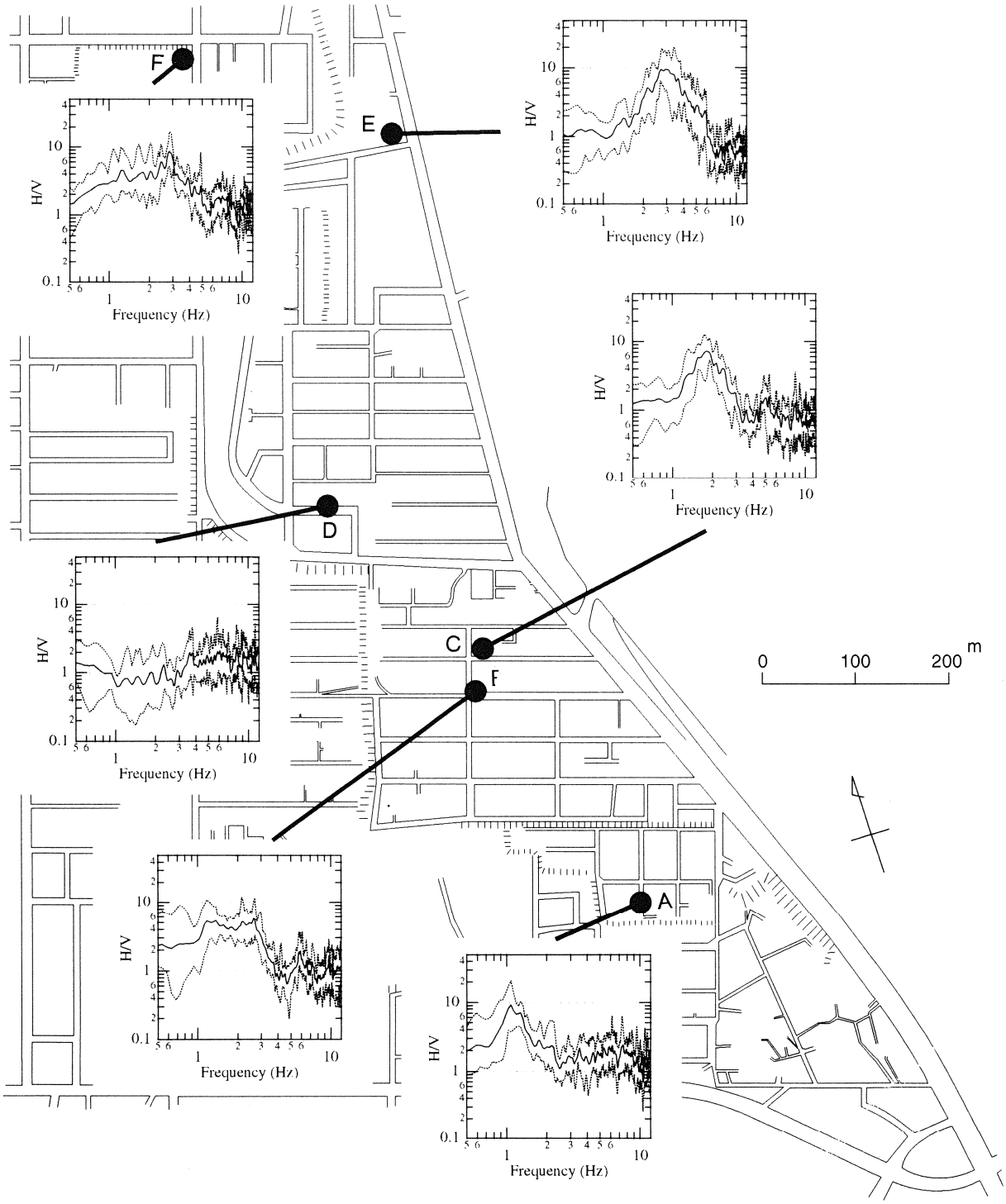

Fig.14 Result of Microtremor Measurements

CONCLUDING REMARKS

There was substantial damage to underground pipelines and buildings in Midorigaoka, Kushiro City during the 1994 Kushiro-oki earthquake. The damage was caused primarily by ground deformations and/or ground movements associated with slope failures, lateral spreading, and liquefaction, and partially by ground shaking.

In summary, Midorigaoka had several adverse conditions such as thickness and density of fills, slope of the ground surface, and subsurface water conditions. The conditions lead to occur various types of ground failures. They were strongly affected to not only locations and pattern of the ground failures but also resulting damage modes of structures. Although the level of damage was much more severe in 1993, it is notable that locations and patterns of sand boils and cracks in 1993 were the same as in the time of the 1973 Nemuro-hanto-oki earthquake.

ACKNOWLEDGEMENTS

The authors wish to thanks several people who assisted in the earthquake reconnaissance and acquisition of information. Special thanks are extended to Associate Prof. K. Miura of Hokkaido University who informed the earthquake damage quickly. Prof. S. Yasuda of Tokyo Denki University, Dr. S. Tsujino, and Mr. I. Suetomi, both of Sato Kogyo Co., who joined in the earthquake reconnaissance investigations and give us valuable suggestions. Dr. R. Imamura and Mr. K. Adachi of Asia Air Survey Co. helped in analyzing aerial photographs. Mr. I. Suetomi and other people in Sato Kogyo Co. conducted microtremor measurements. Thanks also are extended to Mr. Honma and Mr. Taisyu of the Kushiro Water Department, Mr. Okabe and S. Kainuma of the Kushiro Wastewater Department, Mr. M. Masuoka of the Kushiro Urban Development Department, Mr. Sugimura of the Kushiro General Affairs Department, and Mr. Kobayashi of Kushiro Gas Co., all for their help in gathering lifeline and building damage data.

REFERENCES

1) Kushiro City Government, "Document of Earthquake Hazard of the 1993 Kushiro-oki Earthquake," 1993 (in Japanese).
2) Earthquake Disaster Investigation Committee of the Japanese Society of Soil Mechanics and Foundation Engineering, "Report on the Damage Investigation of the 1993 Kushiro-oki and Noto Hanto-Oki Earthquakes," 1994 (in Japanese).
3) The Research Group on Microtremor Joint Measurements Related to the 1993 Kushiro-oki Earthquake, Coordinator: Seo, K., "A Study on Application of Microtremors to Evaluate the Characteristics of Ground Motions during Earthquake," Research Report on Natural Disasters, Supported by the Japanese Ministry of Education, Science and Culture, Group for the study of Natural Disaster, 1994 (in Japanese).
4) Japan Gas Association, "The 1994 Kushiro-oki and Hokkaido Nansei-oki Earthquakes and Urban Gas Facilities," 1994 (in Japanese).

Geotechnical Observations at the Van Norman Complex after the 1994 Northridge Earthquake

C.A. Davis, Associate Engineer,
Department of Water and Power, Los Angeles, CA.

J.P. Bardet, Associate Professor,
University of Southern California, Los Angeles, CA.

ABSTRACT

The January 17, 1994 Northridge Earthquake severely shook the Van Norman Complex, in the northern San Fernando Valley. Throughout the complex, sand boils, liquefaction induced lateral spreading, and ground cracks were observed. The Upper and Lower San Fernando hydraulic fill dams displayed substantial cracking, settlement and lateral movement. One small dike failed at the San Fernando Tailrace Channel at the northern end of the site. Six rolled fill embankments, including the Los Angeles Reservoir, underwent measurable movement.

INTRODUCTION

The Van Norman Complex is owned and operated by the City of Los Angeles Department of Water and Power. As shown in Fig.1, it is located in the northern San Fernando Valley along Interstate 5 between the 405 and 210 interchanges approximately 7 miles north of the January 17, 1994 Northridge Earthquake epicenter. As shown in Fig.2, the complex includes major water facilities which are critical to the Los Angeles Area, and controls 50 to 75 percent of the cities' annual supply of water. The Northridge Earthquake caused damage to both water and power facilities estimated to exceed $75M.

This paper summarizes the most significant geotechnical observations in the Van Norman Complex after the Northridge Earthquake, especially on the Lower and Upper San Fernando Dams, Los Angeles Reservoir and Power Plane Tailrace. A more complete and comprehensive report of observations, field measurements, and strong motion recordings is in preparation, and will be released in the near future.

SEISMICITY AND STRONG MOTION RECORDING

The Northridge Earthquake occurred at 4:31 AM (PST) on January 17, 1994 with a moment magnitude of 6.7 (Trifunac et al., 1994; USGS and SCEC, 1994). The main release of energy occurred on an unmapped blind thrust segment of the Oak Ridge Fault which dips to the south under the San Fernando Valley. The epicenter was located at 34° 12.53' N; 118° 32.44'W at a depth of 19 km. The duration of strong shaking was 6 to 10 seconds (Porcella et al., 1994; Shakal et al., 1994).

A great number of aftershocks took place below the complex. This is easily seen in the aftershock map in Fig.3, and the cross-sections BB' and CC' in Fig.4 (after Hauksson, 1994). The aftershocks in Fig.3 are so dense that they completely cover the complex which had to be situated by its coordinates. As shown in Fig.4, the aftershocks

are located within a narrow band that delineates the fault plane inclined at 35°-40°. The eastern extremity of the fault rupture is just below the Van Norman Complex. As a result, the Van Norman Complex was strongly shaken by the main event, and was continually subjected to numerous, close, and shallow aftershocks.

The Northridge Earthquake produced an unprecedented number of near source seismic recordings. Fig.2 and Table 1 present the site locations and recorded peak ground accelerations of the seismic instruments on and around the Van Norman Complex, which include fourteen accelerographs (1-14) and two seismoscopes (15-16). Fig.5 shows an example of the time history of horizontal and vertical accelerations recorded at the Rinaldi receiving station, located to the southern end of the complex and referred to as No.1 in Fig.2. The horizontal peak acceleration (0.84 g) is observed at about 2.5 second and corresponds to a low-frequency and high-energy pulse, which is noticeable in all the recordings in the complex. The vertical acceleration has a shorter dominant period, but an even larger peak value (0.85 g) than the horizontal components.

The recorded peak accelerations were very large for this earthquake of 6.7 magnitude. In fact, the Van Norman Complex was subjected to some of the largest accelerations ever recorded. In contrast to those large accelerations, relatively low levels of shaking (0.32 g) were also measured near the Los Angeles Reservoir. This provides us with a remarkable example about the rapid variation of ground acceleration intensity over short distances.

Table 1. Location of strong motion recordings in the Van Norman Complex, and peak accelerations recorded during the Northridge earthquake.

Station number	Station name	Owner	Geology/ Foundation	Lat.	Long.	Epicentral Distance (km)	Peak acceleration (g)		
							Horiz. 1	Vert.	Horiz. 2
1	Rinaldi receiving station	DWP/Power	Alluvium	34.281	118.478	10	0.84	0.85	0.48
2	LA Dam - West abutment	DWP/Water	Nonmarine deposit	34.294	118.483	11	0.43	0.32	0.32
3	LA Dam foundation	DWP/Water	Nonmarine deposit	34.295	118.479	11	0.32	0.13	0.28
4	LA Dam crest	DWP/Water	Dam fill	34.294	118.481	11	0.56	0.39	0.43
5	LA reservoir	DWP/Water	Concrete structure	34.296	118.478	11	1.34	0.29	1.18
6	North Dike crest	DWP/Water	Dam fill	34.300	118.487	12	0.65	0.38	0.56
7	Generator building	MWD/USGS	Nonmarine deposit	34.313	118.498	12	0.98	0.52	0.56
8	Adminstration building	MWD/USGS	Alluvium	34.312	118.496	12	0.62	0.40	0.40
9	Reservoir roof	MWD/USGS	concrete structure	34.309	118.499	12	0.84	0.51	0.65
10	Valve group 7	DWP/Power	Alluvium	34.311	118.490	12.5	0.90	0.64	0.61
11	Valve group 7 ground floor	DWP/Power	Alluvium	34.311	118.490	12.5	0.75	0.79	0.60
12	Valve group 16 basement	DWP/Power	Alluvium	34.311	118.490	12.5	0.58	0.53	0.37
13	Free field	DWP/Power	Nonmarine deposit	34.312	118.481	13	0.83	0.38	0.49
14	Valve hall floor	DWP/Power	Nonmarine deposit	34.312	118.481	13	0.79	0.43	0.45
15	Abutment	DWP/Water	Nonmarine deposit	34.294	118.483	11	>0.31	-	-
16	Bypass Reservoir dam crest	DWP/Water	Dam fill	34.292	118.484	11	>0.31	-	-

LOWER SAN FERNANDO DAM

The upstream face of the Lower San Fernando Dam was reconstructed, after it failed during the 1971 San Fernando Earthquake. At the time of the Northridge Earthquake, there was only a small pond of water, a few feet deep, within the upstream basin. Nevertheless, the Lower San Fernando Dam crest and upstream slope substantially cracked and moved. Many sand boils emerged on the upstream face. In addition, a sinkhole occurred at the toe of the dam above the 96 inch drain line which had been crushed laterally.

Fig.6 presents a detailed mapping of the cracks and sand boils observed after the earthquake. Fig.6 also shows the lateral displacements perpendicular to the dam axis. The maximum lateral movement on the upstream slope exceeded 1/2 foot in the upstream direction. Along the crest, the maximum movement was just under 1/2 foot, and was similar to that on the upstream slope. The maximum downstream movement was approximately 3 inches on the downstream slope. Maximum settlement of 8 inches occurred along the crest, while settlement along the upstream slope reached nearly 1/2 foot. The maximum settlement and lateral displacement were measured in the same areas. Settlement along the upstream slope, parallel to the axis, was relatively consistent averaging a little over 4 inches, and increased linearly with the dam height. All settlements and displacements were obtained from the surveys of March 4, 1994 and February 24, 1993.

Earthquake shaking produced extensive cracks along the crest and upstream berm. The cracks were observed to extend across the entire width of the dam. Most cracking occurred in the longitudinal direction. However, there were transverse cracks at the abutments. Some cracks on the berm were observed to have up to 9 inches of vertical displacement. Some small cracking was observed through the grass at the top of the upstream slope. No cracks were observed on the downstream slope which was covered with thick grass. Approximately fifty large sand boils emerged through cracks on the upstream slope of the berm as seen in Fig.6.

A sinkhole approximately 30 feet in diameter and 10 feet deep appeared above the storm basin drain line on the west side of the dam. In addition, a large area subsided over the pipe alignment for a few hundred feet south of the sinkhole. The sinkhole resulted from a loss of material into the 8 foot diameter corrugated metal drain pipe. The earthquake crushed the drain line laterally, over a length of three hundred feet. An additional one hundred feet was severely damaged with lateral buckling up to two feet inward.

UPPER SAN FERNANDO DAM

Water retained behind the Upper San Fernando Dam was limited to a few feet within the backwash ponds (see Fig.2). Similar to the Lower San Fernando Dam, the upper dam also underwent extensive cracking in 1994. Fig.7 presents a detailed mapping of cracks and sand boils observed after the earthquake.

Fig.7 shows the lateral movement at monument locations, and a settlement profile. The movement was obtained by comparing the survey of March 4, 1994 to that of July 29, 1993. Maximum settlement reached nearly 1.5 feet. The maximum settlement curiously corresponds with the minimum lateral movement. After intense shakings, the crest moved laterally a maximum of 7 inches in the upstream direction near the west and

east abutments. Settlement was clearly visible by the protruding grout pipes above the outlet line. These pipes were used to grout voids around the outlet line following the 1971 San Fernando Earthquake. Prior to the Northridge earthquake most of the pipes were hidden below the surface, whereas, after the shaking, some of them extended above the surface, as much as six inches.

An extensive network of cracks emerged on the surface of the upper dam, extending from the west abutment across the entire width of the dam and through the spillway on the east side. The majority of cracks were longitudinal to the axis, and became transverse near each abutment. Similar crack patterns were observed in the 1971 San Fernando Earthquake. However, in 1971, settlement reached 3 feet while movement was up to 5 feet in the downstream direction.

Sand boils surfaced at various locations around the Upper San Fernando Dam. Most erupted upstream on the dikes retaining the backwash ponds. Some boils were detected along the eastern upstream toe near the spillway. Others were found downstream of the dam, near piers supporting a 54-inch pipeline.

The 54-inch pipe supported by concrete piers, located below the dam, collapsed as a result of cumulative earthquake damage since the 1971 San Fernando Earthquake. The piers supporting the pipe leaned toward the east, and contributed to the buckling of the ring girders and subsequent pipe collapse. Many large extension cracks were observed along the road in front of the pipe.

LOS ANGELES RESERVOIR

Completed in 1979, the Los Angeles Reservoir is a modern reservoir which provides storage for treated aqueduct water. The water is impounded by two compacted earth fill dams. The Los Angeles Dam, on the south side of the reservoir, is 155 feet high, whereas the North Dike, on the northern side of the reservoir, is 117 feet high. Both embankments are founded on bedrock. Each is zoned with shell material on the upstream and downstream slopes, and contains a chimney drain in the center section made of coarse materials. The Los Angeles Dam also has a clay zone upstream of the chimney drain. The Los Angeles Reservoir is lined with asphalt concrete pavement along all of the interior slopes and perimeter roadways, except for its reservoir floor that is not paved. After the earthquake, the lining on all of the upstream slopes displayed many cracks, in addition to those caused by weathering prior to the earthquake.

The Los Angeles Reservoir is well equipped with modern instruments. The instruments remained functional throughout the earthquake, and were useful to evaluate the safety of the reservoir. Piezometers and observation wells indicated slight increases in pressures in and around the dams immediately after the earthquake, and a rapid return to normal values soon after. However, seepage in the North Dike substantially increased on the west abutment, and still remains high to date. The outlet tower performed extremely well, registering no permanent displacement or noticeable cracking in spite of being subjected to accelerations over 1g. However, the bridge leading to the tower moved significantly. One of the spans hopped out of its bracket supports, and slid more than 1.5 feet.

As shown in Fig.2 and Table 1, there were five seismographs located at the reservoir. Surprisingly, all their recordings were lower than those throughout the complex, which reached record-breaking levels of accelerations. Thus, the reservoir site was subjected to a much lower level of shaking than the surrounding areas.

Movement and settlement measured immediately after the earthquake showed up to 3 1/2 inches of crest settlement, and lateral downstream movement of over 1 inch on the crest. The downstream slope settled a maximum of 3/4 inch, and had lateral displacements in the downstream direction of over 2 inches. Approximately one inch of settlement was observed on the upstream slope around the outlet tower bridge pier. All displacements were measured by comparing the survey results of January 4, 1994 and January 21, 1994.

As shown in Fig.8, the upstream slope displayed a vast array of cracks, the largest cracks occurring at the east abutment. Settlement in this area reached 3.5 inches. These cracks were associated with a wavy and bulging surface. Many of the cracks on the east side were of compressional nature, unlike on the rest of the dam surface. Transverse oriented cracks occurred along the crest road. In many cases the cracks lined up with diagonal cracks extending to the crest on the upstream face. Trenches were excavated across the largest cracks on the crest and upstream slope, and revealed that the cracks died out rapidly with depth. Within the zone encompassed by cracks, three small slump areas were also observed on the upstream face just west of the outlet tower.

POWER PLANT TAILRACE

In the northern part of the complex, substantial damage resulted at the San Fernando Power Plant and Tailrace. The ground surrounding the power plant subsided as much as two feet. Extensional cracking on the surrounding pavement provided evidence of ground spreading toward the tailrace.

Fig.9 shows a detailed mapping of cracks and sand boils around the tailrace. Extensive cracking occurred on both banks of the channel as a result of the lateral spreading induced by liquefaction. Numerous sand boils erupted around the tailrace, mostly on the west bank, although a few were observed on the east bank. A slide over 200 feet wide occurred on the west bank near the south end of the channel. The concrete liner within the channel was pushed over and up five to six feet. The west bank around the slide area settled a few feet, and displayed numerous cracks, most of them having less than 2 inches in width.

The east bank had fewer but larger cracks, which could be better described as scarps and fissures. These cracks were up to 6 inches wide and had over 1 foot vertical offset. A series of cracking patterns followed the old bank of the Upper Van Norman reservoir basin to the southeast of the tailrace. Many cracks extended northwest over to the abutment of the dike. Unfortunately, most cracks around the dike could not be mapped due to the emergency construction activities. Further south, at the site of the California State Northridge observatory, a slide 150 feet wide occurred leaving a scarp 2 1/2 feet high.

The dike retaining the south end of the tailrace channel breached after the earthquake, leaving a breach about 18 feet deep and 45 feet wide. The failure did not occur immediately after the main shock. Disaster response teams did not observe any sign of distress at 9:30 AM the morning of the earthquake. However, by the next morning, the dike had completely failed. Its failure probably resulted from a series of events, related to liquefaction and lateral spreading. The lateral spreading caused subsidence of the slopes into the reservoir basin. Longitudinal cracks propagated into the dike abutments, and possibly into the dike. The large displacements, high pore pressures in the ground, and weakened foundations presented conditions sufficient for piping to occur. It is quite

possible that large aftershocks later that day compounded the problem and aided in completing the failure.

In 1971, the Tailrace channel banks completely failed, but the dike withstood the San Fernando Earthquake shaking. Cracking around the tailrace and Upper Van Norman Reservoir had similar patterns for both earthquakes.

CONCLUSION

The Van Norman Complex sustained substantial damage from the 1994 Northridge Earthquake. Sand boils, liquefaction induced lateral spreading, cracks and fissures were observed. The two hydraulic fill dams (Upper and Lower San Fernando) sustained substantial cracking along with settlement and lateral movement. One small dike failed on the San Fernando Tailrace Channel at the northern end of the complex. Six rolled fill embankments, including the Los Angeles Reservoir, sustained measurable movement. Large and moderate levels of shaking coexisted within the site, with the Los Angeles Reservoir receiving a lower level of shaking than that at other nearby locations. The peak accelerations of the 1994 Northridge Earthquake were much higher than those of the 1971 San Fernando Earthquake. Although subjected to stronger shaking, the Van Norman Complex performed much better in 1994 than in 1971.

ACKNOWLEDGMENT

The financial support off the National Science Foundation (grant CMS-9414222) is acknowledged. The authors thank R. Tognazzini of the Los Angeles Department of Water and Power, and E. Hauksson of the California Institute of Technology for providing their data. The authors also thank M. Harris for reviewing the manuscript.

REFERENCES

Trifunac, M.D., M.I. Todorovska, and S.S. Ivanovič, 1994, " A Note on Distribution of Uncorrected Peak Ground Accelerations During the Northridge, California, Earthquake of January, 17, 1994", *Soil Dynamics and Earthquake Engineering,* Vol.13, pp.187-196.

United States Geological Survey (USGS) and the Southern California Earthquake Center (SCEC), Scientists of, 1994, "The Magnitude 6.7 Northridge, California, Earthquake of January 17, 1994," Submitted to Science Magazine June.

Porcella, R.L., E.C. Etheredge, R.P. Maley, and A.V. Acosta, 1994, "Accelerograms Recorded at USGS National Strong-Motion Network Stations During the Ms=6.6 Northridge, California Earthquake of January 17, 1994," Department of the Interior, U.S. Geological Society February, Open File Report 94-141.

Shakal, A., M. Huang, R. Darragh, T. Cao, R. Sherburne, P. Malhotra, C. Cramer, R. Sydnor, V. Graizer, G. Maldonaldo, C. Pertesen, and J. Wampole, 1994, "CSMIP Strong-Motion Records from the Northridge, California Earthquake of January 17, 1994," *California Department of Conservation, Division of Mines and Geology, Office of Strong Motion Instrumentation Studies,* Report OSMS 94-07, February.

Hauksson, E., 1994, Private communication, California Institute of Technology, Pasadena, California.

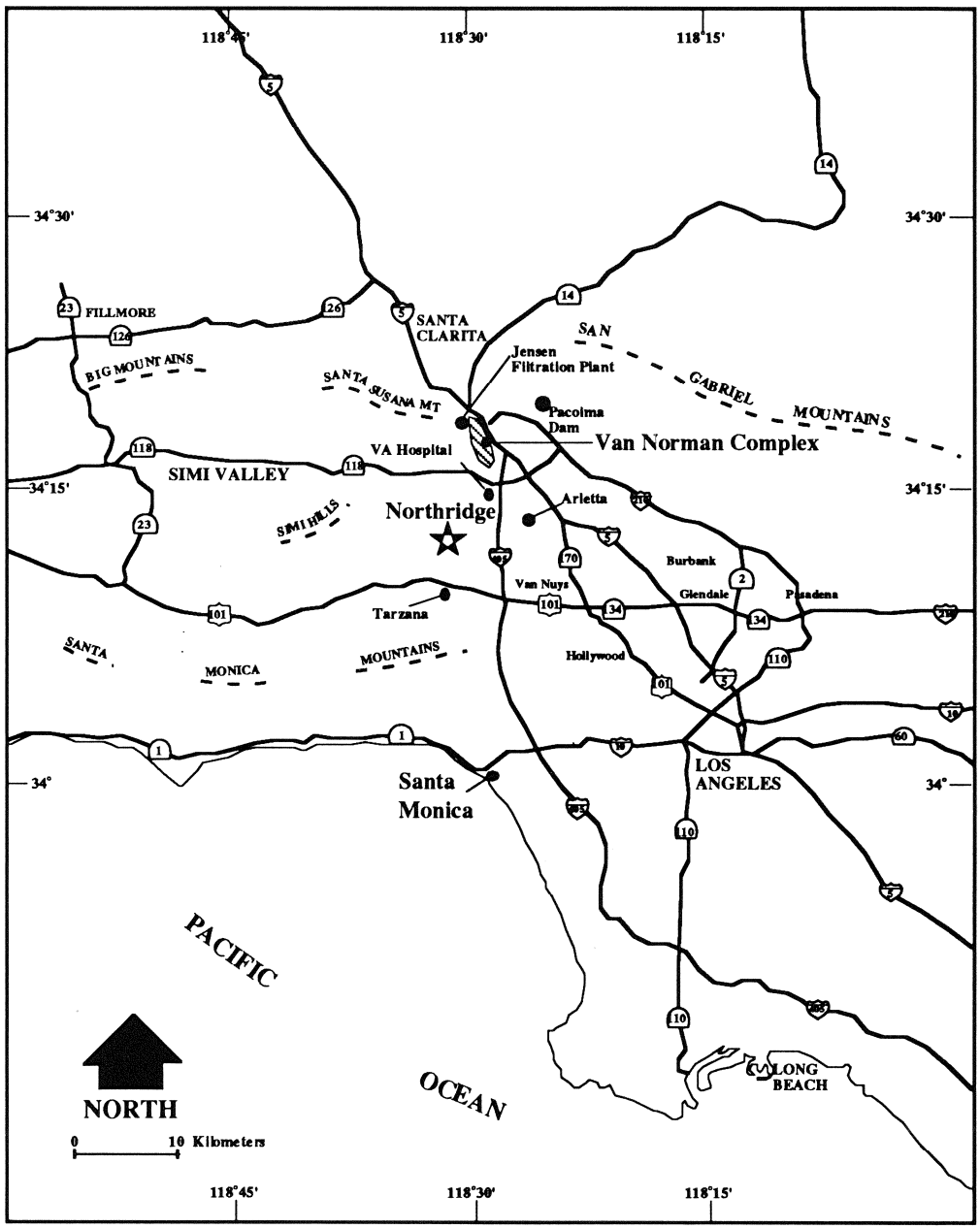

Figure 1. Location of Van Norman Complex in Los Angeles Area.

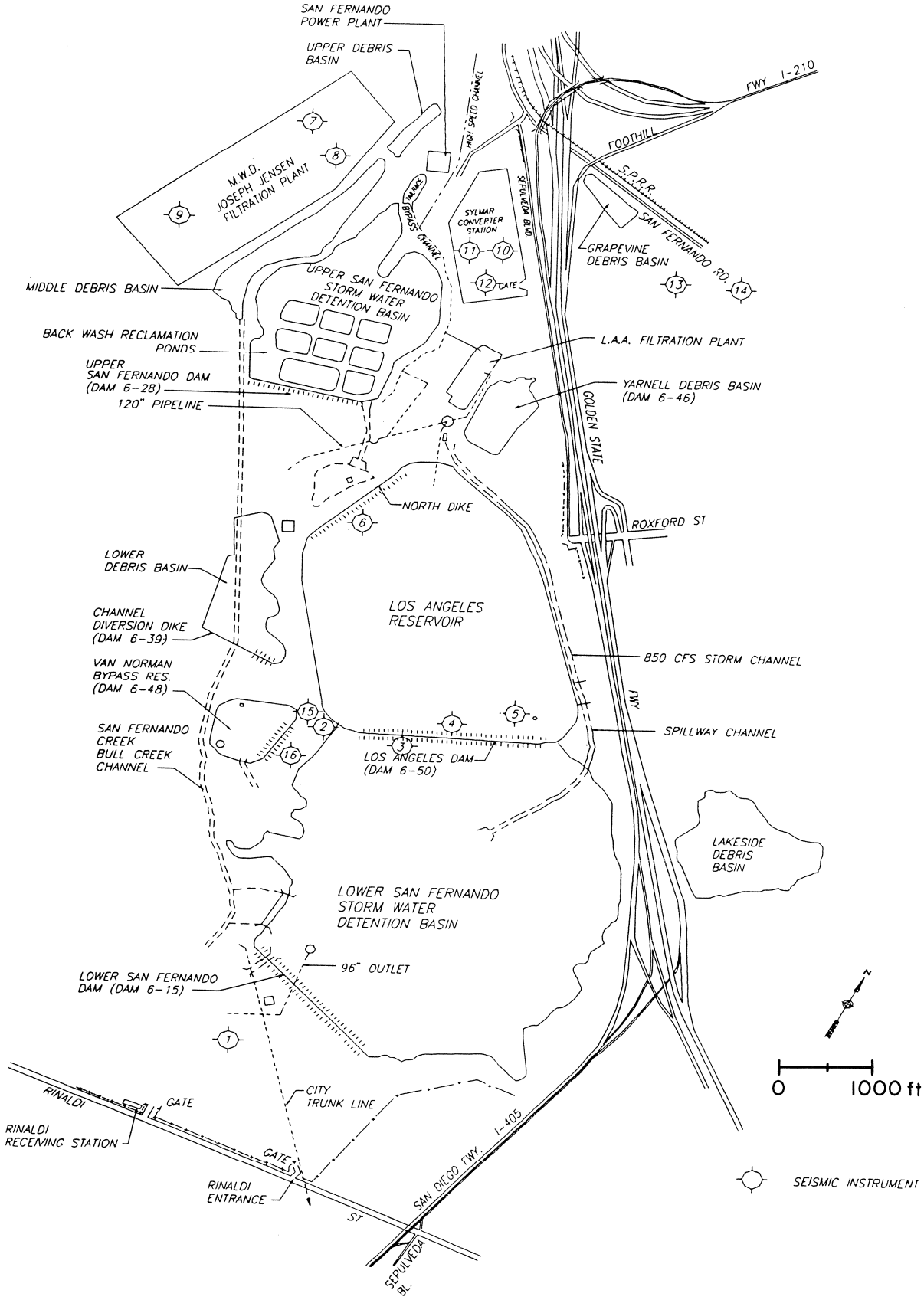

Figure 2. General view, main structures, and location of strong motion recordings of Van Norman complex.

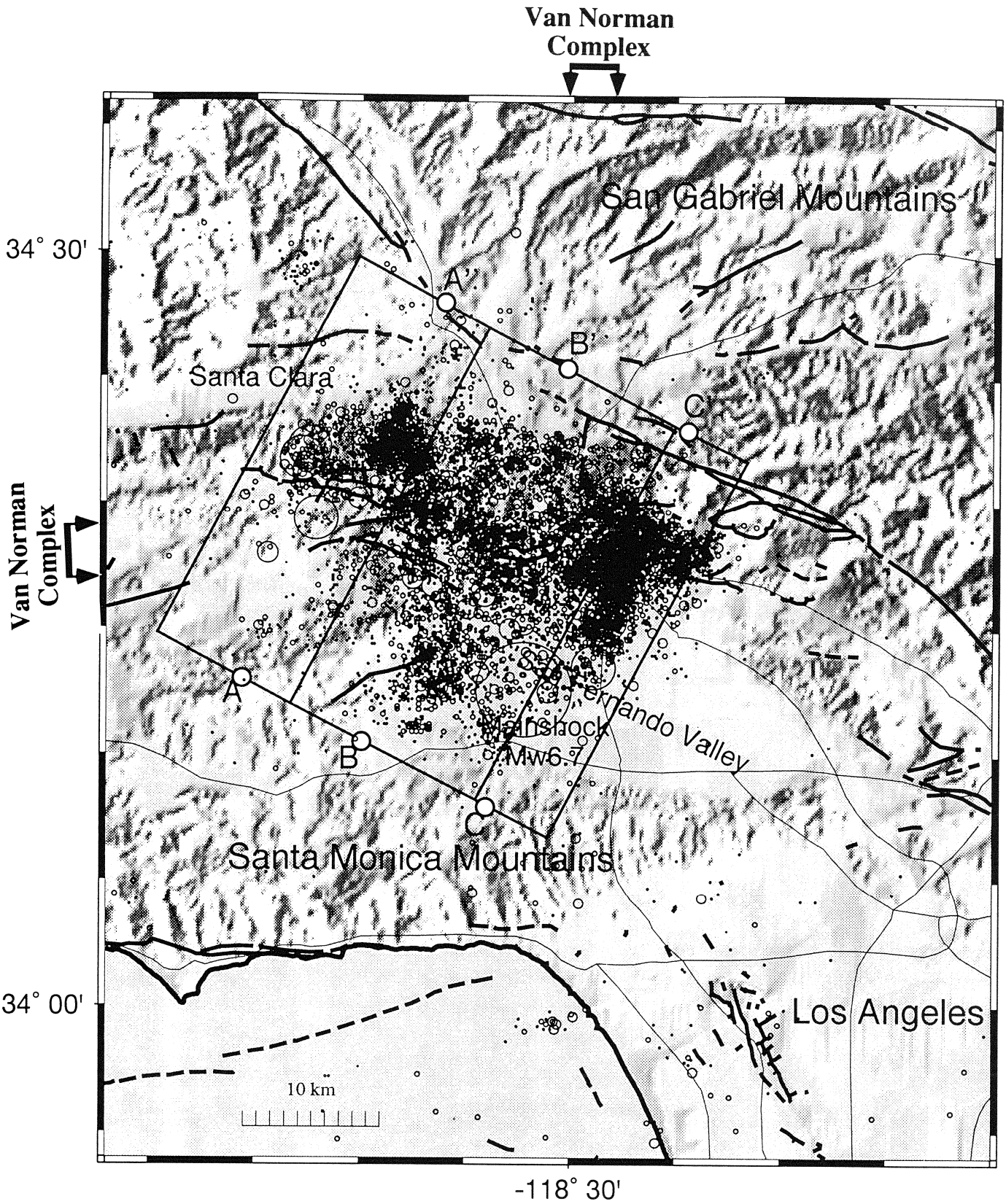

Figure 3. Map of aftershocks after the Northridge earthquake from January to July 1994 (after Hauksson, 1994).

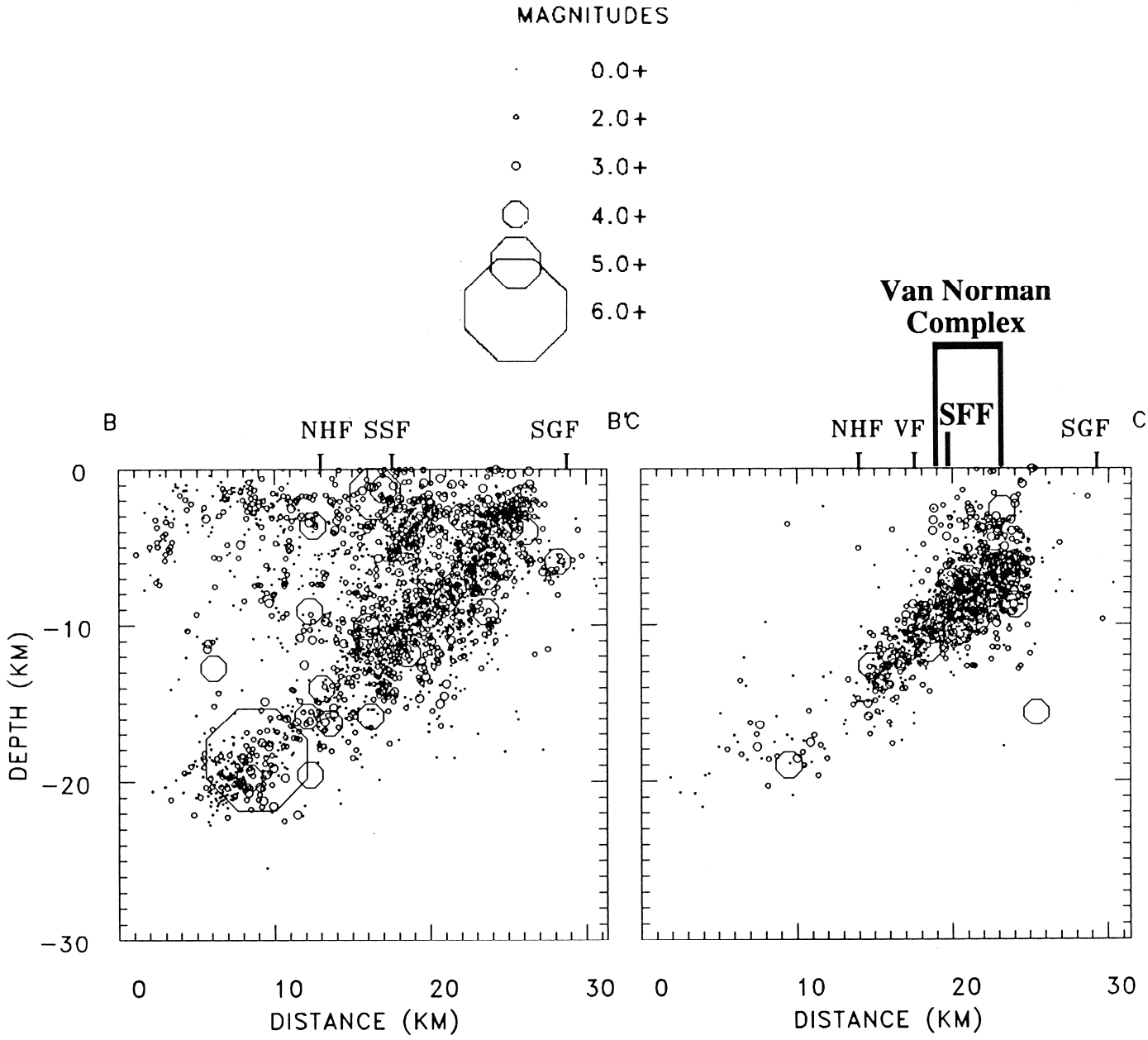

Figure 4. Location and depth of after shocks along sections BB' and CC' of Fig.3 (after Hauksson, 1994).

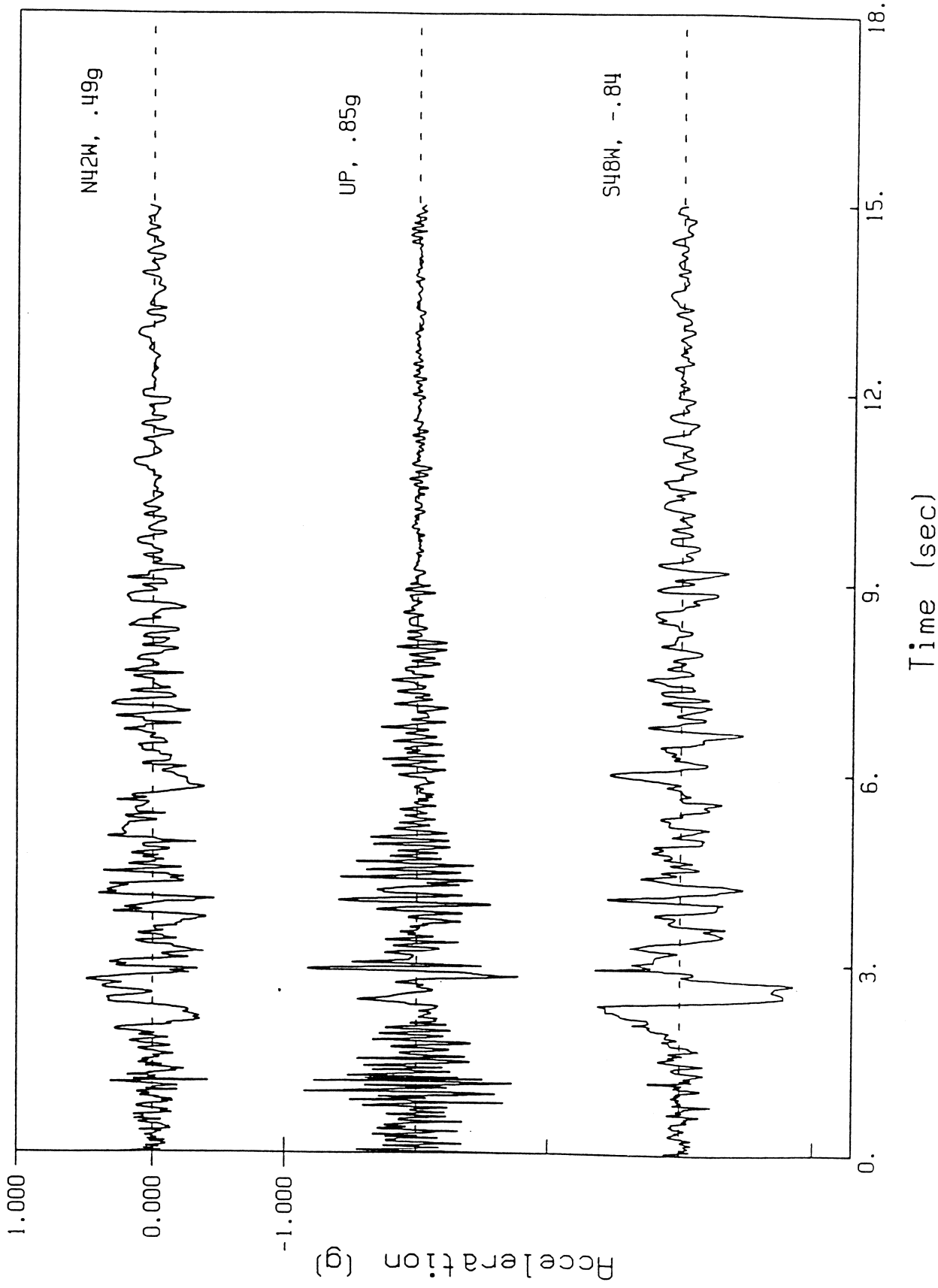

Figure 5. Time history of horizontal and vertical accelerations recorded at Rinaldi receiving station (station No.1 in Fig.2).

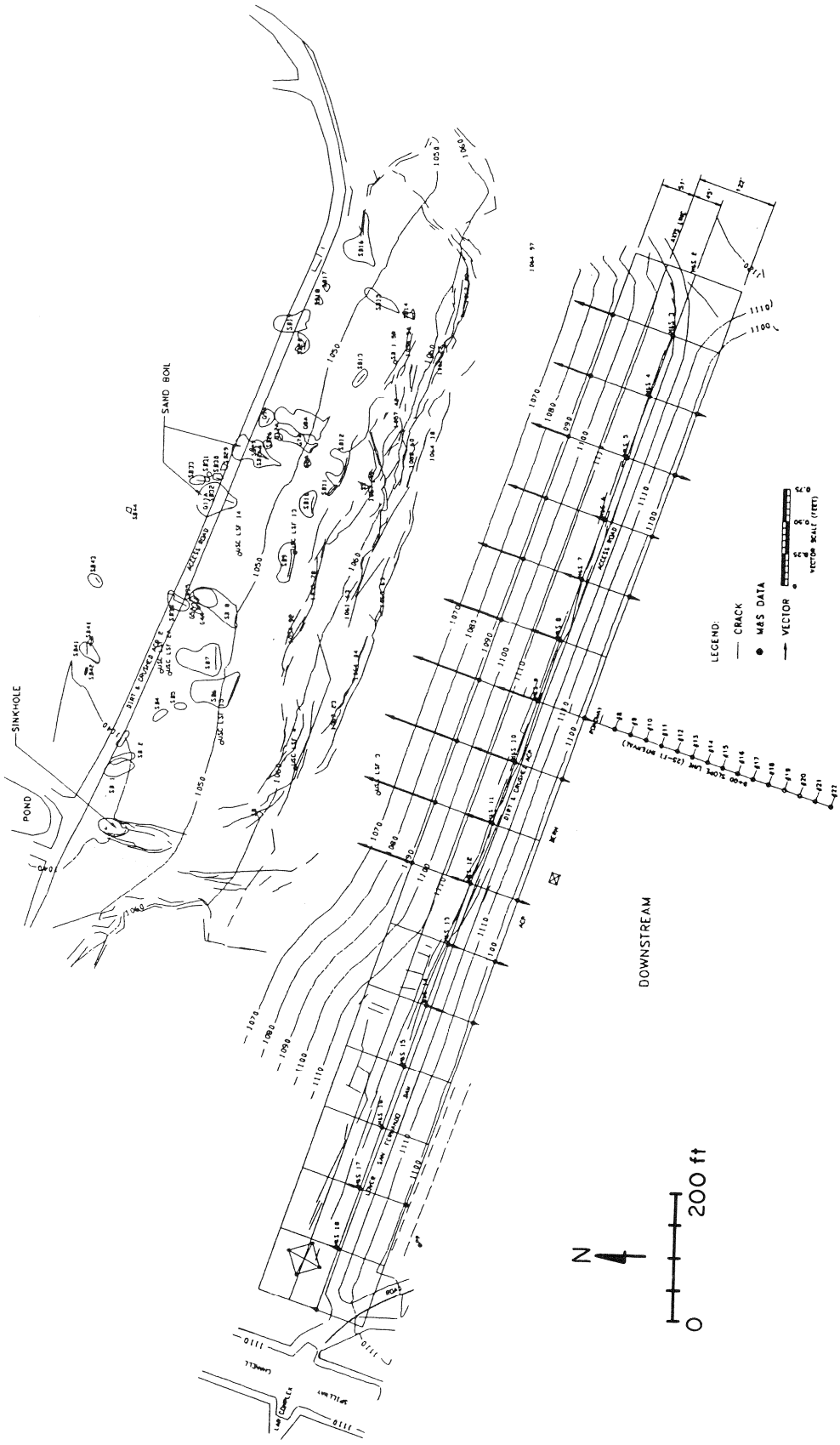

Figure 6. Location of cracks, sand boils, and displacement vectors in Lower San Fernando Dam.

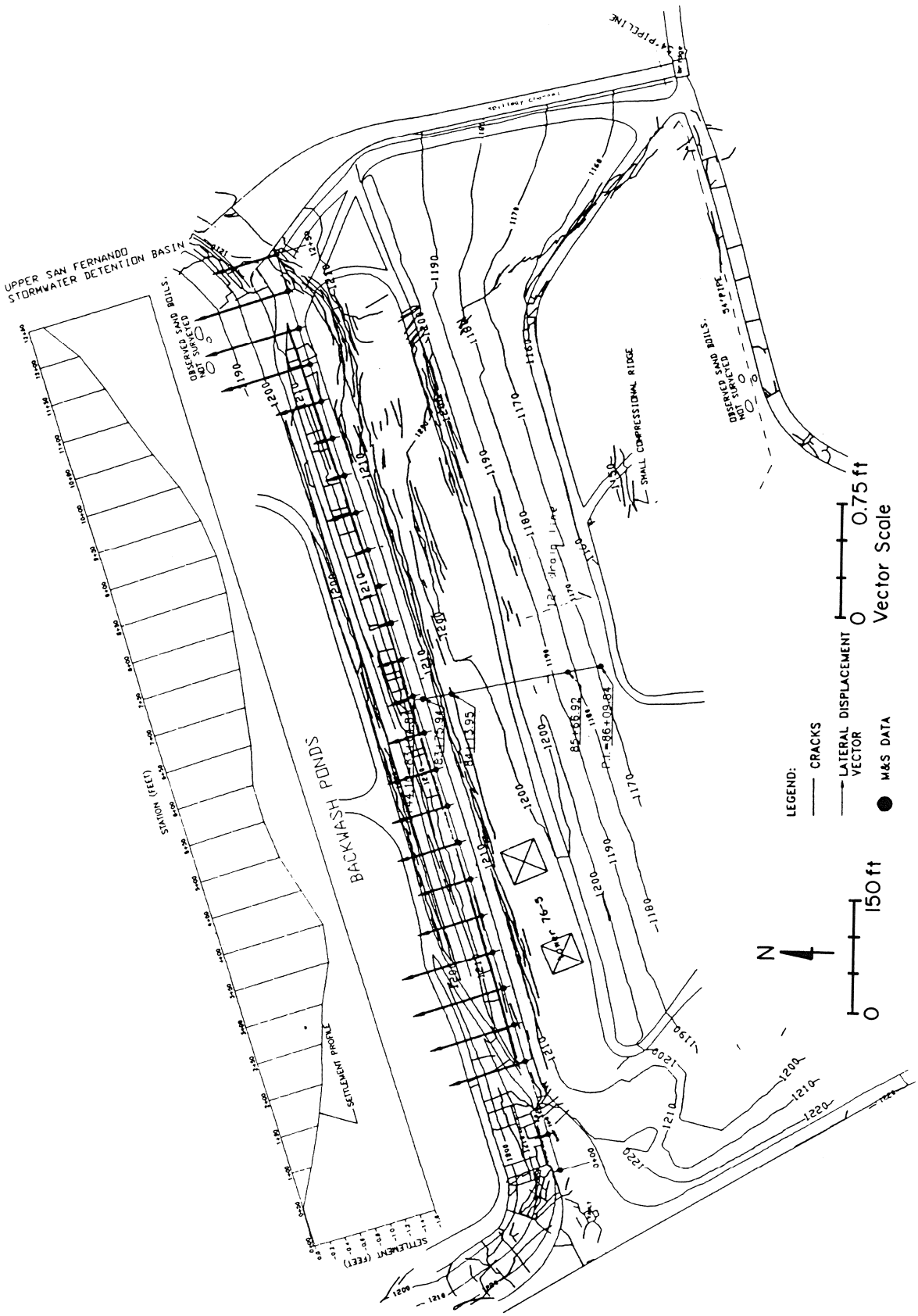

Figure 7. Location of cracks, sand boils, and displacement vectors in Upper San Fernando Dam.

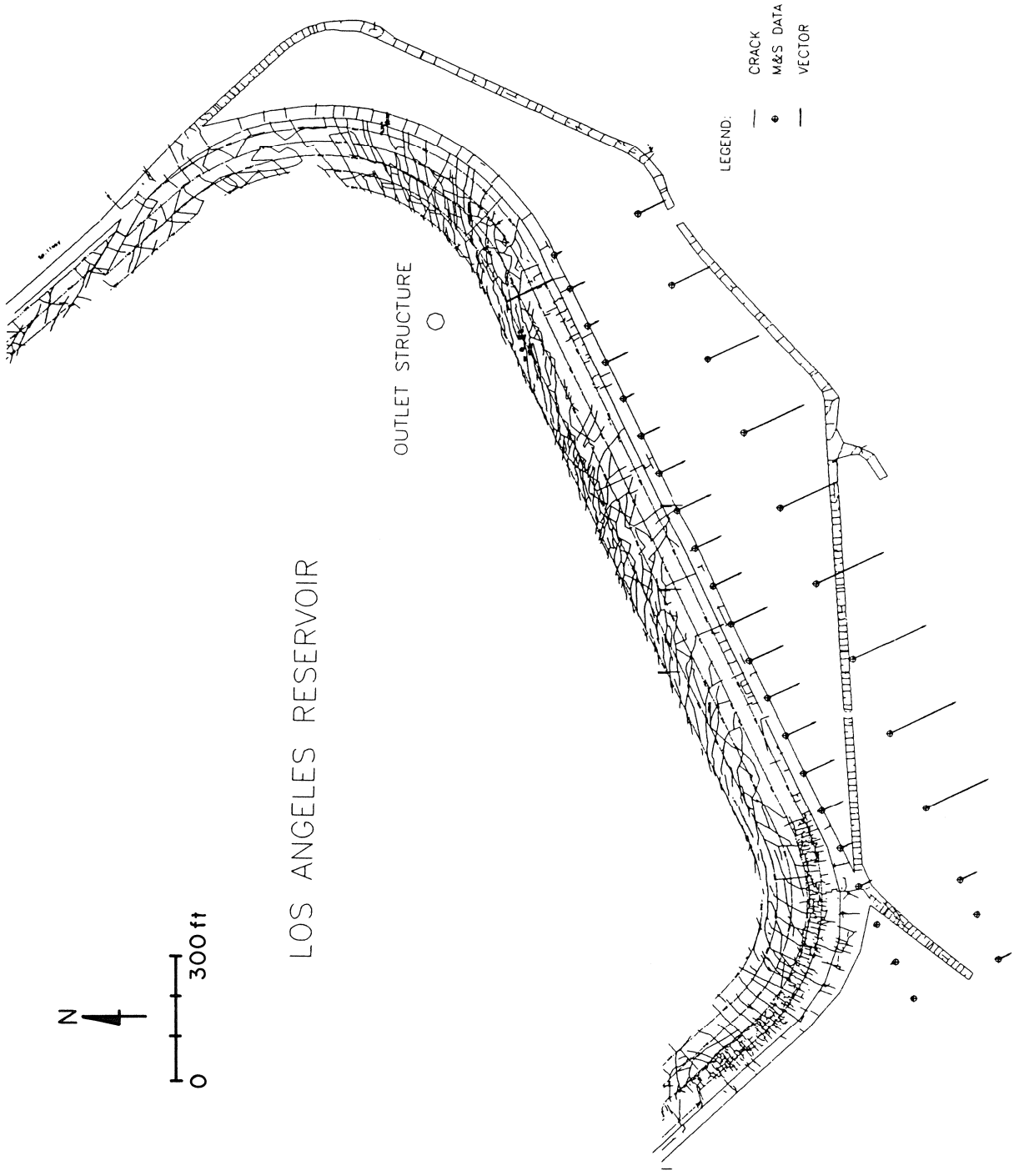

Figure 8. Location of cracks in Los Angeles Resevoir Dam.

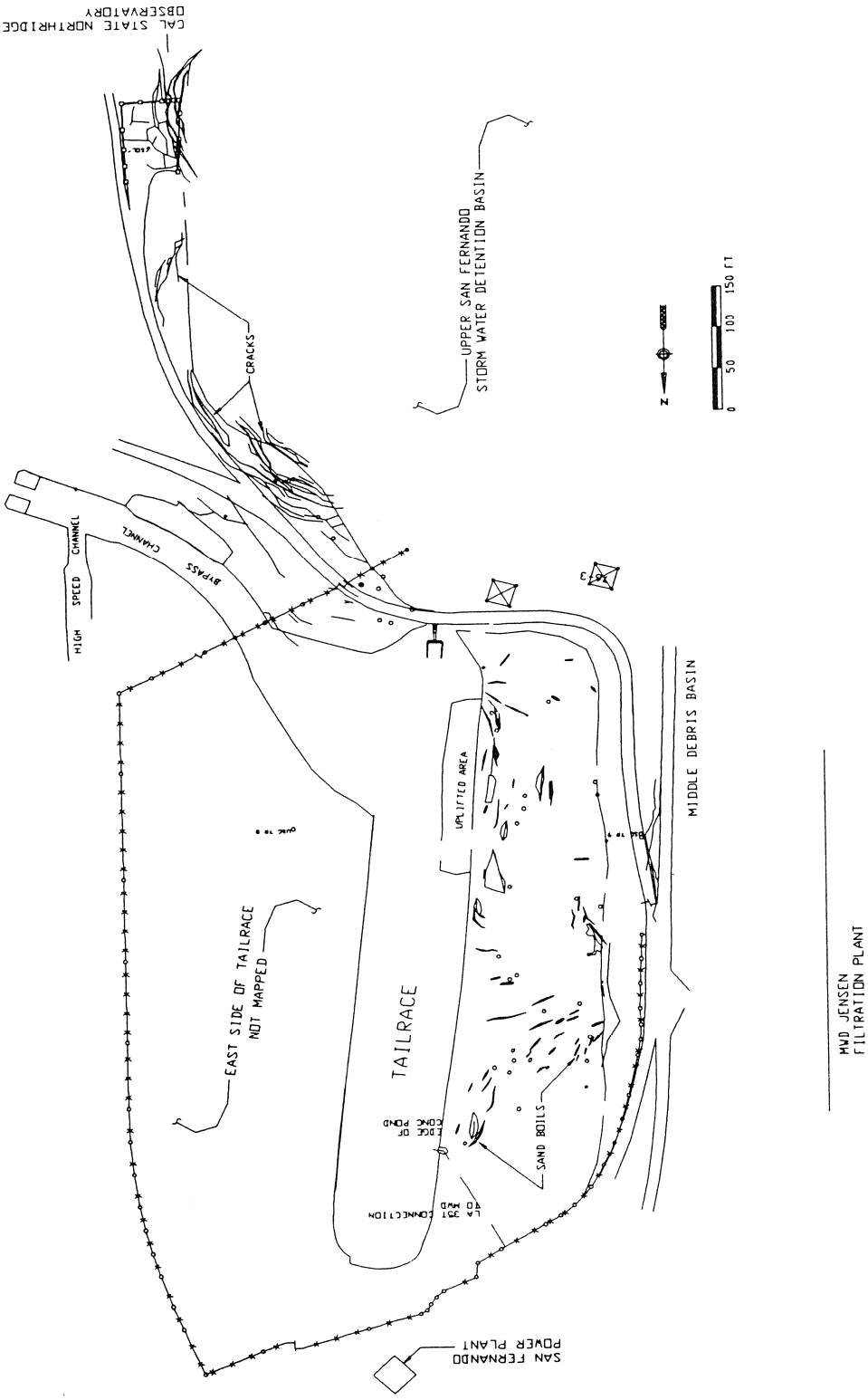

Figure 9. Location of cracks and sand boils in the vicinity of Power Plant Tailrace.

OBSERVED AND PREDICTED GROUND DEFORMATION - MILLER FARM LATERAL SPREAD, WATSONVILLE, CALIFORNIA

Thomas L. Holzer, John C. Tinsley, III, Michael J. Bennett, and Charles S. Mueller

U.S. Geological Survey
345 Middlefield Road
Menlo Park, CA 94025

ABSTRACT

Following the 1989 Loma Prieta, California, earthquake, ground deformation and subsurface conditions were carefully mapped and documented at the east end of a 1.7-km-long lateral spread south of the Pajaro River near Watsonville, California. The lateral spread occurred in natural floodplain deposits that fill a former river channel. Penetration data from geotechnical soundings and correlations of median grain size of sand boils with potential source beds at the east end of the spread indicate that a 6.1-m-thick layer, 4.6 m below the land surface, liquefied. Horizontal extension across ground cracks in the study area ranged from 117 to 160 mm. Settlements ranged from 50 to 240 mm. Empirical predictions of horizontal displacements overpredict observed displacements. Empirical predictions of vertical displacements underpredict observed settlements. We conclude that the lateral spread was a deformation failure, which resulted from transient inertial forces, as contrasted with a flow failure. We also devise a test to establish the maximum displacement by a deformation failure mechanism.

INTRODUCTION

Prediction of horizontal displacement associated with liquefaction poses a significant engineering challenge. Progress has been slowed by uncertainty about potential mechanisms of lateral spreading and a shortage of well-documented field examples. The National Research Council (1985) proposed two mechanisms of lateral spreading: flow and deformation failures. Flow failure occurs by continuous deformation when static gravitational forces exceed the strength of the soil after the strength has been degraded by cyclic loading or pore pressure increase. Deformation failure occurs incrementally when the combined earthquake-induced cyclic and free-field stresses momentarily exceed the resistive strength of the soil mass. The potential for deformation failure is enhanced when liquefaction decouples the surficial soil layer from the underlying nonliquefied soil. As a result of the uncertainty about failure mechanisms, current efforts to predict ground deformation have emphasized case histories and empirical correlations of displacement with site characteristics.

The purposes of this study are: (1) to describe ground deformation within part of a lateral spread that was caused by the October 17, 1989, Loma Prieta, California, earthquake (moment magnitude 6.9), and (2) to compare observed deformation to that predicted by conventional geotechnical methods. The spread, which was near Watsonville, California (Fig. 1), was one of more than 47 lateral spreads that were caused by the Loma Prieta earthquake in the region south of the epicenter (Tinsley and Dupré, 1992). It occurred in floodplain deposits near the Pajaro River. Ground deformation was well exposed in agricultural fields. Following the earthquake, we measured vertical offsets and openings across cracks and surveyed the post-earthquake topography of part of the lateral spread. Comparison of the pre- and post-earthquake topography permitted computation of settlements. In addition, we did 25 cone penetration tests (CPT) and 11 standard penetration test (SPT) borings to characterize the geologic setting and the geotechnical properties of underlying deposits.

LATERAL SPREADING

The lateral spread that we investigated was near the Pajaro River (Fig. 1). South of the river, an approximately 0.2-m-high head scarp could be followed for 1.7 km. The scarp, which undulated in map view, roughly paralleled the river channel. The scarp extended approximately 200 m from the channel, and intersected the channel at its western and eastern ends. Maximum horizontal displacement was approximately 300 mm just west of the study area. Lateral spreading also occurred on the north side of the river, but the head scarp was discontinuous; maximum horizontal displacement there was also approximately 300 mm. Ground deformation on both sides of the river was restricted to the floodplain that is now protected from flooding by man-made flood-control levees. The channelward sense of displacement across the head scarps suggested that lateral spreading on both sides of the river was toward the modern river channel, but nowhere did we see the toe of the lateral spread. Compression of two river bridges, however, suggested that lateral deformation extended into the channel area. The regional downstream slope of the floodplain inferred from the USGS Watsonville East 7½' quadrangle was approximately 0.1 per cent, but land slopes within the floodplain are substantially modified by regrading for irrigation. Before the earthquake, some fields that were subsequently damaged by the lateral spread gently sloped toward the river whereas others sloped away from the river.

Sand boils provided direct evidence of liquefaction. At the eastern end of the lateral spread south of the river, the focus of our investigation, sand boils were restricted to the area affected by lateral spreading. At the western end of the lateral spread, sand boils vented south of, and outside, the head scarp of the lateral spread. Eyewitnesses reported that sediment-laden water flowed gently from vents on the lateral spread during the earthquake and continued to flow for 10 to 20 minutes after the earthquake.

Our investigation concentrated on the eastern end of the lateral spread with particular emphasis on the south side of the river at Clint Miller Farms. This area will be referred to herein as Miller Farm. We also conducted a less extensive investigation on the north side of the river across from Miller Farm. This area will be referred to as Farris Farm.

GEOLOGY

Before construction of flood control levees next to the Pajaro River, flooding deposited a complex interbedded sequence of fluvial deposits. Two Holocene fluvial deposits, older flood-plain deposits (Q_{of}) and younger flood-plain deposits (Q_{yf}) (Fig. 1), which are distinguished primarily based on soil development and geomorphic and stratigraphic position, were mapped in the area (Dupré and Tinsley, 1980). Areas underlain by younger flood-plain deposits are commonly topographically lower and subject to more frequent flooding than areas underlain by older flood-plain deposits.

Lateral spreading at both Farris and Miller Farms was restricted to the area underlain by the younger flood-plain deposits. In fact, the head scarp coincided with the mapped contact between the younger and older flood-plain deposits (Tinsley and Dupré, 1992). The younger flood-plain deposits fill an old river channel. The base of the younger flood-plain deposits consists primarily of point bar and channel sands. This is illustrated in Figure 2, which shows in map view the percentage of the total section in the depth interval from 4.6 to 9.1 m that consists of sand layers at each of our soundings. Sand layers were identified in CPT soundings based on friction ratio (<0.5%) and tip resistance (>3 MN/m^2). As will be described in the section on liquefaction susceptibility, this interval includes most of the zone that liquefied during the Loma Prieta earthquake. Sand-layer percentages in this depth interval in the area underlain by the younger flood-plain deposits range from 67 to 100%, whereas sand-layer percentages in the area underlain by the older flood-plain deposits range from 0 to 27%. Sand in the sandy layers of the younger flood-plain deposits coarsens downward, increasing from fine to medium grained (Fig. 3). Average fines content of the sandy layers is 15%, but ranges from 22% at Miller Farm to 8% at Farris Farm. The older flood-plain deposits are predominantly clay and silt.

The upper 4.6 m of the younger flood-plain deposits is silty and generally contains only a few thin sand layers. Sand-layer percentages in this interval are shown in Figure 2 and range from 0 to 100. There also is an areal variation in the presence of sand layers in the upper interval. Sand-layer percentages in the upper 4.6 m are higher at Miller Farm than at Farris Farm.

The contact between the older and younger flood-plain deposits is sharp and presumably is erosional in origin. The sharpness of the contact can be seen vertically in most CPT soundings and also can be inferred laterally by comparing closely spaced CPT soundings that span the contact as mapped at the surface (Fig. 4). Soundings 2 and 3, which span the contact south of the river, are 79 m apart; soundings 61 and 62, which span the contact on the north side of the river, are 46 m apart. In soundings 3 and 61, which are in the area underlain by younger flood-plain deposits, an abrupt change in stratigraphy occurs at depths of 8.5 and 10.2 m, respectively. Above these depths, a thick sand body, which has a decreasing upward CPT tip resistance, is identifiable. The underlying sequence consists of finely interbedded deposits.

The buried channel is shown in cross section in Figure 5. The thickness of the younger flood-plain deposits varies, but may be as large as 14.5 m at sounding 6 (Fig. 1). The base of the younger flood-plain deposits as inferred from individual soundings at some locations was not clearcut. The underlying older flood-plain deposits locally contain sandy facies that cannot always be texturally distinguished from sands in the younger deposits. Thus, the contact that we identified in the soundings as the boundary between older and younger flood-plain deposits is provisional pending the availability of age dates for these units.

The depth to the water table was 4.6 m 10 days after the mainshock in a hand-augered boring. Most of our geotechnical soundings were conducted the following spring and yielded comparable water depths. The Pajaro River channel was dry during this period because of drought conditions. The water table at the site is probably controlled by river stage.

MAINSHOCK GROUND MOTION

The closest strong motion accelerograph that recorded the Loma Prieta earthquake mainshock is in a four-story building in Watsonville (Fig. 6). The building is 1 km west of Miller Farm and is instrumented with 13 accelerometers (See insert in Fig. 1). Peak horizontal ground-level acceleration recorded in the building was 0.39 g (Shakal and others, 1989). Strong ground shaking lasted for approximately 6 seconds. Comparison of aftershock recordings from portable instruments on the lateral spread south of the river and in the building indicates that site response on the lateral spread is similar to that at the Watsonville building location. The building sits on older flood-plain deposits outside the area that liquefied. Although the Watsonville building recording is not free field, the building is square and rests on a spread footing which suggests that soil-structure interaction probably did not greatly affect the ground-level recording (C.B. Crouse, oral commun., 1994). In addition, the mainshock ground-level peak acceleration in the building is near the median value of free-field sites on similar soils that recorded the Loma Prieta earthquake at comparable distance. A comparison of roof- and ground-level records suggests that the building is excited at 3 Hz (M. Çelebi, written commun., 1994). The ground-level peak acceleration occurs at approximately 4 Hz. The comparison also indicates that the building does not affect ground-level shaking at frequencies less than 2 Hz, which control ground displacement. Thus, we assume that the Watsonville recording closely approximates mainshock ground motion at Miller Farm.

LIQUEFACTION SUSCEPTIBILITY

The sand deposits, which fill the old channel, are heterogeneous. Corrected blow counts, $(N_1)_{60}$, vary from 7 to 28 and increase with depth. Average values for both Miller and Farris Farms are shown in Table 1. Liquefaction resistance as a function of depth beneath the lateral spread is shown in Figure 7. Both induced cyclic stress ratio and liquefaction resistance, which was determined from SPT blow counts, were computed using the simplified procedure (Seed and others, 1985). Comparison of induced cyclic stress ratios to liquefaction resistance indicates that liquefaction occurred primarily in the 6.1-m-thick sand interval from 4.6 to approximately 10.7 m. Below 10.7 m, the overall liquefaction resistance is higher although SPT tests indicate some liquefaction may have occurred below 10.7 m. The interval that is inferred to have been the primary zone of liquefaction also is consistent with the sand boils that vented at Miller Farm. The median grain sizes, d_{50}, of sand boils are shown as inverted triangles on the abscissa in Figure 3. The d_{50}'s of sand boils and the samples from the deposit from 4.6 to 10.7 m are comparable. The larger d_{50}'s of the sands below 10.7 m appear to preclude that sand boils originated from the

deeper part of the deposit.

Although sand boils and ground deformation were restricted to the area underlain by the younger flood-plain deposits, low blow counts in sandy parts of older flood-plain deposits indicate that some parts of it may have liquefied. The thinness and small number of sand layers within the area of older flood-plain deposits at Miller and Farris Farms may have masked surface manifestations of liquefaction if these layers did indeed liquefy.

OBSERVED GROUND DEFORMATION

Horizontal displacements of the land surface at Miller and Farris Farms were measured by summing openings across cracks near head scarps. Horizontal displacements measured in two profiles across the head scarp at Miller Farm were 117 and 160 mm. The profile that yielded 117 mm of horizontal displacement across the head scarp is shown in Figure 8. We also measured 454 mm of extension in this profile across the levee south of the river. We assume, however, that this extension was associated with a bearing capacity failure of the levee as it settled into underlying liquefied soil. Scarps in the levee faced inward toward the crown of the levee (Fig. 8). Extension across one crack at Farris Farm equalled 300 mm, but most of the ground cracking at Farris was affected by a bearing capacity failure of the levee on the north side of the river.

Changes of elevation of the land surface above the lateral spread at Miller Farm were estimated by comparing post- and pre-earthquake topography. Losses of elevation ranging from 50 to 240 mm are estimated in the area affected by lateral spreading (Fig. 9). The profiles indicate that the loss in surface elevation extended over the whole body of the lateral spread, but was greatest in a 30-m-wide zone at the base of the head scarp.

The post-earthquake topography was surveyed in the eastern part of the study area with a combined electronic precision theodolite and electronic distance meter. Pre-earthquake topography was computed from grading specifications provided by the land owner (Fig. 1). Before the earthquake, fields had been carefully graded for irrigation purposes by a laser-controlled grading system. The system can produce gradients at 0.02m/1000m in precision in fine-textured loose soil. To estimate pre-earthquake topography in the area affected by lateral spreading, we projected the land slope determined from grading specifications into the disturbed area from the unaffected area south of the head scarp. Note that the measured post-earthquake land slope in the undisturbed area compares favorably to the pre-earthquake graded slope reported by the landowner (Fig. 9).

PREDICTED GROUND DEFORMATION

Horizontal Displacements

Several empirical methods have been proposed to predict horizontal displacements associated with lateral spreading. The most straightforward method, because it does not involve

site characterization, is described by Youd and Perkins (1987) who proposed a Liquefaction Severity Index (LSI) that provides an upper bound to horizontal displacements on fluvial sites. LSI is predicted only by earthquake moment magnitude (M_W) and distance from the fault (R).

$$\log (LSI) = - 3.49 - 1.86 \log R + 0.98 M_W \quad (1)$$

Hamada and others (1986) used observations of lateral spreading in two earthquakes in Japan to develop a correlation between displacements (D) and thickness of the liquefied interval (H) and average slope (θ).

$$D = 0.75 H^{0.50} \theta^{0.33} \quad (2)$$

Hamada (1992) and Pease and O'Rourke (1993) concluded that the best predictor of displacement is liquefied thickness. Including slope did not materially improve their predictions. Pease and O'Rourke (1993) derived the following regression for displacement with liquefied thickness (H) of fills for the 1906 San Francisco, California, earthquake, which they estimated had a peak acceleration, 0.4 g, comparable to Miller Farm.

$$D = 0.32 H + 0.14 \quad (3)$$

Bartlett and Youd (1992) compiled case histories of lateral spreads in earthquakes in Japan and the United States. They correlated displacements (D) with earthquake moment magnitude (M_W), horizontal distance to seismic source zone (R), slope (θ) or the ratio of the height of the free face to the distance of lateral spreading from the free face (W), and the thickness (H), average fines content (F), and median grain size (d_{50}) of the interval with $(N_1)_{60}<15$.

For a free face:

$$\log (D+0.01) = -16.366 + 1.178 M_W - 0.927 \log R - 0.013 R + 0.657 \log W + 0.348 \log H + 4.527 \log (100 - F) - 0.922 d_{50} \quad (4)$$

For sloping ground:

$$\log (D+0.01) = -15.787 + 1.178 M_W - 0.927 \log R - 0.013 R + 0.429 \log \theta + 0.348 \log H + 4.527 \log (100 - F) - 0.922 d_{50} \quad (5)$$

Horizontal displacements predicted by equations (1) to (5) are shown in Table 2. All of the predictive methods overestimate observed displacements at Miller Farm.

Changes of Elevation

We used the simplified method of Tokimatsu and Seed (1987) to predict settlement from post-liquefaction consolidation at 3 SPT/CPT locations at Miller Farm (Table 3). Unfortunately,

only one SPT/CPT sounding, no. 5, is within the area of the post-earthquake topographic survey. Thus, a direct comparison only can be made at this location. At this location where 100 mm of settlement was observed, we predict only 25 mm of settlement. The other borings, although on the lateral spread, are only useful for predicting the general magnitude of settlement. Predicted settlements at Miller Farm ranged from 20 to 80 mm.

The method uses induced cyclic stress ratio and $(N_1)_{60}$ to predict post-liquefaction strain. Settlement is estimated by multiplying the predicted strain by sand-layer thickness, which we determined from the CPT sounding. Because the method was developed for clean sands, a correction should be applied to account for the effect of fines in diminishing post-liquefaction consolidation. Following the procedure suggested by O'Rourke and others (1991), we increased $(N_1)_{60}$ to account for the influence of fines content. Predicted settlements for both clean sand and sand with corrections for fines content are shown in Table 3.

MECHANISM OF HORIZONTAL GROUND DEFORMATION

Because horizontal displacements were small and the boundary between younger and older flood-plain deposits may be sharp and nearly vertical, we considered the possibility that the observed horizontal displacements were caused by differential vertical displacement at depth. By this mechanism, surficial horizontal displacements were caused by bending of the overburden when differential post-liquefaction consolidation occurred beneath the overburden and across the nearly vertical boundary between the liquefied and nonliquefied zones. No horizontal deformation in the liquefied zone was assumed. We analyzed this mechanism by treating the overburden as an elastic beam subject to differential displacements along its base. Lee and Shen (1969) proposed that horizontal displacement (D) can be estimated by:

$$D = \tfrac{2}{3} T \alpha \qquad (6)$$

where T is the thickness of the overburden and α is the change in slope of the land surface. For a T = 4.6 m and a change in slope of approximately 0.0083 (Fig. 9), equation (6) predicts only about 25 mm of horizontal displacement, which is 16-21% of the observed displacement. Thus, we conclude that horizontal deformation within the liquefied zone was the primary cause of horizontal surface displacement.

A flow failure mechanism for the lateral spread is inconsistent with the pre-earthquake land slopes at Miller Farm provided by the land owner. Land in the western part of the Miller Farm portion of the lateral spread sloped at 0.264% away from the river (Fig. 1). If this slope is valid, and we have no evidence to the contrary, the western part of the lateral spread should have moved away from the channel. Field observations indicated that displacement was channelward. The eyewitness accounts of continued venting from sand boils after the earthquake also are inconsistent with a flow failure. Continued venting implies pore pressures remained elevated which are conducive to large ground displacements.

We also considered the possibility that the flow failure was driven by static stresses associated with the topographic relief of the river channel. When the lateral spread is examined at true scale (Fig. 5B), however, it is unlikely that these stresses would be significant as far away

from the channel as the head scarp. Thus, a progressive failure would be required for these stresses to be the cause of the flow failure. Such a failure is not supported by the field observations that indicated the block remained essentially intact.

To evaluate the feasibility of a deformation failure, we performed a Newmark (1965) sliding block analysis using the Watsonville strong ground motion record for loading. We assumed the failure surface was in the upper part of the liquefied zone because blow counts are lower in this zone and most of the sand boils appear to have been derived from this zone (Fig. 3). A deeper sliding surface also would involve passive resistance of soil beneath the river channel (Fig. 5) which would imply that failure is not occurring on the plane of least resistance. Back-calculated residual strengths for such a failure ranged from 7 to 9 kPa for failure surfaces with slopes ranging from 0.05 to 0.7 degrees. These values of residual strength are consistent with residual strengths inferred from observed corrected blow counts using the correlation by Seed and Harder (1990).

Because both the failure surface and the residual strength of the liquefied soil were uncertain, we devised a method to estimate the maximum possible permanent displacement in a deformation failure. The method requires a nearby strong motion record. The method rests on the assumption that the mechanism for deformation failure is that the lateral spread behaves as a block that is detached from the underlying soil by the liquefied zone and can only move relative to the failure surface in the downslope direction. During cyclic loading, the block cannot keep pace with the underlying soil during upslope dynamic displacements because of the reduction in strength along its base. Hence, relative, but permanent, downslope displacement occurs. During downslope dynamic displacements, the block and underlying soil move together and no relative displacement occurs. The maximum permanent ground deformation then is the summation of the peak-to-peak displacements, calculated by double integration of the acceleration time history, in the upslope direction (Fig. 6). For the Watsonville record, the sum of the peak-to-peak displacements in the southeast direction is 1,156 mm, which is approximately 7 times the observed permanent displacement at Miller Farm, 160 mm, and 3 times the maximum observed displacement on the spread, 300 mm. This implies that ground displacements during the mainshock were large enough to cause the observed permanent horizontal displacements by a sliding block model.

SURFACE MANIFESTATIONS OF LIQUEFACTION

Our observations at Miller and Farris Farms are consistent with the compilation by Ishihara (1985) that describes the conditions under which surface damage from liquefaction is observed. Ishihara (1985) correlated thicknesses of the liquefied layer with the nonliquefied surface layer for areas with and without surface effects for different accelerations. The data point for both farms falls well within the part of his graph where surface manifestations of liquefaction are observed (Fig. 10).

CONCLUSIONS

The 1.7-km-long Miller Farm lateral spread was the largest lateral spread caused by the Loma Prieta earthquake. Empirical methods for predicting horizontal displacement overestimate observed displacements by as much as an order of magnitude. The best predictions are by Bartlett and Youd (1992). Settlements are underestimated by empirical methods. Observed displacements and soil properties are consistent with an inertial deformation failure mechanism. A flow failure mechanism is unlikely because the ground moved opposite to land slope in parts of the lateral spread.

ACKNOWLEDGMENTS

We gratefully acknowledge the help of the following people and organizations that made this investigation possible. Clint Miller Farms and the family of Marie K. Farris permitted access to the land on which we worked. Granite Construction Company and Pacific Bell allowed us to locate portable seismographs at their facilities. J. Hamilton conducted the post-earthquake survey at Miller Farm. C. Criley assisted in drilling and analyzing SPT samples. S.D. Ellen and K.H. Chang measured the profile of ground displacements across the lateral spread. The California Strong Motion Instrumentation Program provided the Watsonville accelerograms. S. Toprak and T.D. O'Rourke performed the Newmark analysis. M. G. Bonilla and R.E. Kayen reviewed drafts of the manuscript. We particularly appreciate the insightful discussions about the Newmark analysis with T.D. O'Rourke, M. Palmer, J. Pease, and H.E. Stewart.

REFERENCES

Bartlett, S. F., and Youd, T. L., 1992, Empirical prediction of lateral spread displacement, *in* Proceedings, 4th U.S.-Japan workshop on earthquake resistant design of lifeline facilities and countermeasures for soil liquefaction, NCEER-92-0019, National Center for Earthquake Engineering Research, Buffalo, p. 351-363.

Dupré, W. R., and Tinsley, J. C., III, 1980, Maps showing geology and liquefaction potential of northern Monterey and southern Santa Cruz Counties, California: U.S. Geological Survey, Miscellaneous Field Studies Map MF-1199 (scale 1:62,500).

Hamada, M., 1992, Large ground displacements and their effects on lifelines - 1964 Niigata earthquake *in* Case Histories of Liquefaction and Lifeline Performance during past Earthquakes: v. 1: Japanese Case Studies, M. Hamada and T.D. O'Rourke, eds., NCEER-92-0001, National Center for Earthquake Engineering Research, Buffalo, p. 3-1 to 3-123.

Hamada, M., Yasuda, S., Isoyama, R., and Emoto, K., 1986, Study of liquefaction induced permanent ground displacements: Association for the Development of Earthquake Prediction, Tokyo, 87 p.

Ishihara, K., 1985, Stability of natural deposits during earthquakes, *in* 11th International Conference on Soil Mechanics and Foundation Engineering, San Francisco, p. 321-376.

Lee, K. L., and Shen, C. K., 1969, Horizontal movements related to subsidence: Journal of Geotechnical Engineering, ASCE, v. 95, no. 1, p. 139-166.

National Research Council, 1985, Liquefaction of soils during earthquakes: National Academy Press, Washington, D.C., 240 p.

Newmark, N. M., 1965, Effects of earthquakes on dams and embankments: Geotechnique, v. 15, p. 139-159.

O'Rourke, T. D., Gowdy, T. E., Stewart, H. E., and Pease, J. W., 1991, Lifeline performance and ground deformation in the Marina during 1989 Loma Prieta earthquake, *in* Proceedings, 3rd U.S.-Japan workshop on earthquake resistant design of lifeline facilities and countermeasures for soil liquefaction, NCEER-91-0001, National Center for Earthquake Engineering, Buffalo, p. 129-146.

Pease, J. W., and O'Rourke, T. D., 1993, Liquefaction hazards in the Mission District and South of Market Street areas, San Francisco, California: U.S. Geological Survey, External Contract No. 14-08-0001-G2128.

Seed, H. B., Tokimatsu, K., Harder, L. F., and Chung, R. M., 1985, Influence of SPT procedures in soil liquefaction resistance evaluation: Journal of Geotechnical Engineering, ASCE, v. 111, no. 12, p. 1425-1445.

Seed, R. B., and Harder, L. F., Jr., 1990, SPT-based analysis of cyclic pore pressure generation and undrained residual strength, *in* Duncan, J. M., ed., H. Bolton Seed: Vancouver, B.C., BiTech Publishers Limited, p. 351-376.

Shakal, A., Huang, M., Reichle, M., Ventura, C., Cao, T., Sherburne, R., Savage, M., Darragh, R., and Petersen, C., 1989, CSMIP strong-motion records from the Santa Cruz Mountains (Loma Prieta), California earthquake of 17 October 1989: California Strong Motion Instrumentation Program Report no. OSMS 89-06, p. 57.

Tinsley, J. C., III, and Dupré, W. R., 1992, Liquefaction hazard mapping, depositional facies, and lateral spreading ground failure in the Monterey Bay area during the 10/17/89 Loma Prieta earthquake, *in* Proceedings, 4th U.S.-Japan workshop on earthquake resistant design of lifeline facilities and countermeasures for soil liquefaction, NCEER-92-0019, National Center for Earthquake Engineering Research, Buffalo, p. 71-85.

Tokimatsu, K., and Seed, H. B., 1987, Evaluation of settlements in sand due to earthquake shaking: Journal of Geotechnical Engineering, ASCE, v. 113, no. 8, p. 861-878.

Youd, T. L., and Perkins, D. M., 1987, Mapping of liquefaction severity index: Journal of Geotechnical Engineering, ASCE, v. 113, no. 11, p. 1374-1392.

Table 1. Geotechnical properties of liquefied layer

Property	Miller Farm	Farris Farm	Combined
Thickness	6.1 m	6.1 m	6.1 m
Fines content	22 %	8 %	15 %
d_{50}	0.16 mm	0.21 mm	0.19 mm
$(N_1)_{60}$	14±7	18±6	16±7

Table 2. Predicted and observed horizontal displacements

Method	Displacement, mm
Hamada and others (1986)	1,040
Pease and O'Rourke (1993)	2,120
Youd and Perkins (1987)	990
Bartlett and Youd (1992)	
Free face	600
Sloping ground	540
Observed	**117 to 160**

Table 3. Predicted settlements

Sounding	Sand layer thickness, m	Predicted Settlement, mm		**Observed Settlement, mm**
		Clean sand	Fines corrected	
3	2.0	30	20	
5	5.2	61	25	**100**
8	6.2	113	80	

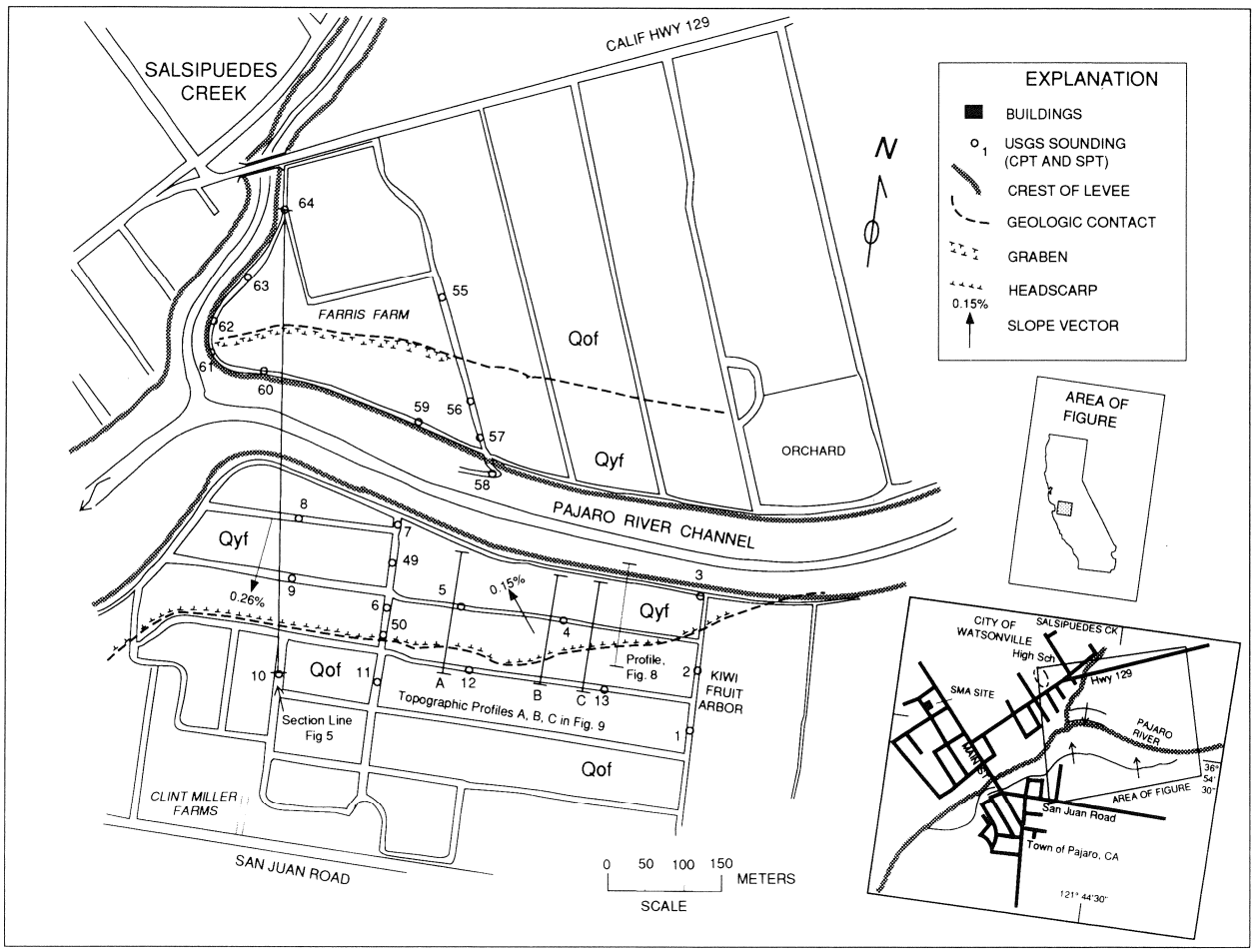

Fig. 1 Map of Miller and Farris Farms showing the lateral spread and locations of soundings and profiles. Arrows at Miller Farm indicate pre-earthquake slope from grading specifications reported by landowner. Map units Q_{yf} and Q_{of} are younger and older flood-plain deposits, respectively (Dupré and Tinsley, 1980).

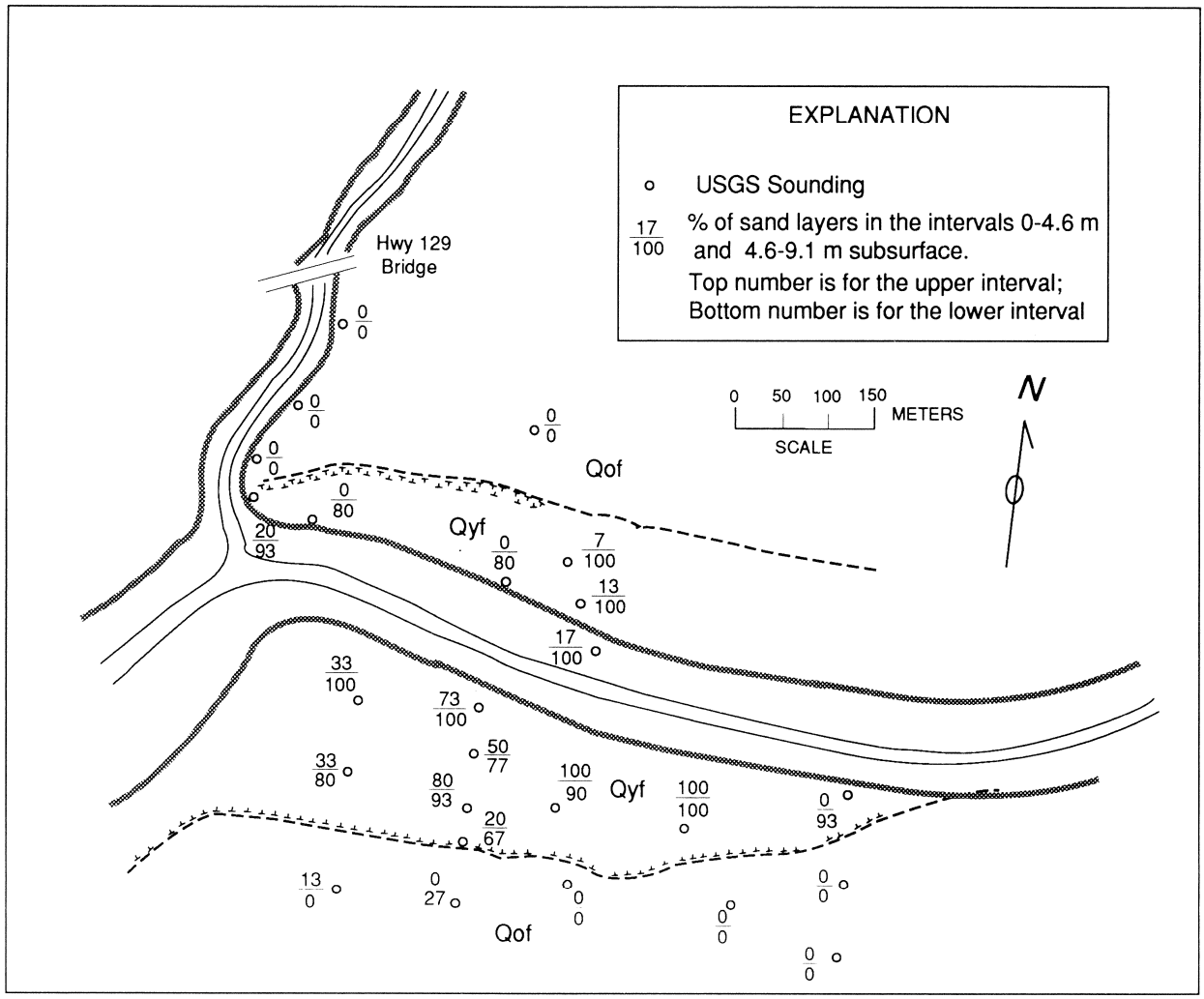

Fig. 2 Map of sandy layers as a percentage of interval thickness for depth intervals 0 to 4.6 m and 4.6 to 9.1 m. Upper and lower values are for upper and lower depth intervals, respectively.

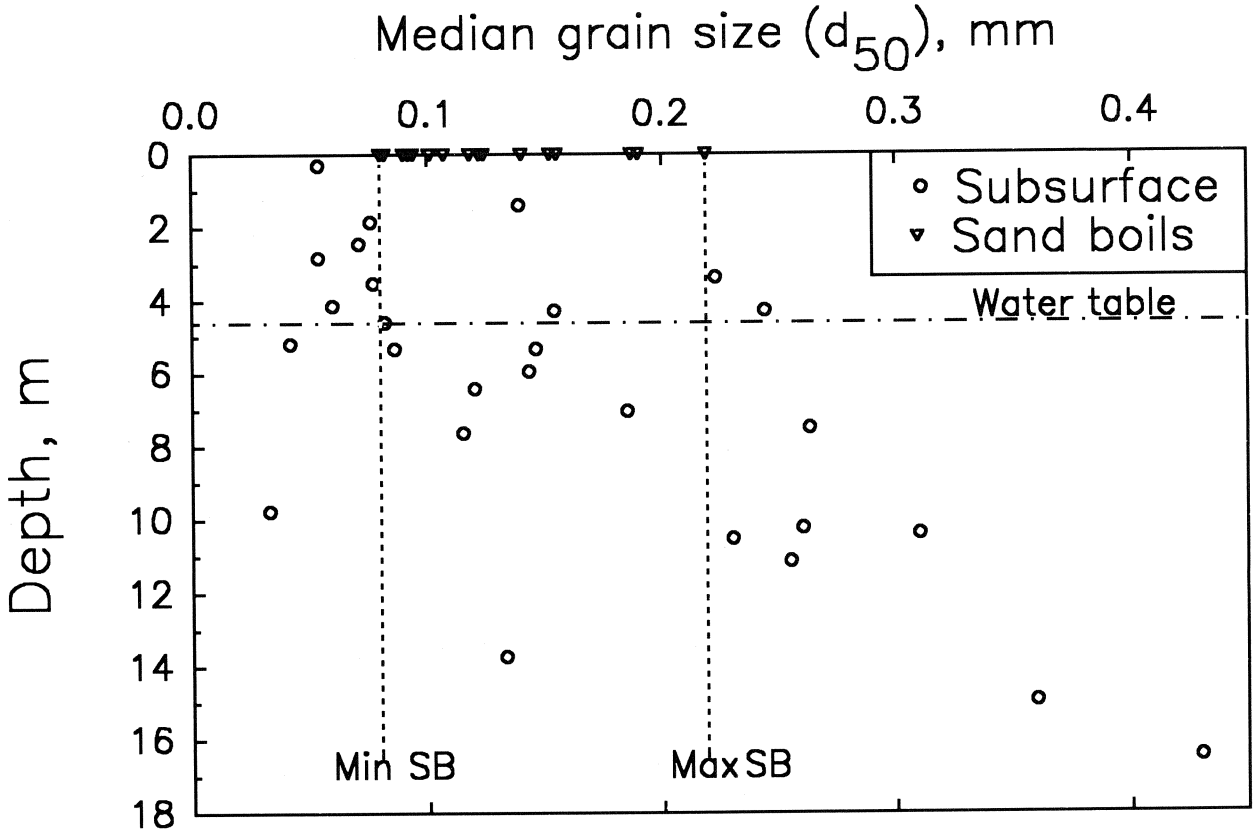

Fig. 3 Median grain size, d_{50}, as function of depth for Miller Farm. Inverted triangles show d_{50} of sand boils. Min SB and Max SB are the minimum and maximum d_{50} of sand boils, respectively.

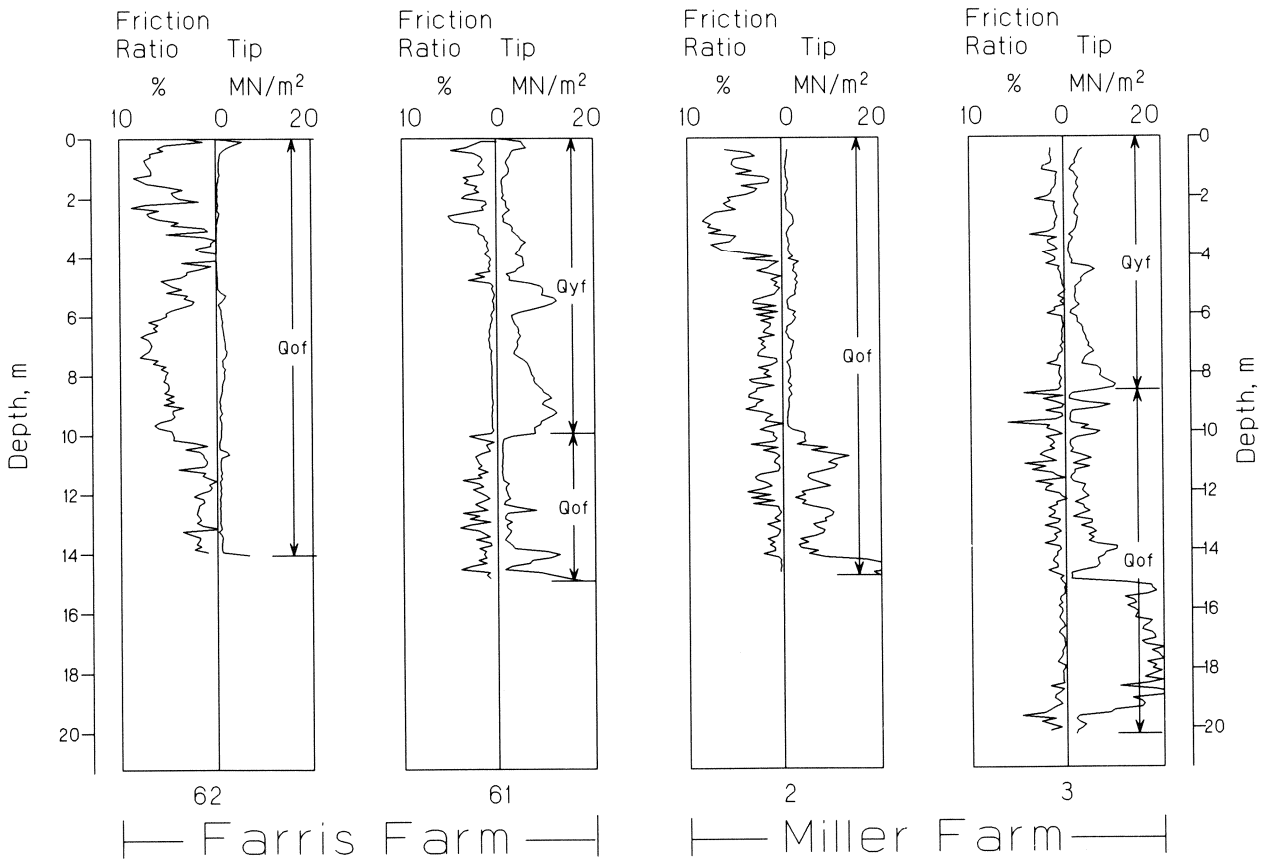

Fig. 4 Comparison of closely spaced cone penetration tests that straddle the contact between older (Q_{of}) and younger (Q_{yf}) flood-plain deposits at Farris and Miller Farms. See Figure 1 for locations.

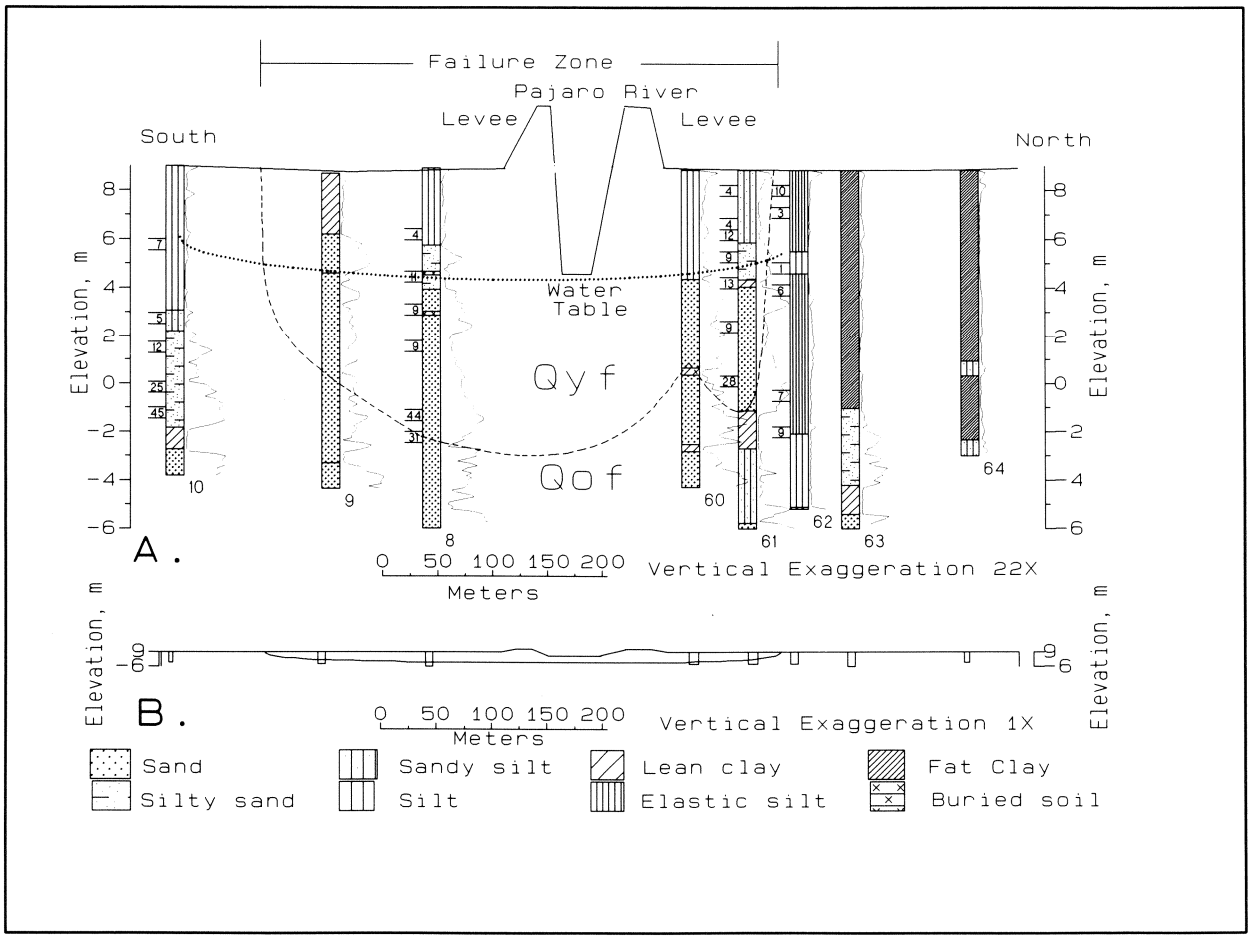

Fig. 5 Geologic cross section of the buried river channel at exaggerated (A) and true (B) scale. Curves to the right of the soundings are CPT tip resistance; numbers to the left are SPT field blow counts in blows/foot. Sounding number is shown at base of log. See Figure 1 for location.

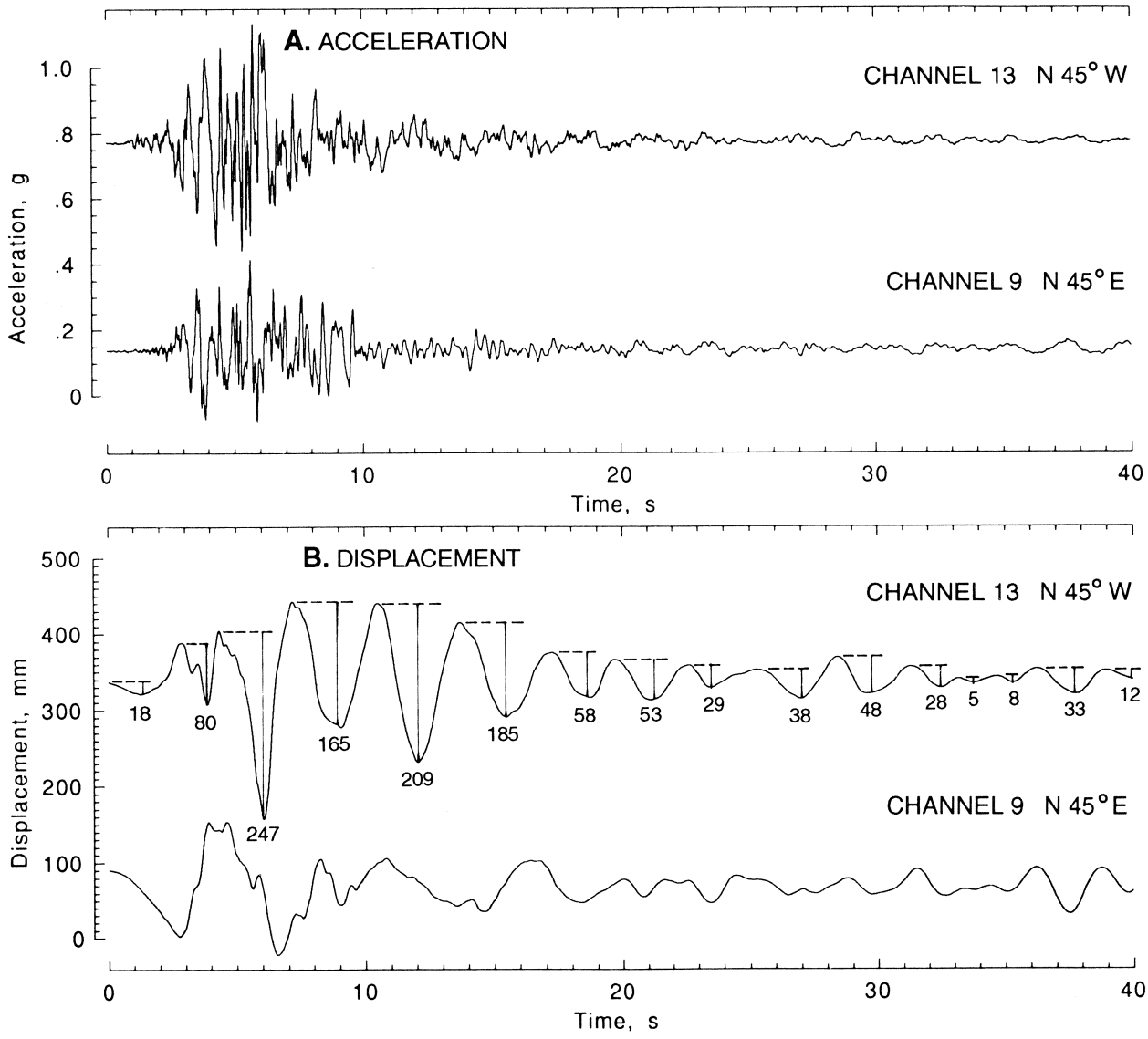

Fig. 6 A. Accelerograms of Loma Prieta earthquake mainshock recorded by orthogonal horizontal accelerometers at ground level in phone company building at Watsonville (the azimuth is the direction of positive acceleration); B. Displacements computed by double integration of acceleration time history. Peak-to-peak displacement, in mm, is shown for channel 13. Total of peak-to-peak displacements equals 1,156 mm. See SMA site in insert in Figure 1 for location.

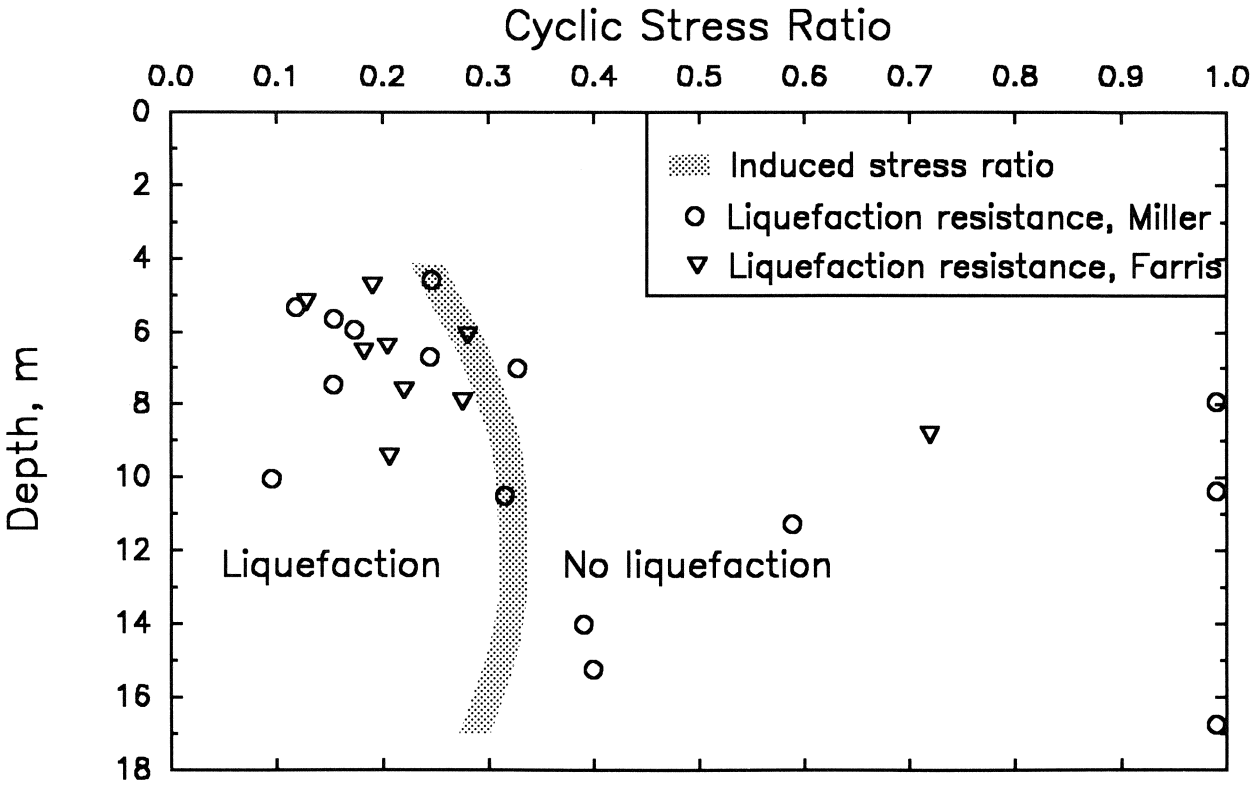

Fig. 7 Comparison of induced stress ratio with the stress ratio required to liquefy as a function of depth for SPT soundings at Miller and Farris Farms. Stress ratios shown as 0.99 are actually much greater than one.

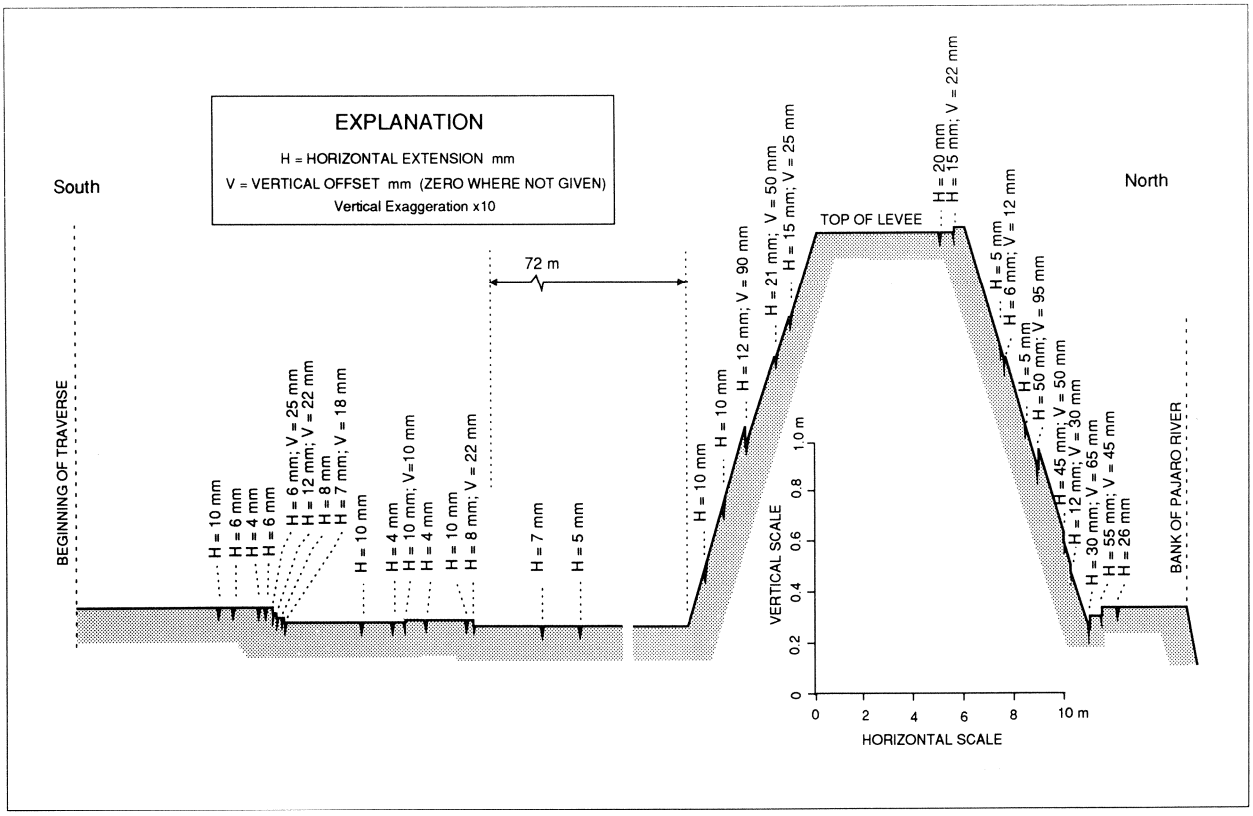

Fig. 8 Vertical offset and horizontal opening across ground cracks at Miller Farm. See Figure 1 for location.

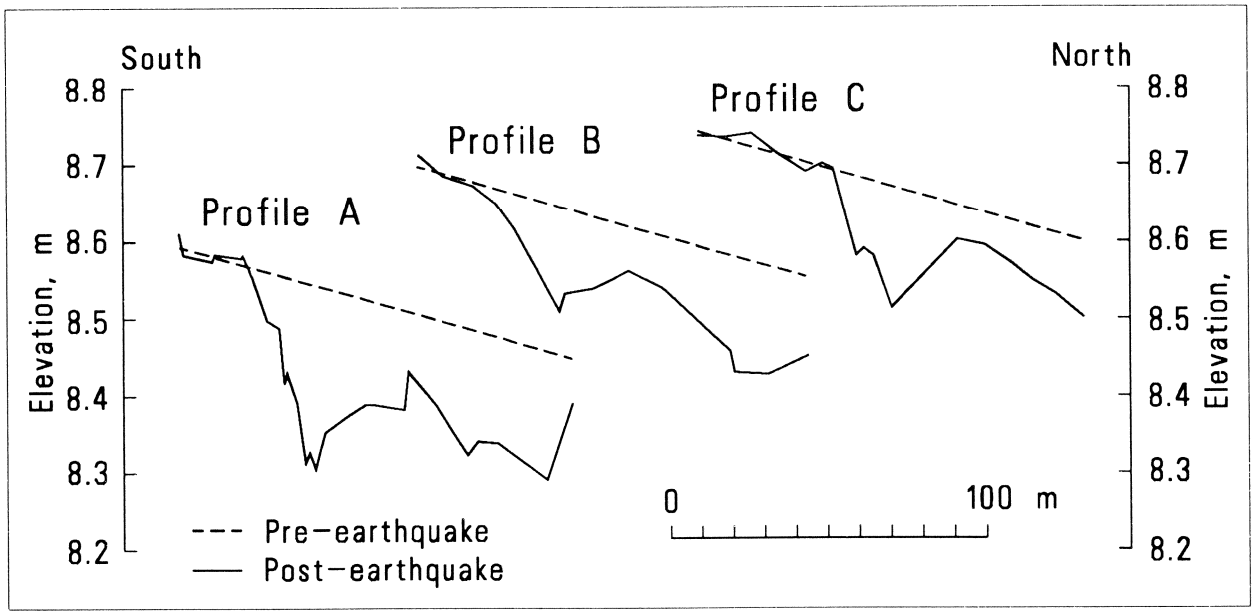

Fig. 9 Pre- and post-earthquake profiles of the land surface on Miller Farm. See Figure 1 for locations.

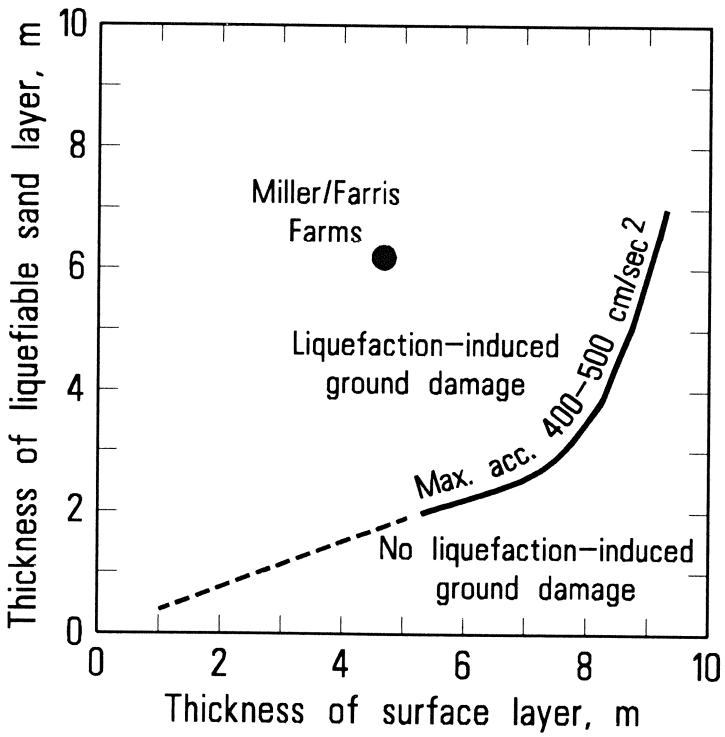

Fig. 10 Comparison of observation at Miller/Farris Farms to Ishihara's (1985) correlation of observation of liquefaction effects with thicknesses of liquefied layer and nonliquefied surficial layer.

Characteristics and Damage Investigation of 1993 Hokkaido Nansei-oki Earthquake

Takahiro Iwatate *, Yoshihiro Sawada **, Daiei Inoue **, and You Sakamoto ***

ABSTRACT

This paper describes the characteristics and earthquake damage of 1993 Hokkaido Nansei-oki Earthquake(M=7.8) by the recorded strong motion accelerograms and damage investigations performed a few days later the earthquake by CRIEPI researchers. The main results imply that: (1) About 80 aftershock records including maximum acceleration of 190 gal were obtained by CRIEPI s temporary observation system in Okushiri island. (2) The tsunami left the run-up height more than 15m along the coast of Okushiri island,particularly more than 30 m at local point. (3) Many houses and civil engineering structures(breakwater, wharfs and etc.) along the coast of Okushiri island were suffered heavy damages from tsunami. (4) Lots of slope failure occurred at Okushiri island. (5) Earthquake has been resulted damages on ground and civil engineering structures(road,raiway, embedded pipes and etc.) which were constructed on(in) soft alluvial deposits, due to the liquefaction of loose sandy deposits. (6) The permanent displacements(Max. 160cm) of the surface ground occurred in the soft alluvial deposit. (7) Volcanic coarse-grained soil liquefied with a wide range at Akaigawa district,resulting in differential settlement of houses. The cause of the liquefaction occurrence of the gravelly soil was verified by the various soil tests. (8) Though the electric power distribution facilities were suffered some damage from tsunami,the facilities were promptly restored.

1 INTRODUCTION

The Hokkaido Nansei-oki Earthquake of 7.8 magnitude occurred at the southern part of the Hokkaido island and its adjacent Okushiri island at 22:17 12 th July 1993, whose seismic center was 34 km in depth. This earthquake has been resulted to the damages on the ground including slope failure, and liquefaction and civil engineering structures(roads, embedded pipes and etc.). The tsunami accompanied by the earthquake brought heavy damage to the Okushiri island and the west coast of Hokkaido.

The damage investigations due to the earthquake motion and the tsunami as well as after shock observation were carried out a few days later the earthquake by CRIEPI researchers.

This paper describes the characteristics of the earthquake by the observation data and earthquake damages on the ground(liquefaction and slope failure) and, civil engineering structures(houses, roads, wharfs and etc.) and electric facilities by means of field survey due to liquefaction and tsumani(Iwatate 1993). Moreover to examine the the permanent displacement of the ground surface occurred at the soft alluvial deposit and the liquefaction of volcanic coarse-grained soil at the Akaigawa district by means of field survey and soil tests.

2 HOKKAIDO NANSEI-OKI EARTHQUAKE

2.1 Earthquake Element

According to Japan Meteorological Agency (JMA), this earthquake was of magnitude 7.8 and the hypocenter was located 42° 47' N, 139° 12' E with focal depth was 34 km(Table 1). This earthquake is the biggest size which occurred in Japan sea of Hokkaido region. Fig.1 shows the map of seismic intensities by JMA, and the intensity of the region near the epicenter was V. This earthquake were caused by the collision between Eurasian Plate and North-American Plate as shown in Fig.2.

* Professor of Tokyo Metropolotan University,Japan
** Central Research Institute of Electric Power Industry(CRIEPI),Japan
*** Hokkaido Electric Power Company Inc.,Japan

Judging from the after shock distribution, the size of earthquake fault were estimated 100 km of NS x 50 km of EW,and stress drop,average slip was estimated about 60 bars and 4 m, respectively as shown in Table 2.

In this particular event, the earthquake indicated a complicated rapture process, and the rupture has started from the north side of the fault to the south side with velocity about 3 km/s.

2.2 Earthquake Observation

(1) Observation Stations

CRIEPI has about 50 strong earthquake observation stations that are located on rock outcrops in mainly the circum-Pacific seismic zone of Japan in order to research the input motion on bedrock (Yajima 1991). Among these stations,the earthquake data of main shock were recorded at the 4 stations(SRN, KUJ, FRF and KMS)located at Tohoku region(Fig.3). And, in order to examine the characteristics of the earthquake motion minutely, two temporary stations near the epicenter for after shock were constructed on the outcrop at Okushiri island(OKS) and Setana-cho(SET) of the west coast of Hokkaido.

(2) Earthquake Observation Data

・ Main Shock

1) Fig.4 shows three-component accelerograms at SRN station which is located 257 km far from the epicenter . The maximum values were 10.3gal(NS component), 9.9gal(EW component), and 7.9gal(UD component), respectively. And Fig.5 shows the Fourier amplitude spectrum, power spectral density, absolute acceleration response spectra, and pseudo velocity response spectra of NS component .

2) Fig.6 shows the three-component accelerogram at JMA Sutsu station(SUT)which is located 69 km far from the epicenter, and the maximum accelerations were 216gal(NS component), 202 gal(EW component), and 51 gal(UD component), respectively.

・ After Shock

1) About 80 after shock events were recorded at OKS and SET stations. The maximum one(M=6.5) occurred at 04:42 8 th August. Fig.7 shows the three-component accelerogram of this earthquake observed at OKS station. The maximum accelerations were 95 gal(NS component),189 gal(EW component), and 65 gal(UD component), respectively. And the Fourier amplitude spectrum, power spectral density, absolute acceleration response spectra, and pseudo velocity response spectra of NS component are shown in Fig.8.

Fig.9 shows the relations between the observed maximum accelerations of the these stations to hypocentral distance. The acceleration values were almost same those predicted from some empirical acceleration-attenuation formula except for the SUT data.

3 TSUNAMI

(1) Characteristics of Tsunami

The tsunami accompanied by the earthquake brought heavy damage to Okushiri island and west coast of Hokkaido. In Okushiri island ,the tsunami left the run-up height more than 15 m along the coast,particularly more than 30 m at local point which is the highest value in 20 th century in Japan, as shown in Fig.10,11.

The tsunami was diffracted and refracted around this island with concentrating the energy at the shoal of the coast.

(2) Damage of Tsunami

Photo 1 shows the overveiw of the damages at Aonae area in Okushiri island. Many houses and harvor facilities (breakwater, wharfs) were suffered heavy damage from tunami and fire. Photo 2 shows the broken breakwater of Okushiri harbor, and Photo 3 shows the damage of the embankment of the coast of Taiseicho in Hokkaido.

4 EARTHQUAKE DAMAGE (Fig.10,11)

Table 3 shows the summary the earthquake damages of houses,civil engineering structures compared to the other past earthquakes with same magnitude. The damages of structures of this earthquake were concentrated in the

Okushiri island and east cast of Hokkaido due to tsunai and the liquefaction of the ground. And lots of slope failure occurred in Okushiri island. The sum of the damage cost of this earthquake was about twice larger than that of Kushiro−oki earthquake,and more than two hundred people died. The main damages show as follows.

(1) Electric Power Facilities

Table 4 shows the summary of the damages of electric power facilities, and Table 5 shows the damages of electric power distribution facilities. In Hokkaido island, Hokkaido electric company has 1 nuclear power station(Tomari), and 3 thermal power stations of the area near epicenter. The damages of the facilities of these power stations were very little,but the electric power distribution facilities were suffered some damages in Kita−hiyama district. From these damages, the electric power supply were cut off in Kitahiyama district, but about 5 hours after the outage was almost restored. On the other hand, in Okushiri island,though the electric power distribution facilities(cable, pole) were suffered severe damages with the electric supply cut off from tsunami as shown in Fig.12. But the emergency electric sources were promptly recovered, and 4 days after the outage was almost restored.

(2) Slope Failure

Lots of slope failure(about 400 points)occurred along the coast of Okushiri island. These failures were classified into 4 types, that is, shallow−seated sliding, deep−seated sliding,landslide and rockfall. In particular, the most of slope failure was the shallow seated sliding with repeated phenomena(more than 80%) and the sliding part of the slope was consisted of fairly efforescented rocks. Photo 4 shows the slope failures of Okushiri island comparison between the before earthquake(a) and after earthquake(b). The slope failure were tremondously increased by the earthquake. And Photo 5 shows the large deep sliding at the back of the Okushiri port. In this case, 37 people died.

(3) Liquefaction

The liquefaction of the ground with loose sand deposits were occurred with wide range along the No. 5 road (from Oshamanbe to Yagumo) and Kitahiyama district, resulting the manholes,gasoline oil−tanks and agricultural culvert built−up as shown Photo 6,7. And ground displacements also occurred at the ground of Nakanosawa elementary school as shown in Photo 8. Fig.13 shows the measured permanent displacement of the ground. The maximum value was about 160 cm resulting the damages of broken piles of the school houses and the fallen concrete walls. But, at the part of compacted alluvial deposit of the ground, the permanent displacement was very little and the backnet for baseball and the plant trees were useful to protect the lateral flow of the liquefied soil.

(4) Damage of roads

Most of damaged roads were constructed on soft alluvial deposits,such as National Highway No.5(from Oshamanbe to Yagumo),Kitahiyama district along the Rishibetu−river. The collapsed embankments,differential settlements and caving in roadbed were occurred as shown in Photo 9. The main cause of them may be liquefaction of loose sand deposits by strong earthquake motions.

(5) Liquefaction of Gravelly Debris Avalanche Deposit

Vocanic coarse−grained soil liquefied with wide range at Aki−gawa district in Mori town near the Ohonuma lake,resulting in differential settlements of houses.

It is rare case that gravelly ground is liquefied and often used for foundation on ground of electric power facilities because of its high stability against liquefaction, so CRIEPI has conducted further site investigations with geological survey,PS−logging, large penetration tests, elastic wave exploration tests, in−situ freeze sampling and some laboratory tests in order to clarify the liquefaction occurrence of the site(Tanaka 1994).

The test results imply that : ① The age of organic soil layers which sandwich the gravally soil deposits,was found about 2000 years. ② According to the results of PS−logging,the average of shear wave velocity of the ground shallower than depth of 7 m is about 100m/s which is very small value for a gravelly soil as shown in Fig.14. ③ The value of shear wave velocity of the ground measured by the refraction method was approximately equal to those by PS−logging.

On the base of these test results and estimated ground surface acceleration values, liquefaction susceptibility of the ground was examined by a practical method. And from the test results ,the cause of the liquefaction occurrence at the site has been verified.

5 CONCLUSION

(1) Hokkaido Nansei-oki earthquake was the biggest one occured in Japan sea of Hokkaido region, and it were caused by the collision between Eurasian Plate and North American Plate.

(2) CRIEPI obtained about 80 earthquake data on the outcrop near the epicenter by the after shock observations. The maximum acceleration was 189gal(NS-component).

(3) The tsunami left the run-up height more than 15 m along the coast of Okushiri-island particularly more than 30 m at local point.

(4) Many houses and civil engineering structures(wharfs, breakwaters) along the cost of Okushiri island and the east coast of Hokkaido were suffered severe damages from tsunami, and though electric power distribution facilities also suffered severe damages from tsunami, the facilities were promptly restored.

(5) Lots of slope failures were occurred along the coast Okushiri island. The most of slope failure was the shallow-seated sliding and the sliding part of the slop was consisted of fairly efforescented rocks.

(6) This earthquake has been resulted the heavy damage on the ground and civil engineering structures(roads, railway embankments and etc.) constructed on (in) soft alluvial deposit due to the liquefaction.

(7) The permanent displacements(Max.160 cm)occurred in soft ground of Nakanosawa elementary school resulting the damage of the piles of school houses.

(8) Volcanic coase-graind soil liquefied with a wide range at Akaigawa district,resulting in differential settlement of houses. The cause of the liquefaction occurrance of the site has been verified by the soil tests.

REFERENCE

- Iwatate T., Sawada Y, Inoue D.and etc.(1993)
  Characteristics and Damage Investigation of 1993 Hokkaido Nansei-oki Earthquake
  Abiko Research Laboratory Report No.U93028 (in Japanese)
- Yajima,H.(1991)
  Strong Motion Earthquake Records of CRIEPI earthquake observation network
  CRIEPI Report No.U90058 (in Japanese)
- Tanaka,Y.(1994)
  Investigation of Causes of Liquefaction of Gravelly Debris Avalanche Deposit occurred during Hokkaido Nansei-oki Earthquake of July 12,1993(Part 1)
  Abiko Research Laboratory Report No.U94007(in Japanese)

Table 1 Earthquake Elements

(1)Origin Time	:1993.07.12. 22h17m(JST=9hours+UT)
(2)Location Name	:Off south-west coast of Hokkaido
(3)Hypocenter	:Longitude 42° 47'N
	Latitude 139° 12'E
	Depth H=34km
(4)Size	:M_{JMA}=7.8
(5)Seismic Intensities by JMA :	
V	:Otaru,Fukaura,Suttsu,Esashi
IV	:Aomori,Muroran,Tomakomai,Mutsu,Kutchan,Hakodate
III	:Rumoi,Sapporo,Hachinohe,Akita,Obihiro,Iwamizawa, Haboro
II	:Asahikawa,Wakkanai,Shinjo,Morioka,Sakata,Urakawa
I	:Yamagata,Abashiri,Miyako,Kushiro,Onahama,Niigata, Ofunato,Wajima,Omu,Hiroo,Sendai

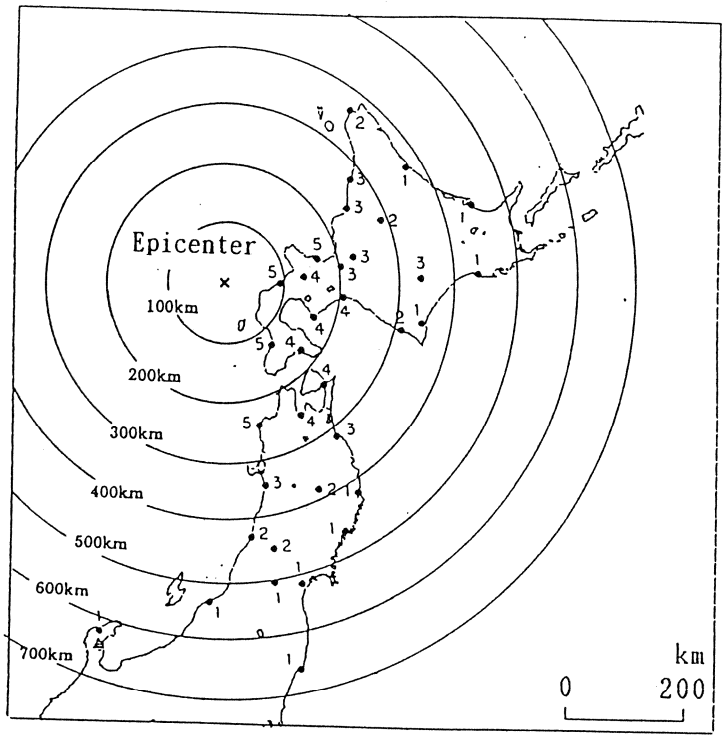

Fig. 1 Map of Seismic Intensity by JMA

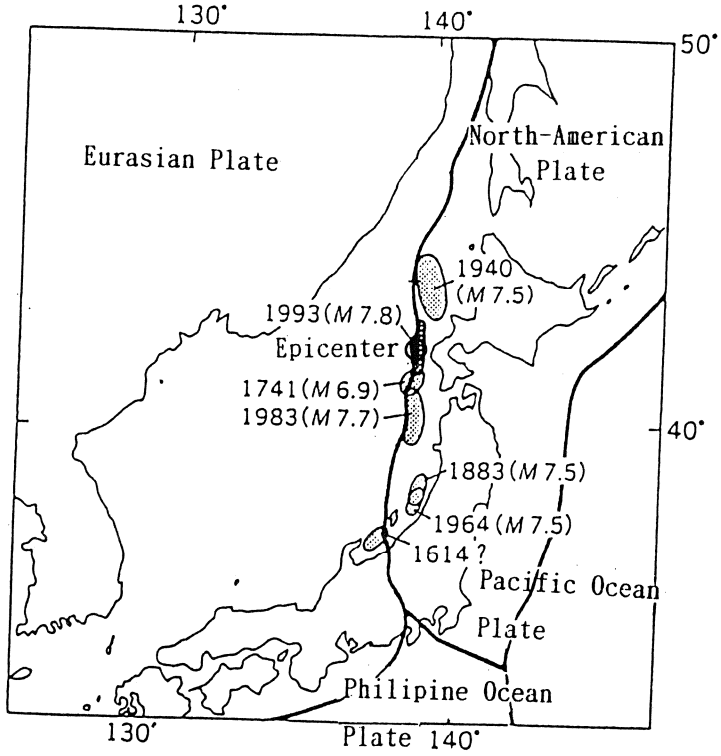

Fig. 2 Seimic Regions of Big Earthquakes occurred in in Japan Sea of Hokkaido Region

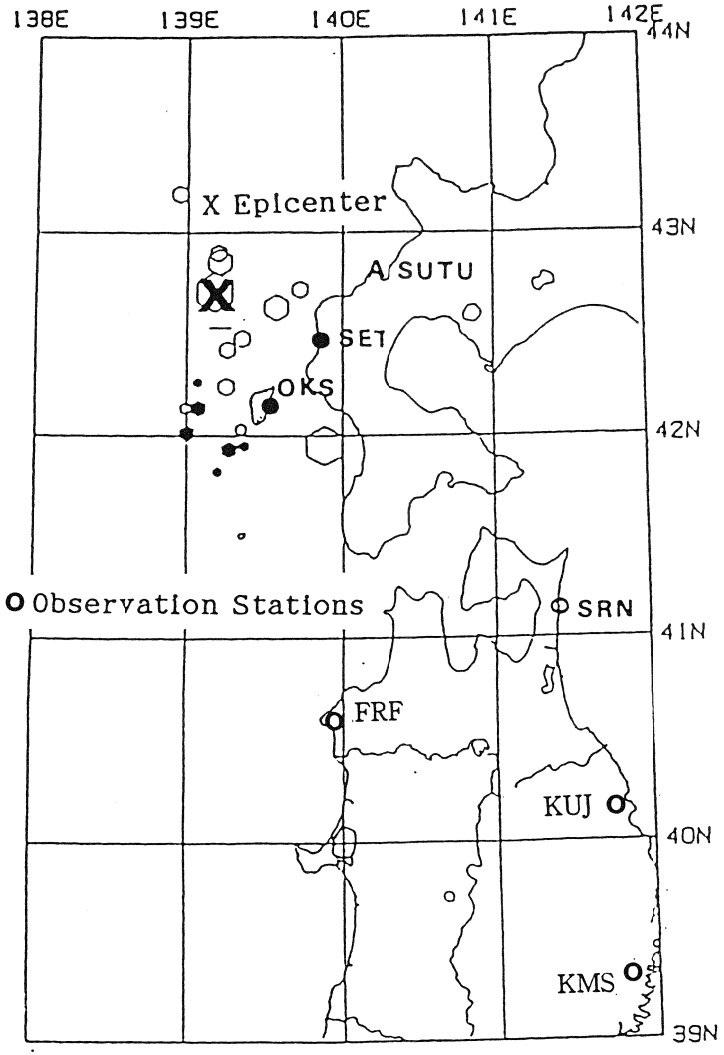

Fig. 3 Observatin Stations of CRIEPI

Table 2 The Source Parameter of The Main Shock

Origin Time	Fault Size (km)	Seismic Moment (dyne·cm)	Stress Drop (bar)	Average Slip (m)
1993, July. 12 22:17	100(NS) x 50(EW)	4.2×10^{27}	60	4.0

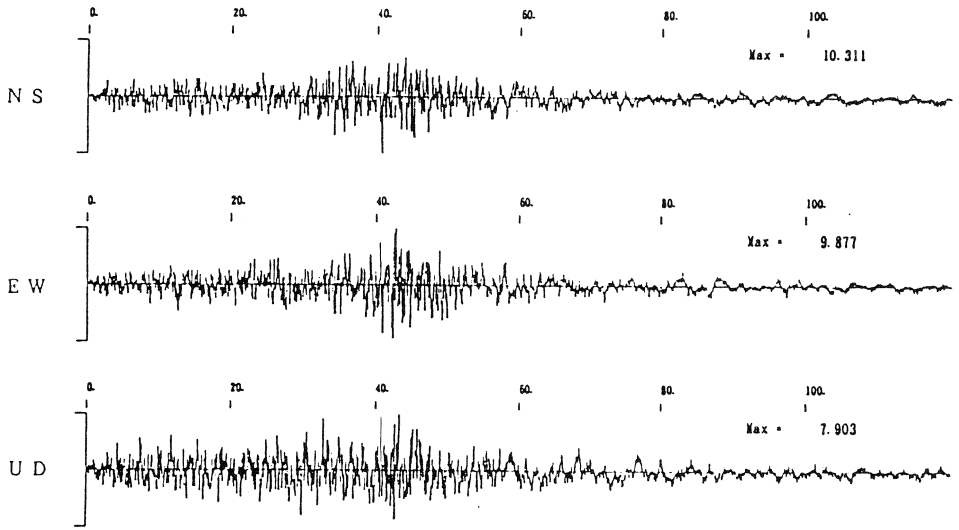

Fig. 4 Observation Accelerograms at CRIEPI's SRN Station

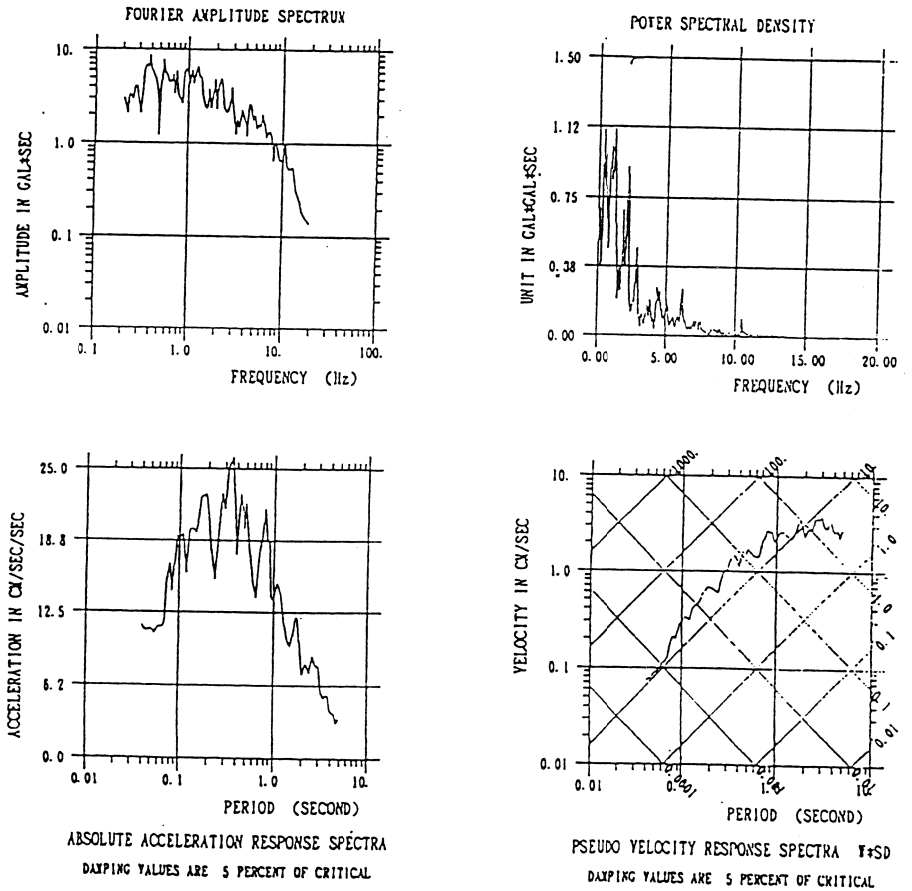

Fig. 5 Fourier Amplitude Spectrum, Power Spectral Density, Absolute Acceleration Response Spectra and Pseudo Velocity Resonse Spectra of SRN Data (NS-component)

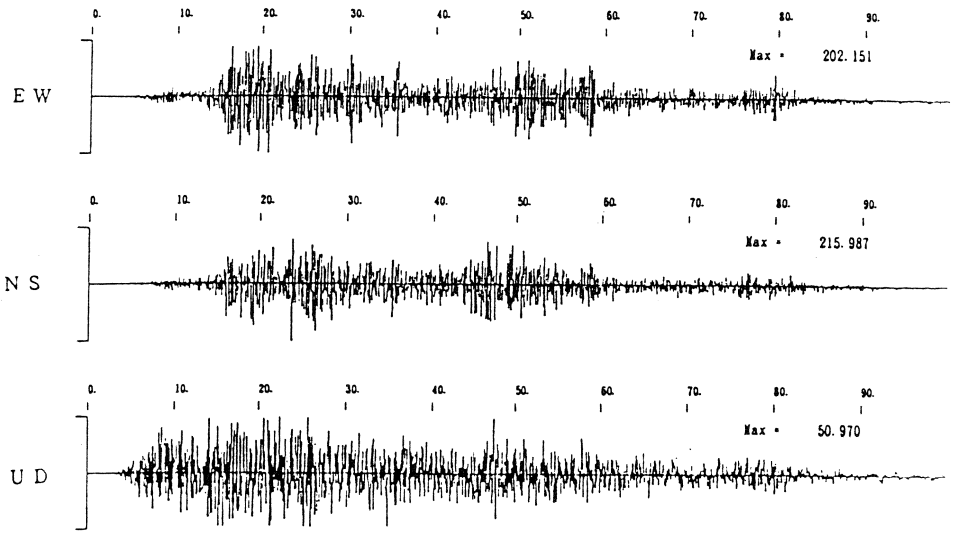

Fig. 6 Observation Accelerograms at JMA Sutu Station (Main Shock)

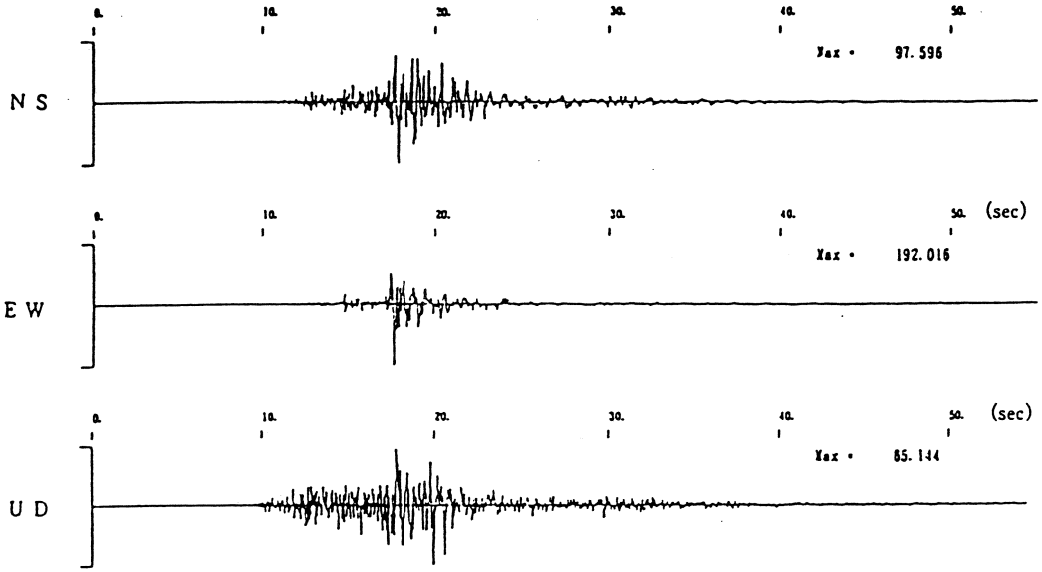

Fig. 7 Observation Accelerograms at CRIEPI' OKS Station

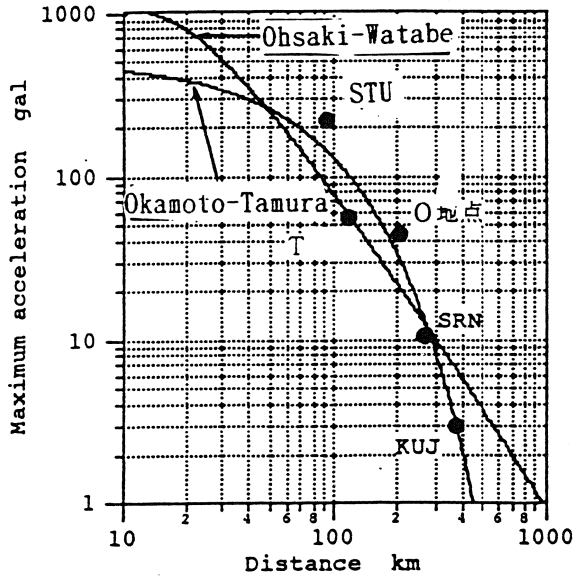

Fig. 9 The Relations between the Observed Maximum Accelerations to Hypocentral Distance

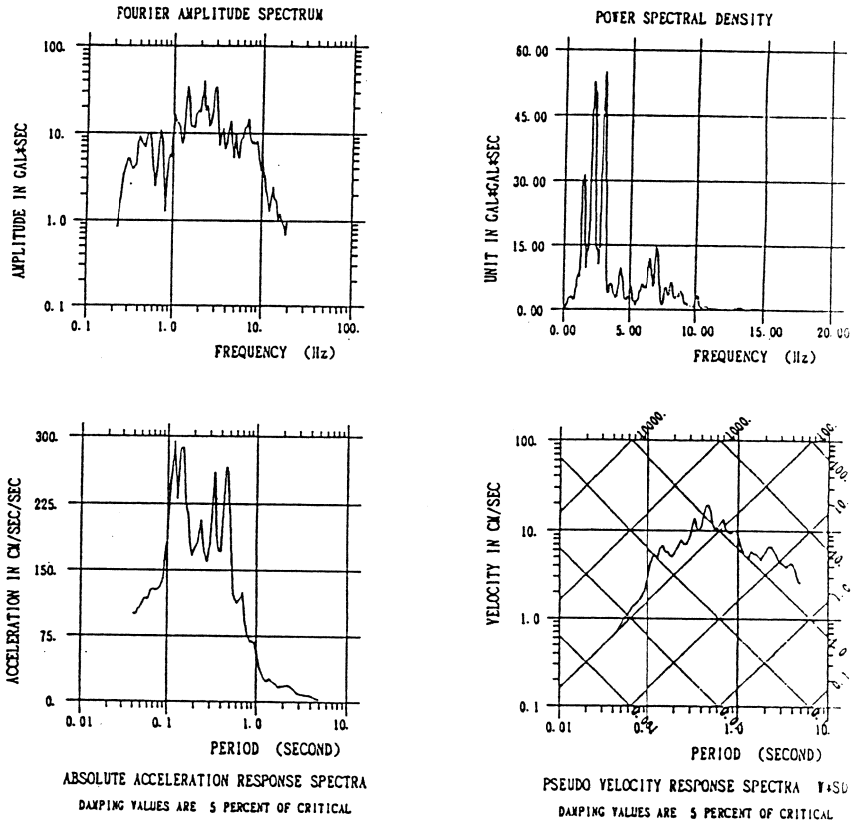

Fig. 8 Fourier Amplitude Spectrum. Power Spectral Density. Absolute Acceleration Response Spectra and Pseudo Velocity Resonse Spectra of OKS Data (NS-component)

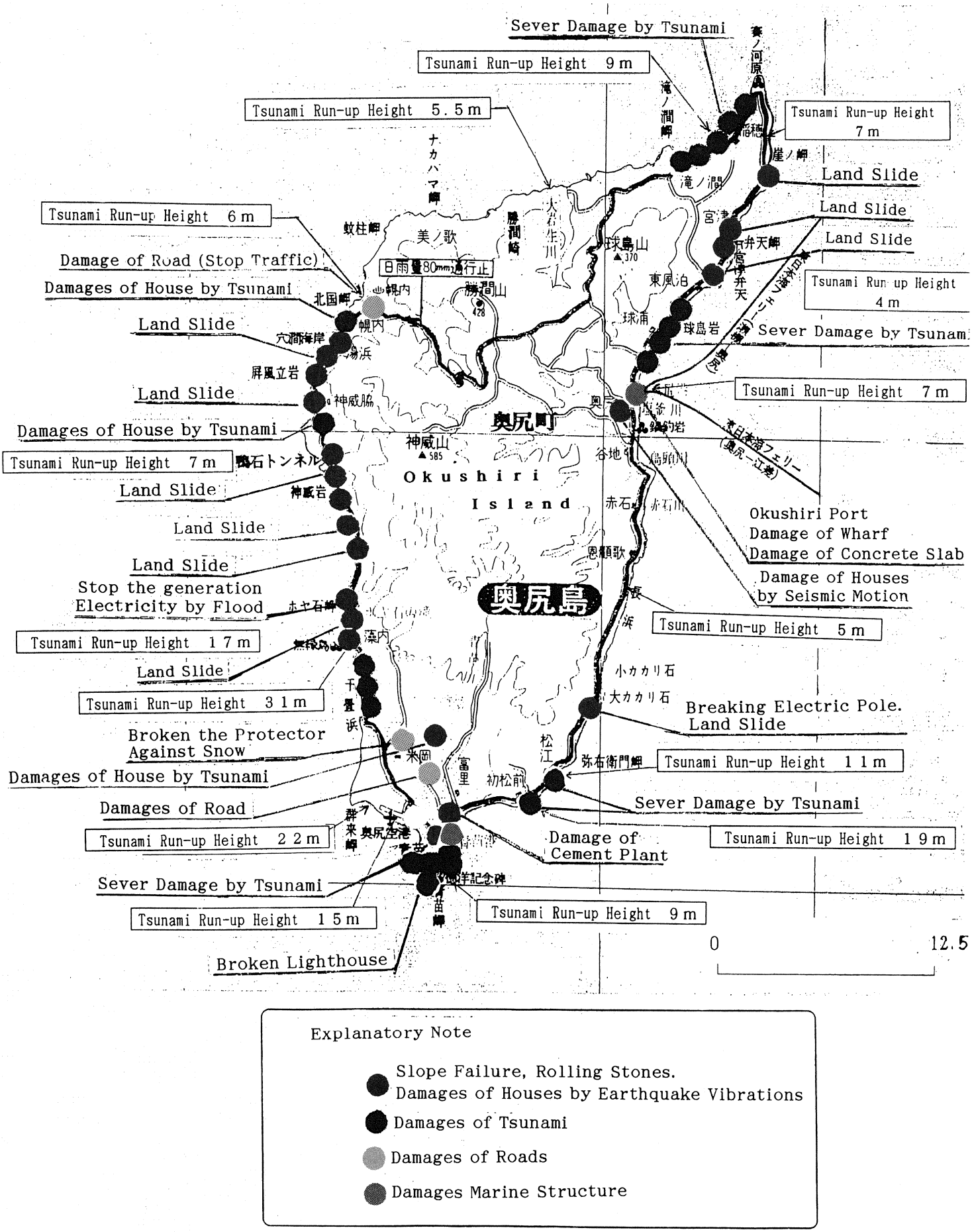

Fig. 10 Earthquake Damage of Okushiri island

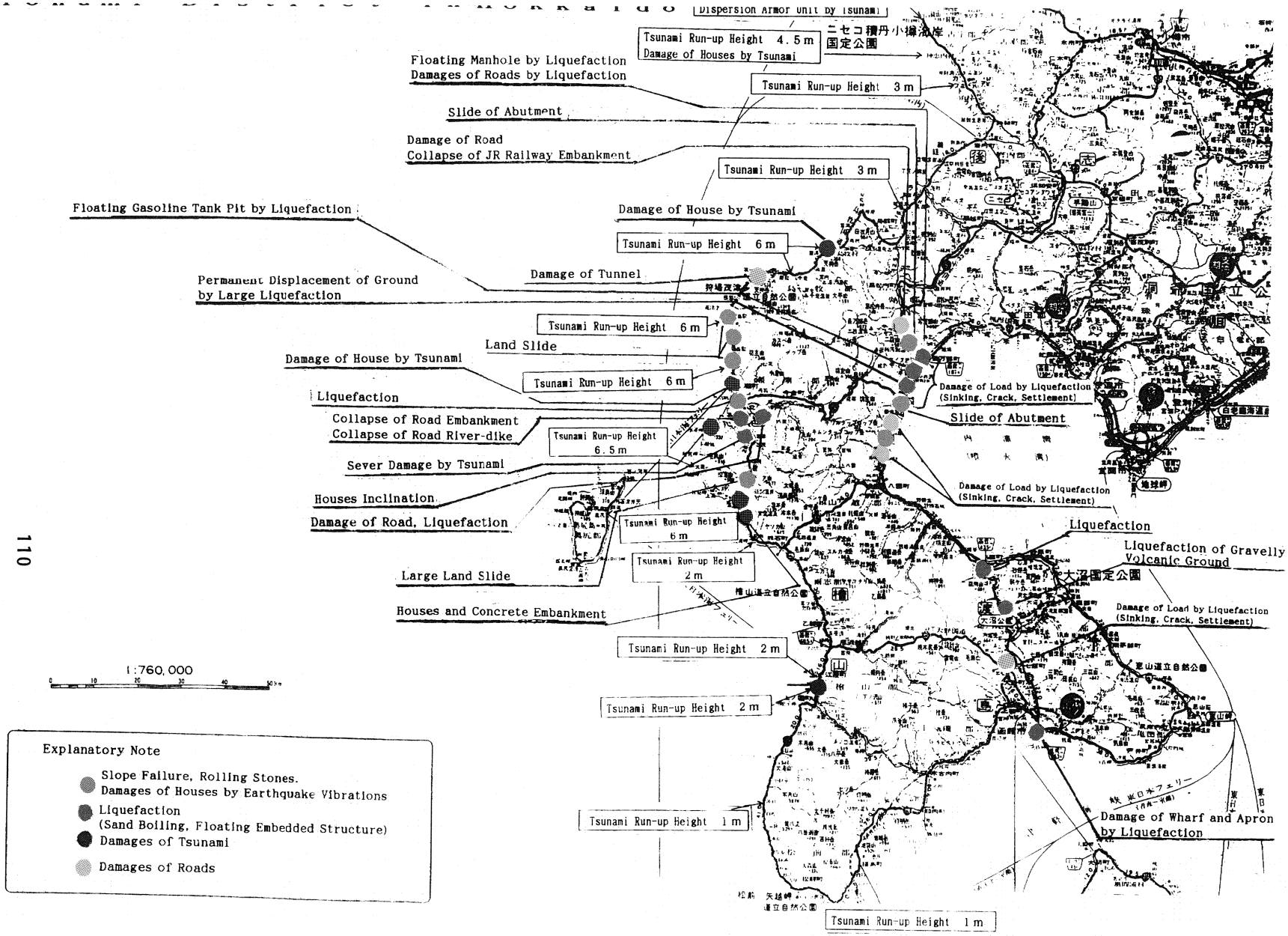

Fig. 10 Earthquake Damage of Hokkaido island

Table 3 Summary of Hokkaido nansei-oki Earthquake Damages compared to the other Earthquake Damages with same magnitude(1993/8/16)

Event	Origin Magnitude Date	Amount of Damage	Human Damage Death Injured Missing	Damage of houses	Damage of Civil Engineering Structures
Hokkaido Nansei-oki	1993 07 12 M7.8	100.7billions	201 305 29	3947	1167
Kushiro-oki	1993 01 15 M7.8	53.1billions	1 927 0	4466	1993
Nihonkai Chyubu	1983 05 26 M7.7	164 billions	104 324	11061	2226

Table 4 Earthquake Damages of Elecrtic Equipments

Equipments	Damage Pattern
1.Power plant	
• Mori(Geo-Thermal:50MW)	Leaking insulting oil for pipes of actuater
• Shiriuchi(Oil:350MW)	Short -circuit of EP Damage of support tower for chimney
• Okushiri(Internal-combustion:3.2MW)	Damage of feul pipelines
• Hoya-ishikawa(Hydraulic:0.17MW)	The generator was submerged by Tsunami
2.Transmission line	
• 33KV(Matsumae-Line)	Broken porcelain component(1)
• 33KV(Toshima-Tohbetsu-Line)	Broken porcelain component(2)
• 33KV(Setana-Line and etc)	Inclined the pale(14)
• 33KV(Hiyama-Line)	Displacement of the base of Iron Tower(3)
3.Substation	
• Ohno	Broken of the part of 187KV Arrester Crack of retaining wall
• Kamiiso	Broken poclain of 72KV Gas-breaker Breaking Jumper
• Oshamanbe	Broken porclain and Leaking insulting of oil
• Fukushima	Broken porclain of 72KV switch

Table 5 Damage of Electlic Power Distribution Facilities

Equipment	Hakodate Area	Okushiri Area	Muroran Area	Otaru Area	Iwamisawa Area	Total
1.Pole	572	278		7		857
2.Cable	27	659		4		690
3.Transformer	633	96	18	57	1	805
4.A Breake and Make Switch	3	11	2		1	17

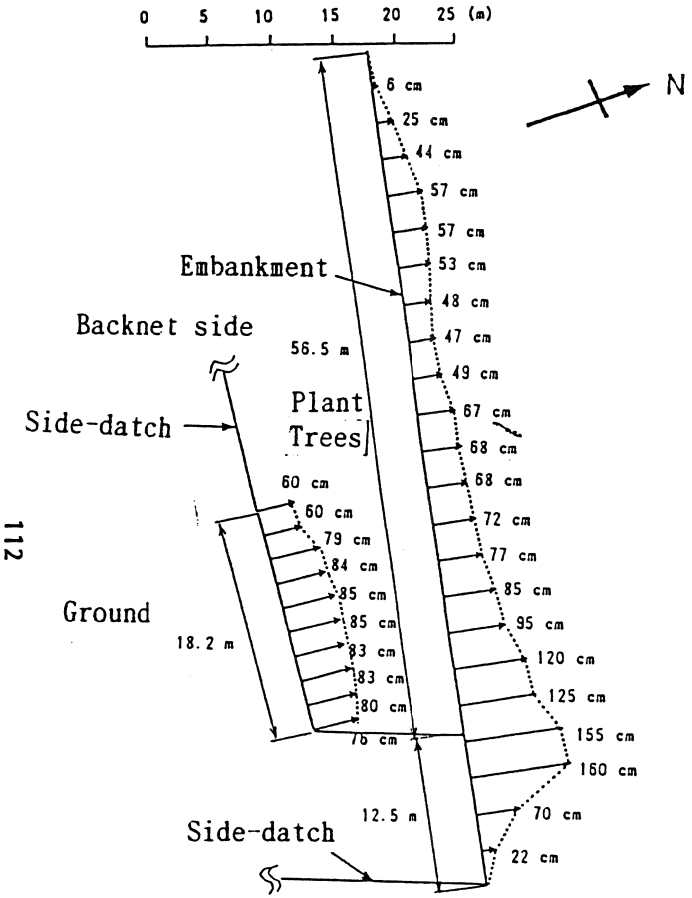

Fig. 13 Permanent Ground Displacement of Nakanosawa Elemerntary School

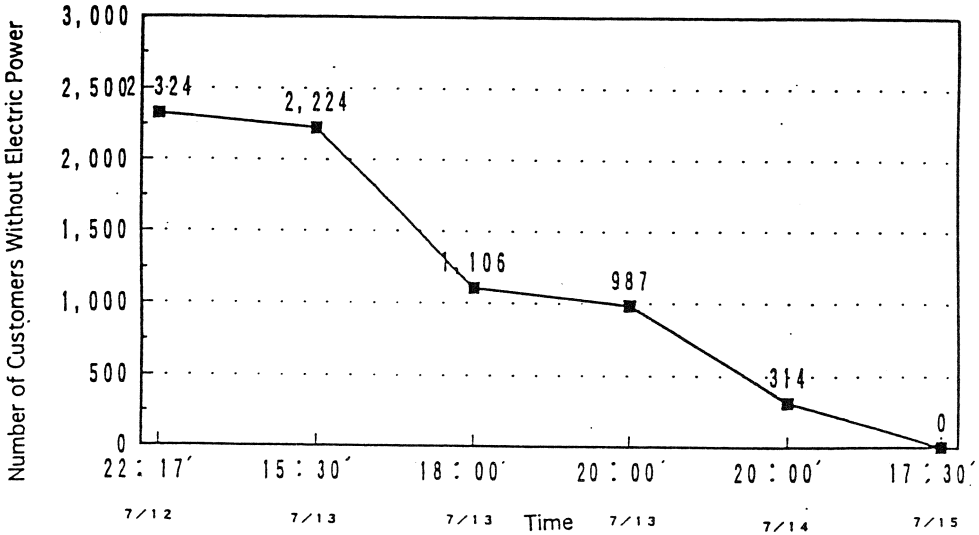

Fig. 12 The Number of Customers in Okushiri island affected by the Earthquake

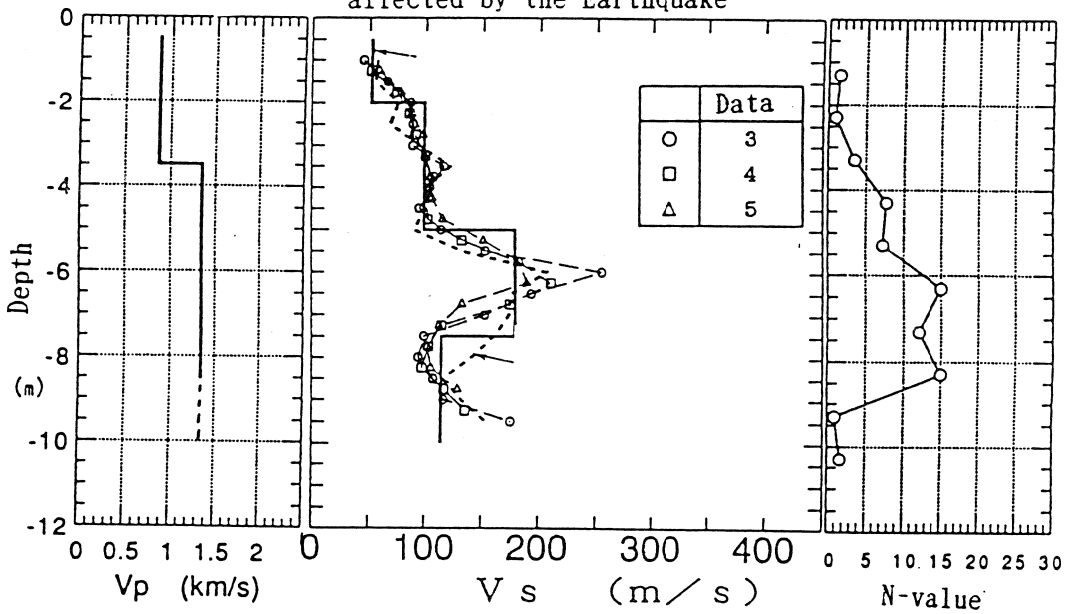

Fig. 14 Distributions of P-wave and S-wave Velocities with Depth of the the Ground N-value(Large Penetration Tests)

Photo 1 Overall View of the Damage of Aonae District
(Destroyed Tunami and Fire)

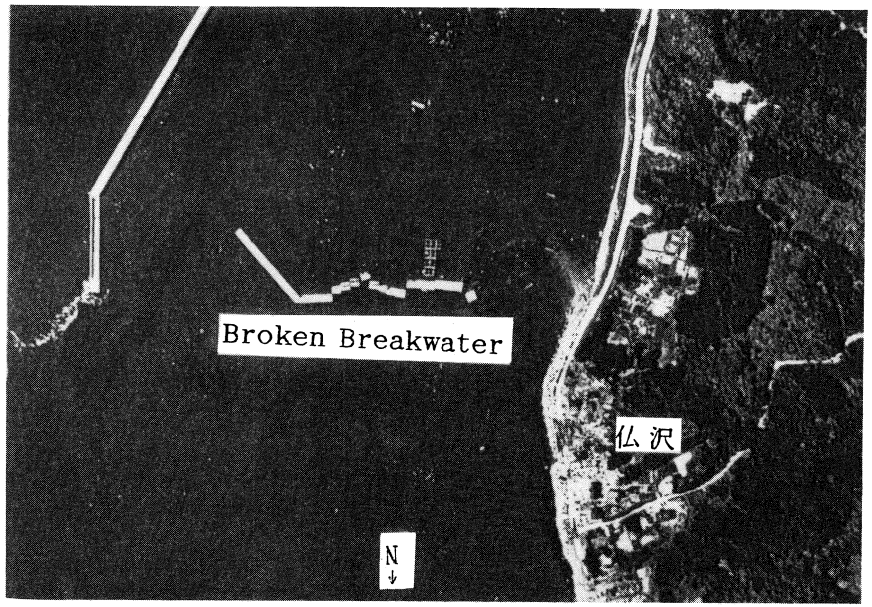

Photo 2 Broken Breakwater due to Tsunami at Okushiri island

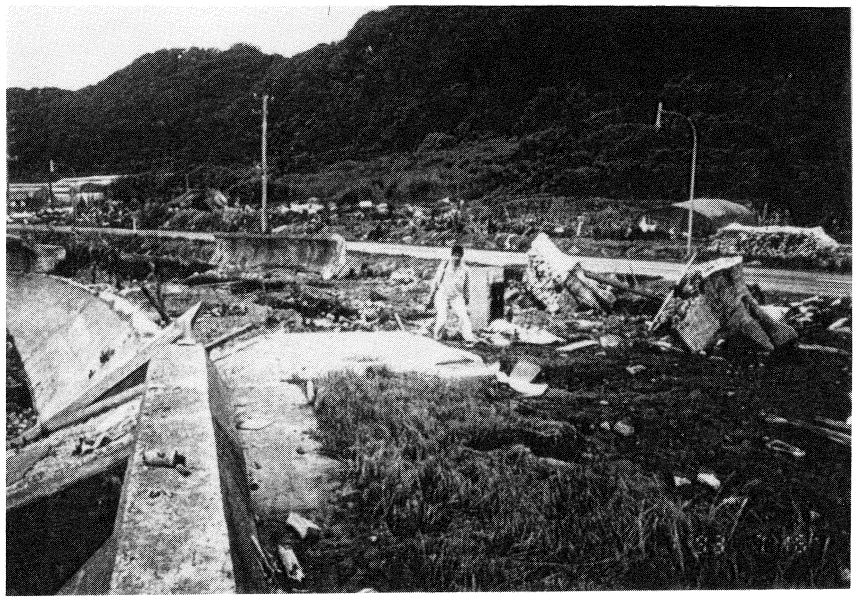

Photo 3 Broken Embankment due to Tsunami at Taisei-cho

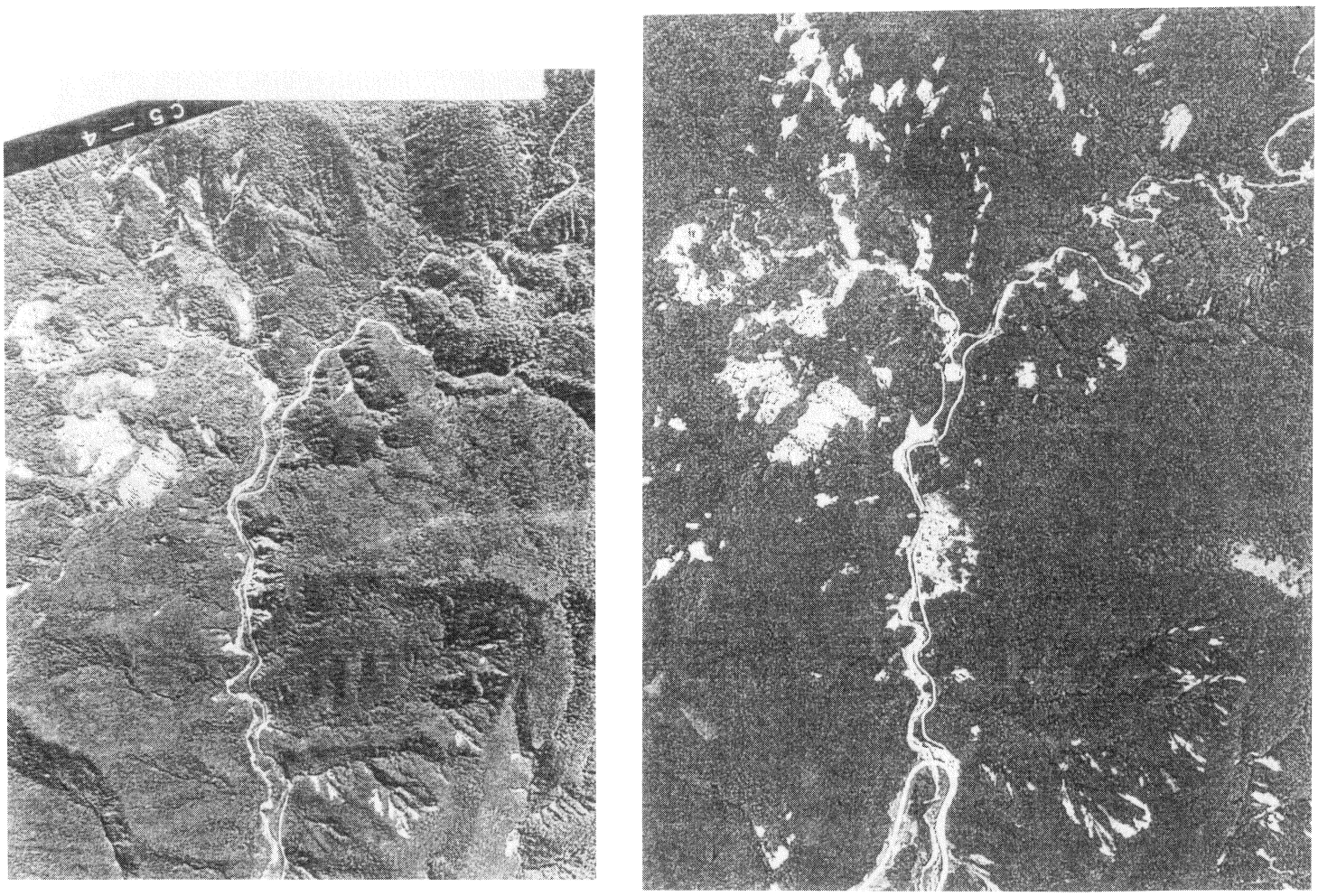

Before Earthquake

After Earthquake

Photo 4 Collapse of the Slope at Okushiri island

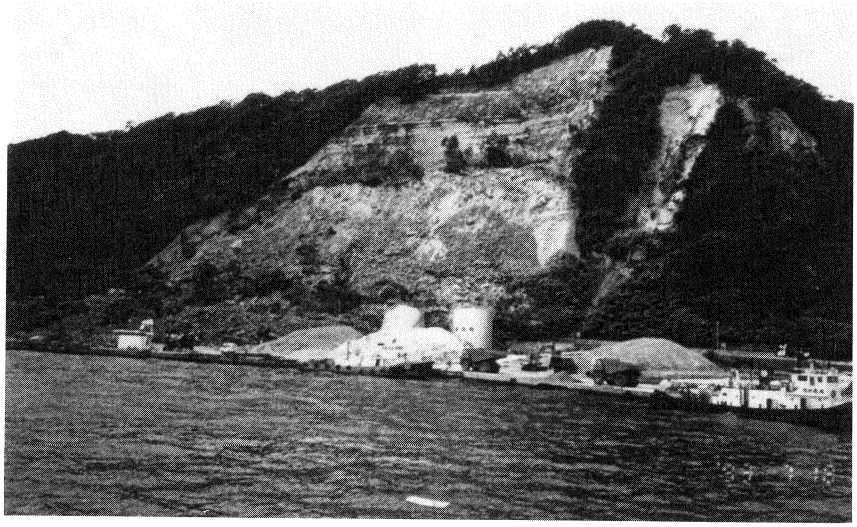

Photo 5 Large Deep Sliding at the Back of The Okushiri-port

Photo 6 Built-up the Oil pit due to Liquefaction

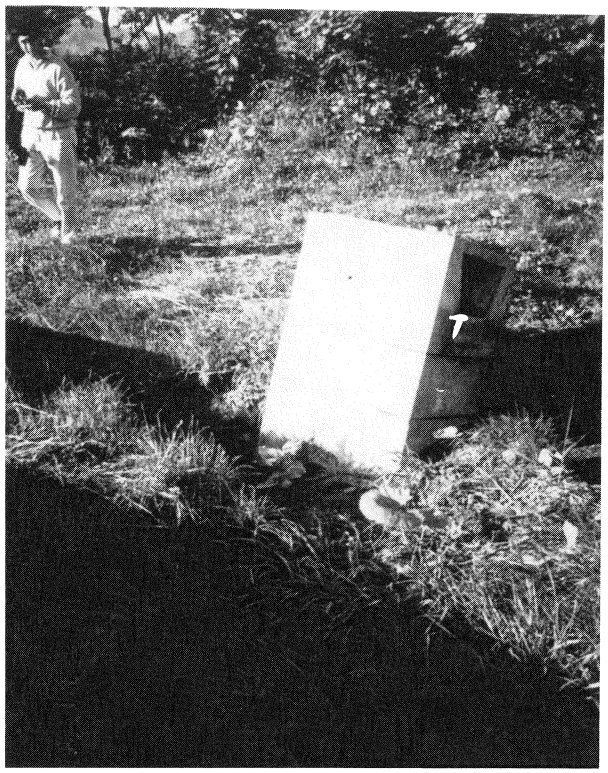

Photo 7 Built up the Agricultural culvert due to Liquefaction

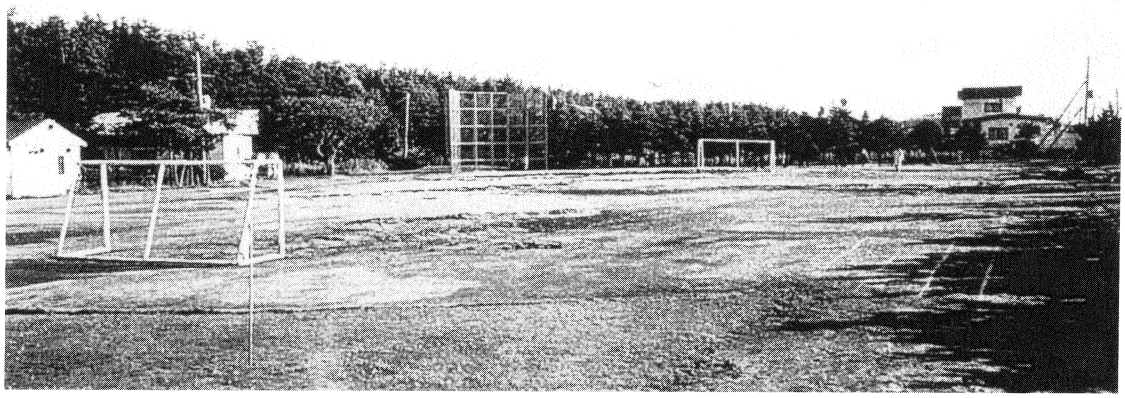

Photo 8 Overview of the Liquefaction of the Ground of Nakanosawa Elementary School

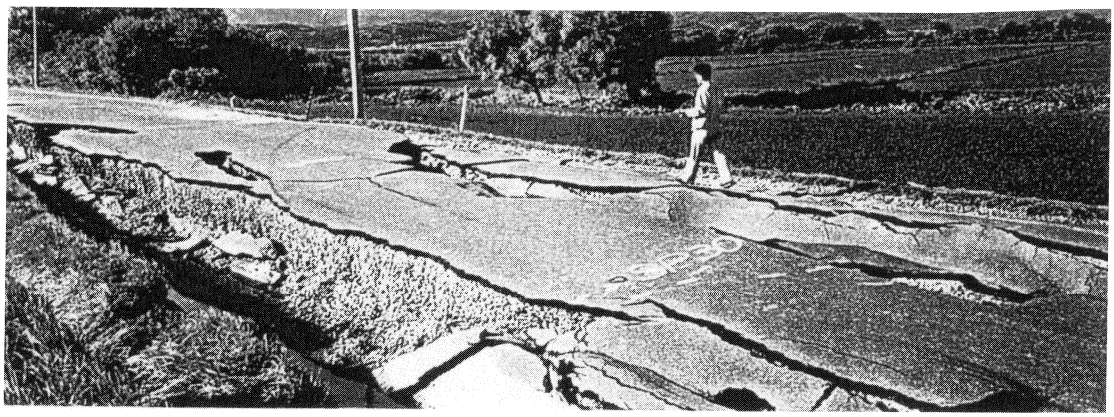

Photo 9 Damage of Road due to Liquefaction

LIQUEFACTION OF CALCAREOUS SANDS AND LATERAL SPREADING EXPERIENCED IN GUAM AS A RESULT OF THE 1993 GUAM EARTHQUAKE

Shahriar Vahdani
Associate Engineer, Treadwell & Rollo, Inc.
San Francisco, California

Robert Pyke
Independent Consultant, Lafayette, California

Ukrit Siriprusanen
President, Geo-Engineering, Tamuning, Guam

ABSTRACT

The August 1993 magnitude 8.1 (moment magnitude, M_w 7.7) Guam earthquake caused soil liquefaction and associated ground failures (lateral spreading and settlement) in the harbor and port areas and along the free-faces of stream channels. Soil liquefaction caused severe damage to the commercial and the U.S. Navy port facilities, where uncontrolled fill had been placed to reclaim land.

The epicenter of the earthquake was adjacent to the Mariana Trench, about 60 kilometers (km) south of the island. Unfortunately, there were no operable strong ground motion instruments in Guam at the time of the earthquake. According to eyewitnesses, the strong ground shaking lasted up to about 60 seconds. Based on published attenuation relationships appropriate for subduction zone earthquakes in the region, for a M_w of 7.7, the island must have experienced a peak ground acceleration (PGA) in the range of 0.20 gravity (g) to 0.3g.

The earthquake provided a unique opportunity to study the behavior of calcareous soils during strong ground shaking caused by a large magnitude earthquake. This paper presents our observations regarding liquefaction-induced ground failures and damage to various facilities. The study was supported by the National Science Foundation (NSF Grant No. CMS-9413272).

INTRODUCTION

The island of Guam is located at the southern end of the Mariana Islands, within the Pacific Rim (Figure 1).

In this region, the relative movement between the Pacific Plate and the Philippine Plate creates a highly active seismic environment; it is characterized by the subduction and underthrusting of the Pacific Plate beneath the Philippine Plate along the Mariana Trench.

As can be seen from Figure 1, the north-south trending Mariana Trench is east of the Mariana Islands; near the island of Guam, it turns westward and approaches the Yap Trench. The 8 August 1993 Guam earthquake occurred adjacent to the Mariana Trench, about 60 km south of Guam.

Three accelerographs are located on the island; however, none of them were operational at the time of the earthquake. The eyewitnesses interviewed indicated that the quake resulted in a rolling motion that lasted more than 90 seconds, with 60 seconds of strong shaking.

The earthquake caused little damage to low-rise, stiff structures and significant damage to some of the high-rise buildings. This indicates that the predominant period of the earthquake must have been between 0.5 and 1.5 seconds.

Using the attenuation relationships appropriate for subduction earthquakes in this region, for a M_w of 7.7, a PGA in the range of 0.2g to 0.3g is computed.

The northern half of the island is relatively flat, and is underlain by limestone. The subsurface conditions in the southern half of the island consist of a thin layer of highly plastic silt (residual volcanic rock) and volcanic rock with intruding layers of limestone. Near the shoreline, there are lagoon deposits consisting of a heterogenous mixture of particles ranging from silt- to gravel-size. Because of their unique depositional environment, the lagoon deposits can be found in soft (loose) states even at great depths. The shorelines are blanketed by a layer of coral sand beach material.

The soil liquefaction and related ground failures, as evidenced by sand boils, ground subsidence, lateral spreading, and differential settlement between pile-supported structures and adjacent areas occurred in the southern half of the island, mostly near the shorelines of Apra Harbor. Soil liquefaction occurred in both the naturally-deposited, loose and silty sand of the lagoon deposits and in the loose sand fill in the reclaimed areas.

Liquefaction-related ground failures resulted in damage to the port facilities, electric power plants, pavements, utilities, oil storage tanks, and other structures in Guam. Our observations of the damage to these facilities are presented in the remainder of this paper.

COMMERCIAL PORT FACILITIES

At the commercial port on Cabras island, the liquefaction-related damage was concentrated in an area between Berth No. 3 and Berth No. 6. This area was reclaimed by:

1) dredging the lagoonal deposits and raising the ground surface from its original grade at Elevation[1] -3 feet to Elevation +1 foot

2) driving the sheet piles to Elevation -45 feet (tip elevation)

3) driving the 15-foot-long deadman sheet piles and installing the tie rods

4) placing additional fill, compacting the fill to 95 percent relative compaction, and raising the grade to Elevation +9 feet at the bulkhead location and to Elevation +10 feet at the deadman location about 100 feet from the bulkhead

5) dredging the material in front of the bulkhead to approximately Elevation -35 feet.

During the first stage of fill placement, the dredged materials were placed below water and directly over the lagoon deposits. The results of a post-earthquake geotechnical investigation in this area indicate that the lagoon deposits contain a layer of loose, silty, fine sands containing about 15 to 25 percent fines. The penetration resistance measured within this layer was less than 10, mostly in the range of 2 to 8. It should be noted that some of the blow counts were obtained through a non-standard penetration testing procedure (i.e., the holes were drilled using a hollow stem auger, and the sampler size was larger than that of the Standard Penetration Test sampler). The blow counts were then converted to the SPT N-values by applying a correction factor to account for the larger-sized sampler.

Figure 2 presents an aerial view of the commercial port facilities. Significant soil liquefaction occurred in the area between Berth Nos. 3 and 6. Soil liquefaction resulted in failure of the bulkhead, and caused up to 24 inches of lateral movement and up to 18 inches of settlement of the ground behind the bulkhead (Figures 3 and 4).

Figure 5 presents the liquefaction-induced differential settlement between the pile-supported crane railing system and the adjacent filled areas. Figure 6 shows the disruption of the surface drainage by the differential ground settlement.

The movement of the bulkhead and lateral spreading resulted in several pavement cracks parallel to the shoreline; the most significant of which occurred near the deadman, about 100 feet from the bulkhead.

---

[1] Mean Low Low Water

Our team is in the process of performing additional field investigations in areas adjacent to but outside of the zone that experienced soil liquefaction. We will attempt to identify critical SPT N-values by comparing the penetration resistances at sites that experienced soil liquefaction and those which did not.

SHELL OIL TERMINAL

The Shell Oil Terminal is on a spit of land branching out from Cabras island near Berth F at the commercial port (Figure 8).

Soil liquefaction resulted in settlement and lateral spreading near the shoreline. No significant damage to the tank or its foundation was reported as the result of the ground failures.

Figure 9 shows that about six inches of settlement and six inches of lateral movement that occurred near the shoreline where the smaller oil tanks are located.

The subsurface condition generally consists of 9 to 10 feet of fill made up of silty, sandy, limestone gravel. The upper 3 to 4 feet of fill appears to be medium-dense, but the lower portion, which was placed below water, is loose. The natural soil underlying the fill is medium-dense to dense, silty, gravelly sand of coral origin.

It is surmised that the mat foundations supporting the oil tanks influenced the pattern of ground failure (i.e., ground settlement and lateral movement were pushed to the landside of the tanks), and performed satisfactorily by maintaining the tanks in a relatively level condition.

PITI ELECTRIC POWER PLANTS

There are two electric power plants (EPP) in Piti (Figure 10). The new EPP belongs to the U.S. Navy and is supported on steel H piles; the older EPP belongs to the government of Guam and is supported on wood piles.

Soil liquefaction resulted in ground settlements (locally up to several inches), and minor lateral movements, except near the stream channel.

The subsurface conditions consist of a 5- to 8-foot-thick silty, sandy, gravel fill underlain by a medium-dense, relatively clean, coral sand layer about six feet thick. The coral sands are, in turn, underlain by coralline limestone at depths ranging from 12 to 14 feet.

As can be seen from Figure 11, lateral spreading caused the power poles to lean towards the stream channel. Figure 12 shows typical ground settlements adjacent to buildings supported either on shallow foundations founded on dense sands below the liquefiable sands or on deep pile foundations.

U.S. NAVY PORT FACILITIES

Figure 13 presents an aerial view of the U.S. Navy port facilities in Apra Harbor and the inner harbor areas. Similar to the commercial port facilities, soil liquefaction, ground settlement, and lateral spreading caused significant damage to the port facilities.

Although the ground failures at each wharf exhibited unique characteristics, soil liquefaction generally resulted in a series of pavement cracks parallel to the shoreline. In all cases, the lateral movements were coupled with ground settlements, making determination of volumetric strain very difficult, if not impossible.

At Wharf V, there was a concentration of lateral ground movement at the deadman location (Figures 14 and 15). Failure of the bulkhead resulted in bulging of the ground surface on the front and about a 24-inch drop on the backside, of the deadman. Upon further investigation, it became apparent that the upper portion of the deadman was embedded within soil that did not liquefy. As a result of soil liquefaction and loss in strength of the lower material, the deadman moved laterally and pushed against the upper, more competent material, and caused the ground surface to bulge.

At Wharf O, soil liquefaction resulted in failure of the bulkhead, lateral movements in the bulkhead and backfill of up to three feet, and ground settlement of up to 24 inches (Figure 16). In addition to a major crack parallel to the shoreline, a classical, circular ground failure also occurred behind the deadman (Figure 17). Our team is in the process of performing a geotechnical field investigation within areas where failure occurred and in the adjacent areas where soil liquefaction did not occur. Again, the purpose of this work is to identify critical SPT N-values by comparing the penetration resistances at sites that experienced soil liquefaction and those which did not.

Figures 18 and 19 show aerial and close-up views of Wharf S, where the maximum lateral movement of the bulkhead (about eight feet) and ground settlement behind the bulkhead (about 30 inches) occurred within the U.S. Navy port facilities.

Lateral ground failure, as manifested by cracking of the pavement, occurred at a relatively large distance (up to 250 feet) away from the shoreline near Wharf S. Available subsurface information from a geotechnical investigation performed for a site about 150 feet away from the shoreline indicates the site is underlain by a layer of granular fill that is 8 to 11 feet thick. Below the fill, down to a depth of 80 feet, the site is underlain by lagoon deposits consisting of alternating layers of loose clean sand, loose silty sand, medium-dense gravel, coralline limestone, and soft sandy silt.

It is clear that settlement and lateral movement in this area are indicative of soil liquefaction within the lagoon deposits, and is not necessarily limited to the surficial fill material. Indeed, the reported lateral movements along the Dry Dock island shorelines and the U.S. Navy fuel pipeline were the results of soil liquefaction within the lagoon deposits consisting of loose silty sand and soft sandy silt.

Of particular interest is the apparent influence of the presence of the Laundromat building on the pattern of lateral ground movement (Figure 20). As indicated in this photograph, as the ground surface crack approached the building, it changed direction, and instead of breaking through the slab, it separated the slab from the wall, then continued its natural course on the other side of the building. This indicates that even the stiffness offered by a building of substandard design and construction could significantly affect the pattern of ground failure.

Figure 21 shows typical settlement and cracking of the pavement immediately behind the bulkhead at the U.S. Navy port facilities.

OTHER SITES WHICH EXPERIENCED SIGNIFICANT SOIL LIQUEFACTION

The largest lateral movement caused by soil liquefaction occurred near the former Andy's hut at the north shoreline of Apra Harbor. Lateral spreading of up to 15 feet caused failure of the sheet piles (Figures 22 and 23) and collapse of the building. The building had been demolished and removed before these photographs were taken.

ACKNOWLEDGMENTS

The authors wish to acknowledge the support of the National Science Foundation (NSF Grant No. CMS-9413272). We would also like to thank Mr. Simeon Delos Santos of the Port Authority of Guam and the U.S. Navy, OICC Guam engineers for providing access to and permitting the release of data. In addition, the useful discussions with Dr. Peter Nicholson, Mr. John Egan, Mr. Peter Kaldveer, and Mr. Robin Lim are greatly appreciated.

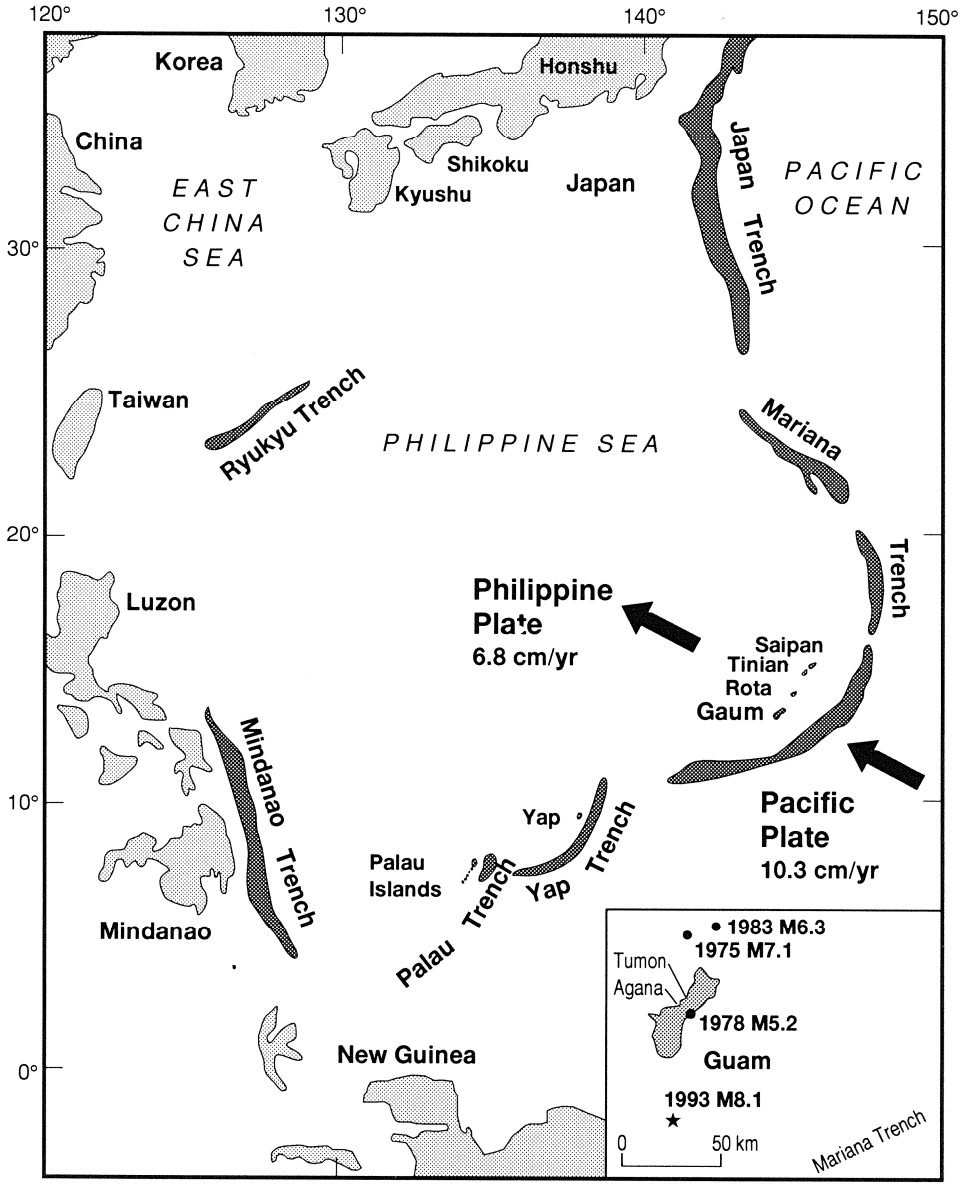

Figure 1: Location map, island of Guam, Mariana Trench, and epicenter of the 1993 earthquake within the Pacific Rim
Reference: EERI Newsletter, v. 27, n. 10, October 1993

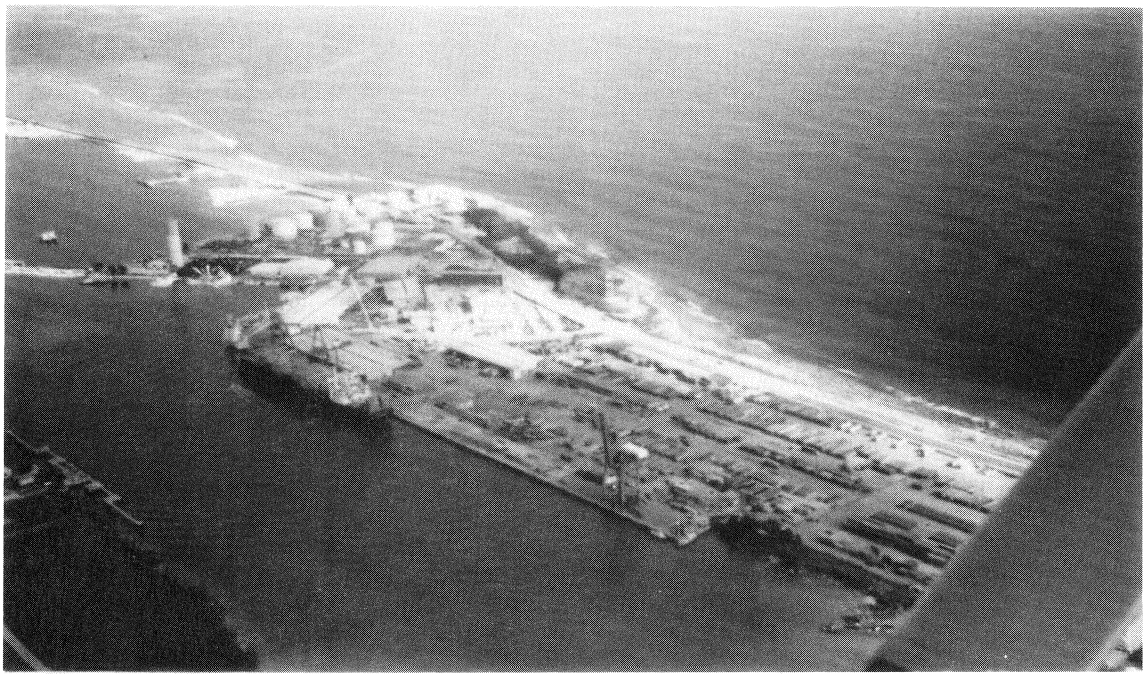

Figure 2: Aerial view of the commercial port facilities

Figure 3: Aerial view of the damage to the commercial port facilities

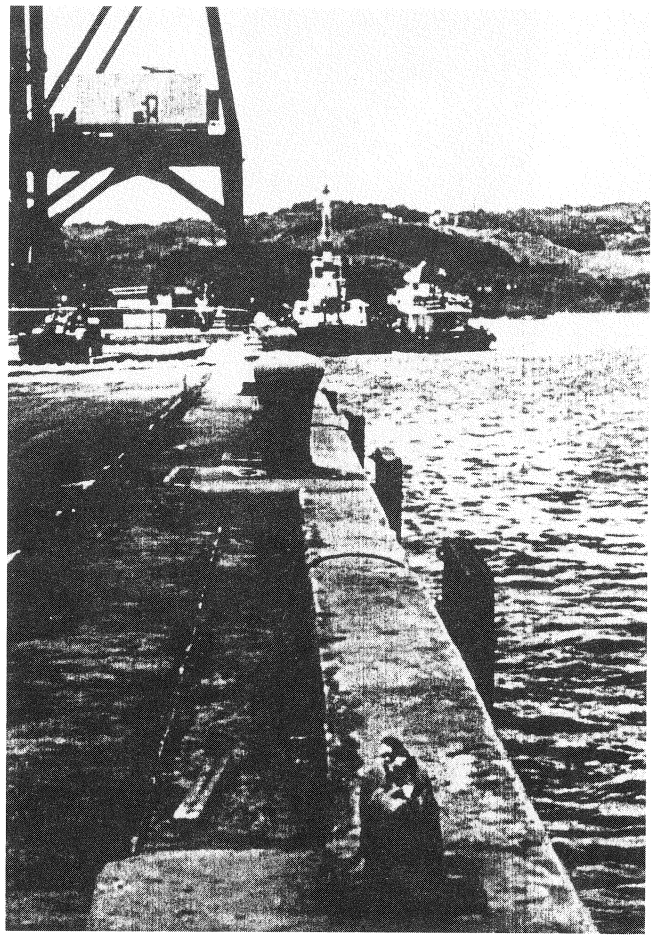

Figure 4: Liquefaction-induced lateral movement of the bulkhead (up to 24 inches) and settlement (up to 18 inches) at the commercial port facilities

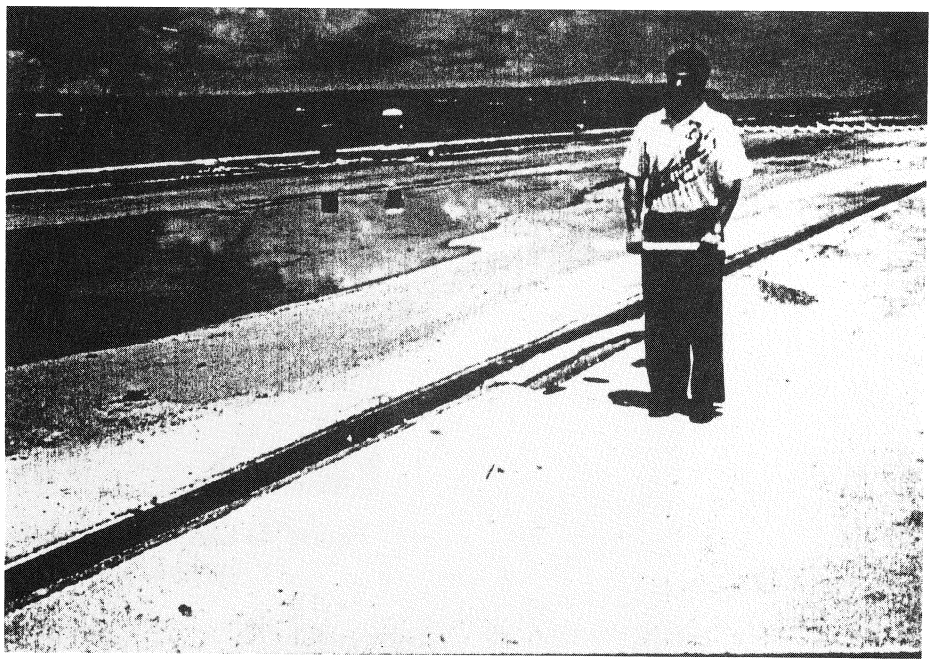

Figure 5: Differential settlement between the pile-supported crane railing and the adjacent filled areas

Figure 6: Settlements of up to 18 inches disrupted the surface drainage at the commercial port facilities

Figure 7: Lateral movement and cracking of the pavement, commercial port facilities

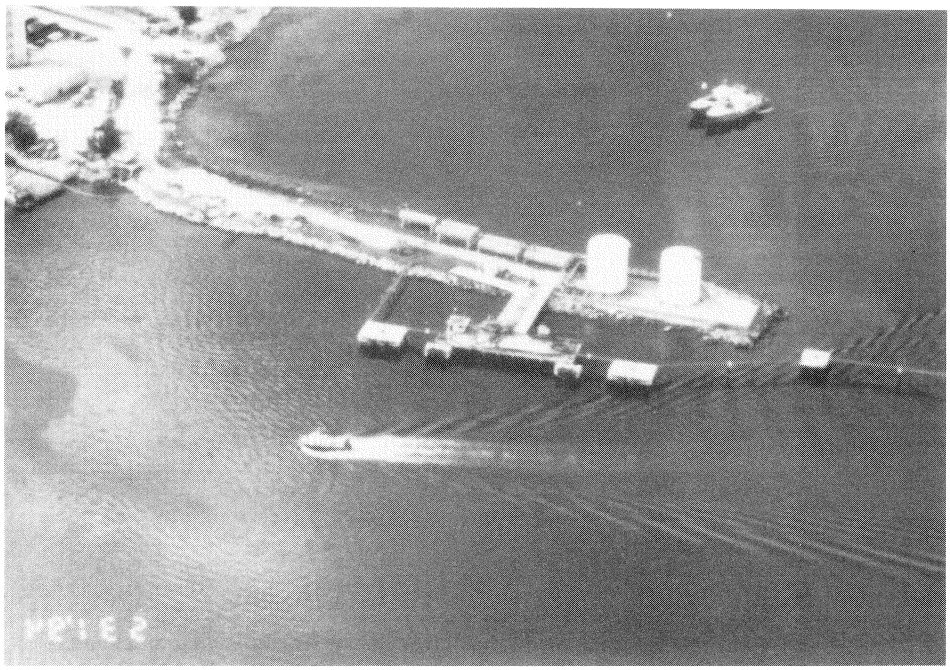

Figure 8: Aerial view of the Shell Oil Terminal

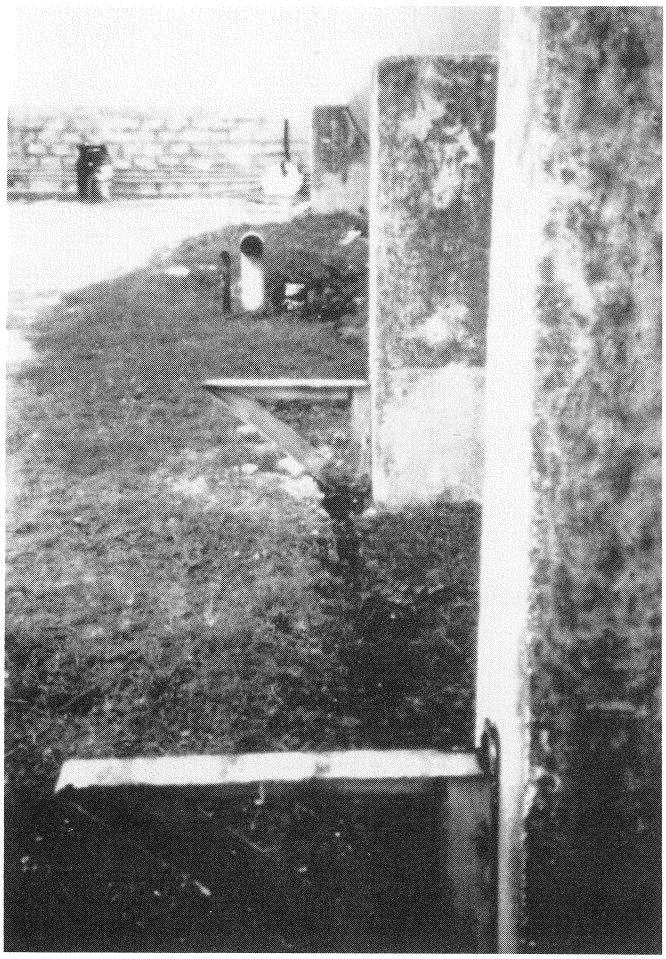

Figure 9: Uniform settlement and lateral movement of the oil tanks, Shell Oil Terminal

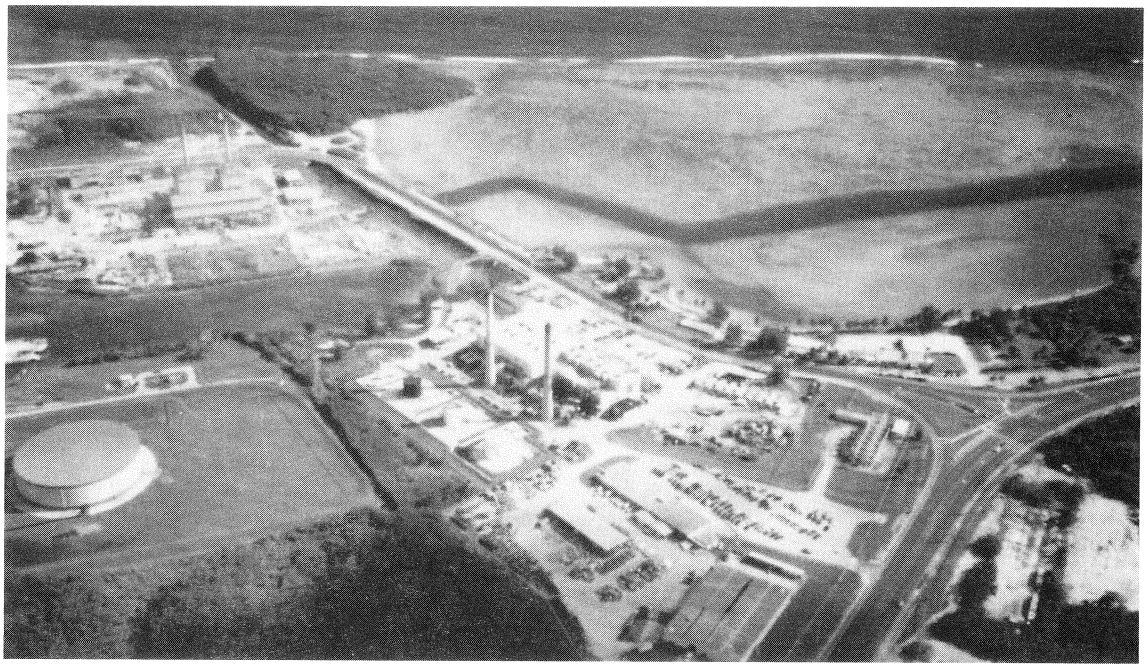

Figure 10: Aerial view of the Piti Electric Power Plant

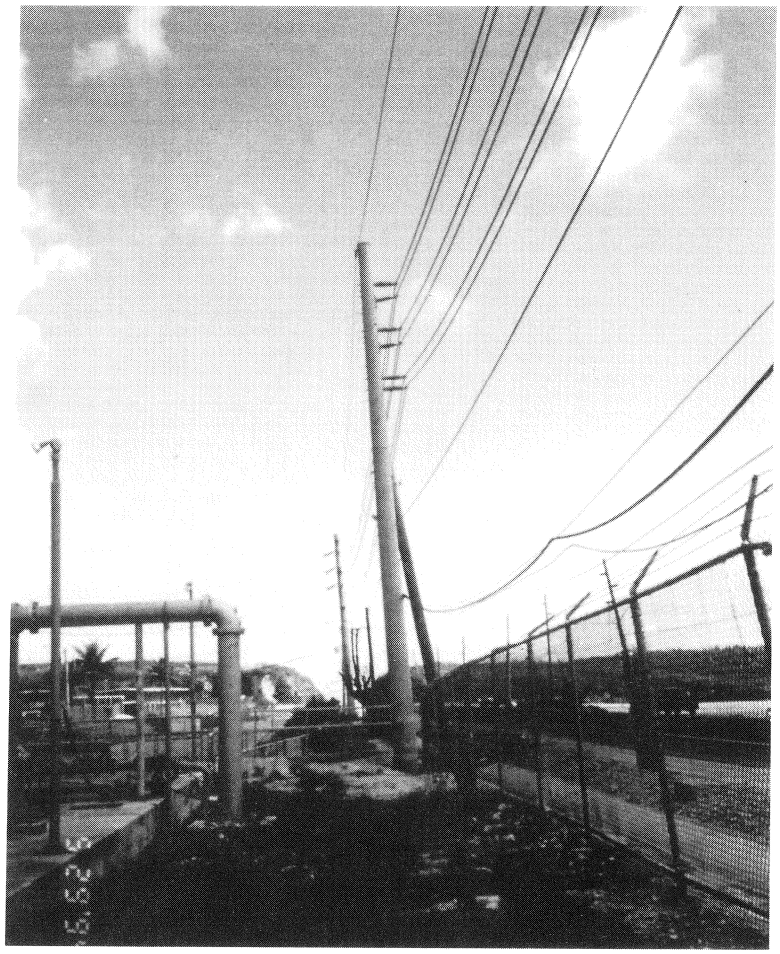

Figure 11: Leaning of the power poles caused by lateral spreading at the Piti Electric Power Plant

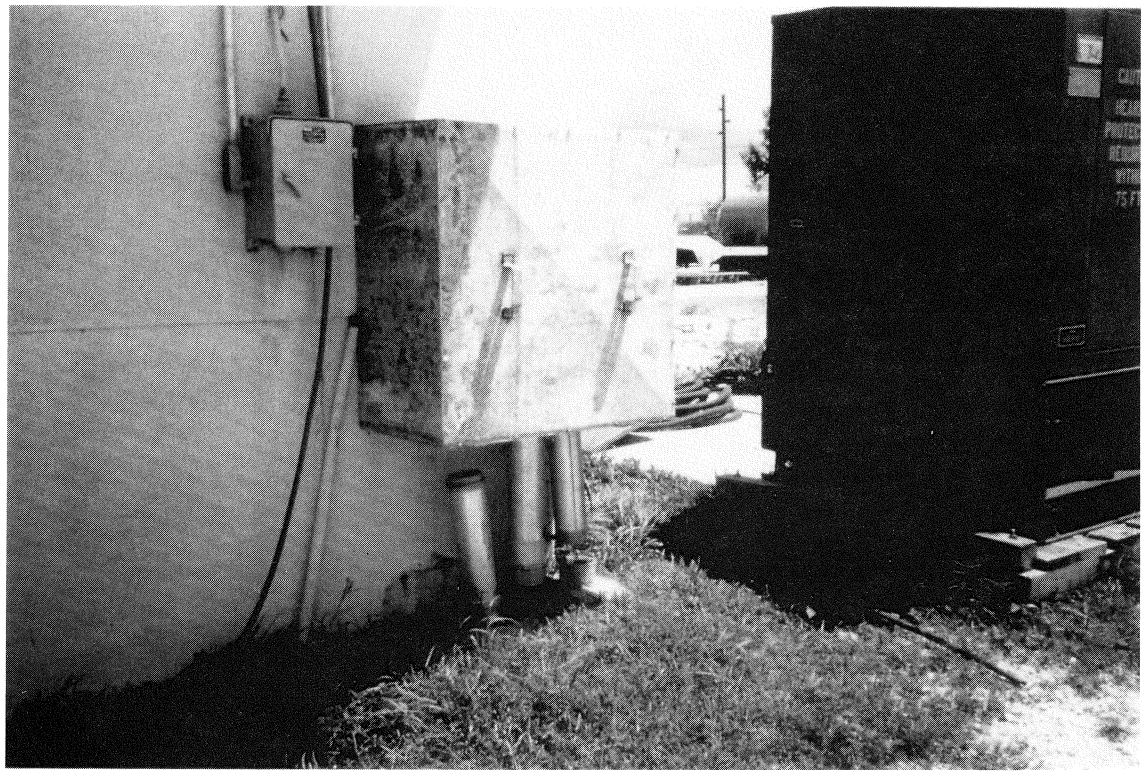

Figure 12: Signs of differential settlement between the pile supported building and the adjacent filled area

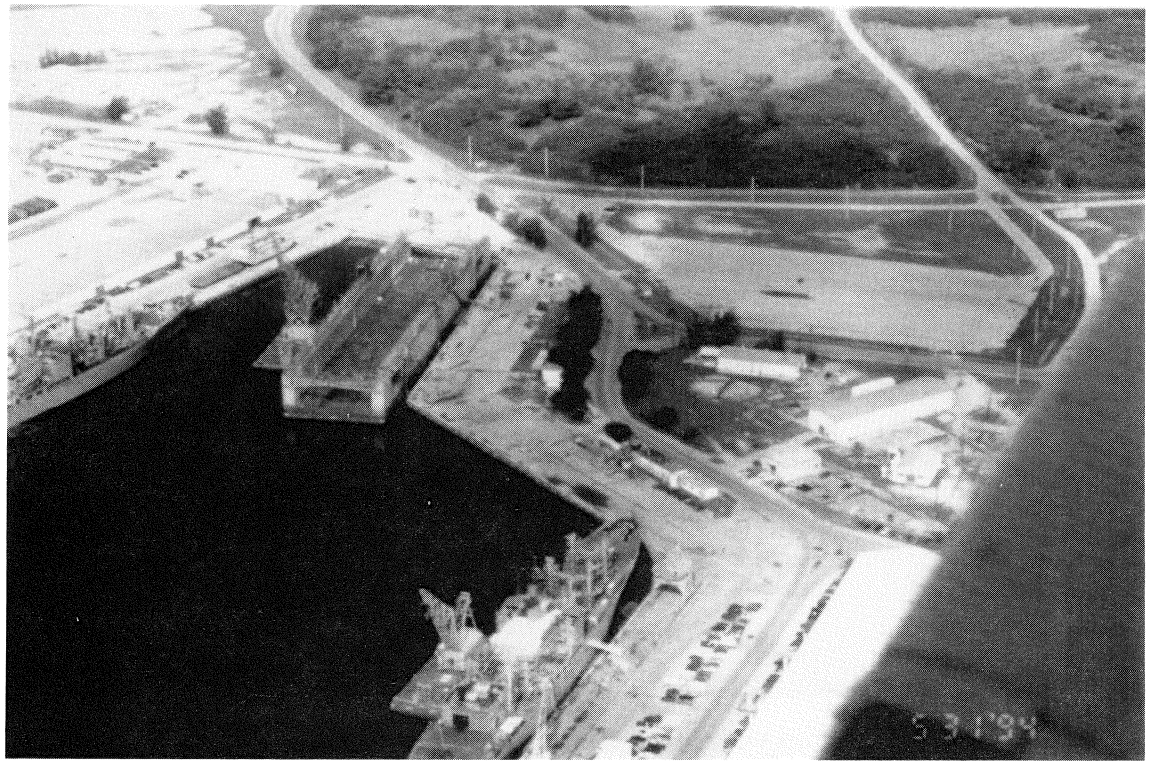

Figure 13: Aerial view of the U.S. Navy port facilities

Figure 14: Aerial view showing concentration of lateral movement and settlement behind the bulkhead, U.S. Navy port facilities

Figure 15: Close-up view of the lateral movement and settlement behind the bulkhead, U.S. Navy port facilities

Figure 16: Lateral movement of the bulkhead, U.S. Navy port facilities

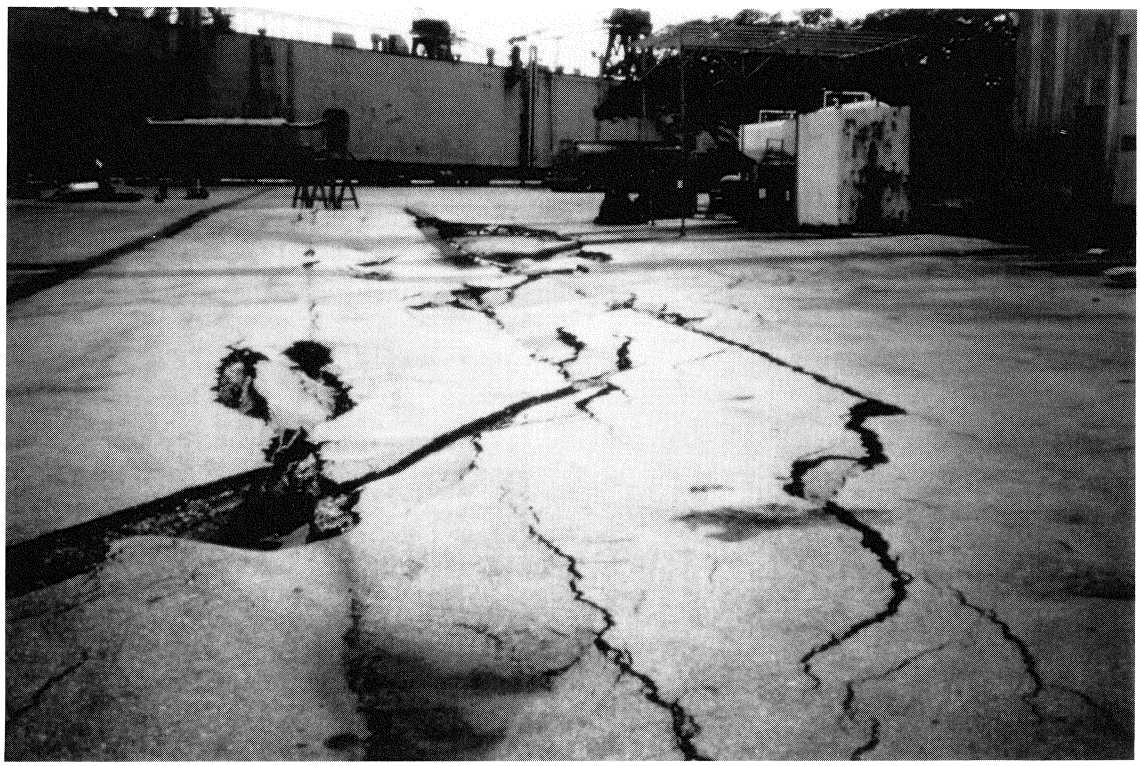

Figure 17: Pattern of lateral soil movement and cracking of the pavement, U.S. Navy port facilities

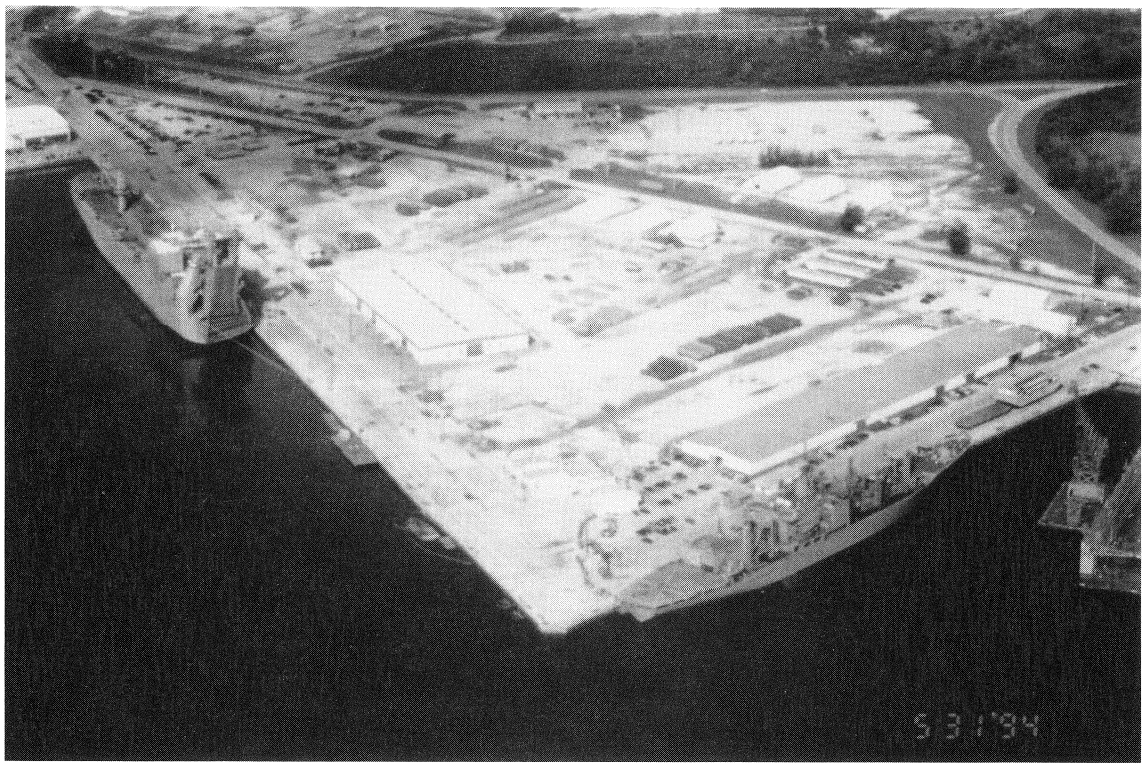

Figure 18: Aerial view of lateral movement of the bulkhead and settlement at the U.S. Navy port facilities

Figure 19: Close-up view of the lateral movement of the bulkhead and settlement at the U.S. Navy port facilities

Figure 20: Influence of the presence of the Laundromat building on the pattern of the lateral ground movement

Figure 21: Typical settlement and cracking behind the bulkhead, U.S. Navy port facilities

Figure 22: Failure of the sheet pile and lateral spreading near the former Andy's hut

Figure 23: Aerial view of failure of the sheet piles and lateral spreading near the former Andy's hut

EFFECTS OF REMEDIAL MEASURES AGAINST LIQUEFACTION AT 1993 KUSHIRO-OKI EARTHQUAKE

S. Iai[1], Y. Matsunaga[1], T. Morita[1], M. Miyata[1], H. Sakurai[1],

H. Oishi[2], H. Ogura[3], Y. Ando[4], Y. Tanaka[5] and M. Kato[5]

1) Port and Harbour Research Institute, Yokosuka, Japan
2) NKK Corporation, Yokohama, Japan
3) GEOTOP Corporation, Tokyo, Japan
4) FUDO Construction Co., Ltd., Tokyo, Japan
5) KONOIKE Construction Co., Ltd., Tokyo, Japan

ABSTRACT

During the 1993 Kushiro-Oki Earthquake of magnitude 7.8, Kushiro Port being located at 15 km from the epicenter was shaken with a peak horizontal acceleration of 0.47g. Many of the quay walls at the Kushiro Port suffered damage due to liquefaction of backfill sand. However, the quay walls having backfill sand compacted as measures against liquefaction survived the earthquake without damage. In these quay walls, gravel drains were also used as a part of the liquefaction remediation in the vicinity of the walls. Since the contrast in the performance of those quay walls are of significance in the engineering practice, the present paper is devoted to report the details including the recorded earthquake motions and the ground conditions.

INTRODUCTION

In recent Japanese practice, measures against liquefaction have often been put into practice in order to mitigate damage to structures sitting on potentially liquefiable foundations. While laboratory data are abundant to evaluate the effectiveness of those measures against liquefaction, in-situ data during strong earthquake shaking are very scarce.

On January 15, 1993, an earthquake of magnitude 7.8 in the scale of Richter-Japan Meteorological Agency (JMA) hit a northern island of Japan called Hokkaido. The epicenter was located 15 km south of Kushiro City as shown in Fig. 1; the earthquake was named the 1993 Kushiro-Oki earthquake. The focal depth was 107 km, being much deeper than the ordinary focal depths of about 40 km for the earthquakes occurring around Japan.

Kushiro Port was shaken with a peak horizontal acceleration of 0.47g. The earthquake caused liquefaction of untreated backfill sand at the port, resulting in damage to many of the quay walls. The extent of the damage was generally moderate; the displacements of the quay walls were less than about 5 percent of the water depth in front of the quay walls. In contrast, the quay walls having the backfill sand compacted as measures against liquefaction survived the earthquake without damage. In these quay walls, gravel drains were also used as a part of the liquefaction remediation in the vicinity of the walls to relieve the influence of compaction to the walls during its installation.

In the present paper, the effects of these liquefaction remediation measures will be reported in detail including the recorded earthquake motions, the ground conditions, and the results of in-situ examination of gravel drains after the earthquake.

KUSHIRO PORT

Kushiro Port is developed at the estuary of the Kushiro River as shown in Fig. 2. As understood by the former beach line shown by the broken line in Fig. 2, most of the port area has been reclaimed from the sea by filling the sand dredged from the nearby sea. The port has been constructed step by step from a quay wall located at the eastern most end toward west direction along the former beach line; the quay wall at the western most end, i.e. Pier No.3 in the West Port District, has been just constructed in 1992.

The natural ground along the former beach line is of sand dune origin, being dense with SPT N-values of about 50. The fill above the original ground gradually increases its thickness from none at the former beach line to about ten meters at the southern end of the piers in the West Port District.

Though Kushiro City is located at the latitude 43 degrees north, at about the same as that of Rome in Italy, the average temperature falls below the water freezing point during winter. When the earthquake hit, the ground surface was said to be frozen with a thickness of about 0.5 to 1.0 meters in Kushiro City. However, the port engineers reported that the materials used for the ground surface layer in the port areas were chosen to serve as anti-freezing layer to prevent the damage to the pavement due to the soil freezing. The anti-freezing layer is made of coarse sand, its thickness about 0.8 meters. At present, the authors could not obtain the definite evidence to determine whether the ground surface in the port area was frozen at the time of the earthquake. When the earthquake occurred, the ground at Kushiro City was not covered with snow. It began to snow the next day and the ground was covered with snow with a thickness of about 0.2 meters.

EARTHQUAKE MOTION AT KUSHIRO PORT

Kushiro Port has a strong motion recording station at its central location. This is one of the station deployed under the network of the Port and Harbour Research Institute in cooperation with the Kushiro Port Construction Office, Hokkaido Development Bureau (Kurata and Iai, 1992).

The strong motion recording station is located on the former beach line at the estuary of the Kushiro River as shown in Fig. 2. The ground condition is shown in Fig. 3. In this figure and the figures to follow, all the borings and the Standard Penetration Tests (SPT) were conducted before the earthquake. The ground at this site consists of a fill with a thickness of about three meters, underlain by a medium to dense sand layer of SPT N-values about 20 with a thickness of about seven meters, underlain by a dense sand layer of SPT N-values of about 50.

The instrumentation at this site consists of two accelerographs; one is installed at the ground surface, the other installed at the base of the bore hole 77 meters below the ground surface. The accelerographs are of force balance servo type, having the flat gain in the frequency range from 0.01 to 30 Hz. The acceleration data are recorded in the digital format in the integrated circuit (IC) cartridge memory with 16 bits/data at the time intervals of 0.01 seconds. The digital recorder is equipped with a pre-event memory to record earthquake motions from ten seconds before triggering.

The recorded earthquake motions during the 1993 Kushiro-Oki Earthquake are shown in Fig. 4. In this figure, main portion of the earthquake motion is plotted out of the original record obtained for a duration of 180 seconds; the origin of the time is ten seconds before the triggering of the recorder. Loci of integrated velocities and displacements computed for the accelerations at the ground surface and the base, shown in Fig.

5, clearly indicate that the predominant motion is in the north-south direction in this earthquake.

By comparing the ground surface motion in the north direction shown in the first row in Fig. 4 with the corresponding base motion at a depth of 77 meters shown in the fourth row, it is easy to notice the sudden change in the response of ground after about 30 seconds; most of the high frequency motions are filtered out; instead, a long period motion with a period of about 1.5 seconds becomes predominant, overlain by a spiky wave form at each peak.

This type of ground response has been often observed in the laboratory (e.g. Lee and Schofield, 1988); it is considered as manifestation of the effect of cyclic mobility of dense sand. The effect of the dilatancy of sand plays a major role when the ground is saturated and shaken with a strong motion as in this earthquake. In the in-situ condition during earthquakes, similar spiky acceleration was observed at loose silty sand deposit at the Wildlife site during the 1987 Superstition Hills Earthquake (Holzer et al, 1989). In the dense clean sand deposit, the present record represents the very evidence that the effect of dilatancy of sand plays a significant role in the ground response during strong earthquake shaking.

In the current practice of ground response analysis such as often done with the equivalent linear model, the effect of the dilatancy of sand has been often neglected. The definite evidence presented here cautions us against the current practice of ground response analysis at strong earthquake motions.

DAMAGE TO GRAVITY QUAY WALLS

The most serious damage to the gravity quay walls in Kushiro Port was found at the North Pier in the East Port District. The location is designated in Fig. 2 as the site A. As shown in Fig. 6, displacement toward sea registered 2.0 meters at maximum, settlement 0.4 meters at maximum. The ground conditions shown in Fig. 7 indicates possibility of liquefaction down to an elevation of about -6.0 meters below the water level.

Among the gravity quay walls affected by liquefaction of backfill sand, quay walls designed with a seismic coefficient of 0.2 suffered relatively minor displacement. An example with a water depth of 12 meters is shown in Fig. 8. This quay wall is located at the south end of the Pier No.2 in the West Port District shown in Fig. 2 designated as the site B. As understood from the height to width ratio of the caisson being close to unity, the quay wall was designed to resist relatively strong earthquake motions.

The backfill sand at this pier was loosely deposited and was of a coarse sand as shown in Fig. 9. It was planned to be compacted as remedial measures against liquefaction; unfortunately the

earthquake hit the Kushiro area before the work was actually done. The backfill sand liquefied due to the earthquake. The caisson suffered deformation as shown in Fig. 8 but the displacement toward sea was only about 0.3 meters.

DAMAGE TO A SHEET PILE QUAY WALL

The most serious damage to the sheet pile quay walls in Kushiro Port was found at the Fishery Pier in the East Port District. The location is designated in Fig. 2 as the site C. The structure of this quay wall is of a steel sheet pile type anchored by battered steel piles. The cross section is shown in Fig. 10. As shown in Fig. 11, the ground at this pier consists of a loosely deposited backfill sand with a thickness of about ten meters, underlain by medium to dense sand deposit which forms the original ground.

The original ground level becomes deeper to the level of 11.5 meters at the eastern end of the quay wall so that this part of the quay wall slightly differs from that shown in Fig. 10; the quay wall at the eastern end uses longer sheet piles with an embedment depth of -20.5 meters and longer anchor piles installed to a depth of -14.9 meters on the sea side and -20.6 meters on the land side.

The earthquake caused liquefaction in the backfill sand, resulting in the serious deformation of the sheet pile wall as shown by the solid line in Fig. 10. In accordance with the deformation of the sheet pile wall, the apron exhibited serious settlement between the sheet pile wall and the anchor piles. Detailed investigation of the sheet pile wall by diving in the sea revealed that cracks opened in the steel sheet pile wall at an elevation of four meters below the water level.

PERFORMANCE OF A SHEET PILE QUAY WALL WITH COMPACTED Backfill SAND

In contrast to the damaged sheet pile quay wall described earlier, quay walls with compacted backfill sand survived the earthquake without damage. An example, shown in Fig. 12, is the quay wall at the south end of the Pier No.1 at the West Port District. The location is designated as the site D in Fig. 2.

The structure of this quay wall is of a steel pipe pile wall anchored by a steel sheet pile wall with a water depth of 12 meters. The ground at this wall had originally consisted of fill sand with a thickness of about ten meters, underlain by the original ground of medium to dense sand. The backfill sand was later treated by a sand compaction pile method as shown in Fig. 12. The SPT N-values of the ground before and after the compaction are shown in Fig. 13. In order to avoid the adverse effect upon the existing steel pipe pile wall during the ground compaction work, gravel drains were installed near the wall as shown in Fig. 12.

Despite the strong shaking of the earthquake, the earthquake caused no effect on this quay wall. The measures against liquefaction as well as the overall design of the quay wall according to the current design practice (Ports and Harbours Bureau, 1991) was proven to be good enough to provide resistance the strong earthquake shaking.

LIQUEFACTION AND DAMAGE TO STRUCTURES

In order to grasp an overall picture of the effects of liquefaction on damage to quay walls at Kushiro Port, Table 1 summarizes the relevant data of the quay walls with water depths deeper than 7.5 meters. In this table, "liquefaction" is identified with respect to the soils within "the area of a quay wall cross section," shown in Fig. 14, which includes the backfill area treated as measures against liquefaction. This similarly applies to the quay walls without measures against liquefaction, including the backfill area which is supposed to be treated as remediation against liquefaction.

As shown in Table 1, the quay walls designed with a seismic coefficient of 0.15 suffered serious sea-ward displacement of more than 20% of the water depth. Both the excessive strong shaking and the liquefaction might be the cause for this. In contrast, the quay walls designed with a seismic coefficient of 0.20 suffered sea-ward displacement of less than 10% even when liquefaction occurred.

A closer look at the displacements of the quay walls with a seismic coefficient of 0.20 reveals that those without measures against liquefaction suffered displacement ranging from 0.5 to 10% whereas those with measures against liquefaction suffered displacement less than 3%, suggesting the remediation measures against liquefaction reduces displacement of quay walls.

Among these features observed above, the effectiveness of measures against liquefaction to reduce displacement of quay walls is what was expected through the laboratory studies; the in-situ evidence observed here is the very confirmation of this fact. The effects of seismic coefficient on displacement of quay walls are also what was expected from the balance of inertial forces and resistant force of quay walls. However, the effects of seismic coefficient also include the resistance against the effects of liquefaction. The larger resistance of gravity body, which becomes massive and large if designed with seismic coefficient of 0.20, may contribute to resist the increase in earth pressures due to liquefaction as well.

From the point of view of measures against liquefaction, the backfilled part of ground consisting of rubble behind a wall shown in Fig. 14 might be regarded as treated area as measures against liquefaction. Though the area of this part is not wide enough to cover whole area of active earth failure zone, this

part still contributes to reduce the effects of liquefaction. Indeed, past case histories of performance of quay walls during earthquakes suggests that the effects of rubble can be regarded to reduce liquefaction induced displacement of quay walls (Tsuchida, 1981).

PERFORMANCE OF GRAVEL DRAINS

There was some concern about the performance of gravel drains during earthquakes. This was partly because the history of gravel drains as liquefaction remediation is rather new; the case history data on its performance during actual earthquakes has been scarce. After the earthquake, a site designated site-E, shown in Fig. 2, where gravel drain was installed as remedial measures against liquefaction, was excavated in order to examine the clogging of gravel drains due to migration of sand from natural ground. The cross section of the quay wall and the remediation measures are similar to that shown in Fig. 14 (a).

The gravel drain piles are 40 cm in diameter, installed at a space of 5.0 meters. The sand consisting of the ground and the gravels used for the drain have those gradations shown in Fig. 15. The 15% diameter of the filtering material (i.e. the gravel) d_{F15} and the 85% diameter of the sand D_{S85} read off from this figure are

$$d_{F15} = 2.50 \text{ mm} \quad (1)$$

$$D_{S85} = 0.90 \text{ mm} \quad (2)$$

resulting in a diameter ratio as

$$d_{F15}/D_{S85} = 2.8 \quad (3)$$

This ratio should be more than adequate for passing such a filtering criterion as

$$d_{F15}/D_{S85} < 5 \quad (4)$$

as suggested by the Design Standard for Dams in Japan (1978) and Sherard et al.(1984).

Excavation was done by at first lowering the existing water level at +1.20m to a level of +0.00 m, then by digging out to a level of +0.00 as shown in Figs. 16 and 17. Close eye inspection of a gravel drain, shown in Fig. 18, found no migration of sand.

Sieving of the gravels sampled from the gravel drain resulted in Fig. 19, suggesting that there is not variation in the percentage of sandy materials (i.e. those with a particle size less than 2.0 mm) within the cross section of the gravel drain. However, there were about 20 percent of the sandy materials contained in the gravels as shown in the same figure. In order to examine the origin of those sandy materials, mineral analysis using X-ray

diffraction method was conducted on the sandy materials in the gravels, to be compared with those results on the sand consisting of the ground and the gravel. The mineral analysis resulted in that tridymite S_iO_2 is commonly found in the sandy materials in the gravel drain and the gravel but not in the sand consisting of the ground. This result also confirmed the fact that no migration of sand into the gravel drain occurred during the earthquake.

CONCLUSIONS

The present paper was devoted to compile the case history data on the effects of remediation measures against liquefaction during the 1993 Kushiro-Oki Earthquake. The further analyses are currently underway and will be reported elsewhere. Implications from the present case history data can be summarized as follows.

(1) The strong motion record with a peak acceleration of 0.47g at Kushiro Port indicates that the effect of dilatancy of sand plays an important role in the ground response during strong shaking.

(2) Performance of the quay walls at Kushiro Port manifests the importance and the effectiveness of the measures against soil liquefaction in the earthquake resistant design of waterfront structures.

(3) No migration of sand into gravel drains occurred during the earthquake, suggesting sound performance of gravel drains.

REFERENCES

Holzer, T.L., Youd, T.L. and Hanks, T.C. (1989) : "Dynamics of liquefaction during the 1987 Superstition Hills, California Earthquake, Science 244, pp.56

Japan Large Dam Conference (1978): "Design Standard for Dams (second edition), Chapter 5," (in Japanese)

Kurata, E. and Iai, S. (1992) : "Annual report on strong motion earthquake records in Japanese ports (1991)," Technical Note of the Port and Harbour Research Institute, No.727

Lee, F.H. and Schofield, A.N. (1988) : "Centrifuge modelling of sand embankments and islands in earthquakes," Geotechnique, Vol.38, No.1, pp.45-58

Ports and Harbours Bureau (ed.) (1991) : "Technical standards for port and harbour facilities in Japan," Overseas Coastal Area Development Institute of Japan

Sherard, J., Dunningan, L.P. and Talbot, J.R. (1984) : "Basic Properties of Sand and Gravel Filters," Journal of Geotechnical Engineering Division, ASCE, Vol.110, No.GT6, pp.684-700

Tsuchida, H. (1981) : "Damage to quay walls affected by liquefaction," 16th Research Conference of Earthquake Engineering, JSCE, pp.201-204 (in Japanese)

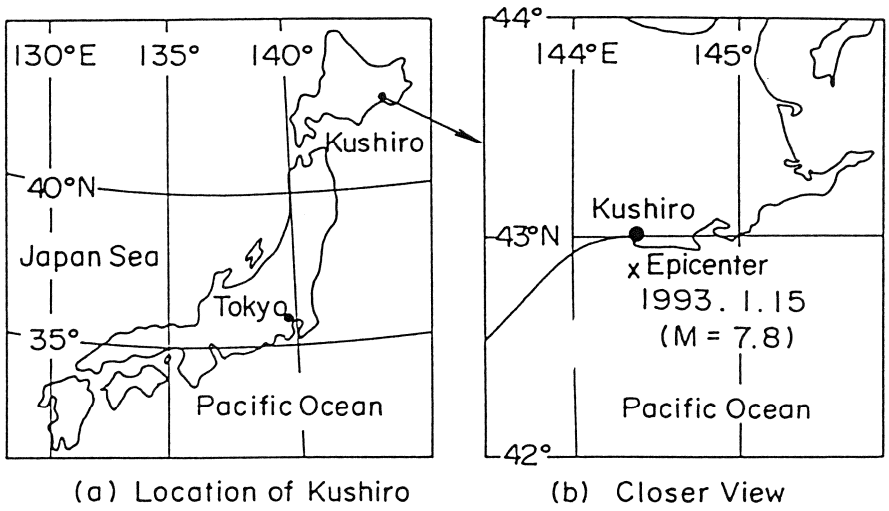

Fig. 1 Location of Kushiro City and the epicenter

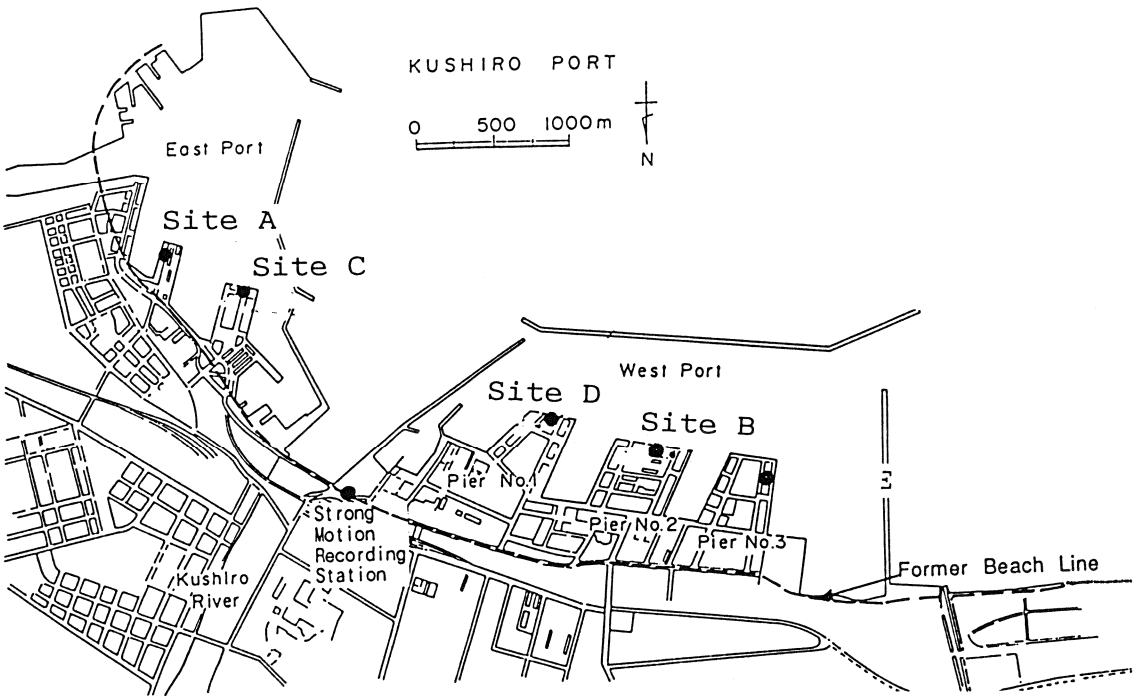

Fig. 2 Plan of Kushiro Port

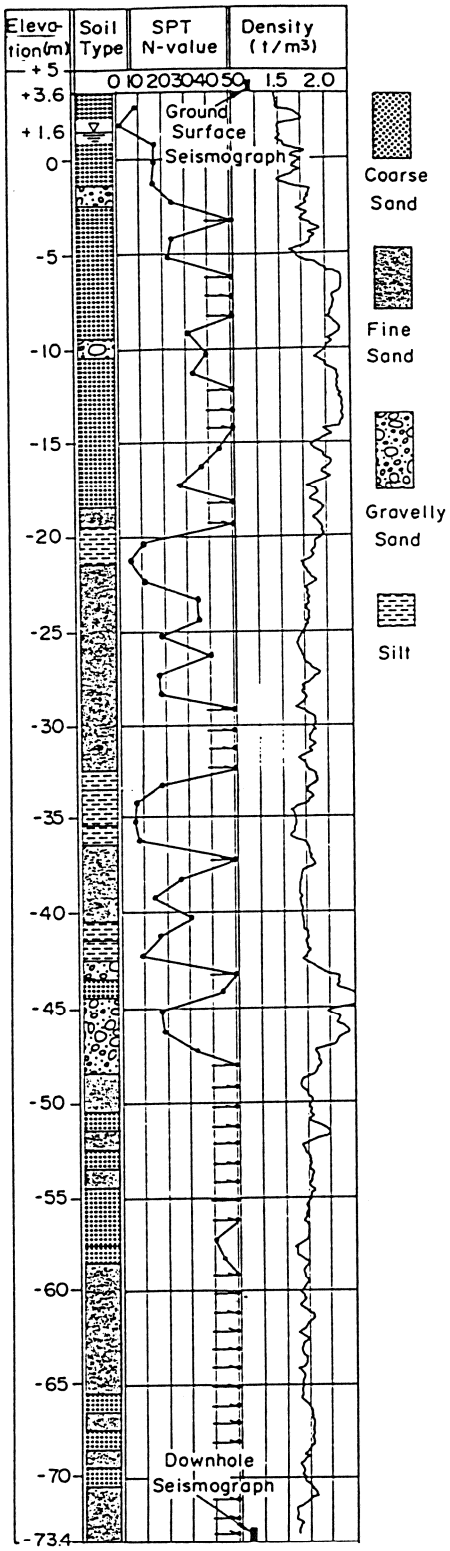

Fig. 3 Ground condition at the strong motion recording station

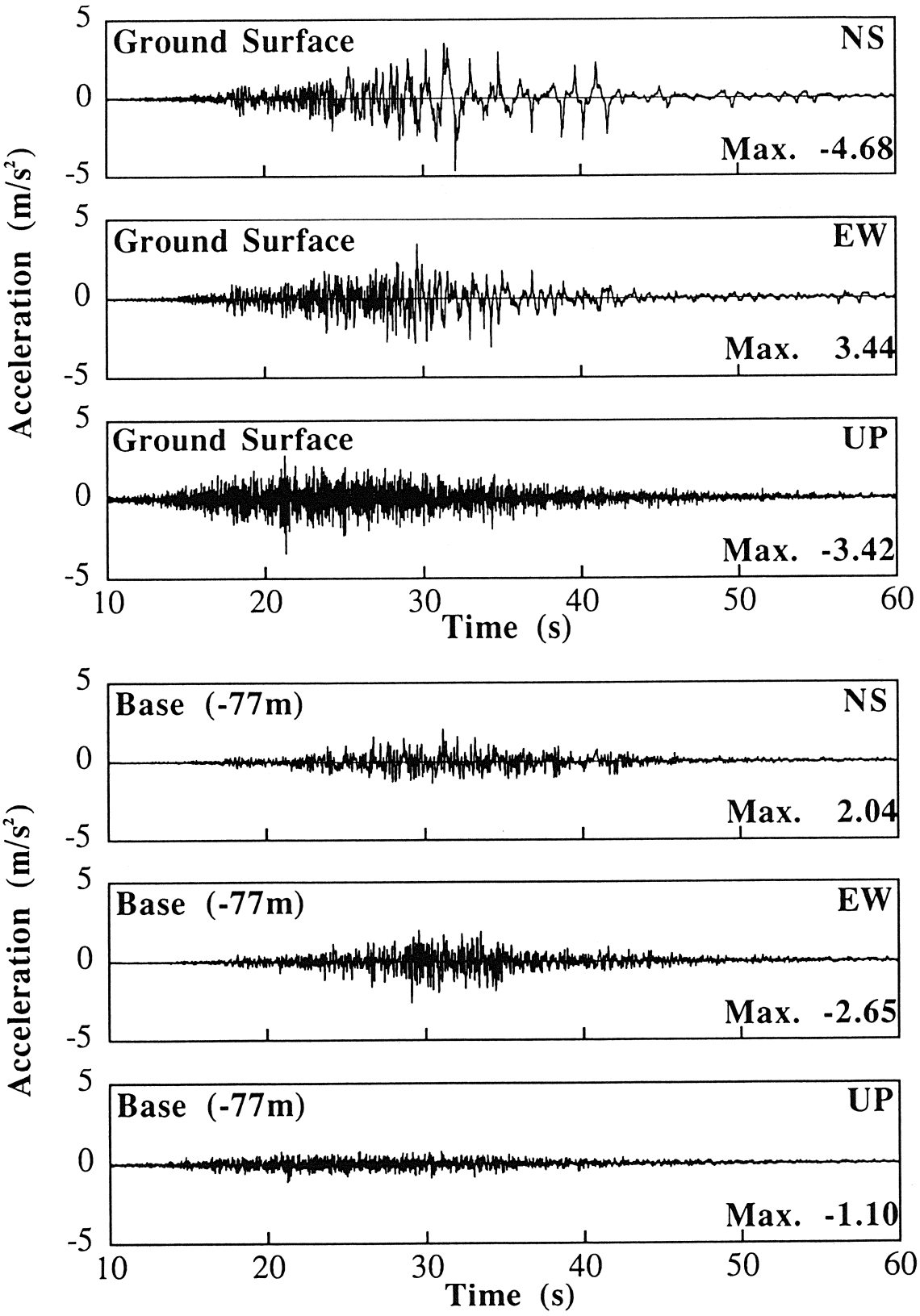

Fig. 4 Strong earthquake motions at Kushiro Port on Jan. 15, 1993

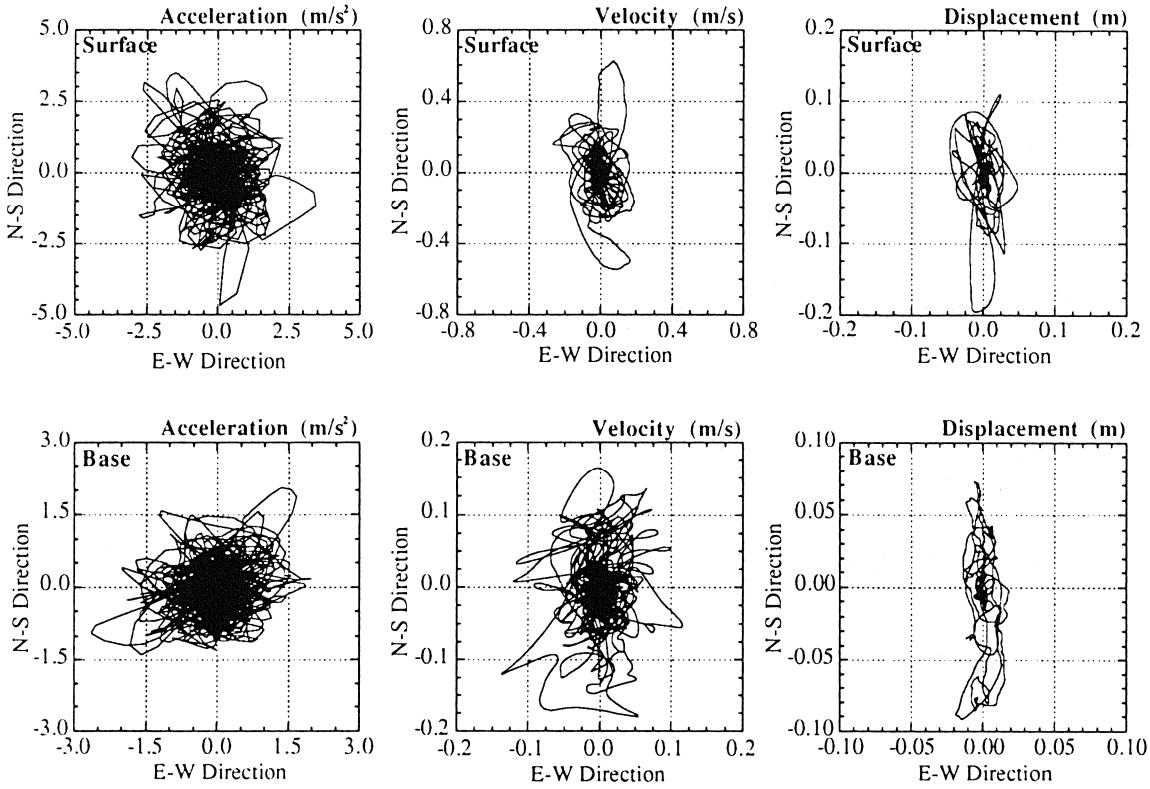

Fig. 5 Loci of accelerations, velocities and displacements

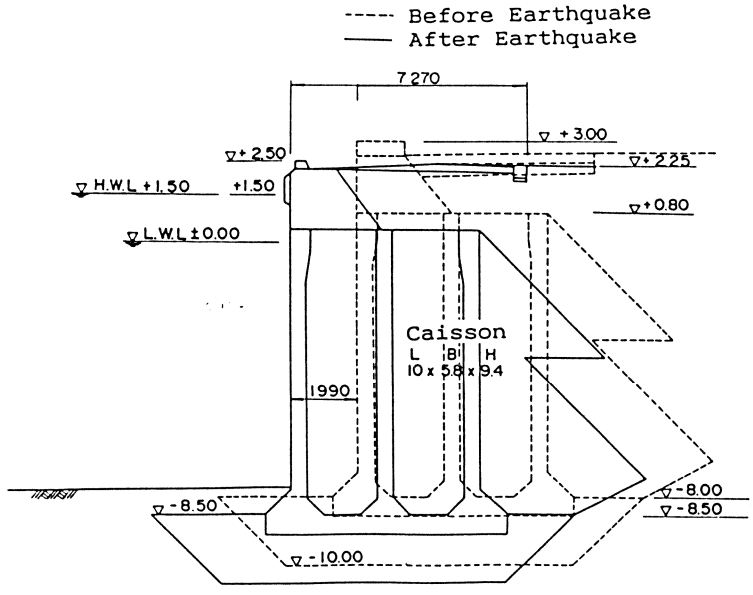

Fig.6 Damage to a quay wall at Site A

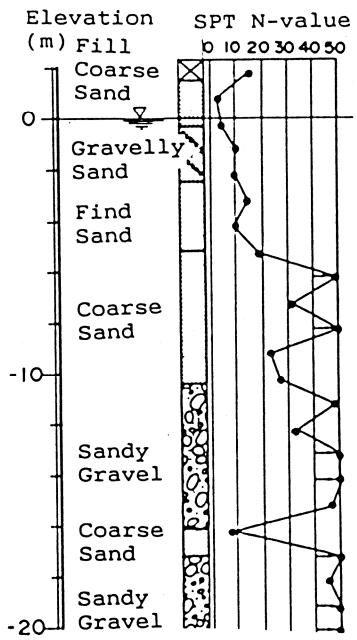

Fig.7 Ground Condition at Site A

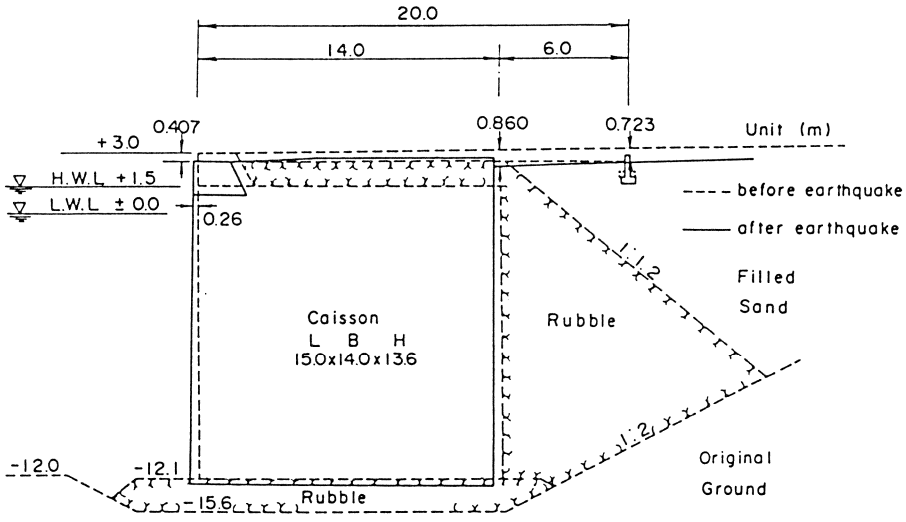

Fig.8 Damage to a quay wall at Site B

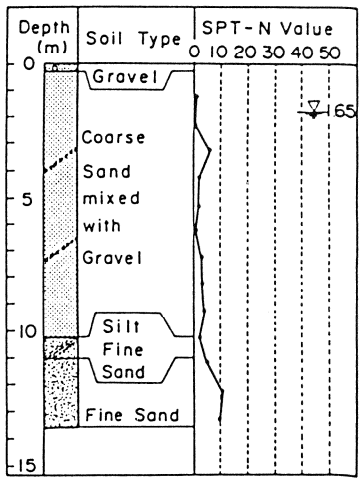

Fig.9 Ground Condition at Site B

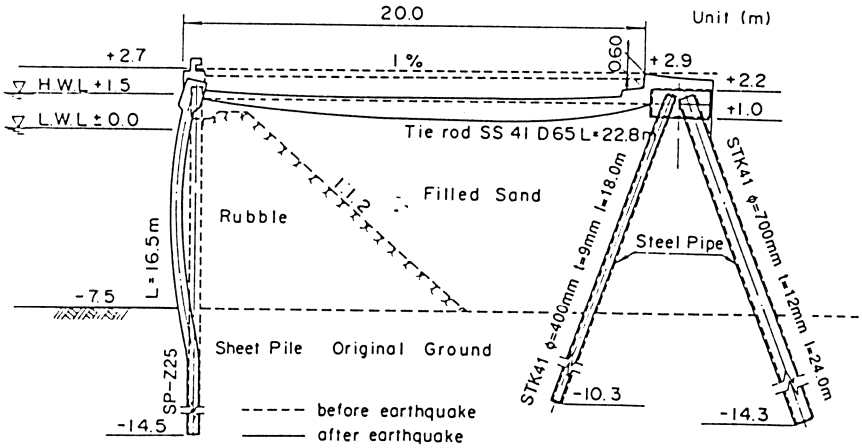

Fig.10 Damage to a quay wall at Site C

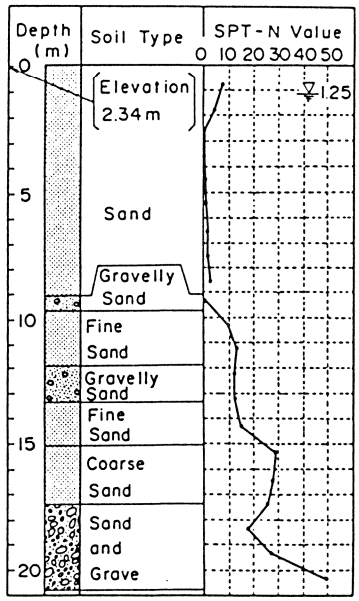

Fig.11 Ground condition at Site C

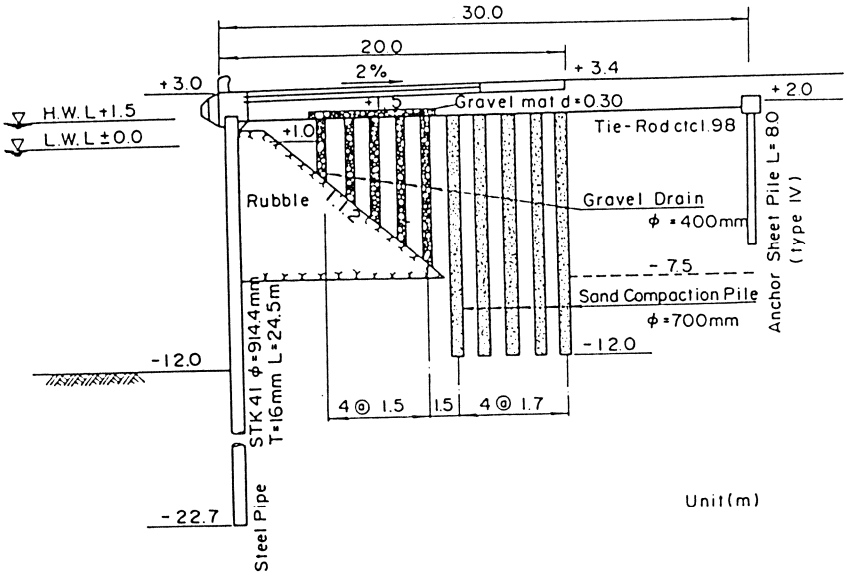

Fig.12 Cross section of a quay wall at Site D

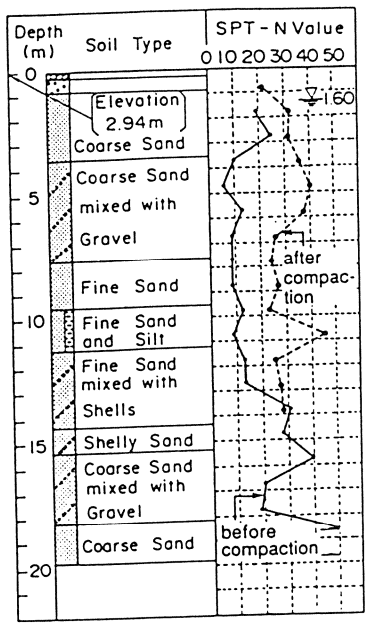

Fig.13 Ground condition at Site D

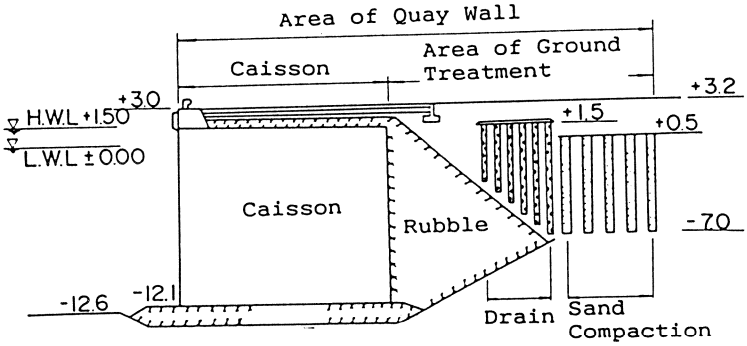

(a) Gravity type quay wall

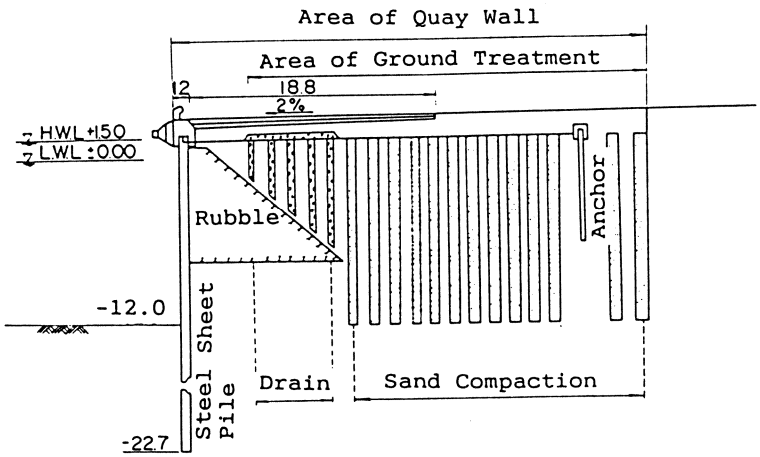

(b) Sheet pile quay wall

Fig.14 Schematic figures of the area of quay walls

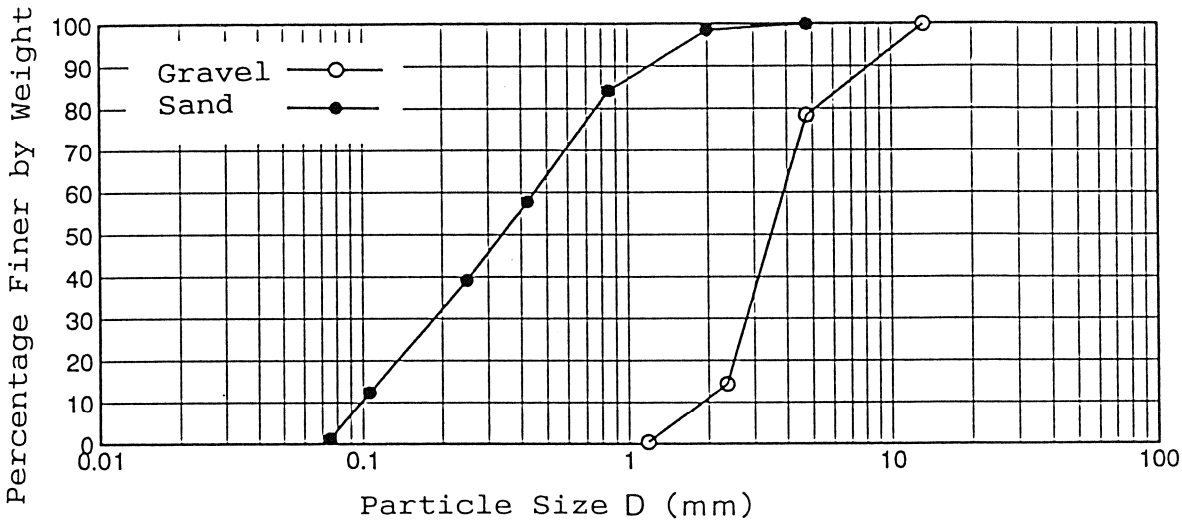

Fig.15 Gradation of sand and gravel

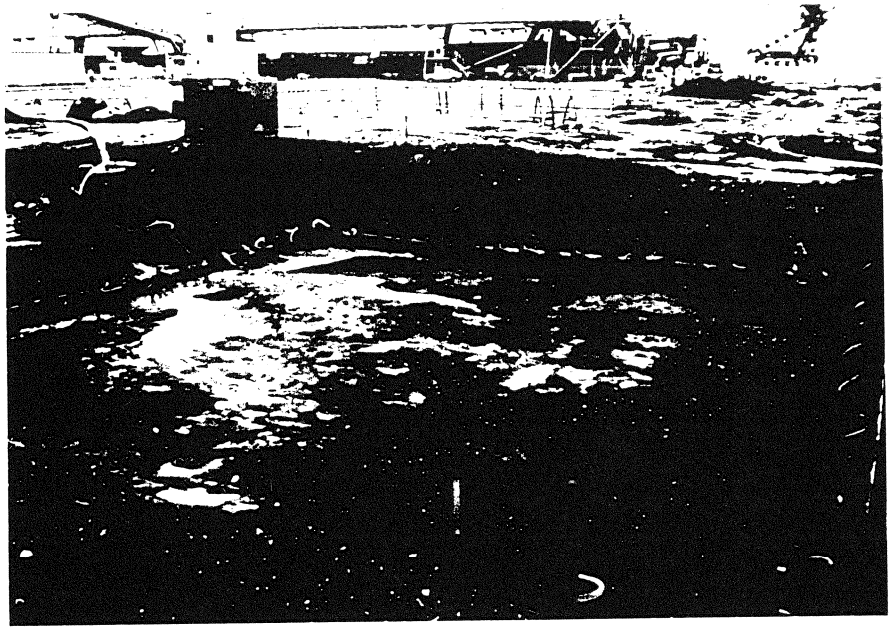

Fig.16 General view of excavation of gravel drain site

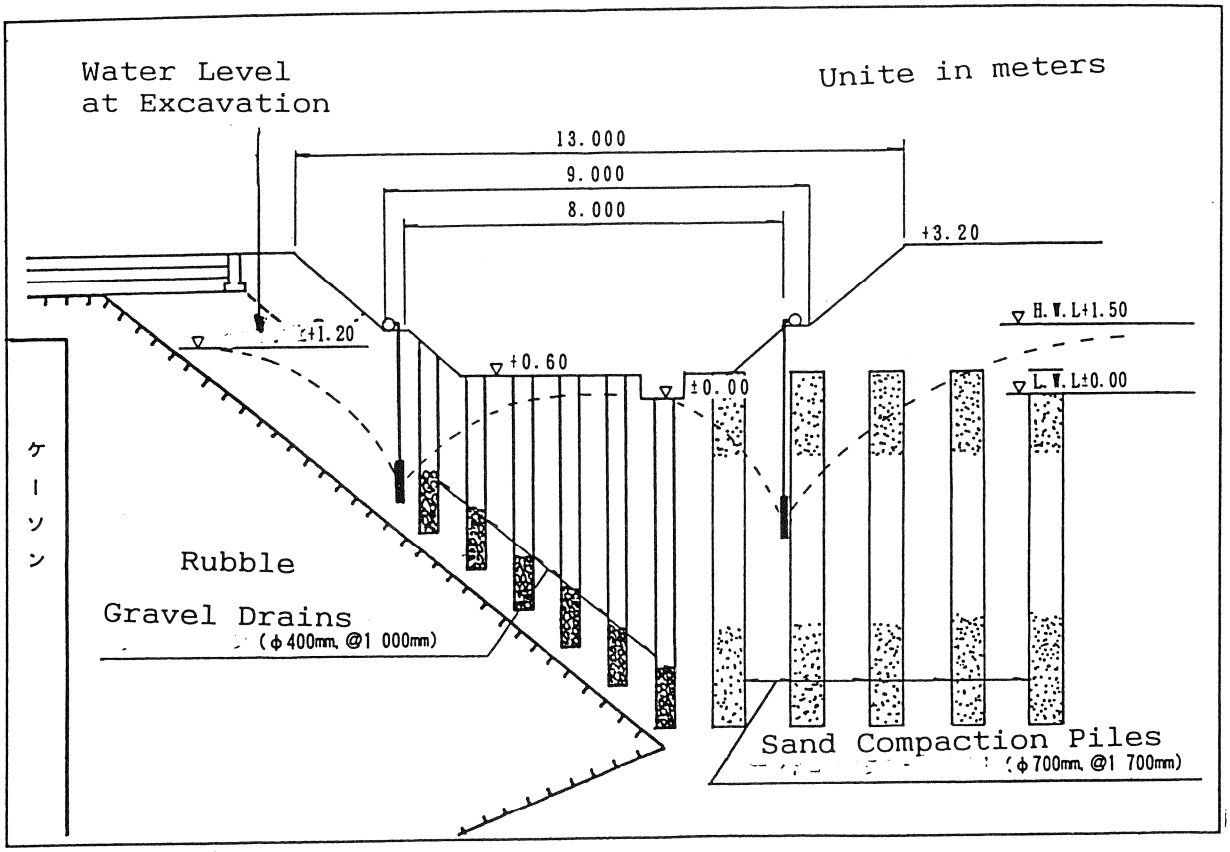

Fig.17 Cross section of excavation details

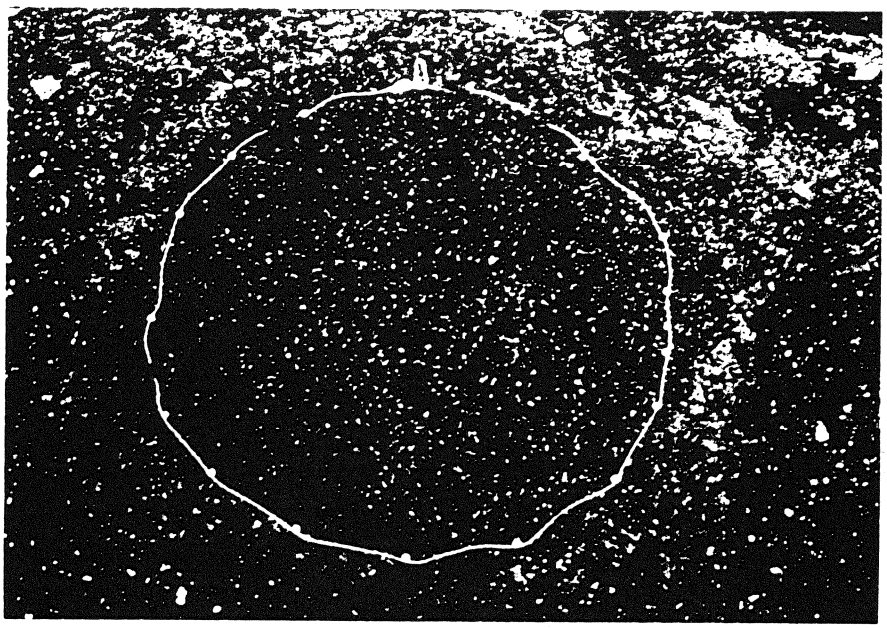

(a) Cross section of gravel drain and surrounding sand

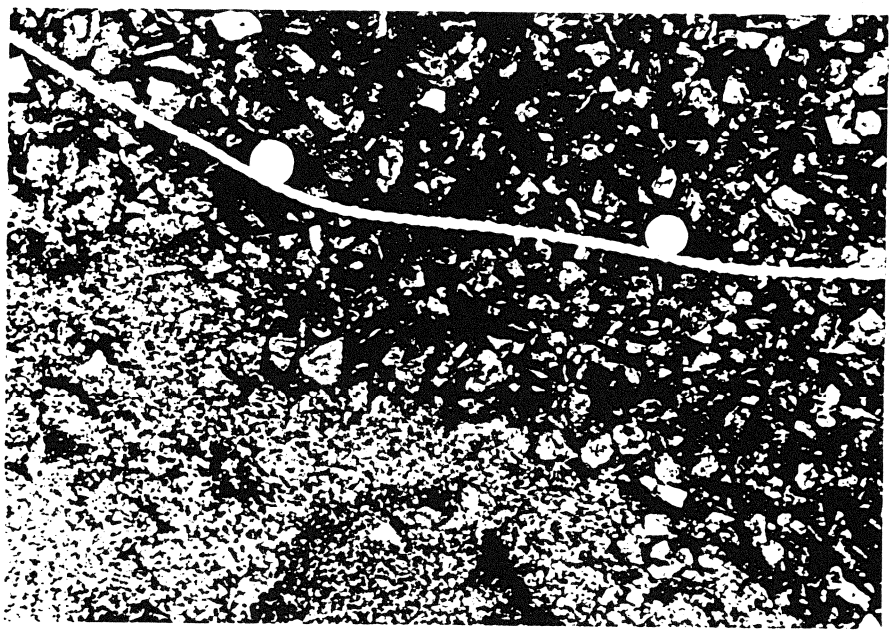

(b) Closer up view

Fig.18 Excavated cross section of gravel drain

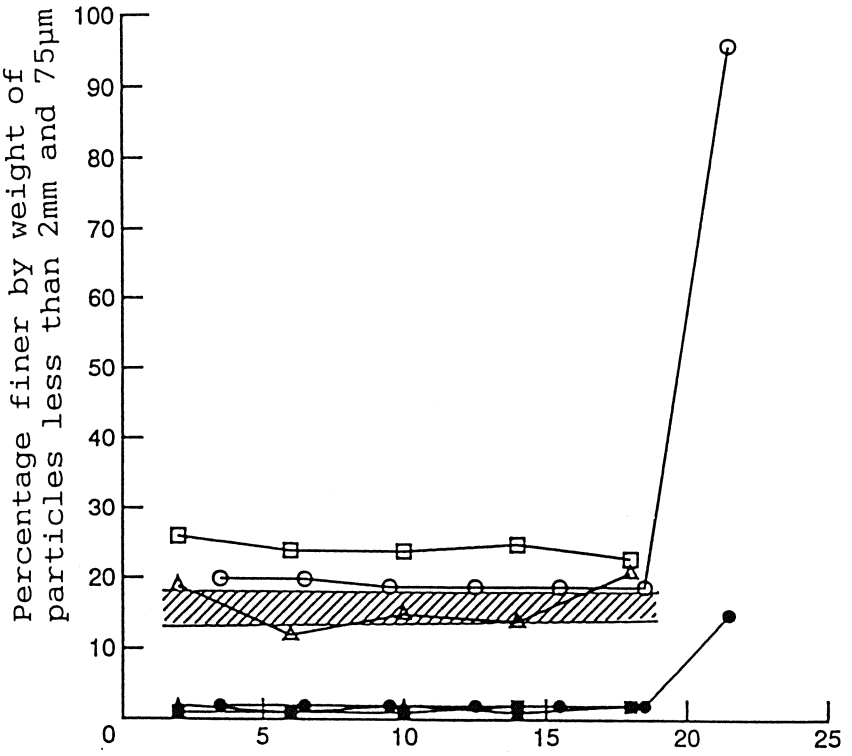

Index

○	No. 1
●	(+0.6m)
□	No. 2
■	(+0.6m)
△	No. 3
▲	(±0.0m)

※ ////// Percentage finer by weight of particles less than 2.36mm of gravels at the installment of the gravel drain

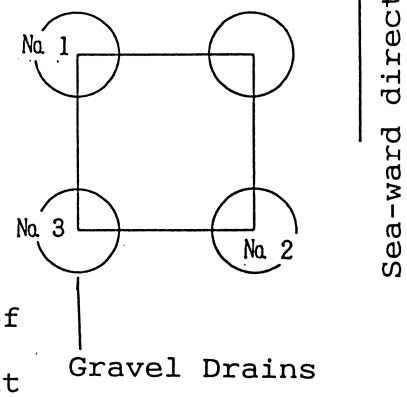

Open Circle : Sandy materials (less than 2 mm)
Closed Circle : Silty materials (less than 75μm)

Fig.19 Fine grained materials and sand contained in the gravels

WATER SYSTEMS PERFORMANCE
NORTHRIDGE EARTHQUAKE, January 17, 1994

Le Val Lund, P.E., M ASCE

Civil Engineer
ASCE - Technical Council on Lifeline Earthquake Engineering

ABSTRACT

Lifelines played an important role in the emergency response and restoring the urban area affected by the Northridge earthquake. Although the earthquake was severe the lifeline disruption only represented a small percentage of the inconvenience to the population served within the large earthquake impact area. The 1994 event showed significant improvement in the seismic performance of lifelines (power, water, sewer, gas and communications) from the 1971 San Fernando event. The 1994 event also revealed some conclusions and new lessons learned in the seismic performance of lifelines which will require attention by lifeline agencies.

The Fifth U. S.-Japan Workshop
on Earthquake Resistant Design of Lifeline Facilities and
Counter Measures Against Soil Liquefaction
September 29 and October 1, 1994
Snowbird, Utah

INTRODUCTION

An earthquake occurred at 4:31 a.m., Pacific Standard Time (PST) on Monday, January 17, 1994. The epicenter was located 20 miles (32 kilometers) from the center of Los Angeles, in the Northridge community (San Fernando Valley) of Los Angeles, California, USA. The magnitude was M 6.7 (Caltech) or M 6.8 National Earthquake Information Center (NEIC). The impact of the earthquake was wide spread in western Los Angeles and eastern Ventura Counties. The earthquake had significant impact on lifelines, in addition to damage to residential and commercial buildings, and freeways. The estimated damage was approximately $15 billion and there were approximately 58 fatalities.

Lifelines

Lifelines are those services vital to the health and safety of the community and the functioning of an urban and industrialized society. Lifelines are critical for the emergency response and recovery of a community after a disaster such as earthquake. Lifelines include electric power, communication, transportation (highways, airports, railroads and harbors), water, sewage, natural gas and liquid fuel systems.

Lifeline Seismicity

No surface rupture that can be associated with the main shock has been found by field geologists from California Division of Mines and Geology (CDMG), US Geological Survey (USGS) and other organizations. Buried pipelines were subjected to both strong shaking and acceleration, and tectonic movement, even though there was no surface faulting.

WATER SYSTEMS

Supply

Water supply to Southern California is provided by local groundwater basins, water reclamation and imported supplies from the Colorado River and Northern California. The earthquake disrupted five of the major pipelines from northern California serving the Santa Clarita, Simi and San Fernando Valleys which supplied four water treatment plants. Three plants were in operation and the fourth was under construction.

The breaks in 54 (1371), 77 (1956), 78 (1981), 85 (2160), and 120-inch (3048-millimeters) diameter steel and concrete pipelines and concrete conduits were repaired in two to 67 days. Some of the repairs were temporary to restore service and permanent repairs will made by summer 1994.

Until these pipelines were repaired water utilities received supplies from local groundwater basins, storage reservoirs and Metropolitan Water District of Southern California (MWD) Colorado River Aqueduct and State Water Project - East Branch.

Supply Pipelines

The State Water Project-West Branch supplies the Jensen Water Treatment Plant from the Castaic Reservoir via the Newhall and Balboa Tunnels. At the south portal of the Balboa Tunnel the 170-in (4320-mm) line branches into two-85-in (2160-mm) by 13/16-in (20-mm) welded steel inlet pipes (WSP) to the treatment plant. The west pipe performed satisfactorily; however, the east pipe circumferentialy cracked on the curved portion of a long bell. The pipe was joined by an inside welded bell and spigot joint. The northerly part of the round crack moved horizontally about 3-in (76-mm) east with respect to the southerly part. Vertical movement was about 1/2-in (38-mm).

An approximately 10-feet (3.0-meters) of the damaged pipe was removed and replaced by two-5-ft (1.5-m) lengths of pipe rolled at the MWD yard. The closure was made by three welded butt straps joints and completed the evening of January 19th. The MWD East Valley Feeder and pumping plant was activated to provide supply from the Colorado River Aqueduct/ State Water Project - East Branch to the areas in western Los Angeles County and eastern Ventura Counties, affected by this outage.

Los Angeles Aqueduct No. 1 supplies the Los Angeles Water Filtration Plant from the Owens Valley by two aqueducts. Aqueduct No. 1 had damage at four locations; however, it was operated at very low flow for about week after the earthquake to allow repairs to be made to Aqueduct No. 2, then was shut off for repairs. After temporary repairs were made, it was operated again at one-half capacity, for about two weeks at the end of March, during a planned MWD shutdown. It was shut down shut down April 1st and was out of service until July for permanent repairs.
Both aqueducts were shut down for a period of three weeks, the last week of February and first two weeks in March, to allow for the repair of the

open concrete channel supplying the water filtration plant. The channel was fractured in many locations requiring replacing concrete sections, low pressure grouting the voids behind the walls and patching the cracks.

At the south end of Aqueduct No. 1 Soledad (inverted) Siphon at two locations occurred the partial cracking of the curved portion of the bell of an 120-in (3050-mm) by 3/8-in (10-mm) welded steel pipe. The pipe was welded on the outside of a bell and spigot joint and was above ground and supported by concrete saddles. The circumferential cracks were about 5-ft (1.5-m) long on the top of the pipe. The repair was made by removing a coupon of the damaged joints and replacing it with a welded steel plates. At Quigley (inverted) Siphon there was split in the top of the 120-in (3050-mm) riveted steel pipe which was welded shut.

At two locations, Whitney and Elsmere Canyons, the 120-in (3050-mm) cast-in-place reinforced concrete (inverted) siphons were shattered, and temporary repairs were made by plugging the cracks from the outside. Permanent repairs were made by placing a steel liner inside the pipe and injecting the cracks with sealing compound from tapped holes in the liner from the inside of the pipe. The steel liners were fitted with a "O" ring gasket at each end. Creek flow was a dewatering problem at Elsmere Canyon. Tunnels were inspected and found in satisfactory condition except for minor cracking and the tunnel through Terminal Hill, which had circumferential cracking at the south end. The cracks were sealed with urethane resin.

Los Angeles Aqueduct No. 2. was out of service for the first week after the earthquake for repairs, and placed in service until the shutdown of both aqueducts for the open channel repair during the last week in February for three weeks. It was put back in service in mid March until April 8th at which time it was removed from service for non earthquake related reasons.

At Terminal Hill the 77-in (1955-mm) welded steel pipeline was shut down twice to repair two pulled mechanical couplings and an eight-inch long split in the wye branch stiffener. This required draining and filling the pipe twice during the first week after the earthquake. The pulled couplings were temporarily repaired by welded butt straps. The wye branch stiffener was rewelded. Two-6-in (13-mm) compression bulges appeared on the north slope of Terminal Hill in the 77-in (1955-mm) pipe in above ground pipe supported on concrete saddles. This represented

almost 2-feet (0.6-m) of compression in the pipeline. At these bulges there were no leaks although significant movement occurred.

At Quigley Canyon a circumferential tear in the top of the buried 77-in (1955-mm) welded steel pipe was repaired by welding a interior patch plate. A number of air and vacuum valves were damaged and required replacement.

Long travel times and traffic were a problem in gaining access to the repair sites north and south of the Interstate 5 and State Highway 14 damaged interchange. All repairs were made by agency personnel. Compliance was required with the Occupational Safety and Health Act (OSHA) for entering confined spaces (tunnels and pipes).

Santa Clarita Valley is served from the Castaic Reservoir, the terminus of the State Water Project-West Branch. The Castaic Conduit from the water treatment plant was video inspected and had 35 leak repairs in the 54 (1370), 39 (990) and 33-in (838-mm) modified prestresed concrete cylinder pipe (MPCCP). One repair occurred on the 54-in (1370-mm) MPCCP inlet pipe to the plant. Breaks occurred at welded fabricated compound (horizontal and vertical) bends and on long horizontal reaches where the rubber gasket joints pulled apart. A pipe manufacturer fabricated new compound bend sections and a contractor welded these sections together with butt straps. The pulled rubber gasket joints were welded in place. Backer rods were used to fill the annular space between the bell and spigot to facilitate the welding. The conduit was placed back in service March 25th. The supply to the Santa Clarita Valley after the earthquake was supplied from local groundwater.

Simi Valley receives water supply from the MWD Jensen Treatment Plant. The supply is transmitted by two pipelines to the storage reservoir at the west end of Simi Valley. The common tunnel at the east end was inspected and found undamaged. At the west tunnel portal in Simi Valley the pipeline separates into 78-in (1980-mm) and 51-in (1295-mm) prestressed concrete cylinder pipelines with rubber gasket joints. Alternate supply was available from reservoir storage and groundwater.

The 78-inch North Branch Feeder (1980-mm) had 15 to 20 major pulled joints and approximately 500 cracks requiring chipping and patching with cement mortar. The rubber gasket joints were welded shut and some of the joints were pressure grouted from the inside behind the weld. External repair plates (diapers) were used at some locations.

Replacement was required of 22 damaged air and vacuum valves. The replacement valves were air freighted by the manufacturer within two days. The 78-in (1980-mm) line was placed back in service on March 4th.

The 51-inch Calleguas Conduit(1295-mm) remained in service intermittently after the earthquake. The earthquake damage occurred at three corroded blind flanges and bolts at future service connections. The flanges, bolts and valves were replaced. Also an air and vacuum valve was damaged.

Lifeline Collocation

An interesting collocation of nine lifelines occurred on Balboa Boulevard, north of Rinaldi Street, in Granada Hills, an apparent tension and compression zone. Located within the street were 3-gas , 3-water, 2-sewer and 1-oil underground lines; 34.5 kv and 4.8 kv power, telephone, and cable TV overhead lines; and ornamental street lighting. Ground movement caused the breakage of some of the underground pipelines. A fire occurred in the street which ultimately burned the overhead lines and five homes. At this location there appeared to be a ground separation (tension) at a location on Balboa Blvd. south of Lorillard Street of approximately 9 to 12-in (230 to 305-mm). Approximately 1,000-ft (300-m) to the south there was ground compression of an equal amount. At both of these locations the gas, water and sewer pipelines were damaged.

Large Diameter Pipelines

Two of the three water lines in Balboa Blvd. were the Granada Trunk Line 48-in (1220-mm) WSP and MPCCP and the Rinaldi Trunk Line 68-in (1727-mm) WSP. The Granada line had four major pulled mechanical couplings and two tension and compression failures on the curved portion of the bell, of the bell and spigot joints. Repairs were made by connecting a short length of pipe with butt straps in the tension zone, a butt strap in the compression zone and interior butt straps (WEKO seals) at other locations. A creek caused dewatering problems at one location. The line was put back in service on January 29th. The Rinaldi line had three pulled welded bell and spigot joints at the bell curve and a tension and compression failure on Balboa Blvd. Repairs were made by connecting a short length of pipe with butt straps in the tension zone, a butt strap in the compression zone and interior butt straps (WEKO seals) at other locations.

There were approximately one dozen other large diameter pipeline failures for the same reasons as described above. Repairs were made using the same methods, requiring the use of similar materials, equipment and personnel.

Distribution System

The most significant damage to the smaller distribution pipeline network was within the earthquake affected area. It was reported (4-1-94) there were approximately 1,400 leaks in mains and services by the water utilities in the San Fernando Valley and approximately 300 in the Santa Clarita and Simi Valleys. Pipes were broken by compression and tension and some pipes weakened by corrosion due most likely to vibration and tectonic movement. The most affected were older cast iron with rigid joints and older steel subjected to corrosion. There also were broken fire hydrants and air and vacuum valves.

The repairs were time consuming requiring draining prior to repair, the repair, the filling the pipe for testing, and chlorination and invariably another leak was observed, requiring the repeat of the process. In a number of cases this process was repeated many times and was more time consuming in larger diameter pipes which required more time to drain and fill. In some areas dewatering of excavations was necessary. Food, water and housing were a problem to the restoration workers in the damaged areas, because of the loss of commercial power and potable water to restaurants and motels.

Water Treatment Plants

The operating plants have a capacity of 25 (95), 550 (2080), and 600 million gallons per day (mgd) (2270 million liters per day) (ml/d) The treatment plants received minor damage, such as ground settlement around the plants; leaks at construction and expansion joints; leaks in plastic chlorine solution lines, overturned filing cabinets and book cases; falling ceiling tiles; and sloshing damage to gratings and wood baffles in the basins. Supply was available in most areas from storage and the other regional sources, but was not immediately available from the treatment plants because of the damage to the distribution systems. The Simi Valley water treatment plant (50 mgd) (190 ml/d) was not in operation and is still under construction.

Booster Pumping Stations and Groundwater Wells

There was no reported damage to booster pumping facilities or groundwater wells, other than loss of commercial power. Many wells did not have emergency power. Pumping stations with emergency power supply worked well. There was minor damage to the enclosures housing these facilities.

In some areas, fire department engine pumpers were used to maintain pressure in area in which the leaks had been repaired. The pumping between fire hydrants by the engine pumpers was used when the primary supply was not available.

Storage Tanks

The Santa Clarita Valley (Valencia-Newhall area) is north of and about eight miles (13-km) from the earthquake epicenter in Northridge. Severe tank damage occurred in this area in that six of the seven Newhall tanks were damaged and were rendered nonfunctional following the earthquake. Principal modes of damage were broken inlet-outlet piping and valves, roof and rafter damage, and shell buckling/elephants foot failures. Lateral movement or sliding/shifting did not appear to occur frequently or, if it did occur, it was in the order of two to four inches (5 to 10-cm).

Similarly, there were two structural failures in the Valencia area, with a third tank suffering damage from an adjacent tank failure. Failure modes were severe shell buckling and uplift, inlet-outlet piping failure, roof/rafter damage and in one case shell ripping at the tank bottom. The two tanks with structural failures have been removed.

The Simi Valley area lies 10 to 12-miles (16 to 20-km) west of Northridge. This area also experience a significant number of functional tank failures, the causes of the failures again being shell buckling and inlet-outlet piping and valve damage . In addition to the these tanks, there were an additional ten tanks in the Simi Valley area which were damaged and rendered nonfunctional; however, many of these tanks were repaired and returned to service.

Those tanks in the San Fernando Valley which had significant damage were in the Santa Monica Mountains south of Northridge. Inlet-outlet piping and valve damage, erosion and roof problems were again the major causes of functional failure. All of these tanks have been repaired and returned to

service. A damaged 1929 riveted steel tank in the Granada hills area has been removed. Good performance was observed by prestressed concrete tanks.

Observations from this earthquake are the significant number of tanks damaged and which became nonfunctional by not being able to contain water-the effects on fire protection of being immediate concern. The principal modes of function failure were inlet-outlet piping failure and roof damage. Also most of the failed tanks were not American Water Works Association AWWA D-100 design basis tanks. Many were of bolted construction and were of relatively small size. The Larwin tank was a used tank, rebuilt in 1986, with AWWA nameplate, tank was anchored, nevertheless suffered severe damage and was removed from the site. Although not mentioned in this report, there were a number of smaller industrial tanks near the Northridge/Canoga Park area which also failed.

Comparing the damage to water tanks during this earthquake with damage in previous earthquakes, this earthquake produced far more extensive and severe damage to water tanks than previously experienced. About 40 tanks were rendered nonfunctional by this earthquake. To the credit of operating and maintenance personnel, many of the tanks without severe damage were returned to service in a short time and the systems were not faced with prolonged outages.

Many of the steel tanks were not AWWA D-100 designed tanks, so its difficult to judge their design criteria. It is noted that roof damage seemed to be more apparent in this event; the occurrence of roof rafters falling off supports was noted at number of locations. The failure of the inlet-outlet piping was the principal cause of functional failure; the lesson here is to provide flexibility in the inlet/outlet piping and possibly use steel valves and fittings.

Reservoirs

There were 120 dams within 46-miles (74 -kilometers) of the epicenter of the Northridge earthquake. Most of the dams are water supply storage reservoirs. Others are flood control and are generally empty or have minimum stored water. 108 of these dams are under the jurisdiction of the California Department of Resources, Division of Safety of Dams (DSOD), the remaining 12 are owned by the federal government. All major DSOD dams were inspected by their owners immediately after the earthquake. Some of the major dams were further inspected by their staff

or contract engineers. In the first five days 101 of the dams under state jurisdiction were inspected by DSOD engineers. The remainder were either dry, under construction, or outside the epicentral area. All were eventually inspected. All state and federal dams performed satisfactorily and no emergency situation existed.

Thirteen of the 108 dams nearest the epicenter had some minor longitudinal and transverse cracking, settlement, minor horizontal movement or increased seepage and one small storm water dam had a minor slope failure.

Pacoima Dam had cracking in both abutments and damage to its access ramps and stairways. The upper left abutment strong motion instrument recorded an acceleration of 1.5 g or greater on the horizontal and 1.4 g on the vertical component. At the same location in the 1971 San Fernando earthquake the record was 1.25 g on the horizontal and 0.7 g on the vertical component. Peak accelerations exceeding 2.0 g were recorded on the dam structure. The total capacity of the flood control basin is 3,770 acre feet, but storage capacity was temporarily limited to 1,000 acre feet, while civil engineers made further investigation of the abutments. The dam performed satisfactorily in the earthquake. Water is released from this dam to enhance the water supply by recharge into the San Fernando groundwater basin.

Dams performed well in the Northridge earthquake. Since the 1971 San Fernando earthquake, most major dams in the state have been dynamically analyzed for the maximum earthquake that could be imposed on the dam. Some dams met this seismic criteria, others were rebuilt, modified, operating at a reduced level or have been removed from service.

Water Quality

This earthquake disrupted treated water to many water systems including Santa Clarita, Fillmore, Moorpark, Simi Valley, Malibu and San Fernando as well as Los Angeles. Water supply was available, some treated and some untreated, from groundwater basins, storage, MWD Colorado River Aqueduct and East Branch of the State Water Project.

Three filtration plants were out of service due to pipeline damage; this meant a loss of over one billion gallons (3.8 billion liters) of water treatment capacity. As a precaution, water purveyors, in cooperation with the California Department of Health Services, Division of Drinking Water

and Environmental Management (DHS), issued "boil water" notices immediately. Although some service areas were not affected, the boil water notices gave water purveyors needed time to assess the damage to their systems. A standard "boil water" notice had been prepared by DHS in advance for use by the water agencies in times of a emergency.

The notice generally stated customers should boil or treat their water before consuming. Rapid boiling for five minutes or treating the water with chlorine would disinfect the water adequately. Specifically, customers were asked to add unscented liquid commercial bleach to their water in the following amounts: 8 drops per gallon (3.8-liter) for water that appears clear, 16 drops per gallon (3.8 -liter) for water that appeared cloudy. Customers were told to mix the chorine and water and let the mixture set for 30 minutes before consuming.

The boil water notices were released by the water purveyors and DHS in the printed and electronic media. Local TV and radio stations became very important disseminators of changes in the boil water notice in the areas. A problem arose when customers from unaffected water systems began to unnecessarily boil water their water and call their water purveyors in panic. This required unaffected water purveyors to issue their own separate notice indicating their water was safe to drink. Even with the confusion water purveyors and DHS felt issuing "boil water" notices was better than taking a chance that someone might drink contaminated water.

In order to lift the "boil water" notice from any service area, the water agency requested permission from the local DHS district engineer. The authorization would only be granted after the water purveyor had completed the repairs to its distribution system, the distribution system was pressurized, had at least a 1 ppm (1 mg/l) chlorine residual in the distribution system and had received satisfactory disinfection and bacteriological testing. The testing took at least one day. It would be desirable to have mobile water quality Laboratory to make field testing of water quality and an expedited method for testing for contaminants in the water.

In areas like Santa Clarita Valley, where well water was chlorinated for the first time, some customers complained about the chlorine taste and odor. In Los Angeles, boil water area was gradually reduced as the system was restored and customers in the last boil water notice area were allowed to use their water on January 29th, in the Simi Valley on January 24th and in the Santa Clarita Valley on February 4th.

Emergency Water Supply

Emergency water supply was provided by bottled water, beer and soft drink beverage companies, MWD, U. S. Army Corps of Engineers, California National Guard and water agencies provided water using agency, contractors and rented tanker trucks. The tanker trucks were disinfected and fitted with taps and hoses for easy dispensing. During the height of the operation in Los Angeles, 72 trucks were being dispatched to nearly as many locations providing over 100,000 gallons (378,500 liters) of water each day. The Los Angeles International Airport was temporarily closed because it fell within the boil water notice area and no airplanes could take off with out potable water. The problem was solved by having the water tanker truck that normally supplies the planes dispatched to a location outside the boil water area to received its potable water for delivery to the aircraft.

Mutual Aid

Volunteer mutual aid was provided by almost a dozen water agencies from the local area and one came from the San Francisco Bay area. Mutual aid agencies provided their own personnel, equipment and materials. Fifty-two people assisted Los Angeles in restoring their system. Contractors familiar with water utility work were also used. the mutual aid agencies had to deal with the limited housing and food in the epicentral area.

CONCLUSIONS

1. Lifelines played an important role in emergency response and restoring the community after the Northridge earthquake. Telecommunications, radio and electronic media played a valuable role in directing emergency response for essential services and the repairing of damaged lifelines. Water supply was necessary where available for public fire protection. Highways and roads were used to move rescue, repair, fire and medical teams and their supplies and equipment to the damaged areas. Although the Northridge earthquake was severe, the lifeline disruption only represented a small percentage of inconvenience to the population served within earthquake impact area.

2. The 1994 Northridge event showed significant improvement in the seismic performance of lifelines from the 1971 San Fernando earthquake. Among the facilities and equipment installed, using modern seismic codes,

which had good seismic performance, but not totally inclusive, is dams, steel and concrete tanks, wells, pumping stations and treatment plants. Also included is welded steel pipe with butt joints, ductile iron pipe with rubber gasket joints and polyethylene pipe.

3. The 1971 San Fernando and 1987 Whittier Narrows earthquakes experience has encouraged lifeline agencies to prepare emergency response plans. These plans have been tested and implemented by lifeline agencies. The regular earthquake exercises generally held, in April, of each year in various communities proved to be invaluable in this earthquake. The month of April is selected because it is the anniversary of the 1906 San Francisco earthquake.

4. Above ground tanks usually have either one or two pipes, with valves, rigidly connected to the tank to provide for the filling the tank and draining the tank to meet the peak water demands in the water service area. In the Northridge earthquake, there were cases were the piping or valves broke because the differential movement between the tank and the piping. Several methods have been developed for providing a more flexible connection between the tank and the piping to withstand the differential movement. There needs to be further study on economical and other methods of preventing storage tank inlet/outlet piping damage due to differential movement.

5. Older steel tanks not seismically designed and constructed suffered buckling at the bottom (elephants foot bulge), in the shell and roof. There is a need to seismically retrofit these older facilities.

6. Welded steel Tanks seismically designed and constructed under American Water Works Association (AWWA) Standards for Welded Steel Tanks for Water Storage (AWWA D-100) and prestressed-concrete water tanks designed and constructed under AWWA Standards for Wire-Wound Circular Prestressed-Concrete Water Tanks (AWWA D 110) performed very well.

7. Water supply lifelines use bell and spigot pipe almost exclusively for welded steel pipe. Bells are fabricated by using a mandrel to expand the cold pipe to create the bell. There were a number of instances in the Northridge earthquake were the large diameter bell was cracked at the curvature point where the bell changes diameter. There is a need to study the seismic strength of welded steel bell and spigot joints and how to improve the seismic performance of the joint. The joint performance

should be compared with the current (AWWA) Standard for Welded Steel Pipe (AWWA C-200)

8. Most damage to the water distribution system piping occurred in cast iron pipe with rigid joints and old steel pipe subject to corrosion. Although there is limited ductile iron pipe with rubber gasket joints installed, the seismic performance of this pipe was very good. Programs are needed, including funding, to replace this older pipe in seismically active areas.

9. Most of the emergency power supplies worked for pumping stations and treatment plants; however, there is a continuing need to regularly test these emergency generators under load; to have adequate fuel for a longer term commercial power outage; provision for transferring fuel from the storage tank to the day tank, when the electric pumps are out of service.

10. There are number of wells, pumping stations and treatment plants without emergency power or that do not have capacity to provide for all their essential operations. There is a need to enlarge the emergency generation capacity to cover all essential operations. Portable generators with "quick electrical connectors" would be of value.

11. Sloshing in large basins in water filtration and water reclamation plants caused damage in the 1989 Loma Preita and 1994 Northridge events. Although not critical, the damaged equipment can cause malfunction of other equipment. As an example sloshing caused the jamming of the chain drive sludge scrapers in seven out of 44 final clarifiers of a water reclamation plant. There is a continuing need to consider sloshing in the design of mechanical equipment and baffles in large basins of water and wastewater treatment plants.

12 Customer water, gas and electrical service was disrupted to a small (5% to 20%) portion of the population impacted by the earthquake and for a short period of time considering the intensity of the earthquake. Most of this disruption was due to distribution system damage and structural damage to residences and buildings. Redundancy was provided in distribution system networks and alternate supplies from other sources for electric and gas supplies and storage, groundwater basins and alternate aqueduct systems for water supplies. Redundancy continues to play an important role in the restoration of lifeline services.

13. The 1994 Northridge event demonstrated the vulnerability of lifelines within essential facilities, such as, hospitals, fire stations and emergency operating centers. Small breaks in water lines and automatic sprinklers caused flooding in lower floors. Roof top HVAC equipment was damaged which caused malfunction of other systems within the building. Internal lifelines in essential facilities require seismic design. There is a need for emergency electric and water supplies for essential facilities.

14. The Northridge earthquake identified several areas were there is a need for enhancing the ability of lifeline employees in their emergency response and recovery activities. This event cause transportation problems, because of the closed freeways, for lifeline employees to get from their homes to their work location. Alternate work locations or telecommuting where feasible should be considered.

15. There is need for emergency food, water and housing; and adequate cash to purchase these items, for lifeline workers in the epicentral areas. Because there is a potential for potable water, gas and electricity not being available, restaurants and motels may not be in operation.

16. There is need for a communications plan, which has been tested for lifeline employees and families to notify each other of their well being. This would allow employees to report directly to a restoration effort without worrying about their families. This was not necessary in the Northridge event because most people were still at home at 4:31 a. m. in the morning.

17. In advance of an emergency, non-emergency response lifeline employees, should be assigned and trained in emergency response activities. For government lifelines there is a need to document repairs for FEMA reimbursement which could be done by non-emergency response personnel.

18. A lifeline agency with its own engineering staff, not involved in the recovery operation, offered their services to help employees with their home earthquake inspections.

19. Consideration should be given to developing a mobile water quality laboratory to expedite, in the field after repairs have been made, the determination if the water is safe for drinking.

20. Currently bacteriological testing takes several days to determine whether water is safe for drinking. Research should be done to expedite this process so the boil notice may be lifted sooner.

21. The entering of large diameter pipes, conduits and tunnels requires compliance with OSHA requirements for entering confined spaces.

22. Air and vacuum valves on pipelines are an inverted pendulum above the ground surface. In the Northridge event many valves toppled, had cracked bodies or damaged floats (balls). The damage may have been caused by transient pressures in the pipeline. A study is required to improve the performance of these valves in an earthquake.

23. The Northridge event showed good performance of structures and equipment which had been seismically upgraded from the 1971 San Fernando event. Seismic upgrade of lifeline equipment, buildings and facilities is very costly, requires prioritizing, budgeting and some form of innovative financing. Innovative financing research is required to further improve the seismic performance of lifelines.

24. All lifeline agencies should make seismic vulnerability assessments of their facilities to determine vulnerability to damage of their system. The assessment should prioritize/schedule any required seismic mitigation.

25. All lifeline agencies should have an emergency response and recovery plan. The plan should be practiced and updated on a regular basis.

References

"Preliminary Reconnaissance Report - Northridge Earthquake, January 17, 1994, Lifeline Section, Earthquake Spectra, Earthquake Engineering Research Institute, Oakland, March 1994.

Persson, V. H., 1994, "Assessment of Damage to State Jurisdictional Dams Caused by the Northridge Earthquake (M_W 6.7) on January 17, 1994", Presented at the California Seismic Safety Commission meeting, March 3, 1994, Burbank, CA.

Lund, L., 1994, "How the Earthquake Affected Water Quality", Association of California Water Agencies, Water Quality Monitor, Volume 6, Number 1, January/February 1994, , Sacramento, CA.

Aqueduct, Metropolitan Water District of Southern California, Los Angeles, March/April 1994.

Intake, Department of Water and Power, Los Angeles, January/February 1994.

Water storage tanks by T. Cooper, ASCE - TCLEE.

Personal Communications and field investigations by L. Lund with numerous water and wastewater agencies.

II MECHANISMS OF LIQUEFACTION AND LARGE GROUND DEFORMATION

Construction of Stress-Strain Histories from Recorded Dynamic Response
R. Dobry, M. Gutierrez, M. Zeghal, and A-W. Elgamal
Behavior of Sand After Liquefaction
N. Yoshida, S. Yasuda, M. Kiku, T. Masuda, and W.D.L. Finn
Post Liquefaction Deformation of Cohesionless Soil
A.K. Hussein and H.E. Stewart
A Consideration on Mechanism of Liquefaction-Related Large Ground Displacement
M. Hamada, H. Sato, and T. Kawakami
A Comparative Study of Predictive Methods for Liquefaction Induced Embankment Displacements
G.R. Martin and P. Qiu
Torsional Shear and Triaxial Compression Tests on Deformation Characters of Sands Before and After Liquefaction
S. Yasuda, T. Masuda, N. Yoshida, H. Nagase, H. Kiku, S. Itafuji, K. Mine, and K. Sato
Ground Motion Characteristics and Their Relation to Soil Liquefaction at the Wildlife Liquefaction Array, Imperial Valley, California
R.E. Kayen, J.K. Mitchell, and T.L. Holzer
Experimental Study on Mechanical Properties of Liquefied Sand
T. Kawakami, N. Suemasa, H. Hamada, H. Sato, and T. Katada
Review of Energy-Based Liquefaction Research at Case Western Reserve University
J.L. Figueroa, A.S. Saada, and L. Liang
Post-Liquefaction Ground Flow in Shaking Table Tests
H. Toyota and I. Towhata
Evaluation of Liquefying Soil through Time Using System Identification
S. Glaser and R. Chung
Recent Research on Liquefaction of Silts and Silty Sands at Santa Clara University
S. Singh
CANLEX (Canadian Liquefaction Experiment): A One Year Update
P.K. Robertson, B.R. List, and B.A. Hofmann

CONSTRUCTION OF STRESS-STRAIN HISTORIES FROM RECORDED DYNAMIC RESPONSE

Ricardo Dobry, Manuel Gutierrez, Mourad Zeghal, and Ahmed-W. Elgamal

Department of Civil and Environmental Engineering
Rensselaer Polytechnic Institute
Troy, New York 12180

ABSTRACT

Instrumented centrifuge laminated box experiments generate acceleration and LVDT displacement histories along the model height. These histories are employed to directly construct the associated dynamic stress-strain histories. Soil shear response at different elevations is explored. Soil strength during liquefaction and lateral spreading is revealed at different elevations along the model height.

INTRODUCTION

Centrifuge dynamic testing offers a highly controlled laboratory environment for exploring soil response. In a laminated soil container, histories of acceleration, LVDT displacements, and pore-pressures are conveniently recorded along the model height. These records constitute the dynamic response of a one-dimensional (1D) shear beam. Through this shear beam idealization, the associated stress-strain histories can be directly constructed from the recorded acceleration and displacement histories. The involved procedure is described below. This procedure was originally developed (Elgamal and Zeghal 1992, Zeghal and Elgamal 1993, 1994a, 1994b, Elgamal *et al.* 1994) to analyze downhole records at Lotung, Taiwan; at Wildlife refuge site, CA (Figure 1); and for VELACS (Arulanandan and Scott 1993) centrifuge experiments (Taboada and Dobry 1993a, 1993b).

TEST SETUP

An instrumented laminar box is shown in Figure 2 (Gutierrez *et al.* 1994). As shown, the histories of displacement are recorded along the outer side of laminates. In this test, a loose saturated layered soil stratum was built of silty sand (7 % silt). Each layer was constructed by pluviation under water, and consolidated before building the next (hydraulic fill method with water employed as pore fluid). The test was conducted at a centrifugal acceleration of 50 gravities. Before shaking, the model was tilted by about 0.2^o to the horizontal in order to simulate the response of a mildly sloping infinite slope. Histories of recorded acceleration and displacement are shown in Figures 3 and 4.

CONSTRUCTION OF SHEAR STRESSES AND STRAINS

Displacement histories yield shear strains through the simple expression

$$\gamma_i(t) = \frac{d_i(t) - d_j(t)}{h_{ij}} \tag{1}$$

where $\gamma_i(t)$ is average shear strain history within the layer bound by LVDTs i and j, $d_i(t)$ is displacement history at station i, and h_{ij} is spacing between stations i and j. Strains derived from accelerations (i.e., using d_i obtained by double integration of acceleration a_i) were superposed on lateral permanent drift traces recorded by the LVDTs at each elevation of interest. The corresponding stress history at any elevation is obtained by (Elgamal *et al.* 1994, Zeghal and Elgamal 1994b): *i*) integrating the acceleration records along the height from the surface downwards, up to the desired elevation, and *ii*) multiplying by the soil mass density.

RESULTS

The stress-strain histories constructed from Figures 3 and 4 are shown in Figure 5. Inspection of these histories reveals:

1- The soil liquefied, and the upper layers became progressively isolated from additional dynamic excitation.

2- Lateral strains are observed to gradually accumulate in the downslope direction during each additional loading cycle. Permanent strains were concentrated within the elevation range of 7 m- 9.5 m below ground surface.

2- Upon liquefaction, and before isolation, a level of strength associated with yielding may be inferred from cyclic loading during the time frame 1 s-2 s. These strength values are listed in Table 1 for selected elevations along the height.

SUMMARY AND CONCLUSIONS

A laminated container testing technique combined with a simple methodology for constructing the involved stress-strain histories was presented. Valuable information is directly extracted concerning soil stiffness and strength during liquefaction along the soil layer height. This information is of direct practical importance, and is also particularly valuable for validating simplified as well as elaborate computational procedures. Finally, the reported testing and analysis techniques constitute a basic methodology for evaluation of cyclic soil response; and offer a compliment to conventional shear and triaxial testing. The involved effort and expense is similar to that involved in these conventional tests.

ACKNOWLEDGMENT

Financial support to this research was provided by grants from NCEER, Buffalo, NY, INTEVEP, Venezuela, US ARMY corps of engineers, Vicksburg MI, and USGS, USA. This support is gratefully acknowledged.

REFERENCES

Arulanandan, K, and Scott, R. F., eds. (1993). *Proceedings of the International Conference on the Verification of Numerical Procedures for the Analysis of Soil Liquefaction Problems, Davis, CA, Oct. 1993*, Vol. 1, "Experimental Results and Numerical Predictions," A. A. Balkemema, 1993.

Elgamal, A.-W. and Zeghal, M. (1992). "Analysis of Wildlife Site Liquefaction During the 1987 Superstition Hills Earthquake," Proceedings of the 4th U.S.-Japan Workshop on Earthquake Resistant Design of Lifeline Facilities and Countermeasures Against Soil Liquefaction,

Tokai University Pacific Center, Hamada, M. and O'Rourke T., eds., Hawaii, 87-96.

Elgamal, A.-W., Zeghal, M., Taboada, V. and Dobry, R. (1994). "Site Liquefaction: An experimental Comparative Study," submitted for journal publication.

Gutierrez, A. M., Dobry, R. and Zeghal, M. (1994). "Centrifuge Tests of Normally Consolidated Silty Sand Deposited in Layers Under Water and Subjected to Seismic Excitations," Report, Civil Engineering Department, Rensselaer Polytechnic Institute, Troy, NY.

Taboada, V. M. and Dobry, R. (1993a). "Experimental Results of Model 1 at RPI," *Proceedings of the International Conference on the Verification of Numerical Procedures for the Analysis of Soil Liquefaction Problems, Davis, CA, Oct. 1993*, Vol. 1, Arulanandan, K. and Scott, R. F., eds. A. A. Balkemema, 1993.

Taboada, V. M. and Dobry, R. (1993b). "Experimental Results of Model 2 at RPI," *Proceedings of the International Conference on the Verification of Numerical Procedures for the Analysis of Soil Liquefaction Problems, Davis, CA, Oct. 1993*, Vol. 1, Arulanandan, K. and Scott, R. F., eds. A. A. Balkemema, 1993.

Zeghal, M. and Elgamal, A.-W., (1993). "Lotung Site: Downhole Seismic Data Analysis," *Report,* submitted to Electric Power Research Institute.

Zeghal, M. and Elgamal, A.-W. (1994a). "Analysis of Site Liquefaction Using Earthquake Records," *Journal of Geotechnical Engineering*, ASCE, Vol. 120, No. 6, pp. 996-1017.

Zeghal, M. and Elgamal, A.-W. (1994b). "Analysis of Soil-System Response During Liquefaction Using VELACS data," Report, Civil Engineering Department, Rensselaer Polytechnic Institute, in preparation.

Table 1: Variation of yield strength with depth.

Depth (m)	σ'_v (kPa)	τ_{yield} (kPa)	τ_{yield}/σ'_v
1.625	18.03	1.0	0.055
3.625	37.70	2.0	0.053
5.125	50.50	2.1	0.042
6.375	62.85	4.0	0.064
8.125	79.63	12.0	0.151
9.250	89.00	22.0	0.247

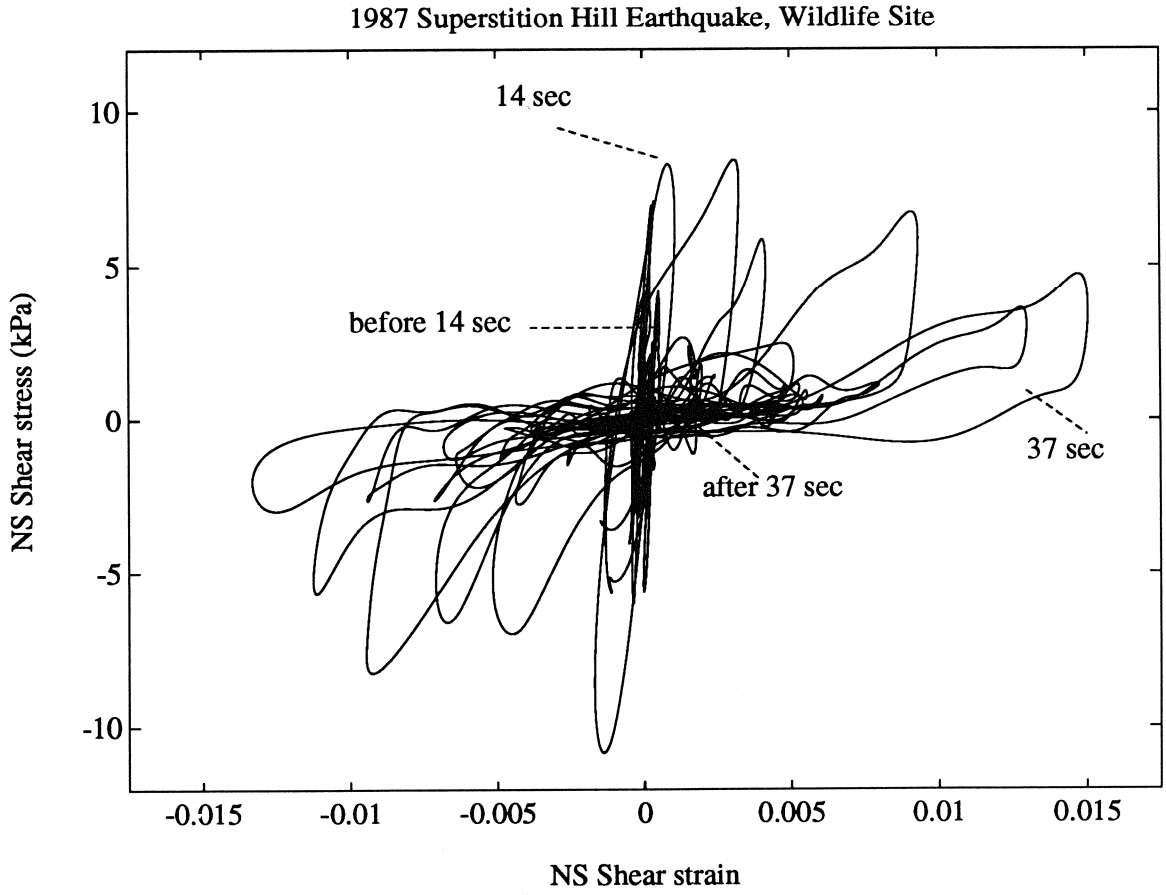

Figure 1: Shear stress strain history at the Wildlife refuge site during liquefaction (Elgamal and Zeghal 1992, Zeghal and Elgamal 1994).

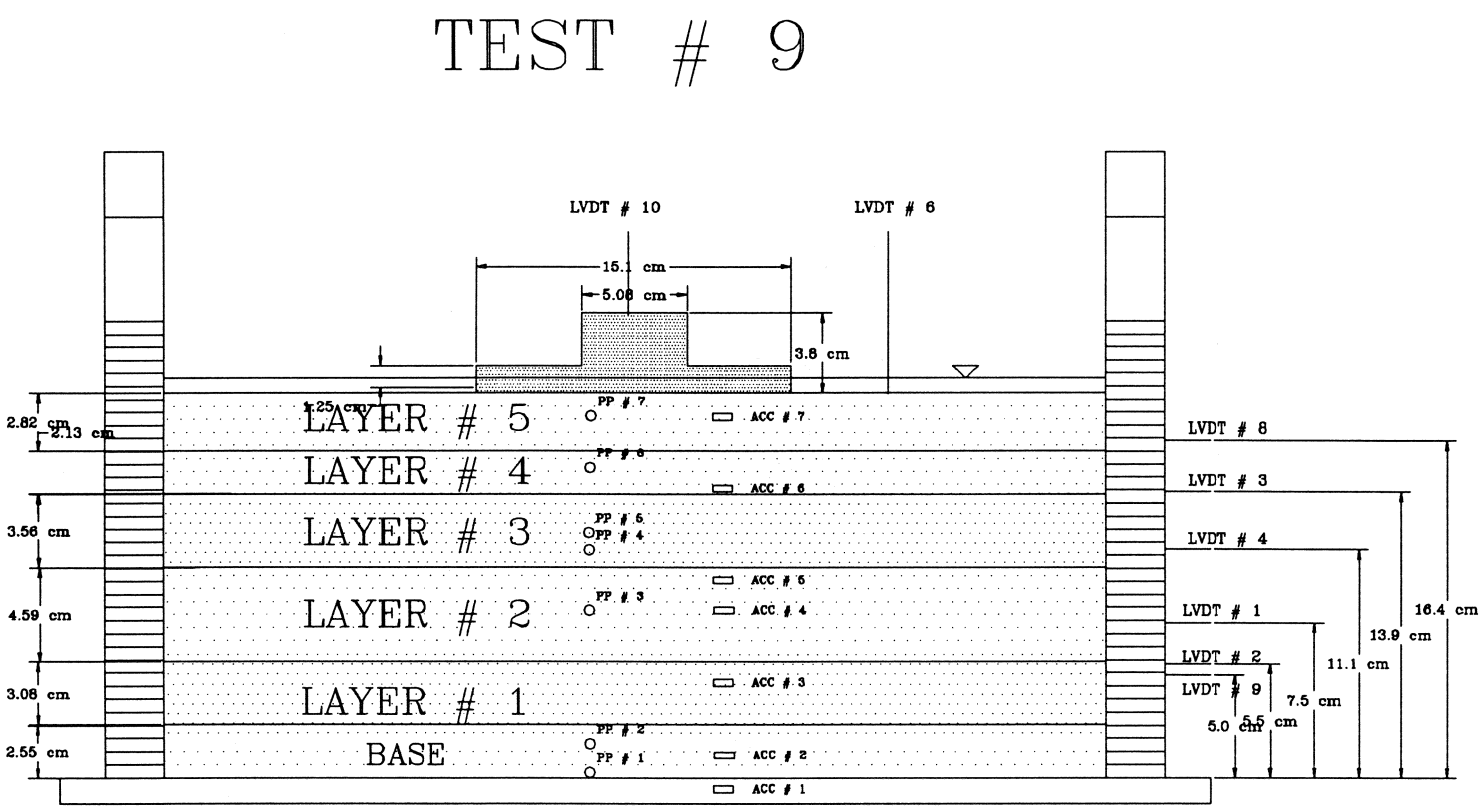

Figure 2: Test setup: soil profile and instrumentation (dimensions given in model scale).

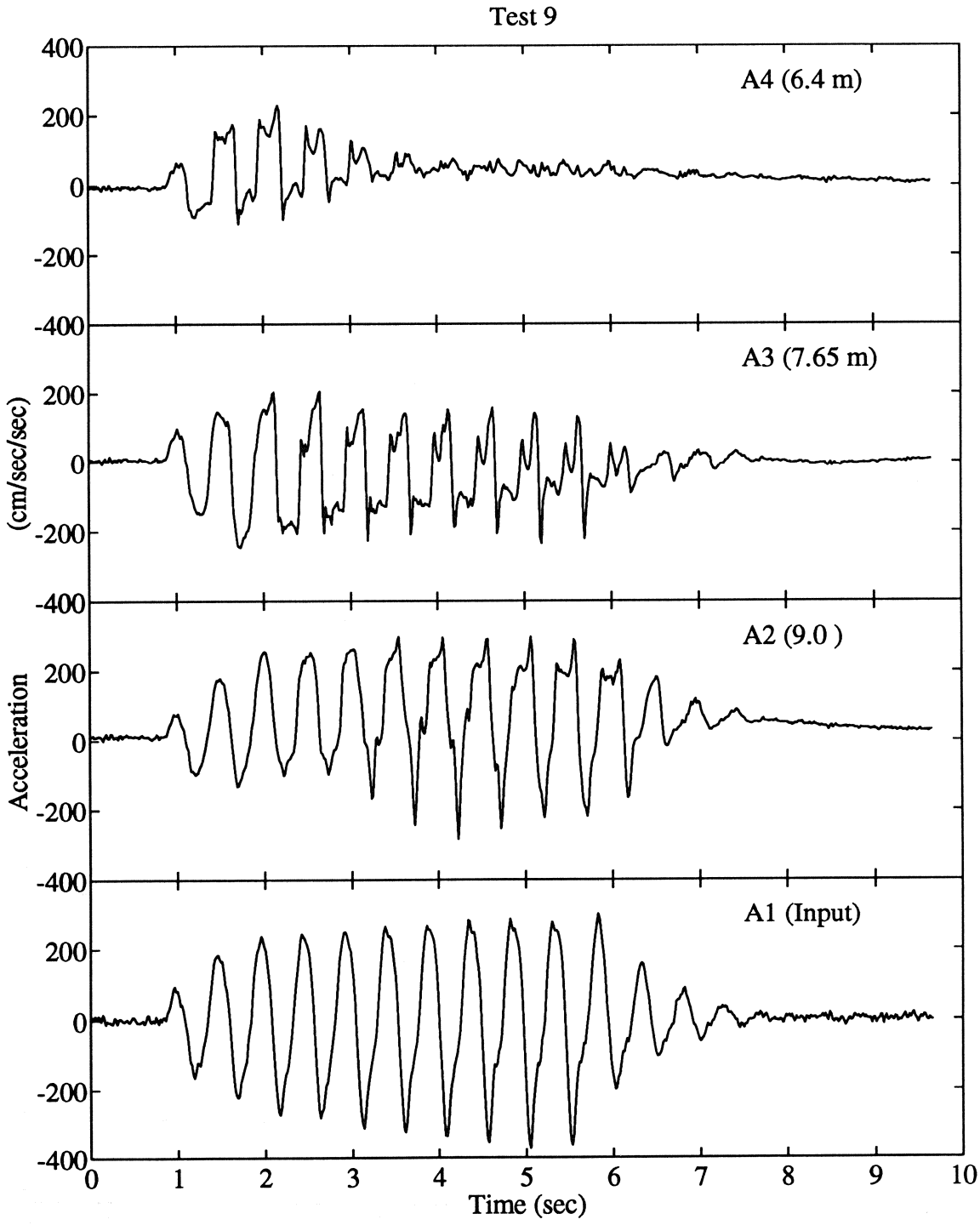

Figure 3: Acceleration histories at 6.4 m depth, 7.65 m depth, 9.0 m depth, and input acceleration history (prototype scale).

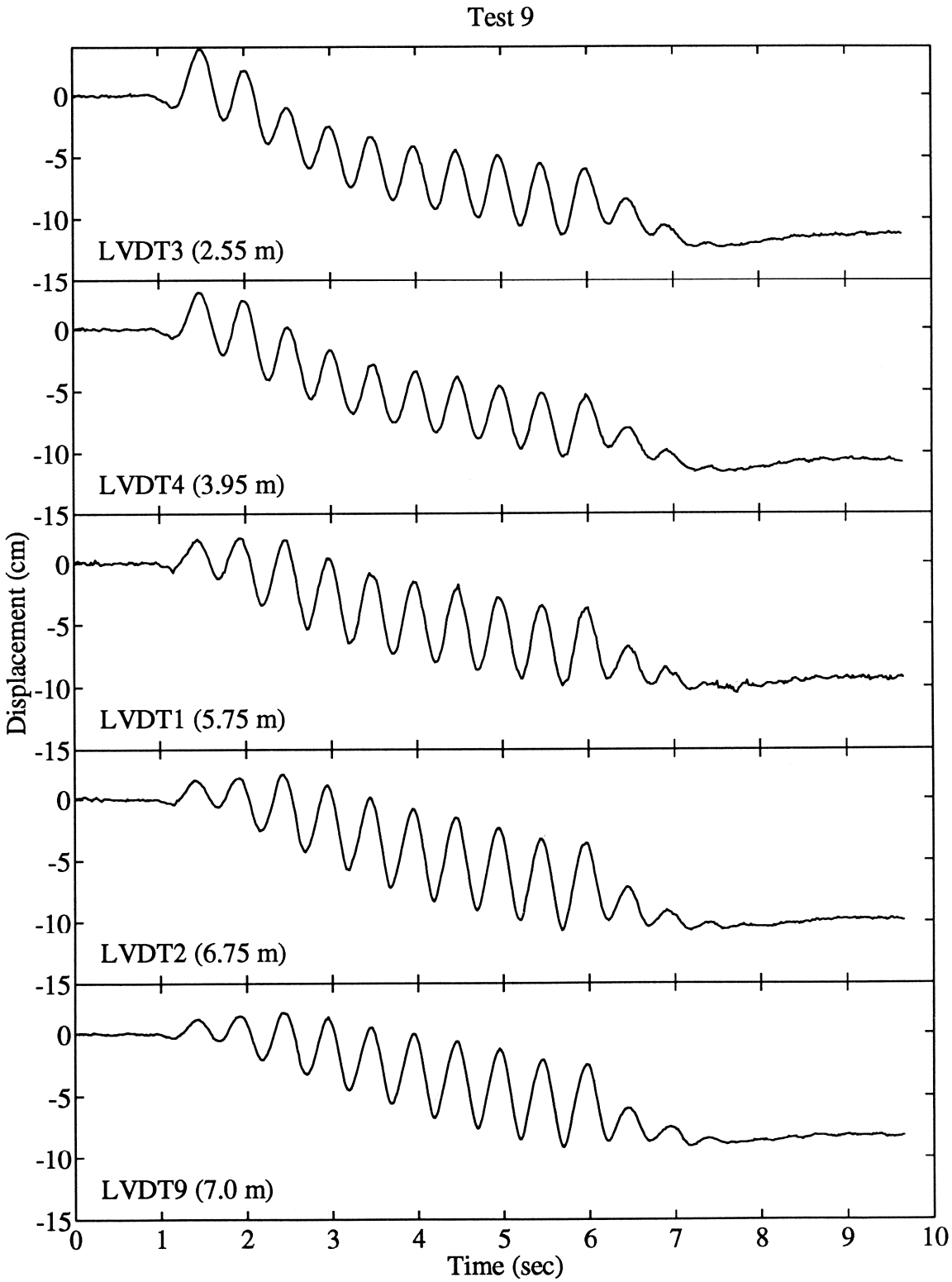

Figure 4: Displacement histories at 2.55 m depth (LVDT3), 3.95 m depth (LVDT4), 5.75 m depth (LVDT1), 6.75 m depth (LVDT2), and 7.0 m depth (LVDT9); prototype scale.

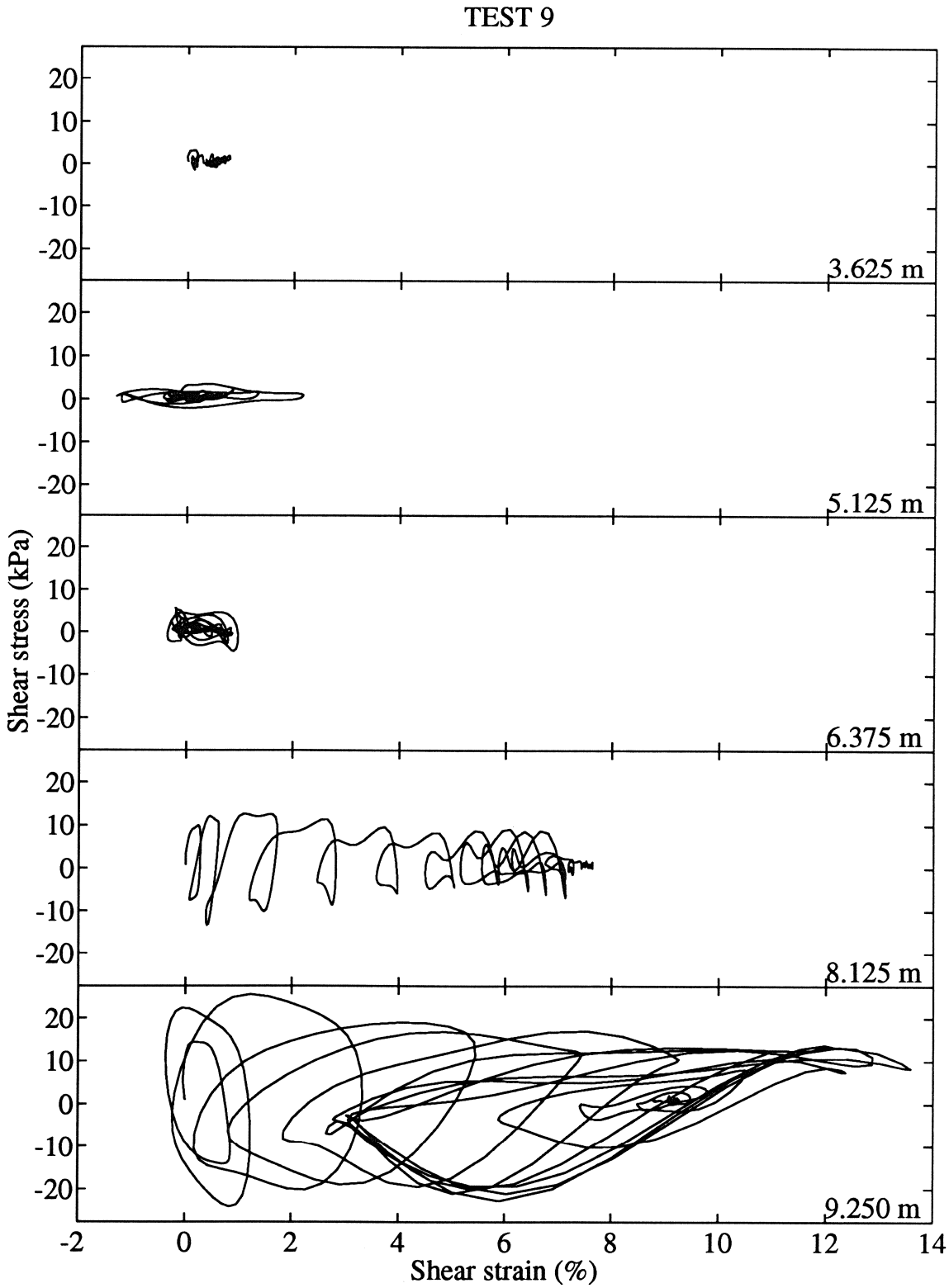

Figure 5: Shear stress-strain histories at 3.625 m depth, 5.125 m depth, 6.375 m depth, 8.125 m depth, and 9.250 m depth (prototype scale).

BEHAVIOR OF SAND AFTER LIQUEFACTION

by
Nozomu YOSHIDA[1], Susumu YASUDA[2], Masanori KIKU[3],
Tamio MASUDA[4], and W.D. Liam FINN[5]

ABSTRACT

Behavior of sand after liquefaction is discussed and formulated. Material properties that are usually assumed constant, such as internal friction angle, is ahown to change due to cyclic loading causing liquefaction. It is also shown that regions with very small stiffness appears by the cyclic loading. They may expand several ten percents, which causes liquefaction-induced large permanent displacement. A simlified model is introduced and improved so as to be able to take into new features such as change of material property and appearance of low stiffness region. The agreement of the numerical calculation and test are very good. Future research needs for evaluating the amount of liquefaction-induced permanent displacement more precisely are also pointed out.

[1] Engineering Research Institute, Sato Kogyo Co., Ltd., Atsugi, Japan

[2] Department of Civil Engineering, Tokyo Denki University, Saitama, Japan

[3] Department of Civil Engineering, Yokohama National University, Yokohama, Japan

[4] Civil Engineering Hydro Generation and Transmission Engineering Department, Tokyo Electric Co., Ltd., Tokyo, Japan

[5] Department of Civil Engineering, University of British Columbia, Vancouver, Canada

INTRODUCTION

Since Hamada et al. (1986) found that large permanent displacement (lateral spreading) occurred when soil liquefied in a widespread area, many efforts have been done to find the mechanism of lateral spreading caused by liquefaction and to evaluate the amount of lateral spreading (Hamada et al., 1994). Through the studies such as shaking table test (Yasuda et al., 1992, for example) and investigation of piles damaged due to lateral spreading (Yoshida et al., 1992; Yoshida and Hamada, 1992), it have been clarified that large deformation occurs in whole liquefied layer but not in a particular slip plane.

Figure 1 shows the mechanism of lateral spreading based on these observations schematically. Line ℓ denotes a backbone curve at the beginning of the earthquake. At this stage, nonzero shear stress exists in the horizontal plane mainly because of the gravity load when the ground is not a level ground. Point A in Figure 1 is then supposed to be an initial state.

When excess pore water pressure generates, material properties such as shear strength and elastic moduli change. Suppose that the backbone curve moves from ℓ to m by the change of material property. Because driving shear stress is caused by gravity, it hardely change under the small change of material property. If it does not change, the state point moves from A to B. Therefore, shear strain increases by the amount of γ_2-γ_1. As shown in this example, additional shear strain is generated if excess pore water pressure generates.

The amount of shear strain increases according to the generation of the excess pore water pressure. If the driving stress keeps constant, shear strain becomes infinite when shear strength becomes less than the driving stress. However, in the actual ground, the driving stress also decreases according to the change of geometry. Therefore actual strain increment from state ℓ to state m is not from A to B but from A to C. In other word, strain increment caused by the change of material property is not γ_2-γ_1 but γ_3-γ_1. Lateral spreading stops when new material property comes to a balance with a new driving stress, which is shown as point D in the figure.

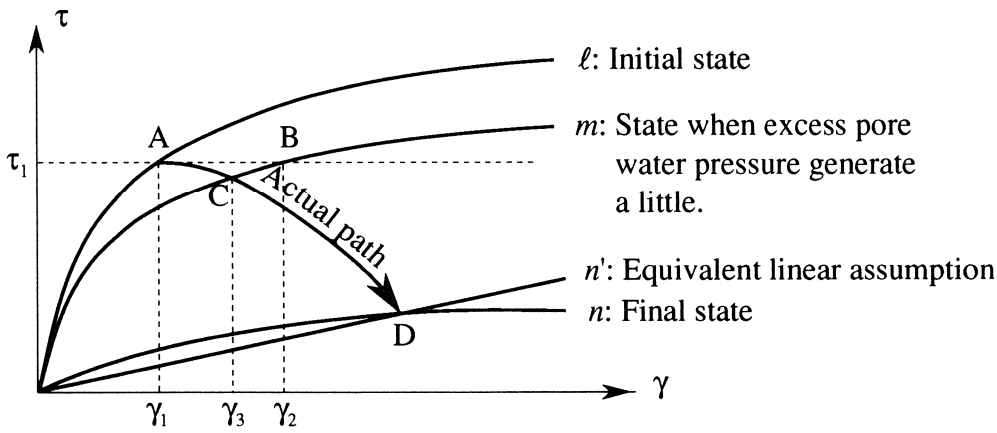

Figure 1 Schematic figure showing the mechanism of lateral spreading

This illustration implies two important features for predicting the amount of lateral spreading. The one is a stress-strain relationship to large strains and the other is a consideration of the change of geometry or large deformation theory.

Several analytical methods have been proposed for predicting the magnitude of lateral spreading based on this mechanism. Yoshida (1989) and Finn et al. (1991) used hyperbolic stress-strain relationships and large deformation theory. However, these methods require lots of computing time because both the change of geometry and that of material property must be considered in the same time. A more simplified methods have also been proposed. Employment of linear stress-strain relationship or zero stiffness on the liquefied layer is one simplification. Towhata et al. (1992) assumed zero stiffness and derived an analytical solution. Yoshida (1990) used equivalent linear concept in the FEM analysis. Yasuda et al. (1992) uses additional simplification, small deformation theory, in addition to linear stress-strain relationship.

In these analyses, stiffness of liquefied layer is assumed to be zero or very small except Finn et al. (1991) who dealt with partial liquefaction as well as complete liquefaction. By this zero stiffness assumption, we may be able to predict maximum possible displacement. In other word, it may be valid if we want to compute the displacement when a tilted ground becomes horizontal. However, all the liquefied ground does not always become a level ground. It is also obvious that the stiffness and the residual strength after the liquefaction affect the displacement prediction very much. In this paper, we discuss the behavior of sand at large strains and that after the liquefaction from the point of view for developing the stress-strain model based on test result.

BRIEF DESCRIPTION OF LABORATORY TEST AFTER LIQUEFACTION

Toyoura sand, with relative density from 30% to 70%, is tested by means of torsional shear test apparatus (Yasuda et al., 1993). Figure 2 shows loading program schematically. Specimen is formed and isotropically consolidated to an effective mean stress p'=0.5kgf/cm^2. Then shear stress with constant amplitude is applied until the safety factor against liquefaction, F_L, decreases to a specified value. Finally, load is applied so that shear strain increases monotonically. The second stage (cyclic loading) and the third state (monotonic loading) of test are conducted under an undrained condition. Only the behavior at the 3rd loading stage is shown and discussed hereafter.

Figure 3(a) shows examples of test result. Here, "static" indicates the test in which there is no cyclic load (2nd stage loading in Fig.2) before monotonic loading. Big difference is seen between the results of static and the of other loadings (called "post-liquefaction loading" hereafter). Shear stress at the beginning of the monotonic loading is nearly zero in the post-liquefaction loading. Figure 3(b) focuses on the behavior at small stresses. The stiffness at the beginning of loading is very small, but not zero although loading starts after the soil liquefied. At certain strain, the sand recovers its stiffness very rapidly, and, as seen in Fig. 3(a), stiffness finally becomes comparable order with the one of static loading. The former part is called low stiffness region and the latter high stiffness region hereafter. Our goal is to predict the behavior of sand in whole these region.

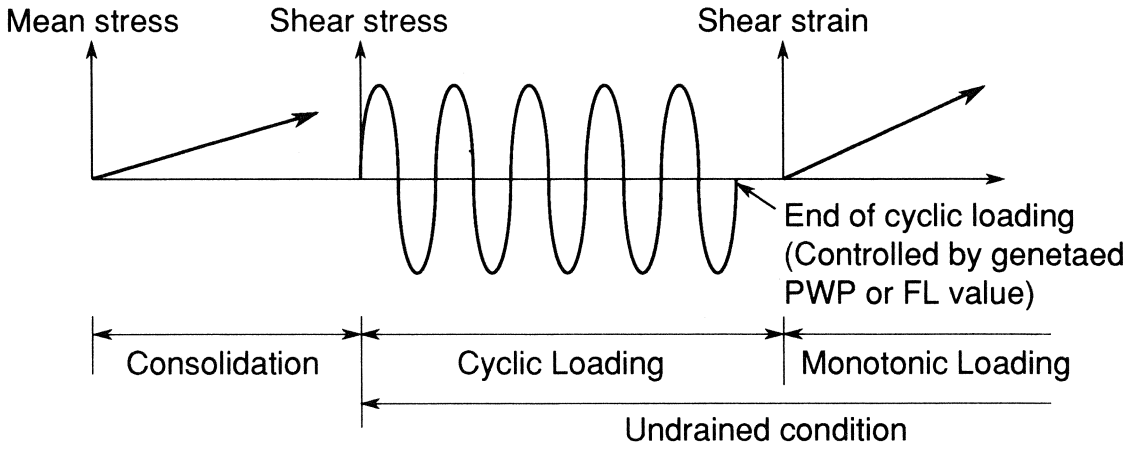

Figure 2 Loading program

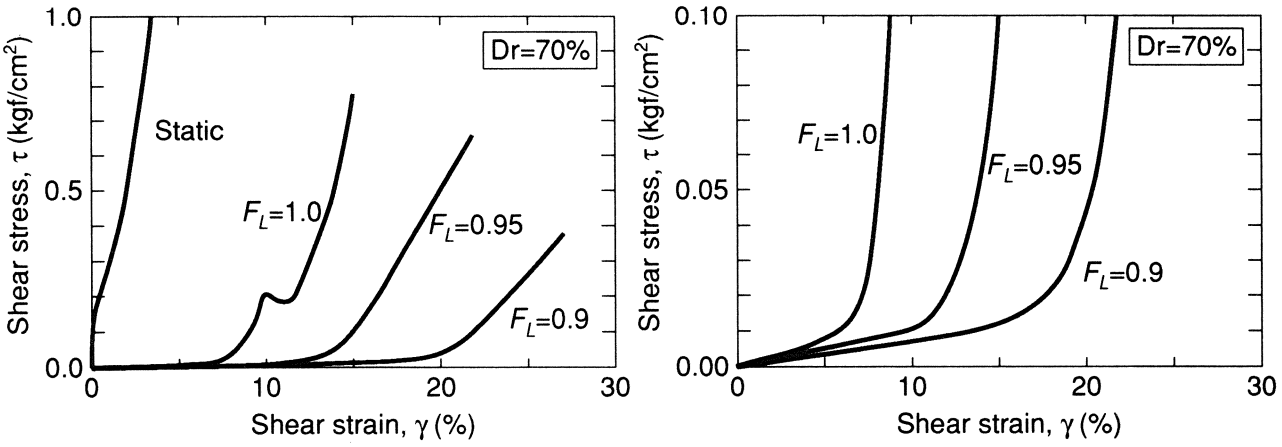

(a) Whole test result (b) Behavior at small stress

Figure 3 Stress-strain relationship of typical test results

BASIC EQUATIONS OF STRESS-STRAIN MODEL

A simplified method (Yoshida et al., 1993a,b) is employed for formulating the basic stress-strain model. Although this method includes wide scope including cyclic plasticity, the simplest form is used so as to make the characteristics of the behavior of sand clear.

Deformation of soil is divided into volume change and shear deformation. Incrementally elastic behavior is assumed for the volume change;

$$dp' = K(d\varepsilon_v - d\varepsilon_{vd}) \tag{1}$$

where

p' : effective mean stress

$K = K_o p'^n$: tangent bulk modulus (2)

K_o : bulk modulus constant

n : bulk modulus exponent

ε_v : volumetric strain

ε_{vd} : volume change due to dilatancy

Volume change ε_{vd} due to dilatancy is computed by using the generalized stress-dilatancy relationship,

$$\frac{d\varepsilon_{vd}}{d\gamma} = \mu - \frac{\tau}{p'} \tag{3}$$

where γ denotes equivalent shear strain, and τ denotes equivalent shear stress (radius of Mohr's cycle). The variable μ is a parameter, but, at present, we put $\mu=\mu_p$ following the ordinary stress-dilatancy relationship, where and μ_p denotes stress ratio τ/p' at phase transform. From Eqs. 1 and 3, we can compute effective mean stress increment for given strain increment $d\varepsilon_{ij}$. Therefore, the value of effective mean stress is known when computing shear deformation in the followings.

Hyperbolic model is employed for shear stress-shear strain relationship, which is expressed in the dimensionless form as

$$\eta = \frac{\xi}{1+\xi} \tag{4}$$

where

$\eta = \tau / \tau_{max}$: shear stress ratio

$\tau_{max} = p' \sin\phi$: shear strength (5)

ϕ : internal friction angle

$\xi = \dfrac{\gamma\, G_{max}}{\tau_{max}}$: shear strain ratio

G_{max} : shear modulus at small strains

Since effective mean stress is already known, both G_{max} and τ_{max} are known quantities. Dimensionless tangent shear modulus g is obtained by differentiating η with respect to ξ, which yields

$$g = \frac{d\eta}{d\xi} = \frac{1}{(1+\xi)^2} \tag{6}$$

Finally, deviatoric stress increment ds_{ij} is obtained from the given deviatoric strain increment $d\gamma_{ij}$ as

$$ds_{ij} = g\, G_{max} d\gamma_{ij} \tag{7}$$

Stress increment is computed from Eqs. 1 and 7.

This formulation is shown to be effective for simulating the behavior of sand in the ordinary shear strain range up to several percent (Yoshida et al., 1993b). However, it does not seem to be valid at very large strains or for the behavior after liquefaction, which will be discussed hereafter. The formulation will be improved based on the discussion of the characteristics of the behavior of sand both at large strains and after the liquefaction.

BEHAVIOR OF SAND AT LARGE STRAINS

In this section, we discuss the stress-strain relationship at large strains where stress point moves along the failure surface. Equivalent shear strain increment $d\gamma$ is easily computed from a given strain increment $d\varepsilon_{ij}$. Then, volumetric change due to dilatancy is computed from Eq.3. Under the undrained condition, however, this volume change does not occur, but effective mean stress changes

by the amount of

$$dp' = -K d\varepsilon_{vd} \tag{8}$$

Substitution of Eq.3 into Eq.8 yields

$$dp' = K\left(\frac{\tau}{p'} - \mu\right)d\gamma \tag{9}$$

Since the stress path moves along the failure surface, the stress ratio τ/p' is approximately expressed as

$$\frac{\tau}{p'} = \sin\phi \tag{10}$$

Therefore, Eq.9 yields

$$dp' = K(\sin\phi - \mu)d\gamma \tag{11}$$

Shear strength increment $d\tau_{max}$ during the change of mean effective stress is computed from Eq. 5 as

$$d\tau_{max} = dp'\sin\phi \tag{12}$$

We again use the assumption that stress path moves along the failure surface. Then, equivalent shear stress increment $d\tau$ is nearly equals to the shear strength increment $d\tau_{max}$. Finally, we obtain stress-strain relationships at large strains in the incremental form

$$d\tau = K(\sin\phi - \mu)\sin\phi \cdot d\gamma \tag{13}$$

Equation 13 implies that a computed stiffness at large strains is strongly affected by the value of μ, because other parameters are well known physical quantities.

The value of μ for static loading is back calculated from Eq. 13 and $d\tau/dp'$ value read off from the test result. Here tangent bulk modulus is computed from

$$K = \frac{2(1+\nu)}{3(1-2\nu)}G_{max} \tag{14}$$

where ν denotes Poisson's ratio. Shear modulus G_{max} at small strains is computed from the empirical equation for Toyoura sand (Kokusho, 1980),

$$G_{max} = 840\frac{(2.17-e)^2}{1+e}p'^{1/2} \quad (\mathrm{kgf/cm^2}) \tag{15}$$

where e denotes void ratio. Kokusho (1980) also showed Poisson's ratio ν as a function of effective confining pressure as shown in Fig. 4. The value at p'=0.5kgf/cm^2 is used in Eq. 14 and the following analysis.

Figure 5 shows computed μ value at large strains, μ_f . The value of μ increases with relative density. This tendency is quite different with the tendency of phase transformation angle which decreases with relative density. Therefore it is obvious that we cannot obtain good prediction at large strains if $\mu=\mu_p$ is used at large strains.

The change of μ value from stress ratio $\eta=\mu_p$ (phase transform) to $\eta=1$ (on failure line) is not known. In the followings, therefore, we use piecewise linear relationship between μ and η. Figure 6 shows the result of analysis for static loading. The agreement between test and analysis is very good.

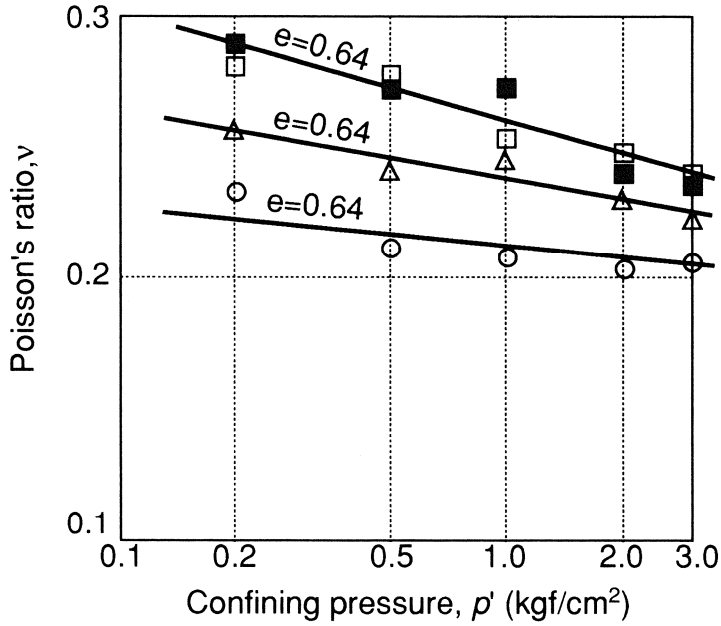

Figure 4 Poisson's ratio versus effective mean stress relationship (Kokusho, 1980)

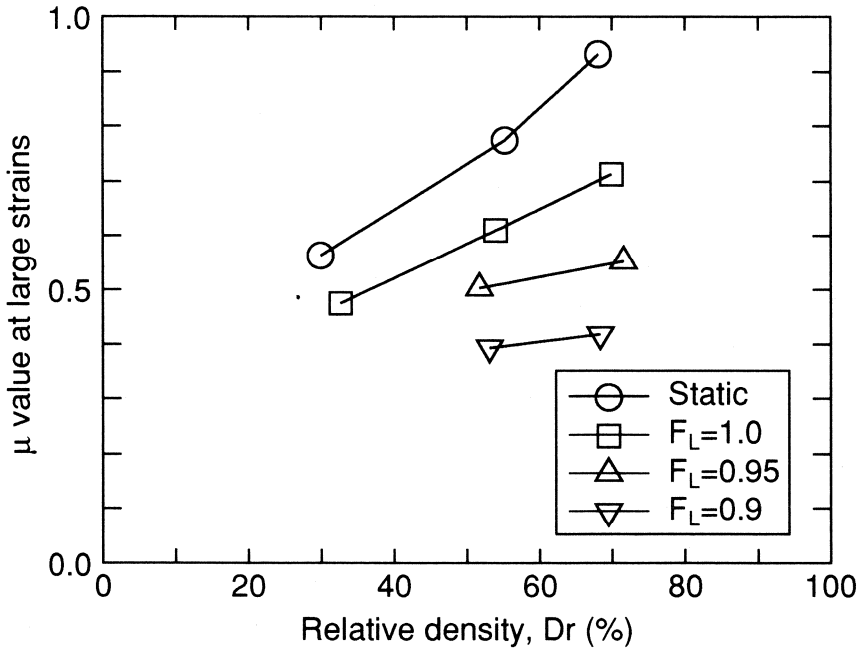

Fig.5 The value of μ at large strains

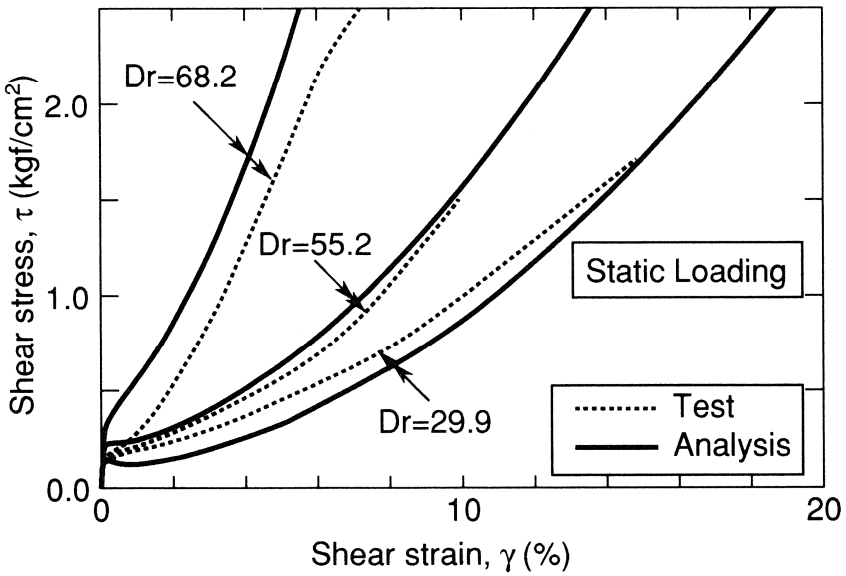

Fig.6 τ-γ relationship for static loading

EFFECT OF OCCURRENCE OF LIQUEFACTION

In almost all constitutive models, material properties with physical meanings such as internal friction angle are assumed to be constant even if liquefaction occurs. As the first trial, therefore, we use similar method; the effect of liquefaction is considered only in the initial condition. Because of the occurrence of liquefaction, effective mean stress decreases very much. So, we use 1/100 of initial effective mean stress, p_o=0.005kgf/cm^2, as initial mean stress.

Figure 7 shows the result of analysis in comparison with test and previous analysis. This analysis (p_o=0.005kgf/cm^2) generates more strain than previous analysis (p_o=0.5kgf/cm^2), which comes from the difference between the behaviors at the beginning of the loading. This analysis starts at very low effective mean stress, therefore stiffness at the beginning is also small, which is the reason why this analysis generates more strain than the previous. However, as discussed in the previous section, this analysis does not improve the behavior at large strains; stress-strain curves are almost parallel to each other. In addition, stiffness at the beginning of loading in this analysis is much smaller than the one by previous analysis, but it is still much larger compared with test results of post-liquefaction loading. Therefore, the resultant strain is still much smaller than the ones of tests with post-liquefaction loading.

Observation of both test result and detailed comparison between test and analysis show following disagreements.

1) Analysis shows larger stiffness at the beginning of loading, because low stiffness region observed in the test is not considered in the analysis.
2) Stiffness at high stiffness region by test decreases depending of F_L, but constant in the analysis.
3) The behavior of post-liquefaction loading changes depending on F_L value, but it is not considered

in the analysis.

These facts imply that material property may change during the cyclic loading conducted before the post-liquefaction loading. In the following sections, we will discuss these and consider the effect of liquefaction in developing the stress-strain modeling.

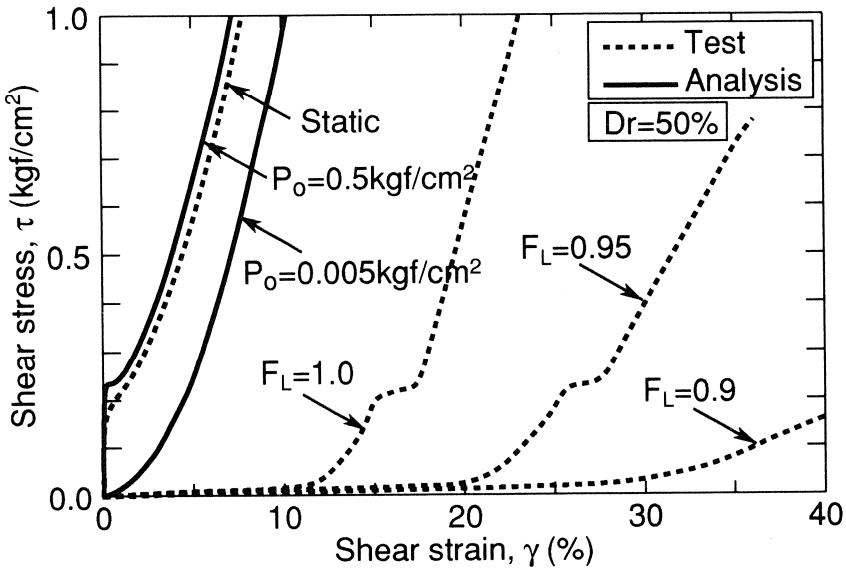

Figure 7 Comparison of stress-strain relationship

INTERNAL FRICTION ANGLE AND PHASE TRANSFORM

Figure 8 shows an example of stress paths of the test of relative density 70%. The stress-strain relationship of this test is shown in Fig. 3. Stress path moves linearly after phase transformed for static loading test. It moves almost linearly from the beginning of loading for post-liquefaction loading test. Therefore, stress point is supposed to move along the failure line. It is clearly observed that the slope decreases with F_L value, which implies that internal friction angle changes depending on the loading before the monotonic loading.

The slope angles are read from stress path trajectory and plotted in Fig. 9. Those obtained from tests with other relative deisities are also plotted in the figure. Here, it is noted that this angle is not an internal friction angle ϕ, but $\tan^{-1}(\sin\phi)$. The dependency of internal friction angle on the loading before liquefaction is also clearly observed.

Phase transform is very difficult or impossible to read from test result of post-liquefaction loading. According to the parametric studies using the final form of the stress-strain model of this paper, however, μ_p value does not affect the whole behavior very much. Therefore, in the following analysis, it is held constant regardless of F_L value.

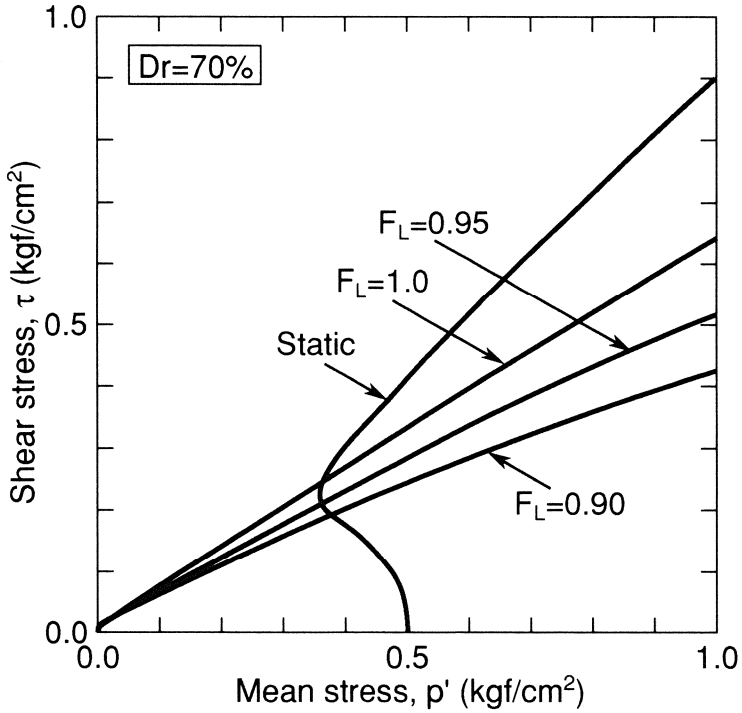

Fig.8 Stress path of test with relative density of 70%

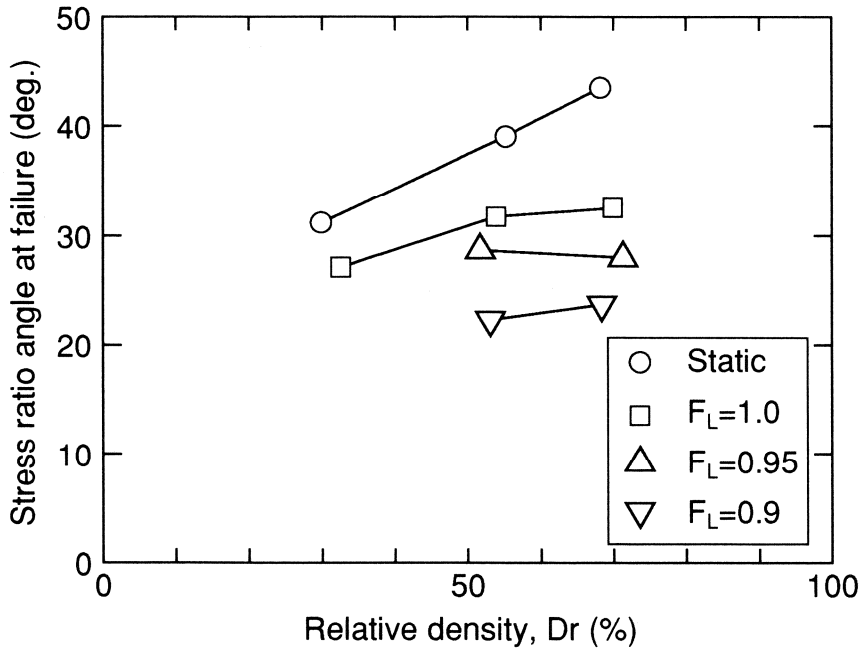

Fig. 9 Change of slope of failure line caused by liquefaction

Knowing the internal friction angle and the slope of the stress-strain curve at high stiffness region, the value of μ_f can be calculated. The result is overplotted in Fig. 5. The value of μ_f decreases as F_L value decreases or cyclic loading after liquefaction increases, which is the similar to the tendency of internal friction angle.

EVALUATION OF LOW STIFFNESS REGION

It is easily recognized from the previous analysis that modification of internal friction angle and μ value will improve the behavior in high stiffness region, but not in low stiffness region. Yoshida et al. (1994) measured the relationship between the volumetric strain and effective mean stress during the process of excess pore water pressure dissipation so as to obtain the settlement characteristics of the ground after liquefaction by means of triaxial shear test apparatus. Figure 10 shows typical result of the test.

The p'-ε_v relationship is divided into two parts. At the beginning of drainage, bulk modulus is very small. It increases very rapidly at certain volumetric strain. This behavior is similar to the test result described in the previous section; low stiffness region and high stiffness region correspond to low and high bulk modulus regions, respectively. The p'-ε_v relationship shown in Fig. 10 is obtained on the process of excess pore water pressure dissipation. If principle of effective stress holds, however, the same relationship is valid for the undrained behavior discussed here.

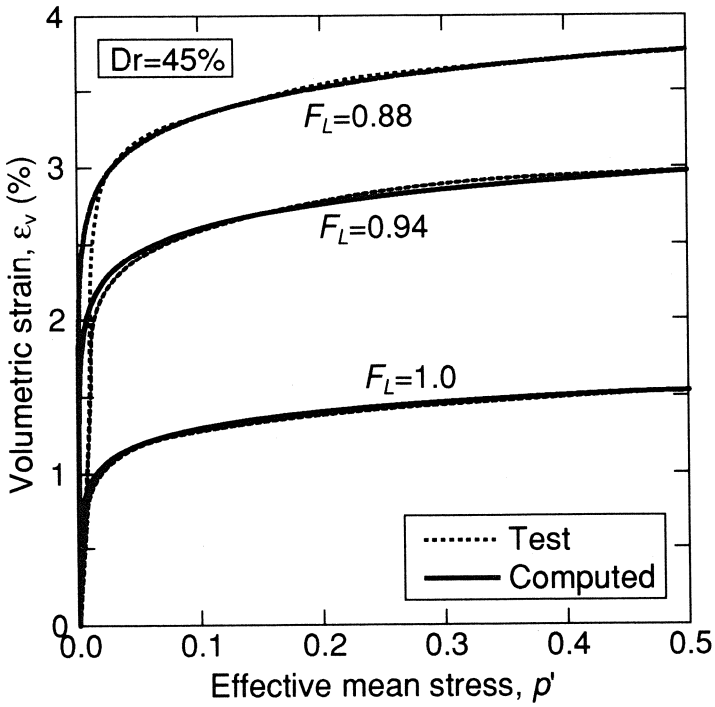

Fig.10 Volumetric strain characteristics during the excess pore water pressure dissipation after liquefaction. (Yoshida and Finn, 1994)

Since there is few change of shear strain on the process of drainage, volume change due to dilatancy is supposed not to include in the measured volumetric change in Fig.10. Yoshida et al. (1994) pointed out that bulk modulus at high bulk modulus region is consistent to the bulk modulus derived from ordinary empirical equation such as Eq. 2. This implies that elastic modulus (tangent bulk modulus) is very small in the low bulk modulus region. If so, it is also reasonable to assume that shear modulus G_{max} at small strains is also very small. Otherwise, Poisson's ratio becomes very small or negative, which is not realistic.

Yoshida and Finn (1994) formulates the behavior in Fig. 10 in the following equation,

$$\frac{p'}{p'_o} = \frac{e^{\frac{\varepsilon_v}{c}} - 1}{e^{\frac{\varepsilon_{vo}}{c}} - 1} \tag{16}$$

where p'_o denotes initial effective mean stress from which cyclic load is applied to cause liquefaction, andε_{vo} denotes a volumetric strain at $p' = p'_o$. The variable c is a parameter, which is expressed as

$$c = 0.053\varepsilon_{vo} + 7 \times 10^{-4} \tag{17}$$

Tangent bulk modulus to be used instead of Eq. 2 is obtained from Eq. 16 as a function of effective mean stress p' as

$$K = \frac{1}{c} \frac{p'_o + p'(e^{\frac{\varepsilon_{vo}}{c}} - 1)}{e^{\frac{\varepsilon_{vo}}{c}} - 1} \tag{18}$$

The shear modulus G_{max} at small strains is then obtained from Eq. 14, where, in the following analysis, the value of Poisson's ratio is kept constant.

In the following analysis, tangent bulk modulus and shear modulus at small strains derived from Eqs. 18 and 14 are used, which covers both low and high stiffness regions. Here, it is noted that ε_{vo} in Eq. 16 was actual value which occurs after excess pore water pressure dissipates, but, when using in the analysis here, it is a fictitious value.

RESULT OF ANALYSIS AND DISCUSSION

In the first part of this paper, we introduced a basic form of stress-strain model, and after that, we have discussed the effect of liquefaction on the behavior of sand at large strains. From the point of view for computing the behavior of soil, they are summarized as follows;

1) Internal friction angle changes during the cyclic loading causing liquefaction, which is shown in Fig.9.
2) The value of μ at phase transform and that at large strains where stress path moves along the failure line are different to each other; the latter is generally larger than the former. Piecewise linear relationship is used in terms of shear stress ratio in this analysis. The value of μ_f is shown in Fig.5, which also changes depending on the amount of cyclic loading.
3) Tangent bulk modulus K is computed from Eq. 18 instead of Eq. 2. Shear modulus G_{max} at small strains is computed from Eq. 14, where Poisson's ratio is kept constant.

In applying Eq. 18, the value of ε_{vo} is not known, because it can be obtained after excess pore water

pressure dissipates. Moreover, since only the test result with relative density of 45% is shown in Fig. 10, ε_{vo} at other relative densities cannot be obtained from the figure. Therefore, at first, we treat ε_{vo} as a fitting parameter.

Figures 11 to 13 show the result of analysis and test result. Here, the value of μ_f cannot be read from the test result of Dr=30% and F_L=0.95 and 0.9, therefore suitable value is assumed. The agreement of analysis with test result is very good for both low stiffness region and high stiffness region, although a little disagreement is seen at the transition between two regions.

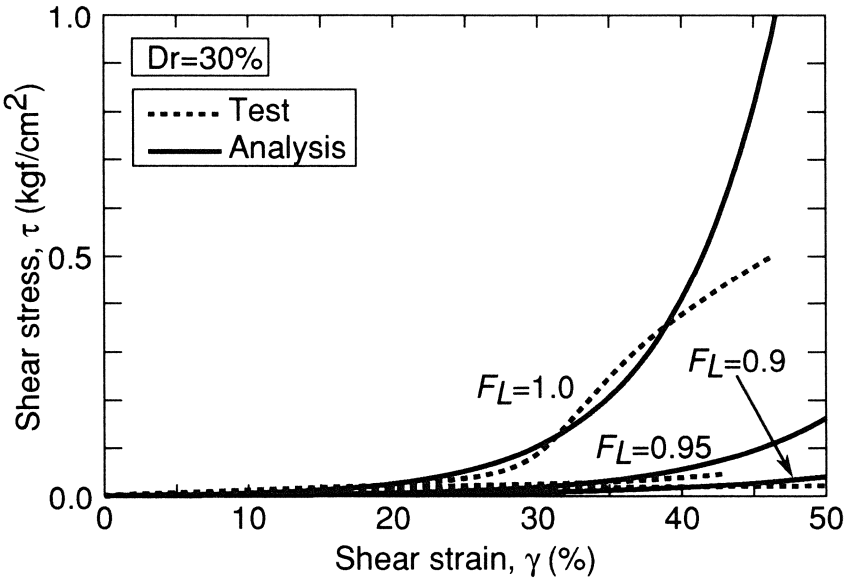

Fig.11 Stress-strain relationship for Dr=30%

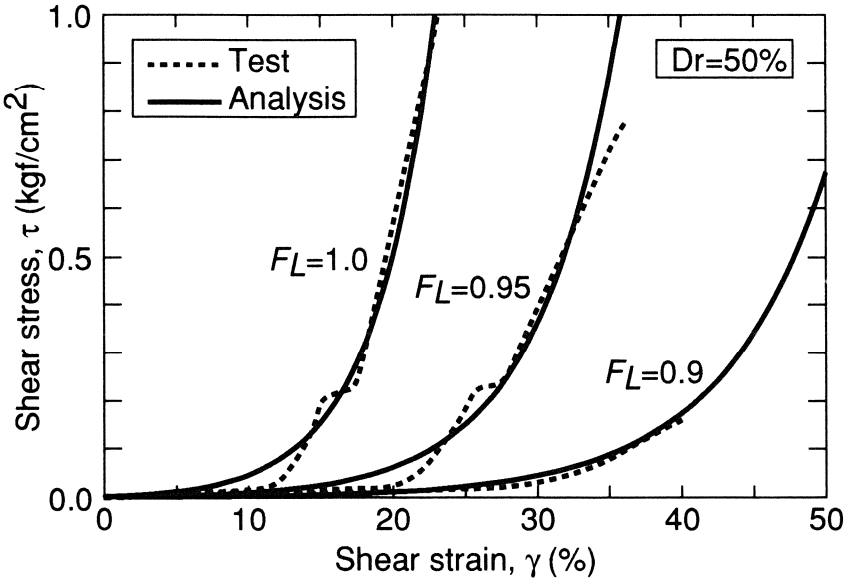

Fig.12 Stress-strain relationship for Dr=50%

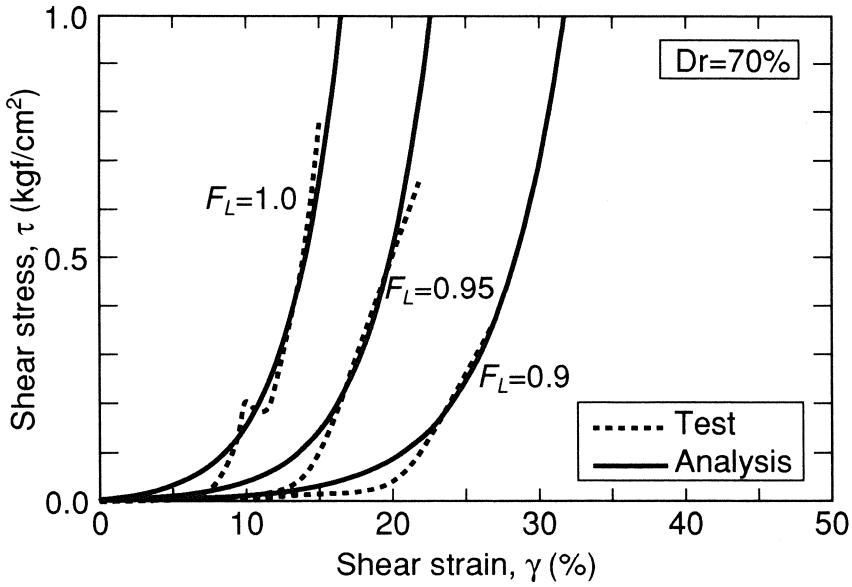

Fig.13 Stress-strain relationship for Dr=70%

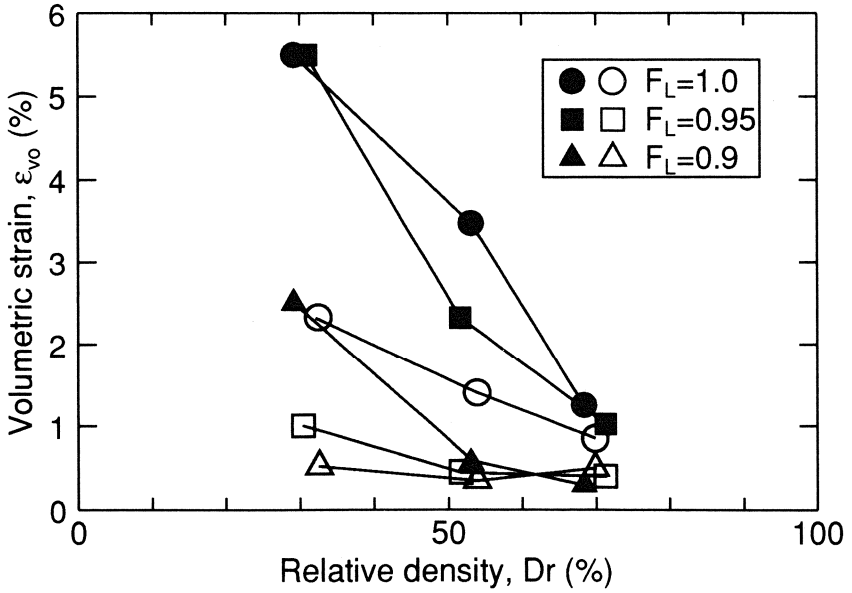

Fig. 14 Fictitious volumetric strain ε_{vo} used in the analysis

In Fig. 14, hollow symbols show evaluated ε_{vo} value in order to get good agreement as shown in Figs. 11-13. Ishihara (1993) produced a design charts as shown in Fig. 15 for evaluating the post-liquefaction volume change. This chart is derived based on random shear stress history loading by means of torsional shear test apparatus. The value of ε_{vo} can be read off from this figure from either F_L value or γ_{max} which is a maximum shear strain generated during the random loading. Here, it is noted that definition of the occurrence of liquefaction is different in the test described here and

Fig. 15. As seen in Fig. 15, F_L=1 corresponds to the generation of 3.5% shear strain under random loading. On the other hand, F_L=1 in the test discussed in this paper corresponds to the generation of 15% double amplitude shear strain under constant amplitude shear stress loading. Therefore, direct use of ε_{vo} value in Fig. 15 may not fit in the analysis. However, there is no direct conversion method. So, we try to use ε_{vo} value assuming that F_L values in both method are identical to each other in the next trial.

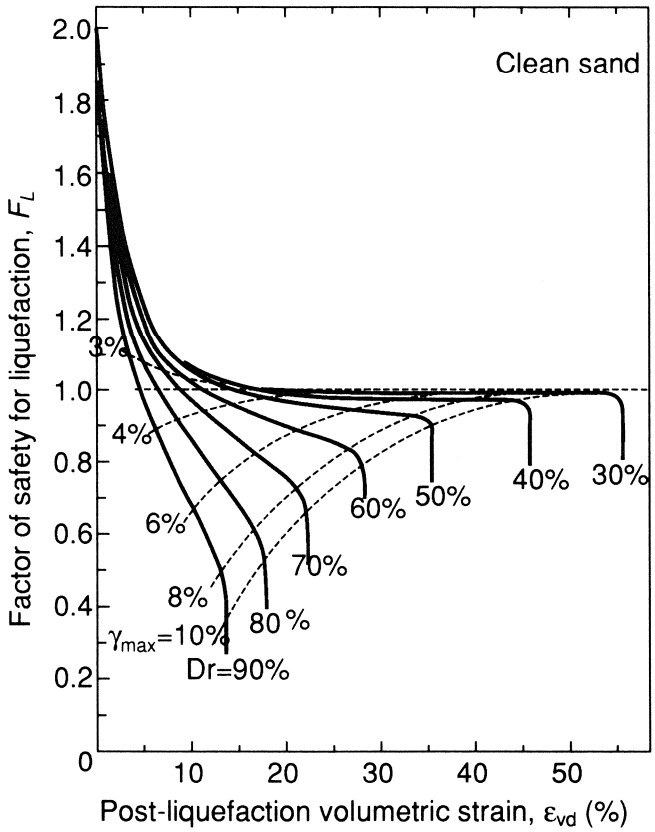

Fig.15 Design chart for obtaining post-liquefaction volumetric change (Ishihara, 1993)

Figure also 14 shows ε_{vo} value read off from Fig. 15 as solid symbols. it symbols is larger than that shown by hollow symbols. The value of ε_{vo} in the case of Dr=30% are the same for F_L=0.95 and 0.9. On the other hand, test result shown in Fig. 11 clearly shows more deterioration for F_L=0.9 than F_L=0.95. This also implies that F_L values in both test may not be of the same definition.

Since ε_{vo} shown by solid symbols in Fig. 14 (read off from Fig.15) is larger than that shown by hollow symbols (derived in this paper), it is obvious that new calculation gives larger low stiffness region than previous if other parameters are kept constant. As shown previously, all the parameters except μ have clear physical meanings in the theory proposed here. Therefore, we treat μ as fitting parameter and get better agreement with test result. Figure 16 shows the result of analysis for Dr=70%. The agreement with test result is also good although the agreement of the stiffness at high stiffness region is a little worse than previous.

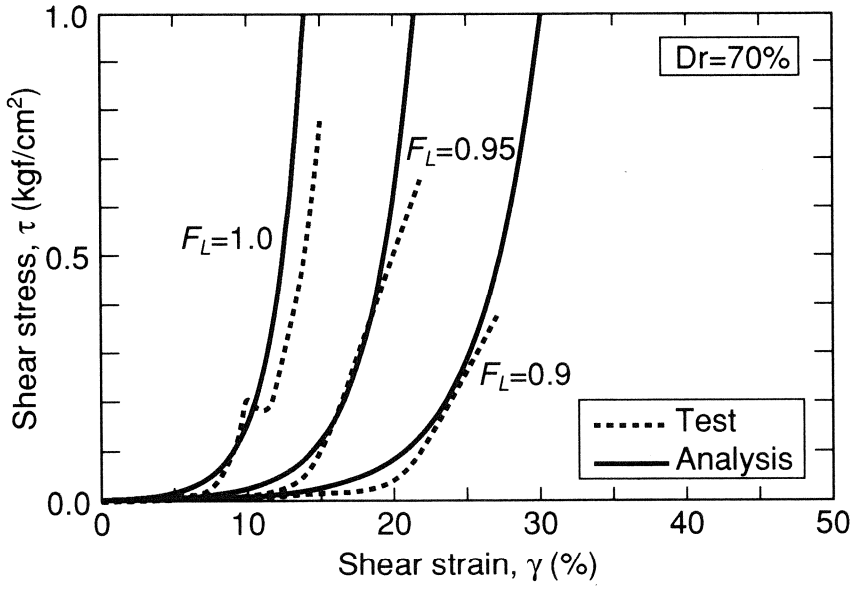

Fig. 16 Comparison between test and analysis in which fictitious volumetric strain shown in Fig. 15 is used and μ is treated as fitting parameters

CONCLUDING REMARKS

Several new features are presented in this paper from the point of view to predict the behavior of sand after liquefaction. The biggest one is the appearance of low stiffness region whose size depends on the amount of cyclic loading. The stiffness of this region is very small, and the strain is as large as several ten percents, which is a sufficient order of shear strain to cause large amount of liquefaction-induced permanent deformation. It may be recognized that this region occurs because soil particle configuration is very unstable, possibly floating up in the pore water or just close to that. The phase change from low stiffness region to high stiffness region occurs because the soil particle comes to a new stable configuration. This concept explains the change of material property due to cyclic loading. Therefore, the mechanism of liquefaction-induced lateral spreading is quite different with the ordinary discussion on residual strength or steady state under monotonic loading without cyclic loading before it.

Several ten percents of shear strain may not be enough to explain the lateral spreading observed in, for example, Niigata city during the 1964 Niigata earthquake (Hamada et al., 1993) where more than 100% of shear strain is supposed to occur. The discussion in this paper is based on the behavior under undrained condition. If configuration of soil particle is unstable at low stiffness region, the configuration may be disturbed by seepage flow. This will create additional displacement. Additional displacement is larger as thickness of liquefied layer increases because seepage flow caused by the excess pore water pressure dissipation continue for long period.

It is also noted that low stiffness region is observed even at F_L=1.0. It implies that this stage appears even before the occurrence of liquefaction. However, constitutive models usually does not consider the appearance of this region.

We also showed that the behavior of soil can be computed with reasonable accuracy by considering the low stiffness region. However, some of the parameters were not evaluated well because empirical experience is short or not conducted to evaluate these values within required accuracy. Therefore, we employed relevant value by our judgement in this paper, which may not be best choice and result in disagreement. For example, Poisson's ratio is assume to be constant in this analysis, but, as shown in Fig.4, it depends on confining pressure. However, since it is not expressed in a formula and value at very low confining pressure is not shown, we do not consider p' dependency of Poisson's ratio. The same things occured for phase transform angle. Moreover, we used Eq. 16 but the validity of this equation is proved only in particular cases. The change of internal friction angle and μ by cyclic loading are also not formulated. Research is required to obtain these behavior and to develop the empirical formulae used in the analysis.

We used F_L value to express the loading causing liquefaction and after liquefaction, and ε_{vo} value as the index of low stiffness region. Obviously, these are not convenient parameters when developing the stress-strain models. Trials to find another, more convenient parameter are also required.

REFERENCES

Finn,W.D.L., Yogendrakumar,M., Ledbetter,R.H. and Yoshida,N. (1991), Analysis of liquefaction induced displacements, 7ICCMAG, pp.913-921

Hamada,M., Yasuda,S., Isoyama,R. and Emoto,K. (1986): Study on Liquefaction Induced Permanent Ground Displacement, Association for the Development of Earthquake Prediction, Tokyo

Hamada,M, O'Rouke,T.D. and Yoshida,N. (1994): Liquefaction-induced Large Ground Displacement, Performance of Ground and Soil Structures during Earthquakes, 13th ICSMFE, New Delhi, JSSMFE, pp.93-108

Ishihara (1993): Rankine lecture

Kokusho,T. (1980): Cyclic Triaxial Test of Dynamic Soil Properties for Wide Strain Range, Soils and Foundations, Vol.29, No.2, pp.45-60

Towhata,I. et al. (1992): Prediction of Permanent Displacement of Liquefied Ground by Means of Minimum Energy Principle, Soils and Foundations, Vol.32, No.3, pp.97-116

Yasuda,S. et al. (1992), The mechanism and a simplified procedure for the analysis of permanent ground displacement due to liquefaction, Soils and Foundations, Vol.32, No.1, pp.149-160

Yasuda,S., Kiku,H., Yoshida,N., Masuda,T. and Itafuji,S. (1993): Torsional Shear Tests on Post Liquefaction Behavior of Sand, Preprint, Japan-US Seminor on Dynamic Behavior and Failure of Ground, Napa Valley, California

Yoshida,N. (1989): Large Deformation Analysis of Liquefaction-induced Ground Displacement by

Reduced Integral Method, Proc., 3rd Symposium on Computational Mechanics, Japan Union of scientists, pp.391-396 (in Japanese)

Yoshida,N., Kobayashi,K. and Nakamura,S. (1990): An Investigation of Pile Foundation of a Building Damaged at the 1964 Niigata Earthquake, Tsuchi-to-Kiso, JSSMFE, Vol.38, No.6, pp.39-44 (in Japanese)

Yoshida,N. and Hamada,M. (1990): Damage to Foundation Piles and Deformation Pattern of Ground due to Liquefaction-induced Permanent Ground Deformations, Proc., 3rd Japan-U.S. Workshop on Earthquake Resistant Design of Lifeline Facilities and Countermeasures for Soil Liquefaction, San Francisco, CA

Yoshida,N. (1990): LIQLARD: A Computer Code for Large Ground Displacement due to Soil Liquefaction, Association for the Development of Earthquake Prediction (in Japanese)

Yoshida,N. (1991): State of Arts of Liquefaction Analysis, Symposium on the Problems of Earthquake Motion and Ground in Water-front Area, AIJ, pp.37-44 (in Japanese)

Yoshida,N. and Tsujino,S. (1993a): A simplified Practical Stress-strain Model for the Multi-dimensional Analysis under Repearted Loading, Proc., The 28th Japan National Conference of Soil Mechanics and Foundation Engineering, pp.1221-1224 (in Japanese)

Yoshida,N., Tsujino,S., Nakajima,T. and Yano,Y. (1993b): A Simplified Practical Model for the Use of Multi-Dimensional Analysis, Part 2, Consideration of Dilatancy, Proc., 48th Annual Conf. of the Japan Society of Civil Engineering, Vol.3, pp.1218-1219

Yoshida,N., Tsujino,S. and Inadomaru,K. (1994): Fundamental Study on the Resudual Settlement of Ground after Liquefaction, Proc.,49th Annual Conf. of the Japan Society of Civil Engineering, Vol.3, pp.

Yoshida,N. and Finn,W.D.L. (1994) : Joint Element for Liquefaction and Consolidation Analysis (in preparation)

POSTLIQUEFACTION DEFORMATION OF COHESIONLESS SOIL

Ashraf K. Hussein and Harry E. Stewart

Graduate Research Assistant and Associate Professor
School of Civil and Environmental Engineering
Cornell University

ABSTRACT

Ground settlements due to reconsolidation of liquefied soils can cause substantial damage to both above ground structures and those buried within the ground. Current methods for predicting the magnitude of settlement rely upon either empirical data collected from a limited number of field sites, or from correlations developed from specialized laboratory tests. Some direct field measurements show that actual settlements can differ significantly from those estimated using the available techniques. Therefore, an understanding of the factors influencing these ground movements is critical for quantifying the magnitude of ground deformations. Constant volume strain-controlled direct simple shear tests at relative densities of approximately 38 and 80% were performed on specimens of Nevada sand. Following liquefaction, an additional 10 to 20 cycles were applied, with shear strains ranging from 0.5 to 15%. The specimens then were allowed to reconsolidate and the volume changes were measured.

Test results indicated that the reconsolidation volumetric strains depended on relative density and initial effective stress. The reconsolidation volume changes were slightly dependent on the shear strain level, up to a shear strain of about 4%, and independent of number of postliquefaction loading cycles. Additional tests were performed in a torsional shear system to confirm the results of the direct simple shear tests. Comparisons of these results with data from other researchers, where reconsolidation strains were found to be related uniquely to the cyclic strains, are discussed in light of design curves used to estimate the magnitude of anticipated ground settlements.

INTRODUCTION

Cyclic ground motion during earthquakes is known to cause volumetric reduction in cohesionless soils, resulting in permanent ground settlement which can cause substantial damage to both above ground structures and those buried within the ground. There are two general mechanisms by which settlements can occur. First, dry cohesionless soils may undergo compaction as a result of repeated shear straining. Mechanisms contributing to settlements of dry soils have been explored and identified by several researchers (Silver and Seed, 1971; Youd, 1972), and analysis methods have been developed to predict settlements in dry soils (Seed and Silver, 1972; Pyke, et al. 1975).

The second general method by which ground settlements develop is related to reconsolidation of saturated deposits as excess pore water pressures generated during undrained cyclic loading are dissipated. Although there are several similarities in the general behavioral aspects of dry and saturated soil settlements, the latter may involve more complex relationships. Simplified and insightful methods for evaluating the anticipated reconsolidation settlements have been proposed, and are very useful for preliminary settlement evaluations. Lee and Albaisa (1974) have proposed methods based on laboratory test results for calculating reconsolidation settlements for situations where the excess pore pressures are less than or just equal to those causing liquefaction. Tokimatsu and Seed (1987) and Ishihara and Yoshimine (1992) have developed more generalized predictive methods that include consideration of not only excess pore pressure dissipation, but also the magnitude of the cyclic shear strain imposed during ground shaking. The importance of including the magnitude of the cyclic shear strains has been demonstrated based on the results of specialized laboratory tests (Ishihara and Yoshimine, 1992; Nagase and Ishihara, 1988; Tatsouka, et al. 1984).

This paper presents the results of a laboratory test program wherein test specimens were liquefied under undrained strain-controlled cyclic loading, subjected to several cycles of straining after initial liquefaction, then allowed to reconsolidate. Constant volume strain-controlled direct simple shear (DSS) tests were performed on a Nevada sand at relative densities, D_r, of approximately 38 and 80%. Following liquefaction, an additional 10 to 20 cycles were applied, with shear strains, γ, ranging from 1 to 15%. The specimens then were allowed to reconsolidate and the volume changes measured. Additional tests were performed in a torsional shear (TS) system for comparison with the results of the direct simple shear tests. Specimen preparation and test procedures are explained, along with test results. Comparisons of these results with data from other researchers, where reconsolidation strains were found to be related uniquely to the cyclic strains, are discussed in light of design curves used to estimate the magnitude of anticipated ground settlements.

TEST PROCEDURES

The tests material in this program was a Nevada sand. The grain size distribution curve for Nevada sand is shown in Figure 1. The sand has a specific gravity of 2.68, and the maximum and minimum void ratios were 0.516 and 0.894, respectively (Arulmoli, et al. (1991). The NGI direct

simple shear device with wire-reinforced rubber membranes was used in this study to perform constant volume cyclic strain-controlled tests. Sand specimens with a diameter of 66.8 mm and a height of approximately 20 mm were prepared using a dry-tamping method. Specimens were prepared in two layers at relative densities slightly lower than the target densities of approximately 38 and 80% to allow for initial consolidation effects. Although constant volume tests often are done using dry specimens, deaired water was circulated through the specimens under gravity head to minimize concerns about potential water lubrication effects. Each specimen was consolidated to an effective vertical stress of $\overline{\sigma}_{vi}$ = 54 kPa or 204 kPa, and the relative density was determined. Then, a constant volume strain-controlled test was conducted using a sinusoidal cyclic strain at frequency of 0.01 Hz until an initial liquefaction condition occurred. The strain amplitudes leading to initial liquefaction were varied over a wide range, up to strain levels wherein liquefaction developed in less than one cycle. Constant volume was achieved using a carefully controlled feedback mechanism throughout testing. After these loadings, the specimen was reconsolidated to the initial effective vertical stress prior to shear, $\overline{\sigma}_{vi}$, and the vertical strain was measured using a linear variable differential transformer. Since tests were conducted using the stiff wire-reinforced membranes, the volumetric reconsolidation strain, ε_v ,was equal to the vertical strain.

A series of cyclic undrained strain-controlled tests were conducted using the hybrid resonant column/torsional shear device described by Stewart and Hussein (1992). Solid cylindrical specimens with a height of 193 mm and a diameter of 71 mm were prepared in a split mold using the undercompaction technique developed by Ladd (1978). Specimens were consolidated isotropically at an effective confining pressure of $\overline{\sigma}_{ci}$ = 150 kPa. This isotropic consolidation pressure was selected so that the mean effective stress level in the torsional shear tests would be roughly equivalent to that in the DSS tests at $\overline{\sigma}_{vi}$ = 204 kPa. After consolidation, undrained strain-controlled cyclic torsional shear tests were performed at shear strain levels ranging from γ_{cy} = 0.1% to 8% until initial liquefaction occurred. Then, the specimens were reconsolidated to the initial effective confining pressure of 150 kPa. The reconsolidation volumetric strain was calculated based on the outflow of pore water and the specimen volume prior to cyclic shear.

TEST RESULTS

The first series of tests was conducted in the DSS device to investigate the effects of cyclic shear strain amplitude, γ_{cy}, relative density, D_r, and initial effective vertical stress, $\overline{\sigma}_{vi}$, on the volumetric strain, ε_v, due to reconsolidation after liquefaction, but without any postliquefaction cyclic straining. After initial liquefaction occurred, specimens were reconsolidated to the initial vertical stress prior to shear of $\overline{\sigma}_{vi}$ = 54 kPa or 204 kPa. The average relative densities of the specimens after consolidation were roughly 38 and 80%. The cyclic shear strain amplitude was constant for each test, and ranged from 0.1 to 15%. For shear strain levels greater than about 1%, the specimens sustained less than one complete cycle prior to failure.

Figures 2 and 3 illustrate typical results from this series of tests. Figure 2 shows pore pressure ratio, $\Delta u/\overline{\sigma}_{vi}$, versus number of loading cycles, N, at various cyclic shear strain levels, for D_r =

38% and $\overline{\sigma}_{vi}$ = 204 kPa. It is clear that the rate at which pore water pressure increases is higher for higher cyclic shear strain levels. The typical effect of relative density on pore water pressure accumulation is shown in Figure 3, wherein the pore water pressure buildup decreases as relative density increases. Figure 3 also indicates that for a given relative density and cyclic shear strain level, pore pressure ratio after a specific number of cycles decreases as initial effective vertical stress increases, although the differences are relatively minor. A similar effect was reported by Dobry, et al. (1982).

Figure 4 shows the effect of relative density and vertical stress on the number of cycles required to cause initial liquefaction, N_L. The symbols represent the averages from all tests. The figure indicates that N_L decreases as cyclic shear strain level increases, and that N_L increases for higher relative densities. Also, there is a slight trend for N_L to increase for higher initial effective vertical stresses at the same relative density.

The first series of tests involved no postliquefaction straining. Thus, volumetric reconsolidation strains measured in these tests should establish a baseline from which the effects of additional straining can be determined. Figure 5 shows the reconsolidation volumetric strains versus the cyclic shear strains for tests conducted at average relative densities of 38 and 80%, and $\overline{\sigma}_{vi}$ = 204 kPa. It can be seen from Figure 5 that at a given relative density, the reconsolidation volumetric strain slightly increases as cyclic shear strain increases up to a shear strain of roughly 4%. However, if γ_{cy} is greater than 4%, the volumetric strain tends to remain constant, independent of the level of cyclic shear strain. Also, it is clear in Figure 5 that the reconsolidation volumetric strain depends on the relative density, with volumetric strain increasing as relative density decreases. Figure 6 shows the effect of initial vertical stress on the reconsolidation volumetric strains. Previous studies generally have indicated that vertical stress does not have a major effect on the magnitude of reconsolidation strains. Yet, there is a clear difference between the tests conducted at $\overline{\sigma}_{vi}$ = 54 kPa and 204 kPa. It can be seen in Figure 6 that the reconsolidation volumetric strain increases by approximately one-third as initial effective vertical stress increased from 54 kPa to 204 kPa. Lee and Albaisa (1974) reported results of cyclic triaxial tests in which the volumetric reconsolidation strains were independent of initial effective confinement, $\overline{\sigma}_{ci}$, for pore pressure ratios, $\Delta u/\overline{\sigma}_{ci}$, less than about 0.6. For higher pore pressure ratios, the volumetric strains increased with increasing confinement, but were small, on the order of 0.8, 1.1, and 1.3% for effective confinements of 103, 207, and 414 kPa, respectively.

The effect of postliquefaction cycling on the volumetric strain due to reconsolidation was studied by bringing specimens to liquefaction at relatively small cyclic strains, $\gamma_{cy\text{-}pre}$, followed immediately by several cycles of large postliquefaction strains, $\gamma_{cy\text{-}post}$. Constant volume strain-controlled tests were performed at D_r = 38%, $\overline{\sigma}_{vi}$ = 204 kPa and preliquefaction cyclic shear strain levels of $\gamma_{cy\text{-}pre}$ = 0.1 and 0.5%, as described before. After liquefaction, the specimens were cycled at constant postliquefaction cyclic shear strain amplitudes ranging from $\gamma_{cy\text{-}post}$ = 0.1 to 15%. The number of postliqeufaction cycles was kept constant at either N_{post} = 10 or 20.

The reconsolidation volumetric strains for specimens cycled up to liquefaction at $\gamma_{cy\text{-}pre}$ = 0.1 and 0.5% with N_{post} = 10 are shown in Figure 7 as a function of the postliquefaction cyclic shear strains, $\gamma_{cy\text{-}post}$. It is clear that the volumetric strain does not depend on $\gamma_{cy\text{-}pre}$, when the

postliquefaction strains are larger than those causing liquefaction. The volumetric strains increase as $\gamma_{cy\text{-}post}$ increases up to about 4%. However, the volumetric strain remains constant as $\gamma_{cy\text{-}post}$ increases beyond 4%. The results of the tests cycled following liquefaction with N_{post} = 10 and 20 are presented in Figure 8. The figure reveals that the number of postliquefaction cycles does not influence the reconsolidation volumetric strains.

A comparison of the results of specimens reconsolidated immediately following liquefaction with the results of specimens reconsolidated after substantial postliquefaction cycling is shown in Figure 9. All the specimens had an average relative density of about 38% and were consolidated at $\overline{\sigma}_{vi}$ = 204 kPa. The figure indicates that the results of the two types of tests are the same. Both sets of data indicate a slight increase in volumetric reconsolidation strains up to a shear strain of about 4%, after which there are no marked changes. Consequently, it can be concluded that the reconsolidation volumetric strain depends on the maximum cyclic shear strain experienced by the sand during the undrained cyclic loading, as long as liquefaction occurs.

As a follow up to the DSS testing at constant preliquefaction shear strain, a series of constant volume strain-controlled tests were carried out to study the effect of the wave form on the reconsolidation volumetric strain. After consolidation to $\overline{\sigma}_{vi}$ = 204 kPa, specimens were cycled at constant shear strain level of 0.3% for five cycles. Then, specimens were cycled at a higher shear strain level ranging from 0.5 to 15% until initial liquefaction occurred. No postliquefaction cycles were applied. Volumetric strains due to reconsolidation after initial liquefaction were calculated and the results are presented in Figure 10, along with the results of tests in which a constant cyclic shear strain was applied until liquefaction occurred. The figure indicates that the volumetric strain in not affected by the wave form and depends on the maximum cyclic shear strain the sand experienced during undrained cycling.

Additional tests were conducted using the torsional shear (TS) device to confirm the trends found in the DSS tests. Specimens were consolidated isotropically to a confining pressure of $\overline{\sigma}_{ci}$ = 150 kPa and D_r = 38%. After initial consolidation, undrained cyclic strain-controlled tests were carried out at cyclic shear strain amplitudes ranging from 0.1 to 15%. No postliquefaction cycles were applied in these tests. Figure 11 compares the torsional shear and direct simple shear test results. The torsional shear results again indicate that the reconsolidation volumetric strain increases as cyclic shear strain increases up to 4%. Beyond γ_{cy} = 4%, the volumetric strain remains constant, as concluded previously from the direct simple shear results.

COMPARISONS AND DISCUSSION

Several findings from the test results require discussion, in particular with respect to differences between trends presented elsewhere. The DSS test results indicated that the volumetric reconsolidation strains were dependent on the level of initial vertical stress, as reported by Lee and Albaisa (1974). Nagase and Ishihara (1988) studied the liquefaction characteristics of Fuji River sand in a torsional shear apparatus. The program involved irregular, stress-controlled, multidirectional shearing of saturated specimens. In that program, acceleration records from six earth-

quakes were converted to shear stress histories, and applied to the test specimens. The shear stress histories were scaled to cause varying levels of pore pressure ratio, $\Delta u/\bar{\sigma}_{ci}$, at the end of cycling. For tests in which the pore pressure ratios were less than one, the reconsolidation volumetric strains increased nearly linearly with increasing pore pressure ratios, and decreased with increasing relative density. These trends are consistent with those reported by others, and consistent with anticipated behavior. However, in the tests in which liquefaction ($\Delta u/\bar{\sigma}_{ci} = 1$) occurred, the measured volumetric strains were not defined uniquely as a function of pore pressure ratio. Nagase and Ishihara (1988) determined that the maximum shear strain, γ_{max}, that occurred at any point in the applied stress record could be used to determine the volumetric reconsolidation strain. This finding is significant, as it implies that reconsolidation strains are dependent on how the pore pressures are generated. In addition, they concluded that when the applied shear stress records were adjusted so that the irregular loading was just large enough to cause liquefaction, the maximum shear strain generated, γ_{max}, in all specimens was approximately 2.5 to 3.5% for relative densities in the range of approximately 50 to 90%. For specimens that did not liquefy prior to the complete application of the irregular loading, the maximum shear strains were less than that limit. Further analysis of the reconsolidation strains for all pore pressure ratios were found to be related directly to the maximum shear strain that occurred at any point in the tests. Ishihara and Yoshimine (1992) developed relationships between reconsolidation strains and maximum shear strains that were based on several important considerations. First, for situations in which liquefaction did not occur, volumetric strains could be related either to pore pressure ratio or cyclic strain. Secondly, liquefaction did not occur unless the cyclic shear strains during a test were at least equal to a threshold value of about 3%. Finally, volumetric strains at any relative density increased nearly linearly with maximum cyclic shear strain up to a second shear strain limit of about 8%, after which the volumetric strains remained constant.

Lee and Seed (1967) identify several ways in which failure in laboratory tests can be defined. One definition is when the zero effective stress condition develops, i.e., $\Delta u/\bar{\sigma}_{ci} = 1$. Another definition is based on a performance criterion in which strains reach some limiting value. A key difficulty with any definition based on a performance criterion such as a defined strain, is that there are many different strain levels that can be considered. Lee and Seed (1967) clearly showed that the strains at initial liquefaction decrease with increasing relative density, and that the onset of liquefaction in stress-controlled triaxial tests on loose sand specimens ($D_r = 38\%$) was accompanied by an immediate increase in the cyclic axial strains, ε_a, to approximately 10%. These trends in strain generation also were exhibited in stress-controlled cyclic simple shear tests (Peacock and Seed, 1968), wherein large strains ($\gamma \approx 15\%$) developed immediately following liquefaction in loose sands ($D_r = 50\%$). Furthermore, Lee and Albaisa (1974) presented test results from a loose sand ($D_r = 40\%$) that showed axial strains on the order of 10 to 14% when pore pressure ratios first become one, corresponding to a shear strain of $\gamma = 1.5\ \varepsilon_a = 15$ to 21%. Thus, establishment of a unique strain at failure in stress-controlled tests is difficult. There are, however, reasonable limits on the amount of strain that can be generated *in situ* during earthquakes, which are dependent on relative density, with maximum shear strains of about 35% at $D_r \approx 50\%$, and perhaps 5% for $D_r \approx$ 90% (Seed, 1979). Such behavior is referred to as cyclic mobility with limited strain potential. Thus, the findings by Nagase and Ishihara (1988) identifying a unique level of shear strain, independent of relative density, with the condition of liquefaction represents a fundamentally new development in understanding stress-controlled testing.

Nagase and Ishihara (1988) and Ishihara and Yoshimine (1992) have shown that reconsolidation volumetric strains are related uniquely to the maximum shear strain developed in the stress-controlled tests, up to strains of about 8%. Tatsuoka, et al. (1984) also investigated the effects of cyclic strain on reconsolidation volumetric strains. Those test results indicated increasing volumetric strains with increasing shear strains, but insufficient data were collected at cyclic shear strains greater than about 5%. Thus, a clear conclusion about a threshold strain limit cannot be drawn from that work, although there is some indication that the strain limit may be near 5%. Finn, et al. (1970) investigated the effects of strain history on the reliquefaction susceptibility of sand. Those tests included a series of strain-limited cyclic simple shear tests in which specimens were brought to liquefaction, and subjected to 15 cycles of shear strain prior to dissipation of the excess pore pressures. The specimens were then allowed to reconsolidate, and were tested again to determine any changes in cyclic strength that occurred as a result of the postliquefaction straining. The postliquefaction shear strains in tests performed by Finn, et al. ranged from $\gamma = 0.5$ to 11%. Thus, these tests are similar to those performed on the Nevada sand in this study. The tests conducted by Finn, et al. indicated that volumetric reconsolidation strains increased with the level of postliquefaction shear strain, for strains up to about $\gamma = 3\%$. However, for higher shear strains the volumetric strains remained nearly constant. The conclusion was drawn that above $\gamma = 3\%$, no further structural rearrangement of the soil skeleton occurs. This implies that cyclic strains following liquefaction in excess of $\gamma = 3\%$ may not lead to additional reconsolidation strain. This finding generally is consistent with the test results for the Nevada sand, although the Nevada sand showed a threshold strain of 4%.

Figure 12 presents reconsolidation volumetric strains measured by several groups, the design curves recommended by Ihsihara and Yoshimine (1992), and the results from the Nevada sand tested at $\bar{\sigma}_{vi} = 204$ kPa. The design curves prepared by Ishihara and Yoshimine (1992) are based on many data generated by Nagase and Ishihara (1988), which are not shown on the figure. Figure 12 indicates a wide range in volumetric strains, and a general increase in volumetric strain for decreasing relative densities. However, the cyclic strain after which the volumetric strains tend to remain constant appears to be on the order of 3 to 5%. The results presented in Figure 12 show fundamental differences in interpreting stress-controlled and strain-controlled tests. Liquefaction can be induced in strain-controlled tests at low strain levels in only a few cycles. However, stress-controlled tests often define liquefaction failure as occurring at much higher strain levels (greater than 3%.).

The methods used most frequently in recent years for prediction liquefaction-induced settlements generally rely upon estimates of shear stress ratios generated by an earthquake and those causing liquefaction, as dependent on some index such as relative density or penetration resistance. (Tokimatsu and Seed, 1987; Ishihara and Yoshimine, 1992). Comparisons between measured and predicted settlements are in reasonable agreement, but are sensitive to the shear strain levels for very loose soil conditions.

Figure 13 presents a simple interpretation of the volumetric strains anticipated following liquefaction. The solid line in the figure represents the relationship given by the Tokimatsu and Seed (1987) design curves for volumetric strain for conditions in which liquefaction has occurred. The data shown on the figure are those from Japanese field observations from the 1968 Tokachioki

earthquake (Ohsaki, 1970), the 1964 Niigata earthquake (Building Research Institute, 1965), and the 1968 Miyagiken Oki earthquake (Tohno and Yasuda, 1981), as used by Tokimatsu and Seed to construct their design curves. Also shown on the figure are the results form this study on Nevada sand. The data from these tests on Nevada sand agree reasonably well with the others. As with the predictive method given by Tokimatsu and Seed (1987) and Ishihara and Yoshimine (1992), Figure 12 indicates that volumetric strains for site conditions having $(N_1)_{60}$ greater than about 30 are limited to about 1%. For sites where the soil is extremely loose, observed settlements may have been affected by other aspects of extensive liquefaction that make reliable measurements of actual ground settlements and back-calculated volumetric strains difficult. For many natural deposits, normal limits on relative densities often have a lower limit of 30 to 40%, with an upper limit on the order of 80%. Thus, it may be that typical maximum volumetric strains are limited to about 4%.

ACKNOWLEDGMENTS

The authors wish to thank the National Center for Earthquake Engineering Research (NCEER) which provided support under Grant No. 93-2301(S). The work of Ali Avcisoy in helping to prepare the figures is appreciated greatly.

REFERENCES

Arulmoli, K., K.K. Muraleetharan, M.M. Hossain, and L.S. Fruth (1991) " VELACS Verification of Liquefaction Analyses by Centrifuge Studies Laboratory Testing Program Preliminary Data Report," The Earth Technology Corporation, Sept.

Building Research Institute (1965) "Niigata Earthquake and Damage to Reinforced Concrete Buildings in Niigata City," Report, Building Research Institute, Ministry of Construction, 43.

Dobry, R., R.S. Ladd, F.Y. Yokel, R.M. Chung, and D. Powell (1982) "Prediction of Pore Water Pressure Buildup and Liquefaction of Sands During Earthquakes by the Cyclic Strain Method," Building Science Series 138, National Bureau of Standards, Washington, D.C., July, 168 p.

Finn, W.D.L., P.L. Bransby, and D.J. Pickering (1970) "Effect of Strain History on Liquefaction of Sand," Journal of the Soil Mechanics and Foundations Division, ASCE, Vol. 96, No. SM6, Nov., pp. 1917-1934.

Ishihara, K. and M. Yoshimine (1992) "Evaluation of Settlements in Sand Deposits Following Liquefaction During Earthquakes," Soils and Foundations, JSSMFE, Vol. 32, No. 1, March, pp. 173-188.

Peacock, W.H. and H.B. Seed (1968) " Sand Liquefaction Under Cyclic Loading Simple Shear Conditions," Journal of the Soil Mechanics and Foundations Division, ASCE, Vol. 94, No. SM3, May, pp. 689-708.

Ladd, R.S. (1978) "Preparing Test Specimens Using Undercompaction," Geotechnical Testing Journal, ASTM, Vol. 1, No. 1, Mar., pp. 16-23.

Lee, K.L, and A. Albaisa (1974) "Earthquake Induced Settlements in Saturated Sands," Journal of the Geotechnical Engineering Division, ASCE, Vol. 100, No. GT4, Apr., pp. 387-406.

Nagase, H. and K. Ishihara (1988) "Liquefaction-Induced Compaction and Settlement of Sand During Earthquakes," Soils and Foundations, JSSMFE, Vol. 28, No. 1, March, pp. 65-76.

Ohsaki, Y. (1970) "Effects of Sand Compaction on Liquefaction During Tokachioki Earthquake," Soils and Foundations, JSSMFE, Vol. 10, No.2, pp. 112-128.

Pyke, R., H.B. Seed, and C.K. Chan (1975) "Settlement of Sand Under Multidirectional Shaking," Journal of the Geotechnical Engineering Division, ASCE, Vol. 101, No. GT4, Apr., pp. 379-398.

Seed, H.B. and M.L. Silver (1972) "Settlement of Dry Sands During Earthquakes," Journal of the Soil Mechanics and Foundations Division, ASCE, Vol. 98, No. SM4, Apr., pp. 381-397.

Seed, H.B. (1979) "Soil Liquefaction and Cyclic Mobility Evaluation for Level Ground During Earthquakes," Journal of the Geotechnical Engineering Division, ASCE, Vol. 105, No. GT2, Feb., pp. 201-255.

Silver, M.L. and H.B. Seed (1971) "Volume Changes in Sands During Cyclic Loading," Journal of the Soil Mechanics and Foundations Division, ASCE, Vol. 97, No. SM9, Sept., pp. 1171-1182.

Stewart, H.E. and A.K. Hussein (1992) "Determination of the Dynamic Shear Modulus of Holocene Bay Mud for Site-Response Analysis," The Loma Prieta, California, Earthquake of October 17, 1989 - Marina District, U.S. Geological Survey Professional Paper 1551-F, June, pp. F75-F83.

Tatsuoka, F., T. Sasaki, and S. Yamada (1984) "Settlement in Saturated Sand Induced by Cyclic Undrained Simple Shear," Proceedings, Eighth World Conference on Earthquake Engineering, San Francisco, Vol. III, pp. 95-102.

Tohno, I. and S. Yasuda (1981) "Liquefaction of the Ground During the 1978 Miyagiken-Oki Earthquake," Soils and Foundations, JSSMFE, Vol. 21, No. 2, pp. 18-34.

Tokimatsu, K. and H.B. Seed (1987) "Volume Changes in Sands During Cyclic Loading," Journal of Geotechnical Engineering, ASCE, Vol. 113, No. 8, Aug., pp. 861-878.

Yoshimi, Y., F. Kuwabara, and K. Tokimatsu (1975) "One-Dimensional Volume Change Characteristics of Sands Under Very Low Confining Stresses," Soils and Foundations, JSSMFE, Vol. 15, No. 3, Sept., pp. 51-60.

Youd, T.L. (1972) "Compaction of Sands by Repeated Shear Straining," Journal of the Soil Mechanics and Foundations Division, ASCE, Vol. 98, No. SM7, July, pp. 709-725.

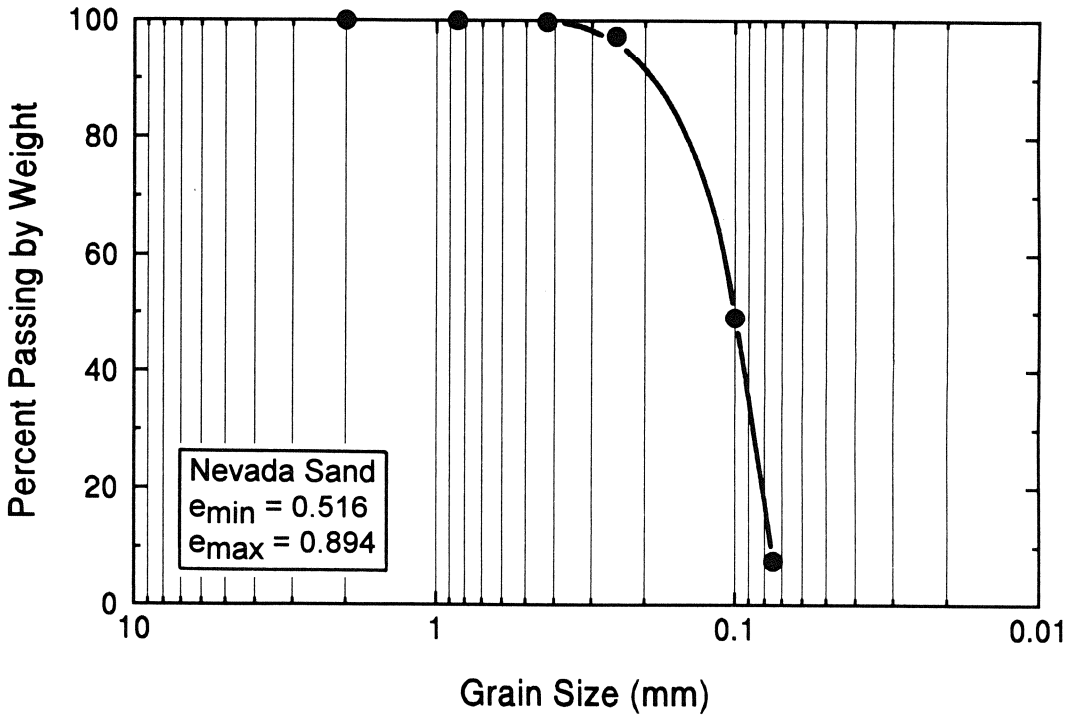

Figure 1. Grain Size Distribution Curve for Nevada Sand

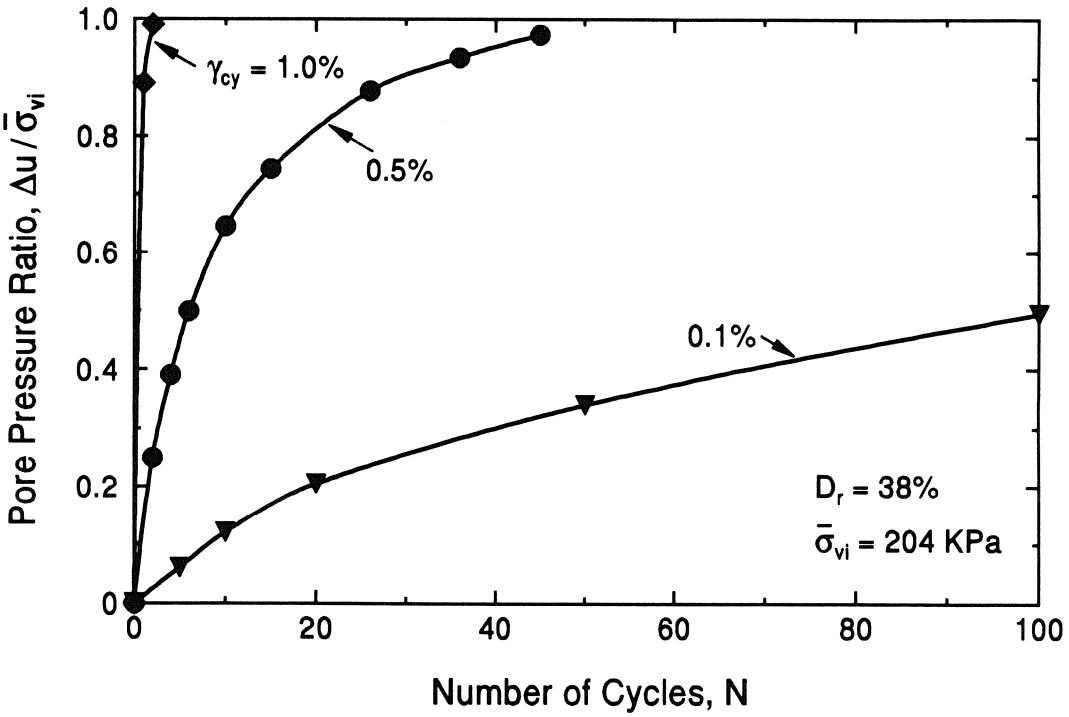

Figure 2. Pore Pressure Ratio versus Number of Cycles at Various Cyclic Shear Strain Levels

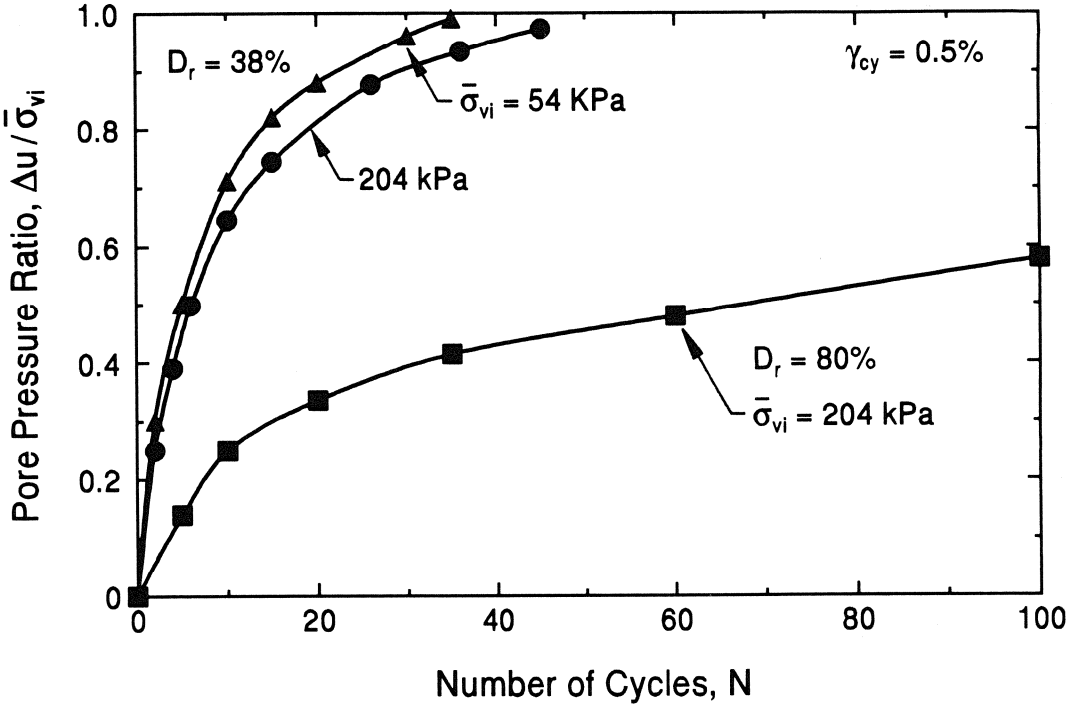

Figure 3. Effect of Relative Density and Initial Effective Stress on Pore Pressure Ratio

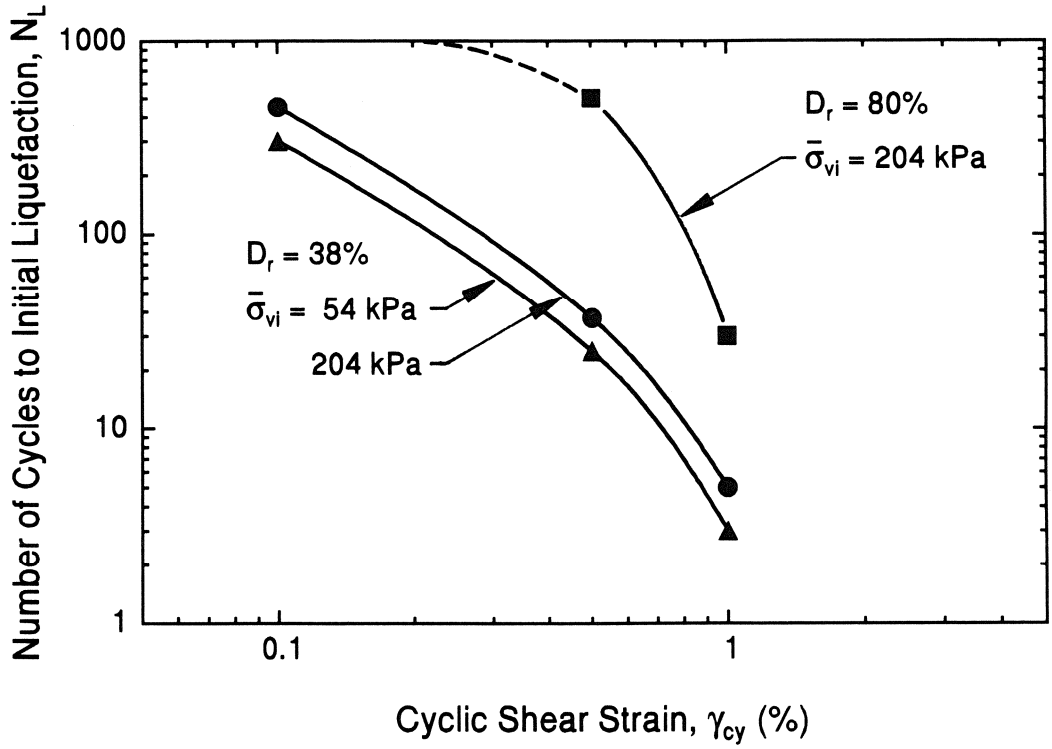

Figure 4. Effect of Relative Density and Initial Effective Stress on Number of Cycles to Liquefaction

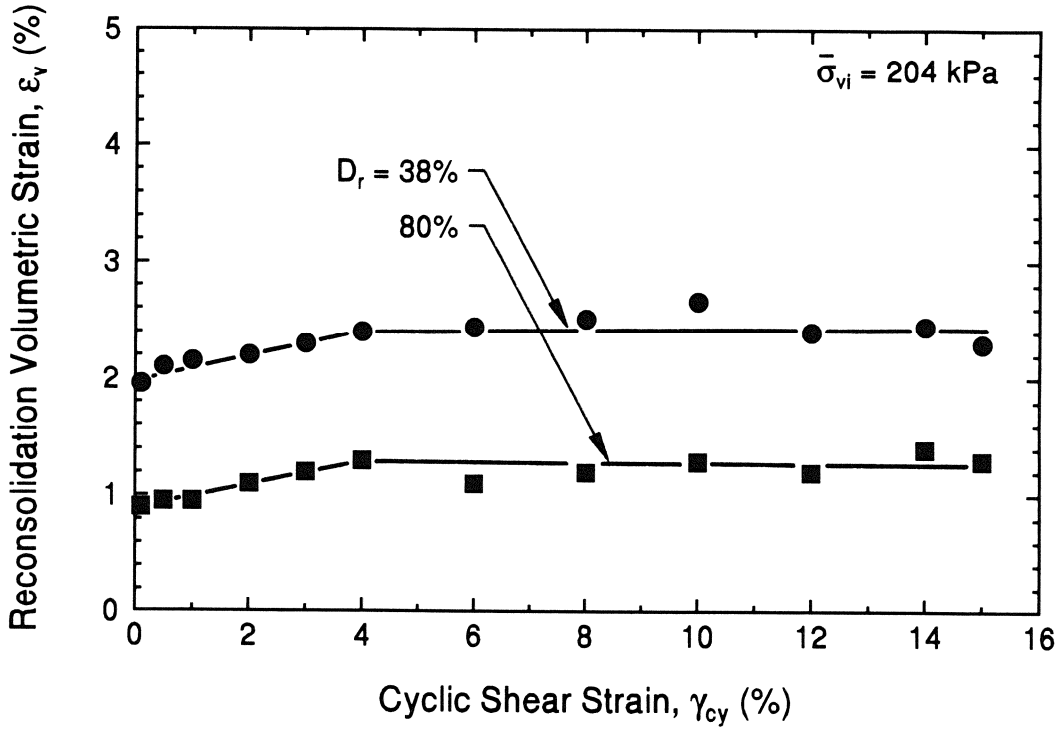

Figure 5. Effect of Relative Density on Reconsolidation Volumetric Strain

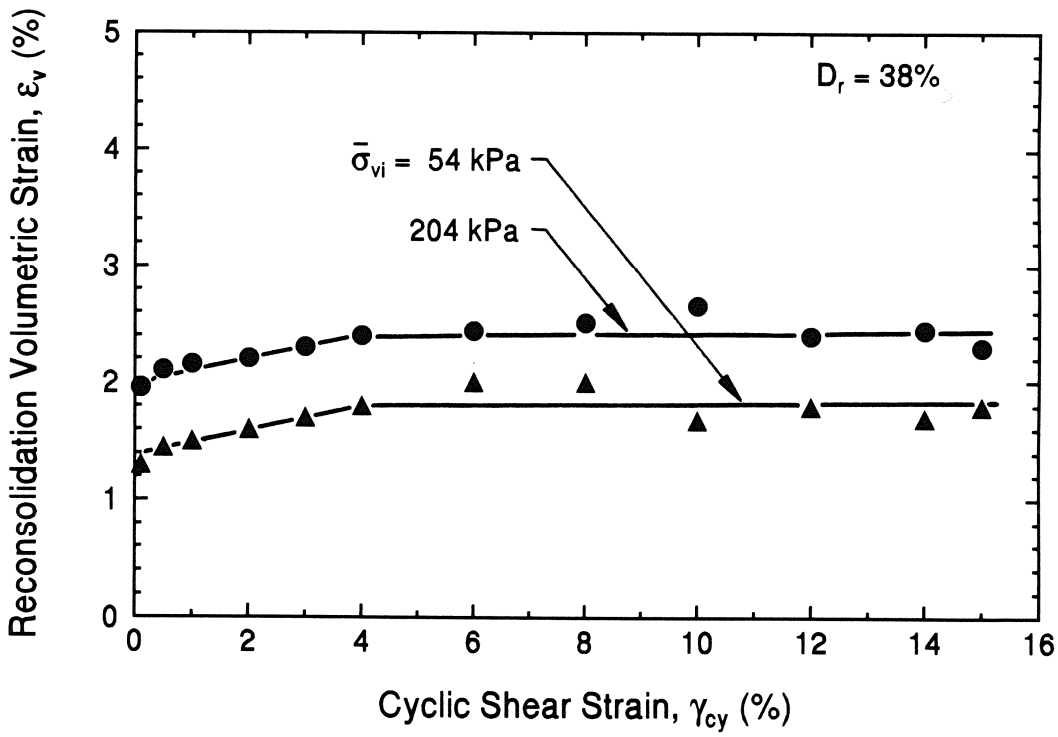

Figure 6. Effect of Initial Effective Stress on Reconsolidation Volumetric Strain

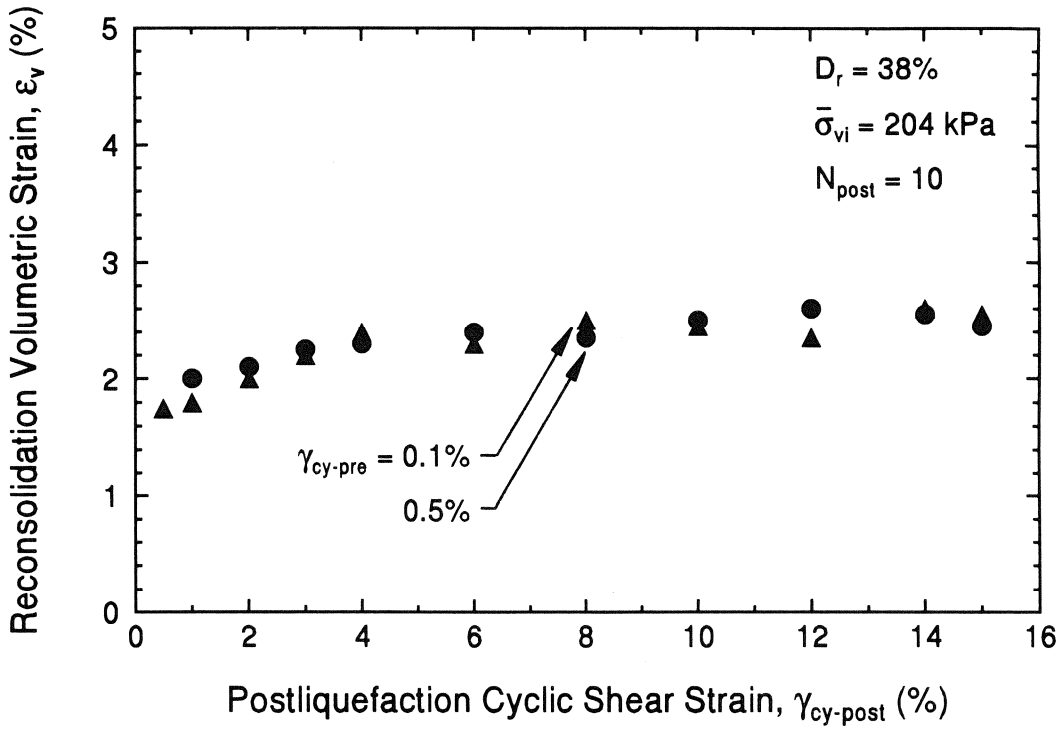

Figure 7. Effect of Postliquefaction Cycling on Reconsolidation Volumetric Strain

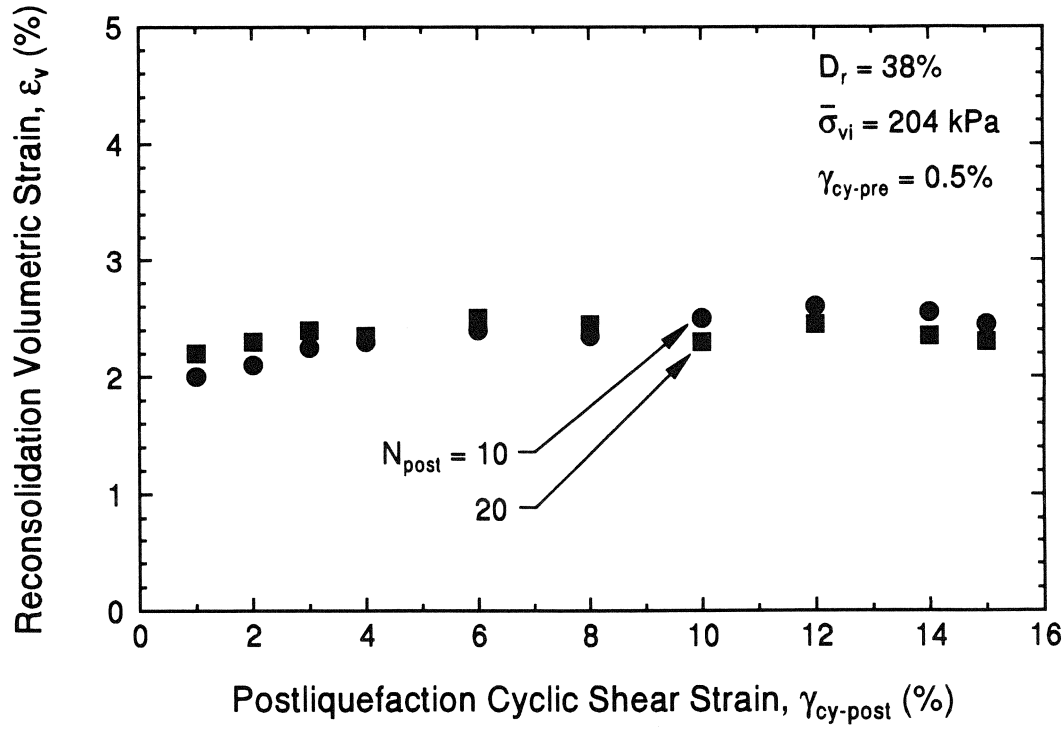

Figure 8. Reconsolidation Volumetric Strains for N_{post} = 10 and 20

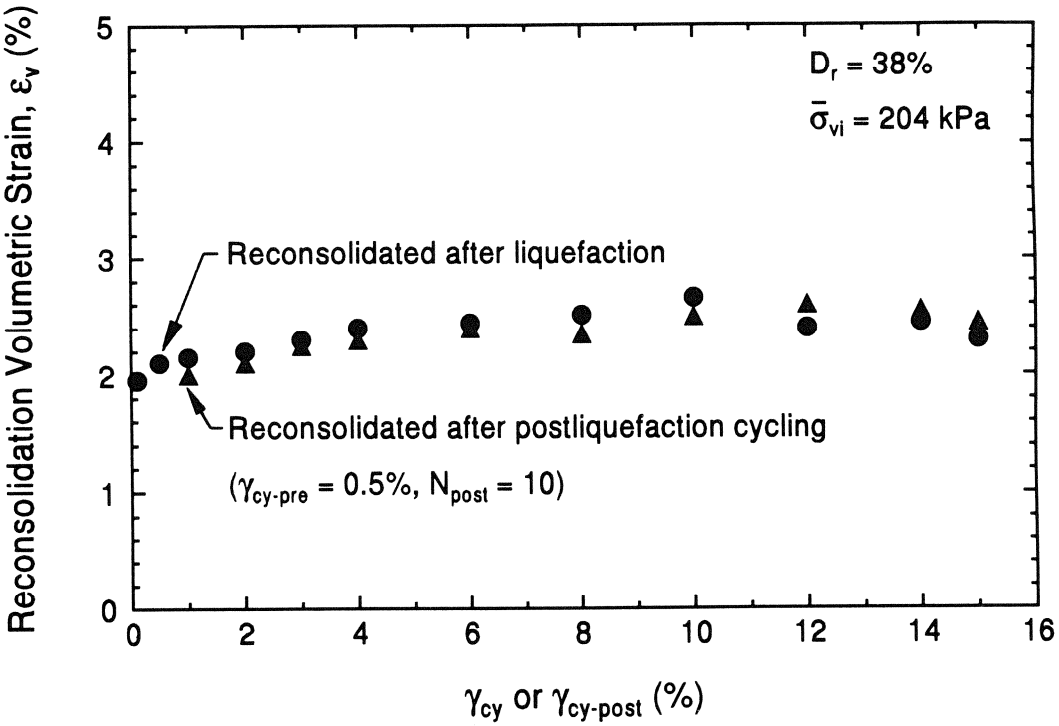

Figure 9. Comparison of Test Results with and without Postliquefaction Cycling

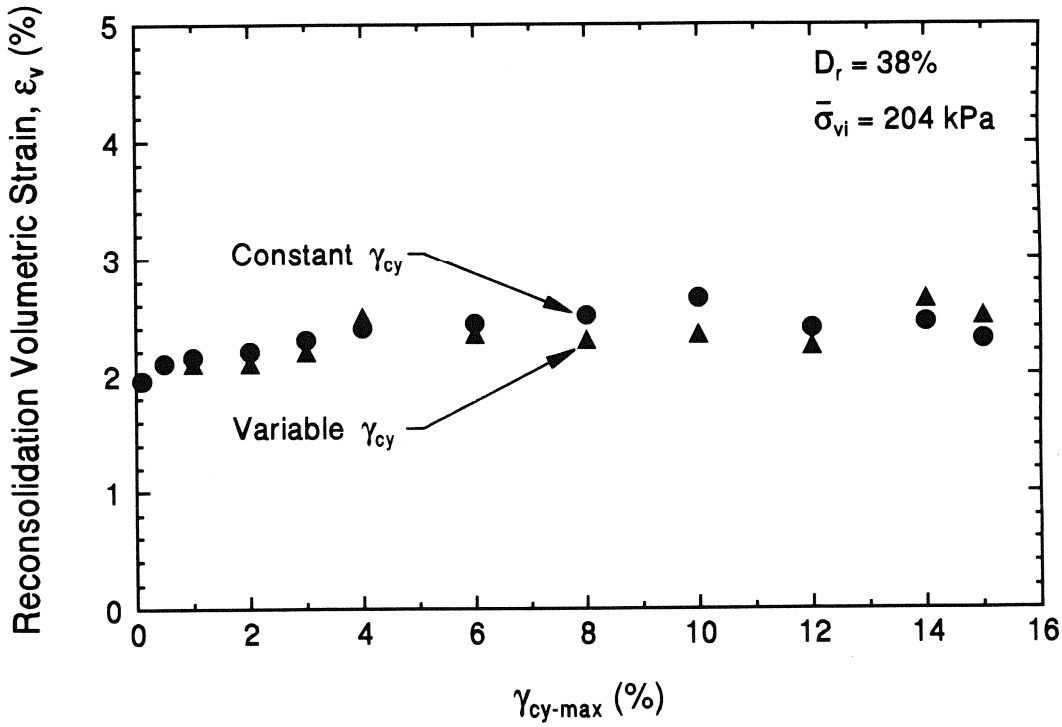

Figure 10. Reconsolidation Volumetric Strains for Different Wave Forms

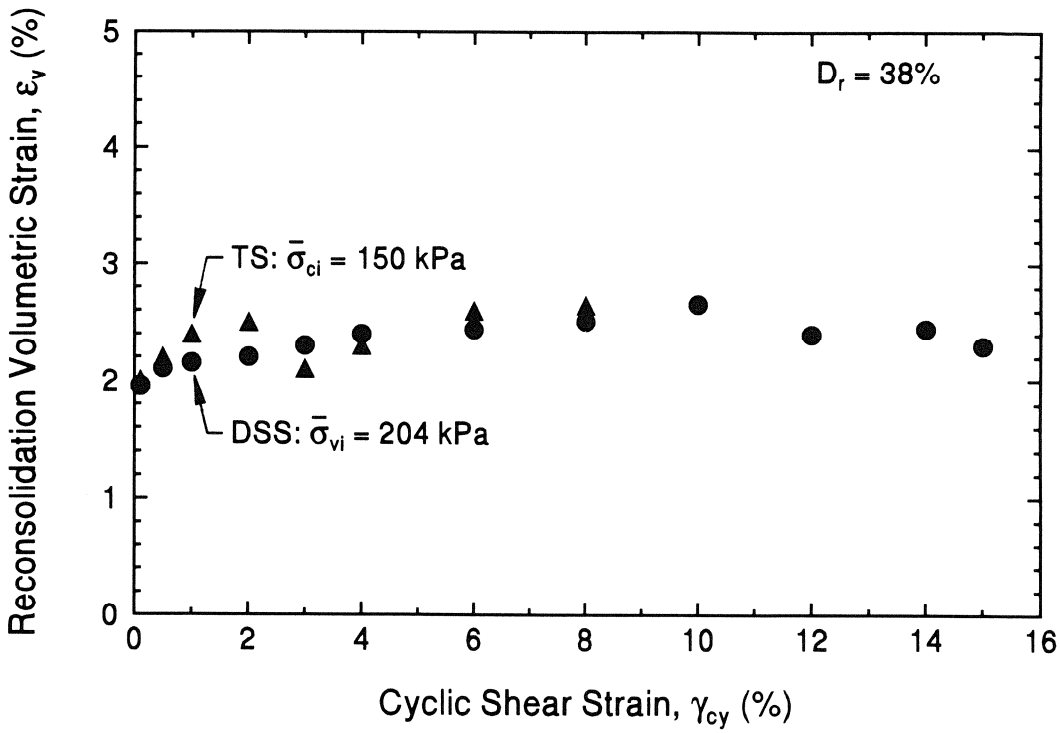

Figure 11. Comparison of Direct Simple Shear and Torsional Shear Tests Results

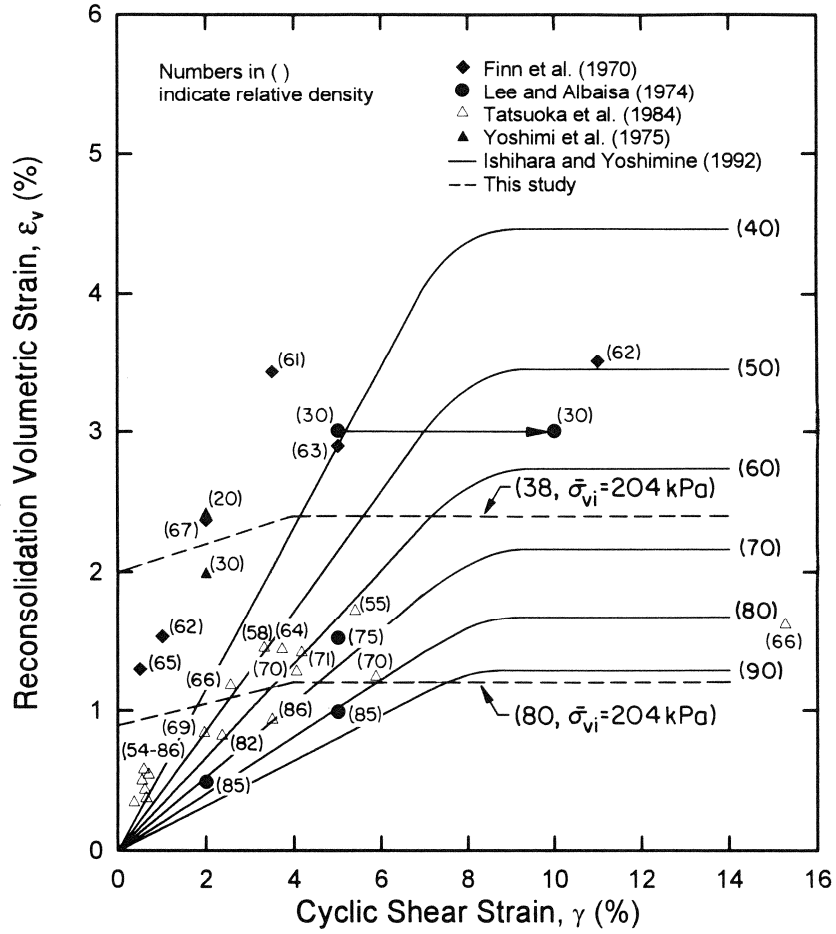

Figure 12. Reconsolidation Volumetric Strains from Various Studies

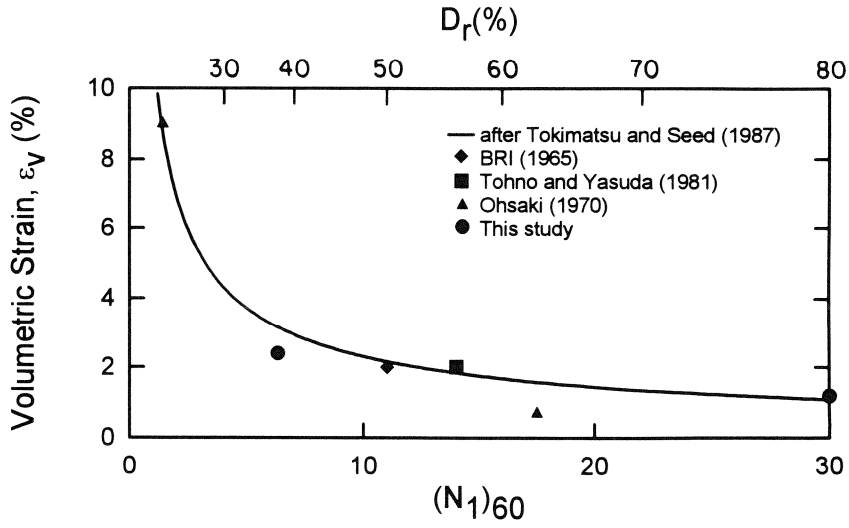

Figure 13. Simplified Curve for Estimating Reconsolidation Volumetric Strain

A CONSIDERATION OF THE MECHANISM FOR LIQUEFACTION-RELATED LARGE GROUND DISPLACEMENT

Masanori Hamada*, Hiroshi Sato** and Tetsutaro Kawakami***

ABSTRACTS

The authors discussed the mechanism of the liquefaction-related large ground displacement by referring the existing researches and an shaking table test result. Firstly, they reviewed the outcomes from case studies on large ground displacement during past earthquakes as well as empirical formulae proposed from regression analyses of the ground displacement with various factors such as gradient of ground surface, and studied fundamental characteristics of the large ground movement. Secondarily, the authors reviewed existing experimental works on ground displacement and on the mechanical properties of liquefied soil during the ground movement.

Furthermore, the authors conducted a shaking table test, where the ground surface was inclined after complete liquefaction of the soil. Based on the the review of the existing researches and on the shaking table test they proposed an idea on the mechanism of the large ground displacement during liquefaction.

* Professor, Dept. of Civil Engineering, Waseda University, Tokyo, Japan.
** Researcher, Institute of Technology, Tokyo Electric Power Company, Tokyo, Japan.
*** Assistant Professor, Dept. of Ocean Civil Engineering, Tokai University, Shimizu, Japan.

INTRODUCTION

Liquefaction-induced large ground displacements were firstly recognized and measured by aerial survey at the time of the 1983 Nihonkai-Chubu earthquake. Since then, case studies on past ten earthquakes have been conducted under a close corporation between U.S. and Japanese researchers. By using the data from the case studies the soil and geological conditions under which the large ground displacements occurred have been studied (Hamada and O'Rourke, 1992a and O'Rourke and Hamada, 1992a).

A number of experimental and numerical researches has been done on the liquefaction-caused large ground displacement and it's effects on the structures. However, the mechanism of the occurrence of the large ground displacement with a magnitude of several meters has not been comprehensively explained, and any adequate knowledge which is applicable for the design and construction of the structures against the large ground displacement has not been provided .

The Liquefaction-induced ground displacement has caused extensive damage to structures, particularly to in-ground structures such as buried pipes and foundation piles. Therefore, it is one of urgent research subjects to investigate the mechanism of the occurrence of the ground displacement as well as to develop effective countermeasures in order to prevent the damage due to the ground displacement.

CASE STUDIES AND PROPOSED EMPIRICAL FORMULAE

Hamada et al. (1986) summarized two types of soil and geological condition where liquefaction induced the large ground displacement as shown in Figure 1 by referring the case studies. First type is that a ground along river or sea largely moves toward the water when quay walls collapses. The mechanism of this type can be easily understood by considering the elevation difference of the ground surface at the collapsed quay walls. Second type is that a slightly inclined ground moves from the higher elevations to the lower one due to liquefaction. It seems difficult to clearly explain the mechanism of the ground displacement of this type with a magnitude of several meters, sometimes above ten meters, which means that the ground strain reaches over 100 %, even when gradient of ground surface is very small, below 1 %.

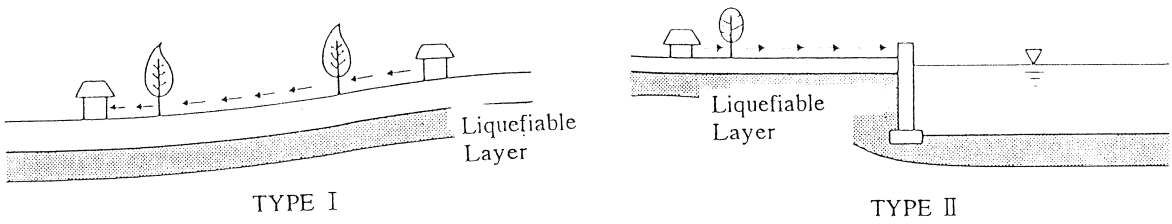

Figure 1. Subsurface Condition for Liquefaction-Induced Ground Displacement

The correlation of the magnitude of the ground displacement with various factors such as gradient of the ground surface and thickness of the liquefiable soil, were studied, and empirical formulae were proposed in order to predict the ground displacement (Hamada et al., 1986, Bartlett et al., 1992).

Hamada et al., conducted a regression analysis by using the data from the 1964 Niigata, the 1971 San Fernando and the 1983 Nihonkai-Chubu earthquakes, and proposed the following empirical formula;

$$D = 0.75 \cdot \sqrt[2]{H} \cdot \sqrt[3]{\theta} \qquad (1)$$

D : Ground displacement in the horizontal direction (m).
H : Thickness of estimated liquefied layer of the ground (m).
θ :Larger value of the gradient of ground surface or that of lower boundary of estimated liquefied layer of the ground (%).

The proposed formula only provides an approximate fit to the field data. The predicted ground displacements by the above formula are actually scattered between half and twice the measured values as shown in Figure 2. In particular, the empirical formula shows the comparatively low correlation between the ground displacement D and the larger value of the gradient of the ground surface or that of lower boundary of liquefied layer θ, since D is proportional to only a cubic root of the gradient.

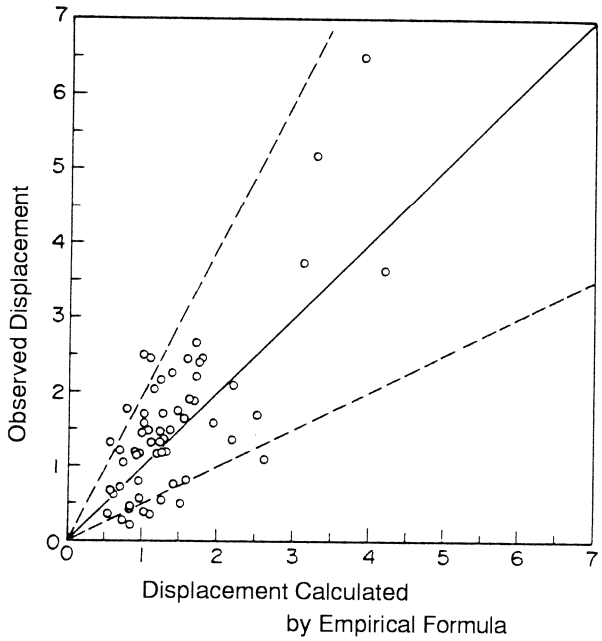

Figure 2. Comparison of Horizontal Ground Displacement Estimated by Regression Formula with Observed One(Hamada et al., 1986)

Figure 3 shows one example of the relationship between the gradient of the ground surface and the magnitude of the ground displacement, which was obtained from the data in Niigata as well as Noshiro, but no significant correlation could not be found. The gradient of the ground surface in the figure was determined as a mean value over a horizontal distance of 5 times of the thickness of the estimated liquefied layer of the ground. The mean gradient over a horizontal distance of 30 times was also calculated, but the correlation was not improved.

If it is assumed that a sloped ground is deformed by the gravity under a condition of large reduction of its shear stiffness due to the liquefaction, the ground displacement should be proportional to the gradient of the ground surface, so that better correlation should have been obtained with the gradient. The lack of the correlation between the ground displacement and the gradient of the ground surface appears to contradict the fact that the ground moved from the higher elevation to the lower one. However, this contradiction can be resolved if it is assumed that the ground displacement was caused by a fluid behavior of the liquefied soil. The gradient of the fluid surface has not any influence on the magnitude of the displacement of the fluid, but does affect its velocity.

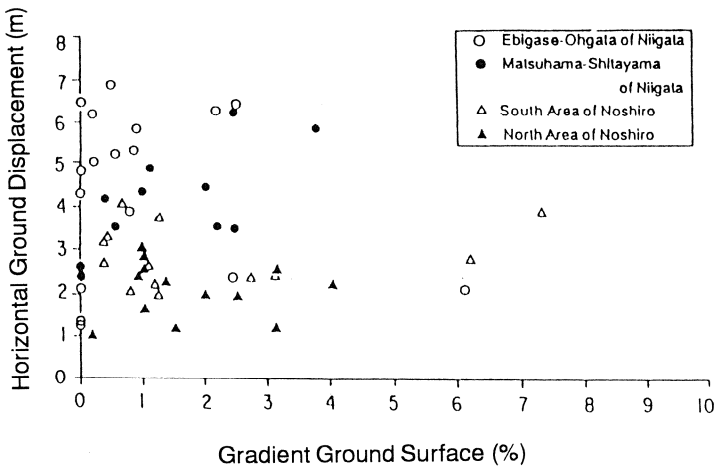

Figure 3. Correlation between Ground Displacement and Gradient of Ground Surface (1964 Niigata and 1983 Nihonkai-Chubu Earthquake)

On the other hand, the magnitude of the ground displacement has a good correlation with the thickness of the liquefied soil in most of case studies. Figure 4 shows the relationship between the ground displacement and the thickness in the case studies on the Niigata and Nihonkai-Chubu earthquakes. This figure clearly demonstrates that the ground displacement increases in proportion to the thickness of the liquefied layer.

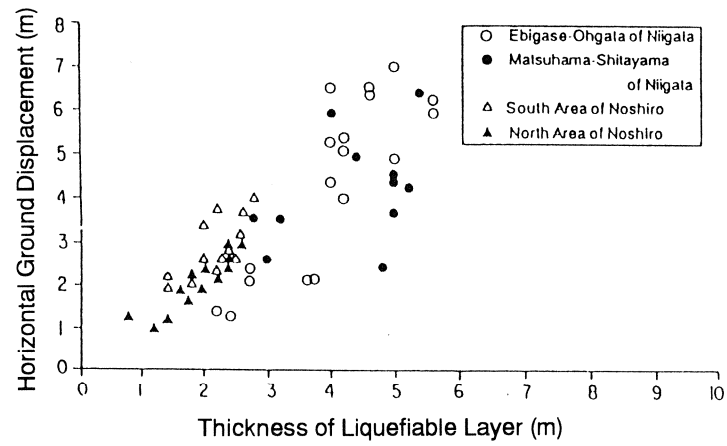

Figure 4. Correlation between Ground Displacement and Thickness of Estimated Liquefied Layer (1964 Niigata and 1983 Nihonkai-Chubu Earthquake)

Bartlett et al. (1992) proposed the following empirical formulae based on a regression analysis of the data from Japanese and U.S. case studies.

$$\text{LOG}\ (D_H + 0.01) = -16.366 + 1.178\ M - 0.927\ \text{LOG}\ R - 0.013\ R + 0.657\ \text{LOG}\ W + 0.3484\ T_{15} + 4.527\ \text{LOG}\ (100 - F_{15}) - 0.922\ D50_{15} \quad (2a)$$

, and

$$\text{LOG}\ (D_H + 0.01) = -15.787 + 1.178\ M - 0.927\ \text{LOG}\ R - 0.013\ R + 0.429\ \text{LOG}\ S + 0.348\ T_{15} - 4.527\ \text{LOG}\ (100 - F_{15}) - 0.922 D50_{15} \quad (2b)$$

D_H : Ground displacement in Horizontal Direction.
M : Earthquake magnitude (moment magnitude).
R : Horizontal distance from the seismic energy source.
W : Ratio of the height(H) of the free face to the distance(L) from a free face.
S : Gradient of ground surface (in percent).
T_{15}: Cumulative thickness of saturated granular layers with corrected blow counts less than 15.
F_{15} : Average fines content of saturated granular layers included in T_{15}.
$D50_{15}$: Average mean grain size in layers included in T_{15}.

Formula (2a) is proposed for the second type of the ground displacement in Figure 1, where a ground along river or sea moves towards the water when the quay walls are collapsed. The formula (2b) is for the first type of the displacement of a slightly sloped ground. However, the predicted ground displacements by these formulae also scattered between half and twice the observed displacement as shown in Figure 5.

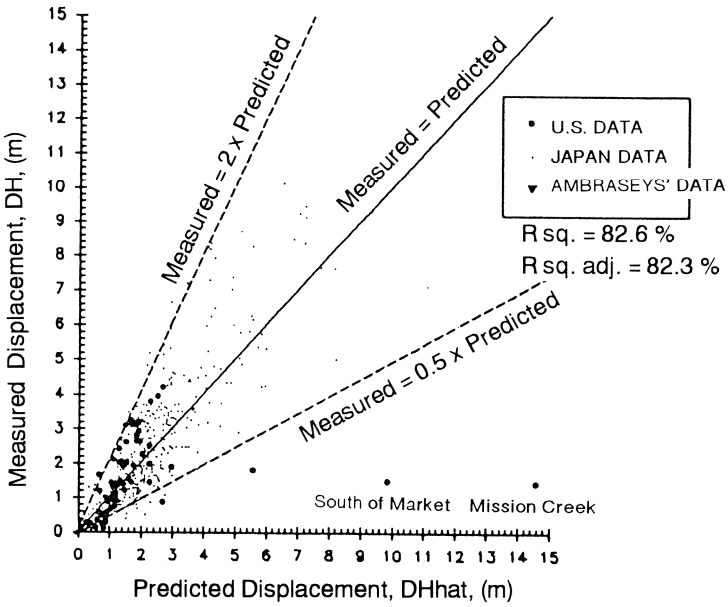

Figure 5. Comparison of Ground Displacement Estimated by Empirical Formula with Observed One (Bartlett et al.)

The correlation between the ground displacement D_H and the gradient of the ground surface S in Formula (2b) is a little higher than that in Formula (1), but is still low because the coefficient of the logarithm of the gradients is only 0.429.

In all cases of the slightly sloped ground the ground displacement was caused to the downward direction. Any case has never been found that ground displacement was caused to the upward direction of the slope. This suggests that the gravity is a key factor of the occurrence of the ground movement. However, the correlation between the magnitude of the ground displacement and the gradient of the ground surface is low. This low correlation should be taken into consideration for the discussion on the mechanism of the occurrence of the large ground displacement.

DISCUSSIONS ON MECHANICAL PROPERTIES OF LIQUEFIED SOIL

There may be two possible ideas about the behaviors of the liquefied soil during the large ground movement. First one is that the liquefied soil behaves as a real liquid and that the large ground displacement is caused as

a flow of the liquefied soil. The second idea is that the liquefied soil still behaves as a solid body with a largely reduced shear stiffness due to liquefaction. According to the second idea, the magnitude of the ground displacement should be proportional to the gradient of the ground surface, because the gravity is governing the deformation of the solid ground as mentioned previously. However, the correlation of the ground displacement with the surface gradient is low in the case studies.

On the other hand, the first idea of the liquid has also a big disadvantage, which is that if the liquefied soil perfectly behaved as a liquid, the ground surface should have been flat after the ground movement. However, according to the case studies the surfaces of the actual grounds still preserved their inclinations.

The third idea where the liquefied soil behaves with a combined characteristics of the fluid and the solid is also possible .

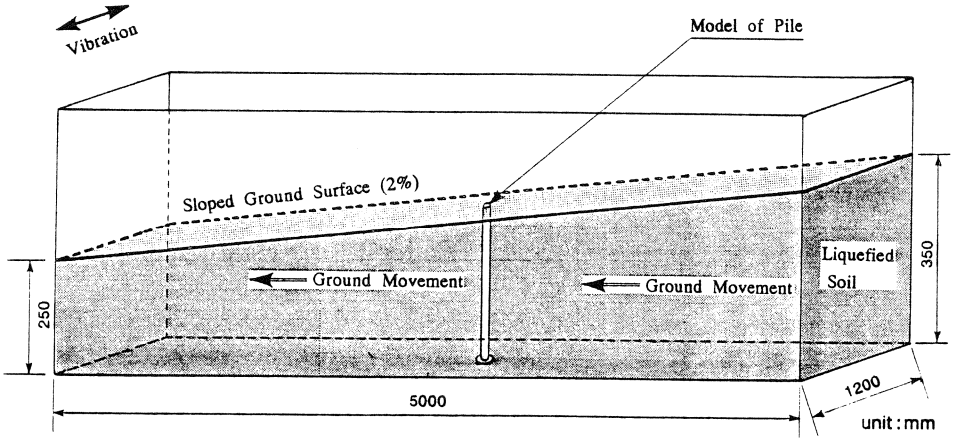

Figure 6. Experiment on Liquefaction-Induced Ground Displacement

As for the fluid properties of the liquefied soil, several experimental works have been conducted. Figure 6 shows an experiment on external force on a foundation pile during ground movement (Hamada et al., 1992b). An acryl model pile with a diameter of 22 mm was installed at the center of a model ground, which is 5 m long, 2 m wide and 0.5 m thick with a surface gradient of 2 %. The liquefaction was induced by shaking the soil box in the direction perpendicular to that of the ground slope, so that the effect of the base excitation on the ground movement could be neglected.

Figure 7 shows time histories of the displacement and the velocity of the ground nearby the model pile and the bending strain of the pile. The good similarity between the time history of the pile strain and that of the ground velocity suggests that the pile was deformed by a fluid force from the laterally moving ground.

From the case studies, some evidences of the liquid behavior of the liquefied ground can be found. Figure 8 shows a movement of a wastewater pipe together with displacement of ground surface measured by aerial survey in Noshiro City after the 1983 Nihonkai-Chubu earthquake. The pipe is asbestos-cement pipe with a diameter of 30 cm. The lateral distance between the straight line connecting two neighboring manholes and the pipe axis was measured. The pipe had been laid in a straight line between two manholes before the earthquake. The measured distance is a relative displacement of the pipe with respect to two manholes.

The maximum movement of the pipe is 160 cm, but the ground displacement at the surface in the lateral direction to the pipe axis is 80 to 110 cm. Here, it should be noted that the movement of the pipe was measured as a relative displacement from the two neighboring manholes. This means that the absolute

displacement of the pipe is more than 160 cm, and the pipe moved much more than the ground surface.

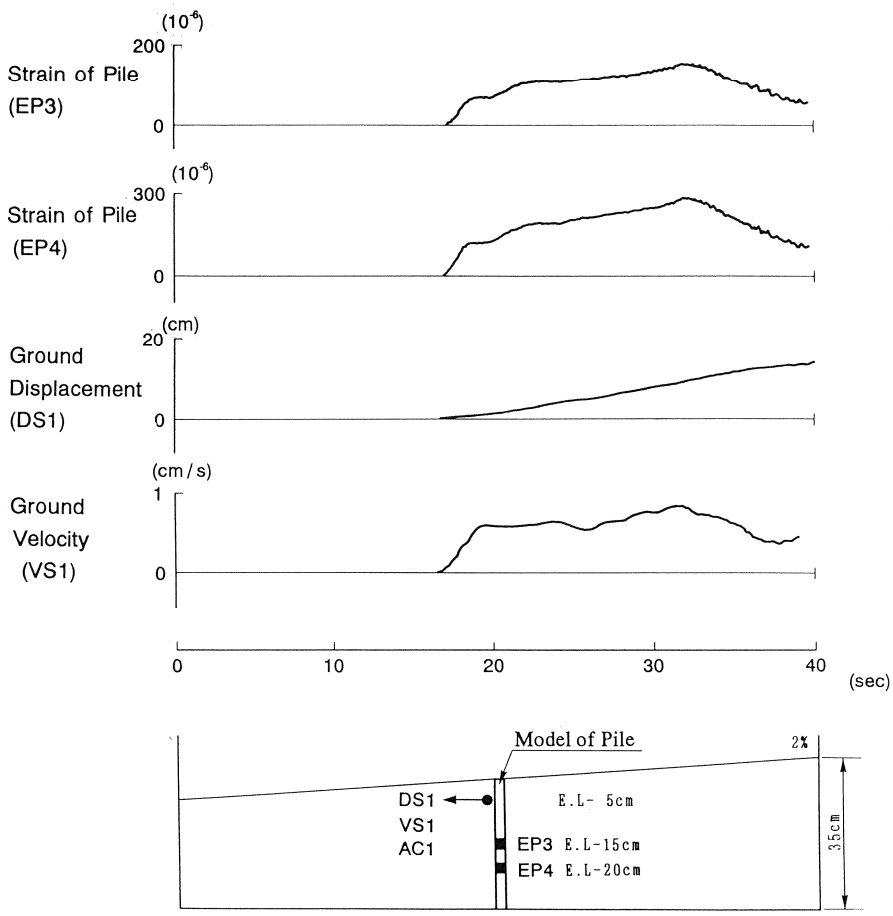

Figure 7. Experimental Result of External Fore on Foundation Pile

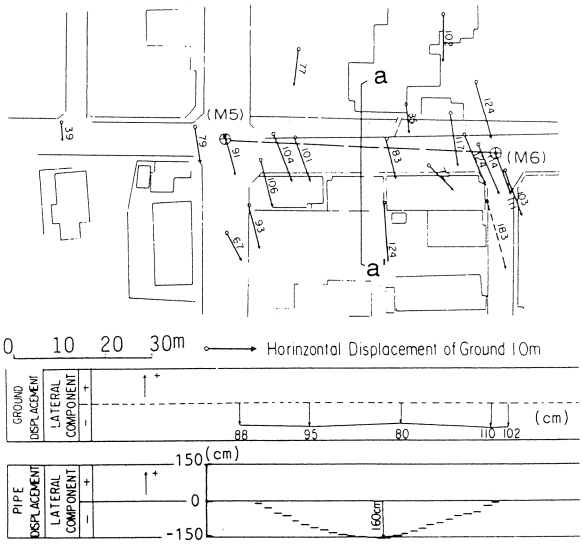

Figure 8. Displacement of Wastewater Pipe and Ground Surface (1983 Nihonkai-Chubu Earthquake)

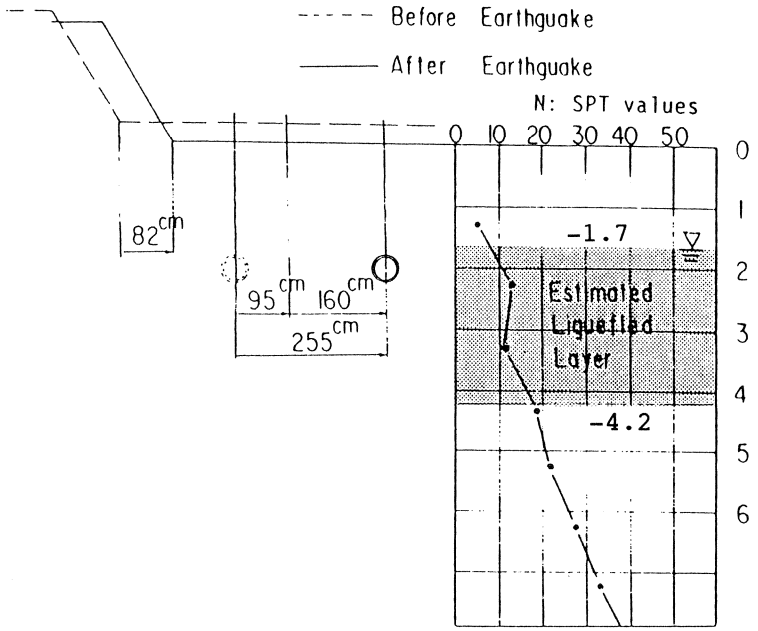

Figure 9. Displacement of Westewater Pipe and Ground Surface in CrossSection a-a'

Figure 9 shows the displacement of the pipe and the ground surface in the cross section along line a-a' in Figure 8, where movement of the pipe was a maximum. The absolute displacement of the pipe was calculated to be 255 cm by adding the maximum relative displacement 160 cm to the mean displacement of the two manholes 95 cm. Along line a-a' the displacement at the ground surface was measured to be only 82 cm.

Figure 9 also shows a soil profile with N-values at a site about 50 m north of the wastewater pipe and an estimated liquefied soil. The subsurface consists of sandy fill and sand dune. The ground water is located at -1.7 m below the ground surface, and the soil between -1.7 m and -4.2 m below the ground surface can be assessed to be liquefied based on the N-values. The wastewater pipe was located in the estimated liquefied layer of the ground. Therefore, the above-mentioned displacement of the wastewater pipe means that the liquefied soil moved much more than the overlaying non-liquefied layer.

A similar story was reported by a witnesses in Niigata City after the 1964 Niigata earthquake. A gas company engineer said that he had found gas pipes underneath side trenches of a road, which had been buried apart from the trenches before the earthquake. Furthermore, it was reported that a main gas pipe buried in a depth of about 1.5 m along the Shinano River, where the ground moved toward the river above ten meters, could not be found even by the thorough excavation after the earthquake. The pipe was guessed to has been flown into the river with the flow of the liquefied soil toward the river.

In order to investigate the mechanism of the large ground displacement, information about the duration of the occurrence is also important. Interviews with witnesses of the area where the ground displacement has been caused were conducted. A resident of the northern slope of the Maeyama in Noshiro City, where the ground displaced downward with a maximum of 5 m responded to a question about the duration of the motion of the 1983 Nihonkai-Chubu earthquake by saying that she had felt that the tremors continued for about 30 minutes, because her house had been making noises during the duration.

Several witnesses of the 1948 Fukui earthquake, when the liquefaction-

induced ground displacement reached over 5 m along the Kuzuryu River (Hamada, et al., 1992a) said that a ground fissure with a gap of about 1.0 m had been caused after the earthquake motion, and that the width had increased to about 3 m two or three hours later after the earthquake. Similar remarks were also reported by witnesses in Kasukabe City, where the ground moved several meters at the time of the 1923 Kanto earthquake (Hamada, et al., 1992a). They said that they had found a ground fissure with a gap of about 1.0 m along a small river just after the earthquake motion ended, and that the fissure had grown up about 3 m wide two or three hours later.

The collapse of the Showa Bridge with a total span of 250 m was one of the worst instance of damage to structures caused by the 1964 Niigata earthquake. Many witnesses reported that the girders had begun to collapse somewhat later after the earthquake motion ceased (Hamada, 1992a). When the earthquake motion started, many people and vehicles were on the bridge, but no lives were lost in spite of the catastrophic collapse. This suggests that there was enough time for people on the bridges to seek refuge on the banks. By taking into consideration the ground displacements measured on the bank of the Showa Bridge, the large bending deformation of the foundation piles and the estimated liquefied layer, it can be concluded that the liquefaction-induced displacement continued long time and reached several meters, consequently deforming the foundation piles and causing the girders to fall (Hamada, 1992a).

The above-mentioned remarks by the witnesses and the instance of the collapse of the Showa Bridge suggest that the liquefaction-induced ground displacement continued for a long period, until the excess water pressure dissipated although the earthquake motion ceased.

SHAKING TABLE TEST

A certain number of shaking table tests under 1 g condition as well as under several ten g condition by centrifuges was conducted on the liquefaction-induced ground displacement of sloped grounds. In most cases of these tests, the base excitation was continued until the surface of the model ground became flat. The horizontal ground displacement was caused by a volumetric transfer of the liquefied soil from the upstream to the downstream. Therefore, the magnitude of the horizontal ground displacement is governed by the total volume of the transferred soil, and proportional to the gradient of the ground surface as well as to the length of the soil box. These test results are not consistent with the outcomes from the case studies.

By referring the remarks from the witnesses that the ground movement had continued after the ground motion ceased, the authors conducted a shaking table test on the ground movement after the shaking ended. Figure 10 shows a rigid soil box, which is 3.0 m long, 1.0 m wide and 0.6 m deep. The model ground with flat surface was made in the soil box, and was vibrated in the direction of the shorter side of the box by sinusoidal waves. After a perfect liquefaction of the model ground which was confirmed by several piezometers in the soil, the soil box was inclined by lifting one side of the box with a specific gradient.

Generally, it can be considered that a large ground displacement started after an achievement of the perfect liquefaction of the soil and continued until the pore water pressure dissipates, even after the earthquake motion ended. The purpose of this experiment is to investigate characteristics of the ground movement after the earthquake motion ceases.

The tests were conducted by varying the initial relative density of the model ground and the inclination of the ground surface. The time history of the ground displacement was recorded by measuring movement of small marks buried in the soil, which were connected by thin strings with displacement

meters out side of the soil box as shown in Figure 11. The strings were protected by stainless tubes in order to cut the friction between the strings and the surrounding soil. The maximum ground displacement was also measured from the movement of elliptical marks in the soil as shown in Figure 12.

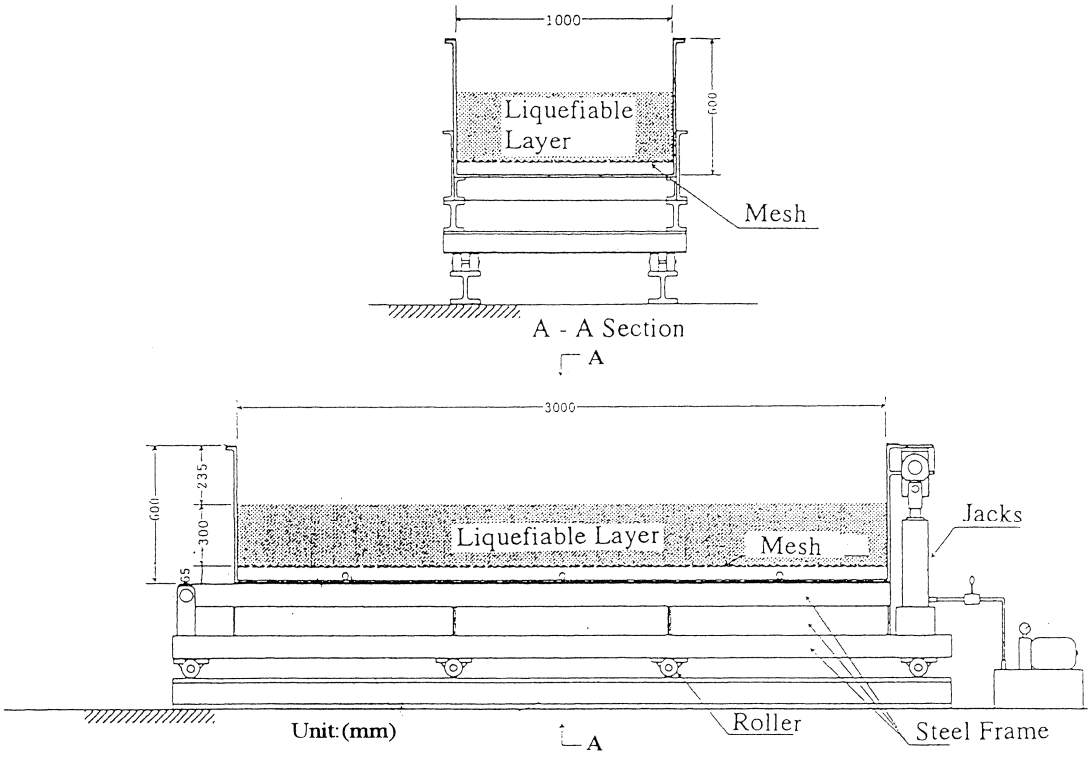

Figure 10. Soil Box and Model Ground for Shaking Table Test

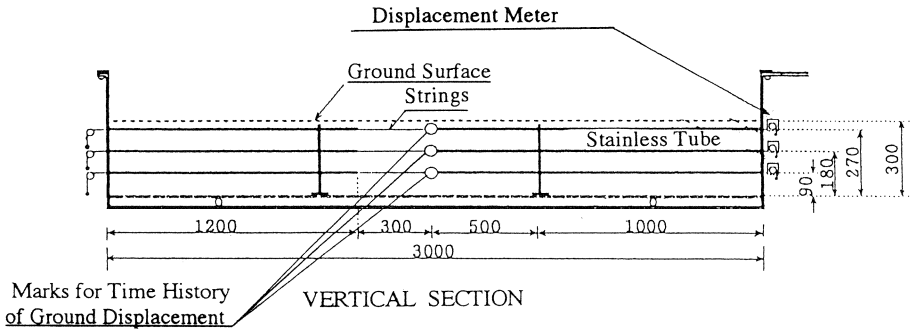

Figure 11. Measurement of Time History Ground Movement

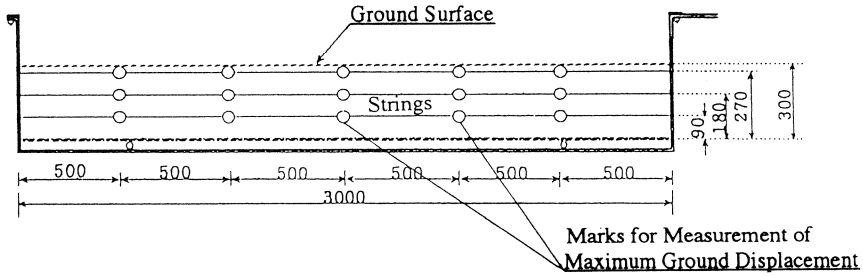

Figure 12. Measurement of Maximum Ground Displacement

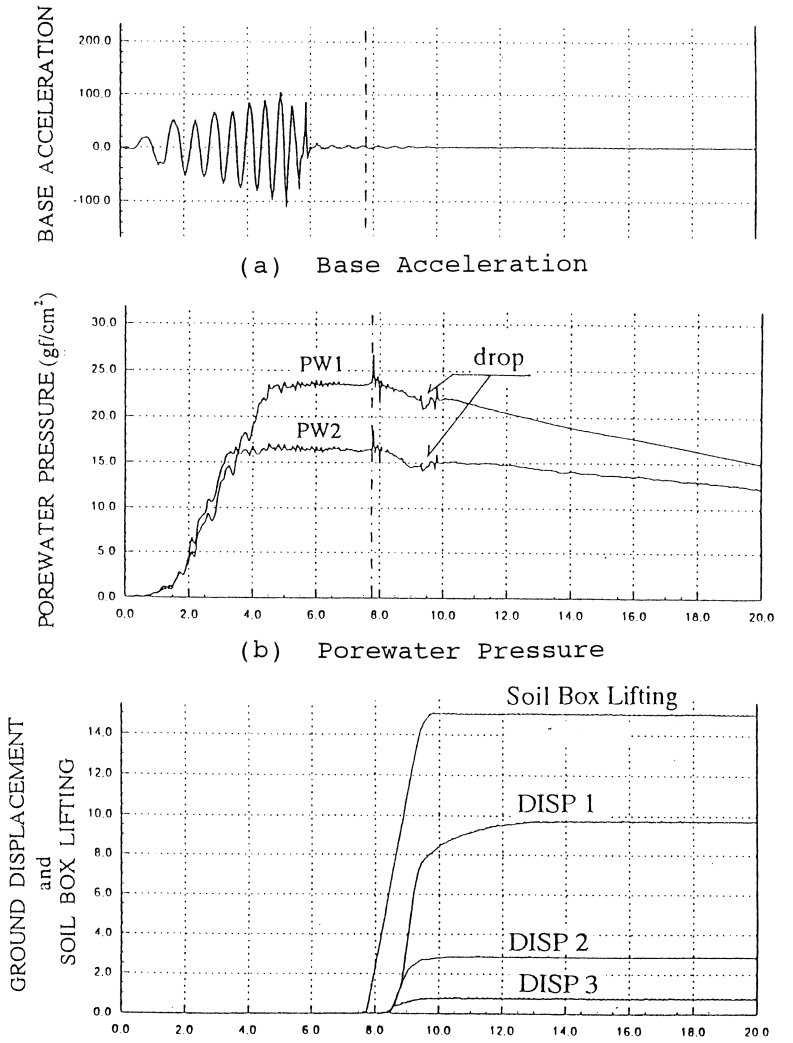

Figure 13. Example of Shaking table Test Results Result (CASE-1, Dr =23 %, θ = 4.2 %)

Figure 13 shows an example of the test results, when the initial relative density and the gradient of the ground surface are 23 % and 4.2 %, respectively. The porewater pressure (Figure(b)) gradually rose and reached the effective overburden pressure at each elevation due to base excitation (Figure(a)). After a complete stop of the base shaking the ground surface started to be inclined by lifting a side of soil box (Figure(c)). The time histories of ground displacements at three elevations were measured as shown in Figure(c). It is noteworthy that the porewater pressure sharply dropped when the ground displacement increased and approached the maximum values. After that, the porewater pressure gradually decreased due to upward dissipation of the porewater. The sharp drop of the porewater pressure suggests a recovery of the effective stress of the soil and a mobilization of the soil stiffness.

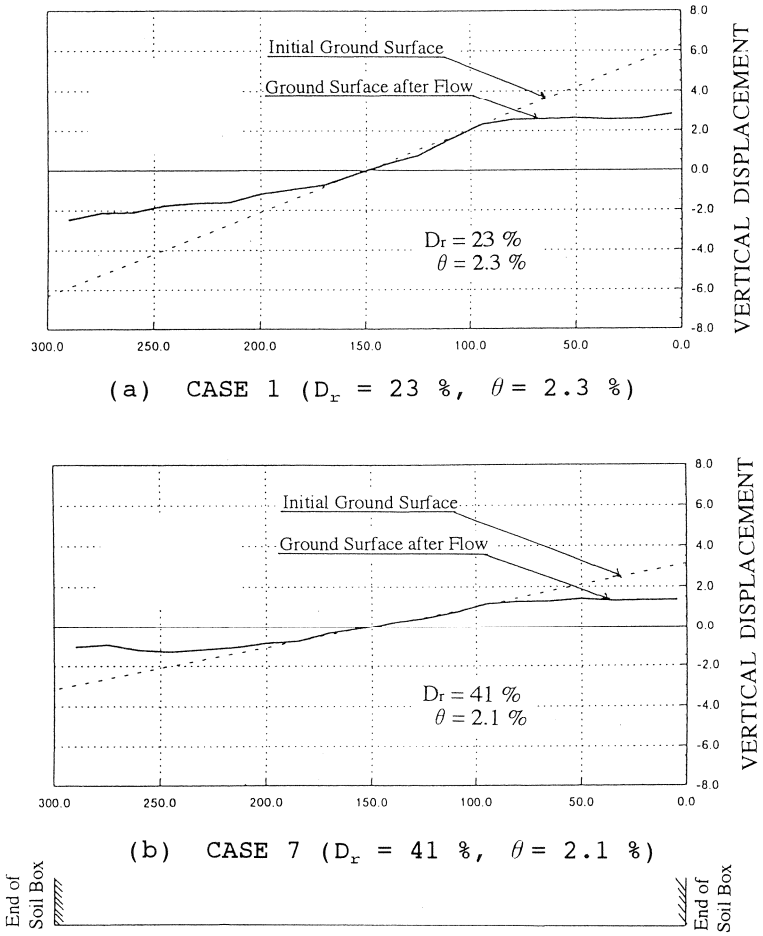

Figure 14. Vertical Movement of Ground Surface

The dotted as well as the solid lines in Figure 14 show the ground surface before and after the ground movement, respectively. The ground surface subsided by compaction of the sand due to liquefaction, but it was completed before lifting the soil box. The elevation of the ground surface before and after the ground displacement was measured by subtracting the mean subsidence from the original elevation. It is interesting to note that the initial inclination of the ground surface was preserved in the central part of the model ground even after the ground displacement. On the contrary, the ground surface became mostly flat nearby the two sides of the soil box. As mentioned later, this result indicates that the liquefied soil behaved as a liquid at first, but after a specific amount of the shear deformation of the ground the soil recovered it's stiffness and behaved as a solid body.

Figure 15 shows the maximum ground displacement at three different elevations at five locations along the direction of the ground displacement. It is noteworthy that the ground displacement in Figure (a), where the initial relative density is 41 % and the gradient is 2.1 %, is mostly same to that in Figure (b), where the relative density is same, but the gradient is 4.2 %, twice that in the case of Figure (a). This result suggests that maximum ground displacement is not necessarily governed by the gradient of the ground surface inclination, which is consistent with the result of the case studies. The displacement in Figure (c), where the initial relative density is small 23 %, is much larger than those in Figures (a) and (b). It can be understood that the maximum ground displacement is governed by the initial relative density of the ground.

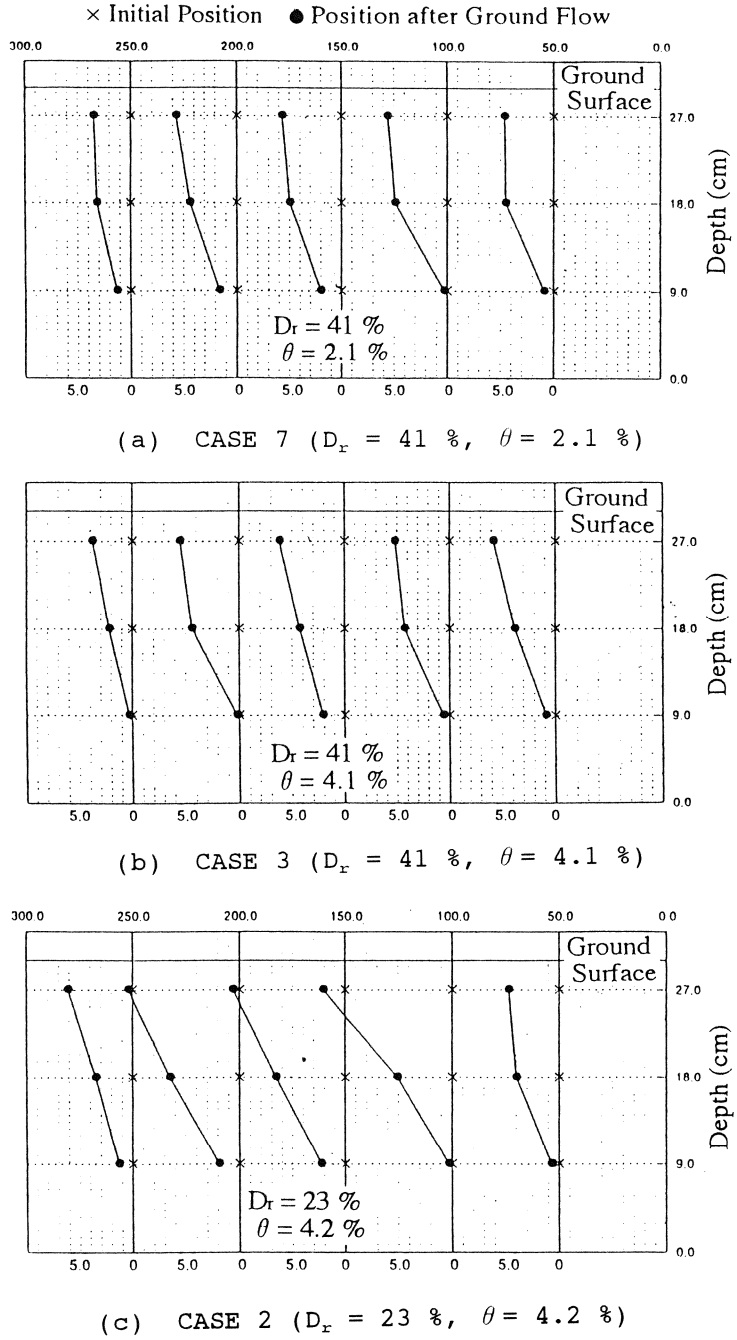

Figure 15. Maximum Ground Displacement at Three Elevations

The above-mentioned test result can be rationally explained by the following hypothesis: Figure 16 shows the half part of the model ground of the upstream side, and line O-C-A is the initial ground surface with a gradient θ. Firstly the ground surface of the upstream side subsides to line O-D-B, and consequently the ground at the center of the soil box (OF) causes horizontal displacement due to a volumetric transfer of the liquefied soil from the upstream side. If the liquefied soil behaves as a real liquid, the volume of $\triangle$ OEF is equal to that of $\triangle$ OBA under as assumption that the horizontal ground displacement distribution along the vertical direction is triangular as shown in the figure.

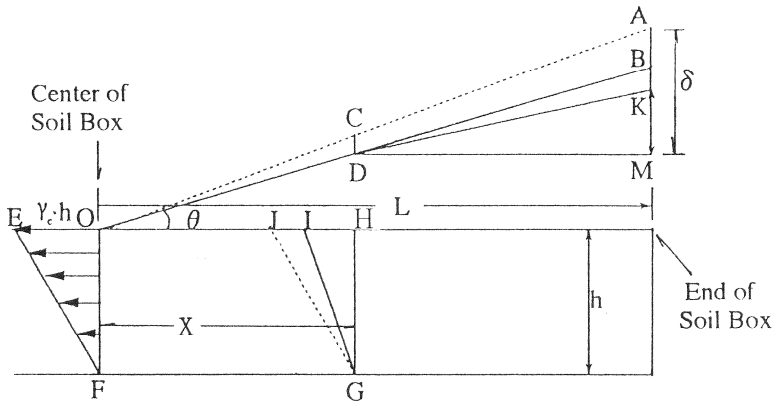

Figure 16. Change of Shape of Ground Surface

When the shear strain of the ground at the center of the soil box reaches so-called critical strain γ_c at which it is assumed that the soil stiffness is mobilized and the soil behaves as a solid body again, the ground displacement stops to increase, and after that the displacement at the surface remains constant $\gamma_c \cdot h$. Here h is the thickness of the ground at the center.

At a location (GH) away from the center, the ground also moves in the horizontal direction due to the volumetric transfer of the liquefied soil. The ground displacement at the surface of this location is HI, and the volume of △HIG is equal to that of □ACDB of the upstream side from GH. At this location the shear strain of the ground dose not yet reach the critical strain γ_c. Therefore, more volume of the liquefied soil (△IJG) can flow into this position. The volume of △IJG is equal to that of △BDK, and is also equal to that of △COD. The ground surface OD returns to OC due to the flow of the liquefied soil with a volume equal to that of △COD. Therefore, the ground surface OC preserve the initial gradient. On the contrary the ground surface becomes flat due to the liquid behavior of the liquefied soil nearby the upstream end of the soil box, because the shear strain does not reach the critical strain γ_c.

According to the above-mentioned explanation, the distance from the center of the inclined part with the initial gradient x and the subsidence at the upstream end of the soil box δ can be easily calculated as follows;

$$x = L - h\sqrt{\gamma_c / \theta} \qquad (3a)$$

$$\delta = \theta \cdot (L - x) \qquad (3b)$$

where L, h and θ are the half length of the soil box, the thickness of the ground and the initial gradient of the ground surface, respectively.

Figure 17 shows an comparison of the calculated ground surface with the one obtained by the experiment. The critical strain γ_c was determined from the ground deformation at the center of the ground. It can be concluded from a good coincidence between the experiment and the calculation that the above-mentioned hypothesis can explain the behavior of the liquefied soil during the large displacement.

Figure 18 shows the relationship between the critical strain γ_c and the initial relative density of the soil D_r. The critical strain increases when the initial relative density decreases.

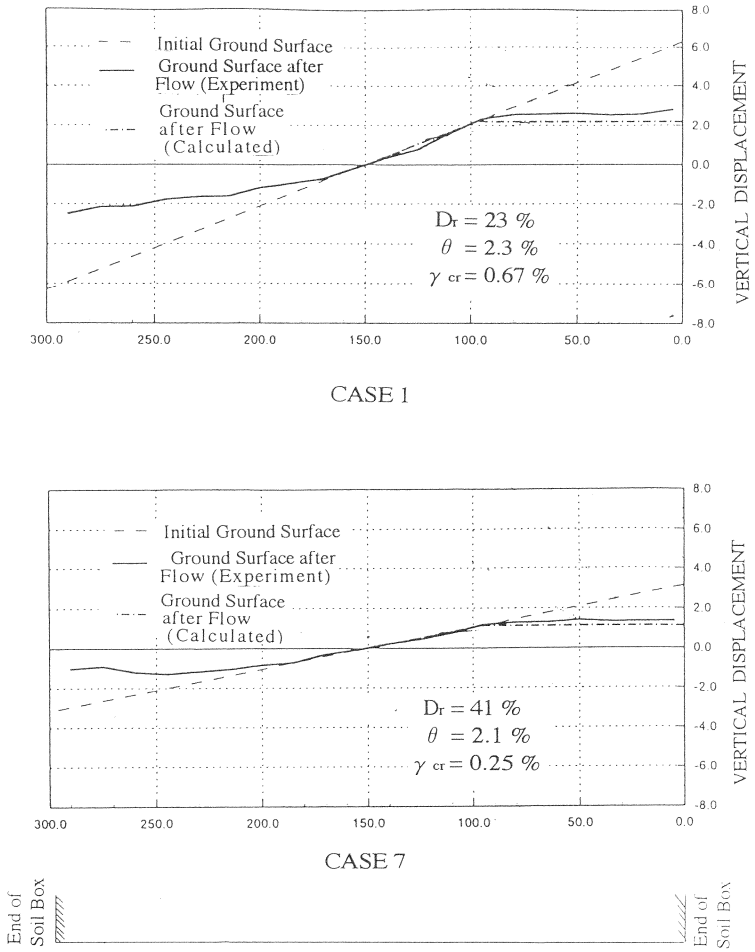

Figure 17. Comparison of Ground Surface between Calculation and Experiment

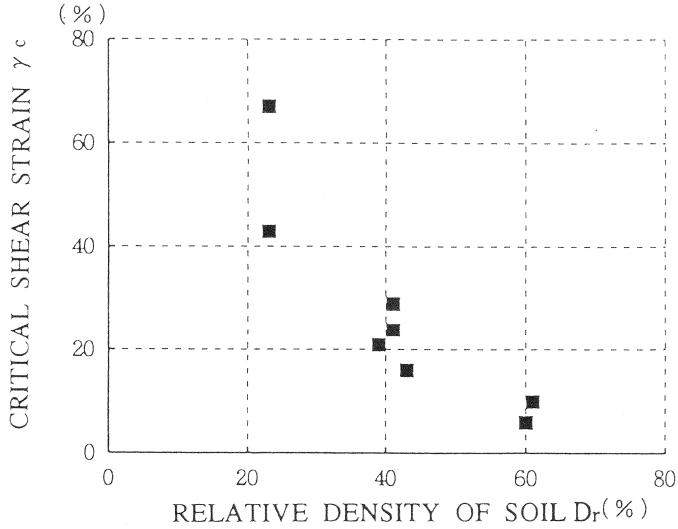

Figure 18. Relationship Between Critical Shear Strain and Relative density of Soil

CONCLUSION

The case studies on the liquefaction-induced large ground displacement showed that the ground moved from the higher elevation to the lower one, but the correlation was low between the magnitude of the ground displacement and the gradient of the ground surface. If it is assumed that the inclined ground was deformed by the gravity due to a large reduction of the soil stiffness, above-mentioned two facts contradict to each other.

The authors conducted a shaking table test on the liquefaction-induced ground displacement and found that the magnitude of the ground displacement did not depend on the surface gradient, but on the relative density of the soil. The test showed that the liquefied soil firstly behaved as a liquid, but after a specific amount of shear deformation which was controlled by the relative density, the soil stiffness was mobilized and the ground behaved as a solid body.

The experimental result is consistent with the fact obtained from the case studies. However there still remains the following research subjects on the liquefaction-induced ground displacement:

i) The magnitude of the ground strain in the test is 10 ~ 50 %, much smaller than that observed in the case studies which is sometime above 100 %. The test was focussed on the ground displacement after earthquake motion ceased. Therefore, the ground displacement during earthquake motion should be investigated.

ii) The test was conducted under 1 g condition. The effect of the confining pressure on the critical strain, at which the soil stiffness is mobilized should be studied.

iii) The test showed that the liquefied soil firstly behaved as a liquid. In order to discuss the duration of the ground displacement and the effect of the ground displacement on the in-ground structures, the fluid properties of the liquefied soil should be investigated.

REFERENCES

Hamada, M. and O'Rourke, T.D., (1992a), Case Studies of Liquefaction and Lifeline Performance during Past Earthquakes, Volumes 1 and 2, Japanese and U.S. Case Studies. Technical Report NCEER-92-0002, National Canter for Earthquake Engineering Research, Buffalo.

Hamada, M., Yasuda, S., Isoyama, R. and Emoto, K., (1986), Study on Liquefaction Induced Permanent Ground Displacement, Association for the Development of Earthquake Prediction (ADEP), Tokyo.

Bartlett, S. F., and Youd, T. L., (1992), Empirical Prediction of Lateral Spread Displacement, Proceedings from the Fourth Japan-U.S. Workshop on Earthquake Resistant Design of Lifeline Facilities and Countermeasures for Soil Liquefaction, Technical Report NCEER-92-0019, Vol. Ⅰ , pp.351~366.

Hamada, M., Ohtomo, K., Sato, H. and Iwatate, T., (1992b), Experimental Study of Effects of Liquefaction-Induced Ground Displacement on In-Ground Structures, Proceedings from the fourth Japan-U.S. Workshop on Earthquake Resistant Design of Lifeline Facilities and Countermeasures for Soil Liquefaction, Technical Report NCEER-92-0019, Vol. Ⅱ, pp481~492.

A Comparative Study of Predictive Methods for Liquefaction Induced Embankment Displacements

Geoffrey R. Martin[1] and Ping Qiu[2]

ABSTRACT

Many bridge failures in past earthquakes have resulted from large post liquefaction lateral deformations of bridge approach fills. In considering the problem of retrofit of existing bridges where liquefiable foundation soils are found, there is a clear need to develop improved predictive methods for post liquefaction deformations of approach fills, prior to the investment of heavy costs related to ground remediation. In this presentation, current design approaches for evaluating post liquefaction lateral deformations are compared by utilizing the simple problem of a thirty-foot high approach fill on a liquefiable sand stratum. The comparative approaches encompass simplified one-dimensional Newmark sliding block analyses and more complex two-dimensional finite difference models. The comparative studies indicate that simplified one-dimensional Newmark sliding block analyses can provide a practical basis for less conservative retrofit design, provided the time at which residual strength is initiated when liquefaction occurs and the effects of initial static shearing stresses are taken into account.

[1] Professor and Chairman, Department of Civil Engineering, University of Southern California, Los Angeles.
[2] Graduate Student, Department of Civil Engineering, University of Southern California, Los Angeles.

INTRODUCTION

In the 1964 Alaska and Niigata earthquakes, liquefaction induced lateral embankment or approach fill deformations were particularly destructive to highway and railway bridges (Bartlett and Youd, 1992). Ninety-two highway bridges in Alaska were severely damaged or destroyed and a further forty-nine bridges received moderate to light damage. Liquefaction induced lateral deformations of embankments have caused similar bridge damage in many more recent earthquakes including those in Japan, Puerto Rico, and the Philippines. Clearly this is a problem that needs to be addressed during the seismic design of bridges in liquefaction prone environments. In the case of the seismic retrofit of existing bridges, however, it is desirable to reduce any conservatism in assessing the magnitude of post liquefaction deformations, prior to the investment of heavy costs related to ground remediation.

In this presentation, differences in lateral displacement predictive methods are examined by utilizing the simple problem of a thirty-foot high approach fill on a liquefiable sand stratum. By examining the assumptions used and comparing displacement predictions, both the sensitivity of analysis methods and inherent conservatism may be assessed.

To simulate the observed failure mode of approach fills in past earthquakes for comparative analytical studies, we have idealized the problem as shown in Fig. 1. The figure is representative of a compacted earth approach fill located above a liquefiable foundation layer. From a vulnerability standpoint, the question arises as to the magnitude of lateral embankment displacement which could be induced during the earthquake adopted for seismic retrofit. A reliable estimate of this displacement would allow evaluation of the vulnerability of the existing bridge to such deformation.

For practical reasons, the Newmark Sliding Block approach for computing earthquake induced embankment displacements (Newmark, 1959) is generally adopted in practice. A common conservative approach to the problem is to assume that a liquefied soil layer mobilizes a residual undrained strength s_{ur} following liquefaction, with the value of s_{ur} determined by correlation with standard penetration blow counts or from laboratory tests. Using limiting equilibrium principles, a horizontal yield acceleration coefficient k_y leading to a factor of safety of one for the most critical sliding block is then determined. Assuming rigid block response, the ground motions which will lead to incremental horizontal block displacements when $k > k_y$, may be represented by the acceleration time history at the base of the sliding block. Assuming residual strength is mobilized at time zero during earthquake loading, the resulting block displacement may be computed for a given time history through use of a simple computer program. Alternatively, non-dimensional

charts may be used, expressing permanent displacements as a function of k_y/k_{max}, where k_{max} is the maximum ground acceleration coefficient.

Research studies to date have examined the assumptions used for the simplified Newmark approach described above with a view to understanding the mechanisms of failure and reducing potential conservatism. The results of these studies are briefly summarized below and illustrate the following aspect of the problem:

- The sensitivity of displacements to input ground motions.
- The time history of pore pressure build up leading to the point at which residual strength should be triggered for analyses.
- The potential influence of horizontal static shearing stresses beneath embankment slopes and their role in the impeding the rate of excess pore pressure build up.
- The use of two-dimensional non-linear response analyses to simulate the embankment displacement mechanism.
- Comparative evaluation of assumptions on displacement predictions.

DISPLACEMENT SENSITIVITY TO INPUT MOTIONS

Embankment displacements predicted by the Newmark Sliding Block model are primarily a function of k_y/k_{max}, peak ground velocity V and peak ground acceleration A. The number of load cycles exceeding yield as reflected by the earthquake magnitude M, could also be a factor. A number of analytical studies to determine displacements as a function of k_y/k_{max} have been made using a variety of earthquake records. However, many of the available displacement charts have been normalized by scaling earthquake records to peak accelerations of 0.5g and peak velocities of 30 inches per second.

To develop a more convenient design chart and to investigate the range of variability of predictive displacements, a study was made using the database published by Hynes and Franklin (1985), where displacements computed using a large number of earthquake records have been documented. For this study, the data was limited to earthquakes with a magnitude range of 6.0 to 7.5. For the purpose of data analysis an equation of the form:

$$d = C\,(k_y/k_{max})^{a1}\,(1 - k_y/k_{max})^{a2}\,A^{a3}\,V^{a4}\,M^{a5}$$

was used. Regression analyses indicated that earthquake magnitude does not have major effect on predictions and that a equation of the form:

$$d = 6.82\,(k_y/k_{max})^{-0.55}\,(1 - k_y/k_{max})^{5.08}\,A^{-0.86}\,V^{1.66}$$

describes the mean displacement with an R^2 error of 0.9247. In the above equation a consistent set of units of inches, and seconds are used. By normalizing the displacement by a factor $A^{-.86}\,V^{1.66}$, a normalized displacement chart showing $d/\,A^{-.86}\,V^{1.66}$ vs. k_y/k_{max} may be plotted and is shown in Fig. 2. Almost 80% of all data fall on a narrow band leading to the nominal upper and lower bounds as shown. Upper bound displacements are about twice those of the mean, while lower bound values are about one quarter of the mean.

TIME HISTORY OF PORE PRESSURE BUILD UP

To pursue analytical studies addressing questions related to the time history of pore pressure build up and two-dimensional response, the idealized embankment configuration and the material properties shown in Fig. 3 were assumed. To study the effects of liquefaction we focused on layer 1 by assuming a low relative of density of 40%. The cohesionless materials in the idealized embankment were assumed to be those of Nevada sand which was used for the VELACS Project (Arulmoli et.al., 1992). Penetration blow counts in $(N_1)_{60} = 8$ and $(N_1)_{60} = 16$ were assumed for layers 1 and 2 respectively. An undrained residual strength of 200 psf was chosen for layer 1 from the standard relationships shown in Fig. 4. Pore pressure build up was suppressed in the lower layer 2 to ensure a dominant lateral sliding mechanism. The 1940 El Centro earthquake with a peak ground acceleration of 0.33g was input at bedrock level.

Time history of pore pressure increases were computed for one-dimensional free field conditions represented by column 1 and column 2, using the effective stress response program DESRA (Lee and Finn, 1978). Modifications to this program were made to make it more user friendly in a practical sense. These modifications included the use of a simplified two-parameter pore pressure model suggested by Byrne (1991) and a generalized non-linear backbone curve with automatic generation of parameters to represent a given curve describing variations in shear modulus with shear strain amplitude. The two pore pressure parameters were selected to match a standard liquefaction strength curve developed from field blow count data and a design earthquake magnitude. The simplifications make the program more amenable to routine design practice. An Iwan model (1967) was used as a non-linear constitutive model and incorporates an array of elasto-plastic elements which simulate a given non-linear backbone curve and provides hysteretic

damping. This physically based mechanistic model provides a good simulation of permanent displacement induced by soil yield.

Fig. 5 shows the G/G_{max} vs. shear strain amplitude curve assumed for analyses and the liquefaction strength curve for layer 1. In the program DESRA, G_{max} values were assigned to layer properties using the equation: $G_{max} = 20000(N_1)_{60}^{1/3}(\sigma'_m)^{1/2}$, where $(\sigma'_m)^{1/2}$ is the mean effective stress. A non-linear backbone or shear stress-shear strain curve was then constructed to be compatible with the G/G_{max} vs. γ curve. The backbone curve was then used to fix the Iwan model parameters, which in turn define the soil behavior under cyclic loading. The field liquefaction strength curve for layer 1 was constructed to be compatible with the assumed blowcount $(N_1)_{60} = 8$. The difference in the two curves shown reflect the effect of initial confining stresses.

The results of the DESRA analyses with respect to pore pressure build up are shown in Fig. 6. For column 1, the loose sand layer 1 liquefied after about two seconds of strong shaking. The corresponding large shearing strains occurring in the layer are interpreted as relative displacements of the soil column above the liquefied layer in Fig. 6a. These displacements can be considered to reflect ground lurch leading to a permanent displacement of the ground of about 0.25 feet. For column 2, liquefaction occurred after about three seconds leading to permanent lurch displacements of the soil column above the liquefied layer of about 0.3 feet. Note the significant reductions in surface accelerations compared to input accelerations. The low 0.05g peak acceleration reflects the limiting inertial loads which can be carried by the upper soil column following mobilization of the post liquefaction residual strength of 200 psf. in layer 1. The shear stress vs. shear strain time history (0 - 4 seconds) for layer 1 (column 2) is shown in Fig. 7.

TWO-DIMENSIONAL RESPONSE ANALYSES

To study the effects of two-dimensional earthquake response on the mechanisms of lateral deformation of the slope and to evaluate the influence of initial static shearing stresses beneath the sloping embankment on liquefaction resistance, a two-dimensional dynamic response program TENSI was used. The program TENSI has been documented by Larkin et.al.,(1991). TENSI is a non-linear two-dimensional total stress response analysis program utilizing a multiple yielding surface model to simulate non-linear soil behavior. The latter model has been described by Iwan (1967), and is a kinematic strain hardening model analogous to the model used for the one-dimensional analyses described above. The original program TENSI has been modified to form

TENSI-M to allow inclusion of the effects of initial static stresses due to embankment construction on the earthquake response. The program is now divided into two parts: static analysis and dynamic analysis. In the static analysis, gravity loading is used to simulate the construction procedure, where the embankment is built in a sequence of layers. For each loading layer, the program runs twice. The first run is under an assumption that loosely placed soil has only very small stiffness, that is, a very low modulus. In the second run, the stiffness matrix is formed using compacted soil modulus values, but resetting displacements and strains from the first run, that is, the position after settlement of loose soil is chosen as a reference position. A Gaussian procedure is used to solve for displacements from layer gravity loading. The embankment shown in Fig. 3 is assumed to be constructed in three layers. The resulting static shear stress distribution over layer 1 is shown in Fig. 8. The highest shear stresses occur beneath the slope, leading to an average ratio of horizontal static shearing stress to initial vertical effective stress beneath the slope of about 0.25. The static shear stress will affect liquefaction strength as described by Vaid and Finn (1979) and will be discussed further below.

As a two-dimensional effective stress constitutive model has yet to be programmed into TENSI-M, in order to study the two-dimensional mechanisms of lateral deformation, the shear modulus and shear strength of the loose sand layer were progressively degraded from initial values to residual values using the average increases in pore pressure from the one-dimensional DESRA analyses. The TENSI-M results at the vertical free field boundaries, columns 1 and 2, are compared to the results from DESRA in Fig. 9. The TENSI-M results are very similar to the DESRA results except for permanent lurch displacements which are about 0.6 feet. This increase may be attributed to the effects of initial static horizontal shearing stresses that extend out as far as column 1.

The displacement pattern as a whole for the TENSI-M analyses, is shown in Fig. 10. The horizontal sliding mode of the embankment is clearly indicated with evidence of passive failure a the toe. The time history of average horizontal slope displacement is shown in Fig. 12.

CALCULATION OF EMBANKMENT DISPLACEMENTS USING THE NEWMARK METHOD

To perform conventional Newmark analyses, it is necessary to first determine the critical sliding block and the corresponding yield acceleration (assuming the residual strength of 200 psf is mobilized in layer 1) using conventional pseudostatic limiting equilibrium methods. The position of the critical sliding block is roughly that shown in Fig. 1. The corresponding yield acceleration is 0.03g. The static factor of safety is 1.15 which provides for static stability under post

liquefaction conditions, that is, a flow failure would not occur. Horizontal displacements of the block induced by the input earthquake acceleration time history were computed using the program DISPLMT (Houston et.al., 1987). The time histories of displacement assuming residual strength triggered following liquefaction either at time = 0 or 2 seconds are shown in Fig. 12, leading to maximum displacements of about 2.8 and 2.5 feet respectively. If liquefaction had not occurred until after about 4 or 5 seconds of strong shaking, the reductions in maximum displacement from the assumption of triggering at t = 0 would have been more significant. A block displacement of about 2 feet was computed from the mean curve shown in Fig. 2, using the average maximum V and A at the base of the liquefied layer from DESRA results. The corresponding upper bound displacement is about 4 feet. The maximum displacement from TENSI-M analyses assuming residual strengths triggered at 2 seconds, is about 3.3 feet.

The embankment displacement estimates assume pore pressure generation under one-dimensional free field conditions and do not reflect the influence of static shearing stress reducing the rate of pore pressure build up. The latter effects were taken into account by utilizing the results of published laboratory data, where simple shear test were conducted with varying initial static shearing stress ratios, as reported by Vaid and Finn (1979), as shown for example in Fig. 11. By modifying the liquefaction strength curve beneath the sloping embankment to account for an average static shearing stress ratio of 0.25, (a liquefaction strength increase of about 25%), it was found that the earthquake induced pore pressure increases reached only about 40% of the values required to induce liquefaction. The effect of reduced strength degradation beneath the sloping embankment to values corresponding to 40% of the difference between static strengths and residual strengths significantly increased the yield accelerations and reduced displacement. The displacement time histories are shown plotted on Fig. 12 and resulted in a maximum of about 0.2 feet of displacement.

SUMMARY AND CONCLUSIONS

From the above sensitivity study it is clear that both the point of time during the earthquake when residual strength is triggered by liquefaction and the effects of initial static shearing stresses in reducing the rate of pore pressure build up, have a major influence on the magnitude of earthquake induced post liquefaction displacements. However, research to date has indicated that the Newmark approach for evaluating post liquefaction embankment deformations can provide a practical basis for design provided the above effects are taken into account. Through on-going research exploring the sensitivity of displacements to the above variables, it is anticipated that simplified final design approaches and charts can be documented for routine use in the field. Additional centrifuge tests as part of an RPI research program will include experiments where

embankment deformations will be measured utilizing a model configuration similar to that shown in Fig. 1. These tests will provide additional verification for the analysis approach.

ACKNOWLEDGMENTS:

The research described above was supported by the National Center for Earthquake Engineering Research Highway Project, funded by the Federal Highway Administration.

REFERENCES

Arulmoli, K, Muraleetharan, K. K., Hossain, M. M. and Fruth, L. S., (1992): "VELACS, Verification of Liquefaction Analysis By Centrifuge Studies Laboratory Testing Program, Soil Data Report", The Earth Technology Corporation, California, Earth Technology Project No. 90-0562.

Bartlett, Steven F. and Youd , T. Leslie, (1992): "Case Histories of Lateral Spreads Caused by the 1964 Alaska Earthquake", Case Studies of Liquefaction and Lifeline Performance During Past Earthquakes, Vol. 2, United States Case Studies, Edited by T.D. O'Rourke and M.Hamada, Technical Report NCEER-92-0002.

Byrne, Peter M., (1991): "A Cyclic Shear-volume Coupling and Pore Pressure Model for Sand", Iwan, Proceedings: Second International Conference on Recent Advances in Geotechnical Engineering and Soil Dynamics, March, pp. 11 - 15, St. Louis, Missouri, Paper No. 1.24.

Houston, Sandra L., Houston, William N. and Padilla, J. Manuel, (1987): "Microcomputer-aided Evaluation of Earthquake-induced Permanent Slope Displacements", Microcomputers in Civil Engineering 2.

Hynes, Mary E. and Franklin, Arley G., (1984): "Rationalizing the Seismic Coefficient Method", Geotechnical Laboratory, Department of the Army, Waterways Experiment Station, Corp. of Engineers, Vicksburg, Mississippi, July.

Iwan, W. D., (1967): "On a Class of Models for the Yielding Behaviors of Continuous and Composite System", Transaction of the ASME, September.

Larkin, T.J. and Marsh, E.J., (1982): "Two Dimensional Nonlinear Site Response Analysis", Proc. Pacific Conference on Earthquake Engineering, Vol. 3, pp. 217-227, Auckland, November.

Lee, Michael K. W. and Finn, W. D. Liam, (1978): "DESRA-2: Dynamic Effective Stress Response Analysis of Soil Deposit with Energy Transmitting Boundary Including Assessment of Liquefaction Potential", Department of Civil Engineering, University of British Columbia, Vancouver, Canada, June.

Newmark, Nathan M., (1959): "A Method of Computation for Structural Dynamics", Journal of the Engineering Mechanics Division, ASCE, Vol. 85, No. EM3, July.

Seed, H. Bolton and Harder, Leslie F., Jr., (1990): "SPT-based Analysis of Cyclic Pore Pressure Generation and Undrained Residual Strength", Memorial Symposium Proceedings, Volume 2, May, BiTech Publishers LTD.

Vaid, Yoginder P. and Finn, W.D. Liam, (1979): "Static Shear and Liquefaction Potential", Journal of the Geotechnical Engineering, ASCE, Vol. 105, No. GT10, October.

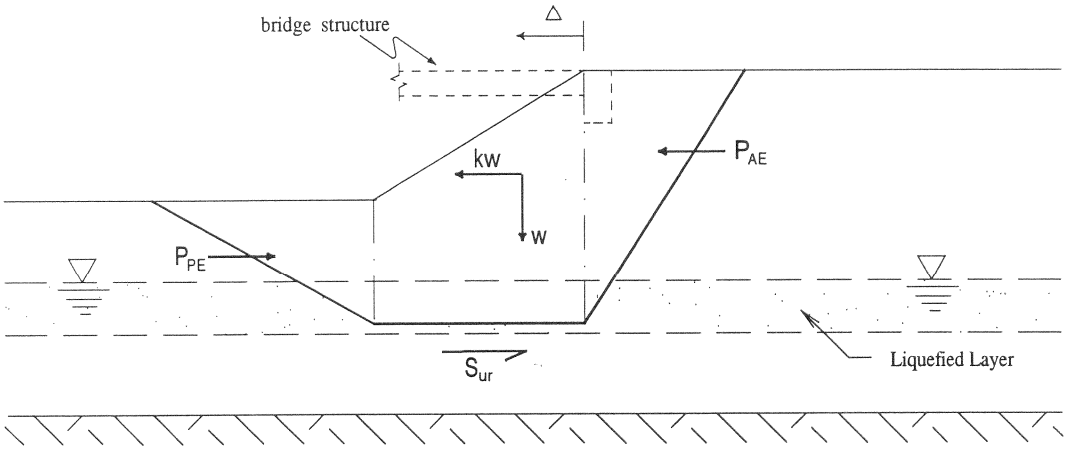

Fig. 1 Idealized Block Failure Mode of Bridge Approach Fill

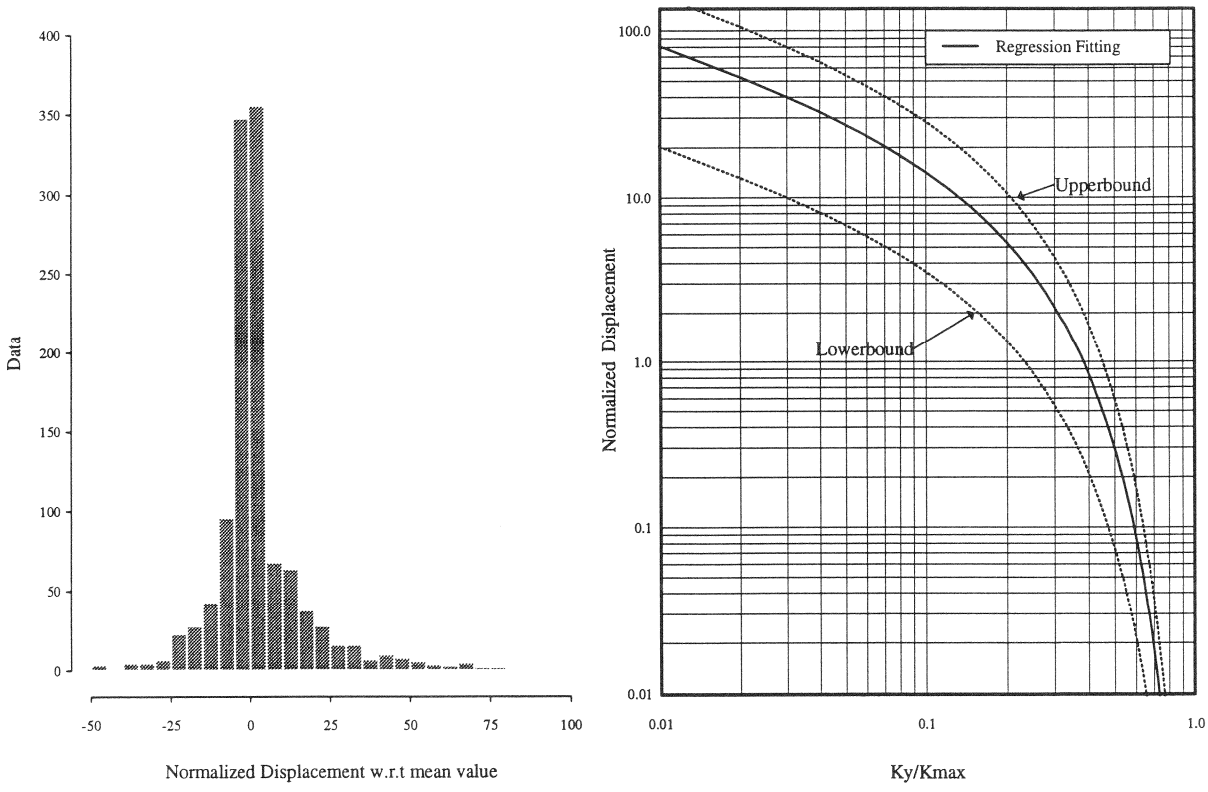

Fig. 2 Newmark Displacement Chart

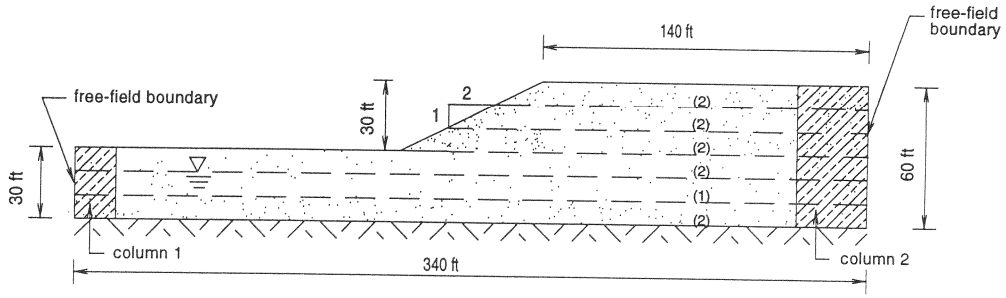

Summary of Material Properties of Nevada Sand

Layer	Relative Density	Poisson's Ratio	Friction Angle	Coefficient of Permeability (m/s)	Residual Strength (psf)
1	40%	0.3	33	6.6×10^{-5}	200
2	60%	0.3	35	5.6×10^{-5}	700

Fig. 3 Configuration of an Idealized Embankment

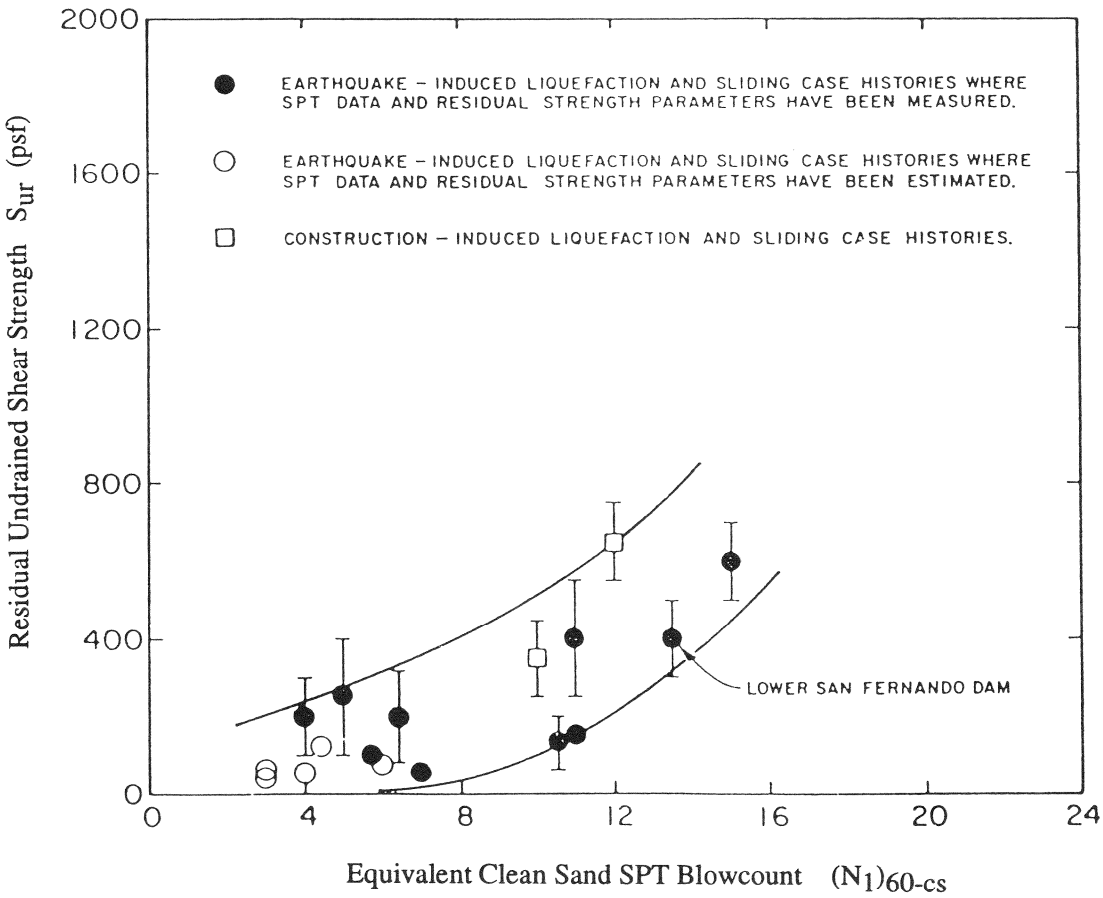

Fig. 4 Relationship Between Clean Sand Blowcount and Undrained Residual Strength from Case Studies

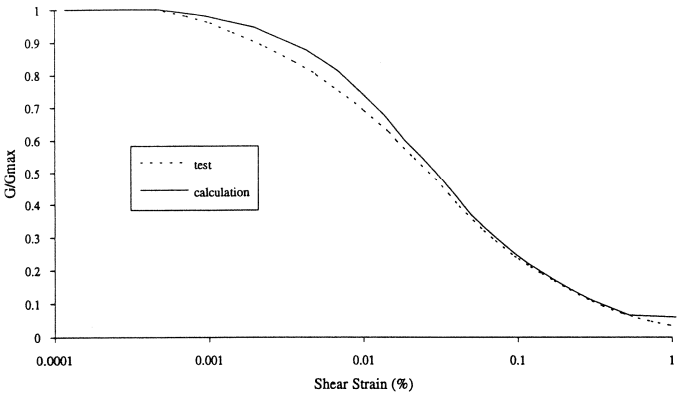

Fig. 5a Modeled versus Standard Shear Modulus-Shear Strain Curve

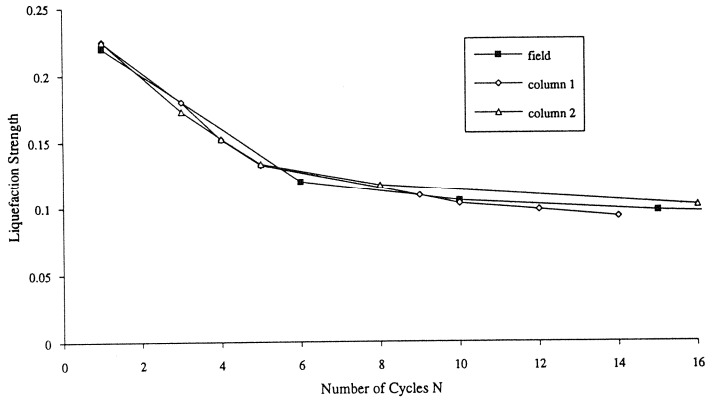

Fig. 5b Modeled versus Field Liquefaction Strengths

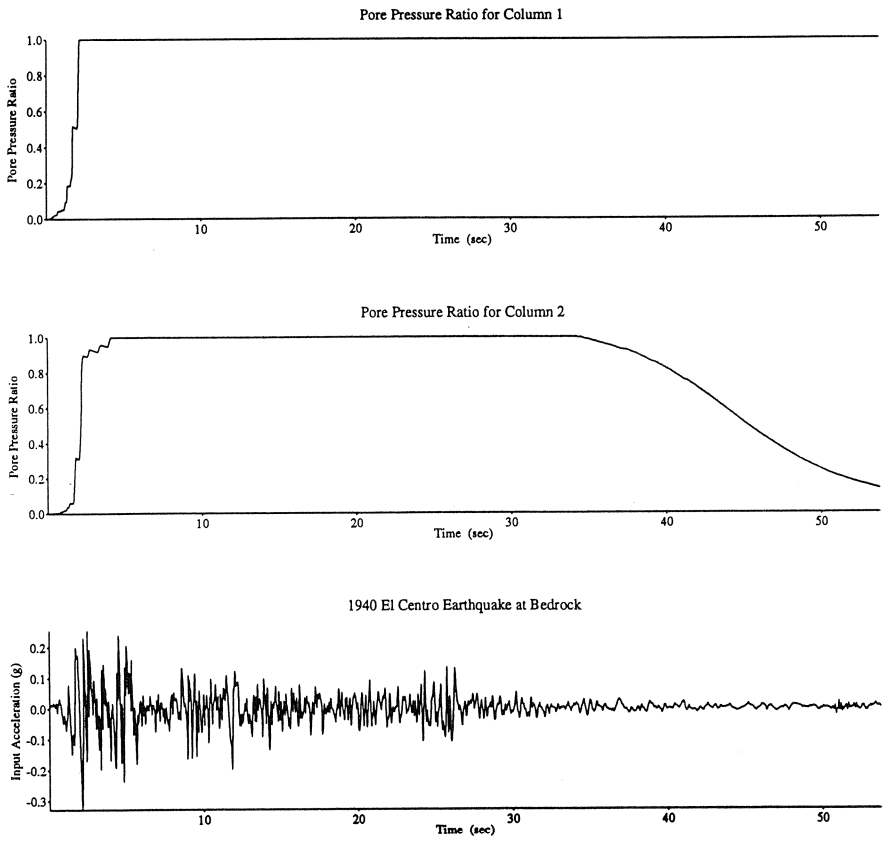

Fig. 6 DESRA-6 Liquefaction Evaluation

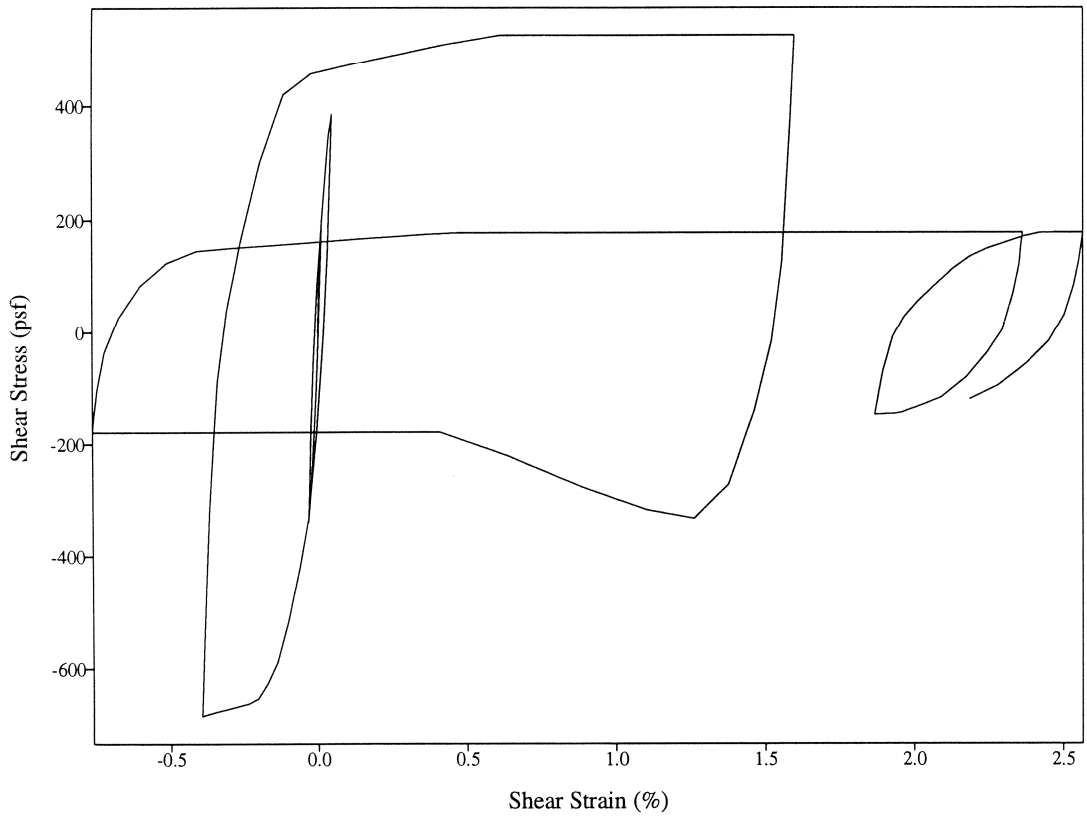

Fig. 7 Shear Stress vs. Shear Strain Time History (0 - 4 seconds) for Layer 1 (Column 2)

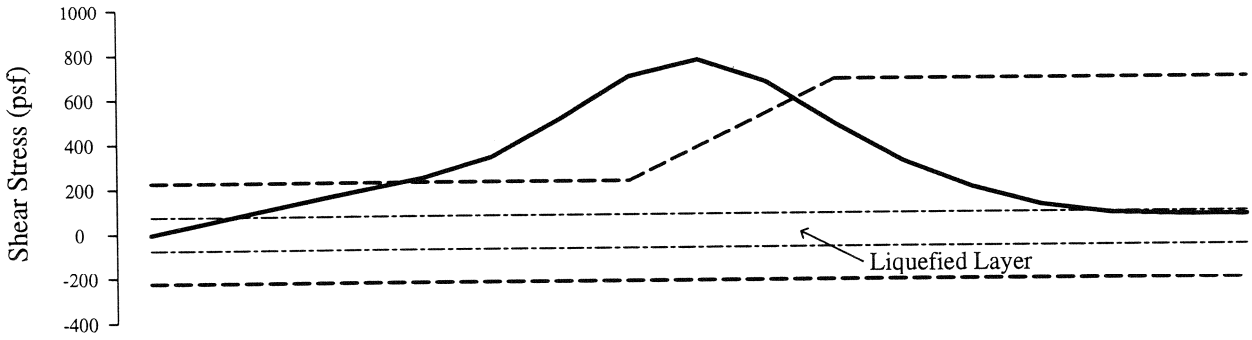

Fig. 8 Horizontal Static Shear Stress Distribution Due to Embankment Construction (Layer 1)

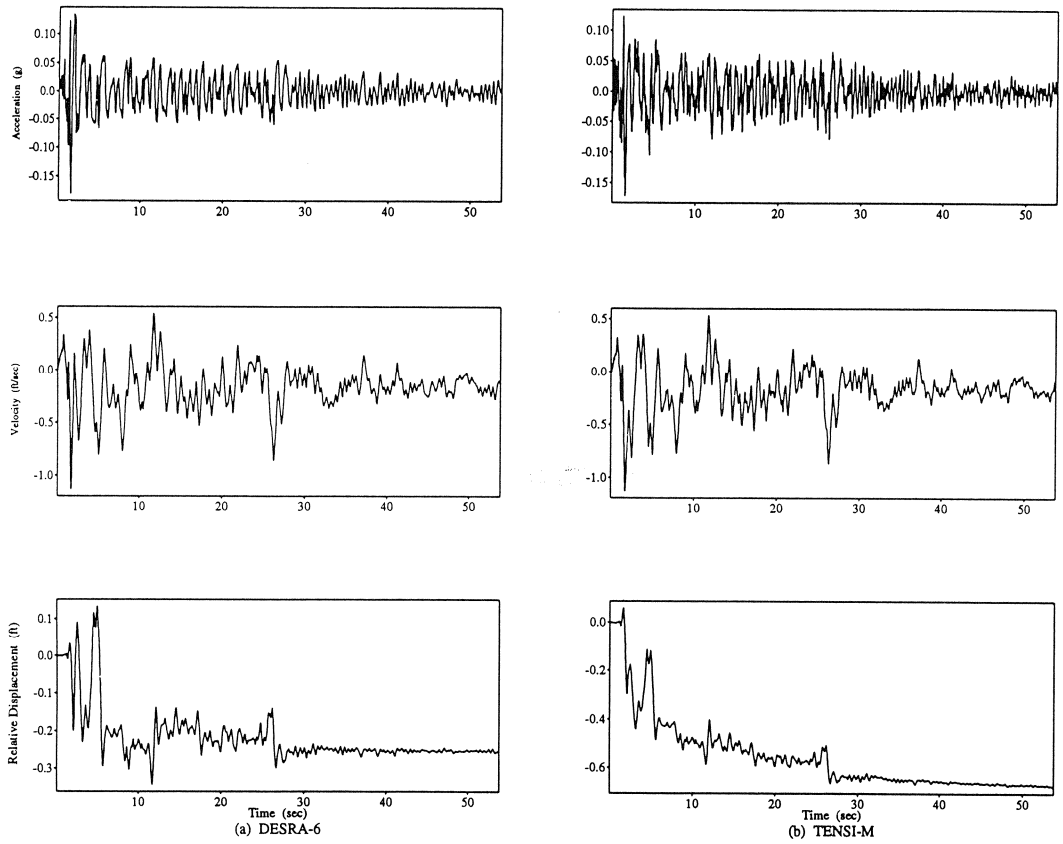

Fig. 9 Comparison of DESRA-6 and TENSI-M Results for Loose sand Layer - Column 1

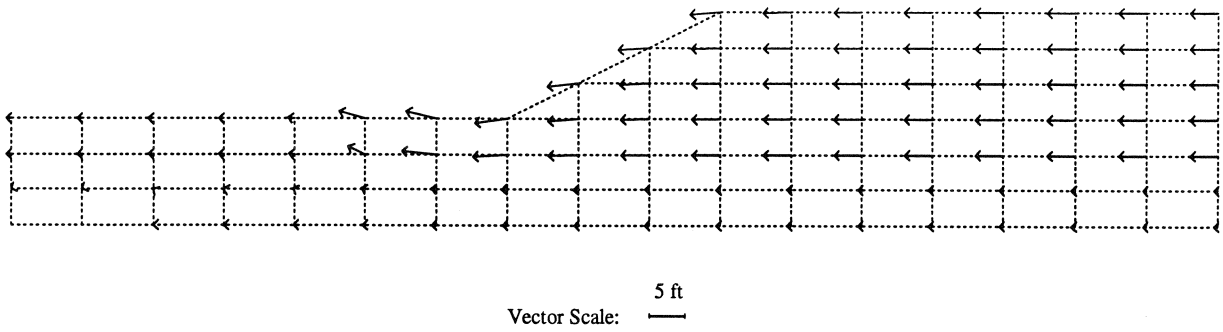

Fig. 10 Displacement Field Vectors

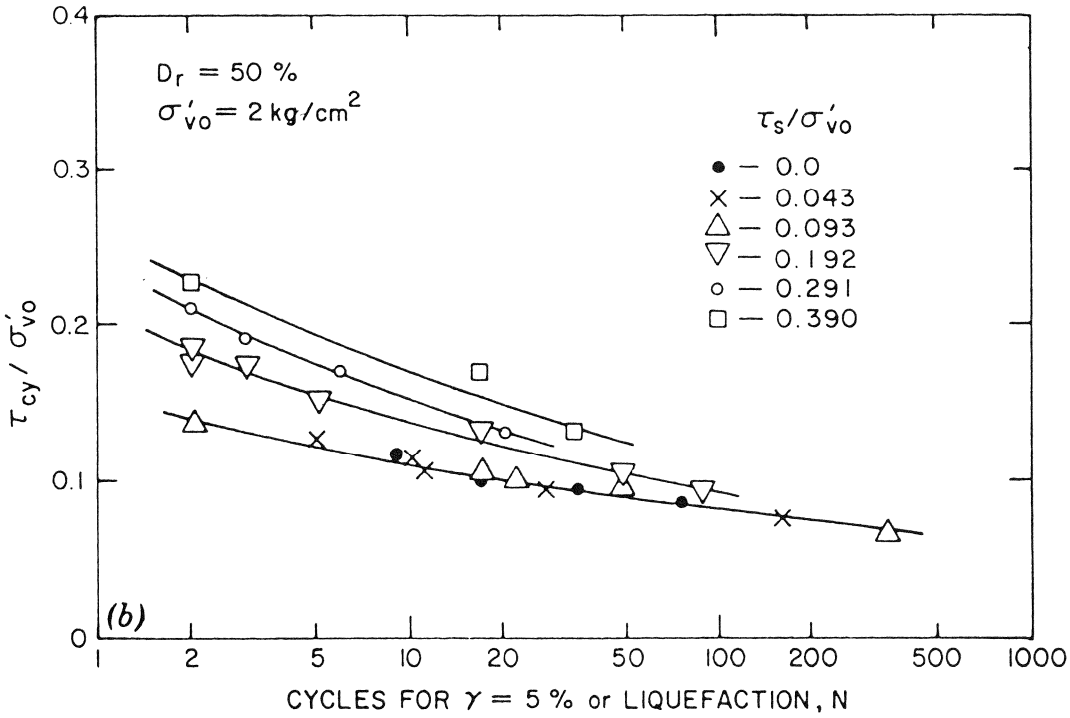

Fig. 11 Cyclic Shear Stress Required to Cause 5% Shear Strain (Loose Ottawa Sand, after Vaid and Finn, 1979)

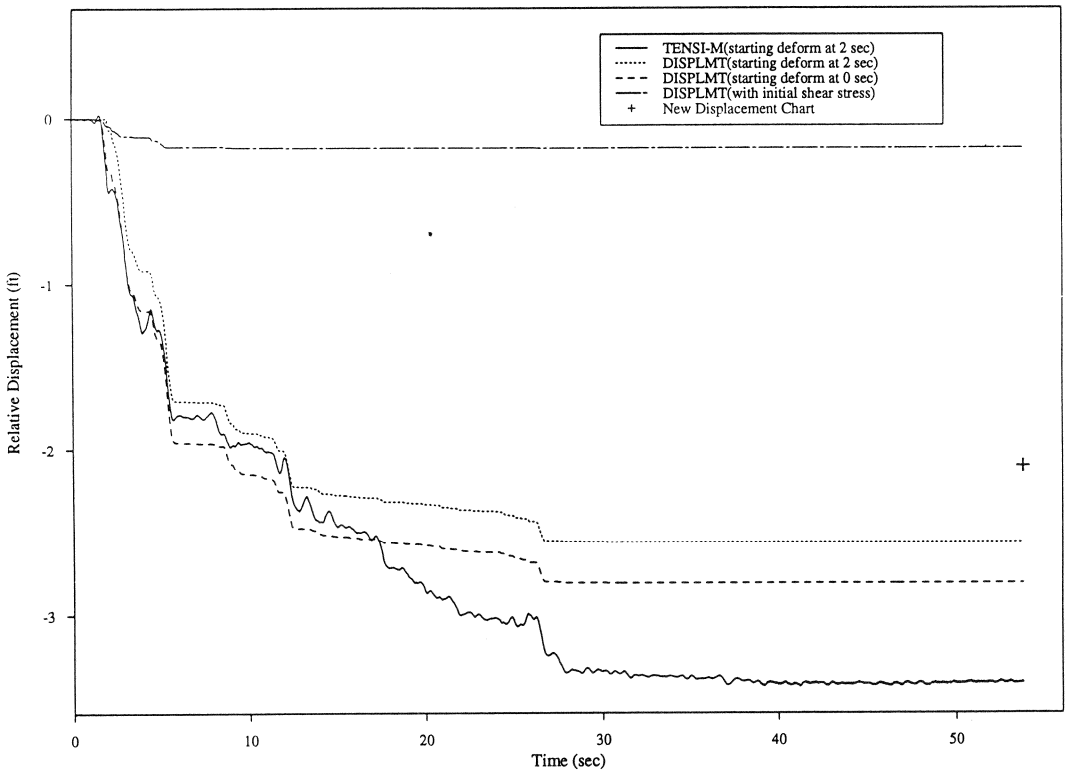

Fig. 12 Comparisons of Newmark Displacements for Liquefied Layer

Torsional Shear and Triaxial Compression Tests on Deformation Characters of Sands Before and After Liquefaction

Susumu YASUDA [1], Tamio MASUDA [2], Nozomu YOSHIDA [3]
Hideo NAGASE [4], Hiroyoshi KIKU [5]
Shigeru ITAFUJI [6], Keiichiro MINE [6] and Kazuya SATO [7]

ABSTRACT

The stress–strain relationships of sand after liquefaction were studied by conducting torsional shear and triaxial compression tests under several conditions. A prescribed number of cyclic loadings were applied first, then a monotonic loading was applied in undrained condition. The stress–strain relationships during the monotonic loading are discussed. The stress–strain curves were affected by the accumulated excess pore pressure ratio and by the severity of liquefaction. The shear and secant modulus decreased to less than 1/1000 due to liquefaction. The shear strain increased more than 10% with very low stress in the liquefied specimen. And, there exists a so called "reference strain at resistance transformation, γ_L" which increases with decreases in soil density, severity of liquefaction and fines content, and with increase with confining pressure.

---

[1] Professor, Dept. of Civil Eng., Tokyo Denki University, Saitama, Japan.
[2] Chief of Section, Tokyo Electric Power Co. Ltd., Tokyo, Japan.
[3] Head of Research, Engineering Research Institute, Sato Kogyo Co., Tokyo, Japan.
[4] Associate Professor, Dept. of Civil Eng., Kyushu Institute of Technology, Kitakyushu, Japan.
[5] Research Associate, Dept. of Civil Eng., Yokohama National University, Yokohama, Japan.
[6] Graduate Student, Dept. of Civil Eng., Kyushu Institute of Technology, Kitakyushu, Japan.
[7] Graduate Student, Dept. of Civil Eng., Yokohama National University, Yokohama, Japan.

INTRODUCTION

It is necessary to know the post liquefaction behavior of sand to estimate large displacement of ground or the settlement of structures due to liquefaction. However, this behavior has not been clarified because studies on liquefaction have focussed mainly on methods to estimate the occurrence of liquefaction.

Therefore, the stress–strain relationships of sand after liquefaction were studied by conducting torsional shear and triaxial compression tests under several conditions of density, confining pressure, fines content and severity of liquefaction. In the tests, a prescribed number of cyclic loading was applied to induce a prescribed excess pore water pressure. Then, a monotonic shear stress was applied.

TEST APPARATUS

Figure 1 shows the torsional shear test apparatus used in this study. Torsional test specimens were hollow cylinders of 10 cm in outer diameter, 6 cm in inner diameter and 10 cm in height. Torsional shear stress was applied at the top of specimens in a horizontal direction with rotational movement of a vertical plunger rod. The rotational movement of the rod was generated with a loading cylinder in cyclic shear stress and with an electric motor in monotonic shear tests. Torsional force, rotational angle and pore water pressure were measured by a torque pick up, a potentiometer and a pressure transducer, respectively. One pair of gap sensors were also used for measuring very small rotational angles.

In triaxial compression tests, column cylindrical specimen of 7.5 cm in diameter and 15 cm in height were used. Axial force, axial displacement and pore water pressure were measured by a road cell, a differential displacement transducer and a pressure transducer, respectively.

TEST CONDITIONS

The sands used in this study were Toyoura sand (G_S=2.64, e_{max}=0.977, e_{min}=0.605, D_{50}=0.16mm, and no content finer) and Narita sand (G_S=2.70, e_{max}=1.371, e_{min}=0.773 D_{50}=0.12mm, and a fine content of 15.2%), as shown in Fig.2.

Most tests were performed using Toyoura sand, which is the standard sand in Japan. The tests were conducted under the following test conditions to clarify the effects of density, confining pressure, excess pore pressure, fines content and severity of liquefaction.

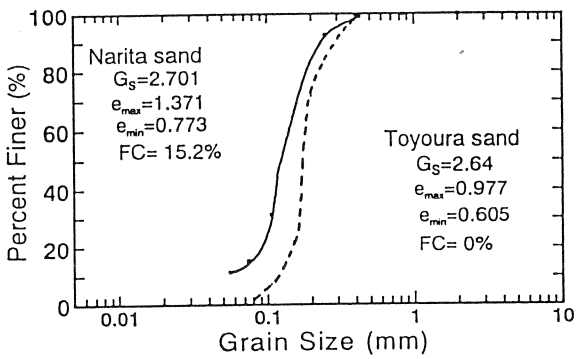

Fig.2 Grain size distribution curves of Toyoura sand and Narita sand

In torsional shear tests

(1) relative density: Dr=0%, 30%, 50% and 70%

(2) effective confining pressure: σ_0' =0.25 kgf/cm^2, 0.5 kgf/cm^2 and 1.0 kgf/cm^2

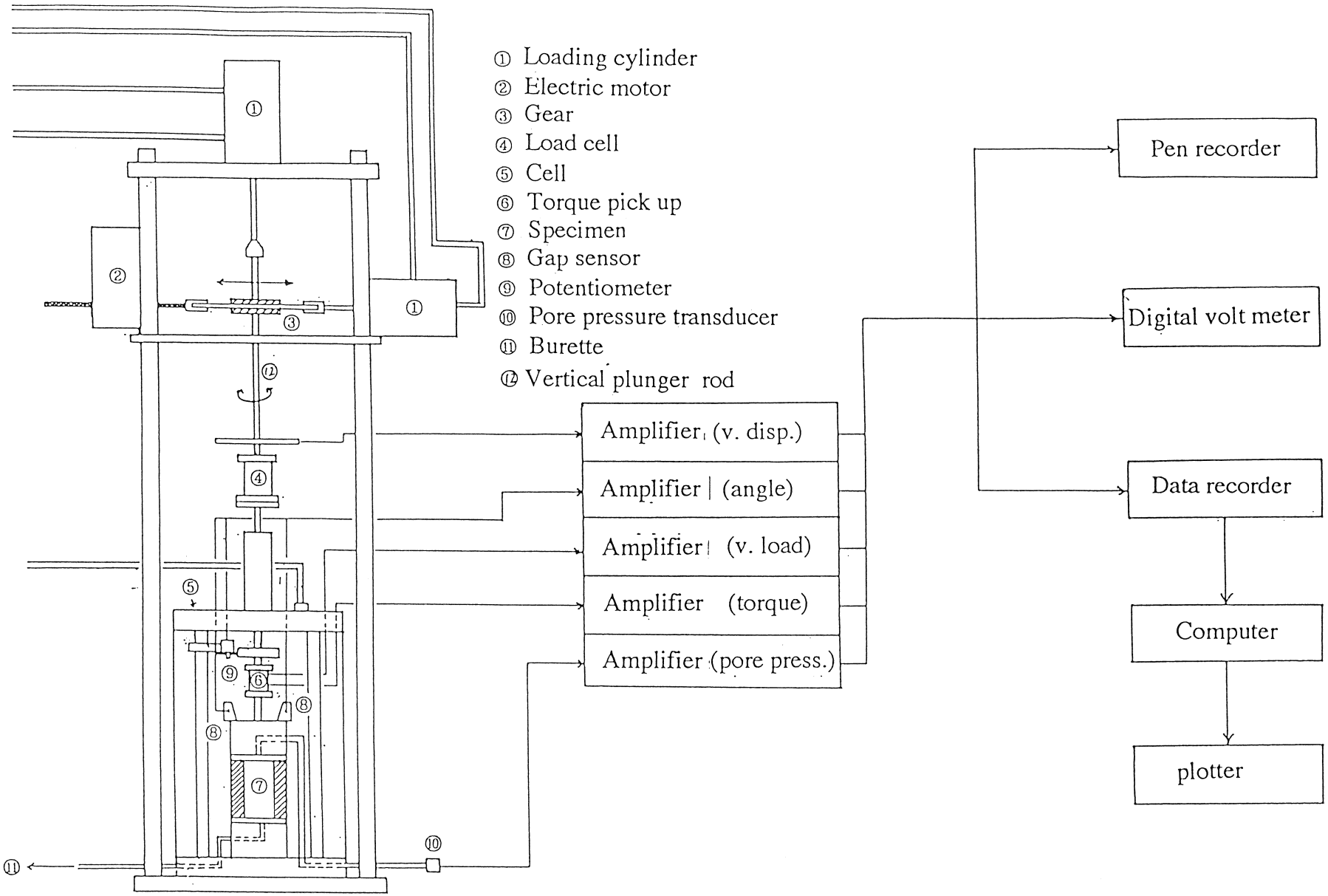

Fig.1 Torsional shear test apparatus

Table 1 Test conditions

No.	Test Device	Sand	Dr %	σ_o' kgf/cm²	$\Delta u/\sigma_v'$ or F_L	No.	Test Device	Sand	Dr (%)	σ_o' kgf/cm²	$\Delta u/\sigma_v'$ or F_L
1	Torsional	C	-1.9	0.5	0	37	Torsional	C	65.4	1.0	0
2	Torsional	C	-5.2	0.5	1.0(F_L=1.0)	38	Torsional	C	73.5	1.0	0.9
3	Torsional	C	29.9	0.5	0	39	Torsional	C	71.9	1.0	1.0(F_L=1.0)
4	Torsional	C	32.6	0.5	1.0(F_L=1.0)	40	Torsional	C	69.4	1.0	1.0(F_L=0.95)
5	Torsional	C	30.5	0.5	1.0(F_L=0.95)	41	Torsional	C	69.9	1.0	1.0(F_L=0.9)
6	Torsional	C	29.2	0.5	1.0(F_L=0.9)	42	Torsional	C	34.7	0.25	0
7	Torsional	C	31.5	0.5	0.3	43	Torsional	C	31.9	0.25	0.9
8	Torsional	C	30.3	0.5	0.6	44	Torsional	C	31.9	0.25	1.0(F_L=1.0)
9	Torsional	C	34.7	0.5	0.9	45	Torsional	C	33.4	0.25	1.0(F_L=0.95)
10	Torsional	C	55.2	0.5	0	46	Torsional	C	33.2	0.25	1.0(F_L=0.9)
11	Torsional	C	53.9	0.5	1.0(F_L=1.0)	47	Torsional	C	45.5	0.25	0
12	Torsional	C	51.7	0.5	1.0(F_L=0.95)	48	Torsional	C	53.5	0.25	0.9
13	Torsional	C	53.1	0.5	1.0(F_L=0.9)	49	Torsional	C	50.0	0.25	1.0(F_L=1.0)
14	Torsional	C	48.3	0.5	0.6	50	Torsional	C	53.1	0.25	1.0(F_L=0.95)
15	Torsional	C	53.0	0.5	0.9	51	Torsional	C	47.9	0.25	1.0(F_L=0.9)
16	Torsional	C	68.2	0.5	0						
17	Torsional	C	69.9	0.5	1.0(F_L=1.0)	52	Triaxial	C	27.8	0.5	0
18	Torsional	C	71.3	0.5	1.0(F_L=0.95)	53	Triaxial	C	28.2	0.5	0.36
19	Torsional	C	68.4	0.5	1.0(F_L=0.9)	54	Triaxial	C	25.3	0.5	0.52
20	Torsional	C	70.2	0.5	0.6	55	Triaxial	C	26.1	0.5	0.9
21	Torsional	C	71.8	0.5	0.9	56	Triaxial	C	23.2	0.5	1.0(F_L=1.0)
22	Torsional	C	-2.2	1.0	0	57	Triaxial	C	49.5	0.5	0
23	Torsional	C		1.0	0.9	58	Triaxial	C	46.4	0.5	0.26
24	Torsional	C	-3.6	1.0	1.0(F_L=1.0)	59	Triaxial	C	49.3	0.5	0.38
25	Torsional	C	-4.6	1.0	1.0(F_L=0.95)	60	Triaxial	C	48.7	0.5	0.94
26	Torsional	C	-4.8	1.0	1.0(F_L=0.9)	61	Triaxial	C	48.0	0.5	1.0(F_L=1.0)
27	Torsional	C	32.7	1.0	0	62	Triaxial	F	38.6	0.5	0
28	Torsional	C	34.5	1.0	0.9	63	Triaxial	F	38.0	0.5	0.44
29	Torsional	C	25.3	1.0	1.0(F_L=1.0)	64	Triaxial	F	39.9	0.5	0.56
30	Torsional	C	25.8	1.0	1.0(F_L=0.95)	65	Triaxial	F	38.8	0.5	0.9
31	Torsional	C	27.3	1.0	1.0(F_L=0.9)	66	Triaxial	F	38.0	0.5	1.0(F_L=1.0)
32	Torsional	C	51.4	1.0	0	67	Triaxial	F	54.8	0.5	0
33	Torsional	C	53.3	1.0	0.9	68	Triaxial	F	54.8	0.5	0.40
34	Torsional	C	46.4	1.0	1.0(F_L=1.0)	69	Triaxial	F	53.3	0.5	0.56
35	Torsional	C	51.0	1.0	1.0(F_L=0.95)	70	Triaxial	F	49.6	0.5	0.9
36	Torsional	C	45.9	1.0	1.0(F_L=0.9)	71	Triaxial	F	53.0	0.5	1.0(F_L=1.0)

sand: C: Clean sand (Toyoura sand)
F: Sand with fines (Narita sand)

(3) excess pore pressure ratio: $\Delta u/\sigma_0' = 0$, 0.3, 0.6, 0.9 and 1.0
(4) severity of liquefaction: FL=1.0, 0.95 and 0.9

Special tests were also carried out in which the excess pore pressure dissipated after liquefaction up to $\Delta u/\sigma_0' = 0.9$ or 0.6 by drainage, then monotonic shear stresses were applied. The test conditions of all the specimens are listed in Table 1.

In triaxial compression tests
(1) relative density: Dr= 30% and 50%
(2) effective confining pressure: $\sigma_0' = 0.5$ kgf/cm^2
(3) excess pore pressure ratio: $\Delta u/\sigma_0' = 0$, 0.4, 0.6, 0.9 and 1.0
(4) fines content: FC=0% (Toyoura sand) and 15.2% (Narita sand)

TEST PROCEDURES

Sample preparation technique

In the tests for relative densities of 30%, 50% and 70%, specimens were prepared by the air–pluviation method; pouring dry sand into molds through a funnel from constant heights. The density of the specimens was controlled by the height. In the tests for 0% relative density, which is very loose, a special technique for preparing the specimen. was adopted; a slightly wet sand with 1–2% moisture content was carefully filled into a mold without tamping. After being saturated, samples were consolidated isotropically at a prescribed effective confining pressure($\sigma_0' = 0.25$, 0.5 and 1.0 kgf/cm^2) with a back pressure, σ_{BP}, of 2.0 kgf/cm^2 in undrained condition.

Loading pattern in torsional shear tests

In torsional shear tests, a prescribed number of cyclic loading of 0.1 Hz was applied to the specimens in undrained conditions. The cyclic loading was terminated when the excess pore pressure ratio, or FL, reached a prescribed value. Then, a monotonic loading was applied during undrained condition with a relatively high speed of $\gamma = 10\%$ in a minute, as shown in Fig. 3. The amplitude of cyclic loading was controlled to a prescribed value which produced liquefaction in 20 cycles. Therefore, the amplitude of each density was different.

If the number of cycles of cyclic loading was less than 20, liquefaction did not occur However, the stress–strain relationships during the monotonic loading were affected by the excess pore pressure induced during the cyclic loading. Cyclic loading was terminated when $\Delta u/\sigma_0'$ reached 0 or 0.3, 0.6, 0.9, 1.0. The number of cycles was 0 when $\Delta u/\sigma_0' = 0$ and 20 when $\Delta u/\sigma_0'$ was 1.0.

On the contrary, liquefaction occurred when the number of cycles during the cyclic loading exceeded 20, and the severity of liquefaction increased with the number of cycles. The severity of liquefaction was indicated by the factor of safety against liquefaction, FL, in this study. If the number of cycles, N, was 20, FL equalled 1.0. In the case of

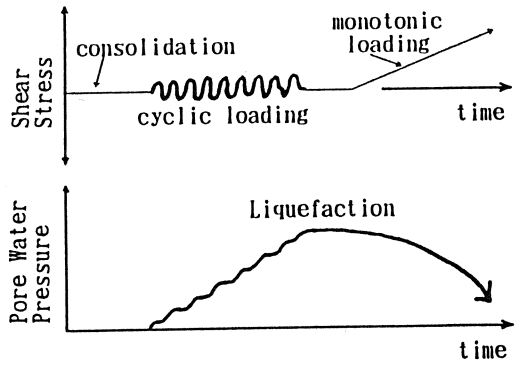

Fig.3 Procedure of cyclic loading and monotonic loading

N>20, N for prescribed FL can be calculated by the following equation, which was derived based on the normalizing method proposed by Tatsuoka et al.(1980).

$$N=20\,(FL)^{1/b} \qquad (1)$$

where: b=−0.17 in clean sand

Therefore, cyclic loading was terminated at N=27 and N=37 in FL=0.95 and FL=0.9, respectively.

Figure 4 shows shear resistance of inner and outer menbrane without a specimen. The shear resistance of membranes was deducted from the measured shear stress.

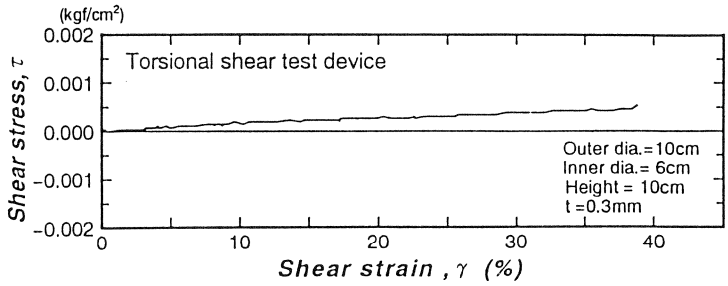

Fig.4 Shear resistance of inner and outer membranes

Loading pattern in triaxial compression tests

In triaxial compression tests, the number of cycles of cyclic loading was fixed for 20 cycles in all specimens. The amplitude of the cyclic loading was controlled to accumulate a prescribed value of excess pore pressure. Therefore, in case of fully−liquefied condition, FL=1 and $\Delta u/\sigma_0' = 1.0$, the cyclic shear stress ratio which produce liquefaction in 20 cycles, $R_{l,20}$, was applied. If the amplitude of cyclic loading was smaller than $R_{l,20}$, liquefaction did not occur and the accumulated excess pore pressure ratio was less than 1.0.

TEST RESULTS

Test Results for Different Pore Pressure Ratio

Relationships among shear stress, τ ,excess pore pressure, Δu, and shear strain, γ , in the monotonic loading are discussed in this study. Figure 5 shows the stress−strain curves and the excess pore pressure−strain curves in the case of $\Delta u/\sigma_0'=0$. Shear stress increased rapidly with shear strain up to $\gamma \fallingdotseq 1\%$. Then, the shear stress increased gradually with shear strain in the cases of Dr ≧ 30%.

On the contrary, the shear stress decreased gradually in the case of Dr=−1.9%. Pore pressure increased with shear strain up to $\gamma \fallingdotseq 2\%$, then decreased, in the cases of Dr ≧ 30%. However, the pore water pressure did not decrease in the case of Dr=−1.9%.

Figure 6 compares the

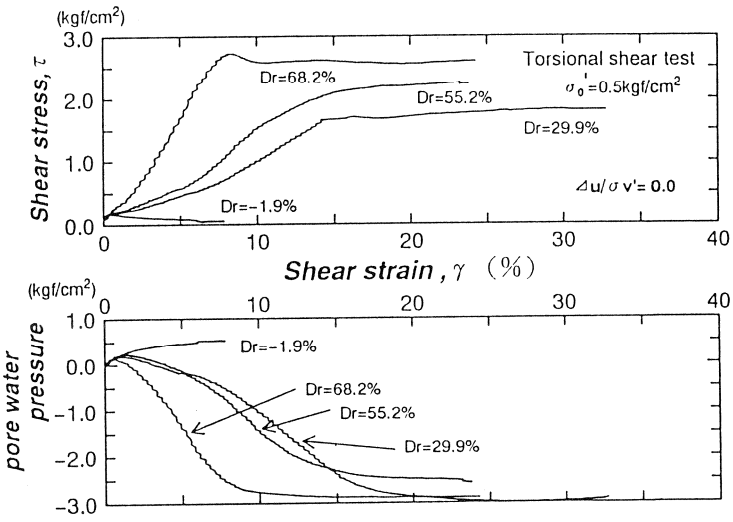

Fig.5 Stress-strain curves and strain-pore pressure curves ($\Delta u/\sigma_0'$=0,static)

stress paths of tests shown in fig. 5. It can be seen that the stress path of Dr=−1.9% proceeded toward the origin of the coordinate axes after having a peak value of shear stress.

Figure 7(a) and Figure 7(b) in which the scales of the axes are enlarged, show stress−strain curves and excess pore water pressure−strain curves in the case of $\Delta u/\sigma_0'$ =1.0 and FL=1.0. Shear strain increased with very low shear stress up to γ >10%. Then, after a resistance transformation point the shear stress increased comparatively rapidly with shear strain, following the decrease of pore water pressure in the cases of Dr ≧ 30%. However, quite little shear stress was generated up to γ =47% without dropping the pore water pressure in the case of Dr=−5.2%.

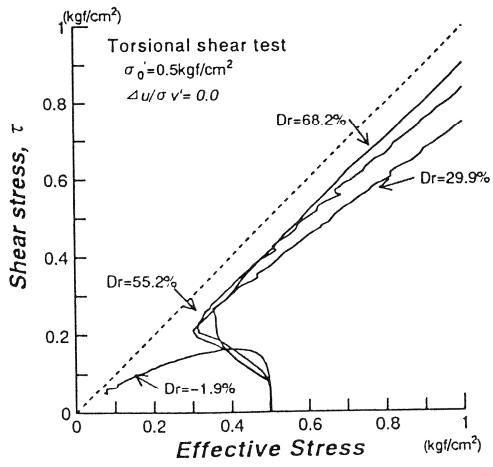

Fig.6 Comparison of stress paths in different densities

Figure 8(a), (b) and (c) compare the stress−strain curves in different pore water pressure ratios and FLs. As shown in these figures, shear stress in some shear strain decreased with the pore water pressure ratio.

Test Results for Different FL

Test results for FL=0.95 and 0.9 are shown in Fig.9(a) and (b). The curves were similar to those of FL=1.0. However, for the similar FL, the resistance transformation point appeared at large strain.

Effect of Drainage

Figure 10(a) and (b) show results of the special tests in which excess pore water pressure dissipated up to $\Delta u/\sigma_0'$=0.9 or 0.6. As shown in these figures, the decreased excess pore water pressure recovered up to $\Delta u/\sigma_0'$=1.0 in small strain. However, shear strains at the resistance transformation points were smaller than those of the data without dissipation.

Effect of Confining Pressure

Figure 11(a), (b), (c) and (d) show the change of stress−strain curves with the development of liquefaction in different confining pressures and relative densities. Comparing the stress−strain curves in the same conditions of relative density and pore pressure ratio, the shear stress in some shear strain increased with the confining pressure when the FL is greater than 1.0. On the contrary, the shear stress in some strain decreased with the confining pressure when the FL is less than 1.0.

Effect of Fine Content

Figure 12(a) and (b) show the relationships between the deviator stress, $\sigma_1-\sigma_3$, and the axial strain, ε, of Toyoura sand during the monotonic loadings using triaxial compression test device. The change of stress−strain curves with different pore pressure ratio in triaxial test were similar to those in torsional test. Figure 13(a) and (b) compare the stress−strain curves of Narita sand, which contains the fines of 15.2%, during the monotonic loading. As shown in Fig.12 and Fig.13, flow deformation was observed also in triaxial tests when the excess pore pressure ratio almost 1.0. The axial strain with low deviator stress was larger in case of clean sand. However, the deviator stress recovered rapidly with axial strain in case of clean sand as compared with that for fine sand.

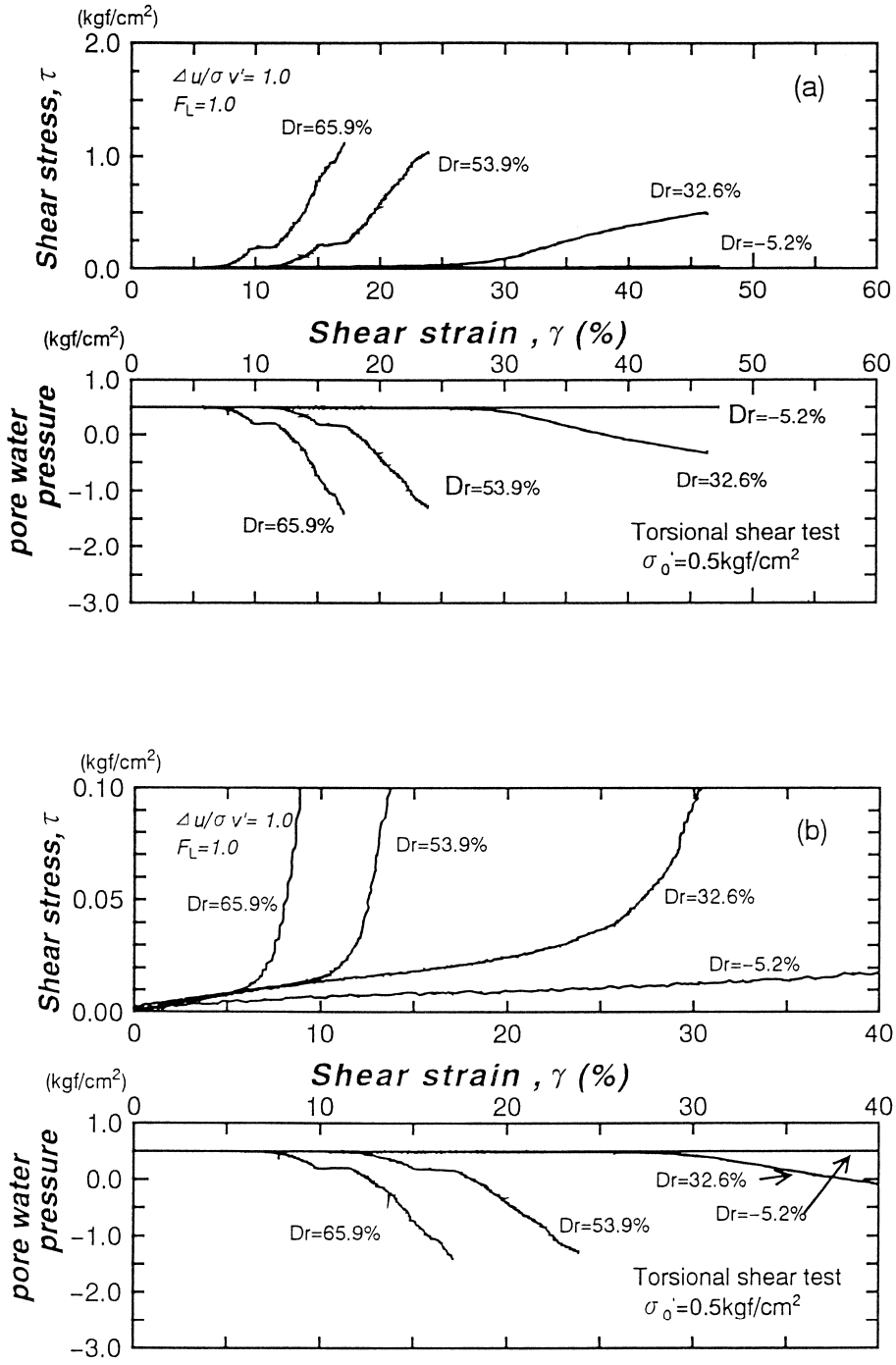

Fig.7 Stress-strain curves and strain-pore pressure curves ($\Delta u/\sigma_0'$=1.0, F_L=1.0)

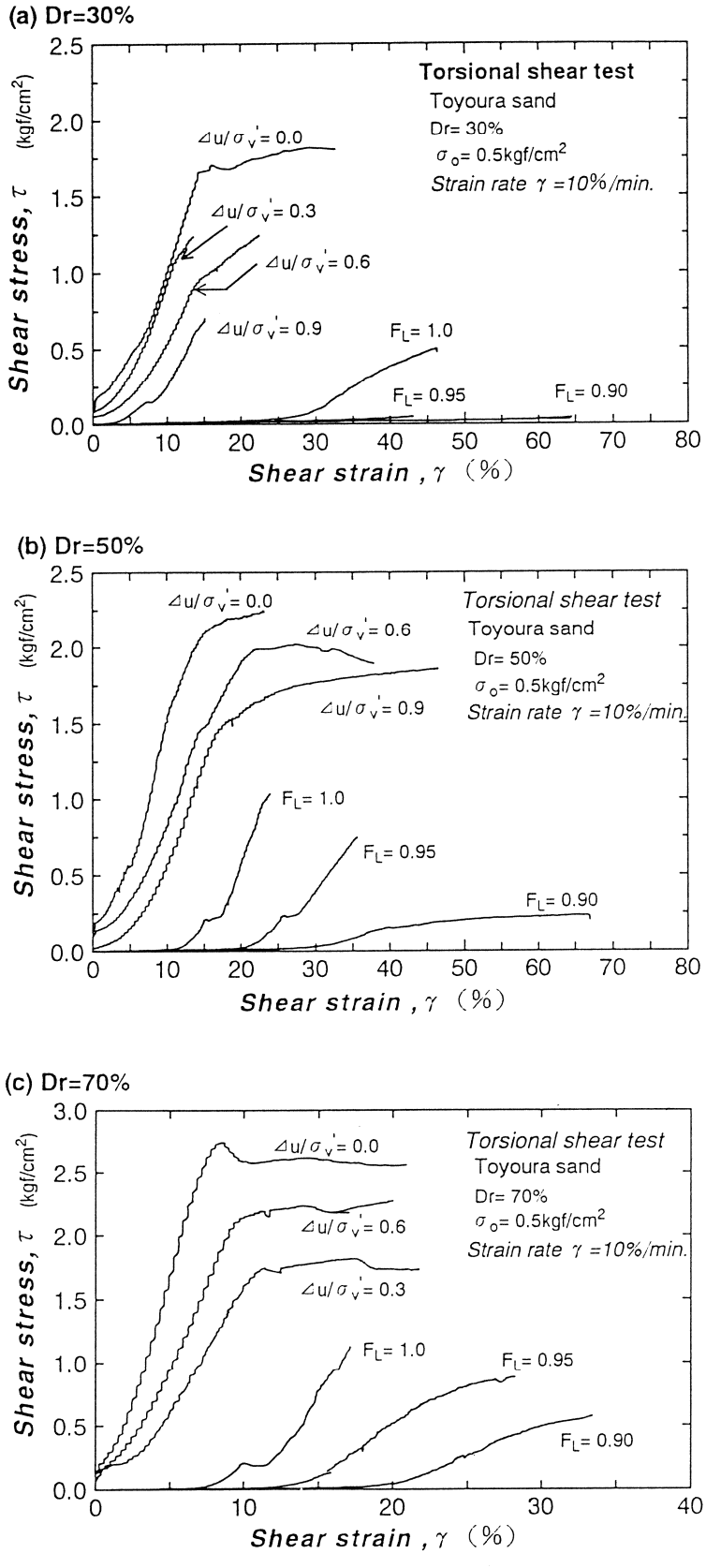

Fig.8 Comparison of stress–strain curves in different densities

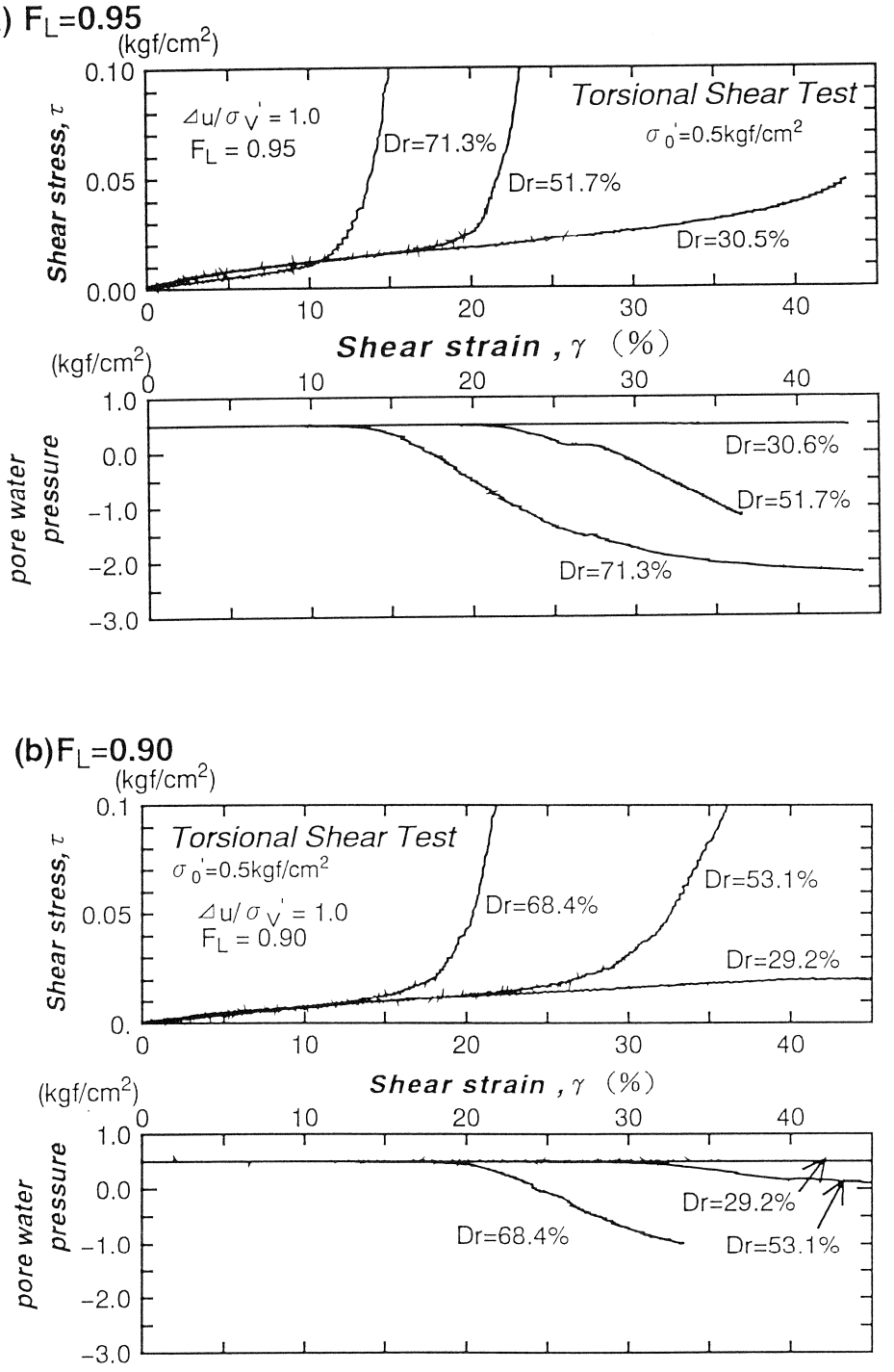

Fig.9 Stress-strain curves and strain-pore pressure curves ($\Delta u/\sigma_0'$=1.0, F_L<1.0)

(a) $\Delta u/\sigma_0' = 1.0 \rightarrow 0.9$

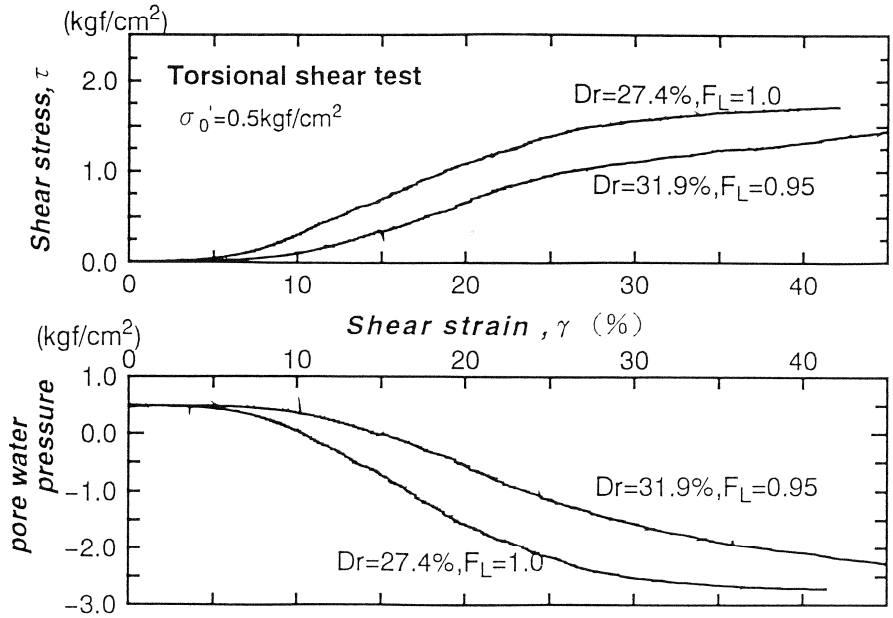

(b) $\Delta u/\sigma_0' = 1.0 \rightarrow 0.6$

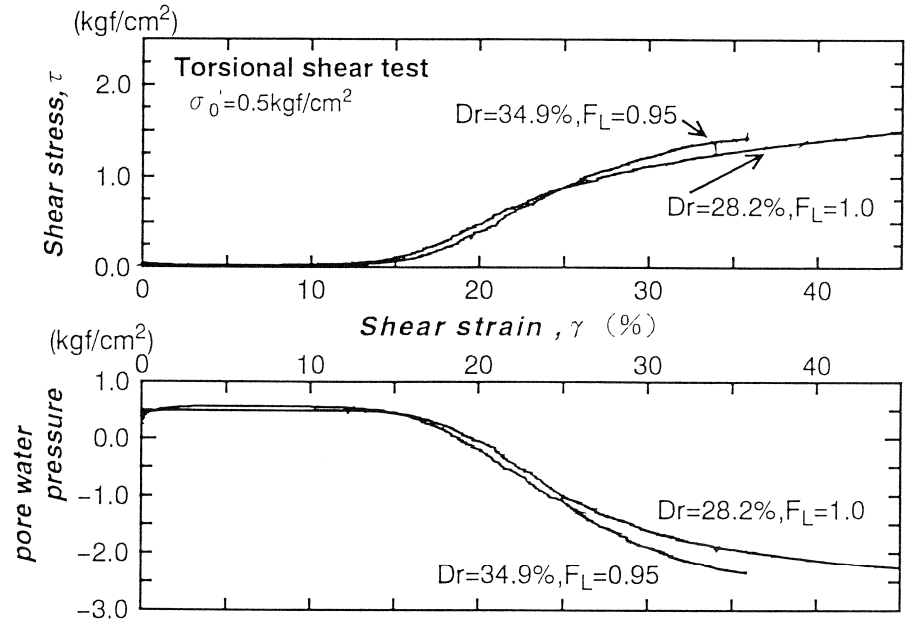

Fig.10 Stress-strain curves and strain-pore pressure curves
($\Delta u/\sigma_0'$=1.0→0.9 or 0.6, F_L=1.0 or 0.9)

(a) Dr=50%, σ_0'=1.0kgf/cm^2

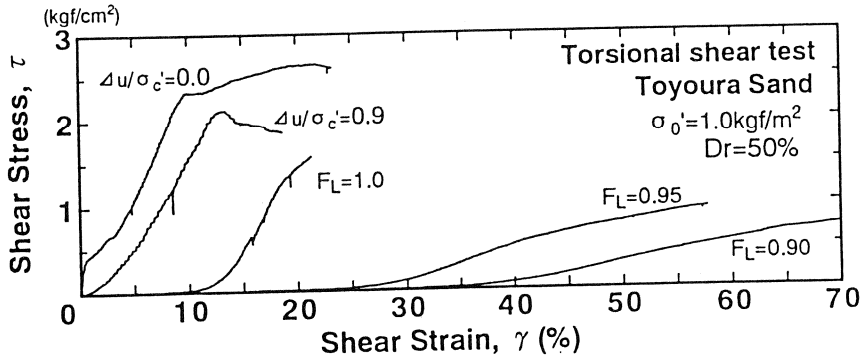

(b) Dr=50%, σ_0'=0.25kgf/cm^2

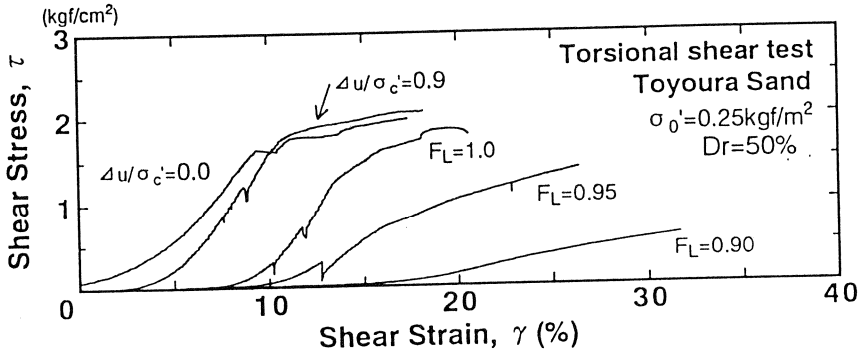

(c) Dr=70%, σ_0'=1.0kgf/cm^2

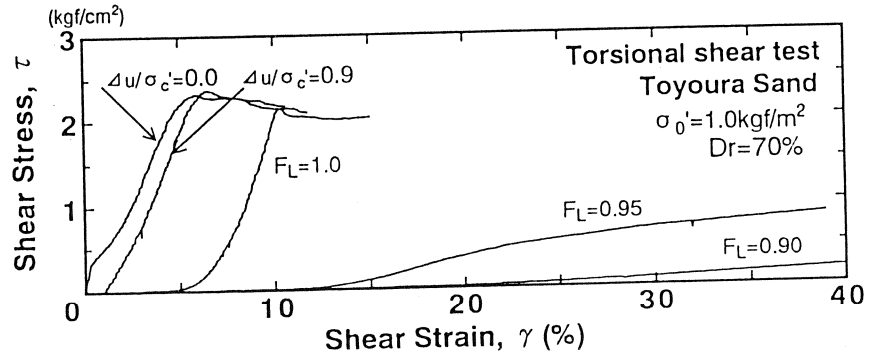

(d) Dr=30%, σ_0'=0.25kgf/cm^2

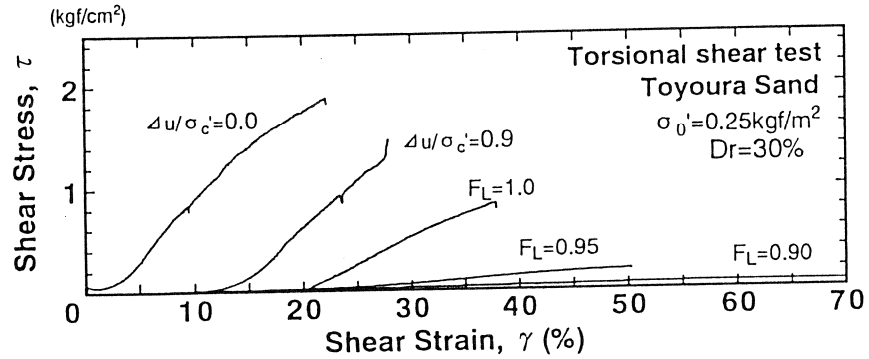

Fig.11 Stress-strain curves in different confining pressures

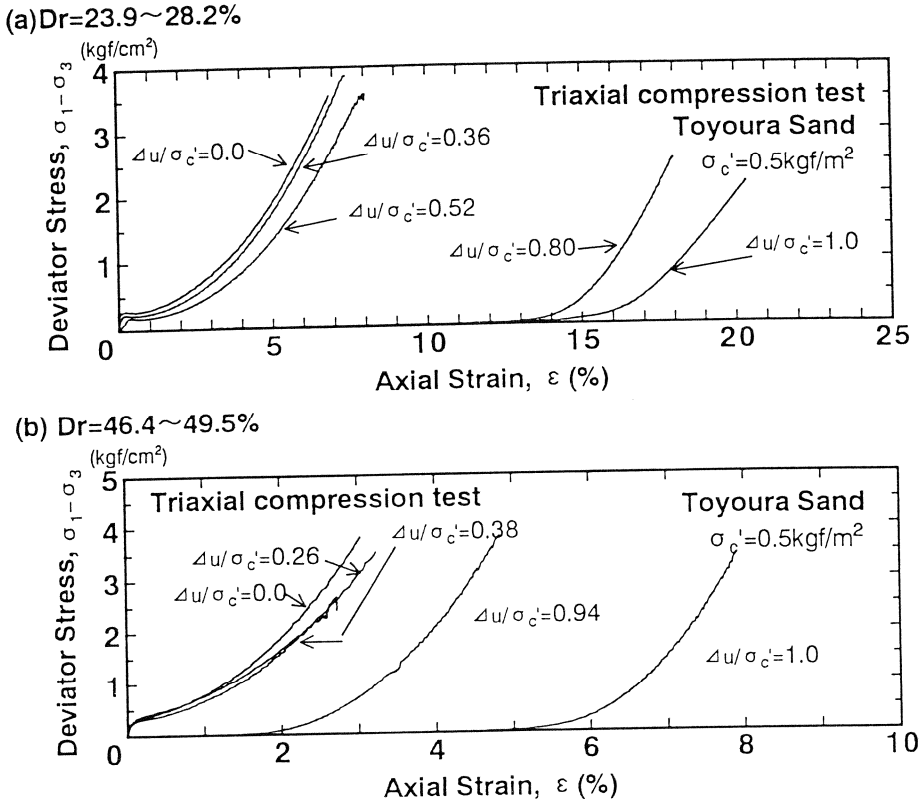

Fig.12 Stress-strain curves in triaxial compression tests (Toyoura sand)

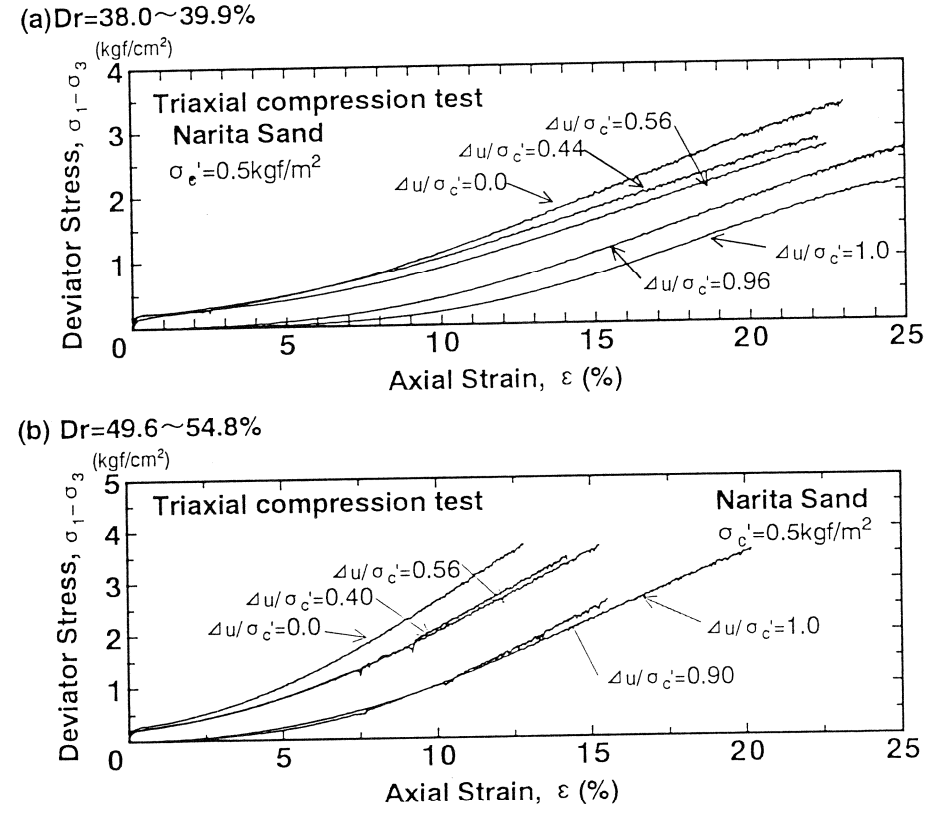

Fig.13 Stress-strain curves in triaxial compression tests (Narita sand)

RELATIONSHIPS BETWEEN $G_i / G_{0.i}$ *AND* $\Delta u/\sigma_0'$ *OR* FL

The rate of reduction of shear modulus, $G_i / G_{0.i}$, was calculated from the torsional test results to know the reduction rate of the rigidity of sand due to liquefaction. $G_{0.i}$ and G_i were defined as the secant moduli of the stress−strain curves at γ =0.1% in the case of $\Delta u/\sigma_0'$=0 and at γ =0.1 or 1.0, 3.0% in the case of $\Delta u/\sigma_0'$>0, respectively. Figure 14 shows relationships between $G_i/G_{0.i}$ and $\Delta u/\sigma_0'$. It can be seen that $G_i / G_{0.i}$ decreased with an increase in $\Delta u/\sigma_0'$ and reached a vary small value. If the $G_{0.i}$ at γ =0.1% and G_i at γ =3.0% are assumed as shear moduli of the ground before and after liquefaction, respectively, $G_i/G_{0.i}$ in Fig. 14(a), (b) and (c) are almost 0.001. This means that the shear modulus of the ground decreased to almost 1/1000 due to liquefaction.

Figure 15 shows relationships between FL and $G_i/G_{0.i}$. FL values greater than 1.0 were also calculated by Eq. (1). As shown in this figure, G_i decreased more than 1/1000 in the range of FL<1.0. Therefore, it can be said roughly that the shear modulus decreases to less than 1/1000 due to severe liquefaction, and varies with the severity of liquefaction.

Yasuda et al. (1992) proposed a simplified analytical method to estimate large ground displacement due to liquefaction. As the parameter $G_i/G_{0.i}$ is used in the method, test results in this study will be utilized in such a kind of analysis.

In the same manner, the rate of reduction of secant modulus, $E_i / E_{0.i}$, was calculated from the triaxial test results. Figure 16(a) and (b) show the relationships between $E_i / E_{0.i}$ and $\Delta u/\sigma_0'$ in Toyoura sand. It can be seen that $E_i / E_{0.i}$ decreased with an increase in $\Delta u/\sigma_0'$ and reached a vary small value, similar in the torsional shear tests. Figure 17(a) and (b) show the relationships between $E_i / E_{0.i}$ and $\Delta u/\sigma_0'$ in Narita sand. The tendency of reduction curves of Narita sand were a little different from those of Toyoura sand, but the obvious difference of the reduction rate between Toyoura sand and Narita sand could not be seen from these figures.

RELATIONSHIPS AMONG γ_L, Dr, FL *AND* σ_0'

As shown in Fig. 7, 8 and 9, shear stress increased comparatively rapidly after a resistance transformation point. The amount of strain up to the resistance transformation point is called here the "value of strain during low resistance, γ_L" as shown in Fig. 18. γ_L thus defined are plotted with Dr and FL in Fig. 19(a), (b) and (c). γ_L increased with decreases in Dr and FL and with increase in σ_0'. In the case of Dr=30%, FL=0.9 and σ_0'=0.5 kgf/cm^2, γ_L reached a very large strain, almost 60%.

A detailed method for the estimation of large ground displacements due to liquefaction based on the γ_L or stress−strain curves studied here will be developed hereafter. However, a simple estimation for permanent ground displacement due to liquefaction is tried here, based on Fig. 19 under the following assumptions;

① A model ground with gentle slope is liquefied from ground surface to the depth of −10m. FL, Dr and unit weight γ_t of the liquefied layer are 0.95, 30% and 1.9 tf/m^3, respectively.

② Shear strain up to γ_L induces due to liquefaction in the liquefied soil.

Figure 20 shows the distribution of the estimated permanent ground displacement. As shown in this figure, the displacement increases from the bottom of the liquefied layer to the ground surface. And the permanent ground displacement at ground surface can be estimated as 3.5m.

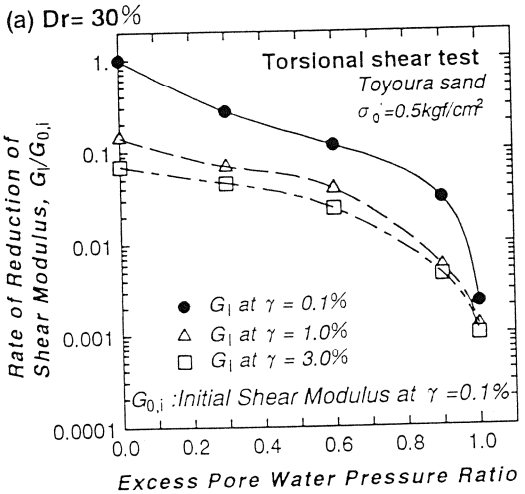

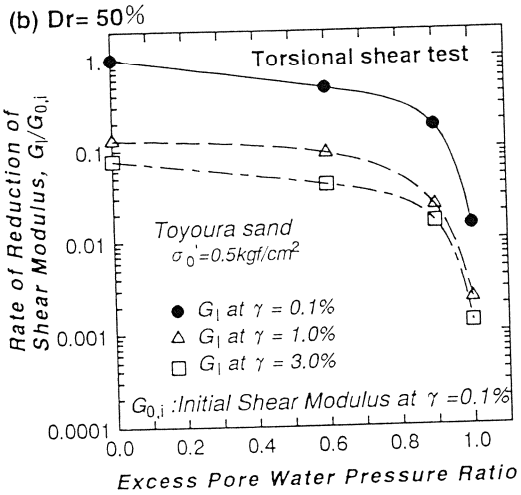

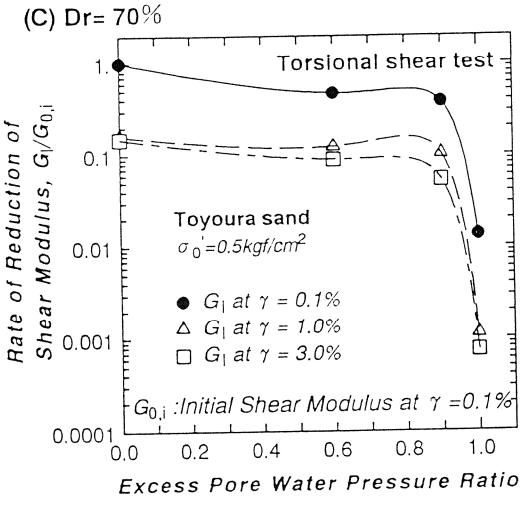

Fig.14 Relationships between $G_l/G_{0,i}$ and $\Delta u/\sigma_0$

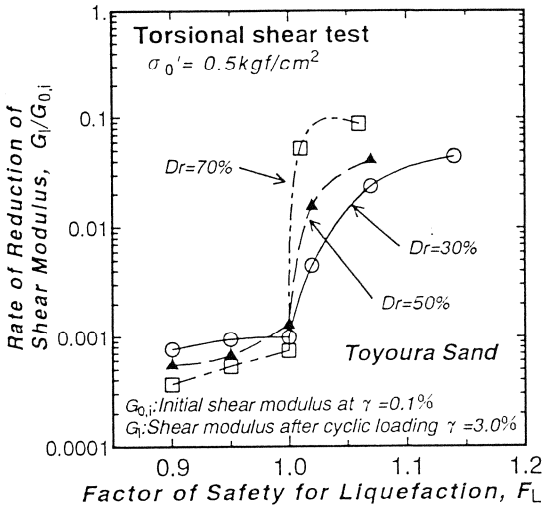

Fig.15 Relationships between $G_l/G_{0,i}$ and F_L

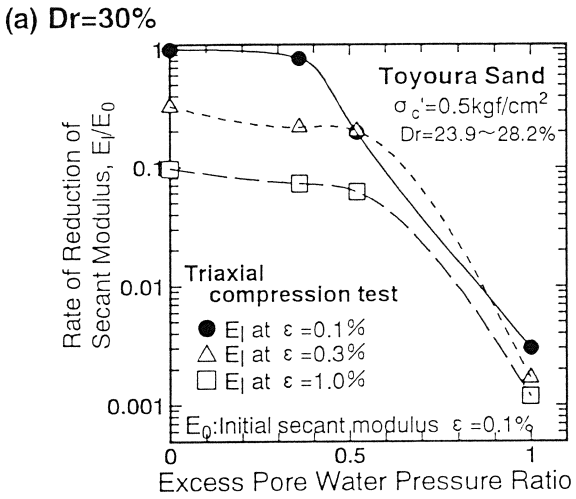

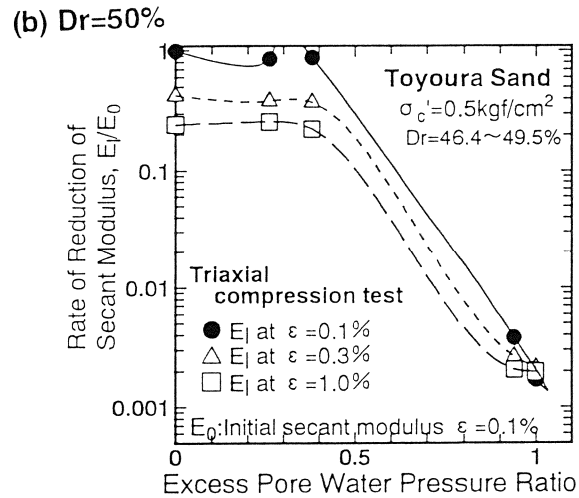

Fig.16 Relationships between $E_l/E_{0,i}$ and $\Delta u/\sigma_0'$

(a) Dr=30%

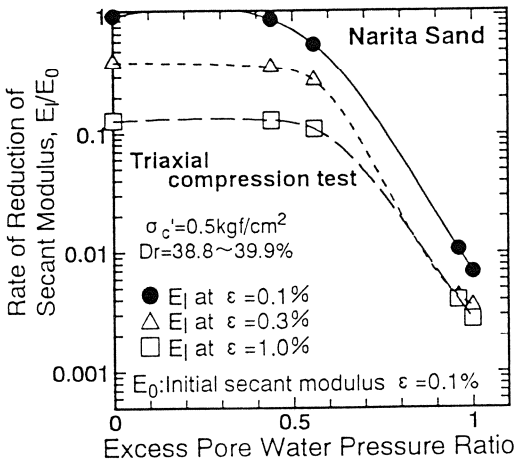

(b) Dr=50%

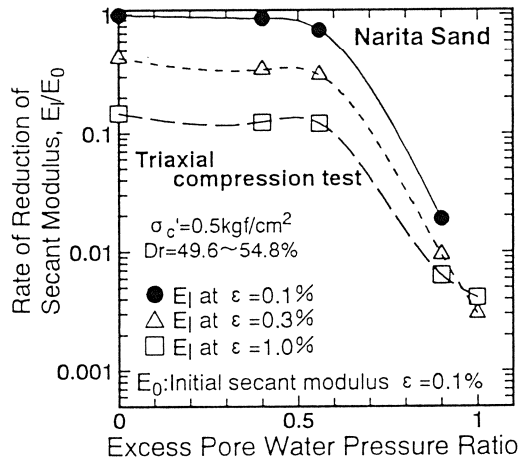

Fig.17 Relationships between $E_I/E_{0,i}$ and $\Delta u/\sigma_0'$

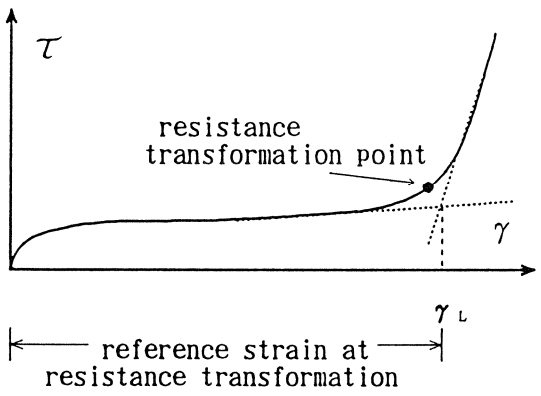

Fig.18 Definition of γ_L

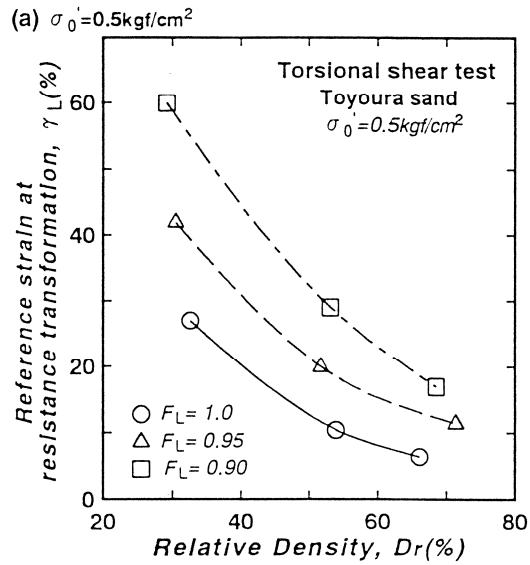

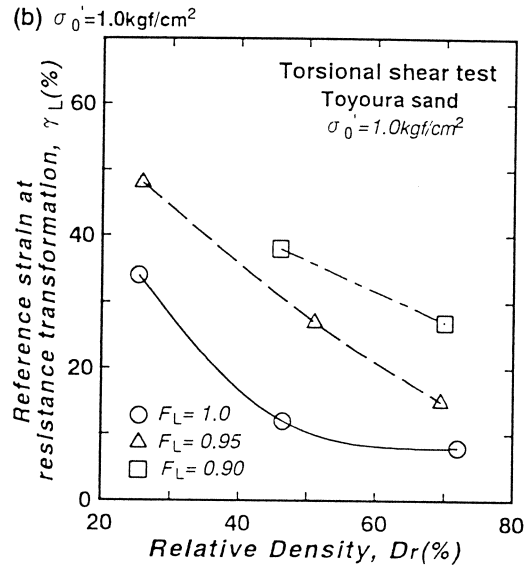

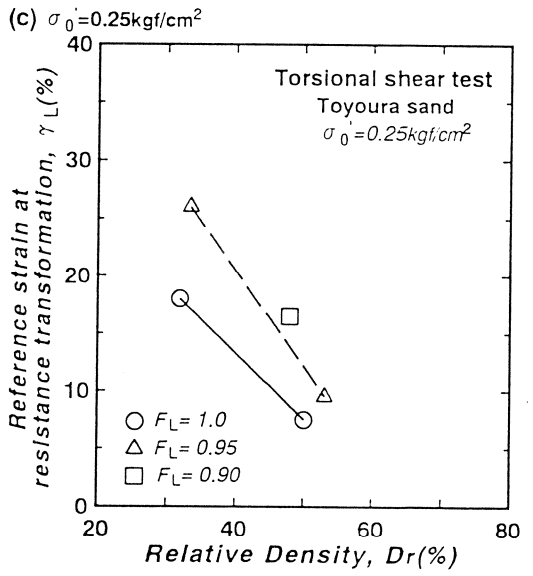

Fig.19 Relationships among γ_L,Dr and F_L

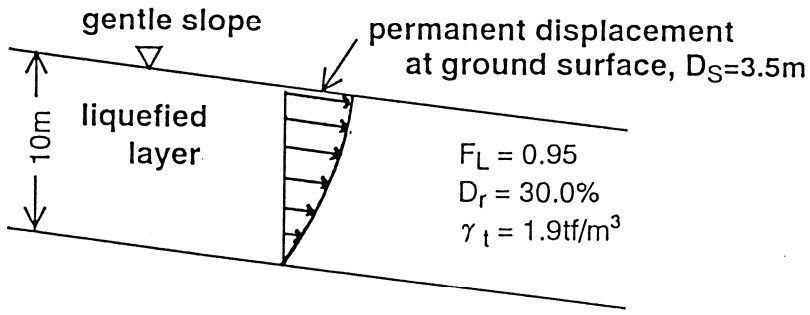

Fig.20 A simple estimation for permanent ground displacement

CONCLUSIONS

Torsional and triaxial shear tests on saturated sands were conducted under several conditions to ascertain the post liquefaction behavior of the sand. The main conclusions are as follows:

(1) stress–strain curves are affected by the excess pore water pressure ratio, $\Delta u/\sigma_0'$, by the factor of safety against liquefaction, FL, and by fine content of the soil.

(2)the shear modulus decreases to 1/1000 or less due to liquefaction and varies with FL.

(3) there exists a so called "reference strain at resistance transformation, γ_L," which increased with decreases in relative density and FL and with increase in with σ_0'.

ACKNOWLEDGEMENTS

Valuable discussions by the members of a committee of the Association for the Development of Earthquake Prediction in Japan. The tests were carried out in the laboratories of Kyushu Institute of Technology and Yokohama National University. The authors would like express their thanks also to Prof. G. Imai of Yokohama National University and Mrs. K. Ushijima of Kyushu Institute of Technology.

REFERENCES

1) Tatsuoka, F., Yasuda, S., Iwasaki, T. and Tokida, K.: Normalized Dynamic Undrained Strength of Sand Subjected to Cyclic and Random Loading, Soils and Foundations, Vol.20, No.3, pp.1–16, 1980.

2) Yasuda, S., Nagase, H., Kiku, H. and Uchida, Y.: The mechanism and A Simplified Procedure for the Analysis of Permanent Ground Displacement due to Liquefaction, Soils and Foundations, Vol.32, No.1, pp.149–160, 1992.

Ground Motion Characteristics and their Relation to Soil Liquefaction at the Wildlife Liquefaction Array, Imperial Valley, California.

Kayen R.E.[1], Mitchell, J.K.[2], and Holzer, T.L.[3]

Abstract

We use the earthquake shaking severity parameter Arias intensity, I_h, to assess the site specific characteristics of ground motion, and investigate the relation of those characteristics to soil liquefaction occurrence at the Wildlife liquefaction array, in response to the Elmore Ranch and Superstition Hills earthquakes of November 23 and 24, 1987. We found that for both earthquake events, the Arias intensities calculated from motions recorded by the downhole seismometer were significantly less than those calculated from recordings of the surface seismometer. By normalizing the downhole cumulative Arias intensity-time history with that of the surface record, it can be shown that the ratio of the recorded intensity response of the downhole seismometer to that of the surface seismometer was essentially a constant during the Elmore Ranch event, when no excess pore-water pressures were observed. In the Superstition Hills event record, this ratio of Arias intensities climbs erratically throughout the period of strong shaking during which there is a rise in pore-water pressure and softening of portions of the soil column. We attribute the erratic rise in the intensity ratio to a de-coupling of the surface and downhole seismometers, caused by liquefaction of a layer between them.

We interprete the data to show that the surface measured intensity of shaking at the site, in response to the Elmore Ranch earthquake (I_h = 0.44 m/sec) , was insufficient to elevate pore-water pressures in soil with a fines corrected $(N_1)_{60}$ penetration resistance of 12-14. During the Superstition Hills event, which occurred the following day, pore-water pressure begins to develop at 13.6 seconds when the surface intensity had reached 0.54 m/sec. Between 27 seconds (I_h = 1.37 m/sec.) and 40 seconds ($I_{h\ surface}$ = 1.70 m/sec.) portions of the soil column fully liquefied. The data suggest that a threshold level of earthquake shaking, as measured by Arias intensity, was required to trigger soil liquefaction at the Wildlife site.

---

[1] Research Civil Engineer, U.S. Geol. Survey, 345 Middlefield Road, Menlo Park, CA 94025
[2] Via Professor of Civil Engineering, Virginia Polytechnic Institute and State University, Blacksburg VA 24061.
[3] Research Geologist, U.S. Geol. Survey, 345 Middlefield Road, Menlo Park, CA 94025

Introduction

The Wildlife liquefaction array (WLA) was established on the flood plain of the Alamo River in the Imperial Valley of California, 36 km north of the town of El Centro, to record the response of a liquefiable soil body, with the potential for lateral displacements, to earthquake motions (Figure 1). The Imperial Valley is situated south of the southerly end of the San Andreas Fault, in the vicinity of the Salton Sea and the Imperial Fault, and is one of the most earthquake-prone regions of the United States. As such, the Wildlife site is exposed to frequent strong motion events. The array, presented in Figure 2, is instrumented with piezometers and strong motion accelerometers at the surface and at 7.5 meters depth (Bennett et al., 1984, Holzer et al., 1989a). Numerous studies have documented the site characteristics and have presented analyses of the WLA, with regard to pore-water pressure response (Dobry, et al., 1989, Thilakaratne and Vucetic, 1989, Youd and Holzer, 1994); initial liquefaction (Holzer et al., 1989b, Elgamal and Zeghal, 1992); and ground deformations (Bazair et al., 1992, Youd and Bartlett, 1988, Holzer et al., 1989a, Dobry, et al., 1992).

The deposits that underlie the Wildlife site are underlain by a 2.3 meter thick fine-grained flood deposit (Figure 2); loose-to-moderately dense silty sand layer is found between 2.3 and 6.8 meters (units B1 and B2, Bennett, et al., 1984); below layer B are dense silty sands and sandy silts not subject to liquefaction. Sand boils found at the Wildlife site after the 1981 Westmorland Earthquake (M=5.9) are derived from material in both units B1 and B2 (Holzer et al., 1989). Fines corrected standard penetration tests (SPT) taken in layers B1 and B2 yield an average calculated $N_{1(60)}$ value of 12-14.

The instrumentation at WLA includes six Data Instruments model AB pore-pressure transducers placed in the soil column, in units B1 at 2.8 and 3.0 meters depth; in unit B2 at 4.0, 5.0, and 5.3 meters depth; and at 12.1 meters depth in the dense underlying soil. The boreholes for the pore pressure transducers were back-filled with bentonite-cement to seal the holes. The accelerometer instrumentation consists of two Kinemetrics model FBA-13 triaxial-accelerometers, one located at the surface, and the other at 7.5 meters depth within a PVC casing (designated FBA-13DH). The surface accelerometer is mounted to a concrete pad and housed within a fiberglass instrument box. The downhole accelerometer was placed at the base of the casing, which was then back-filled with sand.

Methods

We use the earthquake intensity measure Arias Intensity developed by Lange (1968) and Arias (1970) to characterize ground motion at the Wildlife site and investigate its relation to soil liquefaction. Arias intensity is defined by Arias (1970) as the total energy-per-unit-weight absorbed by evenly-spaced single-degree of freedom oscillators between the frequencies 0 and ∞. In practice, Arias intensity is calculated as proportional to the integral of the square of the recorded strong motion acceleration . The 2-component Arias intensity in the horizontal plane, I_h, is given by:

$$I_h = I_{xx} + I_{yy} = \frac{\pi}{2g} \int_0^t a_x^2(t)\, dt + \frac{\pi}{2g} \int_0^t a_y^2(t)\, dt$$

The two orthogonal single component Arias intensities, I_{XX} (intensity in the x-direction, integrated from the x-direction record) and I_{YY}, are integrated from acceleration time histories, where g is the gravitational acceleration, $a_X(t)$ is the acceleration at time-t recorded in the x-direction, and $a_Y(t)$ is the acceleration recorded in the y-direction. Single-component of motion Arias intensity is commonly referred to as I_a. This intensity measure is relatively insensitive to the variation in the damping characteristics of liquefiable soils (Kayen, 1993) and has the advantage of incorporating the entire accelerogram record into the intensity measure, whereas for example, the peak ground acceleration (PGA) utilizes but one-point. Arias intensity is useful because it can be quantified and verified in an objective manner, as opposed to subjective psycho-physical intensity measures, such as the Modified Mercali Intensity (Arias, 1970).

Elmore Ranch and Superstition Hills Earthquake

The epicenter of the 23 November 1987 Elmore Ranch earthquake (***M***=6.2) was located approximately 23 kilometers to the west of the WLA. This earthquake triggered instruments that recorded modest earthquake motions but no elevated pore-water pressures. The peak ground-acceleration and surface-level two-component horizontal Arias intensity for the event were 0.13g and 0.44m/sec, respectively. The acceleration- and cumulative intensity-time histories for the two components of motion at the surface and at 7.5 meters depth are plotted in Figure 3.

On the following day, November 24, 1987, the Superstition Hills earthquake (*M*=6.6), centered 31 kilometers west-southwest of the site, triggered instruments at the Wildlife site that recorded strong motions and elevated pore-water pressures. Acceleration- and Arias intensity-time histories for the Superstition Hills event are plotted in Figure 4. During this event, excess pore-water pressures developed approximately 13.6 seconds (I_h = 0.54 m/sec) into the record. The sand layer began to soften, noted by the loss of phase coherence between the downhole and surface acceleration records (Holzer et al., 1989b). By 16 seconds ($I_{h,16secs}$ = 0.90 m/sec) the pore pressure ratio, r_u, in portions of layer B approached approximately 0.5. Between 27 seconds ($I_{h,27secs}$ = 1.37m/sec) and 40 seconds ($I_{h,40secs}$ = 1.70 cm/sec) portions of the soil column fully liquefied (Youd and Holzer, 1994).

Discussion

The Wildlife strong motion data indicate that the Arias intensity calculated from seismograms at the ground surface is typically greater than that measured at depth within the soil column. Amplification at the ground-level is expected due to the effects of double-amplification at the surface and interference of the upward and downward traveling shear waves within the soil column. To investigate the variation of Arias intensity with depth, we used the Wildlife data to normalize the cumulative Arias intensity at a depth of 7.5 meters with the surface measure of intensity. We define an intensity depth reduction parameter, r_b, as the ratio of the buried to surface cumulative Arias intensities.

$$r_b = \frac{I_{xx}\ (depth)}{I_{xx}\ (surface)}$$

The r_b parameter can be calculated for either the single- or double-component horizontal Arias intensity. The time-history of the cumulative Arias intensity depth reduction factor, r_b, is calculated for the single-components of the Elmore Ranch earthquake, and presented in figure 5. It can be seen that during the first seven seconds of the 360° record, during the period dominated by P-waves, the r_b ratio fluctuates significantly. This fluctuation is due to the influence of the intensity of incident waves on the very low value of the ratio, r_b, during the first 6 seconds of the acceleration time-history. After 7 seconds, when shear waves dominate the strong motion, the intensity ratio plateaus at approximately 0.28 until 13 seconds, and then climbs to 0.38. For the 090° component of motion, a similar response is calculated from the acceleration time histories.

For this record a generally noisy record persists up to 7 seconds, followed by a progressive increase in r_b to 0.33 at 30 seconds.

A noteworthy aspect of both of the above records is the relatively constant ratio of r_b during the principal portion of strong shaking. Holzer et al. (1989b) argued that under non-liquefaction conditions, a linear proportionality constant exists between the downhole and surface cumulative Arias intensity. The relatively flat r_b profiles in Figure 4 support their hypothesis.

Plotting the cumulative Arias intensity ratio, r_b, as a time-history for the Superstition Hills event (Figure 6) shows a strikingly different response, compared to that of the Elmore Ranch record (Figure 5). During the early seconds of shaking there is a high sensitivity to wave interference in the r_b signature, as noted in the Elmore Ranch records. After 7 seconds into the record the intensity ratio plateaus for a period of 5-6 seconds at a value of approximately 0.34 for the 360 record and 0.25 for the 090 record. At 13.5 seconds r_b begins to rise in a rapid and erratic manner until r_b reaches a value of approximately 0.44-0.46.

Accordingly, Holzer et al. (1989b) concluded that the divergence between a scaled-Arias intensity at depth and the surface intensity was due to the onset of strain-softening behavior and the absorption of energy by the intervening liquefied layer. Our observations of the erratic elevation in r_b during the Superstition Hills event support their findings. The rapid rise in r_b indicates a partial de-coupling of the surface layer from the soil beneath the liquefied layer, such that shear waves propagating upwards are attenuated, and perhaps partly reflected downwards, before reaching the surface accelerometer.

The depth reduction characteristics for Arias intensity, calculated from the Wildlife array data, are plotted as a triangle in Figure 7b; the left limb representing the Elmore Ranch Earthquake response, and the right limb representing the Superstition Hills earthquake response. A separate parametric study of the the attenuation of Arias intensity with depth (Figure 7a) was performed by integrating synthetic seismograms generated with the ground-response program SHAKE (Schnabel, et al., 1972) and normalizing the intensities calculated at depth by the surface Arias intensity (Kayen, 1993; Kayen and Mitchell, in progress). The lines in Figure 7a are the r_b profiles generated with SHAKE using a suite of soil-shear modulus profiles and input strong motion records. A statistical synthesis of these profiles are shown in Figure 7b as a mean and ± 1 standard deviation response. The

empirical data from the Wildlife site fall below the mean response of the parametric study, but are in general agreement with those findings.

Liquefaction Response of Soil at the Wildlife liquefaction array

Acceleration time-histories recorded from the Elmore Ranch and Superstition Hills earthquakes are important in that they constrain the relation between shaking severity, as measured by Arias intensity, and liquefaction performance at the Wildlife site. To assess the liquefaction response, we coupled the depth factor, r_b, with surface-measured Arias intensity, I_h, to give an estimate of the energy-per-unit-weight absorbed by a specific soil layer at depth in the soil column, which we term the Arias intensity at depth, $\mathbf{I_{hb}}$. That is, we multiplied the surface intensities I_h measured at the surface accelerometer station at the Wildlife site by the depth-dependent reduction factor, r_b, interpolated between the surface and the measured value at 7.5 meter depth, to estimate Arias intensities within the soil column. In contrast, Egan and Rosidi (1991) have attempted to correlate the surface measure of Arias intensity with the field performance of potentially liquefiable sites. Their findings correctly indicate that the surface measure of Arias intensity correlates poorly with the liquefaction performance at depth in the soil column.

In Figure 8, we plot the intensity of earthquake shaking, $\mathbf{I_{hb}}$, estimated at the depth of soil layer B against the representative $(N_1)_{60}$ value for layer B (Bennett, et. al, 1984); having determined the fines- and effective overburden stress- corrected standard penetration resistance for that layer using the methods prescribed by Seed et al. (1984). The Elmore Ranch event, with a surface measured Arias intensity of 0.44 m/sec and an estimated intensity within layer B of 0.24 m/s, was insufficient to soften the sand layers B1 and B2. The Elmore Ranch event is marked on Figure 8 as no-liquefaction point below the boundary curves.

During the Superstition Hills earthquake, pore pressures developed at approximately 13.6 seconds, at which point the horizontal surface Arias intensity had reached 0.54 m/sec. Full liquefaction appears to have occurred after approximately 27 seconds (surface I_h = 1.37 m/sec) of instrument recording, as determined by the piezometer response (Dobry et al., 1989). The vertical band in Figure 8 represents the transition from a non-liquefied to liquefied soil state during the Superstition Hills event. The response of the Wildlife site is presented with a suite of points representing the field performance of other sites, investigated by Kayen (1993), observed during nine earthquakes in United States and Japan (magnitude range: $6.1 \leq M \leq 7.9$). From this

investigation, Arias intensity-based curves can be drawn which define a threshold boundary for liquefaction occurrence (Kayen and Mitchell, in progress). The integration of both acceleration amplitude and earthquake shaking duration in the parameter Arias intensity is such that these boundary curves are independent of earthquake magnitude . The liquefaction field performance observed at the Wildlife site during the Elmore Ranch and Superstition Hills events is consistent with that observed at the other sites, and supports the basis for a depth-dependent Arias intensity-based boundary in $(N_1)_{60}$-$\mathbf{I_{hb}}$ space defining limiting conditions for liquefaction occurrence.

Conclusions

We have analyzed the characteristics of strong motions of the Elmore Ranch and Superstition Hills Earthquakes, recorded at the WLA, in terms of their progressive Arias intensity build-up. The ratio of the downhole to surface cumulative Arias intensities was essentially a constant during the principal portion of ground shaking in the Elmore Ranch event, when no excess pore-water pressures were observed. The depth reduction factor, r_b, calculated for the two-components of motion for the Elmore Ranch event was 0.36. During the Superstition Hills event, the Arias intensity ratio climbed in an erratic manner in response to a partial de-coupling of the surface and downhole seismometers, between which was a liquefied layer. The Superstition Hills earthquake had a two-component depth reduction factor, r_b, of 0.45.

To assess the liquefaction response of the Wildlife site during the two earthquake events, we multiplied the surface intensities, I_h, by the depth-dependent reduction factor, r_b, interpolated between the surface and 7.5 meter depth. In doing so, we can compare the energy-per-unit-weight absorbed by a layer at depth, $\mathbf{I_{hb}}$, to the penetration resistance of that layer, $(N_1)_{60}$. The Elmore Ranch event had an estimated $\mathbf{I_{hb}}$ intensity within soil layer B of 0.24 m/sec. which was below the threshold required to elevate pore-water pressures within that layer. During the Superstition Hills earthquake, pore pressures began to develop at an $\mathbf{I_{hb}}$ intensity level of 0.27 m/sec. Full liquefaction appears to have occurred after approximately 27 seconds when the Arias intensity at the depth of layer B, $\mathbf{I_{hb}}$, was approximately 0.7 m/sec. The WLA data-set allow us to observe the transition of a site from a non-liquefied to a liquefied state in terms of Arias intensity buildup. This transition is consistent with an investigation of other sites in the United States and Japan where Arias intensity has been correlated with the liquefaction performance in the field.

Acknowledgments

We thank John C. Tinsley III and Michael J. Bennett for their thoughtful reviews of the manuscript.

References

Arias, A. (1970) A Measure of Earthquake Intensity, R.J. Hansen *ed.* Seismic Design for Nuclear Power Plants, The M.I.T. Press, Cambridge, Massachussetts.

Baziar, M.H., Dobry, R., and Alemi, M. (1992) Evaluation of Lateral Ground Deformation Using Sliding Block Model, Earthquake Engineering, Tenth World Conference, Balkema, Rotterdam, pp.1401-1406.

Bennett, M.J., Mc Laughlin, P.V., Sarmiento, J.S., and Youd, T.L., (1984) Geotechnical Investigation of Liquefaction Sites, Imperial Valley, California, USGS Open-File Report 84-252, U.S. Geological Survey, Menlo Park, CA.

Dobry, R., Elgamal, A.W., Baziar, M.H., and Vucetic, M. (1989) Pore Pressures and Acceleration Response of Wildlife Site During the 1987 Earthquake, Proceedings, Second U.S.-Japan Workshop on Liquefaction, Large Ground Deformation, and Effects on Buried Pipelines, Niagra Falls, New York, pp. 145-260.

Dobry, R., Baziar, M.H., O'Rourke, T.D., Roth, B.L., and Youd, T.L. (1992) Liquefaction and Ground Failure in the Imperial Valley, Southern California during the 1979, 1981, and 1987 Earthquakes, U.S.-Japan Case Studies of Liquefaction and Pipeline Performance During Past Earthquakes, Vol. 2, U.S. Case Studies, NCEER Report 92-0002, pp.4-1 to 4-85.

Egan, J.A. and Rosidi, D. (1991) Assessment of Earthquake-Induced Liquefaction Using Ground-Motion Energy Characteristics, Proc. Pacific Conference on Earthquake Engineering, New Zealand.

Elgamal, A.-W. and Zeghal, M. (1992) Analysis of Wildlife Site Liquefaction During the 1987 Superstition Hills Earthquake, Proc. of the Fourth Japan - U.S.Workshop on Earthquake Resistant Design of Lifeline Facilities and Countermeasures for Soil Liquefaction, in M. Hamada and T.D. O'Rourke, eds. Technical Report NCEER-92-0019.

Holzer, T.L., Bennett, M.J., and Youd, T.L. (1989a) Lateral Spreading Experiments by the U.S. Geological Survey, Proceedings from the Second U.S.-Japan Workshop on Liquefaction, Large Ground Deformations and their Effects on Lifelines, *eds.* T.D. O'Rourke and M. Hamada, Technical Report NCEER-89-0032.

Holzer, T.L., Youd, T.L., and Hanks, T.C. (1989b) Dynamics of Liquefaction During the 1987 Superstition Hills California Earthquake, Science, Vol. 244, pp. 56-59.

Kayen, R.E.(1993) Accelerogram-Energy Approach for Prediction of Earthquake-Induced Ground Liquefaction, unpublished Ph.D. dissertation, Department of Civil Engineering, University of California at Berkeley, 289 pp.

Kayen, R.E. and Mitchell, J.K., in progress, Ground-motion energy approach for assessment of earthquake-induced cyclic-liquefaction, J. Geotech. Engrg., ASCE.

Lange, G. (1968) Una Medida de Intensidad Sismica, unpublished Ph.D. Thesis, University of Chile, Santiago, Chile.

Schnabel, P., Lysmer, J., and Seed, H.B. (1972) SHAKE: A Computer Program for Earthquake Ground Response, Univ. Cal. Berkeley, EERC Report No. UCB/EERC-72-12.

Seed, H.B., Tokimatsu, K., Harder, L.F., and Chung, R.M., (1984) Influence of SPT procedures in soil liquefaction resistance evaluation, Earthquake Engineering Research Center Report No. UCB/EERC-84/15.

Thilakaratne, V. and Vucetic, M. (1989) Analysis of liquefaction occurrence at the Wildlife Site during 1987 Superstition Hills Earthquakes, Research Report, Dept. of Civil Engineering, University of California, Los Angeles, p.131.

Youd, T.L. and Bartlett, S.F., (1988) U.S. Case Histories of Liquefaction-Induced Ground Displacement, Proc. of the First Japan-U.S. Workshop on Liquefaction, Large Ground Deformations and their Effects on Lifeline Facilities, Tokyo, Japan.

Youd, T.L. and Holzer, T.L. (1994) Piezometer Performance at Wildlife Liquefaction Site, California. J. Geotech. Engrg., ASCE, 120(6).

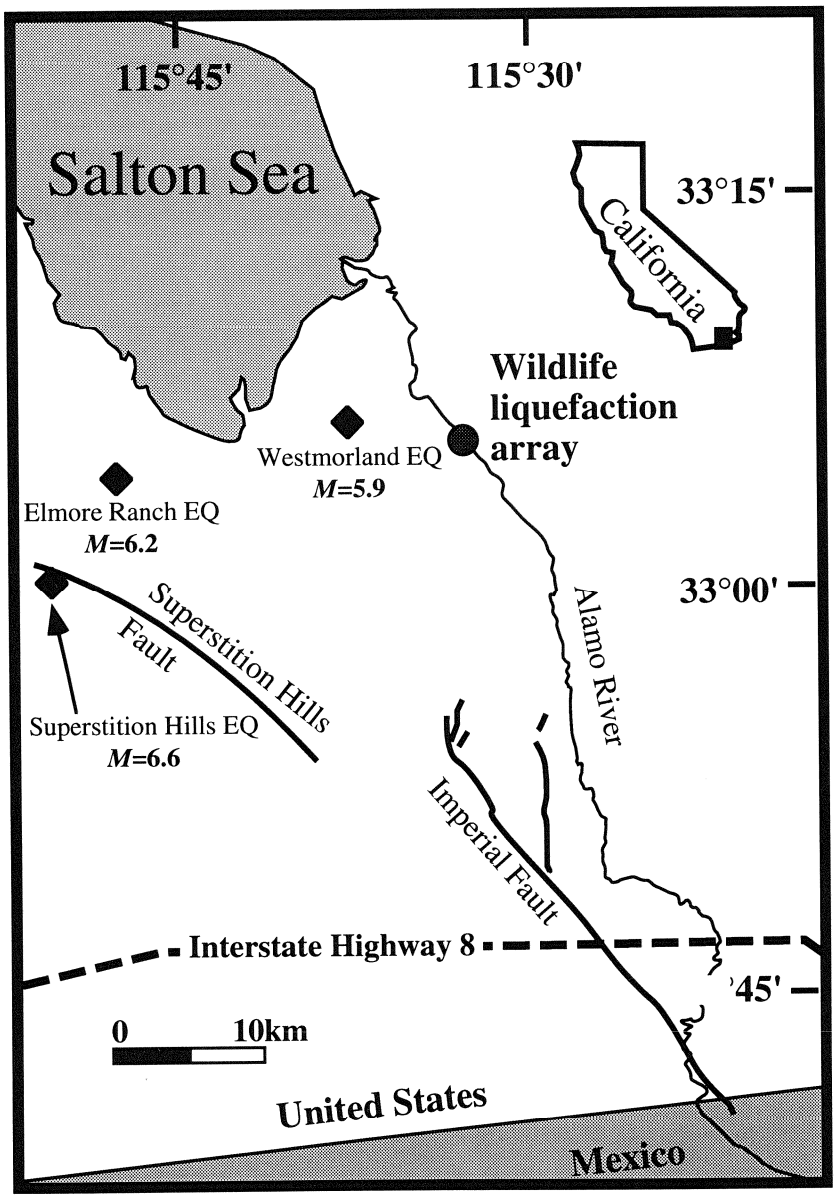

Figure 1. Location map of the WLA, Imperial Valley, Ca. Epicenters for the 1981 Westmorland; 1987 Elmore Ranch; and 1987 Superstition Hills earthquakes are starred.

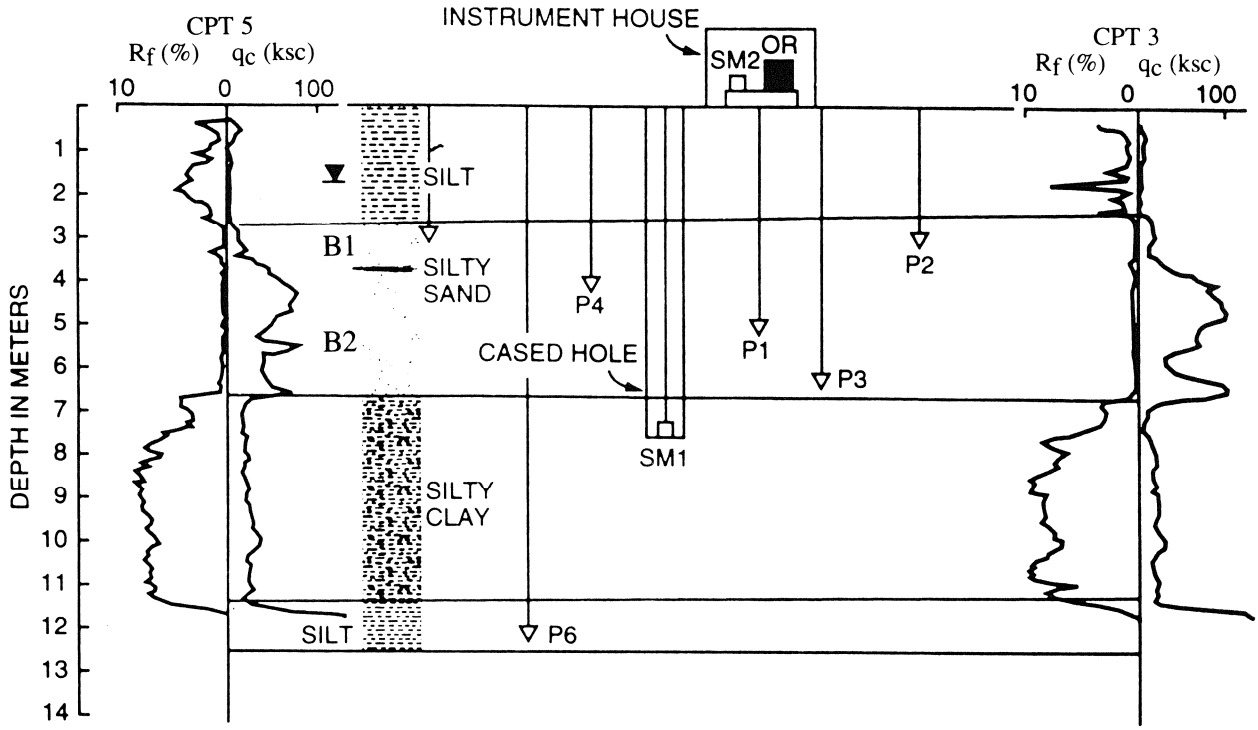

Figure 2. Profile of the Wildlife site with layers A-, from the surface, to-D at 12-meters, and cone penetration test (CPT) profiles (Bennett, et al., 1984). The parameters q_c (kg/cm^2) and r_f (%) are the cone-tip resistance and sleeve friction ratio, respectively. Inverted triangles P1-P6 denotes the pore pressure piezometers; SM1 and SM2 denote the triaxial accelerometers; OR denotes the oscilloscope recorder.

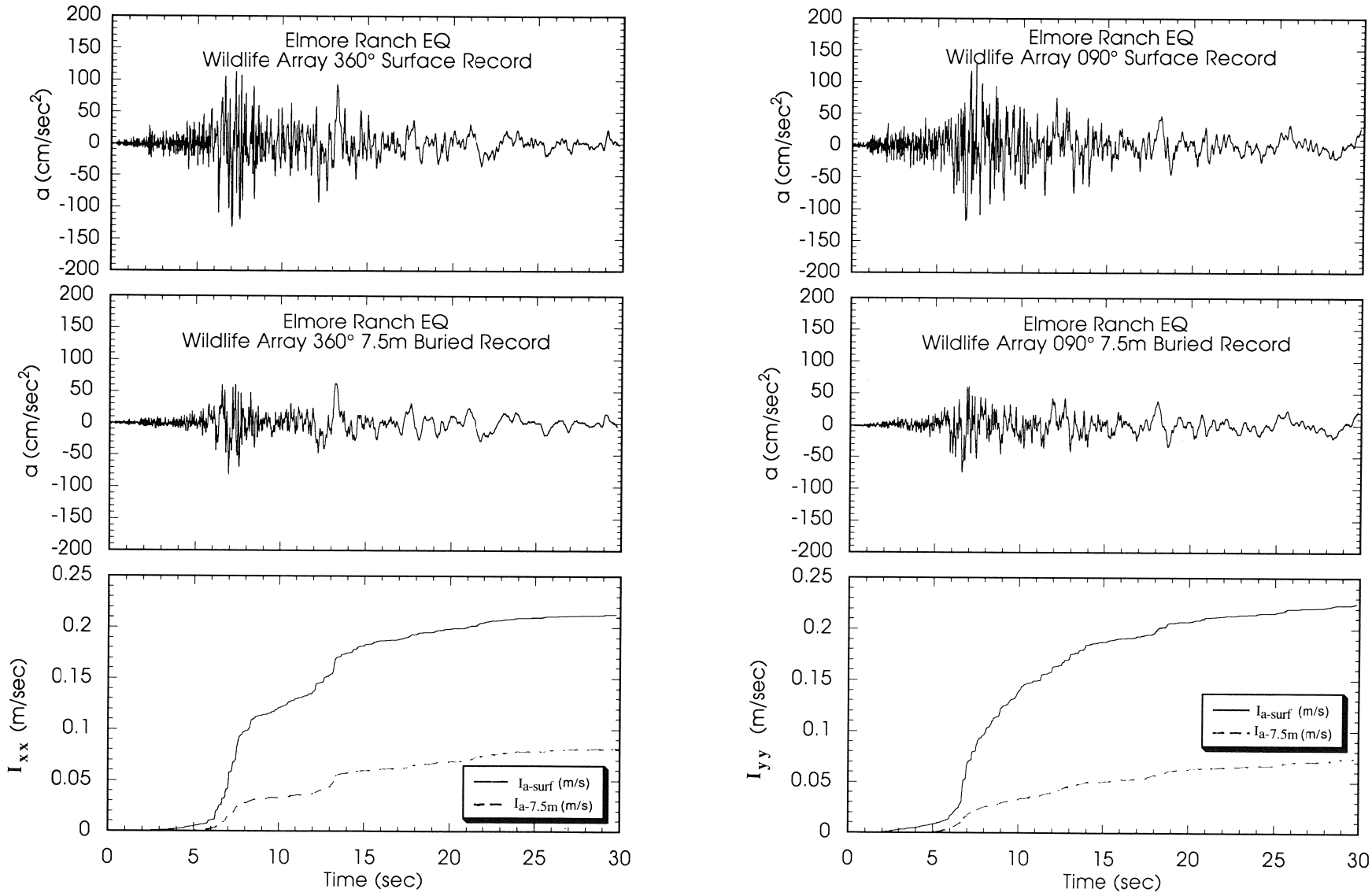

Figure 3. Ground surface and 7.5 m depth recordings from the WLA, recorded during the Elmore Ranch Earthquake. Plotted are accelerations and their computed cummulative Arias intensities for the 360° and 090° components. $I_{a\ top}$ and $I_{a\ mid}$ are the surface and 7.5 meter depth Arias intensities, respectively. Horizontal scaling is the first 30 seconds of recording.

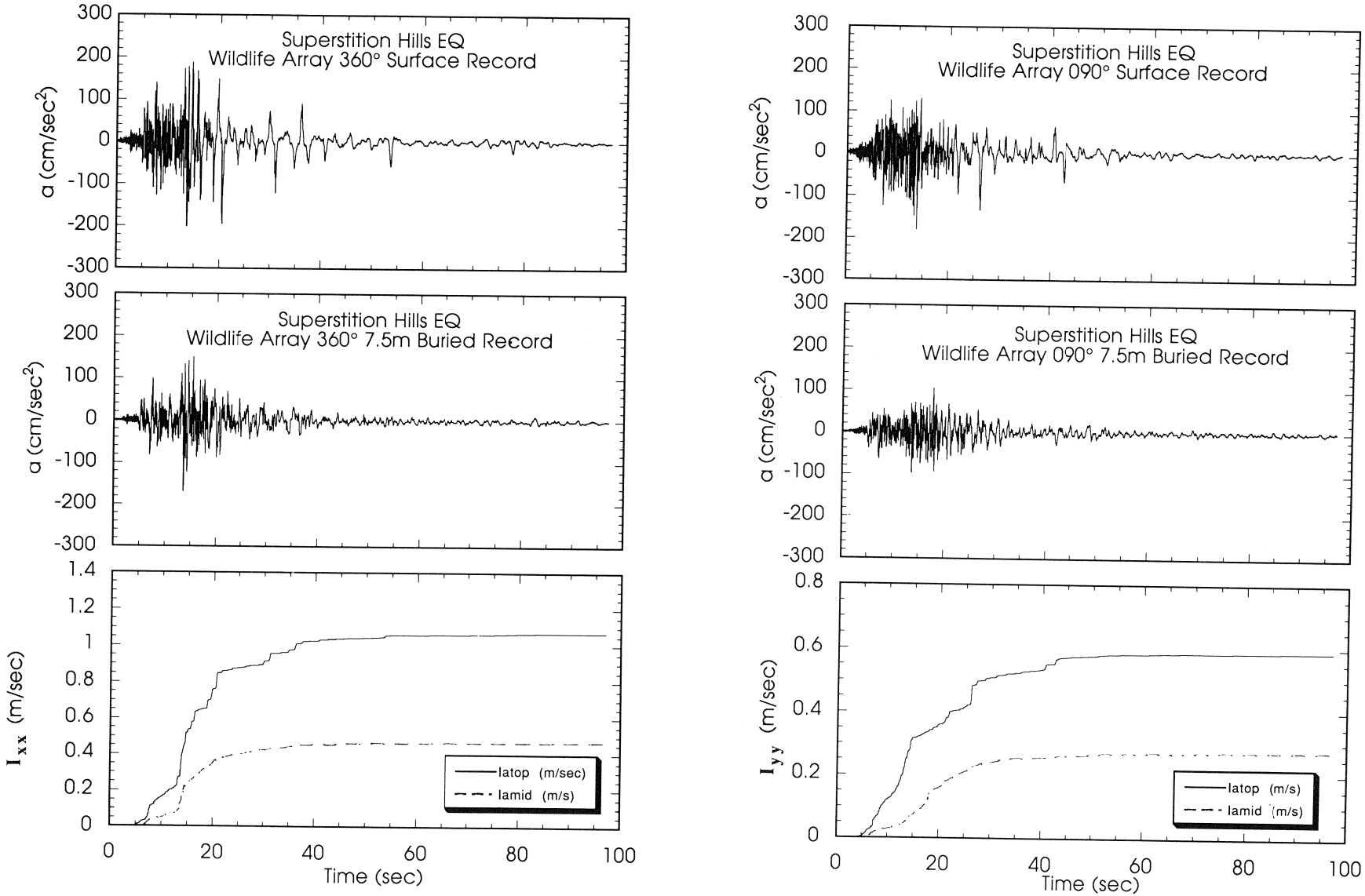

Figure 4. Ground surface and 7.5 m depth recordings from the WLA, recorded during the Superstition Hills Earthquake. Plotted are accelerations and their computed cumulative Arias intensities for the 360° and 090° components. Horizontal scaling is the first 100 seconds of recording.

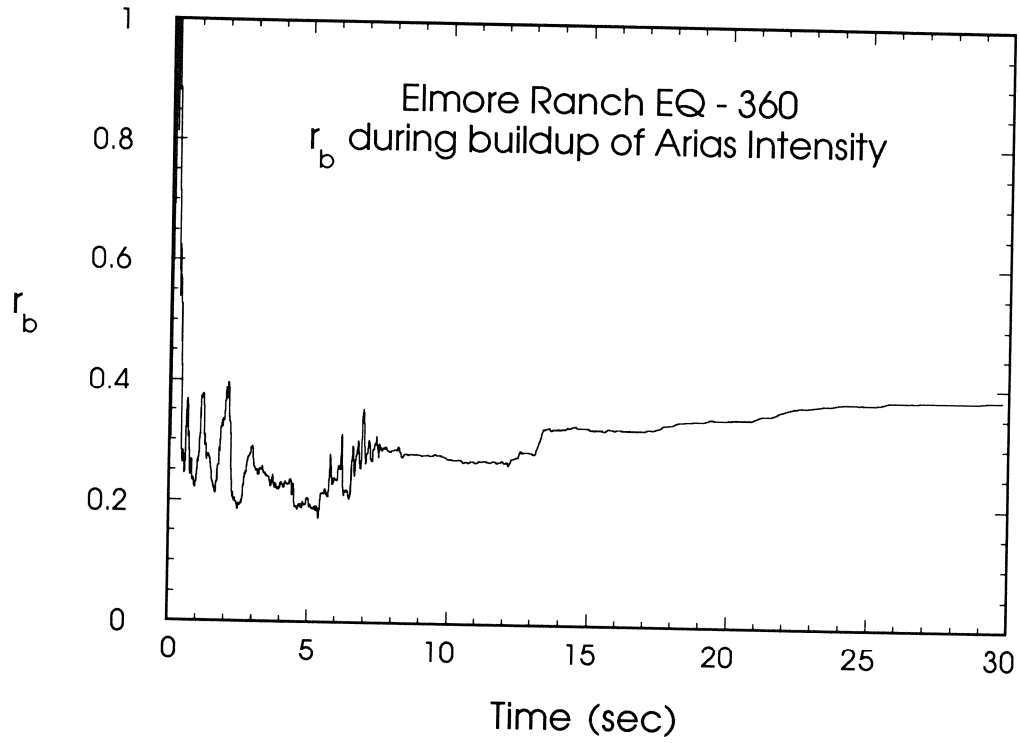

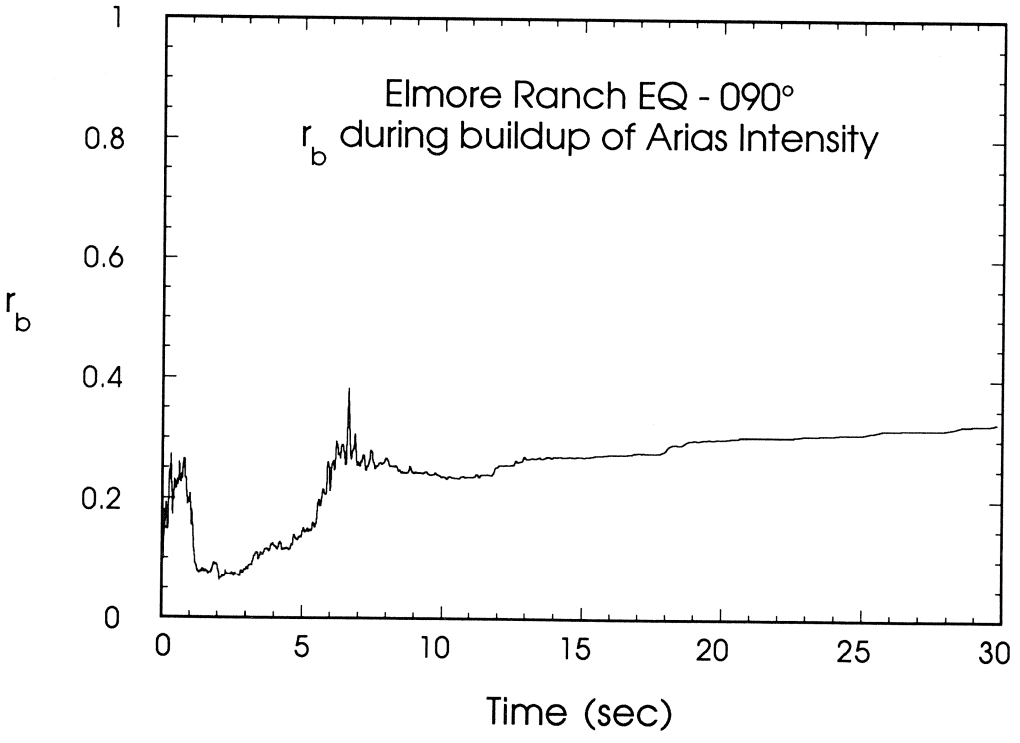

Figure 5. Cumulative r_b time-histories for the 360° and 090° components of the Elmore Ranch Earthquake records.

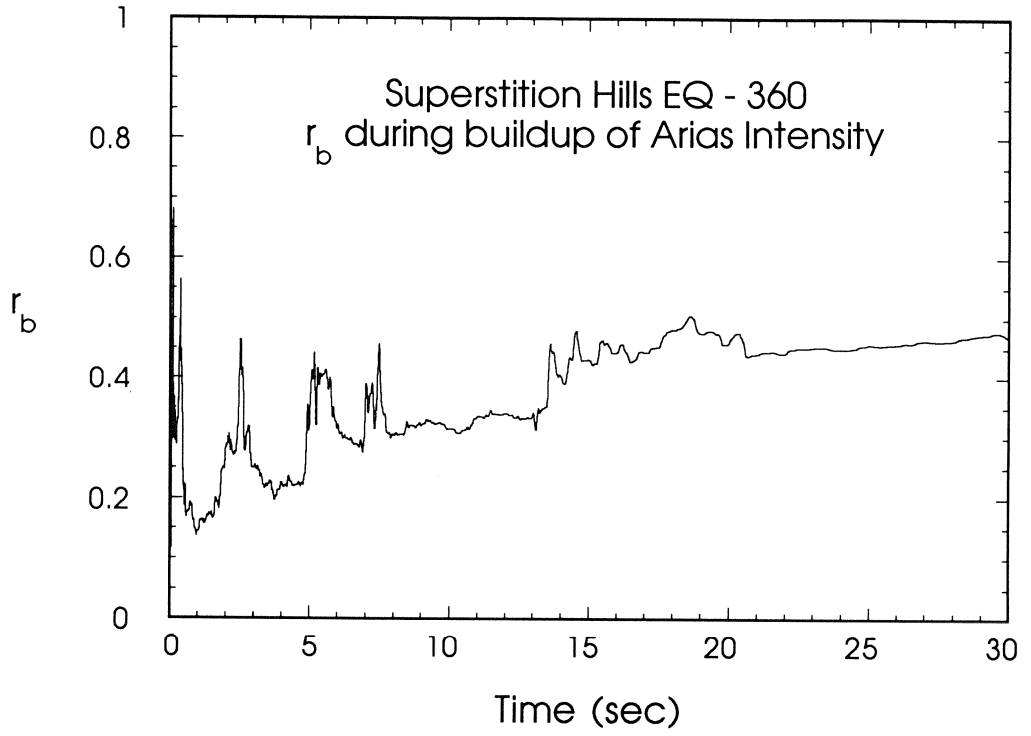

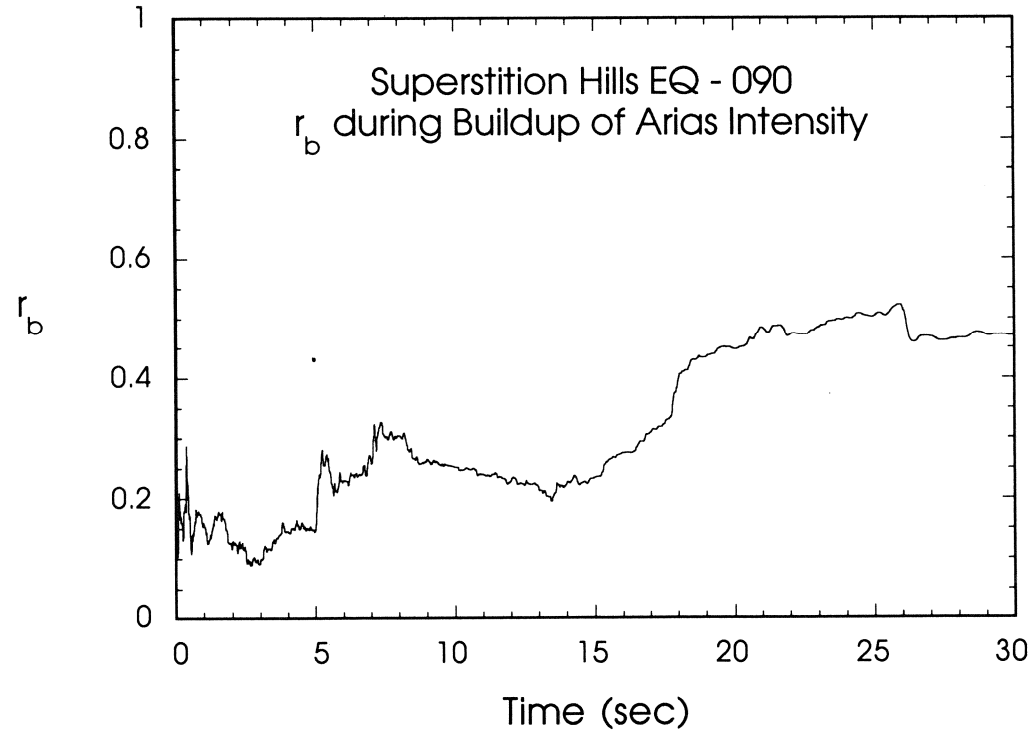

Figure 6. Cumulative r_b time-histories for the 360° and 090° components of the Superstition Hills Earthquake records.

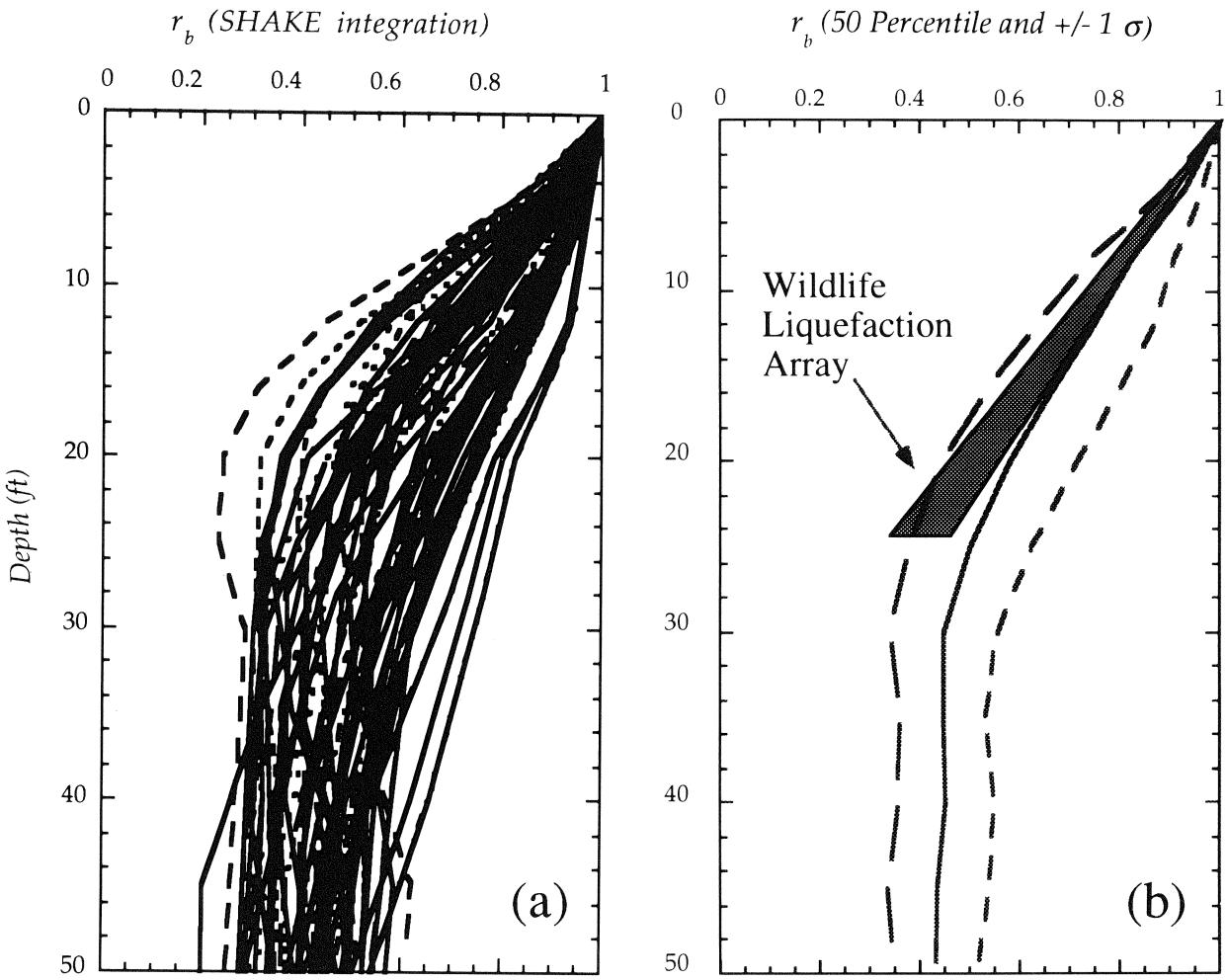

Figure 7. Arias intensity depth reduction profiles modeled using the ground response program SHAKE are presented in Figure 7a. A statistical synthesis of the SHAKE-study is presented in Figure 7b along with the empirical results from the WLA response during the Elmore Ranch and Superstition Hills earthquakes.

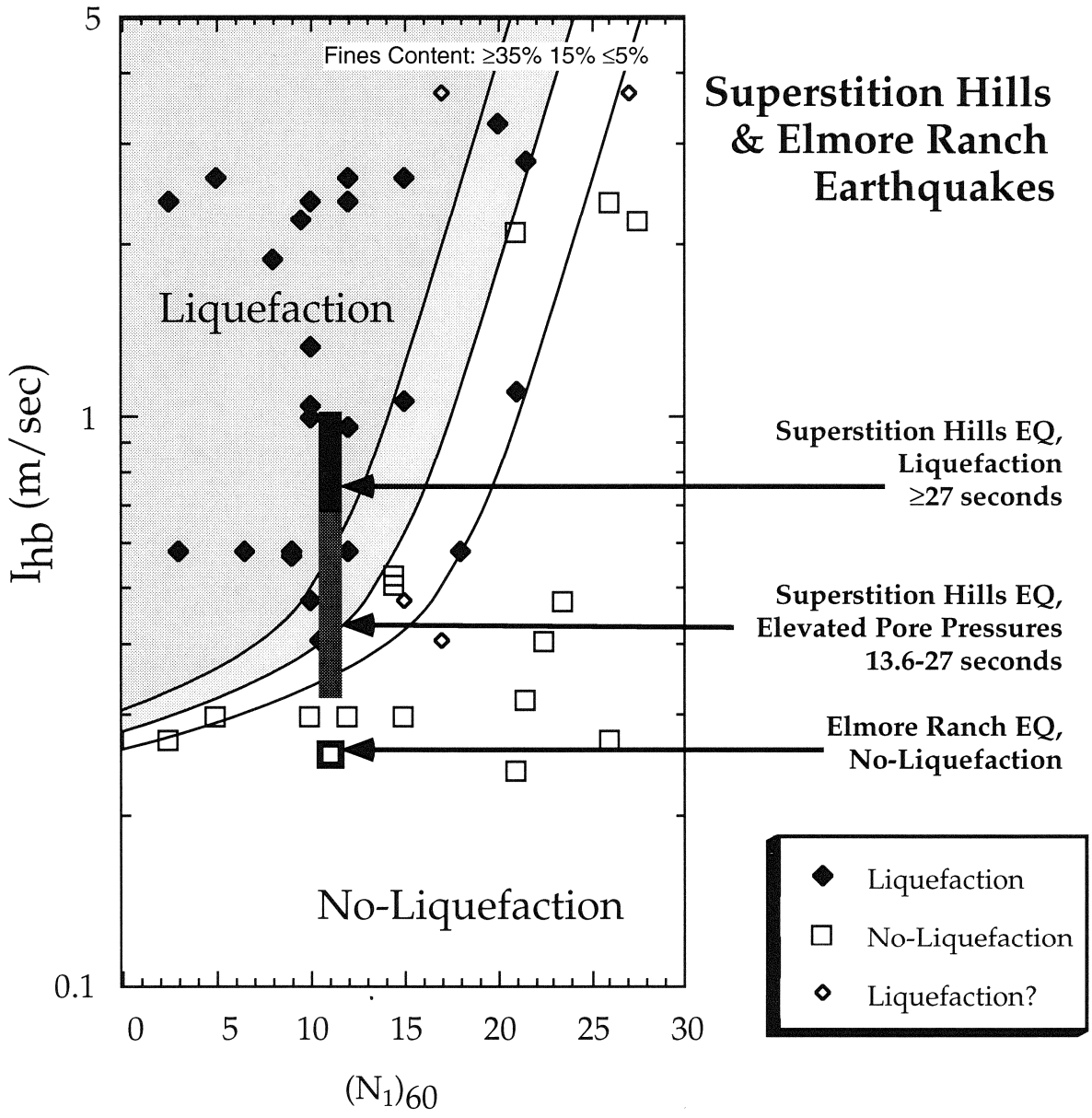

Figure 8. $\mathbf{I_{hb}}$ versus $(N_1)_{60}$ for the WLA site during the Elmore Ranch and Superstition Hills earthquakes. The boundary curves are constrained by field performance data from sites in Japan and United States, whose performance is identified in the legend (Kayen and Mitchell, in progress).

Experimental Study on Mechanical Properties of Liquefied Sand

T. Kawakami[1], N. Suemasa[2], H. Hamada[3], H. Sato[4], and T. Katada[5]

ABSTRACT

The purpose of this study is to understand the mechanical properties of liquefied sand to estimate the behavior of ground after liquefaction and to investigate the mechanism of occurrence of liquefaction-induced large ground displacement. In this paper we consider that the mechanical properties of liquefied sand can be separated the following two phases, (1) the fluid characteristic of liquefied sand as viscous fluid, (2) the solid characteristic of liquefied sand under large deformation.

From the above-mentioned points, the authors carried out laboratory tests on the fluid and solid characteristics of liquefied sand. For the fluid characteristic, two kinds laboratory tests were conducted in order to obtain coefficient of viscosity on liquefied sand. In the first test, coefficient of viscosity was estimated from load acting on sphere in liquefied sand with constant velocities. On the other hand, by using viscometer which measured torque moment of a rotor rotating in liquefied sand. These results suggest that viscosity of liquefied sand depend on relative density of sand and velocity of shear strain. For the solid characteristic a laboratory test was conducted. It was a cyclic torsion shear test, in which maximum shear strain of liquefied sand reaches about 80%. The results of the test show that liquefied sand has a critical maximum shear strain which depend on relative density of sand.

1) Assistant Professor, Dept. of Marine Civil Engineering, Tokai University.
2) Assistant Professor, Dept. of Civil Engineering, Musashi Institute of Technology.
3) Professor, Dept. of Civil Engineering, Waseda University.
4) Senior Researcher, Engineering Research Center, Tokyo Electric Power Company.
5) Associate Professor, Dept. of Civil Engineering, Musashi Institute of Technology.

INTRODUCTION

The authors have been investigating the mechanism for occurrence of the liquefaction-induced large ground displacement and the effects of liquefaction on underground structures, by the case studies on earthquakes in the past (Doi and Hamada, 1992), and by the experimental studies on the behavior of ground after liquefaction (Hamada, et al. 1992). The followings became clear from the above studies, 1) the liquefied soil behaves as a viscous fluid, 2) the load acting on pile which is located in flowing liquefied soil depends on velocity of flowing liquefied soil. These results indicate the possibility of estimating the behavior of ground after liquefaction assuming that flowing liquefied soil is regarded as viscous fluid (Sato, et al, 1993).

However, we consider that the practical phenomena of liquefaction-induced large ground displacement can not be explained by only the above assumption, because of the inclined ground dose not become the level ground after the occurrence of liquefaction. Also, Yasuda, et al. (1993) points out that the stiffness of the liquefied sand is recovered as subject to the large shear strain. Therefore, it is necessary to consider that the mechanical property of the liquefied soil change from the fluid characteristic to the solid characteristic in the process of the liquefied soil flow.

This paper discusses the mechanical properties of liquefied sand to estimate the behavior of ground after liquefaction and to investigate the mechanism of occurrence of liquefaction-induced large ground displacement. In this paper we consider that the mechanical properties of liquefied sand can be separated the following two phases, 1) the fluid characteristic of the liquefied sand which is regarded as viscous fluid, 2) the solid characteristic of liquefied sand under large deformation. From the above-mentioned points, the authors carried out laboratory tests on the fluid and solid characteristics of liquefied sand. For the fluid characteristic, two kinds laboratory tests were conducted in order to obtain coefficient of viscosity on liquefied sand. For the solid characteristic a laboratory test was conducted. It was a cyclic torsion shear test, in which maximum shear strain of liquefied sand reaches about 80%.

LABORATORY TESTS FOR FLUID CHARACTERISTIC

Measurement of Viscosity on Liquefied Sand by Load Acting on Sphere

Procedure of Test

Figure 1 shows the experimental arrangement used to measure the viscosity of liquefied sand, by using the load acting on sphere moving with constant velocity in liquefied sand. The soil box is cylindrical, with a diameter of 100.0 cm and a depth of 87.5 cm. The steel sphere is placed into liquefied sand, which have a diameter of 3.0 cm. Liquefaction was induced by shaking the soil box using sinusoidal waves. Toyoura sand was used as the test material. This sand has followings physical properties, a specific gravity of 2.63, a maximum void ratio of 0.974, a minimum void ratio of 0.598, a maximum grain diameter of 0.85, 50 percent diameter of 0.168 and a uniformity coefficient of 1.74, respectively.

The tests were carried out as follows:

(1) The saturated model sand with the prescript relative density was made in the soil box.

(2) Liquefaction was occurred by shaking the soil box. Subsequently, if the complete liquefaction was confirmed by the pore water pressure meters at all the measuring points, shaking the soil box was stopped.

(3) Immediately, the sphere was pulled up with constant velocity, and load acting on the sphere was measured. In this time, it was necessary that the complete liquefaction was kept around the sphere.

A series of the tests by using above method were conducted with following parameters, velocities of pulled up sphere, initial relative densities. The conditions of the tests are shown in Table 1.

If the liquefied sand is assumed to be a viscous fluid, the relation between viscosity and load acting on the sphere is formulated as the following equation.

$$\eta = \frac{F}{3\pi d U} \tag{1}$$

Where F, d, U are the load, diameter of the sphere and the velocity, respectively, η is the coefficient of viscosity.

Results of Test

A example of the experimental results which in the way described above is shown in Figure 2. Figure 2 (a) shows the incident acceleration, similarly, (b) shows the velocity of the sphere, (c) shows the excess pore water pressure in the liquefied sand, (d) shows the load acting on the sphere, (e) shows the excess pore water pressure at the surface of the sphere, respectively. Where, the line A-A in Figure 2 (e) express the effective normal stress which is considered the effect of pulling up the sphere in the liquefied sand.

From Figure 2, we can see that the load acting on sphere shows the constant value as the velocity of sphere is constant. This relationship between the load acting on sphere and the velocity of sphere satisfy equation (1), if the viscosity is assumed to be constant, and it is suggested that liquefied sand can be approximated viscous fluid.

The relationship between the coefficient of viscosity and the velocity of sphere is shown in Figure 3. The coefficient of viscosity was calculated from the load acting on sphere by using equation (1). Then, the relationship between the coefficient of viscosity and relative density is shown in Figure 4.

The followings became clear from these figures:

(1) The coefficient of viscosity for liquefied sand has a proportional correlation with the velocity of sphere, that the coefficient of viscosity decreases as the velocity of sphere increases.

(2) The correlation is observed between the coefficient of viscosity and relative density, that the coefficient of viscosity increases as the relative density increases.

Measurement of Viscosity on Liquefied Sand by Viscometer

Procedure of Test

In this section, we summarize the measurement of viscosity of liquefied sand using viscometer. The experimental apparatus is shown in Figure 5. The soil container is a transparent plastic cylinder, with a diameter of 8.5 cm and a depth of 30.0 cm. The soil container has a porous disk at the bottom, and the bottom is connected to the water tank. Two pore water pressure meters are installed in the wall of the container to measure the hydraulic gradient. Liquefaction of the sand in the container was occurred by upward seepage. Toyoura sand was used as the test material. The effective normal stress σ' at the depth of z in sand with upward seepage is expressed as following equation,

$$\sigma' = \left(\frac{G-1}{1+e} - i\right)\rho_w g z \ , \tag{2}$$

where, G is a specific gravity of soil particles, e is a void ratio, ρ_w is a density of water

and g is a acceleration due to gravity, respectively. Then, i is a hydraulic gradient, and it is clearly that the effective normal stress σ' becomes 0 if the i denotes as following equation,

$$i = \frac{G-1}{1+e} \quad . \tag{3}$$

Therefore, it can be considered that the sand was liquefied by the upward seepage. In this test, the hydraulic gradient i was obtained by measuring two pore water pressures and using following equation.

$$i = \frac{u_2 - u_1}{L\,\rho_w\,g} \tag{4}$$

Where, u_1 and u_2 are pore water pressures, L is a distance between u_1 and u_2(see Figure 5).

The viscosity of liquefied sand was estimated by viscometer, which measured torque moment acting on a rotor rotating in liquefied sand. A series of the tests by using above method were conducted with following parameters, number of rotation and initial relative density. The conditions of the tests are shown in Table 2.

Results of Test

The relationship between the coefficient of viscosity and the number of rotation is shown in Figure 6. Similarly, the relationship between the coefficient of viscosity and the initial relative density is shown in Figure 7. The followings became clear from the results of the tests:

(1) The coefficient of viscosity of liquefied sand is depended on the number of rotation, that is, the coefficient of viscosity decreases as the number of rotation increases.

(2) The coefficient of viscosity of liquefied sand has a correlation with the initial relative density, that is, the coefficient of viscosity increases as the initial relative density increases.

(3) Above these results agree with the results of the preceding section.

Discussion of Viscosity on Liquefied Sand

In this section, the velocity of shear strain for liquefied sand acting the shear deformation is introduced to discuss the results of two kinds of test for viscosity. The velocity of shear strain D_s on the surface of sphere which is moved with constant velocity in viscous fluid is expressed as following equation by Stokes's stream function.

$$D_s = \frac{3\,U}{d} \tag{5}$$

Similarly, The velocity of shear strain D_s on the surface of rotor rotating in cylindrical container filled with viscous fluid is obtained as following equation by solving Navier-Stokes's equation,

$$D_s = \frac{2\,R^2\,\Omega}{K\,(R^2 - r^2)} \quad , \tag{6}$$

where, R and r are the radius of container and the radius of rotor, Ω is a angular velocity, respectively. K is denoted as a correctional coefficient considering the finite length of the rotor (in this case, K=0.77).

Figure 8 shows the relationship between the coefficient of viscosity and the velocity of shear strain. In this figure, we plotted the coefficient of viscosity of liquefied sand which was obtained by the experiment on liquefaction-induced ground displacement using the model ground and the shaking table (Ogasawara and Hamada,1994), as well as the

results of the tests in this study.

The followings became clear from this figure:

(1) Clearly, the strong correlation is observed between the coefficient of viscosity and the velocity of shear strain.

(2) The coefficient of viscosity decreases as the velocity of shear strain increases.

(3) The results of two kinds of the tests in this study indicate a good agreement.

(4) The results of the experiments on liquefaction-induced ground displacement using the model ground indicate the similar tendency with the above (2). Then, these results agree well with the results of the tests in this study.

LABORATORY TEST FOR SOLID CHARACTERISTIC

Measurement of Strength / Deformation on liquefied sand

Procedure of Test

It is a purpose of this test to explain the strength / deformation characteristics of liquefied sand by a new hollow cylinder torsional shear apparatus, which is that shear loading tests until maximum 80% of shear strains are enabled. An undrained cyclic torsion shear test was carried out by this test machine. The test apparatus is shown in Figure 9. The hollow cylindrical specimen used in the tests was 10.0 cm in outside diameter, 6.0 cm in inside diameter and 10.0 cm in height. Toyoura sand was used as the test material. This sand has a specific gravity of 2.634, and the maximum and minimum void ratio were measured to be 0.993 and 0.614, respectively. The hollow cylindrical specimens were made by pluviation under water.

The parameters in the tests are relative density, frequency of cyclic torsion, shear stress ratio and effective confining pressure. The conditions of the test are shown in Table 3.

Results of Test

As an example on the result of the test, the relationship between shear stress and shear strain shows in Figure 10. In this case, the relative density was a 53%, the shear stress ratio was a 0.2, the effective confining pressure was a 1.0 kgf/cm^2 and the frequency of cyclic torsion was a 0.1 Hz, respectively. From this figure, in the first stage after the occurrence of liquefaction, we can see that the shear strain shows a rapidly increasing rate with increase in the number of cycles. However, if the shear strain reaches one value, the increasing rate of the shear strain decreases.

Figure 11 (a), (b), (c) show the relationships between shear strain and number of cycles considering the influence of the each parameters.

The followings became clear from these figures:

(1) The shear strain shows a rapidly increasing rate after the occurrence of liquefaction, however, the increase of the shear strain has a critical value.

(2) The strongest correlation was observed between the critical value of shear strain (hereafter, it is called the critical maximum shear strain) and the initial relative density of the liquefied sand, as compared with the other parameters.

From the above-mentioned points, Figure 12 is shown in order to clear the relationship between the critical maximum shear strain and the initial relative density. It is suggested from this figure that:

(1) The plotted results are a few scattered, but the correlation is observed between the critical maximum shear strain and initial relative density.

(2) The general tendency is observed that the critical maximum shear strain increases as the relative density decreases.

CONCLUSION

The objective of the study was to clear the mechanical properties of liquefied sand, from two viewpoints those were fluid and solid characteristics. In this study, the coefficient of viscosity on liquefied sand was measured as the fluid characteristic, and the shear strain-shear stress relationship on liquefied sand under large deformation was indicated as solid characteristic, by using the laboratory tests.

The summary of the results is shown below.

(1) The coefficient of viscosity on liquefied sand depends on the relative density.

(2) The correlation was observed between the coefficient of viscosity and the velocity of shear strain.

(3) The existence of the critical maximum shear strain on liquefied sand under large deformation was estimated.

(4) The critical maximum shear strain depends on the relative density.

REFERENCES

1)Doi, M. and Hamada, M. (1992): "A summary of Case Studies on liquefaction-Induced Ground Displacements," Proceedings from the Fourth Japan-U.S. Workshop on Earthquake Resistant Design of Lifeline Facilities and Countermeasures for Soil Liquefaction, Vol. 1, Technical Report NCEER-92-0019, pp. 115-129.

2)Hamada, M., Ohtomo, K., Sato, H. and Iwatate, T. (1992): "Experimental Study of Effects of Liquefaction-Induced Ground Displacement on In-Ground Structures," Proceedings from the Fourth Japan-U.S. Workshop on Earthquake Resistant Design of Lifeline Facilities and Countermeasures for Soil Liquefaction, Vol. 1, Technical Report NCEER-92-0019, pp. 481-492.

3)Ogasawara, Y. (1994) : "Experimental Study on Liquefaction-Induced Ground Displacements by Pressurized Soil box," Master's thesis, Tokai University, Japan.

4)Sato, H., Doi, M., Hamada, M. and Nakamura, T. (1993): "Numerical Analysis on Liquefaction-Induced Ground Displacements," Proceedings of the 22th JSCE Earthquake Engineering Symposium, pp. 87-90.

5)Yasuda,S.,Kiku, H.,Masuda,T. and Bando,S.(1993): "A study on Strength/Deformation Characteristics of Liquefied Sand by Cyclic Torsional Shear Test," Proceedings of the 22th JSCE Earthquake Engineering Symposium, pp. 19-22.

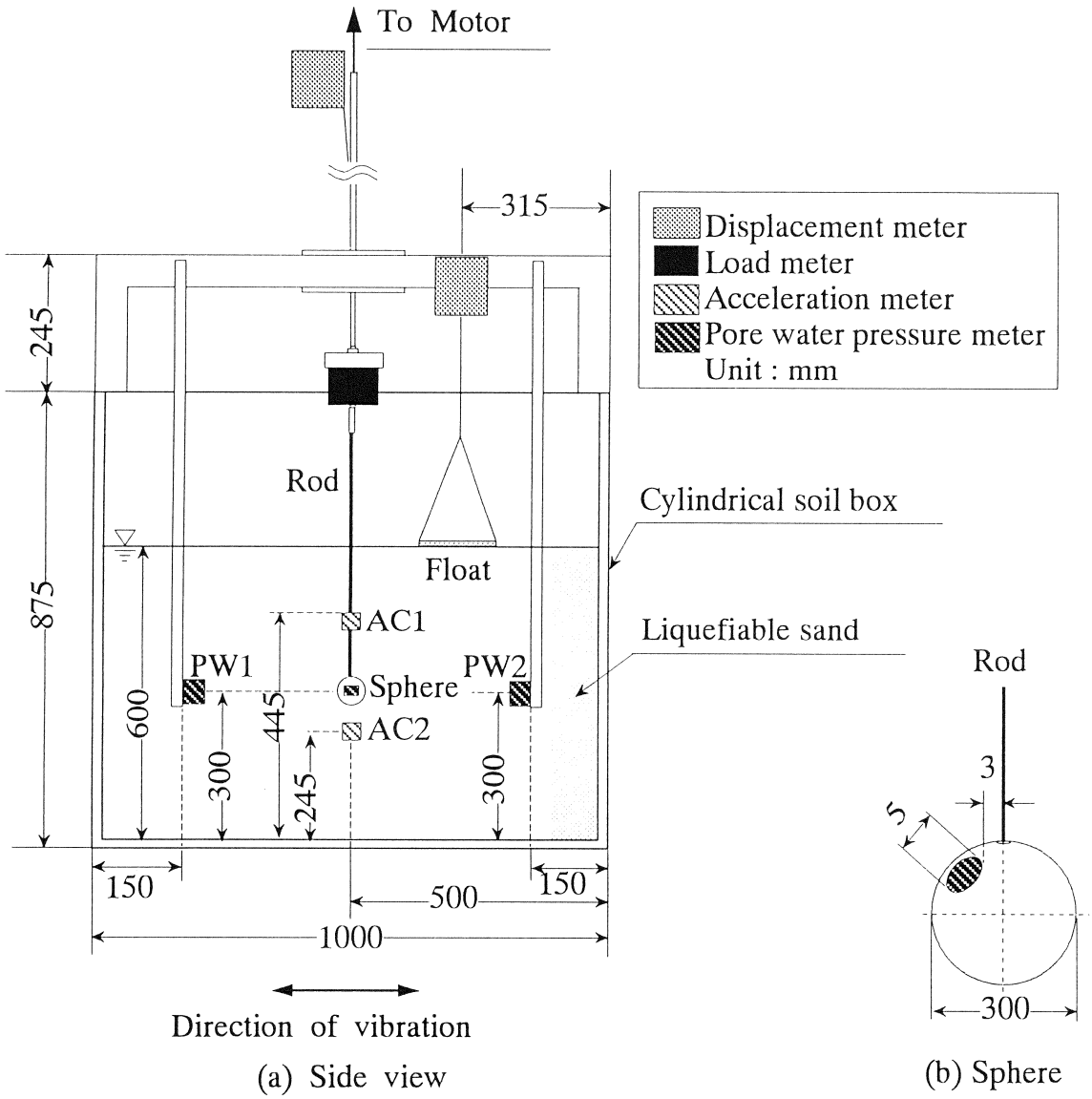

Figure 1 Experimental apparatus for measuring viscosity of liquefied sand by load acting on sphere

Table 1 Conditions of test by load acting on sphere

Diameter of sphere d (cm) : 3.0
Initial relative density Dr (%) : 10 20 30 40 50
Velocity of sphere V (cm/s) : 0.25 0.5 0.75 1.0 1.25 1.5
Acceleration Ac (gal) : 200

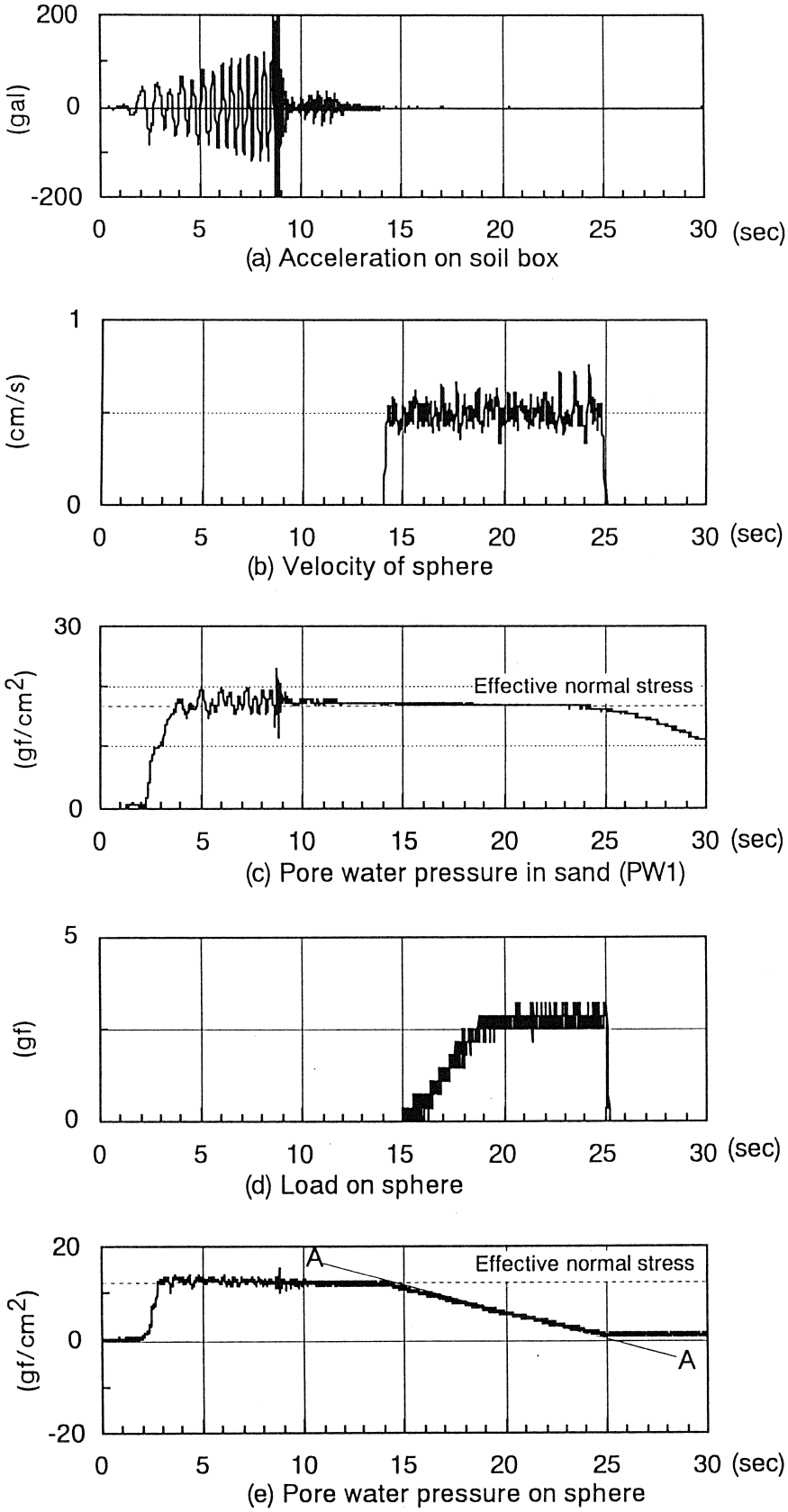

Figure 2 An example of results for test by load acting on sphere (d=3.0 cm, Dr=20%)

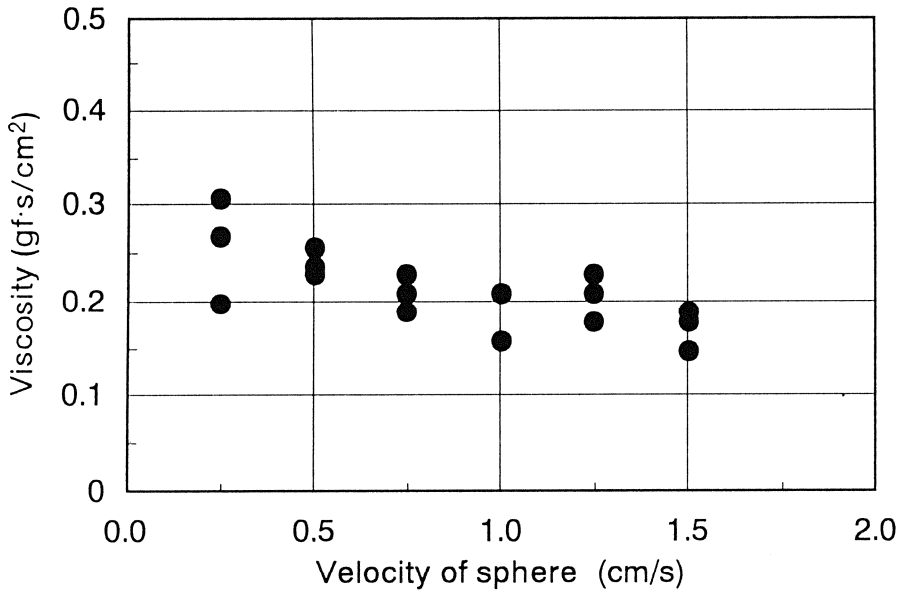

Figure 3 Relationship between coefficient of viscosity and velocity of sphere (d=3.0cm, Dr=20%, Ac=200gal)

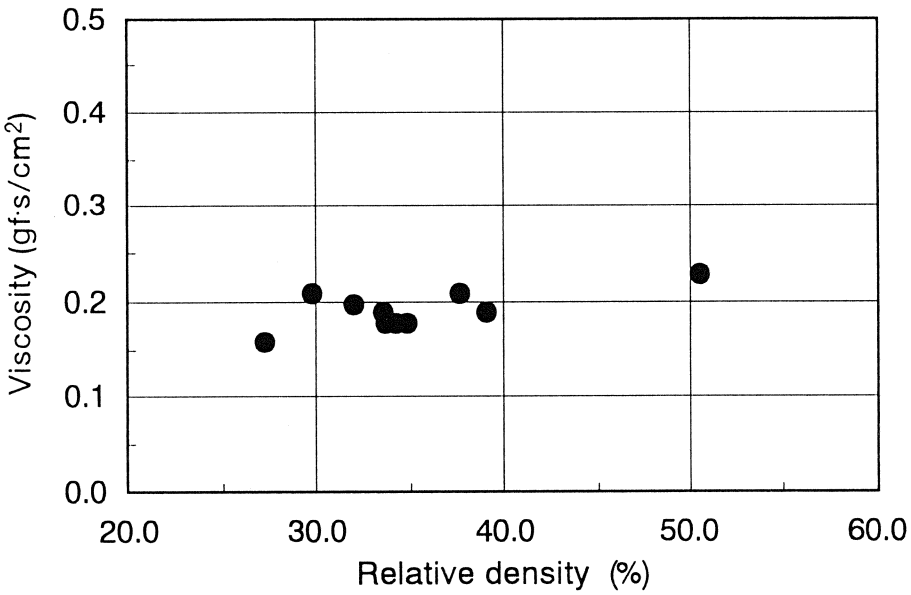

Figure 4 Relationship between coefficient of viscosity and relative density (d=3.0cm, V=1.5cm/s, Ac=200gal)

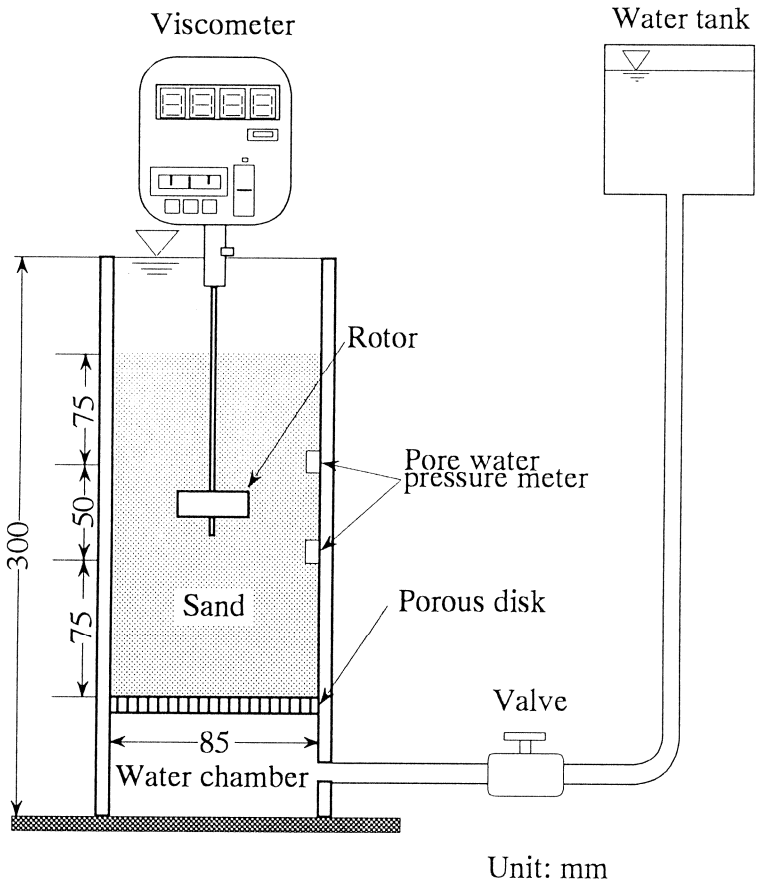

Figure 5 Experimental apparatus of measuring viscosity by viscometer

Table 2 Conditions of test by viscometer

Initial relative density (%) :	20 40 50
Number of rotation (rpm) :	1.5 3.0 6.0 12.0 30.0 60.0

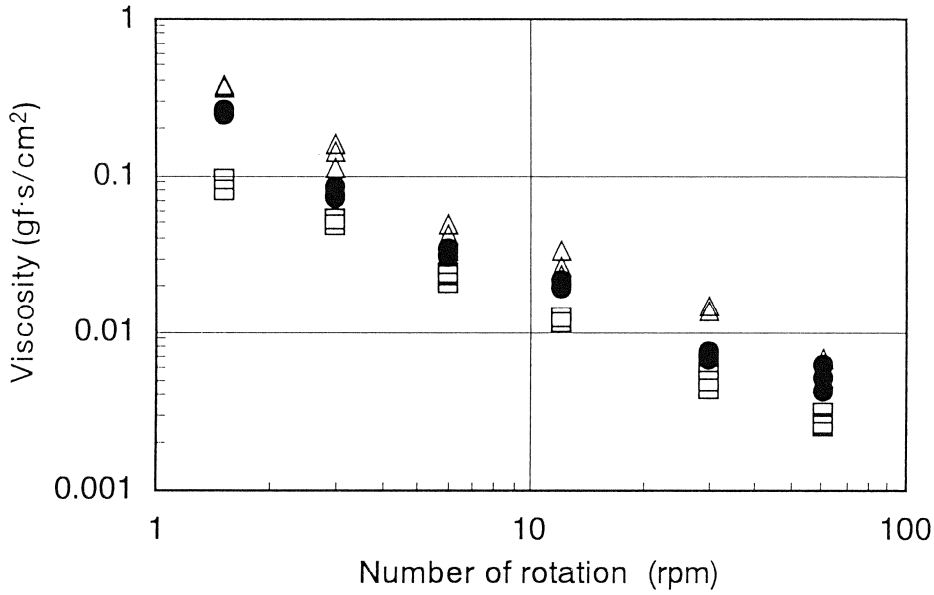

Figure 6 Relationship between coefficient of viscosity and number of rotaition
(□ : Dr=20%, ● : Dr=40%, △ : Dr=50%)

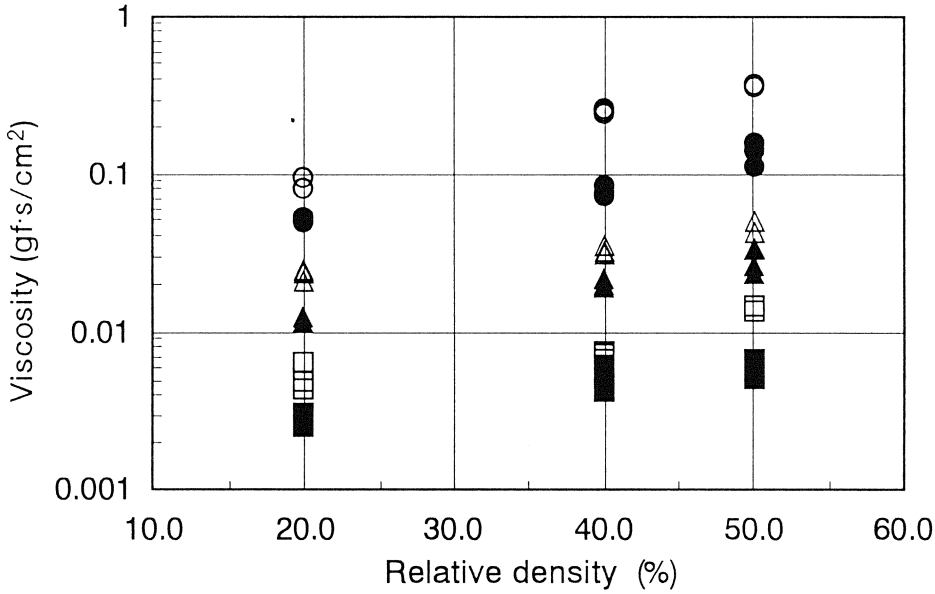

Figure 7 Relationship between coefficient of viscosity and initial relative density
(○ : 1.5rpm, ● : 3.0rpm, △ : 6.0rpm, ▲ : 12.0rpm,
□ : 30.0rpm, ■ : 60.0rpm)

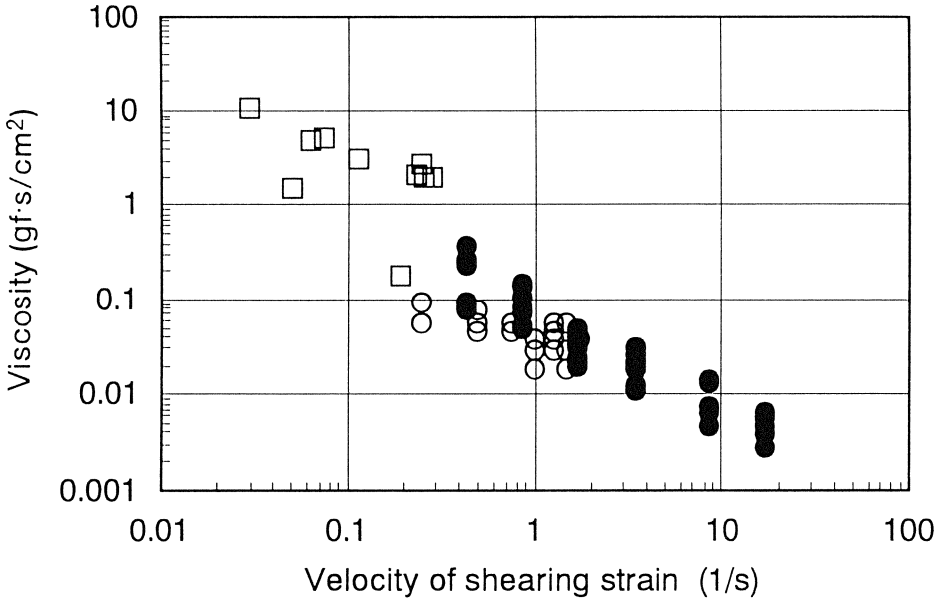

Figure 8 Relationship between coefficient of viscosity and velocity of shear strain

(● : result of test by viscometer, ○ : result of test by load acting on sphere, □ : result of experiment on liquefaction-induced large ground displacement by shaking table)

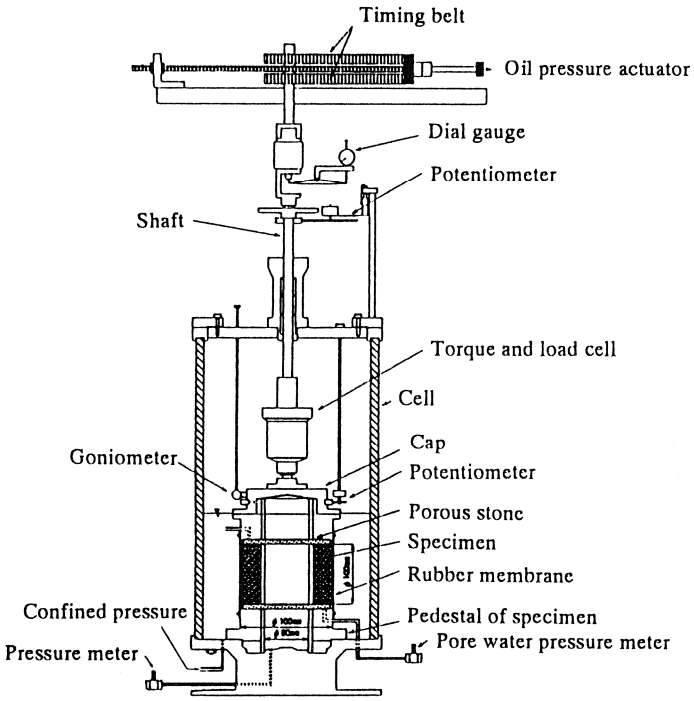

Figure 9 Experimental apparatus for hollow cylinder torsional shear test

Table 3 Conditions of cyclic torsion shear test

Relative density Dr (%)	:	27 ~ 73
Frequency f (Hz)	:	0.01 0.1
Shear stress ratio τ/σ_0'	:	0.1 0.15 0.2
Effective confining pressure σ_0' (kgf/cm^2)	:	0.5 1.0 2.0

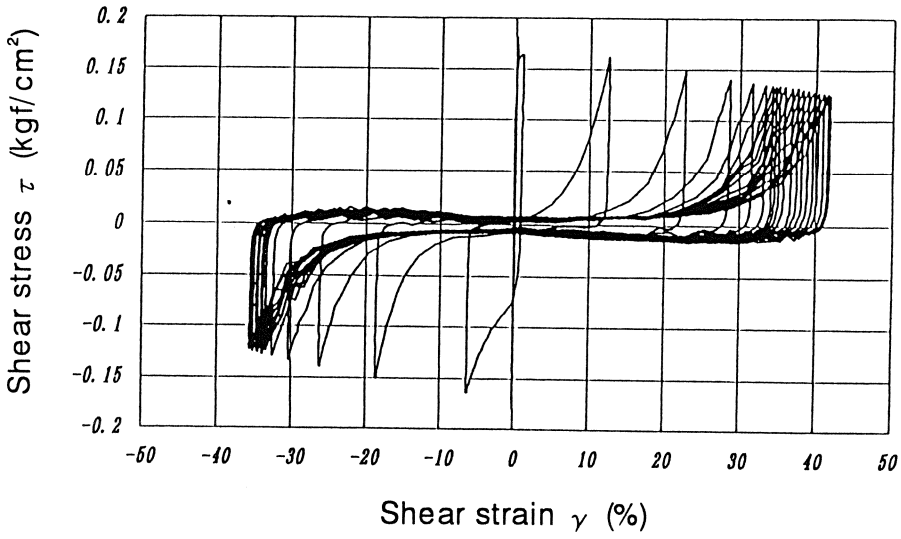

Figure 10 Relationship between shear stress and shear strain
(Dr=53%, τ/σ_0'=0.2, σ_0'=1.0kgf/cm^2, f=0.1Hz)

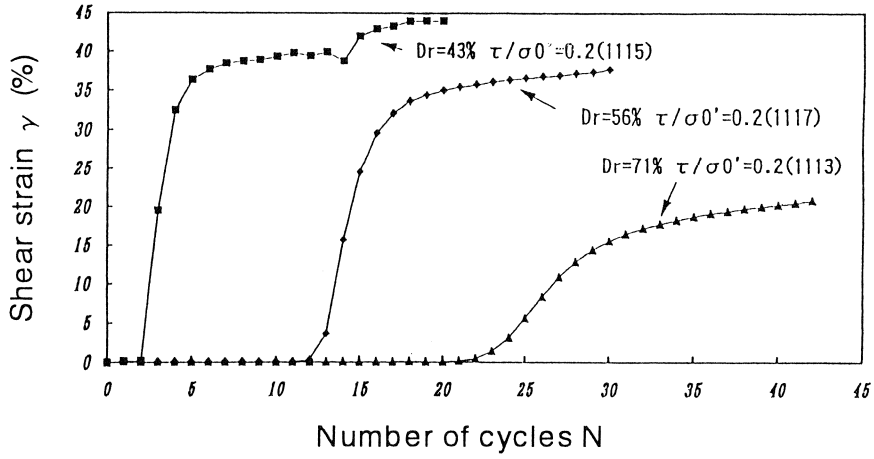

(a) Influence of relative density

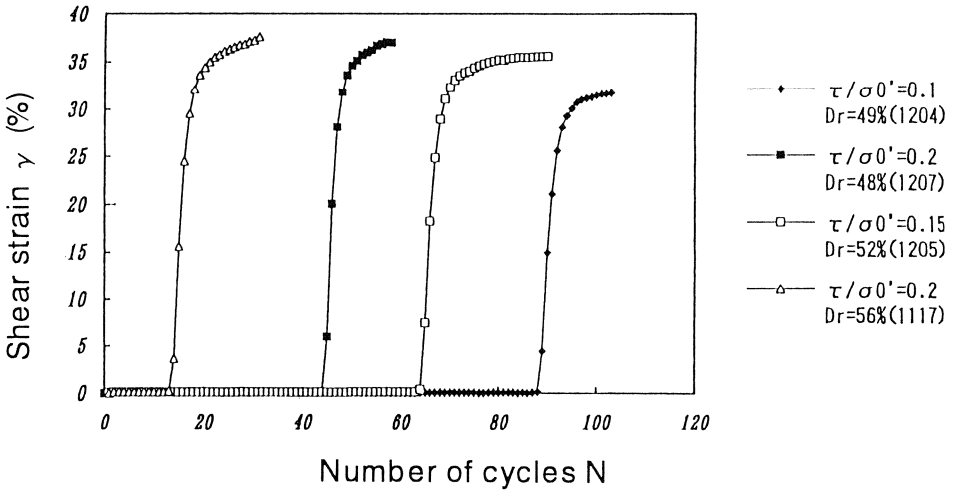

(b) Influence of shear stress ratio

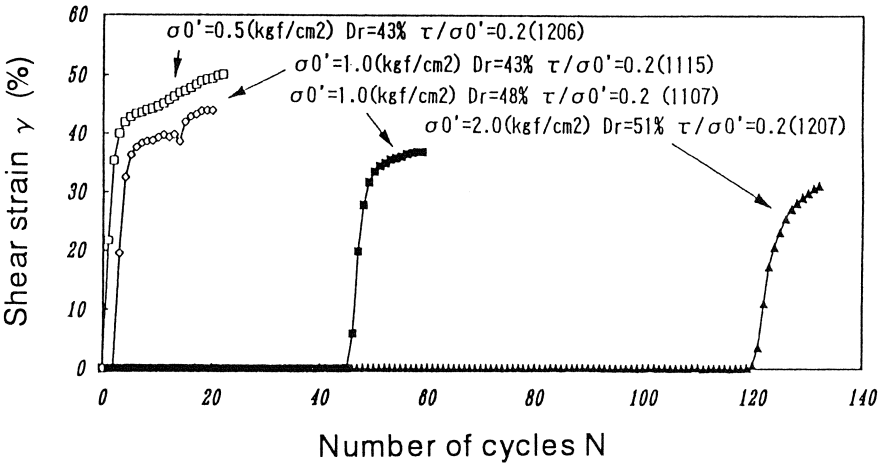

(c) Influence of effective confining pressure

Figure 11 Relationship between shear strain and number of cycles

POSTLIQUEFACTION DEFORMATION OF COHESIONLESS SOIL

Ashraf K. Hussein and Harry E. Stewart

Graduate Research Assistant and Associate Professor
School of Civil and Environmental Engineering
Cornell University

ABSTRACT

Ground settlements due to reconsolidation of liquefied soils can cause substantial damage to both above ground structures and those buried within the ground. Current methods for predicting the magnitude of settlement rely upon either empirical data collected from a limited number of field sites, or from correlations developed from specialized laboratory tests. Some direct field measurements show that actual settlements can differ significantly from those estimated using the available techniques. Therefore, an understanding of the factors influencing these ground movements is critical for quantifying the magnitude of ground deformations. Constant volume strain-controlled direct simple shear tests at relative densities of approximately 38 and 80% were performed on specimens of Nevada sand. Following liquefaction, an additional 10 to 20 cycles were applied, with shear strains ranging from 0.5 to 15%. The specimens then were allowed to reconsolidate and the volume changes were measured.

Test results indicated that the reconsolidation volumetric strains depended on relative density and initial effective stress. The reconsolidation volume changes were slightly dependent on the shear strain level, up to a shear strain of about 4%, and independent of number of postliquefaction loading cycles. Additional tests were performed in a torsional shear system to confirm the results of the direct simple shear tests. Comparisons of these results with data from other researchers, where reconsolidation strains were found to be related uniquely to the cyclic strains, are discussed in light of design curves used to estimate the magnitude of anticipated ground settlements.

INTRODUCTION

Cyclic ground motion during earthquakes is known to cause volumetric reduction in cohesionless soils, resulting in permanent ground settlement which can cause substantial damage to both above ground structures and those buried within the ground. There are two general mechanisms by which settlements can occur. First, dry cohesionless soils may undergo compaction as a result of repeated shear straining. Mechanisms contributing to settlements of dry soils have been explored and identified by several researchers (Silver and Seed, 1971; Youd, 1972), and analysis methods have been developed to predict settlements in dry soils (Seed and Silver, 1972; Pyke, et al. 1975).

The second general method by which ground settlements develop is related to reconsolidation of saturated deposits as excess pore water pressures generated during undrained cyclic loading are dissipated. Although there are several similarities in the general behavioral aspects of dry and saturated soil settlements, the latter may involve more complex relationships. Simplified and insightful methods for evaluating the anticipated reconsolidation settlements have been proposed, and are very useful for preliminary settlement evaluations. Lee and Albaisa (1974) have proposed methods based on laboratory test results for calculating reconsolidation settlements for situations where the excess pore pressures are less than or just equal to those causing liquefaction. Tokimatsu and Seed (1987) and Ishihara and Yoshimine (1992) have developed more generalized predictive methods that include consideration of not only excess pore pressure dissipation, but also the magnitude of the cyclic shear strain imposed during ground shaking. The importance of including the magnitude of the cyclic shear strains has been demonstrated based on the results of specialized laboratory tests (Ishihara and Yoshimine, 1992; Nagase and Ishihara, 1988; Tatsouka, et al. 1984).

This paper presents the results of a laboratory test program wherein test specimens were liquefied under undrained strain-controlled cyclic loading, subjected to several cycles of straining after initial liquefaction, then allowed to reconsolidate. Constant volume strain-controlled direct simple shear (DSS) tests were performed on a Nevada sand at relative densities, D_r, of approximately 38 and 80%. Following liquefaction, an additional 10 to 20 cycles were applied, with shear strains, γ, ranging from 1 to 15%. The specimens then were allowed to reconsolidate and the volume changes measured. Additional tests were performed in a torsional shear (TS) system for comparison with the results of the direct simple shear tests. Specimen preparation and test procedures are explained, along with test results. Comparisons of these results with data from other researchers, where reconsolidation strains were found to be related uniquely to the cyclic strains, are discussed in light of design curves used to estimate the magnitude of anticipated ground settlements.

TEST PROCEDURES

The tests material in this program was a Nevada sand. The grain size distribution curve for Nevada sand is shown in Figure 1. The sand has a specific gravity of 2.68, and the maximum and minimum void ratios were 0.516 and 0.894, respectively (Arulmoli, et al. (1991). The NGI direct

simple shear device with wire-reinforced rubber membranes was used in this study to perform constant volume cyclic strain-controlled tests. Sand specimens with a diameter of 66.8 mm and a height of approximately 20 mm were prepared using a dry-tamping method. Specimens were prepared in two layers at relative densities slightly lower than the target densities of approximately 38 and 80% to allow for initial consolidation effects. Although constant volume tests often are done using dry specimens, deaired water was circulated through the specimens under gravity head to minimize concerns about potential water lubrication effects. Each specimen was consolidated to an effective vertical stress of $\overline{\sigma}_{vi}$ = 54 kPa or 204 kPa, and the relative density was determined. Then, a constant volume strain-controlled test was conducted using a sinusoidal cyclic strain at frequency of 0.01 Hz until an initial liquefaction condition occurred. The strain amplitudes leading to initial liquefaction were varied over a wide range, up to strain levels wherein liquefaction developed in less than one cycle. Constant volume was achieved using a carefully controlled feedback mechanism throughout testing. After these loadings, the specimen was reconsolidated to the initial effective vertical stress prior to shear, $\overline{\sigma}_{vi}$, and the vertical strain was measured using a linear variable differential transformer. Since tests were conducted using the stiff wire-reinforced membranes, the volumetric reconsolidation strain, ε_v ,was equal to the vertical strain.

A series of cyclic undrained strain-controlled tests were conducted using the hybrid resonant column/torsional shear device described by Stewart and Hussein (1992). Solid cylindrical specimens with a height of 193 mm and a diameter of 71 mm were prepared in a split mold using the undercompaction technique developed by Ladd (1978). Specimens were consolidated isotropically at an effective confining pressure of $\overline{\sigma}_{ci}$ = 150 kPa. This isotropic consolidation pressure was selected so that the mean effective stress level in the torsional shear tests would be roughly equivalent to that in the DSS tests at $\overline{\sigma}_{vi}$ = 204 kPa. After consolidation, undrained strain-controlled cyclic torsional shear tests were performed at shear strain levels ranging from γ_{cy} = 0.1% to 8% until initial liquefaction occurred. Then, the specimens were reconsolidated to the initial effective confining pressure of 150 kPa. The reconsolidation volumetric strain was calculated based on the outflow of pore water and the specimen volume prior to cyclic shear.

TEST RESULTS

The first series of tests was conducted in the DSS device to investigate the effects of cyclic shear strain amplitude, γ_{cy}, relative density, D_r, and initial effective vertical stress, $\overline{\sigma}_{vi}$, on the volumetric strain, ε_v, due to reconsolidation after liquefaction, but without any postliquefaction cyclic straining. After initial liquefaction occurred, specimens were reconsolidated to the initial vertical stress prior to shear of $\overline{\sigma}_{vi}$ = 54 kPa or 204 kPa. The average relative densities of the specimens after consolidation were roughly 38 and 80%. The cyclic shear strain amplitude was constant for each test, and ranged from 0.1 to 15%. For shear strain levels greater than about 1%, the specimens sustained less than one complete cycle prior to failure.

Figures 2 and 3 illustrate typical results from this series of tests. Figure 2 shows pore pressure ratio, $\Delta u/\overline{\sigma}_{vi}$, versus number of loading cycles, N, at various cyclic shear strain levels, for D_r =

38% and $\overline{\sigma}_{vi}$ = 204 kPa. It is clear that the rate at which pore water pressure increases is higher for higher cyclic shear strain levels. The typical effect of relative density on pore water pressure accumulation is shown in Figure 3, wherein the pore water pressure buildup decreases as relative density increases. Figure 3 also indicates that for a given relative density and cyclic shear strain level, pore pressure ratio after a specific number of cycles decreases as initial effective vertical stress increases, although the differences are relatively minor. A similar effect was reported by Dobry, et al. (1982).

Figure 4 shows the effect of relative density and vertical stress on the number of cycles required to cause initial liquefaction, N_L. The symbols represent the averages from all tests. The figure indicates that N_L decreases as cyclic shear strain level increases, and that N_L increases for higher relative densities. Also, there is a slight trend for N_L to increase for higher initial effective vertical stresses at the same relative density.

The first series of tests involved no postliquefaction straining. Thus, volumetric reconsolidation strains measured in these tests should establish a baseline from which the effects of additional straining can be determined. Figure 5 shows the reconsolidation volumetric strains versus the cyclic shear strains for tests conducted at average relative densities of 38 and 80%, and $\overline{\sigma}_{vi}$ = 204 kPa. It can be seen from Figure 5 that at a given relative density, the reconsolidation volumetric strain slightly increases as cyclic shear strain increases up to a shear strain of roughly 4%. However, if γ_{cy} is greater than 4%, the volumetric strain tends to remain constant, independent of the level of cyclic shear strain. Also, it is clear in Figure 5 that the reconsolidation volumetric strain depends on the relative density, with volumetric strain increasing as relative density decreases. Figure 6 shows the effect of initial vertical stress on the reconsolidation volumetric strains. Previous studies generally have indicated that vertical stress does not have a major effect on the magnitude of reconsolidation strains. Yet, there is a clear difference between the tests conducted at $\overline{\sigma}_{vi}$ = 54 kPa and 204 kPa. It can be seen in Figure 6 that the reconsolidation volumetric strain increases by approximately one-third as initial effective vertical stress increased from 54 kPa to 204 kPa. Lee and Albaisa (1974) reported results of cyclic triaxial tests in which the volumetric reconsolidation strains were independent of initial effective confinement, $\overline{\sigma}_{ci}$, for pore pressure ratios, $\Delta u/\overline{\sigma}_{ci}$, less than about 0.6. For higher pore pressure ratios, the volumetric strains increased with increasing confinement, but were small, on the order of 0.8, 1.1, and 1.3% for effective confinements of 103, 207, and 414 kPa, respectively.

The effect of postliquefaction cycling on the volumetric strain due to reconsolidation was studied by bringing specimens to liquefaction at relatively small cyclic strains, $\gamma_{cy\text{-}pre}$, followed immediately by several cycles of large postliquefaction strains, $\gamma_{cy\text{-}post}$. Constant volume strain-controlled tests were performed at D_r = 38%, $\overline{\sigma}_{vi}$ = 204 kPa and preliquefaction cyclic shear strain levels of $\gamma_{cy\text{-}pre}$ = 0.1 and 0.5%, as described before. After liquefaction, the specimens were cycled at constant postliquefaction cyclic shear strain amplitudes ranging from $\gamma_{cy\text{-}post}$ = 0.1 to 15%. The number of postliqeufaction cycles was kept constant at either N_{post} = 10 or 20.

The reconsolidation volumetric strains for specimens cycled up to liquefaction at $\gamma_{cy\text{-}pre}$ = 0.1 and 0.5% with N_{post} = 10 are shown in Figure 7 as a function of the postliquefaction cyclic shear strains, $\gamma_{cy\text{-}post}$. It is clear that the volumetric strain does not depend on $\gamma_{cy\text{-}pre}$, when the

postliquefaction strains are larger than those causing liquefaction. The volumetric strains increase as $\gamma_{cy\text{-}post}$ increases up to about 4%. However, the volumetric strain remains constant as $\gamma_{cy\text{-}post}$ increases beyond 4%. The results of the tests cycled following liquefaction with N_{post} = 10 and 20 are presented in Figure 8. The figure reveals that the number of postliquefaction cycles does not influence the reconsolidation volumetric strains.

A comparison of the results of specimens reconsolidated immediately following liquefaction with the results of specimens reconsolidated after substantial postliquefaction cycling is shown in Figure 9. All the specimens had an average relative density of about 38% and were consolidated at $\overline{\sigma}_{vi}$ = 204 kPa. The figure indicates that the results of the two types of tests are the same. Both sets of data indicate a slight increase in volumetric reconsolidation strains up to a shear strain of about 4%, after which there are no marked changes. Consequently, it can be concluded that the reconsolidation volumetric strain depends on the maximum cyclic shear strain experienced by the sand during the undrained cyclic loading, as long as liquefaction occurs.

As a follow up to the DSS testing at constant preliquefaction shear strain, a series of constant volume strain-controlled tests were carried out to study the effect of the wave form on the reconsolidation volumetric strain. After consolidation to $\overline{\sigma}_{vi}$ = 204 kPa, specimens were cycled at constant shear strain level of 0.3% for five cycles. Then, specimens were cycled at a higher shear strain level ranging from 0.5 to 15% until initial liquefaction occurred. No postliquefaction cycles were applied. Volumetric strains due to reconsolidation after initial liquefaction were calculated and the results are presented in Figure 10, along with the results of tests in which a constant cyclic shear strain was applied until liquefaction occurred. The figure indicates that the volumetric strain in not affected by the wave form and depends on the maximum cyclic shear strain the sand experienced during undrained cycling.

Additional tests were conducted using the torsional shear (TS) device to confirm the trends found in the DSS tests. Specimens were consolidated isotropically to a confining pressure of $\overline{\sigma}_{ci}$ = 150 kPa and D_r = 38%. After initial consolidation, undrained cyclic strain-controlled tests were carried out at cyclic shear strain amplitudes ranging from 0.1 to 15%. No postliquefaction cycles were applied in these tests. Figure 11 compares the torsional shear and direct simple shear test results. The torsional shear results again indicate that the reconsolidation volumetric strain increases as cyclic shear strain increases up to 4%. Beyond γ_{cy} = 4%, the volumetric strain remains constant, as concluded previously from the direct simple shear results.

COMPARISONS AND DISCUSSION

Several findings from the test results require discussion, in particular with respect to differences between trends presented elsewhere. The DSS test results indicated that the volumetric reconsolidation strains were dependent on the level of initial vertical stress, as reported by Lee and Albaisa (1974). Nagase and Ishihara (1988) studied the liquefaction characteristics of Fuji River sand in a torsional shear apparatus. The program involved irregular, stress-controlled, multidirectional shearing of saturated specimens. In that program, acceleration records from six earth-

quakes were converted to shear stress histories, and applied to the test specimens. The shear stress histories were scaled to cause varying levels of pore pressure ratio, $\Delta u/\bar{\sigma}_{ci}$, at the end of cycling. For tests in which the pore pressure ratios were less than one, the reconsolidation volumetric strains increased nearly linearly with increasing pore pressure ratios, and decreased with increasing relative density. These trends are consistent with those reported by others, and consistent with anticipated behavior. However, in the tests in which liquefaction ($\Delta u/\bar{\sigma}_{ci} = 1$) occurred, the measured volumetric strains were not defined uniquely as a function of pore pressure ratio. Nagase and Ishihara (1988) determined that the maximum shear strain, γ_{max}, that occurred at any point in the applied stress record could be used to determine the volumetric reconsolidation strain. This finding is significant, as it implies that reconsolidation strains are dependent on how the pore pressures are generated. In addition, they concluded that when the applied shear stress records were adjusted so that the irregular loading was just large enough to cause liquefaction, the maximum shear strain generated, γ_{max}, in all specimens was approximately 2.5 to 3.5% for relative densities in the range of approximately 50 to 90%. For specimens that did not liquefy prior to the complete application of the irregular loading, the maximum shear strains were less than that limit. Further analysis of the reconsolidation strains for all pore pressure ratios were found to be related directly to the maximum shear strain that occurred at any point in the tests. Ishihara and Yoshimine (1992) developed relationships between reconsolidation strains and maximum shear strains that were based on several important considerations. First, for situations in which liquefaction did not occur, volumetric strains could be related either to pore pressure ratio or cyclic strain. Secondly, liquefaction did not occur unless the cyclic shear strains during a test were at least equal to a threshold value of about 3%. Finally, volumetric strains at any relative density increased nearly linearly with maximum cyclic shear strain up to a second shear strain limit of about 8%, after which the volumetric strains remained constant.

Lee and Seed (1967) identify several ways in which failure in laboratory tests can be defined. One definition is when the zero effective stress condition develops, i.e., $\Delta u/\bar{\sigma}_{ci} = 1$. Another definition is based on a performance criterion in which strains reach some limiting value. A key difficulty with any definition based on a performance criterion such as a defined strain, is that there are many different strain levels that can be considered. Lee and Seed (1967) clearly showed that the strains at initial liquefaction decrease with increasing relative density, and that the onset of liquefaction in stress-controlled triaxial tests on loose sand specimens ($D_r = 38\%$) was accompanied by an immediate increase in the cyclic axial strains, ε_a, to approximately 10%. These trends in strain generation also were exhibited in stress-controlled cyclic simple shear tests (Peacock and Seed, 1968), wherein large strains ($\gamma \approx 15\%$) developed immediately following liquefaction in loose sands ($D_r = 50\%$). Furthermore, Lee and Albaisa (1974) presented test results from a loose sand ($D_r = 40\%$) that showed axial strains on the order of 10 to 14% when pore pressure ratios first become one, corresponding to a shear strain of $\gamma = 1.5\ \varepsilon_a = 15$ to 21%. Thus, establishment of a unique strain at failure in stress-controlled tests is difficult. There are, however, reasonable limits on the amount of strain that can be generated *in situ* during earthquakes, which are dependent on relative density, with maximum shear strains of about 35% at $D_r \approx 50\%$, and perhaps 5% for $D_r \approx$ 90% (Seed, 1979). Such behavior is referred to as cyclic mobility with limited strain potential. Thus, the findings by Nagase and Ishihara (1988) identifying a unique level of shear strain, independent of relative density, with the condition of liquefaction represents a fundamentally new development in understanding stress-controlled testing.

Nagase and Ishihara (1988) and Ishihara and Yoshimine (1992) have shown that reconsolidation volumetric strains are related uniquely to the maximum shear strain developed in the stress-controlled tests, up to strains of about 8%. Tatsuoka, et al. (1984) also investigated the effects of cyclic strain on reconsolidation volumetric strains. Those test results indicated increasing volumetric strains with increasing shear strains, but insufficient data were collected at cyclic shear strains greater than about 5%. Thus, a clear conclusion about a threshold strain limit cannot be drawn from that work, although there is some indication that the strain limit may be near 5%. Finn, et al. (1970) investigated the effects of strain history on the reliquefaction susceptibility of sand. Those tests included a series of strain-limited cyclic simple shear tests in which specimens were brought to liquefaction, and subjected to 15 cycles of shear strain prior to dissipation of the excess pore pressures. The specimens were then allowed to reconsolidate, and were tested again to determine any changes in cyclic strength that occurred as a result of the postliquefaction straining. The postliquefaction shear strains in tests performed by Finn, et al. ranged from $\gamma = 0.5$ to 11%. Thus, these tests are similar to those performed on the Nevada sand in this study. The tests conducted by Finn, et al. indicated that volumetric reconsolidation strains increased with the level of postliquefaction shear strain, for strains up to about $\gamma = 3\%$. However, for higher shear strains the volumetric strains remained nearly constant. The conclusion was drawn that above $\gamma = 3\%$, no further structural rearrangement of the soil skeleton occurs. This implies that cyclic strains following liquefaction in excess of $\gamma = 3\%$ may not lead to additional reconsolidation strain. This finding generally is consistent with the test results for the Nevada sand, although the Nevada sand showed a threshold strain of 4%.

Figure 12 presents reconsolidation volumetric strains measured by several groups, the design curves recommended by Ihsihara and Yoshimine (1992), and the results from the Nevada sand tested at $\bar{\sigma}_{vi} = 204$ kPa. The design curves prepared by Ishihara and Yoshimine (1992) are based on many data generated by Nagase and Ishihara (1988), which are not shown on the figure. Figure 12 indicates a wide range in volumetric strains, and a general increase in volumetric strain for decreasing relative densities. However, the cyclic strain after which the volumetric strains tend to remain constant appears to be on the order of 3 to 5%. The results presented in Figure 12 show fundamental differences in interpreting stress-controlled and strain-controlled tests. Liquefaction can be induced in strain-controlled tests at low strain levels in only a few cycles. However, stress-controlled tests often define liquefaction failure as occurring at much higher strain levels (greater than 3%.).

The methods used most frequently in recent years for prediction liquefaction-induced settlements generally rely upon estimates of shear stress ratios generated by an earthquake and those causing liquefaction, as dependent on some index such as relative density or penetration resistance. (Tokimatsu and Seed, 1987; Ishihara and Yoshimine, 1992). Comparisons between measured and predicted settlements are in reasonable agreement, but are sensitive to the shear strain levels for very loose soil conditions.

Figure 13 presents a simple interpretation of the volumetric strains anticipated following liquefaction. The solid line in the figure represents the relationship given by the Tokimatsu and Seed (1987) design curves for volumetric strain for conditions in which liquefaction has occurred. The data shown on the figure are those from Japanese field observations from the 1968 Tokachioki

earthquake (Ohsaki, 1970), the 1964 Niigata earthquake (Building Research Institute, 1965), and the 1968 Miyagiken Oki earthquake (Tohno and Yasuda, 1981), as used by Tokimatsu and Seed to construct their design curves. Also shown on the figure are the results form this study on Nevada sand. The data from these tests on Nevada sand agree reasonably well with the others. As with the predictive method given by Tokimatsu and Seed (1987) and Ishihara and Yoshimine (1992), Figure 12 indicates that volumetric strains for site conditions having $(N_1)_{60}$ greater than about 30 are limited to about 1%. For sites where the soil is extremely loose, observed settlements may have been affected by other aspects of extensive liquefaction that make reliable measurements of actual ground settlements and back-calculated volumetric strains difficult. For many natural deposits, normal limits on relative densities often have a lower limit of 30 to 40%, with an upper limit on the order of 80%. Thus, it may be that typical maximum volumetric strains are limited to about 4%.

ACKNOWLEDGMENTS

The authors wish to thank the National Center for Earthquake Engineering Research (NCEER) which provided support under Grant No. 93-2301(S). The work of Ali Avcisoy in helping to prepare the figures is appreciated greatly.

REFERENCES

Arulmoli, K., K.K. Muraleetharan, M.M. Hossain, and L.S. Fruth (1991) " VELACS Verification of Liquefaction Analyses by Centrifuge Studies Laboratory Testing Program Preliminary Data Report," The Earth Technology Corporation, Sept.

Building Research Institute (1965) "Niigata Earthquake and Damage to Reinforced Concrete Buildings in Niigata City," Report, Building Research Institute, Ministry of Construction, 43.

Dobry, R., R.S. Ladd, F.Y. Yokel, R.M. Chung, and D. Powell (1982) "Prediction of Pore Water Pressure Buildup and Liquefaction of Sands During Earthquakes by the Cyclic Strain Method," Building Science Series 138, National Bureau of Standards, Washington, D.C., July, 168 p.

Finn, W.D.L., P.L. Bransby, and D.J. Pickering (1970) "Effect of Strain History on Liquefaction of Sand," Journal of the Soil Mechanics and Foundations Division, ASCE, Vol. 96, No. SM6, Nov., pp. 1917-1934.

Ishihara, K. and M. Yoshimine (1992) "Evaluation of Settlements in Sand Deposits Following Liquefaction During Earthquakes," Soils and Foundations, JSSMFE, Vol. 32, No. 1, March, pp. 173-188.

Peacock, W.H. and H.B. Seed (1968) " Sand Liquefaction Under Cyclic Loading Simple Shear Conditions," Journal of the Soil Mechanics and Foundations Division, ASCE, Vol. 94, No. SM3, May, pp. 689-708.

Ladd, R.S. (1978) "Preparing Test Specimens Using Undercompaction," Geotechnical Testing Journal, ASTM, Vol. 1, No. 1, Mar., pp. 16-23.

Lee, K.L, and A. Albaisa (1974) "Earthquake Induced Settlements in Saturated Sands," Journal of the Geotechnical Engineering Division, ASCE, Vol. 100, No. GT4, Apr., pp. 387-406.

Nagase, H. and K. Ishihara (1988) "Liquefaction-Induced Compaction and Settlement of Sand During Earthquakes," Soils and Foundations, JSSMFE, Vol. 28, No. 1, March, pp. 65-76.

Ohsaki, Y. (1970) "Effects of Sand Compaction on Liquefaction During Tokachioki Earthquake," Soils and Foundations, JSSMFE, Vol. 10, No.2, pp. 112-128.

Pyke, R., H.B. Seed, and C.K. Chan (1975) "Settlement of Sand Under Multidirectional Shaking," Journal of the Geotechnical Engineering Division, ASCE, Vol. 101, No. GT4, Apr., pp. 379-398.

Seed, H.B. and M.L. Silver (1972) "Settlement of Dry Sands During Earthquakes," Journal of the Soil Mechanics and Foundations Division, ASCE, Vol. 98, No. SM4, Apr., pp. 381-397.

Seed, H.B. (1979) "Soil Liquefaction and Cyclic Mobility Evaluation for Level Ground During Earthquakes," Journal of the Geotechnical Engineering Division, ASCE, Vol. 105, No. GT2, Feb., pp. 201-255.

Silver, M.L. and H.B. Seed (1971) "Volume Changes in Sands During Cyclic Loading," Journal of the Soil Mechanics and Foundations Division, ASCE, Vol. 97, No. SM9, Sept., pp. 1171-1182.

Stewart, H.E. and A.K. Hussein (1992) "Determination of the Dynamic Shear Modulus of Holocene Bay Mud for Site-Response Analysis," The Loma Prieta, California, Earthquake of October 17, 1989 - Marina District, U.S. Geological Survey Professional Paper 1551-F, June, pp. F75-F83.

Tatsuoka, F., T. Sasaki, and S. Yamada (1984) "Settlement in Saturated Sand Induced by Cyclic Undrained Simple Shear," Proceedings, Eighth World Conference on Earthquake Engineering, San Francisco, Vol. III, pp. 95-102.

Tohno, I. and S. Yasuda (1981) "Liquefaction of the Ground During the 1978 Miyagiken-Oki Earthquake," Soils and Foundations, JSSMFE, Vol. 21, No. 2, pp. 18-34.

Tokimatsu, K. and H.B. Seed (1987) "Volume Changes in Sands During Cyclic Loading," Journal of Geotechnical Engineering, ASCE, Vol. 113, No. 8, Aug., pp. 861-878.

Yoshimi, Y., F. Kuwabara, and K. Tokimatsu (1975) "One-Dimensional Volume Change Characteristics of Sands Under Very Low Confining Stresses," Soils and Foundations, JSSMFE, Vol. 15, No. 3, Sept., pp. 51-60.

Youd, T.L. (1972) "Compaction of Sands by Repeated Shear Straining," Journal of the Soil Mechanics and Foundations Division, ASCE, Vol. 98, No. SM7, July, pp. 709-725.

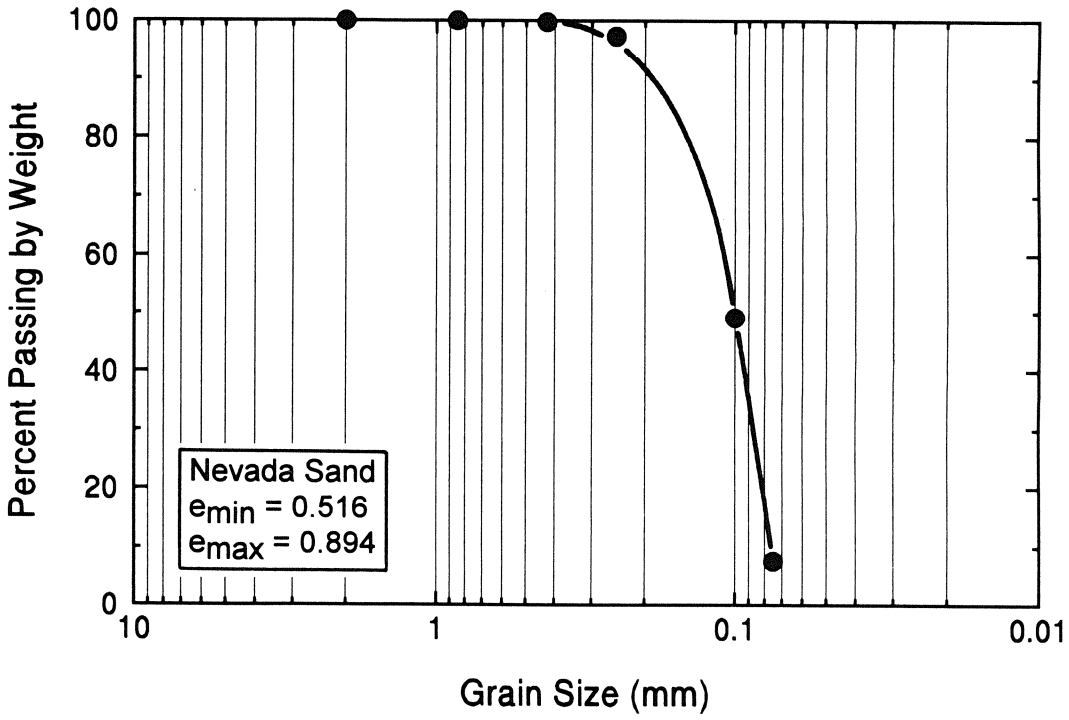

Figure 1. Grain Size Distribution Curve for Nevada Sand

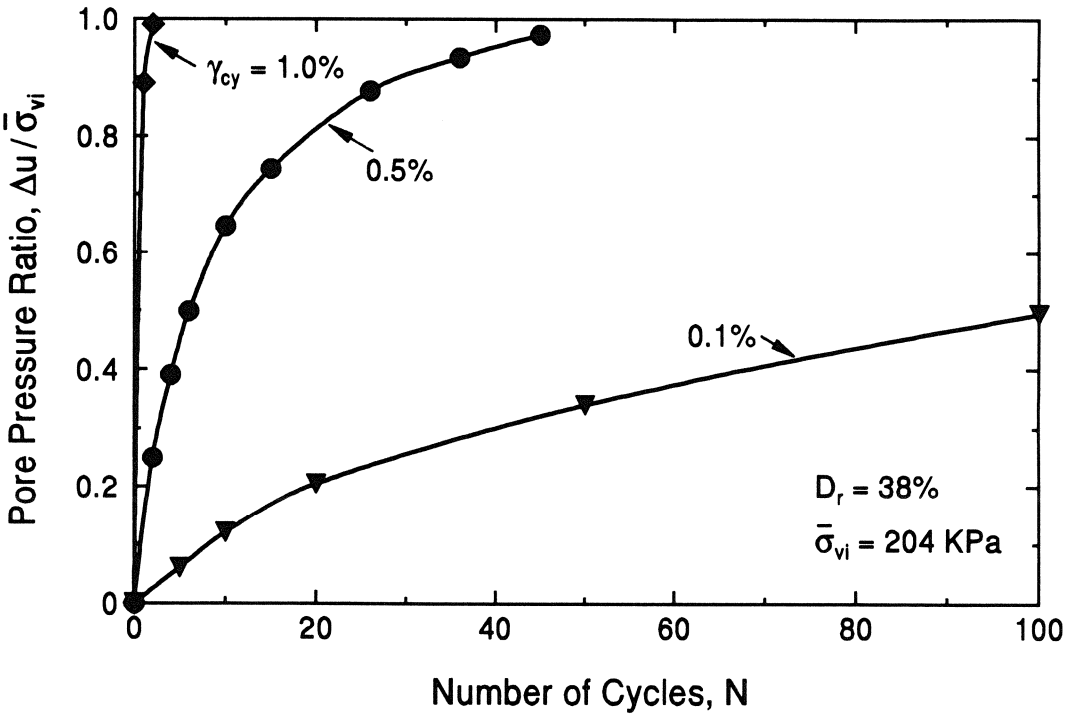

Figure 2. Pore Pressure Ratio versus Number of Cycles at Various Cyclic Shear Strain Levels

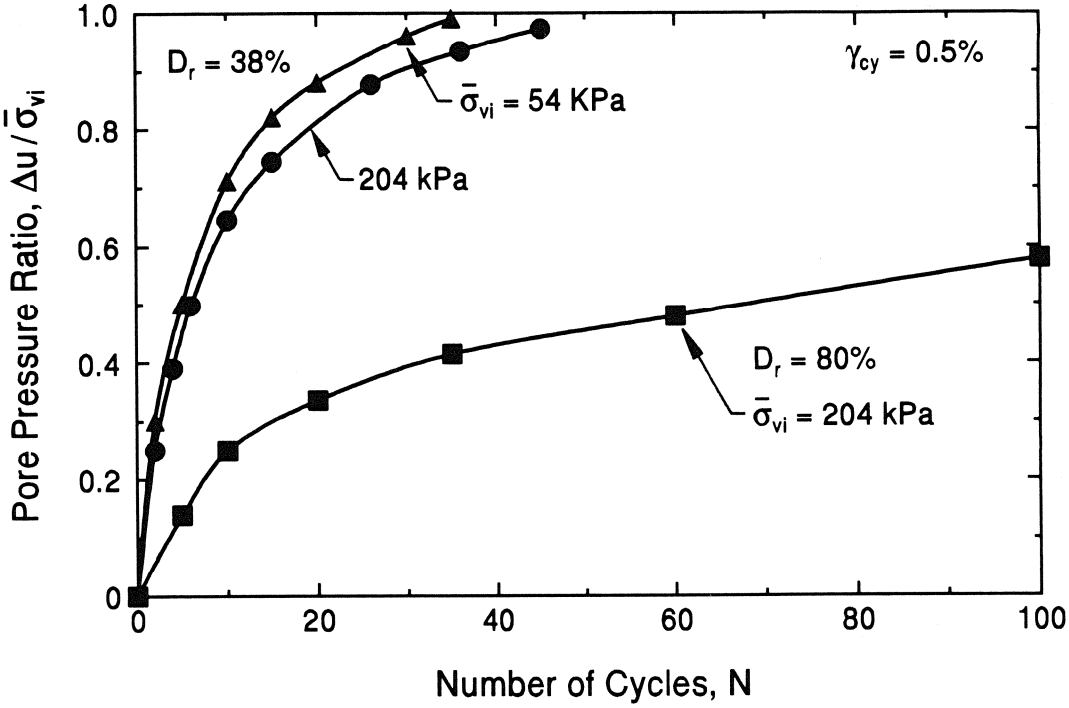

Figure 3. Effect of Relative Density and Initial Effective Stress on Pore Pressure Ratio

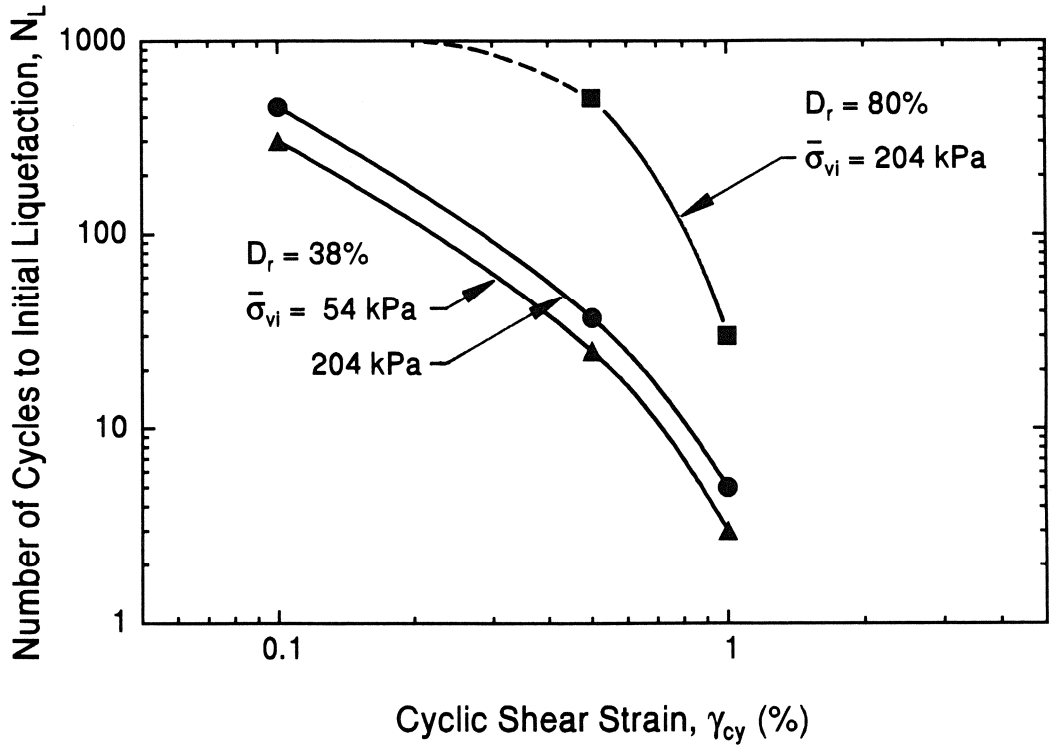

Figure 4. Effect of Relative Density and Initial Effective Stress on Number of Cycles to Liquefaction

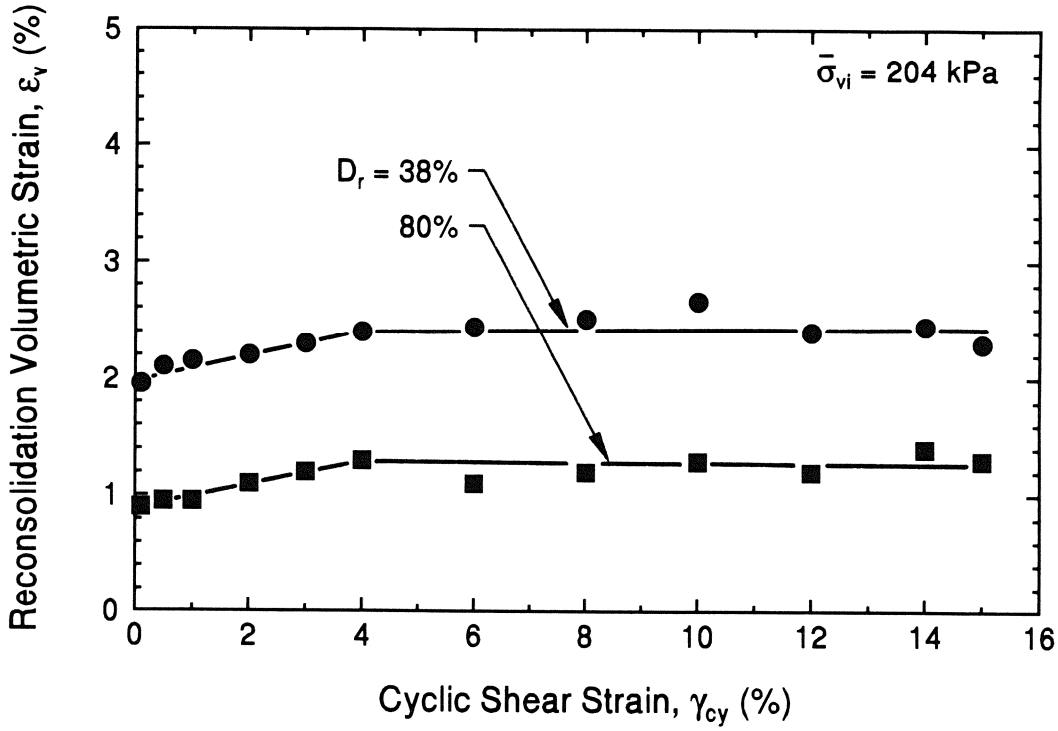

Figure 5. Effect of Relative Density on Reconsolidation Volumetric Strain

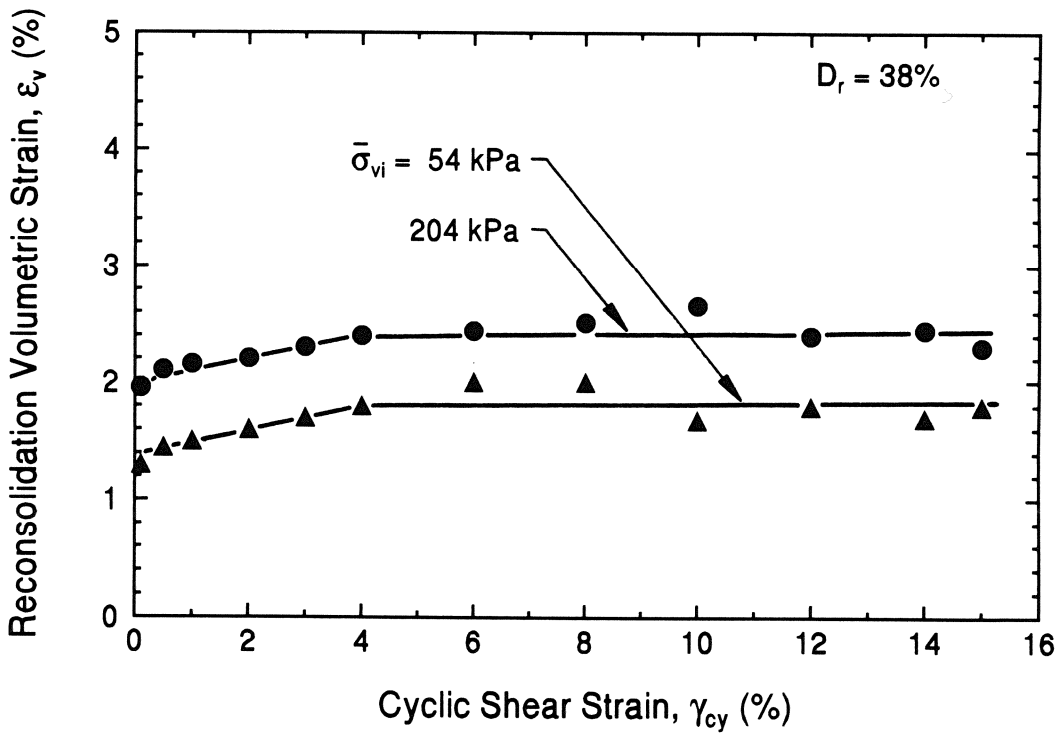

Figure 6. Effect of Initial Effective Stress on Reconsolidation Volumetric Strain

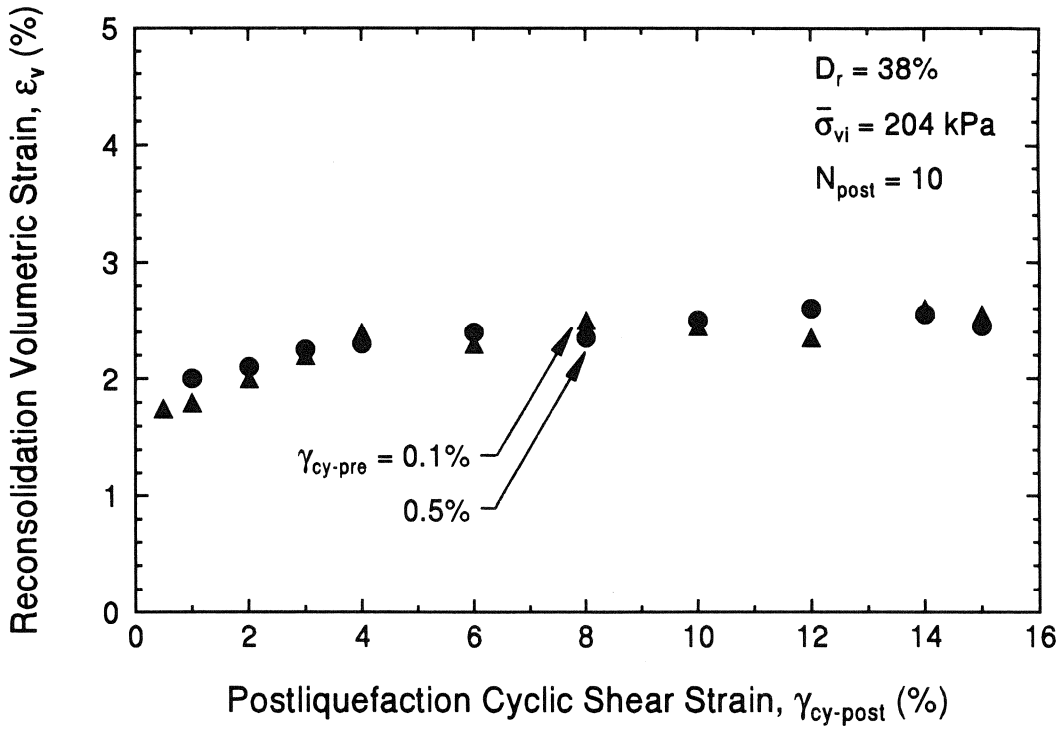

Figure 7. Effect of Postliquefaction Cycling on Reconsolidation Volumetric Strain

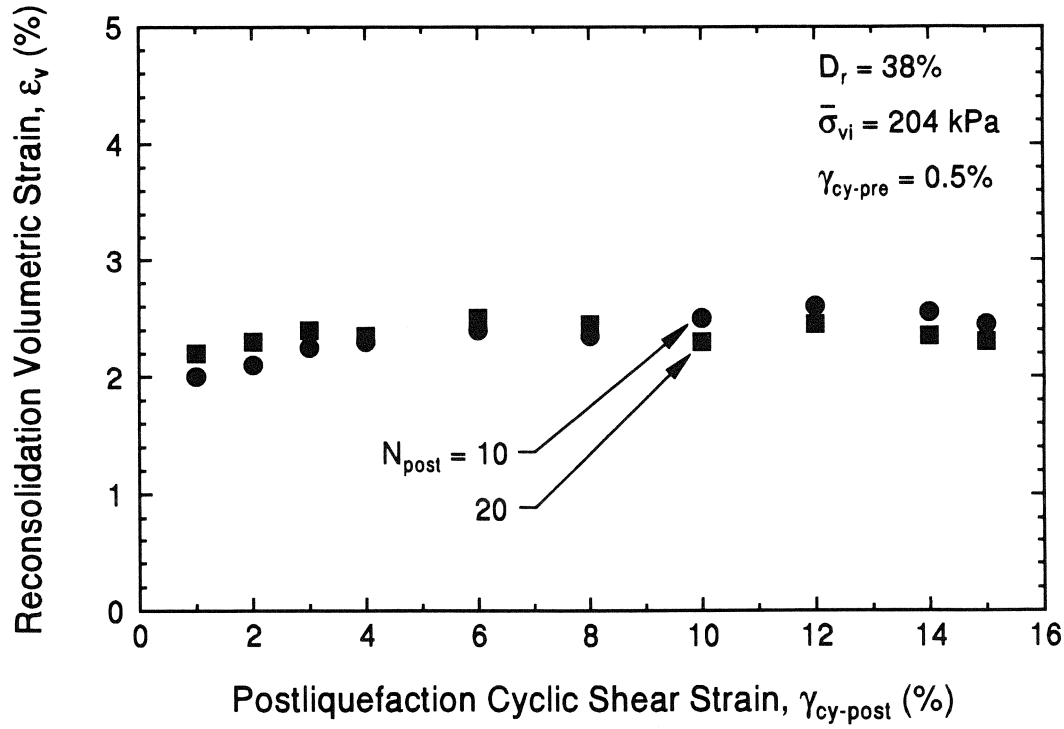

Figure 8. Reconsolidation Volumetric Strains for N_{post} = 10 and 20

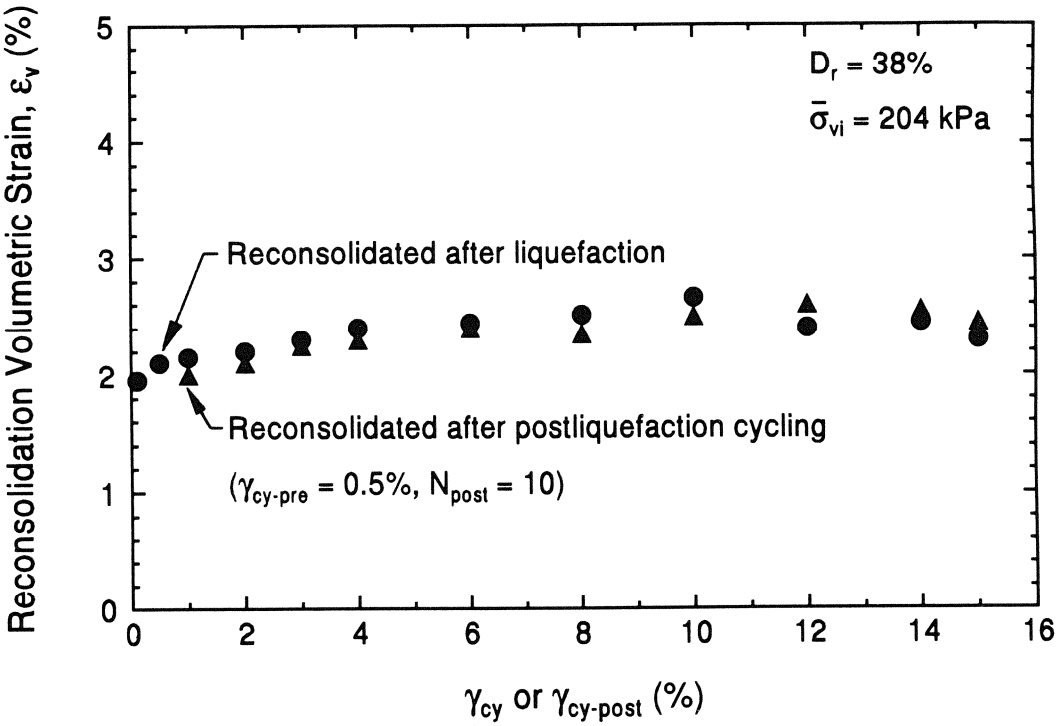

Figure 9. Comparison of Test Results with and without Postliquefaction Cycling

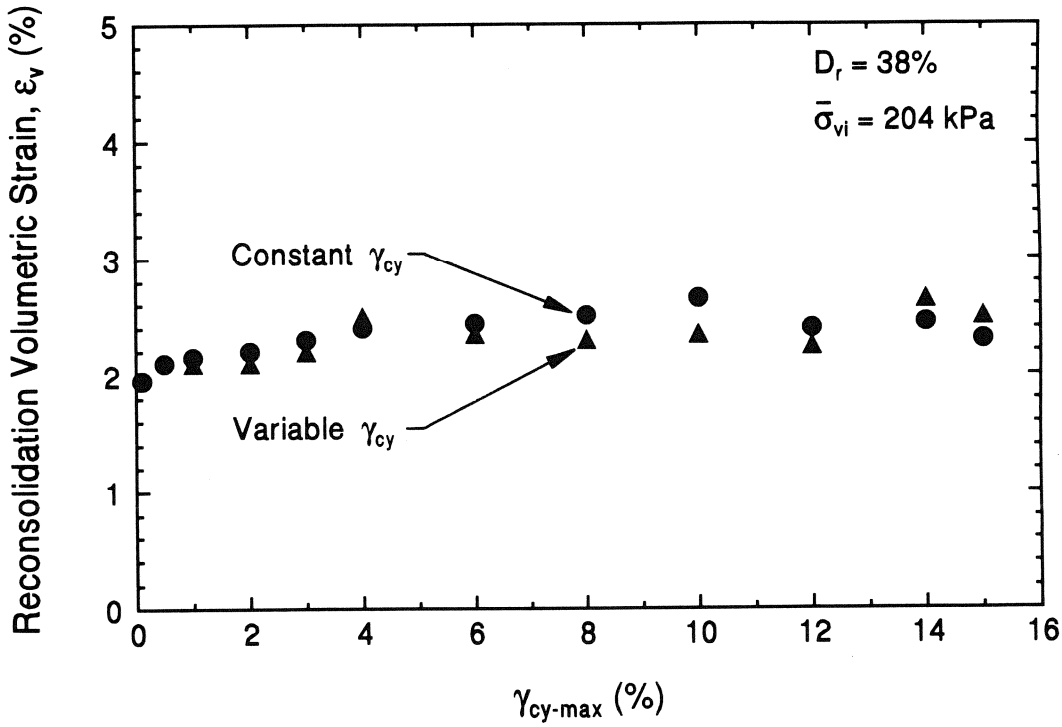

Figure 10. Reconsolidation Volumetric Strains for Different Wave Forms

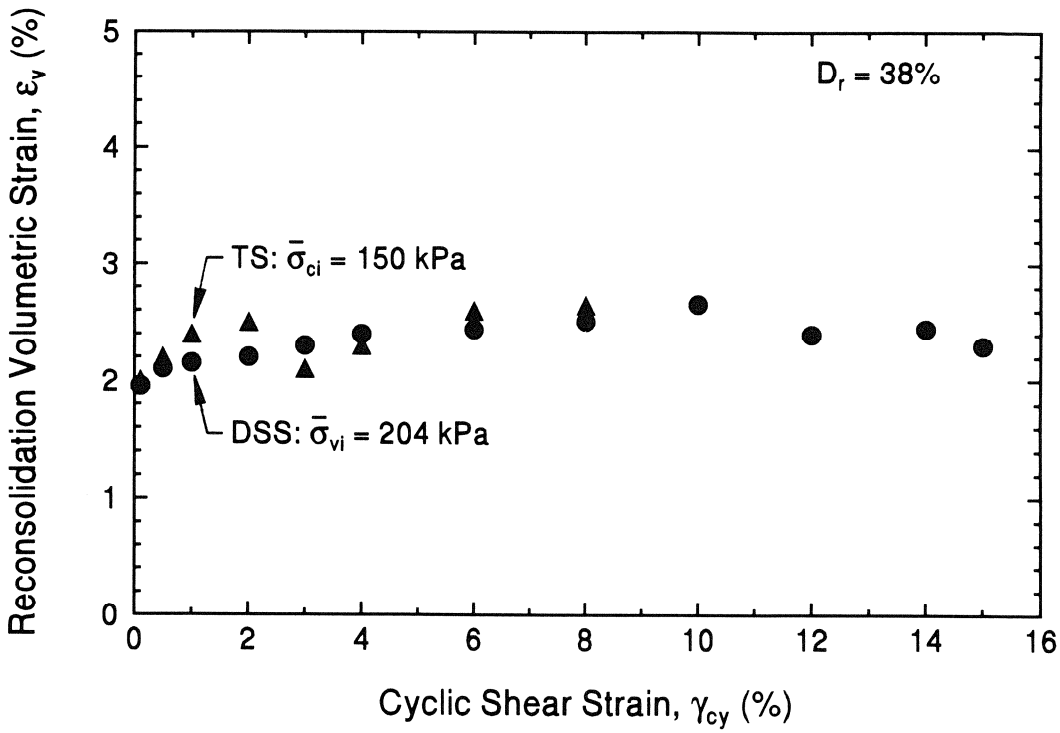

Figure 11. Comparison of Direct Simple Shear and Torsional Shear Tests Results

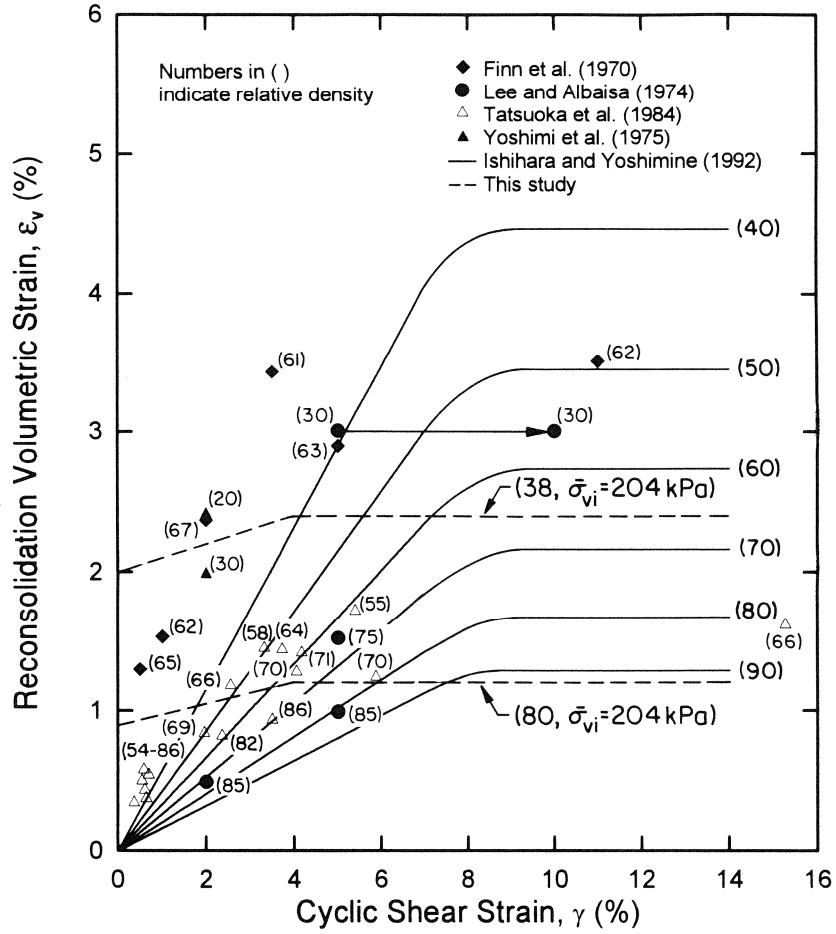

Figure 12. Reconsolidation Volumetric Strains from Various Studies

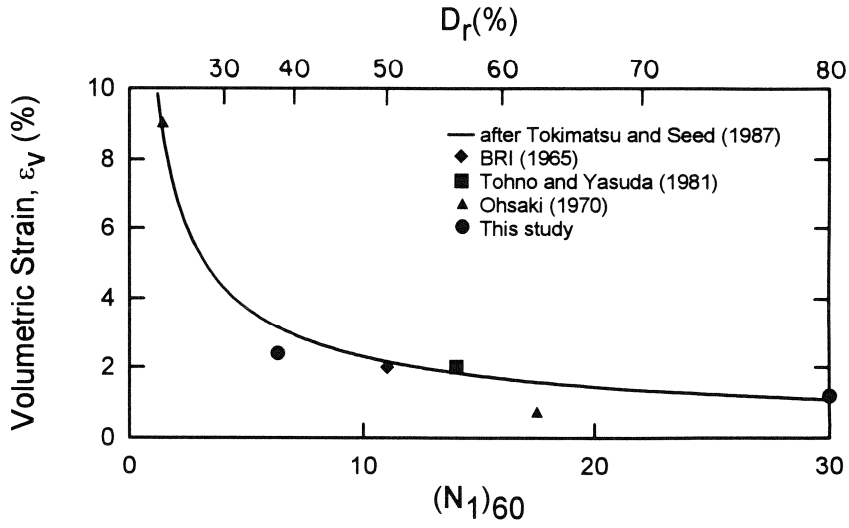

Figure 13. Simplified Curve for Estimating Reconsolidation Volumetric Strain

A CONSIDERATION OF THE MECHANISM FOR LIQUEFACTION-RELATED LARGE GROUND DISPLACEMENT

Masanori Hamada*, Hiroshi Sato** and Tetsutaro Kawakami***

ABSTRACTS

The authors discussed the mechanism of the liquefaction-related large ground displacement by referring the existing researches and an shaking table test result. Firstly, they reviewed the outcomes from case studies on large ground displacement during past earthquakes as well as empirical formulae proposed from regression analyses of the ground displacement with various factors such as gradient of ground surface, and studied fundamental characteristics of the large ground movement. Secondarily, the authors reviewed existing experimental works on ground displacement and on the mechanical properties of liquefied soil during the ground movement.

Furthermore, the authors conducted a shaking table test, where the ground surface was inclined after complete liquefaction of the soil. Based on the the review of the existing researches and on the shaking table test they proposed an idea on the mechanism of the large ground displacement during liquefaction.

* Professor, Dept. of Civil Engineering, Waseda University, Tokyo, Japan.
** Researcher, Institute of Technology, Tokyo Electric Power Company, Tokyo, Japan.
*** Assistant Professor, Dept. of Ocean Civil Engineering, Tokai University, Shimizu, Japan.

INTRODUCTION

Liquefaction-induced large ground displacements were firstly recognized and measured by aerial survey at the time of the 1983 Nihonkai-Chubu earthquake. Since then, case studies on past ten earthquakes have been conducted under a close corporation between U.S. and Japanese researchers. By using the data from the case studies the soil and geological conditions under which the large ground displacements occurred have been studied (Hamada and O'Rourke, 1992a and O'Rourke and Hamada, 1992a).

A number of experimental and numerical researches has been done on the liquefaction-caused large ground displacement and it's effects on the structures. However, the mechanism of the occurrence of the large ground displacement with a magnitude of several meters has not been comprehensively explained, and any adequate knowledge which is applicable for the design and construction of the structures against the large ground displacement has not been provided .

The Liquefaction-induced ground displacement has caused extensive damage to structures, particularly to in-ground structures such as buried pipes and foundation piles. Therefore, it is one of urgent research subjects to investigate the mechanism of the occurrence of the ground displacement as well as to develop effective countermeasures in order to prevent the damage due to the ground displacement.

CASE STUDIES AND PROPOSED EMPIRICAL FORMULAE

Hamada et al. (1986) summarized two types of soil and geological condition where liquefaction induced the large ground displacement as shown in Figure 1 by referring the case studies. First type is that a ground along river or sea largely moves toward the water when quay walls collapses. The mechanism of this type can be easily understood by considering the elevation difference of the ground surface at the collapsed quay walls. Second type is that a slightly inclined ground moves from the higher elevations to the lower one due to liquefaction. It seems difficult to clearly explain the mechanism of the ground displacement of this type with a magnitude of several meters, sometimes above ten meters, which means that the ground strain reaches over 100 %, even when gradient of ground surface is very small, below 1 %.

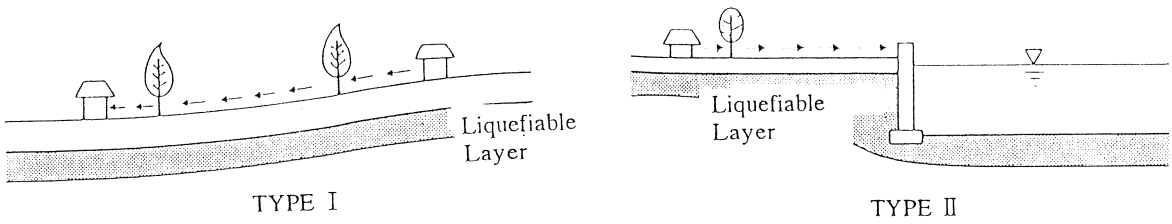

Figure 1. Subsurface Condition for Liquefaction-Induced Ground Displacement

The correlation of the magnitude of the ground displacement with various factors such as gradient of the ground surface and thickness of the liquefiable soil, were studied, and empirical formulae were proposed in order to predict the ground displacement (Hamada et al., 1986, Bartlett et al., 1992).

Hamada et al., conducted a regression analysis by using the data from the 1964 Niigata, the 1971 San Fernando and the 1983 Nihonkai-Chubu earthquakes, and proposed the following empirical formula;

$$D = 0.75 \cdot \sqrt[2]{H} \cdot \sqrt[3]{\theta} \qquad (1)$$

D : Ground displacement in the horizontal direction (m).
H : Thickness of estimated liquefied layer of the ground (m).
θ :Larger value of the gradient of ground surface or that of lower boundary of estimated liquefied layer of the ground (%).

The proposed formula only provides an approximate fit to the field data. The predicted ground displacements by the above formula are actually scattered between half and twice the measured values as shown in Figure 2. In particular, the empirical formula shows the comparatively low correlation between the ground displacement D and the larger value of the gradient of the ground surface or that of lower boundary of liquefied layer θ, since D is proportional to only a cubic root of the gradient.

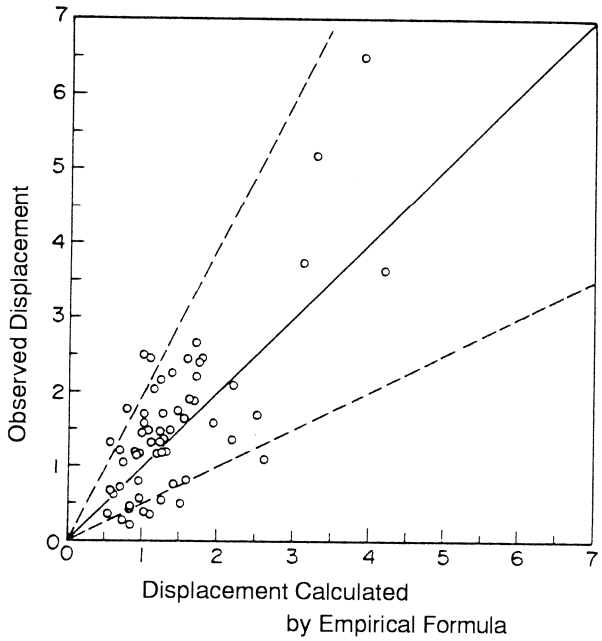

Figure 2. Comparison of Horizontal Ground Displacement Estimated by Regression Formula with Observed One(Hamada et al., 1986)

Figure 3 shows one example of the relationship between the gradient of the ground surface and the magnitude of the ground displacement, which was obtained from the data in Niigata as well as Noshiro, but no significant correlation could not be found. The gradient of the ground surface in the figure was determined as a mean value over a horizontal distance of 5 times of the thickness of the estimated liquefied layer of the ground. The mean gradient over a horizontal distance of 30 times was also calculated, but the correlation was not improved.

If it is assumed that a sloped ground is deformed by the gravity under a condition of large reduction of its shear stiffness due to the liquefaction, the ground displacement should be proportional to the gradient of the ground surface, so that better correlation should have been obtained with the gradient. The lack of the correlation between the ground displacement and the gradient of the ground surface appears to contradict the fact that the ground moved from the higher elevation to the lower one. However, this contradiction can be resolved if it is assumed that the ground displacement was caused by a fluid behavior of the liquefied soil. The gradient of the fluid surface has not any influence on the magnitude of the displacement of the fluid, but does affect its velocity.

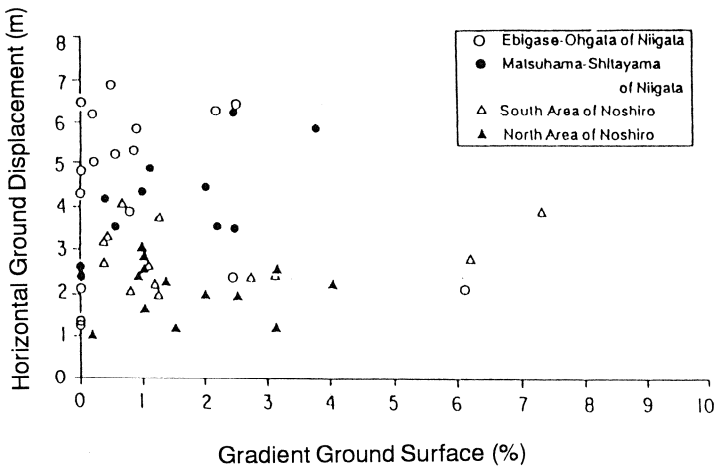

Figure 3. Correlation between Ground Displacement and Gradient of Ground Surface (1964 Niigata and 1983 Nihonkai-Chubu Earthquake)

On the other hand, the magnitude of the ground displacement has a good correlation with the thickness of the liquefied soil in most of case studies. Figure 4 shows the relationship between the ground displacement and the thickness in the case studies on the Niigata and Nihonkai-Chubu earthquakes. This figure clearly demonstrates that the ground displacement increases in proportion to the thickness of the liquefied layer.

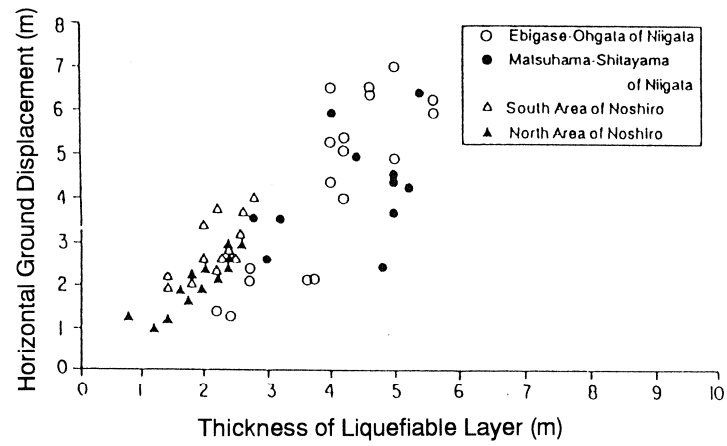

Figure 4. Correlation between Ground Displacement and Thickness of Estimated Liquefied Layer (1964 Niigata and 1983 Nihonkai-Chubu Earthquake)

Bartlett et al. (1992) proposed the following empirical formulae based on a regression analysis of the data from Japanese and U.S. case studies.

$$\text{LOG}\ (D_H + 0.01) = -16.366 + 1.178\ M - 0.927\ \text{LOG}\ R - 0.013\ R + 0.657\ \text{LOG}\ W + 0.3484\ T_{15} + 4.527\ \text{LOG}\ (100 - F_{15}) - 0.922\ D50_{15} \quad (2a)$$

, and

$$\text{LOG}\ (D_H + 0.01) = -15.787 + 1.178\ M - 0.927\ \text{LOG}\ R - 0.013\ R + 0.429\ \text{LOG}\ S + 0.348\ T_{15} - 4.527\ \text{LOG}\ (100 - F_{15}) - 0.922 D50_{15} \quad (2b)$$

D_H : Ground displacement in Horizontal Direction.
M : Earthquake magnitude (moment magnitude).
R : Horizontal distance from the seismic energy source.
W : Ratio of the height(H) of the free face to the distance(L) from a free face.
S : Gradient of ground surface (in percent).
T_{15}: Cumulative thickness of saturated granular layers with corrected blow counts less than 15.
F_{15} : Average fines content of saturated granular layers included in T_{15}.
$D50_{15}$: Average mean grain size in layers included in T_{15}.

Formula (2a) is proposed for the second type of the ground displacement in Figure 1, where a ground along river or sea moves towards the water when the quay walls are collapsed. The formula (2b) is for the first type of the displacement of a slightly sloped ground. However, the predicted ground displacements by these formulae also scattered between half and twice the observed displacement as shown in Figure 5.

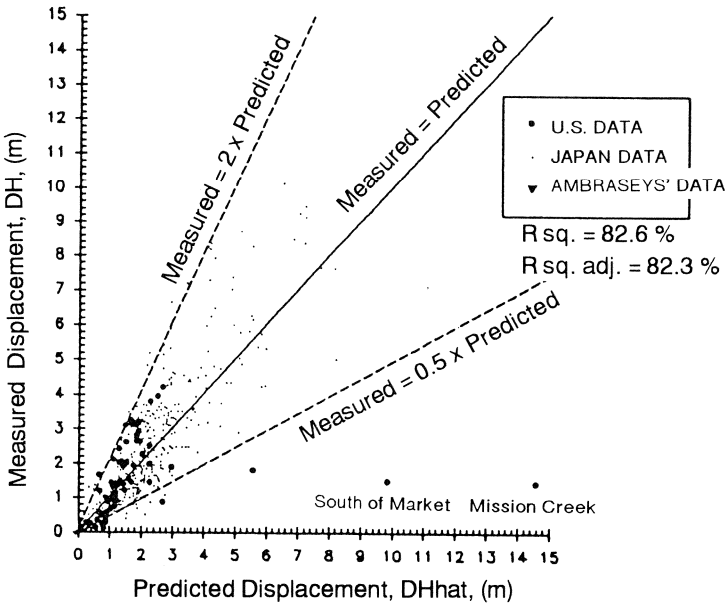

Figure 5. Comparison of Ground Displacement Estimated by Empirical Formula with Observed One (Bartlett et al.)

The correlation between the ground displacement D_H and the gradient of the ground surface S in Formula (2b) is a little higher than that in Formula (1), but is still low because the coefficient of the logarithm of the gradients is only 0.429.

In all cases of the slightly sloped ground the ground displacement was caused to the downward direction. Any case has never been found that ground displacement was caused to the upward direction of the slope. This suggests that the gravity is a key factor of the occurrence of the ground movement. However, the correlation between the magnitude of the ground displacement and the gradient of the ground surface is low. This low correlation should be taken into consideration for the discussion on the mechanism of the occurrence of the large ground displacement.

DISCUSSIONS ON MECHANICAL PROPERTIES OF LIQUEFIED SOIL

There may be two possible ideas about the behaviors of the liquefied soil during the large ground movement. First one is that the liquefied soil behaves as a real liquid and that the large ground displacement is caused as

a flow of the liquefied soil. The second idea is that the liquefied soil still behaves as a solid body with a largely reduced shear stiffness due to liquefaction. According to the second idea, the magnitude of the ground displacement should be proportional to the gradient of the ground surface, because the gravity is governing the deformation of the solid ground as mentioned previously. However, the correlation of the ground displacement with the surface gradient is low in the case studies.

On the other hand, the first idea of the liquid has also a big disadvantage, which is that if the liquefied soil perfectly behaved as a liquid, the ground surface should have been flat after the ground movement. However, according to the case studies the surfaces of the actual grounds still preserved their inclinations.

The third idea where the liquefied soil behaves with a combined characteristics of the fluid and the solid is also possible .

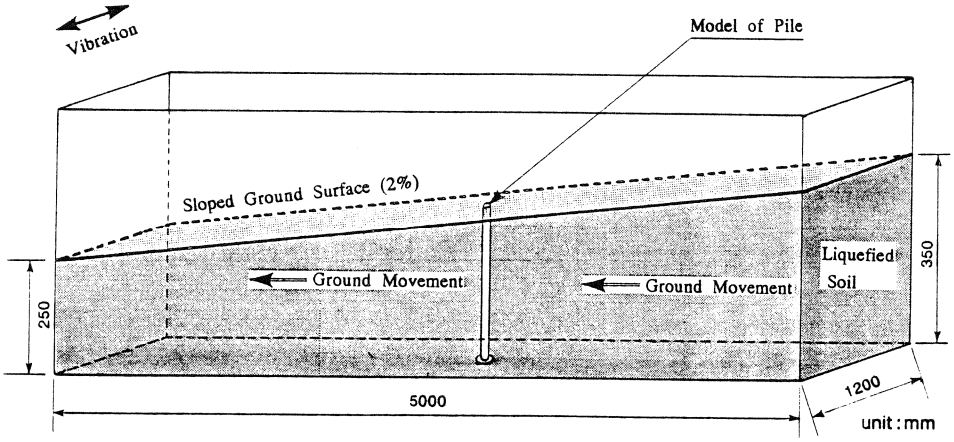

Figure 6. Experiment on Liquefaction-Induced Ground Displacement

As for the fluid properties of the liquefied soil, several experimental works have been conducted. Figure 6 shows an experiment on external force on a foundation pile during ground movement (Hamada et al., 1992b). An acryl model pile with a diameter of 22 mm was installed at the center of a model ground, which is 5 m long, 2 m wide and 0.5 m thick with a surface gradient of 2 %. The liquefaction was induced by shaking the soil box in the direction perpendicular to that of the ground slope, so that the effect of the base excitation on the ground movement could be neglected.

Figure 7 shows time histories of the displacement and the velocity of the ground nearby the model pile and the bending strain of the pile. The good similarity between the time history of the pile strain and that of the ground velocity suggests that the pile was deformed by a fluid force from the laterally moving ground.

From the case studies, some evidences of the liquid behavior of the liquefied ground can be found. Figure 8 shows a movement of a wastewater pipe together with displacement of ground surface measured by aerial survey in Noshiro City after the 1983 Nihonkai-Chubu earthquake. The pipe is asbestos-cement pipe with a diameter of 30 cm. The lateral distance between the straight line connecting two neighboring manholes and the pipe axis was measured. The pipe had been laid in a straight line between two manholes before the earthquake. The measured distance is a relative displacement of the pipe with respect to two manholes.

The maximum movement of the pipe is 160 cm, but the ground displacement at the surface in the lateral direction to the pipe axis is 80 to 110 cm. Here, it should be noted that the movement of the pipe was measured as a relative displacement from the two neighboring manholes. This means that the absolute

displacement of the pipe is more than 160 cm, and the pipe moved much more than the ground surface.

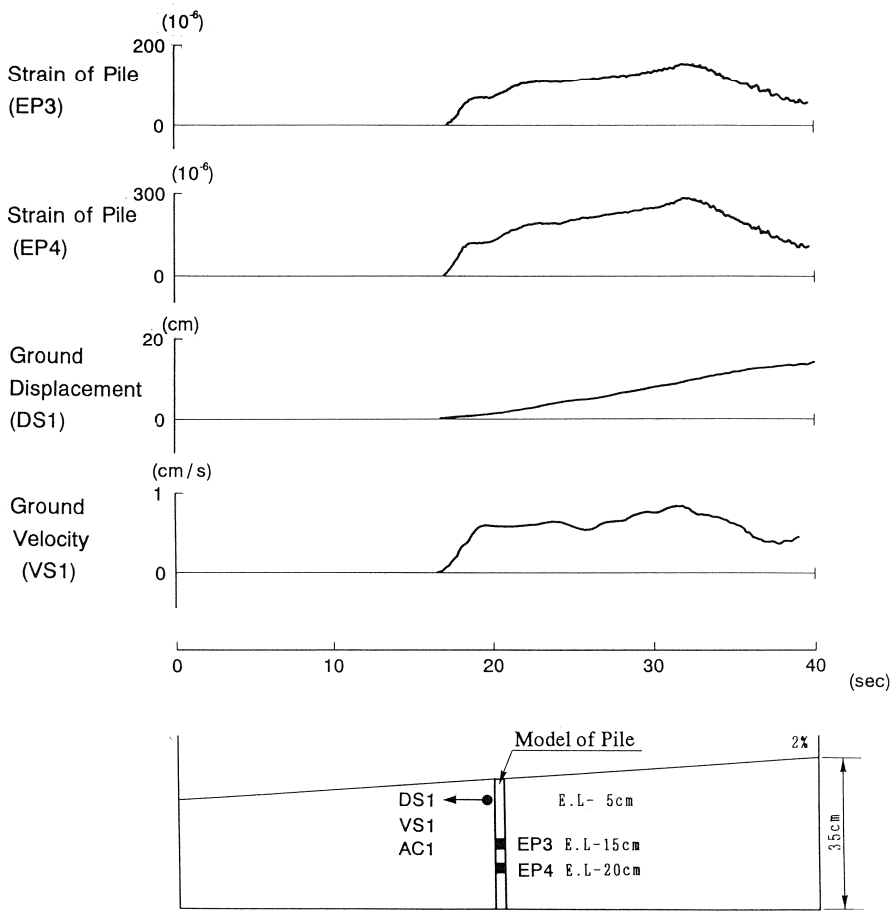

Figure 7. Experimental Result of External Fore on Foundation Pile

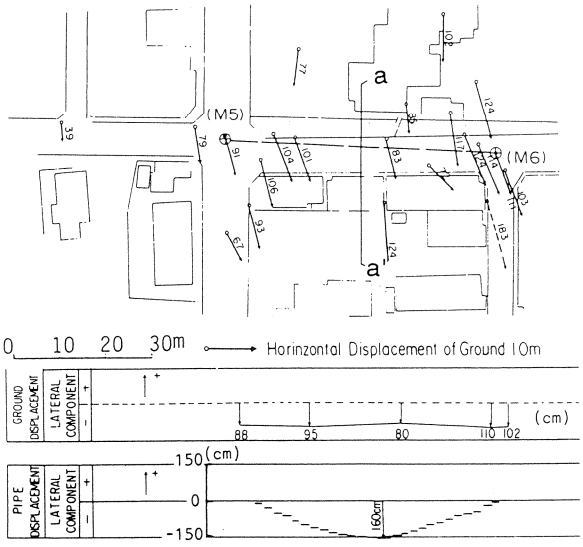

Figure 8. Displacement of Wastewater Pipe and Ground Surface (1983 Nihonkai-Chubu Earthquake)

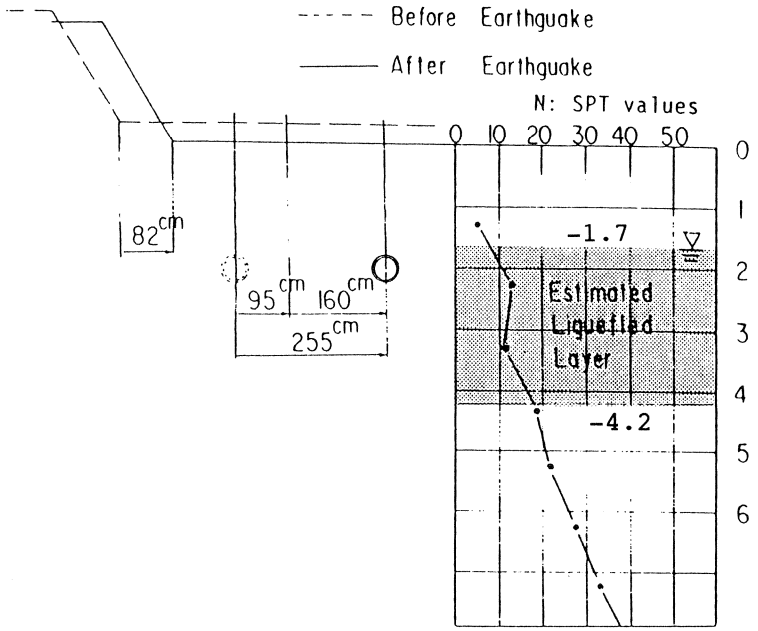

Figure 9. Displacement of Westewater Pipe and Ground Surface in CrossSection a-a'

Figure 9 shows the displacement of the pipe and the ground surface in the cross section along line a-a' in Figure 8, where movement of the pipe was a maximum. The absolute displacement of the pipe was calculated to be 255 cm by adding the maximum relative displacement 160 cm to the mean displacement of the two manholes 95 cm. Along line a-a' the displacement at the ground surface was measured to be only 82 cm.

Figure 9 also shows a soil profile with N-values at a site about 50 m north of the wastewater pipe and an estimated liquefied soil. The subsurface consists of sandy fill and sand dune. The ground water is located at -1.7 m below the ground surface, and the soil between -1.7 m and -4.2 m below the ground surface can be assessed to be liquefied based on the N-values. The wastewater pipe was located in the estimated liquefied layer of the ground. Therefore, the above-mentioned displacement of the wastewater pipe means that the liquefied soil moved much more than the overlaying non-liquefied layer.

A similar story was reported by a witnesses in Niigata City after the 1964 Niigata earthquake. A gas company engineer said that he had found gas pipes underneath side trenches of a road, which had been buried apart from the trenches before the earthquake. Furthermore, it was reported that a main gas pipe buried in a depth of about 1.5 m along the Shinano River, where the ground moved toward the river above ten meters, could not be found even by the thorough excavation after the earthquake. The pipe was guessed to has been flown into the river with the flow of the liquefied soil toward the river.

In order to investigate the mechanism of the large ground displacement, information about the duration of the occurrence is also important. Interviews with witnesses of the area where the ground displacement has been caused were conducted. A resident of the northern slope of the Maeyama in Noshiro City, where the ground displaced downward with a maximum of 5 m responded to a question about the duration of the motion of the 1983 Nihonkai-Chubu earthquake by saying that she had felt that the tremors continued for about 30 minutes, because her house had been making noises during the duration.

Several witnesses of the 1948 Fukui earthquake, when the liquefaction-

induced ground displacement reached over 5 m along the Kuzuryu River (Hamada, et al., 1992a) said that a ground fissure with a gap of about 1.0 m had been caused after the earthquake motion, and that the width had increased to about 3 m two or three hours later after the earthquake. Similar remarks were also reported by witnesses in Kasukabe City, where the ground moved several meters at the time of the 1923 Kanto earthquake (Hamada, et al., 1992a). They said that they had found a ground fissure with a gap of about 1.0 m along a small river just after the earthquake motion ended, and that the fissure had grown up about 3 m wide two or three hours later.

The collapse of the Showa Bridge with a total span of 250 m was one of the worst instance of damage to structures caused by the 1964 Niigata earthquake. Many witnesses reported that the girders had begun to collapse somewhat later after the earthquake motion ceased (Hamada, 1992a). When the earthquake motion started, many people and vehicles were on the bridge, but no lives were lost in spite of the catastrophic collapse. This suggests that there was enough time for people on the bridges to seek refuge on the banks. By taking into consideration the ground displacements measured on the bank of the Showa Bridge, the large bending deformation of the foundation piles and the estimated liquefied layer, it can be concluded that the liquefaction-induced displacement continued long time and reached several meters, consequently deforming the foundation piles and causing the girders to fall (Hamada, 1992a).

The above-mentioned remarks by the witnesses and the instance of the collapse of the Showa Bridge suggest that the liquefaction-induced ground displacement continued for a long period, until the excess water pressure dissipated although the earthquake motion ceased.

SHAKING TABLE TEST

A certain number of shaking table tests under 1 g condition as well as under several ten g condition by centrifuges was conducted on the liquefaction-induced ground displacement of sloped grounds. In most cases of these tests, the base excitation was continued until the surface of the model ground became flat. The horizontal ground displacement was caused by a volumetric transfer of the liquefied soil from the upstream to the downstream. Therefore, the magnitude of the horizontal ground displacement is governed by the total volume of the transferred soil, and proportional to the gradient of the ground surface as well as to the length of the soil box. These test results are not consistent with the outcomes from the case studies.

By referring the remarks from the witnesses that the ground movement had continued after the ground motion ceased, the authors conducted a shaking table test on the ground movement after the shaking ended. Figure 10 shows a rigid soil box, which is 3.0 m long, 1.0 m wide and 0.6 m deep. The model ground with flat surface was made in the soil box, and was vibrated in the direction of the shorter side of the box by sinusoidal waves. After a perfect liquefaction of the model ground which was confirmed by several piezometers in the soil, the soil box was inclined by lifting one side of the box with a specific gradient.

Generally, it can be considered that a large ground displacement started after an achievement of the perfect liquefaction of the soil and continued until the pore water pressure dissipates, even after the earthquake motion ended. The purpose of this experiment is to investigate characteristics of the ground movement after the earthquake motion ceases.

The tests were conducted by varying the initial relative density of the model ground and the inclination of the ground surface. The time history of the ground displacement was recorded by measuring movement of small marks buried in the soil, which were connected by thin strings with displacement

meters out side of the soil box as shown in Figure 11. The strings were protected by stainless tubes in order to cut the friction between the strings and the surrounding soil. The maximum ground displacement was also measured from the movement of elliptical marks in the soil as shown in Figure 12.

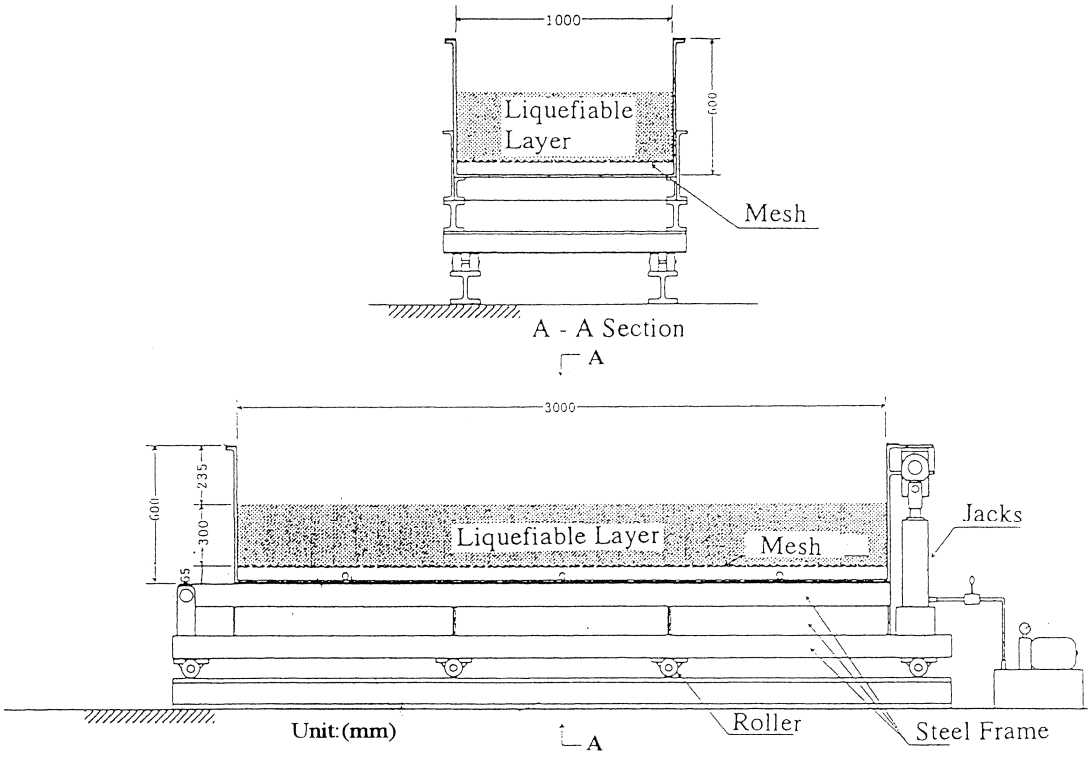

Figure 10. Soil Box and Model Ground for Shaking Table Test

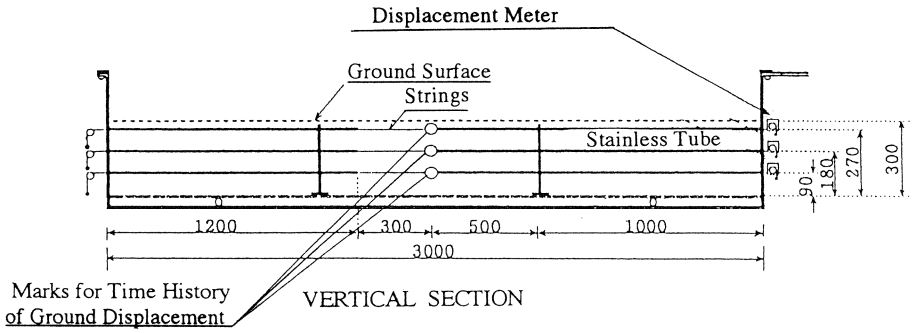

Figure 11. Measurement of Time History Ground Movement

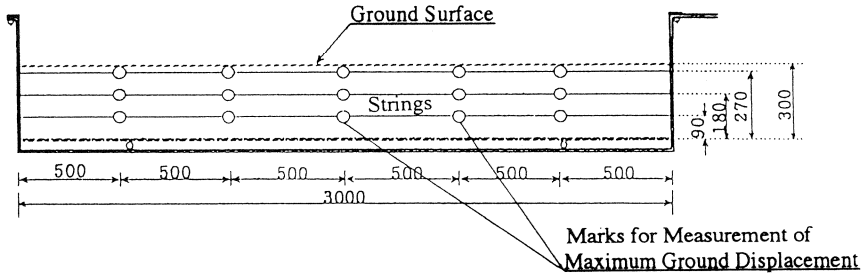

Figure 12. Measurement of Maximum Ground Displacement

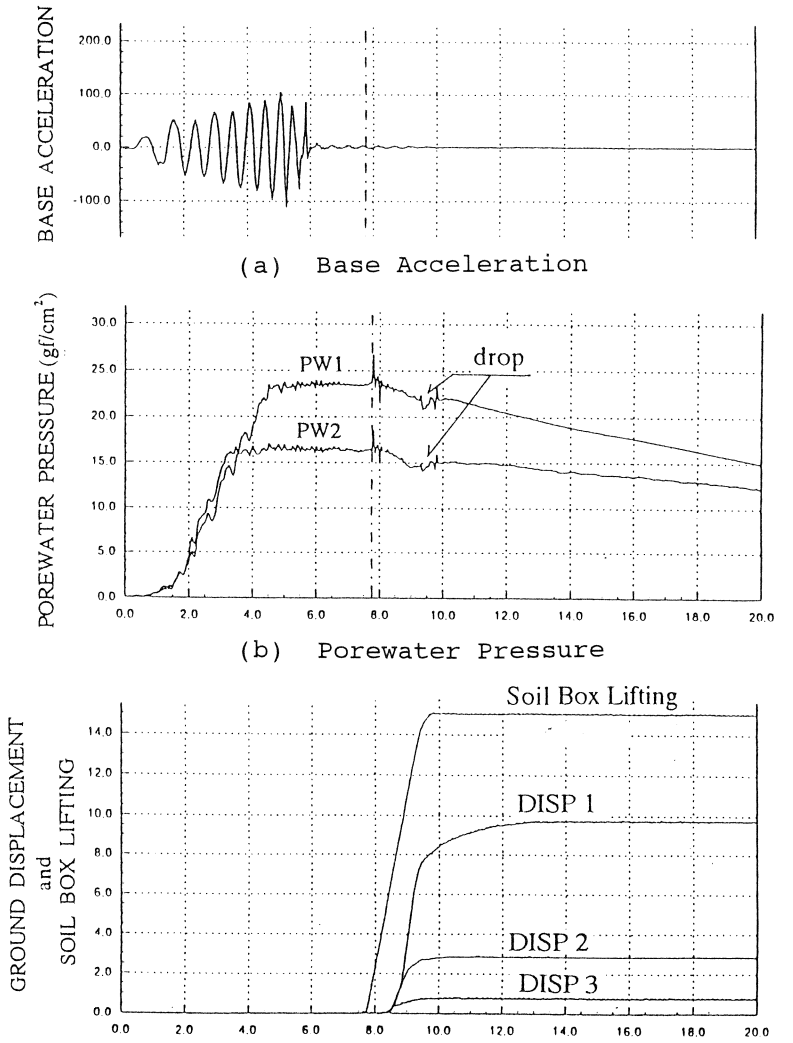

Figure 13. Example of Shaking table Test Results Result (CASE-1, Dr =23 %, θ = 4.2 %)

Figure 13 shows an example of the test results, when the initial relative density and the gradient of the ground surface are 23 % and 4.2 %, respectively. The porewater pressure (Figure(b)) gradually rose and reached the effective overburden pressure at each elevation due to base excitation (Figure(a)). After a complete stop of the base shaking the ground surface started to be inclined by lifting a side of soil box (Figure(c)). The time histories of ground displacements at three elevations were measured as shown in Figure(c). It is noteworthy that the porewater pressure sharply dropped when the ground displacement increased and approached the maximum values. After that, the porewater pressure gradually decreased due to upward dissipation of the porewater. The sharp drop of the porewater pressure suggests a recovery of the effective stress of the soil and a mobilization of the soil stiffness.

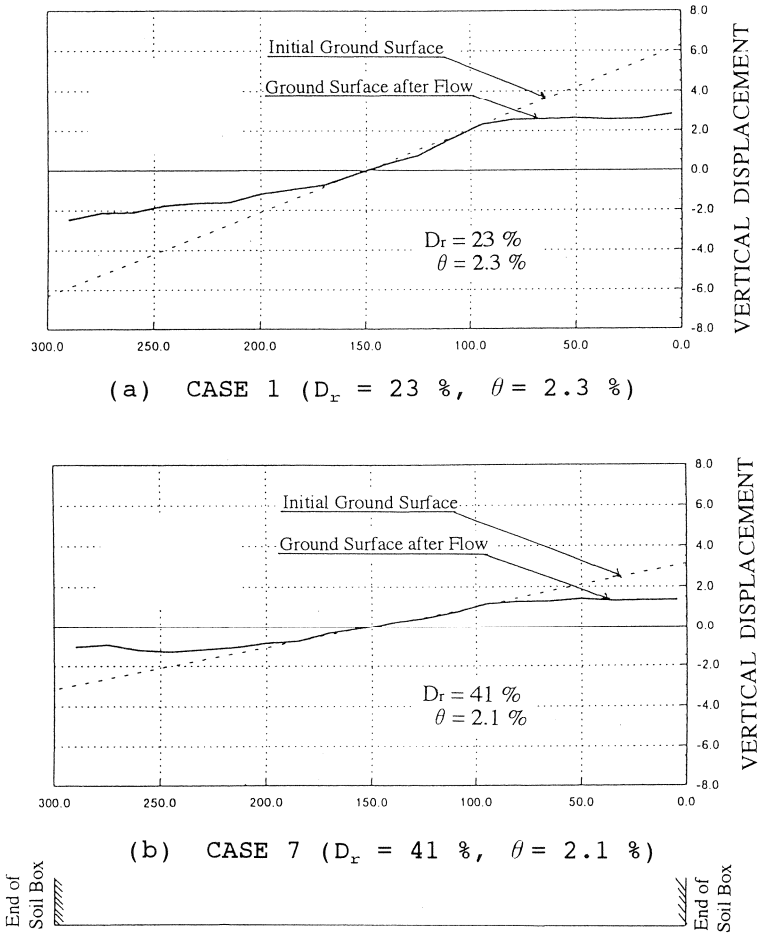

Figure 14. Vertical Movement of Ground Surface

The dotted as well as the solid lines in Figure 14 show the ground surface before and after the ground movement, respectively. The ground surface subsided by compaction of the sand due to liquefaction, but it was completed before lifting the soil box. The elevation of the ground surface before and after the ground displacement was measured by subtracting the mean subsidence from the original elevation. It is interesting to note that the initial inclination of the ground surface was preserved in the central part of the model ground even after the ground displacement. On the contrary, the ground surface became mostly flat nearby the two sides of the soil box. As mentioned later, this result indicates that the liquefied soil behaved as a liquid at first, but after a specific amount of the shear deformation of the ground the soil recovered it's stiffness and behaved as a solid body.

Figure 15 shows the maximum ground displacement at three different elevations at five locations along the direction of the ground displacement. It is noteworthy that the ground displacement in Figure (a), where the initial relative density is 41 % and the gradient is 2.1 %, is mostly same to that in Figure (b), where the relative density is same, but the gradient is 4.2 %, twice that in the case of Figure (a). This result suggests that maximum ground displacement is not necessarily governed by the gradient of the ground surface inclination, which is consistent with the result of the case studies. The displacement in Figure (c), where the initial relative density is small 23 %, is much larger than those in Figures (a) and (b). It can be understood that the maximum ground displacement is governed by the initial relative density of the ground.

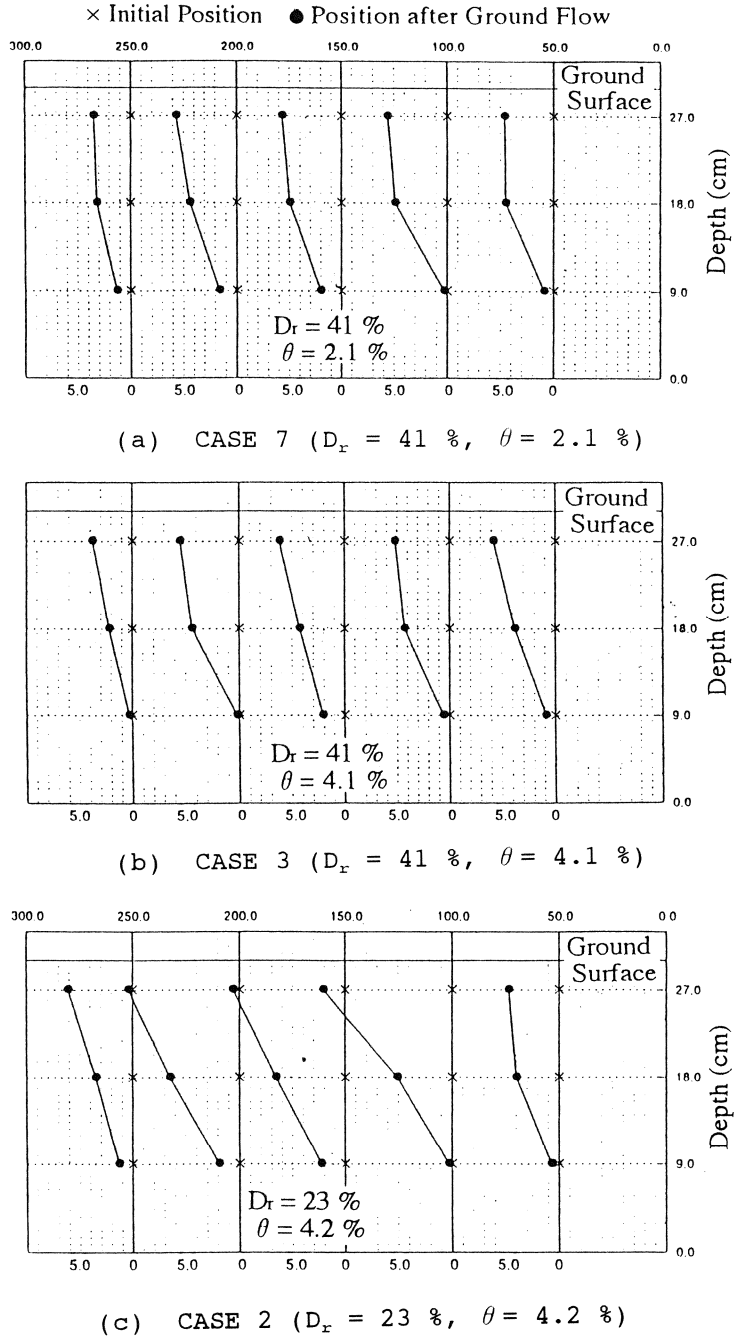

Figure 15. Maximum Ground Displacement at Three Elevations

The above-mentioned test result can be rationally explained by the following hypothesis: Figure 16 shows the half part of the model ground of the upstream side, and line O-C-A is the initial ground surface with a gradient θ. Firstly the ground surface of the upstream side subsides to line O-D-B, and consequently the ground at the center of the soil box (OF) causes horizontal displacement due to a volumetric transfer of the liquefied soil from the upstream side. If the liquefied soil behaves as a real liquid, the volume of $\triangle$ OEF is equal to that of $\triangle$ OBA under as assumption that the horizontal ground displacement distribution along the vertical direction is triangular as shown in the figure.

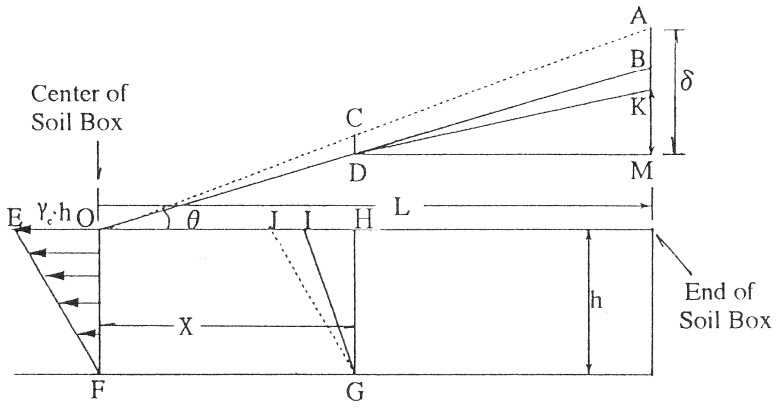

Figure 16. Change of Shape of Ground Surface

When the shear strain of the ground at the center of the soil box reaches so-called critical strain γ_c at which it is assumed that the soil stiffness is mobilized and the soil behaves as a solid body again, the ground displacement stops to increase, and after that the displacement at the surface remains constant $\gamma_c \cdot h$. Here h is the thickness of the ground at the center.

At a location (GH) away from the center, the ground also moves in the horizontal direction due to the volumetric transfer of the liquefied soil. The ground displacement at the surface of this location is HI, and the volume of △HIG is equal to that of □ACDB of the upstream side from GH. At this location the shear strain of the ground dose not yet reach the critical strain γ_c. Therefore, more volume of the liquefied soil (△IJG) can flow into this position. The volume of △IJG is equal to that of △BDK, and is also equal to that of △COD. The ground surface OD returns to OC due to the flow of the liquefied soil with a volume equal to that of △COD. Therefore, the ground surface OC preserve the initial gradient. On the contrary the ground surface becomes flat due to the liquid behavior of the liquefied soil nearby the upstream end of the soil box, because the shear strain does not reach the critical strain γ_c.

According to the above-mentioned explanation, the distance from the center of the inclined part with the initial gradient x and the subsidence at the upstream end of the soil box δ can be easily calculated as follows;

$$x = L - h\sqrt{\gamma_c / \theta} \qquad (3a)$$

$$\delta = \theta \cdot (L - x) \qquad (3b)$$

where L, h and θ are the half length of the soil box, the thickness of the ground and the initial gradient of the ground surface, respectively.

Figure 17 shows an comparison of the calculated ground surface with the one obtained by the experiment. The critical strain γ_c was determined from the ground deformation at the center of the ground. It can be concluded from a good coincidence between the experiment and the calculation that the above-mentioned hypothesis can explain the behavior of the liquefied soil during the large displacement.

Figure 18 shows the relationship between the critical strain γ_c and the initial relative density of the soil D_r. The critical strain increases when the initial relative density decreases.

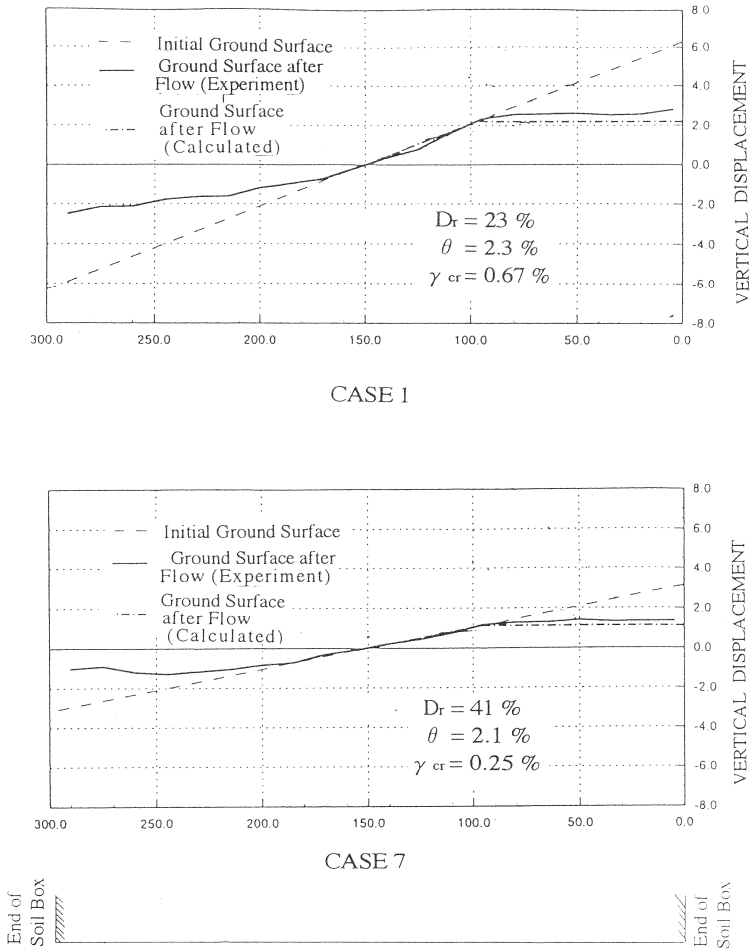

Figure 17. Comparison of Ground Surface between Calculation and Experiment

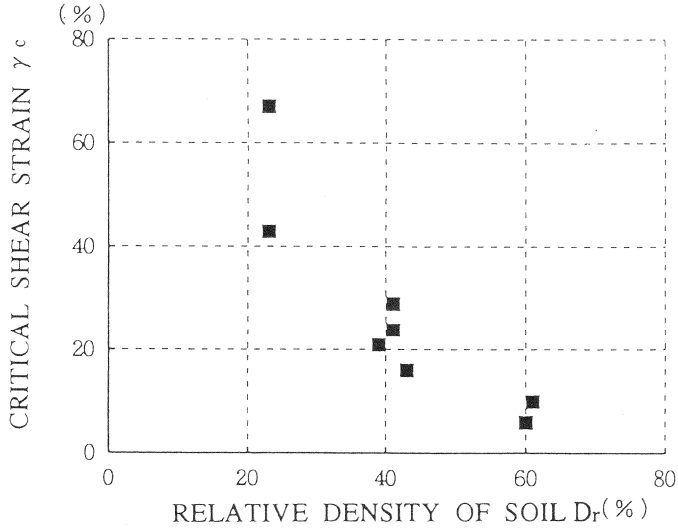

Figure 18. Relationship Between Critical Shear Strain and Relative density of Soil

CONCLUSION

The case studies on the liquefaction-induced large ground displacement showed that the ground moved from the higher elevation to the lower one, but the correlation was low between the magnitude of the ground displacement and the gradient of the ground surface. If it is assumed that the inclined ground was deformed by the gravity due to a large reduction of the soil stiffness, above-mentioned two facts contradict to each other.

The authors conducted a shaking table test on the liquefaction-induced ground displacement and found that the magnitude of the ground displacement did not depend on the surface gradient, but on the relative density of the soil. The test showed that the liquefied soil firstly behaved as a liquid, but after a specific amount of shear deformation which was controlled by the relative density, the soil stiffness was mobilized and the ground behaved as a solid body.

The experimental result is consistent with the fact obtained from the case studies. However there still remains the following research subjects on the liquefaction-induced ground displacement:

i) The magnitude of the ground strain in the test is 10 ~ 50 %, much smaller than that observed in the case studies which is sometime above 100 %. The test was focussed on the ground displacement after earthquake motion ceased. Therefore, the ground displacement during earthquake motion should be investigated.

ii) The test was conducted under 1 g condition. The effect of the confining pressure on the critical strain, at which the soil stiffness is mobilized should be studied.

iii) The test showed that the liquefied soil firstly behaved as a liquid. In order to discuss the duration of the ground displacement and the effect of the ground displacement on the in-ground structures, the fluid properties of the liquefied soil should be investigated.

REFERENCES

Hamada, M. and O'Rourke, T.D., (1992a), Case Studies of Liquefaction and Lifeline Performance during Past Earthquakes, Volumes 1 and 2, Japanese and U.S. Case Studies. Technical Report NCEER-92-0002, National Canter for Earthquake Engineering Research, Buffalo.

Hamada, M., Yasuda, S., Isoyama, R. and Emoto, K., (1986), Study on Liquefaction Induced Permanent Ground Displacement, Association for the Development of Earthquake Prediction (ADEP), Tokyo.

Bartlett, S. F., and Youd, T. L., (1992), Empirical Prediction of Lateral Spread Displacement, Proceedings from the Fourth Japan-U.S. Workshop on Earthquake Resistant Design of Lifeline Facilities and Countermeasures for Soil Liquefaction, Technical Report NCEER-92-0019, Vol. Ⅰ , pp.351~366.

Hamada, M., Ohtomo, K., Sato, H. and Iwatate, T., (1992b), Experimental Study of Effects of Liquefaction-Induced Ground Displacement on In-Ground Structures, Proceedings from the fourth Japan-U.S. Workshop on Earthquake Resistant Design of Lifeline Facilities and Countermeasures for Soil Liquefaction, Technical Report NCEER-92-0019, Vol. Ⅱ, pp481~492.

A Comparative Study of Predictive Methods for Liquefaction Induced Embankment Displacements

Geoffrey R. Martin[1] and Ping Qiu[2]

ABSTRACT

Many bridge failures in past earthquakes have resulted from large post liquefaction lateral deformations of bridge approach fills. In considering the problem of retrofit of existing bridges where liquefiable foundation soils are found, there is a clear need to develop improved predictive methods for post liquefaction deformations of approach fills, prior to the investment of heavy costs related to ground remediation. In this presentation, current design approaches for evaluating post liquefaction lateral deformations are compared by utilizing the simple problem of a thirty-foot high approach fill on a liquefiable sand stratum. The comparative approaches encompass simplified one-dimensional Newmark sliding block analyses and more complex two-dimensional finite difference models. The comparative studies indicate that simplified one-dimensional Newmark sliding block analyses can provide a practical basis for less conservative retrofit design, provided the time at which residual strength is initiated when liquefaction occurs and the effects of initial static shearing stresses are taken into account.

[1] Professor and Chairman, Department of Civil Engineering, University of Southern California, Los Angeles.
[2] Graduate Student, Department of Civil Engineering, University of Southern California, Los Angeles.

INTRODUCTION

In the 1964 Alaska and Niigata earthquakes, liquefaction induced lateral embankment or approach fill deformations were particularly destructive to highway and railway bridges (Bartlett and Youd, 1992). Ninety-two highway bridges in Alaska were severely damaged or destroyed and a further forty-nine bridges received moderate to light damage. Liquefaction induced lateral deformations of embankments have caused similar bridge damage in many more recent earthquakes including those in Japan, Puerto Rico, and the Philippines. Clearly this is a problem that needs to be addressed during the seismic design of bridges in liquefaction prone environments. In the case of the seismic retrofit of existing bridges, however, it is desirable to reduce any conservatism in assessing the magnitude of post liquefaction deformations, prior to the investment of heavy costs related to ground remediation.

In this presentation, differences in lateral displacement predictive methods are examined by utilizing the simple problem of a thirty-foot high approach fill on a liquefiable sand stratum. By examining the assumptions used and comparing displacement predictions, both the sensitivity of analysis methods and inherent conservatism may be assessed.

To simulate the observed failure mode of approach fills in past earthquakes for comparative analytical studies, we have idealized the problem as shown in Fig. 1. The figure is representative of a compacted earth approach fill located above a liquefiable foundation layer. From a vulnerability standpoint, the question arises as to the magnitude of lateral embankment displacement which could be induced during the earthquake adopted for seismic retrofit. A reliable estimate of this displacement would allow evaluation of the vulnerability of the existing bridge to such deformation.

For practical reasons, the Newmark Sliding Block approach for computing earthquake induced embankment displacements (Newmark, 1959) is generally adopted in practice. A common conservative approach to the problem is to assume that a liquefied soil layer mobilizes a residual undrained strength s_{ur} following liquefaction, with the value of s_{ur} determined by correlation with standard penetration blow counts or from laboratory tests. Using limiting equilibrium principles, a horizontal yield acceleration coefficient k_y leading to a factor of safety of one for the most critical sliding block is then determined. Assuming rigid block response, the ground motions which will lead to incremental horizontal block displacements when $k > k_y$, may be represented by the acceleration time history at the base of the sliding block. Assuming residual strength is mobilized at time zero during earthquake loading, the resulting block displacement may be computed for a given time history through use of a simple computer program. Alternatively, non-dimensional

charts may be used, expressing permanent displacements as a function of k_y/k_{max}, where k_{max} is the maximum ground acceleration coefficient.

Research studies to date have examined the assumptions used for the simplified Newmark approach described above with a view to understanding the mechanisms of failure and reducing potential conservatism. The results of these studies are briefly summarized below and illustrate the following aspect of the problem:

- The sensitivity of displacements to input ground motions.
- The time history of pore pressure build up leading to the point at which residual strength should be triggered for analyses.
- The potential influence of horizontal static shearing stresses beneath embankment slopes and their role in the impeding the rate of excess pore pressure build up.
- The use of two-dimensional non-linear response analyses to simulate the embankment displacement mechanism.
- Comparative evaluation of assumptions on displacement predictions.

DISPLACEMENT SENSITIVITY TO INPUT MOTIONS

Embankment displacements predicted by the Newmark Sliding Block model are primarily a function of k_y/k_{max}, peak ground velocity V and peak ground acceleration A. The number of load cycles exceeding yield as reflected by the earthquake magnitude M, could also be a factor. A number of analytical studies to determine displacements as a function of k_y/k_{max} have been made using a variety of earthquake records. However, many of the available displacement charts have been normalized by scaling earthquake records to peak accelerations of 0.5g and peak velocities of 30 inches per second.

To develop a more convenient design chart and to investigate the range of variability of predictive displacements, a study was made using the database published by Hynes and Franklin (1985), where displacements computed using a large number of earthquake records have been documented. For this study, the data was limited to earthquakes with a magnitude range of 6.0 to 7.5. For the purpose of data analysis an equation of the form:

$$d = C\,(k_y/k_{max})^{a1}\,(1 - k_y/k_{max})^{a2}\,A^{a3}\,V^{a4}\,M^{a5}$$

was used. Regression analyses indicated that earthquake magnitude does not have major effect on predictions and that a equation of the form:

$$d = 6.82\,(k_y/k_{max})^{-0.55}\,(1 - k_y/k_{max})^{5.08}\,A^{-0.86}\,V^{1.66}$$

describes the mean displacement with an R^2 error of 0.9247. In the above equation a consistent set of units of inches, and seconds are used. By normalizing the displacement by a factor $A^{-.86}\,V^{1.66}$, a normalized displacement chart showing $d/\,A^{-.86}\,V^{1.66}$ vs. k_y/k_{max} may be plotted and is shown in Fig. 2. Almost 80% of all data fall on a narrow band leading to the nominal upper and lower bounds as shown. Upper bound displacements are about twice those of the mean, while lower bound values are about one quarter of the mean.

TIME HISTORY OF PORE PRESSURE BUILD UP

To pursue analytical studies addressing questions related to the time history of pore pressure build up and two-dimensional response, the idealized embankment configuration and the material properties shown in Fig. 3 were assumed. To study the effects of liquefaction we focused on layer 1 by assuming a low relative of density of 40%. The cohesionless materials in the idealized embankment were assumed to be those of Nevada sand which was used for the VELACS Project (Arulmoli et.al., 1992). Penetration blow counts in $(N_1)_{60} = 8$ and $(N_1)_{60} = 16$ were assumed for layers 1 and 2 respectively. An undrained residual strength of 200 psf was chosen for layer 1 from the standard relationships shown in Fig. 4. Pore pressure build up was suppressed in the lower layer 2 to ensure a dominant lateral sliding mechanism. The 1940 El Centro earthquake with a peak ground acceleration of 0.33g was input at bedrock level.

Time history of pore pressure increases were computed for one-dimensional free field conditions represented by column 1 and column 2, using the effective stress response program DESRA (Lee and Finn, 1978). Modifications to this program were made to make it more user friendly in a practical sense. These modifications included the use of a simplified two-parameter pore pressure model suggested by Byrne (1991) and a generalized non-linear backbone curve with automatic generation of parameters to represent a given curve describing variations in shear modulus with shear strain amplitude. The two pore pressure parameters were selected to match a standard liquefaction strength curve developed from field blow count data and a design earthquake magnitude. The simplifications make the program more amenable to routine design practice. An Iwan model (1967) was used as a non-linear constitutive model and incorporates an array of elasto-plastic elements which simulate a given non-linear backbone curve and provides hysteretic

damping. This physically based mechanistic model provides a good simulation of permanent displacement induced by soil yield.

Fig. 5 shows the G/G_{max} vs. shear strain amplitude curve assumed for analyses and the liquefaction strength curve for layer 1. In the program DESRA, G_{max} values were assigned to layer properties using the equation: $G_{max} = 20000(N_1)_{60}^{1/3}(\sigma'_m)^{1/2}$, where $(\sigma'_m)^{1/2}$ is the mean effective stress. A non-linear backbone or shear stress-shear strain curve was then constructed to be compatible with the G/G_{max} vs. γ curve. The backbone curve was then used to fix the Iwan model parameters, which in turn define the soil behavior under cyclic loading. The field liquefaction strength curve for layer 1 was constructed to be compatible with the assumed blowcount $(N_1)_{60} = 8$. The difference in the two curves shown reflect the effect of initial confining stresses.

The results of the DESRA analyses with respect to pore pressure build up are shown in Fig. 6. For column 1, the loose sand layer 1 liquefied after about two seconds of strong shaking. The corresponding large shearing strains occurring in the layer are interpreted as relative displacements of the soil column above the liquefied layer in Fig. 6a. These displacements can be considered to reflect ground lurch leading to a permanent displacement of the ground of about 0.25 feet. For column 2, liquefaction occurred after about three seconds leading to permanent lurch displacements of the soil column above the liquefied layer of about 0.3 feet. Note the significant reductions in surface accelerations compared to input accelerations. The low 0.05g peak acceleration reflects the limiting inertial loads which can be carried by the upper soil column following mobilization of the post liquefaction residual strength of 200 psf. in layer 1. The shear stress vs. shear strain time history (0 - 4 seconds) for layer 1 (column 2) is shown in Fig. 7.

TWO-DIMENSIONAL RESPONSE ANALYSES

To study the effects of two-dimensional earthquake response on the mechanisms of lateral deformation of the slope and to evaluate the influence of initial static shearing stresses beneath the sloping embankment on liquefaction resistance, a two-dimensional dynamic response program TENSI was used. The program TENSI has been documented by Larkin et.al.,(1991). TENSI is a non-linear two-dimensional total stress response analysis program utilizing a multiple yielding surface model to simulate non-linear soil behavior. The latter model has been described by Iwan (1967), and is a kinematic strain hardening model analogous to the model used for the one-dimensional analyses described above. The original program TENSI has been modified to form

TENSI-M to allow inclusion of the effects of initial static stresses due to embankment construction on the earthquake response. The program is now divided into two parts: static analysis and dynamic analysis. In the static analysis, gravity loading is used to simulate the construction procedure, where the embankment is built in a sequence of layers. For each loading layer, the program runs twice. The first run is under an assumption that loosely placed soil has only very small stiffness, that is, a very low modulus. In the second run, the stiffness matrix is formed using compacted soil modulus values, but resetting displacements and strains from the first run, that is, the position after settlement of loose soil is chosen as a reference position. A Gaussian procedure is used to solve for displacements from layer gravity loading. The embankment shown in Fig. 3 is assumed to be constructed in three layers. The resulting static shear stress distribution over layer 1 is shown in Fig. 8. The highest shear stresses occur beneath the slope, leading to an average ratio of horizontal static shearing stress to initial vertical effective stress beneath the slope of about 0.25. The static shear stress will affect liquefaction strength as described by Vaid and Finn (1979) and will be discussed further below.

As a two-dimensional effective stress constitutive model has yet to be programmed into TENSI-M, in order to study the two-dimensional mechanisms of lateral deformation, the shear modulus and shear strength of the loose sand layer were progressively degraded from initial values to residual values using the average increases in pore pressure from the one-dimensional DESRA analyses. The TENSI-M results at the vertical free field boundaries, columns 1 and 2, are compared to the results from DESRA in Fig. 9. The TENSI-M results are very similar to the DESRA results except for permanent lurch displacements which are about 0.6 feet. This increase may be attributed to the effects of initial static horizontal shearing stresses that extend out as far as column 1.

The displacement pattern as a whole for the TENSI-M analyses, is shown in Fig. 10. The horizontal sliding mode of the embankment is clearly indicated with evidence of passive failure a the toe. The time history of average horizontal slope displacement is shown in Fig. 12.

CALCULATION OF EMBANKMENT DISPLACEMENTS USING THE NEWMARK METHOD

To perform conventional Newmark analyses, it is necessary to first determine the critical sliding block and the corresponding yield acceleration (assuming the residual strength of 200 psf is mobilized in layer 1) using conventional pseudostatic limiting equilibrium methods. The position of the critical sliding block is roughly that shown in Fig. 1. The corresponding yield acceleration is 0.03g. The static factor of safety is 1.15 which provides for static stability under post

liquefaction conditions, that is, a flow failure would not occur. Horizontal displacements of the block induced by the input earthquake acceleration time history were computed using the program DISPLMT (Houston et.al., 1987). The time histories of displacement assuming residual strength triggered following liquefaction either at time = 0 or 2 seconds are shown in Fig. 12, leading to maximum displacements of about 2.8 and 2.5 feet respectively. If liquefaction had not occurred until after about 4 or 5 seconds of strong shaking, the reductions in maximum displacement from the assumption of triggering at t = 0 would have been more significant. A block displacement of about 2 feet was computed from the mean curve shown in Fig. 2, using the average maximum V and A at the base of the liquefied layer from DESRA results. The corresponding upper bound displacement is about 4 feet. The maximum displacement from TENSI-M analyses assuming residual strengths triggered at 2 seconds, is about 3.3 feet.

The embankment displacement estimates assume pore pressure generation under one-dimensional free field conditions and do not reflect the influence of static shearing stress reducing the rate of pore pressure build up. The latter effects were taken into account by utilizing the results of published laboratory data, where simple shear test were conducted with varying initial static shearing stress ratios, as reported by Vaid and Finn (1979), as shown for example in Fig. 11. By modifying the liquefaction strength curve beneath the sloping embankment to account for an average static shearing stress ratio of 0.25, (a liquefaction strength increase of about 25%), it was found that the earthquake induced pore pressure increases reached only about 40% of the values required to induce liquefaction. The effect of reduced strength degradation beneath the sloping embankment to values corresponding to 40% of the difference between static strengths and residual strengths significantly increased the yield accelerations and reduced displacement. The displacement time histories are shown plotted on Fig. 12 and resulted in a maximum of about 0.2 feet of displacement.

SUMMARY AND CONCLUSIONS

From the above sensitivity study it is clear that both the point of time during the earthquake when residual strength is triggered by liquefaction and the effects of initial static shearing stresses in reducing the rate of pore pressure build up, have a major influence on the magnitude of earthquake induced post liquefaction displacements. However, research to date has indicated that the Newmark approach for evaluating post liquefaction embankment deformations can provide a practical basis for design provided the above effects are taken into account. Through on-going research exploring the sensitivity of displacements to the above variables, it is anticipated that simplified final design approaches and charts can be documented for routine use in the field. Additional centrifuge tests as part of an RPI research program will include experiments where

embankment deformations will be measured utilizing a model configuration similar to that shown in Fig. 1. These tests will provide additional verification for the analysis approach.

ACKNOWLEDGMENTS:

The research described above was supported by the National Center for Earthquake Engineering Research Highway Project, funded by the Federal Highway Administration.

REFERENCES

Arulmoli, K, Muraleetharan, K. K., Hossain, M. M. and Fruth, L. S., (1992): "VELACS, Verification of Liquefaction Analysis By Centrifuge Studies Laboratory Testing Program, Soil Data Report", The Earth Technology Corporation, California, Earth Technology Project No. 90-0562.

Bartlett, Steven F. and Youd , T. Leslie, (1992): "Case Histories of Lateral Spreads Caused by the 1964 Alaska Earthquake", Case Studies of Liquefaction and Lifeline Performance During Past Earthquakes, Vol. 2, United States Case Studies, Edited by T.D. O'Rourke and M.Hamada, Technical Report NCEER-92-0002.

Byrne, Peter M., (1991): "A Cyclic Shear-volume Coupling and Pore Pressure Model for Sand", Iwan, Proceedings: Second International Conference on Recent Advances in Geotechnical Engineering and Soil Dynamics, March, pp. 11 - 15, St. Louis, Missouri, Paper No. 1.24.

Houston, Sandra L., Houston, William N. and Padilla, J. Manuel, (1987): "Microcomputer-aided Evaluation of Earthquake-induced Permanent Slope Displacements", Microcomputers in Civil Engineering 2.

Hynes, Mary E. and Franklin, Arley G., (1984): "Rationalizing the Seismic Coefficient Method", Geotechnical Laboratory, Department of the Army, Waterways Experiment Station, Corp. of Engineers, Vicksburg, Mississippi, July.

Iwan, W. D., (1967): "On a Class of Models for the Yielding Behaviors of Continuous and Composite System", Transaction of the ASME, September.

Larkin, T.J. and Marsh, E.J., (1982): "Two Dimensional Nonlinear Site Response Analysis", Proc. Pacific Conference on Earthquake Engineering, Vol. 3, pp. 217-227, Auckland, November.

Lee, Michael K. W. and Finn, W. D. Liam, (1978): "DESRA-2: Dynamic Effective Stress Response Analysis of Soil Deposit with Energy Transmitting Boundary Including Assessment of Liquefaction Potential", Department of Civil Engineering, University of British Columbia, Vancouver, Canada, June.

Newmark, Nathan M., (1959): "A Method of Computation for Structural Dynamics", Journal of the Engineering Mechanics Division, ASCE, Vol. 85, No. EM3, July.

Seed, H. Bolton and Harder, Leslie F., Jr., (1990): "SPT-based Analysis of Cyclic Pore Pressure Generation and Undrained Residual Strength", Memorial Symposium Proceedings, Volume 2, May, BiTech Publishers LTD.

Vaid, Yoginder P. and Finn, W.D. Liam, (1979): "Static Shear and Liquefaction Potential", Journal of the Geotechnical Engineering, ASCE, Vol. 105, No. GT10, October.

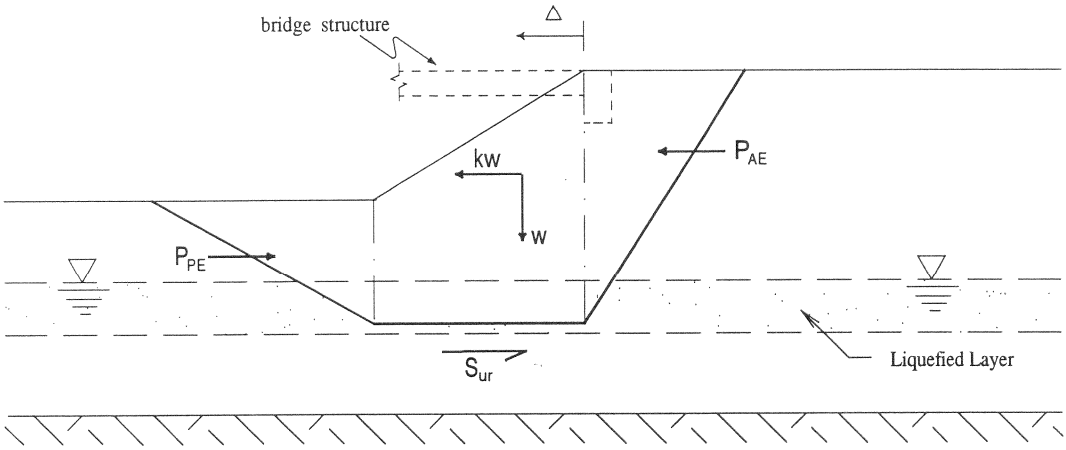

Fig. 1 Idealized Block Failure Mode of Bridge Approach Fill

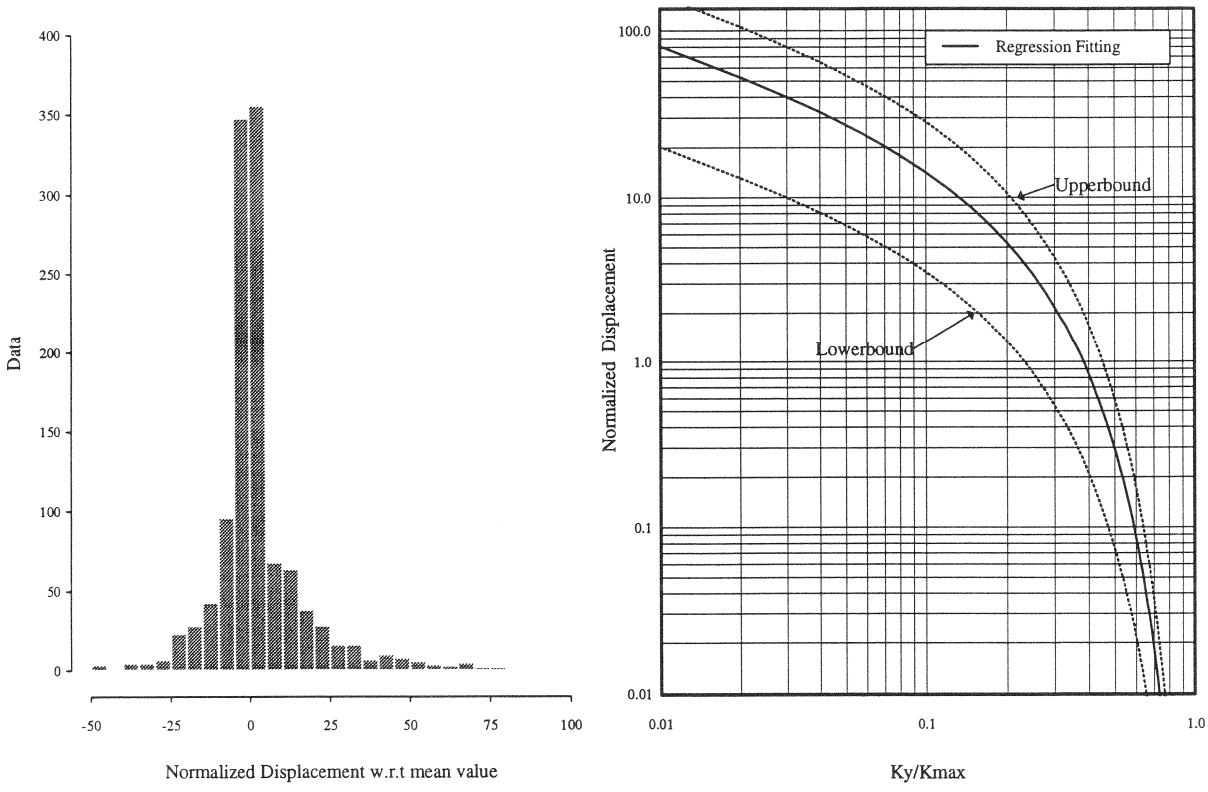

Fig. 2 Newmark Displacement Chart

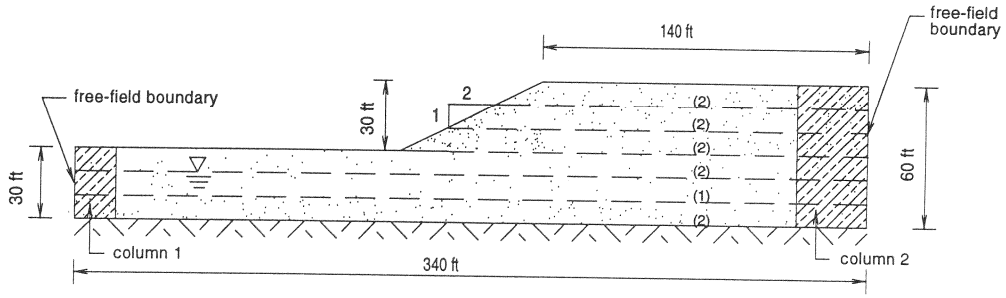

Summary of Material Properties of Nevada Sand

Layer	Relative Density	Poisson's Ratio	Friction Angle	Coefficient of Permeability (m/s)	Residual Strength (psf)
1	40%	0.3	33	6.6×10^{-5}	200
2	60%	0.3	35	5.6×10^{-5}	700

Fig. 3 Configuration of an Idealized Embankment

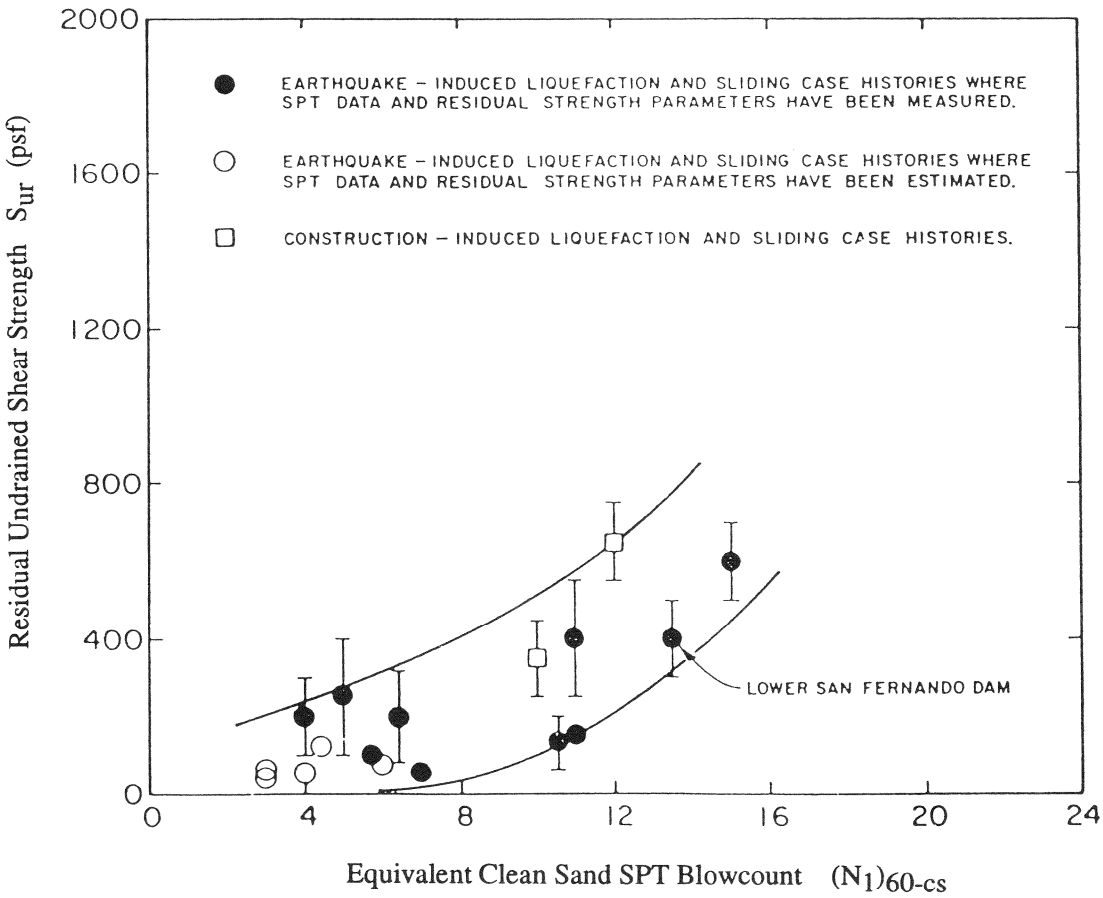

Fig. 4 Relationship Between Clean Sand Blowcount and Undrained Residual Strength from Case Studies

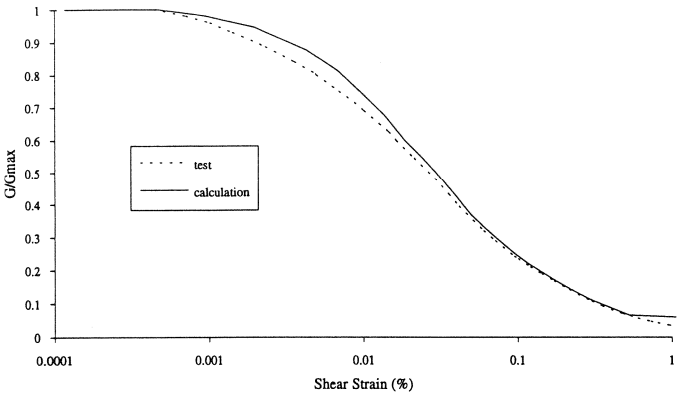

Fig. 5a Modeled versus Standard Shear Modulus-Shear Strain Curve

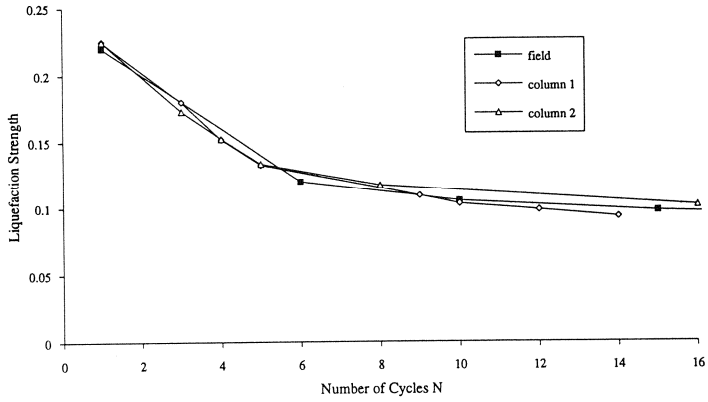

Fig. 5b Modeled versus Field Liquefaction Strengths

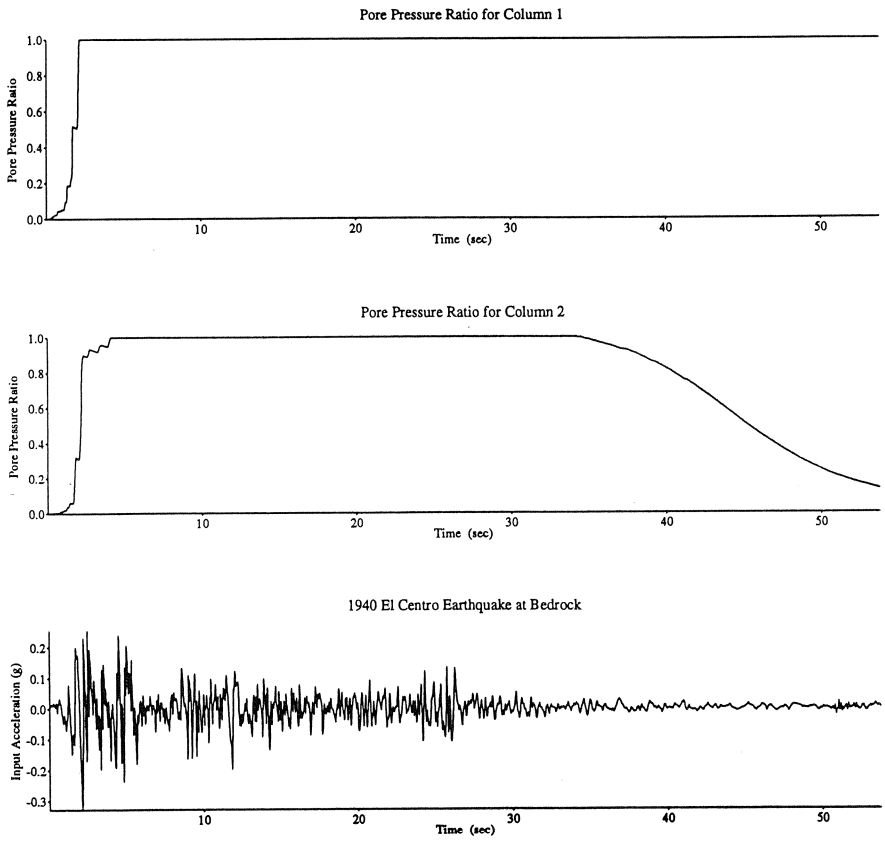

Fig. 6 DESRA-6 Liquefaction Evaluation

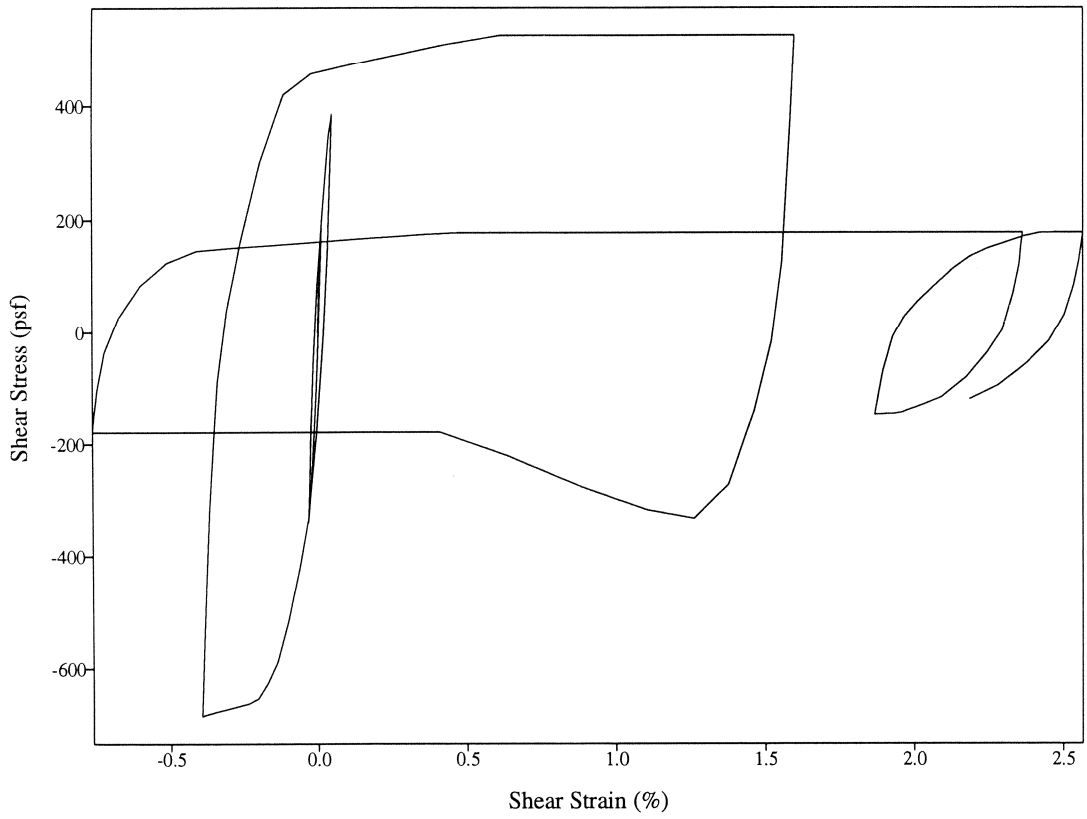

Fig. 7 Shear Stress vs. Shear Strain Time History (0 - 4 seconds) for Layer 1 (Column 2)

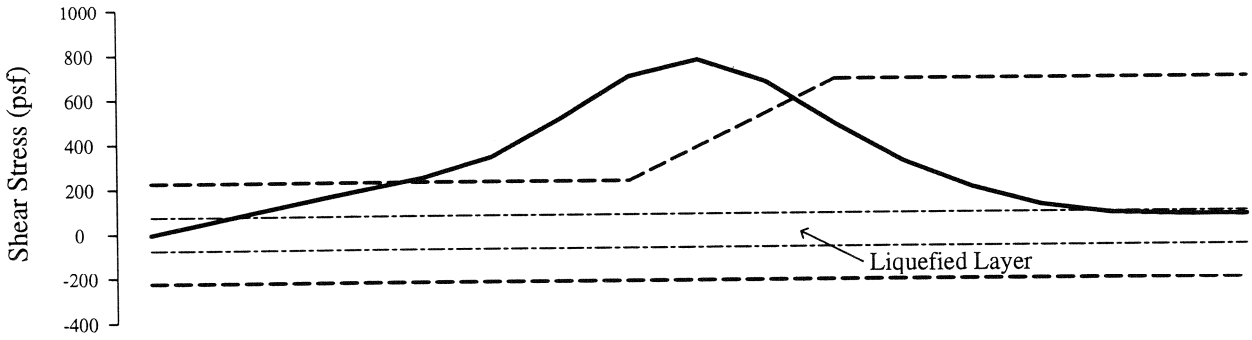

Fig. 8 Horizontal Static Shear Stress Distribution Due to Embankment Construction (Layer 1)

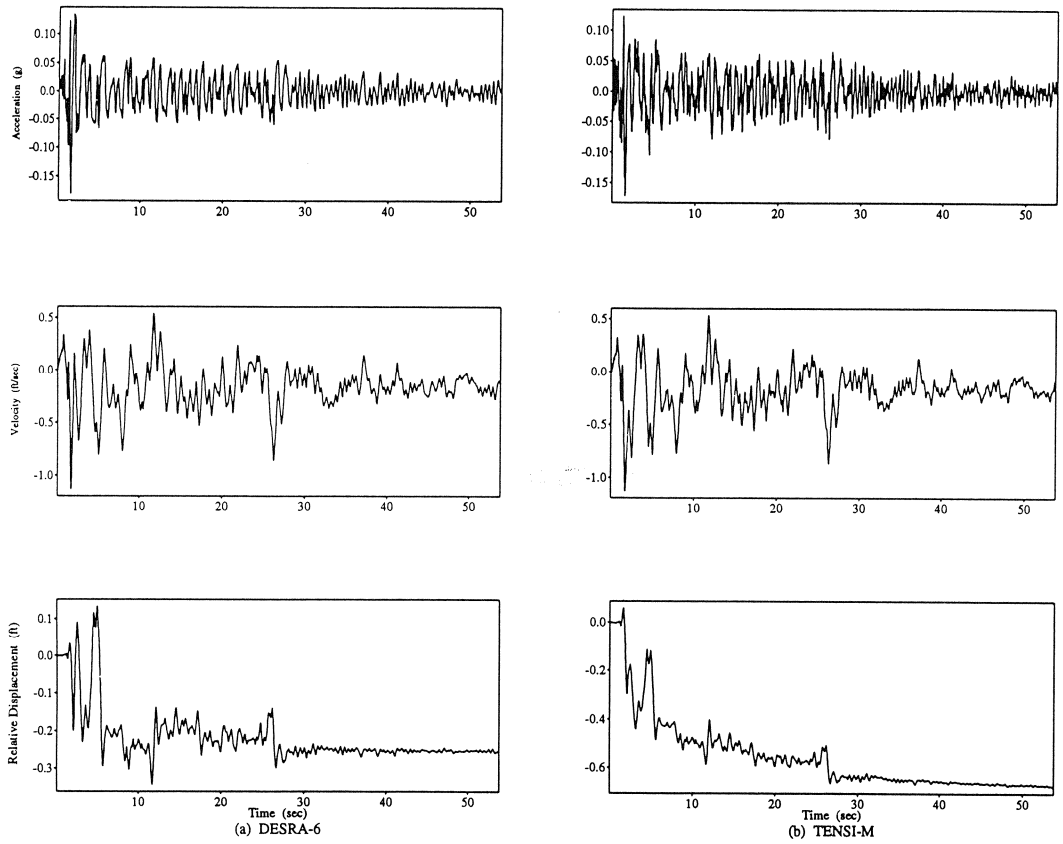

Fig. 9 Comparison of DESRA-6 and TENSI-M Results for Loose sand Layer - Column 1

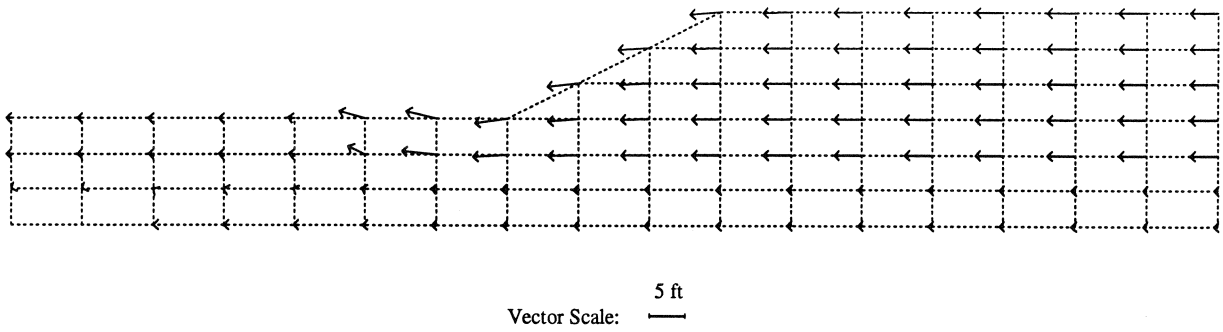

Fig. 10 Displacement Field Vectors

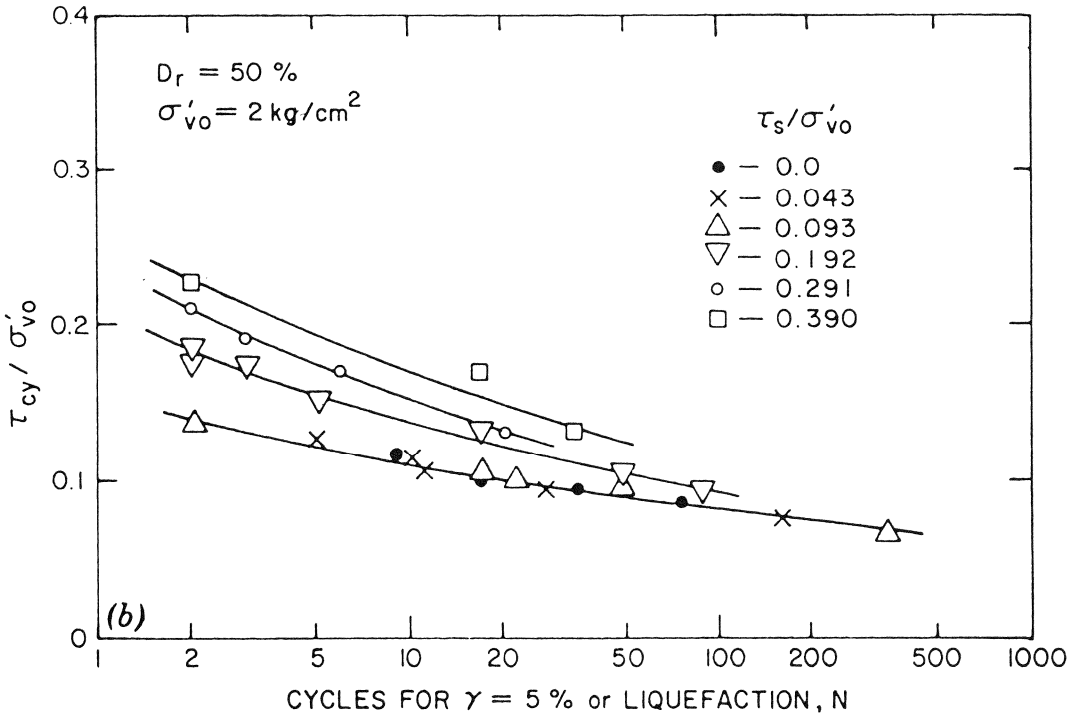

Fig. 11 Cyclic Shear Stress Required to Cause 5% Shear Strain (Loose Ottawa Sand, after Vaid and Finn, 1979)

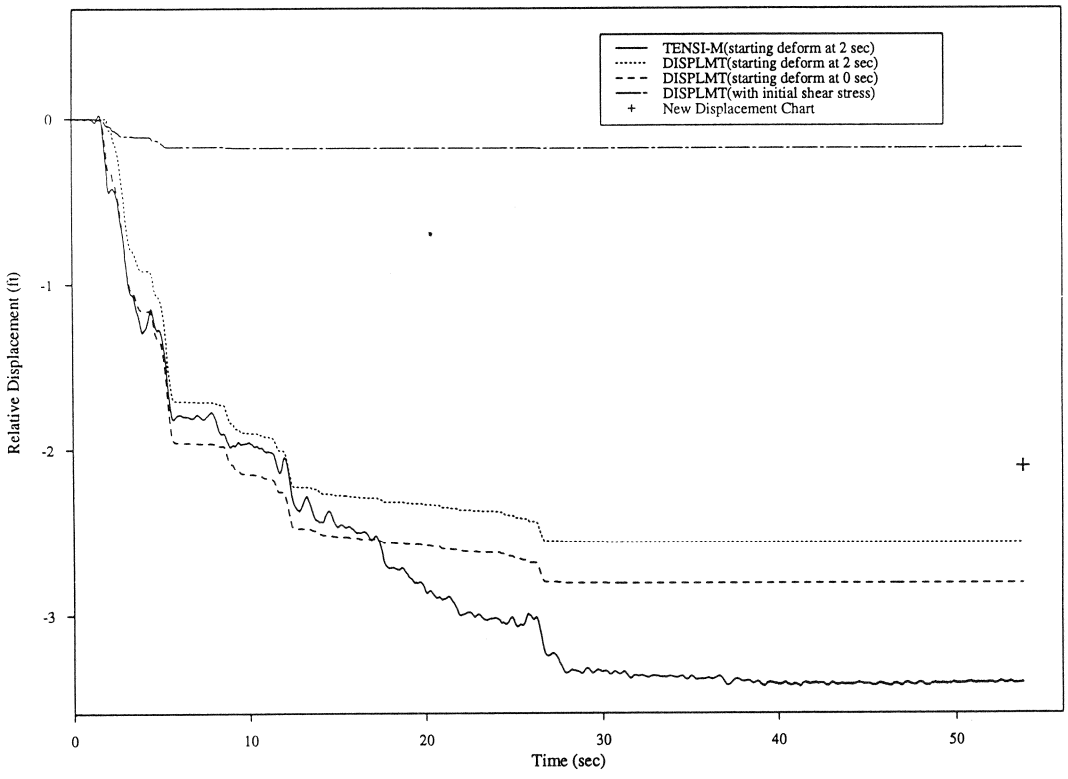

Fig. 12 Comparisons of Newmark Displacements for Liquefied Layer

Torsional Shear and Triaxial Compression Tests on Deformation Characters of Sands Before and After Liquefaction

Susumu YASUDA [1], Tamio MASUDA [2], Nozomu YOSHIDA [3]
Hideo NAGASE [4], Hiroyoshi KIKU [5]
Shigeru ITAFUJI [6], Keiichiro MINE [6] and Kazuya SATO [7]

ABSTRACT

The stress–strain relationships of sand after liquefaction were studied by conducting torsional shear and triaxial compression tests under several conditions. A prescribed number of cyclic loadings were applied first, then a monotonic loading was applied in undrained condition. The stress–strain relationships during the monotonic loading are discussed. The stress–strain curves were affected by the accumulated excess pore pressure ratio and by the severity of liquefaction. The shear and secant modulus decreased to less than 1/1000 due to liquefaction. The shear strain increased more than 10% with very low stress in the liquefied specimen. And, there exists a so called "reference strain at resistance transformation, γ_L" which increases with decreases in soil density, severity of liquefaction and fines content, and with increase with confining pressure.

---

[1] Professor, Dept. of Civil Eng., Tokyo Denki University, Saitama, Japan.
[2] Chief of Section, Tokyo Electric Power Co. Ltd., Tokyo, Japan.
[3] Head of Research, Engineering Research Institute, Sato Kogyo Co., Tokyo, Japan.
[4] Associate Professor, Dept. of Civil Eng., Kyushu Institute of Technology, Kitakyushu, Japan.
[5] Research Associate, Dept. of Civil Eng., Yokohama National University, Yokohama, Japan.
[6] Graduate Student, Dept. of Civil Eng., Kyushu Institute of Technology, Kitakyushu, Japan.
[7] Graduate Student, Dept. of Civil Eng., Yokohama National University, Yokohama, Japan.

INTRODUCTION

It is necessary to know the post liquefaction behavior of sand to estimate large displacement of ground or the settlement of structures due to liquefaction. However, this behavior has not been clarified because studies on liquefaction have focussed mainly on methods to estimate the occurrence of liquefaction.

Therefore, the stress–strain relationships of sand after liquefaction were studied by conducting torsional shear and triaxial compression tests under several conditions of density, confining pressure, fines content and severity of liquefaction. In the tests, a prescribed number of cyclic loading was applied to induce a prescribed excess pore water pressure. Then, a monotonic shear stress was applied.

TEST APPARATUS

Figure 1 shows the torsional shear test apparatus used in this study. Torsional test specimens were hollow cylinders of 10 cm in outer diameter, 6 cm in inner diameter and 10 cm in height. Torsional shear stress was applied at the top of specimens in a horizontal direction with rotational movement of a vertical plunger rod. The rotational movement of the rod was generated with a loading cylinder in cyclic shear stress and with an electric motor in monotonic shear tests. Torsional force, rotational angle and pore water pressure were measured by a torque pick up, a potentiometer and a pressure transducer, respectively. One pair of gap sensors were also used for measuring very small rotational angles.

In triaxial compression tests, column cylindrical specimen of 7.5 cm in diameter and 15 cm in height were used. Axial force, axial displacement and pore water pressure were measured by a road cell, a differential displacement transducer and a pressure transducer, respectively.

TEST CONDITIONS

The sands used in this study were Toyoura sand (G_S=2.64, e_{max}=0.977, e_{min}=0.605, D_{50}=0.16mm, and no content finer) and Narita sand (G_S=2.70, e_{max}=1.371, e_{min}=0.773 D_{50}=0.12mm, and a fine content of 15.2%), as shown in Fig.2.

Most tests were performed using Toyoura sand, which is the standard sand in Japan. The tests were conducted under the following test conditions to clarify the effects of density, confining pressure, excess pore pressure, fines content and severity of liquefaction.

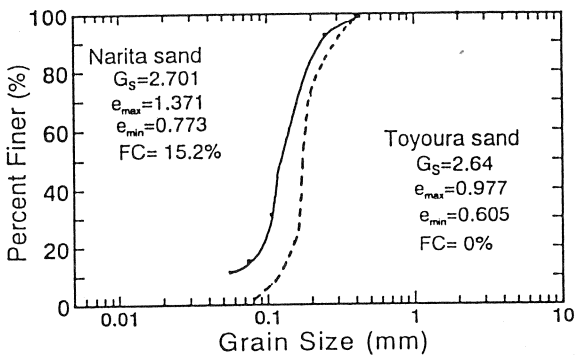

Fig.2 Grain size distribution curves of Toyoura sand and Narita sand

In torsional shear tests

(1) relative density: Dr=0%, 30%, 50% and 70%

(2) effective confining pressure: σ_0' =0.25 kgf/cm^2, 0.5 kgf/cm^2 and 1.0 kgf/cm^2

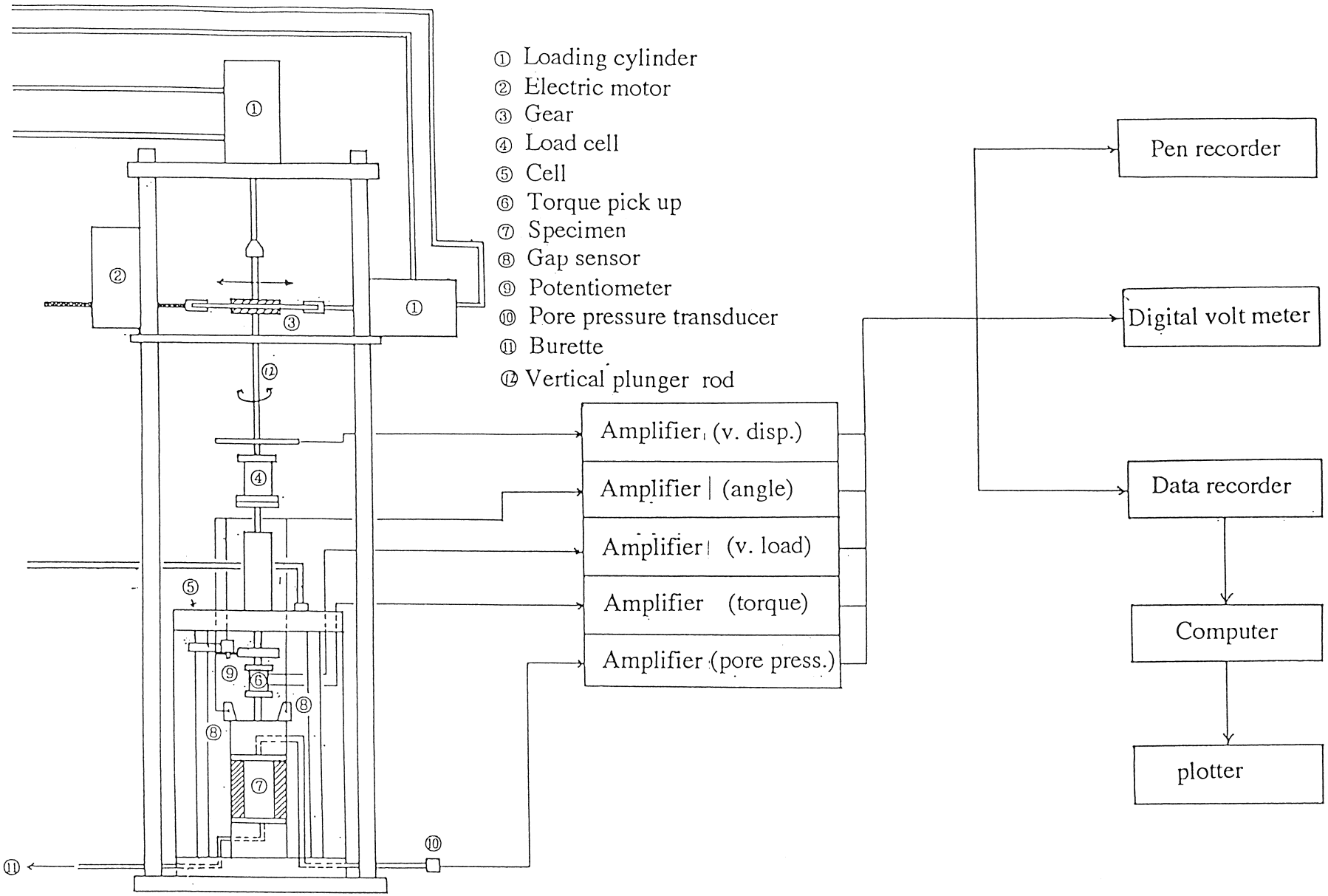

Fig.1 Torsional shear test apparatus

Table 1 Test conditions

No.	Test Device	Sand	Dr %	σ_o' kgf/cm²	$\Delta u/\sigma_v'$ or F_L	No.	Test Device	Sand	Dr (%)	σ_o' kgf/cm²	$\Delta u/\sigma_v'$ or F_L
1	Torsional	C	-1.9	0.5	0	37	Torsional	C	65.4	1.0	0
2	Torsional	C	-5.2	0.5	1.0(F_L=1.0)	38	Torsional	C	73.5	1.0	0.9
3	Torsional	C	29.9	0.5	0	39	Torsional	C	71.9	1.0	1.0(F_L=1.0)
4	Torsional	C	32.6	0.5	1.0(F_L=1.0)	40	Torsional	C	69.4	1.0	1.0(F_L=0.95)
5	Torsional	C	30.5	0.5	1.0(F_L=0.95)	41	Torsional	C	69.9	1.0	1.0(F_L=0.9)
6	Torsional	C	29.2	0.5	1.0(F_L=0.9)	42	Torsional	C	34.7	0.25	0
7	Torsional	C	31.5	0.5	0.3	43	Torsional	C	31.9	0.25	0.9
8	Torsional	C	30.3	0.5	0.6	44	Torsional	C	31.9	0.25	1.0(F_L=1.0)
9	Torsional	C	34.7	0.5	0.9	45	Torsional	C	33.4	0.25	1.0(F_L=0.95)
10	Torsional	C	55.2	0.5	0	46	Torsional	C	33.2	0.25	1.0(F_L=0.9)
11	Torsional	C	53.9	0.5	1.0(F_L=1.0)	47	Torsional	C	45.5	0.25	0
12	Torsional	C	51.7	0.5	1.0(F_L=0.95)	48	Torsional	C	53.5	0.25	0.9
13	Torsional	C	53.1	0.5	1.0(F_L=0.9)	49	Torsional	C	50.0	0.25	1.0(F_L=1.0)
14	Torsional	C	48.3	0.5	0.6	50	Torsional	C	53.1	0.25	1.0(F_L=0.95)
15	Torsional	C	53.0	0.5	0.9	51	Torsional	C	47.9	0.25	1.0(F_L=0.9)
16	Torsional	C	68.2	0.5	0						
17	Torsional	C	69.9	0.5	1.0(F_L=1.0)	52	Triaxial	C	27.8	0.5	0
18	Torsional	C	71.3	0.5	1.0(F_L=0.95)	53	Triaxial	C	28.2	0.5	0.36
19	Torsional	C	68.4	0.5	1.0(F_L=0.9)	54	Triaxial	C	25.3	0.5	0.52
20	Torsional	C	70.2	0.5	0.6	55	Triaxial	C	26.1	0.5	0.9
21	Torsional	C	71.8	0.5	0.9	56	Triaxial	C	23.2	0.5	1.0(F_L=1.0)
22	Torsional	C	-2.2	1.0	0	57	Triaxial	C	49.5	0.5	0
23	Torsional	C		1.0	0.9	58	Triaxial	C	46.4	0.5	0.26
24	Torsional	C	-3.6	1.0	1.0(F_L=1.0)	59	Triaxial	C	49.3	0.5	0.38
25	Torsional	C	-4.6	1.0	1.0(F_L=0.95)	60	Triaxial	C	48.7	0.5	0.94
26	Torsional	C	-4.8	1.0	1.0(F_L=0.9)	61	Triaxial	C	48.0	0.5	1.0(F_L=1.0)
27	Torsional	C	32.7	1.0	0	62	Triaxial	F	38.6	0.5	0
28	Torsional	C	34.5	1.0	0.9	63	Triaxial	F	38.0	0.5	0.44
29	Torsional	C	25.3	1.0	1.0(F_L=1.0)	64	Triaxial	F	39.9	0.5	0.56
30	Torsional	C	25.8	1.0	1.0(F_L=0.95)	65	Triaxial	F	38.8	0.5	0.9
31	Torsional	C	27.3	1.0	1.0(F_L=0.9)	66	Triaxial	F	38.0	0.5	1.0(F_L=1.0)
32	Torsional	C	51.4	1.0	0	67	Triaxial	F	54.8	0.5	0
33	Torsional	C	53.3	1.0	0.9	68	Triaxial	F	54.8	0.5	0.40
34	Torsional	C	46.4	1.0	1.0(F_L=1.0)	69	Triaxial	F	53.3	0.5	0.56
35	Torsional	C	51.0	1.0	1.0(F_L=0.95)	70	Triaxial	F	49.6	0.5	0.9
36	Torsional	C	45.9	1.0	1.0(F_L=0.9)	71	Triaxial	F	53.0	0.5	1.0(F_L=1.0)

sand: C: Clean sand (Toyoura sand)
F: Sand with fines (Narita sand)

(3) excess pore pressure ratio: $\Delta u/\sigma_0' = 0$, 0.3, 0.6, 0.9 and 1.0
(4) severity of liquefaction: FL=1.0, 0.95 and 0.9

Special tests were also carried out in which the excess pore pressure dissipated after liquefaction up to $\Delta u/\sigma_0' = 0.9$ or 0.6 by drainage, then monotonic shear stresses were applied. The test conditions of all the specimens are listed in Table 1.

In triaxial compression tests
(1) relative density: Dr= 30% and 50%
(2) effective confining pressure: $\sigma_0' = 0.5$ kgf/cm^2
(3) excess pore pressure ratio: $\Delta u/\sigma_0' = 0$, 0.4, 0.6, 0.9 and 1.0
(4) fines content: FC=0% (Toyoura sand) and 15.2% (Narita sand)

TEST PROCEDURES

Sample preparation technique

In the tests for relative densities of 30%, 50% and 70%, specimens were prepared by the air–pluviation method; pouring dry sand into molds through a funnel from constant heights. The density of the specimens was controlled by the height. In the tests for 0% relative density, which is very loose, a special technique for preparing the specimen. was adopted; a slightly wet sand with 1–2% moisture content was carefully filled into a mold without tamping. After being saturated, samples were consolidated isotropically at a prescribed effective confining pressure($\sigma_0' = 0.25$, 0.5 and 1.0 kgf/cm^2) with a back pressure, σ_{BP}, of 2.0 kgf/cm^2 in undrained condition.

Loading pattern in torsional shear tests

In torsional shear tests, a prescribed number of cyclic loading of 0.1 Hz was applied to the specimens in undrained conditions. The cyclic loading was terminated when the excess pore pressure ratio, or FL, reached a prescribed value. Then, a monotonic loading was applied during undrained condition with a relatively high speed of $\gamma = 10\%$ in a minute, as shown in Fig. 3. The amplitude of cyclic loading was controlled to a prescribed value which produced liquefaction in 20 cycles. Therefore, the amplitude of each density was different.

If the number of cycles of cyclic loading was less than 20, liquefaction did not occur However, the stress–strain relationships during the monotonic loading were affected by the excess pore pressure induced during the cyclic loading. Cyclic loading was terminated when $\Delta u/\sigma_0'$ reached 0 or 0.3, 0.6, 0.9, 1.0. The number of cycles was 0 when $\Delta u/\sigma_0' = 0$ and 20 when $\Delta u/\sigma_0'$ was 1.0.

On the contrary, liquefaction occurred when the number of cycles during the cyclic loading exceeded 20, and the severity of liquefaction increased with the number of cycles. The severity of liquefaction was indicated by the factor of safety against liquefaction, FL, in this study. If the number of cycles, N, was 20, FL equalled 1.0. In the case of

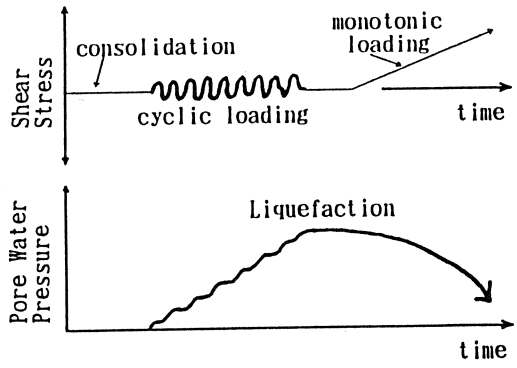

Fig.3 Procedure of cyclic loading and monotonic loading

N>20, N for prescribed FL can be calculated by the following equation, which was derived based on the normalizing method proposed by Tatsuoka et al.(1980).

$$N=20\,(FL)^{1/b} \qquad (1)$$

where: b=−0.17 in clean sand

Therefore, cyclic loading was terminated at N=27 and N=37 in FL=0.95 and FL=0.9, respectively.

Figure 4 shows shear resistance of inner and outer menbrane without a specimen. The shear resistance of membranes was deducted from the measured shear stress.

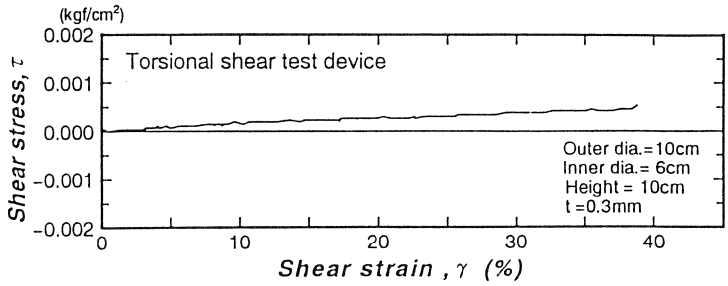

Fig.4 Shear resistance of inner and outer membranes

Loading pattern in triaxial compression tests

In triaxial compression tests, the number of cycles of cyclic loading was fixed for 20 cycles in all specimens. The amplitude of the cyclic loading was controlled to accumulate a prescribed value of excess pore pressure. Therefore, in case of fully−liquefied condition, FL=1 and $\Delta u/\sigma_0' = 1.0$, the cyclic shear stress ratio which produce liquefaction in 20 cycles, $R_{l,20}$, was applied. If the amplitude of cyclic loading was smaller than $R_{l,20}$, liquefaction did not occur and the accumulated excess pore pressure ratio was less than 1.0.

TEST RESULTS

Test Results for Different Pore Pressure Ratio

Relationships among shear stress, τ ,excess pore pressure, Δu, and shear strain, γ , in the monotonic loading are discussed in this study. Figure 5 shows the stress−strain curves and the excess pore pressure−strain curves in the case of $\Delta u/\sigma_0'=0$. Shear stress increased rapidly with shear strain up to $\gamma \fallingdotseq 1\%$. Then, the shear stress increased gradually with shear strain in the cases of Dr ≧ 30%.

On the contrary, the shear stress decreased gradually in the case of Dr=−1.9%. Pore pressure increased with shear strain up to $\gamma \fallingdotseq 2\%$, then decreased, in the cases of Dr ≧ 30%. However, the pore water pressure did not decrease in the case of Dr=−1.9%.

Figure 6 compares the

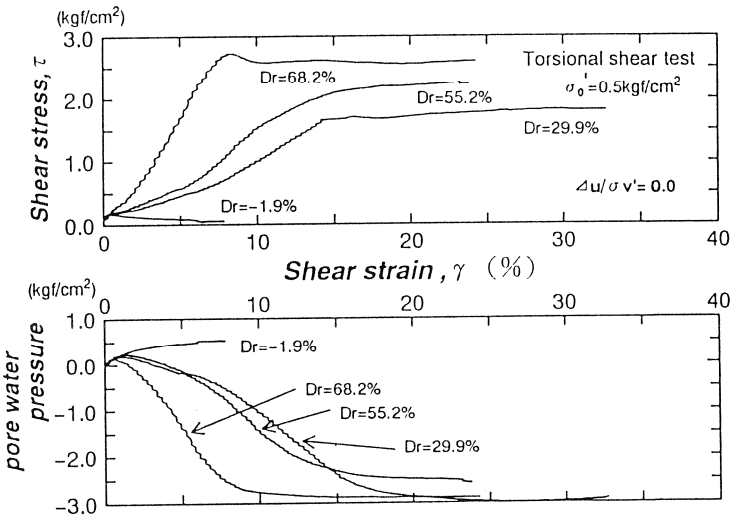

Fig.5 Stress-strain curves and strain-pore pressure curves ($\Delta u/\sigma_0'$=0,static)

stress paths of tests shown in fig. 5. It can be seen that the stress path of Dr=−1.9% proceeded toward the origin of the coordinate axes after having a peak value of shear stress.

Figure 7(a) and Figure 7(b) in which the scales of the axes are enlarged, show stress−strain curves and excess pore water pressure−strain curves in the case of $\Delta u/\sigma_0'$ =1.0 and FL=1.0. Shear strain increased with very low shear stress up to γ >10%. Then, after a resistance transformation point the shear stress increased comparatively rapidly with shear strain, following the decrease of pore water pressure in the cases of Dr ≧ 30%. However, quite little shear stress was generated up to γ =47% without dropping the pore water pressure in the case of Dr=−5.2%.

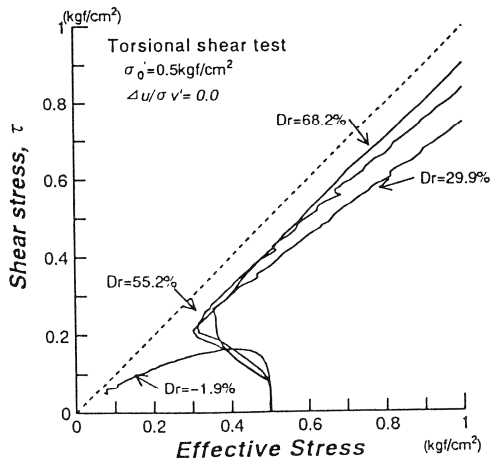

Fig.6 Comparison of stress paths in different densities

Figure 8(a), (b) and (c) compare the stress−strain curves in different pore water pressure ratios and FLs. As shown in these figures, shear stress in some shear strain decreased with the pore water pressure ratio.

Test Results for Different FL

Test results for FL=0.95 and 0.9 are shown in Fig.9(a) and (b). The curves were similar to those of FL=1.0. However, for the similar FL, the resistance transformation point appeared at large strain.

Effect of Drainage

Figure 10(a) and (b) show results of the special tests in which excess pore water pressure dissipated up to $\Delta u/\sigma_0'$=0.9 or 0.6. As shown in these figures, the decreased excess pore water pressure recovered up to $\Delta u/\sigma_0'$=1.0 in small strain. However, shear strains at the resistance transformation points were smaller than those of the data without dissipation.

Effect of Confining Pressure

Figure 11(a), (b), (c) and (d) show the change of stress−strain curves with the development of liquefaction in different confining pressures and relative densities. Comparing the stress−strain curves in the same conditions of relative density and pore pressure ratio, the shear stress in some shear strain increased with the confining pressure when the FL is greater than 1.0. On the contrary, the shear stress in some strain decreased with the confining pressure when the FL is less than 1.0.

Effect of Fine Content

Figure 12(a) and (b) show the relationships between the deviator stress, $\sigma_1-\sigma_3$, and the axial strain, ε, of Toyoura sand during the monotonic loadings using triaxial compression test device. The change of stress−strain curves with different pore pressure ratio in triaxial test were similar to those in torsional test. Figure 13(a) and (b) compare the stress−strain curves of Narita sand, which contains the fines of 15.2%, during the monotonic loading. As shown in Fig.12 and Fig.13, flow deformation was observed also in triaxial tests when the excess pore pressure ratio almost 1.0. The axial strain with low deviator stress was larger in case of clean sand. However, the deviator stress recovered rapidly with axial strain in case of clean sand as compared with that for fine sand.

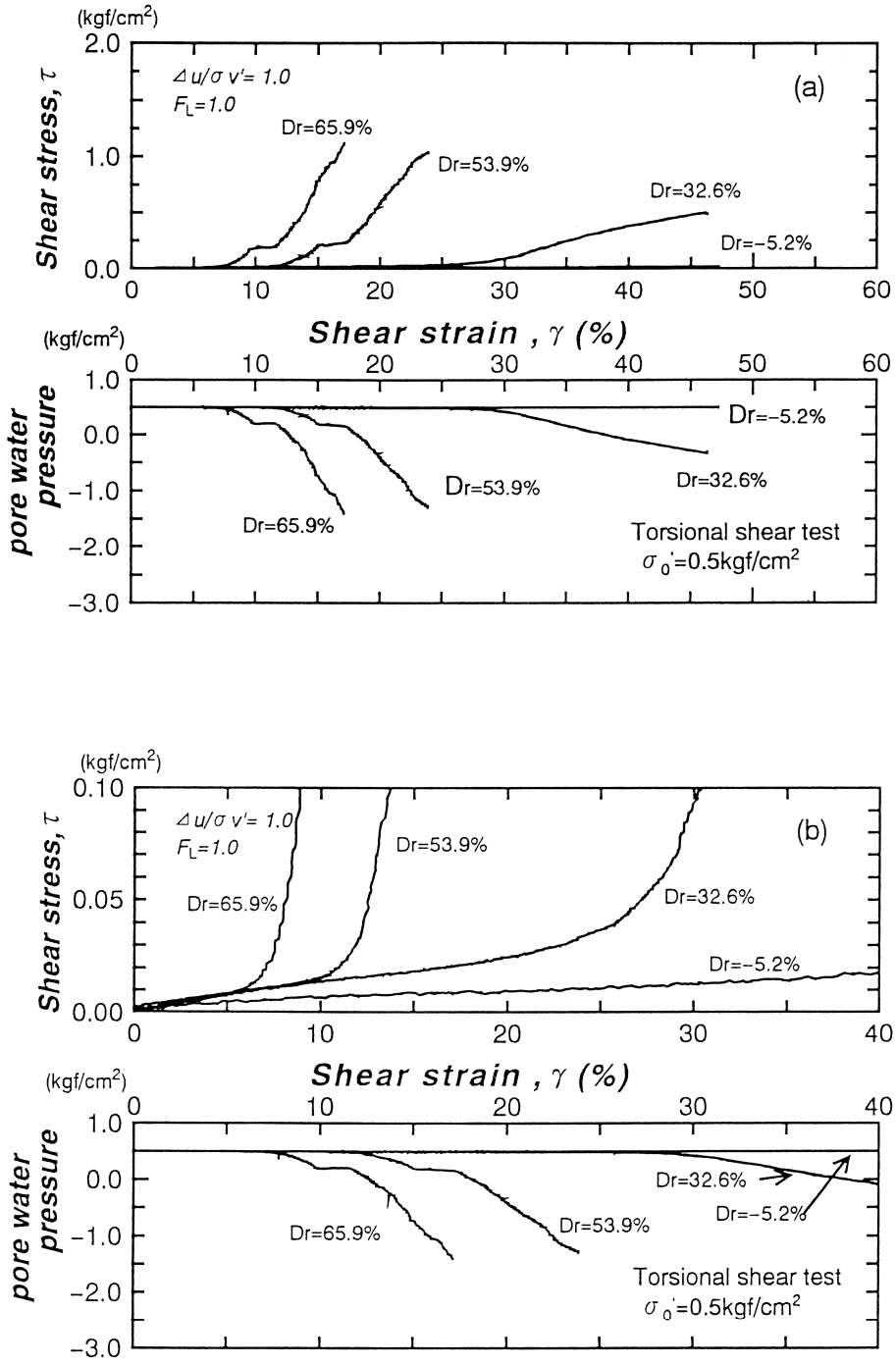

Fig.7 Stress-strain curves and strain-pore pressure curves ($\Delta u/\sigma_0'$=1.0, F_L=1.0)

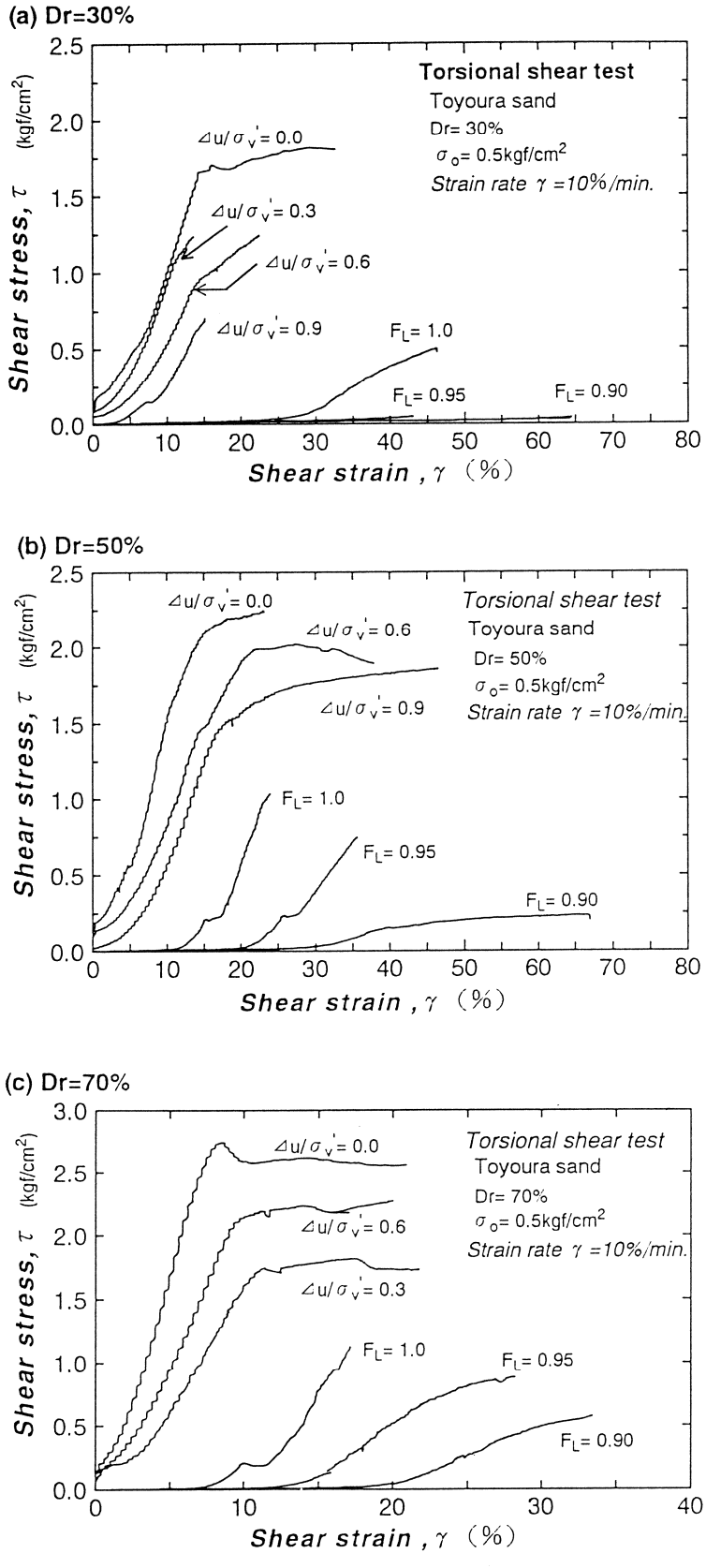

Fig.8 Comparison of stress–strain curves in different densities

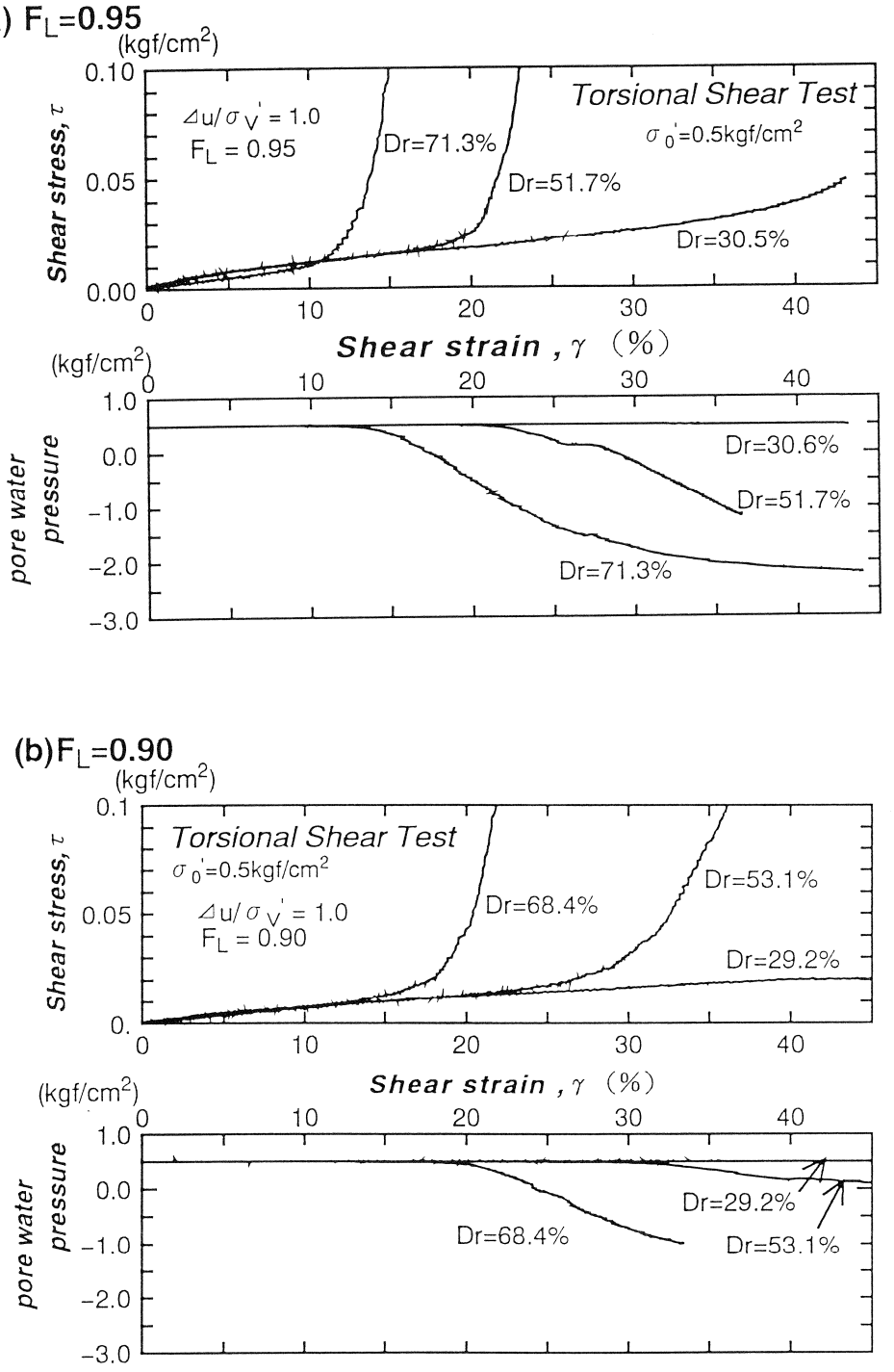

Fig.9 Stress-strain curves and strain-pore pressure curves ($\Delta u/\sigma_0'$=1.0, F_L<1.0)

(a) $\Delta u/\sigma_0' = 1.0 \rightarrow 0.9$

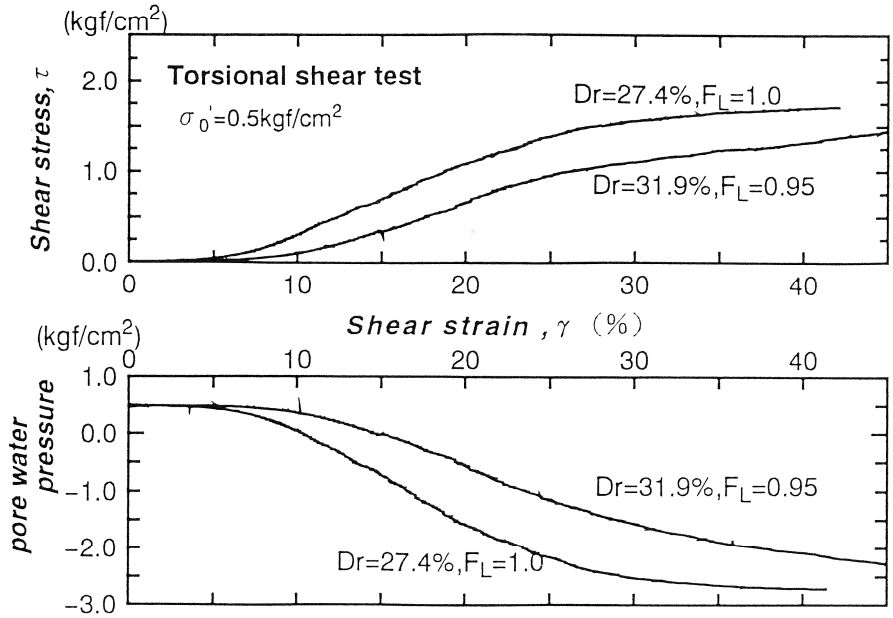

(b) $\Delta u/\sigma_0' = 1.0 \rightarrow 0.6$

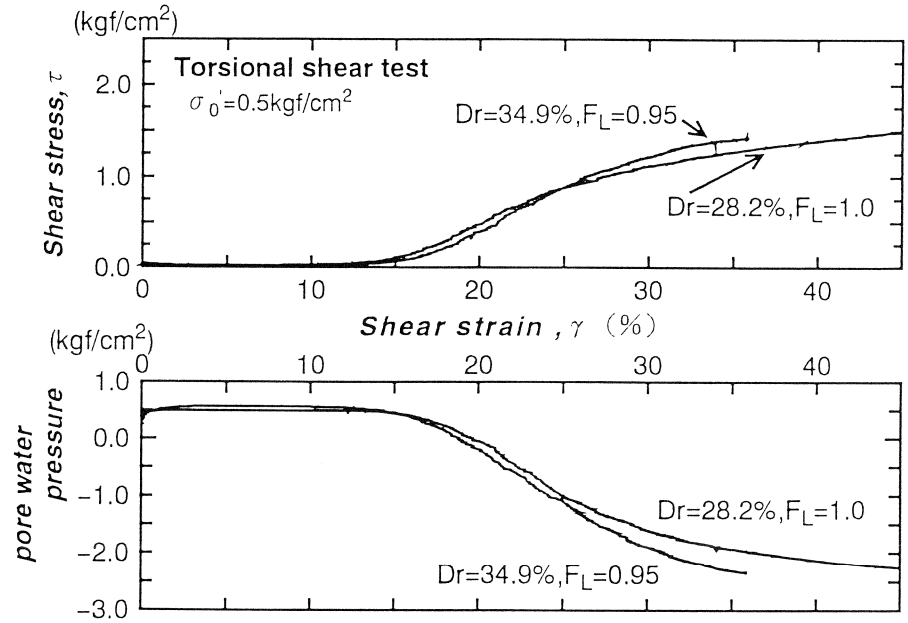

Fig.10 Stress-strain curves and strain-pore pressure curves
($\Delta u/\sigma_0'$=1.0→0.9 or 0.6, F_L=1.0 or 0.9)

(a) Dr=50%, σ_0'=1.0kgf/cm^2

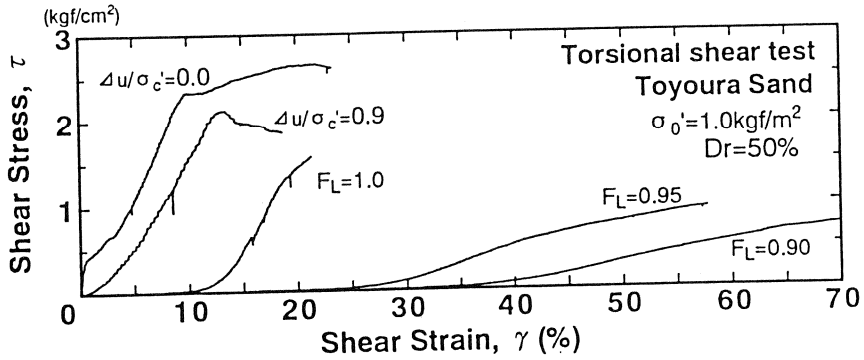

(b) Dr=50%, σ_0'=0.25kgf/cm^2

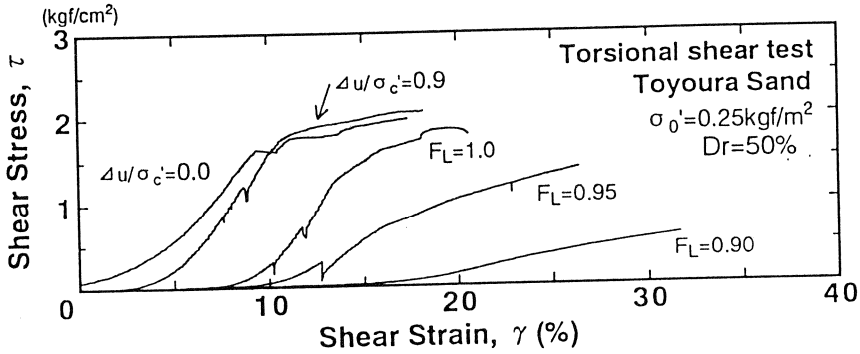

(c) Dr=70%, σ_0'=1.0kgf/cm^2

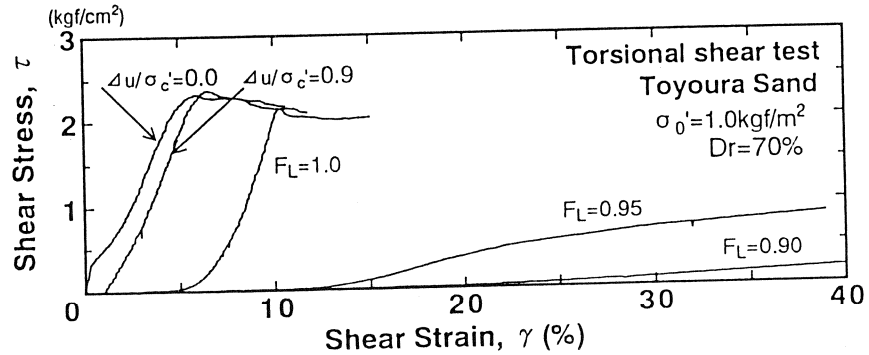

(d) Dr=30%, σ_0'=0.25kgf/cm^2

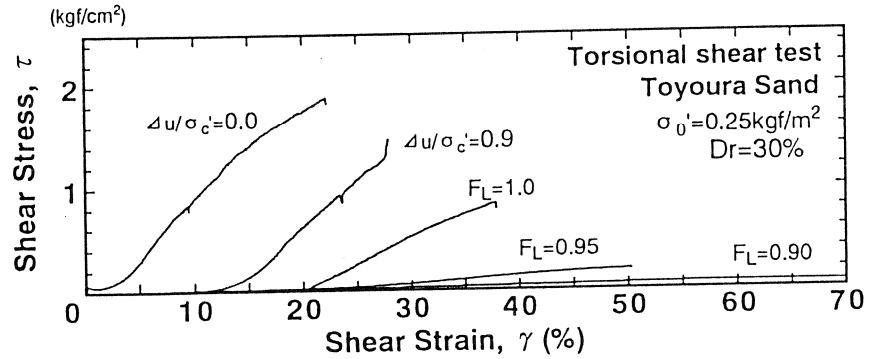

Fig.11 Stress-strain curves in different confining pressures

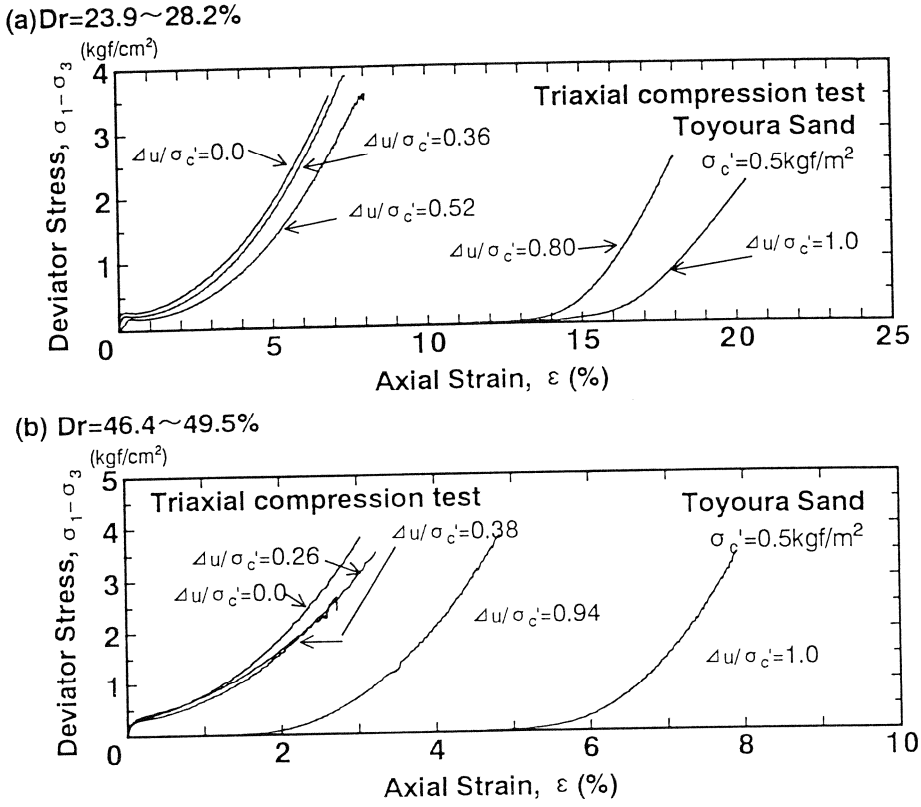

Fig.12 Stress-strain curves in triaxial compression tests (Toyoura sand)

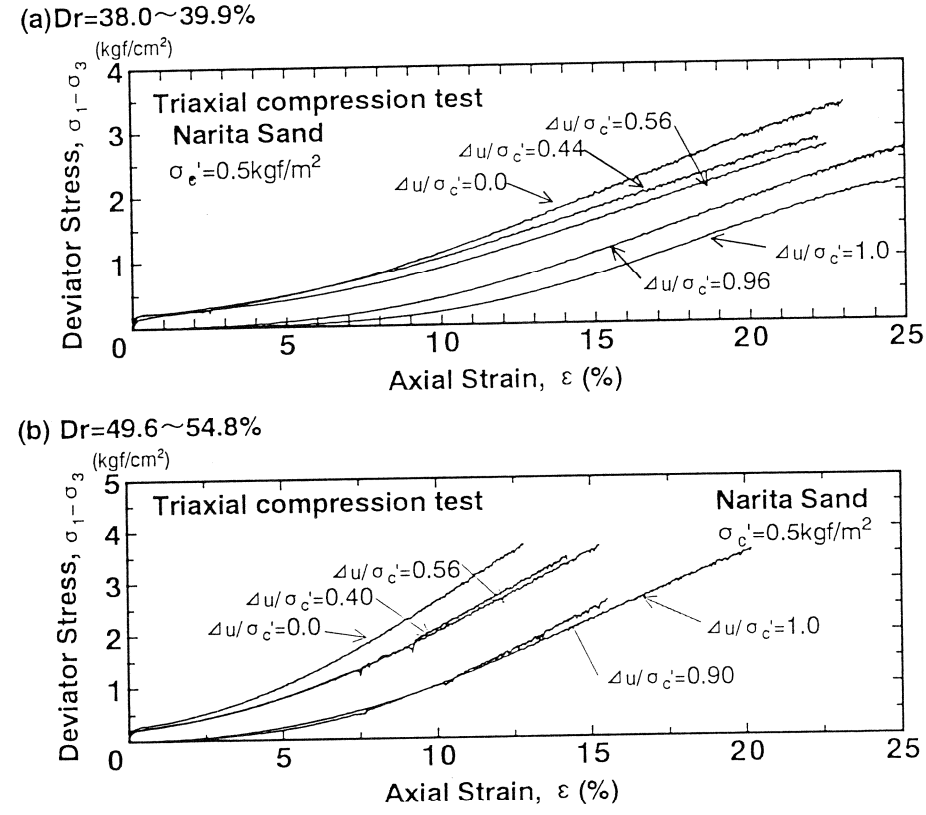

Fig.13 Stress-strain curves in triaxial compression tests (Narita sand)

RELATIONSHIPS BETWEEN $G_i / G_{0.i}$ *AND* $\Delta u/\sigma_0'$ *OR* FL

The rate of reduction of shear modulus, $G_i / G_{0.i}$, was calculated from the torsional test results to know the reduction rate of the rigidity of sand due to liquefaction. $G_{0.i}$ and G_i were defined as the secant moduli of the stress−strain curves at γ =0.1% in the case of $\Delta u/\sigma_0'$=0 and at γ =0.1 or 1.0, 3.0% in the case of $\Delta u/\sigma_0'$>0, respectively. Figure 14 shows relationships between $G_i/G_{0.i}$ and $\Delta u/\sigma_0'$. It can be seen that $G_i / G_{0.i}$ decreased with an increase in $\Delta u/\sigma_0'$ and reached a vary small value. If the $G_{0.i}$ at γ =0.1% and G_i at γ =3.0% are assumed as shear moduli of the ground before and after liquefaction, respectively, $G_i/G_{0.i}$ in Fig. 14(a), (b) and (c) are almost 0.001. This means that the shear modulus of the ground decreased to almost 1/1000 due to liquefaction.

Figure 15 shows relationships between FL and $G_i/G_{0.i}$. FL values greater than 1.0 were also calculated by Eq. (1). As shown in this figure, G_i decreased more than 1/1000 in the range of FL<1.0. Therefore, it can be said roughly that the shear modulus decreases to less than 1/1000 due to severe liquefaction, and varies with the severity of liquefaction.

Yasuda et al. (1992) proposed a simplified analytical method to estimate large ground displacement due to liquefaction. As the parameter $G_i/G_{0.i}$ is used in the method, test results in this study will be utilized in such a kind of analysis.

In the same manner, the rate of reduction of secant modulus, $E_i / E_{0.i}$, was calculated from the triaxial test results. Figure 16(a) and (b) show the relationships between $E_i / E_{0.i}$ and $\Delta u/\sigma_0'$ in Toyoura sand. It can be seen that $E_i / E_{0.i}$ decreased with an increase in $\Delta u/\sigma_0'$ and reached a vary small value, similar in the torsional shear tests. Figure 17(a) and (b) show the relationships between $E_i / E_{0.i}$ and $\Delta u/\sigma_0'$ in Narita sand. The tendency of reduction curves of Narita sand were a little different from those of Toyoura sand, but the obvious difference of the reduction rate between Toyoura sand and Narita sand could not be seen from these figures.

RELATIONSHIPS AMONG γ_L, Dr, FL *AND* σ_0'

As shown in Fig. 7, 8 and 9, shear stress increased comparatively rapidly after a resistance transformation point. The amount of strain up to the resistance transformation point is called here the "value of strain during low resistance, γ_L" as shown in Fig. 18. γ_L thus defined are plotted with Dr and FL in Fig. 19(a), (b) and (c). γ_L increased with decreases in Dr and FL and with increase in σ_0'. In the case of Dr=30%, FL=0.9 and σ_0'=0.5 kgf/cm^2, γ_L reached a very large strain, almost 60%.

A detailed method for the estimation of large ground displacements due to liquefaction based on the γ_L or stress−strain curves studied here will be developed hereafter. However, a simple estimation for permanent ground displacement due to liquefaction is tried here, based on Fig. 19 under the following assumptions;

① A model ground with gentle slope is liquefied from ground surface to the depth of −10m. FL, Dr and unit weight γ_t of the liquefied layer are 0.95, 30% and 1.9 tf/m^3, respectively.

② Shear strain up to γ_L induces due to liquefaction in the liquefied soil.

Figure 20 shows the distribution of the estimated permanent ground displacement. As shown in this figure, the displacement increases from the bottom of the liquefied layer to the ground surface. And the permanent ground displacement at ground surface can be estimated as 3.5m.

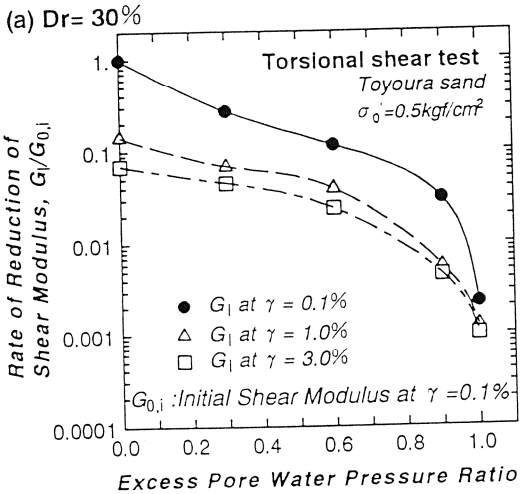

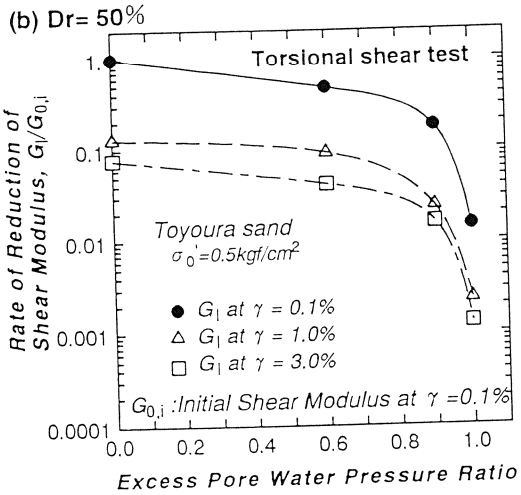

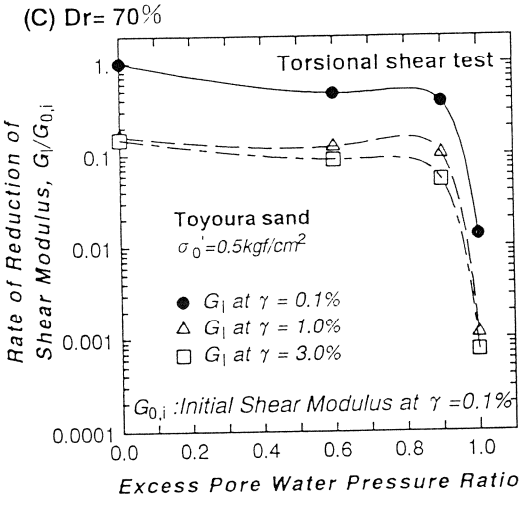

Fig.14 Relationships between $G_l/G_{0,i}$ and $\Delta u/\sigma_0$

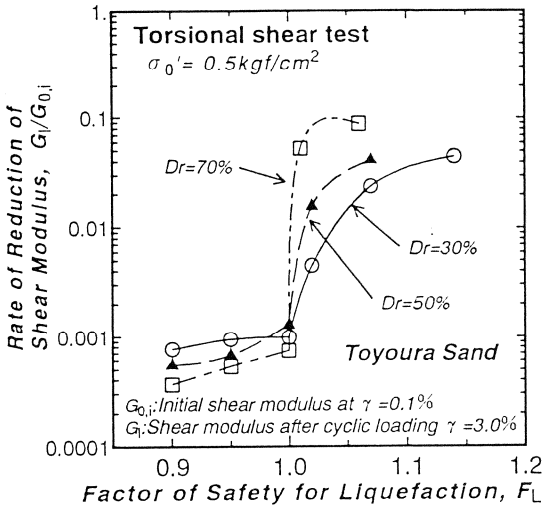

Fig.15 Relationships between $G_l/G_{0,i}$ and F_L

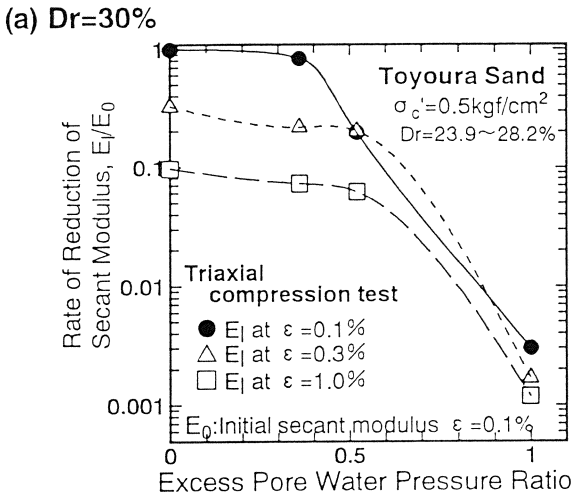

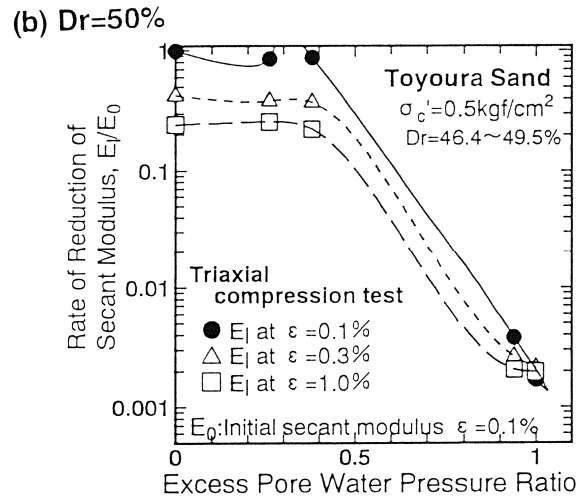

Fig.16 Relationships between $E_l/E_{0,i}$ and $\Delta u/\sigma_0'$

(a) Dr=30%

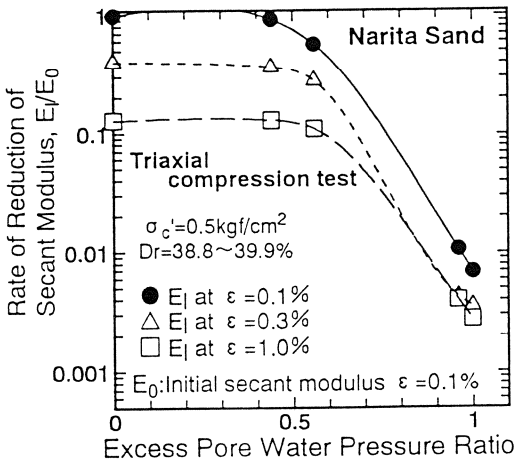

(b) Dr=50%

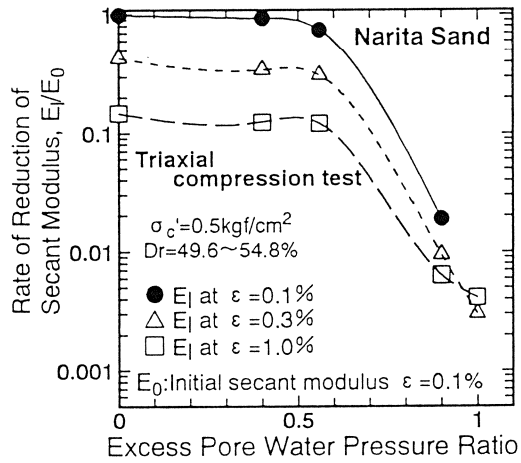

Fig.17 Relationships between $E_I/E_{0,i}$ and $\Delta u/\sigma_0'$

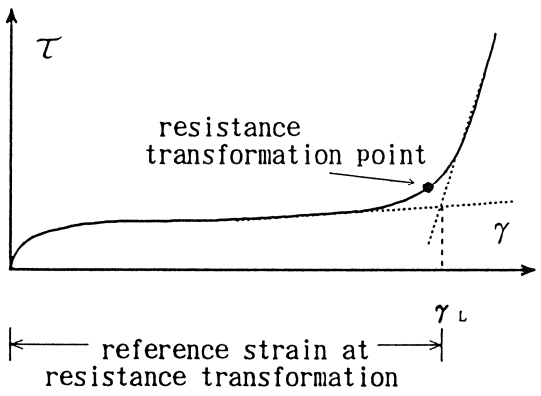

Fig.18 Definition of γ_L

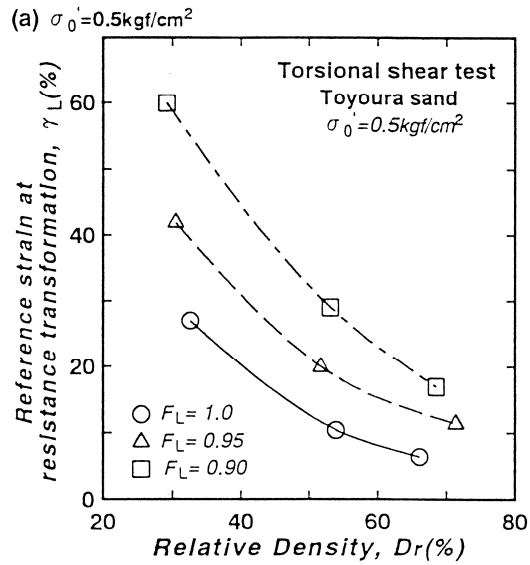

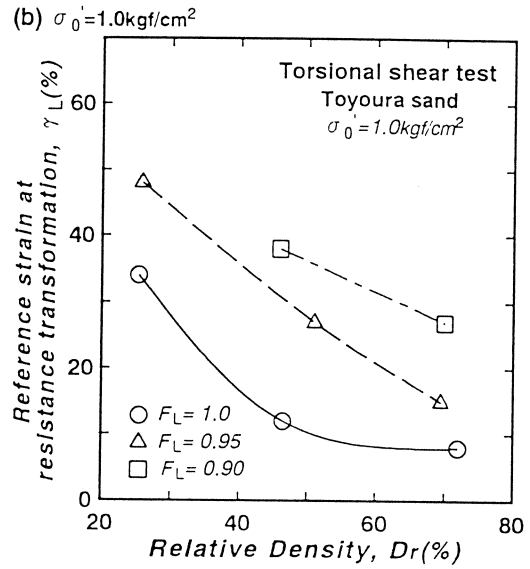

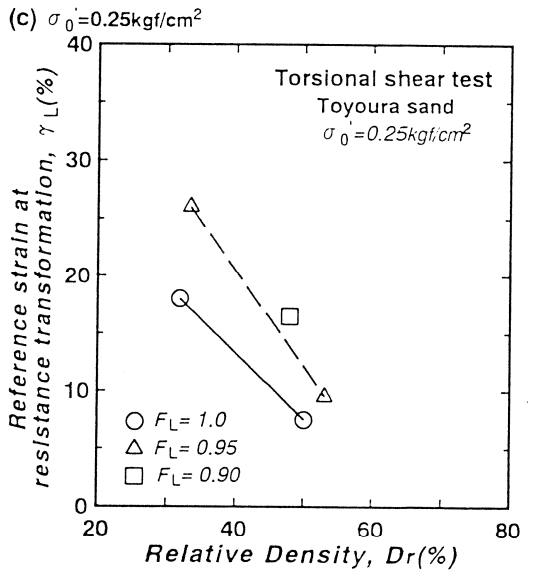

Fig.19 Relationships among γ_L,Dr and F_L

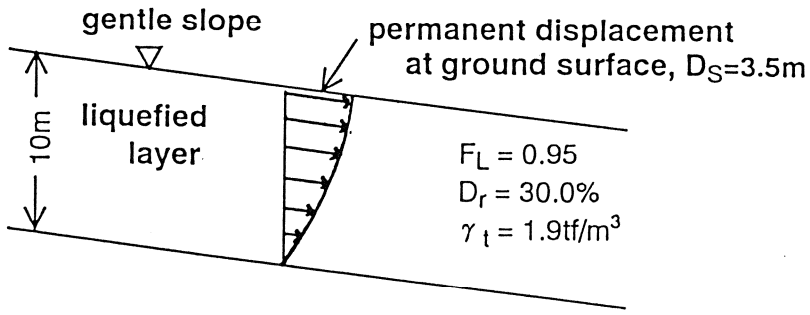

Fig.20 A simple estimation for permanent ground displacement

CONCLUSIONS

Torsional and triaxial shear tests on saturated sands were conducted under several conditions to ascertain the post liquefaction behavior of the sand. The main conclusions are as follows:

(1) stress–strain curves are affected by the excess pore water pressure ratio, $\Delta u/\sigma_0'$, by the factor of safety against liquefaction, FL, and by fine content of the soil.

(2)the shear modulus decreases to 1/1000 or less due to liquefaction and varies with FL.

(3) there exists a so called "reference strain at resistance transformation, γ_L," which increased with decreases in relative density and FL and with increase in with σ_0'.

ACKNOWLEDGEMENTS

Valuable discussions by the members of a committee of the Association for the Development of Earthquake Prediction in Japan. The tests were carried out in the laboratories of Kyushu Institute of Technology and Yokohama National University. The authors would like express their thanks also to Prof. G. Imai of Yokohama National University and Mrs. K. Ushijima of Kyushu Institute of Technology.

REFERENCES

1) Tatsuoka, F., Yasuda, S., Iwasaki, T. and Tokida, K.: Normalized Dynamic Undrained Strength of Sand Subjected to Cyclic and Random Loading, Soils and Foundations, Vol.20, No.3, pp.1–16, 1980.

2) Yasuda, S., Nagase, H., Kiku, H. and Uchida, Y.: The mechanism and A Simplified Procedure for the Analysis of Permanent Ground Displacement due to Liquefaction, Soils and Foundations, Vol.32, No.1, pp.149–160, 1992.

Ground Motion Characteristics and their Relation to Soil Liquefaction at the Wildlife Liquefaction Array, Imperial Valley, California.

Kayen R.E.[1], Mitchell, J.K.[2], and Holzer, T.L.[3]

Abstract

We use the earthquake shaking severity parameter Arias intensity, I_h, to assess the site specific characteristics of ground motion, and investigate the relation of those characteristics to soil liquefaction occurrence at the Wildlife liquefaction array, in response to the Elmore Ranch and Superstition Hills earthquakes of November 23 and 24, 1987. We found that for both earthquake events, the Arias intensities calculated from motions recorded by the downhole seismometer were significantly less than those calculated from recordings of the surface seismometer. By normalizing the downhole cumulative Arias intensity-time history with that of the surface record, it can be shown that the ratio of the recorded intensity response of the downhole seismometer to that of the surface seismometer was essentially a constant during the Elmore Ranch event, when no excess pore-water pressures were observed. In the Superstition Hills event record, this ratio of Arias intensities climbs erratically throughout the period of strong shaking during which there is a rise in pore-water pressure and softening of portions of the soil column. We attribute the erratic rise in the intensity ratio to a de-coupling of the surface and downhole seismometers, caused by liquefaction of a layer between them.

We interprete the data to show that the surface measured intensity of shaking at the site, in response to the Elmore Ranch earthquake (I_h = 0.44 m/sec) , was insufficient to elevate pore-water pressures in soil with a fines corrected $(N_1)_{60}$ penetration resistance of 12-14. During the Superstition Hills event, which occurred the following day, pore-water pressure begins to develop at 13.6 seconds when the surface intensity had reached 0.54 m/sec. Between 27 seconds (I_h = 1.37 m/sec.) and 40 seconds ($I_{h\ surface}$ = 1.70 m/sec.) portions of the soil column fully liquefied. The data suggest that a threshold level of earthquake shaking, as measured by Arias intensity, was required to trigger soil liquefaction at the Wildlife site.

---

[1] Research Civil Engineer, U.S. Geol. Survey, 345 Middlefield Road, Menlo Park, CA 94025
[2] Via Professor of Civil Engineering, Virginia Polytechnic Institute and State University, Blacksburg VA 24061.
[3] Research Geologist, U.S. Geol. Survey, 345 Middlefield Road, Menlo Park, CA 94025

Introduction

The Wildlife liquefaction array (WLA) was established on the flood plain of the Alamo River in the Imperial Valley of California, 36 km north of the town of El Centro, to record the response of a liquefiable soil body, with the potential for lateral displacements, to earthquake motions (Figure 1). The Imperial Valley is situated south of the southerly end of the San Andreas Fault, in the vicinity of the Salton Sea and the Imperial Fault, and is one of the most earthquake-prone regions of the United States. As such, the Wildlife site is exposed to frequent strong motion events. The array, presented in Figure 2, is instrumented with piezometers and strong motion accelerometers at the surface and at 7.5 meters depth (Bennett et al., 1984, Holzer et al., 1989a). Numerous studies have documented the site characteristics and have presented analyses of the WLA, with regard to pore-water pressure response (Dobry, et al., 1989, Thilakaratne and Vucetic, 1989, Youd and Holzer, 1994); initial liquefaction (Holzer et al., 1989b, Elgamal and Zeghal, 1992); and ground deformations (Bazair et al., 1992, Youd and Bartlett, 1988, Holzer et al., 1989a, Dobry, et al., 1992).

The deposits that underlie the Wildlife site are underlain by a 2.3 meter thick fine-grained flood deposit (Figure 2); loose-to-moderately dense silty sand layer is found between 2.3 and 6.8 meters (units B1 and B2, Bennett, et al., 1984); below layer B are dense silty sands and sandy silts not subject to liquefaction. Sand boils found at the Wildlife site after the 1981 Westmorland Earthquake (M=5.9) are derived from material in both units B1 and B2 (Holzer et al., 1989). Fines corrected standard penetration tests (SPT) taken in layers B1 and B2 yield an average calculated $N_{1(60)}$ value of 12-14.

The instrumentation at WLA includes six Data Instruments model AB pore-pressure transducers placed in the soil column, in units B1 at 2.8 and 3.0 meters depth; in unit B2 at 4.0, 5.0, and 5.3 meters depth; and at 12.1 meters depth in the dense underlying soil. The boreholes for the pore pressure transducers were back-filled with bentonite-cement to seal the holes. The accelerometer instrumentation consists of two Kinemetrics model FBA-13 triaxial-accelerometers, one located at the surface, and the other at 7.5 meters depth within a PVC casing (designated FBA-13DH). The surface accelerometer is mounted to a concrete pad and housed within a fiberglass instrument box. The downhole accelerometer was placed at the base of the casing, which was then back-filled with sand.

Methods

We use the earthquake intensity measure Arias Intensity developed by Lange (1968) and Arias (1970) to characterize ground motion at the Wildlife site and investigate its relation to soil liquefaction. Arias intensity is defined by Arias (1970) as the total energy-per-unit-weight absorbed by evenly-spaced single-degree of freedom oscillators between the frequencies 0 and ∞. In practice, Arias intensity is calculated as proportional to the integral of the square of the recorded strong motion acceleration . The 2-component Arias intensity in the horizontal plane, I_h, is given by:

$$I_h = I_{xx} + I_{yy} = \frac{\pi}{2g} \int_0^t a_x^2(t)\, dt + \frac{\pi}{2g} \int_0^t a_y^2(t)\, dt$$

The two orthogonal single component Arias intensities, I_{XX} (intensity in the x-direction, integrated from the x-direction record) and I_{YY}, are integrated from acceleration time histories, where g is the gravitational acceleration, $a_X(t)$ is the acceleration at time-t recorded in the x-direction, and $a_Y(t)$ is the acceleration recorded in the y-direction. Single-component of motion Arias intensity is commonly referred to as I_a. This intensity measure is relatively insensitive to the variation in the damping characteristics of liquefiable soils (Kayen, 1993) and has the advantage of incorporating the entire accelerogram record into the intensity measure, whereas for example, the peak ground acceleration (PGA) utilizes but one-point. Arias intensity is useful because it can be quantified and verified in an objective manner, as opposed to subjective psycho-physical intensity measures, such as the Modified Mercali Intensity (Arias, 1970).

Elmore Ranch and Superstition Hills Earthquake

The epicenter of the 23 November 1987 Elmore Ranch earthquake (***M***=6.2) was located approximately 23 kilometers to the west of the WLA. This earthquake triggered instruments that recorded modest earthquake motions but no elevated pore-water pressures. The peak ground-acceleration and surface-level two-component horizontal Arias intensity for the event were 0.13g and 0.44m/sec, respectively. The acceleration- and cumulative intensity-time histories for the two components of motion at the surface and at 7.5 meters depth are plotted in Figure 3.

On the following day, November 24, 1987, the Superstition Hills earthquake (*M*=6.6), centered 31 kilometers west-southwest of the site, triggered instruments at the Wildlife site that recorded strong motions and elevated pore-water pressures. Acceleration- and Arias intensity-time histories for the Superstition Hills event are plotted in Figure 4. During this event, excess pore-water pressures developed approximately 13.6 seconds (I_h = 0.54 m/sec) into the record. The sand layer began to soften, noted by the loss of phase coherence between the downhole and surface acceleration records (Holzer et al., 1989b). By 16 seconds ($I_{h,16secs}$ = 0.90 m/sec) the pore pressure ratio, r_u, in portions of layer B approached approximately 0.5. Between 27 seconds ($I_{h,27secs}$ = 1.37m/sec) and 40 seconds ($I_{h,40secs}$ = 1.70 cm/sec) portions of the soil column fully liquefied (Youd and Holzer, 1994).

Discussion

The Wildlife strong motion data indicate that the Arias intensity calculated from seismograms at the ground surface is typically greater than that measured at depth within the soil column. Amplification at the ground-level is expected due to the effects of double-amplification at the surface and interference of the upward and downward traveling shear waves within the soil column. To investigate the variation of Arias intensity with depth, we used the Wildlife data to normalize the cumulative Arias intensity at a depth of 7.5 meters with the surface measure of intensity. We define an intensity depth reduction parameter, r_b, as the ratio of the buried to surface cumulative Arias intensities.

$$r_b = \frac{I_{xx}\ (depth)}{I_{xx}\ (surface)}$$

The r_b parameter can be calculated for either the single- or double-component horizontal Arias intensity. The time-history of the cumulative Arias intensity depth reduction factor, r_b, is calculated for the single-components of the Elmore Ranch earthquake, and presented in figure 5. It can be seen that during the first seven seconds of the 360° record, during the period dominated by P-waves, the r_b ratio fluctuates significantly. This fluctuation is due to the influence of the intensity of incident waves on the very low value of the ratio, r_b, during the first 6 seconds of the acceleration time-history. After 7 seconds, when shear waves dominate the strong motion, the intensity ratio plateaus at approximately 0.28 until 13 seconds, and then climbs to 0.38. For the 090° component of motion, a similar response is calculated from the acceleration time histories.

For this record a generally noisy record persists up to 7 seconds, followed by a progressive increase in r_b to 0.33 at 30 seconds.

A noteworthy aspect of both of the above records is the relatively constant ratio of r_b during the principal portion of strong shaking. Holzer et al. (1989b) argued that under non-liquefaction conditions, a linear proportionality constant exists between the downhole and surface cumulative Arias intensity. The relatively flat r_b profiles in Figure 4 support their hypothesis.

Plotting the cumulative Arias intensity ratio, r_b, as a time-history for the Superstition Hills event (Figure 6) shows a strikingly different response, compared to that of the Elmore Ranch record (Figure 5). During the early seconds of shaking there is a high sensitivity to wave interference in the r_b signature, as noted in the Elmore Ranch records. After 7 seconds into the record the intensity ratio plateaus for a period of 5-6 seconds at a value of approximately 0.34 for the 360 record and 0.25 for the 090 record. At 13.5 seconds r_b begins to rise in a rapid and erratic manner until r_b reaches a value of approximately 0.44-0.46.

Accordingly, Holzer et al. (1989b) concluded that the divergence between a scaled-Arias intensity at depth and the surface intensity was due to the onset of strain-softening behavior and the absorption of energy by the intervening liquefied layer. Our observations of the erratic elevation in r_b during the Superstition Hills event support their findings. The rapid rise in r_b indicates a partial de-coupling of the surface layer from the soil beneath the liquefied layer, such that shear waves propagating upwards are attenuated, and perhaps partly reflected downwards, before reaching the surface accelerometer.

The depth reduction characteristics for Arias intensity, calculated from the Wildlife array data, are plotted as a triangle in Figure 7b; the left limb representing the Elmore Ranch Earthquake response, and the right limb representing the Superstition Hills earthquake response. A separate parametric study of the the attenuation of Arias intensity with depth (Figure 7a) was performed by integrating synthetic seismograms generated with the ground-response program SHAKE (Schnabel, et al., 1972) and normalizing the intensities calculated at depth by the surface Arias intensity (Kayen, 1993; Kayen and Mitchell, in progress). The lines in Figure 7a are the r_b profiles generated with SHAKE using a suite of soil-shear modulus profiles and input strong motion records. A statistical synthesis of these profiles are shown in Figure 7b as a mean and ± 1 standard deviation response. The

empirical data from the Wildlife site fall below the mean response of the parametric study, but are in general agreement with those findings.

Liquefaction Response of Soil at the Wildlife liquefaction array

Acceleration time-histories recorded from the Elmore Ranch and Superstition Hills earthquakes are important in that they constrain the relation between shaking severity, as measured by Arias intensity, and liquefaction performance at the Wildlife site. To assess the liquefaction response, we coupled the depth factor, r_b, with surface-measured Arias intensity, I_h, to give an estimate of the energy-per-unit-weight absorbed by a specific soil layer at depth in the soil column, which we term the Arias intensity at depth, $\mathbf{I_{hb}}$. That is, we multiplied the surface intensities I_h measured at the surface accelerometer station at the Wildlife site by the depth-dependent reduction factor, r_b, interpolated between the surface and the measured value at 7.5 meter depth, to estimate Arias intensities within the soil column. In contrast, Egan and Rosidi (1991) have attempted to correlate the surface measure of Arias intensity with the field performance of potentially liquefiable sites. Their findings correctly indicate that the surface measure of Arias intensity correlates poorly with the liquefaction performance at depth in the soil column.

In Figure 8, we plot the intensity of earthquake shaking, $\mathbf{I_{hb}}$, estimated at the depth of soil layer B against the representative $(N_1)_{60}$ value for layer B (Bennett, et. al, 1984); having determined the fines- and effective overburden stress- corrected standard penetration resistance for that layer using the methods prescribed by Seed et al. (1984). The Elmore Ranch event, with a surface measured Arias intensity of 0.44 m/sec and an estimated intensity within layer B of 0.24 m/s, was insufficient to soften the sand layers B1 and B2. The Elmore Ranch event is marked on Figure 8 as no-liquefaction point below the boundary curves.

During the Superstition Hills earthquake, pore pressures developed at approximately 13.6 seconds, at which point the horizontal surface Arias intensity had reached 0.54 m/sec. Full liquefaction appears to have occurred after approximately 27 seconds (surface I_h = 1.37 m/sec) of instrument recording, as determined by the piezometer response (Dobry et al., 1989). The vertical band in Figure 8 represents the transition from a non-liquefied to liquefied soil state during the Superstition Hills event. The response of the Wildlife site is presented with a suite of points representing the field performance of other sites, investigated by Kayen (1993), observed during nine earthquakes in United States and Japan (magnitude range: $6.1 \leq M \leq 7.9$). From this

investigation, Arias intensity-based curves can be drawn which define a threshold boundary for liquefaction occurrence (Kayen and Mitchell, in progress). The integration of both acceleration amplitude and earthquake shaking duration in the parameter Arias intensity is such that these boundary curves are independent of earthquake magnitude . The liquefaction field performance observed at the Wildlife site during the Elmore Ranch and Superstition Hills events is consistent with that observed at the other sites, and supports the basis for a depth-dependent Arias intensity-based boundary in $(N_1)_{60}$-$\mathbf{I_{hb}}$ space defining limiting conditions for liquefaction occurrence.

Conclusions

We have analyzed the characteristics of strong motions of the Elmore Ranch and Superstition Hills Earthquakes, recorded at the WLA, in terms of their progressive Arias intensity build-up. The ratio of the downhole to surface cumulative Arias intensities was essentially a constant during the principal portion of ground shaking in the Elmore Ranch event, when no excess pore-water pressures were observed. The depth reduction factor, r_b, calculated for the two-components of motion for the Elmore Ranch event was 0.36. During the Superstition Hills event, the Arias intensity ratio climbed in an erratic manner in response to a partial de-coupling of the surface and downhole seismometers, between which was a liquefied layer. The Superstition Hills earthquake had a two-component depth reduction factor, r_b, of 0.45.

To assess the liquefaction response of the Wildlife site during the two earthquake events, we multiplied the surface intensities, I_h, by the depth-dependent reduction factor, r_b, interpolated between the surface and 7.5 meter depth. In doing so, we can compare the energy-per-unit-weight absorbed by a layer at depth, $\mathbf{I_{hb}}$, to the penetration resistance of that layer, $(N_1)_{60}$. The Elmore Ranch event had an estimated $\mathbf{I_{hb}}$ intensity within soil layer B of 0.24 m/sec. which was below the threshold required to elevate pore-water pressures within that layer. During the Superstition Hills earthquake, pore pressures began to develop at an $\mathbf{I_{hb}}$ intensity level of 0.27 m/sec. Full liquefaction appears to have occurred after approximately 27 seconds when the Arias intensity at the depth of layer B, $\mathbf{I_{hb}}$, was approximately 0.7 m/sec. The WLA data-set allow us to observe the transition of a site from a non-liquefied to a liquefied state in terms of Arias intensity buildup. This transition is consistent with an investigation of other sites in the United States and Japan where Arias intensity has been correlated with the liquefaction performance in the field.

Acknowledgments

We thank John C. Tinsley III and Michael J. Bennett for their thoughtful reviews of the manuscript.

References

Arias, A. (1970) A Measure of Earthquake Intensity, R.J. Hansen *ed.* Seismic Design for Nuclear Power Plants, The M.I.T. Press, Cambridge, Massachussetts.

Baziar, M.H., Dobry, R., and Alemi, M. (1992) Evaluation of Lateral Ground Deformation Using Sliding Block Model, Earthquake Engineering, Tenth World Conference, Balkema, Rotterdam, pp.1401-1406.

Bennett, M.J., Mc Laughlin, P.V., Sarmiento, J.S., and Youd, T.L., (1984) Geotechnical Investigation of Liquefaction Sites, Imperial Valley, California, USGS Open-File Report 84-252, U.S. Geological Survey, Menlo Park, CA.

Dobry, R., Elgamal, A.W., Baziar, M.H., and Vucetic, M. (1989) Pore Pressures and Acceleration Response of Wildlife Site During the 1987 Earthquake, Proceedings, Second U.S.-Japan Workshop on Liquefaction, Large Ground Deformation, and Effects on Buried Pipelines, Niagra Falls, New York, pp. 145-260.

Dobry, R., Baziar, M.H., O'Rourke, T.D., Roth, B.L., and Youd, T.L. (1992) Liquefaction and Ground Failure in the Imperial Valley, Southern California during the 1979, 1981, and 1987 Earthquakes, U.S.-Japan Case Studies of Liquefaction and Pipeline Performance During Past Earthquakes, Vol. 2, U.S. Case Studies, NCEER Report 92-0002, pp.4-1 to 4-85.

Egan, J.A. and Rosidi, D. (1991) Assessment of Earthquake-Induced Liquefaction Using Ground-Motion Energy Characteristics, Proc. Pacific Conference on Earthquake Engineering, New Zealand.

Elgamal, A.-W. and Zeghal, M. (1992) Analysis of Wildlife Site Liquefaction During the 1987 Superstition Hills Earthquake, Proc. of the Fourth Japan - U.S.Workshop on Earthquake Resistant Design of Lifeline Facilities and Countermeasures for Soil Liquefaction, in M. Hamada and T.D. O'Rourke, eds. Technical Report NCEER-92-0019.

Holzer, T.L., Bennett, M.J., and Youd, T.L. (1989a) Lateral Spreading Experiments by the U.S. Geological Survey, Proceedings from the Second U.S.-Japan Workshop on Liquefaction, Large Ground Deformations and their Effects on Lifelines, *eds.* T.D. O'Rourke and M. Hamada, Technical Report NCEER-89-0032.

Holzer, T.L., Youd, T.L., and Hanks, T.C. (1989b) Dynamics of Liquefaction During the 1987 Superstition Hills California Earthquake, Science, Vol. 244, pp. 56-59.

Kayen, R.E.(1993) Accelerogram-Energy Approach for Prediction of Earthquake-Induced Ground Liquefaction, unpublished Ph.D. dissertation, Department of Civil Engineering, University of California at Berkeley, 289 pp.

Kayen, R.E. and Mitchell, J.K., in progress, Ground-motion energy approach for assessment of earthquake-induced cyclic-liquefaction, J. Geotech. Engrg., ASCE.

Lange, G. (1968) Una Medida de Intensidad Sismica, unpublished Ph.D. Thesis, University of Chile, Santiago, Chile.

Schnabel, P., Lysmer, J., and Seed, H.B. (1972) SHAKE: A Computer Program for Earthquake Ground Response, Univ. Cal. Berkeley, EERC Report No. UCB/EERC-72-12.

Seed, H.B., Tokimatsu, K., Harder, L.F., and Chung, R.M., (1984) Influence of SPT procedures in soil liquefaction resistance evaluation, Earthquake Engineering Research Center Report No. UCB/EERC-84/15.

Thilakaratne, V. and Vucetic, M. (1989) Analysis of liquefaction occurrence at the Wildlife Site during 1987 Superstition Hills Earthquakes, Research Report, Dept. of Civil Engineering, University of California, Los Angeles, p.131.

Youd, T.L. and Bartlett, S.F., (1988) U.S. Case Histories of Liquefaction-Induced Ground Displacement, Proc. of the First Japan-U.S. Workshop on Liquefaction, Large Ground Deformations and their Effects on Lifeline Facilities, Tokyo, Japan.

Youd, T.L. and Holzer, T.L. (1994) Piezometer Performance at Wildlife Liquefaction Site, California. J. Geotech. Engrg., ASCE, 120(6).

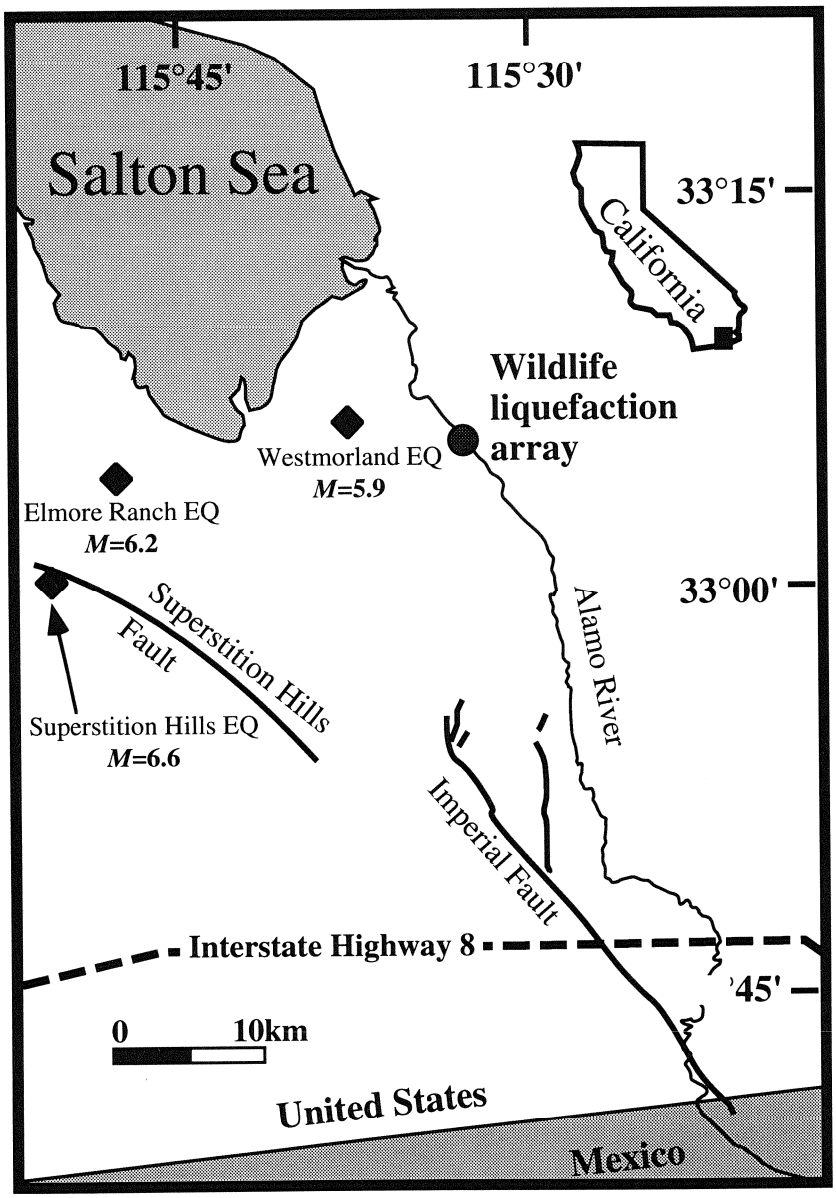

Figure 1. Location map of the WLA, Imperial Valley, Ca. Epicenters for the 1981 Westmorland; 1987 Elmore Ranch; and 1987 Superstition Hills earthquakes are starred.

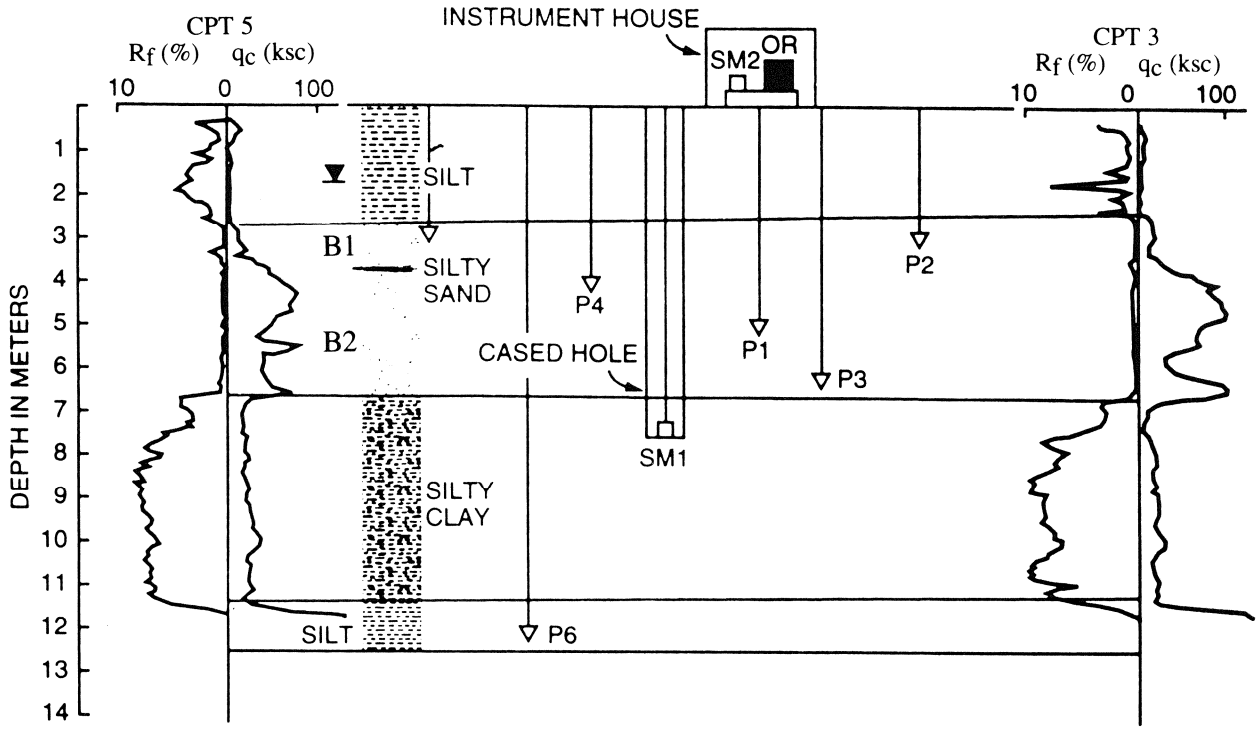

Figure 2. Profile of the Wildlife site with layers A-, from the surface, to-D at 12-meters, and cone penetration test (CPT) profiles (Bennett, et al., 1984). The parameters q_c (kg/cm^2) and r_f (%) are the cone-tip resistance and sleeve friction ratio, respectively. Inverted triangles P1-P6 denotes the pore pressure piezometers; SM1 and SM2 denote the triaxial accelerometers; OR denotes the oscilloscope recorder.

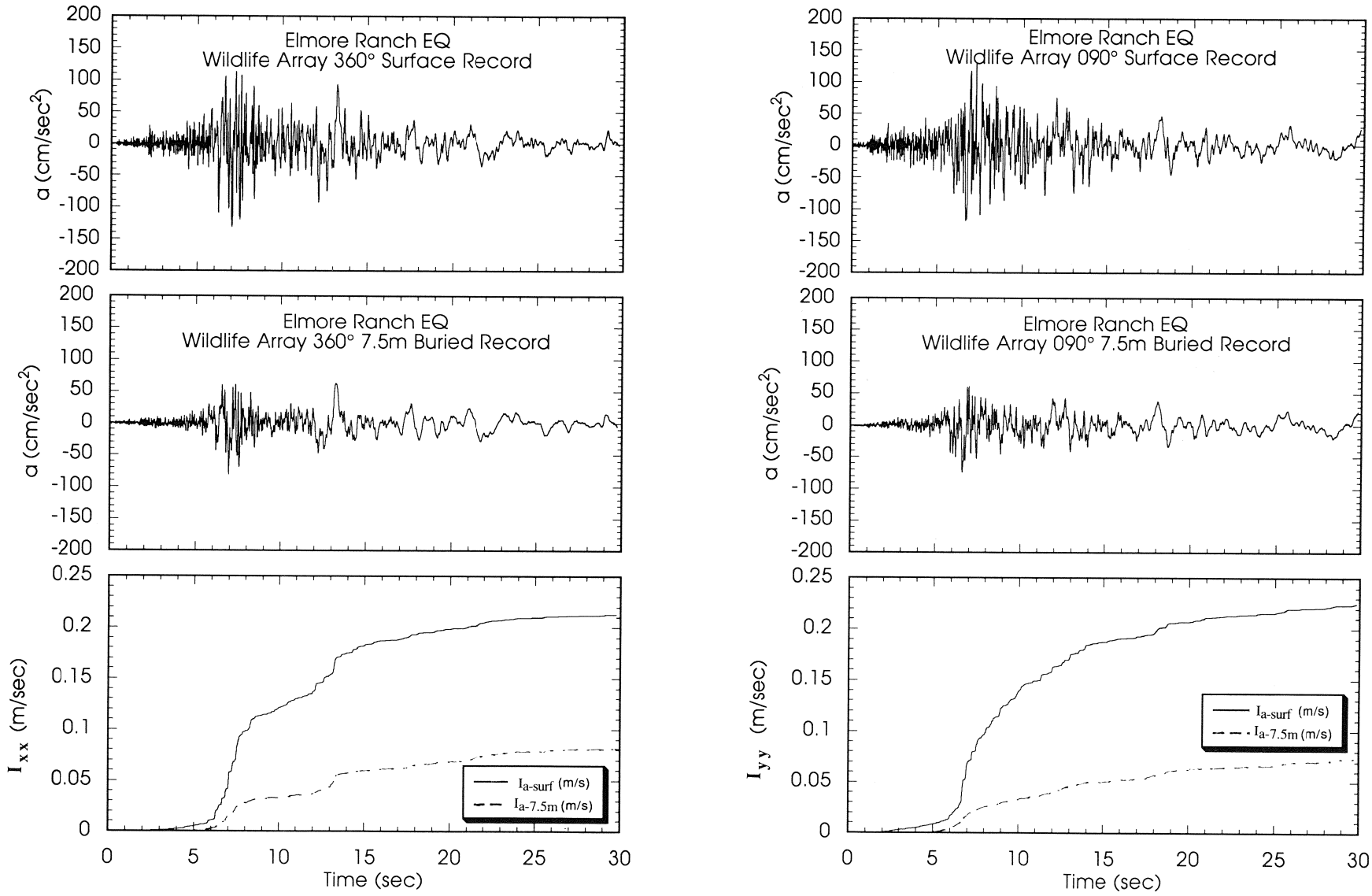

Figure 3. Ground surface and 7.5 m depth recordings from the WLA, recorded during the Elmore Ranch Earthquake. Plotted are accelerations and their computed cummulative Arias intensities for the 360° and 090° components. $I_{a\ top}$ and $I_{a\ mid}$ are the surface and 7.5 meter depth Arias intensities, respectively. Horizontal scaling is the first 30 seconds of recording.

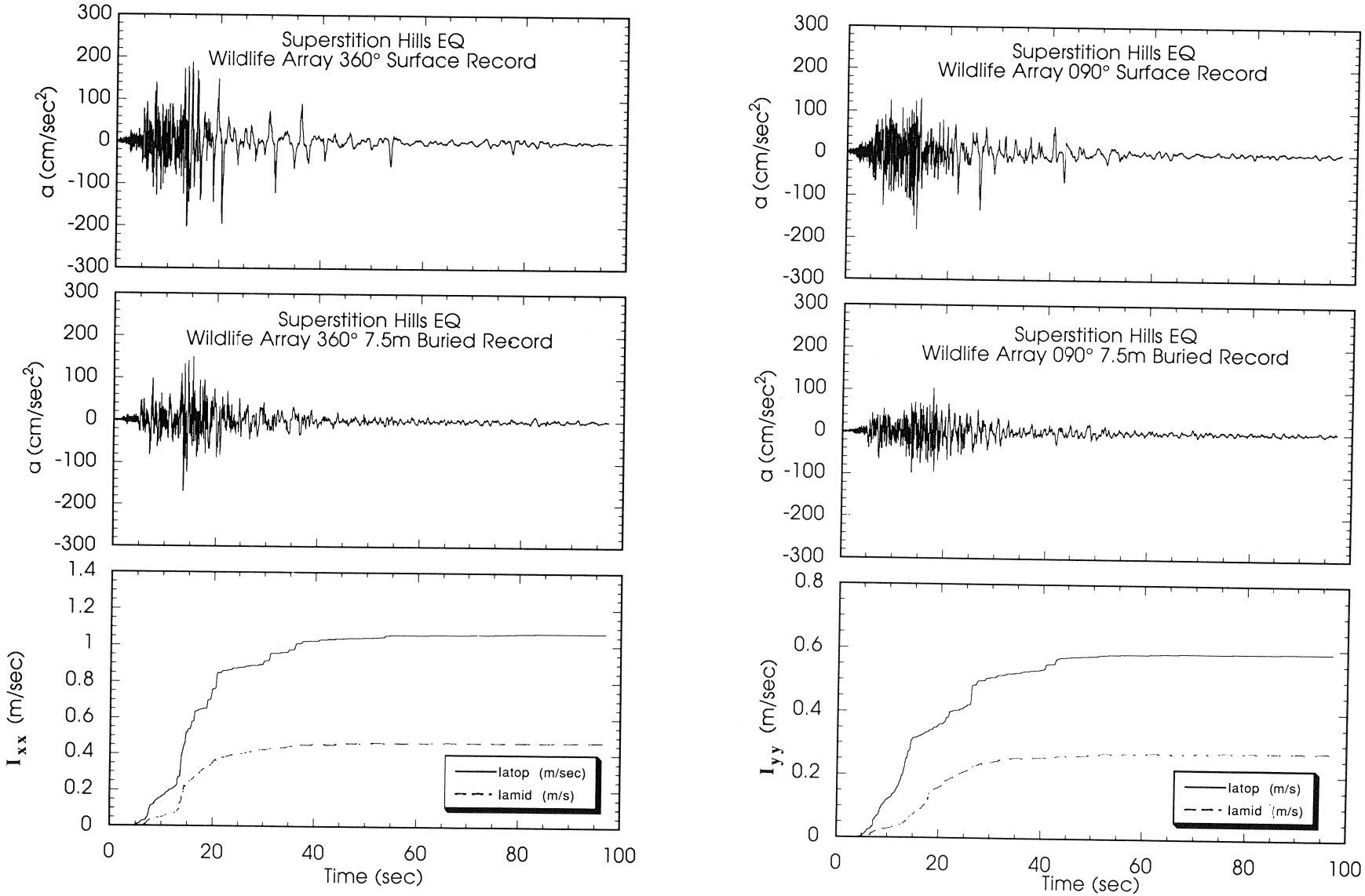

Figure 4. Ground surface and 7.5 m depth recordings from the WLA, recorded during the Superstition Hills Earthquake. Plotted are accelerations and their computed cumulative Arias intensities for the 360° and 090° components. Horizontal scaling is the first 100 seconds of recording.

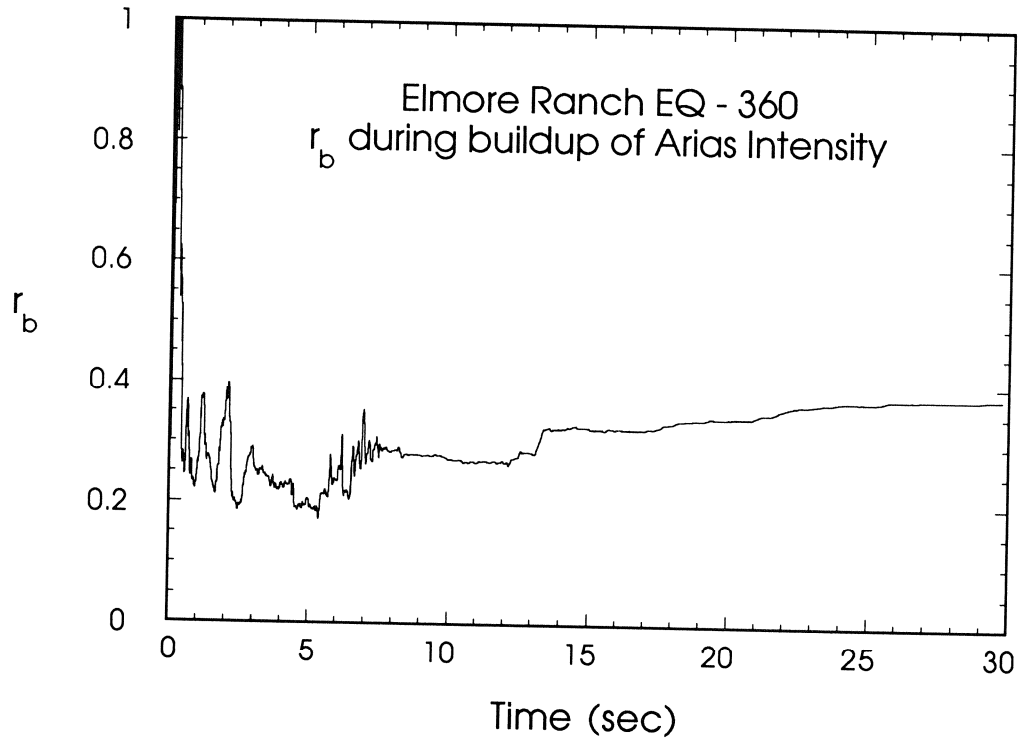

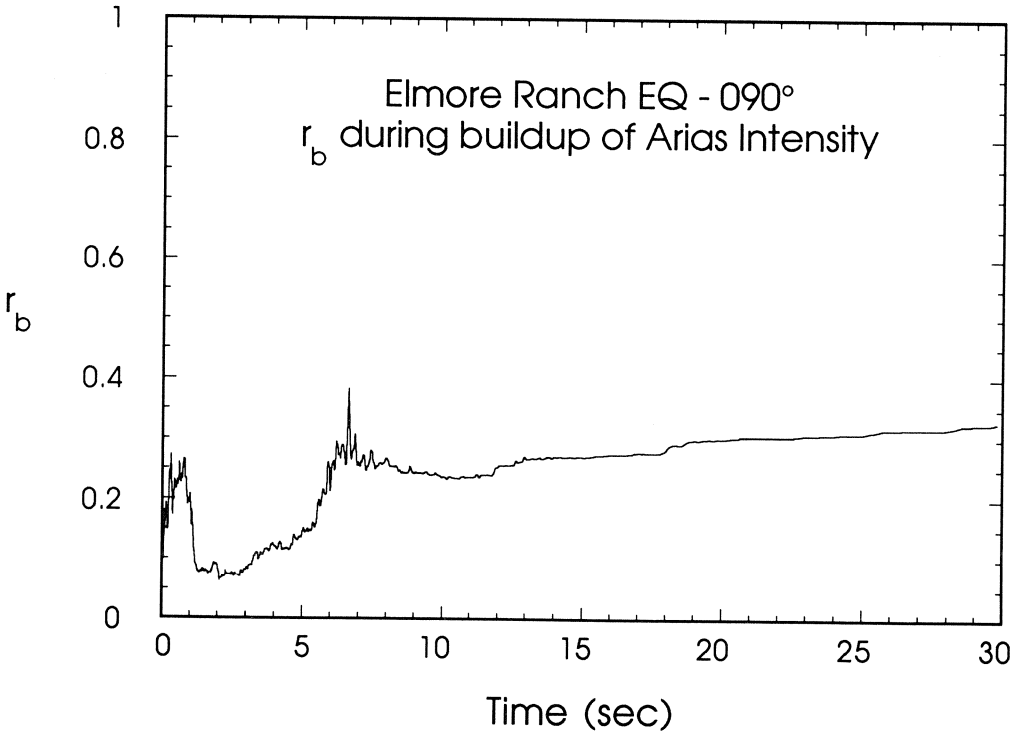

Figure 5. Cumulative r_b time-histories for the 360° and 090° components of the Elmore Ranch Earthquake records.

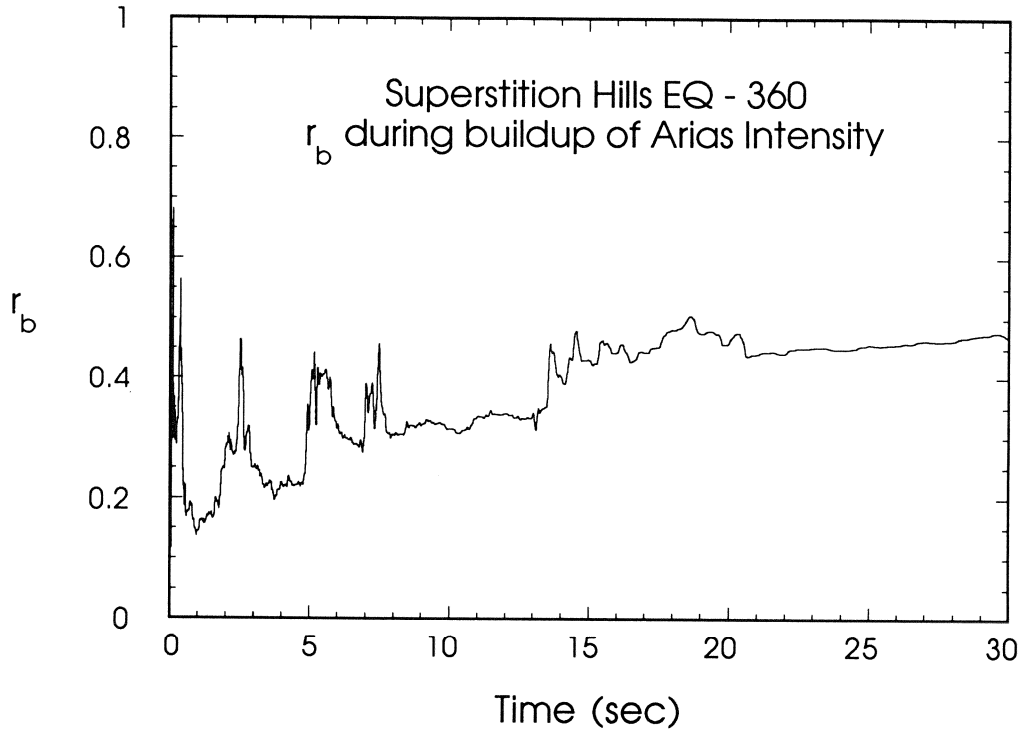

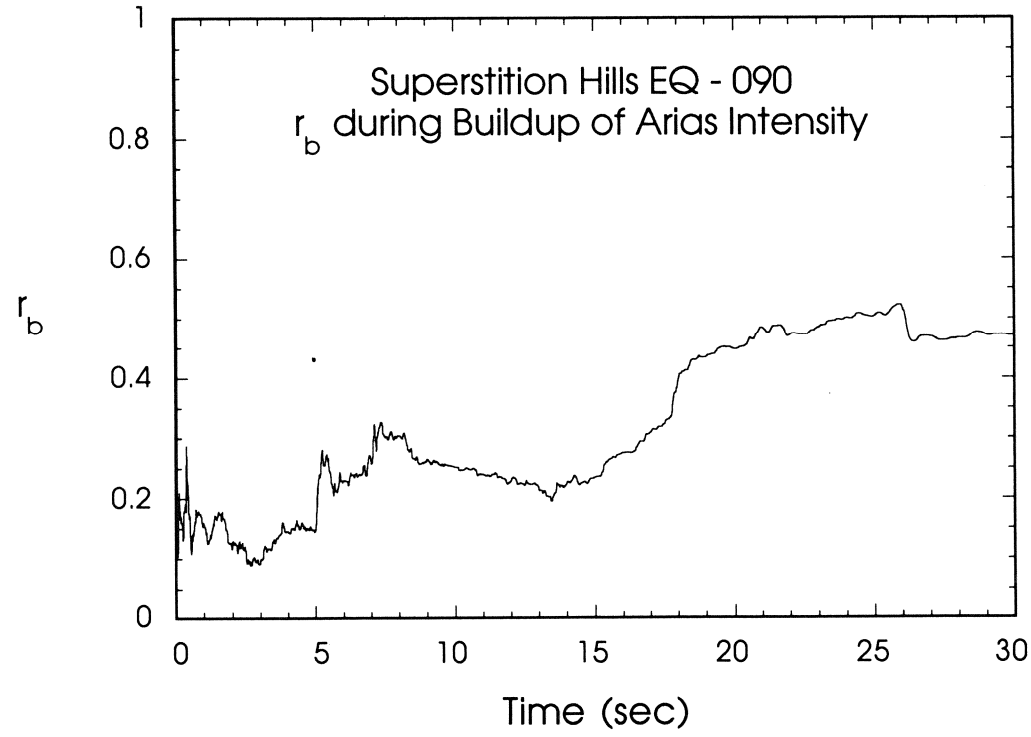

Figure 6. Cumulative r_b time-histories for the 360° and 090° components of the Superstition Hills Earthquake records.

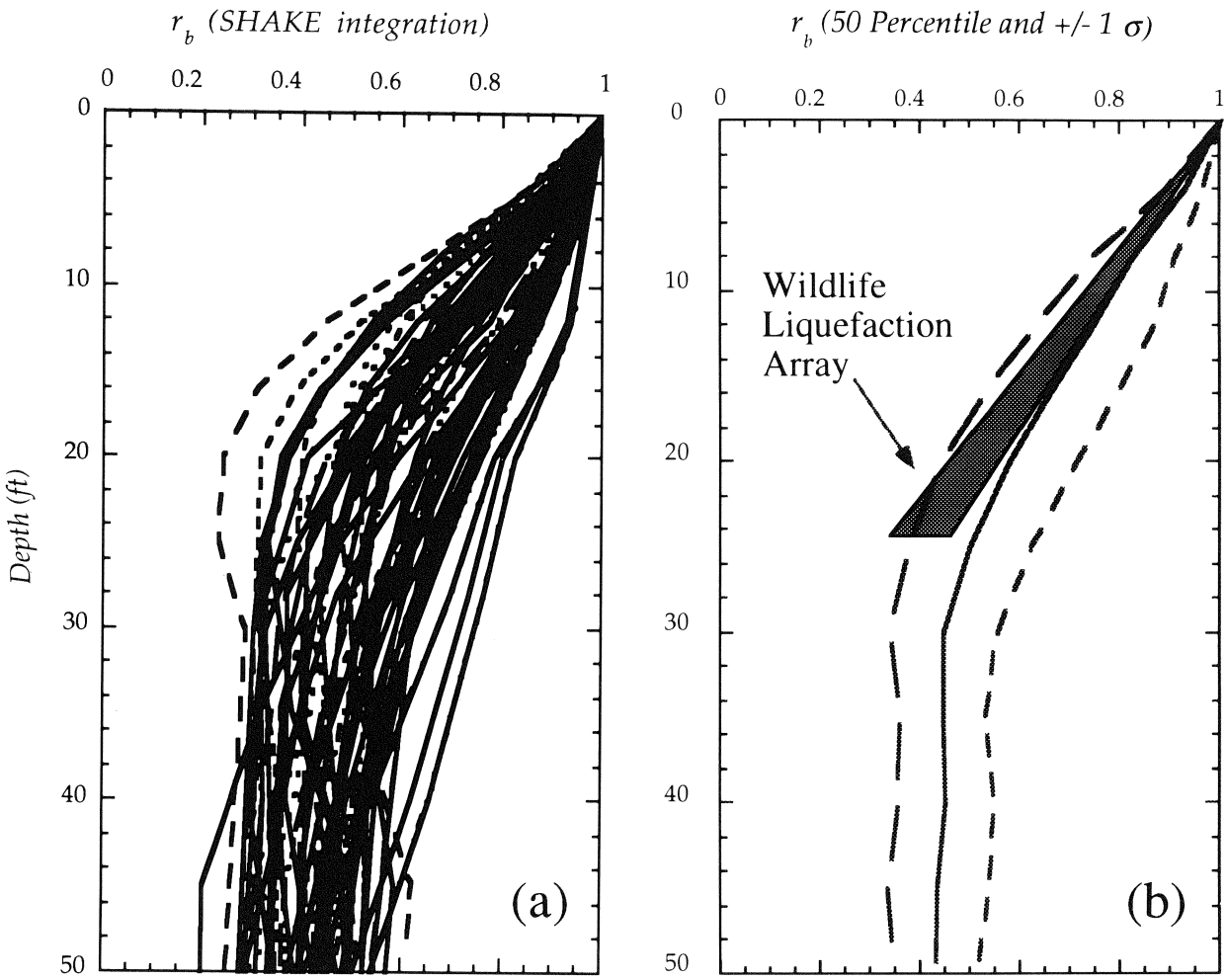

Figure 7. Arias intensity depth reduction profiles modeled using the ground response program SHAKE are presented in Figure 7a. A statistical synthesis of the SHAKE-study is presented in Figure 7b along with the empirical results from the WLA response during the Elmore Ranch and Superstition Hills earthquakes.

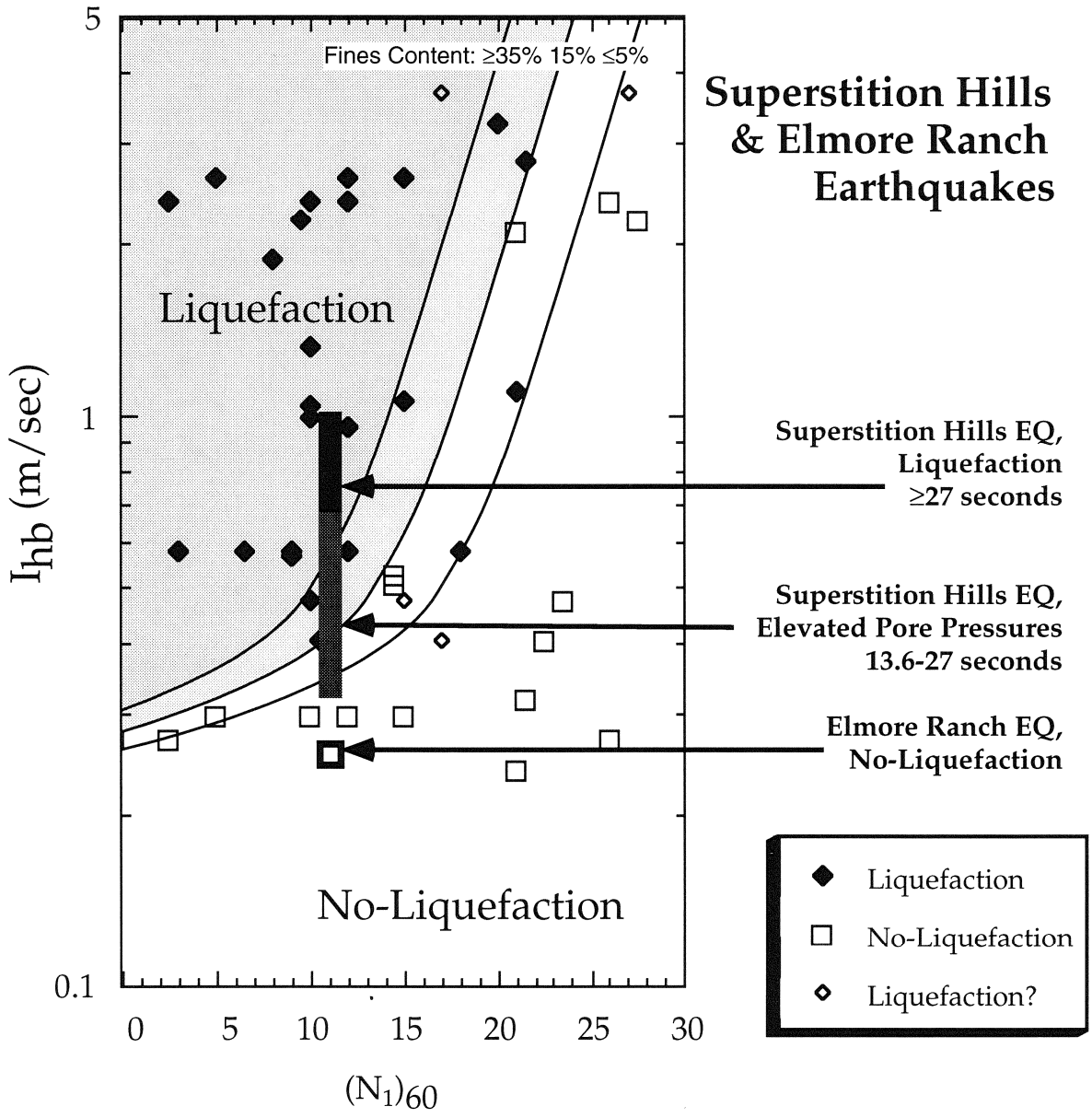

Figure 8. $\mathbf{I_{hb}}$ versus $(N_1)_{60}$ for the WLA site during the Elmore Ranch and Superstition Hills earthquakes. The boundary curves are constrained by field performance data from sites in Japan and United States, whose performance is identified in the legend (Kayen and Mitchell, in progress).

Experimental Study on Mechanical Properties of Liquefied Sand

T. Kawakami[1], N. Suemasa[2], H. Hamada[3], H. Sato[4], and T. Katada[5]

ABSTRACT

The purpose of this study is to understand the mechanical properties of liquefied sand to estimate the behavior of ground after liquefaction and to investigate the mechanism of occurrence of liquefaction-induced large ground displacement. In this paper we consider that the mechanical properties of liquefied sand can be separated the following two phases, (1) the fluid characteristic of liquefied sand as viscous fluid, (2) the solid characteristic of liquefied sand under large deformation.

From the above-mentioned points, the authors carried out laboratory tests on the fluid and solid characteristics of liquefied sand. For the fluid characteristic, two kinds laboratory tests were conducted in order to obtain coefficient of viscosity on liquefied sand. In the first test, coefficient of viscosity was estimated from load acting on sphere in liquefied sand with constant velocities. On the other hand, by using viscometer which measured torque moment of a rotor rotating in liquefied sand. These results suggest that viscosity of liquefied sand depend on relative density of sand and velocity of shear strain. For the solid characteristic a laboratory test was conducted. It was a cyclic torsion shear test, in which maximum shear strain of liquefied sand reaches about 80%. The results of the test show that liquefied sand has a critical maximum shear strain which depend on relative density of sand.

1) Assistant Professor, Dept. of Marine Civil Engineering, Tokai University.
2) Assistant Professor, Dept. of Civil Engineering, Musashi Institute of Technology.
3) Professor, Dept. of Civil Engineering, Waseda University.
4) Senior Researcher, Engineering Research Center, Tokyo Electric Power Company.
5) Associate Professor, Dept. of Civil Engineering, Musashi Institute of Technology.

INTRODUCTION

The authors have been investigating the mechanism for occurrence of the liquefaction-induced large ground displacement and the effects of liquefaction on underground structures, by the case studies on earthquakes in the past (Doi and Hamada, 1992), and by the experimental studies on the behavior of ground after liquefaction (Hamada, et al. 1992). The followings became clear from the above studies, 1) the liquefied soil behaves as a viscous fluid, 2) the load acting on pile which is located in flowing liquefied soil depends on velocity of flowing liquefied soil. These results indicate the possibility of estimating the behavior of ground after liquefaction assuming that flowing liquefied soil is regarded as viscous fluid (Sato, et al, 1993).

However, we consider that the practical phenomena of liquefaction-induced large ground displacement can not be explained by only the above assumption, because of the inclined ground dose not become the level ground after the occurrence of liquefaction. Also, Yasuda, et al. (1993) points out that the stiffness of the liquefied sand is recovered as subject to the large shear strain. Therefore, it is necessary to consider that the mechanical property of the liquefied soil change from the fluid characteristic to the solid characteristic in the process of the liquefied soil flow.

This paper discusses the mechanical properties of liquefied sand to estimate the behavior of ground after liquefaction and to investigate the mechanism of occurrence of liquefaction-induced large ground displacement. In this paper we consider that the mechanical properties of liquefied sand can be separated the following two phases, 1) the fluid characteristic of the liquefied sand which is regarded as viscous fluid, 2) the solid characteristic of liquefied sand under large deformation. From the above-mentioned points, the authors carried out laboratory tests on the fluid and solid characteristics of liquefied sand. For the fluid characteristic, two kinds laboratory tests were conducted in order to obtain coefficient of viscosity on liquefied sand. For the solid characteristic a laboratory test was conducted. It was a cyclic torsion shear test, in which maximum shear strain of liquefied sand reaches about 80%.

LABORATORY TESTS FOR FLUID CHARACTERISTIC

Measurement of Viscosity on Liquefied Sand by Load Acting on Sphere

Procedure of Test

Figure 1 shows the experimental arrangement used to measure the viscosity of liquefied sand, by using the load acting on sphere moving with constant velocity in liquefied sand. The soil box is cylindrical, with a diameter of 100.0 cm and a depth of 87.5 cm. The steel sphere is placed into liquefied sand, which have a diameter of 3.0 cm. Liquefaction was induced by shaking the soil box using sinusoidal waves. Toyoura sand was used as the test material. This sand has followings physical properties, a specific gravity of 2.63, a maximum void ratio of 0.974, a minimum void ratio of 0.598, a maximum grain diameter of 0.85, 50 percent diameter of 0.168 and a uniformity coefficient of 1.74, respectively.

The tests were carried out as follows:

(1) The saturated model sand with the prescript relative density was made in the soil box.

(2) Liquefaction was occurred by shaking the soil box. Subsequently, if the complete liquefaction was confirmed by the pore water pressure meters at all the measuring points, shaking the soil box was stopped.

(3) Immediately, the sphere was pulled up with constant velocity, and load acting on the sphere was measured. In this time, it was necessary that the complete liquefaction was kept around the sphere.

A series of the tests by using above method were conducted with following parameters, velocities of pulled up sphere, initial relative densities. The conditions of the tests are shown in Table 1.

If the liquefied sand is assumed to be a viscous fluid, the relation between viscosity and load acting on the sphere is formulated as the following equation.

$$\eta = \frac{F}{3\pi d U} \tag{1}$$

Where F, d, U are the load, diameter of the sphere and the velocity, respectively, η is the coefficient of viscosity.

Results of Test

A example of the experimental results which in the way described above is shown in Figure 2. Figure 2 (a) shows the incident acceleration, similarly, (b) shows the velocity of the sphere, (c) shows the excess pore water pressure in the liquefied sand, (d) shows the load acting on the sphere, (e) shows the excess pore water pressure at the surface of the sphere, respectively. Where, the line A-A in Figure 2 (e) express the effective normal stress which is considered the effect of pulling up the sphere in the liquefied sand.

From Figure 2, we can see that the load acting on sphere shows the constant value as the velocity of sphere is constant. This relationship between the load acting on sphere and the velocity of sphere satisfy equation (1), if the viscosity is assumed to be constant, and it is suggested that liquefied sand can be approximated viscous fluid.

The relationship between the coefficient of viscosity and the velocity of sphere is shown in Figure 3. The coefficient of viscosity was calculated from the load acting on sphere by using equation (1). Then, the relationship between the coefficient of viscosity and relative density is shown in Figure 4.

The followings became clear from these figures:

(1) The coefficient of viscosity for liquefied sand has a proportional correlation with the velocity of sphere, that the coefficient of viscosity decreases as the velocity of sphere increases.

(2) The correlation is observed between the coefficient of viscosity and relative density, that the coefficient of viscosity increases as the relative density increases.

Measurement of Viscosity on Liquefied Sand by Viscometer

Procedure of Test

In this section, we summarize the measurement of viscosity of liquefied sand using viscometer. The experimental apparatus is shown in Figure 5. The soil container is a transparent plastic cylinder, with a diameter of 8.5 cm and a depth of 30.0 cm. The soil container has a porous disk at the bottom, and the bottom is connected to the water tank. Two pore water pressure meters are installed in the wall of the container to measure the hydraulic gradient. Liquefaction of the sand in the container was occurred by upward seepage. Toyoura sand was used as the test material. The effective normal stress σ' at the depth of z in sand with upward seepage is expressed as following equation,

$$\sigma' = \left(\frac{G-1}{1+e} - i\right)\rho_w g z \ , \tag{2}$$

where, G is a specific gravity of soil particles, e is a void ratio, ρ_w is a density of water

and g is a acceleration due to gravity, respectively. Then, i is a hydraulic gradient, and it is clearly that the effective normal stress σ' becomes 0 if the i denotes as following equation,

$$i = \frac{G-1}{1+e} \quad . \tag{3}$$

Therefore, it can be considered that the sand was liquefied by the upward seepage. In this test, the hydraulic gradient i was obtained by measuring two pore water pressures and using following equation.

$$i = \frac{u_2 - u_1}{L\,\rho_w\,g} \tag{4}$$

Where, u_1 and u_2 are pore water pressures, L is a distance between u_1 and u_2(see Figure 5).

The viscosity of liquefied sand was estimated by viscometer, which measured torque moment acting on a rotor rotating in liquefied sand. A series of the tests by using above method were conducted with following parameters, number of rotation and initial relative density. The conditions of the tests are shown in Table 2.

Results of Test

The relationship between the coefficient of viscosity and the number of rotation is shown in Figure 6. Similarly, the relationship between the coefficient of viscosity and the initial relative density is shown in Figure 7. The followings became clear from the results of the tests:

(1) The coefficient of viscosity of liquefied sand is depended on the number of rotation, that is, the coefficient of viscosity decreases as the number of rotation increases.

(2) The coefficient of viscosity of liquefied sand has a correlation with the initial relative density, that is, the coefficient of viscosity increases as the initial relative density increases.

(3) Above these results agree with the results of the preceding section.

Discussion of Viscosity on Liquefied Sand

In this section, the velocity of shear strain for liquefied sand acting the shear deformation is introduced to discuss the results of two kinds of test for viscosity. The velocity of shear strain D_s on the surface of sphere which is moved with constant velocity in viscous fluid is expressed as following equation by Stokes's stream function.

$$D_s = \frac{3\,U}{d} \tag{5}$$

Similarly, The velocity of shear strain D_s on the surface of rotor rotating in cylindrical container filled with viscous fluid is obtained as following equation by solving Navier-Stokes's equation,

$$D_s = \frac{2\,R^2\,\Omega}{K\,(R^2 - r^2)} \quad , \tag{6}$$

where, R and r are the radius of container and the radius of rotor, Ω is a angular velocity, respectively. K is denoted as a correctional coefficient considering the finite length of the rotor (in this case, K=0.77).

Figure 8 shows the relationship between the coefficient of viscosity and the velocity of shear strain. In this figure, we plotted the coefficient of viscosity of liquefied sand which was obtained by the experiment on liquefaction-induced ground displacement using the model ground and the shaking table (Ogasawara and Hamada,1994), as well as the

results of the tests in this study.

The followings became clear from this figure:

(1) Clearly, the strong correlation is observed between the coefficient of viscosity and the velocity of shear strain.

(2) The coefficient of viscosity decreases as the velocity of shear strain increases.

(3) The results of two kinds of the tests in this study indicate a good agreement.

(4) The results of the experiments on liquefaction-induced ground displacement using the model ground indicate the similar tendency with the above (2). Then, these results agree well with the results of the tests in this study.

LABORATORY TEST FOR SOLID CHARACTERISTIC

Measurement of Strength / Deformation on liquefied sand

Procedure of Test

It is a purpose of this test to explain the strength / deformation characteristics of liquefied sand by a new hollow cylinder torsional shear apparatus, which is that shear loading tests until maximum 80% of shear strains are enabled. An undrained cyclic torsion shear test was carried out by this test machine. The test apparatus is shown in Figure 9. The hollow cylindrical specimen used in the tests was 10.0 cm in outside diameter, 6.0 cm in inside diameter and 10.0 cm in height. Toyoura sand was used as the test material. This sand has a specific gravity of 2.634, and the maximum and minimum void ratio were measured to be 0.993 and 0.614, respectively. The hollow cylindrical specimens were made by pluviation under water.

The parameters in the tests are relative density, frequency of cyclic torsion, shear stress ratio and effective confining pressure. The conditions of the test are shown in Table 3.

Results of Test

As an example on the result of the test, the relationship between shear stress and shear strain shows in Figure 10. In this case, the relative density was a 53%, the shear stress ratio was a 0.2, the effective confining pressure was a 1.0 kgf/cm^2 and the frequency of cyclic torsion was a 0.1 Hz, respectively. From this figure, in the first stage after the occurrence of liquefaction, we can see that the shear strain shows a rapidly increasing rate with increase in the number of cycles. However, if the shear strain reaches one value, the increasing rate of the shear strain decreases.

Figure 11 (a), (b), (c) show the relationships between shear strain and number of cycles considering the influence of the each parameters.

The followings became clear from these figures:

(1) The shear strain shows a rapidly increasing rate after the occurrence of liquefaction, however, the increase of the shear strain has a critical value.

(2) The strongest correlation was observed between the critical value of shear strain (hereafter, it is called the critical maximum shear strain) and the initial relative density of the liquefied sand, as compared with the other parameters.

From the above-mentioned points, Figure 12 is shown in order to clear the relationship between the critical maximum shear strain and the initial relative density. It is suggested from this figure that:

(1) The plotted results are a few scattered, but the correlation is observed between the critical maximum shear strain and initial relative density.

(2) The general tendency is observed that the critical maximum shear strain increases as the relative density decreases.

CONCLUSION

The objective of the study was to clear the mechanical properties of liquefied sand, from two viewpoints those were fluid and solid characteristics. In this study, the coefficient of viscosity on liquefied sand was measured as the fluid characteristic, and the shear strain-shear stress relationship on liquefied sand under large deformation was indicated as solid characteristic, by using the laboratory tests.

The summary of the results is shown below.

(1) The coefficient of viscosity on liquefied sand depends on the relative density.

(2) The correlation was observed between the coefficient of viscosity and the velocity of shear strain.

(3) The existence of the critical maximum shear strain on liquefied sand under large deformation was estimated.

(4) The critical maximum shear strain depends on the relative density.

REFERENCES

1)Doi, M. and Hamada, M. (1992): "A summary of Case Studies on liquefaction-Induced Ground Displacements," Proceedings from the Fourth Japan-U.S. Workshop on Earthquake Resistant Design of Lifeline Facilities and Countermeasures for Soil Liquefaction, Vol. 1, Technical Report NCEER-92-0019, pp. 115-129.

2)Hamada, M., Ohtomo, K., Sato, H. and Iwatate, T. (1992): "Experimental Study of Effects of Liquefaction-Induced Ground Displacement on In-Ground Structures," Proceedings from the Fourth Japan-U.S. Workshop on Earthquake Resistant Design of Lifeline Facilities and Countermeasures for Soil Liquefaction, Vol. 1, Technical Report NCEER-92-0019, pp. 481-492.

3)Ogasawara, Y. (1994) : "Experimental Study on Liquefaction-Induced Ground Displacements by Pressurized Soil box," Master's thesis, Tokai University, Japan.

4)Sato, H., Doi, M., Hamada, M. and Nakamura, T. (1993): "Numerical Analysis on Liquefaction-Induced Ground Displacements," Proceedings of the 22th JSCE Earthquake Engineering Symposium, pp. 87-90.

5)Yasuda,S.,Kiku, H.,Masuda,T. and Bando,S.(1993): "A study on Strength/Deformation Characteristics of Liquefied Sand by Cyclic Torsional Shear Test," Proceedings of the 22th JSCE Earthquake Engineering Symposium, pp. 19-22.

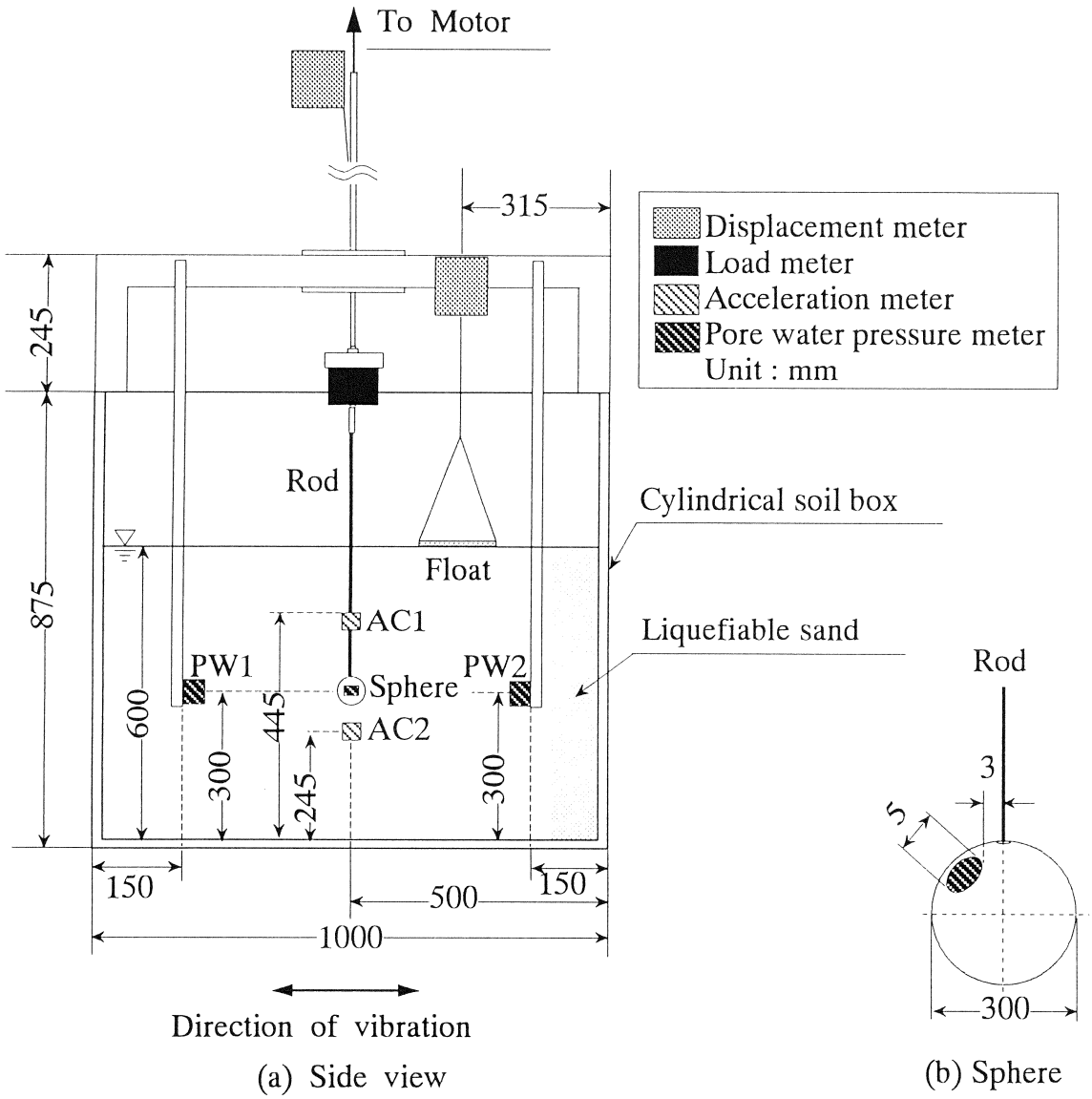

Figure 1 Experimental apparatus for measuring viscosity of liquefied sand by load acting on sphere

Table 1 Conditions of test by load acting on sphere

Diameter of sphere d (cm) : 3.0
Initial relative density Dr (%) : 10 20 30 40 50
Velocity of sphere V (cm/s) : 0.25 0.5 0.75 1.0 1.25 1.5
Acceleration Ac (gal) : 200

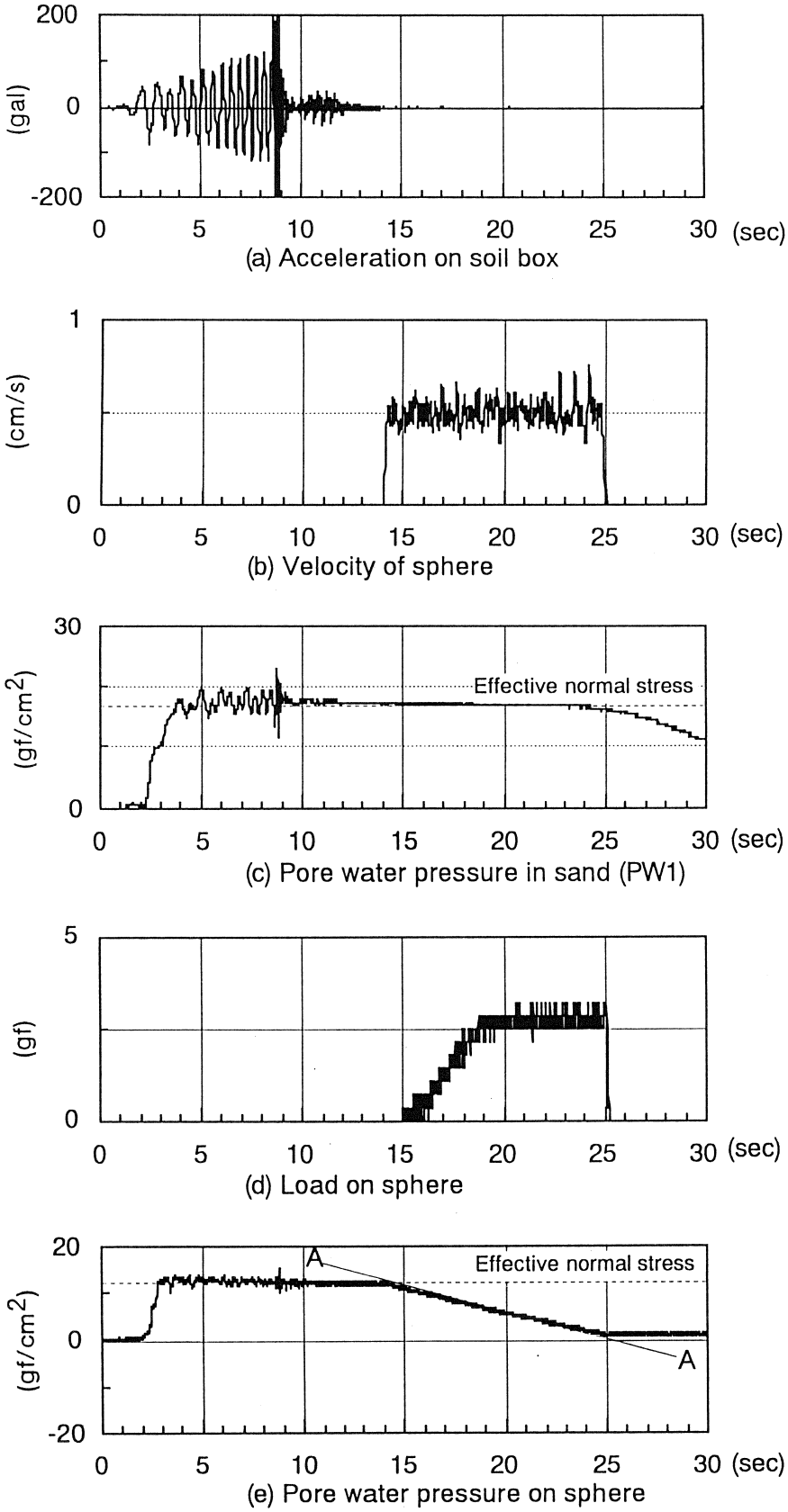

Figure 2 An example of results for test by load acting on sphere (d=3.0 cm, Dr=20%)

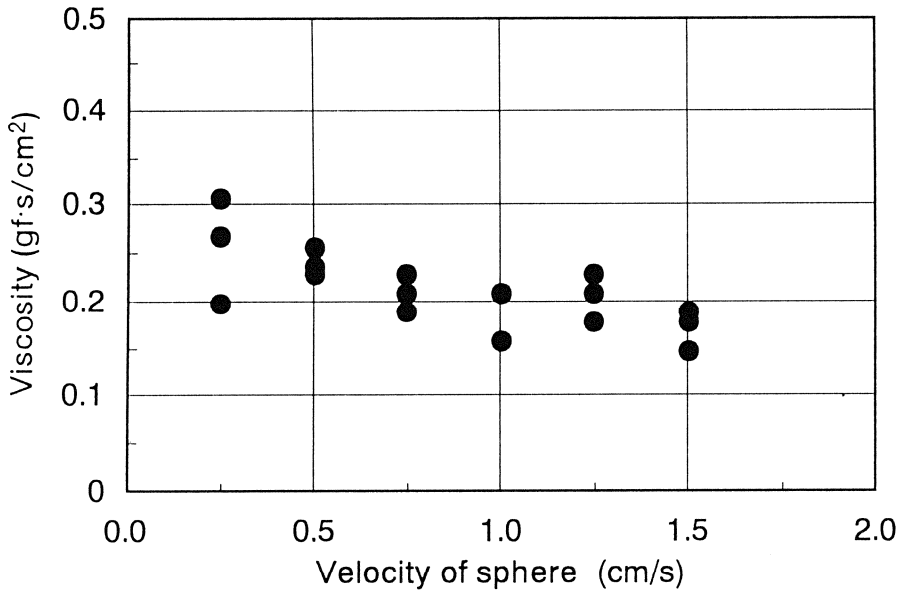

Figure 3 Relationship between coefficient of viscosity and velocity of sphere (d=3.0cm, Dr=20%, Ac=200gal)

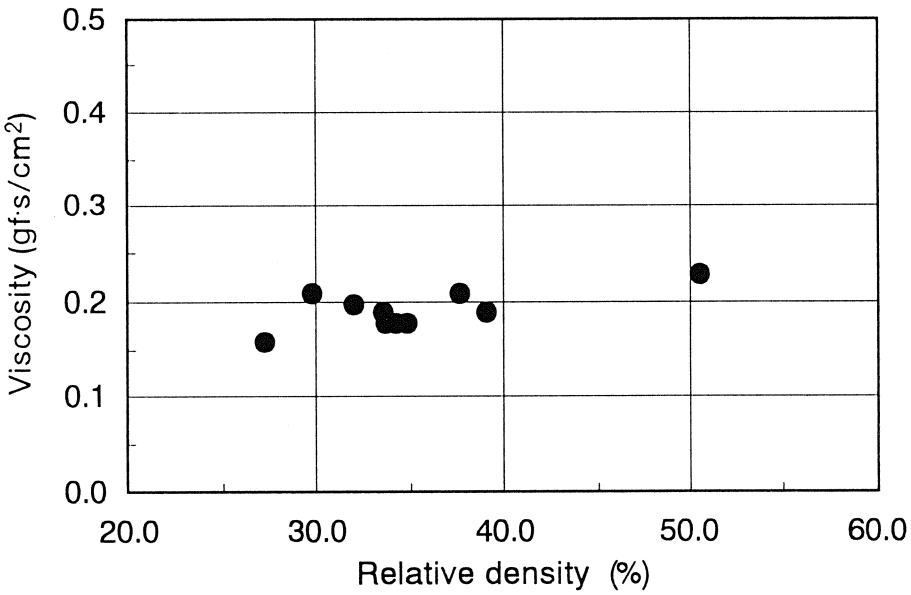

Figure 4 Relationship between coefficient of viscosity and relative density (d=3.0cm, V=1.5cm/s, Ac=200gal)

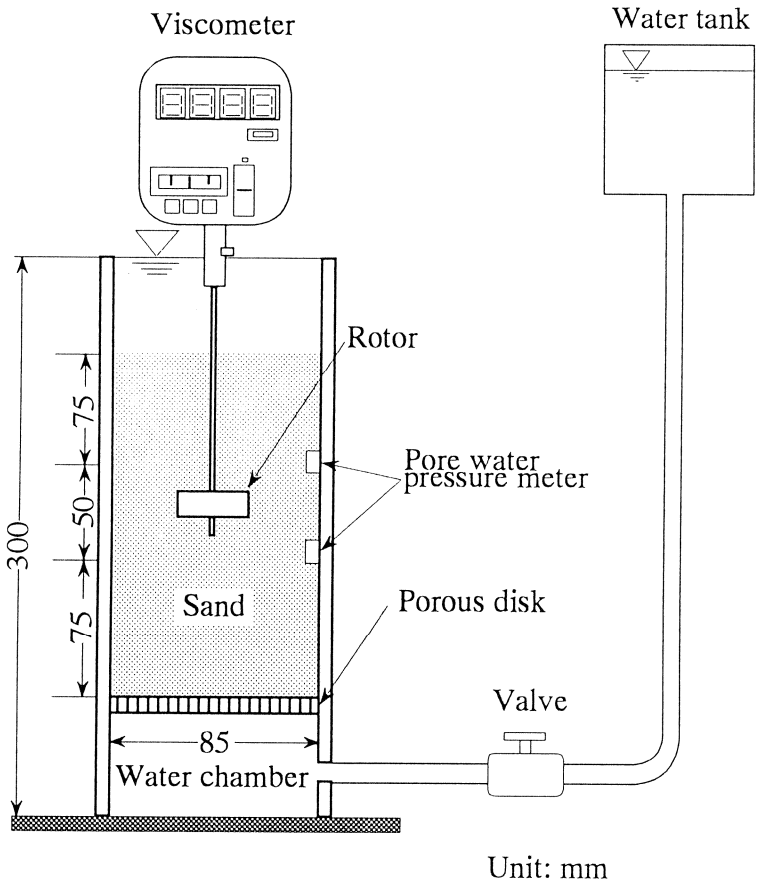

Figure 5 Experimental apparatus of measuring viscosity by viscometer

Table 2 Conditions of test by viscometer

Initial relative density (%) :	20 40 50
Number of rotation (rpm) :	1.5 3.0 6.0 12.0 30.0 60.0

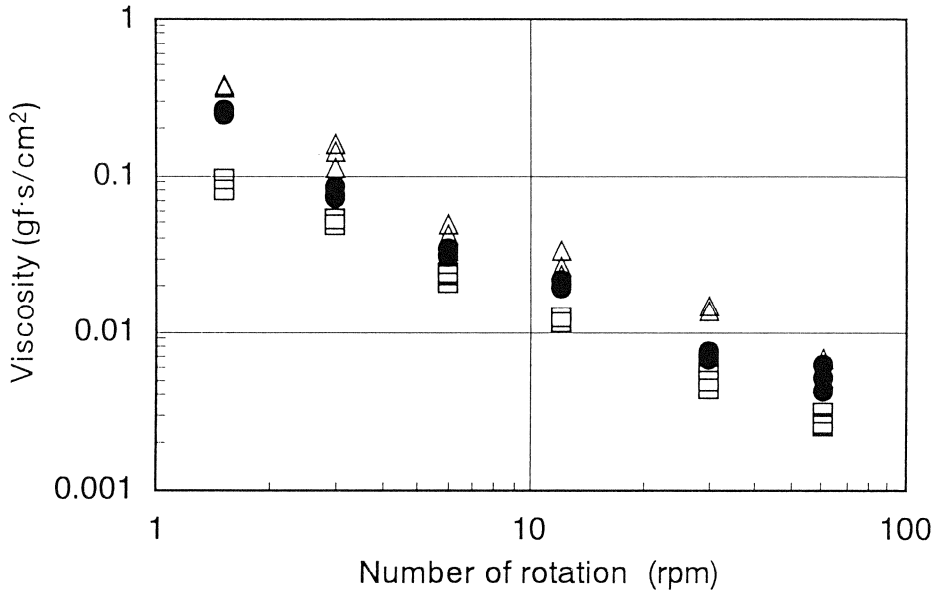

Figure 6 Relationship between coefficient of viscosity and number of rotaition
(□ : Dr=20%, ● : Dr=40%, △ : Dr=50%)

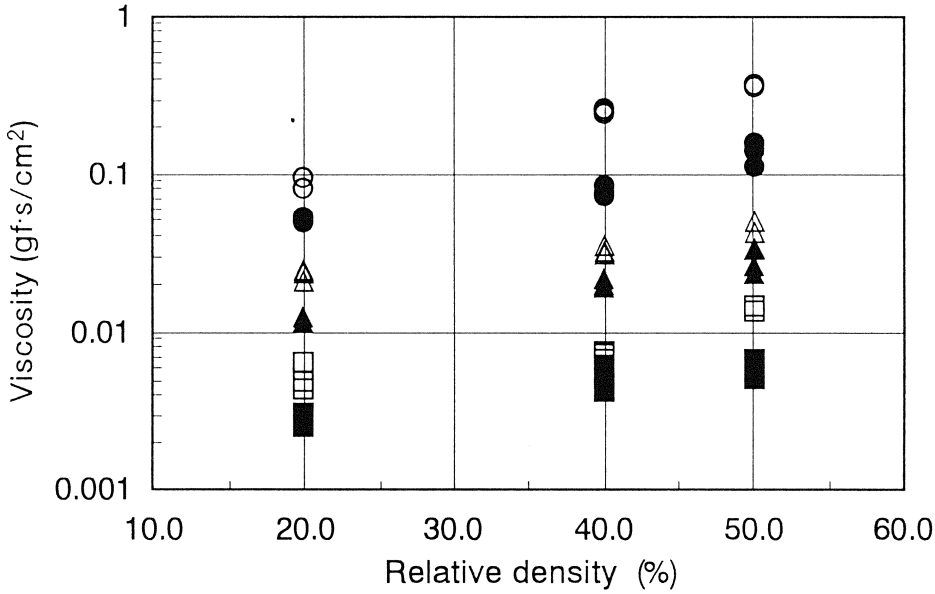

Figure 7 Relationship between coefficient of viscosity and initial relative density
(○ : 1.5rpm, ● : 3.0rpm, △ : 6.0rpm, ▲ : 12.0rpm,
□ : 30.0rpm, ■ : 60.0rpm)

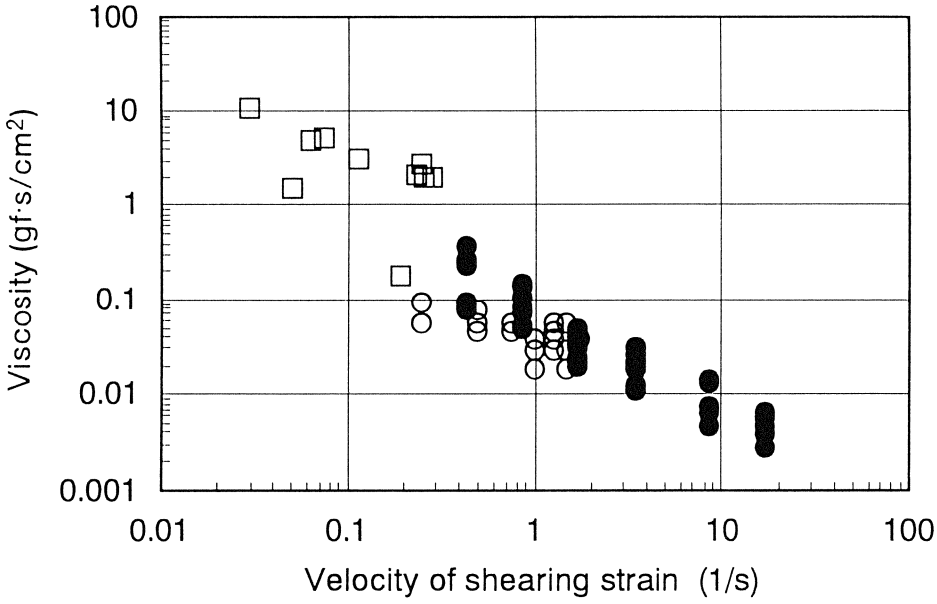

Figure 8 Relationship between coefficient of viscosity and velocity of shear strain

(● : result of test by viscometer, ○ : result of test by load acting on sphere, □ : result of experiment on liquefaction-induced large ground displacement by shaking table)

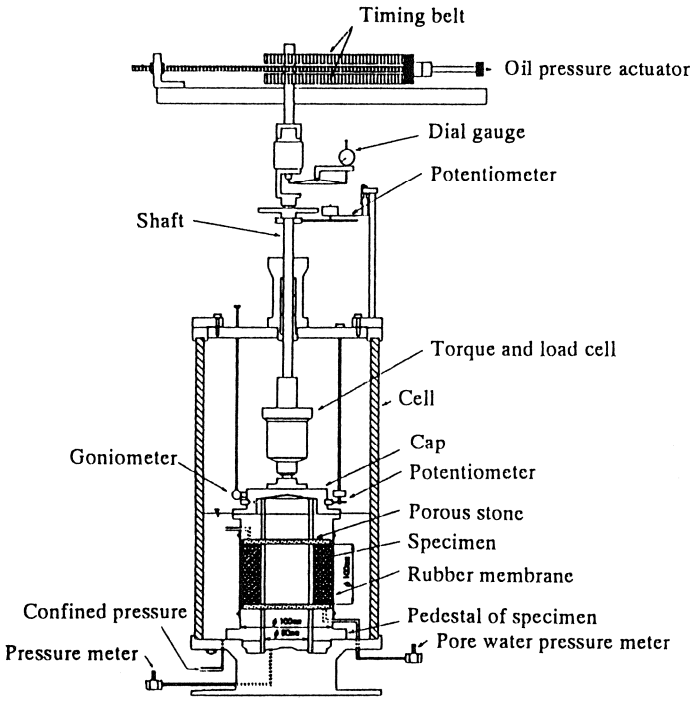

Figure 9 Experimental apparatus for hollow cylinder torsional shear test

Table 3 Conditions of cyclic torsion shear test

Relative density Dr (%)	:	27 ~ 73
Frequency f (Hz)	:	0.01 0.1
Shear stress ratio τ/σ_0'	:	0.1 0.15 0.2
Effective confining pressure σ_0' (kgf/cm^2)	:	0.5 1.0 2.0

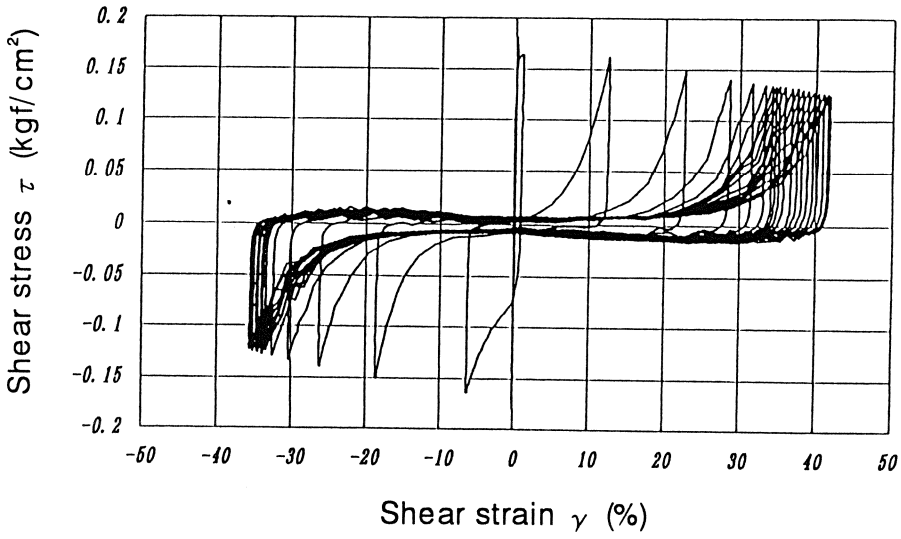

Figure 10 Relationship between shear stress and shear strain
(Dr=53%, τ/σ_0'=0.2, σ_0'=1.0kgf/cm^2, f=0.1Hz)

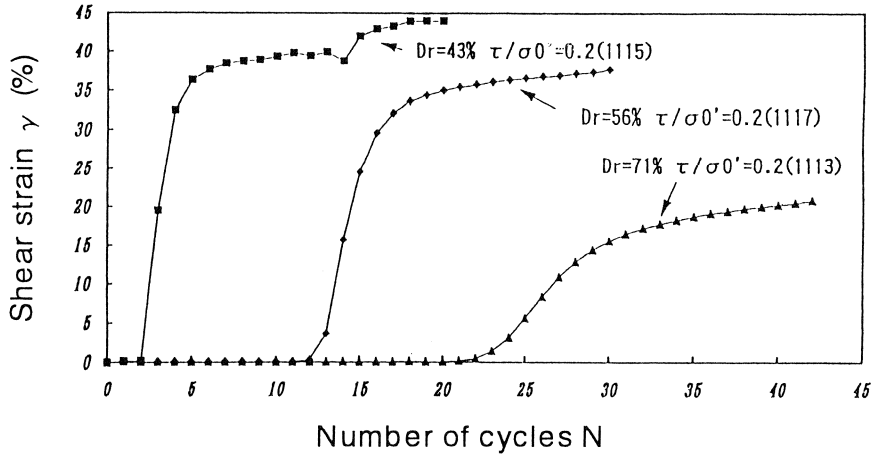

(a) Influence of relative density

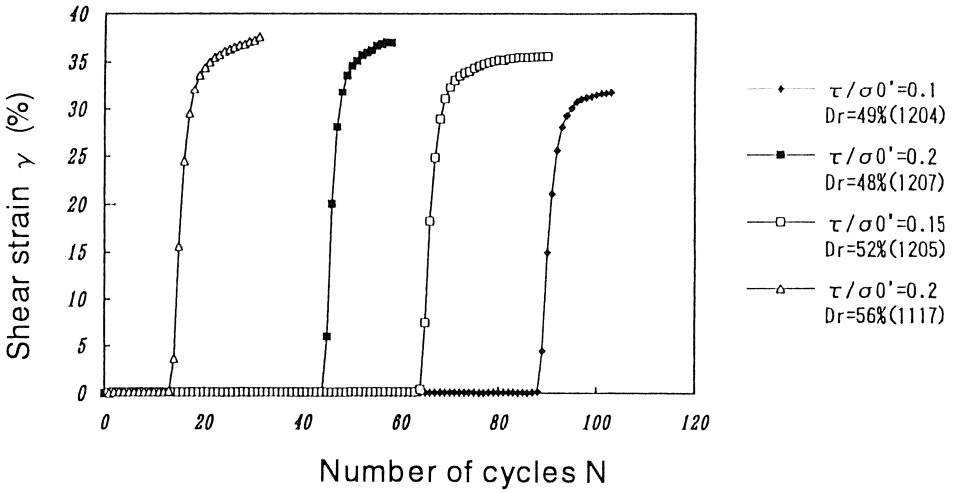

(b) Influence of shear stress ratio

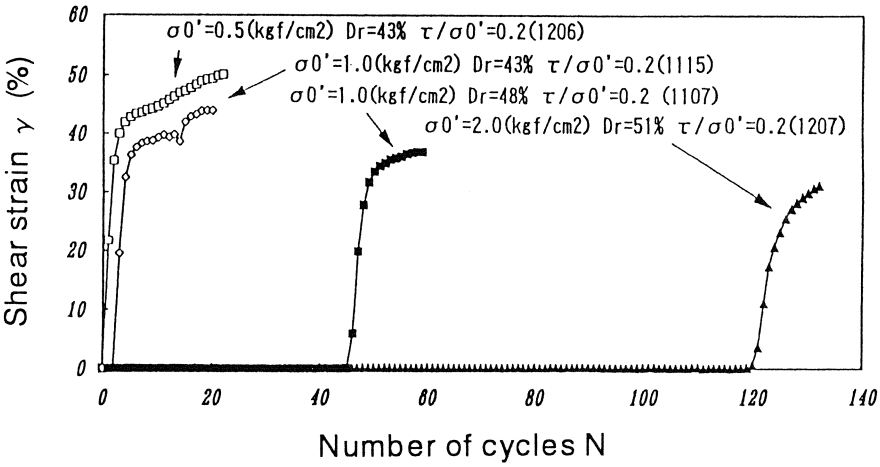

(c) Influence of effective confining pressure

Figure 11 Relationship between shear strain and number of cycles

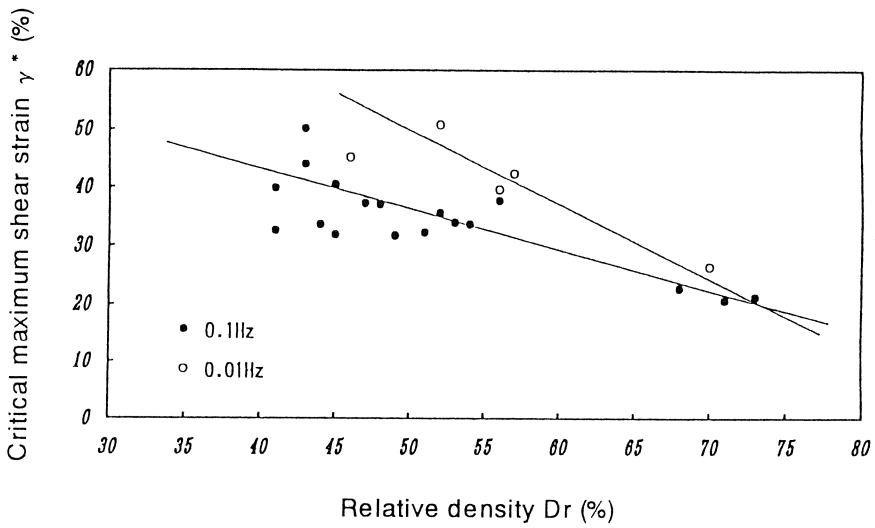

Figure 12 Relationship between critical maximum shear strain and relative density

REVIEW OF ENERGY-BASED LIQUEFACTION RESEARCH AT CASE WESTERN RESERVE UNIVERSITY

J. Ludwig Figueroa, Associate Professor
Adel. S. Saada, Frank H. Neff Professor and Chairman
Liqun Liang, Graduate Student
Department of Civil Engineering
Case Western Reserve University
Cleveland, OH 44106.

ABSTRACT

The development of pore pressure leading to liquefaction of soils subjected to earthquake loadings has been associated by several researchers in recent years to the amount energy imparted to the soil during the dynamic motion. More recently, exploratory laboratory work conducted at Case Western Reserve University indicated that regardless of the mode of stress application, sinusoidal or random, the unit energy needed to initiate liquefaction is nearly constant for a given effective confining stress and a specific relative density. This work also demonstrated that the unit energy imparted to the soil to induce liquefaction is independent of the shear strain amplitude. Data obtained during torsional shear tests made possible the development of relationships between the unit energy required for liquefaction (as the dependent variable) and the effective confining pressure and the relative density (as the independent variables). This paper summarizes these significant developments, and includes preliminary results of tests conducted on soils that liquefied during the recent Northridge Earthquake (Lower San Fernando Valley Dam). The fundamentals of an energy-based method to determine the liquefaction potential of a soil deposit are also presented.

INTRODUCTION

Liquefaction of saturated sandy soils is a common problem in earthquake-prone zones, leading to major damage to buildings, dams and other civil engineering structures. Extensive liquefaction research over the past few decades has helped determine some of the parameters influencing the liquefaction potential of a soil deposit, and procedures to identify these deposits have been developed, combining field and laboratory tests.

After the original introduction of the energy concept in the analysis of the densification and liquefaction of cohesionless soils by Nemat-Nasser and Shokooh (1979), a number of experimental studies conducted by Davis and Berrill (1982), Simcock et al (1983), Berrill and Davis (1985), Law et al (1990), Figueroa (1990) and Figueroa and Dahisaria (1991), Figueroa et al. (1994), and Liang et al (1995) have been aimed at establishing relationships between pore water pressure increases during the dynamic motion and the dissipated energy; and to explore the validity of using the energy concept in the evaluation of the liquefaction potential of a soil deposit.

Using hollow cylindrical specimens of Reid Bedford Sand subjected to sinusoidal torsional loading Figueroa et al (1994) developed a relationship between the dissipated energy per unit volume to reach liquefaction and the effective confining pressure, the relative density and the shear strain amplitude. They found that the dissipated energy per unit volume could conceivably replace both the amplitude of the shear strain and the number of cycles to predict the onset of liquefaction. Later, Liang et al. (1995) presented the results of torsional shear tests conducted at different relative densities and confining pressures, using an earthquake-type time series of loading, demonstrating that the energy per unit volume needed to induce liquefaction was independent of the dynamic loading form, and could be used to evaluate the liquefaction potential of soils subjected to earthquakes. Figueroa et al. (1995) also tested silty sands that liquefied during the recent Northridge Earthquake (Lower San Fernando Valley Dam), and compared the amount of energy per unit volume required for the liquefaction of these soils with that for the Reid Bedford sand, to determine the influence of the grain size distribution.

The following sections summarize liquefaction-related research conducted at Case Western Reserve University; its goal being the development of an energy-based practical procedure to determine the liquefaction potential of a soil deposit.

LABORATORY TESTING

The soils selected for study were Reid Bedford Sand, obtained from the Reid Bedford Bend, located south of Vicksburg, Mississippi, and Lower San Fernando Dam (LSFD) silty sand, obtained from the Lower San Fernando Dam, in the Los Angeles, California area. Classification tests to determine the properties of these soils included sieve analysis, specific gravity and relative density. Their results are shown in Table 1.

The long, thin, hollow cylindrical specimens used in the torsional shear liquefaction testing had the following dimensions:

Outside diameter	=	7.1 cm
Inside diameter	=	5.1 cm
Height	=	12.9 cm
Volume	=	247.2 cm^3

Sample preparation is described in detail in Figueroa et al. (1994).

Test Program

Tests were conducted on specimens at nominal relative densities of 50, 60 and 70 percent for the Reid Bedford Sand, and at relative densities ranging between 57 and 92 percent for the LSFD Silty Sand. Three initial effective confining pressures were used, namely 41.4 kPa, 82.7 kPa and 124.1 kPa; for each relative density.

Some of the Reid Bedford Sand tests were conducted using a controlled-strain type device which applies a sinusoidal torsional deformation, through and eccentric mechanical drive. The remaining tests on this soil, as well as all tests on the LSFD Silty Sand were conducted with a controlled-stress type device applying a random torsional loading.

Torsional Loading Control

The magnitude of shear strain in the controlled-strain device is a function of the eccentricity in the mechanical drive. While the shear strain is maintained constant throughout the test, the shear stress decreases as the soil begins to liquefy.

A synthetic earthquake time series generation computer package was used to generate a random torsional loading proportional to the time history of the ground acceleration (Seed and Idriss, 1971; Ishihara and Yasuda, 1972 and 1975). Input parameters to this package include: the duration of the earthquake, maximum ground acceleration, intensity envelope function, target response spectrum, and damping ratio. A typical synthetically generated time history of ground acceleration is shown in Figure 1. The controlled-stress torsional shear device is computer-controlled. The digital signal from the synthetic time series of acceleration is converted to an analog form and sent to an Electric-to-Pneumatic Transducer to provide the needed actuating forces.

RESULTS AND ANALYSIS

Liquefaction is considered to occur when the developed pore water pressure becomes equal to the applied effective confining pressure at all stages of loading. Torsional shear testing of granular soils permits the determination of hysteresis loops showing the variation of the shear stress with the shear strain up to liquefaction. Figure 2 shows an example of the characteristic decay in the shearing resistance of a Reid Bedford Sand specimen before the development of liquefaction; and the progressive flattening of the loops, indicating the softening of the soil as the pore water pressure increases. The specimen was prepared at a nominal relative density of 60%, and was subjected to sinusoidally varying torsional loading, at an effective confining pressure of 124.1 kPa and a shear strain amplitude of 0.47%.

Results of a series of sinusoidal torsional tests on this sand showed that the accumulated unit energy to liquefaction is constant for a certain combination of parameters affecting the development of liquefaction. The accumulated energy per unit volume (δW) absorbed by the specimen up to liquefaction can be calculated from the hysteresis loops (Figueroa et al., 1994):

$$\delta W = \sum_{i=1}^{n-1} \frac{1}{2}(\tau_i + \tau_{i+1})(\gamma_{i+1} - \gamma_i) \qquad (1)$$

where:

τ = shear stress;
γ = shear strain;
n = number of points recorded to liquefaction.

Generalized relationships were obtained by Figueroa et al. (1994), after conducting 27 liquefaction tests, by performing regression analyses between the energy per unit volume dissipated in generating liquefaction as the dependent variable and the relative density, confining pressure and amplitude of the applied shear strain as the independent variables. Following are the most significant relationships (those with the highest coefficient of determination R^2) which were developed:

$$\delta W = -2124.23 + 14.05\,\sigma_c' + 37.16\,Dr + 174.66\,\Gamma; \qquad R^2=0.934; \qquad (2a)$$

$$\delta W = -2028.13 + 14.05\,\sigma_c' + 37.15\,Dr; \qquad R^2=0.922; \qquad (2b)$$

where:

δW = Energy per unit volume (J/m^3);
σ_c' = Initial effective confining pressure acting on the sample (kPa);
D_r = Relative density of the sample (%);
Γ = Amplitude of the applied shear strain (%);
R^2= Coefficient of determination;

$$Log_{10}(\delta W) = 1.982 + 0.00477\,\sigma_c' + 0.0116\,Dr + 0.0376\,\Gamma; \qquad R^2=0.942; \qquad (3a)$$

$$Log_{10}(\delta W) = 2.002 + 0.00477\,\sigma_c' + 0.0116\,Dr; \qquad R^2=0.937; \qquad (3b)$$

Equations 2a and 3a use all of the parameters in the regression while equations 2b and 3b use two of the three parameters, which are relative density and effective confining pressure. By comparing equation 2a with equation 2b and 3a with 3b, it can be seen that including the effect of the amplitude of shear strain (Γ) only improves the coefficient of determination by 0.012 for equation 2a and 0.005 for equation 3a. Inclusion of the shear strain changes the constants by less than 5%; and barely changes the coefficients corresponding to other parameters. It can be concluded that for the tests conducted in this program, the effect of the shear strain amplitude (Γ) can be ignored in establishing the relationship between the energy per unit volume for liquefaction and the influence parameters. Because of the high Coefficient of Determination which is obtained for Equation 3b, it is also concluded that this equation provides the best fit for the data. However, the linear fit expressed by equation 2b also yields a very high coefficient of determination and may be preferred because of its simplicity. These equations show that:

1. For the same initial effective confining pressure, the energy per unit volume increases with the relative density of the soil. Thus a higher amount of energy is required to liquefy a sand with a higher relative density.

2. For the same relative density, more energy per unit volume is dissipated with increased applied effective confining pressure.

3. There is very little difference between the energy per unit volume needed for the onset of liquefaction under sinusoidal and under random loading. Regression analysis will now be used to judge the significance of these differences.

Figure 3 shows characteristic hysteresis loops obtained after testing Reid Bedford Sand using a non-uniform shear stress. As in the sinusoidal torsional loading (constant strain) tests, the loops tend to become progressively flatter as the sample begins to liquefy; and after liquefaction the stress-strain relationships are almost horizontal. The area of the hysteresis loops also nears zero at liquefaction. The specimen was prepared at a relative density of 59.9% (nominal 60%) and was subjected to an initial effective hydrostatic pressure of 124.1 kPa.

At the beginning of the test, the specimen is stiff and the shearing resistance can build up without large displacements. However as the stiffness (shear modulus) decreases, larger deformations take place with decreasing shearing resistance. This resistance is almost negligible when the sample liquefies. Similar observations were made by other researchers using stress controlled hydraulic or pneumatic loading systems (Ishihara and Yasuda, 1972).

The response time history of the resisting shear stress and the corresponding power spectrum show a frequency band width similar to that of the excitation (Liang et al., 1995) However,

specimens prepared at a higher relative density and subjected to a higher initial effective confining pressure develop a shear stress power spectrum closer to the excitation spectrum than the spectrum of specimens prepared at a lower relative density and subjected to a lower initial effective confining pressure.

As in the sinusoidal torsional tests, relationships were obtained by performing regression analyses between the energy per unit volume at the onset of liquefaction as the dependent variable and the relative density and the initial effective confining pressure as the independent variables. Several relationships such as linear, second order polynomials and logarithmic were examined; however, the following equation provided the best fit to the data obtained from nine non-uniform torsional loading tests, conducted at combinations of three relative densities and three effective confining pressures:

$$\text{Log}_{10}(\delta W) = 2.062 + 0.0039\ \sigma_c' + 0.0124\ Dr; \qquad R^2=0.925; \qquad (4)$$

The similarity of Equations. 3b and 4 is striking, and it may be stated that they are equivalent. A statistical F-test, as described by Sen and Srivastava (1990), was used to test this hypothesis. Results of the F-test, presented by Liang et al. (1995) strongly support the validity of the hypothesis.

The influence of grain size on the amount of energy per volume at the onset of liquefaction was examined by conducting random-loading torsional shear tests on soils that liquefied during the recent Northridge Earthquake (Lower San Fernando Valley Dam). Index properties and classification of these finer soils were already shown in Table 1. The LSFD Silty Sand contains up to 28% of silt, as compared to a negligible amount in the Reid Bedford Sand. Testing was conducted using the same time series of non-uniform torsional stress as in the Reid Bedford Sand with combinations of four nominal relative densities and three effective confining pressure for a total of twelve tests (Figueroa et al., 1995).

Figure 4 compares the amount of energy per unit volume to the onset of liquefaction for the Reid Bedford Sand and for the LSFD silty sand. The finer LSFD soil requires lower unit energy for liquefaction, within the ranges tested, than the coarser Reid Bedford Sand at the same effective confining pressure. The influence of relative density on the energy per volume is practically eliminated with increased silt content, regardless of the value of the effective confining pressure, as can be seen in the following equations:

$$\text{Log}_{10}(\delta W) = 2.484 + 0.00471\ \sigma_c' + 0.00052\ Dr; \qquad R^2=0.995; \qquad (5)$$

$$\text{Log}_{10}(\delta W) = 2.529 + 0.00474\ \sigma_c'; \qquad R^2=0.994; \qquad (6)$$

The elimination of the relative density from the regression (Equation 6) barely affects the constant, the coefficient for σ_c' and the coefficient of determination, as compared with Equation 5. This may be the result of modifying the kinematics of the granular soil by the significant presence of silt in the inter granular spaces.

SUMMARY AND CONCLUSIONS

The use of the energy concept to define the liquefaction potential of a soil has been examined through a series of laboratory tests conducted on Reid Bedford sand and Lower San Fernando Dam Silty Sand. Results of nine torsional shear tests conducted at different relative densities and confining pressures, using an earthquake type time series of torsional loading, were compared to those obtained from tests conducted under sinusoidally applied strains. This comparison, supported by regression analysis, confirms the conclusion that the energy per unit volume needed to induce liquefaction is independent of the dynamic loading form and can be used to evaluate the liquefaction potential of a soil under earthquake excitation.

Similarly, the influence of relative density on the energy per volume was examined by comparing the results of liquefaction testing of Lower San Fernando Dam Silty Sand , with similar tests using Reid Bedford Sand. Its influence is practically eliminated with increased silt content, regardless of the value of the effective confining pressure. This may be the result of modifying the kinematics of the granular soil by the significant presence of silt in the inter granular spaces

All these findings provide a link between laboratory and field behavior and provide the basis for the development of an energy-based method to evaluate the liquefaction potential of a soil deposit. In simple terms, the energy per unit volume needed for liquefaction and determined in the laboratory through the torsional shear testing of undisturbed (if possible) or reconstructed soil specimens from a specific deposit would be compared to the energy per unit volume induced by the random excitation of an earthquake. If the latter, determined with the aid of advanced soil response models to earthquake loadings, is higher than the former, the deposit would experience liquefaction.

ACKNOWLEDGMENTS

This research is supported by the National Science Foundation under Grant No. MSS-9215006.

REFERENCES

Berrill, J.B. and Davis, R.O., "Energy Dissipation and Seismic Liquefaction of Sands: Revised Model," Soils and Foundations, Vol. 25, No. 2, pp. 106-118, 1985.

Davis, R. O. and Berrill, J. B., "Energy Dissipation and Seismic Liquefaction in Sands," Earthquake Engineering and Structural Dynamics, Vol. 19, pp. 59-68, 1982.

Figueroa, J.L., "A Method for Evaluating Soil Liquefaction by Energy Principles," Proceedings, Fourth U.S. National Conference on Earthquake Engineering, Palm Springs, CA - May 1990.

Figueroa, J.L., Dahisaria, M.N., "An Energy Approach In Defining Soil Liquefaction," Proceedings, Second International Conference on Recent Advances in Geotechnical Earthquake Engineering and Soil Dynamics - University of Missouri-Rolla - March 1991.

Figueroa, J.L., Saada, A.S., Liang, L. and Dahisaria, M.N., "Evaluation Of Soil Liquefaction By Energy Principles," Journal of the Geotechnical Engineering Division, ASCE, Vol. 120, No. 9, Proc. Paper 1841, pp. 1554-1569, 1994.

Figueroa, J.L., Saada, A.S., and Liang, L. "Effect of Grain Size on the Energy per Unit Volume at the Onset of Liquefaction" Accepted for Presentation and Publication, Proceedings, Third International Conference on Recent Advances in Geotechnical Earthquake Engineering and Soil Dynamics - University of Missouri-Rolla - April, 1995

Ishihara, K. and Yasuda, S., "Sand Liquefaction In Hollow Cylinder Torsion under Irregular Excitation," Soils and Foundations, Vol. 15, No. 1, pp. 45-59, 1975.

Ishihara, K. and Yasuda, S., "Sand Liquefaction Due To Irregular Excitation," Soils and Foundations, Vol. 12, No. 4, pp. 65-77, 1972.

Law, K.T., Cao, Y.L., and He, G. N., "An Energy Approach for Assessing Seismic Liquefaction Potential," Canadian Geotechnical Journal, Vol. 27, pp. 320-329, 1990.

Liang, L., Figueroa, J.L., and Saada, A.S. "Liquefaction Under Random Loading: A Unit Energy Approach," Accepted for Publication Journal of the Geotechnical Engineering Division, ASCE, 1995

Nemat-Nasser, S., Shakooh, A., "A Unified Approach to Densification and Liquefaction of Cohesionless Sand in Cyclic Shearing," Canadian Geotechnical Journal, Vol. 16, pp. 659-678, 1979.

Seed, H.B and Idriss, I.M., "Simplified Procedure for Evaluating Soil Liquefaction Potential," Journal of the Soil Mechanics and Foundations Division, ASCE, Vol.97, No.SM9, September, pp.1249-1274, 1971.

Sen, A. and Srivastava, M., "Regression Analysis: Theory, Methods and Applications," Springer-Verlage, New York Inc., 1990.

Simcock, J., Davis, R.O., Berrill, J.B. and Mallenger, G., "Cyclic Triaxial Tests with Continuous Measurement of Dissipated Energy," Geotechnical Testing Journal, GTJODJ, Vol. 6, No. 1, pp. 35-39, 1983.

Table 1. - Index Properties and Classification (Figueroa et al., 1995)

Property	Reid Bedford Sand	LSFD Silty Sand
USCS Group	SP	SM
Specific Gravity	2.65	2.67
Max. Void Ratio	0.85	1.22
Min. Void Ratio	0.58	0.71
D_{50}	0.26 mm	0.13 mm

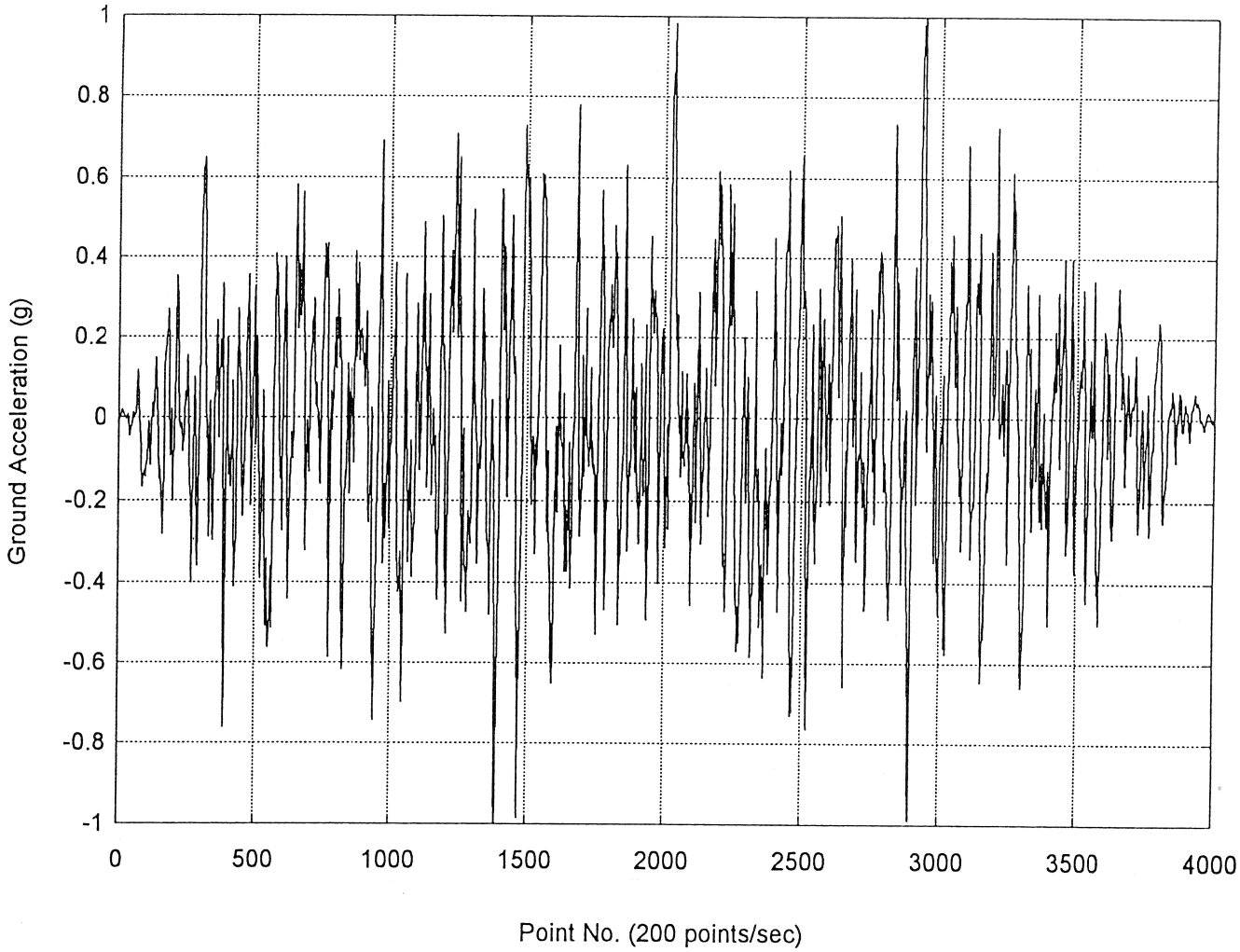

Figure 1. Simulated Ground Acceleration (Liang et al., 1995)

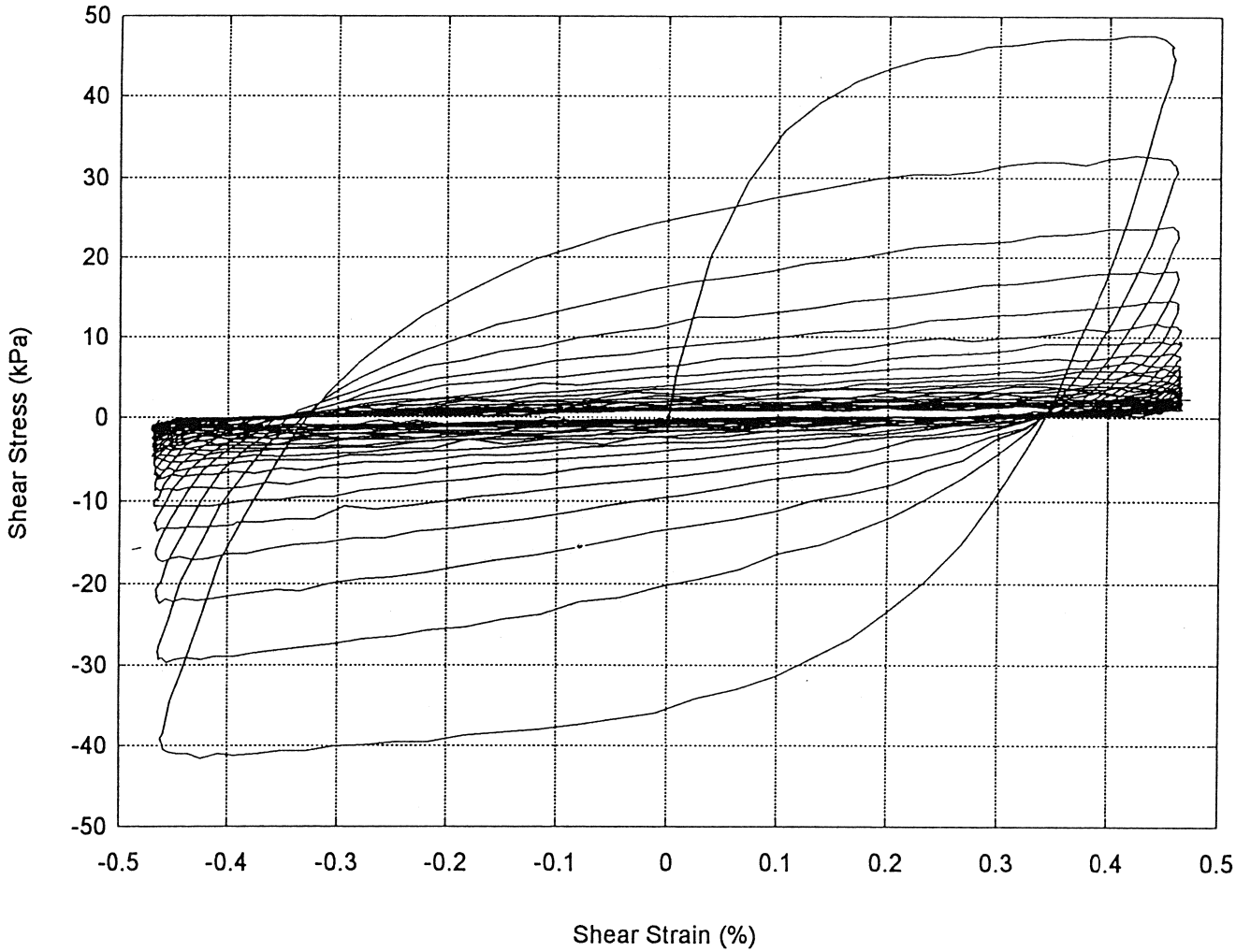

Figure 2. Shear Stress-Strain Relationships During Sinusoidal (Strain Controlled) Torsional Shear Testing (Figueroa et al., 1994)

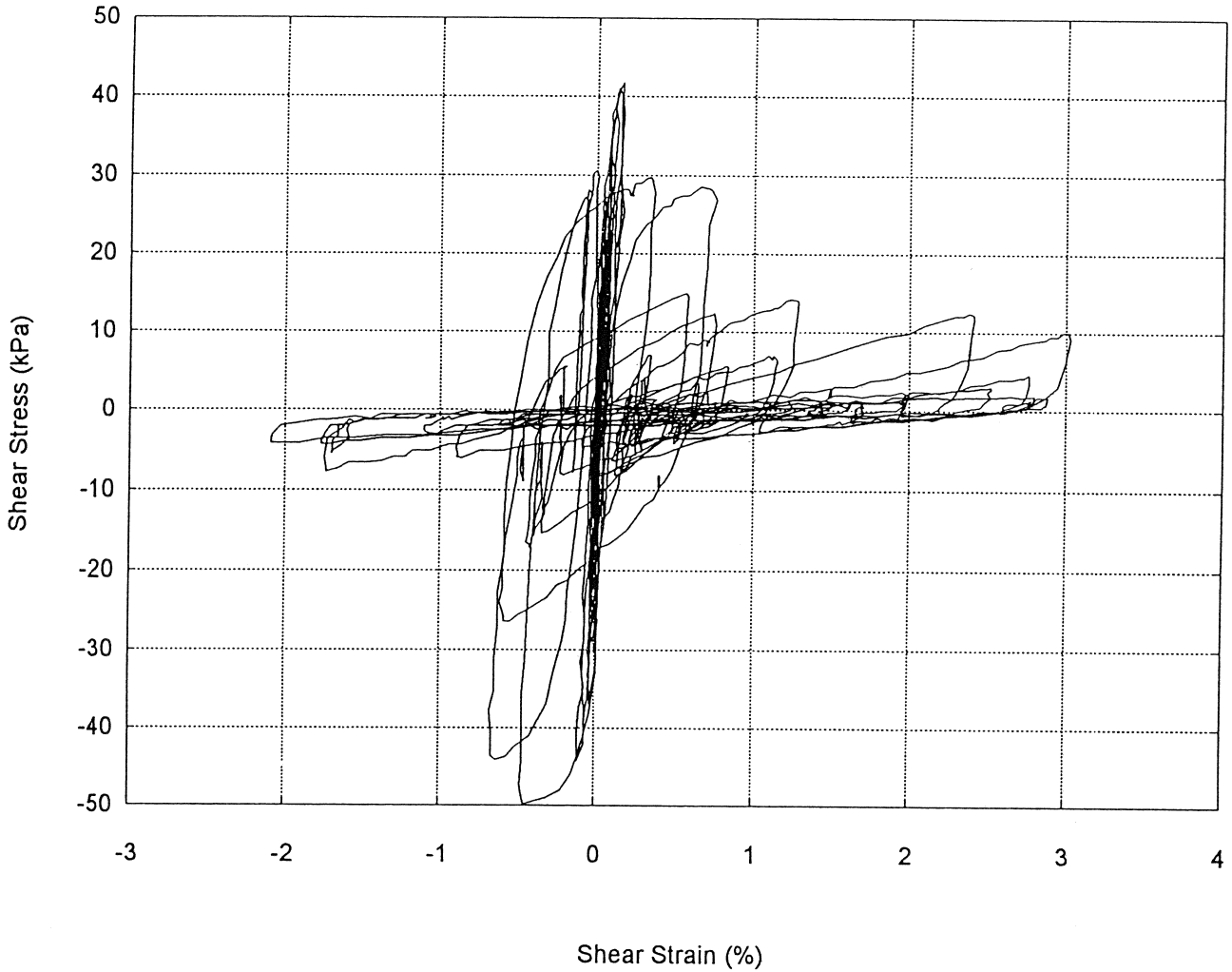

Figure 3. Shear Stress-Strain Relationships During Random (Stress Controlled) Torsional Shear Testing (Liang et al., 1995)

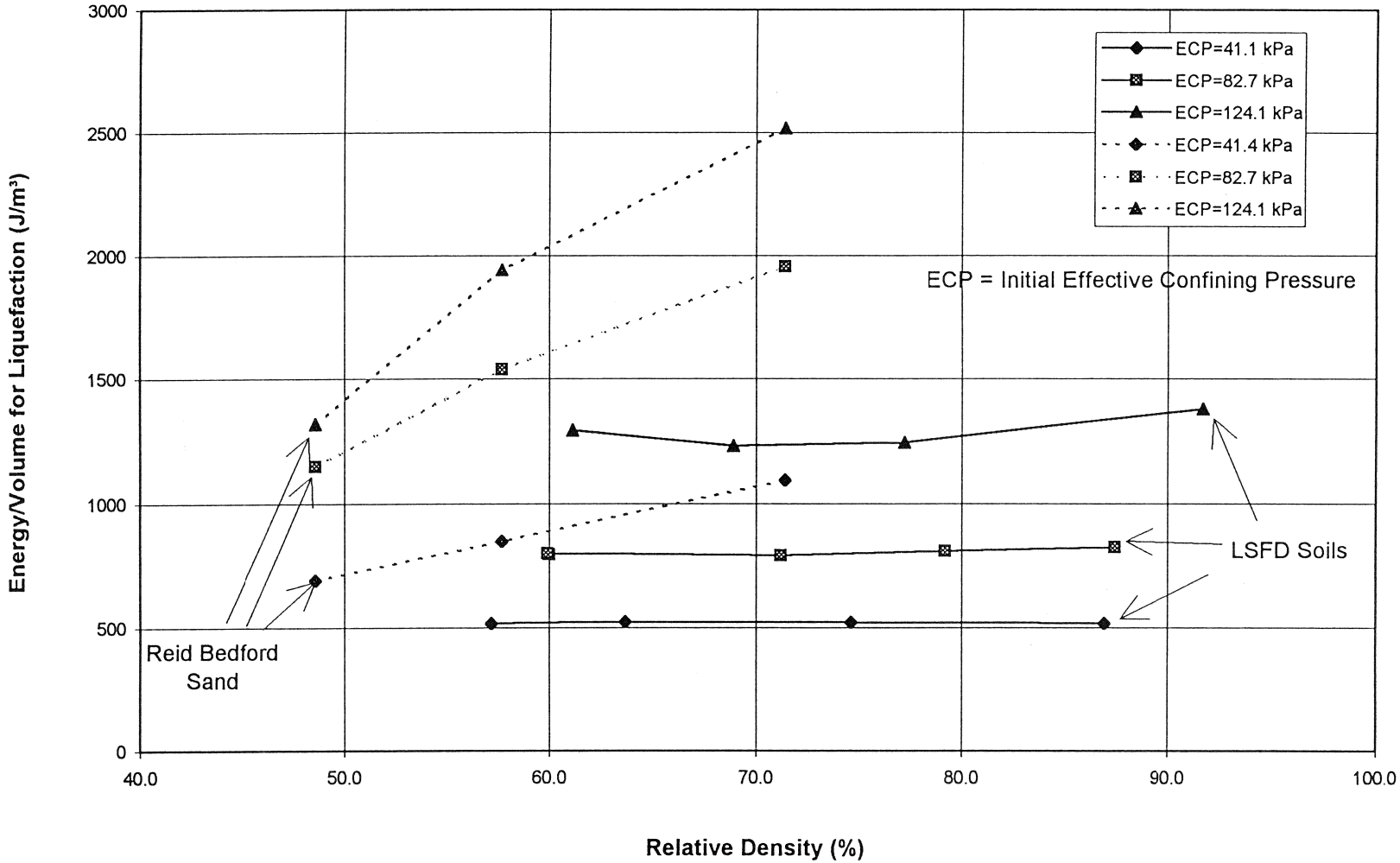

Figure 4. Effect of Grain Size on the Energy/Volume for Liquefaction (Figueroa et al., 1995)

Post-Liquefaction Ground Flow in Shaking Table Tests

Hirofumi Toyota[1] and Ikuo Towhata[2]

ABSTRACT

The behavior of liquefied ground in lateral flow was studied in shaking table using a smaller and a larger container. Tests were conducted in a submerged model slope made with Toyoura sand. The dilatancy characteristics were considered to be very important. Since the shear deformation behavior of model ground at low confining pressure is dilative, the flow created in regular 1-G shaking table tests is limited and cannot continue after shaking stops. However, this problem was solved by using a very loose model ground with contractive behavior. The model ground was prepared by moist placement and wet tamping methods. In order to trigger free flow an impact load was applied in the direction perpendicular to the slope (Transverse direction). Some tests were conducted with continuous shaking applied in the direction parallel to the slope (Longitudinal direction).

In order to observe the soil deformation in detail, markers made from dyed sand were placed in contact with the transparent side wall of container. The displacement obtained from markers and a transducer placed in the center of the ground were compared. A relationship between the velocity of flow and the void ratio was obtained. Results of experiments with free flow triggered by an impact load and flow applied by continuous shaking were also examined.

INTRODUCTION

Lateral flow may occur when inclined ground of sandy soil is liquefied by seismic shaking. This has caused big damages to underground structures, such as lifeline facilities and piers of bridges. According to damage reports of the 1964 Niigata earthquake, the Showa Bridge collapsed 0.5~1 minute after the main shake (Horii, 1968). Also, the collapse of the Lower San Fernando Dam occurred about 30 seconds after the main shaking stopped (Seed, 1979). These experiences suggest that deformation continued even after shaking stopped. Model experiments on lateral flow of liquefied ground have been conducted using

[1]Graduate Student, University of Tokyo, Japan

[2]Professor, University of Tokyo, Japan

shaking tables (Sasaki et al., 1992). However, ground deformation terminated at the end of shaking in those experiments.

In the present experiments, lateral flow under the static gravity force was reproduced by making a very loose deposit. Two type of lateral flows were generated. One was free flow in which lateral deformation developed without shaking, and the other was flow with continuous shaking. The progress of lateral flow with time was examined in detail. The relationships of flow velocity with density of ground and effects of shaking were studied in the present research.

TESTING PROCEDURE

The results of a series of undrained triaxial compression tests are shown in Fig. 1. For a given density, strain softening occurs at high confining stress level but the specimen behavior is dilative at low confining stress level. Thus, the possibility of flow depends on the confining stress level. To get a stress-strain behavior with softening in low stress level, the specimen should be made looser. The shear behavior of a model ground with void ratio similar to field condition is dilative, because it is tested at very low stress level. Thus a model ground should be looser in order to achieve a similar behavior as in the field.

The model ground in the larger container was prepared as follows:

1. Sand was mixed with about 5% of water.
2. Transducers for measuring pore water pressure, acceleration and displacement were placed inside the container as shown in Fig. 11 and 12.
3. The model ground was prepared by placing or tamping wet sand in layers 4~5cm thick with a small flat-bottom tamper. Markers were made by placing dyed sand in a grid in contact with side wall. The final shape was a slope of 20% gradient as shown in Photo 1.
4. In order to avoid lateral deformation during saturation the container was inclined until the surface of the model slope was almost horizontal.
5. Carbon dioxide was supplied through the bottom into the container in order to improve saturation.
6. Water was supplied at a very low rate from the bottom. When the target void ratio was very high, some pre-estimated collapse occurred in the ground.

7. The container was lowered slowly with the rise of water level above the ground surface. The model slope obtained in this way was fully submerged.

Shaking was generated by two methods. One was an impulse in the transverse direction. The duration time of the impulse was very short. Inertia force in the longitudinal direction did not develop. Flow failure of liquefied ground occurred under a static force (free flow). The second was cyclic shaking in the longitudinal direction. Cyclic shaking was continued until the liquefied ground reached the ultimate configuration of stability.

EXPERIMENTS IN A SMALLER CONTAINER

Firstly, experiments were conducted using smaller container to study the characteristics of flow. The input load was an impulse in the transverse direction in these experiments. The size of the model ground and location of transducers are illustrated in Fig. 2. Toyoura sand was used to create very loose ground (Void ratios 1.07~1.09) using the moist placement method. The time histories of input acceleration and pore water pressure are shown in Fig. 3. Markers made with dyed Toyoura sand were placed as shown in Fig. 4 (a) to observe and to measure lateral deformation. The deformation of markers was recorded in a video tape. Lateral displacement stopped when the gradient of the slope decreased from 25% to 17% (Fig. 4).

Secondly, a different material was used to achieve flow failure. This material was Toyoura sand with fines made by crushing the same sand. The grain size distribution is shown in Fig. 5. The ground was prepared by the moist placement method. The recorded measurements (pore pressure, acceleration) and the deformation of markers are shown in Fig. 6 and 7 respectively. Larger deformation than that with clean sand was achieved. The gradient of slope became less than 10% after the test. One reason for this difference is that the shear behavior of sand with 10% fines is contractive. Hence, it is difficult for the ground to recover shear strength with progress of shear strain. Another reason is that the dissipation rate of pore pressure was reduced by the presence of fines. Therefore, recovery of strength with time was slow (Compare Fig. 3 and 6).

The relationship between void ratio and ultimate lateral displacement obtained from markers is shown in Fig. 8 for Toyoura sand with 10% fines. Void ratio was controlled by the tamping energy. There is a big change in lateral displacement near void ratio of 1.05 (Dr≈-19%). Therefore, free flow was observed in model ground of very loose sand (e≈1.05) which contained 10% fines by weight.

Further, a viscous liquid was used to prevent the quick dissipation of pore pressure. This liquid was made by dissolving cellulose in water. It was ten times more viscous than normal water. The moist placement method was used to prepare the model ground. The results of this experiment are shown in Fig. 9 and 10. Dissipation of pore pressure was slower than in other cases (See Fig. 3, 6 and 9) but deformation was not large. The viscous liquid was very good in preventing the quick dissipation but not good at generating flow failure.

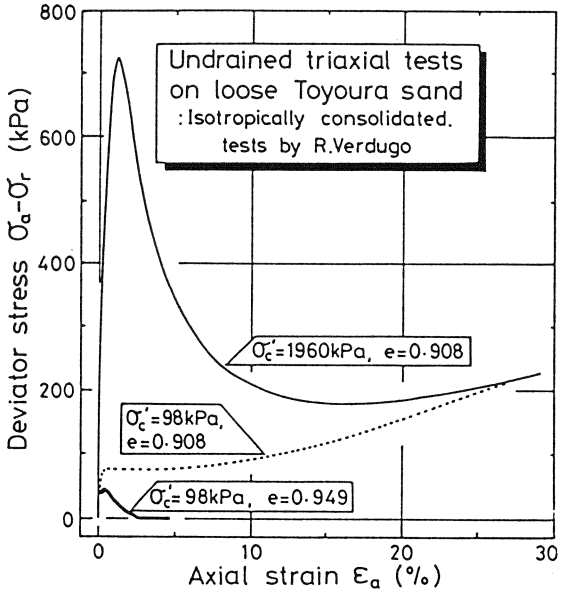

Fig. 1 Undrained behavior of loose sand

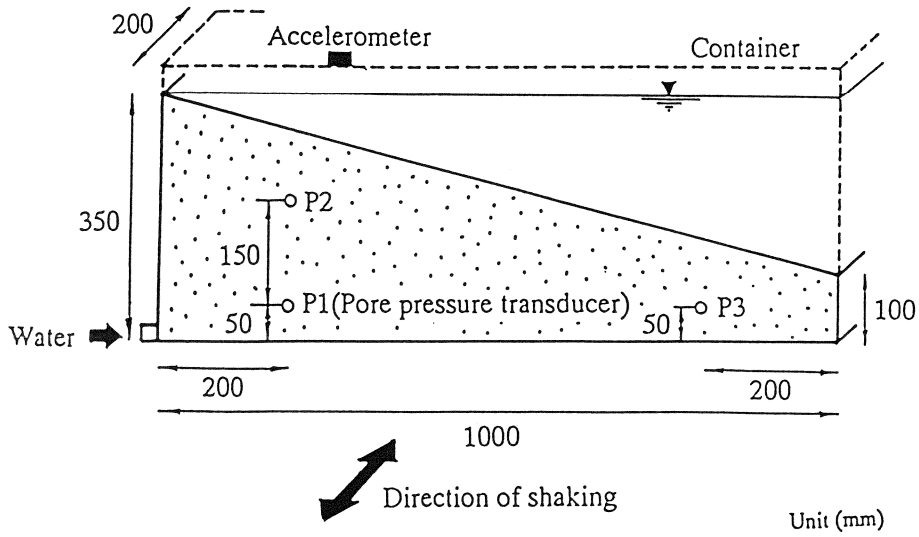

Fig. 2 Model configuration in tests with the smaller container

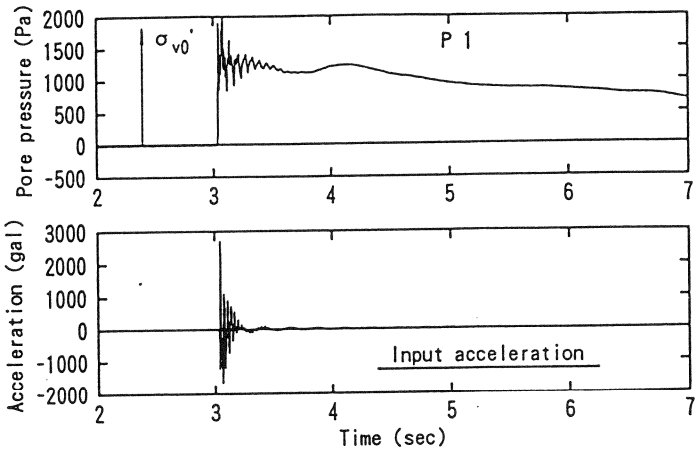

Fig. 3 Measurements in the test with clean sand (e=1.09)

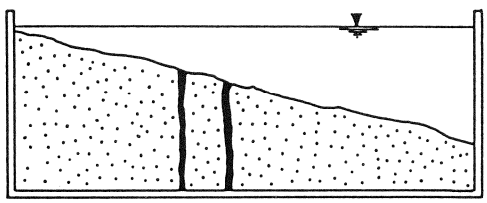

(a) Before shaking

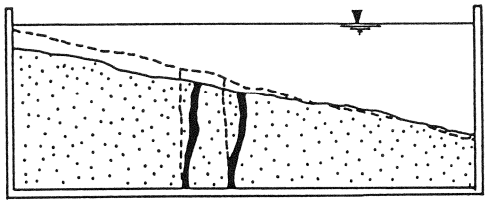

(c) 0.6 sec. after the beginning of shaking

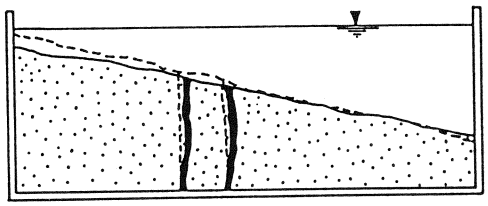

(b) 0.3 sec. after the beginning of shaking

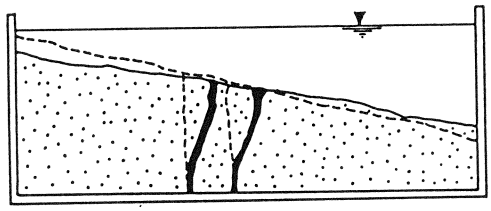

(d) After test

Fig. 4 Deformation of markers in the test with clean sand (e=1.09)

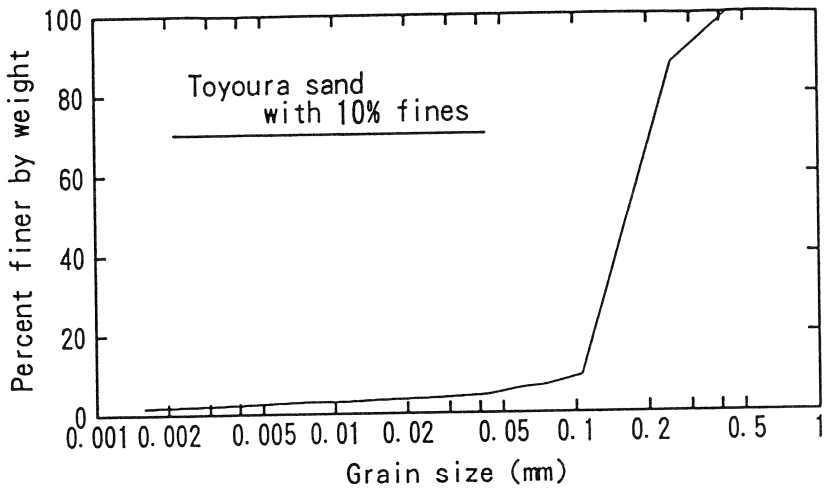

Fig. 5 Grain size distribution of Toyoura sand with 10% fines

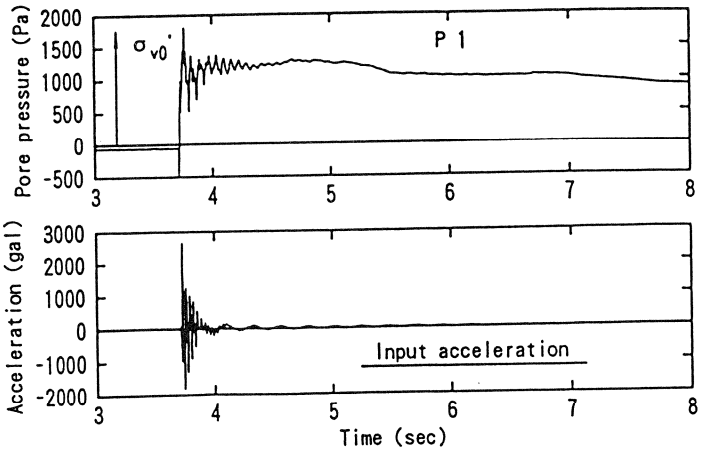

Fig. 6 Measurements in the test with sand containing 10% fines (e=1.07)

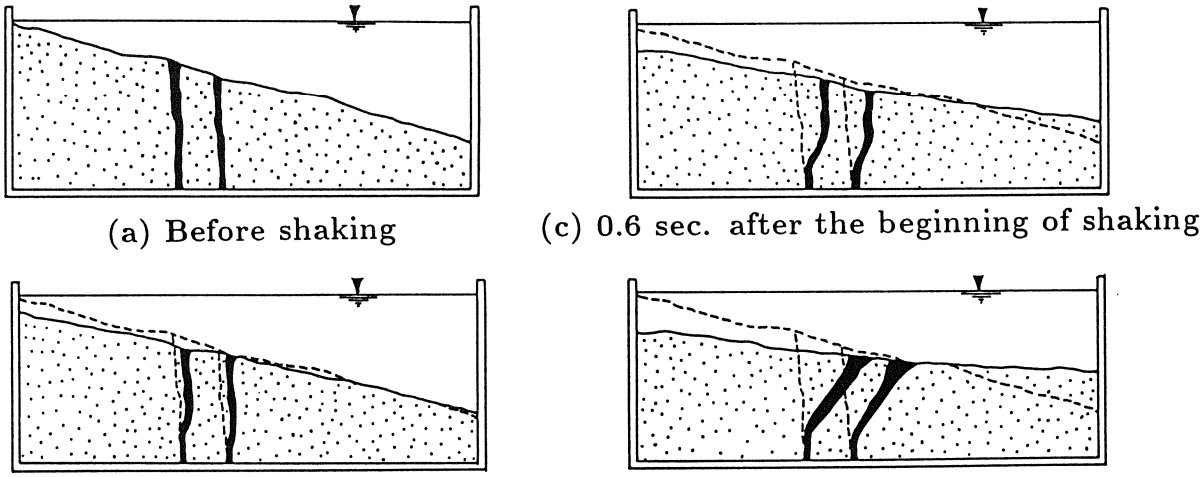

(a) Before shaking

(c) 0.6 sec. after the beginning of shaking

(b) 0.3 sec. after the beginning of shaking

(d) After test

Fig. 7 Deformation of markers in the test with sand containing 10% fines (e=1.07)

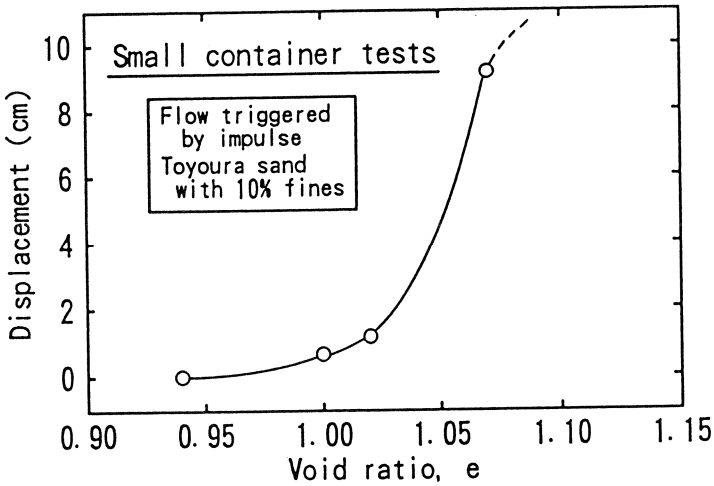

Fig. 8 Ultimate displacement obtained from markers for various tests

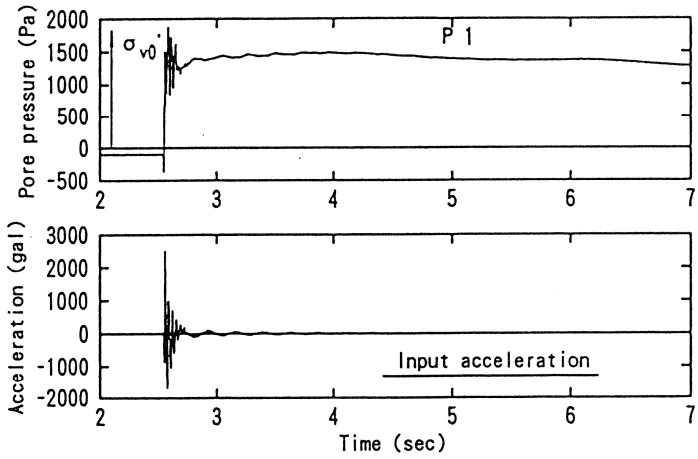

Fig. 9 Measurements in the test with viscous liquid (e=1.09)

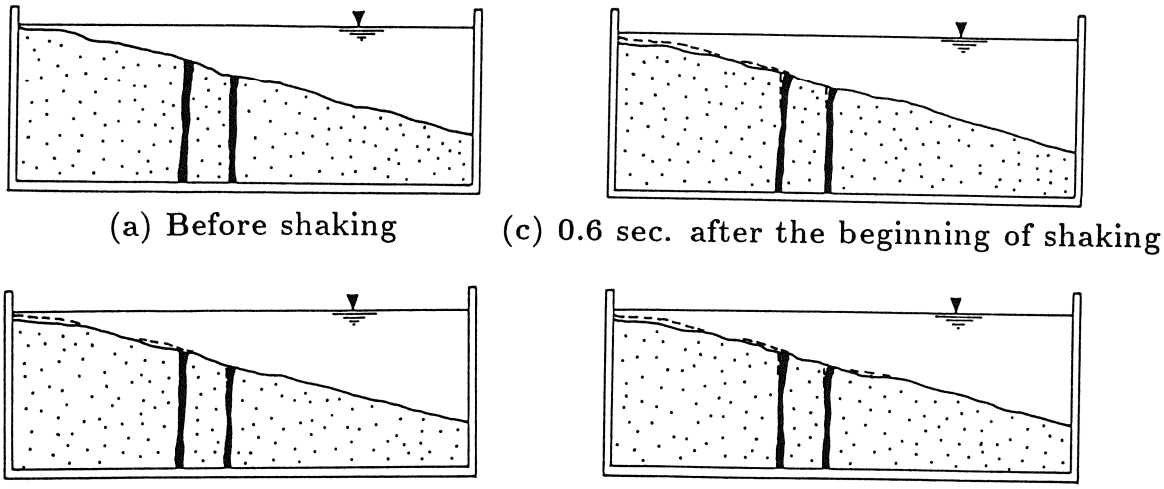

(a) Before shaking

(c) 0.6 sec. after the beginning of shaking

(b) 0.3 sec. after the beginning of shaking

(d) After test

Fig. 10 Deformation of markers in the test with viscous liquid (e=1.09)

EXPERIMENTS IN A LARGER CONTAINER

In the next step, experiments in a larger container were conducted in order to reduce the effects of wall friction. The size of the container, the model ground and location of transducers are illustrated in Fig. 11. Only Toyoura sand was used to prepare the model ground and flow could be reproduced. A displacement transducer was placed inside the ground to measure the time history of lateral displacement (Fig. 12). Markers were created in a square pattern in the ground in contact with the transverse side wall of the container to help in measuring the distribution of shear strain with depth. The deformation of markers was recorded by continuous photographing and in a video tape.

Flow induced by impulse shaking

A comparison between the time histories of displacement obtained from the transducer and the markers is shown in Fig. 13. The displacement of markers was obtained from the photographs using a digitizer. The displacement of markers was smaller than that obtained from the displacement transducer. If the displacement of markers is multiplied by some factor, good agreement is achieved. This means that, although the displacement was smaller than that obtained from a transducer, markers show the real deformation pattern of model ground. Thus, deformation of ground is similar between inside and at the side wall.

Fig. 14 and 15 show general results of tests in which impulse load was applied to a 20% slope with void ratios of 1.03 and 0.95 respectively. Impulse was used to induce liquefaction and lateral flow occurred. Lateral flow stabilized when an almost level surface was attained in the test with a void ratio of 1.03 (Photo 2). It is clear that there was no shear strength in the ground that could stop the movement before level surface was attained. Photo 2 indicates that the large deformation of the ground consisted of a continuous shear distortion with depth. A slip plane was not observed. Denser ground retained some inclination of the slope at the end of flow (Photo 3), because some shear strength (Residual strength) developed with progress of shear strain. Therefore, the inclination of the slope in the final stable condition depended on the density.

Similar experiments were conducted by employing a variety of densities. The time histories of displacement are summarized in Fig. 16. Displacement advanced with higher flow velocity just after applying the impulse but velocity decreased about 0.4 seconds after shaking. It was inferred that initially displacement advanced faster with the collapse of the unstable structure of the loose deposit caused by the impulse. Later, flow velocity was reduced by the dilatancy generated by the high shear-strain rate. After this, flow continued in an almost steady condition. Looser ground attained greater displacement. An interesting fact is that flow ended almost always at the same time. This means that the duration time of flow to achieve a final stable condition whether the inclination was steep or gentle, was independent of density. It is clear from this fact that looser ground attained grater flow velocity.

Flow induced by cyclic shaking

The model ground was cyclically shaken in the longitudinal direction. Shaking was continued until ground movement stopped. Fig. 17 illustrates the results of a test with a

void ratio of 0.93. Although density was higher than that in impulse tests, the lateral soil movement continued for a longer period and the ultimate displacement was greater than that of impulse tests. Finally the ground surface became level (Photo 4).

The type of shaking, impulse or continuous, has an important effect on ground movement. The ultimate displacement was larger in the case of continuous shaking. This means that the ground subjected to shaking has much lower strength than the ground in which shear deformation advances only under the static gravity force.

The average flow velocity was calculated in each case. The comparison between velocity for free flow and flow with continuous shaking is shown in Fig. 18. Density has some effect on the velocity of ground attained by the two methods of shaking. Flow velocity is almost the same in looser ground ($e>0.99$), independent of type the of shaking, but a difference appears in denser ground ($e<0.99$), depending on type of shaking. The lateral displacement measured at the end of flow is summarized in Fig. 19. When liquefied ground was subjected to continuous cyclic shaking, the displacement was constant and independent of density. Surface always became level, suggesting null residual strength. Conversely, the displacement of ground shaken by impulse was strongly affected by density. There seems to be a residual strength which develops with shear strain and increases with density. Based on these results, Towhata et al. (1994) calculated the residual strength (Fig. 20).

Other experiments were conducted with denser ground in a variety of amplitudes and frequencies of input acceleration. Constant amplitude of shaking was continued until ground movement stopped. The average flow velocity was calculated using the initial portion of the displacement (40~70% of the ultimate displacement). Fig. 21 shows the relationship between flow velocity and input acceleration for model ground with nearly the same density. Flow velocity increases with the amplitude of input acceleration. The effect of frequency (4~16Hz) of input acceleration is almost negligible. Liquefied ground subjected to strong input acceleration becomes softer than that subjected to weak input acceleration. Input shaking has very complicated effects on the characteristics of lateral flow in denser ground ($e<0.99$).

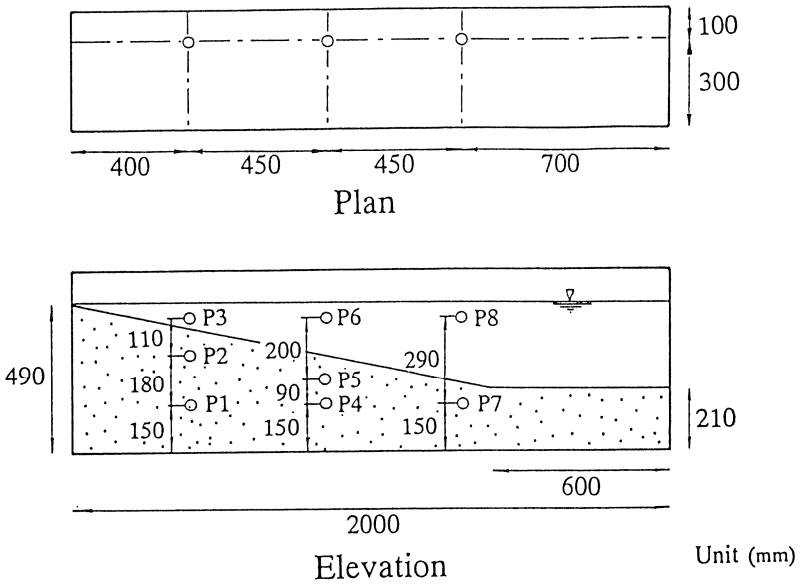

Fig. 11 Model configuration in the tests with the larger size container

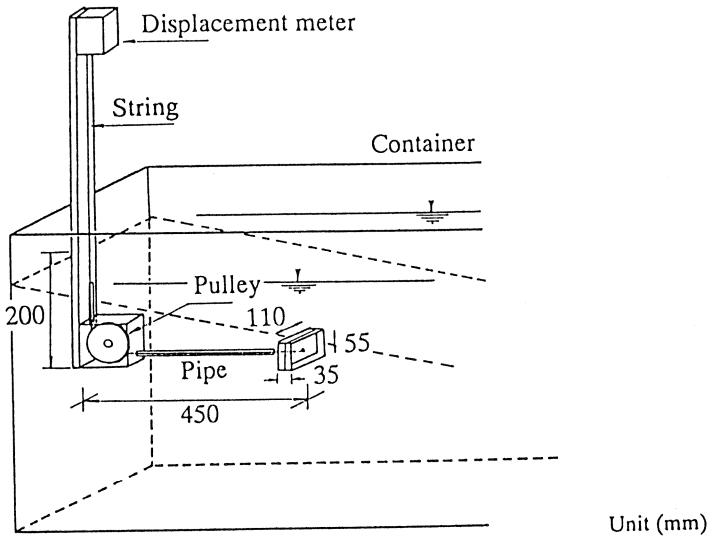

Fig. 12 Location of displacement meter

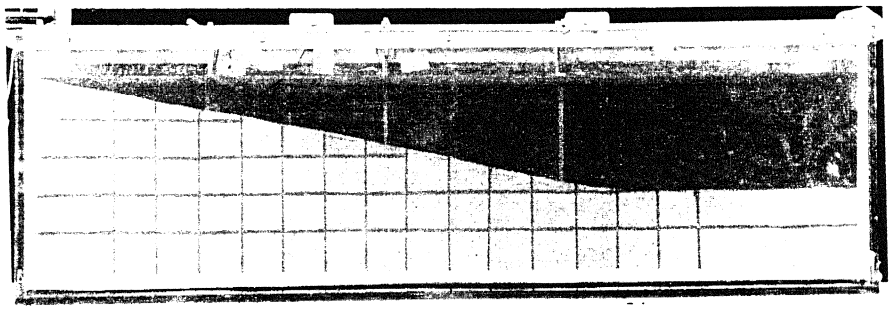

Photo 1 Array of dyed sand markers

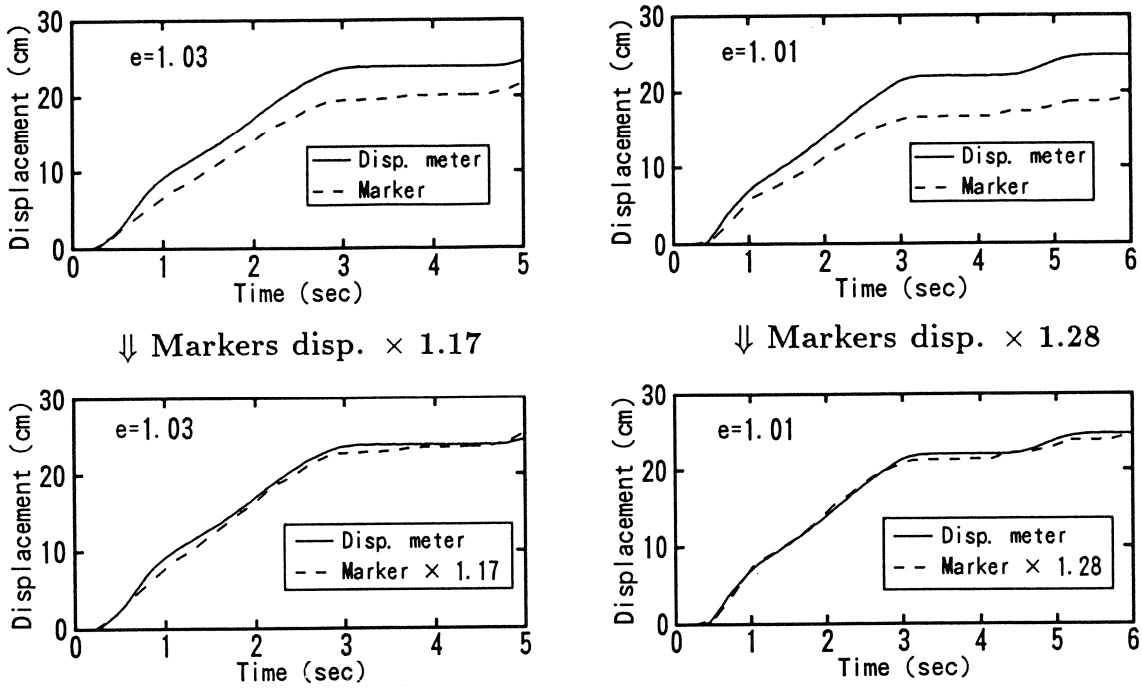

Fig. 13 Comparison of displacement records obtained from transducer and markers

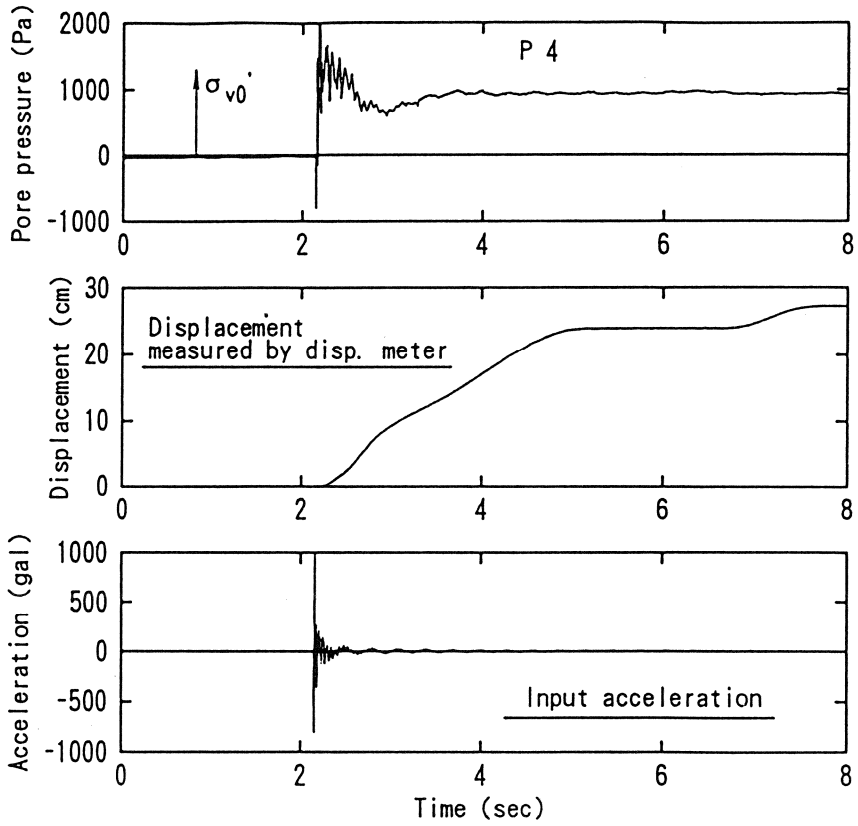

Fig. 14 Measurements in the test with the larger size container (e=1.03)

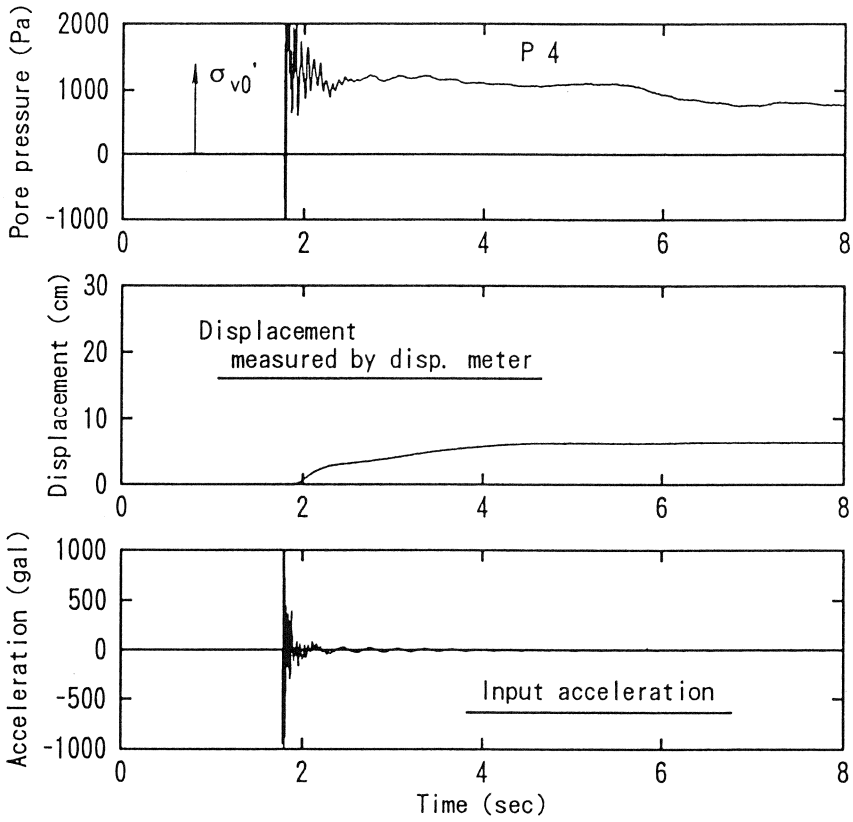

Fig. 15 Measurements in the test with the larger size container (e=0.95)

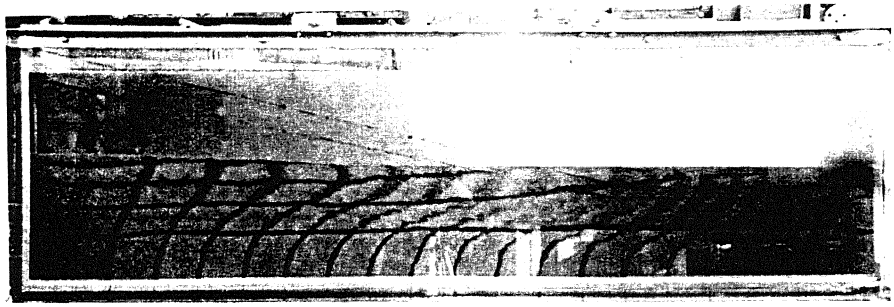

Photo 2 Model ground after free flow (e=1.03)

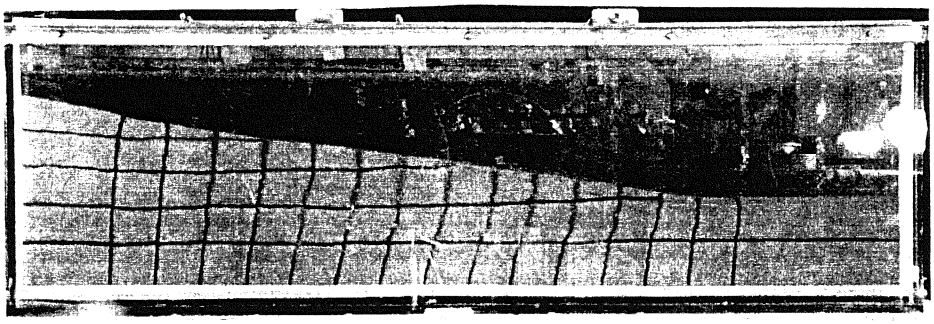

Photo 3 Model ground after free flow (e=0.95)

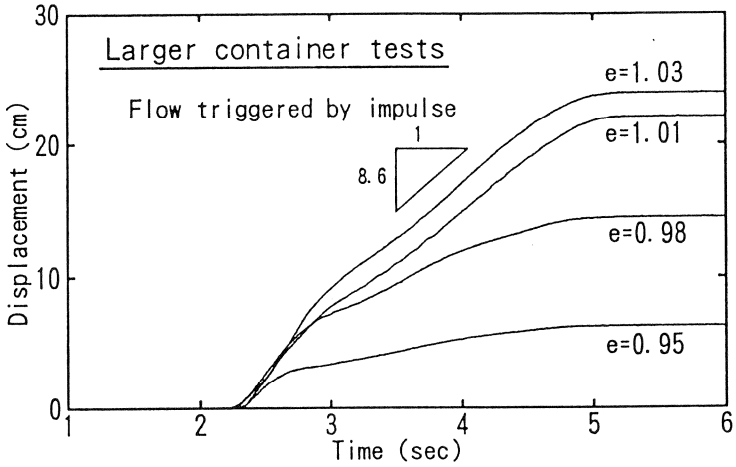

Fig. 16 Effect of density on free flow

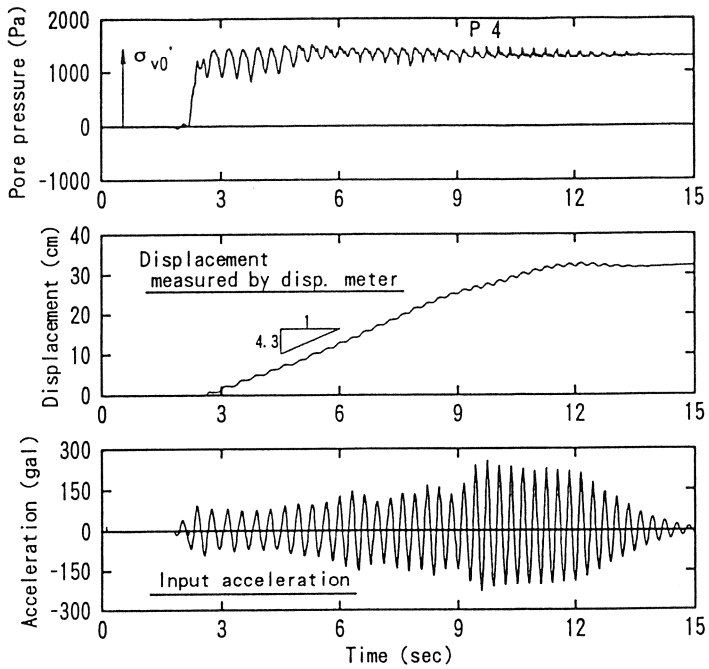

Fig. 17 Measurements with cyclic shaking (e=0.93)

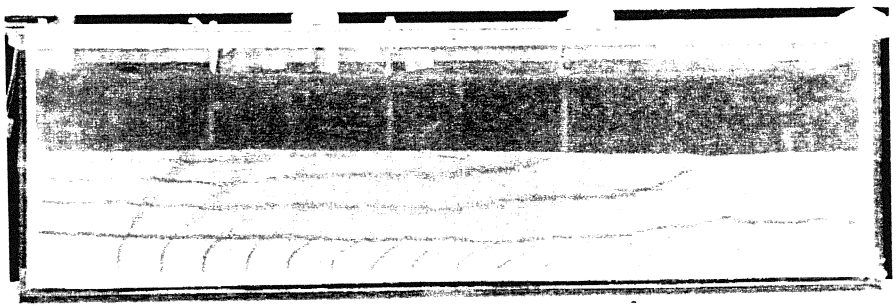

Photo 4 Model ground after cyclic shaking (e=0.93)

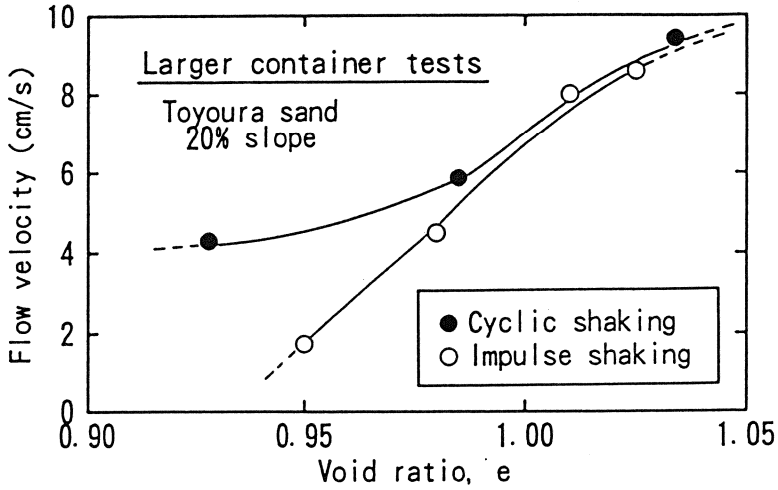

Fig. 18 Flow velocity for various tests

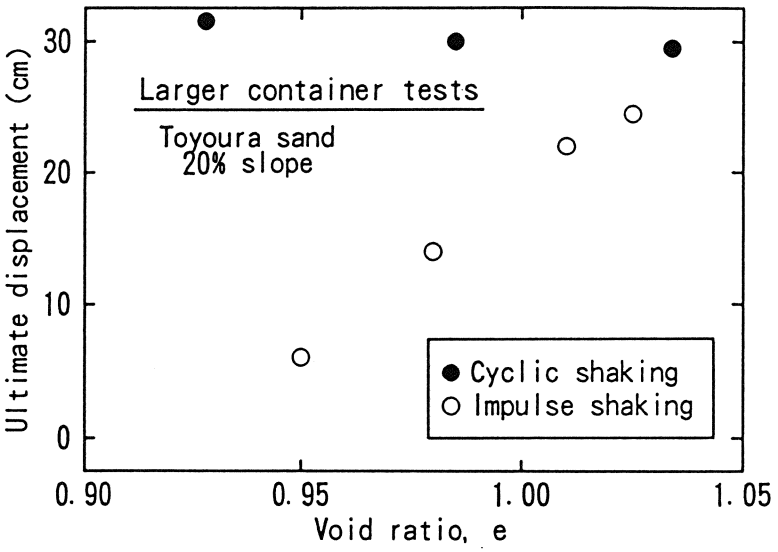

Fig. 19 Ultimate displacement for various tests

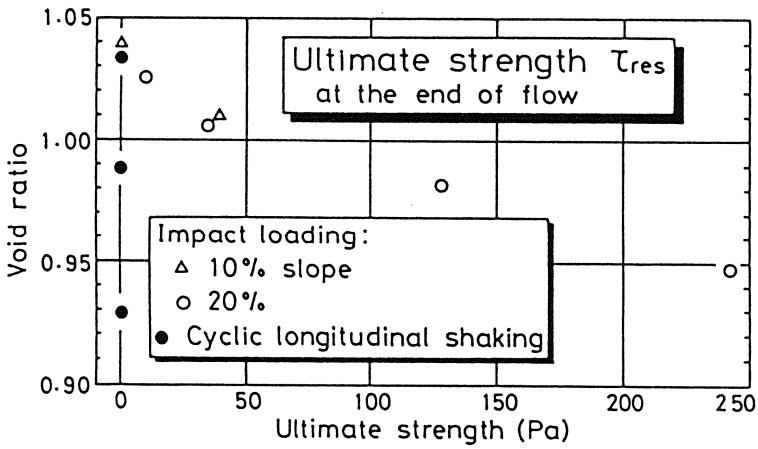

Fig. 20 Ultimate strength for various tests

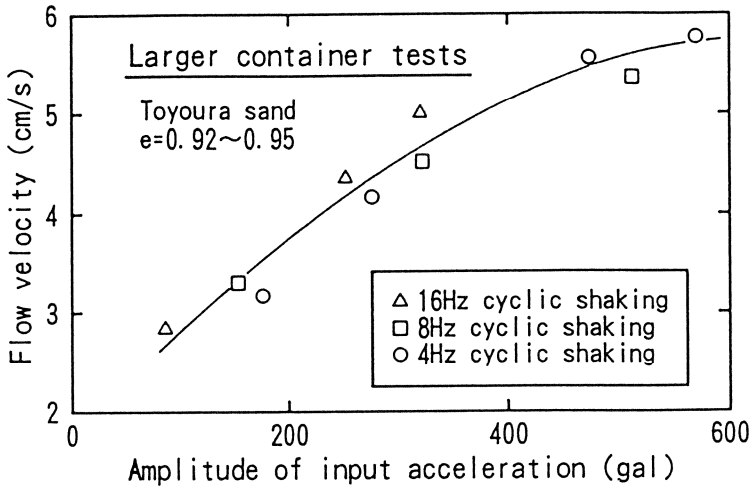

Fig. 21 Effect of input acceleration on flow velocity

CONCLUSIONS

Shaking table tests with model ground were conducted in order to examine the characteristics of lateral flow after liquefaction in detail. The experiments were carried out using very loose deposits made by moist placement and wet tamping for taking into account the dependency of undrained stress-strain behavior (dilatancy) on the stress level.

Following are the conclusions from experiments with a smaller container.

- It was easier to achieve flow using sand with 10% fines than with clean sand.
- Viscous liquid was not good to attain flow in 1-G model tests with impulse shaking.

Following are the conclusions from experiments with a larger container.

- It was easier to achieve flow than in the case of a smaller container.
- Although the displacement obtained from markers was slightly smaller than that obtained from the transducer, markers show the real deformation pattern of model ground.
- Two types of flow were produced. One was free flow which advanced only under the static gravity force and the other was flow under continuous shaking.
- Liquefied ground had some residual strength in the static shear condition, depending on the density.
- The residual strength of liquefied ground subjected to continuous shaking was almost null.

- The duration time of free flow was constant and independent of density.
- Flow velocity was affected by density and type of shaking. Looser ground flowed faster. The effect of shaking was negligible in the looser condition (e>0.99) when flow occurred.
- In experiments with denser ground (e≈0.93), the amplitude of input acceleration strongly affected flow velocity. Conversely, frequency of input acceleration (4∼16Hz) did not have much effect on flow velocity.

ACKNOWLEDGEMENTS

The present experiments were conducted with S. Imamura, K. Kudoh, former undergraduate students at the Department of Civil Engineering, University of Tokyo and Chiba Institute of Technology respectively, and A. Ghalandarzadeh, current graduate student at the Department of Civil Engineering, University of Tokyo. The authors express their gratitude to them.

REFERENCES

Horii, K., Chapter on *Highway Bridges*, General Report on the Niigata Earthquake, Tokyo Electrical Engineering College Press, pp.431-450, 1968.

Sasaki, Y., Towhata, I., Tokida, K., Yamada, K., Matsumoto, H. and Tamari, Y., *Mechanism of Permanent Displacement of Ground Caused by Seismic Liquefaction*, Soils and Foundations, Vol.32, No.3, pp79-96, 1992.

Seed, H.B., *Consideration in Earthquake-resistant Design of Earth and Rockfill Dams*, Geotechnique, Vol.29, No.3, pp215-263, 1979.

Towhata, I. and Toyota, H., *Shaking Table Tests on Transient Flow of Liquefied Ground*, Submitted to 3rd International Conference on Recent Advances in Geotechnical Earthquake Engineering and Soil Dynamics, Missoui-Rolla, 1994.

Verdugo, R., *Characterization of Sandy Soil Behavior under Large Deformation*, Ph.D. Thesis, University of Tokyo, 1992.

EVALUATION OF LIQUEFYING SOIL THROUGH TIME USING SYSTEM IDENTIFICATION

Steven Glaser, Division of Engineering, Colorado School of Mines
Riley Chung, Structures Division, National institute of Standards and Technology

ABSTRACT

A new approach to evaluating earthquake strong motion, parametric modeling (System Identification) is introduced. This method avoids many of the problems inherent in Fourier Methods. Both stationary and recursive parametric modeling methods are applied to input-output data sets from the Wildlife Site, CA, which was subjected to two large earthquakes on November 24, 1987. During the second, larger, earthquake (Superstition Hills earthquake) the site soils liquefied. The data set collected is unique since it is the only available record of buried and surface motions publicly available. Existing seismological analyses of the two earthquakes show that the Superstition Hills earthquake actually consisted of three distinct subevents. The strong motion records and pore water pressure records show excellent correlation with the subevents. The results show weakening of the soils system as pore pressure increases, with estimates of natural frequency, damping ratio, and participation factor given.

INTRODUCTION

The traditional method of geotechnical analysis of dynamic soil motions in earthquake engineering is by the Fourier transform. However, serious problems arise when this method is applied to short data streams, and to signals changing through time — non-stationary signals. These and other serious limitations of the Fourier method are examined in detail in many books and journals (e.g., Glaser, 1993; Johansson, 1993; Pandit, 1991). This study was undertaken to show the effectiveness of a different type of model, a parametric mode commonly used in automatic control and geophysics. An important aspect of the parametric models used, is that there is a theoretical link between the system parameters and the damping and stiffness on an N-Degree-of-Freedom System. This method requires (as do all inverse methods!) a time history if the signal input into the system, and a corresponding system output. The method allows estimates of a system's dynamic properties to be to be made if an input-output data set is available.

An obvious application of this method, commonly referred to as system identification (SI), is to estimate the dynamic soil properties of a profile excited by earthquake strong motion. This would yield large strain soil properties, and avoid sampling disturbance. The records of the two (Elmore Ranch and Superstition Hills) 1987 earthquakes at the Wildlife Site in the Imperial Valley, California are the only publicly available true input-output data sets.

This paper applies several parametric models to the input-output data set recorded during the 1987 Superstition Hills earthquake. Since the inverse problem is non-unique, it is necessary to understand the mechanistic behavior of the system being modeled in order to select the correct model and solution. To this end detailed geotechnical, geological, and seismological analyses of the Wildlife site and earthquake events are presented

SYSTEM IDENTIFICATION

Parametric Modeling of the Soil System

The goal of system identification is to model a system in a manner that provides needed mechanical information about that system. The system is often visualized as a filter with a known input and output. In the time domain, the linear filtering process of a signal passing through a soil layer is represented as a convolution. The process of inversion, or deconvolution, allows the estimation of the system response function (filter) if the input and output signals are known. A simple model for characterizing a system is as a ratio of weighted polynomials. The weights are the parameters relating system input and output. Such a model, referred to as an autoregressive-moving average (ARMA) model, is based on discrete time series analysis:

$$y_t = b_0 x_t + b_1 x_{t-1} + \ldots + a_1 y_{t-1} + a_2 y_{t-2} + \ldots \quad (1)$$

where y_j is the actual output data sequence, x_j is the input sequence (assume white noise for simple spectral estimation), and t is the time step counter. Equation 1 is often rearranged to give

$$y_t = a_1 y_{t-1} + a_2 y_{t-2} + \ldots + b_0 x_t + b_1 x_{t-1} + \ldots \equiv \left(\sum_{j=0}^{nb} b_j x_{t-j} + \sum_{k=1}^{na} a_k y_{t-k} \right) \tag{2}$$

where *na* and *nb* are the AR and MA orders, respectively. The output is seen as a combination of the input history acted upon by the "*b*" coefficients plus the past outputs acted upon by the "*a*" coefficients. The input series, involving the "*b*" coefficients, is a causal moving average (MA) process (convolutional). The series involving weighted past output values ("*a*" coefficients) is a noncausal autoregressive (AR) process. The lengths of the AR and MA processes (model order) must be explicitly chosen so that the model best represents the process.

Applying the shifting theorem to Eq. 2. yields the Fourier transform (Bracewell, 1978)

$$Y_\omega \left(1 + a_1 e^{i\omega} + a_2 e^{2i\omega} + \ldots \right) = X_\omega \left(b_0 + b_1 e^{i\omega} + b_2 e^{2i\omega} + \ldots \right) \tag{3}$$

where i is $\sqrt{-1}$ and ω is circular frequency. Applying the Z-transform (Bracewell, 1978), where $z^k = e^{ki\omega}$, and rearranging, yields the frequency domain transfer function H_ω

$$H_\omega = \frac{Y_\omega}{X_\omega} = \frac{b_o + b_1 z^1 + b_2 z^2 + \ldots}{1 - a_1 z^1 - a_2 z^2 + \ldots} \tag{4}$$

The ARMA model is very powerful in that it can easily model sharp drops, sharp peaks, and smooth spectral behavior. It is also the most parsimonious estimator (Robinson, 1982), describing a complex process with very few parameters calculated from a small length of data, avoiding many of the difficulties inherent in the traditional Fourier methods.

The ARMA model has special significance since it can be derived directly from the differential equation of motion for an *N*-degree-of-freedom system, with the damping ratio and resonant frequency as the model parameters (e.g., Gersch and Luo, 1970). A 2*n*-2*n* ARMA model is therefore a valid model for a layered soil system, or soil-structure interaction problem. The damping ratio and resonant frequency of the *N*-degree-of-freedom oscillators are contained in the 2*n* AR parameters. Phase relations are preserved in the MA parameters. Extensions of this model, e.g., ARMAX, ARX, Box-Jenkins, allow input, system, and output noise to be expressly modeled (Ljung, 1987). In particular, the ARX model includes the effect of uncertainties and noise as a white noise term. The structure is written as

$$A_i y_t = B_j x_{t-k} + e_t \tag{5}$$

where k is a time step delay and e_t is a white noise sequence.

Stationarity

Traditional methods of system estimation, both parametric and non-parametric, are strictly valid only for stationary data. A stationary signal is one whose statistics do not change with time. The commonly invoked, loose definition of stationarity requires that the signal variance be constant over any and all time windows. Inherent in a stationary transformation is the averaging of the signal components over the sampling period *T*. The energies present at each component frequency are integrated over the entire time period *T*. The difficulty with non-stationary signals is that these energies are changing during this period. If the frequencies present are changing over this time window, the resulting estimation, regardless of method used, will be a smeared average as if all the frequencies with energy were active throughout the period.

The field of adaptive (recursive) filtering was developed to model non-stationary processes. As the statistics of the signal change through time, the filter "adapts" to the changing variance with new parameter values that reflect the structure of the system at that point. The predicted value for the next time step can be compared with the actual value, and the difference will give a measure of how well the filter is doing its job. ARMA or AR parameters can be sequentially estimated so that the parameters are adaptive to the changing nature of the process (Ljung, 1987). The parameters are updated after each data point, tracking slowly non-stationary signals. The spectral estimation can be made at any time step by evaluating the AR parameters around the unit circle, giving the spectral description of the behavior of the process at that time. The most popular direct adaptive filter, or process model, is the Kalman filter (Kalman, 1960). Sorenson (1970) points out that the Kalman approach is a direct descendant of Gauss's least squares, except now neither the signal nor the noise model is stationary — the state may change from sample point to sample point. The so-called extended Kalman filter has been very successfully applied to non-linear estimation problems

THE WILDLIFE SITE IN THE IMPERIAL VALLEY

Introduction

The Wildlife site is located in the Western Imperial Valley, 13 km north of Brawley, Imperial County, California. The Imperial Valley is one of the most seismically active regions of the United States (Hudnut and Sieh, 1989). The Wildlife site is located in the Imperial Wildlife Management Area, on an incised flood plain of the Alamo river (Bennett et al., 1984). The deposits consist of various flood plain, fluvial, and lacustrine materials with 7 distinct units in the first 26 m. The top three units were investigated thoroughly since they were believed to be the seat of any liquefaction (Holzer et al., 1989).

The geotechnical cross-section of the first 13 m of soil at the Wildlife is shown in Fig. 1. The water table, controlled by the near-by Alamo river, was approximately 1.2 m below the surface when the Superstition Hills earthquakes struck. Unit A is a very soft sandy to clayey silt, which grades into the silty clay of at the bottom of Unit B below. The upper meter of Unit B, B1, is a very loose poorly graded silty sand which phases towards the denser silty sand of subunit B2. In general, the materials in Unit B grade from coarsest at the bottom (7 m) to the finest at the top. Unit C ranges

from a medium-to-stiff clayey silt to a very stiff silty clay. Unit D is a dense, well-graded silt, cemented towards the top of the unit.

The U.S. Geological Survey (USGS) chose to install an instrumentation array at the Wildlife site because it liquefied during the 1981 Westmoreland earthquake (shear magnitude, M_S, 6.0) and its location in a very seismically active area. Besides surface and buried (8 m) accelerometers, an array of pore pressure transducers was installed at various depths, making this one of four piezometric arrays in the U.S. (Holzer et al., 1989; Brady et al., 1989). Fig. 1 presents the physical relation of the piezometers to the soil units. Two piezometers were installed in subunit B1, three in B2, and one in the dense clayey silt of Unit D.

The USGS undertook a thorough site investigation at the time the instrumentation array was installed (Bennett et al., 1984), and other researchers performed geophysical investigations to determine the in situ shear-wave velocity (Bierschwale, 1984; Nazarian and Stokoe, 1984). Both standard penetration tests and cone penetration tests, as well as an analysis of the soil description, indicated that subunit B1 would be the most likely to liquefy in the event of strong enough dynamic excitation. Piezometer P5 and P2 were installed in this subunit.

Two large earthquakes, the Elmore Ranch and Superstition Hills, occurred on November 24, 1987. The shaking was strong enough to induce liquefaction at the Wildlife site, which suffered more than 2 m of lateral spread towards the Alamo river, and sand boils occurred over at least 33 hectares (Holzer et al., 1989). Accelerograms from the buried and surface transducers, as well as pore pressure histories, were captured for both the Elmore Ranch and Superstition Hills earthquakes (Brady et al., 1989). This is the only full input-output data set known to exist for a site experiencing liquefaction, and the only set of records complete enough to allow an unambiguous system identification analysis.

Geology

The Imperial Valley is a structural depression caused by the active spreading of the Gulf of California (Magistrale et al., 1989). The Wildlife site is located 32 km west of the Superstition Hills temblor epicenter. The Valley flanks are continental crystalline plutonic and metamorphic rocks, about 2 km deep on the west, while the center of the central Valley is comprised of metamorphosed sedimentary rocks beneath 5 km of sediment (Magistrale et al., 1989).

The surface sediments in the areas of interest are Holocene lacustrine silty sand and claystone, interbedded with alluvial deposits, below which are slightly consolidated Pleistocene silty and clayey lake deposits with sand and gravelly units (Bennett et al., 1984). The impedance contrasts of the geology are such that the vertical motions due to a local earthquake are primary-waves (P-waves), while the horizontal motions are manifestations of the passage of shear-waves (S-waves) (Wald et al., 1990). This assertion is borne out by the phase shift that occurred between the buried and surface horizontal motion records and by the lack of shift in the vertical records.

The Superstition Hills fault is a northwest-trending fault that can be seen as a continuation of the San Andreas and San Jacinto fault zones. Evidence shows that the Superstition Hills fault delineates a section of the boundary between the steeply sloping crystalline basement and the sedimentary materials, with a great amount of historical northwest-trending tectonic activity in the region (Magistrale et al., 1989).

Seismology

On the evening of November 23, 1987, an earthquake occurred along the previously unknown Elmore Ranch fault, with an M_S of 6.2 and a hypocenter depth of about 11 km (Magistrale et al., 1989). The fault was a north-east trending, left-lateral displacement made up of a multitude of small displacements or fault zones. The maximum measured surface horizontal displacement was 125 mm, which occurred during the event itself. Twelve hours after the Elmore Ranch earthquake, a larger, long-duration earthquake struck on the Superstition Hills fault. This 6.6 M_S seismic event was caused by a northwestward-striking right lateral displacement coincident with previous earthquakes in 1968 and 1979 (Magistrale, 1989). The two 1987 temblors, Elmore Ranch and Superstition Hills, are associated with a well-defined conjugate fault system (Hudnut et al., 1989). The left-lateral motion relieved normal stress on the existent major northwest-striking fault system, allowing the shear stress from the Pacific plate to be relieved.

The Superstition earthquake was a complicated event characterized by an extended period of strong motion (Wald et al., 1990). Figure 2 shows the acceleration record for the north-south acceleration, recorded at a depth of 8 meters. There appears to be arrivals of energy at approximately 3 and 9 seconds following the arrival of the initial S-wave. Thorough and independent study of the strong motion and teleseismic records by several researchers indicates the event was made up of three distinct subevents that had to have occurred over an extended area (Hwang et al., 1990; Wald et al., 1990; Frankel and Wennerberg, 1989) The physical location of these subevents is given in Fig. 3 in both the map and plan view. While all three studies reached essentially the same general conclusions, the study by Wald et al. was the most exhaustive and their quantitative results will be used in this paper.

Wald et al. (1990) calculated the arrival times relative to initial energy arrival, seismic magnitude, and horizontal extent of the three subevents. While the M_S of the three subevents are very similar, the energy released by subevent 3, characterized by the seismic moment, is almost 3 times larger than the combined energy release of the first two subevents. The source durations of the first two subevents were short (less than 2 s for subevent 2), while it was estimated that subevent 3 required about 7.5 s for the displacement to propagate the 18 km (Wald et al., 1990). The calculated arrival times of the three subevents are shown in Fig. 2, exactly matching the visually perceived arrival of packets of energy. The extended shaking due to subevent 3 continued for slightly longer than the 7.5 s duration of source displacement. While the propagation velocity of each subevent was greater or equal to the S-wave velocity, the very slow rupture velocity for the entire earthquake implies an overall rupture mechanism reminiscent of progressive failure (Frankel and Wennerberg, 1989).

Pore Pressure History

Analysis of pore pressure histories recorded during the Elmore Ranch and Superstition Hills earthquakes yields additional understanding of the mechanistic behavior of the Wildlife site. Complete pore pressure records were made during both temblors at five different depths (Brady et al., 1989). Records show that an increase in pore water pressure was measured during both the Elmore Ranch and Superstition Hills earthquakes.

This paper will focus on the pore water pressure history of piezometer P5, which was buried at a depth of 2.9 m, the top of soil layer B1. This transducer is being singled out for several reasons: it unambiguously indicated that the excess pore pressure exceeded the total overburden pressure; it was located at the top of the layer expected to liquefy during the Superstition Hills shaking and therefore would be at the point of initial liquefaction (Scott, 1987; Florin and Ivanov, 1962).

Figure 4 introduces the pore pressure ratio r_u (ratio of excess pore pressure u to initial effective overburden stress $\bar{\sigma}_v$) history for piezometer P5, Superstition Hills earthquake, compared to the acceleration record of Fig. 2 (Brady et al., 1989). The pore pressure history is addressed here to enhance mechanistic understanding of the recorded strong motion signals and thus simplify and strengthen later interpretation. There is some controversy whether the pore pressure transducers at the site were operating properly (Hushmand et al., 1992, 1991), however, it was decided to utilize what clues the data provides without making a value judgement.

At time t_0 (Fig. 4) the initial S-wave energy from the first subevent arrived, and a very slight increase in pore pressure was recorded by P5. At approximately time $t_{3.1}$ (subscript is elapsed time) energy from subevent 2 excited the accelerometer, and the pore pressure started to increase at a steady rate. Finally, at time $t_{9.8}$ strong shaking was triggered by the arrival of subevent 3, and the pore pressure ratio at P5 increased at a rapid rate to a maximum greater than 1.2. After $t_{9.8}$ the rate of increase of r_u was relatively constant for the duration of source motion ($\approx$7.5 s), until it reached 0.6, a level often considered as functional liquefaction. The rate of pore pressure increase slowed until approximately time t_{23}, at which time r_u was approximately 1 and the rate of increase remains nearly constant. This strong correlation between pore pressure and seismic history indicates more than serendipity.

IDENTIFICATION OF THE WILDLIFE SITE SOIL SYSTEM

Analysis Methods

For the problem at hand, estimating the soil parameters during the Superstition Hills earthquake at the Wildlife site, both the system input and output are known. Analysis of the records was undertaken using the standard routines contained in the MATLAB System Identification Toolbox (MathWorks, 1991). Since there is little known about the statistics of the system, a direct method was used to determine whether a given model accurately captured the system — the output simulated by the calculated system had to accurately model the actual measured output.

The input-output data record was initially broken into segments based on the mechanistic understanding discussed in previous sections. Segment 1 is the segment from the start of the time history to the arrival of subevent 2 at approximately $t_{2.8}$ seconds (171 data points). Segment 2 runs from the arrival of subevent 2 to the arrival of subevent 3 at approximately $t_{8.8}$ seconds (150 data points). The segment corresponding to the shaking due to subevent 3 is assumed to be very non-stationary due to the nature of the signal and the rapid rise of pore pressure. Segment 3 encompassed the coda of the signal after the shaking stopped at approximately t_{17} seconds, to the end of the record at 93 seconds (1870 data points). If the stationary model could not accurately and parsimoniously simulate the segment output, a non-stationary recursive model was used. In addition, the residual autocorrelation function, and the cross-correlation function between the input and output residuals were white with 99 percent confidence (Bohlin, 1987). A final verification on independent input-output data was made using the 90° Superstition Hills record, and the Elmore Ranch time histories.

Once the relevant model is determined and the parameters calculated, a spectral representation of the system is easily obtained from Eqn. 4. The statistical approach used in parametric modeling allows the calculation of confidence intervals of the spectral estimate. The modal natural frequencies ξ_j, percent of critical damping ω_j, (Ghanem et al., 1991) and power participation factor p_j (Pandit, 1991; Safak, 1988) are calculated from the system poles and residues found from partial-fraction expansion of Eq. 2.

Results

The first two segments, corresponding to the beginning of the record up to the arrival of subevent 3, can be accurately modeled by stationary ARX models. Segment 1 is modeled as a 4-DOF system, with an RMS error between simulated and actual velocity of 0.26. Segment 2 proved to be representable as a 3-DOF system, with an RMS error between simulated and actual velocity of 1.1. A comparison of the spectral estimates is shown in Fig. 5, along with the estimates of modal parameters. These values are summarized in the top of Table 1. Note that the system natural frequency diminished slightly after the arrival of subevent 2, an indication of system softening.

The change in the soil system was so slight during the initial 8.8 s of excitation, that it proved possible to model a combined initial segment (subevents 1 and 2) accurately with one 4-DOF ARX model (RMS error = 0.59), with the characteristics of the second subevent swamping the lower energy first arrival. The suitability of this model is verified by comparing the actual surface velocities from the Elmore Ranch 360° horizontal record with the record simulated for the relevant Elmore Ranch input by the selected model. The congruity between simulation and real-life is shown in Fig. 6, which match with an RMS error of only 0.72.

In order to see the evolution of the soil system through the initial 20 s of the Superstition Hills earthquake, the system was modeled with a recursive technique employing a Kalman filter model with 3-DOF. The spectral time history of the top 8 m of the Wildlife site for the initial 20 s of shaking is shown in Fig.7. The softening corresponds with the initial increase in pore water

pressure to about 3.1 kPa, accounting for the downward shift in natural frequencies and increase in damping.

The system behavior during the subevent 3 strong shaking is obviously non-stationary and non-linear due to the rapid build-up of pore water pressure and irregular shaking. The point at which a stationary model could no longer model the system behavior corresponds to the time when the pore pressure ratio reached approximately 0.6, at $t_{16.5}$. The modal estimates from a Kalman filter model showed that the natural frequency diminished and damping ratio increased as the effective stress in soil layer B decreased, and are summarized in the bottom of Table 1.

The final segment (post-energy input) proved to be quite non-stationary due to the constant increase in phase shift between buried and surface signals, and it was not possible to accurately model the soil as a time invariant system. Application of a 3-DOF, 0 delay Kalman filter captures the essence of the soil response through time (RMS error = 0.76), with the spectral time history shown in Fig. 8. As indicated by the time dependent values for resonant frequency and damping, the soil system is slowly changing as the pore water pressure comes to equilibrium.

CONCLUSIONS

The Wildlife Site, CA was subjected to two large earthquakes on November 24, 1987. During the second, larger, earthquake (Superstition Hills earthquake) the site liquefied. The data collected are unique since they are the only available records of buried and surface motions publicly available. In addition, pore water pressure records were recorded at several depths during the temblor.

The Superstition Hills earthquake was actually three distinct subevents. The third subevent was the largest, associated with displacement along 18 km of fault. The strong motion records and pore water pressure records were examined, and showed excellent correlation with the subevents. A significant rise in pore pressure that resulted in liquefaction of layer B occurred at the onset of subevent 3.

Both stationary and recursive parametric modeling methods are applied to the unique input-output data set from the two temblors. These unique results show weakening of the soils system as pore pressure increased. A summary of the calculated dynamic system properties is given in Table 1. The parametric models used in this study are powerful tools for the qualitative and quantitative estimation of in situ soil properties. The recursive methods allow the behavior of the soil system to be monitored throughout the excitation process and liquefaction. Figures 7 and 8 present a unique insight into the liquefaction process. The confidence in the estimates is increased by comparison with independent data from the E-W direction, and the Elmore Ranch temblor. The estimates all converged on the values reported. The soil was 'tested' in its natural condition, with no man-made disturbances or other difficulties encountered in the laboratory.

BIBLIOGRAPHY

Bennett, M. J., McLaughlin, P. V., Sarmiento, J. S., & Youd, T. L. (1984). *Geotechnical investigation of liquefaction sites, Imperial Valley, California,* Open File Report 84-252. p. 103. Menlo Park, CA: United States Geological Survey.

Bierschwale, J. G. (1984). Analytical evaluation of liquefaction potential of sands subjected to the 1981 Westmoreland earthquake. *University of Texas geotechnical engineering report GR-84-15. p.* 231. Austin TX: University of Texas Geotechnical Engineering Center.

Bohlin, T. (1987). Model validation. *Encyclopedia of systems and control* (Singh, M.) Oxford: Pergamon Press.

Bracewell, R. N. (1978). *The Fourier transform and its applications.* p. 443. New York: McGraw-Hill.

Brady, A. G., Mork, P. N., Seekins, L. C., & Switzer, L. C. (1989). *Processed strong-motion records from the Imperial Wildlife liquefaction array, Imperial County, California, recorded during the Superstition Hills earthquakes, November 24, 1987.* Open File Report 97-87. p. 115. Menlo Park, CA: United States Geological Survey.

Florin, V. A., & Ivanov, P. L. (1961). Liquefaction of saturated sandy soils. *Proceedings of the fifth international conference on soil mechanics and foundation engineering. I* Paris. 107-111. Paris: Dunod.

Frankel, A., & Wennerberg, L. (1989). Rupture Process of the MS 6.6 Superstition Hills, California, earthquake determined from strong-motion recordings: application of tomographic source inversion. *Bulletin of the Seismological Society of America,* 79(2), 515-541.

Gersch, W., & Luo, S. (1972). Discrete time series synthesis of randomly excited structural system response. *Journal of the acoustic society of America, 51*(1), 402-408.

Ghanem, R. G., Gavin, H., & Shinozuka, M. (1991) *Experimental Verification of a number of structural system identification algorithms.* p. 302. Technical Report NCEER-91-0024. Buffalo: National Center for Earthquake Engineering Research.

Glaser, S. (1993). *Estimating soil parameters important for lifeline siting using system identification techniques.* NISTIR 5145. p. 91. Gaithersburg, MD:NIST.

Holzer, T. L., Youd, T. L., & Bennett, M. J. (1989). In situ measurement of pore pressure build-up during liquefaction. N. J. Raufaste, *Proceedings of the 20th joint panel meeting of the U.S.-Japan cooperative program in wind and seismic effects. 24* Gaithersburg, MD. (NIST SP 760) 118-130.

Hudnut, K. W., & Sieh, K. E. (1989). Behavior of the Superstition Hills fault during the past 330 years. *Bulletin of the Seismological Society of America,* 79(2), 309-329.

Hushmand, B., Scott, R. F., & Crouse, C. B. (1992). In-place calibration of USGS pore pressure transducers at Wildlife Liquefaction Site, California, USA., *Proceedings of the Tenth World Conference on Earthquake Engineering. 3* Madrid. 1263-1268. Rotterdam: Balkema.

Hushmand, B., Scott, R. F., & Crouse, C. B. (1991). In-situ calibration of USGS piezometer installations. *Recent advances in instrumentation, data acquisition and testing in soil dynamics.* G.S.P. 29, Orlando, FL. 49-69. ASCE: New York.

Hwang, L. J., Magistrale, H., & Kanamori, H. (1990). Teleseismic source parameters and rupture characteristics of the 24 November 1987, Superstition Hills earthquake. *Bulletin of the Seismological Society of America,* 80(1), 43-56.

Johansson, R. (1993). *System identification and modeling.* p.512. Englewood Cliffs, NJ: Prentice-Hall.

Kalman, R. E. (1960). A new approach to linear filtering and prediction problems. *Transactions of the ASME, journal of basic engineering,* (3), 35-45.

Ljung, L. (1987). *System identification: theory for the user.* Englewood Cliffs, NJ: Prentice-Hall.

Ljung, L. (1979). Asymptotic behavior of the extended Kalman filter as a parameter estimator for linear systems. *IEEE transactions on automatic control, AC-24*(1), 36-50.

Magistrale, H., Jones, L., & Kanamori, H. (1989) The Superstition Hills, California earthquakes of 24 November 1987). *Bulletin of the Seismological Society of America*, 79(2), 239-251.
MathWorks, (1991). *System identification toolbox*, (Ljung, L. J.). Natick, MA: The MathWorks Inc.
Nazarian, S., & Stokoe II, K. H. (1984). In situ shear wave velocities from spectral analysis of surface waves. *Proceedings, eighth world conference on earthquake engineering. III* San Francisco, CA. 31-38. Englewood Cliffs: Prentice-Hall.
Pandit, S. M., (1991). *Modal and spectrum analysis: data dependent systems in state space*. p. 415. New York: Wiley.
Robinson, E. A. (1982). A historical perspective of spectrum estimation. *Proceedings of the IEEE, 70*(9), 885-907.
Safak, E. (1988). *Analysis of recordings in structural engineering: adaptive filtering, prediction, and control.* (Open-File Report 88-647). Menlo Park, CA: U.S. Geological Survey.
Scott, R. F. (1986). Solidification and consolidation of a liquefied sand column. *Soils & foundations, 26*(4), 23-31.
Sorenson, H. W. (1970). Least-squares estimation: from Gauss to Kalman. *IEEE spectrum*, 7(7), 63-68.
Wald, D. J., Helmberger, D. V., & Hartzell, S. H. (1990). Rupture process of the 1987 Superstition Hills earthquake from the inversion of strong-motion data. *Bulletin of the Seismological Society of America*, 80(5), 1079-1098.

TABLES

Table 1 Summary of system parameters estimated for pertinent times during the Superstition-Hills earthquake.

	1st Mode			2nd Mode			3rd Mode		
Time (s)	**f (Hz)**	**ζ (%) crit.**	**p**	**f (Hz)**	**ζ (%) crit.**	**p**	**f (Hz)**	**ζ (%) crit.**	**p**
*-4:2.8**	*3.7*	*4*	*0.82*	*6.2*	*16*	*-0.03*	*11*	*14*	*-2.5*
*2.8:8.8**	*2.4*	*87*	0.26	3.5	*15*	*0.95*	9.2	*7*	*-0.72*
26♣	0.8	5	0.19	5.3	22	0.26	10.1	*9*	0.43
32♣	0.42	27	0.13	5.3	27	0.24	10.1	*13*	0.31
37♣	0.35	34	0.10	5.3	28	0.24	10.1	*14*	0.30
56♣	0.35	20	-0.02	5.8	44	-0.20	10.0	*23*	0.22
72♣	0.21	45	0.08	7.1	66	0.50	9.8	*31*	0.41

f = resonant frequency; ζ = critical damping; P = participation factor.

NOTE – * indicates ARX (stationary) estimate using combined model; ß indicates instantaneous Kalman (recursive) estimate (i.e., the best values for the point in time shown).

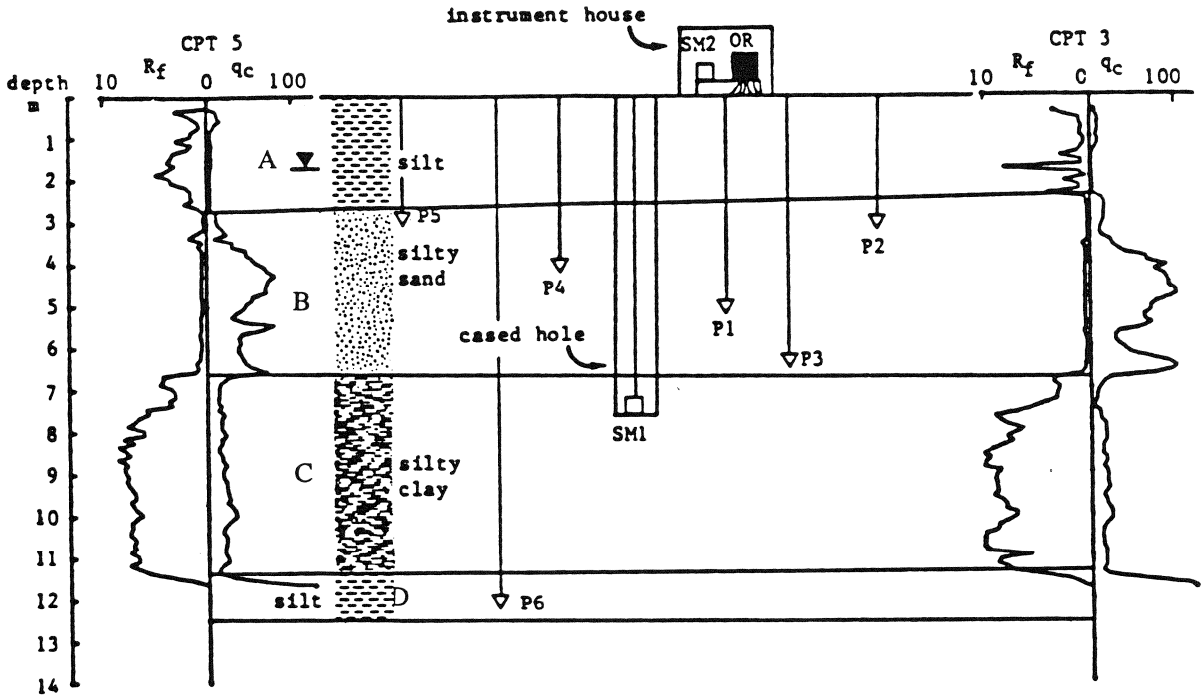

Fig. 1 Layout of the instrumentation at the Wildlife Site (Bennett et al., 1984).

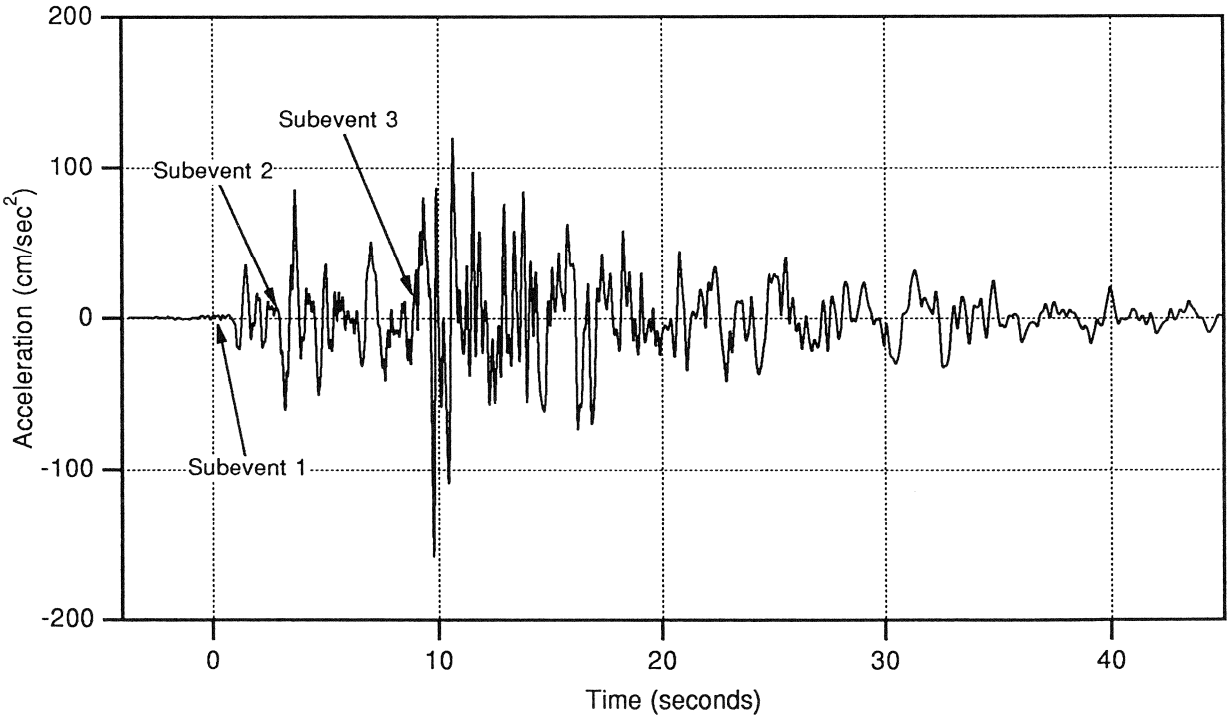

Fig. 2 Acceleration record at a depth of 8 m, N-S direction, Superstition Hills earthquake.

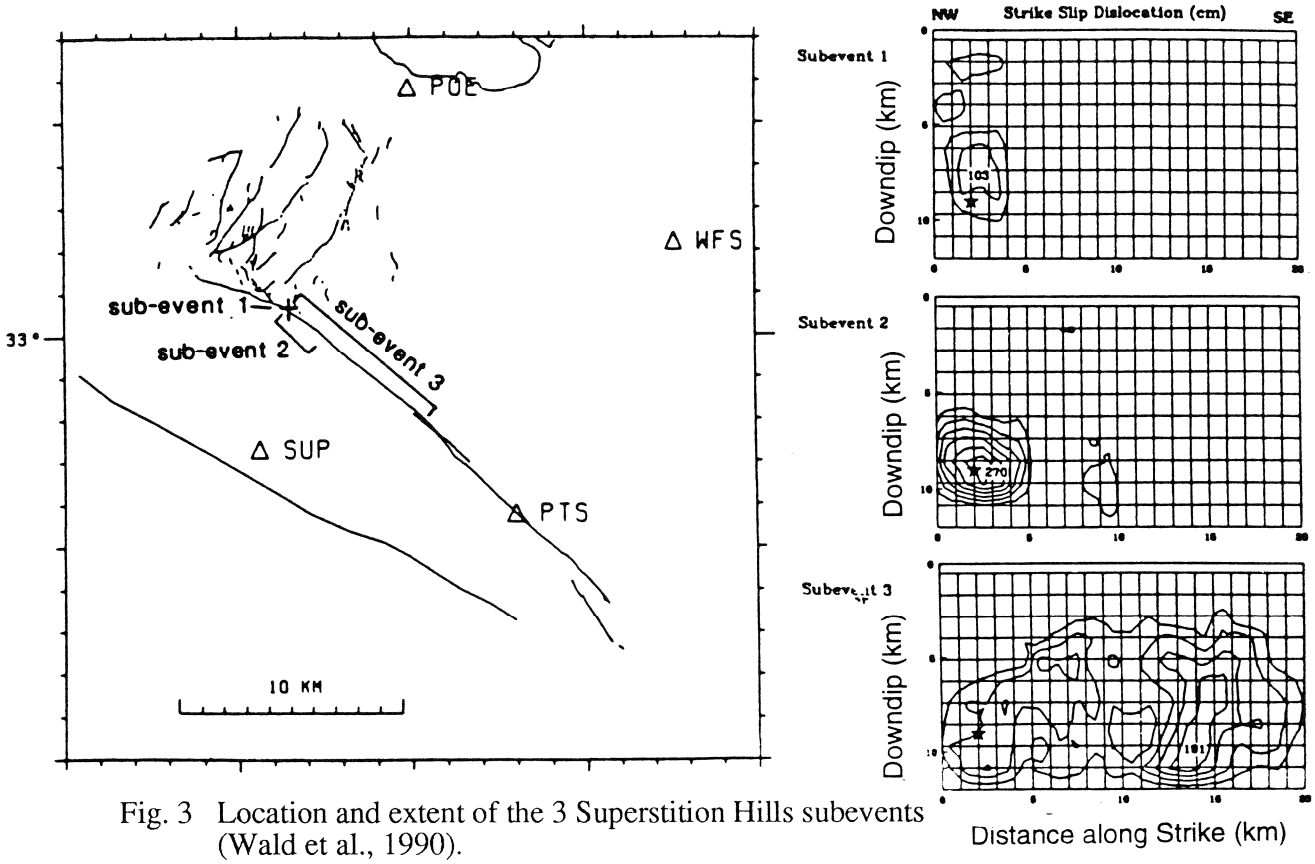

Fig. 3 Location and extent of the 3 Superstition Hills subevents (Wald et al., 1990).

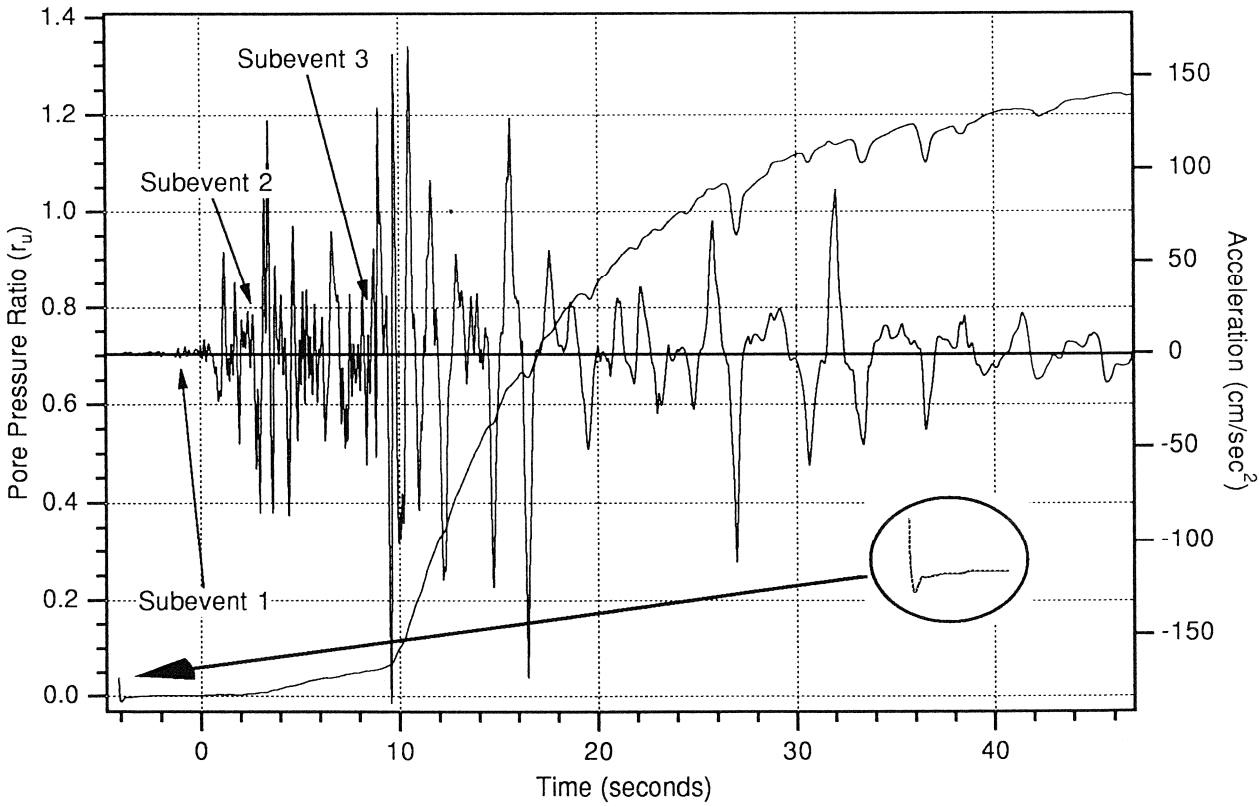

Fig. 4 Pore pressure ratio history compared to top N-S acceleration. Note warm-up detail in inset.

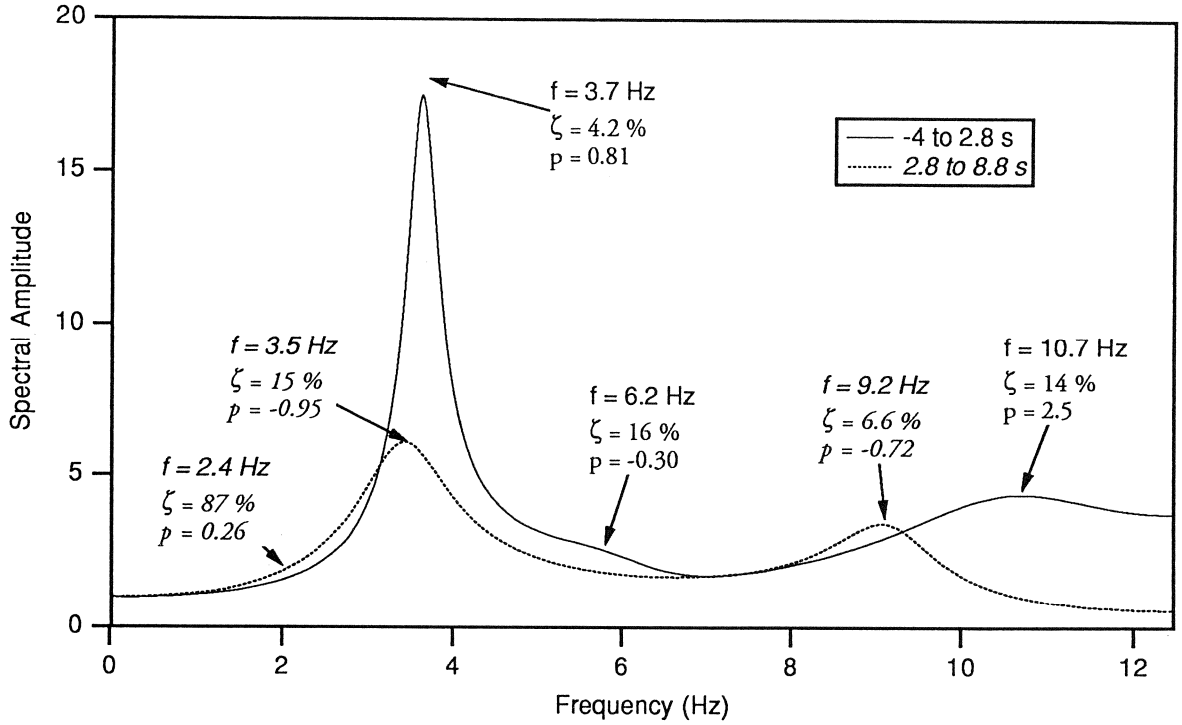

Fig. 5 Spectral estimates for the first and second segments, with estimates of natural frequency, damping ratio, and participation factor.

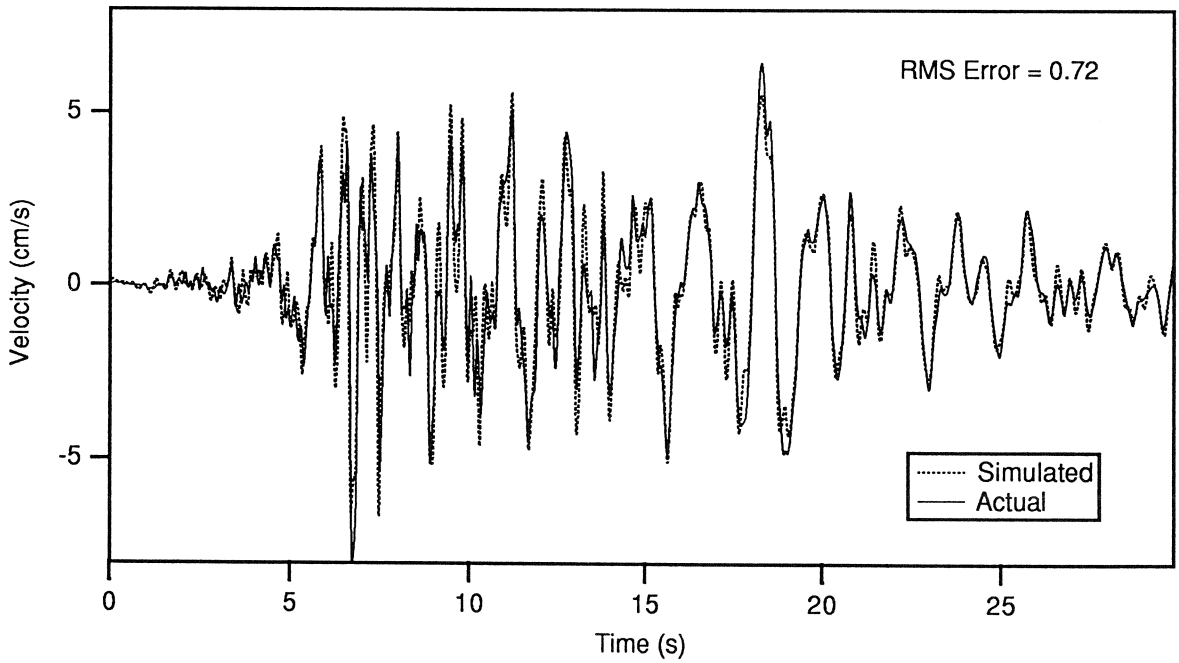

Fig. 6 Comparison between the Elmore Ranch velocity history simulated by the second segment Superstition Hills filter, and the actual velocity history.

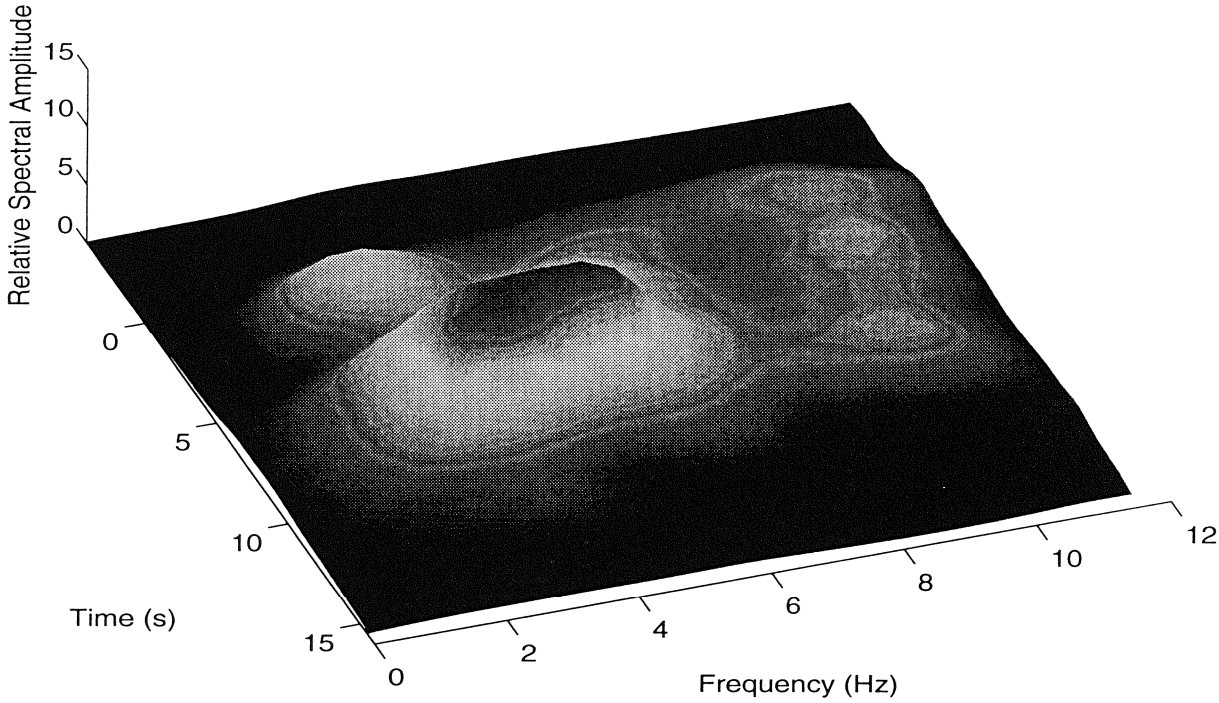

Figure 7 Soil system evolutionary time history for the initial 20 s of the Superstition Hills earthquake. The changing system is shown in spectral representation.

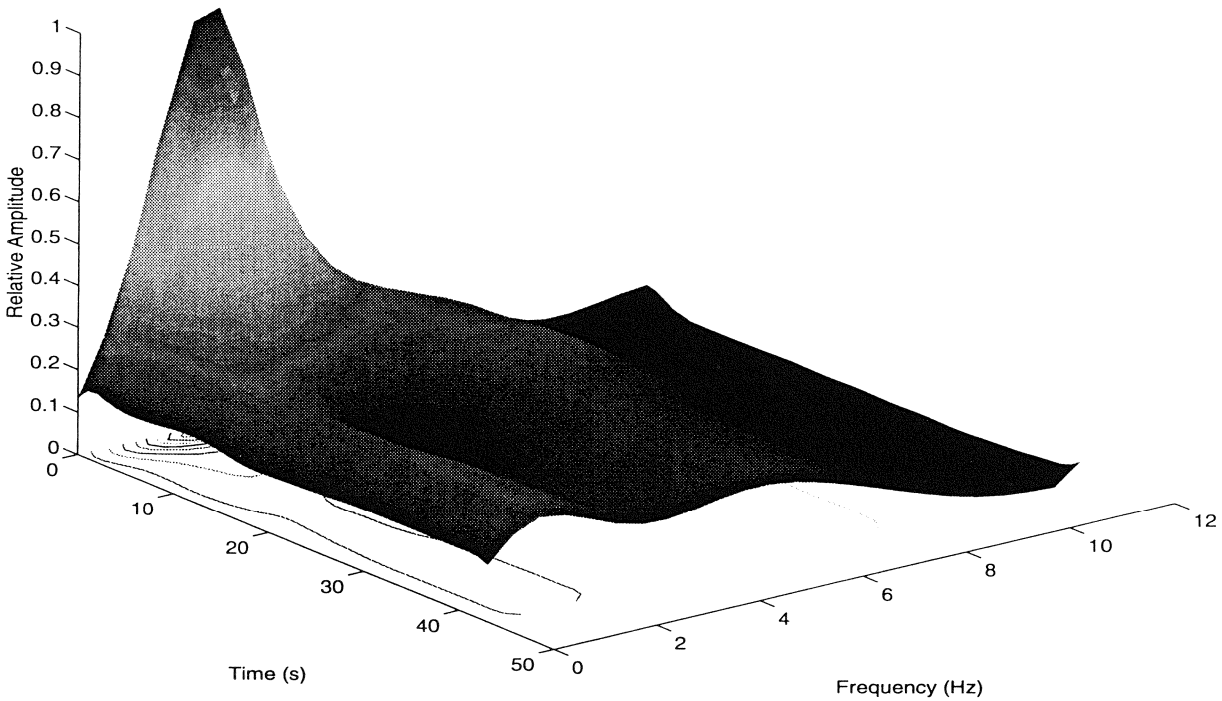

Figure 8 Soil system evolutionary time history for the coda of the Superstition Hills earthquake. The changing system is shown in spectral representation.

Recent Research on Liquefaction of Silts and Silty Sands at Santa Clara University

Sukhmander Singh*

Abstract

The paper presents a summary of the results of cyclic triaxial load testing of samples of silt, and silty sands. The paper emphasizes differences in behavior observed between reconstituted triaxial samples of clean sand, of sand containing 10, 20, 30 and 60 percent silt, pure silt, and undisturbed samples of silt and silty sand. An important observation is that the mechanisms of deformation for silt are different for reconstituted and undisturbed samples, the undisturbed sample having a specific "geologic" structure which seems to slow down the excess pore water pressure accumulation, but which still results in cyclic deformations regularly increasing from the very beginning of the test and rapidly reaching high levels. The other important observation is that fine grained non-cohesive soils such as silts and silty sands can be as or even more susceptible to liquefaction as clean sands. Test results on samples of sands containing 10, 20 or 30 percent of silt indicate lesser resistance to liquefaction than that of pure sand samples. The paper shows the difficulty in identifying a representative parameter to compare the behavior of silts and silty sands with pure sand, and it seems that more research will be needed in this area.

Introduction

Liquefaction behavior of silts and silty sands is routinely evaluated or studied in terms of the parameters used for sands. However, testing of undisturbed samples of silts (Singh and Chew, 1988) indicated that the pore pressure generation and deformation characteristics of silty samples were quite different than that of sand samples. In order to resolve this a systematic study of the cyclic strength behavior of laboratory prepared samples of sand containing different percentages of silt and pure silt were undertaken to compare with test results from undisturbed samples, and to re-examine the influence of non-cohesive fines (silts) on the liquefaction behavior of sands.

Test Results on Undisturbed Samples

A wide range of undisturbed samples of silts, silty sands, and claying silt were tested and results were discussed by Singh and Chew (1988). With the exception of very loose silts, large strains occurred more quickly in the silts as opposed to the sands, while pore pressure buildup was slower in the silts (**Figure 1**).

---

*Professor and Chairman Department of Civil Engineering, Santa Clara University, Santa Clara, California 95053, U.S.A.

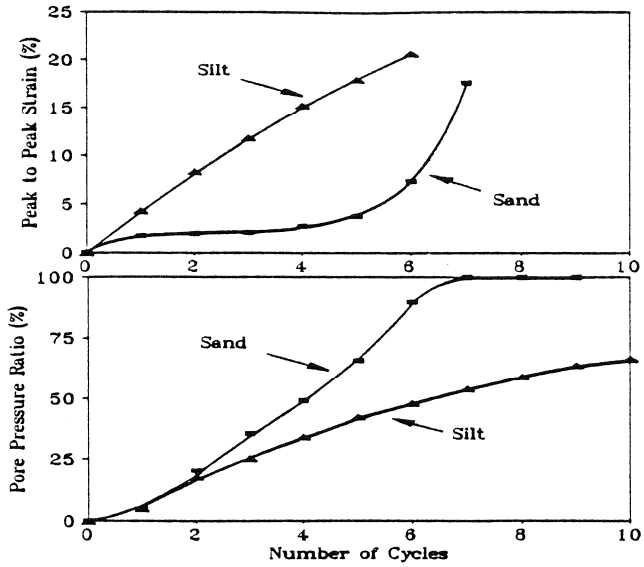

Fig. 1. Strain and pore pressure development in a typical silt and loose sand (from Singh and Chew, 1988)

The behavior of silty sands with less than 20 percent silt was dominated by the sands, while sandy silts with more than 60 percent silt would be controlled by the silt. On the basis of these observations, it appears that the pore pressure buildup was not a good criteria for undisturbed but large straining silts during cyclic loading because the large strains are observed before significant pore pressure buildup occurs.. For more detailed discussions, the reader is referred to a more recent work by Singh (1994).

Test Results on Reconstituted Samples

Flint shot #4 sand, a uniform sand, was used for testing. Uniform non-cohesive silt was obtained by sieving fine sand from Pasadena, California, through a #200 sieve. Moist tamping method was used for sample preparation. Preparation of silt samples was a challenge. In all of the test series involving silt, it was found that the results were very sensitive to the mixing moisture and tamping procedure for sample preparation. Consistencies in all aspects such as mixing, tamping and handling were very important to achieve consistent results. The presence of a somewhat weaker layer was readily evident from the manner in which the sample would fail. Further details of sample preparation are given in Singh (1994). Figure 2 shows the relationship between cyclic stress ratio and number of cycles to initial liquefaction for reconstituted samples of pure sand, pure silt and silty sand.

It may be noted from **Figure 2** that sands containing 10, 20, or 30 percent of silt have lesser cyclic strength than that of 100 percent sands. These samples were prepared to approximately the same relative density of 50%. Maximum and minimum densities were determined separately for each case, and 50% relative density estimated from the maximum and minimum densities. It has been suggested that relative density is not a suitable index for characterizing behavior of silty sands (Ishihara et al., 1980). Laboratory controlled studies on the

effect of silt content on cyclic strengths of clean sands have been reported by Chang et al. (1982) and Kuerbis et al., 1988).

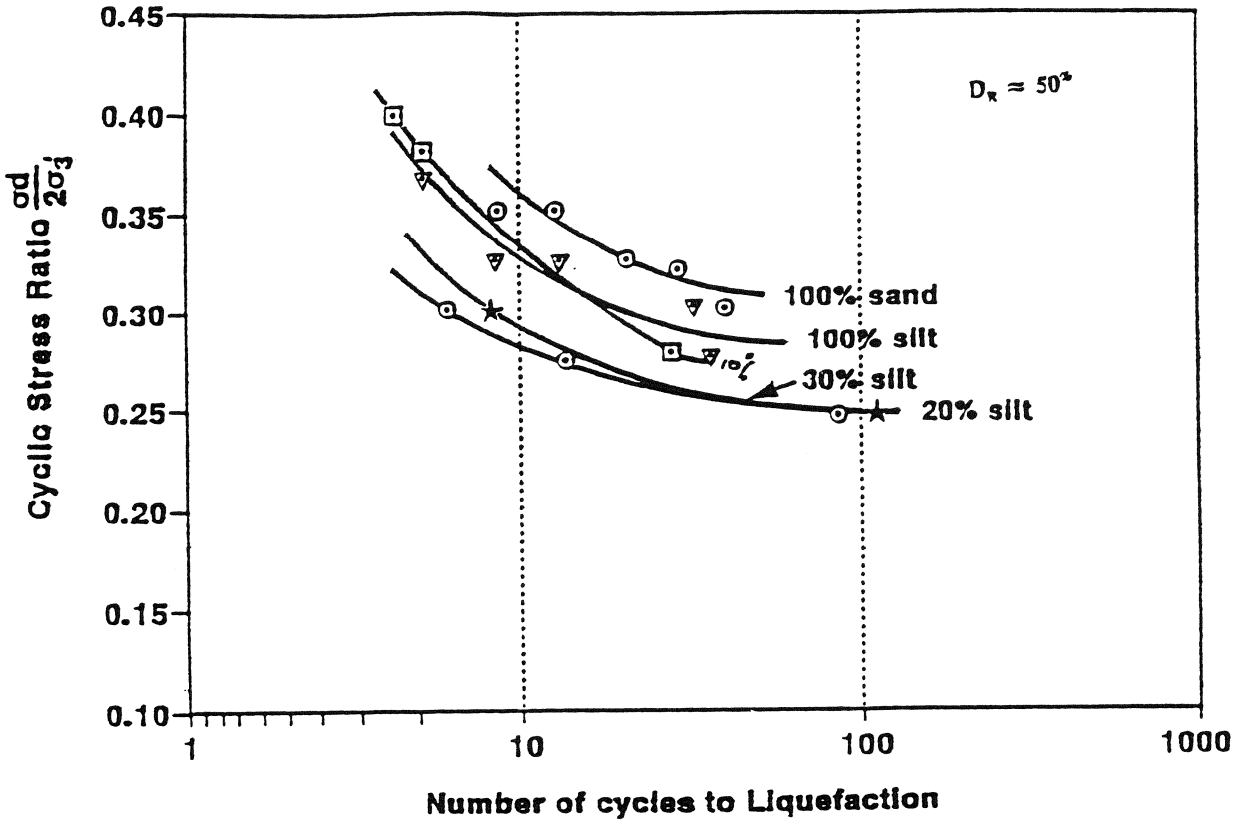

Fig. 2. Relationship Between Cyclic Stress Ratio and Number of Cycles to Initial Liquefaction for Reconstituted Samples of Sand, Silty Sand and Silt (from Singh, 1994)

Chang et al. used void ratio as the basis for comparison and tested silty sand samples at the same void ratio as the 100 percent sand samples, and concluded that the cyclic resistance increases as the silt content increases; that the increase is slight, up to 10% silt content, and begins to develop more as the silt content increases to 30 % silt. Chang et al. explains this behavior in terms of sand grain to sand grain contact in the soil structure. But it appears to be due to the increase in relative density as the more silt is added and the samples are prepared at the same void ratio.

Studies by Kuerbis et al. (1988) suggest that the higher the silt content, the lower the cyclic resistance for given relative density. Studies reported herein indicate similar results (Figure 2). Kuerbis et al. also reported that over the range of overlapping void ratios of various silty sands, the cyclic resistance at a given void ratio decreases with increase in silt content. Kuerbis et al. used the concept of sand-skeleton void ratio to explain the results and concluded that the rather small change in behavior with increasing silt can be explained by the fact that the sand skeleton void ratio remains virtually unaltered with the addition of silt. Silt merely acts as a filler

of sand skeleton voids and hence behaves as an inert component (up to about 20% of silt). Tokimatsu and Yoshimi (1984) and Seed et al. (1985) suggested on the basis of field performance of sandy soils with fines that soils containing more than 20% clay (finer than 5μm) would hardly liquefy unless their plasticity indexes are low.

From the foregoing, it appears that it is not easy to clarify the influence of fines on the behavior of sands under cyclic loading, and that the liquefaction characteristics of silts may not be estimated on the basis of criteria currently used for sands. In an attempt to explain the behavior in terms of void ratio, **Figure 3** was prepared; and it appears that whereas, void ratio may be the

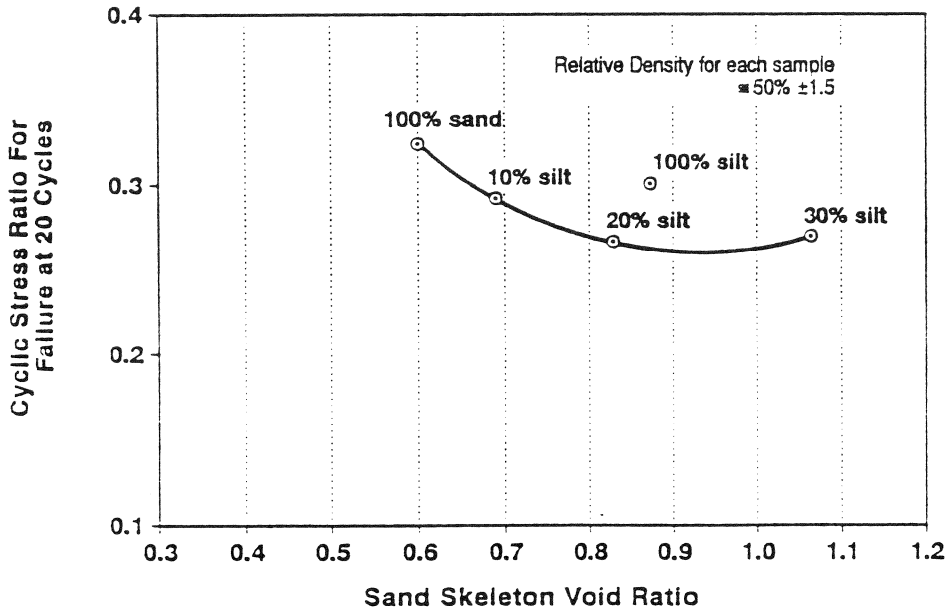

Fig. 3. Relationship between Cyclic Stress Ratio and Sand Skelton Void Ratio (from Singh, 1994)

better index than relative density, to explain the influence of fines on sand behavior, the interpretation in terms of void ratio alone beyond a percentage of fines of 60% (**Figure 4**) need further studies and should be made with caution. As also pointed out by Chang, et al. (1982), it appears that when the silt content reaches 60 percent or more, the soil fabric becomes one of sand grains embedded in silt with practically no sand grain to sand grain contact, so the specimen behavior is totally determined by the silty fines. conversely, it may be suggested that a silt sample containing about 30 percent or more of sand content will have its pore pressure generation characteristics approaching that of sand. However, additional data is needed to draw definitive conclusions on this aspect.

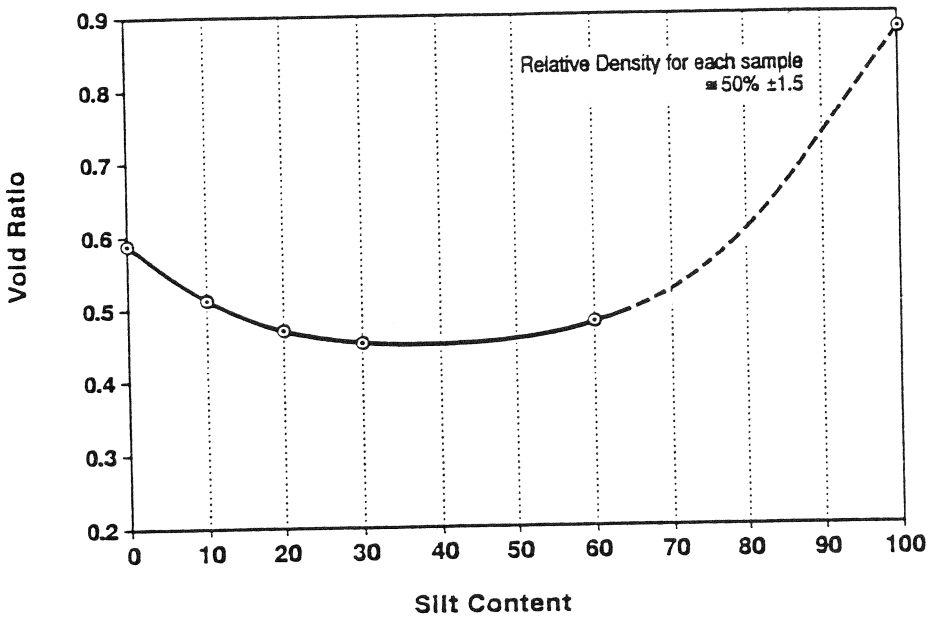

Fig. 4. Effect of Silt Content on the Void Ratios of Samples Prepared at 50% Relative Density (from Singh, 1994)

Conclusions

On the basis of the studies reported herein, the following conclusions may be drawn:

1. There is a difference in the strain developments and the pore pressure generation characteristics of undisturbed and laboratory prepared samples of silts tested under cyclic triaxial loading conditions.

2. There is a problem in establishing criteria for liquefaction of undisturbed silts in terms of joint consideration of pore pressure and deformation.

3. For a given relative density, sands containing 10, 20 or 30% of silt by weight have lesser resistance to liquefaction than pure sands. The loss of resistance appears to be consistent when results are compared in terms of void ratio, thus implying that void ratio may be a better index to use for silty fine sands and silts.

4. One hundred percent silt samples tested at the same relative density as the 10, 20, and 30% silt in sand showed higher strengths, but not higher than pure sands.

Acknowledgements

The research reported herein was supported through the National Science Foundation Grant No. 9013422 and is gratefully acknowledged. Dr. David G. Toll of Durham University is acknowledged for his constructive suggestions. Manjula R. Mannem along with Aparna and Ray Davies meticulously performed the cyclic triaxial testing and assisted in the research. Their efforts are highly appreciated.

References

1. Chang, N.Y., S.I. Yeh, and L. P. Kaufman, (1982), "Liquefaction Potential of Clean and Silty Sands," Third International Earthquake Microzonation Conference, Proceedings, Seattle, Washington, Vol. II, pp. 1017-1032.

2. Ishihara, K., Troncosco, J., Kawase, Y., and Takahashi, Y. (1980). Cyclic Strength Characteristics of Tailings Materials. *Soils and Found*, 20(4):127-142.

3. Kuerbis, R., D. Nequssey, and Y. P. Vaid, (1988), "Effect of Gradation and Fines Content on the Undrained Response of Sand," Proceedings, of the ASCE Geotechnical Division Specialty Conference on Hydraulic Fill Structures, Colorado State University, Fort Collins, Colorado, August.

4. Prakash, S. and V. K. Puri, (1982), "Liquefaction of Loessial Soils," Third International Earthquake Microzonation Conference, Proceedings, Seattle, Washington, Vol. II, pp. 1101-1107.

5. Seed, H. B., K. Tokimatsu, L. F. Harder, and R. M. Chung, (1985), "Influence of SPT Procedures in Soil Liquefaction Resistance Evaluations," Journal of Geotechnical Engineering Division of ASCE, Vol. III, No. 12, December.

6. Singh, S., and R. Y. Chew, (1988), "Dynamic Strain in Silt and Effect on Ground Motions," Paper presented and published at American Society of Civil Engineers Division of the Geotechnical Engineering's Earthquake Engineering and Soil Dynamics Ii conference, Park City, Utah, June 27-30.

7. Singh, S., (1994) "Liquefaction Characteristics of Silts," Geotechnical Special Publication of Session 27 on Ground Failures Under Seismic Conditions (Silty Soils), American Society of Civil Engineering 1994 Annual Convention and Special Exposition, Atlanta, Georgia, October 9-13.

8. Tokimatsu, K., and Y. Yoshimi, (1984), "Criteria of Soil Liquefaction with SPT and Fines Content," Proceedings, of the 8th World Conference on Earthquake Engineering, Vol. III, San Francisco, California, July.

9. Zhaoji, S., (1988) "Study of Silt Liquefaction During Earthquakes," Institute of Engineering Mechanics, SSB Harbin, China.

CANLEX (Canadian Liquefaction Experiment):

A One Year Update

P.K. Robertson[1], B.R List[2] and B.A Hofmann[1]

[1] University of Alberta,
[2] Syncrude Canada Ltd.

ABSTRACT

The Canadian Geotechnical engineering community has embarked on a major study regarding the liquefaction of sand entitled The Canadian Liquefaction Experiment (CANLEX) through a collaborative effort of industry, engineering consultants and university participants, with the support of the Natural Sciences and Engineering Research Council of Canada (NSERC). The study is examining the characterization of sand for dynamic and static liquefaction. The project was started in 1993 and is expected to last at least 3 years with equal funding by both industry and NSERC for a total of about C$1.8M. This paper provides a brief progress report on the Project. Three test sites have been selected and characterized using in-situ testing, conventional sampling as well as in-situ freezing to obtain undisturbed samples. Laboratory testing is underway on both reconstituted samples and undisturbed samples. A full scale liquefaction event is planned for year three of the Project and a feasibility study regarding the event has been completed. As part of the planning for the liquefaction event some preliminary centrifuge testing has been carried out. A static liquefaction flow failure has been successfully produced in the centrifuge. As part of the Project, a set of definitions for liquefaction have been defined and a flow chart developed to aid in the liquefaction analyses.

INTRODUCTION

The Canadian Geotechnical engineering community has embarked on a major study regarding the liquefaction of sand entitled The Canadian Liquefaction Experiment (CANLEX) through a collaborative effort of industry, engineering consultants and university participants, with the support of the Natural Sciences and Engineering Research Council of Canada (NSERC). The study is examining the characterization of sand for dynamic and static liquefaction. The project was started in 1993 and is expected to last at least 3 years, with equal funding by both industry and NSERC for a total of about C$1.8M. The industry participants are B.C. Hydro, Quebec Hydro, Syncrude Canada Ltd., and Suncor Inc. The geotechnical consultants are AGRA Earth and Environmental Limited, EBA Engineering Consultants Ltd., Golder Associates Ltd., Klohn-Crippen Consultants Ltd.and Thurber Engineering. The study is also collaborative with faculty and students from the University of Alberta, University of British Columbia, Carleton University, Universite de Laval and the Universite de Sherbrooke.

In many parts of the world large structures are constructed on or comprised of sand. Examples of such structures are tailings impoundments developed by the mining industry and some of the major earth dams used for hydro electricity generation. The behavior of loose sand deposits can be difficult to predict but can have a significant financial impact on these types of structures. The characterization of loose sand deposits is an area of uncertainty in geotechnical engineering. Unlike clay deposits, it is almost impossible to obtain undisturbed samples of loose saturated sand, especially at depth, using conventional methods. The CANLEX Project enables a focused, coordinated effort by Canadian geotechnical engineers to advance our understanding in the areas of site characterization and soil liquefaction. The main objectives of the project are;

- Develop test sites to study sand characterization
- Develop economical undisturbed sampling techniques, considering that in-situ freezing is seen as the most promising technique
- Obtain a greater understanding of soil liquefaction

The Project has been divided into Phases, with each Phase extending for approximately one year. The paper predominately describes the progress during Phase I.

LIQUEFACTION

The CANLEX Project has agreed on terminology to be used to define soil liquefaction (Robertson, 1994). The following section briefly describes this terminology.

If a soil structure, such as an earth dam or tailings dam, is composed entirely of a strain softening soil and the in-situ gravitational shear stresses are larger than the ultimate steady state strength (i.e. a relatively steep slope), a catastrophic collapse and flow slide can occur if the soil is triggered to strain soften. The collapse can be triggered by either cyclic or

monotonic undrained loading. If a soil structure is composed entirely of a limited strain softening soil and the in-situ gravitational shear stresses are larger than the quasi-state strength, a catastrophic flow slide is unlikely. However, large deformations can occur before the soil stiffens as it strain hardens towards its ultimate state.

If a soil structure is composed entirely of strain hardening soil, undrained collapse and a flow slide can not occur and deformations will, in general, be small. If a soil structure is composed partly of strain softening (SS) and strain hardening (SH) soil and the SS soil is triggered to strain soften, a collapse and flow slide will only occur if, after stress redistribution due to the softening of the SS soil, the SH soil can not support the gravitational shear stresses. The trigger mechanism can be cyclic, such as earthquake loading, or monotonic, such as a rise in the ground water level or rapid undrained loading. Gu et al (1993a) used the collapse surface approach to explain the failure of the Lower San Fernando Dam shortly after the 1971 San Fernando earthquake. Gu et al (1993b) also used the collapse surface approach to explain the continued buildup of pore pressure and deformation after the 1987 Superstition Hills earthquake at the Wildlife Site in the Imperial Valley, California.

During cyclic undrained loading, almost all granular soils develop positive pore pressures due to the contractant response of the soil at small strains. If there is shear stress reversal, the effective stress state can progress to the point of zero effective stress. For shear stress reversal to occur, ground conditions are generally level or gently sloping. When a soil element reaches the condition of zero effective stress, the soil has very little stiffness and large deformations can occur during cyclic loading. For very dense soils, the cyclic loading may not be sufficient to reduce the state to zero effective stress and hence, deformations essentially stop, except those due to local pore pressure redistribution. Gu et al (1993b) showed that the deformations due to pore pressure redistribution were very small at the Wildlife Site in the Imperial Valley. If there is no shear stress reversal, the stress state can not reach zero effective stress and cyclic mobility with limited deformations will occur.

PROPOSED DEFINITIONS OF LIQUEFACTION

Based on the above description of soil behavior in undrained shear, the following definitions of liquefaction are suggested.

Flow Liquefaction

- Requires strain softening response in undrained loading resulting in constant shear stress and effective stress, (i.e. ultimate steady or critical state).

- Requires that in-situ shear stress is greater than undrained residual or steady state shear strength.

- Flow liquefaction can be triggered by either monotonic or cyclic loading.

- For failure of a soil structure to occur, such as a dam or a slope, a sufficient volume of material must show strain softening response. The resulting failure can be a slide or a flow depending on the material characteristics and slope geometry. The

resulting movements are due to internal causes and can occur after the trigger mechanism.

- Can occur in saturated, very loose granular deposits, very sensitive clays and loose loess deposits.

Cyclic Liquefaction

- Requires undrained cyclic loading where shear stress reversal or zero shear stress can develop (i.e. where in-situ static gravitational shear stress is low compared to cyclic shear stress).

- Requires sufficient undrained cyclic loading to allow effective confining stress to reach essentially zero.

- At point of zero effective confining stress no shear stress can exist. When shear stress is applied, pore pressure drops and a very soft initial stress strain response can develop resulting in large deformations. Soil will strain harden with increasing shear strain.

- Deformations during cyclic loading when effective stress is approximately zero can be large, but deformations stabilize when cyclic loading stops, unless pore pressure redistribution effects are large. The resulting movements are due to external causes and occur during the cyclic loading.

- Can occur in almost all sands provided the size and duration of cyclic loading are sufficiently large. For very dense sands the size and duration of cyclic loading will be large and hence, the condition of zero effective confining stress may not always be achieved.

- Clays can experience cyclic liquefaction but deformations at zero effective stress are generally small due to the cohesive strength at zero effective stress and deformations are often controlled by rate effects (creep).

Cyclic Mobility

- Requires undrained loading where shear stress is always greater than zero, i.e. no shear stress reversal develops.

- Zero effective stress does not develop.

- Deformation during cyclic loading will stabilize. The resulting movements are due to external causes and only occur during the cyclic loading.

- Can occur in almost any sand provided the size and duration of cyclic loading are sufficiently large and no stress reversal occurs. Can also occur in very dense sand with shear stress reversal, provided cyclic loading is not sufficient to cause zero effective stress to develop.

- Clays can experience cyclic mobility but deformations are often controlled by rate effects (creep).

PROPOSED FLOW CHART TO EVALUATE LIQUEFACTION

Figure 1 presents a suggested flow chart for the evaluation of liquefaction according to the above definitions. The first step is to evaluate the material characteristics in terms of strain softening or strain hardening response. If the soil is strain softening, flow liquefaction is possible if the soil can be triggered to collapse and if the gravitational shear stresses are larger than the ultimate residual or steady state strength. The trigger to cause collapse can be either monotonic or cyclic. Whether a slope or soil structure will fail and slide will depend on the amount of strain softening soil or limited strain softening soil relative to the strain hardening soil within the structure and on the brittleness of the strain softening soil. Dawson et al (1993) have shown that at high effective stresses some strain softening granular soils appear to become less brittle with increasing confining stress. The resulting deformations of a soil structure with both strain softening and strain hardening soils will depend on many factors, such as: distribution of soils, geometry of structure, amount and type of trigger mechanism, brittleness of strain softening soil and drainage conditions.

If the soil is strain hardening, flow liquefaction will not occur. However, cyclic liquefaction can occur due to cyclic (seismic) undrained loading. The amount and extent of deformations during cyclic loading will depend on the size and duration of the cyclic loading and on whether shear stress reversal occurs. If shear stress reversal occurs it is possible for the effective stress to reach zero and hence, cyclic liquefaction can take place. At the condition of zero effective stress large deformations can occur. If shear stress reversal does not take place or if the sand is very dense and it is not possible to reach the condition of zero effective stress, deformations will be smaller, hence, cyclic mobility will occur. Pore pressure redistribution can occur after cyclic liquefaction that can result in large deformations after the cyclic loading. Pore pressure redistribution generally takes place when a layer of low permeability soil is overlying the liquefied soil.

TEST SITES

Three sites have been selected for the initial phases of the CANLEX Project. The Phase I site is located on the Syncrude Canada Ltd. site near Ft. McMurray, Alberta (see Figure 2), and consists of hydraulically placed sand as part of the Mildred Lake Settling Basin. The Phase II sites are located in the Fraser River Delta near Vancouver, B.C. (see Figure 2) and consist of natural deposits of alluvial sand.

The Syncrude Canada Ltd. site was fully characterized during Phase I, and will be described in more detail in this paper. The Fraser River sites were fully characterized during Phase II, and will only be partly described in this paper.

Phase I Test Site (Syncrude Canada Ltd.):

The Syncrude Canada Ltd. surface mine, located near Ft. McMurray in northeastern Alberta, produced approximately 128 million tonnes of oil sand feed in 1993 generating approximately 280,000 tonnes of tailings solids daily. The Mildred Lake Settling Basin, commissioned in 1978, was designed as an all encompassing storage facility, accommodating the tailings slurry comprised of process water, sand, fine clay particles, and trace amounts of unrecovered hydrocarbons. The tailings slurry is pumped hydraulically via 600 mm diameter pipelines. Since start-up, the majority of tailings have been stored in the Mildred Lake Settling Basin, as shown in Figure 3.

Tailings sand is used to hydraulically construct containment dykes and supporting beaches of the storage facility, while the process water, released through the sand structures, is retained and re-introduced into the extraction process. This hydraulically constructed basin is currently comprised of about 600×10^6 m^3 of solids and contains approximately 280×10^6 m^3 water and fine tails in suspension. The fine tails, primarily clay particles, accumulating in the basin are allowed to settle and consolidate over time. The settling basin profile, as illustrated in Figure 4, includes a freewater layer, a consolidating fine tails zone, and a mature fine tails zone within the sand containment structure.

Two primary sand deposition techniques have been utilized to construct the settling basin containment structure: cell construction and overboarding. Cell construction techniques are utilized to develop the 17 km long perimeter dyke. Accompanied by mechanical compaction, a dense containment structure is developed. The majority of tailings is deposited through overboarding forming beaches within the perimeter dyke. The beaching techniques employed yield two modes of deposition; Beach Above Water (BAW) and Beach Below Water (BBW). Coarse tailings are the first to settle out from the point of discharge on the way to the water body forming a BAW deposit of medium density. The finer materials eventually reach and settle in the water body forming a BBW deposit of lower density. During the early stages of construction of the settling basin, some sand size tails were deposited below water to form BBW deposit of lower density in small localized parts of the basin system. These looser sand deposits, have now been covered by both BAW and cell construction and can be up to 40 m below existing ground surface. It was these looser sand deposits that were to be characterized by the CANLEX Project.

In June 1993, an initial field screening program was conducted through ConeTec Investigations Ltd. on the Mildred Lake Settling Basin to verify the exact test site location. A site was located within Cell 24 along the west portion of the perimeter dyke. The ground conditions comprise about 27 m of dense clean fine sand from BAW and cell construction. From 27 m to 40 m the sand is looser probably due to BBW construction. The phreatic surface during site characterization was at a depth of 21 m, hence the vertical effective stress from 27 m to 40 m varies from about 400 kPa to 600 kPa. The target zone for the CANLEX site characterization was from 27 m to 37 m.

A circular test site plan was developed, as shown in Figure 5. At the center of the test area in-situ freezing was carried out to obtain undisturbed samples. Around the center, at a radius of 5 m, various in-situ testing and sampling techniques were carried out. Testing included; seismic cone penetration tests (SCPT), standard penetration tests (SPT) with rod energy measurements, self-boring pressuremeter tests (SBPMT) and geophysical logging. High quality conventional sampling using a fixed piston sampler and Christiansen double

tube core sampler was also carried out. The penetration testing (SCPT and SPT) was carried out through the University of British Columbia under the direction of Professor R.G. Campanella. The field program was coordinated by Mr. M.P. Davies utilizing a Cone Testing Vehicle supplied by the B.C. Ministry of Transportation and Highways. The self-boring pressuremeter testing was carried out by Dr. J.M.O. Hughes. The SBPMT's were carried out in two parts; an initial evaluation of the pressuremeter technique was carried out in November 1993 followed by a more detailed testing program in March, 1994. Figure 6 shows a summary of the normalized penetration resistance values from the CPT's performed around the central in-situ freeze zone. The penetration resistance values have been normalized with respect to the effective vertical overburden stress and plotted against elevation. The elevation of the ground surface at the time of the field work was approximately 352 m.

The geophysical tests were completed in November 1993 and provided detailed profiles of interpreted density, moisture content and degree of saturation with depth (Plewes et al, 1989). Geophysical tools used in the field program included slim-line compensated gamma-gamma density, natural gamma, compensated neutron, resistivity and caliper measurements. The geophysical tests were carried out through Century Geophysical under the supervision of Dr. A. Küpper (AGRA Earth and Environmental Limited).

The conventional sampling was also carried out in the November field program with specially modified Fixed Piston Sampler and a Christiansen double tube core sampler under the supervision of H.D. Plewes (Klohn-Crippen Consultants Ltd.). A total of 17 piston samples of approximately 0.5 m length, totalling about 15 m of continuous core were successfully retrieved. Samples were frozen at the ground surface to improve handling and transportation. Details of the geophysical and conventional sampling procedures are given by Plewes et al, (1988) and Plewes et al., (1993).

Phase II Test Sites (Fraser River Delta)

A careful review and classification of over 14 potential sites was carried out by a team of engineers from the Vancouver area. Many different sites were reviewed and a short list developed. Two sites were selected for detailed site characterization. As with the Phase I site, a clear selection criteria was developed in order to select the most suitable sites. The selection was based on criteria such as, availability, security, size and the representativeness of the sand deposit.

The selected sites, located in the Fraser River delta, are the KIDD 2 substation in north Richmond, owned by B.C. Hydro and the Massey Tunnel (south portal) in Delta, owned by the B.C. Ministry of Transportation and Highways, as shown in Figure 7.

The subsoil's at the KIDD 2 substation are typical of those found in the Richmond area, comprising a surfical cover of organic silt and clayey silt to a depth of about 4 m over a loose to medium dense clean sand which extends to a depth of 22 m. The sand is generally considered susceptible to cyclic liquefaction under the design earthquake for the region using current methods.

The Massey Tunnel (south) site consists of a relatively loose, clean sand from 6 m to approximately 32 m below ground surface. This deposit is also considered to be

susceptible to cyclic liquefaction. At both the KIDD 2 and Massey Tunnel sites the groundwater level is approximately 1.5 m below ground surface. Similar circular test areas have been established at both Fraser River delta sites.

The sand at both Phase II sites in the Fraser River delta are considered to be part of the same extensive distributary channel sand complex (Monahan et al., 1993).

IN-SITU FREEZING

One of the primary objectives of the CANLEX Project is to develop and enhance the process of in-situ freezing to obtain undisturbed samples. Careful laboratory studies have shown that sand can be frozen without causing disturbance to the density or fabric (e.g. Sasitharan et al, 1993). Davila et al (1992) has shown that sands with fines can be frozen without disturbance provided the amount and type of fines are below certain limits. The disturbance due to freezing appears to be controlled primarily by clay minerals present in the fines. If the fines contain no clay minerals, the sand can have a large fines content and still be frozen without disturbance. However, small amounts of highly active clay minerals can cause disturbance during freezing. Davila et al (1992) proposed guidelines to define the limits for undisturbed freezing based on the amount and type of fines.

During the summer of 1993 a team from the University of Alberta, under the supervision of Professor D.C. Sego, evaluated and enhanced the in-situ freezing technique to "target freeze" certain depths around a single freeze pipe. During the November 1993 field program, this team carried out in-situ freezing to obtain undisturbed samples from the target depth of 27 m to 37 m at the Phase I test site. In-situ freezing was carried out from a central freeze pipe using liquid nitrogen. Radial freezing produced a column of frozen sand with a radius of 1 m. A total length of 20 m of frozen core was obtained using a 100 mm diameter CREEL core barrel. The in-situ freezing at the Phase I site represents a significant achievement due to the great depth of overburden (27 m), high ground temperature (approximately +12°C), and lateral ground water flow (approximately 0.25 m/day).

LABORATORY TESTING

The objectives of the laboratory testing program has been to determine the response of the sand to both static (monotonic) and dynamic (cyclic) loading. The role of the monotonic testing is to determine the state of the sand relative to its ultimate steady or critical state, and then to relate this back to the various in-situ test results.

In order to process all of the expected laboratory samples in a cost effective and efficient manner, and in keeping with the specific interests of the participants, testing is underway at laboratories at four different universities and one engineering consulting company. To provide some level of quality assurance within a given laboratory and among different

laboratories, a testing protocol has been developed that describes the thawing, consolidation and shearing procedures. Each laboratory has been asked to test essentially identical frozen reconstituted samples of Syncrude sand to evaluate the proposed protocol. Laboratory testing is underway and results will be published in subsequent reports and papers.

LIQUEFACTION EVENT

To evaluate our ability to predict liquefaction response of sand structures a full scale liquefaction event is planned for Phase III of the CANLEX Project. Currently, millions of dollars are spent to retrofit structures in seismic areas due to expected liquefaction. Major concerns with the design process relate to the level of disturbance required to trigger liquefaction, the resulting residual undrained strength and the likely deformation. Two possible events have been studied:

Event 1: Flow Slide

This would involve loose sand and a steep slope such that when triggered flow liquefaction will result in a flow slide and provide a measure of residual strength. The trigger could be static or dynamic.

Event 2: Lateral Spread

This would involve either loose or medium dense sand and a more moderate slope such that when triggered cyclic liquefaction would result in lateral spreading rather than flow. The trigger must be dynamic, i.e., blasting, impact or vibroseis.

A feasibility study has been completed that has selected a potential test zone in an area of the future toe berm along the north side of the Syncrude Setting Basin. A flow slide event has been given highest priority with a static trigger. The trigger will likely be induced by rapid construction of a berm over about 10 m of very loose, saturated Syncrude sand. Approximate dimensions of berm and test cell will be confirmed by numerical and physical modeling.

To evaluate and plan the proposed event, preliminary centrifuge testing has been conducted in 1993 by C-CORE under the direction of Dr. R. Phillips and Prof. P.M. Byrne. An 18 degree submerged slope of Syncrude sand was rapidly loaded to trigger a liquefaction flow slide. This represents, what is believed to be, the first static liquefaction failure carried out in a centrifuge. Full details are given by Phillips & Byrne, (1994).

The results of the centrifuge tests are currently being analyzed to assist in the event planning. Analyses are underway by Prof.'s Finn and Byrne at the University of British Columbia, Prof.'s Chan, Robertson and Morgenstern at the University of Alberta and Dr. Gu at EBA Engineering Consultants Ltd.

Additional centrifuge tests are planned to clarify details of the proposed event.

SUMMARY

This paper has briefly presented a summary of the work completed during Phase I and part of Phase II of the CANLEX Project. Three test sites have been selected and site characterization has been essentially completed. Characterization has included in-situ testing, such as, CPT, SPT, SBPMT and geophysical logging. Samples have been obtained using high quality conventional techniques with a fixed piston sampler as well as in-situ freezing techniques. Feasibility planning which has included preliminary centrifuge testing has been completed for a full scale liquefaction event.

This work has been a collaborative effort between industry and universities in Canada.

ACKNOWLEDGMENTS

This work was partly supported by CANLEX (Canadian Liquefaction Experiment), which is a project funded through a Collaborative research and development Grant from the Natural Science and Engineering Research Council of Canada (NSERC), B.C Hydro, Quebec Hydro, Syncrude Canada Ltd. and Suncor Inc. The collaboration includes the geotechnical consultants, AGRA Earth and Environmental Limited, Klohn-Crippen Consultants Ltd., Golder Associates Ltd., Thurber Engineering Ltd. and EBA Engineering Consultants Ltd., as well as faculty and students from the Universities of Alberta, British Columbia, Laval, Carleton and Sherbrooke.

REFERENCES

Dawson, R.F., Morgenstern, N.R., and Sego, D.C., 1992. Geotechnics of Mine Waste Audits. Second International Conference on Environmental Issues and Management of Waste in Energy and Mineral Production, Calgary, Vol. 2, pp. 1003-1014.

Davila, R.S., Sego, D.C., Robertson, P.K., 1992. Undisturbed Sampling of Sandy Soils by Freezing. 45th Canadian Geotechnical Conference, Toronto, October 26-26, 10 p.

Gu, W.H., Morgenstern, N.R. and Sego, D.C., 1993a. Progressive Failure of Lower San Fernando Dam. Journal of Geotechnical Engineering, American Society of Civil Engineering, 119: 333-349.

Gu, W.H., Morgenstern, N.R., and Robertson, P.K., 1993b. Post Earthquake Deformation Analysis of Wildlife Site. ASCE, Vol. 119.

Monahan, P.A., Luternauer, J.L., and Barrie, J.V., 1993. A Delta Plain Sheet Sand in the Fraser River Delta, British Columbia, Canada. Quaternary International, Vol 20, pp. 27-38.

Phillips, R., and Byrne, P.M., 1994. Modelling Slope Liquefaction Due to Static Loading. 47th Canadian Geotechnical Conference, Halifax, 1994, pp.317-326.

Plewes, H.D., McRoberts, E.C., and Chan, W.K., 1988. Downhole Nuclear Density Logging in Sand Tailings. Proceedings of the ASCE Specialty Conference on Hydraulic Fill Structures, Fort Collins, Colorado.

Plewes, H.D., Morgan, M.R., and Kilpatrick, B.L., 1993. In-situ Sampling, Density Measurements and Testing of Foundation Soils at Duncan Dam. 46th Canadian Geotechnical Conference, Saskatoon, Saskatchewan, September 1993.

Robertson, P.K., 1994. Suggested Terminology for Liquefaction: An Internal CANLEX Report.

Sasitharan, S., Robertson, P.K., and Sego, D.C., 1993. Preliminary Evaluation of Flow Liquefaction of Silty Sands Using Shear Wave Velocity. 46th Canadian Geotechnical Conference, September 27-29, Saskatoon, Saskatchewan, pp. 505-513.

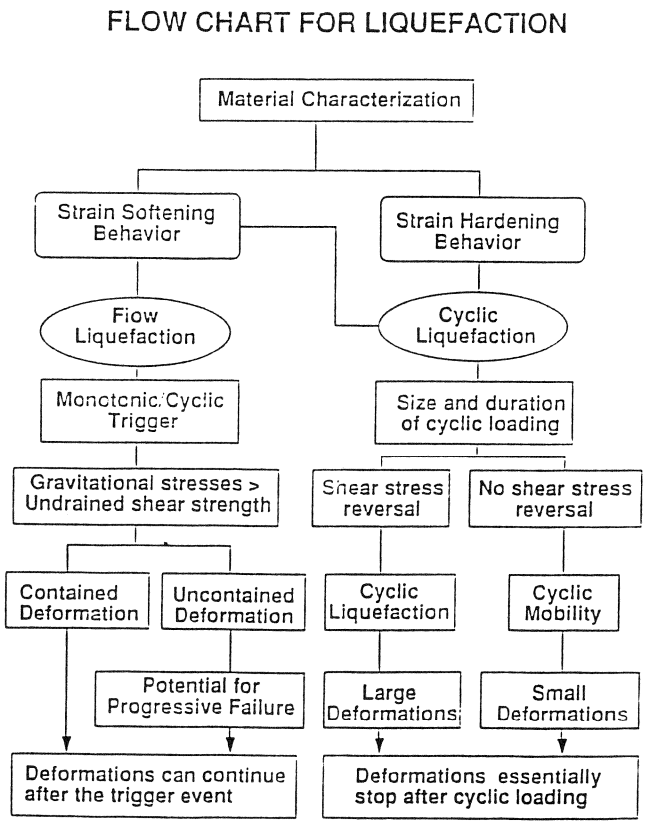

Figure 1 Proposed Flow chart for evaluation of liquefaction (After Robertson, 1994)

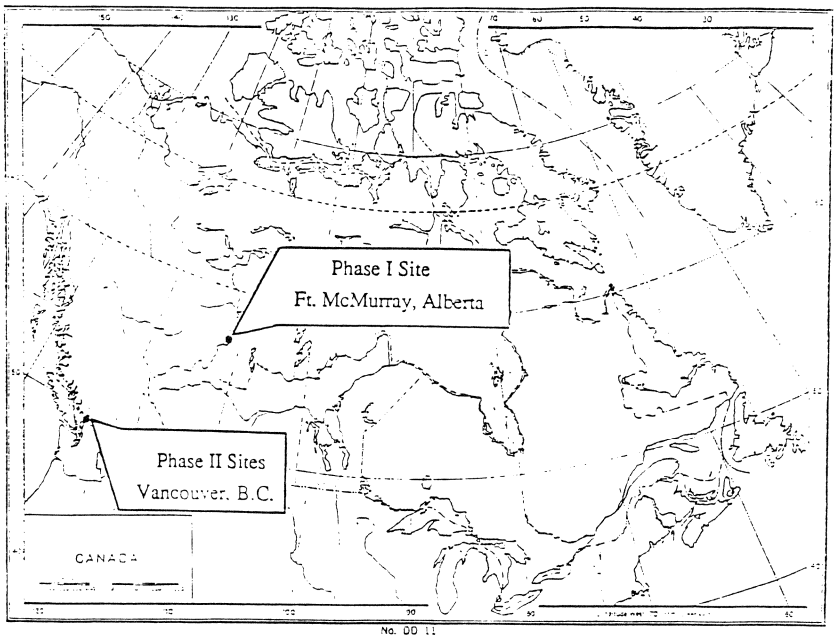

Figure 2 Site location for CANLEX Phase I and II sites.

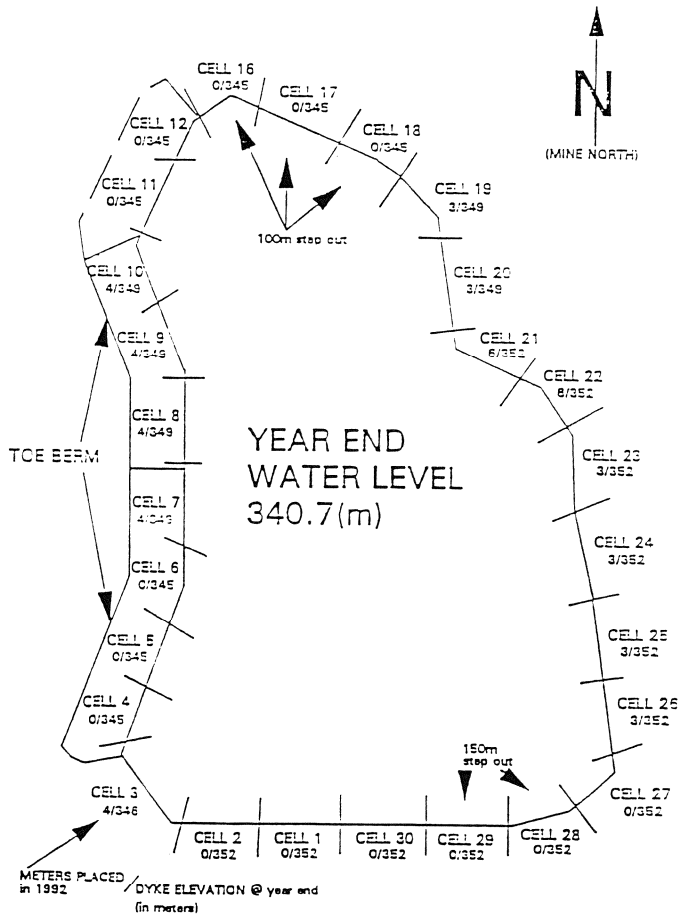

Figures 3 Site plan of Mildred Lake Settling Basin at Syncrude Canada Ltd site.

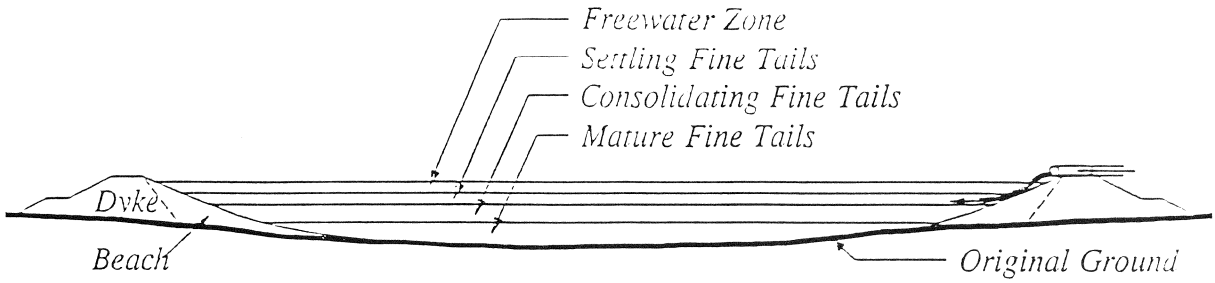

Figure 4 Schematic of Mildred Lake Settling Basin cross section.

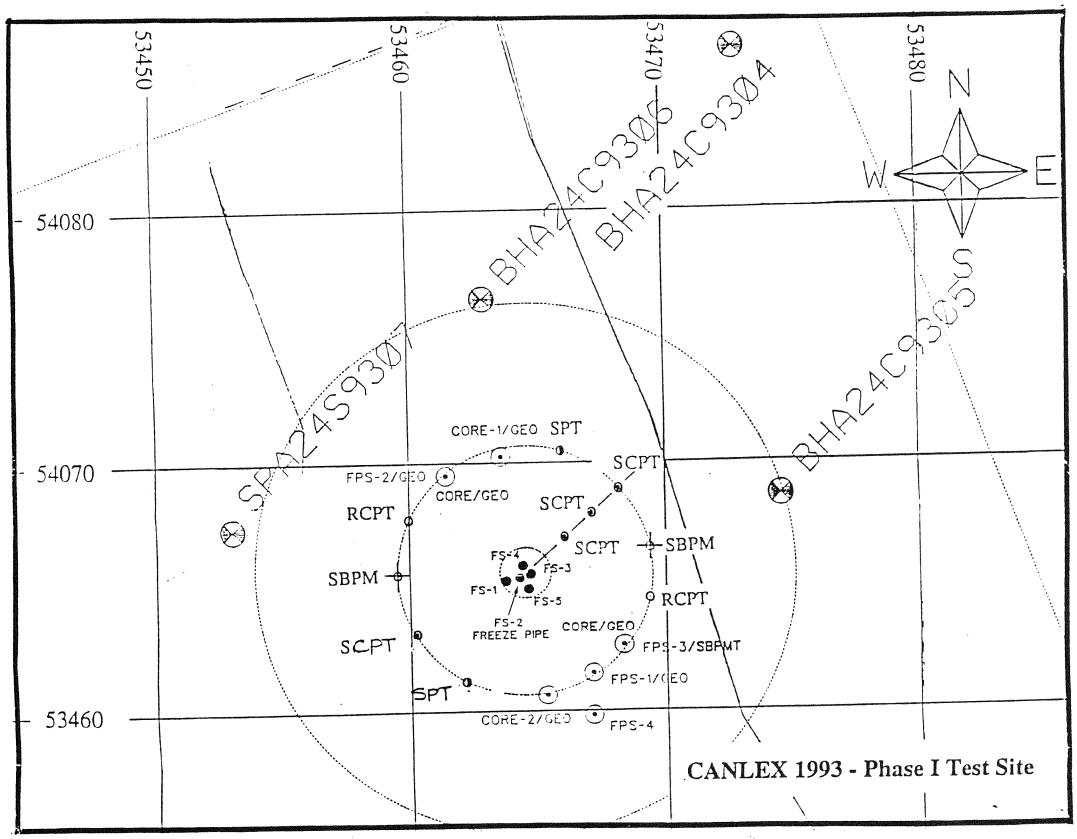

Figure 5 Phase I site plan showing test locations.

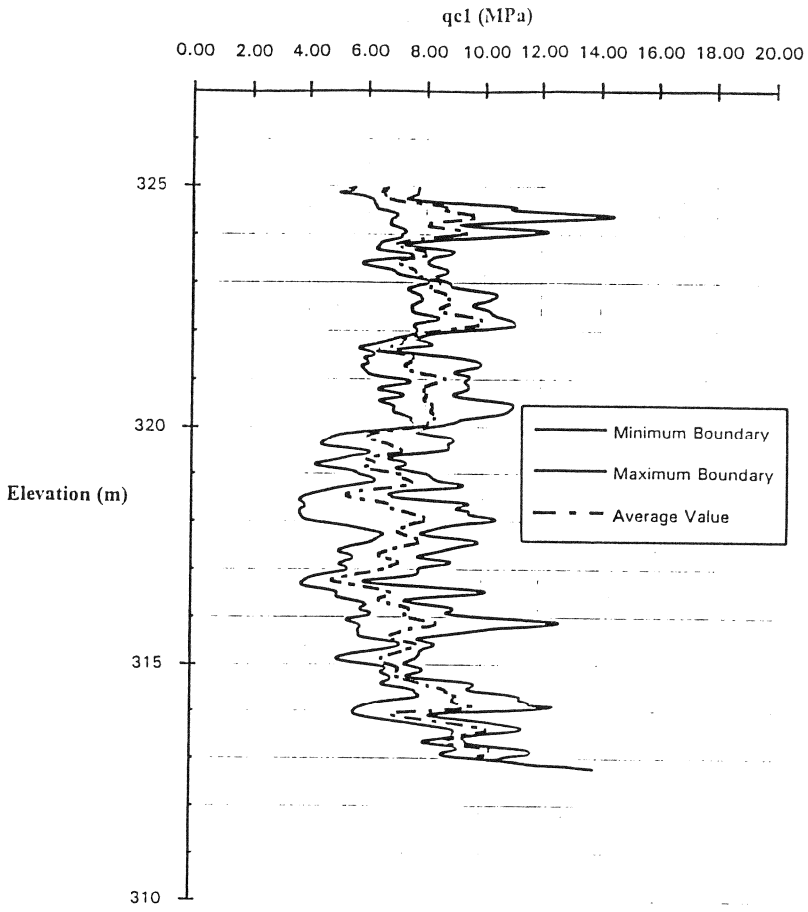

Figure 6 Normalized CPT penetration resistance profiles at Phase I test site.

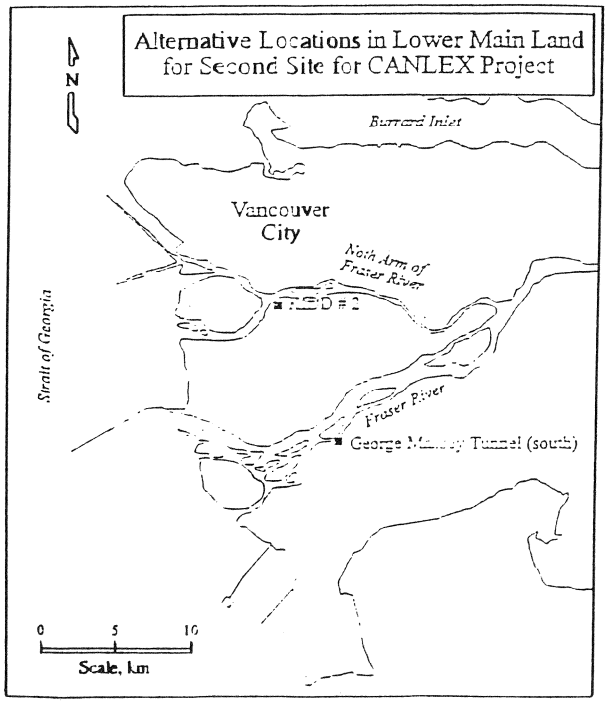

Figure 7 Locaction Plan for Phase II sites near Vancouver, B.C.

III LIQUEFACTION AND DYNAMIC RESPONSE OF UNDERGROUND STRUCTURES

Evaluation for Earthquake Ground Motion of Sediment-Filled Basin Under Seismic Observation
K. Sato, T. Iwatate, S. Sasaki, and H. Yajima
Dynamic Analysis of Lateral Flow of Liquefied Ground
I. Towhata and H. Toyota
VELACS Project: A Summary of Achievements
M.T. Manzari, K. Arulanandan, and R.F. Scott
An Experimental Study of Effects of Laterally Flowing Ground on In-Ground Structures
H. Sato, M. Hamada, and M. Doi
An Assessment of VELACS "Class A" Predictions
J.H. Prevost and R. Popescu
A New Interpretation Method of Surface Wave Measurements to Obtain Representative Shear Wave Velocity Profiles of Soils
C.J. Poran, J.A. Rodriguez-Ordonez, T. Satoh, and R. Borden

EVALUATION FOR EARTHQUAKE GROUND MOTION OF SEDIMENT-FILLED BASIN UNDER SEISMIC OBSERVATION

K. Sato[1], T. Iwatate[2], S. Sasaki[3], H. Yajima[1]

ABSTRACT

Characteristics of Earthquake ground motion and seismic wave propagation were investigated with reference to earthquake records, which were obtained at K site of horizontal sedimentary layer and at O site of sediment-filled basin. Seismic response analyses were also examined by comparing with those records.

Amlificaion of earthquake ground motion between basic and surface layer at K-site, are quite stable in any recorded earthquake. For that reason, it was confirmed that one-dimensinal response analysis is good enough to evaluate earthquake ground motion at horizontal sedimentary layer like this site.

On the other hand, underground distributions of maximum accerelation and amplification at O-site, have strong local effect of surface geology and also have different dynamic characteristics between NS and EW components. Evolutionary power spectrum of ground motion for longitudinal and transverse components to epicenter were analyzed to realize these phenomena. As a result, dispersional Love-wave generated through surface geology were indicated.

Further, availability of the super-imposed method combined both of one-dimensional analysis by the SHAKE and two-dimensinal anlysis by the Aki-Larner method were investigated for earthquake in seismic response at O-site.

[1] Senior Research Engineer, Central Research Institute of Electric Power Industory

[2] Professor of Civil Engineering, Tokyo Metropolitan University

[3] Research Fellow, Central Research Institute of Electric Power Industory

INTRODUCTION

Seismic response of soil layer or local soil amplification due to strong earthquake plays an important role for the seismic safety of structure. Dynamic soil properties are among incident wave parameters, topographical and base-rock irregularities, etc.In this report, seismic response analyses is examined by the deep down-hole array earthquake measurement in the granular soil layer with horizontal and irregular interface. Numerial analyses is introduced with a focus on evaluation for effect of surface geology.

SITE CHARACTERISTICS AND SOIL PROPERTIES (K-SITE)

The array was set up in K-site in a coastal Flat area about 80km east of Tokyo (see Fig.1) by drilling several boreholes in the same site to accomodate the down-hole array instrumentation at nine different levels as shown in Fig.2. The deepest hole was drilled down to 502m from the ground surface so that the Pleistocene sedimentation rock with the shear-wave velocity of 650m/sec was reached. Above the rock a rather uniform horizontal layer consisting of Pleistocene cemented fine sand of about 480m thick is resting with a thin horizontal gravelly layer of about 2.5m thick and a loose to medium sand surface layer of 16m thick capping it. The P-and S-wave velocities measured down to 502m by the PS logging method are shown in Fig.2, indicating the sher-wave velocity almost monotonically increasing with depth.

MEASURED SEISMIC RESPONSE (K-SITE)

Thirty six eartquake records were obtaind for about four years from Dec. 1988 to Jan. 1994.Among them the largest magnitude was M=6.0 with the epicentral distance $\triangle$=27m and the largest value of the peak horizontal acceleration at the ground surface 114cm/sec^2 in a M=5.2 earthquake event(EQ-15) with $\triangle$=43km (see Fig.1). In Fig.3, an example of the recorded motions are shown for an event of M=5.6 , $\triangle$=71.1km (EQ-8).

Fig.4 exemplifies the vertical distribution of the computed maximum horizontal accelceration compared with the measured values as well as the distributions of the mazimum shear stress and the maximum shear strain for a larger seismic motion recorded in the site. The dotted curve in the geaph correspond to the case in which the strain-dependency of the damping ratio, h, is modified so that the lowest value of h is fixed as 5% as shown in Fig.4 on the ground that the seismic records optimization evaluates the damping ratio of the sand layers as about 5%.

Fig.5 shows the distribution of the peak horizontal accelertion amplification alog the depth with respect to the reference value at the deepest G1 point(GL.-502m) for the recorded earthquake of M=4.9 , $\triangle$=33km (EQ-36). It is noted that the amplification factors do not increase but stay almost constant from the deepest G1 point up to the depth of 17m below the surface. Marked amplification takes place solely in the top part shallower than 17m . These amplification characteristics are quite similar in two perpendicular horizontal directions and also very stable for different earthquakes with various intensities, magnitudes and epicentral distances, Leading to the standaard deviations of the amplification factor for the 35 earthquakes being about $\pm$20 percent of the average value and quite stable for all the down-hole levels,

In Fig.6 the transfer functions calculated as the average of the recorded larger earthquake motions between the ground surface level G9 (GL.-1m) and the down-hole levels, G3(GL.-50m), are shown for the two perpendicular horizontal motions. Evidently, the functions are much the same in two orthogonal directions, indicating the soil layer in this site is quite isotropic in its dynamic

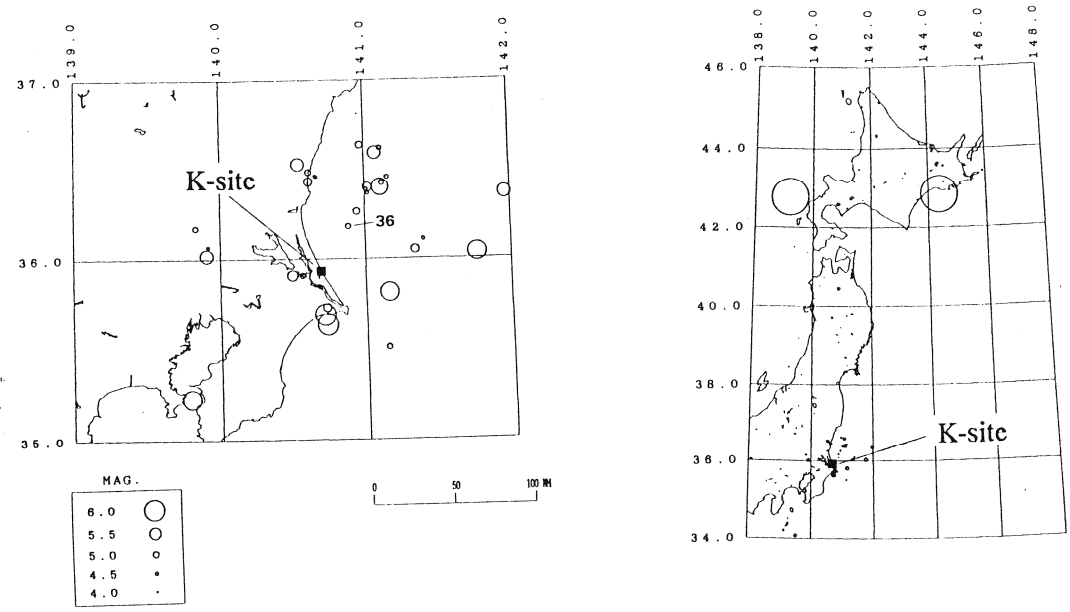

Fig.1 Location map of earthquake recorded at K-site

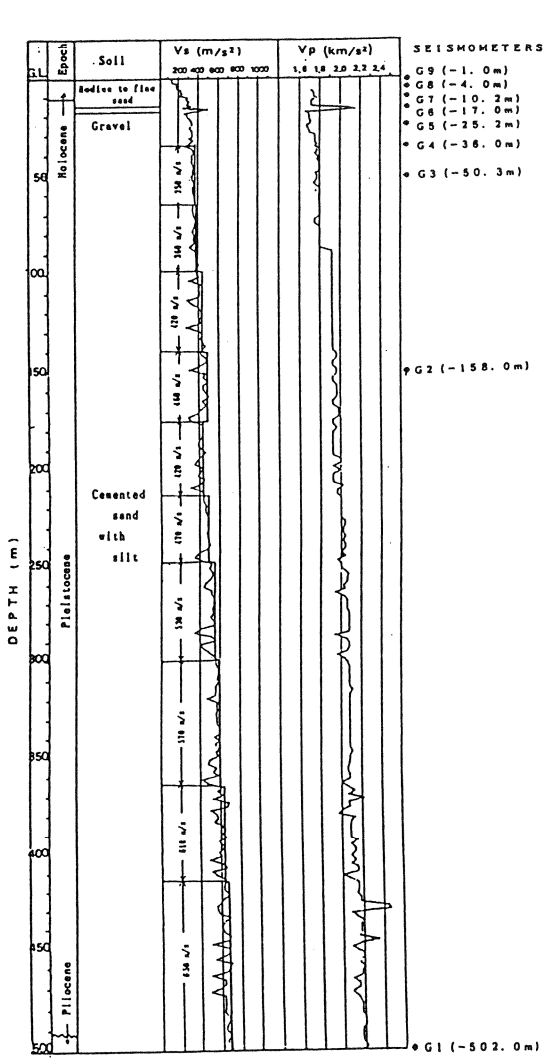

Fig.2 PS logging and down-hole seismometer

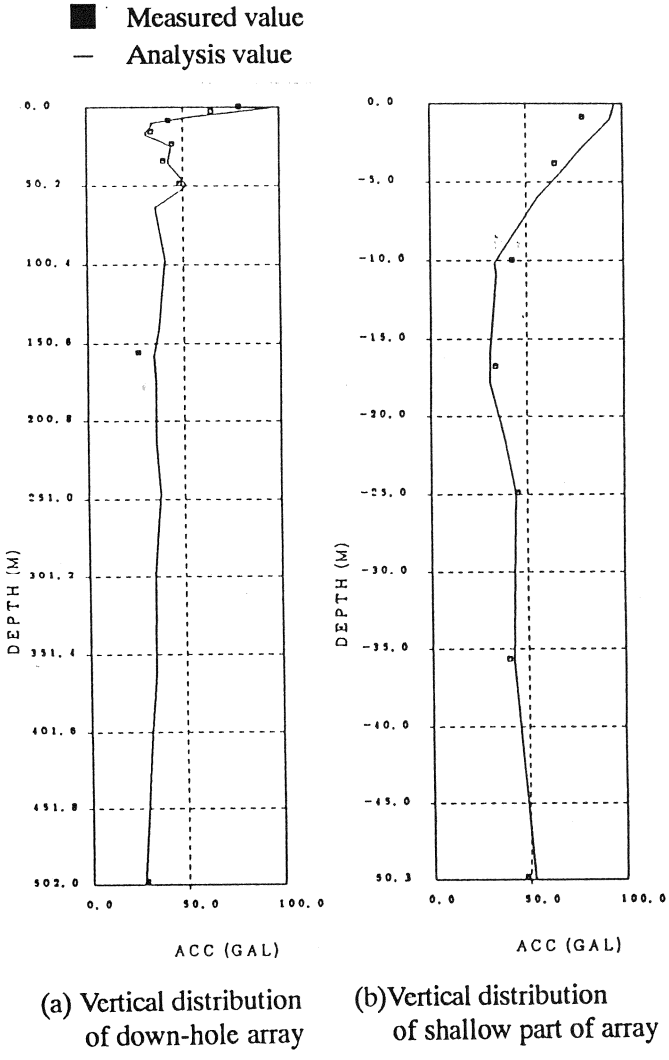

Fig.3 Maximum horizontal accceleration (EQ-8)

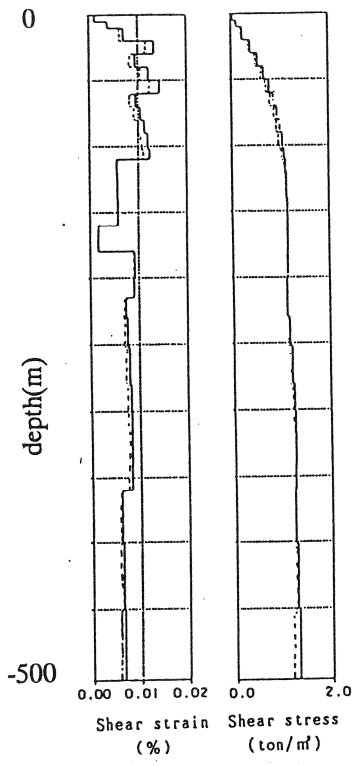

Fig.4 Distributions of Max. Values Computed by SHAKE Analysis (EQ-8, N55W)

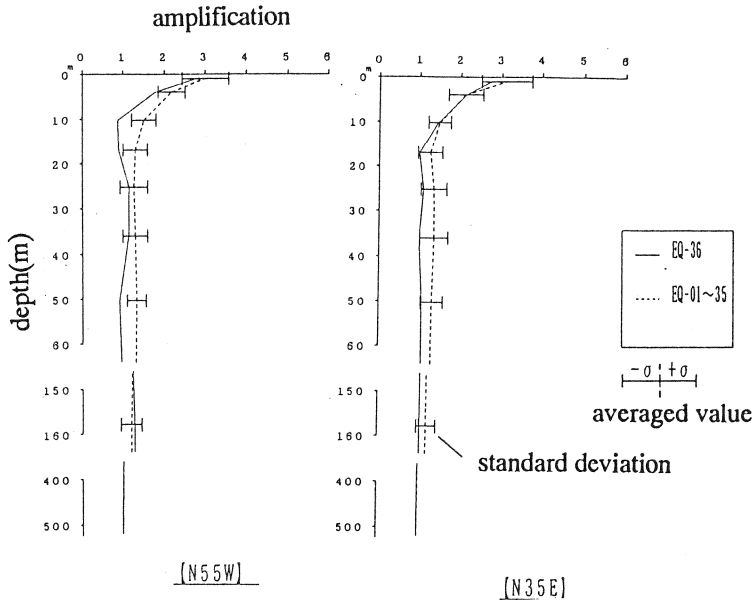

Fig.5 The average, standard deviation and EQ-36 of Max. Acc.

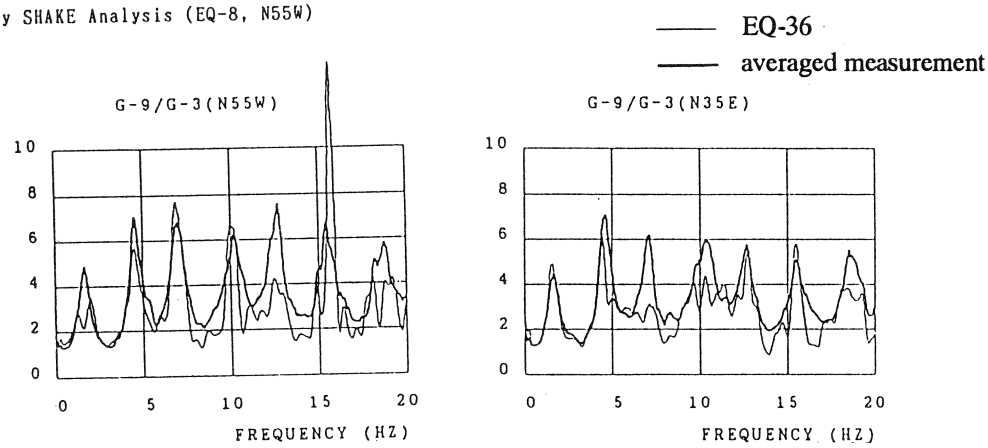

Fig.6 Transfer function compared between averaged and EQ-36

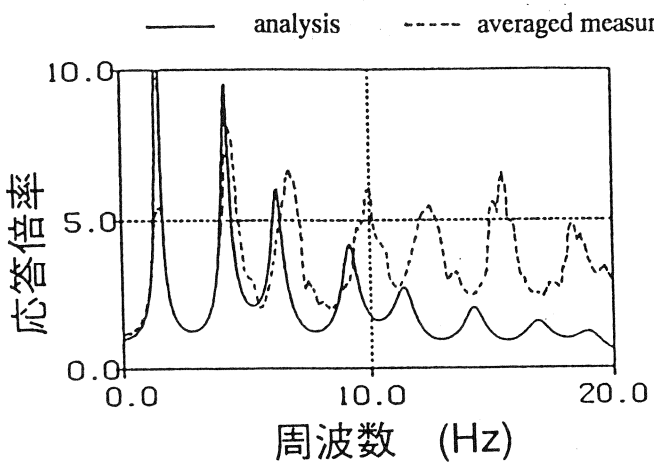

Fig.7 Transfer function (G9/G3) compared betweeen analysis and averaged measurement

response.The transfer functions between G9 and G3 for the same earthquake motion is shown in Fig.7. Hower, there exists a striking difference between the actual and computed responses irrespetive of the damping values in that the peak amplitudes in the transfer function of the SHAKE analysis tend to monotonically decline for higher frequency while those of the actual response stay at almost the same level. This may imply the hysteretic damping incorporated in the SHAKE analysis may not approiately represent the actual damping mechanism exerted in the small strain oscillation.

TOPOGRAPHY AND GEOLOGY OF ASHIGARA VALLEY

The Ashigara Valley, about 80 km southwest of Tokyo, lie in the Southern Kanto region, which is located near the triple junction of the philippin Sea Plate, the Eurasian Plate and the Pacific Plate(See Fig.8). In particular,Ashigara Valley and its vicinities are geologically complicated and have high seismic activities, because they are on the extension of the Sagami trough on the boundary of the Philippine Sea Plate and the Eurasian Plate and under them the Philippine Sea Plate collides with the Eurasian Plate. Naturally, this region has often suffered significant earthquake damage. Under such a situation, the study on the topography and geology of this region has been conducted for a long time. Recent works, For example, are those done by Kanagawa Prefecture(1980) and Yamazaki et al.(1982).

As illustrated by the surface geological map in Fig. 8 and the Ashigara Valley, surrounded by the Hakone Volcano to the west, by the Oiso Hills to the east and by the Tanzawa Mountains to the north, is about 4 km wide and 12 km long. It is a rectangular alluvial plain developed along the lower reaches of the Sakawa River. O-Site is located on the west of this alluvial plain.

GEOTECHNICAL MODEL OF O-SITE

Fig. 9 shows the locations of the surface seismic observation points and three lines of profile in the O-site. The epicenter of the earthquake recorded on this site is indicated in Fig 10 with circle simbol whose diameter size means maghitude of earthquake, Fig.11(a)-(c) show the geotechnical cross sections along the three lines of profile, respectively, giving some image of the three-dimensional structure of the test area.

The O-site in Ashigara Valley and its vicinity have been geophysically explored for investigating the structure and the physical properties of the substructure. Logging provides valuable data for understanding the physical properties of the ground layers in and around the O-site. To estimate the P-wave and S-wave velocities which are indispensable for seismic motion analysis, P-and S-wave velocity logging has been carried out in three boreholes. the suspension method was used in the seismic wave velocity logging. Further,electrical logging (normal method) and density logging were also conducted in the three identical boreholes (OA,OC and OD) in the test site to determine the continuity of the geological structure and the soil layers.

MEASURED SEISMIC RESPONSE (O-SITE)

Seventeen eartquake records were obtaind for about three years from Feb. 1992 to Mar. 1994.Among them the largest magnitude was M=7.8 with the epicentral distance $\triangle$=955km (Kushiro-oki 1993) and the largest value of the peak horizontal acceleration at the ground surface 94.3cm/sec^2 in a M=5.9 earthquake event with $\triangle$=58.5km. An example of the recorded motions are shown for an event of M=4.9 and $\triangle$=65.3km (EQ-3). Fig.12 exemplifies the vertical distribution of the computed maximum horizontal acceleration compared with the measured values for a larger seismic motion recorded in the OA-site of deep down-hole array. It shows the distribution of the peak horizontal acceleration amplification along the depth with respect to the reference value at the deepest G1 point(GL.-300m) . It is noted that the amplification factors do not increase but stay almost constant

from the deepest G1 point up to the depth of 13m below the surface. Marked amplification takes place solely in the top part shallower than 13m. These amplification characteristics are almost similar in two perpendicular horizontal directions.
Revolutionary spectra with the transverse direction to epicenter of the recorded seismic data (EQ-3) was analyzed, which shows ampfification and wave propagation of subsurface seismic motion. Each spectral peak shows arrival time of predominant propagating wave with respect to the frequency. Those peaks' time as shown dot simbol in Fig.13 are gradually changing and dispersional in the frequency boundary from 1 to 3 Hz, but same in the other frequency boundary. It was recognized that those peaks' frequency agree to the sharp curve point of the dispersional curve for Love wave phase velocity on the subsurface structure up to the depth of 13m (See Fig.14). In Fig.15 the transfer functions calculated as the average of the recorded larger earthquake motions between the granular ground surface level G6 (GL.-13m) and the down-hole levels, G1(GL.-300m), are shown for the two perpendicular horizontal motions. The functions are not so much same in two orthogonal directions, indicating the soil layer in this site is quite heterogenuous in its dynamic response.

SEISMIC RESPONSE ANALYSIS(O-SITE)

North to south direction soil profile for the surrounding of OA-site was modelized like as sediment-filled basin in Fig.16,that consist of five lateral heterogeneous soil layers.Seismic response was analyzed by Aki-Larner Method with fast fourier transform, which has periodicity in the horizontal direction of soil model.Fig.17 shows propagating subsurface motion from the ridge side of sediment-filled basin due to incident SH ricker wave of 0.7 sec natural period.Some secondary surface waves are generating from the ridge of sediment-filled basin and then, propagating toward the deepest position of the basin.As a result, seismic response on the central part of the basin shows confused dynamic behavior by both of shear wave propagating from bottom layer and secondary surface Love-wave generating through the geological structure.
In this report, seismic response analysis was calculated by Super-Imposed method combined both of the AL-method in the frequency boundary lower than 3.0 Hz and the SHAKE analysis in the other one higher than 3.0 Hz. Pseudo velocity response spectra for two perpendicular horizontal components of event EQ-3 was obtained in Fig.18. Calculated response spectra in NS component almost agree to observed one except response spectral amplitude peak in the period of 1.0 sec.The amplitude peak in the period of 0.5 sec (2.0 Hz) indicate the seismic response depend on the two-dimensional geological structure. It was founded more clearly by comparing between the two-dimensional analysis(Super-Imposed method) and one-dimensional analysis (SHAKE). Response spectra in EW component are somewhat different with another one mentined above. This different dynamic characteristics is needed to research as site dependent phenomina taking account to the effect of three-dimensional soil structure.The availability of Super-Imposed method was approxemately confirmed on the seismic records of OA-site.

AKNOWREDGEMENTS
The authors are indebted to members of the electric power companies in Japan for their financial suports and encouragements to promote the systematic research in K-site.and O-site. We thanks Mr. Shimada and Mr. Fujitani of Tokyo Electric Company for their special support.

REFERENCE
T.Kokusho,et al. 1992, Sesimic response of soil layer and its dynamic properties, 10 WCEE (Madrid Spain).
Japanes National Working Group on the Effects of Surface Geology onSeismic Motion (JESG) 1991,Ashigara Valley Blind Prediction Test.

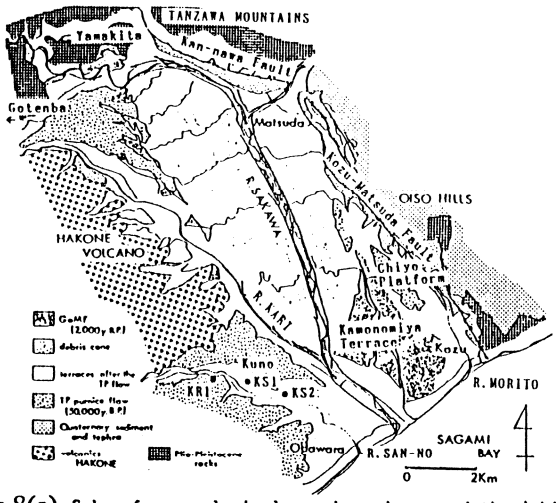

Fig.8(a) Subsurface geological map in and arround the Ashigara Valley (modified Yamazaki et al.,1982)

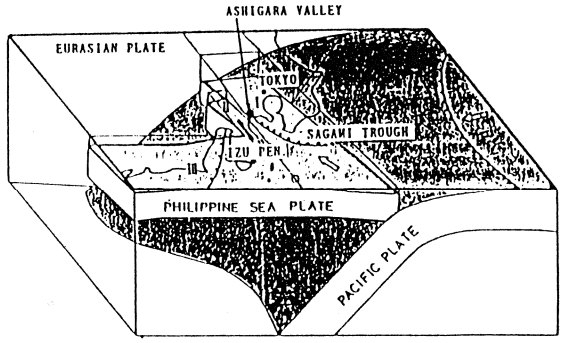

Fig.8(b) Unified plate model for interpreting the techtonics of the Kanto-Tokai area (modified Kasahara, 1985)

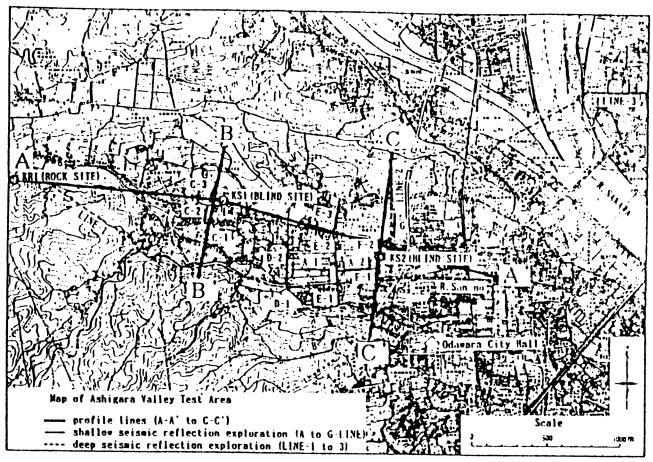

Fig.9 Location map of seismic observation point

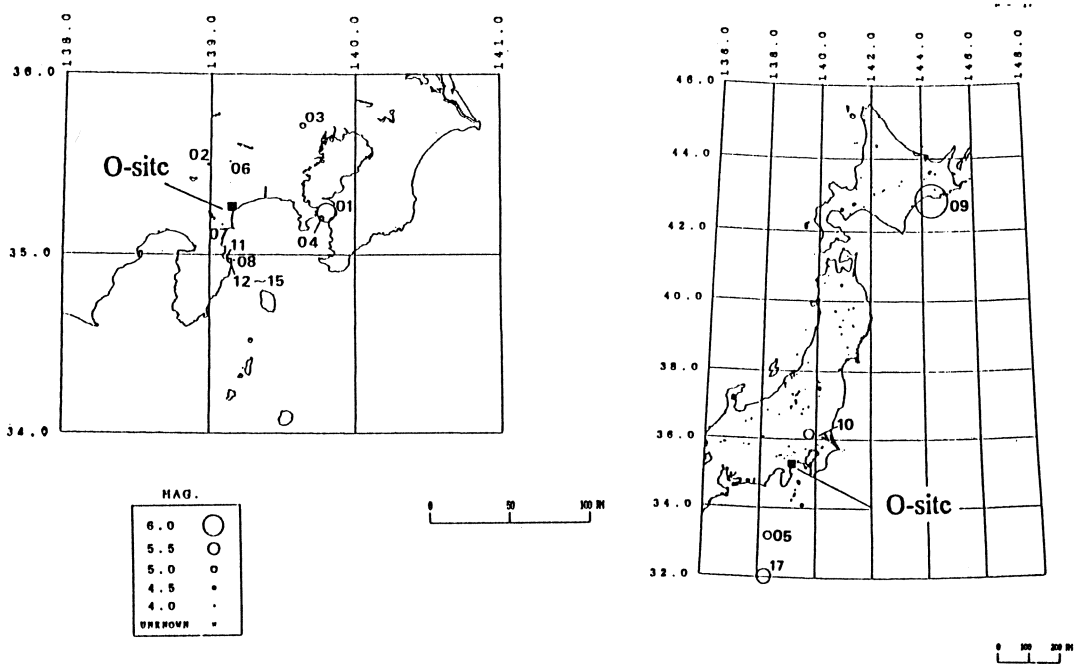

Fig.10 Location map of earthquake recorded at O-sitc

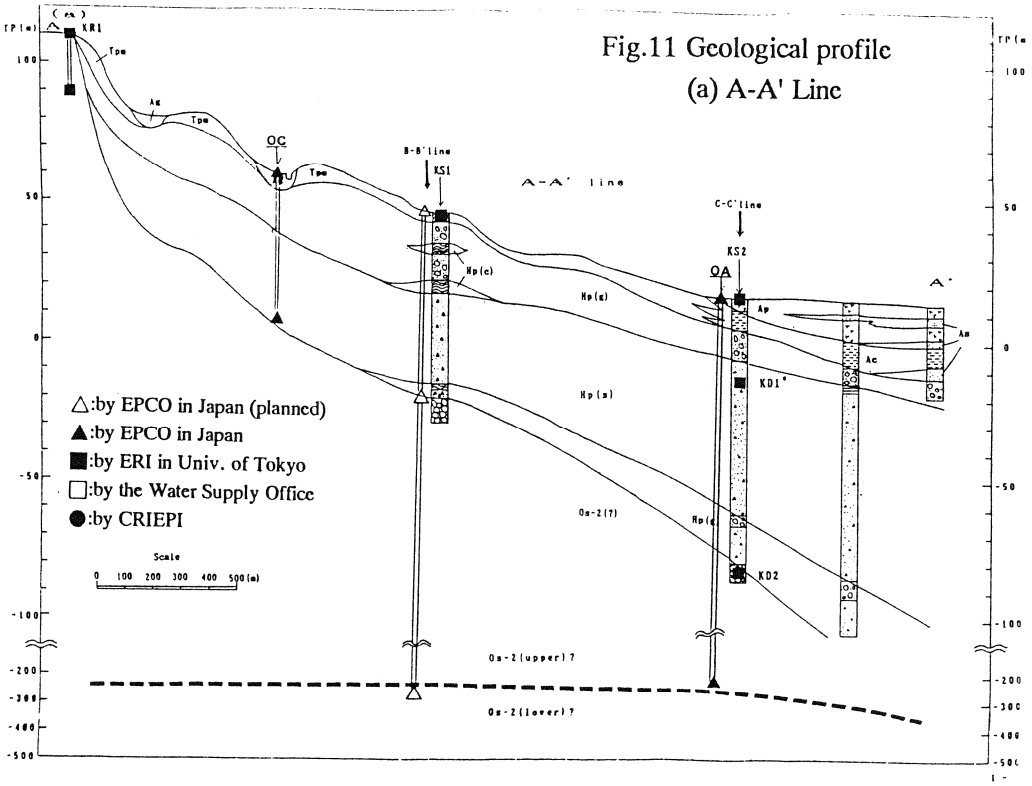

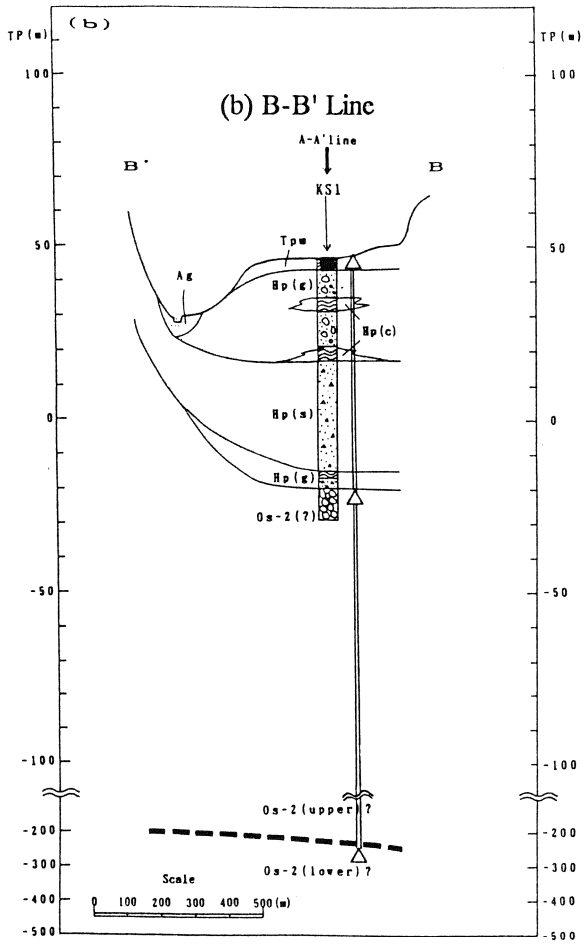

Fig.11 Geological profile

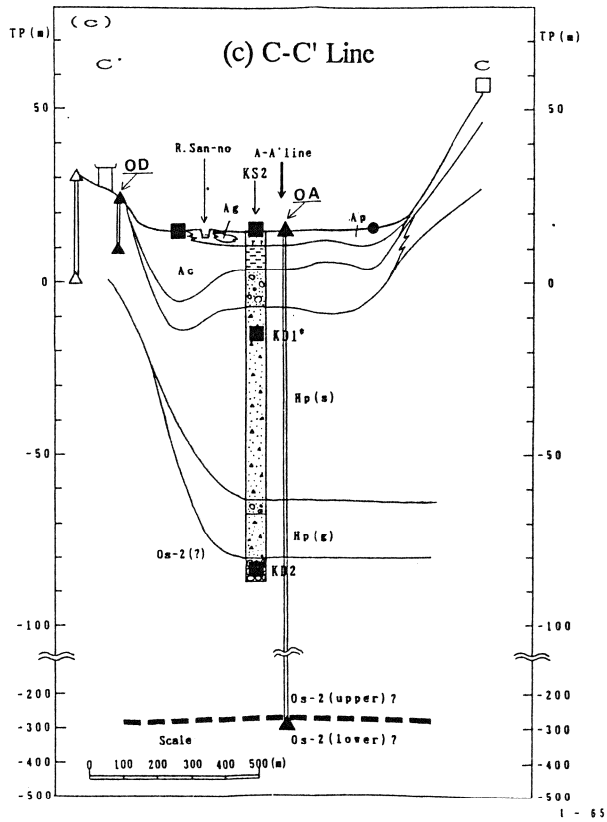

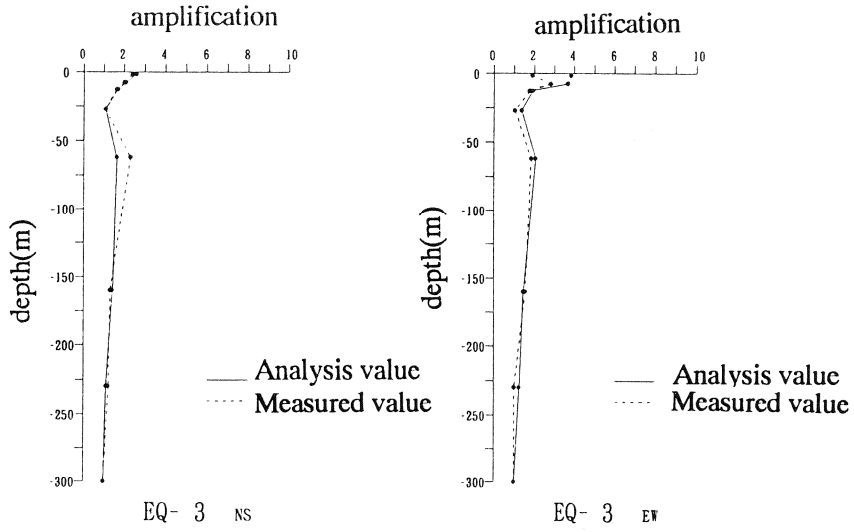

Fig.12 Maximum horizontal acceleration (EQ-3)

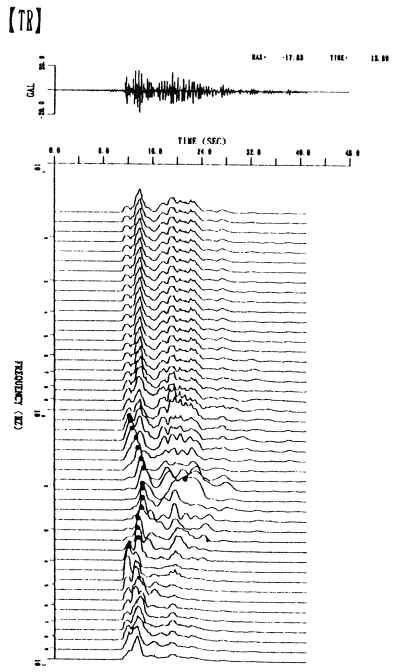

Fig.13 Revolutionary spectra (h=5%)

	H (m)	ρ (t/m³)	V. (m/s)
1	7.0	1.8	66
2	6.0	1.8	157
3	∞	2.0	645

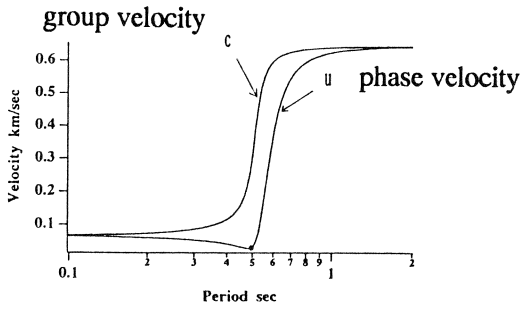

Fig.14 Love-wave dispersional curve of phase velocity

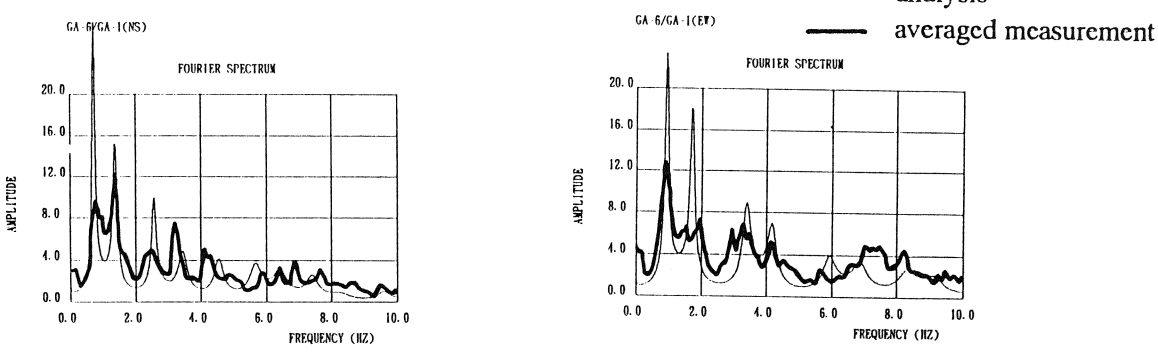

Fig.15 Transfer function (G6/G1) compared betweeen analysis and averaged measurement

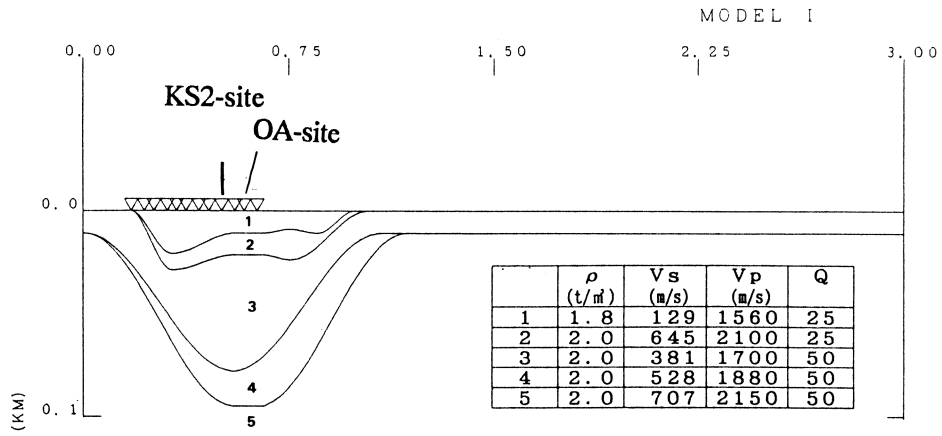

	ρ (t/m³)	Vs (m/s)	Vp (m/s)	Q
1	1.8	129	1560	25
2	2.0	645	2100	25
3	2.0	381	1700	50
4	2.0	528	1880	50
5	2.0	707	2150	50

Fig.16 Sediment-filled model on C-C' line

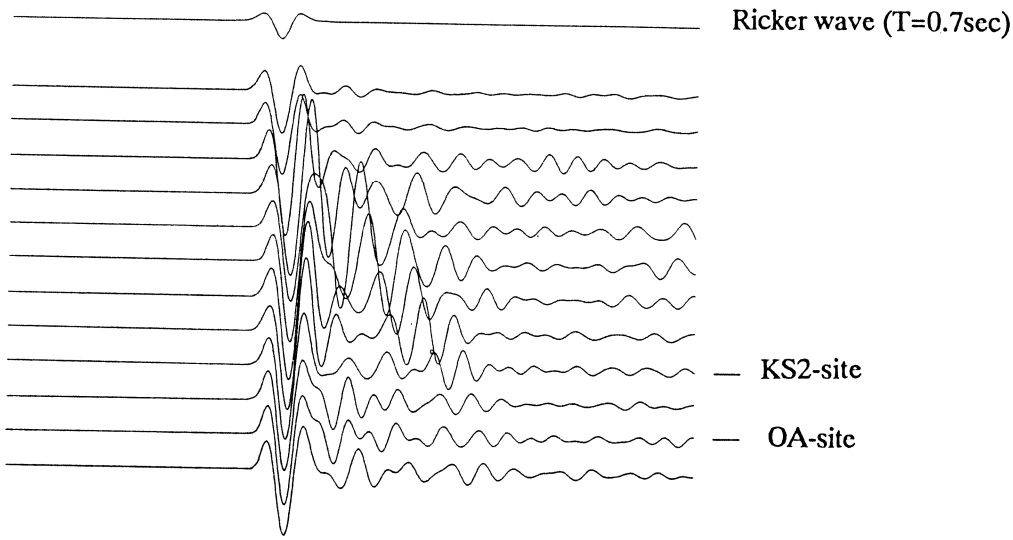

Fig.17 Subsurface motion by AL-method (EQ-3)

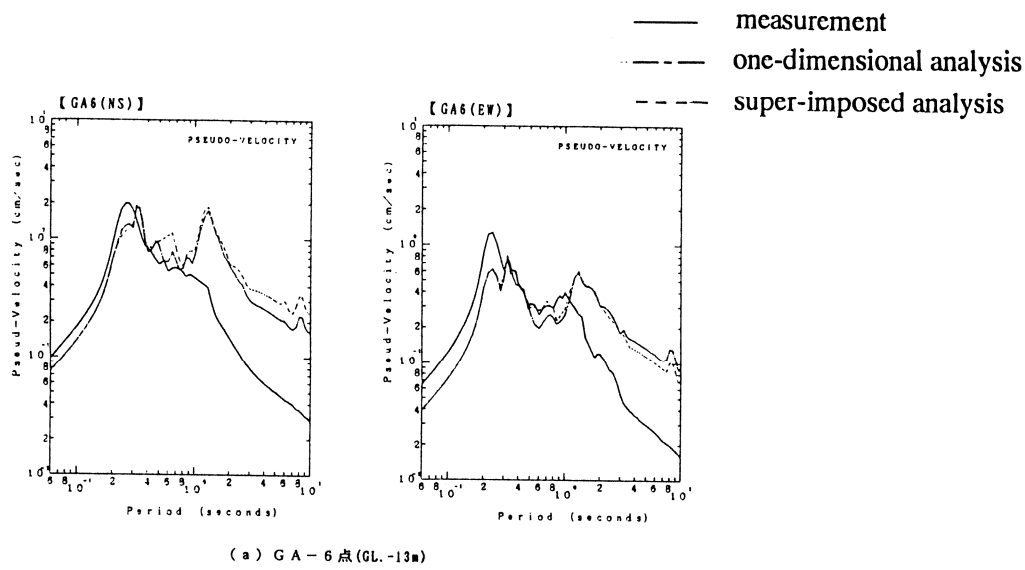

(a) GA－6点(GL.-13m)

Fig.18 Pseudo-velocity response spectra (EQ-3)

Dynamic Analysis of Lateral Flow of Liquefied Ground

Ikuo Towhata
Professor of Civil Engineering, University of Tokyo

and

Hirofumi Toyota
Graduate Student, University of Tokyo

ABSTRACT

A theory of dynamic analysis was derived in order to make it possible to follow the time history of lateral ground motion triggered by seismic liquefaction. This theory obtains a single-degree-of-freedom differential equation, by solving which the time history is calculated. Since the equation have a viscous term and a residual strength that need a detailed study to understand, model shaking tests were performed. Those tests revealed that liquefied sand has a rate-dependent nature that is viscous as well as that the magnitude of the residual strength of liquefied sand is strongly affected by the presence of inertia force. Consequently, several cases were analyzed and compared with observation. Their agreement seems to be good.

INTRODUCTION

The lateral displacement of liquefied sandy ground has been analyzed by a variety of method. Since the damage to pipelines caused by this displacement is induced by the deformation of ground, whether compression or extension, the tool of displacement prediction is required to calculate the ground deformation. Therefore, an analysis on a rigid-block movement, in which there is no deformation, is not very suitable. A finite element analysis that features nonlinear stress-strain behavior of sand, development of excess pore water pressure, dynamic response of ground, and large deformation seems to be more useful. However, an analysis of this type requires a heavy computer duty. In this regard, Towhata et al. (1992) developed a closed-form solution of ground displacement.

The closed-form solution gave the ultimate displacement of ground that is associated with the minimum potential energy of ground and is possible to be reality only when the state of flow continues for a sufficiently long time. In contrast, shaking table tests (Toyota and Towhata, 1994) demonstrated that the state of flow is ceased when shaking ends. Only exception is a very loose sand that can continue to flow after shaking under the effects of gravity force. Consequently, it was found that the predicted displacement is greater than those observed in the field after earthquakes (Towhata et al., 1992).

The present study aims at a development of dynamic analysis that can trace the time-development of ground displacement during and after liquefaction. Since the original theory was closed-form, the present dynamic analysis was desired to be closed-form as well.

THEORY OF DYNAMIC ANALYSIS

Shaking table tests by Toyota and Towhata (1994) revealed that the lateral movement of liquefied ground is associated with a large shear deformation of soil in place of a rigid-block movement. The variation of lateral displacement in the vertical (z) direction is reasonably approximated by a sinusoidal function. Accordingly, the lateral displacement of ground, "u", at a location of (x,z) and at time "t" is expressed by

$$u(x,z,t)=\lambda(t)U(x,z) \tag{1}$$

in which x and z are horizontal and vertical coordinates respectively. U(x,z) is the ultimate displacement that would occur after a sufficiently long period of flow. As illustrated in Fig.1, the effects of x and z components are separated from the time variation denoted by λ. Since U is able to be predicted by a closed-form solution (Towhata et al., 1992), the present study is

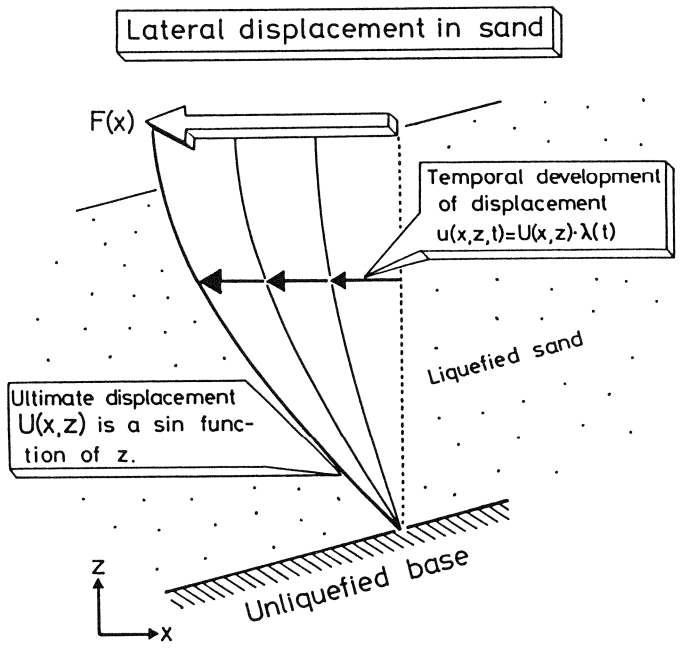

Fig.1 Modeling development of displacement with time.

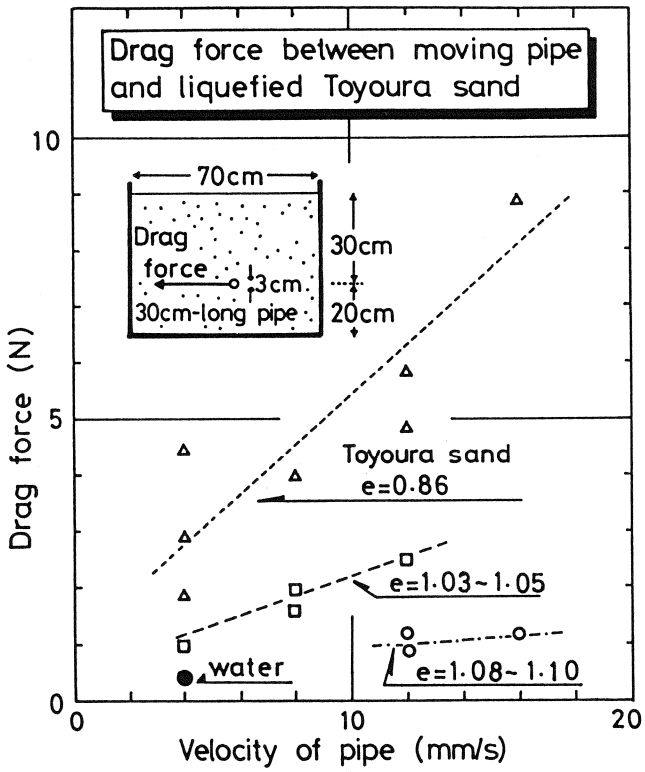

Fig.2 Rate-dependent nature of liquefied sand (Vargas, 1994).

focused on the derivation of $\lambda(t)$, a function of time.

The vertical displacement at time "t" is similarly expressed in terms of λ and W(x,z) that would occur after a sufficiently long period of flow;

$$w(x,z,t)=\lambda(t)W(x,z) \tag{2}$$

where W(x,z) was obtained by a closed-form solution (Towhata et al. 1992).

The velocity of ground is expressed by λ, U, and W;

$$\frac{\partial u}{\partial t}=U\frac{d\lambda}{dt} \quad \text{and} \quad \frac{\partial w}{\partial t}=W\frac{d\lambda}{dt} \tag{3}$$

The strain of soil is expressed similarly;

$$\varepsilon_x=\frac{\partial u}{\partial x}=\lambda\frac{\partial U}{\partial x} \qquad \varepsilon_z=\frac{\partial w}{\partial z}=\lambda\frac{\partial W}{\partial z} \quad \text{and}$$
$$\gamma=\frac{\partial u}{\partial z}+\frac{\partial w}{\partial x}=\lambda\left(\frac{\partial U}{\partial z}+\frac{\partial W}{\partial x}\right) \tag{4}$$

By using Eqs.3 and 4, it is possible to calculate the kinematic and the potential components of energy of ground at any x and z. The energy is thereafter integrated all over the ground to derive the global energy components, denoted by K and Q. Note that the kinematic energy, K, consists of $d\lambda/dt$ while the potential energy, Q, is composed of λ.

K and Q as derived above were substituted in the Lagrangean equation of motion;

$$\frac{d}{dt}\left\{\frac{\partial(K-Q)}{\partial(\partial\lambda/\partial t)}\right\}-\frac{\partial(K-Q)}{\partial\lambda}=0 \tag{5}$$

Consequently, a single-degree-of-freedom equation of motion in terms of λ was derived;

$$m\frac{d^2\lambda}{dt^2}+k\lambda=k \tag{6}$$

Eq.6 shows that the static equilibrium occurs at $\lambda=1$ that means u=U.

Earlier, the liquefied soil was considered to be of zero shear stiffness and constant volume, similar to liquid. Moreover, the unliquefied dry layer at the surface was regarded as an elastic column that resists against lateral compression. Accordingly, the initial analyses were carried out by using Eq.6. However, the results were poor because Eq.6 gives a free oscillation without damping, which is hardly the case in reality. The rate of displacement was found to be much faster than observed in tests. Furthermore, the equation could not reproduce the experimental fact that a ground of a slightly higher density stops movement when the surface is still inclined, probably due to some shear resistance at large deformation. Thus, two more terms were added to Eq.6;

$$m\frac{d^2\lambda}{dt^2}+c\frac{d\lambda}{dt}+k\lambda=k-r\tau_r \tag{7}$$

The second term added to the left-hand side stands for viscosity and the last term on the right-hand side indicates the contribution from a residual strength of sand at large distortion.

SIGNIFICANCE OF VISCOSITY TERM

It appears necessary to examine the viscous nature of liquefied sand as included in Eq.7, because liquefied sand consists of sand grains and pore water both of which have no viscous characteristics. For this purpose, model shaking tests were conducted in which a pipe embedded in a liquefied sand was pulled laterally. The drag force needed for a constant-velocity movement of the pipe was recorded together with the pipe velocity so that the rate-dependent nature of the drag force was studied.

Fig.2 illustrates the test results. Model sandy ground was of a range of density. The drag force increased with the pipe velocity, revealing a viscous nature of sand. The intensity of viscosity increased with the density of sand. Although the true mechanism of the viscosity is not known yet, the use of the viscosity term in Eq.7 appears to be reasonable.

ON RESIDUAL STRENGTH OF LIQUEFIED SAND

The residual strength of liquefied sand was needed to be studied as well. The residual strength at large shear deformation under undrained conditions has been studied by many people (e.g., Poulos et al., 1984; Ishihara, 1993) and it is to date known that the denser sand has the greater strength. However, those studies have been made by running laboratory element tests such as a triaxial one. It is important, however, that there are many differences between laboratory element tests and a shaking liquefied ground. The present study mentions two of them among others; the existence of inertia force induced by seismic acceleration and the effects of seepage force.

The differences mentioned above can be quantitatively studied to a certain extent by examining the results of model shaking tests (Toyota and Towhata, 1994). Unless the involved sand was very loose, the lateral motion of liquefied model ground stopped when excess pore water pressure was still high and the ground surface was inclined, (Fig.3). The cease of motion as observed at an inclined configuration took place because the sand maintained some shear strength.

The closed-form solution of the ultimate displacement (Towhata et al., 1992) already considered the effects of residual strength of liquefied sand. This solution was applied to interpret the present model tests in order to assess the strength of sand. The results of this assessment is indicated in Fig.4 by hollow symbols. Since the ultimate surface slope was greater when the sand was denser, the residual strength at the ultimate displacement is greater as well for denser materials.

In contrast to the impact-shaking tests as mentioned above, several model tests were carried out by continuously shaking the ground until the ultimate displacement was achieved. It was therein observed that the ground surface became level, irrespective of the sand density. Consequently, the sand strength assessed from these tests is negligible as indicated by solid symbols in Fig.4.

The effects of shaking demonstrated in Fig.4 were further studied by model-pipe tests in which a model pipe moved in the horizontal direction cyclically in a liquefied Toyoura sand. Similar to Fig.3, the drag force required for a pipe movement (10mm/sec.) was recorded together with the pipe displacement and the excess pore water pressure. Fig.5 indicates a case where the void ratio was 1.05 and the model ground was shaken by 500gal input motion with 3.5 Hz. The relationship between the drag force and the pipe displacement is qualitatively equivalent to the stress-strain behavior of tested sand, whilst the diagram of force vs. pore pressure suggests the shape of a stress-path diagram.

The force-displacement diagram in Fig.5 reveals a clear difference in the drag force during and after shaking. When shaking was going on, the magnitude of the force was held small, although fluctuating to some extent due to the inertia force. After the shaking was turned off,

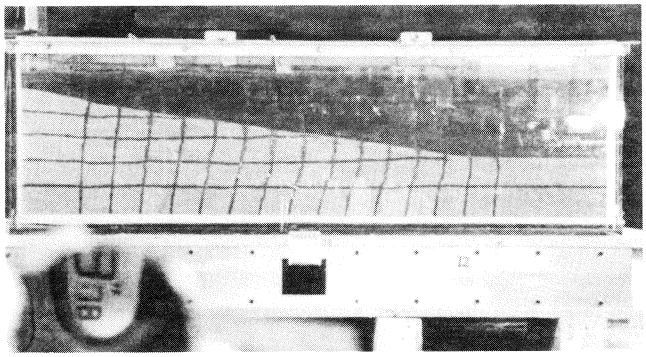

(a) Case with e=0.95

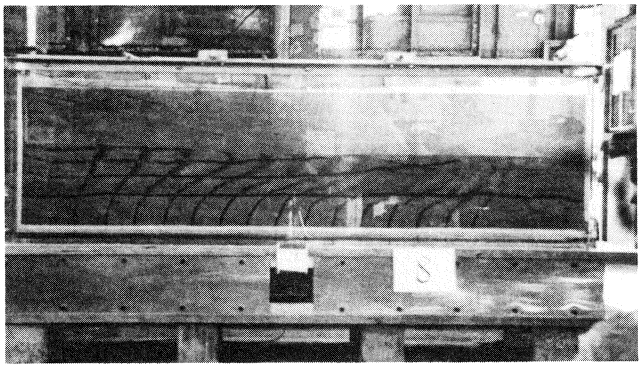

(b) Case with e=1.03 (very loose)

Fig.3 Configuration at the end of flow.

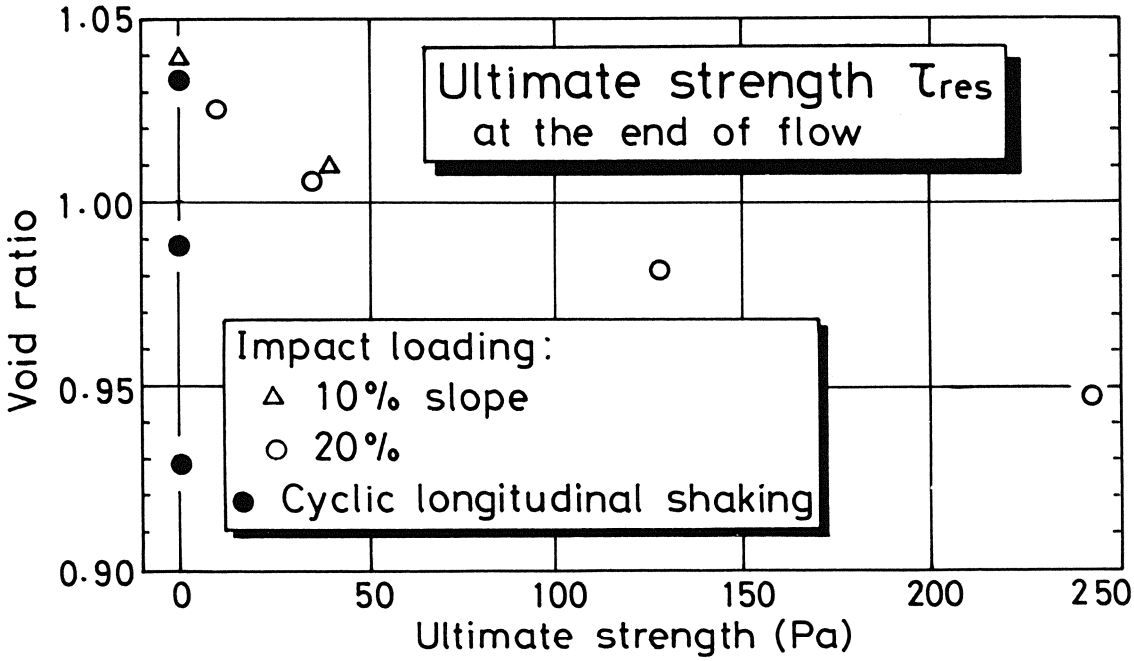

Fig.4 Variation of residual strength with sand density.

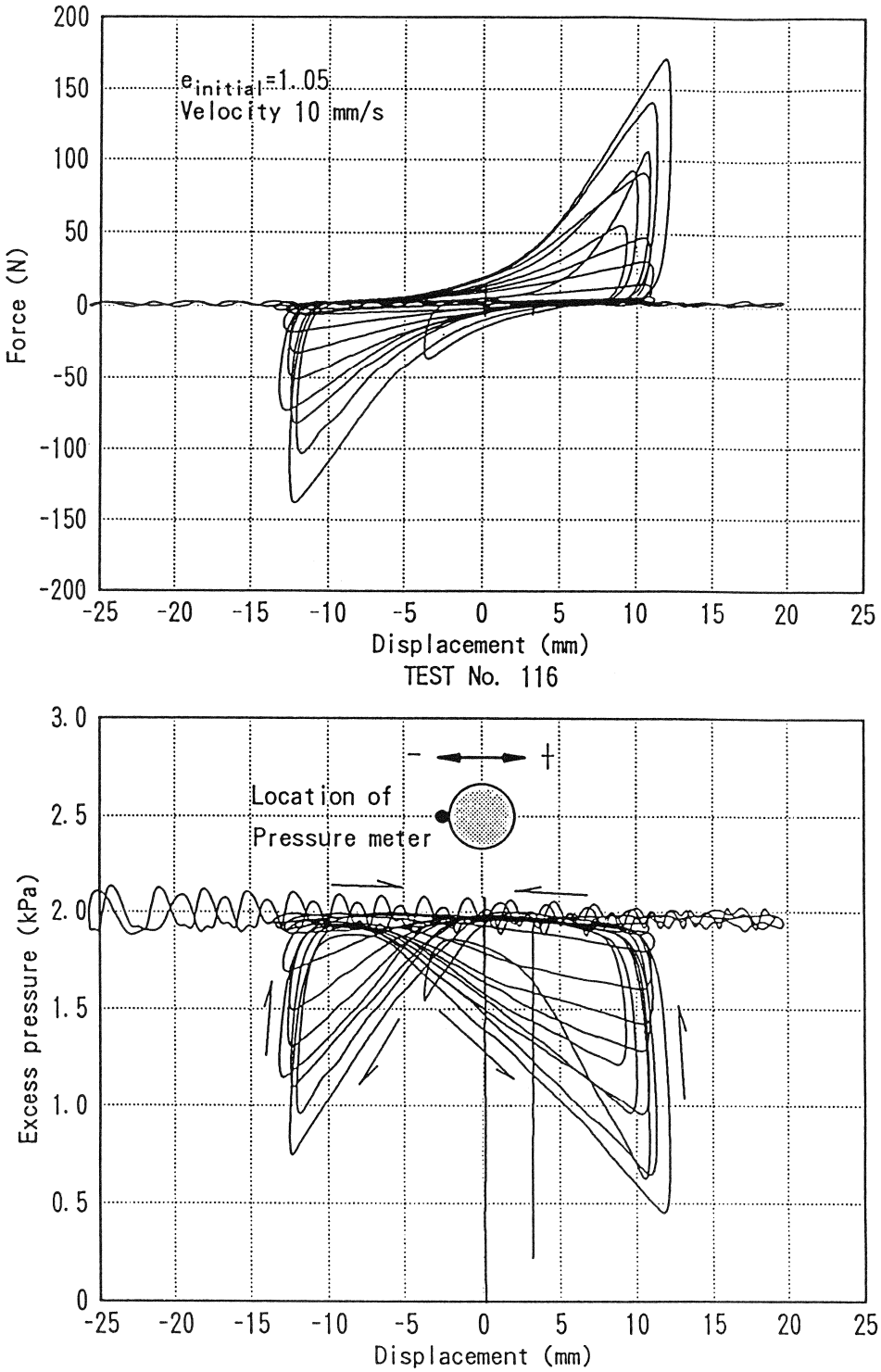

Fig.5 Model pipe test in liquefied ground.

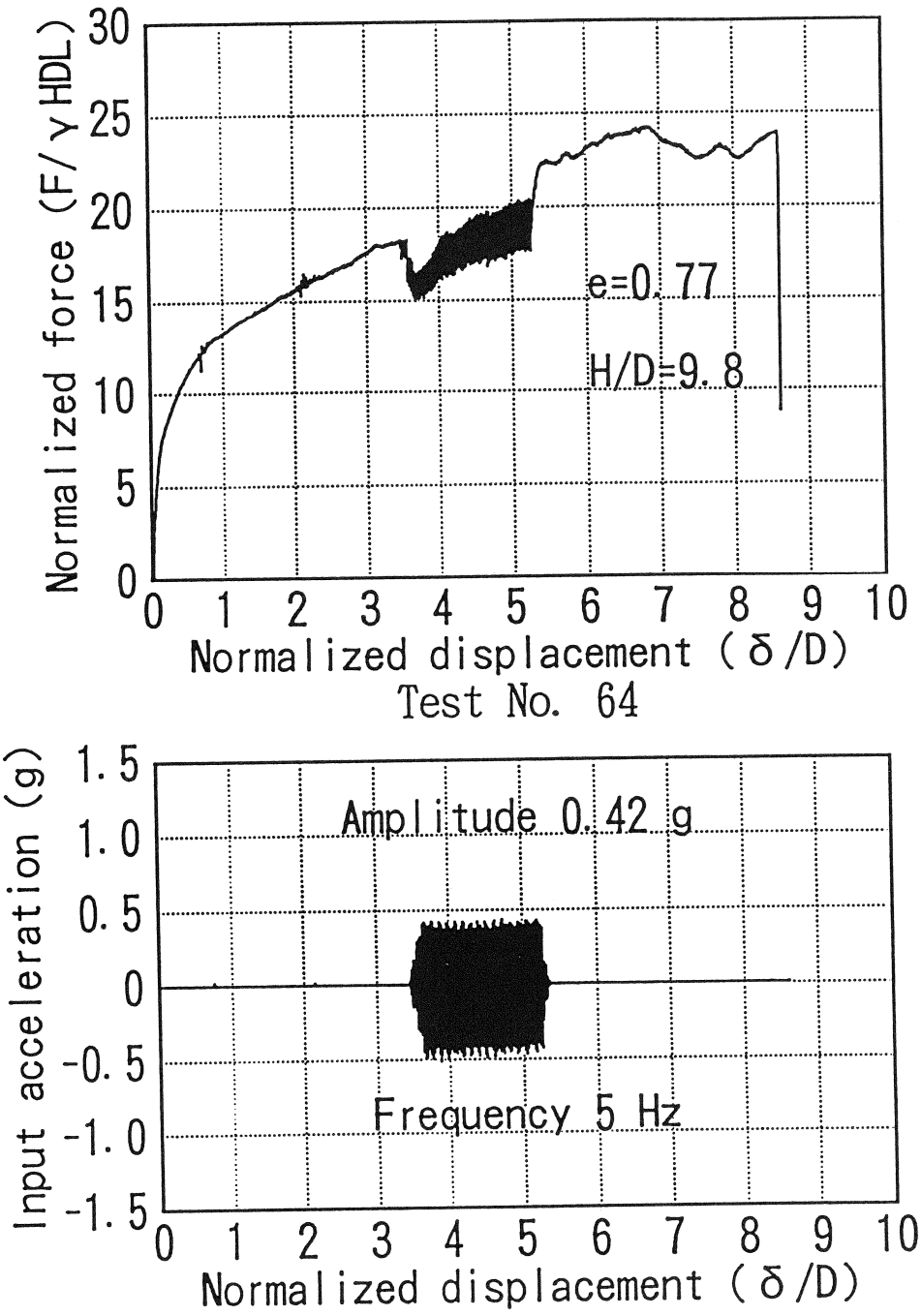

Fig.6 Model pipe test in dry sand.

on the contrary, the amplitude of the force started to be larger. The observed shape of the force-displacement curve is very similar to the undrained stress-strain behavior of loose sand.

Moreover, the variation of excess pore water pressure with displacement (Fig.5) indicates the effects of shaking similarly. In the course of shaking, the excess pore water pressure was held high and constant, indicating 100% development of liquefaction. After the end of shaking, in contrast, a temporary reduction of pore pressure towards the maximum displacement was observed. This behavior is similar to the undrained stress path diagram in which a dilatancy of grain packing induces a reduced pore pressure upon stress loading.

The reason of the difference as stated above is speculated below. The dilatancy of granular packing occurs when a sand grain is pushed by an intergranular force towards an adjacent grain. Sliding up along the surface of the second grain leads to the overall expansion of sand. When undrained, sand cannot absorb water from outside and cannot compensate for the dilatancy of packing. Consequently, the excess pore water pressure drops and the effective stress develops; thus increasing the shear stiffness. When the inertia force is superimposed upon sand during shaking, the intergranular contact force fluctuates in a very complex manner and the state of dilatant particle contact is easily destroyed. Thus, a drop of pore pressure is not necessary very much and the effective stress does not develop.

The idea of destroyed particle contact is further studied by pipe test performed in a dry sand deposit. A pipe embedded in a dry Toyoura sand (e=0.760) was pulled laterally at a rate of 4mm/sec. in a similar manner as in Fig.5. Since the sand was dry, no excess pore water pressure developed. Initially, the pipe was moved in a monotonic manner without shaking. The drag force increased with the displacement, indicating the subgrade reaction of model ground. At sometime, a lateral shaking started and the drag force decreased in magnitude. When the shaking was switched off later, the drag force came back to the extrapolation of the original loading curve. Thus, the drag force or the sand stiffness was reduced only during shaking. This observation suggests that the particle contact pressure which mainly generates the sand stiffness was destroyed to some extent by the induced cyclic inertia force.

EXAMPLE ANALYSES

Eq.7 was applied to several cases in model and insitu situations. The ultimate displacement was calculated first and then the time history of λ was obtained so that the time development of displacement, u, was calculated. The residual strength needed for analysis was determined by using Fig.4, in accordance with the static and shaken conditions. Since much is not known yet about the viscosity of liquefied sand, the viscosity coefficient, c, in Eq.7 was determined to make the critical damping equal to 0.62. Note that this value of damping ratio is equal to the one of a rigid-plastic material (see Fig.7).

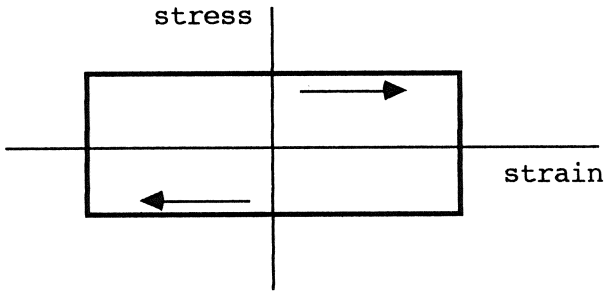

Fig.7 Rigid-perfectly plastic stress-strain curve.

Fig.8 illustrates the calculated displacement of a model ground with a variety of density. Since the flow occurred under static gravity, the residual strength under static conditions in Fig.4 was employed. The observed displacement as well as the size of the ground is demonstrated in Fig.9. See that the duration time of flow is independent of sand density or the magnitude of displacement in both calculation and observation.

Fig.10 indicates the displacement when the motion occurred under sustained shaking. The

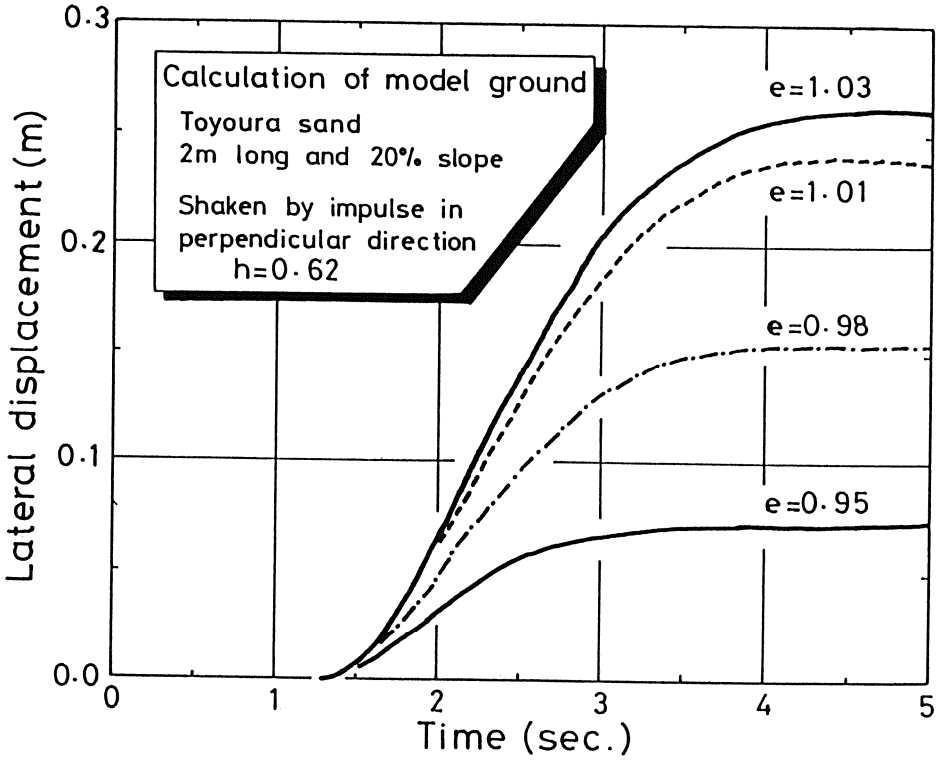

Fig.8 Calculated time history of model slope under static gravity.

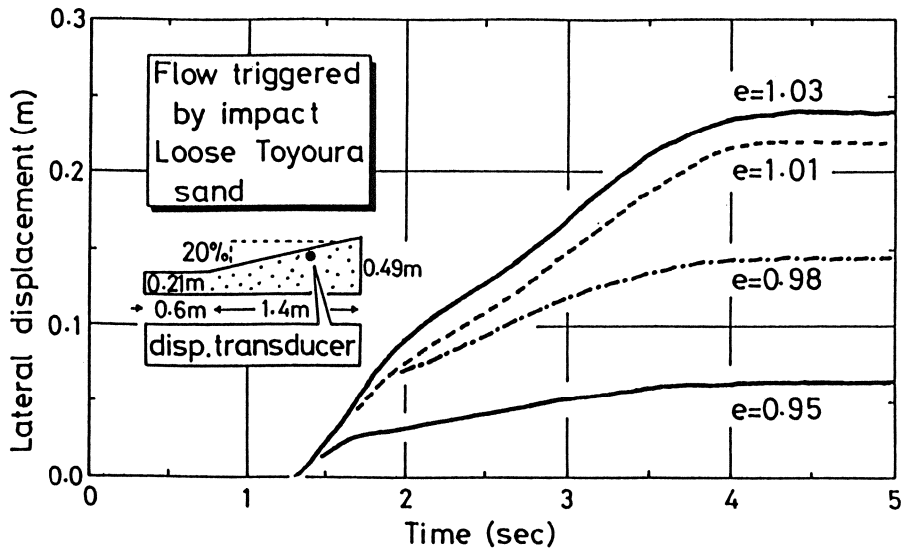

Fig.9 Observed time history of model slope under static gravity.

385

residual strength was set equal to zero as revealed in Fig.4. The viscosity was again determined to make the critical damping ratio equal to 0.62. Consequently, a good agreement between calculation and observation was achieved.

Fig.11 compares the prediction and calculation of a displacement in Noshiro City where a substantial ground displacement occurred at the time of the 1983 Nihonkai-Chubu earthquake. Since no earthquake motion was recorded at this site, a harmonic base motion of 150 gals and 2 Hz were assumed to continue for 10 seconds after the onset of subsoil liquefaction. During this shaking, the residual strength was set equal to zero and λ equal to about 0.75 was attained at the end of shaking. Since a greater strength was needed under static conditions after this time, the movement could not develop further. Hence, the ultimate deformation as obtained previously (Towhata et al., 1992) was multiplied by λ=0.75, and the displacement illustrated in Fig.11 was obtained. There appears to be a good agreement between calculation and observation by Hamada et al. (1986).

CONCLUSION

An attempt was made to develop an analytical measure to predict the time history of lateral ground movement induced by seismic liquefaction. The lack of knowledge about nature of soil undergoing lateral flow and large deformation was compensated for by running several model shaking tests. Accordingly, the following conclusions were drawn;

(1) An application of the theory of Lagrangean equation of motion made it possible to derive a single-degree-of-freedom equation of motion that is easy to solve.
(2) This equation of motion includes a viscosity term and the residual strength of liquefied sand.
(3) Model tests indicated that the resistance of liquefied sand against lateral movement of an embedded pipe is affected by the rate of pipe movement. Hence, there is a viscous nature in liquefied sand.
(4) Dilatancy of sand that could develop negative pore pressure and shear resistance against large distortion is destroyed by seismic inertia force. Hence, liquefied sand during shaking is of negligible shear strength.
(5) Sand loses strength during shaking even when it is dry.
(6) The residual strength starts to occur after shaking.
(7) It is possible to obtain a good agreement between calculation and observation.

ACKNOWLEDGMENT

The model tests described in this text were conducted by Mr.W.Vargas and Mr.M.Yao. Their contribution is deeply appreciated by the authors.

REFERENCES

Hamada,M., Yasuda,S., Isoyama,R., and Emoto,K. (1986) "Generation of Permanent Ground Displacements Induced by Soil Liquefaction," Proc. JSCE, 1986. No.376/III-6, pp.211-220.

Ishihara,K. (1993) "Liquefaction and Flow Failure during Earthquakes," Geotechnique, 1993. Vol.43, No.3, pp.351-415.

Poulos,S.J., Castro,G. and France,J.W. (1984) "Liquefaction Evaluation Procedure," Proc. ASCE, Vol.111, GT6, pp.772-792.

Towhata,I. Sasaki,Y., Tokida,K., Matsumoto,H., Tamari,Y. and Yamada,K. (1992) "Prediction of Permanent Displacement of Liquefied Ground by Means of Minimum Energy Principle," Soils and Foundations, Vol.32, No.3, pp.97-116.

Toyota,H. and Towhata,I. (1994) "Post-liquefaction Deformation of Cohesionless Soils," Proc. 5th US-Japan Workshop on Earthquake Resistant Design of Lifeline Facilities and Counter-Measures against Soil Liquefaction.

Vargas-Monge,W (1994) "Study on Flowing Liquefied Ground by Means of Model Pipe Tests", Master thesis, University of Tokyo.

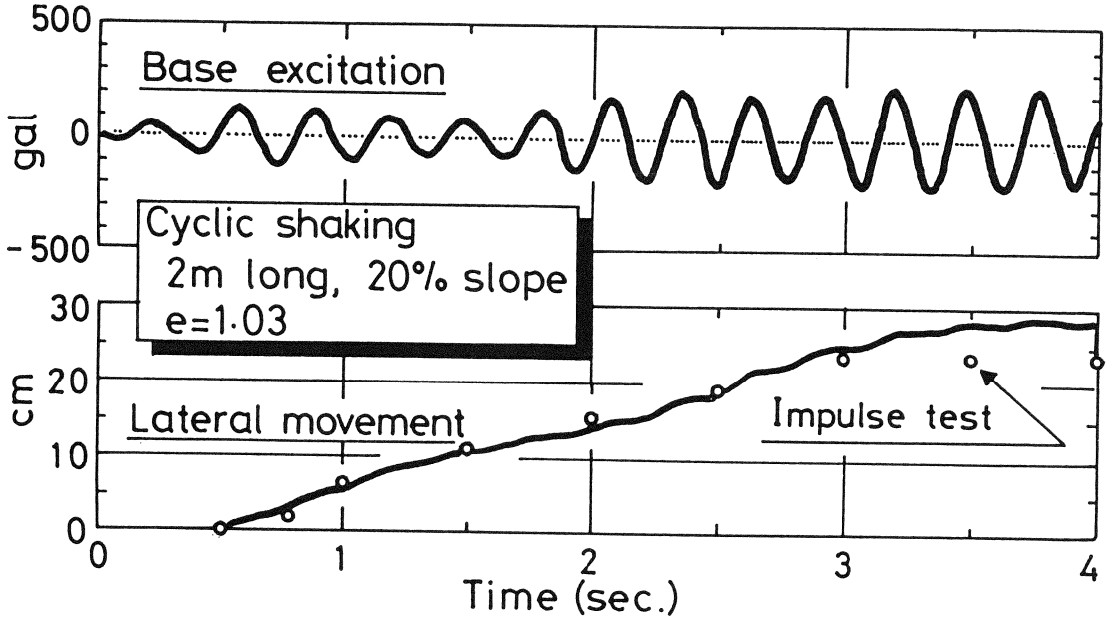

Fig.10 Displacement of slope undergoing shaking.

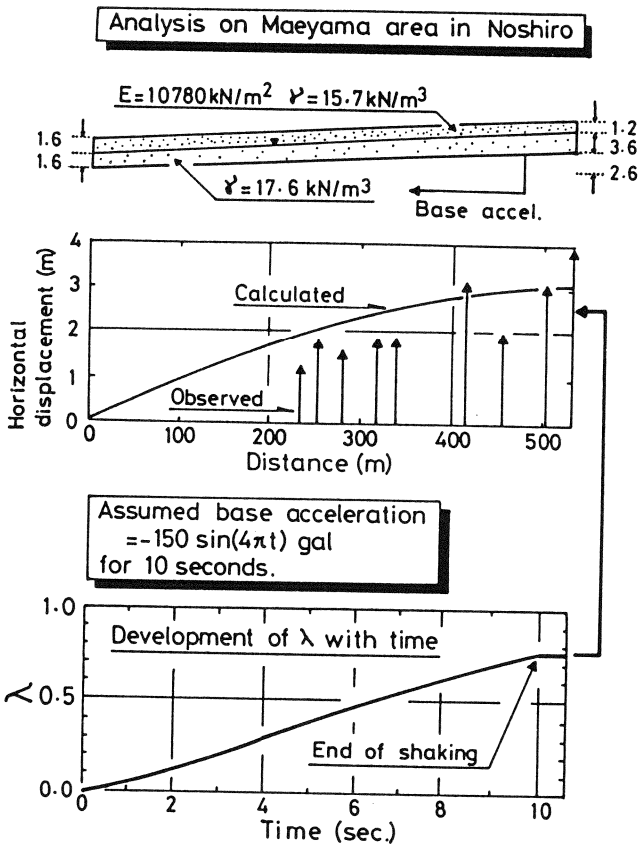

Fig.11 Calculated and observed displacement in Noshiro City.

VELACS Project: A SUMMARY OF ACHIEVEMENTS

Majid T. Manzari and K. Arulanandan
University of California at Davis

R. F. Scott
California Institute of Technology

ABSTRACT

In a collaborative and unprecedented effort, seven major universities from United States and England studied the liquefaction phenomena and its consequences by conducting extensive centrifuge tests on nine carefully selected centrifuge models. In addition, more than 20 groups of researchers from all over the world participated in a Class-A prediction exercise to predict the response of centrifuge models before they were conducted. This paper summarizes the lessons learned from the VELACS project in relation to repeatability of centrifuge models and performance of the existing numerical procedures in analyzing soil liquefaction and its consequences.

INTRODUCTION

The VELACS project (VErification of Liquefaction Analysis using Centrifuge Studies) was a collaborative effort among seven universities: University of California, Davis; California Institute of Technology; Cambridge University; University of Colorado, Boulder; Massachusetts Institute of Technology; Princeton University; and Rensselaer Polytechnic University. The project was the most extensive effort ever undertaken to determine the mechanisms involved in liquefaction, and to evaluate the consequences of soil liquefaction. Nine significant boundary value problems were modeled and tested at different centrifuge facilities, including uniform level ground, stratified layers, heterogeneous embankments, waterfront structures, and a soil structure interaction problem. More than twenty groups from different parts of the world, including USA, England, France, and Japan participated in the Class A prediction exercise which "predicted" the responses of the centrifuge models. The results of experimental studies as well as the Class A predictions are reported in the first volume of the Proceedings of the VELACS International Conference held from October 17 to October 20, 1993 at the University of California, Davis. In addition, an extensive series of overview papers, discussing different aspects of the centrifuge tests and the Class A predictions, was presented in the VELACS conference. A Second Volume of conference proceedings containing these papers will be published in September of 1994.

ACHIEVEMENTS OF THE VELACS PROJECT

Some of the primary technical conclusions of the VELACS project are summarized below.

1. Centrifuge modeling was found to be a reliable tool for studying the mechanisms of soil behavior in boundary value problems. It can produce repeatable results in different facilities provided that the centrifuge modelers follow a unified method of model preparation, and that the centrifuge facilities are capable of producing simulated earthquake motions consisting of a wide range of frequencies (See for example the results of Models 1, 2, 4a and 4b in the VELACS proceedings, Vol. 1, edited by Arulanandan and Scott, 1993; Also see Figures 1 to 5 which show the model configuration, planned base motion, and partial results for model 4-a). However, the effect of the frequency characteristics of the shaker, the boundary effects of the model container, and the minimization of undesirable effects such as unwanted vertical base motions should be thoroughly studied in future applications of centrifuge modeling. Figures 7 to 9 show the model configuration, and difficulties in achieving repeatable results in model 7 of the VELACS project.

2. The existing numerical procedures for soil liquefaction analysis are generally effective in simulating the onset of liquefaction in contractive cohesionless soils. However, a wide range of differences exist in the predictions of liquefaction induced deformations made by different procedures. (See for example the lateral displacements predicted by different groups for Model #2. It ranges from less than 10 cm to more than 80 cm, while the measurements showed a maximum of 40 cm - see VELACS Proceedings, Vol. 1, 1993) Comparison of the results reported by different predictors with the experimental results shows that fully coupled effective stress based procedures which utilize plasticity based constitutive model are more promising for the prediction of deformation than partially coupled procedures or total stress based procedures which utilized empirical relationships to correlate pore pressure generation with the volumetric soil strain (see for example the predictions reported in pages 153-168 of the VELACS proceedings, Vol. 1). The VELACS Class A predictions revealed that the latter procedures may also produce unrealistic trends of deformation for contractive soils during the shaking phase (See for example Figs. 25-30, pp. 243--245 and Figs. 16-20, pp. 407-410, VELACS Proceedings, Vol. 1, 1993; Also see Figures 10 to 12 which show the model configuration, planned base motion, the recorded acceleration and pore pressure time histories, and the predicted time histories of the vertical settlement in model no. 1 of the VELACS project.

3. All the available numerical procedures are generally deficient and inadequate in simulating the behavior of dilative soils. A close examination of the Class A predictions reported by four different groups of predictors for the VELACS Model #6 (a heterogeneous embankment consisting of a relatively dense sand core overlain by a silt layer) reveals that predictions of pore water generation in the sand core generally do not agree with the experimental results (see predictions reported in pp. 773 and 779 compared to those reported in pp. 741-742 of the VELACS proceedings, Vol. 1, 1993). Such a discrepancy between numerical simulations and experimental results is expected since the existing constitutive models used to simulate the cyclic behavior of dense sands are inadequate.

4. One of the major lessons learned form the VELACS project is in any effective stress based procedure, the constitutive model plays a key role in the analysis of soil liquefaction and deformation. A comparison of the different predictions made by effective stress based procedures in the VELACS Class A prediction exercise shows significant differences in the predictions made with only slightly different u-p or u-U formulations. (See for example, the predictions reported in pp. 745-765 compared to the predictions reported in pp. 777-779, VELACS Proceedings, Vol. 1, 1993). These differences may have been caused by many factors, including:

a) The inability of existing models to simulate the stress-strain response of non-cohesive soils for different stress (or strain) paths using a unique set of parameters. In most of the models, a compromise is made in choosing an average set of parameters which should most closely represent the stress path in the boundary value problem. When using this calibration procedure, considerable engineering judgement is required. In general, predictors try to get the best fit to laboratory tests. However, the lack of a standardized procedure for achieving the "best fit" results in various sets of material parameters, even for those using the same constitutive model to predict the same problem. (See for example the calibrated parameters for one of the constitutive models used by two different groups in the VELACS Class A predictions; pp. 187 and 248 in the VELACS proceedings, Vol. 1). The major reason for the use of different calibration procedures is that the models are not capable of producing reasonable simulations for different stress paths and different relative densities in non-cohesive soils. Therefore, predictors try to get the best out of a deficient model by using their previous experience in the application of the model to other boundary value problems. Evidently, difference in experiences will result in differences in calibrated parameters.

b) Different methods have been used to implement the plasticity based models in the computer codes. The accuracy and stability of these methods has not been thoroughly studied. A close examination of the published materials on the constitutive models used in the VELACS project reveals that most of the constitutive equations are integrated using conventional integration procedures for general plasticity models. In most cases, the special features of the constitutive models used for non-cohesive soils such as the pressure-dependent moduli have not been adequately accounted for in the integration procedure. Recent studies (Borja, 1991) show that even in the case of the simplest soil plasticity model (modified cam clay) special treatments are necessary if accurate and reliable results are to be obtained.

REFERENCES

Arulanandan, K. and Scott, R. F. (1993), "Verification of Numerical Procedures for the Analysis of Soil Liquefaction Problems." Proceedings of the International Conference on the Verification of Numerical Procedures for the Analysis of Soil Liquefaction Problems, held at the University of California, Davis on October 17 to 21, 1993. Balkema Press, Rotterdam.

Borja (1991), "Cam Clay Plasticity. 2., Implicit Integration of Constitutive Equation Based on a Nonlinear Elastic Stress Predictor." Computer Methods in Applied Mechanics and Engineering, Vol. 88, No. 2, pp. 225-240, July.

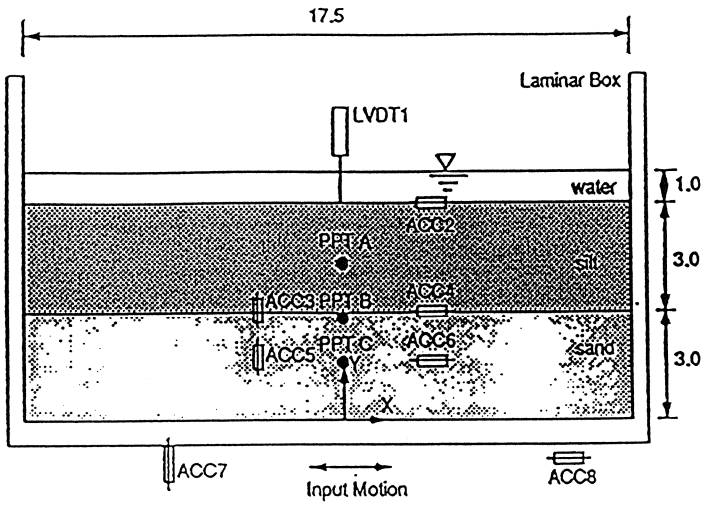

Coordinates of transducers unit: m

transducer	X	Y	Z	transducer	X	Y	Z
ACC2	2.54	6.00	0.00	ACC8	6.35	-0.63	0.00
ACC3	-2.54	3.00	0.00	PPT A	0.00	4.50	0.00
ACC4	2.54	3.00	0.00	PPT B	0.00	2.90	0.00
ACC5	-2.54	1.50	0.00	PPT C	0.00	1.50	0.00
ACC6	2.54	1.50	0.00	LVDT1	0.00	5.00	3.00
ACC7	-6.35	-0.63	0.00				

Fig. 1 Cross-sectional view of the centrifuge model no. 4a of the VELACS project.

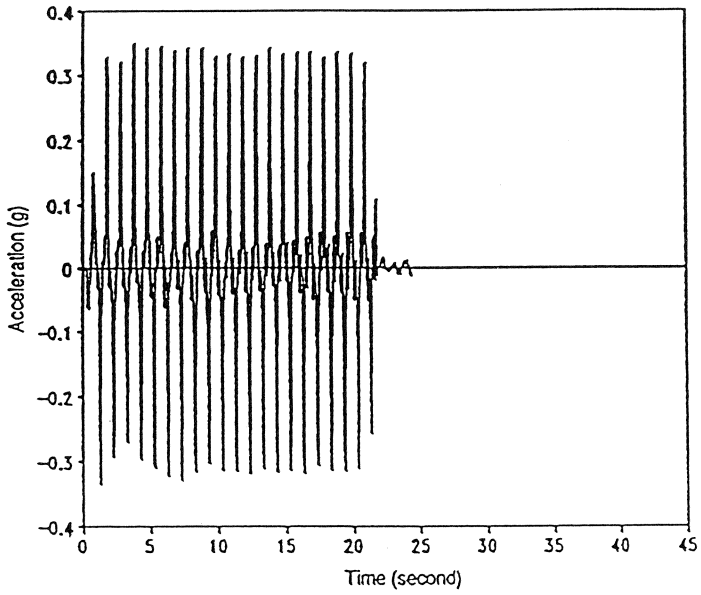

Fig. 2 Planned horizontal input motion for model no. 4a of the VELACS project

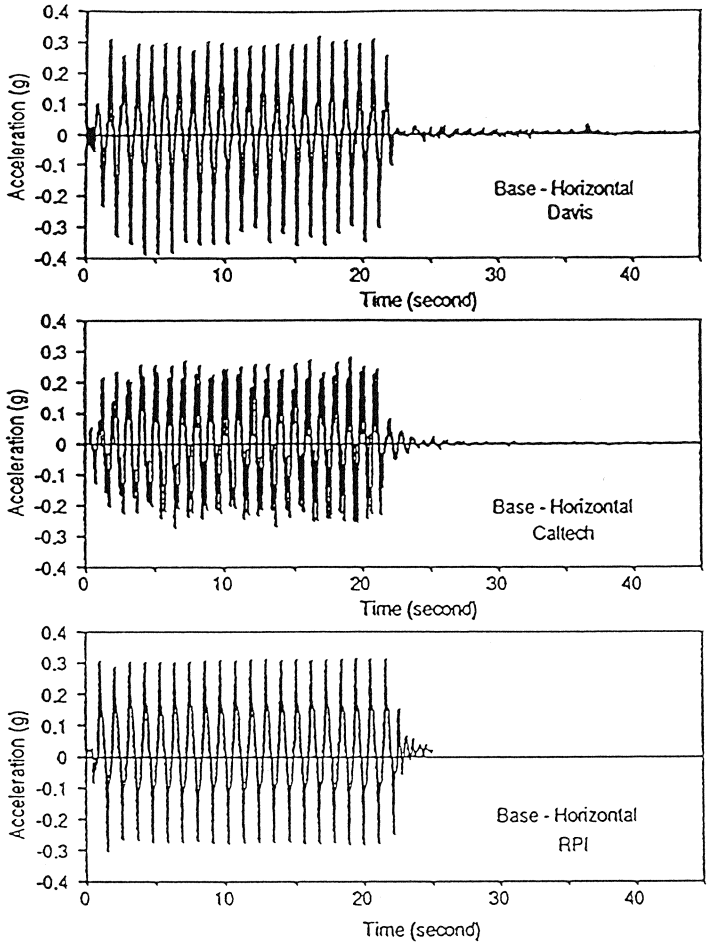

Fig. 3 Horizontal achieved input motion of model no. 4a of the VELACS project.

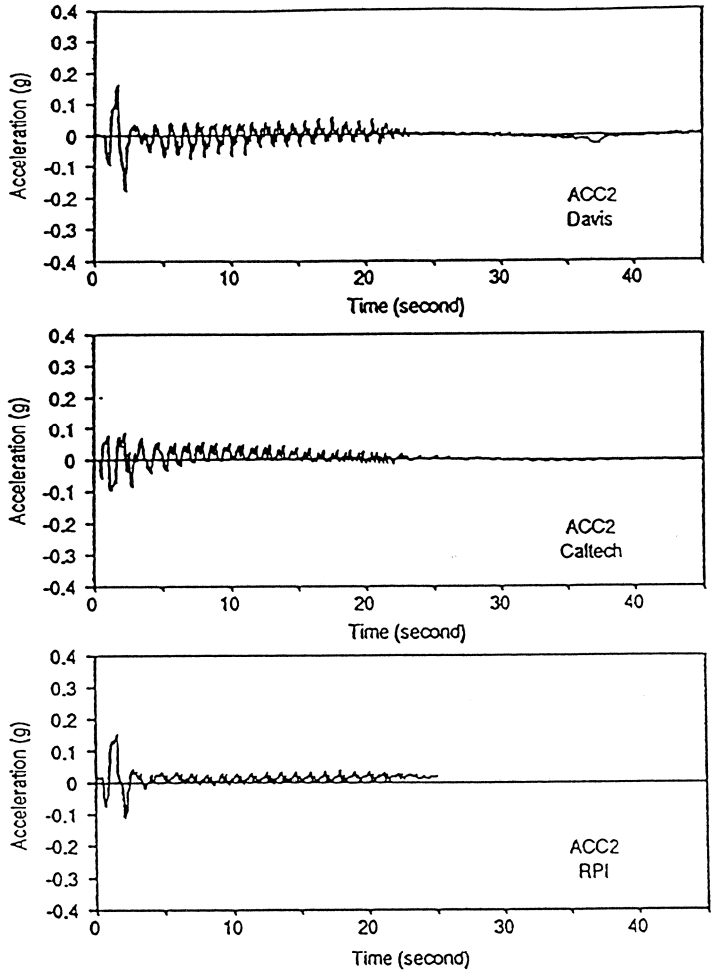

Fig. 4 Horizontal acceleration recorded at the surface, model 4a of the VELACS project

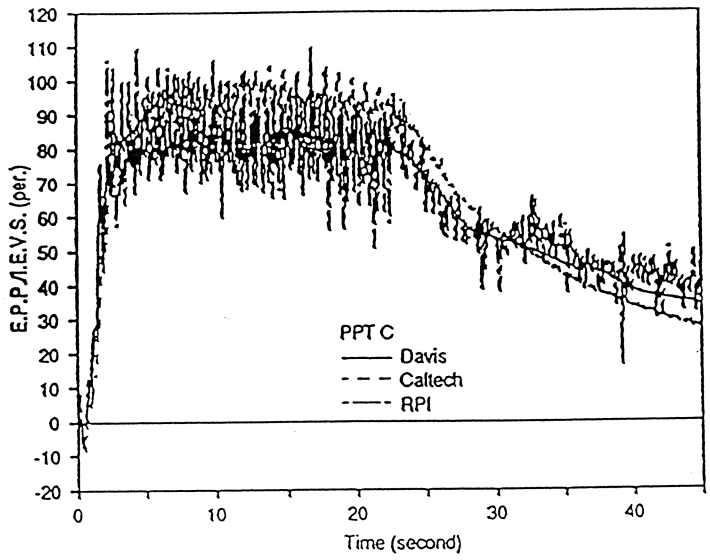

Fig. 5 Excess pore pressure measured at mid-depth of sand layer, model 4a of the VELACS project.

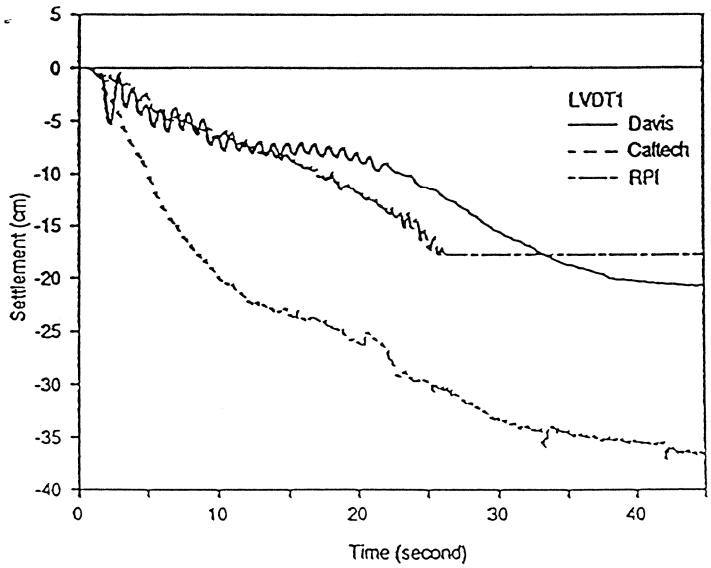

Fig. 6 Settlement of the silt surface, model 4a of the VELACS project

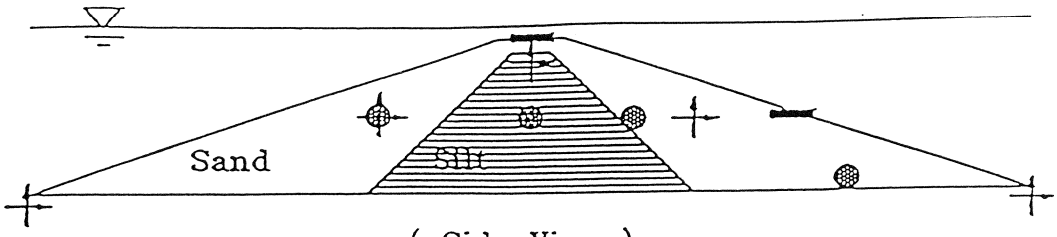

(Side View.)

LEGEND

Horizontal Accelerometer

Vertical Accelerometer

Pore Pressure Transducer

Displacement Transducer

a: Model #7 configuration at CU
(from Astaneh et al. (1993))

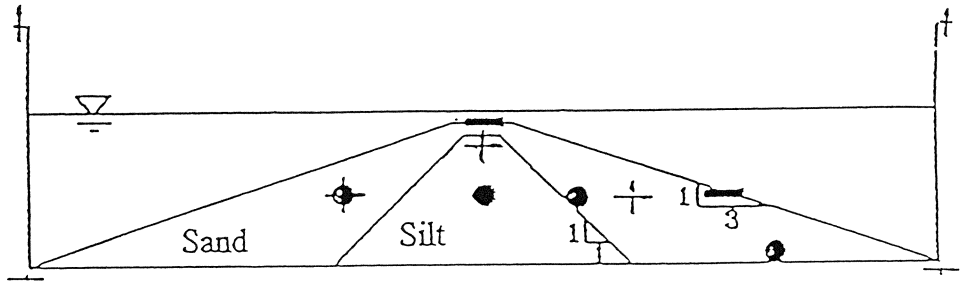

b: Model #7 configuration at RPI
(from Adalier et al. (1993))

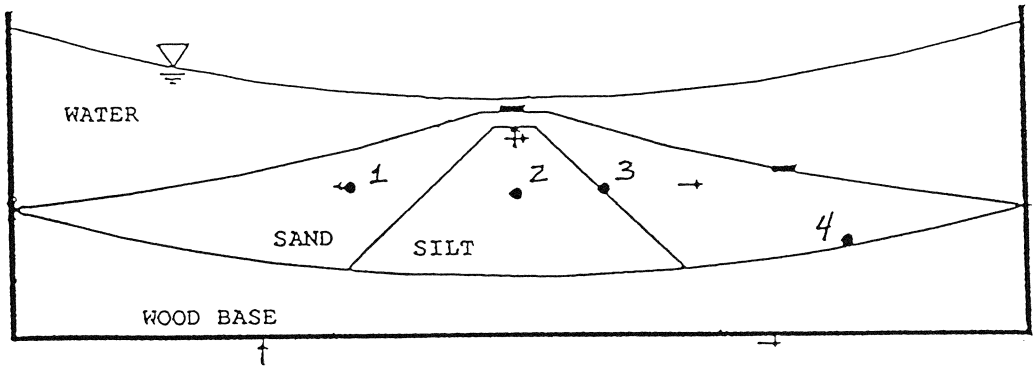

c: Model #7 configuration at UCD

Fig. 7 Cross-sectional view of the centrifuge model no. 7 as constructed at different facilities in the VELACS project

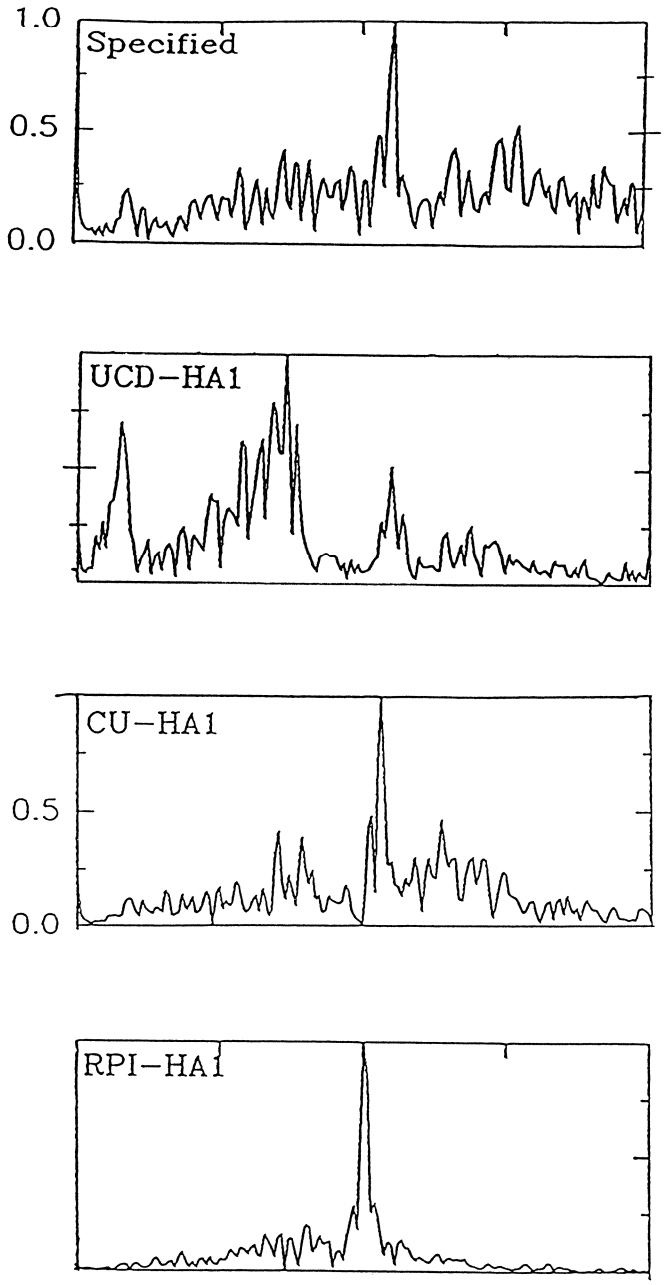

Fig. 8 Fourier spectrums of the achieved base motion at different facilities for model no. 7 of the VELACS project.

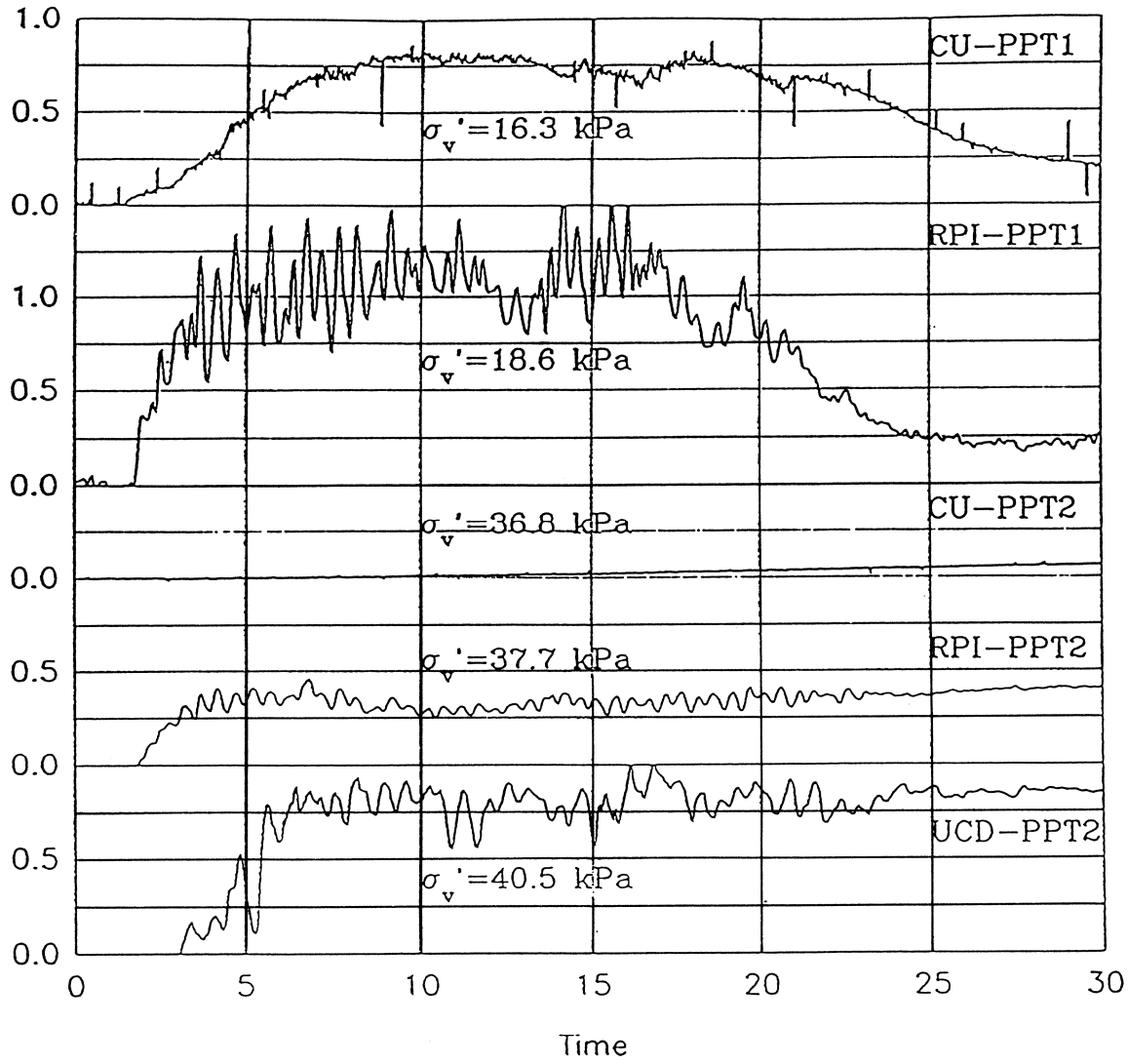

Fig. 9 Normalized excess pore pressure measured at different centrifuge facilities for model no. 7 of the VELACS project.

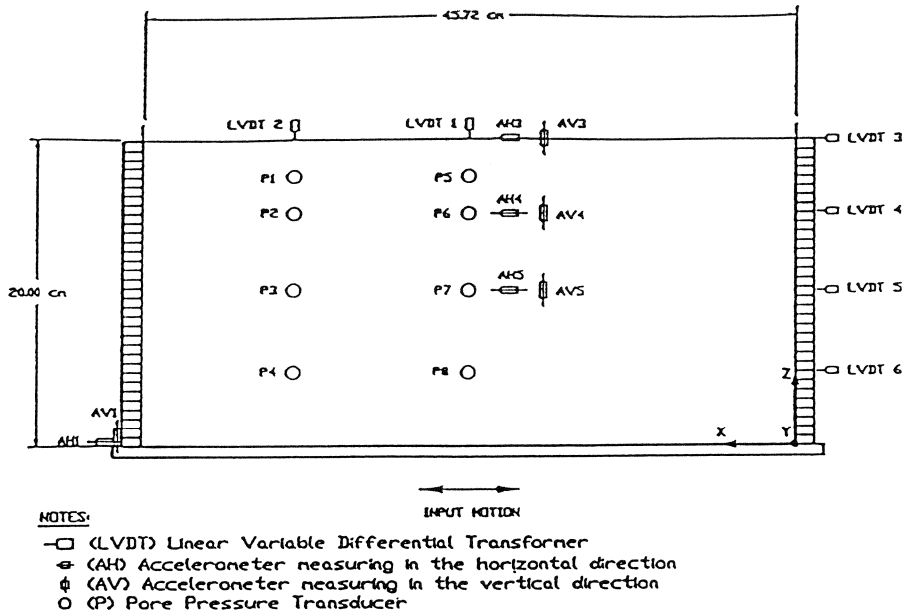

SIDE VIEW OF MODEL No. 1

R.P.I. Laminar Box and Model No. 1.

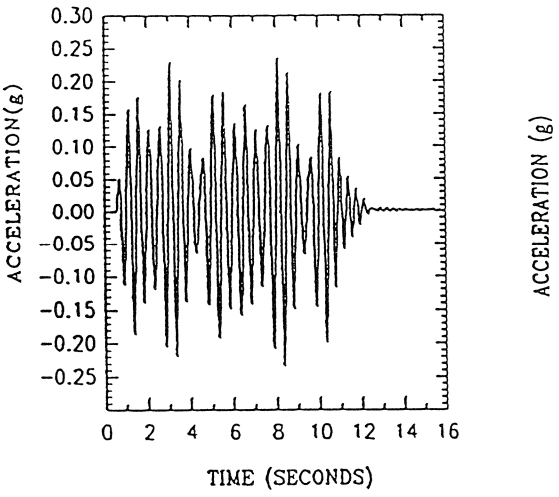

Prototype Horizontal Input Acceleration Proposed for Model No.1.

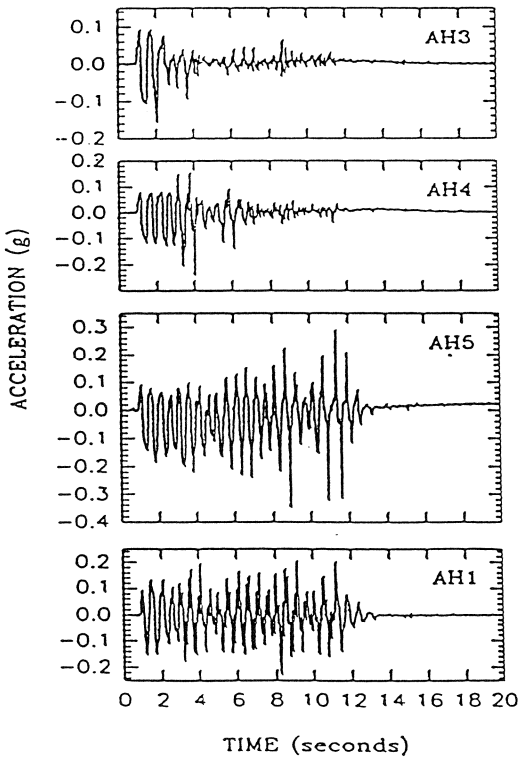

Plot Group 4, Horizontal Accelerations AH1-AH5.

Fig. 10 Model Configuration, planned base motion, and some measured acceleration time histories for model #1 of the VELACS project.

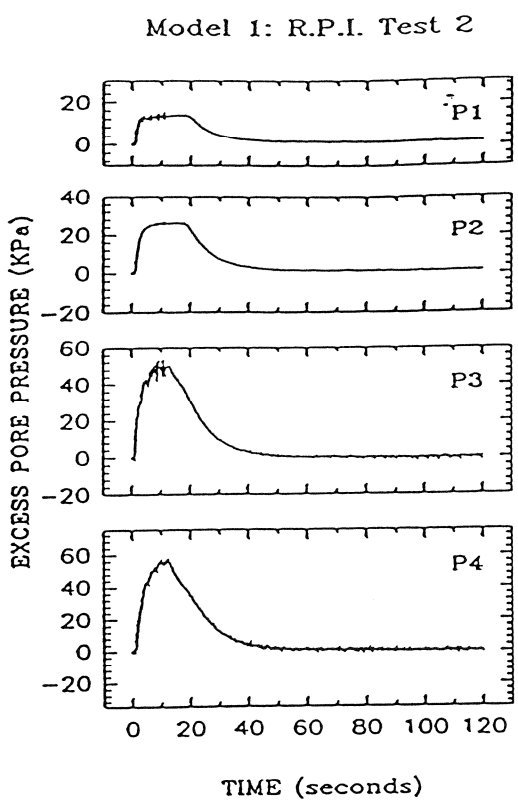

Plot Group 1, Long Term Excess Pore Pressure Histories of P1-P4.

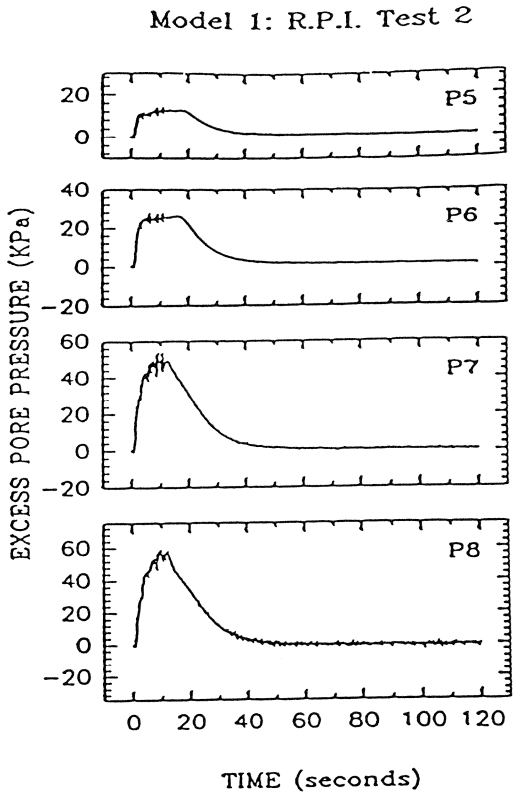

Plot Group 1, Long Term Excess Pore Pressure Histories of P5-P8.

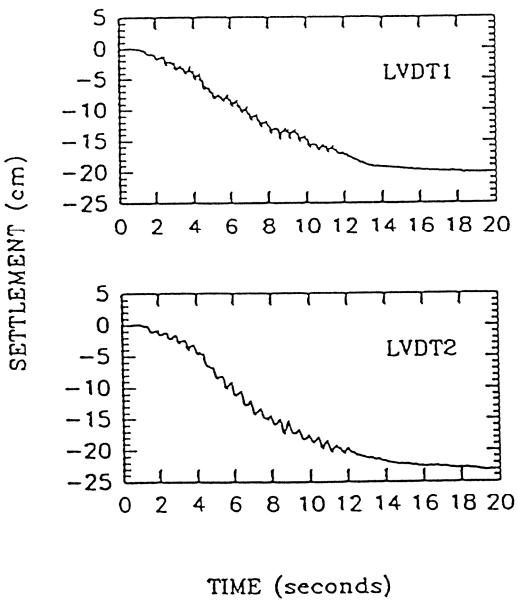

Plot Group 5, Short Term Vertical Settlements of Ground Surface.

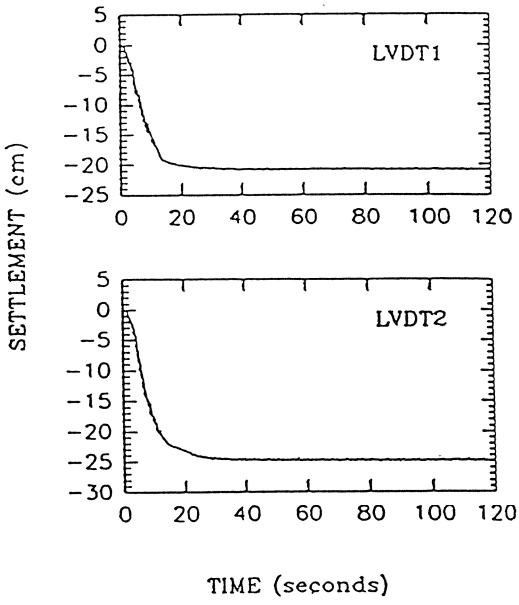

Plot Group 6, Long Term Vertical Settlements of Ground Surface.

Fig. 11 Pore pressure time histories and vertical displacement time histories for model no. 1 at RPI.

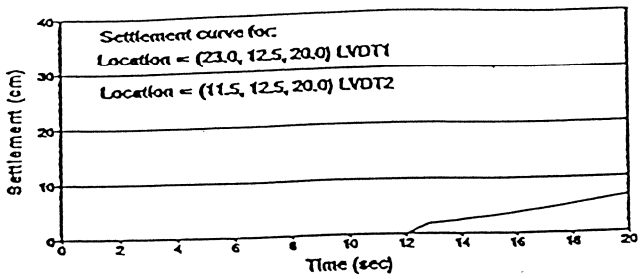

Total Stress or Uncoupled Results:

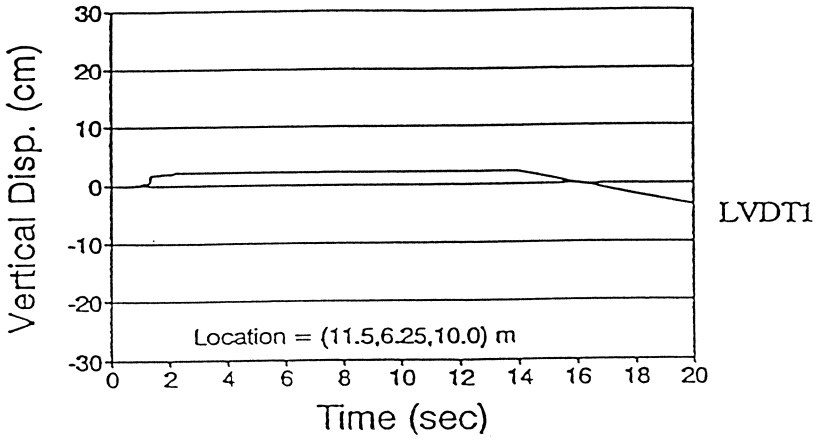

Partially Coupled Results:

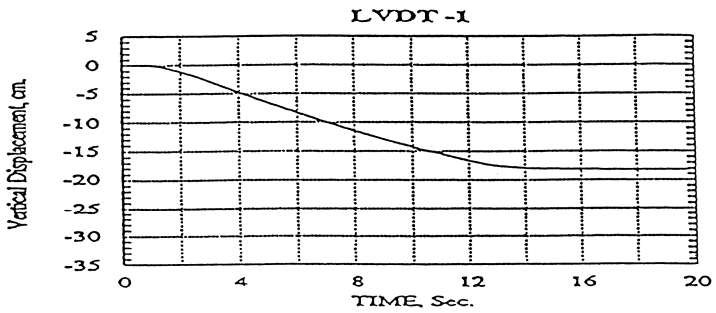

Fully Coupled Results:

Fig. 12 Predictions for contractive soils (Model no. 1 of the VELACS project)

AN EXPERIMENTAL STUDY OF EFFECTS OF LATERALLY FLOWING GROUND ON IN-GROUND STRUCTURES

H. Sato[1], M. Hamada[2] and M. Doi[3]

ABSTRACT

This paper describes an experimental study of effects of laterally flowing ground induced by liquefaction on in-ground structures. In order to investigate the effects, the authors conducted shaking table tests concerning the mechanical properties of liquefied soil.

Generally, there are two kinds of view points for the evaluation of the behavior of liquefied ground. In the first view point, the liquefied ground is assumed to behave as a fluid, and in the second, it is assumed to still behave as a solid with largely reduced stiffness. In this paper, the authors took the first view point based on the findings from the case studies on liquefaction-induced ground displacements during past ten earthquakes.

The following shaking table tests were conducted to investigate the mechanical properties of liquefied soil as a viscous material:

1) Test using a sphere which is drawn up vertically in liquefied soil
2) Test using a pipe which is drawn horizontally in liquefied soil

From the results of both tests, it was recognized that the coefficient of viscosity of liquefied soil, which was calculated from the reactive load acting on the sphere and the pipe, depended on the magnitude of input acceleration and also on the relative density of liquefied soil, namely it depended on the degree of liquefaction severity. In this paper, F_L-value was adopted as an index to estimate the degree of liquefaction severity and the relationship between the coefficients of viscosity and the F_L-values was investigated. From the two kinds of tests it was concluded that the coefficient of viscosity of liquefied soil had a close correlation with the degree of liquefaction severity, and could be estimated quantitatively by F_L-value.

Introduction

At the time of 1983 Nihonkai-Chubu earthquake, liquefaction-induced large ground

[1]Senior Researcher, Engineering Research Center, The Tokyo Electric Power Company, Chofu, Tokyo, Japan
[2]Professor of Civil Engineering, Waseda University, Tokyo, Japan
[3]Researcher, Engineering Research Center, The Tokyo Electric Power Company, Chofu, Tokyo, Japan

displacements were for the first time measured on aerial photographs which were taken at the pre- and post-earthquake (Hamada et al., 1986). After that, case studies of past ten earthquakes in Japan, U.S. and Philippines have been conducted under a cooperation between Japanese and U.S. researchers (Hamada and O'Rourke, 1992). Based on the results from the case studies, influential factors for the magnitude of liquefaction-induced large ground displacements were examined, and empirical formulae for the prediction of the ground displacements were proposed (Hamada, 1986, Bartlett et al., 1992).

One of research subjects on liquefaction-induced large ground displacements is to investigate the mechanism of the occurrence of the ground displacements with a magnitude of several meters, which were recognized even in almost flat ground with a gradient less than 1 %. Another research subject is to study the effect of large ground displacements on in-ground structures such as foundations and buried pipes.

Generally, there are in principle two kinds of view points to evaluate the behavior of the soil that constitutes liquefied ground which is deforming toward large ground displacement. The first is that the liquefied soil behaves as a fluid. The second is that it still behaves as a solid, but its stiffness is largely reduced due to the liquefaction. As a combination of the two, furthermore, a third view point is possible, where the liquefied soil behaves with dual phases of a liquid and a solid.

Based on the first view point, we conducted experimental studies on the mechanical properties of liquefied soil.

Methods of Laboratory Tests

The following two tests were conducted for the evaluation of the mechanical properties of liquefied soil:

1) Sphere test: Test using a sphere which is drawn up vertically in liquefied soil

2) Pipe test: Test using a pipe which is drawn horizontally in liquefied soil

Outline of each test is shown in Figures 1 and 2 respectively. The sphere test was conducted with a cylindrical and rigid box with a diameter of 1.0 m and a height of 1.0 m, and Toyoura sand was used. Liquefaction of the soil was induced by sinusoidally shaking the box, and after complete liquefaction, a steel sphere was lifted up in the liquefied soil with a constant velocity, and the reactive load acting on the sphere during the lifting was measured. Sixty cases of tests were conducted with four variable parameters, i.e., diameter of the sphere, input acceleration for shaking table, relative density of the soil and lifting velocity of the sphere, as shown in Table 1.

Table 1. Parameters of sphere test.

Diameter of the Sphere (mm)	Input Acceleration for Shaking Table (cm/s^2)	Relative Density of the Soil (%)	Lifting Velocity of the Sphere (cm/s)
30, 50, 100	150, 250, 350	10, 30, 50	1, 3, 6

The pipe test was done in a similar way to the sphere test's. The rigid soil box has a length of 1.8 m, a width of 0.8 m and a height of 1.0 m. An aluminum pipe with a diameter of 5 cm and a length of 70 cm was moved horizontally with a constant velocity

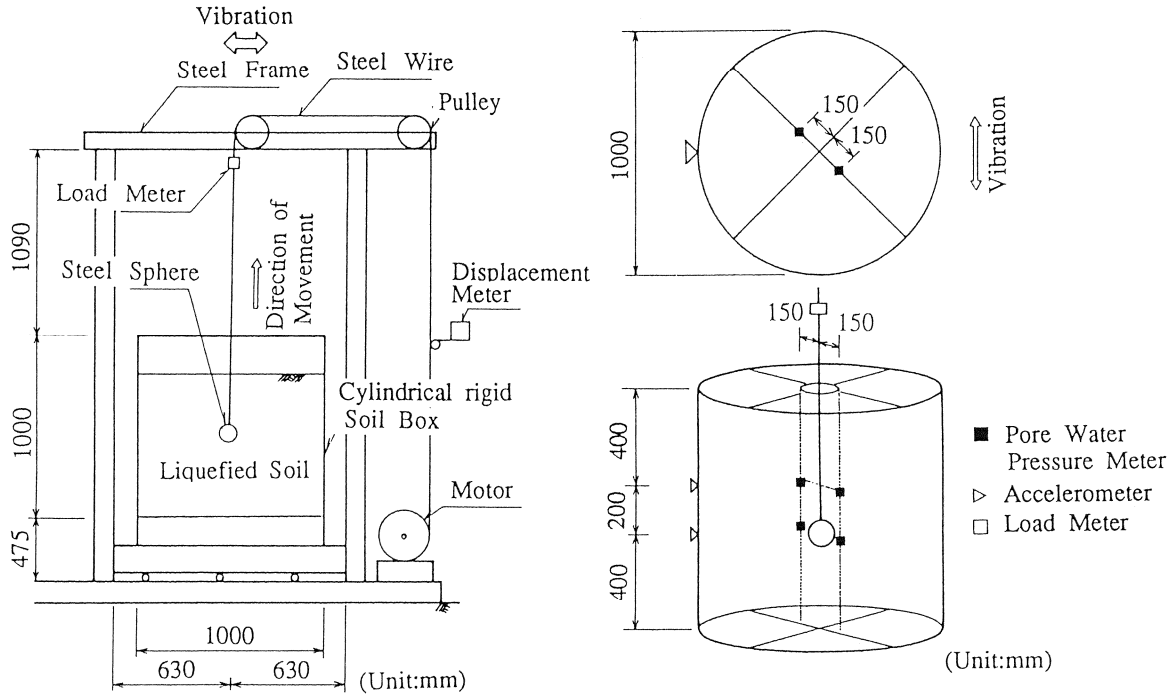

(a) Equipment of sphere test (b) Arrangement of instruments

Figure 1. Outline of sphere test.

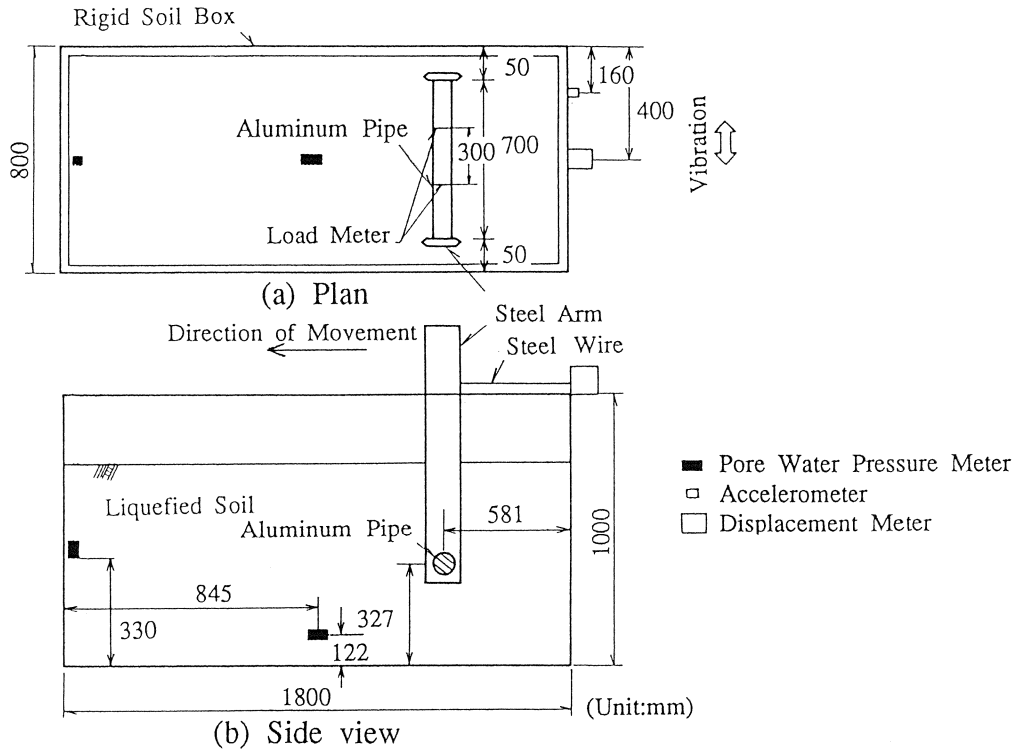

Figure 2. Outline of pipe test.

after complete liquefaction of Toyoura sand. The soil box was shaken in the direction perpendicular to the direction of pipe movement, so that the effects of the inertia force acting on the pipe could be neglected. The reactive load acting on the pipe during the moving was measured by load meters installed in the pipe. Twenty-three cases of tests were conducted with three variable parameters, i.e., input acceleration for shaking table, relative density of the soil and moving velocity of the pipe, as shown in Table 2.

Table 2. Parameters of pipe test.

Input Acceleration for Shaking Table (cm/s^2)	Relative Density of the Soil (%)	Moving Velocity of the Pipe (cm/s)
80 - 500	25, 35, 45	1, 5

Results of Tests

Results of Sphere Tests

Two examples of the results of sphere tests are shown in Figure 3. For both cases, the diameters of spheres are 5 cm, and the relative density and the lifting velocity are almost the same, about 30 % and 3.4 cm/s respectively. However, the input accelerations at the basement of the soil box in each cases are different, 122 cm/s^2 and 379 cm/s^2. The pore water pressure shows that the sand is completely liquefied before and throughout the lifting. The load on the sphere firstly decreases due to the buoyancy of the liquefied soil. The maximum load in the case of larger input acceleration is less than that in the case of smaller input acceleration. Furthermore, according to other tests, while the other three parameters are almost the same, it is also recognized that the maximum load in the case of smaller relative density is less than that in the case of larger relative density.

Figure 4 shows the relationship between the load on the sphere and the excess pore water pressure on the surface of the sphere in preliminary tests. The excess pore water pressure gradually decreases and fluctuates as the sphere is lifted, and this fluctuation coincides well with the load fluctuation. Namely, when the excess pore water pressure has a negative peak, the load has a positive peak, and *vice versa*. The reason is inferred such that the completely liquefied soil around the sphere would recover its stiffness temporarily due to the mobilization induced by the lifting of the sphere and afterwards this incompletely liquefied soil with recovered stiffness would be liquefied again completely by shaking the soil box, and this phenomenon occurs repeatedly around the sphere during the lifting, which can explain the fluctuation of the load in full tests shown in Figure 3.

From above observation, while the soil is completely liquefied in the full tests, the degree of liquefaction severity is greater in the case of larger input acceleration than that in the case of smaller input acceleration, and that is why the load in the case of larger input acceleration is less than that in the case of smaller input acceleration, as shown in Figure 3. In addition, such interpretation might help to explain the difference of the load in the different relative density tests. These results suggest that the mechanical properties of liquefied soil depend on the degree of liquefaction severity, and that the coefficient of viscosity of liquefied soil is governed by the degree of the liquefaction severity.

Therefore, the Factor of Liquefaction Intensity F_L (Iwasaki, et al., 1978) was adopted

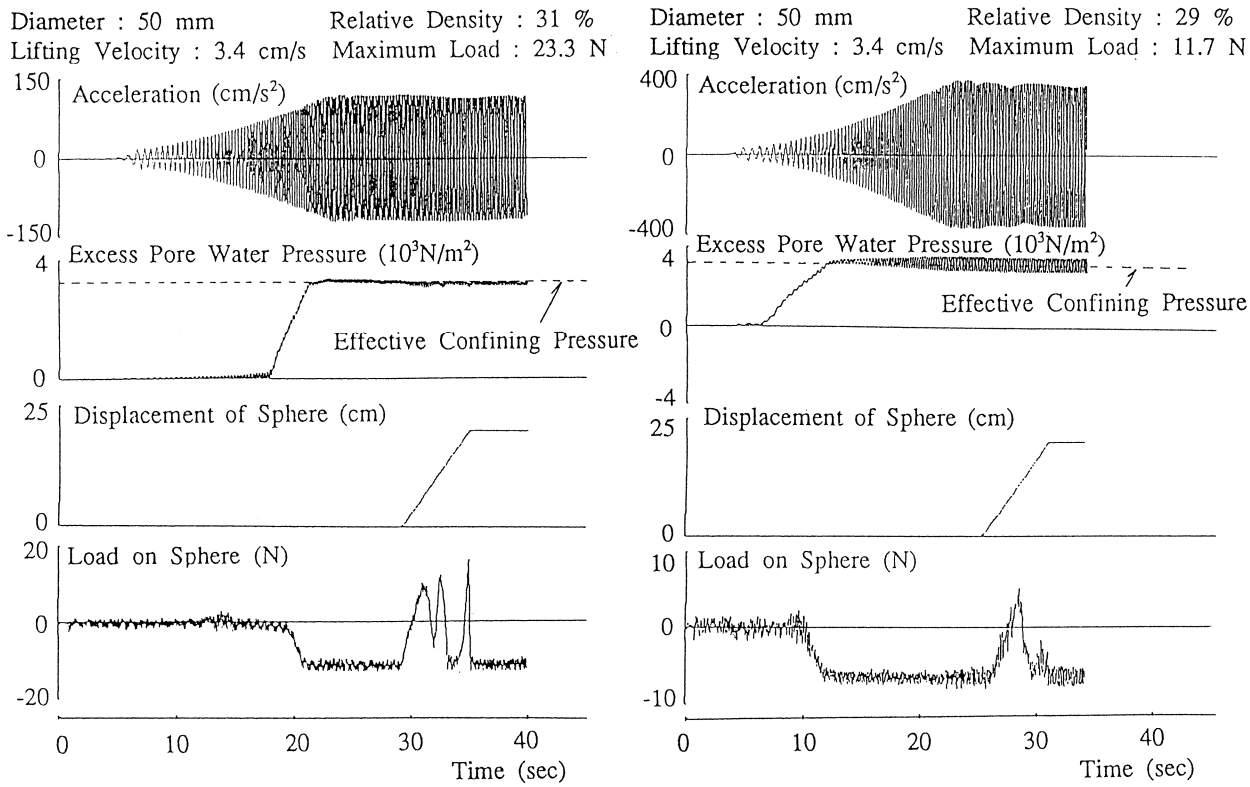

(a) Input acceleration : 122 cm/s² (b) Input acceleration : 379 cm/s²

Figure 3. Examples of sphere test results.

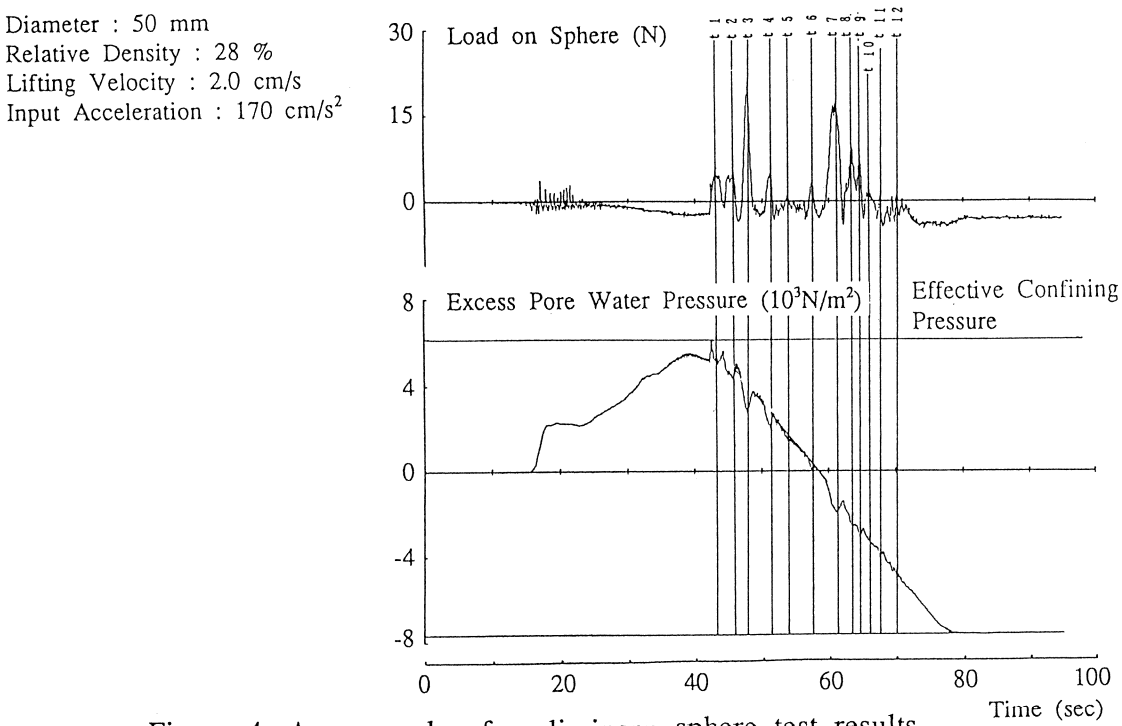

Figure 4. An example of preliminary sphere test results.

as one of the indices to estimate the degree of liquefaction severity. F_L was defined as follows (Japanese Road Association, 1990);

$$F_L = R / L \quad (1)$$

$$R = 0.0042 D_r \quad (2)$$

$$L = (\alpha_{max}/g) \cdot (\sigma_v/\sigma_v') \quad (3)$$

where,

D_r : relative density of the soil
α_{max} : input maximum acceleration of the soil box
σ_v : total overburden pressure
σ_v' : effective overburden pressure
g : gravitational acceleration

The coefficient of viscosity of liquefied soil was estimated with the following formula, because the liquefied soil was assumed as a viscous liquid in this study;

$$\eta = F / 3\pi dV \quad (4)$$

where,

η : coefficient of viscosity of liquefied soil
F : load on the sphere
d : diameter of sphere
V : lifting velocity of sphere

Figure 5 shows the relationship between the coefficients of viscosity of liquefied soil and the F_L-values. When the F_L-value decreases, namely the degree of liquefaction severity increases, the coefficient of viscosity of liquefied soil decreases, while the coefficient of viscosity becomes a little larger as the diameter of the sphere increases. A parabola line calculated by the method of least squares is drawn as well in Figure 5.

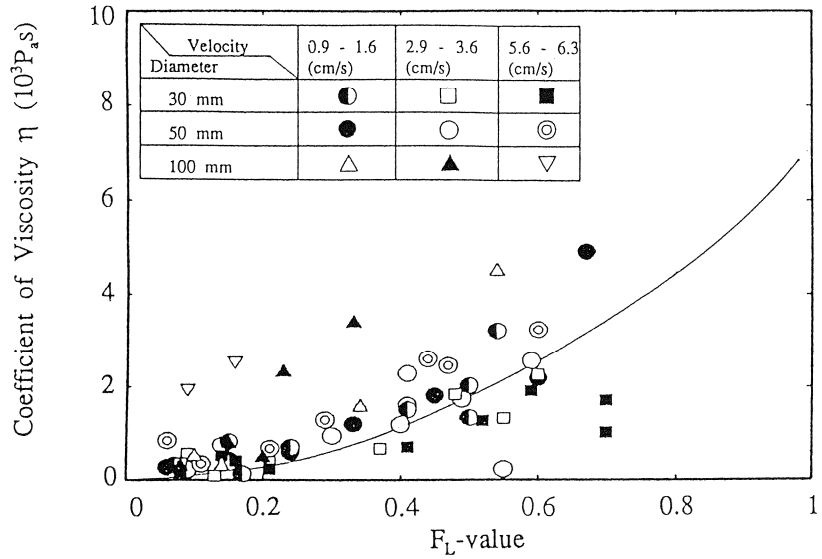

Figure 5. Coefficient of viscosity of liquefied soil in sphere test.

Results of Pipe Tests

Two examples of the results of pipe tests are shown in Figure 6 in a similar way to the sphere test's. For both cases, the relative density and the velocity of the pipe are almost the same, about 34 % and 5.1 cm/s respectively. However, the input acceleration at the basement of the soil box are different, 128 cm/s^2, 255 cm/s^2. As the same as for the sphere tests, the maximum load on the pipe in the case of larger input acceleration is less than that in the case of smaller input acceleration, while the method of the test is different from the sphere test.

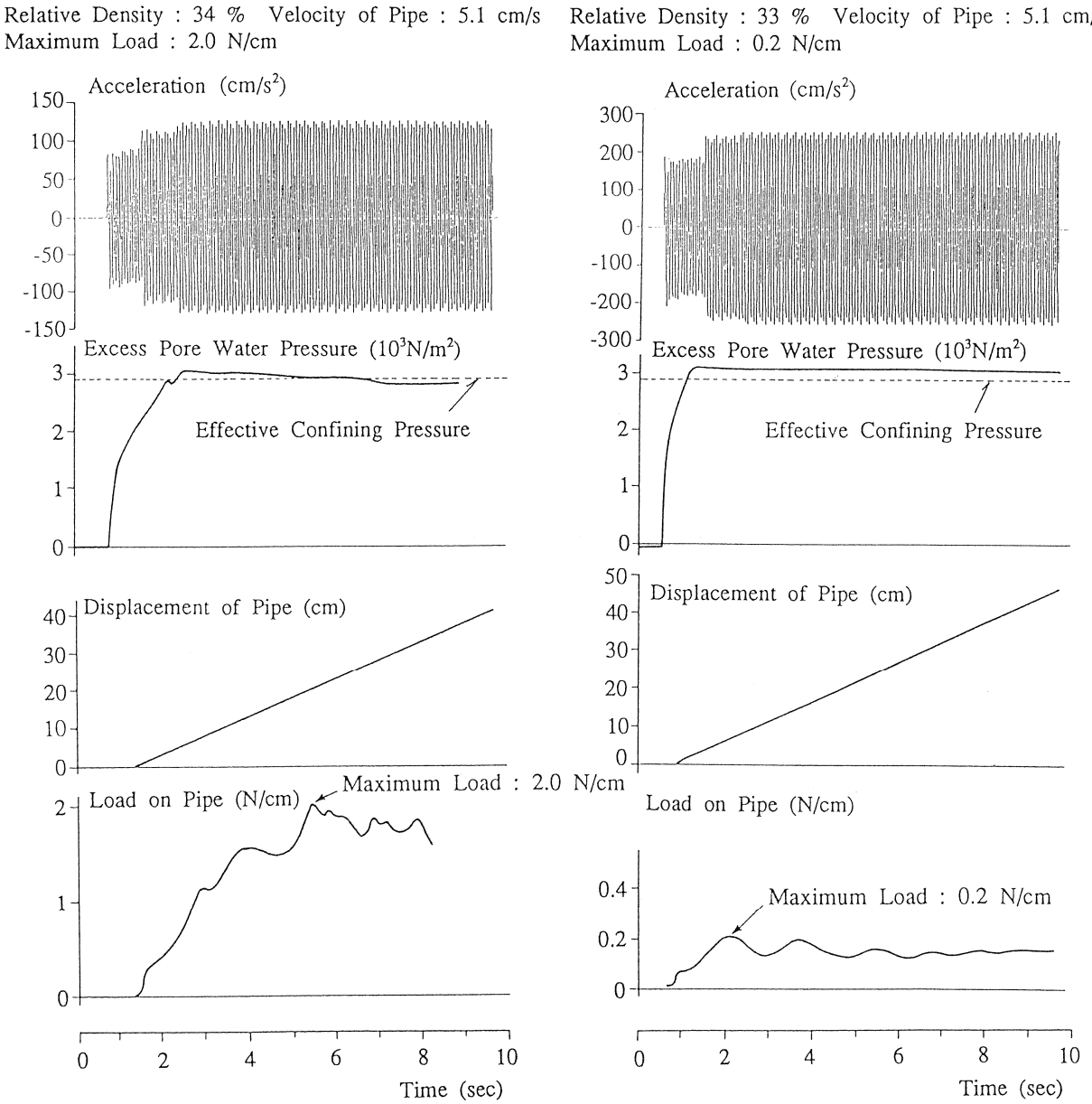

(a) Input Acceleration : 128 cm/s^2 (b) Input Acceleration : 255 cm/s^2

Figure 6. Examples of pipe test results.

The coefficient of viscosity of liquefied soil was calculated with the following formula using the measured load F on the pipe;

$$F = 4\pi\eta V / (2.002 - \log_n Re) \quad (5)$$

where,

η : coefficient of viscosity of liquefied soil
Re: Reynolds Number ($=\rho Vd/\eta$)
V : velocity of pipe
ρ : density of liquefied soil
d : diameter of pipe

Figure 7 shows the coefficient of viscosity estimated from the pipe test, which retains a good correlation with the F_L-value, as the same as for the sphere test.

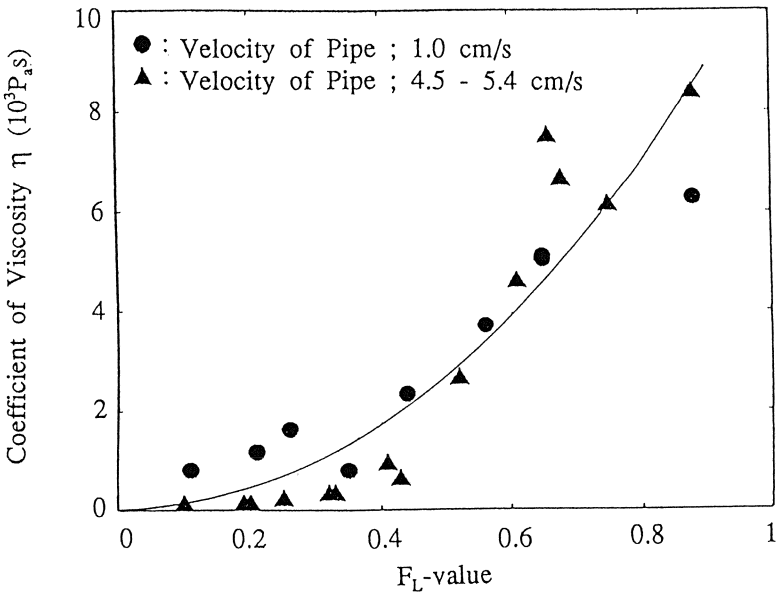

Figure 7. Coefficient of viscosity of liquefied soil in pipe test.

Comparison of Both Tests

Figure 8 shows the results of both kinds of tests. It is notable that the coefficients of viscosity obtained from the pipe tests well coincide with those from the sphere tests, which suggests that it is possible to estimate the coefficient of viscosity quantitatively by F_L-value.

Conclusion

Based on the view point to assume the liquefied soil as a fluid, two kinds of laboratory tests were conducted to evaluate the mechanical properties of liquefied soil, i.e., test using a sphere and test using a pipe. The test results show that the coefficient of viscosity of liquefied soil depends on the degree of liquefaction severity, and that the coefficient can be estimated quantitatively by F_L-value.

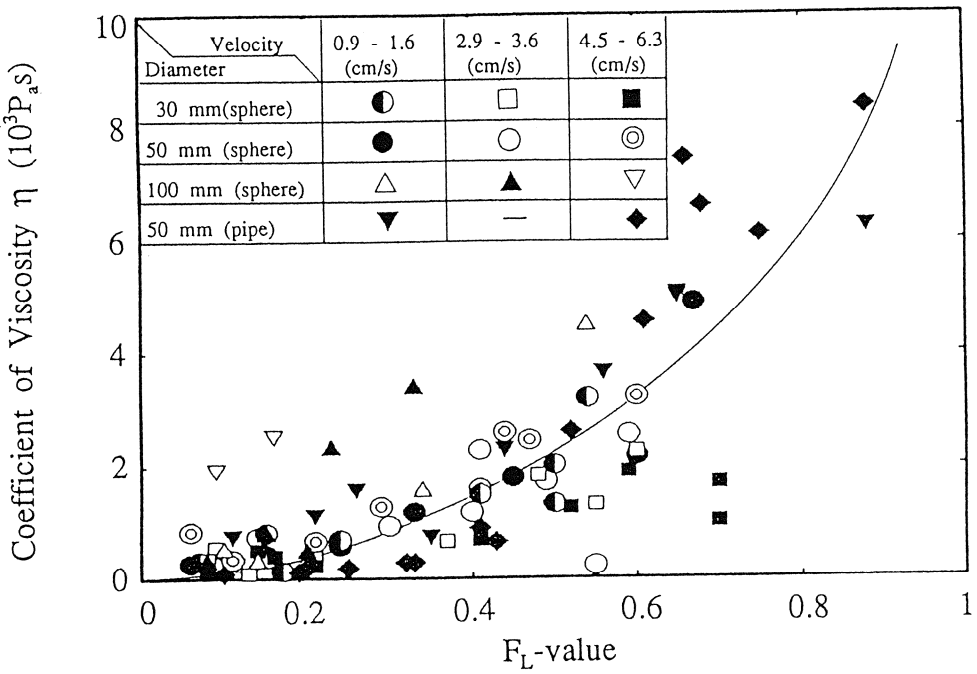

Figure 8. Coefficient of viscosity of liquefied soil in both tests.

In order to prove the proposed assumption that the liquefied ground behaves as a fluid, it is necessary to investigate the behavior of the liquefied soil during ground deformation by experimental studies as well as analytical studies in which the coefficients of viscosity obtained from the sphere test and pipe test are used. Furthermore, it is also necessary to do more research based on the view point to assume the liquefied soil as a solid in order to obtain a rational explanation on the mechanism of the occurrence of large ground displacements.

References

Bartlett, S. F., and Youd, T. L. "Empirical Prediction of Lateral Spread Displacement." *Proceedings from the Fourth Japan-U.S. Workshop on Earthquake Resistant Design of Lifeline Facilities and Countermeasures for Soil Liquefaction, Technical Report NCEER-92-0019* 1 (1992): 351-365.

Hamada, M., Yasuda, S., Isoyama, R., and Emoto, K. *Study on Liquefaction Induced Permanent Ground Displacements.* Tokyo, Japan: Association for the Development of Earthquake Prediction, 1986.

Hamada, M., and O'Rourke, T. *Case Studies of Liquefaction and Lifeline Performance During Past Earthquakes, Technical Report NCEER-92-0001 and 0002.* Buffalo, NY, U.S.A.: National Center for Earthquake Engineering Research, 1992.

Iwasaki, T., Tatsuoka, F., and Tokida, S. "A Practical Method for Assessing for Soil Liquefaction Potential Based on Case Studies at Various Site in Japan." *Proceedings, Fifth Japan Earthquake Symposium,* (1978): 641-648 (in Japanese).

Japan Road Association *Specifications for Highway Bridges, Part V, Earthquake Resistant Design.* Tokyo, Japan, 1990.

AN ASSESSMENT OF VELACS "CLASS A" PREDICTIONS

Jean H. Prevost[1] and Radu Popescu[2]

Department of Civil Engineering and Operations Research
Princeton University
Princeton, New Jersey 08544

ABSTRACT

A method to compare numerical predictions with experimental recordings is presented. Two comparison indices are proposed: (1) the root mean square error of the predictions with respect to the mean of the experimental results; and (2) the size of a confidence interval centered at the predicted value which contains the estimated true value of the experimental results with a 75% probability. The reliability of experimental results is accounted for by the second index.

The method is used to compare numerical "Class A" predictions performed within the framework of the VELACS Project with experimental results recorded in centrifuge experiments. The comparison is made in terms of excess pore pressures.

[1]Professor of Civil Engineering
[2]Graduate Student

INTRODUCTION

The VELACS (VErification of Liquefaction Analysis by Centrifuge Studies) project is a coordinated NSF–sponsored geotechnical centrifuge study of earthquake like loading on a variety of soil models, aimed at studying the mechanisms of soil liquefaction–induced failure and at aquiring data for the verification of various analysis procedures for liquefaction problems. A program of dynamic centrifuge model tests (Figure 1) consisting of nine geotechnical models constructed from or founded on liquefiable soil deposits have been performed [1], as listed in Table 1.

The Class "A" prediction phase of the VELACS project included *a–priori* predictions, in which the relevant experiments were not performed until the computations had been made and the results submitted. The numerical predictions were based on the results of conventional laboratory soil tests [3] performed on the soil materials used in the centrifuge models, and on the anticipated base input motion (viz. "target motion"). The verification and validation of the various analysis procedures were to be carried out by comparing their predictions with the measurements recorded in the centrifuge experiments (in terms of excess pore water pressure, acceleration and displacement time histories). However, it should be pointed out that to this date no firm experimental verification and validation of centrifuge test results with the corresponding prototype situations have been made.

Overview presentations of "class A" predictions and comparisons with the experimental results have already been made within the framework of the VELACS Project [2]. The present study provides a unitary and concise presentation of the prediction performance relative to the experimental measurements, in terms of the excess pore water pressures induced by dynamic loading. The results of the comparison study are dependent on the assumption that the systematic errors or bias in centrifuge experimental results can be neglected. As discussed in ref. [7], this assumption is imposed by the current lack of knowledge on the bias in centrifugal experiment results, as compared to corresponding full scale prototype behaviour.

As shown in Table 1, most of the centrifuge experiments have been duplicated, by repeating the experiment under identical conditions at different laboratory facilities. Studies [7, 6] were conducted to assess the reliability of the experimental recordings obtained in the centrifuge experiments which had been duplicated. These studies sought to address the reliability of the mean of a series of test results as an estimate of the (unknown) **true value**, regarded as the true mean as would result from **very many** nominally identical experiments. The reliability assessment was carried out in terms of the likelihood γ that the true value of the test outcome lies within a $\pm 10\%$ interval of the mean of the experimental measurements. A subjective acceptability limit was set in ref. [7] by accounting for the degree of complexity of the centrifuge experiments as compared to other soil tests, and by comparing the reliability of centrifuge test results with that of conventional laboratory soil tests [3]. According to that limit, and under the reserve of some simplifying assumptions (viz., random sampling, gaussianity of the test outcomes) and of the low number of experiments (typically 2 or 3) imposed by the circumstances, some of the conclusions were as follows:

- In terms of recorded excess pore water pressures, four out of the seven centrifuge experiments which had been duplicated (namely models #2, 4a, 4b and 12) provide reliable results and offer a meaningful data base for comparisons with "class A" predictions. The other three models (1, 3, and 7) were deemed as providing results with relatively

low reliability, in the sense that the comparisons between numerical predictions and the average values obtained from the recordings should be carefuly evaluated and not used for arriving at definite conclusions.

- In terms of displacements and accelerations, the experimental recordings obtained by different laboratories for the same centrifuge model display relatively large variability for all the seven models which were duplicated.

Consequently, in the following the comparisons "class A" predictions vs. centrifuge experiment results are only performed in terms of excess pore pressures.

COMPARISON INDICES

In order to assess the closeness of two time histories (e.g. recorded vs. predicted), one may look at the extreme values only, or one may plot and compare the whole time histories. The first method provides very scarce and incomplete information in the case of dynamic events. The second one becomes tedious when a large amount of information is available [5]. The comparison indices proposed in the following, root–mean–square error ε_{rms} and size $b_n^{av}(\beta)$ of β confidence interval, offer a measure of the overall closeness of the predicted time histories with the experimental recordings. No information is provided as to the sign of the errors (i.e. lower or higher predicted than recorded values), nor as to the time instants at which the differences in predictions vs. recordings are concentrated. However, the fact that these two indices convert the information contained in a whole time history into single numbers makes them convenient for comparison studies involving a large amount of data.

Root mean square error

Given two pore pressure time histories $p_p(t)$ and $p_r(t)$, over a certain time interval $T_{initial} \leq t \leq T_{final}$, the overall root mean square error of p_p (predicted) with respect to p_r (recorded) is computed as:

$$\varepsilon_{rms} = \frac{\left\{ \int_{T_{initial}}^{T_{final}} [p_p(t) - p_r(t)]^2 \mathrm{d}t \right\}^{\frac{1}{2}}}{\sigma'_{v0} \sqrt{T_{final} - T_{initial}}} \tag{1}$$

where the denominator is a normalizing factor, expressed in terms of the initial effective vertical stress σ'_{v0} and the duration $(T_{final} - T_{initial})$.

For each transducer location, the errors are evaluated by using the average of the recorded values, i.e. p_r in eqn. (1) is computed as:

$$p_r(t) = \frac{1}{N_{\exp}} \sum_{i=1}^{N_{\exp}} p_i^{\text{recorded}}(t) \tag{2}$$

with: $N_{\exp}$ – the number of centrifuge experiments reported for that particular model and $p_i^{\text{recorded}}(t)$ – the values recorded in experiment "i". The root mean square error as defined

by eqn. (1) can also be used to assess the quality of each centrifuge experiment, by comparing each experiment with the mean of the experiments. Thus, whenever more than one experimental result is available for a specific transducer, a range of experimental errors is computed with respect to the mean of the recordings and the prediction errors are reported to that range. For the models for which only one centrifuge experiment is reported (Models 6 and 11) the recorded values are used as the basis for the comparison.

Size of confidence interval centered at the prediction, containing the "true value"

A comparison based on the root mean square error takes for granted the validity of the average of the experimental recordings and does not account for the influence that the reliability of the experimental results (function of the scattering of the experimental results and the number of tests [7]) should exercise over the quantitative reliability assessment of the numerical predictions. A second comparison index is used for that purpose. The index is based on the measure of the half length "b" of the confidence interval centered at the predicted value "p" which contains the estimated true mean value "$\mathbf{m}_R$" of the experiment with the probability β. In other words, β is the likelihood that the true value $\mathbf{m}_R$ lies within the confidence interval of length $2b$, centered at the predicted value p:

$$\beta = \mathrm{P}[p - b \leq \mathbf{m}_R \leq p + b] \tag{3}$$

This "b" index can only be evaluated when more than one experimental result is available for comparisons with "class A" predictions. The methodology to evaluate the "b" index is described in ref. [6].

An overall measure of how close the predicted time history is to the experimental measurements is obtained by averaging the value $b(\beta, t)$, computed at every time instant t, over the analysis time interval $T_{initial} \leq t \leq T_{final}$. Finally, to get a nondimensional index, the average value is normalized with respect to the initial effective vertical stress σ'_{v0}:

$$b_n^{av}(\beta) = \frac{\int_{T_{initial}}^{T_{final}} b(\beta, t)\mathrm{d}t}{\sigma'_{v0}(T_{final} - T_{initial})} \tag{4}$$

The quantity $b_n^{av}(\beta)$, evaluated for a certain β value, will be refered to as "size of β confidence interval".

ASSESSMENT OF "CLASS A" PREDICTION PERFORMANCE

The comparison indices previously presented – normalized root–mean–square error, ε_{rms}, and normalized size b_n^{av} of 75% confidence interval – are used for a concise presentation of the "class A" predictions performance. According to the reliability studies reported in refs. [7, 6], the relatively low reliability of the recorded experimental displacements and accelerations makes the comparisons with numerical predictions pointless and is not addressed here. Consequently, the present comparison study is restricted to predicted and recorded excess pore pressures.

As presented in Table 2, about 75% of the "class A" predictions submitted for the VELACS project were available for this study. Since no previous experience exists in terms

of the proposed indices, the comparison study cannot provide information on the absolute quality of the "class A" predictions. However, the large amount of predictions involved (56 "class A" predictions, for 9 centrifuge models with a total of 41 pore pressure transducers) allows a meaningful **comparative** evaluation of these predictions.

A summary of the comparison study results [6] is presented in Figure 2 in terms of the above described indices. For each centrifuge model (Figure 1), the root–mean–square errors and 75% confidence intervals computed for each predictor were averaged over all pore pressure transducers and are shown in Figure 2. A specific marker is assigned to each predictor and used through all the centrifuge models. The same type of markers (e.g. stars, circles, etc.) is assigned to predictors using similar constitutive models, as classified in ref. [4] and listed in Table 2. For the centrifuge models with more than one experiment reported, the ranges of root–mean–square errors and 75% confidence intervals of the experimental records themselves are shown with shaded areas. The expected value of b_n^{av} index is computed for each centrifuge model function of the experimental recording reliability [6], and shown in Figure 2 with vertical bars.

CONCLUSIONS

1. The VELACS project offers a good opportunity to verify and validate various analytical procedures for numerical simulation of soil liquefaction, by comparing the "class A" predictions with the centrifuge experimental results.

2. A methodology to assess the goodness of fit of predicted pore pressure time histories with respect to the values recorded in the experiments is presented. The proposed comparison indices are: (1) normalized root–mean–square error (ε_{rms} index) of the predicted values with respect to the average of experimental recordings, and (2) normalized size b_n^{av} of a confidence interval centered at the predicted value, which contains the estimated true value of the experimental results with 75% probability.

3. The results of a comparative evaluation of about 75% of the "class A" predictions submitted for the VELACS project are presented in an informative and concise manner, in terms of the ε_{rms} and b_n^{av} indices.

4. Once more, it is important to emphasize that the comparison study was performed under the assumption that the centrifuge experimental results have negligible bias or systematic errors. Further studies, involving comparisons between centrifuge experiment results and corresponding full scale prototype behaviour, are needed to verify this assumption.

ACKNOWLEDGEMENTS

The work reported in this study was supported in part by a grant from Kajima Corporation, Japan to Princeton University. This support is most gratefully acknowledged. The authors are also indebted to the VELACS project Steering Committee and experimenters, for providing the results of the "class A" predictions and centrifuge experiments discussed in this study. The authors would also like to thank Prof. Erik H. Vanmarcke for his valuable suggestions.

References

[1] K. Arulanandan and R.F. Scott, editors. *Proc. Int. Conf. on Verif. Numerical Proc. for the Analysis of Soil Liq. Problems*, volume 1. Balkema, Rotterdam, 1993.

[2] K. Arulanandan and R.F. Scott, editors. *Proc. Int. Conf. on Verif. Numerical Proc. for the Analysis of Soil Liq. Problems*, volume 2. Balkema, Rotterdam, 1994.

[3] The Earth Technology Corporation. VELACS laboratory testing program soil data report. Technical report, Earth Technology Project No. 90-0562, 1992.

[4] Y.F. Dafalias. Overview of constitutive models used in VELACS. In *Proc. Int. Conf. on Verif. Numerical Proc. for the Analysis of Soil Liq. Problems*, volume 2, pages 1293–1303. Balkema, Rotterdam, 1994.

[5] R. Popescu and J.H. Prevost. Numerical Class "A" predictions for Models No. 1, 2, 3, 4a, 4b, 6, 7, 11 and 12. In *Proc. Int. Conf. on Verif. Numerical Proc. for the Analysis of Soil Liq. Problems*, volume 1, pages 1105–1207. Balkema, Rotterdam, 1993.

[6] R. Popescu and J.H. Prevost. Comparison between VELACS numerical "class A" predictions and centrifuge experimental soil test results. *Soil Dynamics and Earthquake Eng.*, 1994. submitted for publication.

[7] R. Popescu and J.H. Prevost. Reliability assessment of centrifuge soil test results. *Soil Dynamics and Earthquake Eng.*, 1994. submitted for publication.

Table 1. Centrifuge experiments for VELACS Project [1]

Centrifuge (University)	Experiments		Refered as
	Primary	Duplicating	
Rensselaer Polytechnic Inst.	Models 1 and 2	Mod. 3, 4a, 4b, 7, 12	RPI
California Inst. of Technology	Model 3	Models 2 and 4a	Caltech
University of California, Davis	Mod. 4a, 4b, 6	Mod. 1, 2, $3^{(NA)}$, 7, 12	UC Davis
Colorado University at Boulder	Model 7	Models 1 and 4b	CU Boulder
Cambridge University (UK)	Model 11		Cambridge
Princeton University	Model 12		Princeton

$^{(NA)}$ – results not available for this study

Table 2. Class "A" Predictions for VELACS Project [1]

First predictor	Refered as (in this study)	Predicted excess pore pressures for model #									Constitutive model, as in [4]
		1	2	3	4a	4b	6	7	11	12	
Bardet — Univ. of Southern California	USC	A		A				NA			bounding surface
Been — Golder Associates (UK)			NA								classical plasticity
Chan — Glasgow University (UK)	Glasgow Univ.	A	A	A	A	A		A	A		generalized pl.
Hamada — Tokai University (Japan)			NA						NA		direct (empirical)
Iai — Port and Harbour Research Institute (Japan)		NA	NA						NA	NA	multi–mechanism
Ishihara — University of Tokyo (Japan)	U. Tokyo (Ishihara)	A									bounding surface
Kimura — Tokyo Inst. of Techn. (Japan)		NA		NA				NA	NA		multi–mechanism
Lacy — Tufts University	Tufts Univ.	A	A	A	A			A			nested surfaces
Li — University of California, Davis	UC Davis	A									bounding surface
Manzari — Univ. of California, Davis		NA									bounding surface
Muraleetharan — The Earth Technology Corporation	ETC	A			A						bounding surface
Prevost — Princeton University	Princeton Univ.	A	A	A	A	A	A	A	A	A	nested surfaces
Rollins — Brigham Young University	Brigham Young U.	A						NA		A	total stresses
Roth — Dames and Moore	Dames & More	NA	NA					A			direct (emp.)
Shiomi — Takenaka Corp. (Japan)	Takenaka Corp.	A	A						A	A	classical plasticity
Siddharthan — University of Nevada, Reno	U. Nevada Reno	A	A	A	A						direct (empirical)
Sture — Colorado University at Boulder	CU Boulder			NA			A		NA	A	classical plasticity
Towhata — University of Tokyo (Japan)	U. Tokyo (Towhata)		A						A		direct (empirical)
Yogachandran — Leighton & Associates	Leighton & Assoc.	A			A	A	A				bounding surface
Zienkiewicz — University College of Swansea (UK)	U. Coll. Swansea	A	A	A	A	A	A	A	A		generalized plasticity

Explanation: **A** predicted excess pore pressures – available for this study;
NA predicted excess pore pressures – not available for this study.

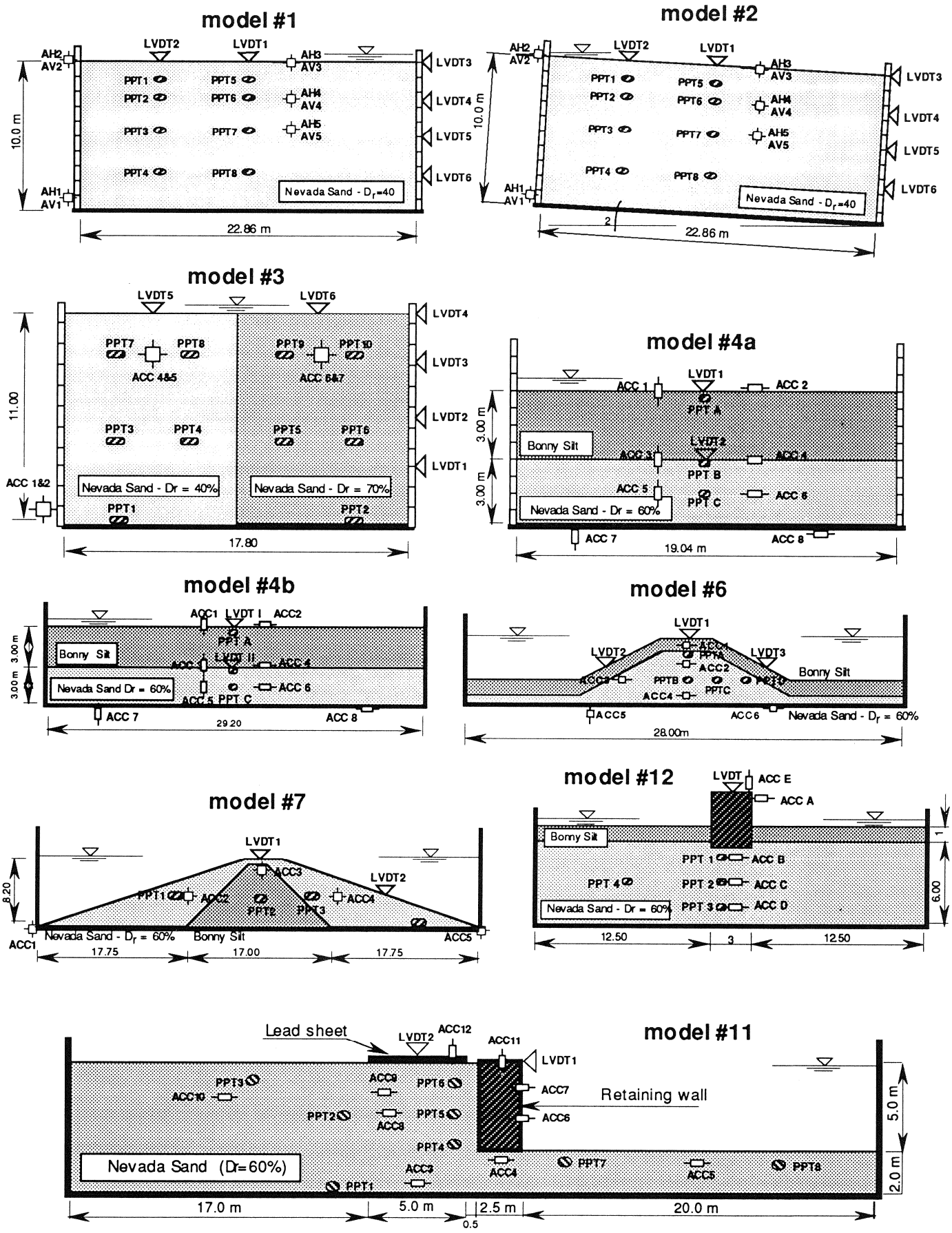

Figure 1. Centrifuge experiments performed for the VELACS Project.

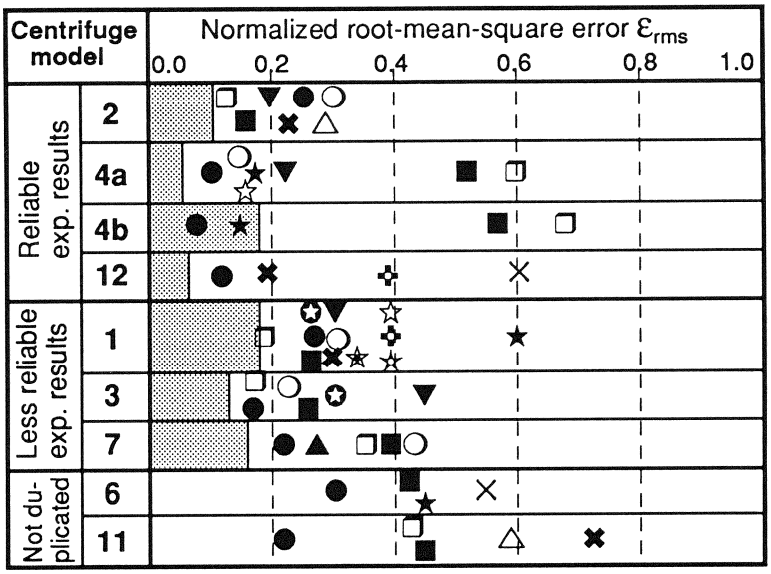

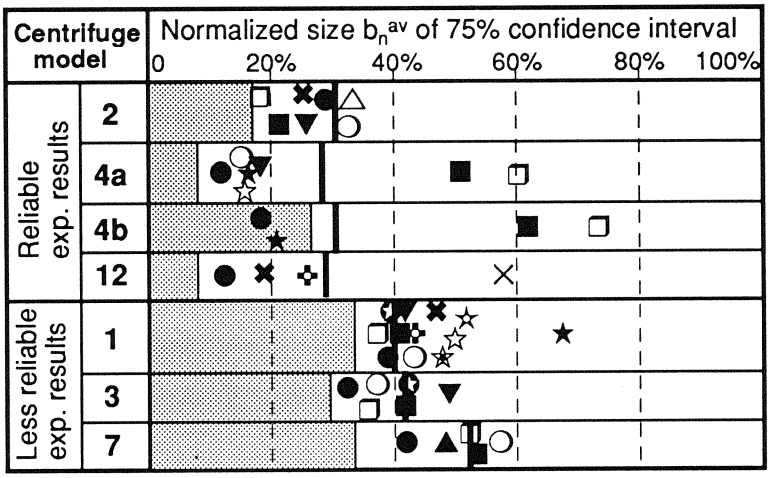

PREDICTOR	CODE	SYMBOL	MODEL
Princeton Univ.	DYNAFLOW	●	nested surfaces
Tufts Univ.	DYNAFLOW	○	
U. Coll. Swansea	SWANDYNE4	■	generalized plasticity
Glasgow Univ.	DIANA-SWAN.	❐	
Leighton & Assoc.	DYSAC2	★	
ETC	DYSAC2	☆	
USC	LINOS	✪	bounding surface
UC Davis	SUMDES	☆	
U. Tokyo (Ishihara)		✯	
CU Boulder	LIQCA	×	classical plasticity
Takeneka Corp.		✖	
U. Nevada Reno	TARA-2	▼	direct (empirical)
Dames & Moore	FLAC	▲	
U. Tokyo (Towhata)	close form soln.	△	
Brigham Young U.	QUAD4	✣	total stress

experimental record range | $E[b_n^{av}]$

Figure 2. Summary of comparison study results: averages of ε_{rms} and b_n^{av} indices over all the transducers of each centrifuge model.

A New Interpretation Method of Surface Wave Measurements to Obtain Representative Shear Wave Velocity Profiles of Soils

by

Chaim J. Poran[1], Jorge A. Rodriguez-Ordonez[2], Takenori Satoh[3], and Roy Borden[4]

ABSTRACT

Recently, the importance of obtaining a representative average shear wave velocity (SWV) profile has significantly increased with new methods proposed for the evaluation of site amplification. The new methods may require engineers to obtain cost-effective measurements of SWV profiles reaching significant depths. Non-invasive SWV profiling of soil deposits has long been recognized as a cost-effective approach to obtain such SWV data. The controlled-source measurement of surface wave dispersion (CXW) is a relatively new non-invasive method that is used for site characterization in the USA and abroad. The CXW method uses harmonic controlled sources to produce steady state Rayleigh waves in order to measure the dispersion characteristics of soil and rock. It may be regarded as a combination of the traditional spectral analysis of surface waves and steady-state Rayleigh waves methods. Several interpretation techniques may be used to obtain SWV structure from Rayleigh waves dispersion data (in a process that is referred to as the Vf-Vs method). CXW measurement data from more than 200 soil and rock sites were analyzed. These results were used to formulate a new interpretation procedure for the Vf-Vs method based on the concept of reference profiles that describes the average dispersion curve and SWV structure. The reference profiles functional form was formulated by taking into account the SWV dependency on confining pressure (depth) in soils. Simple equations for a direct inversion of the reference profile were developed. This paper presents the reference profile concept and shows that it fits well with measured CXW data. Reference SWV profiles may be obtained in the field almost immediately following the measurements and may be used as representative profiles for site amplification evaluations eliminating the need for computationally intensive inversion solutions used with other Vf-Vs methods.

---

1 President, ENSOL, Inc., 2809 Old Orchard Road, Raleigh, NC 27607, USA. Tel: 919-782-8886, Fax: 919-510-4500.

2 Research and Development Engineer, Vibration Instruments Company, Ltd., 6-12-16 Honkomagome, Bunkyo-ku, Tokyo, 113 Japan. Tel: 03-3947-7716, Fax: 03-3947-7675.

3 Chairman, Vibration Instruments Company, Ltd., 6-12-16 Honkomagome, Bunkyo-ku, Tokyo, 113 Japan. Tel: 03-3947-7716, Fax: 03-3947-7675.

4 Professor, Civil Engineering Department, North Carolina State University, Box 7908, Raleigh, NC 27695-7908, USA. Tel: 919-515-7630, Fax: 919-515-7908.

INTRODUCTION

Shear wave velocities of soil and rock deposits are essential data for the analysis of soil behavior under earthquake and other dynamic loading. Shear wave velocity (SWV) can also be used to define low strain elastic moduli for soil characterization and analysis of static problems. Dobry (1991) and others introduced the impedance ratio concept for the evaluation of site amplification. It is possible that this approach will affect design procedures and building codes in the near future. In this approach it is important to obtain representative SWV data to considerable depths. It appears that for this application layered data details are less important and since it is the average SWV structure of the deposit that is used in the computation of impedance ratio and resulting site amplification. This lends itself to application of non-invasive cost-effective surface wave methods.

Several seismic methods have been developed for situ SWV evaluation. These methods are based on the propagation of elastic waves generated at one point (source) and monitored at other locations (receivers). Among them there is one group of methods that is based on non-invasive Rayleigh wave measurements at the ground surface. Because it is a non-invasive method it provides an attractive alternative to more costly intrusive methods such as down-hole and cross-hole SWV measurements. Other advantages of this group of non-invasive methods include its simple measurement procedures and the accuracy of measured data. Its disadvantages include difficult data interpretation and inherent resolution limitations.

The propagation velocity of surface waves depends on the SWV (**Vs**) structure of the soil. If the properties of the soil profile are constant with depth, surface waves of different wavelengths (or frequencies) travel at the same velocity. However, if soil properties vary, surface waves of different wave lengths travel at different phase velocities. This variation of the phase velocity (**Vf**) with wave length is referred-to as dispersion. In this paper, the process of obtaining **Vs** structure from measured **Vf** data is referred to as the Vf-Vs method. The Vf-Vs principle is used in several different methods such as the spectral analysis of surface waves (SASW), the controlled source spectral analysis of surface waves (CXW), and other techniques based on the use of background vibrations or earthquake data to define the surface wave dispersion.

The objective of the Vf-Vs method is to obtain a SWV profile for a site by using the measured dispersion curve. This is an inverse problem in which the properties of the system are computed from the response to an excitation of stress waves. The main tool available for the solution of this inverse problem is the forward modeling of elastic wave propagation. Using these models the dispersion curves can be computed for a known soil profile. Nonlinear optimization formulations are used with the forward modeling to compute a soil profile with a dispersion curve that is compatible with the measured.

Inversion procedures for Vf-Vs methods available to date have serious limitations. Even if the intent is to produce a "smooth" SWV profile, they require extensive computations, their results are not unique, and there are no appropriate means to evaluate the resolution and

accuracy of the results. These procedures also require highly specialized and experienced analysts. These drawbacks have limited the general use of Vf-Vs methods. This paper presents a new reference profile concept that extends the application areas of these methods.

THE CXW METHOD

General

The CXW method may be regarded as a combination of the steady-state Raleigh waves and the spectral-analysis of surface waves, offering the advantages of both methods (Rodriguez-Ordonez 1994, Poran et al. 1992 and 93, Arbelaez-Hoyos 1992, and Satoh 1989 and 91).

In the CXW method, a powerful electromagnetic exciter (the controlled-source) generates operator-selected, repeated surface vibrations that are recorded by two vertically oriented receivers placed near the controlled source as shown in Figure 1. Various modes of repeated source excitation may be used for accurate data averaging. The control unit (CU) of the system is used both as signal generator and as a advanced signal analyzer.

Typically, the on-site time required for a complete CXW measurement and data interpretation (to generate a SWV profile) may range between 10 minutes for profiling depths of 10 m with a small exciter (70 kg maximum dynamic force) to 50 minutes for profiling depths of 35 m with a larger exciter (250 kg maximum dynamic force).

Computation of the Dispersion Curve by Spectral Methods in CXW Measurements

In a CXW test the receivers are located colinearly with the source at known distances. The acceleration or velocity response is measured at the receiver locations and the cross power spectrum is computed. The phase of the cross power spectrum of the recorded signals contains the information on the propagation velocity as a function of the frequency that is the basis of the spectral analysis of Rayleigh waves.

During the tests, the phase shift, ϕ, between the two receivers is automatically computed by the CU. The computation of phase velocity is based on the consideration that the travel time for one wave length is the period **T**, that is the inverse of the frequency **f**. The travel time, **t,** equivalent to the phase shift is given by:

$$t = \frac{\phi}{360} f \qquad (1)$$

During this time the wave traveled over the distance between the receivers, **X**, at a velocity Vf. This phase velocity ($\mathbf{V_f = X/t}$) is automatically computed as:

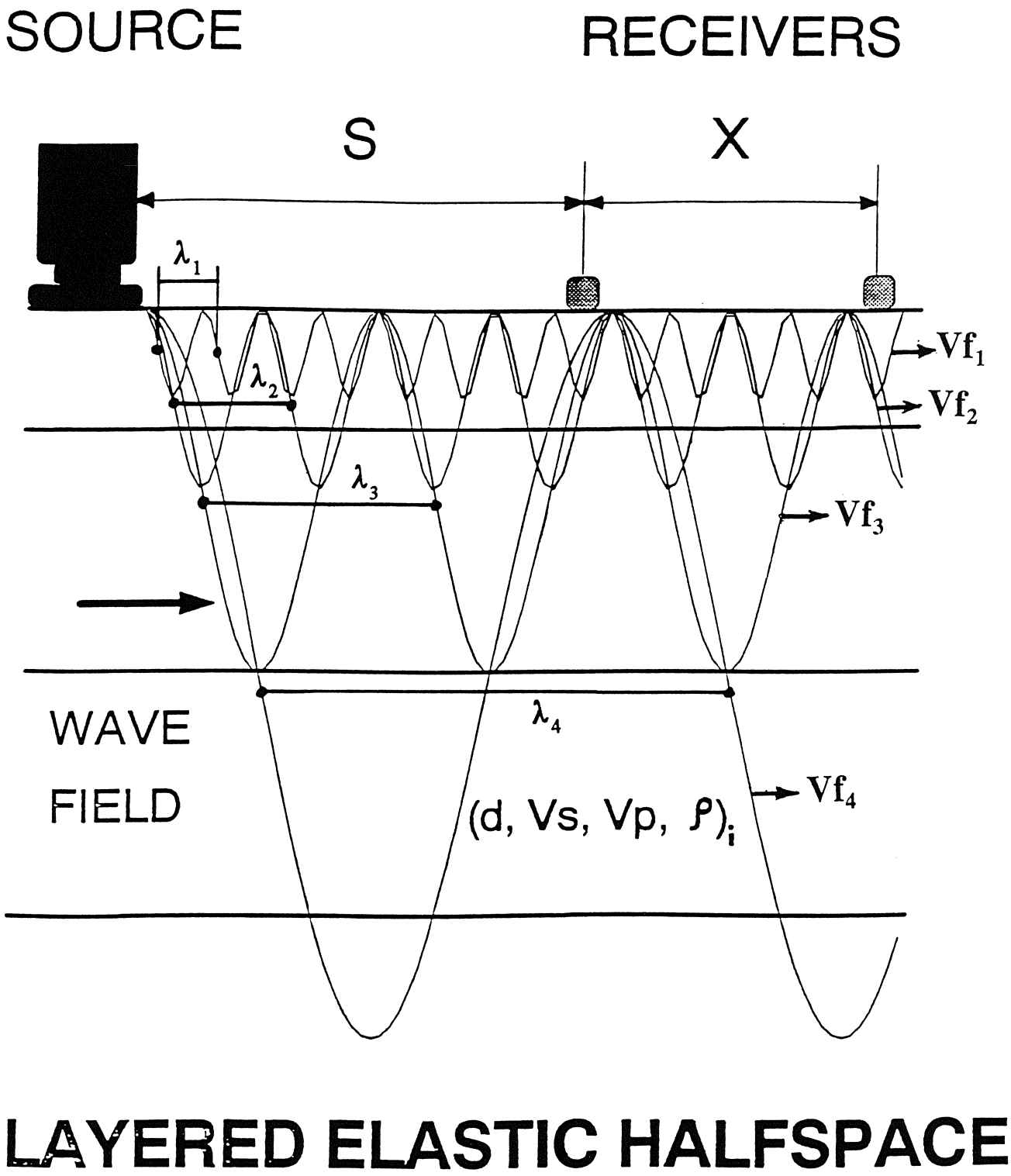

Figure 1. CXW Test Configuration

$$V_f = \frac{360 X f}{\Phi} \qquad (2)$$

The wavelength, λ, is computed as $\lambda = V_f/f$. The results from Equation 2 for the descritized frequency range used for the test define the experimental dispersion curve. These data are the basis for the interpretation of the SWV structure that is the purpose of the test as shown in Figure 2.

THE REFERENCE PROFILE CONCEPT

Phase and SWV Reference Profiles

Generally, CXW results show that the variation of phase velocity with wave length in soil profiles can be defined by a simple function of two parameters (Rodriguez-Ordonez 1994). This is based on data from more than 100 sites of different geological deposits and supported by SASW data from the literature. The function that best fit the experimental data is defined as the reference phase velocity profile. The reference profile in a uniform soil site is defined by two parameters, **Vof** and $\mathbf{m_f}$ which relate the phase velocity **Vf** with the wave length λ by the equation:

$$Vf = Vof \left(\frac{\lambda}{2} \right)^{m_f} \qquad (3)$$

The purpose of test data interpretation is to obtain a SWV profile with a dispersion curve that is close to the measured dispersion within a given tolerance. Experience has shown that there are different SWV profiles with a similar dispersion curve. The main difference between them is in their smoothness. This effect is illustrated in Figure 2 where a profile composed of a few layers like that shown in Figure 2.b have the same dispersion curve as the smoothly varying profile shown in Figure 2.c. Even in situations like the dotted line SWV profile, relatively thin layers with large SWV changes do not produce substantial change in the dispersion curve as shown in Figure 2.a.

Rodriguez-Ordonez (1994) concluded that a smoother profile is in a sense an average of the other rougher profiles that produce a similar dispersion curve. By increasing the smoothness it is possible to obtain a continuous **Vs** profile that matches the target data and resembles its dispersion curve.

The main problem in data interpretation is how to select the most representative profile. The Vf-Vs method by itself cannot provide a good answer to this question, since the data consist of the dispersion curve that can be equally well fitted by several different profiles.

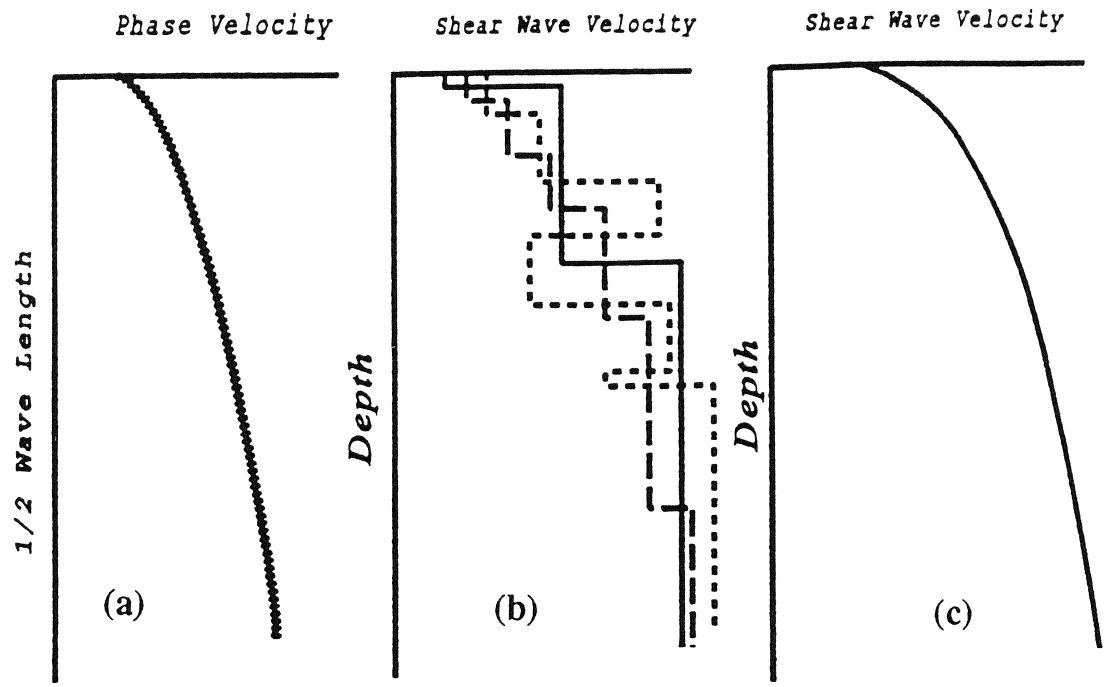

Figure 2. Illustration of: a) Dispersion Curves; b) Corresponding SWV Profiles; and, c) The Corresponding Reference SWV Profile

One can consider different criteria to constraint the solution (the smoothing criteria for the interpreted profile). The criteria may be the mathematical formulation of the optimization, or physical considerations. All the interpretation formulations used to date have used standard minimization formulations, some of them including smoothing constraints. The new interpretation procedure smoothing criteria is based on the reference profile concept that is based on physical, experimental and theoretical considerations.

The main assumption of the new method is that the form of the reference profile described by Equation 3 is a direct consequence of the actual variation of the SWV with depth in soil profiles. Since most available data show that SWV profile and the dispersion curve correlate in a similar way, the reference SWV profile may be described by an equation that is similar to Equation 3. The SWV reference profile in a uniform soil site is defined by two parameters **Vos** and $\mathbf{m_s}$ (Rodriguez-Ordonez 1994), which relate the SWV (**Vs**) to depth **Z** by the equation:

$$Vs = Vos\, Z^{m_s} \qquad (4)$$

This assumption is based on the typical results illustrated in Figure 2, where the smooth SWV profile is also similar to the measured dispersion curve.

Physical Basis of the Reference Profile

SWV of soils depend on several parameters. According to Mitchell (1993), the most important are:

- The type of soil, defined by compositional and environmental factors such as mineralogy, internal structure, cementation, overconsolidation, and geologic age.
- The cyclic strain, strain rate and number of loading cycles.
- The effective confining stress.

The basic form of the relationship between these parameters was determined by Seed et al. (1984) and others from laboratory tests. For non cohesive materials the form is given by:

$$G = 4572\, K_2 \sqrt{\sigma_m} \qquad (5)$$

The equation units are in kPa, where **G** is the shear modulus, σ_m is the mean effective stress and $\mathbf{K_2}$ is a coefficient that depends primarily on grain size, relative density, and shear strain. The shear modulus or shear stiffness is defined as the ratio of the shear stress and the shear strain.

For cohesive soils, the following equation was reported (Dobry and Vucetic 1987) to

compute the shear modulus at low strains **Gmax**:

$$G_{max} = 625 \frac{OCR^{k}}{0.3 + 0.7\, e^{2}} \sqrt{P_a\, \sigma_m} \qquad (6)$$

where **OCR** is the overconsolidation ratio, **e** is the void ratio, **Pa** is atmospheric pressure and σ**m** is the mean effective stress, all in any consistent units. This equation was also developed based on laboratory tests data.

Equations 5 and 6 show that for all soils the shear modulus depends on a function of the soil type and strain level multiplied by the square root of the mean effective stress.

For the elastic waves used with the Vf-Vs method, the strain levels in the soil are very low. The shear modulus has its maximum value at low strains as given by Equation 6. In Equation 5 the value of $\mathbf{K_2}$ is also a decreasing function of the strain level with the maximum at low strain level values. Therefore, for the Vf-Vs measurements the form of Equations 5 and 6 is in general:

$$G = F_1 \sqrt{\sigma_m} \qquad (7)$$

where $\mathbf{F_1}$ is a function of the soil type.

The shear modulus is related to the SWV by the equation:

$$Vs = \sqrt{\frac{G}{\rho}} \qquad (8)$$

where ρ is the mass density ($\rho = \gamma/\mathbf{g}$), γ is the total effective unit weight and **g** is the gravity acceleration. Also, the mean effective stress in geostatic conditions is:

$$\sigma_m = \frac{(\sigma_1 + \sigma_2 + \sigma_3)}{3} = \frac{(1 + 2\,Ko)}{3} \sigma_v \qquad (9)$$

where **Ko** is the at-rest coefficient of earth pressure, which is a function of soil type and geologic history, and σ_v is the vertical effective stress which is given by:

$$\sigma_v = \gamma_{avg}\, Z \qquad (10)$$

where γ_{avg} is the average effective unit weight from the surface to the depth considered.

Substituting Equations 8 through 10 into Equation 7, we have:

$$Vs = \sqrt{\frac{g}{\gamma} F_1 \sqrt{\frac{1 + 2\,Ko}{3} \gamma_{avg} Z}} = F_2 Z^{0.25} \qquad (11)$$

Equation 11 shows that the SWV is a function of depth. For a uniform granular, recently deposited soil $\mathbf{F_2}$ is approximately constant. However, $\mathbf{F_1}$, **Ko** and γ are functions of **Z** and, therefore, lead to the more general expression of Equation 4. This finding was supported with a very large data base of CXW measurements (Rodriguez-Ordonez 1994, USC 1993). In Equation 4, the parameter **Vos** depend on the type of soil, while $\mathbf{m_s}$ reflects the combined effect of soil properties variation with depth and the SWV change with the confining stress.

The predicted range of **Vos** and $\mathbf{m_s}$ from Equation 4 was compared with the values obtained from the interpretation of CXW test data to verify consistency. Typical values of the parameters in Equations 5 through 11 are discussed in the following.

- Non dimensional parameter $\mathbf{K_2}$: The values of this parameter for low strains depend on the type of soil as shown in Table 1 (Seed et al. 1984, Seed and Idriss 1970).

  The values of $\mathbf{K_2}$ were obtained mostly from laboratory tests conducted on remolded soil samples. It is well recognized (Schmertmann 1991) that field values of $\mathbf{K_2}$ are higher than laboratory results due to effects such as aging, cementation, densification due to earthquake shaking, water table variations and other causes that can not be reproduced in the laboratory. Over time, such effects have been found to cause an increase in the shear modulus up to 50 to 100% with respect to laboratory values. The shear modulus increase with time at a diminishing rate which is approximately linear with the logarithm of time. At any given site, measured properties may be significantly higher (up to two times or even more) than the values from laboratory tests.

- Unit weight: varies between 12 to 22 kN/m^3 depending on the soil type and particularly dependent on mineralogy and void ratio.

- Earth pressure coefficient **Ko**: depends on the mineralogy, fabric and the overconsolidation ratio. It varies typically between 0.4 and 0.6, although it may reach values of 1.0 or higher in some cases.

Table 1 - Range of Laboratory Values of K_2

Type of Soil	Relative Density	K_2
Loose sand	30-50%	34-45
Medium sand	60%	52
Dense sand	75-90%	59-70
Sandy gravel with some clay		90
Dense sand and gravel		122
Dense sand and sandy gravel		190

- Void ratio **e**: depends on the soil type and structure. For granular soils it varies between 0.4 and 0.9. It can be much higher in some cohesive soils.

Based on typical soil parameters form laboratory tests, the range of **Vos** values in Equation 4 is between 50 and 150 m/s. When field effects previously discussed are taken into account, this range can be extended to 300 m/s. This range compares well with the results from the CXW measurements.

Rodriguez-Ordonez (1994) showed that **Vos** values vary between 80 and 250 m/s depending on the soil type. He also showed that typical $\mathbf{m_s}$ values in soils range between 0.25 and 0.50. His results show that the reference profile is qualitatively and quantitatively consistent with published laboratory data of soil behavior under dynamic loads at low strain.

INVERSION OF THE REFERENCE PROFILE

Vf-Vs Relationship Approximation

The use of a reference profile that represents an average of the actual SWV variation in the soil deposit is also the basis of a new inversion procedure that was developed by Rodriguez-Ordonez (1994) for detailed layered SWV data. However, due to length limitations the new interpretation procedure will not be discussed in this paper.

Rodriguez-Ordonez (1994) showed that if the relationship between **Vf** and the corresponding **Vs** profile could be found, it is possible to establish a direct method for inversion of the reference profile. He performed a large scale, comprehensive parametric analysis to obtain **Vs** profiles over the range of values of **Vof** and $\mathbf{m_f}$ that occur in actual soil deposits and obtained an optimal correlation based on error minimization, as follows.

The dispersion curve for the fundamental mode of plane Rayleigh waves was computed for

the assumed soil profile by using the transfer matrix method (Saito 1987). A nonlinear curve-fitting procedure was used to obtain the reference phase velocity profile parameters from the computed dispersion curve. This formulation minimizes the deviations between Equation 2 and the target dispersion curve to obtain the parameters **Vof** and $\mathbf{m_f}$ that produce the best fit by a least squares criteria. The NOLSOL computer routines based on the method by Dennis et al. (1981) were used for this computation.

The step to obtain the reference profile parameters used for the parametric analysis is similar to that which was used to compute those parameters from field test data. This is a very efficient optimization to obtain only two parameters from many phase velocity-wave length points. As expected, the curve-fitting of Equation 6.1 with the computed dispersion curve was very good for all cases, with average relative variations within ±1% for most cases.

Based on his results Rodriguez-Ordonez (1994) concluded that the variation of **Vf** may be described by the following equation:

$$Vof = \frac{0.94 - 0.36\, m_s^{1.19}}{1.04 - 0.04\, m_s}\, Vos \qquad (12)$$

The corresponding equation obtained for $\mathbf{m_f}$ is as follows:

$$m_f = 0.09\ \ln(1.48\, Vos)\, m_s \qquad (13)$$

With Equations 12 and 13 the SWV reference profile may be obtained from the phase velocity reference profile very efficiently. The problem is reduced to solving this non linear system of equations for **Vos** and $\mathbf{m_s}$. This is accomplished without any difficulty by using the Newton method with analytical Jacobian.

The reference SWV profile provides a very good approximation to the actual average SWV structure of the soil. For many cases this is all the meaningful information that may be obtained from the Vf-Vs measurements. In those cases, the Vf-Vs inversion is reduced to an optimization to obtain **Vof** and $\mathbf{m_f}$ and the solution for **Vos** and $\mathbf{m_s}$. This process is accomplished in a few seconds with any personal computer (PC) currently used.

Other formulations are available to obtain comparable results. However, several soil layers are needed for these formulations in order to model the basic variation of SWV with depth. These formulations are iterative and require appropriate smoothing restraints for the optimization procedure. At each iteration the dispersion curve and the gradients of all the parameters in the model should be obtained. The computational effort of such formulations is several orders of magnitude higher.

Accuracy of the Approximation

Equations 12 and 13 are approximations to the actual variation of the **Vf** profile parameters. In order to use these equations for an interpretation procedure it is important to know their accuracy. Rodriguez-Ordonez (1994) showed that even for the cases where the relative errors may be large, the actual absolute errors of **Vof** are small, under 15 m/s over the entire range of **Vos** and $\mathbf{m_s}$ values. These absolute errors are less than the standard deviation that can be obtained from experimental data from CXW, SASW, or any other surface wave measurement.

These results show that the reference profile inversion may be obtained with a degree of accuracy that is consistent with the resolution of the CXW method (and other surface wave measurement techniques), by means of a simple procedure. This procedure may be used for field evaluation of CXW data or as an excellent starting point for an additional optimization step, and in some cases it may be used as a final result.

Reference Profile for Multiple Soil Layers

The reference profiles considered so far assumed that the soil deposit is relatively uniform or that when there are some soil layers in the deposit, they may be determined from the deviations with respect to the reference profile. In other words, a profile described by Equation 3 provides a good approximation to the average of the measured dispersion data. There are cases where a sequence of soil layers with relatively similar properties overlay a stiffer material, such as bedrock. In other cases, the soil profile may be composed of two or more different soil layers with significant thicknesses. In these cases the considerations for the reference profile development apply for each distinct layer, and a single reference profile for the whole deposit is not appropriate.

Rodriguez-Ordonez (1994) showed that two or more reference profiles with parameters pairs $\mathbf{(Vof, m_f)i}$ may be obtained to fit the measured data over different ranges of wave length as shown in Figure 3. The parameter sets of this reference model are obtained by using a procedure similar to the case where there is a single profile. A curve fitting procedure based on nonlinear least squares is used to minimize the difference between the reference model and the measured data. This model is described by pairs of $\mathbf{(Vof, m_f)i}$ applicable over certain ranges of wave length. The ranges are defined by the values of half wave length $\mathbf{(D_f)i}$ over which there is an optimal fit. The SWV reference profile is also obtained from two or more pairs of parameters $\mathbf{(Vos, m_s)i}$ that are valid over their corresponding depth ranges.

An optimization is used to obtain the parameters of the **Vs** profile. This optimization is similar to the formulation used for the refinement of the shear wave velocity reference profile of a uniform soil. The purpose of this optimization is to minimize the sum of squares of the differences between the phase velocity reference curve (Figure 3.a) and the dispersion curve obtained by using the shear wave velocity profile shown in Figure 3.b. The reference phase velocity profile is computed using the parameters shown in the left of the figure. The

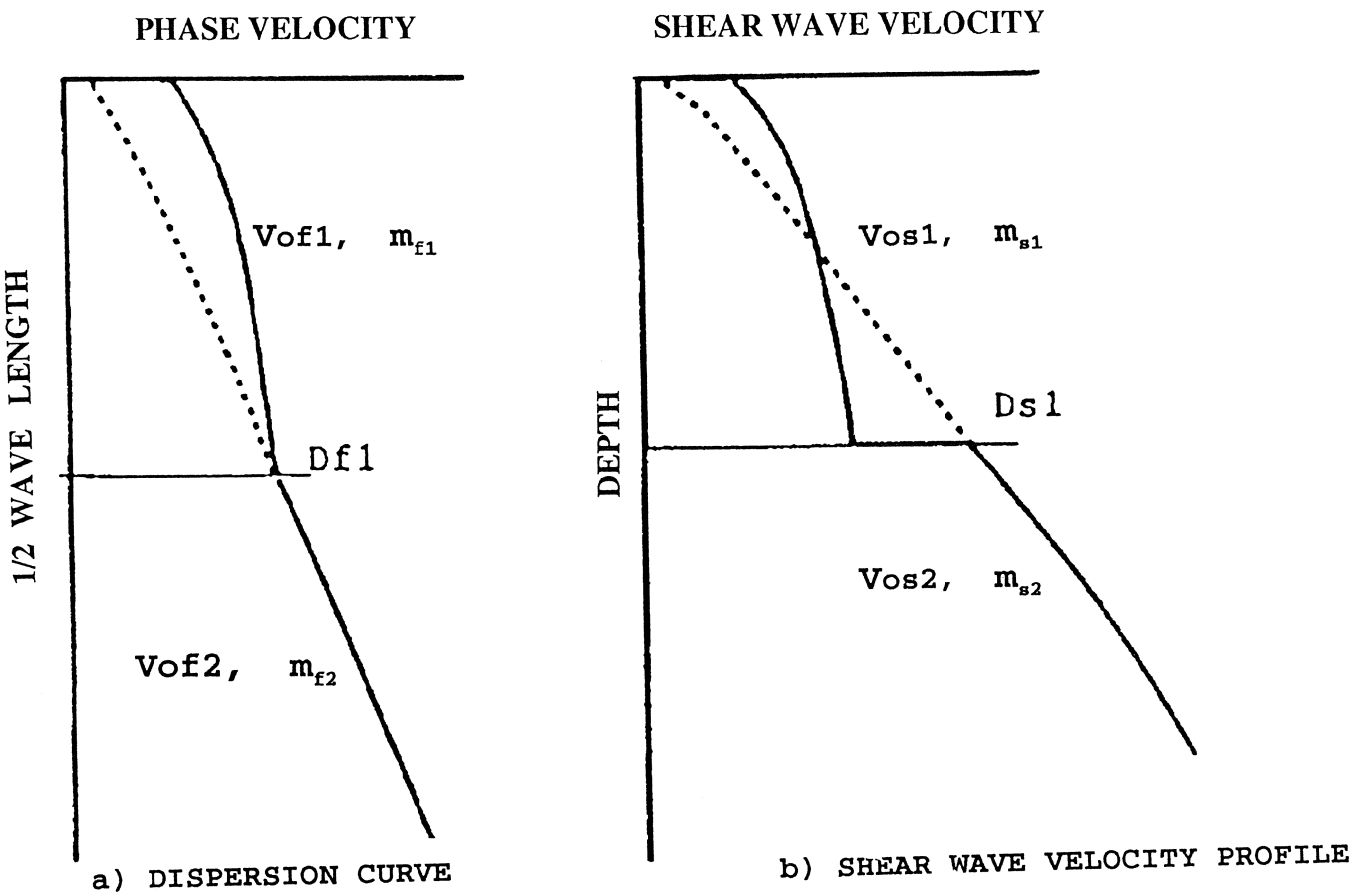

Figure 3. Example of a Reference Profile with Two Materials

variables for the optimization are the parameters shown in the right. The dispersion curve is computed by using the transfer matrix formulation (Saito 1987).

The initial guess for the optimization is obtained by using Equations 12 and 13 with each **(Vof, m_f)i** pair under consideration. The initial value of **Ds1** may be selected as the same value obtained for **Df1**. Computations show that **Ds1** is generally very close to **Df1**, therefore, this parameter can usually be considered as known and not as one of the parameters subject to optimization. With this initial guess the computation of the shear wave velocity profile parameters is very efficient and takes only a few iterations.

If **Ds** is estimated directly, the number of parameters subject to optimization is twice the number of materials in the model. For two materials there are four parameters. The dispersion curve should be defined at a minimum number of frequencies that is larger than the number of parameters in the model. The number of points must be adequate to accurately compare the computed dispersion curve with the reference phase velocity profile. Numerical experiments showed that by using three or four points for each material, the model produces satisfactory results. Therefore, for each iteration of the optimization for a two-material model the dispersion curve should be computed at 6 to 8 frequencies. If needed, these computations can be performed at the site in a few seconds by using a typical notebook PC.

INTERPRETATION PROCEDURE

The complete interpretation procedure (Rodriguez-Ordonez 1994) also handles distinct layers with SWV that deviates from the reference profile. However, the focus of this paper is on obtaining only the reference SWV profile of the soil from the measured dispersion curve. It is assumed that the SWV reference profile has a typical form (as most soils do) and that it is composed of one or more relatively uniform materials.

Figure 4 shows the flow chart for the new interpretation procedure to obtain a SWV reference profile. It has three main components:

1- Definition of the target dispersion curve from the Vf-Vs measurement, $\mathbf{F}(\lambda)$: This component describes the phase velocity as a function of wavelength λ. $\mathbf{F}(\lambda)$ is compared with the dispersion curve of the SWV profile obtained from the interpretation. The new interpretation procedure is useful for cases where the dispersion curve is controlled by the fundamental mode of Rayleigh waves.

2- Computation of the phase velocity reference profile: The parameters describing the reference profile are obtained by minimizing the sum of squares of the difference between the target data and the reference profile, **Ro**, as follows:

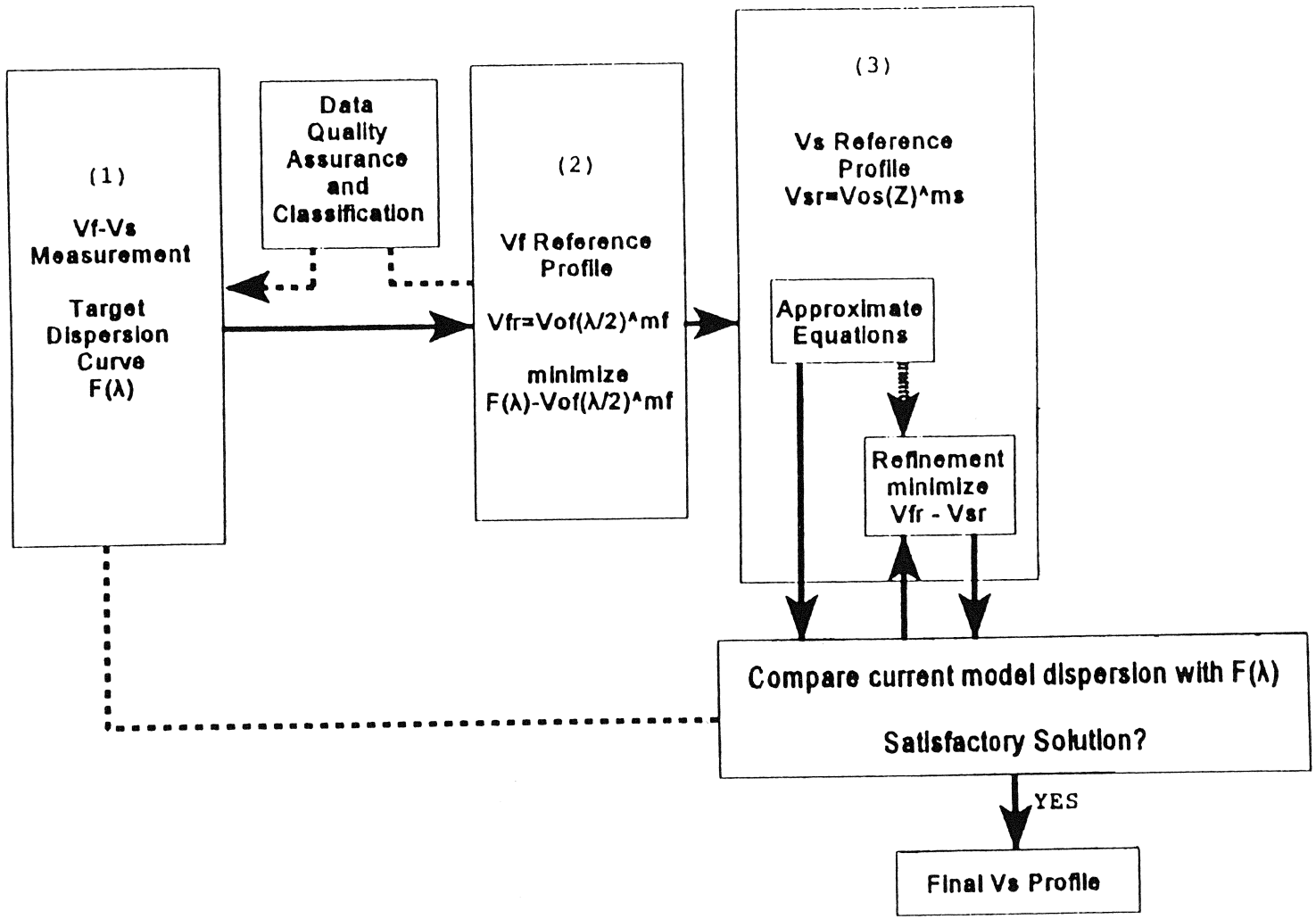

Figure 4. **Flow-Chart of the New Vf-Vs Interpretation Procedure to Obtain a Reference SWV Profile**

$$Ro = \sum_i \left(F(\lambda_i) - Vof\left(\frac{\lambda}{2}\right)_i^{m_f} \right)^2 \qquad (17)$$

3- Computation of the SWV reference profile: The dispersion curve of the SWV reference profile matches the phase velocity reference profile. It is assumed that both the SWV and the phase velocity reference profiles have the same functional form. Equations 12 and 13 may be used to compute the SWV reference profile parameters when only one material is considered. An optional optimization may be carried out to refine the parameters obtained from the equations, although usually this is not required for a single material model.

When there are several materials, Equations 12 and 13 can be used to compute a first estimate of the parameters for the SWV reference profiles associated with each material. A refinement is then obtained by minimizing **R1**, the sum of squares of the difference between the phase velocity reference profile and the dispersion curve obtained with the SWV reference profile parameters:

$$R1 = \sum_i \left(Vof\left(\frac{\lambda}{2}\right)_i^{m_f} - Vos\, Z_i^{m_s} \right)^2 \qquad (18)$$

The computation of this optimization phase is also efficient, and may be performed in a few seconds using a typical PC.

At this point, the dispersion curve obtained from the reference profile is compared with the target dispersion curve $\mathbf{F(\lambda)}$. Often the approximation obtained from the reference profile is good enough for a final interpretation within the resolution limits of the Vf-Vs method. In the case of site amplification evaluation these data are adequate.

CASE STUDIES

Rodriguez-Ordonez (1994) applied the new interpretation procedure in several case studies where cross-hole SWV data were available. An example of these results is shown in Figure 5 with data from the Hollywood Storage Building Site located in the Piedmont of Santa Monica Mountains in California (USC 1993). At this site the reference profile was obtained based on measured CXW dispersion curve. Two distinct materials were used for the reference profile interpretation. Interpretation results show that the reference profile provides a good average to the SWV distribution obtained from the cross-hole results. Such a reference profile (that may be obtained about 5 minutes after the CXW measurement is completed) may be used for site amplification evaluation. This and other case studies (Rodriguez-Ordonez 1994) show that the new method may be applied successfully even in soil deposits were there are several distinct soil layers with large SWV differences.

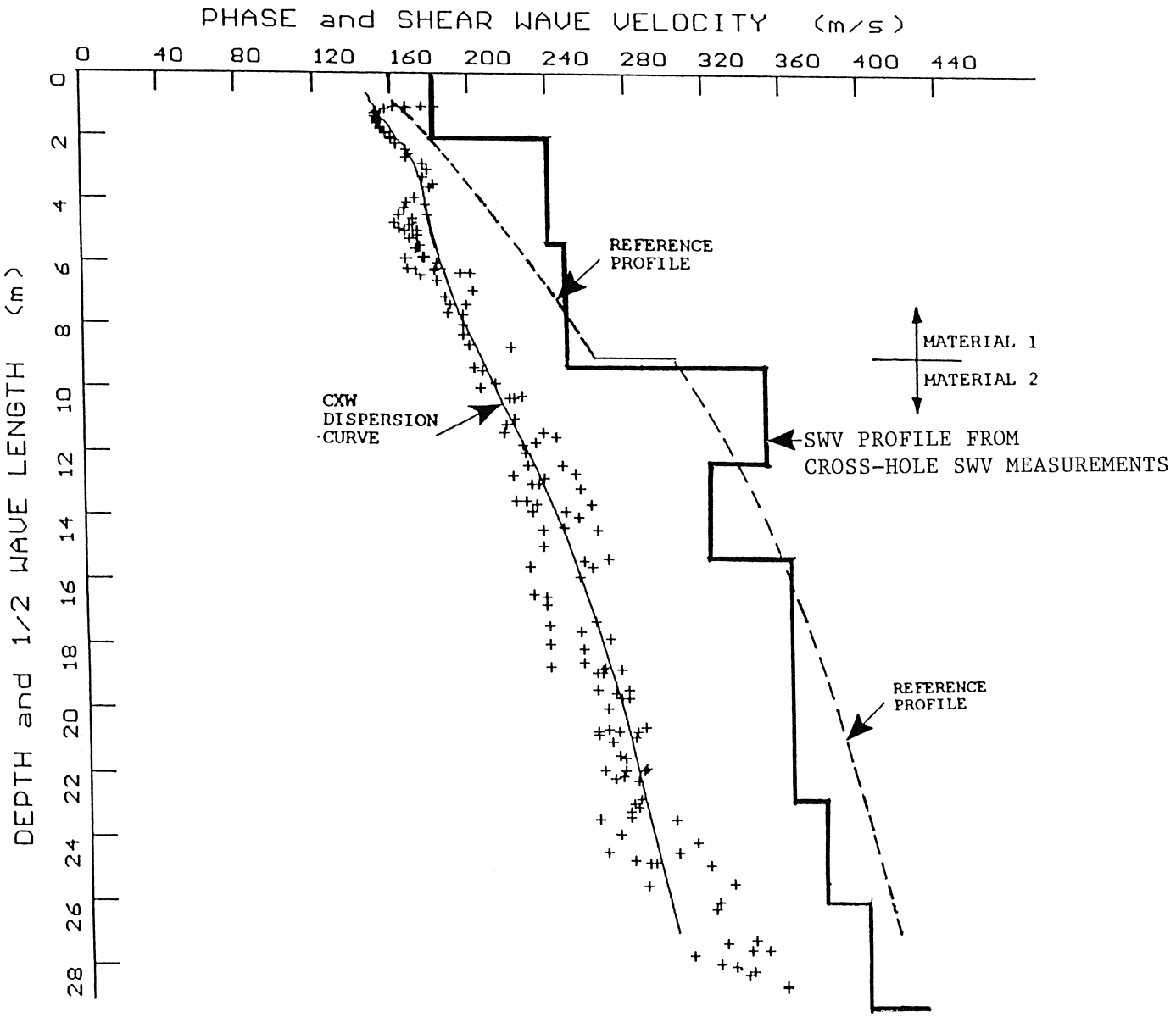

Figure 5. **Measured Cross-Hole SWV Profile and CXW Data, and Computed SWV Reference Profile at the Hollywood Storage Building Site**

SUMMARY AND CONCLUSIONS

The new approach to the interpretation of SWV structure from Rayleigh waves dispersion data (the Vf-Vs method) is based on the reference profile concept. A reference profile describes the average dispersion curve and corresponding SWV structure and is consistent with the fundamental dependency of SWV on confining pressure (depth) in soils. Simple equations were developed for direct inversion of the reference profile based on data from more than 100 sites.

The new reference profile concept is particularly useful for site amplification evaluations using the impedance ratio approach. Non-invasive, controlled-source surface wave measurements provide cost-effective dispersion data to great depth. These data are used to obtain reference profiles for most soil formations. The procedure is rapid and computationally efficient and its results are more representative of actual soil structure than results obtained from other non-invasive methods. This method was verified at several sites where accurate cross-hole SWV data was also available.

REFERENCES

- Arbelaez-Hoyos, M.C. (1992). "Soil profiling using controlled source spectral analysis of surface waves," MS Thesis in Civil Engineering, University of North Carolina at Charlotte.

- Dennis J., Gay D., and Welsch R., (1981). "An adaptive nonlinear least-squares algorithm," *ACM Trans. Math. Software,* Vol. 7, No.3, 348-367.

- Dobry, R. (1991). "Soil Properties and earthquake Ground Response," Key-Note Lecture, Proceedings of the IX Panamerican Conference on Soil Mechanics and Foundation Engineering, Vol. III, Vina del Mar, Chile, August.

- Dobry, R., and Vucetic, M. (1987). "State-of-the-art report: Dynamic properties and response of soft clay deposits," Proceedings of the International Symposium on Geotechnical Engineering of Soft Soils, Mexico City, Vol. 2, 51-87.

- Mitchell, J.K. (1993). Fundamentals of Soil Behavior 2nd Edition. John Wiley & Sons, Inc. New York.

- Poran, C.J., Rodriguez, J.A., and Satoh, T. (1993). "Controlled source surface waves measurements for shear wave velocity profiling of soils," Proceedings, National Science Foundation Workshop on Geophysical Techniques for Site and Material Characterization, Atlanta, Georgia, June, 231-242.

- Poran, C.J., Rodriguez, J.A., Arbelaez, M.C., Satoh, T., and Kavazanjian, E. Jr. (1992). "Non-invasive Rayleigh wave measurement system for soil profiling in ports," Proceedings of Ports '92, ASCE Specialty Conference, Seattle, July, Vol 1., 390-402.

- Rodriguez-Ordonez, J.A. (1994). "A New Method for Interpretation of Surface Wave Measurements in Soils," PhD Dissertation, North Carolina State University, Civil Engineering Department, August.

- Satoh, T. (1989). "On the controlled source spectral Rayleigh wave excitation," Research Report, Vibration Instruments Company Ltd., Tokyo.

- Satoh, T., Yamagata, K., Poran, C.J., and Rodriguez, J.A. (1991). "Soil profiling by spectral analysis of surface waves," Second International Conference on Recent Advances in Geotechnical Earthquake Engineering and Soil Dynamics, St. Louis, 2,1429-1434.

- Saito M., (1987). "Transfer Matrix Approach for Rayleigh Waves Analysis," Research Report to Vibration Instruments Company Ltd., Tokyo (translated from Japanese).

- Schmertmann, J. (1991). "The mechanical aging of soils," *Journal of Geotechnical Engineering ASCE*, Vol. 117, No.9, 1288-1330.

- Seed H.B. and Idriss I.M. (1970). "Moduli and damping factors for dynamic analyses," Earthquake Engineering Research Center Report No. UCB/EERC-70/10, University of California, Berkeley.

- Seed H.B., Wong, R.T., Idriss, I.M., and Tokimatsu, K. (1984). "Moduli and damping factors for dynamic analyses of cohesionless soils," Earthquake Engineering Research Center Report No. UCB/EERC-84/14, University of California, Berkeley.

- USC (1993). "Shear wave velocity profiling of instrumented sites in the greater los angeles area using Rayleigh waves measurements," Research Report for Subcontract Between the University of Southern California and Vibration Instrument Company, Ltd., CALTRANS Contract No. O7G297, May.

IV MITIGATION OF EARTHQUAKE AND LIQUEFACTION EFFECTS

Experiments on Force Acting on Underground Structures in Liquefaction-Induced Ground Flow
M. Miyajima and M. Kitaura
Evaluation of Pile Response to Liquefaction-Induced Lateral Spread
T.D. O'Rourke, W.D. Meyersohn, Y. Shiba, and D. Chaudhuri
High Ductility Aseismic Joint Spliced Pile Behavior When Subjected to Liquefaction-Induced Large Ground Displacements
F. Miura, T. Miyasaka, and T. Hirata
Mitigation of Liquefaction Hazards at Three California Bridge Sites
K. Jackura and A. Abghari
Assessing Vulnerability of BC Gas Pipelines to Lateral Spread Hazards
D.G. Honegger
Pipeline Design Against Sand Liquefaction in Isla Del Carmen, Mexico
V. Trueba-López and R. Flores-Berrones
Preliminary Evaluation of the Use of Compaction Piles for Improvement of the Foundation Soils of the Coastal Dikes of Lake Maracaibo, Venezuela
B. Villegas and J. Murria

EXPERIMENTS ON FORCE ACTING ON UNDERGROUND STRUCTURES IN LIQUEFACTION-INDUCED GROUND FLOW

Masakatsu MIYAJIMA[1] and Masaru KITAURA[2]

ABSTRACT

The present paper focuses on the effects of force induced by liquefied ground flow on underground structures. Small scale tests were conducted using model sand deposits in order to understand the characteristics of liquefied soil. According to the tests, the soil layers showed performance like a liquid when the excess pore water pressure ratio was equal to 1.0, that is, complete liquefaction. Next, the viscous coefficient of completely liquefied soil was estimated from the test that was called dropping ball method. As a result, the viscous coefficient of completely liquefied sand was about 10^5 times greater than that of water. Moreover, bending strains of a model pile in liquefied ground flow were measured and compared with those calculated by using the viscous coefficients obtained from the previous experiments. It is concluded that the viscous coefficient obtained from the dropping ball method could be applied to estimation of the force acting on underground structures in liquefied ground flow.

1) Associate Professor, Dept. of Civil Engineering, Kanazawa University, 2-40-20 Kodatsuno, Kanazawa 920 JAPAN.
2) Professor, ditto.

INTRODUCTION

Permanent ground displacement induced by soil liquefaction is one of the most serious liquefaction hazards. Many civil engineering structures, especially lifeline facilities have been damaged by the liquefaction-induced permanent ground displacement. Hamada and O'Rourke investigated liquefaction-induced permanent ground deformation and lifeline performance during past earthquakes in Japan and U.S.A. from the 1906 San Francisco earthquake to the 1989 Loma Prieta earthquake through the Japan-U.S. cooperative research program [1]. Many studies have been performed in order to clarify the mechanisms of generation of liquefied ground flow and to estimate the value of permanent ground displacement [2-5].

A soil spring constant is usually used for the evaluation of seismic response of underground structures so far. Therefore, some liquefaction-related experiments dealing with the soil spring constant have been conducted [6-8]. They concluded that the soil spring constant of liquefied ground became less than 1/10 to 1/1000 of that in the non-liquefied ground. It is, however, considered that the behavior of soil deposits with so small spring constant is close to liquid rather than solid. From the point of view, some studies dealing with liquefied ground flow as viscous flow were conducted [9-12]. Takada et al. and Ohtomo et al. concluded that the viscous coefficient of completely liquefied sand layer was about 10^5 times greater than that of water [9,12].

In the present paper, effects of degree of liquefaction on characteristics of soil deposit were clarified. Then, the viscous coefficient of completely liquefied soil was investigated through the small scale tests, so called dropping ball method. Furthermore, vibration tests using a model pile were conducted and the performance of the model pile in liquefied ground flow was measured. The response of the pile was compared with that calculated by using the viscous coefficients obtained from the previous tests.

EFFECTS OF DEGREE OF LIQUEFACTION ON CHARACTERISTICS OF SOIL DEPOSITS

A general view of test apparatus is shown in Fig. 1. The sand box was 220 mm in width, 380 mm in length and 250 mm in height. River sand was used in the experiments. Table 1 lists its material properties. Water flow was generated from the bottom of sand deposits and the excess pore water pressure ratio in the sand deposits was controlled by the discharge of water. A ball on two rails was pulled by a motor horizontally. The force was measured by a load cell shown in Fig. 1 when the motor pulled the ball. The displacement of the ball was also measured.

Fig. 2 indicates one of the results obtained here. This figure shows the relationship between the load and displacement of the ball. Five curves in this figure shows the results in case of the excess pore water pressure ratios of 0.00, 0.25, 0.50, 0.75, 1.00, respectively. The velocity of the ball was 1.1 cm/s in this case. The load increased at first, then kept a constant value.

Fig. 3 illustrates the maximum load in relation to the pulling velocity and excess pore water pressure ratio. The maximum load decreased with an increase in the excess pore water pressure ratio. In case of the excess pore water ratio of less than 1.0, the maximum load decreased with an increase in the pulling velocity. Since the load depends on the pulling velocity in case of the excess pore water pressure ratio of less than 1.0, the effects should be considered in evaluation of force acting underground structures. While the load increased with an increase in the pulling velocity when the excess pore water pressure was 1.0, so called complete liquefaction. This means that the soil layers showed the behavior of viscous fluid when the excess pore water pressure ratio was

equal to 1.0. The present paper focuses on the force induced by completely liquefied ground because the soil layers with a slope deformed after complete liquefaction.

VISCOSITY OF COMPLETELY LIQUEFIED SOIL

Viscous coefficients of completely liquefied soil were measured in order to evaluate the force acting on underground structures in liquefied ground flow. The general view of test apparatus was shown in Fig. 4. The sand container was plastic cylinder with 380 mm in diameter and 500 mm in height. The sand used in the tests was the same as that in the previous tests. The sand container was vibrated by a sinusoidal wave with 5 Hz in frequency. When the sand layer completely liquefied, the ball began to fall into the liquefied sand layer. At this stage, the viscous coefficients of the liquefied soil layer can be evaluated from the equilibrium of viscosity resistance, weight of the ball and buoyancy acting on the ball. Two balls were used in the tests. One was 7.8 cm in diameter and 1,160 gf in weight. The other was 3.6 cm in diameter and 150 gf in weight, respectively. The excess pore water pressures and displacement of the ball were measured at each point shown in Fig. 4.

The viscous coefficient was calculated using the following equations. A completely liquefied ground was assumed as the Newtonian fluid in this study. According to the Stokes' formula, the viscosity resistance acting on a ball in the Newtonian fluid can be expressed as Eq. (1) when the ball with diameter a fell in viscous fluid at a steady speed of V [13].

$$F = 6\pi a \mu V \tag{1}$$

Here F is resistance acting on a ball , a is diameter of the ball, μ is viscous coefficient and V is relative velocity between the ball and surrounding soil. The equilibrium equation of viscosity resistance, weight of ball and buoyancy acting on the ball when the ball is falling at a steady speed in the viscous fluid is as follows:

$$6\pi a \mu V = 4\pi a^3 (\rho' - \rho) g / 3 \tag{2}$$

Here ρ is density of fluid, ρ' is density of the ball and g is acceleration of gravity. The viscous coefficient μ can be obtained from the following equation.

$$\mu = \frac{4\pi a^2 (\rho' - \rho) g}{18\pi V} \tag{3}$$

Fig. 5 illustrates one of the test results. The time histories of response acceleration of the sand container, displacement of the ball and excess pore water pressure ratios are indicated, respectively. These figures indicate that the ball began to fall when the excess pore water pressure ratio reached 1.0, then the ball was falling in the liquefied soil layer at a steady speed for more than 5 seconds.

Fig. 6 indicates the viscous coefficient calculated from Eq. (3) in relation to the input acceleration. According to this figure, the viscous coefficient obtained here was not correlated with the input acceleration and ball diameter despite a somewhat scatter in individual data points. The data points distribute from 0.71 gf s/cm^2 to 3.22 gf s/cm^2, and the average in this figure is 1.67 gf s/cm ^{2}.

RESPONSE OF MODEL PILE IN LIQUEFIED GROUND FLOW

Model Test

The diagram of the experimental apparatus is shown in Fig. 7. The sand box was 500 mm in width, 1500 mm in length and 350 mm in height. The model sand deposits had a slope of 6 % to 10 %. The sand deposit was made from loose saturated sand, whose material properties were the same as those listed in Table 1. The model pile was simulated by a rubber rod with 10 mm in diameter and 130 mm in length. Its elastic modulus was 810 kgf/cm^2 and its weight per unit volume was 1.14 gf/cm^3 as listed in Table 2. Two strain gauges were utilized at the model pile. Twenty-four pins were installed at the surface of the sand stratum to measure horizontal residual displacements of the ground surface. The deformation of the ground surface during excitation was measured by means of a video camera. The model sand stratum was vibrated by a harmonic wave with 5 Hz. Input acceleration of the table was 150 cm/s^2.

Fig. 8 illustrates the average velocity of the pins shown in Fig. 7. The pins did not move till the excess pore water pressure ratio reached 1.0. Therefore, the average velocities after completely liquefaction were shown in Fig. 8. The average velocity was evaluated from the displacement for 2 seconds at every time step. This figure indicates the duration time of ground deformation for 6 % slope is shorter than that for 10 % slope despite that the duration time of complete liquefaction was almost same. This could be considered as follows. The upper portion of soil deposit subsided and the lower potion heaved up when the liquefaction of sand layer occurred. The slope of soil deposit became gentle and finally horizontal. Therefore, it is conceivable that the larger the slope of soil deposit is, the longer the duration of ground deformation is. The average velocities of the pins, that is, velocity of ground deformation, were 1.6 cm/s for 10% slope and 0.9 cm/s for 6% slope, respectively. It suggests the velocity of ground deformation increases with an increase in slope of ground. This result is similar to other test results conducted by Miyajima et al. [14].

Discussion

Now, a vertical distribution of velocity is considered here when a viscous fluid flows on an inclined plate under the condition of stationary, shown in Fig. 9. The equation governing the motion of a viscous fluid is given as follows:

$$\mu \frac{\partial^2 V_g}{\partial x^2} + \rho g \cos\beta = 0 \tag{4}$$

in which V_g is velocity of a fluid, ρ is density of the fluid, μ is viscous coefficient, β is slope of the inclined plane and δ is thickness of the fluid, respectively. The boundary conditions are

$$x = 0 : \frac{dV_g}{dx} = 0 \tag{5}$$

$$x = \delta : V_g = 0 \tag{6}$$

By integrating Eq. (4) with respect to x using the boundary conditions Eqs. (5) and (6), the analytical solution is obtained as follows:

$$V_g(x) = \frac{\rho g \delta^2 \cos\beta}{2\mu} \left\{ 1 - \left(\frac{x}{\delta} \right)^2 \right\} \tag{7}$$

Fig. 10 shows the vertical distribution of velocity calculated by using Eq. (7). The viscous coefficient of 1.67 gf s/cm^2 was used in this case. This value was obtained from the tests in the previous chapter. According to this figure, the maximum velocities of liquefied sand deposit at the surface were 10.07 cm/s for 10% slope and 8.07 cm/s for 6% slope, respectively. These values are larger than those obtained from the model tests. The velocity is evaluated as larger value if the viscous coefficient obtained from the tests is used. The equation governing the motion of the fluid is constructed under the condition of stationary, however the model tests were not stationary state. It is conceivable that this could cause the difference of the values. The effect of the wall of sand box was also considered as one of reasons.

The liquefied ground flow is assumed as the viscous fluid on inclined plate here. The bending moment of the model pile was calculated using the distribution of velocity shown in Fig. 10. The force acting on the pile in the liquefied ground flow was evaluated as follows.

$$f = \rho C_d V_r^2 D/2 \tag{8}$$

Here f is the force, ρ is density of liquefied ground, C_d is resistance factor, V_r is relative velocity between the model pile and liquefied ground flow and D is diameter of the model pile. The resistance factor for a cylinder in the fluid with low Reynolds' number can be expressed as:

$$C_d = 8\pi / R_e \{0.5 - \alpha - \ln(R_e/8)\} \tag{9}$$

in which R_e is Reynolds' number and α is Euler's constant. Reynolds' number can be given as:

$$R_e = V_r D/\nu \tag{10}$$

Here ν is kinematic viscosity. The relation between viscous coefficient and kinematic viscosity can be expressed as follows.

$$\mu = \nu\rho \tag{11}$$

Fig. 11 illustrates the bending moment of the model pile calculated by using equations above mentioned. the dots in this figure show the bending moment calculated from the bending strains measured in the tests. The values calculated show good agreement with the measured values. It suggests that the viscous coefficient obtained from the dropping ball method can be used for estimation of the force acting on underground structures in liquefied ground flow.

CONCLUDING REMARKS

The effects of force acting on underground structures in liquefied ground flow were investigated in the present paper. The sand soil layers behaved as a viscous fluid after the excess pore water pressure ratio reached 1.0, that is, after complete liquefaction. Therefore, the completely liquefied soil was treated as a viscous liquid. Small scale tests were conducted in order to measure the viscous coefficient of liquefied sand. The dropping ball method gave the viscous coefficient of 1.67 gf s/cm^2. The viscous coefficient obtained here were about 10^5 times greater than that of water.

Furthermore, vibration tests using a model pile were conducted and the response of the model pile in liquefied ground flow was measured. The response of the pile was compared with that calculated by using the viscous coefficients obtained from the previous tests. As a result, the viscous coefficient obtained from the small scale tests can be used for estimation of the force acting on underground structures in liquefied ground flow.

ACKNOWLEDGEMENTS

The authors wish to thank Mr. Masamichi Hasegawa (graduate student of Kanazawa University) and Mr. Hidemasa Hosaka (student of Kanazawa University) for their cooperation in experiments. A part of expense of this study was defrayed by Kawasaki Steel Corporation.

REFERENCES

1) Hamada, M. and O'Rourke T.D. (Edit.): Case Studies of Liquefaction and Lifeline Performance During Past Earthquake, Vols. 1 and 2, Technical Report NCEER-92-0001, 0002, 1992.
2) Hamada, M., Yasuda, S., Isoyama, R. and Emoto, K.: Study on Liquefaction-Induced Permanent Ground Displacements and Earthquake Damage, Proceedings of JSCE, No. 376, pp. 221-229, 1986 (in Japanese).
3) Towhata, I.: Finite Element Model to Predict Permanent Displacement of Ground Induced by Liquefaction, Proc. 2nd Int. Conf. Numer. Meth. Geomech., pp. 689-697, 1986.
4) Miyajima, M., Kitaura, M. and Nomura, Y.: Study on Response of Buried Pipelines Subjected to Liquefaction-induced Permanent Ground Displacement, Proceedings of JSCE, No. 404, pp. 163-172, 1989.
5) Yasuda, S., Nagase, H., Kiku, H. and Uchida, Y.: The Mechanism and a Simplified Procedure for the Analysis of Permanent Ground Displacement Due to Liquefaction, Soils and Foundations, Proceedings of JSSMFE , Vol. 32, No. 1, pp. 149-160, 1992.
6) Yasuda, S., Saito, K. and Suzuki, N.: Soil Spring Constant on Pipe in Liquefied Ground, Proceedings of the 19th JSCE Earthquake Engineering Symposium, pp. 189-192, 1987 (in Japanese).
7) Tanabe, K.: Fundamental Study on Seismic Assessment and Design of Buried Pipeline Subjected to Ground Failure During Earthquake, Doctoral Dissertation Submitted to Kobe University, Chapter 5, 1988 (in Japanese).
8) Miyajima, M. and Kitaura, M.: Experiments on Soil Spring Constants During Liquefaction, Proceedings of the 2nd Intl. Conf. on Recent Advances in Geotechnical Earthquake Engineering and Soil Dynamics, Vol. 1, pp. 487-490, 1991.
9) Takada, S. and Nagai, J.: Dynamic Stiffness and Damping in Liquefied Ground, Construction Engineering Laboratory Report, No. 29, pp. 53-72, 1987 (in Japanese).
10) Sato, H., Doi, M, Hamada, M. and Nakamura, T.: Analysis of Liquefied Ground Flow and Its Consideration, Proceedings of the 22nd JSCE Earthquake Engineering Symposium, pp. 87-90, 1993 (in Japanese).
11) Doi, M., Sato, H. and Hamada, M.: Experimental Study on Behavior of Liquefied Ground Flow and Its Characteristics, Proceedings of the 22nd JSCE Earthquake Engineering Symposium, pp. 91-94, 1993 (in Japanese).
12) Ohtomo, K., Iwatate T., Shimizu, M., Shumuta, Y. and Hamada, M.: Characteristics of Load Acting on Pile Foundation in Liquefied Ground Flow, Proceedings of the 22nd JSCE Earthquake Engineering Symposium, pp. 95-98, 1993 (in Japanese).
13) Graf, W. H.: Hydraulics of Sediment Transport, McGraw-Hill Book Co., N.Y., 1971.
14) Miyajima, M., Kitaura, M. and Ando, K.: Experimental Study on Permanent Deformation of Liquefied Ground, Proceedings of the 8th Japan Earthquake Engineering Symposium, pp. 939-944, 1990 (in Japanese).

Table 1 Physical properties of sand.

Specific Gravity	2.67	
Uniformity Coefficient	2.96	
Maximum Void Ratio	1.030	
Minimum Void Ratio	0.721	
50 Percent Diameter	0.2	(mm)
Coefficient of Permeability	1.92×10^{-2}	(cm/s)

Table 2 Physical properties of pile model.

Young's modulus	810	(kgf/cm^2)
Unit weight	1.14	(gf/cm^3)
Length	130	(mm)
Diameter	10	(mm)

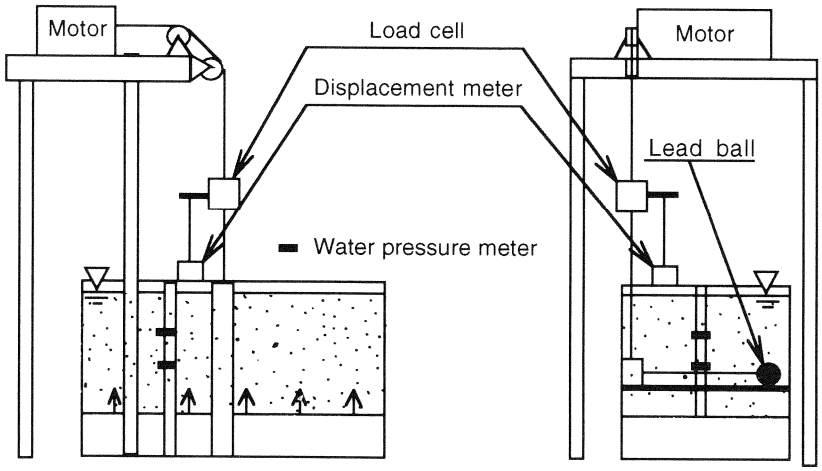

Fig. 1 General view of test apparatus.

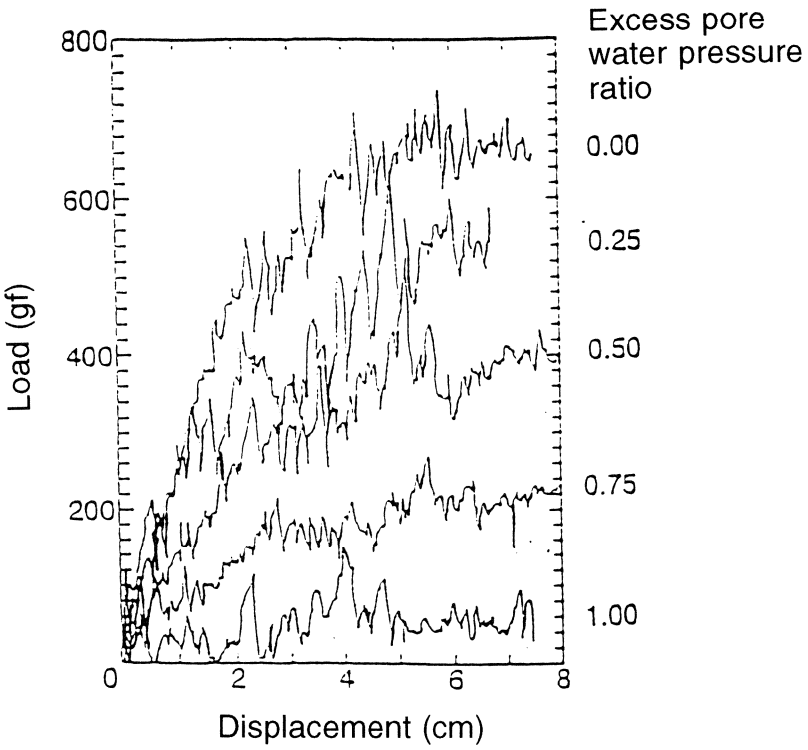

Fig. 2 Relationship between load and displacement.

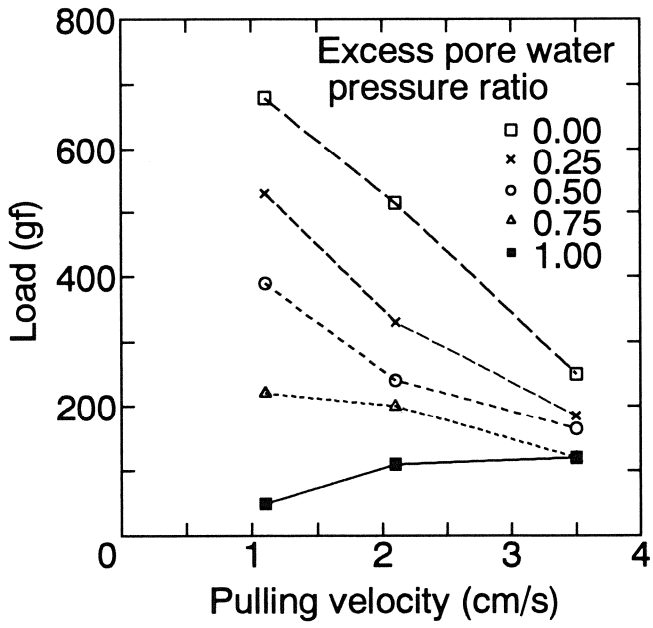

Fig. 3 Relationship between maximum load and pulling velocity.

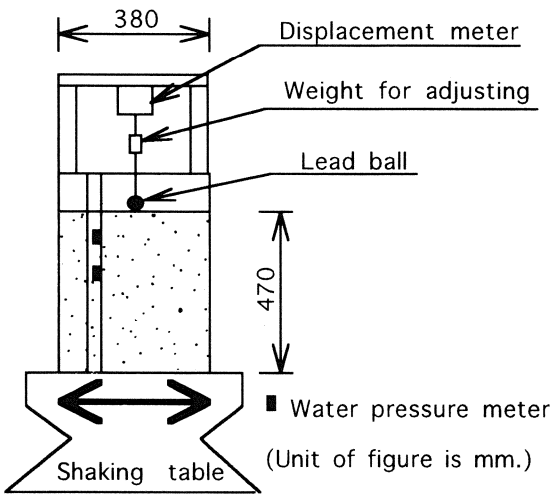

Fig. 4 General view of test apparatus for dropping ball method.

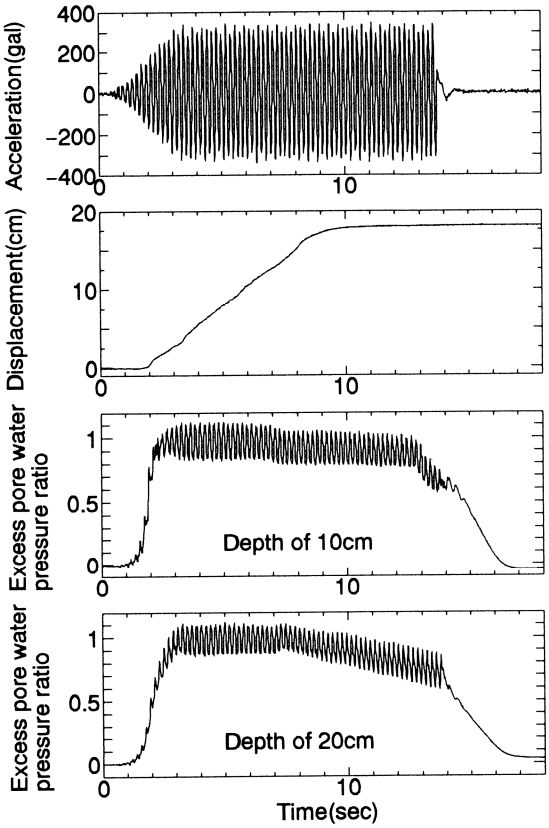

Fig. 5 Time histories of response acceleration, displacement and excess pore water pressure ratios.

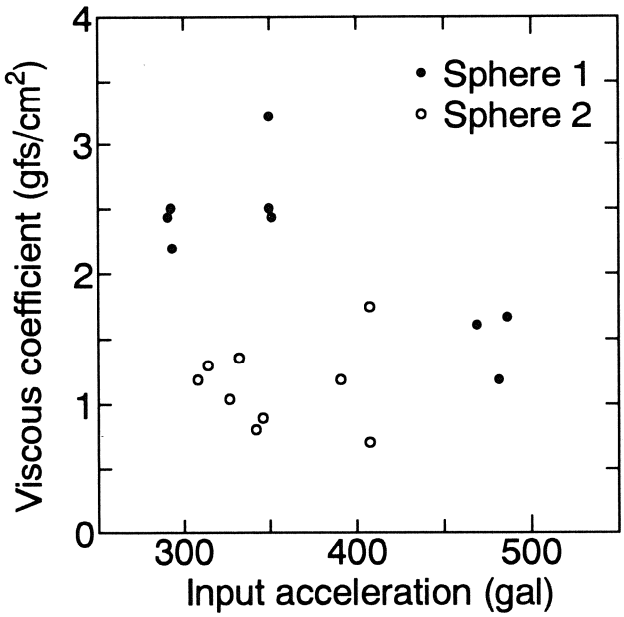

Fig. 6 Relationship between input acceleration and viscous coefficient.

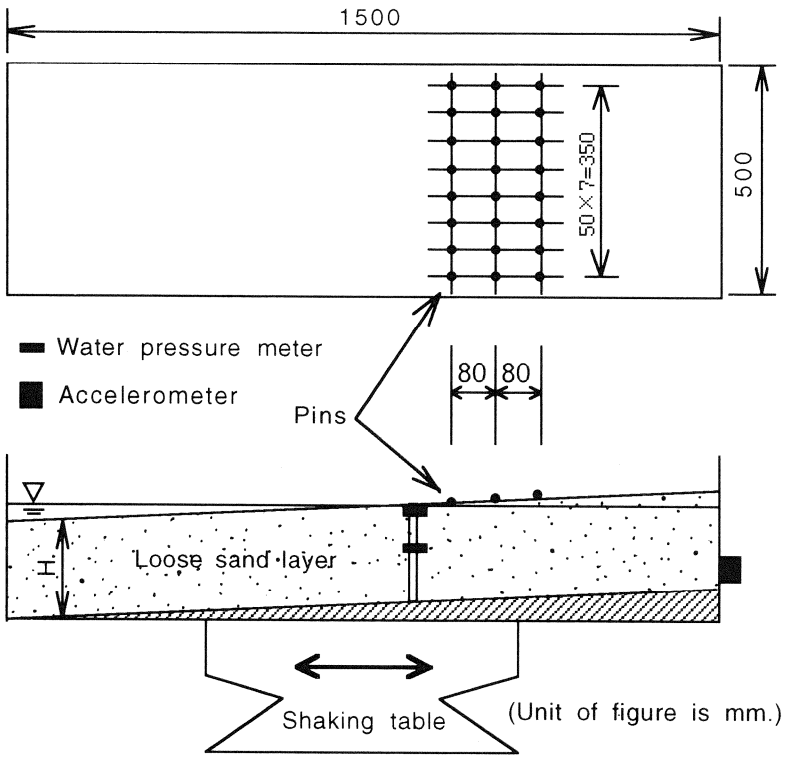

Fig. 7 General view of test apparatus for liquefied ground flow.

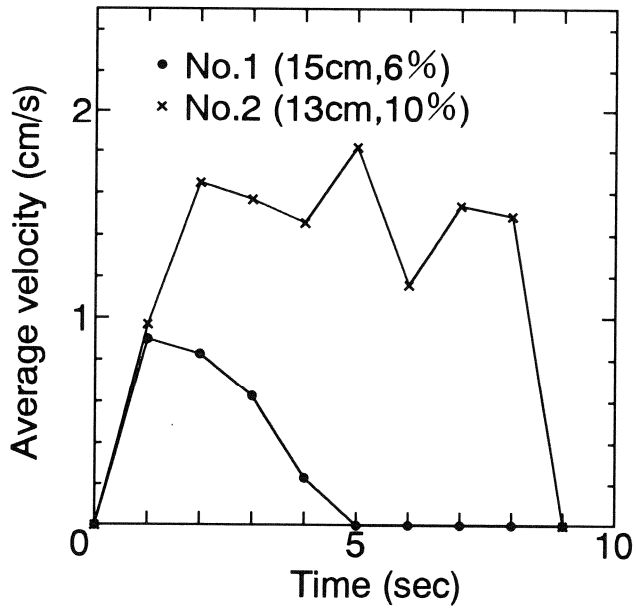

Fig. 8 Velocity of ground deformation at surface.

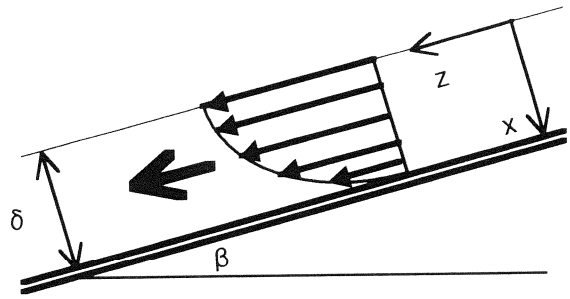

Fig. 9 Model of liquid flow on inclined plate.

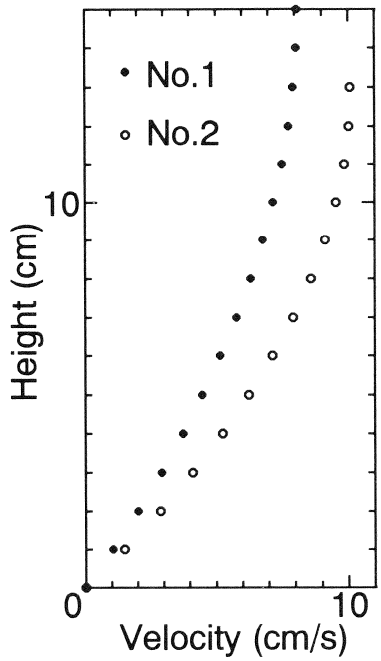

Fig. 10 Theoretical distribution of velocity.

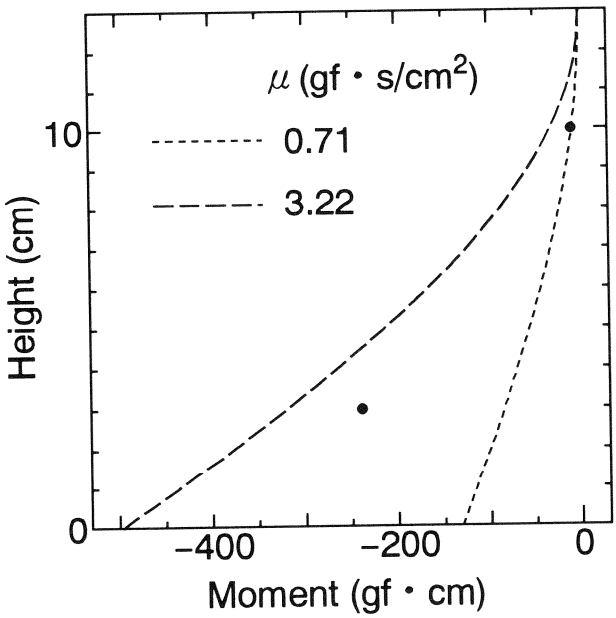

Fig. 11 Relationship between bending moment obtained by model test and analysis.

EVALUATION OF PILE RESPONSE TO LIQUEFACTION-INDUCED LATERAL SPREAD

by

T. D. O'Rourke[1]
W. D. Meyersohn[2]
Y. Shiba[3]
D. Chaudhuri[4]

ABSTRACT

This paper presents the results of a comprehensive analytical study of pile foundation response to lateral spread. Analyses were performed with the computer code B-STRUCT, which has been shown to provide results which compare favorably with field observations of pile deformation under ground failure conditions. Analytical results are combined to develop dimensionless plots which allow for the determination of failure mechanisms on the basis of relative stiffness and applied axial load. For the first time, these results show quantitatively how the behavior of deep foundations changes as the ground alters its force-displacement characteristics from a soil-like to a fluid-like medium. Dimensionless plots also are developed to determine surface soil displacement required to induce the formation of a plastic hinge under excessive bending conditions.

[1]Professor, School of Civil & Environmental Engineering, Cornell University, Ithaca, NY
[2]Staff Engineer, Dames and Moore, 221 Main Street, Suite 600, San Francisco, CA
[3]Visiting Scientist, School of Civil & Environmental Engineering, Cornell University, Ithaca, NY
[4]Graduate Research Assistant, School of Civil & Environmental Engineering, Cornell University, Ithaca, NY

INTRODUCTION

The lateral movement of liquefied soil against single piles and pile groups is an important problem in the design of deep foundations for buildings and bridges constructed in seismically active areas. As shown by Hamada, et al. [1986], the lateral spreading of loose saturated sands caused substantial damage to isolated pile foundations during the 1964 Niigata earthquake. Considerable work on modeling the interaction between piles and liquefied soil has been undertaken in response to the Niigata observations [e.g., Miura and O'Rourke, 1991; Meyersohn, et al., 1992], with the result that analytical procedures now are available to evaluate and design deep foundations affected by liquefaction-induced lateral spread.

This paper describes an analytical approach for assessing pile and pile group response to large ground deformation caused by liquefaction. Models for pile and liquefied soil behavior are embodied in a computer code, B-STRUCT, developed at Cornell University as a result of cooperative U.S. and Japanese research. The paper explains the general characteristics of the analytical procedures, and describes the models adopted to represent the material nonlinearities of reinforced concrete. Analytical results are compared with both laboratory test data and measured pile response to lateral spreads. The failure modes of piles subjected to lateral spread are discussed, and the results of parametric studies are summarized to show how soil properties and subsurface geometry affect the axial load-carrying capacity of a pile and its lateral deformation.

ANALYTICAL APPROACH

The analytical approach adopted for the assessment of soil-pile interaction is illustrated in Figure 1. The analytical approach is explained in detail elsewhere [Meyersohn, 1994; Meyersohn, et al., 1992], and only the salient features are described in this paper.

The water table in Figure 1 is at the top of a liquefiable stratum of thickness, H_L, above which is the nonliquefiable soil cover, L_L. The pile is embedded at a distance, L_b, into a firm, nonliquefiable base. Soil displacements are applied in a series of load increments until the maximum soil displacement at ground surface, d_h, is achieved. Any distribution of soil displacement can be simulated. For purposes of illustration, a trapezoidal distribution is applied in the figure. Axial load, shear, and moment can be specified at the top of the pile.

The B-STRUCT program models the pile foundation by a series of beam elements, while the surrounding soil is modeled by means of transverse and longitudinal bilinear spring-slider elements. Although the diagram shows only springs offering lateral resistance, the program accounts for the effects of skin friction and adhesion as well.

Each beam element is formulated as a nonlinear elastic member, with material nonlinearities concentrated at nodal points. An updated Lagrangian formulation is used to account for geometric nonlinearities in the simulation of large deformation. A solution algorithm, based on the modified

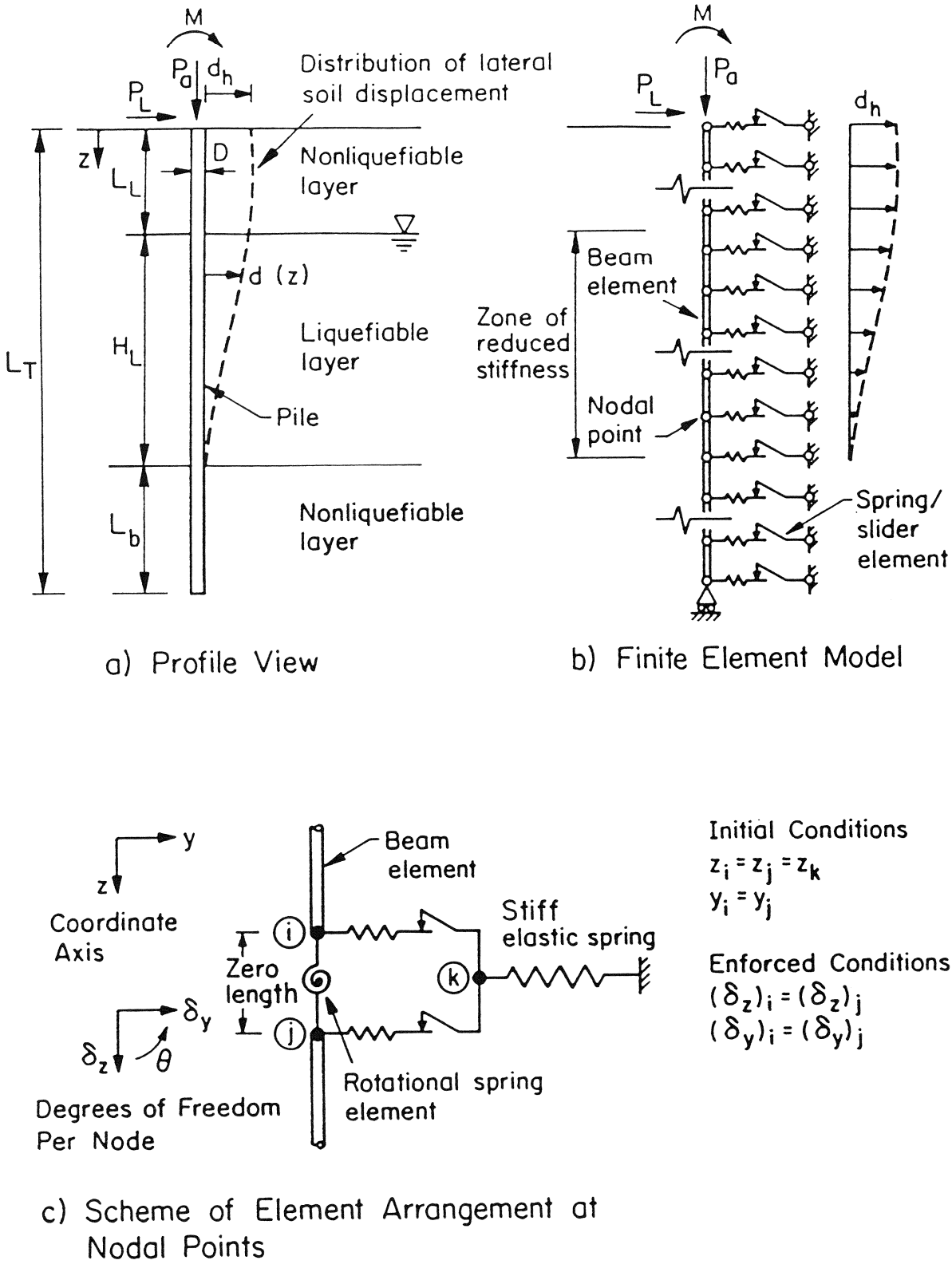

FIGURE 1. Analytical Model for the Soil-Pile System

Newton-Raphson method with a mixed-step iteration technique, is used for convergence. Beam elements are formulated with the capability of detecting buckling states.

Because the mechanical behavior of liquefied soil is complex and imprecisely understood, a relatively simple procedure has been adopted to account for soil strength and stiffness. The choice of a simple interaction mechanism permits the evaluation of important trends and influential parameters, without introducing undue complexity in the formulation of the problem. As will be shown in a forthcoming section of this paper, the simple model adopted herein leads to analytical results which compare very favorably with observed earthquake performance.

The soil yielding force, p_u, is determined from lateral bearing capacity factors proposed by Hansen [1961]. The soil spring stiffness is determined from the coefficient of horizontal subgrade reaction, k_h, proposed by Terzaghi [1955], which is given by the expression:

$$k_h = n_h \frac{z}{D} \tag{1}$$

in which n_h is the constant of horizontal subgrade reaction, z is the depth, and D is the pile diameter. The yielding spring displacement was determined by dividing the yielding force by the spring stiffness. Stiffness and yielding force reduction due to liquefaction are accomplished by dividing k_h and p_u, respectively, by a reduction factor, R_f, larger than 1. The spacing of the spring-slider elements was chosen to conform with the maximum spacing required for beam on elastic foundation analysis [i.e., Boresi, et al., 1978].

Nonlinear flexural behavior of the pile material is accounted for by means of rotational springs, which utilize nonlinear moment-rotation laws. The rotational springs, which connect individual beam elements, are used to represent cracking and ultimate flexural states of reinforced concrete piles. Figure 1c illustrates a typical beam element-rotational spring connection. A zero-length rotational spring is placed between adjacent beam elements. A condition is enforced in which both axial and transverse displacements of nodes i and j are the same.

Since the material nonlinearity of the model is concentrated at the rotational springs, the lateral deflection of the pile is the combined result of elastic bending of the beam elements and nonlinear rotation of the connecting rotational springs. On the basis of modeling techniques proposed by Miura and O'Rourke [1991], the relation between moment and curvature of the pile is converted into a relation between moment and rotation of the rotational spring elements.

ANALYTICAL MODELING OF REINFORCED CONCRETE

Figure 2 illustrates the cross-section, as well as the strain and stress distribution, in the concrete of a circular reinforced pile. The axial load acting on the cross-section is assumed to be constant and equal to P_a. The combined action of applied axial load and bending moment causes the pile to bend and crack. The resulting strain distribution in both concrete and steel is presented in the figure. The depth of the neutral axis, c, indicates the extent of the compressed portion of the pile.

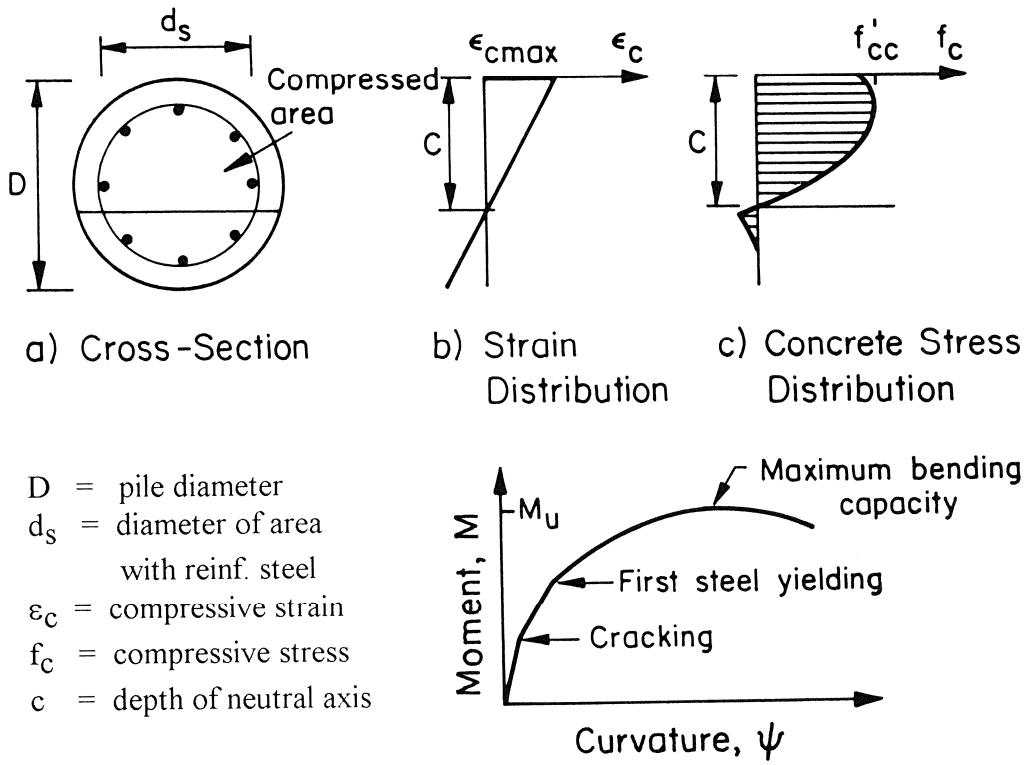

FIGURE 2. Cross-Section, Strain, and Stress Distribution for Theoretical Calculation of Moment-Curvature Relationships for Reinforced Concrete Sections

Concrete stresses are determined from the linear distribution of strain within the compressed area of the pile.

To calculate the theoretical moment-curvature relationship for a given axial load, a value of maximum compressive strain in the extreme fiber, ε_{cmax}, is specified. Then an iterative procedure is performed to determine the neutral axis depth at which the resulting internal forces balance the externally applied axial load and moment. In this process, for an assumed value of c, the strain distribution in the section can be determined. The resulting concrete force and its position, as well as the steel reinforcement loads, are calculated.

If the total resisting force does not balance the external axial load, the depth of the neutral axis is changed and the process is repeated. When the error between internal and external forces is less than a specified tolerance, typically 0.01%, the resulting moment of the internal forces with respect to the center of the section is that being resisted by the pile. The curvature associated with that moment is calculated as the ratio between the maximum concrete strain and the distance to the neutral axis, c.

The maximum bending capacity of concrete piles usually is achieved at maximum concrete compressive strains of 0.003 to 0.0035 [e.g., Kent and Park, 1971]. In this work, moment-curvature determinations were carried to a maximum concrete strain of 0.0035.

Bending test data were obtained from quality control tests performed on production piles fabricated by Daido Concrete Co., Ltd., of Japan. The Daido Concrete Co. produces both reinforced and prestressed concrete piles by centrifuge, or spun, processing. Data for 400-mm-diameter, 8-m-long piles were provided. The piles either were reinforced concrete piles (RC) with a wall thickness of 70 mm, or prestressed concrete piles (PHC) with a wall thickness of 65 mm. Material properties and pile geometries, as well as details of the analytical modeling, are described by Meyersohn [1994]. All piles were tested in pure bending without axial load. Figure 3 illustrates the general test set-up. Piles were placed on supports 4.8 m apart. A transverse load was applied such that an approximately constant moment region occurred in the middle of the pile.

Moment-curvature relationships for each pile were calculated using the stress-strain curve for confined concrete in compression proposed by Mander, et al. [1988]. Tensile stiffening of reinforced concrete piles was modeled as the linear falling branch of Mier [1987], while that of prestressed concrete piles was determined according to the model of Marzouk and Chen [1993].

If the analytical moment-curvature relationship is correct, the estimation of displacements from this relationship should give the correct pile deflections. From the bending moment distribution, which includes the actions of both self-weight and external load, the curvature distribution along the test specimen was determined from the moment-curvature relationship. Then, the integration of curvature was used to calculate deflections along the pile.

Figure 4 shows comparisons between the analytical and measured load-displacement plots. The agreement in both cases is excellent. Initial cracking of the reinforced concrete specimen is evinced by a sharp change in slope at low levels of externally applied load. Cracking also is successfully predicted by the analytical model. Curves for the prestressed concrete specimen change in slope at a load of about 95 kN. This load corresponds, approximately, to the development of full cracking, which occurs once all contribution from tension stiffening has disappeared. After cracking develops, the experimental load-displacement curve shows a quasi-linear trend in parallel with the analytical results.

COMPARISON OF FIELD OBSERVATIONS AND ANALYTICAL RESULTS

Detailed measurements of reinforced concrete pile deformation caused by lateral spread at the NHK and Niigata Family Courthouse (NFCH) Buildings in Niigata have been reported by Hamada [1992]. Analytical studies of the NHK Building foundations have been published and discussed elsewhere [e.g., Miura and O'Rourke, 1991; Meyersohn, et al., 1992]. In this work, attention will be focused on the NFCH Building.

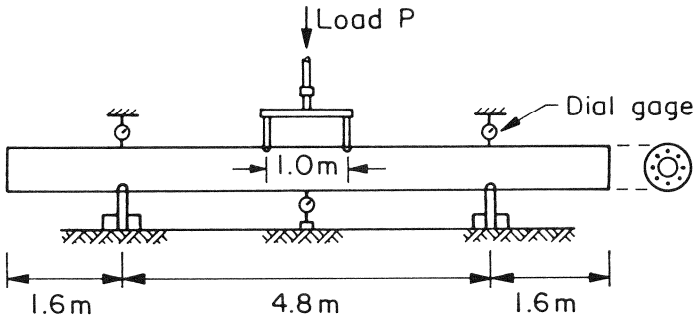

FIGURE 3. Set-Up Test for Daido Concrete Pile Specimens

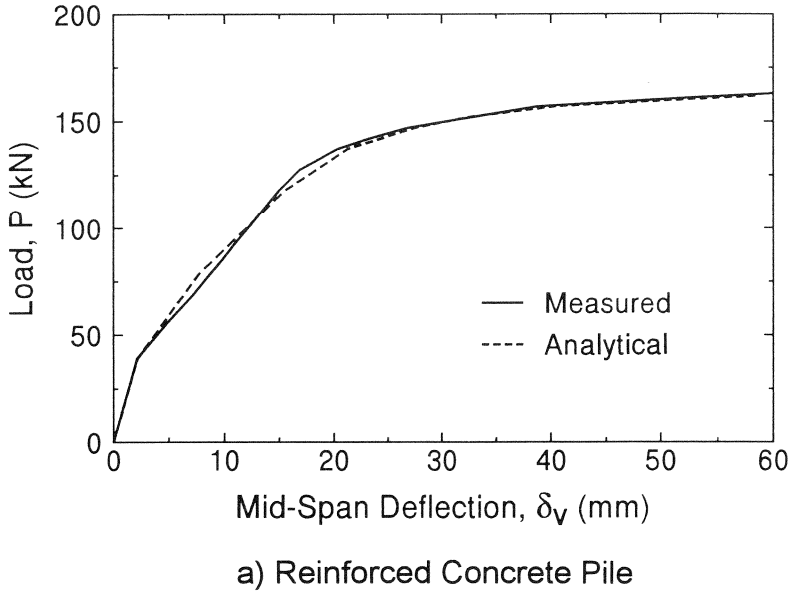

a) Reinforced Concrete Pile

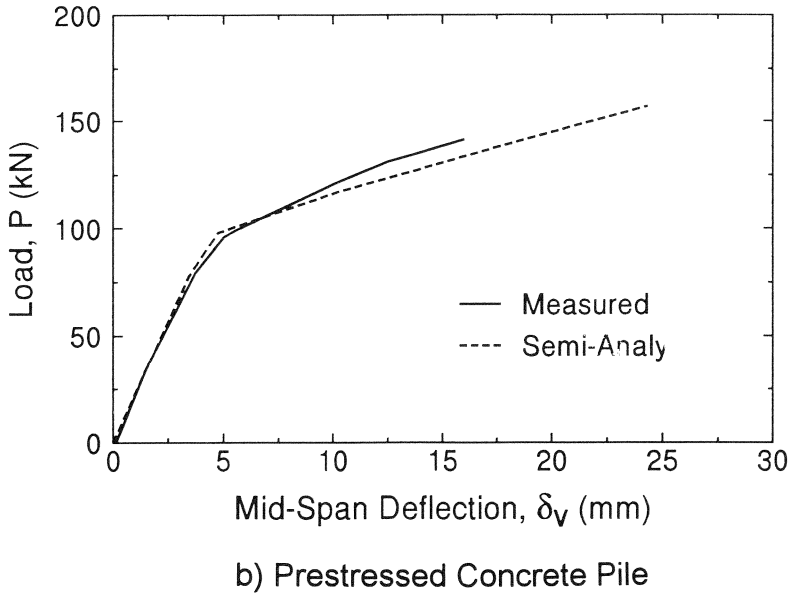

b) Prestressed Concrete Pile

FIGURE 4. Comparison of Analytical and Measured Load Displacement Plots

The NFCH Building was a three-story reinforced concrete structure founded on reinforced concrete piles. As a result of lateral spread during the 1964 Niigata earthquake, the building displaced horizontally approximately 0.5 to 1.5 m, according to photogrametic studies performed by Yoshida and Hamada [1991].

As explained by Meyersohn, et al. [1992], two 350-mm-diameter piles, referred to as Piles 1 and 2, were carefully excavated and examined. Each supported a small footing. Figure 5 shows a scale diagram of the damage state of each pile, along with the measured SPT values. The piles were separated from each other in the field by about 24 m. The uncorrected SPT values are mostly less than 10 for depths up to 8 m, but sharply increase at greater depths. The water table is located at a depth of 1.70 m, however, that value was measured 25 years after the earthquake [Hamada, 1992].

Pile 1 did not reach the lower interface, whereas Pile 2 penetrated into the lower nonliquefied soil. Both piles were damaged at about 2 m from the ground surface, which roughly coincides with the upper interface between liquefied and nonliquefied soil. At this location, Pile 1 showed bending cracks, while Pile 2 showed a severe shear dislocation of about 180 mm. In addition, severe bending cracks at depths between 6.5 and 8.5 m were observed in Pile 2.

Deflection values were obtained for Piles 1 and 2 along their lengths. Pile 1 was "dragged" into its deflected shape by liquefied soil. Its deformation was related to the forces conveyed by liquefied soil and the relative soil/pile stiffness, both of which depend on R_f. By iterative analyses, therefore, a value of R_f was identified which results in the most favorable comparison between predicted and observed deformations. If this value of R_f also results in a suitable match between the prediction and measurement of Pile 2 deformation, then the value of R_f so chosen should provide a reliable measure of the average stiffness reduction experienced by the liquefied soil.

The soil profile and displacement pattern for Pile 1 are presented in Figure 6a. The maximum soil displacement at the ground surface, d_h, was taken as 0.66 m, which is equal to the measured offset in the pile. An explanation of the modeling assumptions and procedures is given by Meyersohn [1994].

Figure 6b plots the ratio between calculated and measured pile offset as a function of R_f for a maximum surface soil displacement of 0.66 m. Measured and calculated offsets agree for R_f = 60, which may be regarded as representative of the state of the liquefiable soil at the site.

Results of the analyses for Pile 1 with R_f = 60 are presented in Figure 7, which shows pile deflections and bending moments at different stages of soil displacement. Superimposed are the measurements of transverse deflections obtained by Yoshida and Hamada [1991] from the excavated pile. Pile 1 develops a plastic hinge at the upper interface between the liquefiable and overlying soil when displacement reaches a magnitude of about 0.54 m. With additional soil displacement, the angle formed at the plastic hinge increases. When the surface soil displacement reaches the maximum specified value of 0.66 m, the observed deflected shape of the pile agrees closely with the analytical deformation pattern. The bending moment diagrams indicate that very little redistribution of moment occurs after hinge formation.

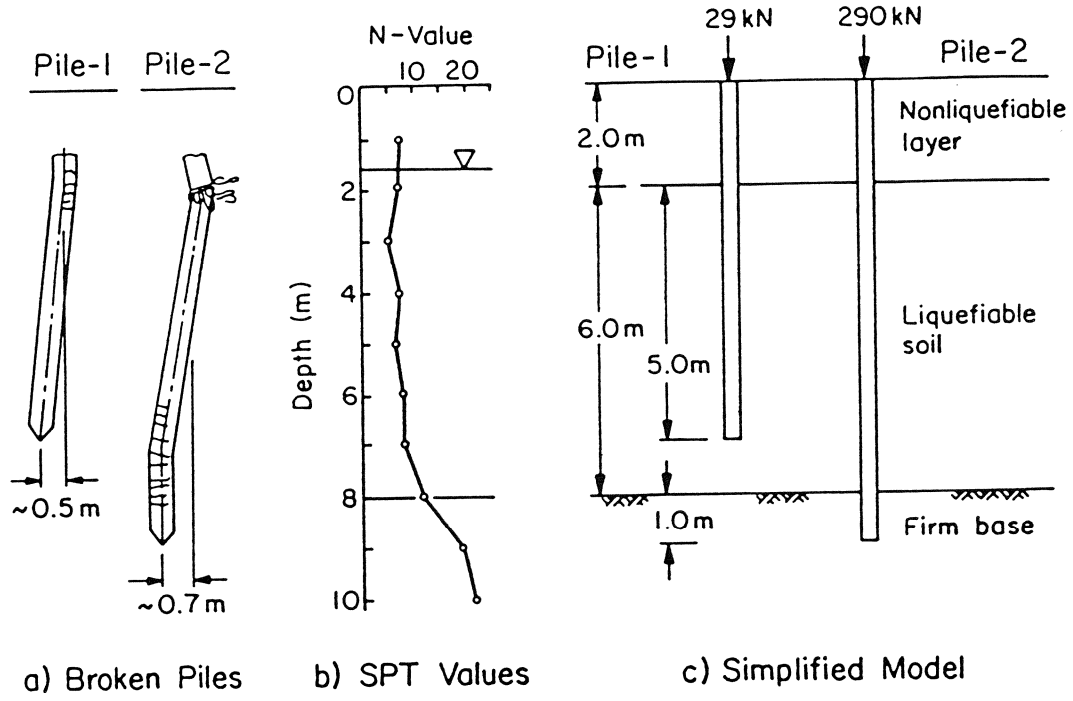

FIGURE 5. Observed Pile Deformation and Soil Conditions at NFCH Building

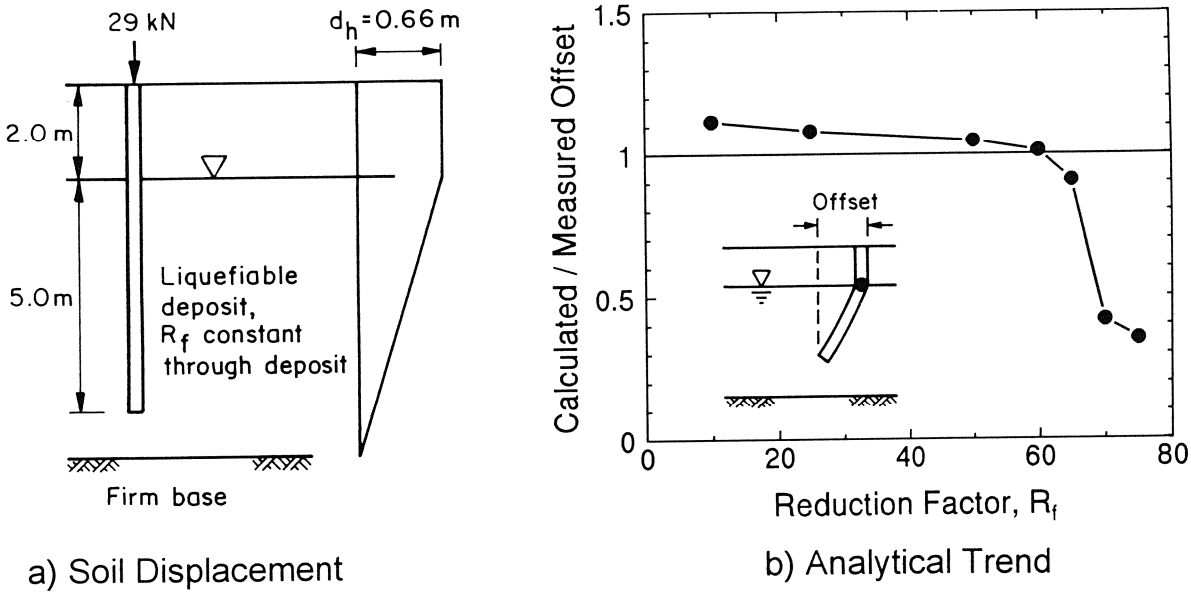

FIGURE 6. Soil Displacement Pattern and Ratio of Calculated to Measured Offset as a Function of R_f

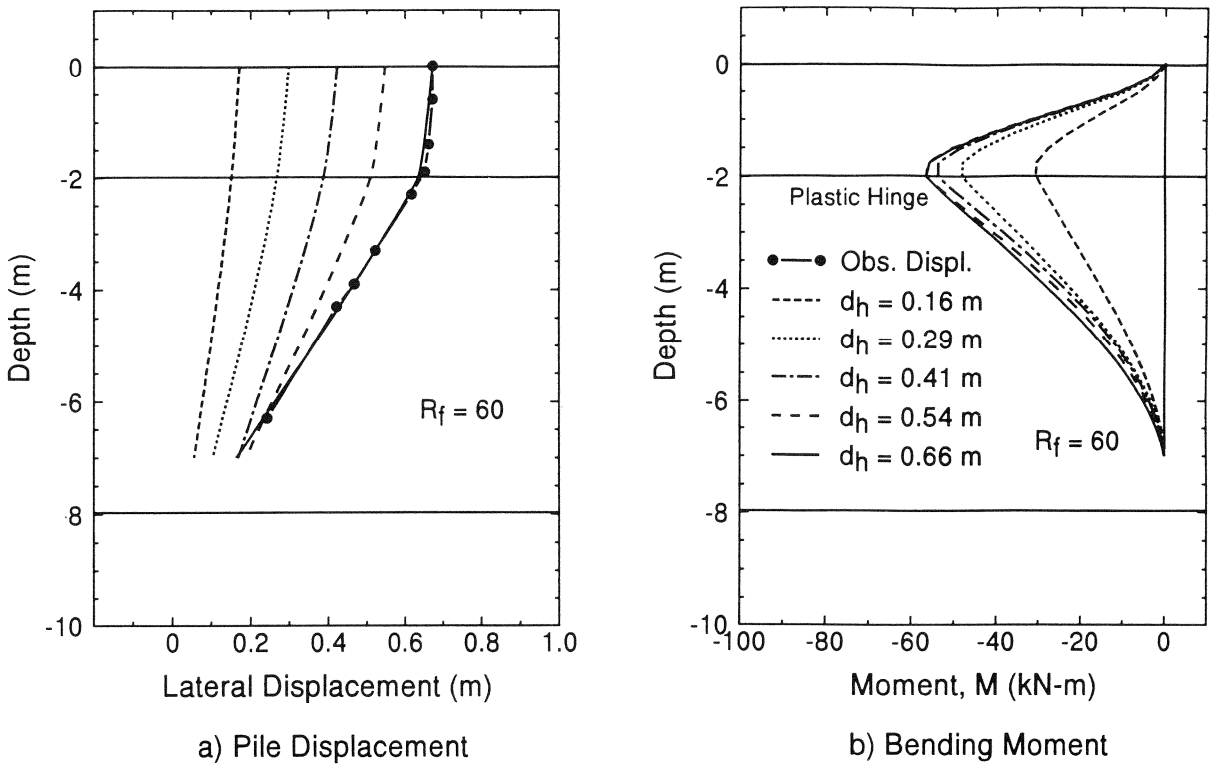

FIGURE 7. Analytical Results for Pile 1 at the NFCH Building

An examination of the measured shape and photographs provided by Yoshida and Hamada [1991] indicates that the failure at the lower end of Pile 2 was distributed over its bottom 2 m. The absence of a sharp kink at this location suggests that the soil offered higher lateral resistance than the liquefied soil above, limiting in this way pile deflections.

In the analysis of Pile 2, liquefaction was assumed between the depths of 2.0 and 7.0 m, thereby resulting in the soil displacement profile shown in Figure 8. A R_f of 60 was assigned to the soil profile between 2.0 and 7.0 m. Between the depths of 7.0 and 8.0 m, the value of R_f was taken as 1.

Numerical results are presented in Figure 9, which shows pile lateral deflections and bending moments at various stages of soil displacement. Numerical results indicate that plastic hinge formation occurs first at the lower interface, when the surface soil displacement is about 0.24 m. A second hinge develops at the upper interface at a soil displacement of about 0.32 m.

The agreement between measured and analytical deformations is good. If it is assumed that upper plastic hinge formation weakened the pile, thereby contributing to shear offset at this location, the analytical results for a 0.66 m soil displacement compare very favorably with observed deforma-

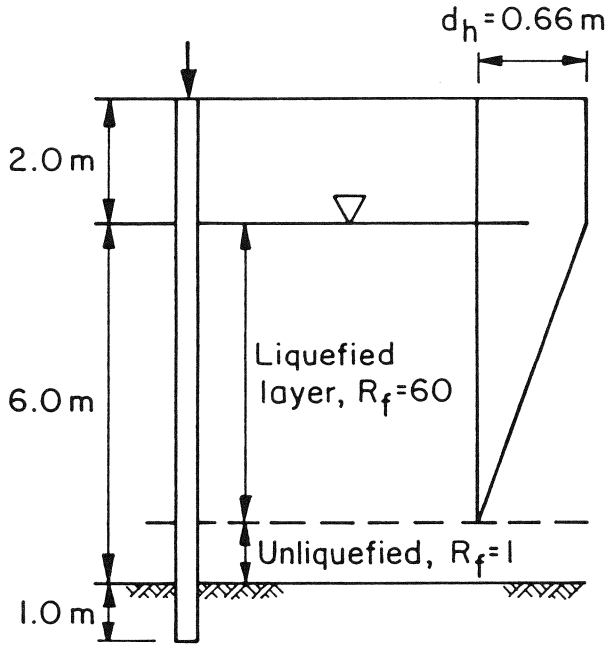

FIGURE 8. Simplified Soil Profile and Assumed Soil Displacement Pattern for Pile 2 at the NFCH Building

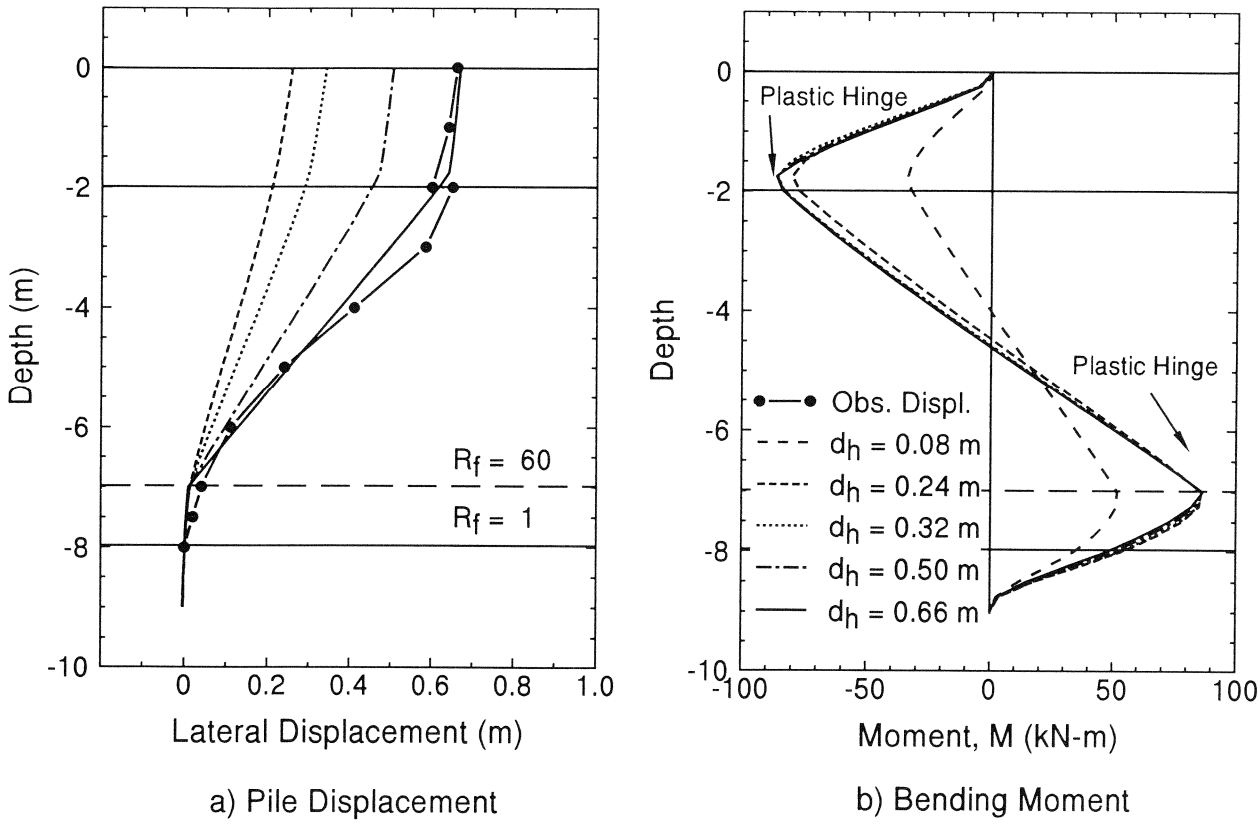

a) Pile Displacement

b) Bending Moment

FIGURE 9. Analytical Results for Pile 2 at the NFCH Building

tion. In this case, hinge formation would have been followed by shear failure, leading to the observed relative movement between the head and underlying body of the pile.

FAILURE MODES AND DEFORMATION CHARACTERISTICS

Two distinctive failure modes can be recognized in piles subjected to lateral spreads resulting from soil liquefaction. In the first one, lateral pile deflections induced by horizontal soil displacement may result in the pile reaching its bending capacity, thus developing a plastic hinge. On the other hand, the lack of sufficient lateral support due to the reduced stiffness of the liquefied soil and the lateral deflection imposed on the pile, may result in buckling.

Figure 10 illustrates the possible failure mechanisms. The depth to water table in the diagrams simply indicates the possible extent of an upper nonliquefied layer. Buckling and plastic hinge formation are shown in Figures 10 a and b, respectively. Whether the bending capacity of the pile is first reached in the vicinity of the upper or the lower interface depends on the amount of lateral restraint offered by the nonliquefied soil. In general, hinge formation will tend to occur at the lower interface, since the higher confining effective stress at a greater depth results in larger lateral resistance than at a shallower depth (Figure 10b).

A third type of failure is illustrated in Figure 10c. It involves excessive rigid body rotation of the pile, which is a characteristic of large diameter piles and piers. This type of response to lateral soil displacement arises primarily from a lack of sufficient restraint at the bottom of the pile, either due to an inadequate imbedment length or to low resistance of the foundation material against lateral movement. With increasing soil movement, this form of pile response may be followed by the formation of a plastic hinge at the lower interface, or by a premature collapse of the foundation due to a combination of excessive rotation and lack of lateral support.

Another behavioral mode is soil flow, which is characterized by flow of liquefied soil around the pile. It usually is associated with stiff foundations, such as large diameter piles, piers, and groups of closely spaced piles. Under these conditions, a relatively stiff pile will flex until the soil has mobilized its full resistance against the pile. Additional soil movement occurs as a flow relative to the pile. This form of response may not lead necessarily to pile failure, since soil will displace without causing additional pile deflection.

B-STRUCT accounts for the effects of geometric nonlinearities, that is to say, it performs a second-order analysis. The coupled action of axial load effects and geometric nonlinearities enables the program, in certain cases, to achieve convergence in a post-buckling analysis.

PARAMETRIC STUDY OF ACCEPTABLE AXIAL LOAD

Parametric studies were performed [Meyersohn, 1994] to develop two sets of dimensionless

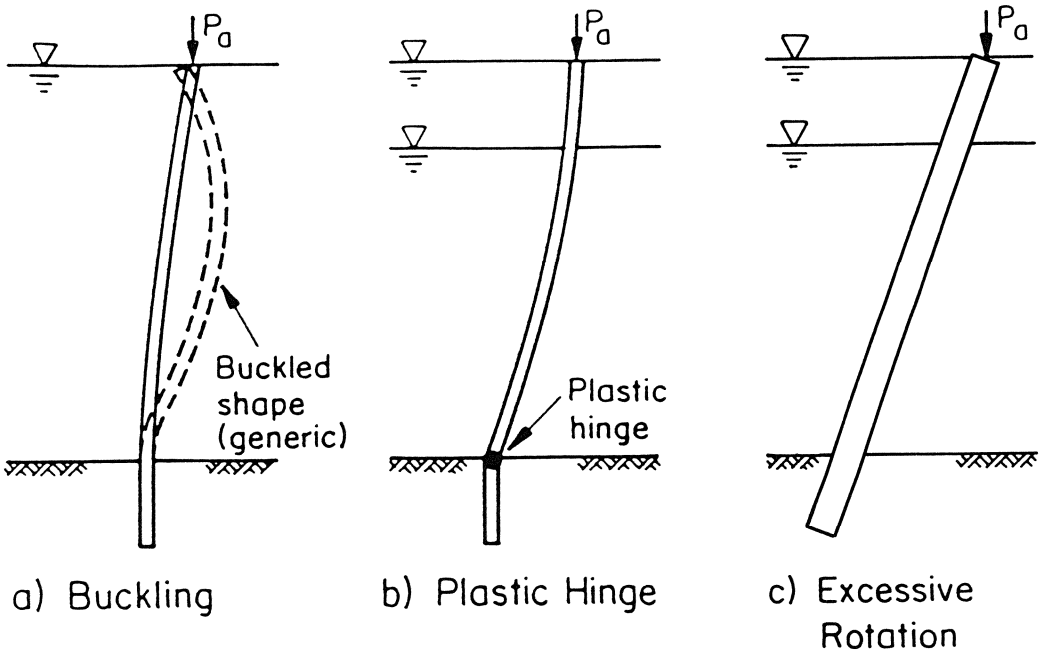

FIGURE 10. Pile Failure Modes

curves, which provide for 1) the determination of acceptable levels of axial load that do not result in pile buckling, and 2) the maximum lateral soil movement at which excessive pile flexure occurs, given that axial load is below the buckling limit. As an illustration of typical results obtained in the parametric study, Figure 11 summarizes the analytical trends for the 350-mm-diameter pile. The inset in the figure shows the conditions associated with the analyses: the water table is at the ground surface with a total thickness of liquefied soil of 8.5 m. The figure plots surface ground displacements as a function of applied axial force for different values of R_f. The soil displacement in the vertical axis denotes the displacement at which the pile either buckles or develops a plastic hinge.

The abrupt change of slope in curves associated with R_f values of 10, 50, and 100 indicates a transition load, P_t, which is the axial load at which the pile buckles simultaneously as it develops a plastic hinge. At axial loads smaller than P_t, the pile fails by excessive bending, while at higher loads, the pile buckles. Note that, as the axial load increases above P_t, the soil displacement, d_h, decreases significantly. The transition load increases as R_f decreases because the increased soil stiffness provides additional lateral support against buckling.

As the stiffness and strength of the soil decrease as a result of liquefaction, lateral pile confinement also decreases, which tends to induce buckling at lower axial loads. As the degree of lique-

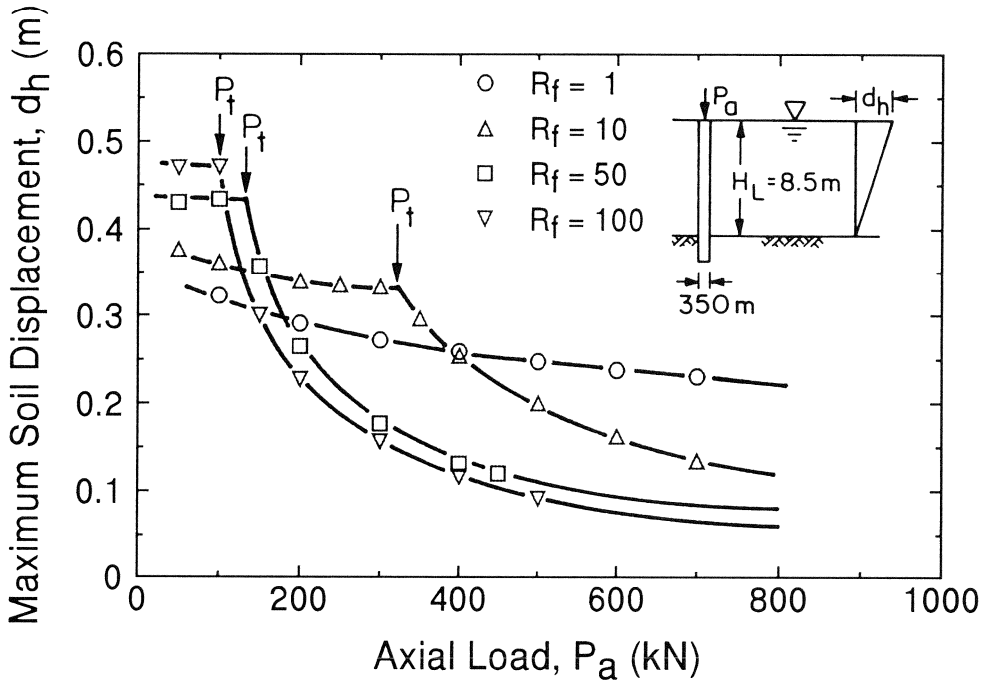

FIGURE 11. Maximum Soil Displacement versus Axial Load for a 350-mm-Diameter Pile, H_L = 8.5 m, L_b = 2.5 m, L_L = 0.0 m

faction becomes more severe, however, its stiffness eventually decreases to a state in which the buckling capacity begins to increase because the liquefied soil movement cannot impose additional pile deflections. Under these conditions, the soil flows relative to the pile, and buckling capacity increases.

These two opposing trends are illustrated schematically in Figure 12, in which the axial load is plotted as a function of the relative stiffness between soil and pile. For illustration purposes, the relative stiffness between the soil and the pile is expressed as the ratio between the modulus of lateral subgrade reaction of liquefied soil, k_{hl}, and the bending stiffness of the pile, EI. The two straight lines in the figure separate stable from unstable states. Line AB defines the boundary for soil flow between stable conditions and buckling, while line BC defines the boundary between potential bending failure and buckling.

An axial load along line AB, which divides soil flow from pile buckling states, is referred to in this work as the flow load, P_f. A load lying along line BC is called the transition load, P_t. In the absence of soil, the relative stiffness between soil and pile is zero. For these conditions, point A in Figure 12 should be equal to the Euler buckling load, provided the pile is restrained fully against rotation at the bottom of the liquefied layer.

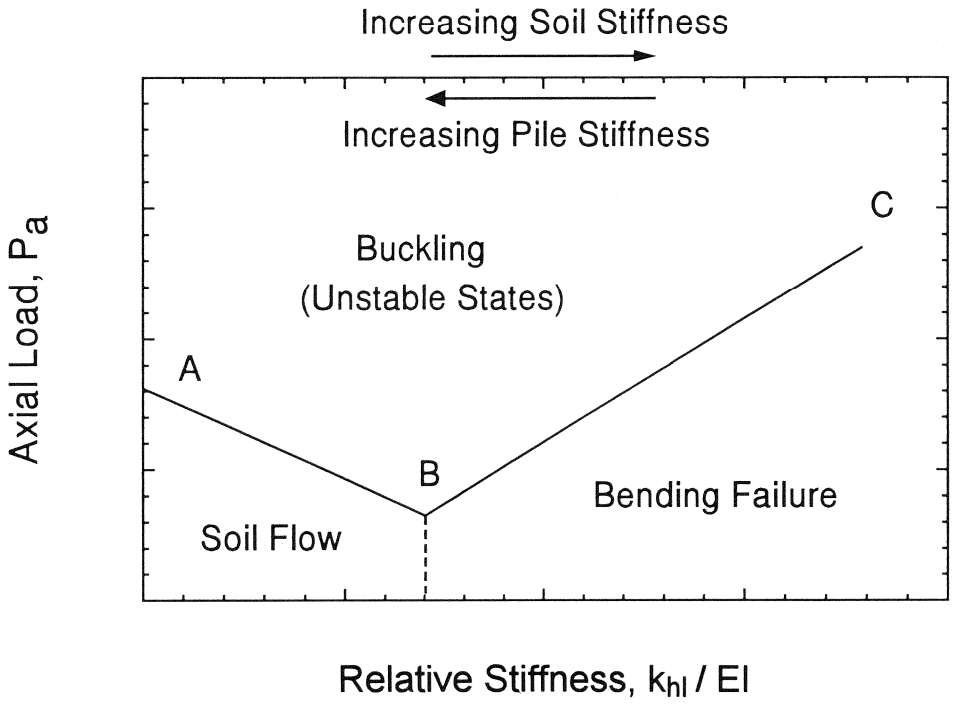

FIGURE 12. Failure States of Piles Subjected to Lateral Spread

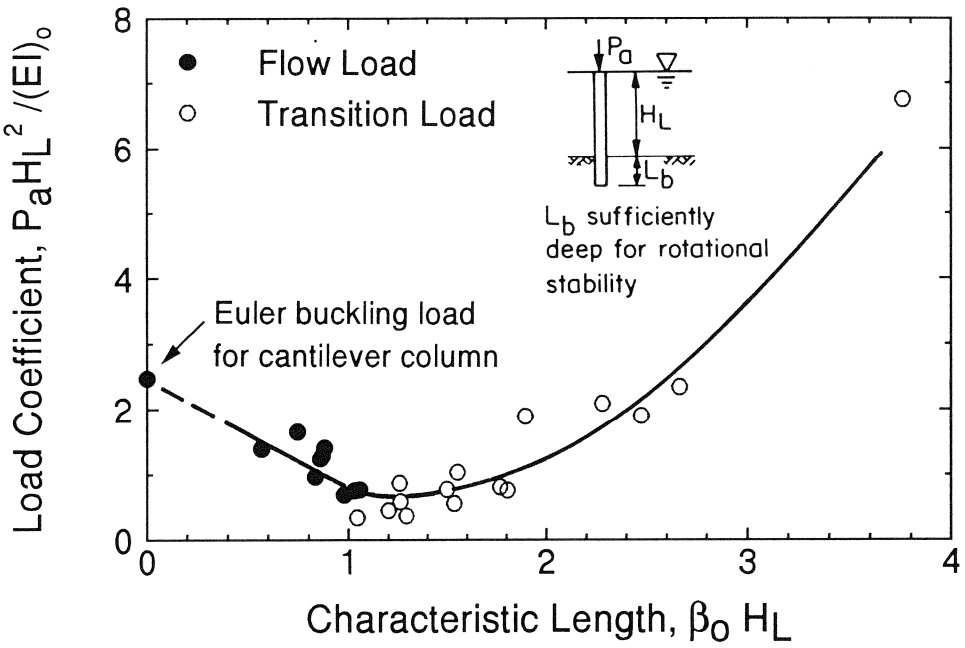

FIGURE 13. Analytical Results for Flow and Transition Loads, L_L = 0.0 m

The ability to predict the potential for buckling is of significant practical importance. If a pile develops a plastic hinge, or if the soil flows around it, the pile generally can accommodate more lateral soil displacement than if it were to buckle. To provide guidance for the problem, transition and flow loads were identified from the computer results and are plotted in Figure 13. In general, flow loads were associated almost exclusively with the condition in which the water table is at the ground surface and with reduction factors larger than about 50. Results in Figure 13 correspond to the case in which the water table is at the ground surface. The horizontal axis, $\beta_o H_L$, is a dimensionless number, referred to as the characteristic length, which depends on the flexural rigidity of the pile, as well as the stiffness of the soil. The parameter β_o is defined as:

$$\beta_o = \sqrt[4]{\frac{n_{hl} D}{(EI)_o}} \tag{2}$$

in which n_{hl} is the coefficient of horizontal subgrade reaction of the liquefied soil, D is the pile diameter, and $(EI)_o$ is the initial, uncracked stiffness of the reinforced concrete pile.

It should be recognized that, for liquefied soil, the coefficient of horizontal subgrade reaction will be obtained by dividing the value for intact soil by the reduction factor (i.e., $n_{hl} = n_h/R_f$). The value of $(EI)_o$ corresponds to the bending stiffness of the uncracked section of the pile, and can be determined by the expression:

$$(EI)_o = \frac{M_c}{\psi_c} \tag{3}$$

in which M_c and ψ_c are the cracking moment and the cracking curvature, respectively.

The axial load has been plotted as a dimensionless coefficient defined as:

$$\frac{P_a H_L^2}{(EI)_o} \tag{4}$$

In Figure 13, open symbols indicate cases in which buckling occurred simultaneously with the formation of a plastic hinge. Solid symbols denote cases of buckling caused by soil flow. Numerical results indicate that the transition load increases, while the flow load decreases, as the characteristic length of the system increases. The observed scatter arises mainly as a result of the nonlinearities of the system that are not accounted for completely by the terms used to define both axes.

Trends shown in Figure 13 agree with the conceptual framework of pile behavior presented in Figure 12. The characteristic length at which flow failure and bending failure occurs (point B in Figure 12) ranges from 1.0 to 1.1, with an average of 1.06. Since this point delineates the boundary between two different pile responses, the characteristic length associated with this limit will be referred to herein as the critical characteristic length, L_c.

Hence, a soil-pile system with a value of L_c smaller than about 1.0 is a potential candidate to develop flow failure. At higher characteristic lengths, soil flow can not occur and the pile will fail in bending. Without soil, the characteristic length takes a value of zero and the flow load would be equal to the Euler critical load for a cantilever column perfectly embedded at the bottom of the liquefied layer. The load coefficient associated with the critical Euler load of a cantilever column takes a value of $\pi^2/4$, or about 2.47.

PARAMETRIC STUDY OF MAXIMUM SOIL DISPLACEMENT

If the axial load acting on the pile is of such magnitude that buckling will not occur, and if the characteristic length of the soil-pile system is such that flow failure can not develop, the next logical step is to assess the amount of soil displacement required to cause bending failure. At the moment of bending failure, a large portion of the pile is in a post-cracked state. Hence, a more representative characteristic length of the system can be defined on the basis of reduced pile stiffness. The characteristic length of the cracked section, $\beta_\alpha H_L$, is expressed as:

$$\beta_\alpha H_L = \sqrt[4]{\frac{n_{hl} D}{(EI)_\alpha}} H_L \tag{5}$$

in which $(EI)_\alpha$ is a secant bending stiffness, the value of which is illustrated with the aid of Figure 14. The value of $(EI)_\alpha$ is taken as the slope between the point of maximum bending capacity (M_u, ψ_u) and a point that results from the intersection between the initial slope line, $(EI)_o$, and a horizontal line drawn at a value of α times M_u. Here α is a positive number less than 1.0. The value of α determines the slope of the secant stiffness. It can be shown that $(EI)_\alpha$ is given by the expression:

$$(EI)_\alpha = \frac{(1-\alpha)}{1-\dfrac{\alpha (EI)_u}{(EI)_o}} (EI)_u. \tag{6}$$

in which $(EI)_u$ is simply M_u/ψ_u, the maximum moment divided by the maximum curvature at a concrete strain of 0.0035.

Examination of numerical results indicates that a value of α equal to 0.70 represents a good measure of secant stiffness, which helps collapse numerical results into well defined trends. Hence, $\alpha = 0.70$ was used in the definition of the characteristic length of the cracked section in Equation 5.

From the numerical results of the parametric study, soil displacements at bending failure were determined and are plotted in Figure 15. The horizontal axis is the normalized length $B_{70}H_L$, while

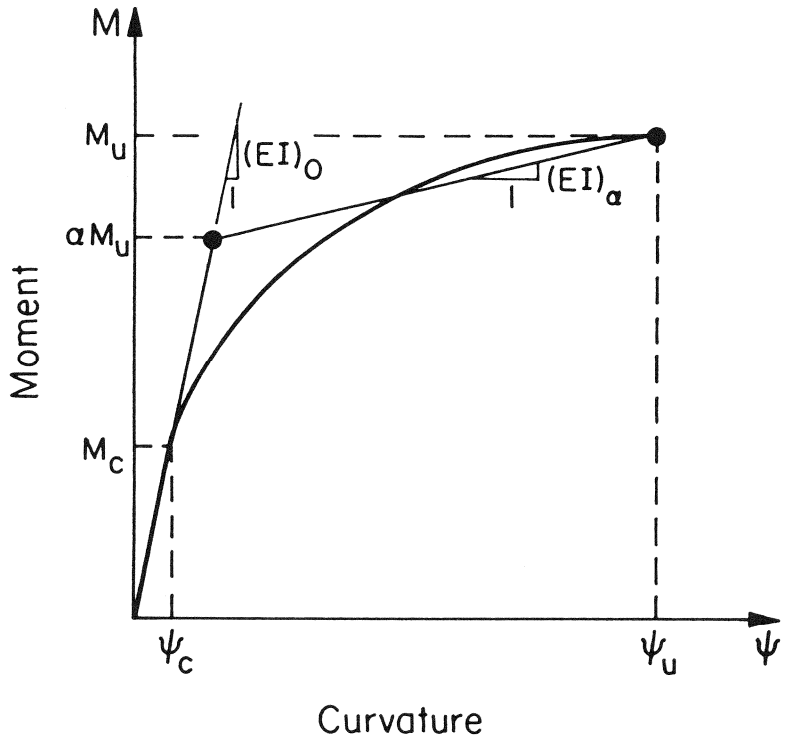

FIGURE 14. Definition of Secant Bending Stiffness, $(EI)_\alpha$

the vertical axis is given as a function of the dimensionless expression Δ_h, defined as:

$$\Delta_h = \frac{d_h D}{H_L^2} \sqrt[4]{R_f} \tag{7}$$

The normalized soil displacement, Δ_h, is a measure of the average strain developed in the pile, as explained by Meyersohn, et al. [1992].

Curves in Figure 15 were developed for axial loads less than the transition load, P_t, and generally equal to about one-fourth to one-third of the ultimate bearing capacity of the pile. They represent a reasonable practical range of working loads that contribute to moments in the pile, and hence, to flexural failure under horizontal soil displacement. As indicated in the figures, upper limits for the analytical trends are associated with 350-mm-diameter piles, while the lower limit defines Δ_h values associated with 1.0-m-diameter piles.

As discussed in the preceding section, there exists a value of $\beta_o H_L$ that establishes the boundary between bending failure and soil flow, which is called the critical characteristic length of the soil-pile system, L_c. These L_c values were calculated to be 1.06 and 0.68, for L_L of 0.0 and 1.5

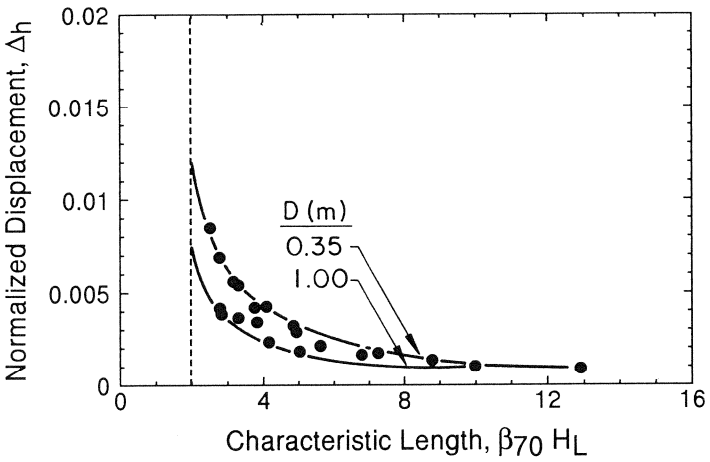

a) L_L = 0.0 m

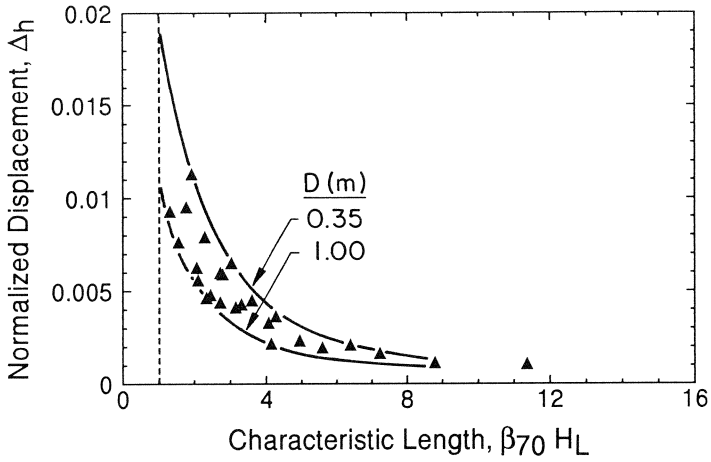

b) L_L = 1.5 m

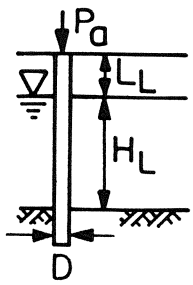

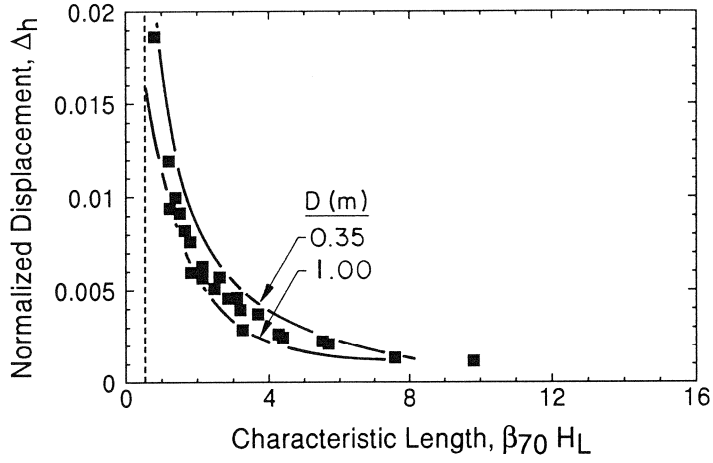

c) L_L = 3.0 m

FIGURE 15. Normalized Soil Displacement versus Characteristic Length to Evaluate Lateral Spread Movement to Cause Bending Failure

m, respectively. In terms of the new definition of the characteristic length, $\beta_{70}H_L$, there is a corresponding critical characteristic length, L_{c70}. The differences in their numerical values arise because β_o and β_{70} are defined on the basis of a different characterization of the bending stiffness of the pile. The ratio between $(EI)_o$ and $(EI)_{70}$ depends on the diameter of the pile and the axial load, and generally ranges between 5 and 100. Thus, the ratio between β_{70} and β_o normally would vary from 1.5 to 3.2, for the same H_L, with an average value of 2. An examination of $(EI)_{70}$ values associated with cases of flow failure reveals that L_{c70} is approximately equal to 2.0 and 1.0 for L_L equal to 0.0 and 1.5 m, respectively.

Vertical dashed lines define the critical characteristic length, L_{c70}, below which there is flow failure. It is apparent that all cases of bending failure plot to the right of the limiting lines. However, there is a tendency for the normalized displacement, Δ_h, to increase as $\beta_{70}H_L$ approaches the limiting line. This increase is consistent with the tendency of the soil to flow as the characteristic length of the system decreases.

Figure 15 indicates a decrease in Δ_h as the characteristic length of the cracked section increases. A very flexible pile will have a larger characteristic length than a relatively stiff pile. Since the flexible pile will try to conform to the soil displacement, large curvatures will develop near the interfaces between liquefied and intact soil. The pile will, therefore, experience bending failure at a relatively low value of soil deformation. A stiff pile will provide a greater resistance to soil displacement, allowing for larger relative movement.

PRACTICAL APPLICATION

The practical application of the work presented in this paper can be illustrated with an example. Consider a bridge abutment founded on 400-m-diameter reinforced concrete piles. The spacing between individual piles is such that group effects are minimal and can be disregarded. The site is underlain by a potentially liquefiable deposit of loose alluvial sands, with an average thickness of about 7.0 m. This deposit is susceptible to lateral spread.

The mechanical properties of the piles are:

Concrete compressive strength:	27.6 MPa
Yield stress of reinforcement:	413.4 MPa
Longitudinal Reinforcement:	10 bars No. 4
Diameter of reinforcing cage:	300 mm

The piles penetrate the 7-m-thick stratum of potentially liquefiable sand into an end-bearing stratum of dense gravel, and the water table is at the ground surface. The coefficient of lateral subgrade reaction of the submerged loose sand is about 1.4 MN/m^3. The axial load acting on each pile is estimated as 300 kN.

Cracking and ultimate moments and curvatures for an axial load of 300 kN are:

M_c = 19.2 kN-m $\quad \Psi_c = 5.145 \times 10^{-4}$

M_u = 117.6 kN-m $\quad \Psi_u = 3.270 \times 10^{-2}$

The initial bending stiffness, $(EI)_o$, is 37.2 MN-m^2, while the secant stiffness, $(EI)_{70}$ is about 1157 kN-m^2.

Assuming a reduction factor of $R_f = 50$ for the stiffness of the liquefiable layer, the characteristic length of the soil-pile system, $\beta_o H_L$, is about 0.92. According to Figure 13, these conditions would result in soil flow. The load coefficient for flow condition is about 1.0, which results in a flow load of 759 kN to induced buckling. Therefore, the factor of safety against buckling under soil flow conditions 759/300, or 2.53. These results were duplicated with the computer program B-STRUCT. The numerical results indicate that the induced pile deflection at the pile top due to soil flow is about 38 mm.

CONCLUDING REMARKS

This paper describes an analytical approach to evaluate the response of single piles and pile groups to horizontal ground displacements caused by soil liquefaction. The analytical model is implemented in a computer program called B-STRUCT. The program has been validated against benchmark problems and by comparing numerical predictions with observed pile foundation damage resulting from lateral spread during earthquakes.

Three failure mechanisms, excessive bending, buckling, and soil flow, are recognized under lateral spread conditions. Each is a function of the relative stiffness between soil and pile, and the axial load carried by the pile. At high relative stiffness, piles may fail by excessive bending. With decreasing relative stiffness, a soil flow condition may develop in which the liquefied soil flows around the pile without inducing additional pile deflections. This mode of pile response is considered safe and provides the basis for acceptable design against structural failure.

Buckling may develop as a result of lateral pile displacement and reduced soil stiffness. As the relative stiffness of soil to pile increases, the buckling load increases and the failure mode of the pile becomes one of excessive bending. Analytical results are combined to develop dimensionless plots which allow for the determination of failure mechanisms on the basis of relative stiffness and applied axial load. For the first time, these results show quantitatively how the behavior of deep foundations changes as the ground alters its force-displacement characteristics from a soil-like to a fluid-like medium. Dimensionless plots also are developed to determine surface soil displacement required to induce the formation of a plastic hinge under conditions when the axial pile load does not lead to buckling.

ACKNOWLEDGMENTS

The research represented in this paper was supported by the National Center for Earthquake Engineering at Buffalo, NY. Thanks are extended to Professor F. Miura of Yamaguchi University and Dr. T. Miyasaka of the Daido Concrete Company for providing information on reinforced concrete piles. K.J. Stewart prepared the manuscript, and A. Avcisoy drafted the figures.

REFERENCES

Boresi, A.P., Sidebottom, O.M., Seeley, F.B., and Smith, J.O., Advanced Mechanics of Materials, 3rd Ed., John Wiley & Sons, New York, NY, 1978.

Hamada, M., "Large Ground Deformations and Their Effects on Lifelines: 1964 Niigata Earthquake," Case Studies of Liquefaction and Lifeline Performance During Past Earthquakes, Vol. 1, Japanese Case Studies, Technical Report NCEER-92-0001, NCEER, Buffalo, NY, Feb. 1992.

Hamada, M., Yasuda, S., Isoyama, R., and Emoto, K., "Study on Liquefaction-Induced Permanent Ground Displacements," Association for the Development of Earthquake Prediction, Tokyo, Japan, Nov. 1986.

Hansen, J.B., "The Ultimate Resistance of Rigid Piles Against Transversal Forces," Report 12, Danish Geotechnical Institute, Copenhagen, 1961, pp. 5-9.

Kent, D.C. and Park, R., "Flexural Members with Confined Concrete," Journal of the Structural Division, ASCE, Vol. 97, No. ST7, July 1971, pp. 1969-1990.

Mander, J.B., Priestley, M.J.N., and Park, R., "Theoretical Stress-Strain Model for Confined Concrete," Journal of Structural Engineering, ASCE, Vol. 114, No. 8, Aug. 1988, pp. 1804-1826.

Marzouk, H. And Chen, Z., "Tension Stiffening Model for High Strength Slabs," Proceedings, 1993 CSCE/CPCA Structural Concrete Conference, Toronto, Canada, May 1993, pp. 127-140.

Meyersohn, W.D., "Pile Response to Liquefaction-Induced Lateral Spread," Ph.D. Thesis, Cornell University, Ithaca, NY, Jan. 1994.

Meyersohn, W.D., O'Rourke, T.D., and Miura, F., "Lateral Spread Effects on Reinforced Concrete Pile Foundations," PWRI Technical Memorandum No. 3198, U.S.-Japan Workshop on Earthquake Disaster Prevention for Lifeline Systems, Public Works Research Institute, Tsukuba Sience City, Japan, Oct. 1992, pp. 173-193.

Mier, J.G.M. van, "Examples of Non-Linear Analysis of Reinforced Concrete Structures with DIANA," HERON, Delft University of Technology, Delft, Netherlands, Vol. 22, No. 3, 1987.

Miura, F. and O'Rourke, T.D., "Nonlinear Analysis of Piles Subjected to Liquefaction-Induced Large Ground Deformation," 3rd U.S.-Japan Workshop on Earthquake-Resistant Design of Lifeline Facilities and Countermeasures for Soil Liquefaction, Technical Report NCEER-91-0001, NCEER, Buffalo, NY, Feb. 1991, pp. 497-512.

Terzaghi, K., "Evaluation of Coefficients of Subgrade Reaction," Geotechnique, Vol. 4, No. 4, Dec. 1955, pp. 297-326.

Yoshida, N. And Hamada, M., "Damage to Foundation Piles and Deformation Pattern of Ground Due to Liquefaction-Induced Permanent Ground Deformations," 3rd U.S.-Japan Workshop on Earthquake-Resistant Design of Lifeline Facilities and Countermeasures for Soil Liquefaction, Technical Report NCEER-91-0001, NCEER, Buffalo, NY, Feb. 1991, pp. 147-161.

High Ductility Aseismic Joint Spliced Pile Behavior When Subjected to Liquefaction-induced Large Ground Displacements

F. Miura[1], T. Miyasaka[2], and T. Hirata[3]

ABSTRACT

Instead of traditional welding splicer, a High Ductility Aseismic Joint (HDAJ) was newly developed for pile splicing. In order to examine the energy dissipating effect of HDAJ and pile responses to large ground displacements, the following procedures were performed. First, we conducted a series of bending experiments to elucidate the characteristics of the splicing. Then, we simulated the results of the experiments by using a nonlinear FEM which took into account both geometric and material nonlinearities to check the validity of the method. Finally, we performed numerical analyses to investigate the effectiveness of HDAJ spliced piles when subjected to liquefaction-induced large ground displacements. The numerical analyses revealed that the new pile structure would sustain ground displacements almost twice the magnitude of that sustained by ordinary piles for a given axial load.

---

1 - Professor, Yamaguchi University, Ube, Yamaguchi Pref., Japan

2 - Chief Engineer, Daido Concrete Co. LTD, Tokyo, Japan

3 - Graduate Student of Masters Course, Yamaguchi University, Ube, Yamaguchi Pref., Japan

INTRODUCTION

Earthquake damage to underground structures is classified into two categories; first, that caused by inertia and, second, that caused by permanent ground displacements. A typical example of the latter is liquefaction-induced large ground displacements. The effect of these displacements on underground structures such as buried pipes and pile foundations has been studied in the past decade. Stewart et al. (1988) and Miura et al. (1989, 1990) proposed a nonlinear finite element method to analyze the performance of piles when subjected to liquefaction-induced permanent ground displacements. The geometric and material nonlinearities of the pile and the material nonlinearity of the soil were taken into consideration in the method.

The authors also examined the performance of Prestressed High-strength Concrete (PHC) piles when subjected to large ground displacements and found that the piles would develop a plastic hinge at the interface between the liquefied layer and nonliquefied layer when the lateral displacement of the ground reached 10 to 20 cm (Miyasaka et al.1994). Meanwhile, according to field observations from the 1964 Niigata earthquake, the magnitude of lateral ground displacements was 1 m or so in highly urbanized areas, and several meters along rivers. This means that almost all piles would be broken if such lateral ground displacements took place. If a pile has higher ductility and can sustain larger lateral ground displacements, for instance 1 m or so, the safety of structures supported by pile foundations will be dramatically increased.

With this in mind, we developed a new pile structure. That is, a pile with a High Ductility Aseismic Joint (HDAJ) as pile splicing instead of the traditional welding splicer. In this paper, we first explain the mechanism and basic principle of the HDAJ. Second, the results of a series of bending experiments conducted to obtain the essential properties of piles with HDAJ are discussed. Third, the procedure for modeling the pile and ground nonlinear system and the numerical analysis method based on the FEM are explained. After checking the validity of the numerical analysis method by simulating the experiment results, we investigate the pile responses to liquefaction-induced permanent ground displacements, and discuss the effectiveness of HDAJ spliced piles.

HIGH DUCTILITY ASEISMIC JOINT

(1) Basic structure

The basic structure of the HDAJ is shown in Figure 1. In this joint structure, three main components are provided: pile tip fittings with circumferential grooves which are connected to the end of upper and lower piles, a circumferentially multi-divided cylindrical inner ring, and a

cylindrical outer ring. The joint is assembled by first setting the upper pile vertically onto the lower pile, then engaging the inner rings on the grooves of the tip fittings, and finally pushing the outer ring longitudinally upward. Both the outside surfaces of the inner ring and the inside surface of the outer ring have conical tapers. Since the taper directions are opposite, pushing the outer ring upward results in a firm coupling of the piles.

(2) Bending characteristics

We performed a series of bending experiments on piles with and without HDAJ. A schematical diagram of the specimen and the observation points is shown in Figure 2. The length of the span is 7.2 m. The angle of rotation, θ (4 points), strain, ε (4 points), and deflection, δ (5 points), were observed as shown in the figure. Table 1 summarizes the conditions of the four test cases used in the experiment. All the tested piles were PHC piles with outer diameters of 400 mm.

The test results are shown in Figures 3(a) and (b). Figure 3(a) compares the results from Cases 1 and 2, i.e., the cases with zero axial load and Figure 3(b) the results from Cases 3 and 4, i.e., the cases with an axial load of 60 tf. This magnitude of 60 tf corresponds to two thirds of the allowable design bearing capacity. Arrows in these figures designate the ultimate bending moment for each case. These values and corresponding rotational angles are listed in Table 2. The values given in Table 2 are for a pile length of 0.5 m, corresponding to the length of the beam element used to model piles in the following numerical analyses. From these figures and Table 2, we can see that piles with HDAJ have ultimate rotational angles three to four times larger than those without HDAJ. In other words, HDAJ provides piles with higher ductility.

NUMERICAL SIMULATION OF BENDING EXPERIMENTS

(1) Analysis method

a) Model for analyses

Figure 4 illustrates the model for the numerical analyses. A pile is modeled by arranging beam elements and Rotational Spring-Slider Elements (RSSE) one after the other in order to express the geometric and material nonlinearity of the pile. The stiffness matrix of the beam element is given as;

$$\begin{bmatrix} \frac{EA}{l} & 0 & 0 & -\frac{EA}{l} & 0 & 0 \\ & \frac{12EI}{l^3}+\frac{6P}{5l} & \frac{6EI}{l^2}+\frac{P}{10} & 0 & -\left(\frac{12EI}{l^3}+\frac{6P}{5l}\right) & \frac{6EI}{l^2}+\frac{P}{10} \\ & & \frac{4EI}{l}+\frac{2PL}{15} & 0 & -\left(\frac{6EI}{l^2}+\frac{P}{10}\right) & \frac{2EI}{l}-\frac{Pl}{30} \\ & & & \frac{EA}{l} & 0 & 0 \\ & \text{symm.} & & & \frac{12EI}{l^3}+\frac{6P}{5l} & -\left(\frac{6EI}{l^2}+\frac{P}{10}\right) \\ & & & & & \frac{4EI}{l}+\frac{2PL}{15} \end{bmatrix} \quad (1)$$

in which l is the length of the element, E is Young's modulus, A is the area of the section, I is the moment of inertia, and P is the axial load. This stiffness matrix is a function of P, and this makes it possible to express the so called P-Δ effect. When P is equal to zero, this stiffness matrix is equal to the ordinary linear stiffness matrix of small deflection problems.

The coordinates of the nodal points of the beam elements and therefore the stiffness matrices of the elements are updated at each iteration for each load step. By virtue of the update and iteration, geometric nonlinearity of the pile is realized. The material nonlinearity of the pile is expressed by the RSSE. The usage of the element, with the exception of the relationships between the bending moment and rotational angle, is explained in detail by Stewart et al. (1988) and Miura et al. (1989, 1990). In this study, the relationships between the bending moment and rotational angle obtained from the experiments, shown in Figure 3, are used although bi-linear or tri-linear approximations for the relationships were used in the references. The values used in the analyses for Young's modulus are summarized in Table 3. These values are obtained from the experimental bending moment-rotational angle curves below the cracking moment level. It should be noted that the values from Cases 3 and 4, in which axial load exists, are larger than those from Cases 1 and 2 in which no axial load exists.

(2) Results

Figures 5(a) and (b) compare the load-deflection curves obtained from the experiments and the numerical simulations. Figure (a) compares the results from Cases 1 and 2, and (b) from Cases 3 and 4. Solid lines show the results from the experiments and broken lines from the numerical simulations. These figures show good agreement between the experimental results and the simulation results at all times. This verifies the validity of the simulation method which we employed.

PILE PERFORMANCE WHEN SUBJECTED TO LIQUEFACTION-INDUCED LATERAL GROUND DISPLACEMENTS

(1) Analysis method

a) Modeling of pile

In this study, four cases are analyzed as listed in Table 4. In all four cases, an axial load of 60 tf is assumed. Two kinds of piles are analyzed; piles without HDAJ and piles with HDAJ. For each kind, two pile cap connectivity conditions are assumed. One is a "free-end condition" , a model of which is shown in Figure 6(a). Nodal point "a" has three degrees-of-freedom, i.e., horizontal, vertical and rotational. The other is a "fixed-end condition", a model of which is shown in Figure 6(b). Nodal point "a" has two degrees-of-freedom, i.e., horizontal and

vertical. Rotational movement is fixed. An RSSE is inserted between nodal points "a" and "b". Nodal points "a" and "b" move in the same way until the bending moment of this RSSE reaches the cracking moment of the pile. In this study, the nonlinear characteristics of the RSSE at the pile cap are set to be equal to those of piles. Therefore, a plastic hinge develops here when the bending moment at the pile cap reaches the ultimate bending moment of the pile. The actual situation of pile cap connectivity lies in between the free-end condition and fixed-end condition.

b) Modeling of ground

We assumed a three-layer system for the ground model, the surface nonliquefiable layer, the middle liquefiable layer and the basal nonliquefiable layer as shown in Figure 7. The surface layer slides as a coherent mass atop the underlying liquefiable layer. In the liquefiable layer, the lateral movements are distributed linearly from the base to the top of the deposit. Shear distortion in the liquefiable soil combined with horizontal translation of the upper nonliquefiable layer results in the trapezoidal distribution of horizontal movements shown in Figure 7, which was used to model displacements in this study. We assumed a bi-linear relationship for the force-displacement relationship of pile-soil interaction as in our previous works.

(2) Analysis results

a) Free-end connectivity

Figures 8(a) and (b) show the change in distribution of pile displacements when the amplitude of ground displacement was incrementally increased from zero to 100 cm. Figure (a) shows the results from Case Pfr and (b) from Case Jfr. Both figures seem to show very similar tendencies. When the magnitude of ground displacement was very small a plastic hinge developed at the lower boundary between the basal nonliquefiable layer and liquefiable layer, but not at the upper boundary between the surface nonliquefiable layer and liquefiable layer. Judging from these figures, the effect of HDAJ seems to be negligible. However, there is a significant difference between these two cases.

In order to make clear the difference, Figures 9(a) and (b) depict the relationship between the bending moments and ground displacements. Arrows in these figures designate the ground displacements at which the bending moment induced in the pile at the lower boundary reached their ultimate values. In Case Jfr the value is almost twice as large as that in Case Pfr. On the other hand, the difference in the responses at the upper boundary is negligible.

b) Fixed-end connectivity

Figures 10(a) and (b) show the change in pile deformation as ground displacement increases as shown in Figure 8. Figure (a) is from Case Pfx and (b) from Case Jfx. The piles are almost

vertical in the surface nonliquefiable layer and large curvature exists just above the upper boundary in Case Pfx and at the boundary in Case Jfx. There is a small difference in the actual location of maximum curvature in Cases Pfx and Jfx, however, the general tendencies are very similar and a plastic hinge developed at the upper boundary in each case. Comparing Figures 10(a) and (b) with Figures 8(a) and (b) respectively, we can identify the differences between them, particularly at the upper boundary where no plastic hinge developed in Cases Pfr and Jfr.

Figures 11(a) and (b) show the bending moment-ground displacement relation curves at the locations where plastic hinges developed in Cases Pfx and Jfx. Arrows in these figures again designate the magnitude of ground displacement at which a plastic hinge developed. The ground displacements in Case Jfx are much larger than those in Case Pfx, which demonstrates the effectiveness of HDAJ.

Finally, Table 5 summarizes the ground displacements at which plastic hinges developed in all cases. These results indicate that piles with HDAJ will sustain ground displacement of almost twice the magnitude of that sustained by piles without HDAJ for a given axial load.

CONCLUDING REMARKS

A new pile structure, a pile spliced with a high ductility aseismic joint instead of traditional welding splicer, was developed. The bending characteristics of the pile were obtained by a series of bending experiments. After checking the validity of the numerical analysis method which we employed, we investigated the responses of the new pile structure to liquefaction-induced large ground displacements. From the numerical analyses, we found that the piles with HDAJ could sustain ground displacements of almost twice the magnitude as that sustained by piles without HDAJ for a given axial load. The numerical results imply the effectiveness of HDAJ, however, the number of models and conditions in this study were limited, we need further analyses to obtain more general conclusions.

ACKNOWLEDGEMENT

Finally we would like to express our sincere thanks to Professor M.Hamada of Waseda University and Mr. Y.Itoh of Daido Concrete Co. LTD for valuable suggestions and information on pile damage caused by past earthquakes. Thanks are extended to Professor T.D.O'Rourke of Cornell University and Dr. W.D.Meyersohn, former graduate student of Cornell University, for providing information on the newest version of computer code "B-STRUCT".

REFERENCES

H.E. Stewart, F. Miura, and T.D. O'Rourke: Pile damage due to large ground displacement, Proc. of the first Japan-U.S. workshop on liquefaction, large ground deformation and their effects on lifeline facilities, pp.99-126, 1988.

F. Miura, H.E. Stewart, and T.D.O'Rourke: Lateral spreading effects on pile foundations, Proc. of the second U.S.-Japan workshop on liquefaction, large ground deformation and their effects on lifeline facilities, pp.295-307, 1989.

F. Miura and T.D.O'Rourke: nonlinear analyses of piles subjected to liquefaction-induced large ground deformation, Proc. of the third Japan-U.S. workshop on earthquake resistant design of lifeline facilities and countermeasures for soil liquefaction, pp.497-512, 1990.

T. Miyasaka, F. Miura, and J. Kiyono: Effects of P-Δ and connectivity on the nonlinear response of piles subjected to liquefaction-induced large ground displacements, Proc. of the second international conference on earthquake resistant construction and design, Berlin, pp.413-420, 1994.

Table 1 Test cases

	Pile length (m)	Span (m)	Axial load (tf)	HDAJ
Case 1	12.0	7.2	0.0	Without
Case 2	12.0	7.2	0.0	With
Case 3	8.0	7.2	60.0	Without
Case 4	8.0	7.2	60.0	With

Table 2 The ultimate bending moments and corresponding ultimate rotational angle

	The ultimate bending moment (tf-m)	The ultimate rotational angle (° /0.5m)
Case 1	19.8	0.733
Case 2	19.8	2.263
Case 3	27.4	0.343
Case 4	27.4	2.423

Table 3 Young's modulus used in the analyses (kg/cm^2)

Case 1	3.5×10^6
Case 2	3.5×10^6
Case 3	4.2×10^6
Case 4	4.2×10^6

Table 4 Analysis cases

	HDAJ	Pile cap connectivity
Case Pfr	Without	Free-end
Case Jfr	With	Free-end
Case Pfx	Without	Fixed-end
Case Jfx	With	Fixed-end

Table 5 Ground displacements at which plastic hinges developed

	Position of the hinge from the pile cap (m)	Ground displacement at the surface (cm)	Ratio
Case Pfr	8.5	20.4 ①	
Case Jfr	8.5	43.7 ②	②／①＝2.14
Case Pfx	8.5 2.5	17.2 ③ 31.4 ④	
Case Jfx	8.5 3.0	37.3 ⑤ 56.4 ⑥	⑤／③＝2.17 ⑥／④＝1.80

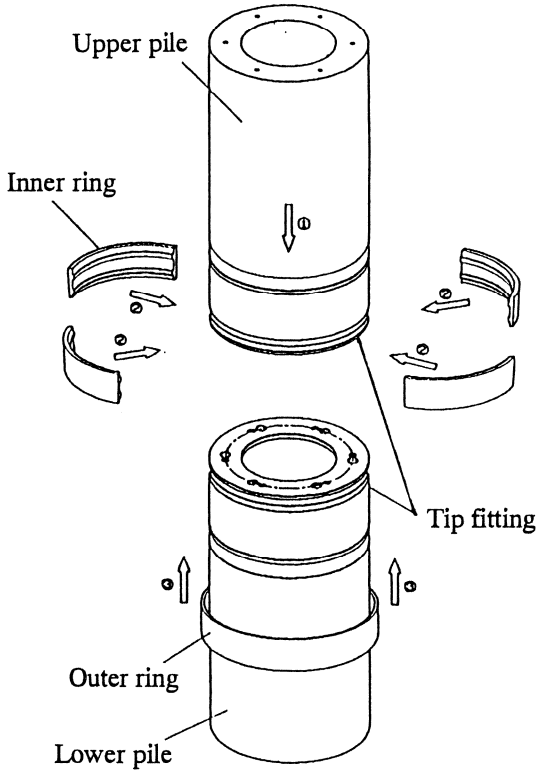

Figure 1 High ductility aseismic joint

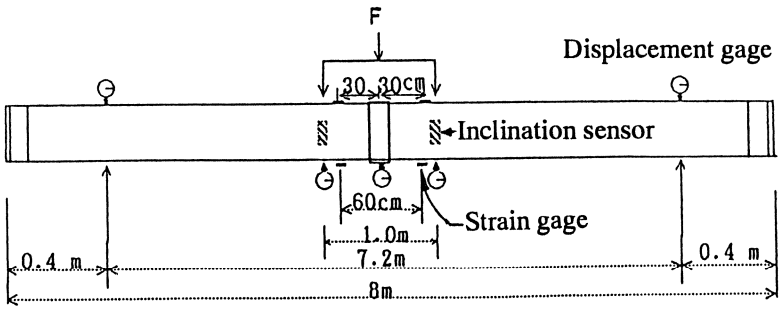

Figure 2 Schematic diagram of bending test

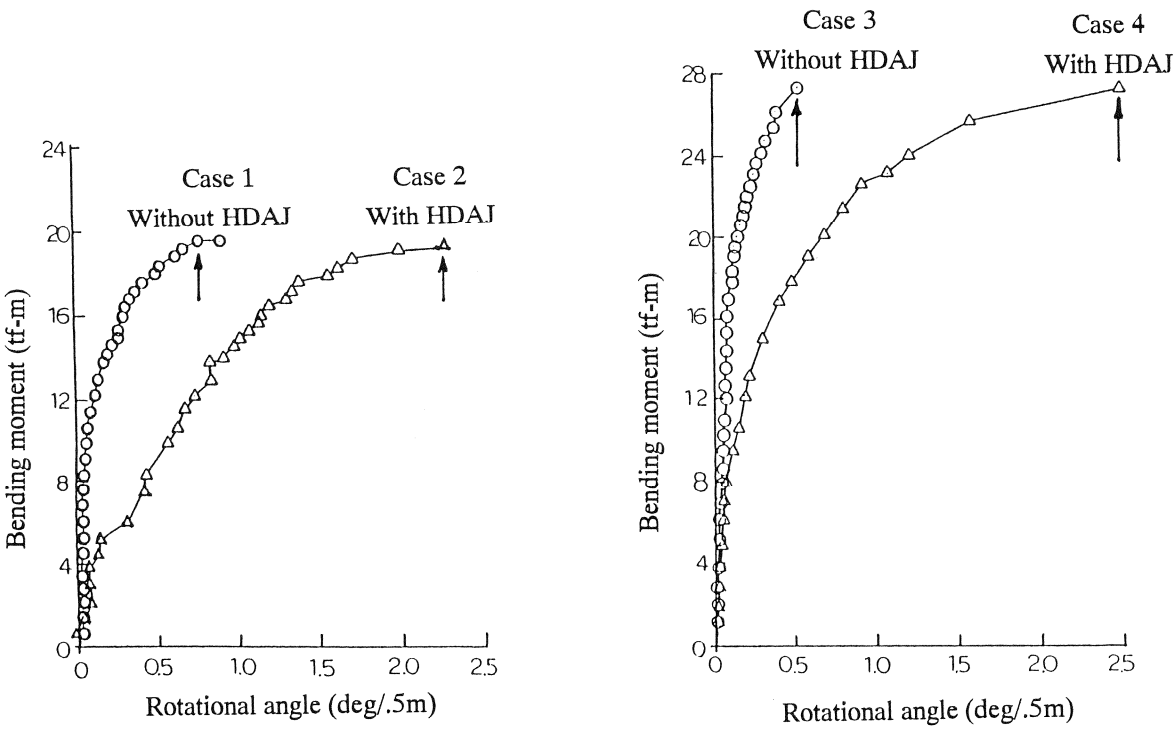

(a) Axial load = 0 tf

(b) Axial load = 60 tf

Figure 3 Resulting bending moment-rotational angle curves

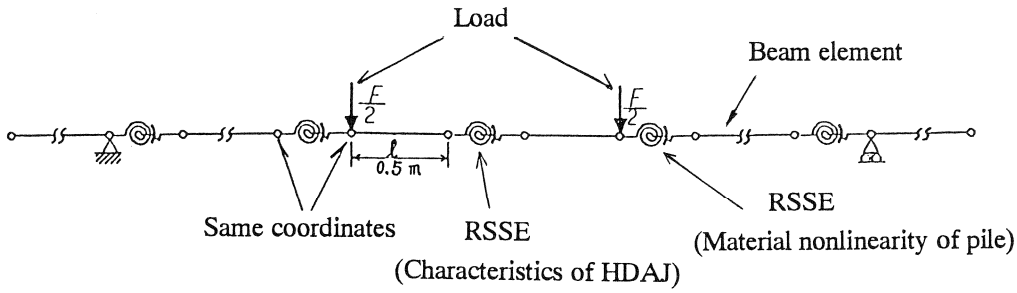

Figure 4 Pile model for numerical simulation

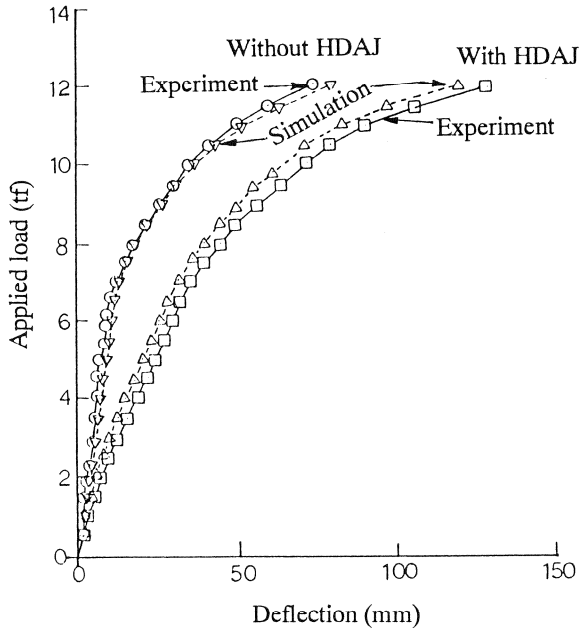

(a) Axial load = 0 tf

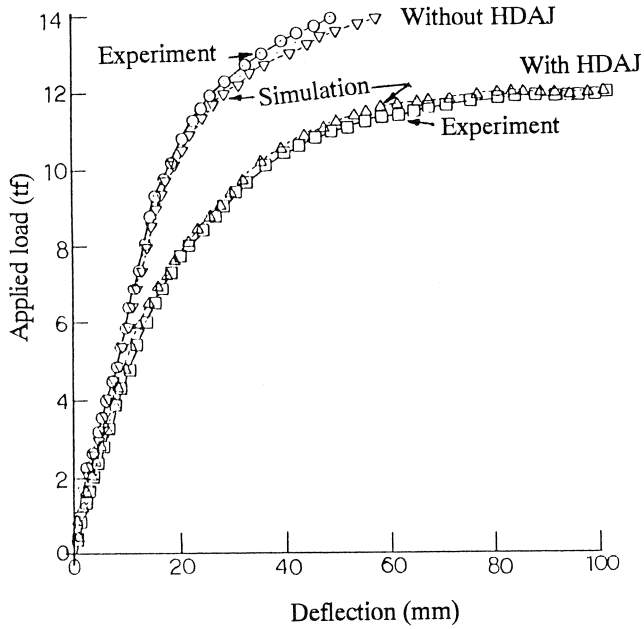

(b) Axial load = 60 tf

Figure 5 Comparison of load-deflection curves obtained from simulations with those from experiments

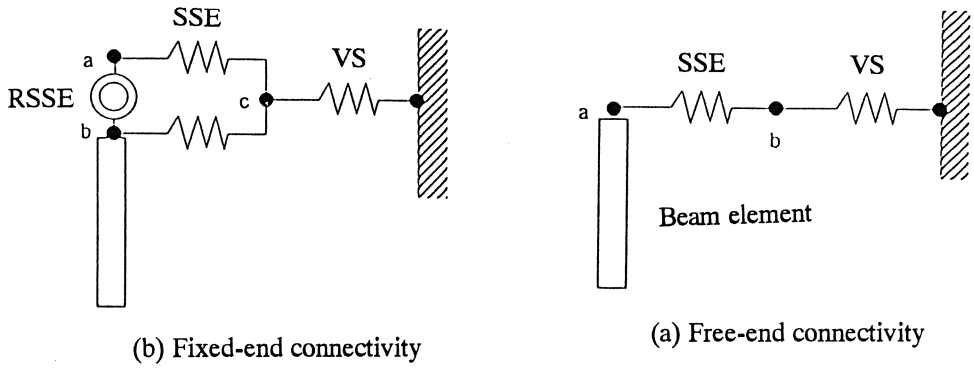

(b) Fixed-end connectivity

(a) Free-end connectivity

Figure 6 Model of pile cap

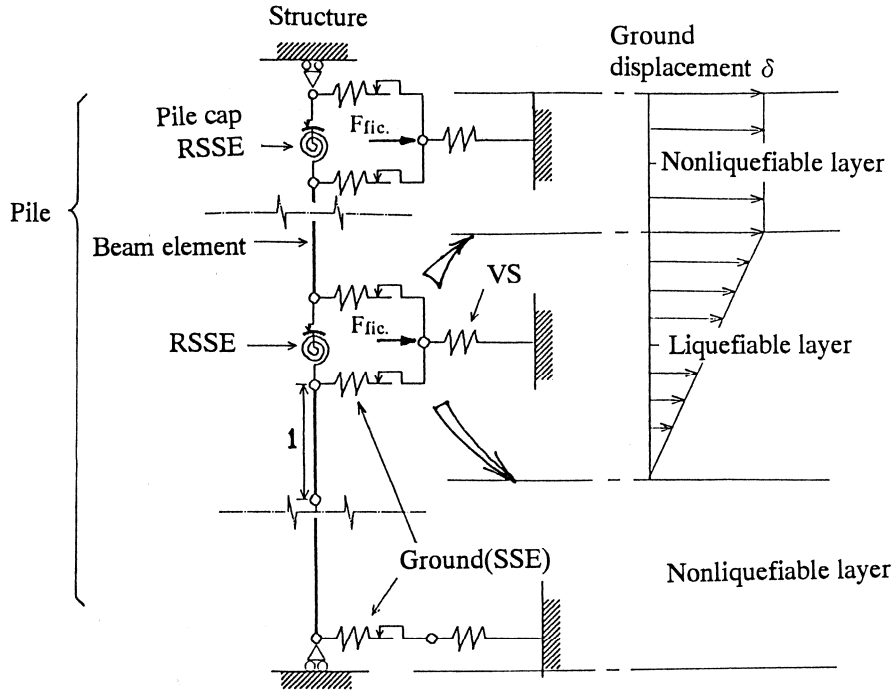

Figure 7 Model of pile and soil interaction for numerical simulation

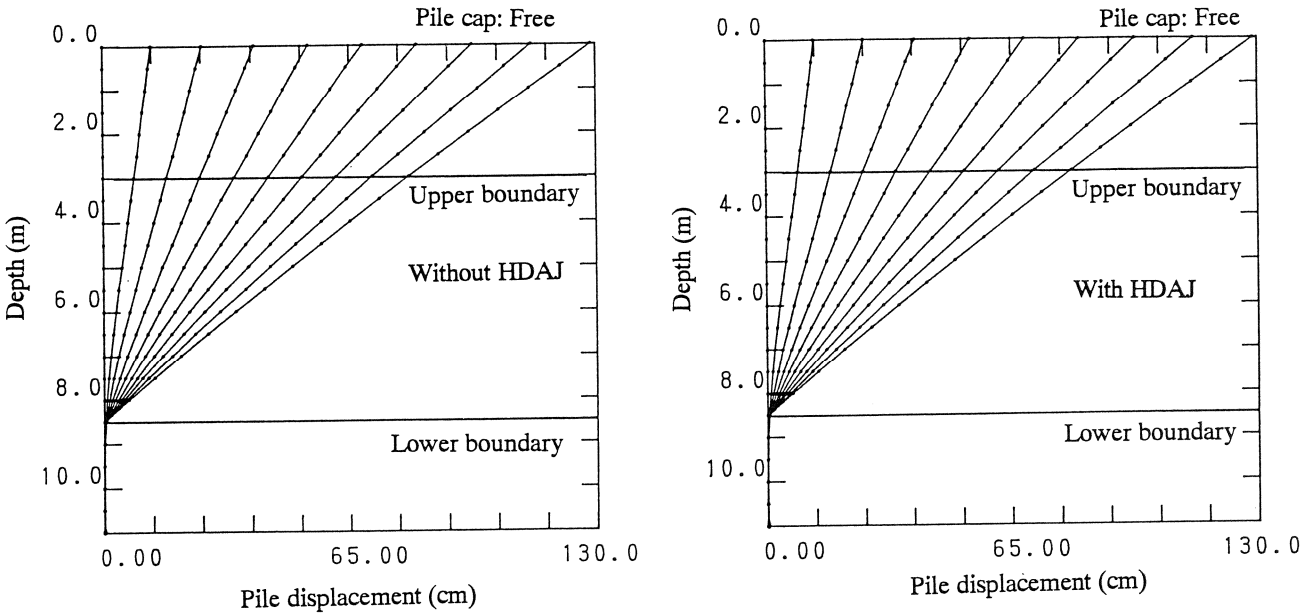

(a) Pile without HDAJ (Case Pfr)

(b) Pile with HDAJ (Case Jfr)

Figure 8 Change of pile displacement with increasing ground displacement (free-end)

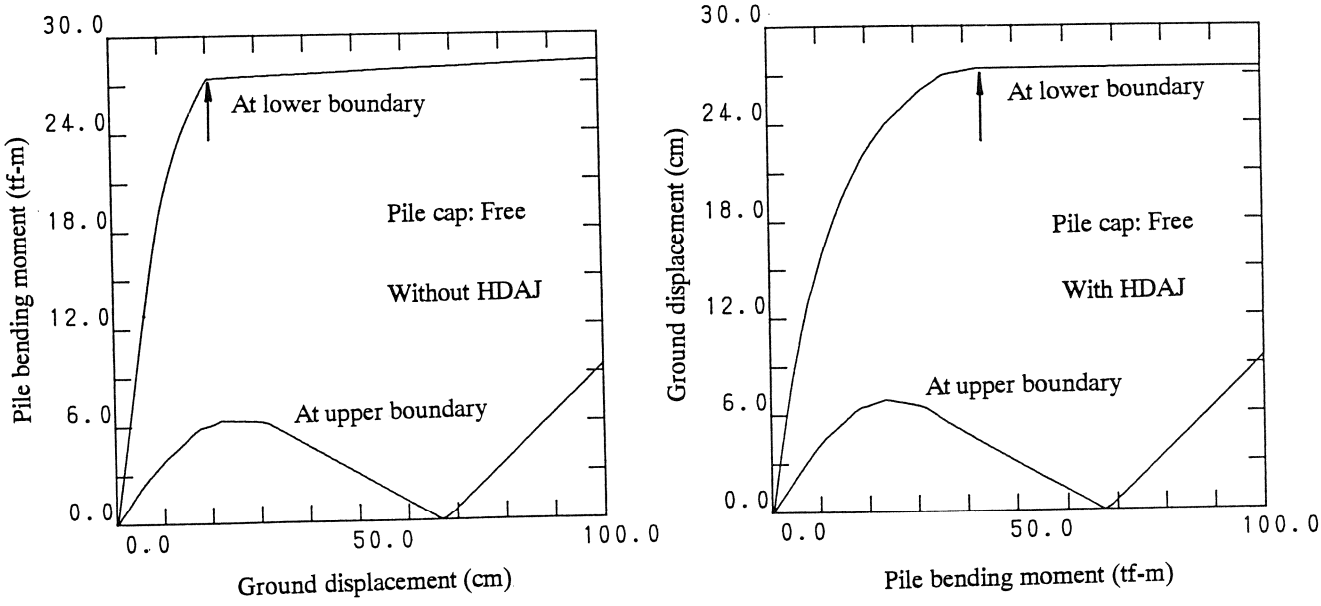

(a) Pile without HDAJ (Case Pfr)

(b) Pile with HDAJ (Case Jfr)

Figure 9 Bending moment-ground displacement curves (free-end)

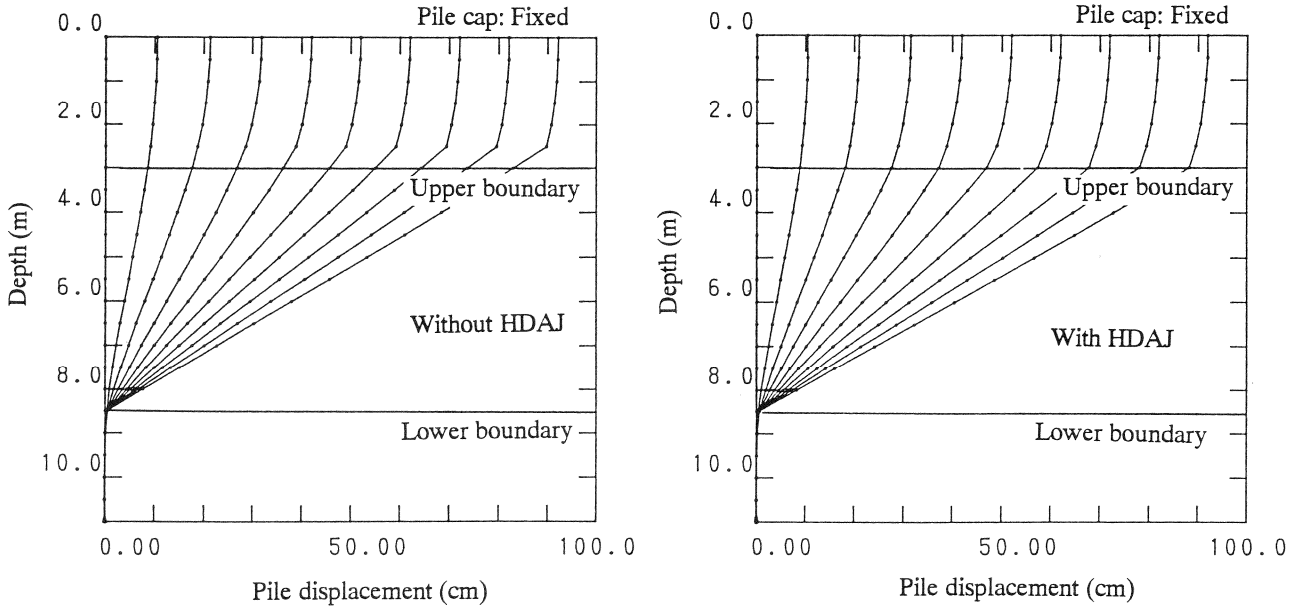

(a) Pile without HDAJ (Case Pfx)

(b) Pile with HDAJ (Case Jfx)

Figure 10 Change of pile displacement with increasing ground displacement (fixed-end)

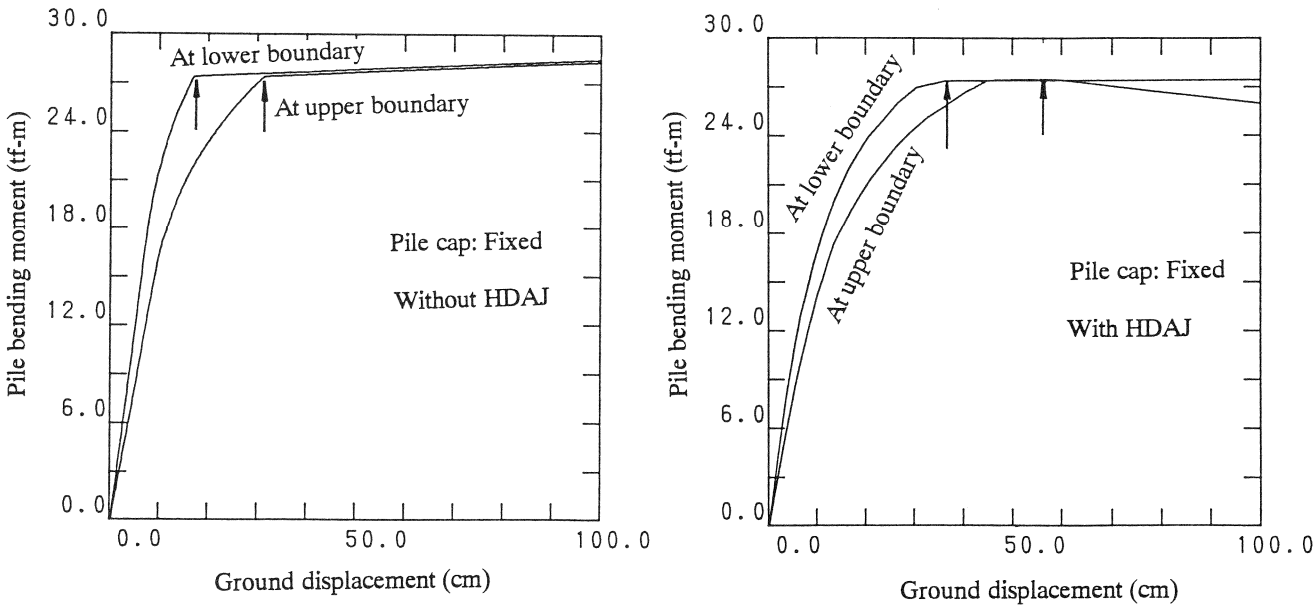

(a) Pile without HDAJ (Case Pfx)

(b) Pile with HDAJ (Case Jfx)

Figure 11 Bending moment-ground displacement curves (fixed-end)

MITIGATION OF LIQUEFACTION HAZARDS AT THREE CALIFORNIA BRIDGE SITES

By

Ken Jackura and Abbas Abghari
California DOT, Geotechnical Unit

ABSTRACT

Certain bridge sites in California are requiring ground and substructure modifications to overcome foundation strength loss due to liquefaction as a result of a major seismic event. This paper includes a discussion on two major interchange sites in the San Diego area and a third in the San Francisco Bay Area. The first site is being modified to develop increased lateral pile support via stone column islands. The second site uses underground stone column buttresses for minimizing lateral spreading. A third site, the east approach to the San Francisco-Oakland Bay Bridge overlies liquefiable sands that are susceptible to lateral spreading. Ductile moment resisting piles are recommended at the third site to provide resistance to accommodate the expected soil and inertial loads because overhead restrictions prevent ground modifications.

INTRODUCTION

The California Department of Transportation has been aggressively incorporating stringent geotechnical criteria into the seismic analysis of bridges since the Loma Prieta event of 1989. This event had caused significant damage to certain structures that were both designed before 1972 and founded over soft clay deposits in and around San Francisco. For example, it caused the collapse of approximately 1.1 km (0.7 miles) of the elevated Cypress (I-880) Viaduct, a structure constructed in the late 1950's and also founded on soft clay (Figure 1). Subsequently, the Governor's Board of Inquiry (1) assembled to review and comment on the damage, recommended, among other things, that ". . . the retrofit program should continue to focus on the structure as a whole, including its foundations and supporting soils. Elements should not be abstractly considered outside the context of their use."

Caltrans engineers immediately implemented a full scale geotechnical investigation program whereby site specific acceleration response spectra (ARS) based on maximum credible events, peak relative soil displacements, and liquefaction assessment would be routinely taken into account. This new program replaces standardized ARS curves and the assumption that peak relative soil displacements would have little or no impact on the sub-structure system. As a consequence, soil-pile-superstructure interaction analyses have since become a norm for many of our structures. However, serious technical and analytical problems arise when sites susceptible to liquefaction are encountered. Seismic motions passing through liquefied layers can be dramatically different than motions that pass through layers with no liquefaction, generally resulting in significant differences in the ARS (Figure 2a) as well as differences in peak relative soil displacements (Figure 2b), even though the deflection of the pile system may or may not coincide with the free field motion. Additionally, liquefaction can pose an even greater threat if there is a potential for large horizontal displacements due to lateral spreading. With these ideas in mind, the following three Caltrans projects are presented, illustrating, in a cursory fashion, the

geotechnical design philosophy utilized in evaluating sites where-in liquefaction hazards are present, as well as the ground and sub-structure modifications proposed for design.

Route 5/56 Interchange (Proposed)

The 5/56 Interchange is a new construction project lying approximately 24 km (15 miles) north of San Diego (Site 1 on Figure 3). New construction will begin in 1995 and consist of embankments to 12 m (40 ft) in height, and elevated connectors approximately 24 m (80 ft) high at their apex and 910 m (3000 ft) long. The interchange will be located in a tidal flat area at a distance of about 5.6 km (3.5 miles east) from the active strike-slip Rose Canyon Fault. This fault has a maximum credible event of moment magnitude M_w=7 which generates a peak bedrock acceleration of 0.6g.

More than 100 borings including Standard Penetration Tests (SPT's) together with a number of Cone Penetrometer Tests (CPT's) provided information on the soil conditions. The foundation soils consist of young alluvial and estuarine sediments comprised of clays, silts and sands that vary in depth and consistency throughout the area. Corrected blow counts $(N_1)_{60}$ in the upper 15 m (50-ft) of the sandy deposits vary from 3 to 50 with the predominate portion falling between 10 to 18. Ground water elevation fluctuates seasonally from the ground surface to 3 m (10 ft) below ground surface. Depth to bedrock varies from 6 m (20 ft) to 30 m (100 ft).

Figure 4 illustrates the soil profile for a portion of the site and is fairly typical of other sections. This section also shows a typical slope of less than 1%.

Analysis

The analysis commenced in 1991 with downhole seismic surveys for the development of shear wave velocity profiles for use in computing ground motions. These profiles are used in program SHAKE to provide estimates of peak ground accelerations under total stress conditions as well as estimates of peak spectral accelerations (Figure 5). In figure 6 an example is given of the range of peak cyclic stress ratios as determined by the ground motion study. These ratios are used to estimate liquefaction potential. Blow counts were corrected for percent fines (-#200) and plasticity (PI). Recognition of the liquefaction potential warranted concern in three areas: 1) Loss of lateral support for the pile foundation; 2) Excessive pile curvature due to large relative soil displacements and/or lateral spreading; and 3) Approach fill instability.

Because of the ±60 acre areal extent of the interchange, ground modification of the entire site would not be feasible by any technique. Consequently, ground modifications were made with stone columns only around each of the 35 bents supporting the large connectors and at each approach fill where-in instability by overturning posed a problem.

In a quasi-static analysis method to determine the survivability of the substructure, the first step is to determine the soil spring constants (P-Y curves) for the liquefied state. A literature search (1991) failed to uncover any information on appropriate P-Y values to use. Therefore, the assumption was made to use a soft clay criteria (Matlock (2)) with a residual shear strength based on the liquefied state (Alba et al Figure 7) and a 2% strain for ε_{50}. Information gathered since

then (3) indicated that 10% would be a closer approximation for ε_{50}. A lower bound $(N_1)_{60}$ value of 10 was chosen for the liquefied state to be consistent with the residual shear strength.

This information was then used to determine the deflection of a ductile pipe pile system consisting of twenty-four 406 mm dia, x 12.7 mm thick (16 in x 0.5-in) piles per bent. The deflection study was based on a single pile analysis program (BMCOL76 (4)), modified by Caltrans to incorporate non-linear beam elements, a much improved convergence algorithm, and maximum curvature warning statements). Peak inertial loads applied to the pile system were determined based on the total stress ARS. At that time it was questionable whether or not a total stress analysis would be too conservative but it was argued that the proposed ground modification would require leaning more towards a total stress approach.

Assuming that liquefaction would extend to a depth of 12+ m (40 ft) with a constant residual shear strength of 19.2 KPa (400 psf), it was determined that buckling of the pile system would occur at 60% of the design load. After evaluating various ground modification techniques, 30 m (100 ft) diameter stone column islands (Figure 8) turned out to be the most cost effective alternative for increasing lateral pile support. The principal mechanisms for such support include quick drainage and the densification of the surrounding soil. Using the assumption that a $\emptyset = 30°$ would prevail within the stone column islands reduced the deflections significantly (Figure 9).

Preliminary field testing of 0.9 m (30 in) diameter stone columns placed at 2.4 m (8 ft) C-C spacing to determine the increase in foundation strength indicated a dramatic improvement in the CPT tip resistance between 1.5 to 6.1 m (5 to 20 ft) and 12 to 16.7 m (40 to 55 ft). At that particular test location, only slight increases were noted between the 6.1 to 12 m (20 to 40 ft) depths (Figure 10).

Lateral spreading estimates were attempted, but due to the variability of the non-liquefiable soil deposits at spot locations and the small surface gradient (< 0.7%), any flow whatsoever was assumed to be absorbed by a crush zone in the fringe of the stone columns at any impacted island, thus preventing additional loading on the substructure system.

The installation of stone columns is also planned for areas with high approach fills where-in safety factors less than 1.0 were computed. Residual shear strengths were incorporated as soil resistance factors for the liquefied zone beneath the embankments and from there, a normal static analysis was carried out. Stone column dimensions were chosen to provide minimum factors of safety of at least 1.05 (Figure 11), for all approach fills.

8/805 Interchange (Retrofit)

The 8/805 Interchange was constructed in 1972 in San Diego (Site 2 on Figure 3) and requires extensive seismic retrofit of the substructure and columns. Interstate 805 is the main viaduct at this site with a N-S orientation, a span of some 1500 m (5000 ft), a 36 m (120 ft) height, and a cast-in-place, prestressed box girder design with eight reinforced concrete connector ramps attached (See photo 1). The main viaduct joins the north and south canyon bluffs which are separated by the wide flood plain of the westerly flowing San Diego River, and the east-west I-8 freeway. Foundation soils to depths of 12 m (40 ft) below the original ground (OG) consist of loose to moderately dense deposits of sand and gravel interspersed with clayey silt and silt layers. Beneath these deposits lie very dense sands and gravel mixes which extend to the sandstone/siltstone deposits some 18 m (60 ft) below OG, (see Figure 12). The water table remains near the river elevation throughout the year. Beneath the structure, portions of the

canyon flood plain have been overlain by well compacted fill to thicknesses of up to 6 m (20 ft) for the support of several multi-story businesses and associated parking facilities. The ground slopes toward the river and varies in grade from 2-7%. Two active strike-slip faults are located nearby, the Rose Canyon (M_W=7.0) and the La Nacion (M_W=6.75), both capable of generating a peak rock acceleration between 0.5 and 0.6g's. Fault distances are 5.4 km east and 3.8 km southwest, respectively.

Analysis

More than 50 site borings including SPT's exist and indicate a range of $(N1)_{60}$ blow counts between 6 to 59 in the upper native 8 m (26 ft) with a mean lower bound lying between 10 to 20. To model the liquefiable soil, an average value of 12 was used as a basis for design. For these approximations of the liquefiable soil, a peak ground acceleration of 0.6g's was estimated using the total stress analysis program, SHAKE, while the design ARS was based on the average of the ARS from SHAKE and the ARS from an effective stress analysis program SUMDES (5). Since the required ground surface acceleration for initiating liquefaction was less than 0.2g's, inertial loads from the design ARS were imposed on the pile system while using soil resistance values for liquefied conditions as per the previous site study. An s_u of 28.8 KPa (600 psf) and an ε_{50} of 10% were implemented for estimating the liquefied P-Y relationship. From there, pile cap deflections were computed. Initial studies included full inertial loads and indicated significant lateral instability of the existing H-pile system for bents near the San Diego River where liquefaction extended to the ground surface.

Further studies in which peak relative soil displacements (0.5 m (1.7 ft) computed from SUMDES assuming horizontally layered conditions), coupled with 25% of the peak inertial loads, were imposed on the pile using a single pile analysis. The results indicated that many more additional bents would fail by hinging and/or buckling. Furthermore, large overturning forces were exceeding the piles uplift capacity in certain bents due to weak pile-to-pile cap connections and/or insufficient uplift resistance as a result of strength loss in the liquefied zone (strength = zero for all zones where $(N1)_{60} \leq 25$).

New pile systems were therefore designed consisting of 42-inch diameter steel pipe piles for the viaduct, and 24-inch diameter pipe piles for the ramps. Depending on bent location these piles were designed to accommodate up to 0.9 m (3 ft) of relative deflection over a pile length of 7.6 m (25 ft) before ductile capacities were exceeded. The new piles will be grouped around the old pile system and the existing cap will be extended to accommodate the additional piles.

Because relative displacement, rather than load, was the controlling factor for pile and superstructure design, it became important to evaluate any additional movement due to lateral spreading and then incorporate it into the design. Several factors against lateral spreading such as the fact that blow counts were not uniformly small and the existence of plasticity in portions of the profile where there are low blow counts (PI @ 10-20), were overridden by the following factors supporting the likelihood of lateral spreading: a) an open face to the river, b) impedance of vertical drainage due to the impervious nature of the overlying fill causing high excess pore pressures to persist for some time in the loose to moderately dense native strata resulting in continued straining due to gravity loads, c) large magnitude post mainshock loading very soon after the mainshock is likely, and d) the extremely dense nature of the overlying fill and its proximity to the cap and column, resulting in displacements that coincide with the fill. Thus, a number of published papers on lateral spreading were examined (3, 6, 7, 8) and displacements were

computed based on the product of limiting strain (γ_{lim}) (2) and the thickness of the liquefiable layer (assumed at 40% and 7.6 m (25 ft), respectively). Potential displacement estimates ranged from 1.5 to 4.5 m (5 to 15 ft), with an average value of 3 m (10 ft).

Ductility calculations indicated that a maximum additional displacement of 0.3 m (1 ft) beyond the peak relative displacement of 0.5 m was tolerable and resulted in the conclusion that ground modification was necessary. Due to the site's large areal extent, only localized ground modifications were considered economical through the use of stone columns acting as an underground buttress. The next best alternative is permanent dewatering. Mobilized shear resistance for this additional displacement was computed under the assumption that it would develop proportionally to the full residual strength (28.9 KPa (600 psf) at the 3 m (10 ft) displacement, Figure 13, Byrne (3)). Thus, a minimum of 1.44 KPa (30 psf) was estimated as the average mobilized strength for the 0.3 m (1 ft) displacement. Incorporating this strength into static stability calculations, stone column dimensions were determined assuming the treated areas would develop a phi of 39°. Figure 14 illustrates the static factor of safety for the 'before' and 'after' stone column addition. A plan view of the stone column area is shown in Figure 15. Since lateral spreading could be skewed to the downhill direction, the buttress was carried parallel to the drip line of the viaduct on the north side of the river. This ground modification location scheme was also dictated by right-of-way restrictions that limited construction activities to the confines of state-owned property.

Oakland Bay Bridge - East Approach

The San Francisco-Oakland Bay Bridge was constructed in the mid 1930's and is considered to be one of the engineering marvels of our time. At that time it was the world's longest steel structure [7 km (4.4 mi)], consuming 18 percent of all the steel fabricated in the United States in 1933. It includes the deepest pier in the world [Pier E3, 71 m (235 ft)] with its tip located on a stratum of stiff clay and sand just short of bedrock at 91 m (300 ft).

Figure 16 shows a plan and aerial view of the West Bay suspension crossing, a portion of the East Bay crossing, and Yerba Buena Island. The east approach cannot be seen in the aerial view, but it is on this section (Piers E23 to E39) that the discussion centers. The east approach superstructure consists of a number of simple-span deck systems that use steel and concrete stringers supported on transverse concrete bents. The pile systems consist of 0.45 m (18 in) tapered timber piles supported primarily by friction in sand and clay sublayers. Two strike-slip faults, the San Andreas (M_w=8.0), and the Hayward (M_w=7.3) are located 22 km (13.8 mi) west, and 7.5 km (4.7 mi) east respectively. Peak site rock accelerations were estimated at 0.5g's.

Figure 17 illustrates the soil profile between Piers E23 - E39, along with a typical cross-section of the bridge. The upper 6.1 to 9.1 m (20 to 30 ft) of fill is hydraulically placed with $(N_1)_{60}$ values between 7 and 30, with an average lower bound between 8 to 10. The fill was placed during the time of construction and displaced up to 5.5 m (18 ft) of the soft bay mud. The undrained shear strength of the soft bay mud ranges from 7 KPa (150 psf) near the mud line to between 22 to 37 KPa (460 to 800 psf) just beneath the fill. Not shown are the sands, silts, and stiff clay mixtures which prevail below this soil to depths of 140± m (460 ft) where bedrock is encountered.

Analysis

Output from SHAKE demonstrated that the ARS varies only slightly from the pile cap level, approximately 1.5 to 3 m (5 to 10 ft) below top-of-fill, to the bay mud-fill interface. Analysis also revealed that the sand fill would liquefy. This liquefaction results in reduced pile resistance and lateral spreading into the bay causing additional pile loading where the head scarp extends into the substructure.

An analysis of the pile foundation using peak inertial loads, liquefied P-Y relationships of the sand based on its estimated residual strength of 14.4 KPa (300 psf), and cyclically degraded strength of the soft bay mud indicated (not surprisingly) complete failure of the timber piles. Due to overhead restrictions of the lower deck to top-of-fill (2.4 to 5.5 m (8 to 18 ft)) and restrictions on lane closures, ground modifications were extremely limited and a decision was made to bypass the liquefied sands with ductile moment resisting piles.

The overhead space limitations prevented the use of a standard pile installation process. A specialty pile by FUNDEX (10) was examined as the best alternative. The recommended FUNDEX pile is a 508 mm (20 in) OD steel pipe pile with a thickness of 25 mm (1 in) at its top and thinner 12 mm (0.5 in) thickness at depth and has a unique 673 mm (26.5 in) fluted tip for helping relieve tip and side friction as the pile is rotated to depth. Piles are segmented into 3 m (10 ft) sections and butt-welded as they are driven. Cement slurry grout, placed under pressure, will fill the annulus between the soil and the pile throughout its length. This reduces gapping and increases P-Y stiffness and corrosion resistance. The new piles will be placed around the existing pile system and new pile caps will be constructed. (As a side note, the excavation required for this operation adds to the project complexity and cost since both the soil and the water are considered hazardous due to high concentrations of lead from repeated painting operations, and must be either cleaned before replacement, or disposed.)

The number of piles to be used at each bent was based on the peak inertial loads determined from the ARS in addition to imposed loads as estimated from soil pressures induced by lateral spreading. Lateral displacement estimates were made using a mechanistic method by Newmark (11) where-in the full residual strength of the liquefied sand was considered. Random block failure surfaces in conjunction with a progressive failure technique proposed by Idriss (12) were used to evaluate the advancement of the scarp head. Strength reductions to 1/3 of the initial undrained shear strength of the soft clay were considered where critical failure planes penetrated into this strata. The 1/3 s_u value was based on the fact that the sensitivity of the bay mud in this vicinity is in the range of 2-4.

The analysis, in general, assumes that for the design earthquake, the peak ground acceleration (PGA) is at a maximum at the beginning and tapers logarithmically to zero. For simplicity, a linear reduction was assumed on this project. The Hayward Fault (M_w=7.3 earthquake) was determined to be the most damaging for this location and was considered to have twelve significant stress pulse cycles associated with its duration. Using two cycles per failure surface as a trial, the PGA reduction relationship described above, and the seismically induced displacement relationship proposed by Makdisi and Seed (13) (Figure 18), a progressive failure scheme evolved based on the M_w=7.5 curve after reducing it to a per cycle basis. For each time step, cross-sectional geometry continually flattened to accommodate a likely progressive failure scenario. Figure 19a -19e summarizes the results of such an analysis for a portion of the east bay approach.

Using the results of this analysis as a guide, an estimate of the possible extent of the head scarp into the substructure region was gleaned. Based on this analysis, lateral pressures equivalent to a value of up to 50 percent of the passive pressure on the pile system for 1/2 the full cap width (maximum extent of scarp head) was imposed as an additional load on the pile system in the lateral direction. Due to a possible skewing of the lateral spreading material, a component of this load was taken longitudinally and added to the longitudinal inertial loads. Figure 20 illustrates the results of our quasi-static analysis of the newly designed pile system. Maximum lateral deflections of the subsurface system are estimated to be in the range of 25 to 75 mm (1 to 3 in).

Axial and lateral load tests on the proposed pile system will start sometime in late 1994 with bridge reconstruction to begin shortly thereafter. Further studies incorporating a full dynamic soil-pile interaction analysis will be pursued using the Program PAR (14). It has an extensive support base for P-Y and T-Z cyclic degradation and radiation damping and can include multi-pile systems as well as superstructure components. The program runs on a DOS based PC and preliminary results look promising. Results compare quite favorably with a quasi-static analysis using another project as a test case. Results on the Bay bridge using this approach will be completed by November 1994 and included for review and design.

REFERENCES

1. The Governor's Board of Inquiry on the 1989 Loma Prieta Earthquake, "Competing Against Time," Department of General Services, Publications Section, P.O. Box 1015, North Highlands, CA 95660, May 1990.

2. Matlock, H., "Correlations for Design of Laterally Loaded Piles in Soft Clay," Paper No. OTC 1204, Proceedings, Second Annual Offshore Technology Conference, Houston, TX, Vol. 1, 1970, pp. 557-594.

3. Byrne, Peter M., "A Model for Predicting Liquefaction Induced Displacements," Soil Mechanics Series No. 147, Department of Civil Engineers, University of British Columbia, Vancouver, Canada, September 1990.

4. Matlock, H., Bogard, D., and Lam, I.P., "BMCOL 76: A Computer Program for the Analysis of Beam-Columns Under Static Axial and Lateral Loading," University of Texas at Austin under grant from Fugro, Inc., Program Documented at Ertec, Inc., the Earth Technology Corp., 3777 Long Beach Blvd., Long Beach, CA 90807, June 1981.

5. Li, X.S., Wang, Z.L., and Shen, C.K., "SUMDES, a Nonline Procedure for Response Analysis of Horizontally-layered Sites Subjected to Multi-directional Earthquake Loading," Report to the Department of Civil Engineering, University of California, Davis, 1992.

6. Hamada, M., Towhata, I., Yasuda, S. and Isoyama, R., "Study on Permanent Ground Displacement Induced by Seismic Liquefaction," Computers and Geotechnics 4, 1987, pp. 197-220.

7. Towhata, I., Yasuda, S., Ohtomo, K., and Yamada, K., "Experimental Studies on Liquefaction Induced Permanent Ground Displacement," Proceedings, First Japan-U.S. Workshop on Liquefaction, Large Ground Deformation and Their Effects on Lifeline Facilities, Tokyo, Japan, November 1988.

8. Youd, T., and Bartlett, S., "US Case Histories of Liquefaction-induced Ground Displacements," Proceedings, First Japan-U.S. Workshop on Liquefaction, Large Ground Deformation and Their Effects on Lifeline Facilities, Tokyo, Japan, November 1988.

9. Seed, H.B., Tokimatsu, K., Harder, L. and Chung, R., "The Influence of SPT Procedures in Soil Liquefaction Resistance Evaluations," Report No. UCB/EERC-84/15, College of Engineering, University of California, Berkeley, California, 1984.

10. FUNDEX Corp, Head Office; Brugsevaart 6, P.O. Box 55, 4500 AB Oostburg, the Neatherlands.

11. Newmark, N.M. (1965). Effects of earthquakes on dams and embankments. Geotechnique, 15(2), pp. 139-160.

12. Idriss, I.M., 1985. Evaluating Seismic Risk Engineering Practice, Proceedings, Theme Lecture No. 6, XI International Conference on Soil Mechanics and Foundation Engineering, San Francisco, CA, August, Vol. 1, pp. 244-320.

13. Makdisi, F. I., and H.B. Seed (1978) "Simplified Procedure for Estimating Dam and Embankment Earthquake-Induced Deformations," Journal of the Geotechnical Engineering Division, ASCE 104 (GT7):849-867.

14. PAR, A Pile Analysis Program, PMB Engineering Inc., 500 Sansome St., San Francisco, CA 94111.

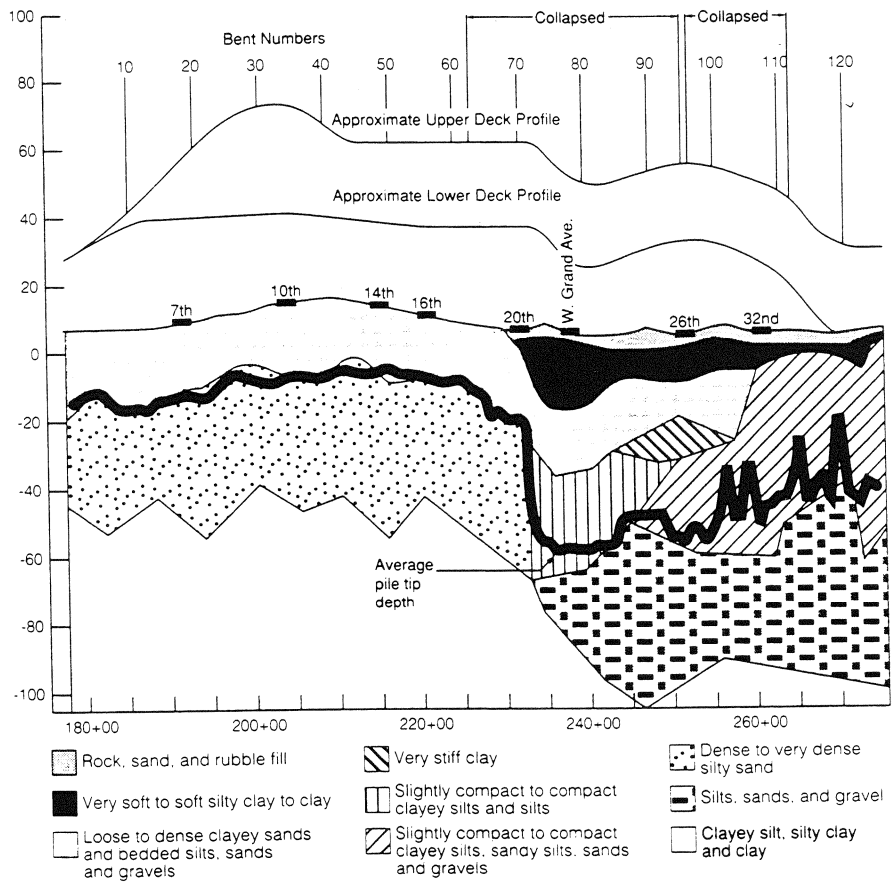

Fig. 1 Soil Profile of Cypress Viaduct Based on Boring Information From 1953-1990

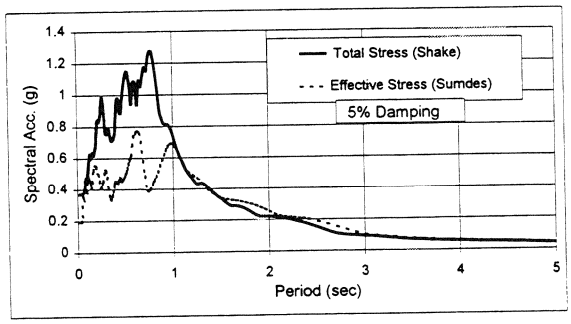

Fig. 2a Comparison of ARS Between Effective And Total Stress Analysis

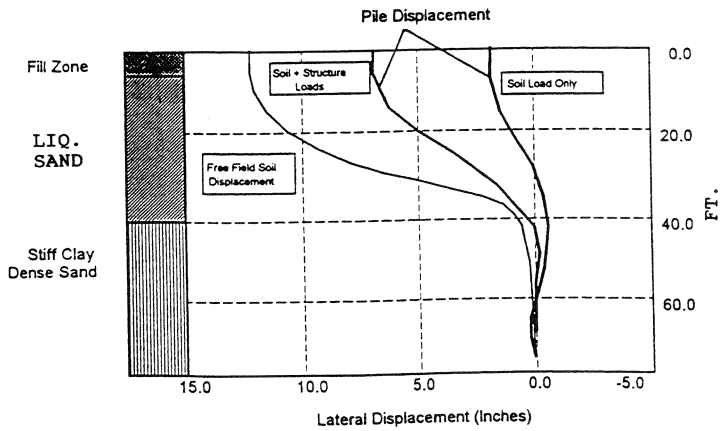

Fig. 2b Loaded Pile and Free Field Soil Displacement Profile

Fig. 3 Site Map of San Diego Vicinity

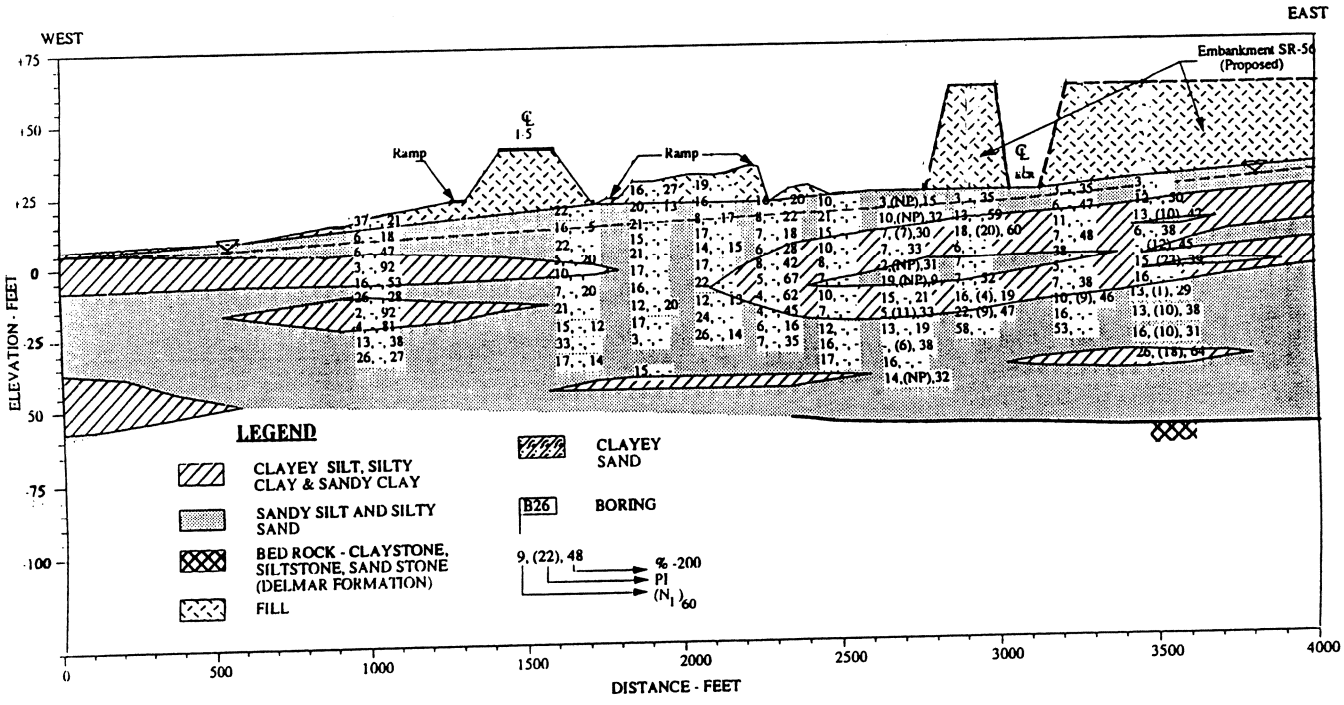

Fig. 4 Soil Profile for Portion of the I-5/56 Interchange

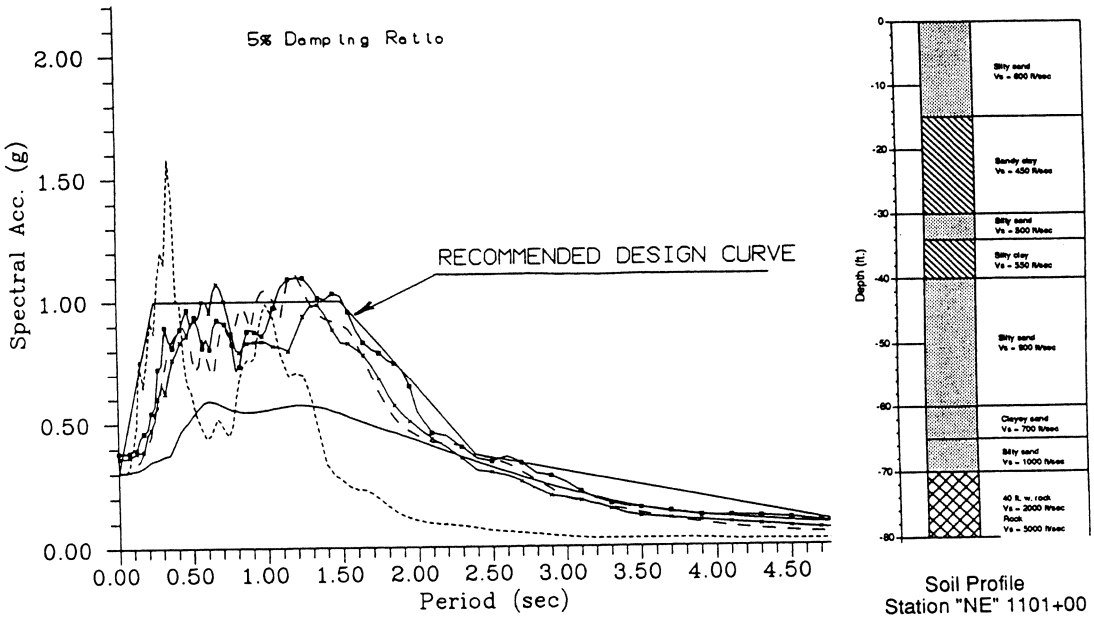

Fig. 5 Acceleration Response Spectra for I-5/56 Interchange

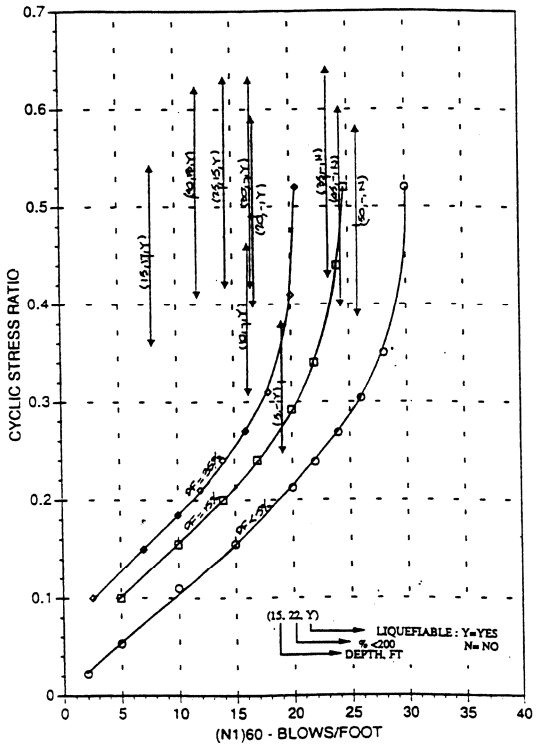

Fig. 6 Liquefaction Potential

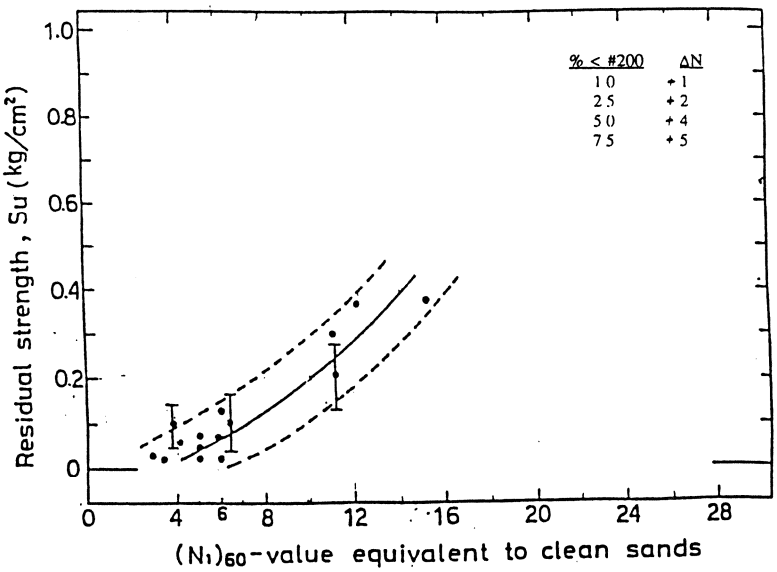

Fig. 7 Residual Strength of Liquefied Sands (Alba et al. 1988)

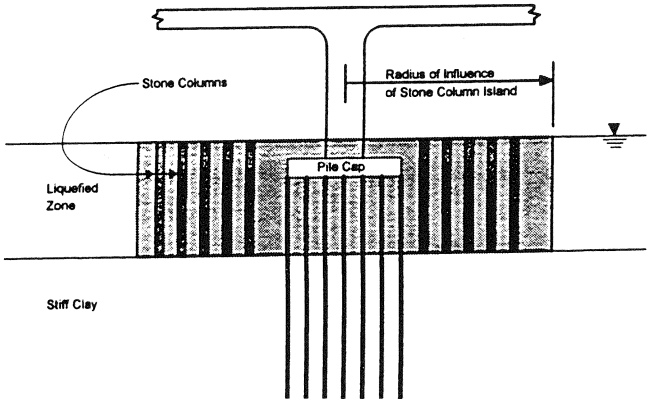

Fig. 8 Schematic Illustrating Stone Column Island Providing Substructure Support in the Liquefied Zone

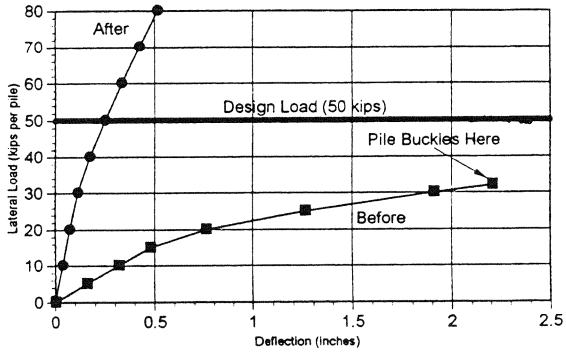

Fig. 9 Load-Deflection Curves for I-5/56 Interchange Before and After Ground Modification

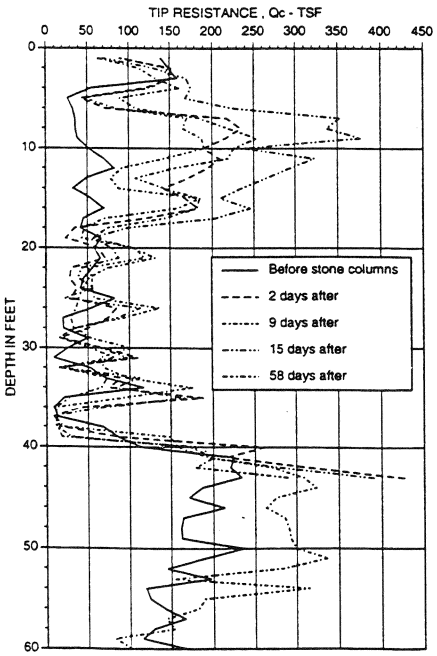

Fig. 10 Cone Tip Resistance Varying With Time After Placement of Stone Column

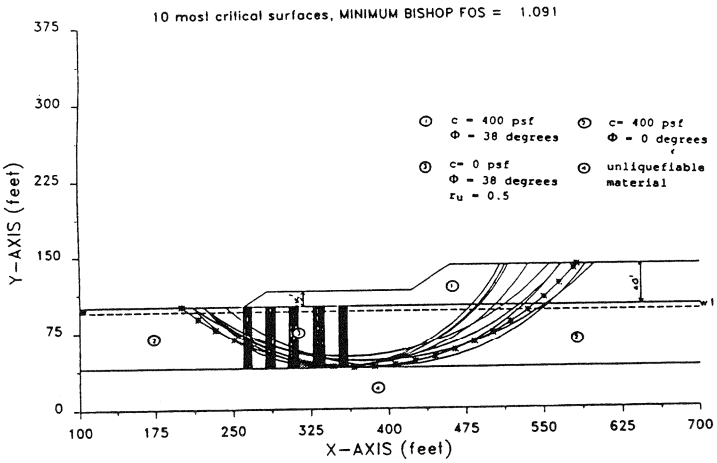

Fig. 11 Stability of 40-ft Embankment With Berm And Stone Column Support

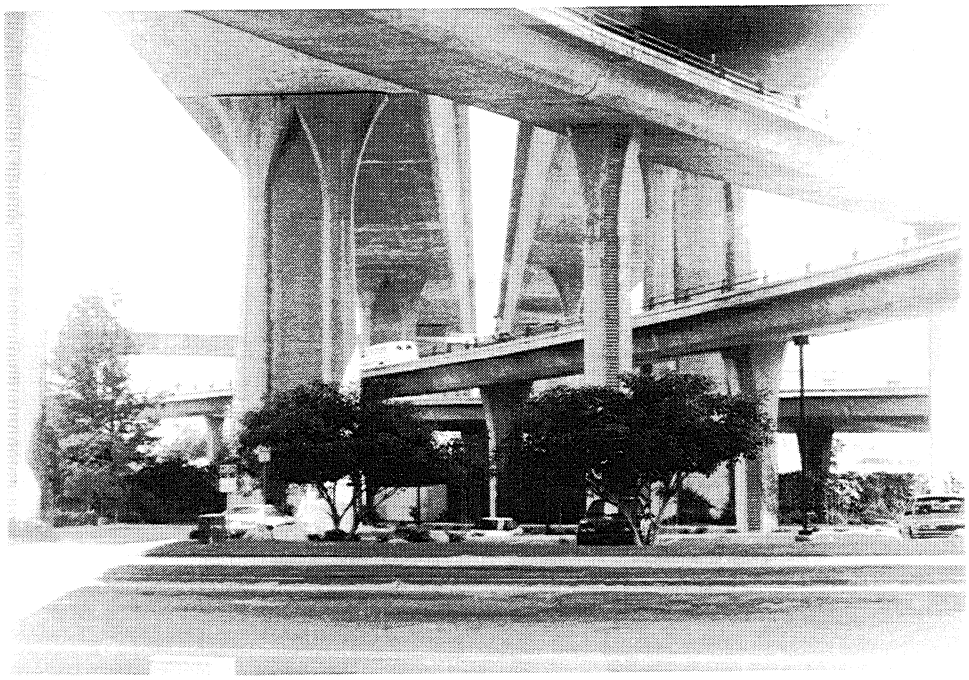

Photo 1 Portion of the I-8/805 Interchange Showing the Overhead Mainline Viaduct and Adjoining Connector Ramps (Viaduct is 120 ft at its Highest Point.)

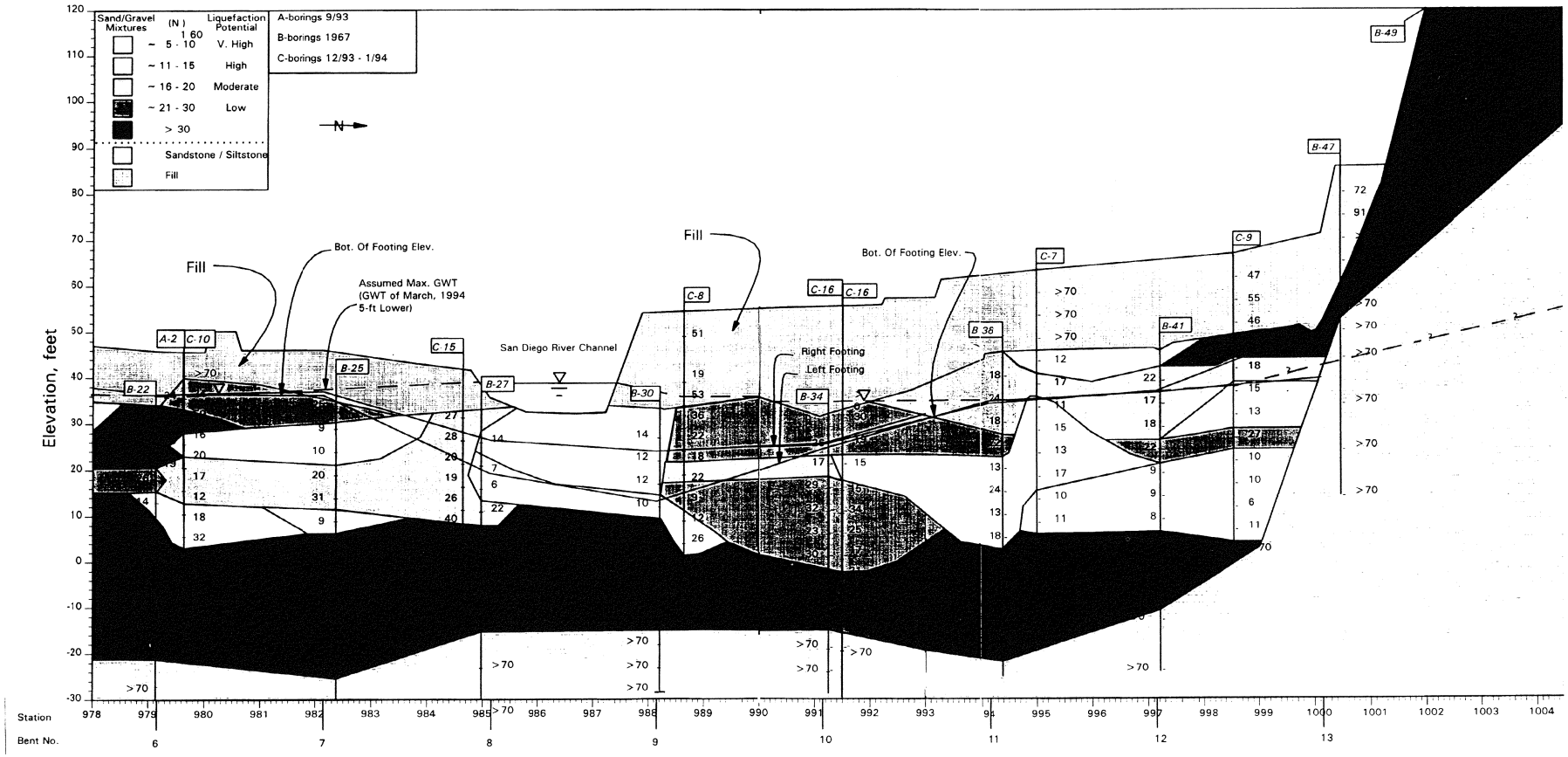

Fig. 12 - Portion of I8/805 interchange soil cross-section running north-south beneath main line viaduct. Black areas are dense non-liquefiable deposits. Lighter shading represents increasing sensitivity to liquefaction. Vertical scale exaggerated x8.

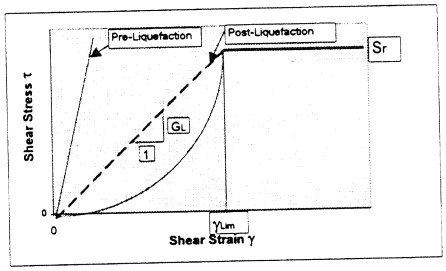

Fig. 13a Linear and Non-linear Stress-Strain Mode (Byrne el at.)

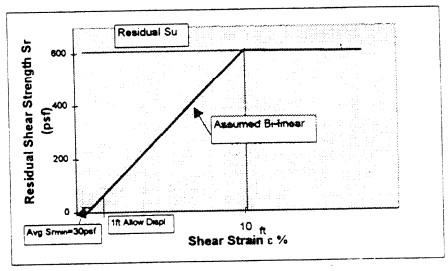

Fig. 13b Liquefied Sand Lateral Displacement Relationship Assumed in Stability Studies

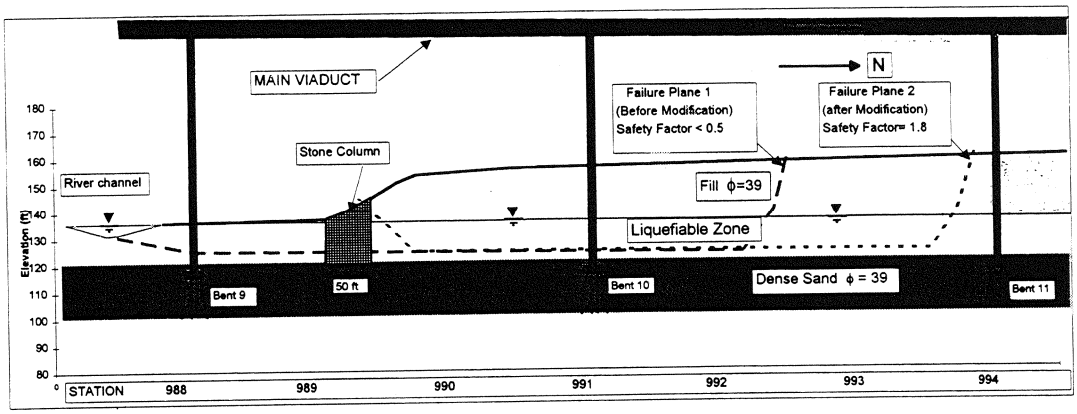

Fig. 14 Soil Profile Beneath Main viaduct (North Side) Illustrating Before and After Ground Modification Safety Factors Against Displacement < 1.0 ft

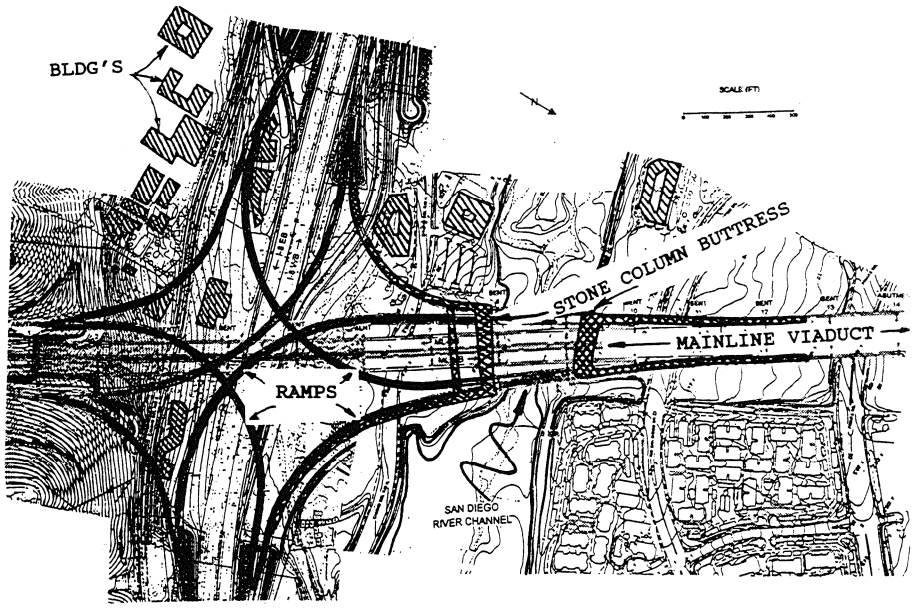

Fig. 15 Plan View of I-8/805 Interchange Showing Location of Underground Stone Column buttress

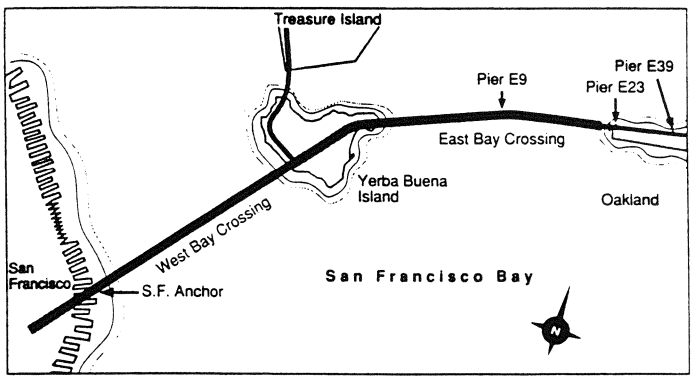

Fig. 16 Plan and Aerial View of the San Francisco-Oakland Bay Bridge

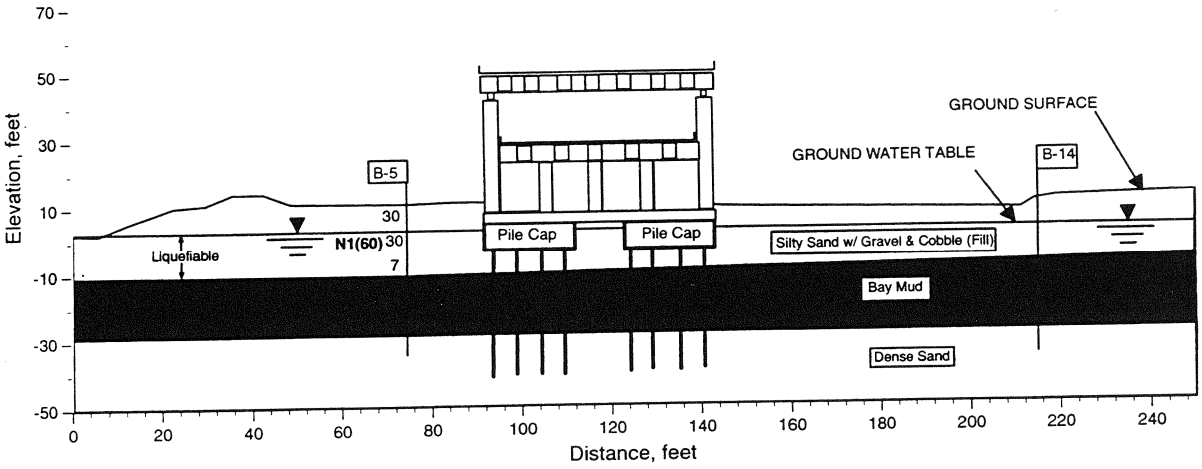

Fig. 17 San Francisco - Oakland Bay Bridge east approach cross section (typical).

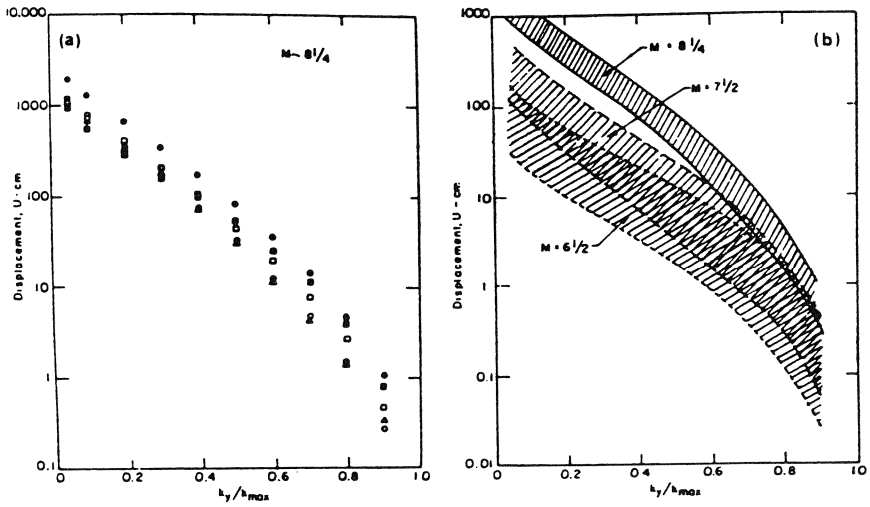

Fig. 18 Permanent Displacement From Sliding Block Analyses: (a) Results Obtained Using Several Input Ground Motions, Typical of Earthquakes With Magnitude 8.25; (b) Summary of Results From Different Magnitudes of Earthquake. Source: Makdisi and Seed (1978)

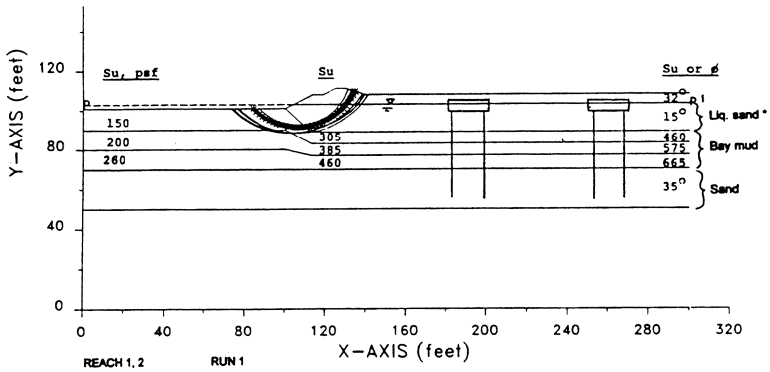

Fig. 19a Original strengths, earthquake time cycle 0 - 2.
(Ky = 0.03, Kmax = 0.5, Dy disp. ~ 10')

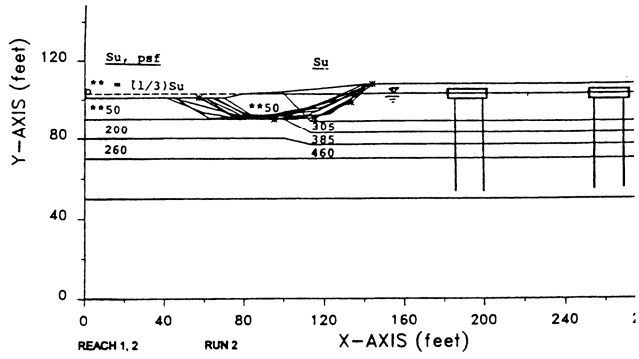

Fig. 19b Modified strengths, earthquake time cycle 2 - 4.
(Ky = 0.03, Kmax = 0.45, Dy disp. ~ 3')

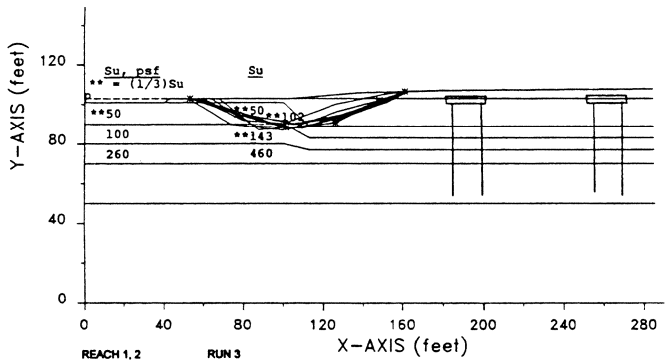

Fig. 19c Modified strengths, earthquake time cycle 4 - 6.
(Ky = 0.06, Kmax = 0.35, Dy disp. ~ 1')

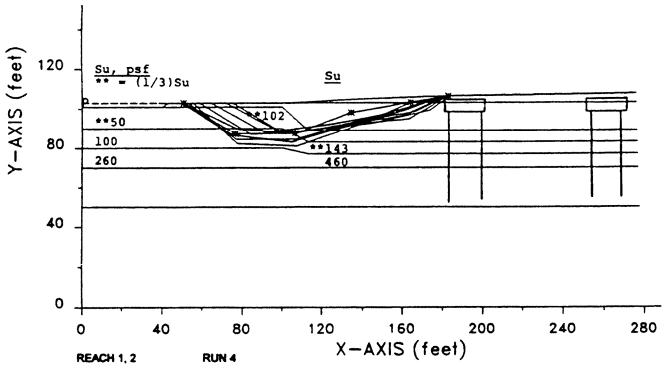

Fig. 19d Modified strengths, earthquake time cycle 6 - 8.
(Ky = 0.06, Kmax = 0.25, Dy disp. ~ 0.6')

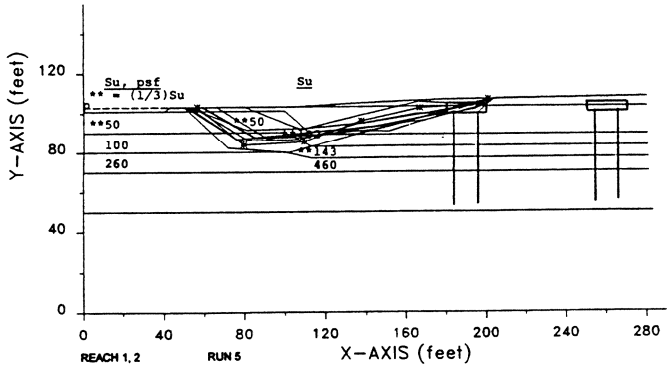

Fig. 19e - Modified strengths, earthquake time cycle 8 - 10.
(Ky = 0.08, Kmax = 0.15, Dy disp. ~ 0.1')

Fig. 19 Progressive failure analysis of liquefied sand and softened bay mud for east approach to Bay Bridge

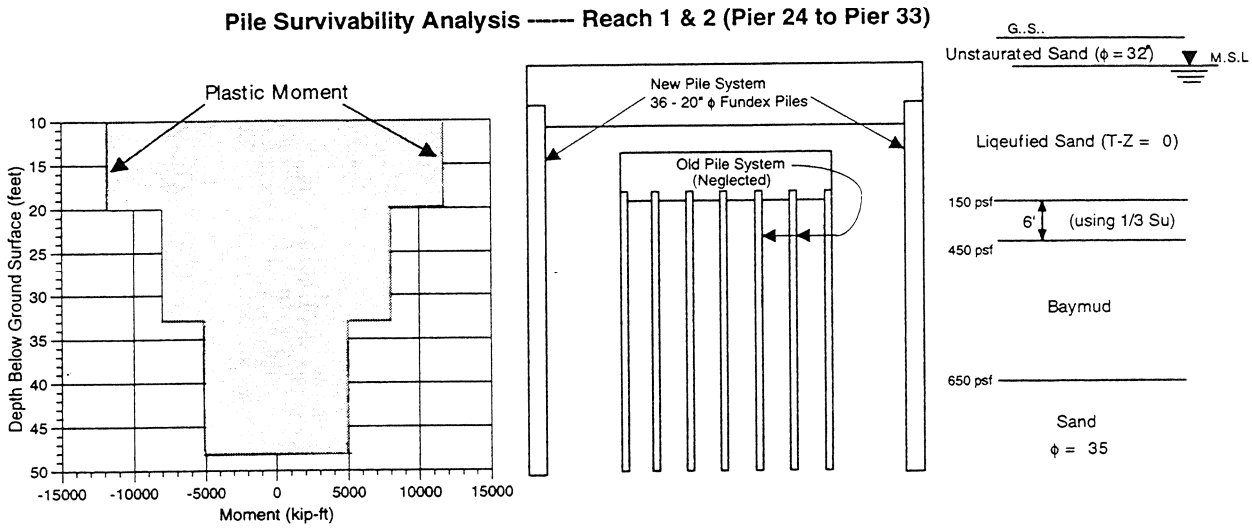

Substructure System Loading and Analysis (three cases evaluated)

Axial: 3240 kips compression
Column Shear: 1725 kip (peak)
Moment: 13,000 kip-ft

Case 1	Case 2	Case3
Driving Force a. 1/2 Pp over full cap length and pile system b. 1/2 inertial load and full axial load c. 7 ft unsaturated fill (ϕ= 32) and 14 ft liq. sand (ϕ= 20).	Same as Case 1 except ϕ=0 and Sr=300 psf for liq. sand . Δl=0.8 in and Δt=1.2 in	Same as Case 2 except full Pp Δl=1.3 in and Δt=1.8 in
Resisting Force a. using Sr=200 psf p-y for liq. sand b. using 1/3 Su p-y for 6 ft baymud below the liq. sand c. full Pa on cap and pile system		
Peak Pile Cap Displacement Δl=0.5 in (longitudinal) and Δt=0.9 in (transverse)		

Fig. 20 Typical Components included in Analysis of New Pile System
(Analysis Involved Studying Three Possible Scenarios for Soil Loading)

ASSESSING VULNERABILITY OF BC GAS PIPELINES TO LATERAL SPREAD HAZARDS

Douglas G. Honegger

Technical Manager
EQE International

ABSTRACT

A systematic review of seismic risks was performed for the BC GAS Lower Mainland natural gas transmission system using a probabilistic approach to define potential earthquake hazards and pipeline response. Potentially liquefiable deposits were identified and mapped into a Geographical Information System (GIS). Lateral spread displacements were made based on the methodology of Bartlett and Youd. There are two very unique features of the BC GAS study. First, finite element analyses were used to define pipeline vulnerability. Second, published data on lateral spread displacements were used to estimate the likelihood of lateral spreading at specific pipeline locations. This study highlights research needs to define lateral spread hazard and is believed to be a model for future seismic risk studies of pipeline systems

INTRODUCTION

A systematic review of seismic risks was completed for the BC Gas Lower Mainland natural gas distribution system. The BC Gas Coastal Pipeline System is located in the Lower Mainland Region of British Columbia. The Lower Mainland covers a triangular shaped area of about 3000 km^2 bounded by the Coast Mountains to the North, the Cascade mountains to the south and southeast, and by the Strait of Georgia to the west. The Fraser River extends through the area and has developed a delta some 31 km long by 24 km wide. Water tables in the study area are typically very close to the surface.

The scope of the pipeline review included transmission and large diameter (greater than NPS 8) intermediate pressure pipelines. All of these pipelines are considered modern steel (post-1950 construction) and are fabricated with full penetration butt-welded joints. The objective of the risk assessment was to identify features of the BC Gas pipeline system that had a potential for long term disruption of gas supply. Given the lack of redundancy in the gas supply pipelines, a very low level of risk was determined to be acceptable. Based on a comparison with other seismic assessments conducted for electric and water utilities and highway bridges, an annual exceedance probability for disruption in the natural gas supply of 0.05% was assigned as an acceptable level of risk.

Past studies of buried gas pipeline systems in the United States and Japan have relied upon earthquake data as a means to predict future performance. In these studies, pipeline damage is expressed in terms of the number of breaks occurring per unit length of pipeline, typically per mile or per kilometer. These vulnerability relationships are limited to the types of pipelines that have been damaged in past earthquakes and the types of earthquake hazard causing the damage. They also suffer from an inability represent variation in pipeline performance with diameter, wall thickness or material yield strength. As a result, a newly installed pipeline system designed to criteria based on earthquake hazards is evaluated as having the same risk as a similar pipeline installed with no consideration for earthquake hazards. A further inadequacy in past studies is their inability to identify specific locations of pipeline damage. Because of these limitations, past evaluations of earthquake performance of buried pipelines only have merit when one is interested in knowing general information such as the total number of repairs. They are totally inadequate for studies of system performance.

Recognizing that past methodologies were incapable of providing the information desired by BC Gas, pipeline vulnerability was based on numerous detailed analysis of generic pipeline configurations. Detailed analysis of pipeline response to large ground deformation has been in use for over 20 years. The analyses are typically carried out using finite element modeling techniques that account for post-yield pipe strains, large deformation and non-linear soil strength characteristics.

Assessment of the likelihood of catastrophic pipeline damage was performed by comparing the capacity of the pipeline to withstand imposed ground deformations with the estimated occurrence of ground motions in excess of this capacity. Inputs to the loading portion of the assessment

included the probability that lateral spreads would occur at a particular point of the pipeline alignment, the orientation of the direction of lateral spreading with respect to the pipeline alignment, computed magnitude of lateral spreading displacements, and lateral spread size. On the capacity side, required information included the pipeline diameter and configuration. Based on a review of the pipeline system, configurations investigated for vulnerability were limited to straight sections, ells and tees.

SEISMICITY OF STUDY REGION

The Lower Mainland Region of British Columbia is located in Seismic Zone 4, which is one of the zones of highest seismic risk as defined in the National Building Code of Canada (NBCC, 1990). The seismicity results from the thrusting of the offshore Juan de Fuca Plate beneath the continental North America Plate. Three basic sources of earthquakes affect the study area:

1. Relatively shallow crustal earthquakes (depths in the order of 20 km);
2. Deeper earthquakes (about 60 km depth) within the subducted plate; and
3. Very large inter-plate earthquakes, often referred to as "mega-thrust" or "subduction" earthquakes.

Earthquakes within the first two categories (intra-plate) have been recorded at regular intervals during the last several decades. The largest are those near Campbell River in 1946 (M = 7.3), near Olympia in 1949 (M = 7.1) and near Seattle/Tacoma in 1965 (M = 6.5). A very large earthquake is also reported to have occurred in central Washington state in 1872. Earthquakes from these sources are commonly included in probabilistic and deterministic seismicity models, such as the NBCC model.

Large subduction earthquakes have not occurred in the region in historic time. However, there is geological evidence that they have occurred in the past (possibly at 300 to 400 year intervals), and the measured accumulation of strain between the tectonic plates suggests that they should be expected in the future. The general consensus is that the upper-board magnitude of a large subduction earthquake would be in the order of 8.0 to 8.5. However, because of the greater epicentral distance from the Lower Mainland, the intensity of ground shaking is not expected to be greater than for the smaller intra-plate earthquakes. The primary concern with respect to the subduction earthquake is the duration of shaking, expected to be in the order of 2 to 3 minutes, or more than five times that of the intra-plate earthquakes.

Earthquake hazard definitions for the BC Gas risk assessment were based upon regional seismic zonation procedures comparable to those used in recent seismic hazard studies for other utilities in the Vancouver region. Probabilistic estimates of earthquake ground shaking hazard were made for selected locations within the BC Gas study area. To avoid overly conservative estimates of failure probabilty, median estimates of seismic hazard were used. This was a departure from the

standard practice in the NBCC which uses ground motions estimated at one standard deviation above the mean.

Probabilistic ground motions formed the input to semi-empirical approaches for estimating lateral spread potential and resulting lateral spread displacement. A separate, deterministic assessment of the potential contribution of a very large event associated with the Cascadia Subduction Zone was also included as part of the earthquake hazard definition process. Estimates of potential lateral spread deformations were obtained using a method based upon the correlation of data from past earthquakes (Bartlett and Youd, 1992). Input required for estimating potential lateral spread displacements on a regional basis included earthquake magnitude, epicentral distance and general soil properties.

Lateral spread movement associated with liquefaction is the principal seismic hazard to the pipelines. Wave propagation and local subsidence was eliminated early in the program as significant seismic hazards because of their inability to produce sufficient levels of strain in the pipe to lead to rupture under the conditions assumed for the risk assessment. The impact of pipeline ruptures on the gas distribution were not investigated as part of this study. An evaluation of the response of the gas distribution system to possible pipeline ruptures at high risk locations is expected to be performed by BC Gas. The systems evaluation is essential to determining the priority for implementation of future mitigative measures.

APPROACH TO EVALUATION OF PIPELINE RISK

The approach used to assess the BC Gas pipeline system incorporated probabilistic estimates of the occurrence of lateral spread movement along a specific portion of the pipeline alignment, the amount of spread displacement, the length of pipeline subjected to lateral spread movement, and the cumulative effect of contributions to risk from various levels of earthquake hazard. The basic approach for identifying portions of the pipeline at risk is described below:

1. Identify portions of the pipeline alignment for which the slopes of the terrain are greater than 0.5%.

2. Determine the subset of the pipeline alignments identified in Step 1 for which lateral spread displacements are estimated.

3. Assign portions of pipeline alignments from Step 2 to one of the basic configurations used in quantifying pipeline vulnerability (straight, ell, or tee). This assignment will also identify whether pipeline vulnerability is governed by lateral spread displacement or the length of pipeline within the lateral spread.

4. For a particular level of earthquake hazard (annual exceedance probability of 0.002, 0.001, or 0.0005), determine the mean lateral spread displacement.

5. Compute the probability that spread displacement or spread length will exceed the failure criteria determined in Step 3.

6. Adjust the probability computed in Step 5 to account for the overall probability of lateral spread occurrence. This is the probability of failure associated with the specific level of seismic hazard.

7. Repeat Steps 4 through 6 for the remaining levels of seismic hazard.

8. Estimate the cumulative probability of failure by adding the products of the failure probabilities at various levels of earthquake hazard and the level of earthquake hazard.

9. Prioritize the locations identified in Step 2 according to the failure probability computed in Step 8.

The above approach accounts for the contribution to overall risk at varying levels of earthquake hazard in a very approximate fashion. Given the considerable level of uncertainty associated with the entire risk assessment process, further refinement was considered unnecessary.

CHARACTERIZATION OF LATERAL SPREAD DEFORMATIONS

A key challenge to the BC Gas study was the definition of lateral spread movements in a fashion suitable for use with the analytical pipeline vulnerabilities. The author knows of no systematic review of the physical size attributes of lateral spreads in past earthquakes. Since these attributes were essential to the BC Gas risk assessment, a limited amount of new research was necessary to characterize the lateral spread phenomena.

A review of the technical literature on lateral spreading revealed that this level of detail had not previously been investigated. For the BC Gas study, an investigation was made to determine if the necessary information could be extracted from reported permanent ground deformations caused by past earthquakes. Two of the most detailed and voluminous studies on lateral spread displacements include papers on observations following the 1964 Niigata and 1983 Nihonkai-Chubu earthquakes in Japan Hamada and O'Rourke (1992).

For the BC Gas study, data from the Niigata and Nihonkai-Chubu earthquakes were reexamined to determine the distribution of lateral spread dimensions and the occurrence of lateral spreading. These data were considered appropriate for extrapolation to the BC Gas study for two reasons. First, the earthquakes had duration of strong shaking that bound those considered applicable for the source mechanisms used to generate ground shaking hazard estimates for the BC Gas study. The Niigata earthquake had a duration of well over 2 minutes with peak ground acceleration on the order of 0.16g. The Nihonkai-Chubu earthquake had duration of approximately 20 seconds with peak ground acceleration on the order of 0.22g. Second, the source mechanisms for the Japanese earthquakes were roughly similar to those used in the BC Gas study. Both earthquakes were related to offshore subduction mechanisms, had relatively large magnitudes (7.5 for Niigata

and 7.7 for Nihonkai-Chubu), and epicentral distances to the areas where displacements were studied of 50 km to 150 km.

From the reported observations of permanent ground deformation in Hamada and O'Rourke (1992), boundaries were drawn around regions judged to be limits of lateral spread deformation. This approach to identification and interpretation of lateral spread boundaries was based on several assumptions:

1. Areas where permanent ground deformations were not measured had no lateral spread movements

2. The total area mapped in the figures in Hamada and O'Rourke (1992) was susceptible to lateral spread movement

3. Large changes in displacement vector direction were indications of lateral spread boundaries

The scope of the BC Gas study did not permit a thorough assessment of the potential impact of these assumptions. The author is hopeful that this paper will spur other investigators to critically examine practical representation of lateral spread hazards necessary for regional risk evaluations.

Past earthquake investigations have identified a dependence of lateral spread boundaries and direction of movement on surface topography and the subsurface profile of the liquefiable stratum. Where additional surface information could be obtained from the maps in Hamada and O'Rourke (1992), it was used to temper judgments on the location of lateral spread boundaries. No attempt was made to characterize patterns in the Hamada and O'Rourke (1992) maps. The pattern of movement within the lateral spread is nearly always a minor issue. This is based on past analytical experience with site specific evaluations of pipeline response to imposed ground deformations.

Information collected for the lateral spread data included longitudinal length, transverse length and circumference. The longitudinal length of the lateral spread was measured as the greatest spread dimension parallel to the predominant direction of spread displacement. Transverse length was measured as the greatest spread dimension perpendicular to the predominant direction of spread movement.

Measurement of Lateral Spread Dimensions

To test the potential uses of previously mapped displacement data, measurements were first collected from mapped displacements along the Shinano River between the Bandai Bridge and Sekiya-Cho. An example of the determination of lateral spread dimensions from the Hamada and O'Rourke (1992) report is provided in Figure 1. The results were plotted in histogram format as shown in Figure 2. It was immediately apparent that there was a strong trend in measurements. This initial investigation into estimating extent of lateral spreads included a population of only 50. These results were encouraging and the process was repeated for other displacement maps for the

two Japanese earthquakes. A total of 156 lateral spread zones were identified. When the measurements from these additional data sources were examined, their distribution(Figure 3) was found to be nearly identical to those collected in the first set of data. The consistency in the results of the interpretation of lateral spread boundaries from the mapping of displacements appears to indicate a large degree of insensitivity to the precision in boundary determination.

The histograms of measurement data were the basis of empirical probability density functions. A cumulative probability curve was constructed for longitudinal spread length as shown in Figure 4. This curve was used to estimate the probability of spread lengths greater than that associated with the pipeline failure criteria. A similar relationship was not needed for the transverse direction as vulnerability was established as a function of ground displacement magnitude for ground movements perpendicular to the pipeline axis.

Estimates of Lateral Spread Coverage

Even in areas experiencing severe lateral spread damage, there is a considerable area in which lateral spread movements are absent. This is an important characteristic when assessing the risk to specific portions of the pipeline alignment. The preferred approach to evaluating lateral spreads occurrence in a region would be to measure the areas within estimated lateral spread boundaries for regions with similar potential for forming lateral spreads. In such a study, similarity would be established by the propensity for liquefaction and the physical geology of the setting (e.g., topography, liquefied layer thickness, slope of the underlying non-liquefied soil deposit).

For the assessment of BC Gas pipelines, a uniform risk factor was estimated based on simplifying assumptions regarding the ratio of lateral spread area to total area. It was assumed that all of the areas ground displacements were mapped had the same potential for lateral spread formation. An upperbound estimate of lateral spread area was related to measured longitudinal and transverse spread dimensions using assuming a rectangular spread shape.

$$A_{LS} = L_T * L_L \tag{1}$$

where A_{LS} = area assigned to lateral spread
L_T = transverse dimension of lateral spread
L_L = longitudinal dimension of lateral spread

The formula is based upon lateral spread boundaries being rectangular in shape. Given the limited amount of data and the assumptions and approximations used, it was decided to use an upperbound value of 34%. The 34% estimate was felt to be applicable to those areas within a kilometer of major river channels or the coast. At other locations, this percentage should be much less. In the BC Gas study, a 50% reduction to 17% was assumed.

PIPELINE VULNERABILITY

The finite element computer code ANSYS (a product of Swanson Analysis Systems, Inc.) was used to perform analyses for the BC Gas pipeline risk assessment. The analysis approach is discussed in detail in numerous references including ASCE (1984) and Honegger (1991, 1992). Pipeline configurations for which vulnerability relationships were computed are illustrated in Figure 5.

The analyses produced a wealth of information regarding pipeline response to ground deformations. A typical plot of strain variation for a 24-inch ell configuration is shown in Figure 6. In all cases, significant pipeline strains are limited to within 50 feet of the application of relative ground deformation, an elbow or a tee. Interpretation of the analysis results was greatly simplified by examining only the point of greatest pipeline strain. A consequence of this approach was that supplemental information that might have led to better extrapolation of vulnerabilities to non-analyzed conditions was not reviewed in detail. This was not felt to be a detriment to the risk assessment since extrapolation was only necessary for 5 of 26 configurations. Four of these cases only involved extrapolation to account for a different soil type.

Soil Resistance Representations in the Analyses

In a regional assessment, such as the one performed for the BC Gas system, there is considerable uncertainty with respect to assigning soil properties. The range of soil loading relationships for the general soil classifications identified for the BC Gas system are illustrated in Figures 5 and 6. These relationships were estimated using the approaches outlined in ASCE (1984) with the following general assumptions:

1. The coefficient of earth pressure at rest was equal to 0.7 for all cases

2. 3 feet of soil cover exists in all cases

3. Soil density was assumed to be representative of unsaturated soil

4. All pipelines are buried with relatively dense sand backfill

Assumptions 1, 3, and 4 were believed to be conservative. Assumption 2 was only expected to be violated at river crossings where much deeper cover exists. However, other conditions assumed for the river crossings result in an overestimate of soil strength and were believed to compensate for any unconservatism regarding the depth of soil cover.

For the analyses, soil resistance relationships were simplified by the use of only three relationships. For axial restraint, only dense sand backfill was assumed. For lateral restraint, two soil restraint relationships were assumed. These were labeled Soil Type I and Soil Type II. Soil Type I was assumed to be representative of the more competent materials in the region. Soil Type II was assumed to be representative of the poorer soil deposits consisting of weak clayey silts and peat deposits.

Criteria for Pipeline Rupture

Rupture of buried, welded steel pipelines is most often a result of severe compressive buckling of the pipe wall. Compressive buckling can result from axial loads or locally high bending moments. Because of the poor understanding of pipe wall response following the onset of compressive wrinkling, considerable conservatism is used in specifying compressive strain values for new design or for evaluation of pipelines for continued long-term service.

For the BC Gas study, we were interested in realistic estimates for relating analytical strains to pipeline rupture. A review of numerous studies and experimental investigations revealed very little useful information on pipeline rupture criteria (ASCE, 1984; Bouwkamp and Stephan, 1973; Meyersohn and O'Rourke, 1991; Meyersohn, 1991, NASA, 1968; Sorenson et al., 1970;). For the BC Gas study, a very simple criterion was used based upon recommendations in ASCE (1984) that compressive strains be kept below about 1/4 to 1/3 the value given by Southwell (1914).

$$\varepsilon_c < 0.6\ t/R \qquad (2)$$

where: ε_c = theoretical compressive strain for onset of wrinkling
t = pipe wall thickness
R = pipe radius

Equation 2 was used to represent the median value of longitudinal compressive strain associated with pipeline rupture. Strains corresponding to 10% and 90% likelihood of rupture were assumed to be equal to 1/3 and 2 times the value given by equation 2, respectively.

Analyses were not performed for the case of a straight run of pipeline subjected to relative ground deformation in a direction parallel to the pipeline. Instead, estimates of pipeline capacity were made by computing the length of lateral spread movement necessary to produce various stress levels in the pipeline. Stress levels of σ_y, $1.5\sigma_y$, and $2\sigma_y$ were assumed to correspond to 10%, median and 90% chances of pipeline rupture, respectively. A similar approach was taken for analyses in which longitudinal soil loading on the pipeline was modeled as a force acting on an ell or tee. The force associated with pipeline rupture was converted to an equivalent length of pipeline subjected to longitudinal soil movement using the appropriate axial soil resistance relationship.

CONCLUSIONS

The approaches outlined above were successfully employed in the evaluation of the BC Gas transmission pipeline system. We were able to rank specific segments of the pipeline system and identify the basis for specific vulnerabilities. Results from the study are being used to prioritize allocation of resources for seismic improvement measures and to augment system planning.

The rupture criteria used in the BC Gas study resulted in the determination that nearly all pipelines could withstand at least 4 meters of lateral movement in a straight configuration. This conclusion was partially tested following the study when a non-seismic ground failure in the vicinity of one pipeline produced approximately 3.5 meters of lateral ground movement over approximately 30 meters of pipe length. No leakage occurred in the pipe.

Because of the lack of existing methodologies to provide sufficient practical information, several unique approaches were developed during the project. The most important technical by-product of the BC Gas study was the utilization of mapped ground deformation information to quantify lateral spread hazard in a manner that is practical for use in a risk assessment. It is estimated that most other investigations of lateral spread risk for regions without previous evidence of lateral spread movement may overestimate the likelihood of occurrence by a factor of 3 to 6.

Development of the methodology used in the BC Gas study was driven by the need to provide needed information to a client. There is clearly a need for more investigation to understand the impact of assumptions used in the study and improve upon the simplified approaches taken. It is hoped that more research resources will be directed to the refinement of the methodology described in this paper.

ACKNOWLEDGEMENTS

I would like to acknowledge BC Gas. Ltd for granting permission to describe the approach taken in assessing the seismic risk to their gas supply system. Also, without the support and suggestions of project team members, the innovations employed in the BC Gas study would not have been possible. My special thanks go to T.L. Youd (Brigham Young University), T.D. O'Rourke (Cornell University), T.P. Fitzell (Golder Associates, Ltd.) and C.B. Crouse (Dames and Moore, Inc.).

REFERENCES

1. ASCE, 1984, Seismic Design Guidelines for Oil and Gas Pipeline Systems, Gas and Liquid Fuel Lifelines Committee.

2. Bartlett, S.F. and T.L. Youd, 1992, "Empirical Analysis of Horizontal Ground Displacement Generated by Liquefaction-Induced Lateral Spreads," Technical Report NCEER-92-0021, National Center for Earthquake Engineering, State University of New York at Buffalo.

3. Bouwkamp, J.G. and R.M. Stephan, 1973, "Large Diameter Pipe Under Combined Loading," ASCE Journal of Transportation Engineering, vol. 99, no. TE3.

4. Hamada, M. and T.D. O'Rourke (editors), 1992, "Case Studies of Liquefaction and Lifeline Performance During Past Earthquakes: Japanese Case Studies," Technical Report NCEER-92-0001, vol. 1, National Center for Earthquake Engineering, State University of New York at Buffalo.

5. Honegger, D.G., 1991, "Application of Lateral Spread Hazard Definition Using Liquefaction Susceptibility Index to the Design of Buried Pipelines," Lifeline Earthquake Engineering, Proceedings of the Third U.S. Conference, Michael Cassaro ed., Technical Council on Lifeline Earthquake Engineering Monograph No. 4.

6. Honegger, D.G., 1992, "Research Needs Related to Detailed Evaluation of Pipeline Response to Large Ground Deformations," Proceedings, Fourth Japan-U.S. Workshop on Earthquake Resistant Design of Lifeline Facilities and Countermeasures for Soil Liquefaction, San Francisco, California, Technical Report NCEER-92-0019, National Center for Earthquake Engineering, State University of New York at Buffalo.

7. Meyersohn, W.D. and T.D. O'Rourke, 1991, "Pipeline Buckling Caused by Compressive Ground Failure During Earthquakes," Proceedings, Third Japan-U.S. Workshop on Earthquake Resistant Design of Lifeline Facilities and Countermeasures for Soil Liquefaction, San Francisco, California, Technical Report NCEER-91-0001, National Center for Earthquake Engineering, State University of New York at Buffalo.

8. Meyersohn, W.D, 1991, "Analytical and Design Considerations for the Seismic Response of Buried Pipelines," Masters Thesis, Cornell University.

9. NASA, 1968, "Buckling of Thin-Walled Circular Cylinders, NASA Space Vehicle Design Criteria (Structures), NASA SP-8007.

10. National Building Code of Canada (NBCC), 1990

11. O'Rourke T.D. and M. Hamada, (editors), 1992, "Case Studies of Liquefaction and Lifeline Performance During Past Earthquakes: United States Case Studies," Technical Report NCEER-92-0001, vol. 2, National Center for Earthquake Engineering, State University of New York at Buffalo.

12. Sorenson, J.E., R.E. Mesloh, E. Rybicki, A.T. Hopper, and T.J. Atterbury, 1970, "Buckling Strength of Offshore Pipelines," Summary Report, vol. 1, Offshore Pipeline Group, Battelle Memorial Institute.

13. Southwell, R.V., 1914, Philosophical Transactions, Royal Society, London, Series A, vol. 213.

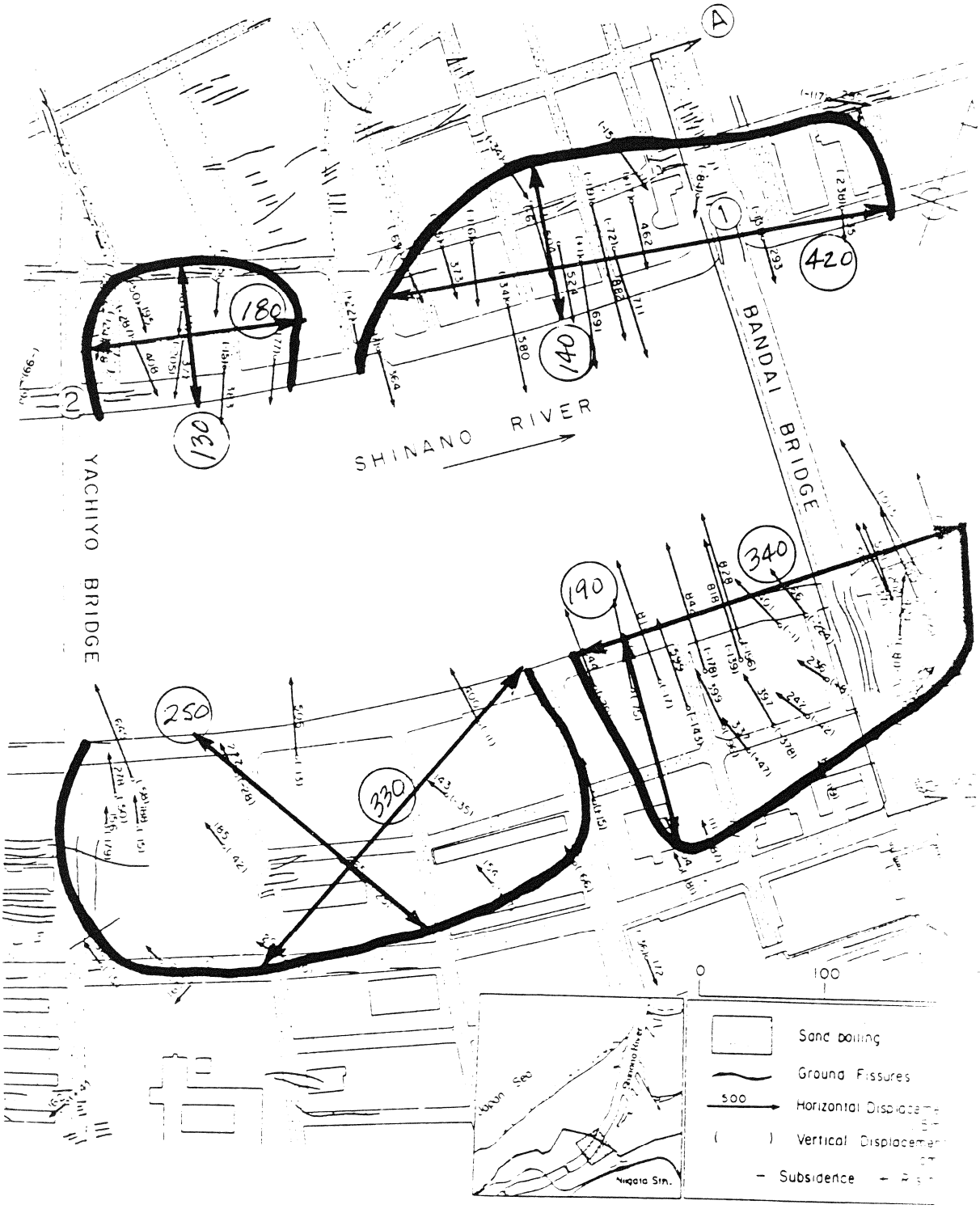

Figure 1: Example Extraction fo Lateral Spread Information

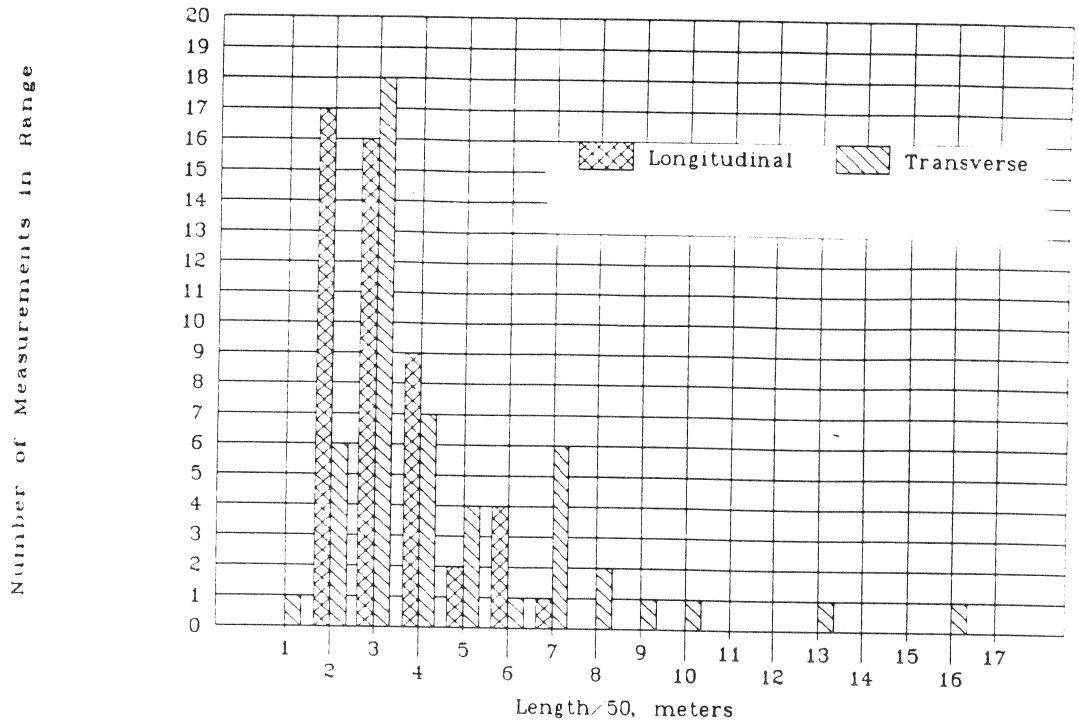

Figure 2: Distribution of Lateral and Transverse Dimensions for 50 Lateral Spread Zones

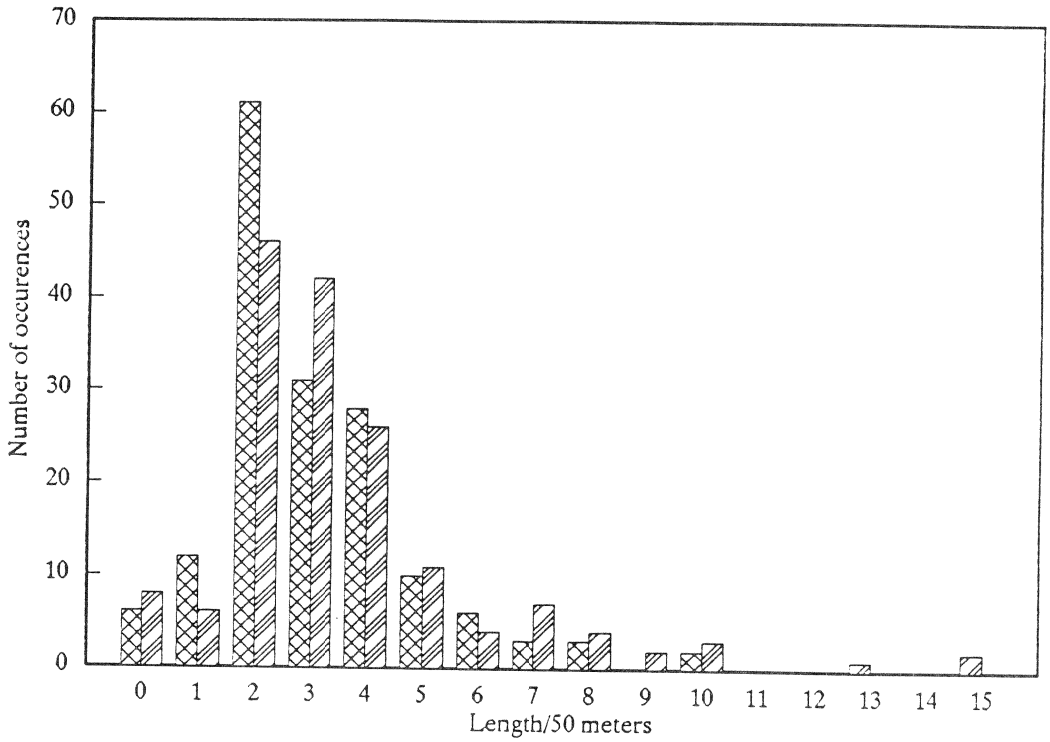

Figure 3: Distribution of Lateral and Transverse Dimensions for 150 Lateral Spread Zones

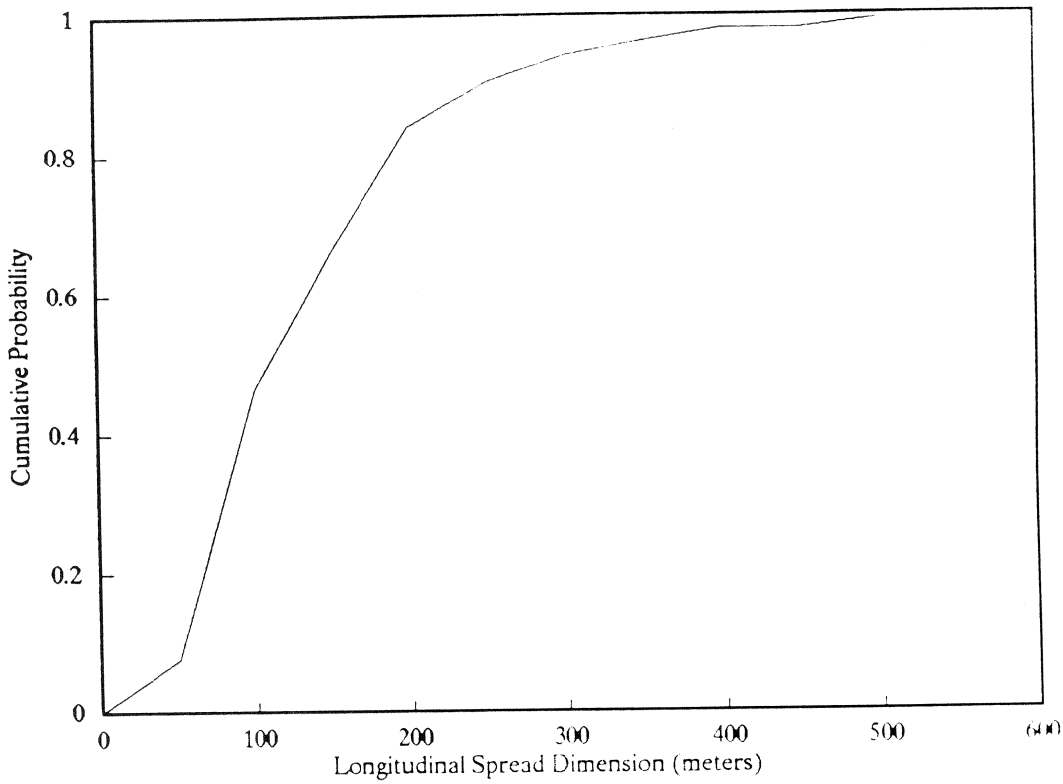

Figure 4: Probabilistic Density Function for Lateral Spread Longitudinal Dimension

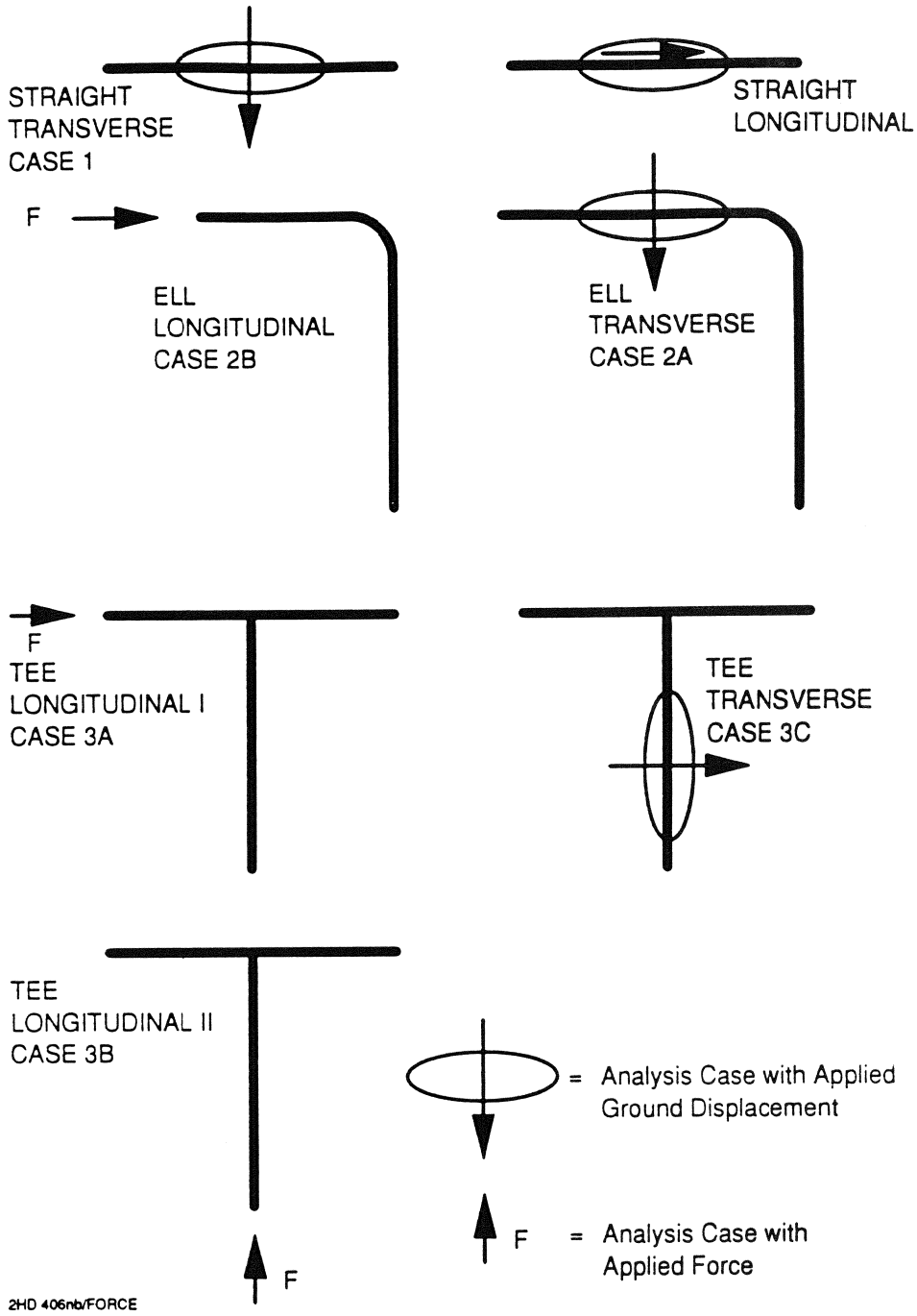

Figure 5: Pipeline Configurations Analyzed for BC Gas Study

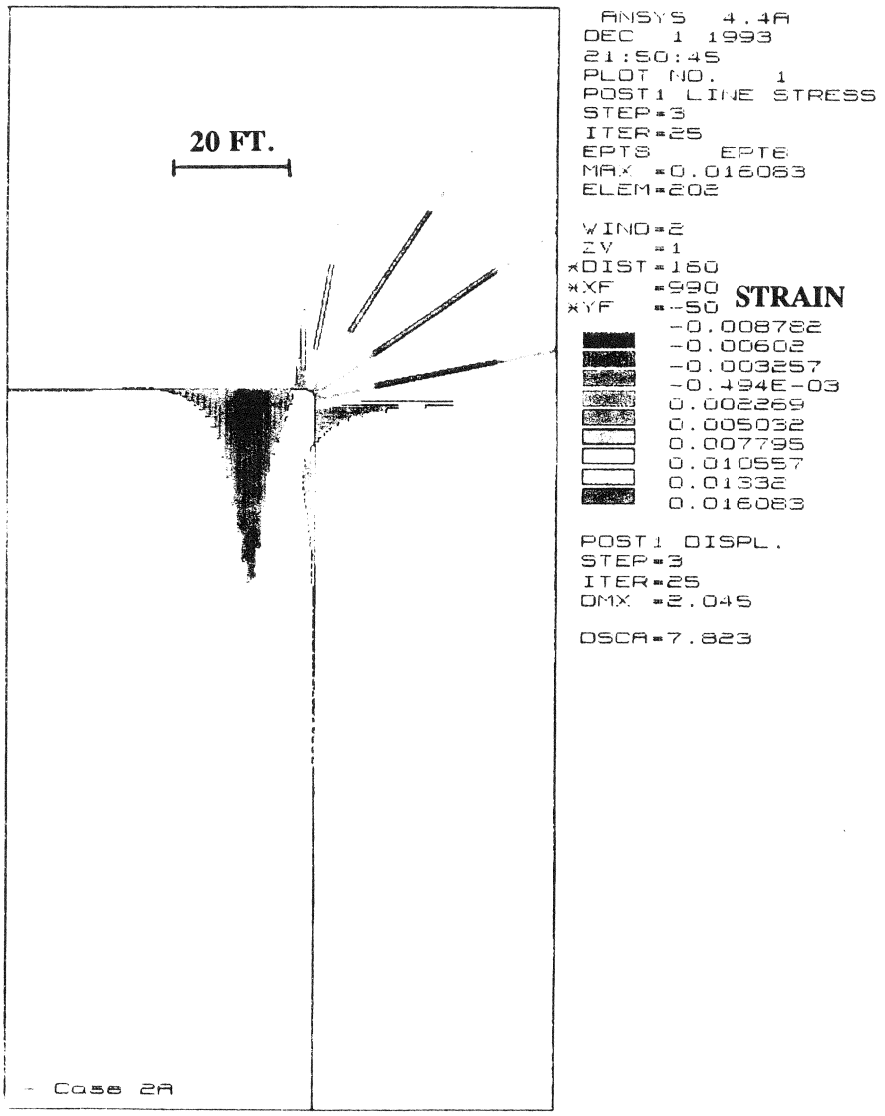

Figure 6: Example of Analysis Output for 24-inch Diameter Ell Configuration

PIPELINE DESIGN AGAINST SAND LIQUEFACTION IN ISLA DEL CARMEN, MEXICO

VENANCIO TRUEBA-LÓPEZ[1] AND RAUL FLORES-BERRONES[2]

[1]Institute of Electrical Research (IIE), Mexico
[2]Mexican Institute of Water Technology (IMTA), Mexico

ABSTRACT

The seismic design analysis for the sewage pipeline system in the city of Carmen at "Isla del Carmen", in the State of Campeche, Mexico, is presented. This city is founded on very fine loose silty sand deposits, in an area where the groundwater level is very shallow. Due to the seismic risk of this area, it was necessary to carry out cyclic triaxial tests to measure the susceptibility of soil liquefaction, and to study the stress and strain conditions of the segmented pipelines. These pipelines made of asbest-cement, varied between 60 to 180 cm in diameter. The results of these studies showed that the liquefaction of the soil deposits in that area will not occur under the effects of an earthquake of magnitude in the order of 6.4. Regarding the effects of ground strain and curvature on pipelines, the results obtained indicated that the expected displacements during an earthquake can be absorbed by the displacement capacity of the pipeline joints.

INTRODUCTION

The sewage pipeline system of Ciudad del Carmen, Mexico, represents more than 20 km of mains and more than 100 km of networks. The pipelines are made of asbest-cement and have a diameter that varies between 0.60 to 1.80 m. These pipeline system is actually under construction.

Since the groundwater level is very shallow (0.5 to 1.5 m), and a relatively thick loose fine silty sand deposit was encountered at the site, it was necessary to verify if an earthquake motion could cause liquefaction of this deposit or induce ground displacements that might yield pipeline displacements larger than those allowed by the pipeline joints.

Therefore liquefaction analysis was performed in order to investigate and evaluate the seismic risk potential of the loose silty fine sand deposit. In a first step, deterministic and probabilistic approaches were used. Further, an experimental program was carried out in order to assess the crucial parameters of soil behavior when subjected to cyclic loading. Thus, the results provided

essential information in order to decide if special construction methods should be applied to alter the soil characteristics and to prevent liquefaction, or design the sewage lifelines for earthquake effects.

The analyses included the effects of ground strain and curvature on pipelines and joints subjected to movements caused primarily by wave propagation during the earthquake. Special considerations were taken to design the junction between pipes and buried structures, such as inspection-wells and pumping plants.

SITE DESCRIPTION

Ciudad del Carmen is located at the Campeche State of Mexico (91°45'W and 18°45'N). This city has a particular importance because it is an access to the petroleum activities in the Campeche Sonde, where PEMEX takes out about 65% of the total national production. The city was founded on the Isla del Carmen, near the west mouth of the Terminos Lagoon, which ends in the Gulf of Mexico. The batimetry is about 20 cm/km at this point, and the topographic contour of the city is noticeably flat, with altitudes typically less than 2 m above the sea level. Pluviometry is high, and can reach 419 mm in 24 hours, with 1800 mm at a year. The wind velocity can be as strong as 160 km/h, and the sea level can raise between some centimeters to 0.5 m during calm and storm conditions, respectively.

From a tectonic point of view, the Isla del Carmen is located near the boundary between the Yucatan Platform at the north, the Massif of Chiapas at the south, and the Macuspana Basin of the flexured Reforma-Akal Calcareous Belt at the west-northwest. The island is closely from a very complex tectonic ocean deep named the Paleocanyon of Chilam formed during the Pleistocene ocean regression, which is plenty of normal and inverse faults, angular discordances, and pronounced compressional folds. At about 50 km from the island there is a group of normal faults, caused by compressional stresses, with general alignment NW-SE. It has been assumed that there is 650 m of Quaternary sediments at this place. The tectonic characteristics on the one hand, and the influence of strong earthquakes in the Pacific Subduction zone on the other, leads to put Ciudad del Carmen into the seismic zone B of Mexico; according to the last Seismic Risk Zonation for Mexico, the maximum ground horizontal acceleration (a_{max}) is 0.09g, with a maximum ground velocity (V_{max}) of 14.8 cm/sec.

STRATIGRAPHY

Based on 17 boring performed for this investigation, the typical stratigraphy between the ground level and the explored depth of 18 m, can be described as follows.

The most shallow strata consists of 2 to 3 m thick of light brown calcareous fine to medium SAND (SP), with 3 to 12% of gravel (<2") to sand sized intact and fragmented shells, and 3

to 5% of low compressibility silt, mica (SP-SM). Sometimes, this strata presents a very high shell content and must be classified as shell layer (GP, GM). Relative density is erratic from medium to dense, and loose in few thin lenses. The unit weight was estimated to be in the range of $17.2 \leq \gamma_m \leq 19.6$ kN/m^3, as computed from moisture content (w) and gravity of solids (G_s).

Underlying the most shallow strata it is a deposit of dark greenish gray SILTY FINE SAND ($d_{50} \leq 0.15$ mm), with some thin lenses of intact and fragmented little shells (5%, $d < 8$ mm); the silt content is 15 to 39% of ML. At someplace there are thin layers of soft dark and light greenish brown CLAY (CH) with traces of fine sand, shells and colloidal organic matter. This deposit extend up to 7.2 to 9.8 m depth, thus with a variable thickness between 3.9 to 7.3 m. Relative density is also erratic: medium to loose at the west side of the city, medium to dense at the East side, and otherwise it is at a loose to very loose state. The unit weight of this soil was assumed to be $\gamma_m = 17.9$ kN/m^3.

Below this strata and up to 14 m depth, there is a sequence of soft and very soft light greenish gray CLAY (CH) layer with lenses of soft SILTY CLAY and loose CLAYEY SAND. For a depth greater than 14 m and up to 20 m, the soil is similar in nature but its consistency is firm to hard. The unit weight was measured in the range of $1650 \leq \gamma_m \leq 1875$ kg/m^3 between 9 and 14 m, and in the range of $18.6 \leq \gamma_m \leq 20.1$ kN/m^3 below 14 m. Undrained strength was measured as $\phi_{uu} = 0°$ with $24 \leq c_{uu} \leq 42$ kN/m^2 between 9 to 14 m, and $\phi_{uu} = 0°$ and $c_{uu} \geq 136$ kN/m^2 for depth over 14 m. Fig 1 shows the stratigraphy at boring SM-9.

LIQUEFACTION ANALYSIS

Lateral spread due to soil liquefaction could be triggered when the layers slope is over 0.5 to 1% [Youd and Perkins (1978), Nyman *et al.* (1984), and Flores-Berrones and O'Rourke (1992)]. However, the topographic and geologic characteristics of Ciudad del Carmen allow to assume that this kind of failure has a very little probability to occur, because the ground slopes are really very flat. On the other hand, liquefaction of the saturated sand deposit may induce ground settlements and/or pipe flotation during earthquake, even for flat ground, and then, liquefaction susceptibility of the sand deposit must be analyzed.

Hamada *et al.* (1985) report that gas and sewage pipelines damage at Noshiro City was relatively reduced where the ground surface is almost flat and the permanent displacements were very small. These authors report also that severe damage on lifelines was observed where lateral spread take place and the permanent ground displacement became large. Kawashima *et al.* (1985) report that for main sewage pipes at Noshiro City failures were concentrated at reinforced concrete pipes joints of tongue and groove joint type, with 95% of failures for pipes with diameter between 6 and 60 cm; a 67% of pipe failures was observed for an embedment less than 1.8 m; while a 72% of joint failures was observed between 1.5 to 3 m depth.

Liquefaction susceptibility has been analyzed in regarding the following fundamental aspects of the problem: (a) the Seed procedure based on standard penetration test and for the earthquake to considered in design; a liquefaction susceptibility safety factor was computed at different depths. (b) Cyclic load undrained triaxial tests with pore pressure measurement were carried out on reconstituted and "intact" soil samples with different fines content. (c) In-Situ recognition and inspection of ancient buildings in the city as well as observation damages during past earthquakes.

The susceptibility analyses are based principally on the works of Seed and Idriss (1971, 1982), Seed (1979, 1987), Seed *et al.* (1983, 1984), Castro (1975), Tokimatsu y Yoshimi (1983, 1984) and Tokimatsu andy Seed (1987), as well as others reported in the references.

Seed and Idriss assume that for practical purposes the average shear stress (τ_{av}) due to the earthquake is about 65% of the shear stress computed at the maximum horizontal ground acceleration. Thus, it can be obtained as follows,

$$\tau_{av} \cong 0.65 \frac{\gamma_m z}{g} a_{\max} r_d \qquad (1)$$

where **g** is the acceleration of gravity, **z** is the ground depth under consideration, and $\mathbf{r_d}$ is a stress reduction factor recommended by Seed and Idriss (1971, 1982) to take into account the soil deformation during the shaking.

Data from the Geophysics Institute of UNAM as well as those of seismic risk studies performed by Guerra and Esteva (1978), Guzmán (1982) and Chávez (1987) for the Campeche Bay, lead to suppose that seismic magnitude could be in the order of 6. Moreover, a very recent seismic risk study (MDOC, 1993) allows to assume that a_{max} is 0.09g, for a return period of 100 years.

Seed *et al.* (1984) suggest to use a scale coefficient ($\mathbf{r_m}$) in order to take into account the earthquake magnitude for a particular site and to allow using of charts normalized to a magnitude of 7.5. For this case $\mathbf{r_m} = 1.2$, when considering the Jáltipan-Coatzacoalcos, August 29, 1959 earthquake, which had a magnitude of 6.4 at the epicentral area.

In order to take into account several factors which affects the in situ **N** value obtained in the standard penetration test, correction factors were applied based on the works of Tokimatsu and Yoshimi (1983, 1984), Skempton (1986), and Liao and Whitman (1986). The in situ **N** value was normalized to a vertical effective soil stress of 98.1 kN/m^2; and the other factors were also considered by reducing the obtained values by a factor of 0.75. Furthermore, in order to include the fines particle influence on liquefaction, as has been pointed out by Seed *et al.* (1984) and Ishihara (1985), equivalent blows could be added as $\Delta\mathbf{N_1}$, which might be computed as a function of the soil fines content (**F**), as: $\Delta\mathbf{N_1}=0$; $=0.6(\mathbf{F}-5)+1$; and $=0.1(\mathbf{F}-10)+4$; for $\mathbf{F}<5\%$, $5\leq\mathbf{F}\leq10\%$, and $\mathbf{F}\geq10\%$, respectively. $\mathbf{N_1}$ was then corrected according with

$$(N_1)_{60} = 0.75 \left(\frac{167}{69 + \gamma_m z} \right) N + (\Delta N_1) \quad (2)$$

where γ_m is the unit weight of soil (kN/m^3) and **N** is the blow count, at a depth **z** (m).

The equation leading to compute the susceptibility factor ($\mathbf{F_L}$) at a depth **z**, as it has been used for the analysis presented in this paper, can be expressed as follows

$$F_L = \frac{r_m \tau_{hz}}{\tau_{av}} \quad (3)$$

where (τ_{hz}) is the shear stress to induce liquefaction.

Alternatively, the probabilistic criteria proposed by Liao, Veneziano and Withman (1986), have been used in order to have an estimate of the liquefaction probability $\mathbf{P_L}$. The resulting equation for Ciudad del Carmen is as follows,

$$P_L = \frac{1}{1 + \exp\left(- \left(10.167 + 4.1933 \ln\left(0.65\, a_{max} \frac{\sigma_z}{\sigma_z'} \frac{r_d}{r_m} \right) - 0.24375\, (N_1)_{60} \right) \right)} \quad (4)$$

where σ_z' and σ_z are the effective and total overburden stresses, respectively.

RESULTS

Liquefaction susceptibility and probability have been estimated for selected borings and the results are presented in fig 2. This figure shows that only in the SPE-2 boring the liquefaction susceptibility factor was less than 1.1, considering that this is a reasonable minimum value to assume that no liquefaction take place. For this case the liquefaction probability was $\mathbf{P_L}$=0.39, that is very near to the maximum acceptable value of 0.40. Alternatively, Ishihara (1985) proposed that $\Delta \mathbf{N_1} = \mathbf{6.5}\, log_{10}\mathbf{N}$, and in this case the factor $\mathbf{F_L}$ will be 1.47.

Because the exposed method can be used as a reference or for estimation purposes only, a laboratory test program was proposed and carried out in order to confirm these preliminary results. Silty sand samples recuperated by thin wall sampler, and reconstituted soil samples with

different densities and fines content were tested. Cyclic load undrained triaxial tests with pore pressure measurements were performed and representative results are presented herein in table 1 and in fig 3. In order to have reliable pore pressure measurements, relatively high backpressure was applied to keep a Skempton B parameter greater than 0.98 in all cases. After pore pressure stabilization, the samples were subjected to 30 cycles of load as follows: 15 cycles with a cyclic deviatoric stress (q_C) selected to be at least twice those stress induced in the subsoil during the earthquake. For the last 15 cycles q_C was incremented up to 6 times the induced stress.

The results showed soil dilatance for samples recuperated or prepared with fines content varying from 15 to 90%. Thus, these results as well as those obtained by the empirical method based on SPT and by the probabilistic method, allow to assume that liquefaction of the loose silty sand deposit will not occur under the effects of an earthquake of magnitude of 6.4.

It is believed that the sharp angles of the sand and silty grains, together with the carbonate content of the soil deposits, are factors that contributed to these results.

EFFECTS OF GROUND MOTION

The effects of ground strain and curvature on pipelines, in addition to relative joint displacement and rotations were analyzed for Rayleigh waves for which the dispersion curve was computed as show in fig 4. Furthermore, the particle velocity at Isla del Carmen has been estimated as $\mathbf{V_{max}}$ = 14.8 cm/sec, and the ground acceleration as a_{max} = 88.3 cm/sec^2. As the pipelines will be embedded at a depth greater than 1.8 m, the soil-pipe interaction was taken into account.

A simplified analysis was also performed considering the propagation of a plane wave traveling in the longitudinal and transverse axes of the pipeline. In this analysis, it is assumed that the pipe has no stiffness or mass and, hence, the strain and curvature are the same as those experimented by the soil (*i.e.* an analysis without soil-pipe interaction). Thus, the axial strain of the pipe is equal to the maximum free-field ground strain, ϵ_g, due to the seismic waves and was computed as

$$\epsilon_g = \pm \frac{V_{max}}{C_L} \tag{5}$$

where $\mathbf{V_{max}}$ is the maximum ground velocity and $\mathbf{C_L}$ is the apparent longitudinal propagation velocity of the seismic waves.

The upper bound for the curvature of the pipeline corresponds to the maximum soil curvature, θ_g, and has been computed as

$$\theta_g = a_{max} / C_T^2 \tag{6}$$

where C_T is the apparent transverse propagation velocity of the seismic waves.

In order to compute the effects on the pipeline joints spaced at a distance L_p, it is assumed that the pipeline consists of rigid segments at which the middlepoints move with the soil. Thus, the maximum relative motion-rotation between two points on the ground will be entirely accommodated by movement at the joints. Hence the upper bound of the maximum joint displacement (Δ_J) was conservatively computed as

$$\Delta_J = \epsilon_g L_p = \pm \frac{V_{max} L_p}{C_L} \tag{7}$$

And the upper bound of the maximum joint rotation (θ_J) was conservatively computed as

$$\theta_J = \theta_g L_p = \frac{a_{max} L_p}{C_T^2} \tag{8}$$

On the other hand, if the relative displacements between the pipeline and the ground are taken into account, the resultant force due to the friction at the interface (t_U) during the earthquake can be computed as

$$t_U = \pi D \left(\frac{1 + K_o}{2} \right) \gamma_m H \tan\delta \tag{9}$$

where **D** is the external pipe diameter computed as 1.08 times the internal or nominal diameter of the pipe; K_0 is the horizontal earth pressure coefficient at rest which was taken as 0.63 for ϕ=22°; γ_m is the unit weight of the soil overlaying the pipe (18.64 kN/m^3); **H** is the backfill thickness; and δ was equal to 20° for 0.9 tan ϕ.

According with O'Rourke and El-Hmadi (1985 and 1988), the maximum length over which the relative displacement between the pipe and soil takes place (L_S) can be computed as

$$L_S = \frac{\epsilon_g E_p A_p}{t_U} \tag{10}$$

where $\mathbf{E_p}$ is the Young's modulus of the pipe (25,000 MN/m^2); and $\mathbf{A_p = \pi t_p(D_e - t_p)}$, is the transversal area of the pipe, with $\mathbf{t_p}$ and $\mathbf{D_e}$ the pipe thickness and its external diameter respectively.

Assuming that the wave propagation is harmonic, the maximum strain occurs at each 1/4 of the wave length. Thus, the pipe strain will be equal to ϵ_g, and can be computed as follows,

$$\epsilon_a = \frac{\lambda \, t_U}{4 \, E_p \, A_p} \tag{11}$$

where λ is the wave length in meters (m).

The results obtained for pipes of nominal diameter of 45 and 110 cm, when the soil-pipe interaction is taken into account for different thickness of the backfill ($\mathbf{H_{BACKFILL}}$ of 1.5, 3, 3.5, 4, 4.5 and 5 m thick), together with those obtained without soil-pipe interaction, are show in fig 5.

From fig 5, the longitudinal (or axial) strain for design of a pipeline with a nominal diameter **D**, corresponds to the intersection between the curves obtained with and without soil-pipe interaction.

For the pipelines with flexible joints, considering that the longitudinal and transverse Rayleigh waves velocity is 140 m/sec, and for a pipe length of $\mathbf{L_p}$ = 5 m, the maximum estimated displacement in the joints are $\Delta = \pm 5.3$ mm, and the rotation $\theta_J = 0.01°$.

The asbest-cement pipelines for Ciudad del Carmen consist of straight pipes class B-7.5, jointed spigot-to-spigot and separated 10 mm. The segments are jointed using a straight cylindrical pipe coupling with special rubber gasket joints.

The manufacturer had determine experimentally that for this kind of flexible pipe coupling the allowable relative displacements and rotation have the magnitudes indicated in table 2. The pipes have a longitudinal compressional strength of 50 MN/m^2, a flexure permissible strength of 25 MN/m^2 and, and a permissible internal pressure of 2.5 MN/m^2.

Regarding the values reported in table 2, the results obtained show that the expected displacements during the earthquake can be absorbed by the displacement capacity of the pipeline joints, assuming that the maximum total displacement in the joint is less or equal than 5 mm.

From the obtained results, it was concluded that the selected pipelines constitute an economical and secure solution for the sewage pipeline system of the city.

CONCLUSIONS

The main conclusions of this paper are the following:

1) The uncertainties related to the possibility of occurring soil liquefaction in the loose silty sand deposits of Ciudad del Carmen, Mexico, where a sewage pipeline system of asbest-cement has to be installed, were dissipated after carrying out a soil liquefaction analysis, and performing several cyclic undrained triaxial tests with both, undisturbed and reconstituted soil samples; these studies were complemented by a probabilistic approach to know the susceptibility of liquefaction. The experimental results as well as those obtained by the empirical method based on SPT and by the probabilistic method, allow to assume that liquefaction of the loose silty sand deposit will not occur under the effects of an earthquake of magnitude of 6.4.

2) The results of the cyclic triaxial tests showed soil dilatance for samples recuperated or prepared with fines content varying from 15 to 90%. It is believed that the sharp angles of the sand grains and the medium (15%) to high (78%) content of silt, together with the carbonate ($CaCO_3$) content of the soil deposits, are factors that effectively contributed to these results.

3) For the pipelines of asbest-cement with flexible joints, considering a backfill of 3 m and a maximum particle velocity of 14.8 cm/sec, a maximum ground acceleration of 88.3 cm/sec^2, a Rayleigh wave velocity of 140 m/sec, and a pipe length of 5 m, the estimated maximum displacement in the joints was 5.3 mm, and the maximum rotation of 0.01°. According to the manufacturer information, give in table 2, those values are well bellow the permissible ones. Therefore, the selected pipelines for the sewage system in Ciudad del Carmen might be considered, from the seismic point of view, on the safe side.

4) More refined mathematical modelling of the soil-pipe interaction could be possible if the mechanical behavior of the joints of the asbest-cement pipes is correctly taken into account. In order to do this, experimental results on the stress-strain relationship and stiffness, obtained from tests carried out on real joints subjected to similar forces or displacements as it will be under the effects of the earthquake for design, are needed. The authors expect that, with the collaboration of the manufacturer, a research program could be undertaken in this direction in the very near future by the National Water Commission of Mexico (CNA).

ACKNOWLEDGEMENTS

The authors want to express their gratitude to the authorities of the National Water Commission of Mexico (CNA), for the opportunity to participate in the solution of this project.

REFERENCES

Castro, G. (1975). Liquefaction and cyclic mobility of saturated sands. *J. of the Soil Mechanics and Foundations Div., ASCE.* **101**(SM6), pp. 551-569.

Chávez, M. (1987). *Análisis de riesgo sísmico en varios sitios de la Bahía de Campeche.* I.I.-UNAM and Proceedings of the Mexican Congress on Earthquake Engineering VIII y IX.

EUREKA, S.A. *Tubería de Fibrocemento para Alcantarillado.* Technical Bulletin. Also: Personal communication from Mr. V. Serrano, Manager of The Development and Hydraulic Operation Department.

Flores-Berrones, R. and M. O'Rourke (1992). Seismic effects on underground pipelines due to permanent longitudinal ground deformations. *Proceedings from the Fourth Japan-U.S. Workshop on Earthquake Resistant Design of Lifeline Facilities and Countermeasures for Soil Liquefaction.* Ed. M. Hamada and T.D. O'Rourke. Technical Report NCEER-92-0019. **I**. pp. 465-480.

Guerra, R. y L. Esteva (1978). *Espectros de diseño sísmico en Paraíso, Tab. y Cd. del Carmen, Camp.* I.I.-UNAM and Proceedings of the Mexican Congress on Earthquake Engineering VIII y IX.

Guzmán, R.A. (1982). *Estudio de riesgo sísmico para la Bahía de Campeche, Golfo de México.* I.I.-UNAM and Proceedings of the Mexican Congress on Earthquake Engineering VIII y IX.

Hamada, M, K. Kubo, and K. Saito (1985). Large ground displacement and buried pipe failure by soil liquefaction during 1983 Nihonkai-Chubu earthquake. *Proceedings of the 1985 Pressure Vessels and Piping Conference: Seismic Performance of Pipelines and Storage Tanks.* Ed. S.J. Brown, ASME, New Orleans, junio 23-26, PVP-**98**(4), pp. 11-24.

Ishihara, K. (1985). Stability of Natural Deposits During Earthquakes. State-Of-The-Art. *Proceeding of The XI Int. Conference on Soil Mechanics and Foundation Engineering,* ISSMFE, San Francisco, CA. **1**(7), pp. 321-376.

Kawashima, K., N. Obinata, K. Gotoh, and T. Kanoh (1985). Seismic damage of sewage pipes caused by the 1983 Nihonkai-Chubu earthquake. *Proceedings of the 1985 Pressure Vessels and Piping Conference: Seismic Performance of Pipelines and Storage Tanks.* Ed. S.J. Brown, ASME, New Orleans, junio 23-26, PVP-**98**(4), pp. 139-145.

Liao, S.S.C. and R.V. Whitman (1986). Overburden correction factors for sand. *J. of the Geotechnical Eng. Div., ASCE.* **112**(3), pp. 373-377.

Liao, S.S.C., D. Veneziano, and R.V. Whitman (1988). Regression Models for Evaluating Liquefaction Probability. *J. of the Geotechnical Eng. Div., ASCE.* **114**(4), pp. 389-411.

MDOC (1993). Manual for the Design of Civil Works. Chapter C.1.3 Earthquake Engineering Design. Federal Commission of Electricity. A new revised version by J. Avilés, J. Avila, R. Gómez, M. Ordáz y V. Trueba, (in spanish).

Nyman, D.J. *et al.* (1984). *Guidelines for the seismic design of oil and gas pipeline systems.* Prepared by the Committee on Gas and Liquid Fuel Lifelines of the ASCE Technical Council on Lifeline Earthquake Engineering, ASCE, Grant CEE-7923559, 471 p.

O'Rourke, M.J., G. Castro, and I. Hossain (1984). Horizontal soil strain due to seismic waves. *J. of Geotechnical Engineering, ASCE.* **110**(9), pp. 1173-1187.

O'Rourke, M.J. and K. El-Hmadi (1985). Earthquake ground wave effects on buried piping. *Proceedings of the 1985 Pressure Vessels and Piping Conference: Seismic Performance of Pipelines and Storage Tanks*. Ed. S.J. Brown, ASME, New Orleans, junio 23-26, PVP-**98**(4), pp. 165-171.

O'Rourke, M.J. and K. El-Hmadi (1988). Analysis of continuous buried pipelines for seismic wave effects. *Int. J. on Earthquake Engineering and Structural Dynamics*. **16**(6), pp. 917-929.

Seed, H.B. and I.M. Idriss (1971). Simplified procedure for evaluating soil liquefaction potential. *J. of the Soil Mechanics and Foundations Div., ASCE*. **97**(SM9), pp. 1249-1274.

Seed, H.B. (1979). Soil liquefaction and cyclic mobility evaluation for level ground during earthquakes. *J. of the Geotechnical Eng. Div., ASCE*. **105**(GT2), pp. 201-255.

Seed, H.B. and I.M. Idriss (1982). *Ground motions and soil liquefaction during earthquakes*. Ed. Earthquake Engineering Research Institute, Monograph Series, Berkeley, California, 134 p.

Seed, H.B., I.M. Idriss and I. Arango (1983). Evaluation of liquefaction potential using field performance data. *J. of the Geotechnical Eng. Div., ASCE*. **109**(3), pp. 458-482.

Seed, H.B. (1983). Evaluation of the dynamic characteristics of sands by in-situ testing techniques. Conférènce Spéciale dans les Cômptes-Rendus des Rapports Généraux du Symposium International *Reconnaissance des Sols et des Roches par Essais en Place*, organisé par les Comités Français de Mécanique des Sols, de Roches et de Géologie de l'Ingénieur, Paris, 18-20 mai. **III**, pp. 91-99.

Seed, H.B., K. Tokimatsu, L.F. Harder y R.M. Chung (1984). *The influence of SPT procedures in soil liquefaction resistance evaluations*. Report No. UCB/EERC-84/15, Earthquake Engineering Research Center, College of Eng., University of California - Berkeley, 50 p. The results of this investigation was also published in: Seed *et al.* (1985). Influence of SPT procedures in soil liquefaction resistance evaluations, *J. of the Geotechnical Eng. Div., ASCE*. **111**(12), pp. 1425-1445.

Seed, H.B. (1987). Design problems in soil liquefaction. *J. of Geotechnical Engineering, ASCE*. **113**(8), pp. 827-845.

Skempton, A.W. (1986). Standard penetration test procedures and the effects of overburden pressure, relative density, particle size, aging and overconsolidation. *Géotechnique*. **XXXVI**(3), pp. 425-447.

Tokimatsu, K. and Y. Yoshimi (1983). Empirical correlations of soil liquefaction based on SPT N-values and fines content. *Soils and Foundations*. **23**(4), pp. 56-74.

Tokimatsu, K. and Y. Yoshimi (1984). Criteria of soil liquefaction with SPT and fines content. Proceedings of the 8th World Conference on Earthquake Engineering, july 21-28, San Francisco USA, ed. Prentice Hall. **III**(5.1), pp. 255-262.

Tokimatsu, K. and H.B. Seed (1987). Evaluation of settlements in sands due to earthquake shaking. *J. of Geotechnical Engineering, ASCE*. **113**(8), pp. 861-878. Also: Discussion by D.W. Sykora, **114**(4), pp. 429-431, 1988, april.

Youd, T.L. and D.M. Perkins (1978). Mapping liquefaction-induced ground failure potential. *J. of the Geotechnical Eng. Div., ASCE*. **104**(GT4), pp. 433-446.

Table 1. Cyclical undrained triaxial tests with pore pressure measurements and constant volume on reconstituted samples

INDEX PROPERTY	Initial		Final	
	SM-9	SM-3	SM-9	SM-3
Moisture content (w) %	6.70	10.3	35.8	30.8
Dry unit weight (γ_d) kN/m^3	13.36	14.40	13.34	14.41
Wet unit weight (γ_m) kN/m^3	14.25	15.88	18.12	18.85
Saturation degree (S_r) %	18.4	33.5	98.0	99.0
Void ratio (e)	0.984	0.831	0.988	0.841
Property or parameter	**Sample: SM-9**		**Sample: SM-3**	
SUCS classification: SP (fines ML, $CaCO_3$) F	28		78	
Relative gravity of solids (G_S)	2.703		2.704	
Effective consolidation pressure (p_o') kN/m^2	58.86		58.86	
Parameter B (Skempton)	0.985		0.993	

Cyclic load was applied in 3 sets of 15 cycles each with $\frac{\tau_{cyc}}{\sigma_{vo}}$ of: 0.53, 0.76 and 1.53

Table 2. Manufacturer permissible displacements for asbest-cement pipeline joints

Nominal Diameter Asbest-Cement Pipe Class B-7.5 (mm)	Relative displacement between coupled pipes		Permissible rotation for coupled pipes (degrees)
	Pull-out (Tension) (mm)	Pull-in (Compression) (mm)	
450	≥ 40	10	2.5°
600 to 750	≥ 45	10	2.5°
900 to 1100	≥ 50	10	2.0°
1500	≥ 100	10	1.5°
1800	≥ 100	10	1.0°

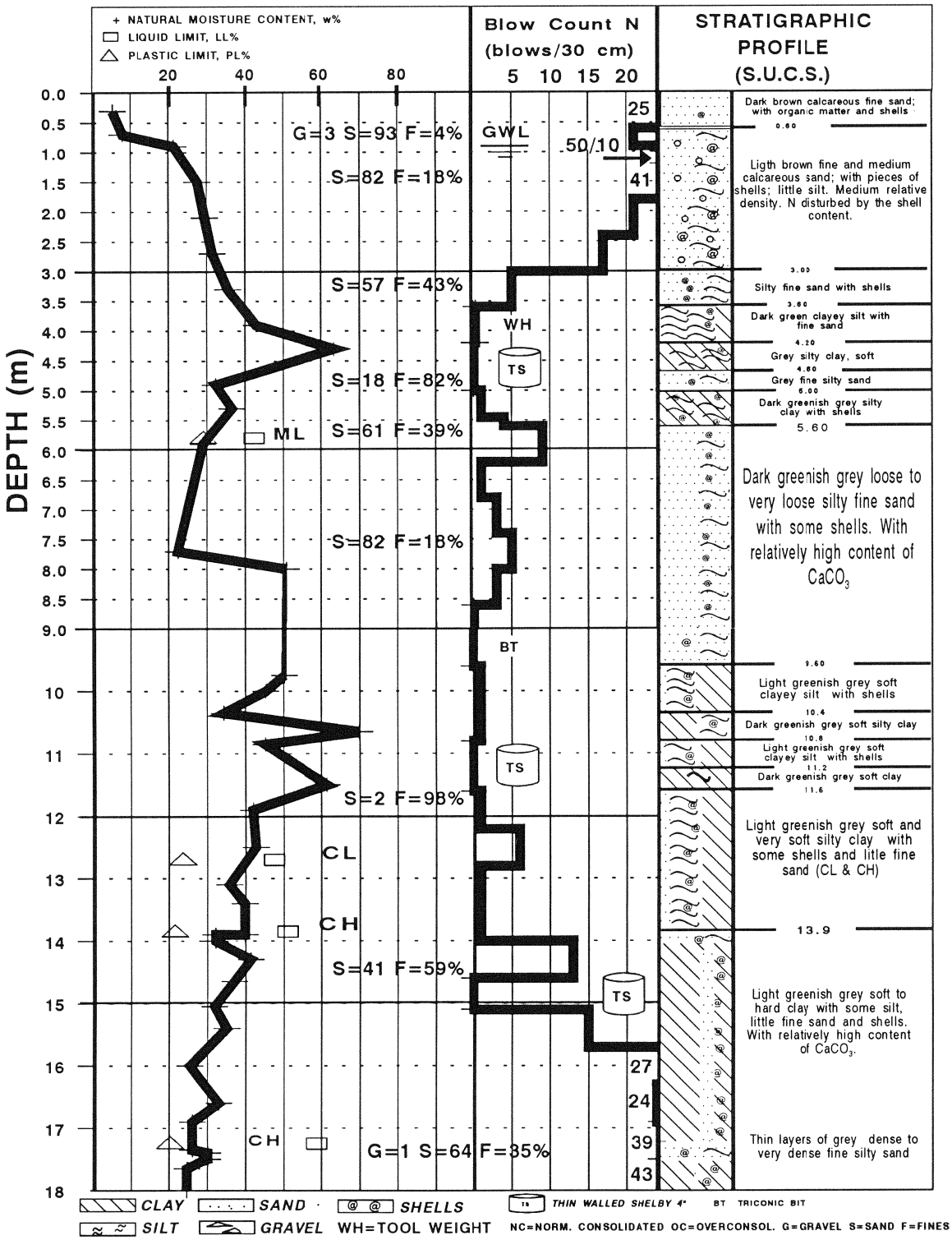

Fig. 1 Stratigraphy of the subsoil in Ciudad del Carmen

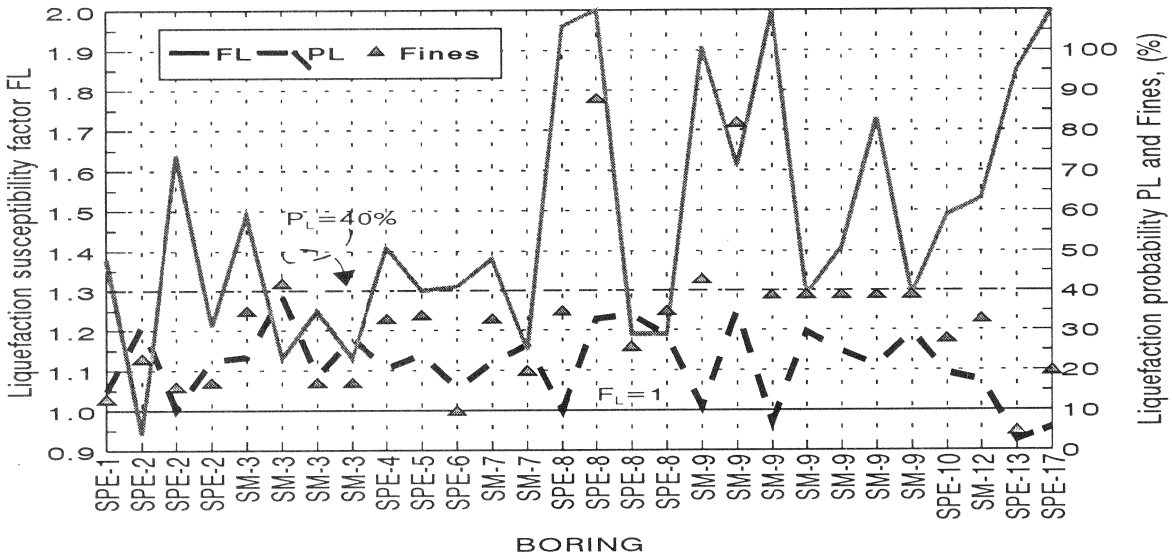

Fig. 2 Liquefaction susceptibility factor and probability computed for Ciudad del Carmen

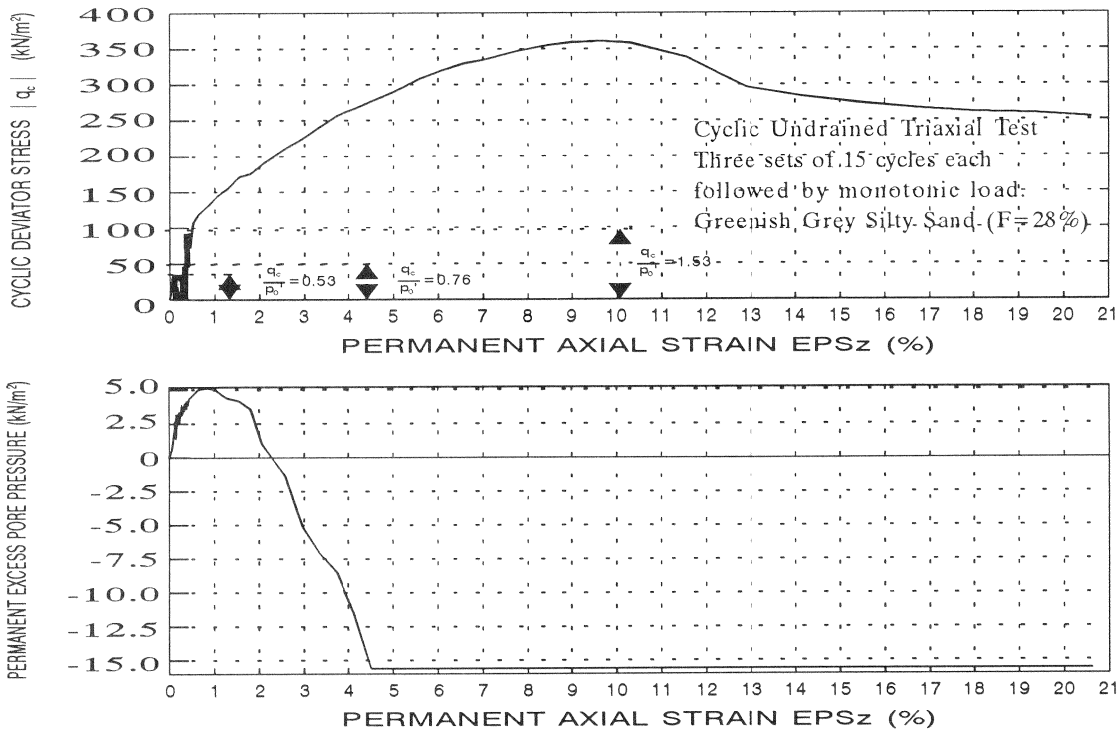

Fig. 3 Cyclic undrained triaxial tests results (F=28%)

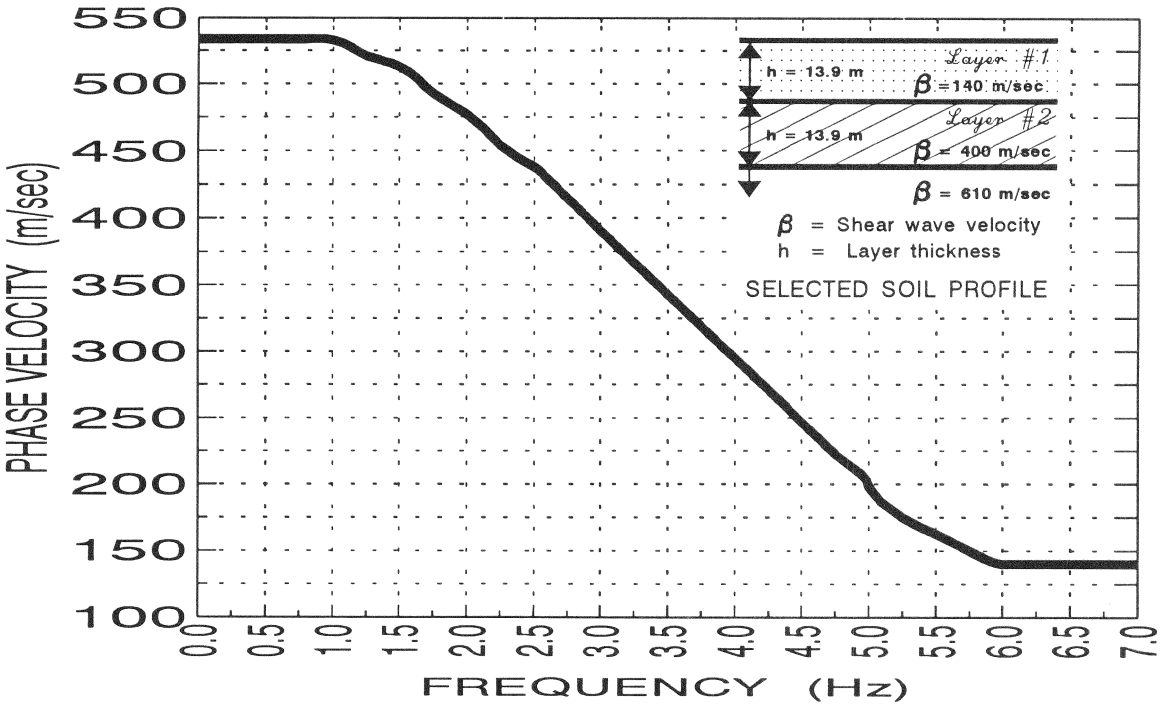

Fig. 4 Computed dispersion curve for Rayleigh waves in Ciudad del Carmen

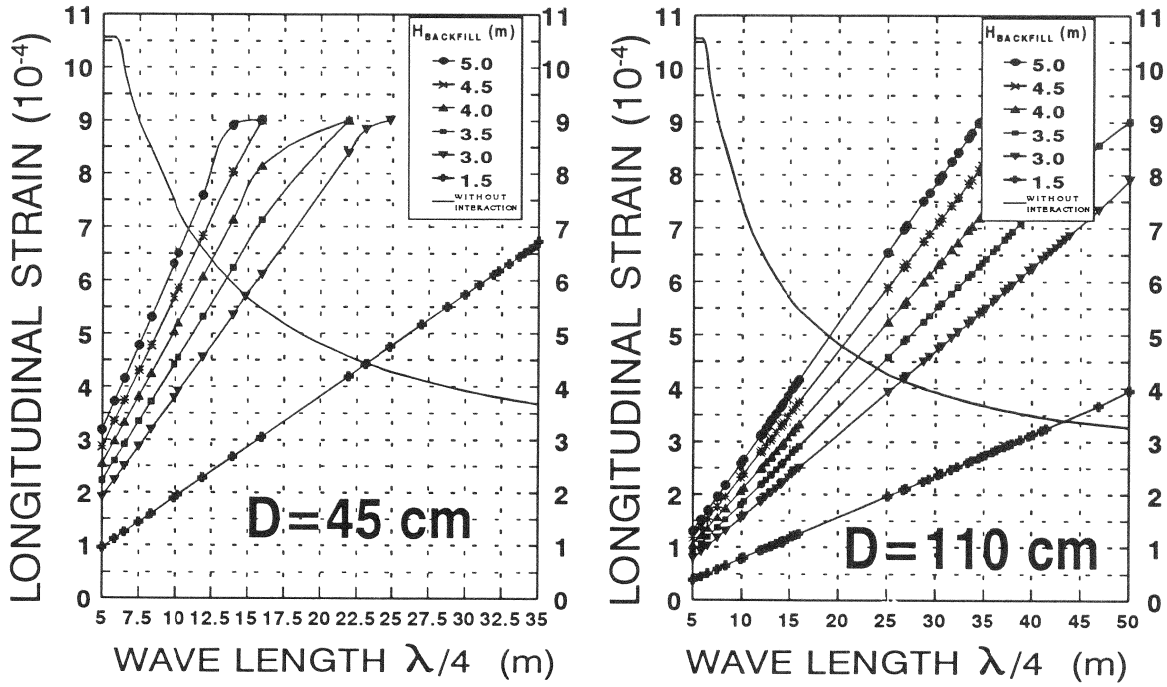

Fig. 5 Computed longitudinal strains with and without pipe-soil interaction in Ciudad del Carmen

PRELIMINARY EVALUATION OF THE USE OF COMPACTION PILES FOR IMPROVEMENT OF THE FOUNDATION SOILS OF THE COASTAL DIKES OF LAKE MARACAIBO, VENEZUELA

Bernardo Villegas, Project Engineer
Juan Murria, Consultant

MARAVEN, S.A., Apartado 173
Lagunillas 4016-A, Venezuela

A B S T R A C T

Recent studies have confirmed the liquefaction potential of the foundation soils of the coastal dikes of the Eastern Coast (Costa Oriental) of Lake Maracaibo, in western Venezuela, a region of moderate seismicity.

Mitigative measures consisting of downstream berms, with or without compaction piles, are being implemented. To evaluate the effectiveness of compaction piles against liquefaction of the silty sands and the improvement of low resistance clays, two field tests were performed, one in Bachaquero and one in Lagunillas.

The 0.60m diameter, 13m long piles were implanted in an 8 row, 5 column arrangement, 3m on centers. A ground levelling network was established. Piezometers, accelerometers and inclinometers readings were taken before, during and after pile implantation. The results obtained to date have confirmed that the berm and the compaction piles improve the properties of both the sandy and clayey soils and are, therefore, a valid method to improve the seimic stability of the coastal dikes of Lake Maracaibo.

INTRODUCTION

Subsidence associated with oil production in the east coast of Lake Maracaibo in western Venezuela was detected in the late 1920's (Murria and Jaeger, 1992). The geomorphology of the area (low, swampy lands) prompted the need to protect inhabitants and oil industry facilities from lake waters by means of coastal dikes.

The coastal protection system consists of 47 km coastal dikes, 59 km of inner (diversion) dikes, 90 km of drainage channels and 31 pumping stations with a combined installed capacity of 350.000 m3/h.

Western Venezuela is an area of moderate seismicity. Recent evaluation of the behavior of the coastal dikes under earthquake shaking have indicated the possibility of dike failure due to liquefaction of the foundation soils. Mitigative measures, consisting basically of downstream (landside) berms and upstream (lakeside) additional riprap, are being implemented. Post seismic stability analyses of different sections along the dike indicate required berms widths between 10 and 85m. Berm width is restricted in some areas by the presence of housing and/or oil facilities. It was decided for practical purposes to limit the berms width to 40m and to improve the foundation soils as needed.

The chosen improvement method has been stone compaction piles (Fig. 1). In order to evaluate the stone columns effectiveness, two pilot tests were performed, one in Bachaquero and one in Lagunillas (Fig. 2). The site selected for the first field test is located inland of the Bachaquero dike. It covers a rectangular area of approximately 1100 m2. The site was chosen because it is located in a very low risk area, away from any community or oil installations, and because the soil stratigraphy was considered typical of the areas where this methodology might be applied. The objectives of the Bachaquero pilot test were as follows (Sgambatti, Echezuria and Blanco, 1989):

1. Evaluate the effectiveness of the stone columns on the improvement of the geotechnical properties of the dike foundation soils,

2. Compare the effectiveness achieved by two different construction methods: vibro-replacement and casing-ramming,

3. Assess the influence of column spacing,

4. Study the effect of stone colums installation on the strength of clays and organic soils,

5. Evaluate pore water pressure variation during stone column construction and,

6. Evaluate time effects.

The site selected for the second field test is located on a dike section with 40m wide berm of the Lagunillas dike. (Fig. 2). The main reason to choose this area was the presence of high plasticity clay strata in the foundation soils.

The design of this field test was based upon the experience acquired from the Bachaquero pilot test. The objectives of the Lagunillas field test were the same as Bachaquero and, in addition, to avaluate the effect of stone column installation on the strenght of high plasticity clays.

Evaluation of soil site conditions at the different stages of the field tests was accomplished by means of standard penetration tests (SPT), cone penetration tests (CPT), in situ vane shear tests (VST), laboratory tests, and shear wave velocity determinations.

Pore pressure build-up during construction was monitored by means of piezometers installed at different depths. Additionally, movemments within the soil mass were monitored by inclinometers placed conveniently in the test areas. Ground deformation was monitored by means of a precise survey network.

BACHAQUERO PILOT TEST

The effect of strengthening the foundation soil by means of stone columns depends on many factors (Datye and Nagajaru, 1981), including:

- Method of construction and equipment characteristics,
- In-situ soil conditions, (soil type, gradation and fines content, relative density, state of stresses, and soil structure),
- Construction procedure and sequence of pile implantation and,
- Grid pattern and spacing between columns.

When programming the Bachaquero pilot test, some of these influencing factors were taken into account to permit later comparisons of their relative effectiveness. Two different construction techniques were tested: vibro-replacement and casing driving and ramming. To evaluate the effect of column arrangement, 2m, 2.5m, 3m and 4.0m c/c spacings were tested. An equilateral triangular array was decided upon as being considered the most efficient and economical.

A detailed testing program and an instrumentation set up were plannned for five different stages:

1. Stage 0: prior to any construction
2. Stage 1: after the construction of a 3m height embankment, which was used as a working platform,
3. Stage 2: immediately after columns construction,
4. Stage 3: two months after column construction and
5. stage 4: eight months after column construction.

A total of 120 stone columns were constructed by the two different constructions methods. Sixty by vibro-replacement and 60 by ramming-

compaction. All the columns were constructed down to a depth of 16m, bearing on a firm silty clay. The nominal diameter varied between 0.55m and 0.60m. Actual diameters increased to as much as 1.20m in the very soft clay stratum.

During the construction of the stone columns, most of the instrumentation was badly damaged or rendered useless. Moreover, the inclinometer tubes were broken and filled with soil, indicating very large movements of the soil mass.

Site Stratigraphy

Table 1, below, summarizes the major soil strata encountered at the test site and their engineering properties.

TABLE 1. Summary of site stratigraphy

Stratum	Depth (m) From	Depth (m) To		Nspt	Su (Kg/cm2)	qc (Kg/cm2)
I	0	4-4.40	Very silty yellowish brown to dark greenish gray loose fine sand coarse very sandy non plastic silt, with inclusions of soft silty clay layers, locally organic.	13	-	50
II	4-4.40	8.20-8.70	Very soft to soft dark gray low plasticity silty clay and clayey silt.	1-2	0.22	4
III	8.20-8.70	9.10	Medium dense to dense yellowish to dark gray silty fine sand, which thins or pinchs out towards the south-western part of the area.	3-7	-	80
IV	9.10-10.0	13+	Soft to firm dark silty gray clay and clayey silt.	2	0.24	5

Construction Methods

Vibro-replacement Method

The vibro-replacement method is used to improve cohesive soils containing more than 18% passing # 200 U.S. standard sieve (Brown, 1976). The equipment used is the vibroflot which is sunk into the ground under its own weight, assisted by water or air jets as a flushing medium until it reaches the predetermined depth. The method can be used either with the wet or dry process. In the wet process, a hole is formed in the ground by jetting a vibroflot down to the desired depth with water. When the vibroflot is

withdrawn, it leaves a borehole of greater diameter than the vibrator. The uncased hole is flushed out and filled in stages with 12mm-75mm size gravel. The densification is provided by an electrically or hydraulically actuated vibrator.

Casing Driving and Ramming Method

This method uses the energy delivered by a falling hammer to drive an open-ended hollow casing into the soil. The hole created by the lateral displacement of the soil, as the sleeve advances to the desired depth, begins to be filled with backfill material when the final depth is reached and the casing is progressively retrieved . The literature consulted so far (Datye and Nagajaru, 1981; Ghazali and Khan, 1986) indicates that there are no serious restrictions for its aplication to any type of soil, although this is not totally certain for cohesive soils.

Bachaquero Test Results

Soil Penetration Resistance

Evaluation was to be based on SPT and CPT results. However, CPT testing had to be discarded due to equipment problems. The only available comparable CPT data show that the vibro-replacement method increases penetration resistance of the granular strata even at 4m c/c column separation. Penetration resistance in the clayey materials does not seem to increase. On the other hand, the results corresponding to the casing driving and ramming method indicate that even columns spaced 4m c/c increased the penetration resistance of both cohesive and granular soil in the range from 100 to 250% and the cohesive soils increased their penetration resistance in a range from 25% to 50%.

The data obtained from Nspt values, comparig results previous to column construction with those approximately two months after column construction, indicate a considerable increase in penetration resistance in the area where the driving and ramming method was used, whereas the results show a moderate improvement in Nspt values in the area where the vibro-replacement method was used.

Shear Strength from Field Vane Tests

The data obtained from in-situ vane tests show that both construction methods increase soil shear strength. Recorded values for both methods are very similar for either peak or residual strengths. However, the scatter in the vibro-replacement test is much larger.

Peak and residual strength values after treatment tend to be lower (around 6m to 7m and near 10.5m to 11.5m depths) for the two construction techniques. Strength values in the vibro-replacement area are lower than those in the casing driving and ramming area. This may be a consequence of the level of consolidation reached by the clay at the time of performing the field vane tests.

Shear vane results in the vibro-replacement area indicate that strength

values are larger in the zones adjacent to sand stratum for organic silt layers. The improvement achieved in the cohesive soils with both methods was in a order from 100% to 40%.

LAGUNILLAS FIELD TEST

Based on the Bachaquero pilot test results the following was decided for the Lagunillas field test:

- Adopt the casing driving and ramming method
- Keep the 0.60m nominal pile diameter and adopt a 13.5m pile length
- Adopt the triangular array 3m c/c

The Lagunillas field test involved: (1) determination of the original site soil conditions, (2) installation of the instrumentation to monitor pore water pressures, ground acceleration and ground deformation, (3) construction of 20 stone columns and (4) determination of the "after column construction" soil properties. The columns were constructed down to a depth of 13.5m, bearing on a firm high plasticity clay.

The field work was programmed to be performed in three phases, as follows:

- Determination of the "before" soil conditions and installation of the instrumentation,
- Construction of stone columns and monitoring of the construction process
- Determination of the "after column construction" soil conditions

Site Stratigraphy

The site stratigraphy consists of alternate layers of granular, organic and cohesive soils. Minor textural and color variations and inclusions of other soil types within each generalized stratum are present.

Major strata of the site stratigraphy are summarized in Table 2, below:

TABLE 2. Summary of site stratigraphy

Stratum	Depth (m) From	To	Soil Description
I	3.35	6.50	Medium dense, very sandy plastic silt (MNP)
II	6.50	7.95	Medium compact, low plasticity silt (ML).
III	7.95	12.15	Very soft to soft, low plasticity silty clay (CL).
IV	12.15	14.40	Stiff, high plasticity clay (CH)

Test Program

Soil improvement was evaluated by means of penetration tests (SPT and CPT), in-situ vane shear tests (VST) and laboratory tests conducted on undisturbed samples. All the in-situ tests have been conducted in four stages as follows: inmediately after columns construction (3-7 days), one month later, three months later, and eleven months later. The in-situ tests program is shown in Figure 3. Results from laboratory tests are not presented in this paper.

Test Instrumentation

The pore pressure behaviour before, during, and after the columns construction were monitored by electrical and vibrating wire piezometers at different depths.

The surface movements were monitored through precise surveying of object points. The location of the instrumentations is shown in Fig. 3.

Lagunillas Test Results

Pore Pressure Build Up

The construction sequence (Fig. 4) has an effect on the generation and dissipation of pore water pressures. The relative increments with respect to the pressure before construction have an irregular pattern, which is believed to be a consequence of partial dissipation and redistribution of pore pressures due to the construction period.

Soil Penetration Resistance

Fig. 5 illustrates the corrected average values of Nspt for stages zero and 4. Fig. 6 presents the trend of the cone resistance (qc) for different stages. These figures indicate a considerable increase in penetration resistance. This increase ranges between 30% and 300% in the first stratum with the largest values toward the upper portion of the layer. Only slight increments in penetration resistance were obtained in cohesive soils. Nonetheless, penetration resistance tests are not sensitive enough to evaluate strength changes in cohesive soils.

Shear Strength from Field Vane Tests in Cohesive Soils

A series of in-situ vane tests were conducted to monitor the variation in Su with time after construction. In order to interpret the results, it was necessary to examine general trends rather than specific details since the soils at the test section vary considerably across the area.

The increase of peak shear strength values range between 30% and 60%. The residual shear strength values presents an increment between 40% and 100%. Fig. 7 shows the trends of the field vane tests results.

Monitoring of Ground Deformation

Based on the experience from the Bachaquero pilot test, three control point were placed away from the test section in order to guarantee their stability (Pedroza et al, 1992). Twenty two object points conformed the survey network, conveniently spread within the test section to provide a complete picture of the ground deformation (vertical and horizontal) due to stone column construction. (Fig. 8).

Horizontal Displacements

Field data were reduced to compute adjusted coordinates of object and control points. This adjustment provided displacement vectors of each point and its associated error ellipse at 95% confidence level. Significant vectors are shown in Fig. 9. The results shown by these vectors indicate the trend of the body displacement due to pile construction. The maximun horizontal displacement measured was of the order of 0.7m. As expected, some points returned to their initial position once the stone columns were constructed, thus confirming the elastic component of ground deformation.

Vertical Displacements

A total of 17 campaigns of high precision first order levelling were performed using two bench marks as controls located near the test section. The reduced height differences from the field measurements were introduced in a graphic computer file for continuous evaluation. An increment of height was obtained in the first five campaigns until construction stopped, with a total displacement of 0.076m. A height decrease was monitored later on with a total displacement of 0.156m. (Fig. 10).

It was, therefore, shown that eight months after the construction, berm vertical displacement had not stopped.

CONCLUSIONS

- In the Bachaquero pilot test the casing driving and ramming method showed the most effectiveness.
- The geotechnical instrumentation design for the Lagunillas field test was based on experience obtained from the Bachaquero pilot test. The entire design was conceived in order to monitor the pore water pressure build up and the surface movements.
- Results obtained from penetration tests and in-situ vane shear tests in the Lagunillas field test, show that the casing driving and ramming technique improves the engineering properties of both granular and high plasticity soils.
- The construction sequence appears to have an important effect on the pore water pressure generation. The highest excess pore pressure was registered in stratum III, during the casing driving operation.

- No increment of pore pressure due to stone columns construction was registered 10-12 meters away from the piezometers.

- Vertical displacements, as expected, showed heave during stone column construction. When construction stopped, ground level started to settle down to values even lower than the initial ones. This indicates soil compaction after the appropiate time period.

- Horizontal displacements showed the pattern followed by the berm, when subjected to strong compaction of the soil. This means that the berm deformed landwards.

REFERENCES

- Blanco, C. Villegas and Sgambatti, J. (1992), "Compaction Columns Field Tests in Heterogeneous Soil Profile", Proc. 3rd. Int. Conf. Case Histories in Geotechnical Engineering., St. Louis.

- Brown, R. E. (1976), "Vibroflotation Compaction of Cohesionless Soils", ASCE Nat. Water Res. Conv.

- Datyl, K.R. and Nagajaru, S. S., "Design Aproach and Field Control for Stone Columns", X Int. Conf. on Soil Mec. and Found. Eng., Stockolm.

- Ghazali, F. and Khan, A. (1986), "Granular Soil Improvement, Some New Physical Methods for Saudi Arabian Projects", Journal of Engineering and Applied Sciences, Vol 3, pp 113-123.

- Murria, J., Leal, J. and Jaeger, L. (1992), "Monitoring and Modelling Ground Subsidence in Western Venezuela Oilfields: An Update", 6th. International FIG-Symposium Deformation Measurements, Hanover Germany.

- Pedroza, M., Villegas, B., and Murria, J. (1992), "Monitoring of Ground Deformation Caused by Stone Pile Construction to Mitigate Liquefaction Potential, Costa Oriental Dikes, Venezuela", 6th. International FIG-Symposium Deformation Measurements, Hanover Germany.

- Sgambatti, J., Echezuría H. and Blanco C. (1989), "Compaction Pile Field Test on a Heterogeneous Soil Profile, Unpublished INTEVEP report, Los Teques.

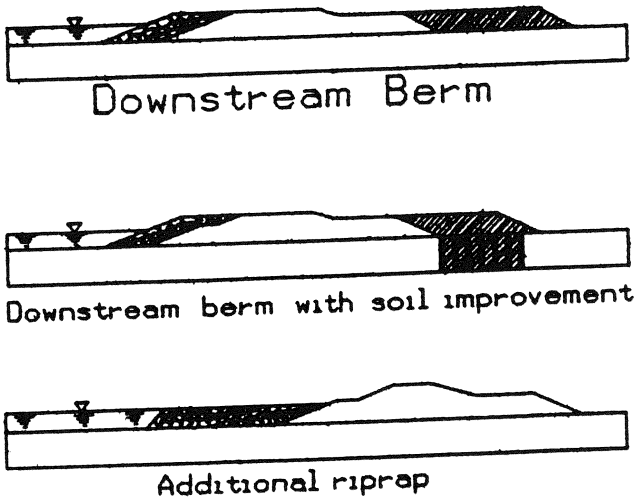

FIGURE 1. MITIGATIVE MEASURES

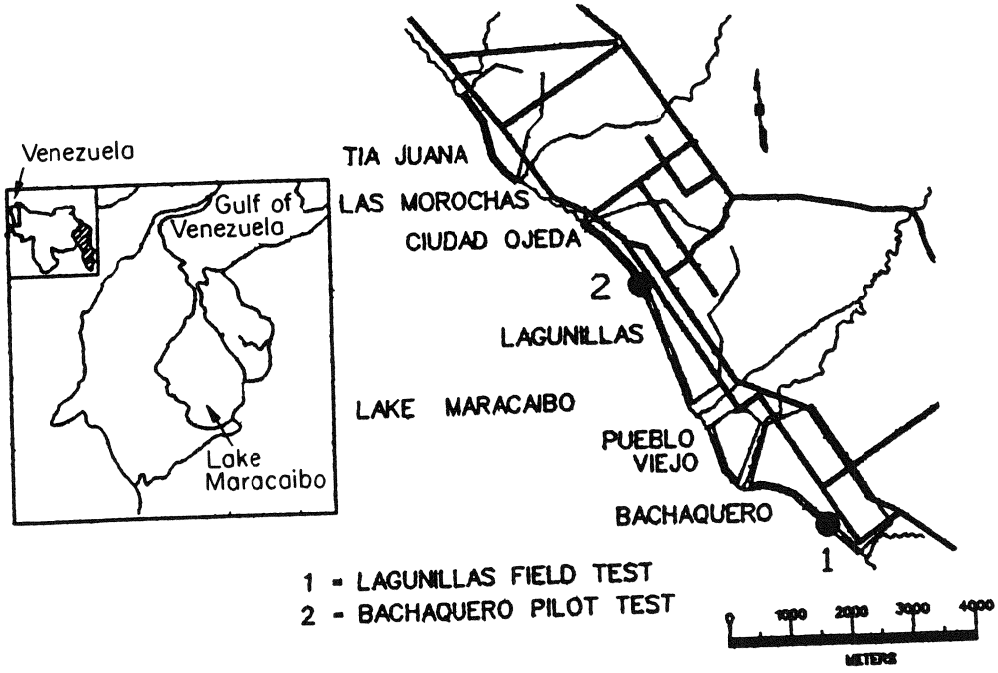

FIGURE 2. LOCATION OF FIELD TESTS

SYMBOLS	DESCRIPTION	STAGES P0	P1 DIA 3-7	P2 DIA 30	P3 DIA 90	P4 DIA 320
⊕	BORING AND WASHING FOR SHELBIES SAMPLES	2	2	-	-	2
□	C.P.T.	5	5	-	2	2
○	S.P.T.	1	2	1	2	2
○	V.S.T.	3	9	3	6	6
▼	PERMEABILITY	2	2			
◐	CROSS HOLE	1				
◆	OPEN PIPE PIEZOMETERS	8				
◇	DYNAMICS PIEZOMETERS	3				
■	ELECTRICS PIEZOMETERS	4				
◧	ACELEROMETERS	10				
●	INCLINOMETERS	4				
◉	HORIZONTAL-VERTICAL CONTROL DISPLACEMENTS	22				
⊕	HYDRAULIC FRACTURE TEST					3

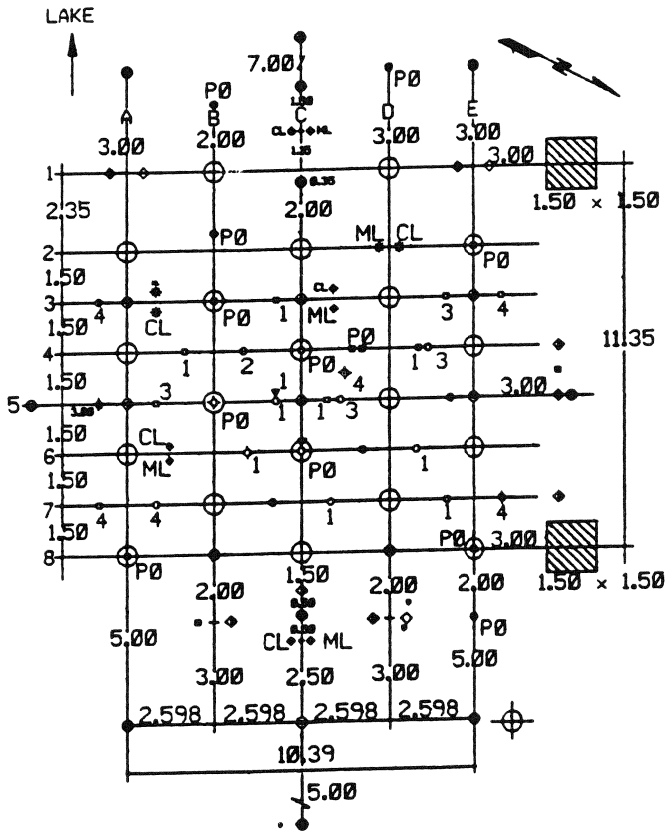

FIGURE 3. LAGUNILLAS PILOT TEST LAYOUT OF INSTRUMENTATION

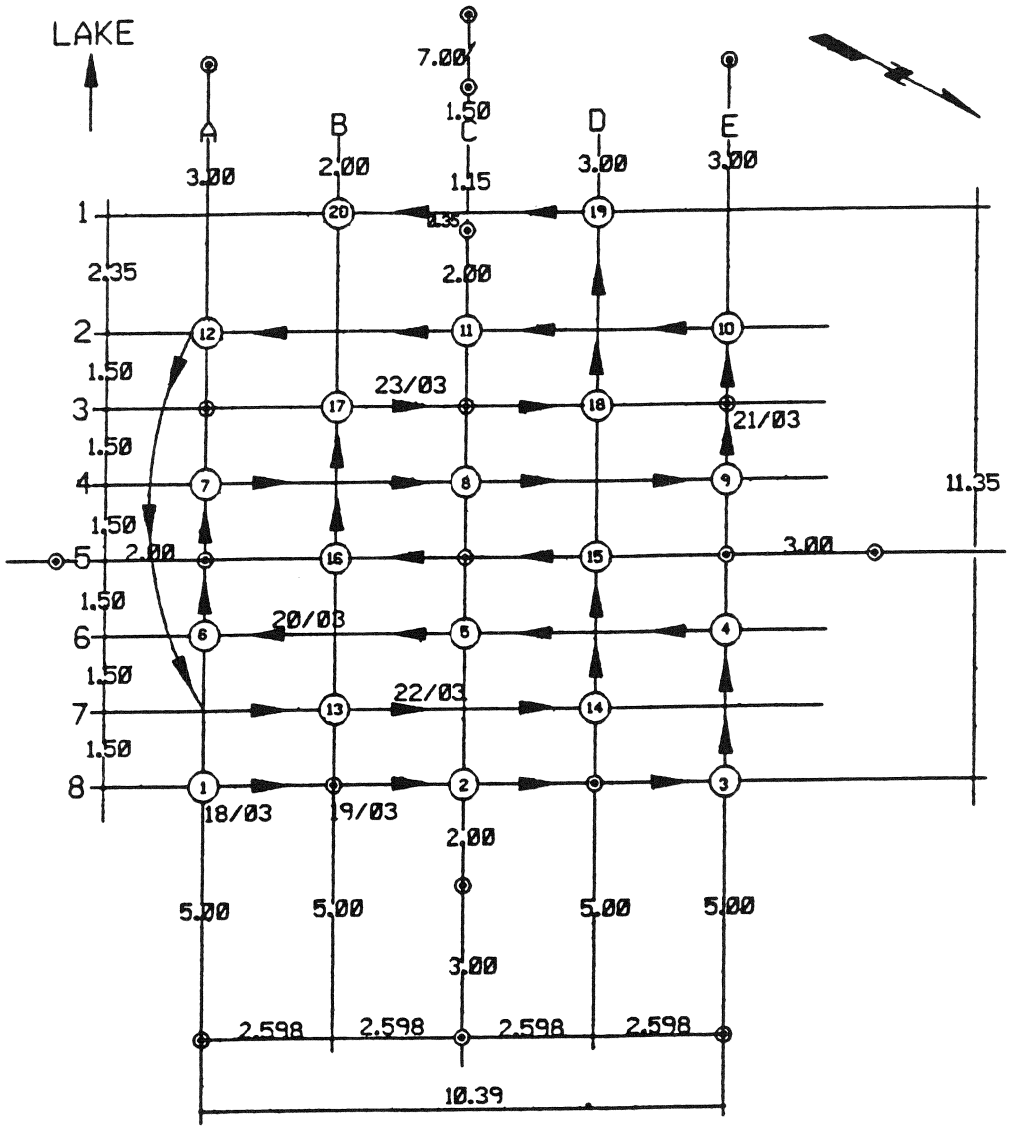

FIGURE 4. LAGUNILLAS TEST COLUMN CONSTRUCTION SEQUENCE

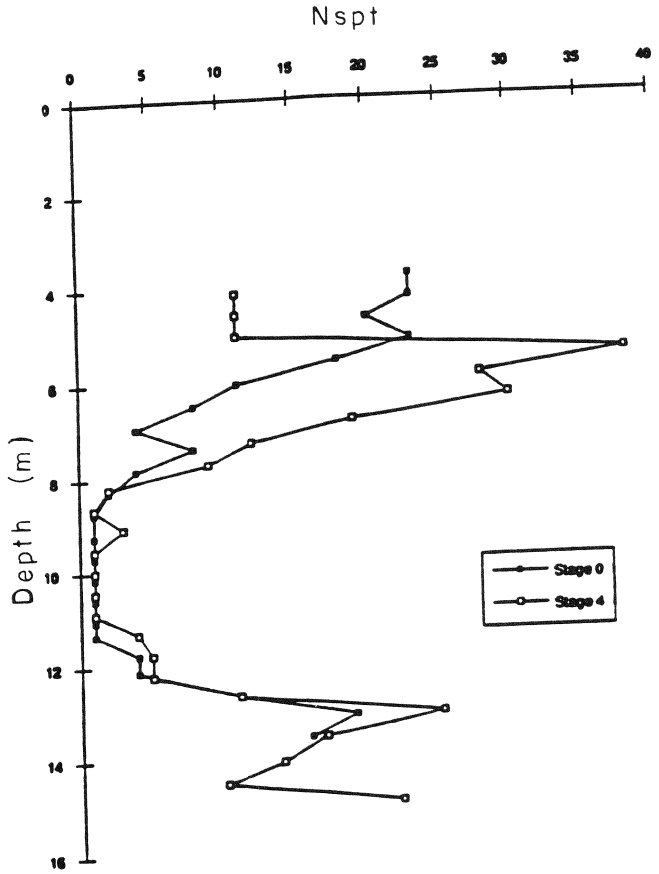

FIGURE 5. SPT RESULTS, STAGES "0" AND "4"

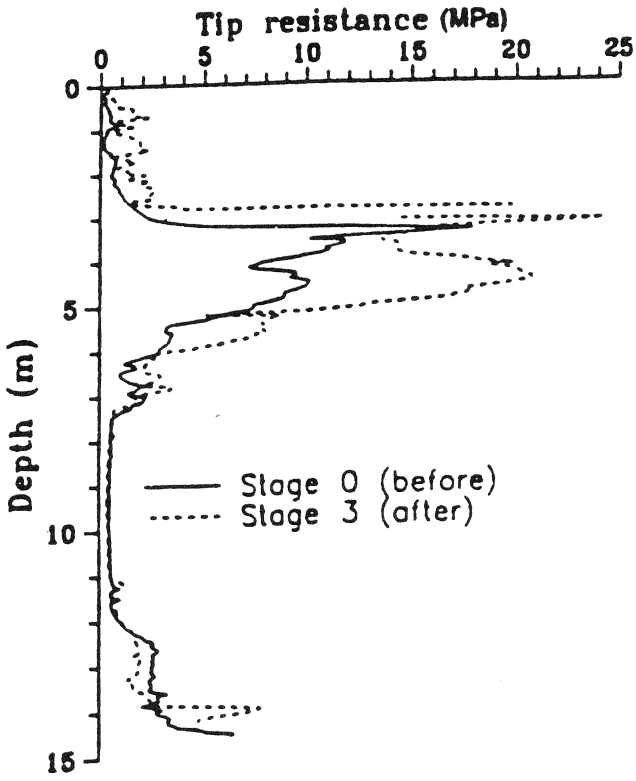

FIGURE 6. CPT RESULTS, STAGES "0" AND "3"

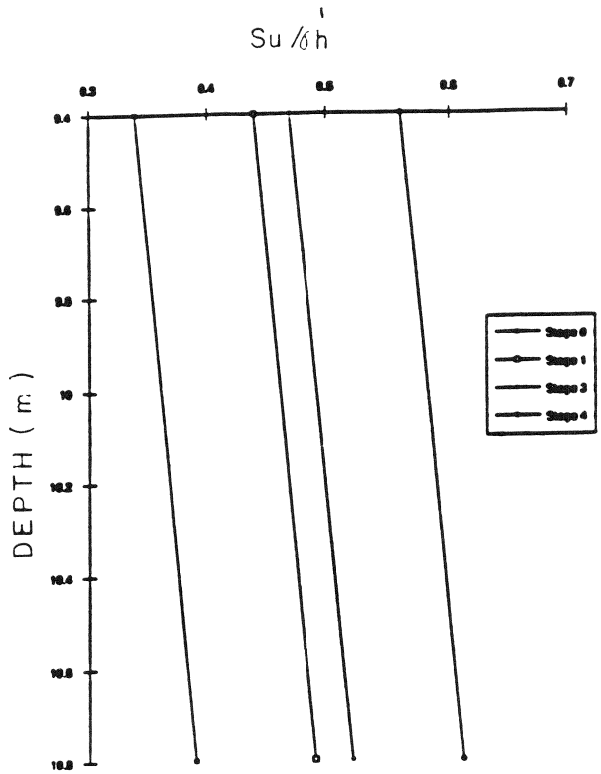

FIGURE 7. UNDRAINED SHEAR STRENGTH TREND AT VARIOUS STAGES

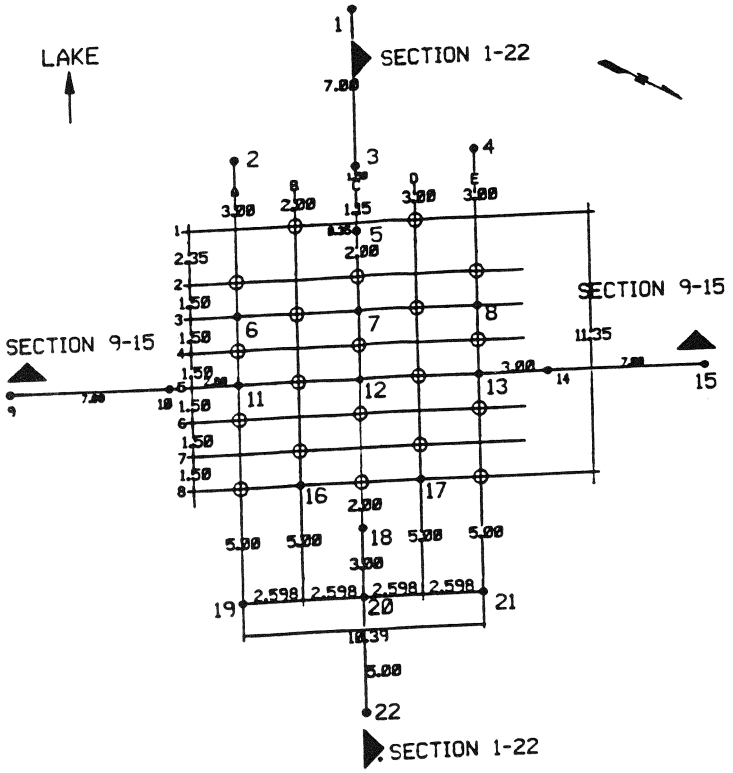

FIGURE 8. LOCATION OF OBJECT POINTS 1 TO 22

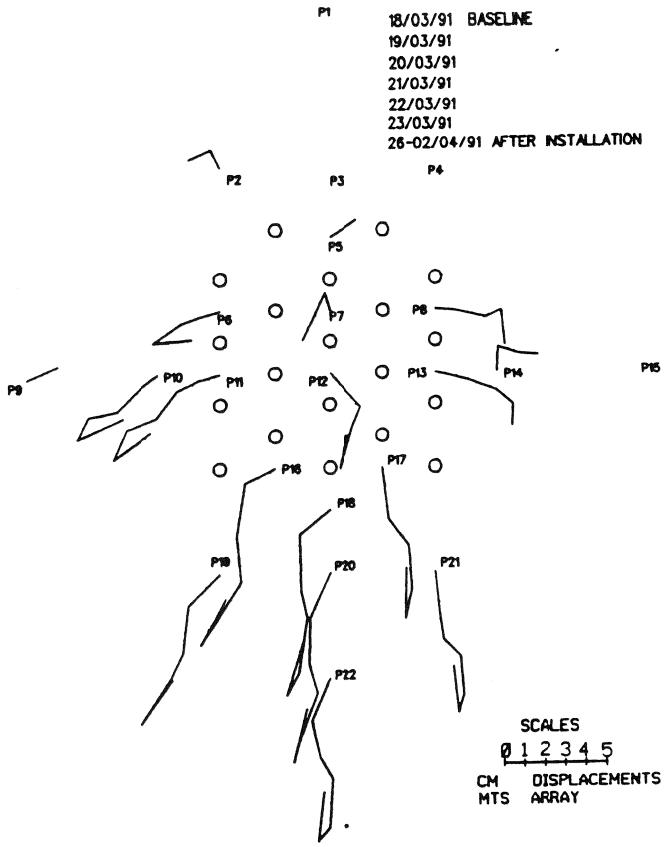

FIGURE 9. HORIZONTAL DISPLACEMENT VECTORS

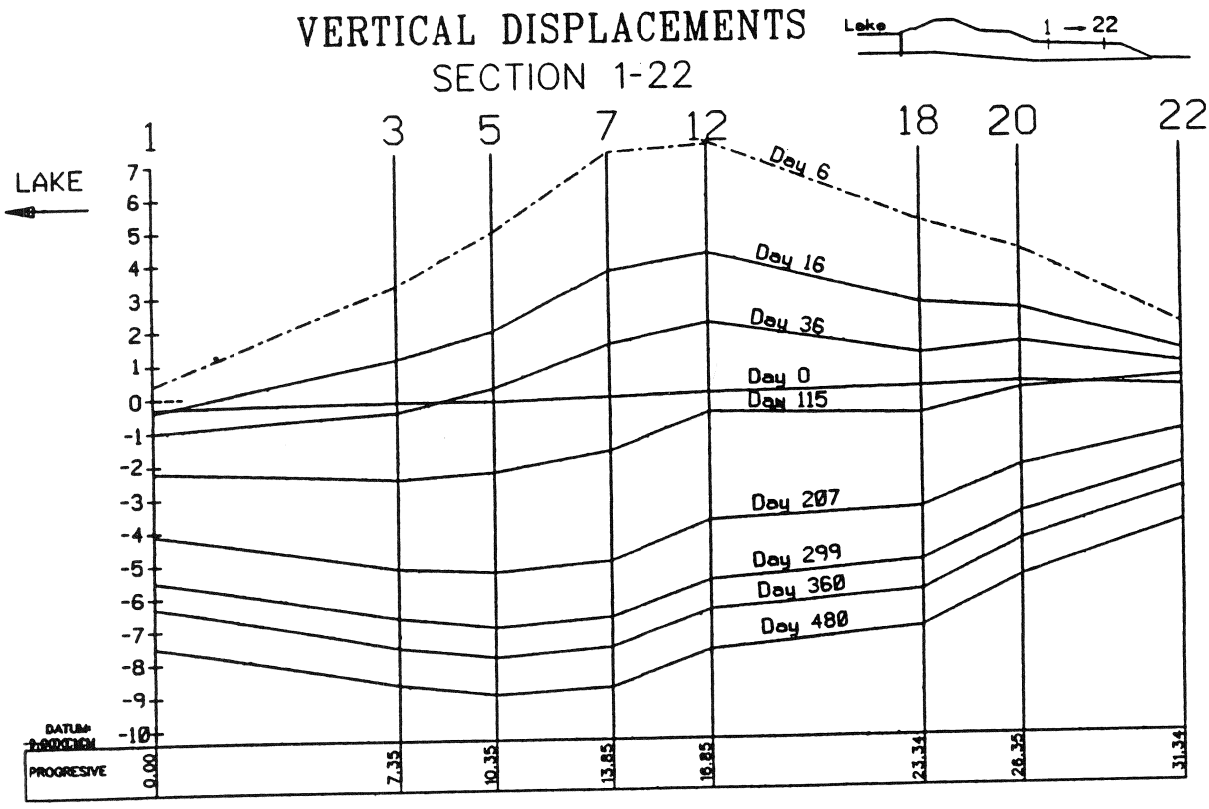

FIGURE 10. VERTICAL DISPLACEMENTS ALONG SECTION 1-22

V LIFELINE PERFORMANCE AND LIQUEFACTION DURING EARTHQUAKES

Minimization of Seismic Damages
K. Kubo
Estimation of Indirect Losses Caused By Disruption of Lifeline Service: A Pilot
Study of the Memphis Light, Gas and Water System
R.T. Eguchi and H.A. Seligson
Time History Analysis of Seismic Serviceability of a Water Supply System
I.J. Markov, M.D. Grigoriu, and T.D. O'Rourke
Troubles People Have to Suffer When Lifelines Fail to Function After Earthquake
H. Hayashi, H. Kameda, and N. Nojima
Guide to Documenting Earthquake Damage to Power Systems
A.J. Schiff
Probabilistic Evaluation of Liquefaction Spread for Lifeline Structures
I. Katayama, J.A Pires, and A.H.-S. Ang
Failure Criterion for Buried Pipe Subject to Longitudinal PGD: Benchmark Case History
M.J. O'Rourke and X. Liu
Changing Needs for Hazard Information for Pipeline Loss Estimation
D. Ballantyne
Shaking Table Tests on Floatation of Buried Pipes Due to Liquefaction of Backfill Sands
S. Yasuda, H. Nagase, S. Itafuji, H. Sawada, and K. Mine
Earthquake Performance of Gas Transmission Pipelines
T.D. O'Rourke and M.C. Palmer
Magnitude Scaling Factors for Analysis of Liquefaction
T.W. Loertscher and T.L. Youd
Damage to Water Pipes During the 1994 Northridge Earthquake
M. Hamada, T. Tazoh, T. Iwamoto, N. Suzuki, J. Ejiri, and K. Ohtomo

MINIMIZATION OF SEISMIC DAMAGES

K. KUBO

It is the sincere wishes of all the people, and also just the dream of human kinds to wipe out any kind of natural disaster, including seismic damages from the earth. However, the real situation is far from our dream. For an example in Japan, a volcanic eruption of Mt. Fugen has been damaging villages on its foothill and is forcing people to lead the long and much uncomfortable refugee lives. Recently, elevated highway bridges were heavily damaged, and gas- and water pipes were broken in the event of Northridge earthquake. People in Southern California are badly threatened due to a couple of strong earthquakes which have occurred in succession since 1971 San Fernando Earthquake, and civil engineers are now very anxious about advent of new type of damages to building and civil engineering structures.

United Nations Educational and Scientific and Cultural Organization (UNESCO) had Inter- governmental Conference on Seismology and Earthquake Engineering in Paris in 1964, aiming the extermination of seismic damage and the construction of the safer national land with such good cooperative contribution of earthquake engineers as international exchange of technical knowledge. In spite of UNESCO effort, strong earthquakes have attacked many times, and a lot of human lives and properties have been lost so far. In 1976 UNESCO again convened the Intergovernmental Conference for mitigating seismic damages, where conference members paid special attention to Haisheng earthquake of Feb. 4, 1975, M=7.3, in China, as it was successfully predicted and people in Haisheng area were forced to evacuate five and half hour in advance the occurrence of the earthquake. In the conference, most of the attendant were thinking that earthquake prediction would be a main resolution for mitigating seismic disasters. However, in the next year, Tangshang earthquake broke out and most of brick apartment houses collapsed and it is said that about 400,000 peoples were killed and injured. So far, only one earthquake and no more has been successfully predicted, and recently discussion items of many seismologists are focussing on the difficulty of earthquake prediction. For reducing seismic damage as low as possible, efforts of earthquake engineers to design and construct earthquake-proof structures are indispensable highly evaluated.

In Japan, there were 36 earthquakes between Nohbi earthquake, 1891, M=7.0 and Hokkaido-Nansei-Oki earthquake M=7.6, 1993, that means that our country has been attacked by earthquakes every about 3 years. Fortunately, no earthquake with so many victims has not occurred since the Fukui earthquake, 1948, where more than 1000 people were killed, but there were several earthquakes causing several thousands, or more than ten thousands victims, in underdeveloping countries.

The writer would like to point out 4 reasons as stated in the followings, for why seismic damage can not be wiped out, 1) Structural design is based on principles of economics, 2) Many kinds of unsolved factors ruling structural seismic damages, 3) Occurrence of new damage patterns which have not been investigated clearly so far, 4) Existence of many new construction materials and structures, which have not baptized by severe earthquakes.

It is surely possible for us to design and construct no-damaged structures even though they were shaken by very severe earthquakes, if no principle of economics would be taken into consideration. Generally speaking, it is of very low possibility for a structure to be shaken by destructive earthquakes during its life time, and the cost which is needed to make overstrung structures is rarely paid unless the structure experiences the strongest earthquakes, and shows its earthquake-proof.

It is well-known that ground conditions have the direct effect on degree of seismic damage to structures, but there are very few cases, in which seismic design coefficients are changed from on a structure to another one, based upon precise test results of soil conditions, and dynamic characteristics of each structures. It is concluded that structures designed by the principle of economics will be sustained seismic damage.

In the event of Northridge earthquake, Jan. 17, 1994, peak ground acceleration as much as 2000 gal was recorded on free field in Tarzana region, and the strong motion seismo graph installed in Kushiro meteorology indicated 922 gal as the maximum value during Kushiro-Oki earthquake, Jan. 15, 1993. In spite of very high ground acceleration, there were low percentage of damage ratio in San Fernando valley as well as in Kushiro City, even though there were seismic damages to buried lifeline pipes. Since 1915, when static seismic coefficient design method was proposed by Prof. R. Sano, degree of seismic damages to structures is said to be dependent on the maximum value of peak ground acceleration, but this scenario has become useless, and seismic damage to structures can not be discussed only by peak ground acceleration. The value of 2000 gal has never been recorded in the past earthquakes and therefore this is very shocking for designers of nuclear power plants.
In the event of Niigata earthquake 1964, RC buildings subsided, tilted or overturned, and man-holes floated up as sandy ground in Niigata City liquefied widely, as well as perfectly, and also bridge piers were shifted horizontally or buried pipes sustained large deformation due to lateral spreading of liquefied ground, whose maximum movement reaches about 12 meter.

In 1978, Sendai city experienced an earthquake of M=7.4. The epicenter of which was about 100 kilometers away from the city center, The specific damage was to the pipe joints of small diameters. It is clear that collar rings of threaded pipes can be easily deformed, causing loose connection under repeated axial loading, not withstanding the fact that arc-welded steel pipes perform very well and survived without any damage in Niigata earthquake. In the event of Kushiro earthquake, 1993, damage ratios for threaded small diameter steel pipes of the Kushiro Gas Co. were very high in comparison with the ratios of the other kinds of pipe joints.

It is concluded that in future, there remains some possibility of occurrence of the damage performances of structures which can not be anticipated scientifically, and severe failures of buildings as well as civil engineering structures.

Another reason for which seismic damages to structures can not be eradicated is like that such new types of structures as high-rise buildings or very long bridges and new construction materials, for an example high-tensile

steel and welded joints are now widely applied to various kinds of structures, whose performance during strong earthquakes has not yet fully checked and verified. It is needless to say that their earthquake-proof is corroborated by using up-to-date analytical method, and laboratory test results, but it can not be denied for civil engineers to have vague anxiety, as these structures have never baptized by strong earthquakes.

It is said that anti-seismic design coefficient of 0.06 specified in 1950 s was enough for buildings of regular shapes and constructed with good workmanship. Seismic coefficient of the same value has been used for buildings of irregular shapes as well as bridges, and therefore many seismic damages to building and civil engineering structures have occurred in the events of recent severe earthquakes. It is good lesson obtained through strong earthquakes that since 1971 San Fernando earthquakes, seismic coefficients for bridges has been pressed upon re-examination.

The most important research item of earthquake engineering is to design and construct structures of enough resistance against earthquakes, since the establishment of the Investigation Committee for Earthquake Disaster Prevention in 1892, one year after the Nohbi earthquake of 1891. This concept is still correct at present, by using which many researchers and engineers are devoting themselves for mitigating seismic damages.

As it is very difficult for us to eradicate seismic damages concretely so far, and a lot of money is needed for strengthening the existing vulnerable structures, new design concept has been spotlighted in which damaged structures and facilities are restored as early as possible, for reducing the stopping period of services.

It is very useful software countermeasure for gas engineers to divide the whole service area into many blocked districts before a future earthquake, for stopping gas-supply only in limited damaged districts, and for doing restoration works rapidly. Another kinds of software earthquake programs are quick collection (within several minutes) and dissemination of the earthquake information as well as damage ones, technical development of detecting damage patterns of lifeline buried pipes, preparation of restoration machines and equipments, medicine for emergency use, foods as well as drinking water, and disaster drill.

Both hardware technology and software countermeasures are considered to be very useful for mitigating seismic damages to human lives and properties and quick restoration of the lifeline facilities.

ESTIMATION OF INDIRECT LOSSES CAUSED BY DISRUPTION OF LIFELINE SERVICE

A Pilot Study of the Memphis Light, Gas and Water System

By

Ronald T. Eguchi
Hope A. Seligson

EQE International
Irvine, California

ABSTRACT

A general methodology for estimating the indirect losses caused by a disruption of lifeline service is presented. This methodology is different from previous approaches in that it attempts to incorporate local data on lifeline usage patterns and detailed information on regional economics into the analysis. Although the analysis is presented using natural gas as the pilot system, the methodology is general enough to have application for other lifeline systems. Since the conduct of this study is part of a larger National Center for Earthquake Engineering Research (NCEER) effort that involves multiple investigators, parts of the analysis are still being performed. Therefore, what is presented in this paper is a snapshot of the analysis with particular focus on model development. Models for natural gas usage, economic productivity and natural gas outage are presented. In order to provide the reader with some understanding of how the results of the analysis will feed into the overall loss assessment procedure, a general discussion of the methodology is presented along with a discussion of future activities. This study is part of the Urban Seismic Risk Project that is being sponsored in whole by the NCEER.

INTRODUCTION

The past performance of many lifeline systems has demonstrated that these systems can be highly vulnerable to disruptions during natural disasters and that economic losses associated with their disruption may far exceed the cost to repair the damaged system. Even with this recognition, few studies have attempted to quantify these indirect losses. The most notable study was performed for the Applied Technology Council (ATC-25, 1992) in an assessment of national lifeline vulnerabilities. Even at this coarse scale, the ATC study identified the significance of lifeline dependencies and suggested that in a major earthquake, business interruption losses could be as much as three times the repair costs for the system. The current study attempts to improve upon the methodology developed in the ATC-25 study by developing more refined models of lifeline usage and economic output.

From many respects, the approach used to model the economic integrity of a region is based on empirical models derived from an examination of local and state economic data. To our knowledge, little information exists on the requirements of businesses for lifeline services. As part of a larger National Center for Earthquake Engineering (NCEER) effort, the Disaster Research Center (DRC) of the University of Delaware is conducting a survey of Memphis businesses to assess the importance of various lifeline systems to these businesses. As part of this survey, questions regarding the length of time that a business can operate without a specific lifeline service are being asked. This information will be essential in completing the current study which attempts to quantify the economic impact on a region that suffers some level of lifeline disruption.

In addition to the survey above, various other empirical models have been developed that quantify the level of gas usage by customer type, and the economic productivity associated with various sectors of the economy. Although economic models exist (e.g., input-output) that can relate changes in economic output to changes in various economic sectors, this type of approach cannot consider in detail the influence of lifeline loss or availability. The drawback of the current approach is that a more comprehensive dataset is required to execute the methodology.

This paper presents an interim report of the analysis. Because this effort is part of a larger study being performed for NCEER (Project title: Urban Seismic Risk), some parts of the analysis are being performed by other members of NCEER. It is expected that all parts of the analysis will be completed by the end of 1994. At that time, a complete summary of expected indirect losses can be reported on. In the meantime, this paper presents our final gas usage and economic models.

METHODOLOGY

The methodology for assessing direct and indirect economic losses due to earthquake-induced utility disruption is shown in Figure 1. Although this study deals specifically with a natural gas utility, the methodology, as shown, can be generalized to apply to many other urban utility networks, such as water, power and telecommunications.

For the purpose of demonstrating the methodology, an assessment of losses related to the disruption of natural gas service provided by Memphis Light, Gas and Water (MLGW) in the event of a large earthquake in the New Madrid Seismic Zone (NMSZ) is being made. MLGW serves Shelby County, Tennessee, which includes the city of Memphis.

The first step in the loss assessment is the seismic hazard analysis. This includes the development of earthquake scenarios, and estimates of Modified Mercalli intensity and liquefaction potential. For this study, seismic hazard analyses performed by Hwang et al. (1991) have been utilized.

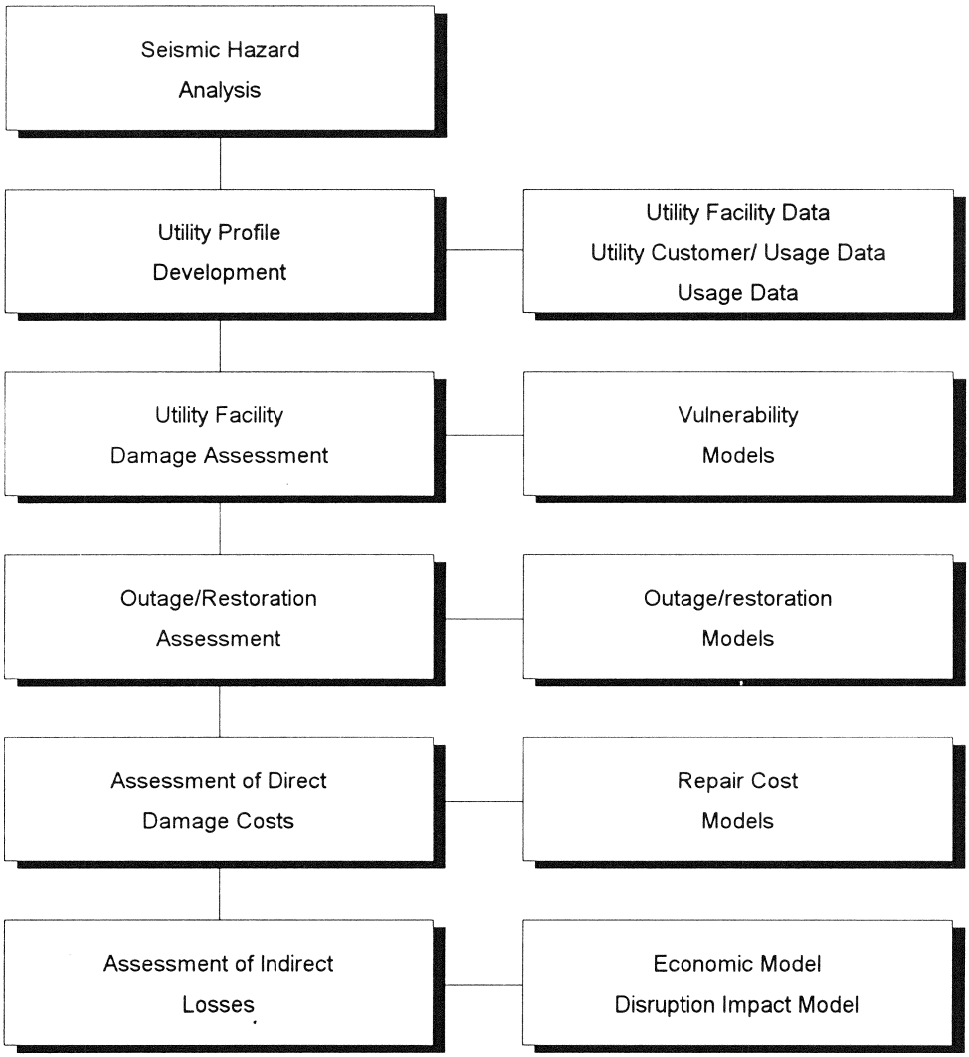

Figure 1
Methodology for the Assessment of Direct and Indirect Losses Due to Earthquake-Induced Utility Disruption In An Urban Enviroment

The next major step is the development of a utility profile. This profile includes data on utility facilities, such as pipeline and storage facility specifications, and pipeline system maps, including the locations of compressor stations. Additional data required for the analysis includes customer and gas usage data, such as the number of residential, commercial and industrial customers, average annual quantities of gas sold, and annual revenues. Regional data on natural gas usage patterns are available through various national organizations, while MLGW customer and facility data have been collected by

Hwang and others at the Center for Earthquake Research and Information (CERI) at Memphis State University.

The facility damage assessment for this study was performed by various NCEER investigators; this effort was coordinated by Professor M. Shinozuka of Princeton University. Preliminary results of their damage assessment of the MLGW transmission system have been made available for use in this study.

The fourth step in the loss analysis procedure is the outage and restoration assessment. This outage assessment takes the results of the damage analysis as input, and applies restoration models to determine the length of time that various utility service areas and customers will be without service, or operating at reduced service levels.

Following the outage assessment, the estimation of losses due to direct damage is performed. These direct losses include both the cost of facility repair, such as pipeline repair or replacement, as well as revenue lost by the utility as a result of service interruption. The first cost is estimated through the use of generalized repair cost models, while the second cost is estimated from annual customer revenues.

The final step in the methodology is the assessment of indirect losses, or loss of regional economic productivity as a result of the loss of utility service. These losses may be estimated in dollars, and as a percent of gross state product (GSP). Two models are required for the implementation of this step; models of the region's economic activity in terms of percent of GSP, and disruption impact models which relate decline in economic activity to reduced utility service. The final model used in this study, the impact disruption model, may be refined following completion of the related NCEER study by Prof. Kathleen Tierney of the Disaster Research Center in Delaware, which includes the survey of businesses in the Memphis area to develop a more detailed business profile, including an assessment of utility dependence.

Natural Gas Usage Data

Data on regional and national natural gas utilization are available from two sources: the American Gas Association (AGA) and the Department of Energy's Energy Information Administration (DOE/EIA). The American Gas Association annually publishes "Gas Facts", a statistical record of the gas utility industry. "Gas Facts" contains data on energy reserves, natural gas supply, underground storage, energy consumption, customers, sales, revenues and prices. Relevant data is presented for the U.S. as a whole, for census divisions, and for individual states. "The Natural Gas Annual", published by DOE/EIA, presents similar information, and includes a set of summary statistics for each state. In addition to data on natural gas deliveries by utilities, the DOE/EIA statistics include natural gas purchased directly from producers and delivered to end users through transportation agreements with pipeline companies. These "transportation volumes" or "deliveries for the accounts of others" are, by definition, not included in the gas industry figures presented by theAGA. While damage to the pipeline companies will impact these

transportation volumes and deliveries, this study is concerned with the impact of natural gas utility disruption on an urban area, and therefore, the AGA statistics are utilized here.

Specific data on local natural gas usage for Shelby County is presented in Table 1. This data includes number of customers, consumption, revenue and supply (MLGW, 1991). This data will be combined with outage estimates to determine the percent of impacted households and commercial and industrial enterprises, and the subsequent economic impact, as well as the resulting loss of revenue for the utility. Other data, such as consumption data, are important to complete the overall picture of regional natural gas usage.

Table 1. Natural Gas Data for Shelby County, Tennessee (1990)

Measure	Res	Comm	Industr	Elec. Gen.	Other	Total
Customers	245,600	18,600[a]	400[b]	-	-	264,600
Annual Consumption[c] (mil BTUs)	81.6	694.8	89,296.0	-	-	-
Annual Sales[c] (Tril BTUs)	20.0	12.9	31.6	-	-	64.5
Annual Revenue[c] (1000 $)	88,389	46,508	24.245	-	-	159,142
Average Price[c] ($/mil BTU)	4.41	3.60	0.77	-	-	-

Notes:

a) MLGW "general services" customers are assumed to represent mostly commercial customers

b) MLGW "demand" customers are assumed to represent mostly industrial customers

c) Derived from 1991 consumption data from MLGW (1992)

In developing average daily revenues per customer for each user group, it is important to consider seasonal fluctuations in natural gas usage. An examination of U.S. quarterly sales volumes (AGA, 1991) for a five-year period (1986-1990) reveals a consistent pattern of greater usage in the winter months (1st and 4th quarters, October through March) than in summer months (2nd and 3rd quarters, April through September). The extent of this fluctuations varies among the different user groups, as follows:

- Residential Users
  - summer usage accounts for ~25% of annual sales by volume
  - winter usage accounts for ~75% of annual sales by volume

- o Commercial Users
  - summer usage accounts for ~30% of annual sales by volume
  - winter usage accounts for ~70% of annual sales by volume
- o Industrial Users
  - seasonal fluctuation in usage is negligible

It is assumed that these national figures, representing typical seasonal fluctuation patterns, are sufficient to capture the average seasonal variation in the current study area. This information has been used to calculate two average daily sales volume figures from total annual sales for each user group - one for summer and one for winter. From the average daily sales figures, average price data allows calculation of average daily revenues, which, when combined with customer data, yields average daily revenues per customer. Table 2 lists seasonal average daily revenues per customer derived for Shelby County.

Table 2. Average Daily Revenue per Gas Utility Customer for Natural Gas Sales in Shelby County, Tennessee (Dollars)

Customer Group	Winter	Summer
Residential	$1.48	$0.49
Commercial	$9.63	$4.10
Industrial	$188.16	$187.13

Economic Models

Various data on the national and state economies are collected and published by the U.S. Department of Commerce, Economics and Statistics Administration, Bureau of Economic Analysis (BEA) and the Bureau of the Census (BOC). Economic censuses are performed by the BOC every five years, most recently in 1987 (published in 1990). Data is collected on various sectors of the economy: Manufacturers, Wholesale Trade, Retail Trade, Service Industries, Mineral Industries, Construction Industries, and Transportation Industries. Other economic data are published monthly by the BEA under the auspices of the "Survey of Current Business".

Data relevant to this study are those that provide an indication of the relative productivity of various business sectors, as defined by the Standard Industrial Classification (SIC). Two such economic indicators are value added and gross state product. Although value added has been used in previous indirect earthquake loss studies (ATC-25, 1991; Dames and Moore, 1991), it is by definition, an industrial measure and is not applicable to the trade and service industries that constitute a significant portion of the economy of an urbanized area. For this reason, gross state product was used.

Gross state product (GSP) is defined as the market value of goods and services produced by labor and property in a State, and is collected for industry categories according to SIC code. GSP is the state counterpart of the national gross domestic product (GDP). The GSP is organized into 13 major economic sector groups according to SIC codes. Table 3 presents 1989 GSP figures for the State of Tennessee, and for the U.S. as a whole.

Table 3. 1989 Gross State Product (Millions of Dollars)

SIC Division	SIC Major Groups	Tennessee	United States
A	Farms	1,426	88,587
A	Agricultural Services, Forestry and Fisheries	312	24,896
B	Mining	354	80,254
C	Construction	4,013	247,721
D	Manufacturing	22,161	965,997
E	Transportation and Public Utilities	7,326	460,863
F	Wholesale Trade	6,271	339,468
G	Retail Trade	9,903	485,979
H	F.I.R.E	13,981	896,652
I	Services	15,494	970,539
J	State and Local Govt.	6,772	413,123
-	Fed. Civilian Govt.	3,716	125,481
-	Fed. Military	537	65,111
	TOTAL	92,267	5,164,671

While GSP data reflects economic activity for all sectors of the economy relevant to this urban analysis, it does so for the State of Tennessee as a whole. To utilize this data for one county within the state, Shelby County, some means of extracting Shelby County's share of the state's economic activity must be developed.

The approach for deriving estimates of county contributions to GSP was to compare economic indicators for the County to those of the State, and to identify any differences that are important to capture in the resulting model. County Business Patterns 1989, published for each State by the Bureau of the Census (1991), presents estimates of employment, payroll and number of establishments by detailed industry category. Table 4 presents summary statistics for Tennessee and Shelby County. As shown in the table, Shelby County accounts for about 22% of the state's payroll, 20% of the state's employees and 18% of the state's business establishments. The number of businesses (19,888) compares favorably with the total number of MLGW commercial and industrial customers (19,000).

Table 4. 1989 Business Patterns for Tennessee and Shelby County (Source: County Business Patterns, 1989; Tennessee, BOC, 1991)		
Measure	**Tennessee**	**Shelby County**
No. of Establishments	112,337	19,888
No. of Employees	1,829,371	364,349
Annual Payroll ($1,000)	34,792,660	7,620,976

To determine which economic indicator was the most appropriate for use in estimating Shelby County's contribution to GSP, we compared industry contribution to GSP to various state economic indicators, by industry. Figure 2 shows a comparison of industry contribution to 1989 GSP and annual payroll for the State of Tennessee by SIC group. The comparison shows that as a percent of total contribution, annual payroll represents a reasonable indicator of the GSP when compared with each of the different SIC divisions. Comparisons for SIC divisions H (F.I.R.E) and I (Services) show the largest discrepancies. Other comparisons were made using information on number of establishments and number of employees as possible indicators. However, the correlations with GSP were not as good as that presented using annual payroll.

Table 5 shows Shelby County's contribution to Tennessee's GSP as estimated from annual payroll data. As the table indicates, Shelby County's share of the GSP is estimated at $20.8 billion. The amount of GSP on a per day basis is estimated at $57.1 million. Also indicated in Table 6 is the share of GSP per day, per establishment.

Figure 2 - Comparison of Industry Contribution to 1989 GSP and Annual Payroll for the State of Tennessee by SIC group

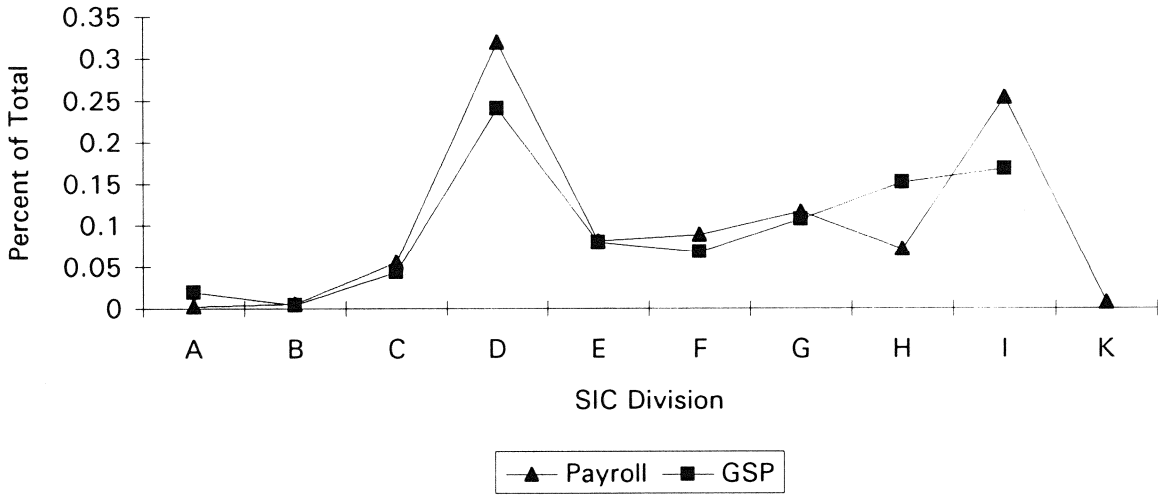

To utilize the economic data described here in the assessment of indirect economic impacts of natural gas disruption, the economic activity of each industry group needs to be assigned to a customer category. Two basic business customer types exist within the State of Tennessee, and Shelby County - Commercial and Industrial. Using the information presented in this section, as well as the previous section on gas usage, the following average daily GSP per establishment ($/day/est.) have been established:

	Shelby Co.	State of Tenn.
Commercial	2,640	1,820
Industrial	7,150	8,510

This data may be combined with outage estimates to quantify loss of economic productivity due to natural gas disruption.

Table 5. Shelby County's Contribution to Tennessee GSP

SIC Division	Share of GSP (million $)	Share of GSP per day (million $)	Share of GSP per day, per establishment[a] ($)
A	399	1.1	5,630
B	5	0.01	1,150
C	871	2.4	1,610
D	2,629	7.2	7,220
E	3,084	8.4	9,230
F	2,014	5.5	2,690
G	2,183	6.0	1,230
H	3,539	9.7	5,410
I	3,709	10.2	1,570
J	1,483	4.1	--[b]
Other[c]	932	2.6	--[b]
TOTAL	20,848	57.1	

Notes:

a) Calculated using the 1989 estimates of the number of establishments by SIC for Shelby County (County Business Patterns, 1989; Tennessee, BOC, 1991).

b) No estimates for the number of government and military establishments are available.

c) Federal government, military

FUTURE ACTIVITIES

Two major activities will place in the next research period: vulnerability assessment and estimation of indirect losses. In order to perform the seismic vulnerability asssessment, the

results from the damage analysis being performed by Professors Hwang and Shinozuka will be utilized. This analysis is based on assessing the seismic vulnerability of major natural gas transmission pipelines that serve the Memphis area. The scenario used in this assessment is a magnitude 8+ earthquake in the New Madrid Seismic Zone. Although this analysis will not identify where specific pipeline breaks will occur, it will provide an assessment of probable outage areas. Based on this analysis and on an assessment of potential shaking intensity levels in the Memphis area, the current project team will determine what the likely impact will be on distribution pipelines. As is evident from past California earthquakes, natural gas distribution pipelines may also be vulnerable to earthquake, even if located outside the immediate epicentral area. For purposes of demonstrating the current methodology, the project team will estimate the number of repairs that may result from the NMSZ scenario and the time for repair (both partial and full restoration.) Based on this analysis, we will apply these outage times to the economic models discussed previously to estimate the likely loss of productivity caused by a disruption of natural gas service.

In addition, as mentioned in the introduction to this paper, the results from the DRC business survey will be incorporated to the fullest extent possible. The results of this survey should identify the lengths of time over which little or no impact on business operations should be observed. To incorporate this survey data, businesses will be classified into commercial and industrial categories. Timelines that indicate when essential lifeline services are needed will be plotted against an assessment of likely outage periods based on the NMSZ scenario. When these outage periods extend beyond non-critical outage periods, indirect losses will be computed.

The methodology that has been described in this paper has focused on the performance of natural gas systems. While these systems are critical for the long-term welfare of a city, they may not be critical for immediate post-earthquake life safety reasons. Therefore, application of this methodology may need to be modified in the investigation of other lifeline services. As part of the Urban Seismic Risk project, the current project team is planning to apply this methodology to water and finally electric power systems. It is anticipated that the economic losses associated with the disruption of these two systems will far exceed those computed for natural gas. Nevertheless, it is anticipated that few changes would be made to the general methodology; the majority of the effort for these other two systems will be in the construction of the usage and economic models.

ACKNOWLEDGEMENTS

The research reported on in this paper was sponsored in whole by the National Center for Earthquake Engineering Research. This support is gratefully acknowledged. In addition, the authors would like to personally thank Professors H. Hwang and M. Shinozuka for their support and help in collecting data on the MLGW systems, as well as regional seismic hazard information. Finally, the authors would like to thank Professor K.J. Tierney for furnishing the results of her Memphis survey. The results from this survey are

helping to reconstruct a more meaningful methodology for examining the indirect effects causes by lifeline disruption.

REFERENCES

Applied Technology Council (1991), Seismic Vulnerability and Impact of Disruption of Lifelines in the Conterminous United States, prepared for the Applied Technology Council by EQE International, funded by the Federal Emergency Management Agency, ATC-25.

American Gas Association (1991), Gas Facts.

Bureau of the Census (1991), County Business Patterns 1989, Tennessee, U.S. Department of Commerce, Economics and Statistics Administration, Bureau of the Census Publication CBP-89-44.

Bureau of the Census (1990), 1987 Census of Manufacture, Geographic Area Series; Tennessee, U.S. Department of Commerce, Economics and Statistics Administration, Bureau of the Census Publication MC87-A-43.

Dames & Moore (1991), Study of Indirect Economic Consequences from a Catastrophic Earthquake: Impact on National Energy Distribution Network, Prepared for Development Technologies, Inc., under contract with the Federal Emergency Management Agency.

Department of Energy/Energy Information Administration (1992), "Natural Gas Annual 1990, Supplement: Company Profiles", Publication DOE/EIA-0131(90).

Hwang, H.H.M. (1991), Seismic Hazards for Memphis Water Delivery System, Proceedings of the Third U.S. Conference on Lifeline Earthquake Engineering, American Society of Civil Engineers, pp.510-519.

Memphis Light, Gas and Water (1992), "Interdepartmental Communication dated October 13, 1992 - Subject: Gas System Information for CERI".

Trott, E.A., Jr., A.E. Dunbar and H.L. Friedenberg (1991), "Gross State Product by Industry, 1977-89", Survey of Current Business, Volume 71, Number 12, December, published by the U.S. Department of Commerce, Economics and Statistics Administration, Bureau of Economic Analysis.

TIME HISTORY ANALYSIS OF SEISMIC SERVICEABILITY OF A WATER SUPPLY SYSTEM

I.J.Markov[1], M.D.Grigoriu[2], and T.D.O'Rourke[2]

[1] Ph.D., Cornell University, Ithaca
[2] Professor of Civil Engineering, Cornell University, Ithaca

ABSTRACT

A new method is presented for estimating the time-dependent serviceability of water networks damaged during earthquakes. The method accounts for the uncertainty in seismic ground motion, soil conditions, current system damage state, required water demand and the finite supply of water in reservoirs and tanks. The analysis is based on the Monte-Carlo simulation method and involves a large number of hydraulic analyses of a water supply system in various damage states. The hydraulic analysis uses an algorithm that eliminates the portions of the network experiencing negative pressures. A computer code with graphic capabilities, GISALLE, developed at Cornell University is modified for calculating the time-dependent seismic serviceability measures. The Auxiliary Water Supply System in San Francisco and an earthquake of the similar intensity as the 1989 Loma Prieta earthquake are used to demonstrate the proposed method of analysis.

INTRODUCTION

Seismic serviceability is an accurate measure for evaluating the seismic performance of water supply systems. The determination of this measure posses significant difficulties because of the uncertainty in the system damage state and the water demand, and because of unavailability of a general algorithm for hydraulic analysis. Current codes for hydraulic analysis have been developed for ideal systems with no leaks. This model does not apply to actual systems in seismic regions. Two computer codes are available for finding realistic criteria of the seismic serviceability of water supply systems [1, 4]. A limitations of these codes is the assumption that the water supply in reservoirs and tanks is infinite. This restrictive assumption is eliminated in this study.

The seismic serviceability of a system depends on the local seismicity, soil conditions, system state, operational strategies, and fire vulnerability. A Monte-Carlo simulation method is used to develop measures for the serviceability analysis of water supply systems. The analysis requires to: (1) generate samples of all random parameters, (2) perform hydraulic analysis of the water supply system in various damage states, (3) develop statistics for serviceability measures and evaluate confidence level, and (4) develop time-dependent serviceability measures.

The computer code GISALLE (Graphical Interactive Serviceability Analysis of Life-Lines subjected to Earthquakes) developed at Cornell is extended to account for the limited water supply of reservoirs and tanks of a system. The code accounts for all uncertain parameters and is based on an algorithm for hydraulic analysis that can model leaks and breaks.

The extended GISALLE algorithm is applied to evaluate the seismic serviceability of the Auxiliary Water Supply System (AWSS) in San Francisco. The seismic event considered in this analysis is the 1989 Loma Prieta earthquake.

EXTENDED GISALLE CODE

The main modules of the code are shown in Figure 1. They include: definition, modification, damage, hydraulic analysis, statistical, time-history, and results modules. The modules allow *preprocessing*, *analysis*, and *postprocessing* capabilities.

The *preprocessor* module allows access to a library of undamaged water supply systems stored as data files. Figure 2 shows the graphical representation of the AWSS on the computer screen as provided by GISALLE. This is an approximation of the as-built

system that does not include pipelines of diameter smaller than 10-in and some of the nodes. Pipelines of different diameters are represented by lines of thicknesses increasing with the pipe diameter. Three water supply sources are also shown in the figure: the Twin Peak Reservoir, the Ashbury Tank, and the Jones St. Tank. There are five fire boat manifolds along the bay line. Fire boats may be connected to one or more manifolds. The figure shows also pump stations 1 and 2. These stations are modeled as single pumps or combinations of pumps.

The data file provides a full description of a water supply system. It contains information on pipes, valves, and nodes. The pipes are characterized by size, length, roughness coefficient, soil condition, and nodal connectivity. A valve on a pipe is modeled by two new nodes on this pipe at 10ft distance. There are two types of valves: valves that can be closed or open and check valves that allow flow in a single predetermined direction. The nodes are specified by coordinates, elevation, specified demand, soil condition, fire risk, and connectivity to pipes. Description of nodes include additional information if nodes are connected to fixed or variable grade components. Fixed grade nodes are nodes connected to reservoirs, storage tanks or a discharge point where pressure is specified. Variable grade nodes are nodes, connected to pumps and fire boats.

The initial data file stored by the GISALLE library can be modified to correspond to a particular supply-demand scenario by a modification module containing interactive computer graphics code. The module allows to activate/deactivate or edit a particular component of the water supply system. The modification module can be skipped to call the analysis module directly.

The preprocessor module also can generate damage states and water demands in the water supply system consistent with the site seismicity, soil conditions, conflagration risk and network characteristics. Damage states are characterized by pipe and hydrant breaks. A Poisson model is used to generate randomly distributed pipe breaks in the system. A Bernoulli model is used to generate randomly distributed hydrant breaks in the system. Water demands correspond to the location of the hydrant closest to a fire. The fire ignition is modeled by a Bernoulli distribution. The fire intensity is characterized by a water demand required for fire fighting. The water demand is modeled as a random variable with a lognormal probability density function.

The *analysis* module determines available flows and pressures at critical hydrant locations for a fire scenario and earthquake intensity. The core of this module is an algorithm for hydraulic analysis. Currently available computer codes for the hydraulic analysis of water supply systems, are based on the assumption that the pressure remain positive at all nodes [5]. The assumption is invalid when dealing with realistic systems that are not air tight because of breaks and leaks. These codes, when applied to analysis of damaged systems,

can predict unrealistically negative pressures at some nodes. Moreover, pressures at hydrants and nodes can not be specified when these codes are used. Therefore, alternative hydraulic analyses are needed for estimating the seismic serviceability of water supply systems.

The hydraulic analysis in GISALLE code can determine flows and pressures in a damaged water supply system. The solution is based on the Hazen-Williams formula and involves an iterative procedure. The computer code identifies the nodes with negative pressures at every step of the iteration procedure. A node i with negative pressure and the pipes connecting this node are eliminated from the system if the total energy at node i is greater than the total energy at all nodes j at the other end of the connecting pipes because there is no flow in this set of pipes. The node i is classified as no-flow node. A node i is classified as a partial-flow node if the energy condition is satisfied only for some nodes j.

The partial flow or open channel flow is characterized by the existence of a free water surface. The surface represents a boundary subject to the atmospheric pressure. The hydraulic analysis in this case is complex and the GISALLE code performs only an approximate partial flow analysis. The approximate method replaces partial flow pipes with full flow pipes by increasing the roughness coefficient such that the pressure at the partial flow node is equal to the atmospheric pressure.

The hydraulic analysis module has two options for elimination of the negative pressure nodes: automatic and interactive. The automatic option eliminates all nodes with negative pressure below a specified pressure threshold. The threshold is specified as a percentage level of the highest negative pressure in the system at every iteration step. The interactive subroutine allows the user to specify a different threshold for the negative pressure at each iteration. The interactive option is useful for verification of the results obtained by the automatic option.

The *postprocessor* module presents graphically: (1) results of selected hydraulic analyses, (2) fragility curves, and (3) results of time-history analyses. Figure 3 show results of a hydraulic analysis of the Auxiliary Water Supply System. The doted and solid lines represent, respectively, disconnected or broken pipelines and pipelines with nonzero flow. The pipeline flow is color coded as shown in the Figure 3 and can be used to detect parts of the system with low flow condition. Similar graphical information is available for node pressure distribution as shown in Figure 4. The postprocessor allows the user to recall the full information for each pipe and node. The pipe information includes flow in the pipe, pipe number, pipe diameter, roughness coefficient and seismic amplification factor. The node information includes node pressure, elevation, demand, seismic amplification factor for hydrant breaks and amplification factor for fire ignition.

SEISMIC SERVICEABILITY

Fragility curves are developed to evaluate seismic serviceability of a water supply system. These curves show the average seismic performance and confidence intervals of seismic serviceability as a function of earthquake intensity. Two performance indices are used to measure seismic serviceability: the damage index S_d and the serviceability index S_s. The damage index is equal to the ratio of total available flow corresponding to the damaged system to the total available flow corresponding to the undamaged system. The serviceability index can be obtained from the ratio of the total available flow of the system for a specified damage state to the total required flow. This index depends on the current demand state of the system.

The determination of the fragility curves involves four steps. First, hydraulic analyses are performed for the undamaged system and generated fire scenarios. Second, damage states are generated for the water supply system consistent with the local seismicity. The Monte-Carlo simulation method is used to generate damage states and fire scenarios. Third, the performance indices are calculated for these damage states and fire scenarios. The seeds of the random numbers used to generate damage states are recorded. Fourth, regression lines, referred as the fragility curves, are constructed based on the values of the performance indices corresponding to the damage states generated in the second phase. Exponential and polynomial regression lines, and confidence intervals for these lines are available.

Figure 5 shows a regression line for the damage index S_d. The line is based on 10 earthquake intensities in the range (VI,VII) of the Modified Mercali Intensity (MMI). Three damage states were generated for each of the earthquake intensity. The figure also shows the 95% confidence interval for S_d. The coefficient of determination R^2, and mathematical expression for the regression curve are available in the upper right window. Similar representation is available for the serviceability indices S_s.

TIME-HISTORY ANALYSIS

The time-history module provides transient values of the performance indices for a water supply system subject to earthquake. The analysis accounts for the decrease of the available water of the tanks and reservoirs supplying the system. The performance indices defined earlier can still be used to measure serviceability in this case but these indices become time-dependent.

The determination of time-dependent performance indices is time consuming because it

has to account for changes that may occur in the water supply system. The analysis involves the following steps:

1. Generate a fire scenario using the fire module. The seed used to generate fire scenario is recorded.
2. Perform the hydraulic analysis for the generated fire and the undamaged water supply system. Available flows are recorded at tanks and fire hydrants.
3. Generated a damage state using the pipe break module and the hydrant break module. The corresponding seeds are recorded.
4. Calculate the damage index $s_{d,j}(t)$ and the serviceability index $s_{s,j}(t)$ for sample $j = 1, 2, ..., n_s$, where n_s is the total number of samples used in the analysis.
5. Calculate the time
$$t_{0,i} = \frac{c_{0,i}}{f_{0,i}} \quad i = 1, ..., n_t \tag{1}$$
to empty tank i, where $c_{0,i}$ is the tank capacity, $f_{0,i}$ is the flow from the tank i, and n_t is the number of tanks in the system. The first tank to empty corresponds to the minimum value of $t_{0,i}$.
6. Shut off the empty tank.
7. Repeated Steps 1-6. Hydraulic analysis is repeated for the same fire scenario obtained in step 1 and damage scenario obtained in step 3.

Statistics are obtained for the damage and serviceability indices as well as for the times required to empty the tanks. Figure 6 shows typical samples of the time-dependent damage index. The dotted line in the figure shows the mean value of the damage indices throughout the time.

The damage index is in this case a stochastic process $S_d(t)$ with mean

$$\mu(t) = E[S_d(t)] \tag{2}$$

and covariance function

$$\gamma(t, s) = E(S_d(t) - \mu(t))(S_d(s) - \mu(s)) \tag{3}$$

The correlation coefficient of damage indices at times t and s is

$$\rho(t, s) = \frac{\gamma(t, s)}{\sqrt{\gamma(t, t)\gamma(s, s)}} \tag{4}$$

The coefficient of variation (C.O.V.) of the time required to empty a tank i is

$$C.O.V. = \frac{\sigma_i}{\mu_i} \tag{5}$$

where μ_i is mean and σ_i is standard deviation for this time. Similar procedure is used to determine the time-dependent serviceability index.

The time-history module provides graphical presentation of the history of the performance indices. Figure 7 show the results of time-history analysis performed on AWSS. Three tanks are supplying water to the system, the Ashbury Tank, the Jones St. Tank, and the Twin Peak Reservoir. Two pumps supply water to the system with four engines running. The analyses were performed for an earthquake intensity of VII MMI. Ten samples were produced. The figure show time-history of the damage index. The index decrease in time to a constant value maintained by the pumps operation. The mean values to empty the Ashbyry Tank, the Jones St. Tank, and the Twin Peak Reservoir are graphically shown on the time axis with the letters "A", "J", and "T", respectively. Numerical values for the mean and coefficient of variation of the time to empty the tanks are shown in the upper left window. A similar presentation is in Figure 8 for the time history analysis of the serviceability index $S_s(t)$.

CONCLUSION

The GISALLE code was extended to incorporate potential changes in the available water supply of a water supply system. These changes can be caused by the complete use of water stored in one or more reservoirs and tanks. The extended GISALLE code uses the same seismic performance indices as GISALLE: the damage and the serviceability indices. However, these indices become time-dependent. The extended GISALLE code was applied to evaluate the seismic performance of the Auxiliary Water Supply System in San Francisco subject to an earthquake of the similar intensity as the 1989 Loma Prieta earthquake.

References

[1] Markov J.I., M.D. Grigoriu, T.D.O'Rourke,"Seismic Serviceability of Water Supply Systems" *Proceeding*, The 4th US-Japan Workshop on Earthquake Resistant Design of Lifeline Facilities and Countermeasures for Soil Liquefaction, Honululu, Hawai, May, 1992.

[2] Markov J.I, M.D. Grigoriu, and T.D.O'Rourke,"An Evaluation of Seismic Serviceability of Water Supply Networks with Application to San Francisco Auxiliary Water Supply System," *Technical Report NCEER-94-0001*, National Center for Earthquake Engineering Research, Buffalo, NY, Jan. 1994.

[3] O'Rourke D.T., M.M. Khater, and M.D. Grigoriu"Earthquake Performance on the San Francisco Water Supply," *Technical Report*, NCEER, 1985. for Earthquake Engineering Research, Buffalo, NY, Jan. 1990.

[4] Shinozuka M. "New Developments in Earthquake Enginering," Proceedings of US/Korea/Japan Trilateral Seminar on Frontier R&D for Constructed Facilities, October 21-24, 1991, Honolulu, Hawaii.

[5] Wood,D.J.,"Computer Analysis of Flow in Pipe Networks Including Extended Period Simulation," Users Manual, Unv. of Kentucky, 1980.

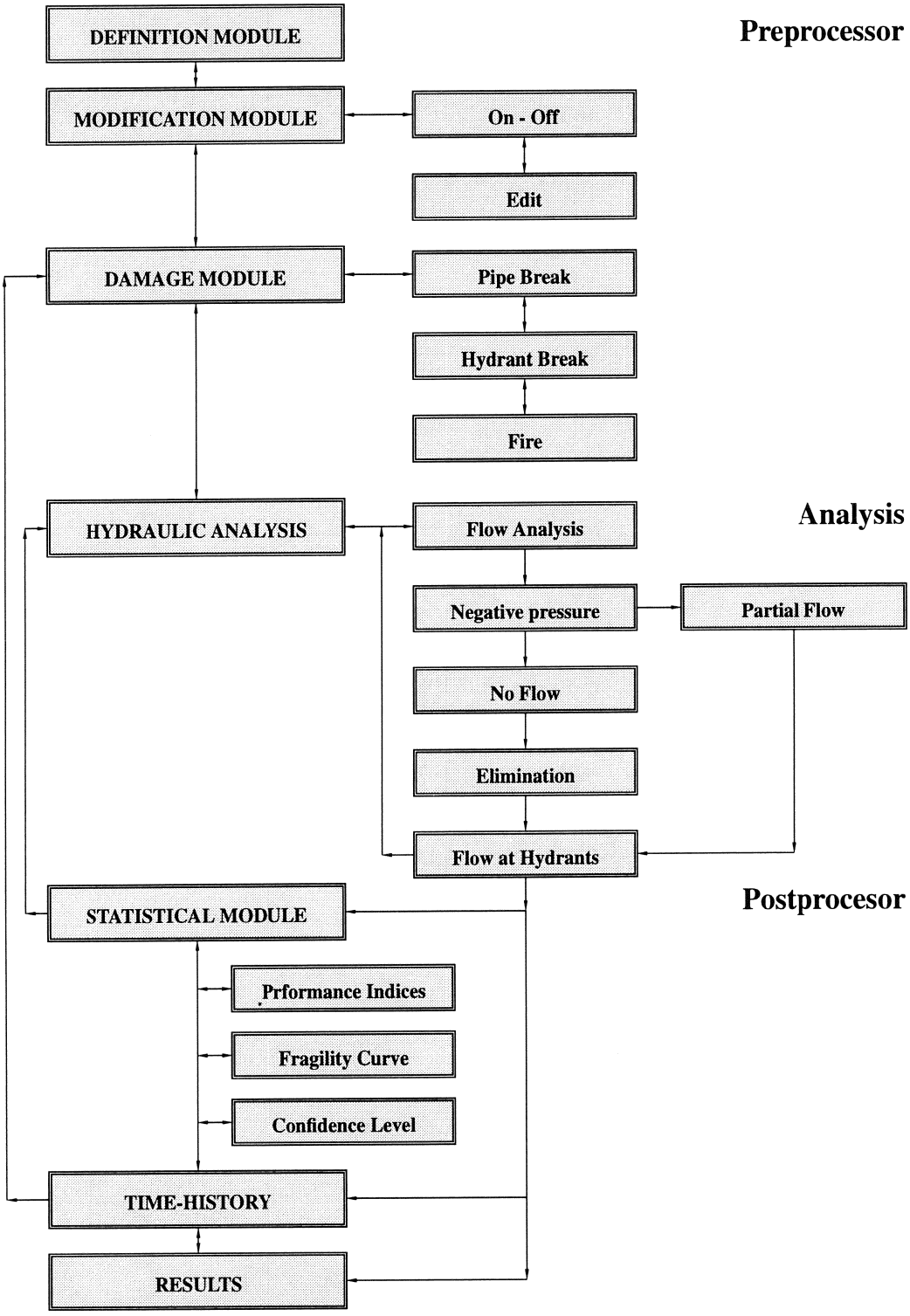

Figure 1: GISALLE Flow-Chart

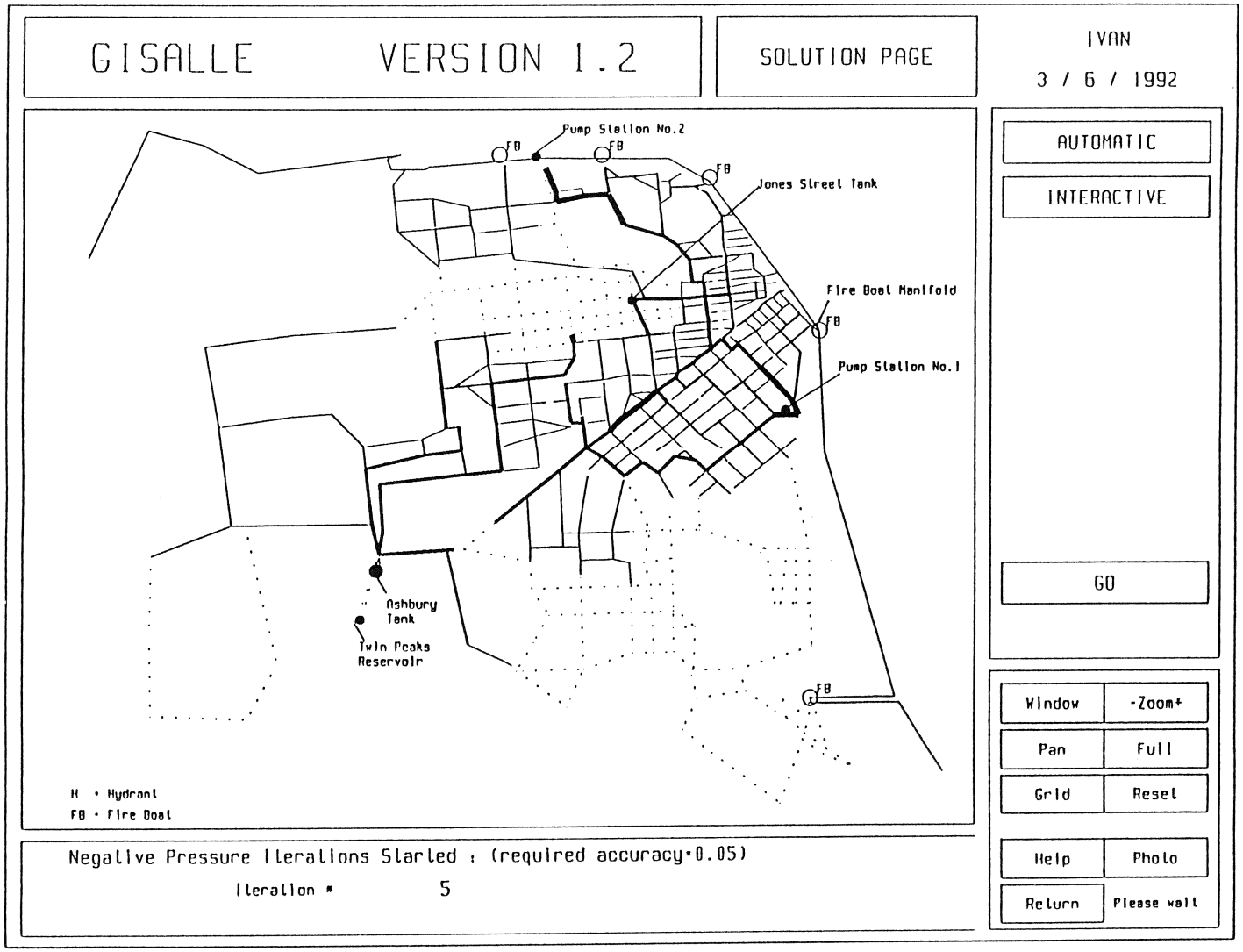

Figure 2: Computer Presentation of the AWSS

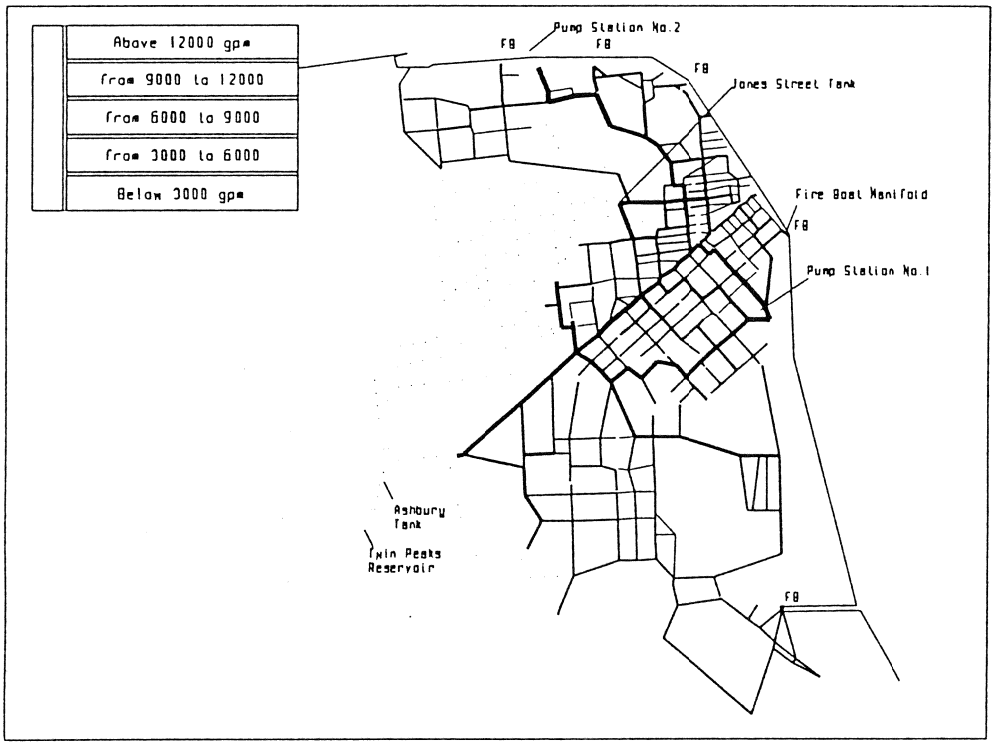

Figure 3: Graphical Presentation of the Flow Distribution

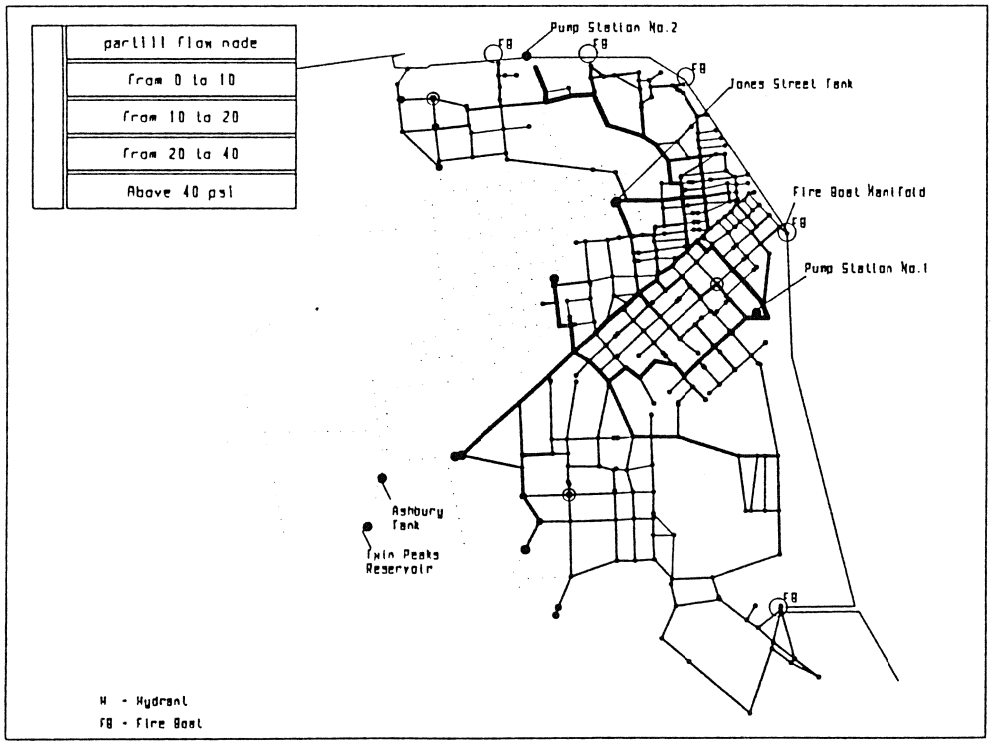

Figure 4: Graphical Presentation of the Pressure Distribution

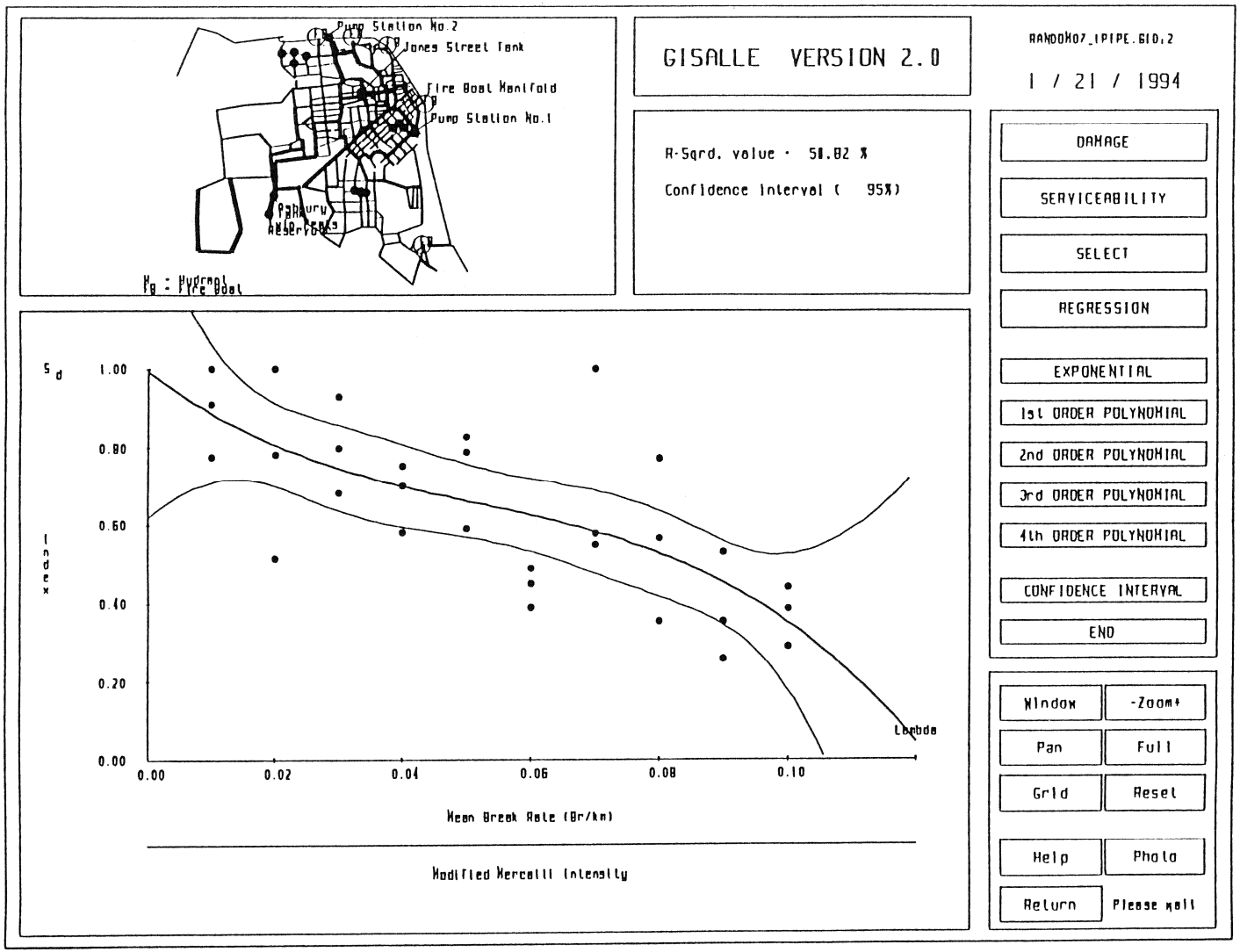

Figure 5: Computer Displays of Fragility Curve and 95% Confidence Level for Damage Indices S_d

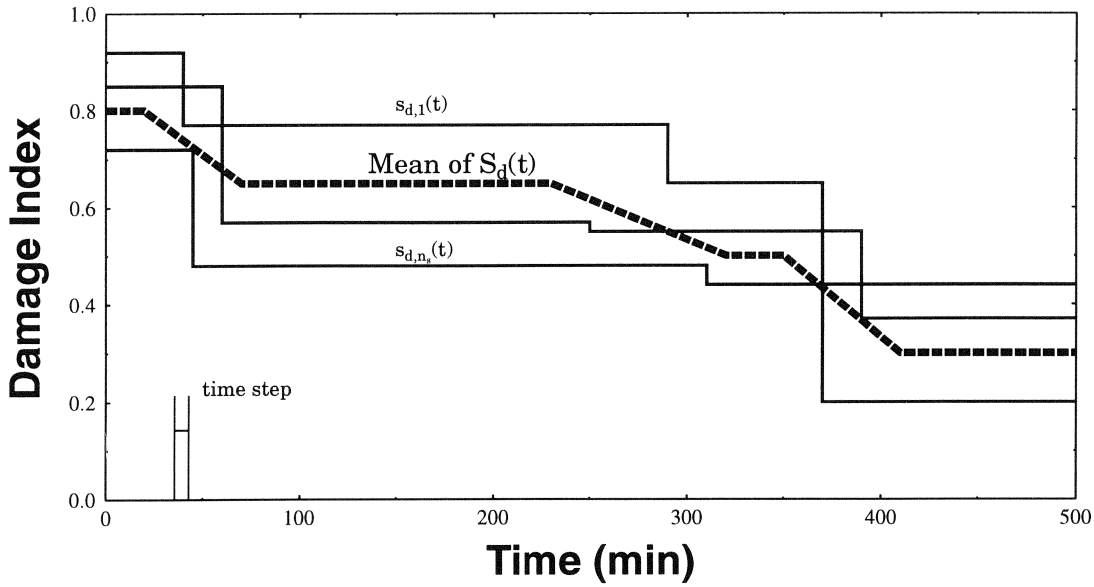

Figure 6: Time-History Analysis of Performance Indices

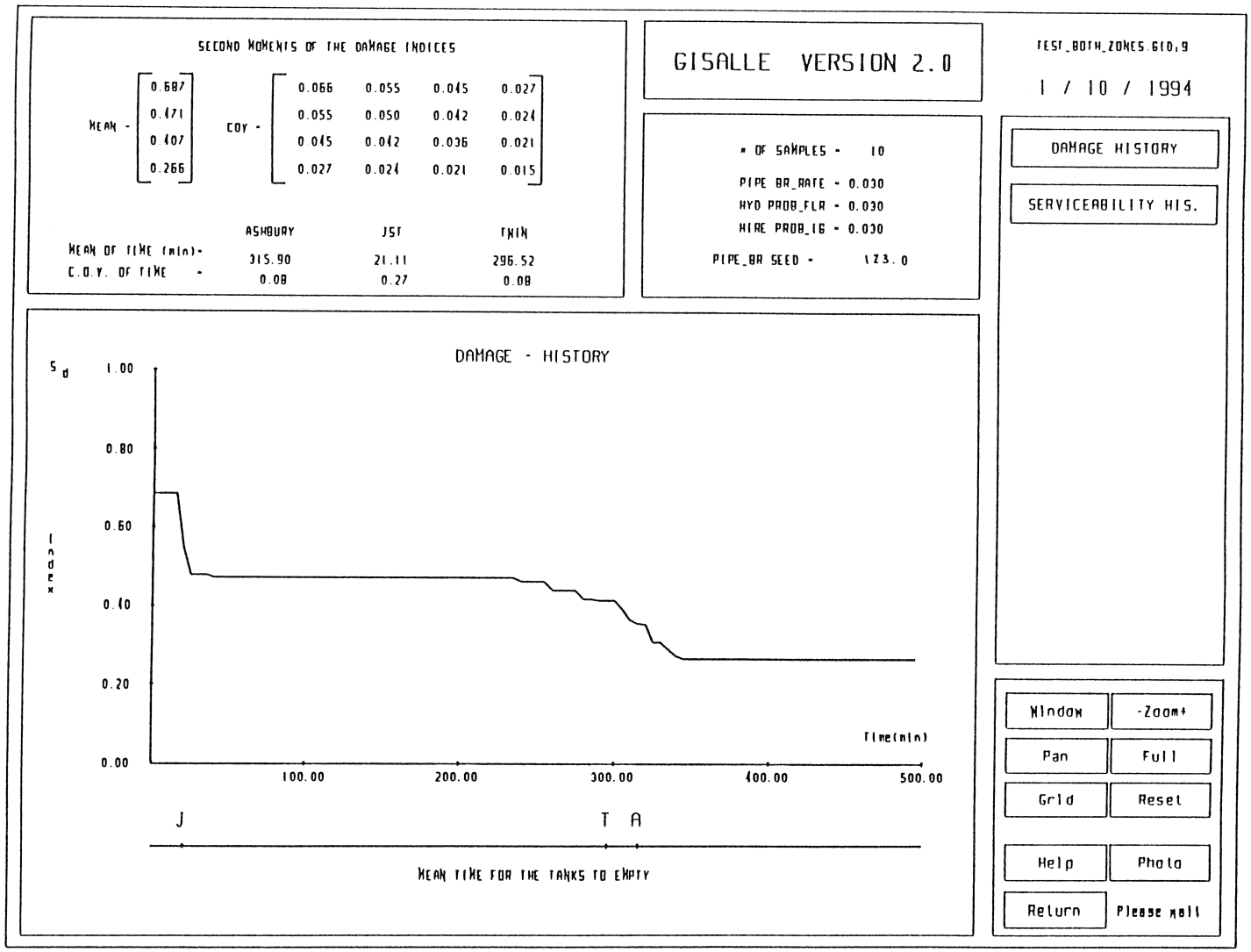

Figure 7: Graphical Presentation of the Time-History for Damage Indices

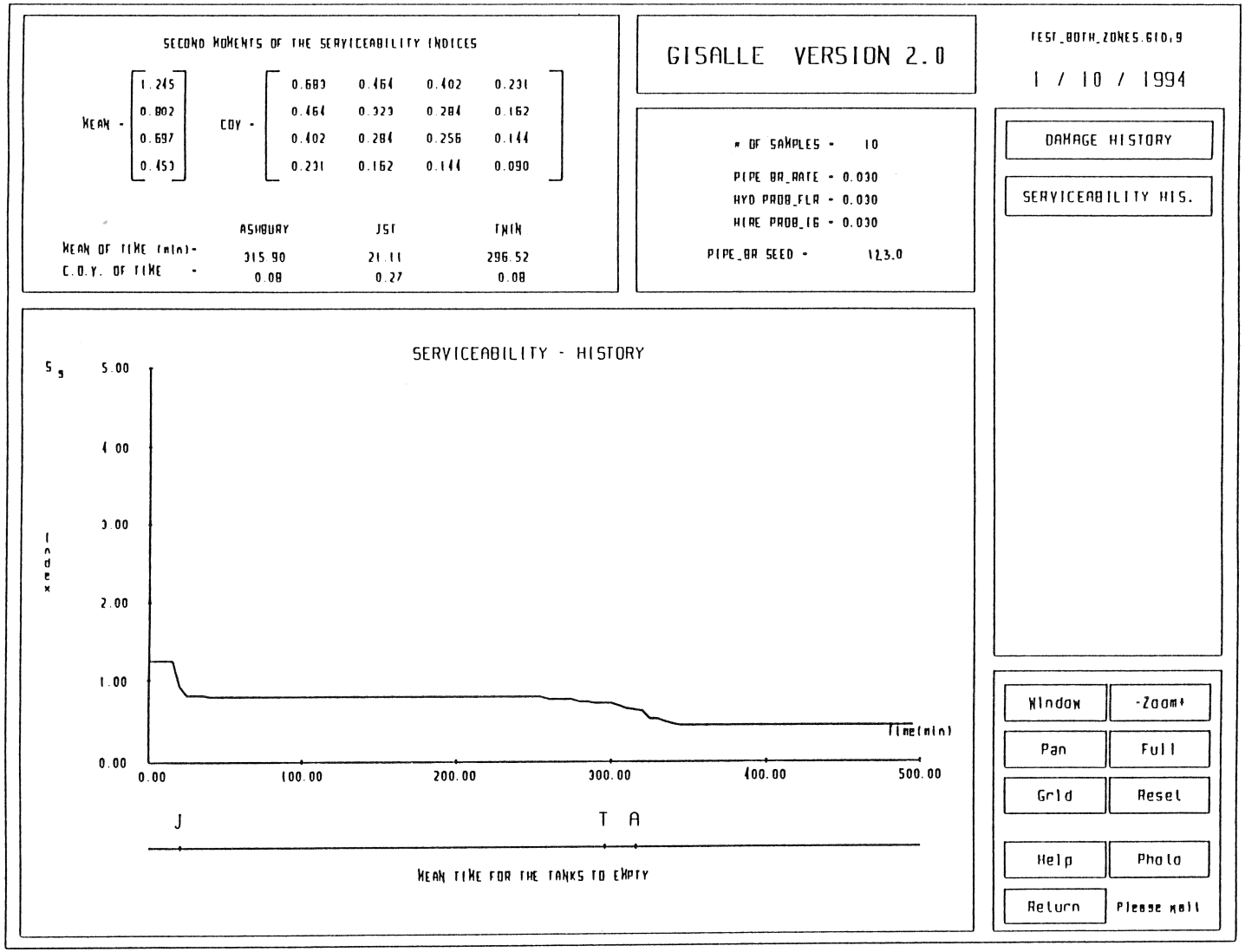

Figure 8: Graphical Presentation of the Time-History for Serviceability Indices

TROUBLES PEOPLE HAVE TO SUFFER WHEN LIFELINES FAIL TO FUNCTION AFTER EARTHQUAKE

HAYASHI, HARUO

Associate Professor, DRS, DPRI, Kyoto University

KAMEDA, HIROYUKI

Professor, UEHR, DPRI, Kyoto University

NOJIMA, NOBUOTO

Assistant Professor, Hiroshima Institute of Technology

ABSTRACT

In the rehabilitation stage of lifelines after earthquake, there would be no room for argument that people tend to experience various kinds of inconvenience due to the functional failure of lifeline systems. However, we do not know yet the exact nature and degree of such inconvenience people may experience during the lifeline functional failure. In order to make it the optimal the rehabilitation processes of lifelines after earthquake, we need to have some empirical data for the quantitative understanding of the incontinences. In this paper, we would like to present a model that describe the inconveniences due to lifeline functional failure based on the experiences by those who lived in Noshiro-city at the time of 1983 Nihonkai-chubu earthquake.

INTRODUCTION

Lifeline systems are one of the indispensable infrastructures for those people living in cities, and they include water supply systems, energy supply systems, disposal systems, transportation systems, and telecommunication systems. Lifeline systems are, however, vulnerable to earthquake. As a result, lifeline services in those cities located near the epicenter were sustained at the every major severe earthquake occurred in Japan for the last 30 years. For example, those people had to suffer severe inconveniences due to lifeline functional failure in such cities as Niigata city at 1964 Niigata earthquake, Sendai city at 1978 Miyagikenoki earthquake, Noshiro city at 1983 Nihonkai-chubu earthquake, and Kushiro city at 1993 Kushirooki earthquake. Thus, the maintenance of reliability of lifeline services became increasingly important issue in the field of urban earthquake engineering along with the rapid development of urbanization of society.

In this paper, we would like to propose a new perspective of lifeline earthquake engineering which integrates the present perspective based heavily on mechanical engineering and system engineering with social scientific perspective which take into account how people would respond to the suspension of lifeline services after earthquake. After explicating our basic assumptions of human behavior as need-reduction sequence, we present our "management model of lifeline earthquake engineering whose goal is the minimization of the inconveniences experienced by the people living in city. Based on the data taken from our intensive survey that asked about 3,000 Noshiro-city residents for their experiences of Nihonkai-Chubu earthquake (1983), some data will be shown to examine the validity of our model.

LIFELINE EARTHQUAKE MANAGEMENT PERSPECTIVE

Lifelines sectors have being taking the every effort to protect the system from earthquakes in all the stages of disaster mitigation, preparedness, responses, and recovery [1]. The prime goal of these efforts has been the minimization of the damages, which is evaluated by the post-earthquake service restoration curve. The main path to achieve this goal is to make the components of lifeline system physically robust and/or to make the lifeline system reliable as network. In this paper, this approach will be called as "pure engineering" approach. Pure engineering approach has been successful in reducing the magnitude of lifeline functional failure. Based on the present state-of-arts and practices in Japan, it is expected in such cities with the population of less than 300,000 people that the normal post-earthquake service suspension period of electric power would be for one day, that of water supply for one week, and that of gas for one month.

Even though pure engineering approach has been successful in reducing the magnitude of lifeline functional failure, it is too expensive and/or virtually impossible to make the lifeline systems free from any damages due to earthquake. People living in cities still have to suffer some inconveniences due to the suspension of lifeline services after earthquake. In case of the earthquake that hits some big city where millions of people live, is it possible or realistic to extrapolate the present level of post-earthquake lifeline performance? The answer would be negative if we take into account the size and complexity of lifeline systems operating in metropolitan regions like Tokyo and Osaka. In any case, it remains as an important issues how to minimize the inconveniences experienced by the people living in cities because of the suspension of lifeline services after earthquake. In challenging this issue, we need to have a new approach which take into account how people would respond to lifeline functional failure after earthquake. In this paper, we call this approach as "management approach".

Both the management approach and the pure engineering approach share the same aim to maintain the quality of lifeline services even in the time of crisis. These two approaches, however, set different goals to actualize the common aim. In the pure engineering approach, the goal is the minimization of the damages. The efforts of the lifeline sector is organized in order to reduce the initial service suspension rate as low as possible and to make the restoration curve as steep as possible. The management approach aims at the minimization of psychological dissatisfaction experienced by the people living in the city with the inconveniences due to the post-earthquake suspension of lifeline services. Even though the minimization of damages itself is the tactics used for the front attack, the management approach also try to reduce the psychological dissatisfaction by providing the information that people want to know.

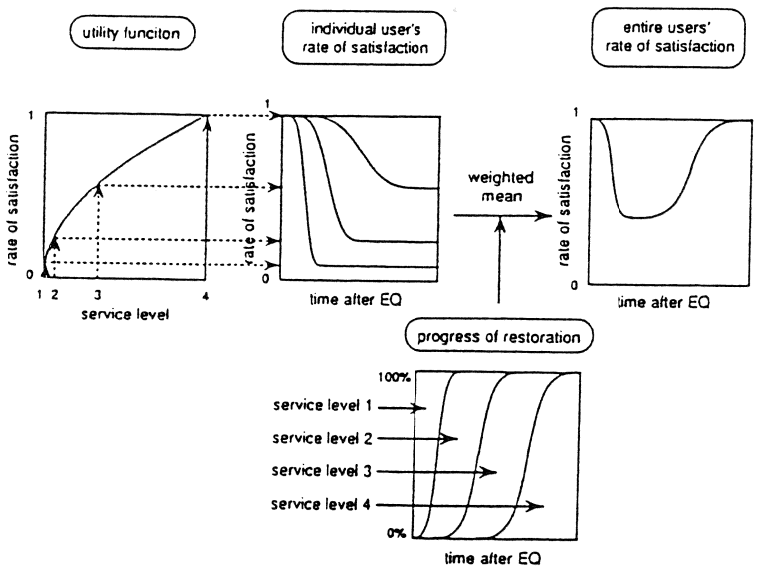

Fig. 1 Schematic Illustration of engineering/Psychological Evaluation of Post-Earthquake Performance of Lifelines [Adopted from Kameda & Nojima (1992)]

Kameda & Nojima [2] introduced a new framework of post-earthquake lifeline performance based on the management approach. They evaluated the post-earthquake lifeline performance not in terms of the in-service rate of lifelines, but in terms of the rate of user's satisfaction, as depicted in Fig. 1. Right after the earthquake lifeline service level is the lowest, at the same time customers' demand is the lowest. As time goes by, both lifeline service rate and customers' demand gradually go back to the normal level. The post-earthquake lifeline performance is determined as a joint function of temporal changes in customers' demand level and those in lifeline service level. There would be no room for argument that both human factors and engineering factors should be included in the management approach for a better understanding of post-earthquake lifeline performance. Based on this framework, what we need to do next is to elaborate these two factors to have a more specific model of post-earthquake lifeline performance. First step should be the clarification of human factors.

HOW HUMAN FACTORS SHOULD BE INCORPORATED INTO LIFELINE EARTHQUAKE ENGINEERING

Lifeline systems provide the satisfaction of human motives. Basically, there are three kinds of human motives. First, there are such biologically based motives that are essentially unlearned and that pertain to the individual alone rather than to his/her interaction with others. Examples are hunger and thirst, the desire for safety, and the need for rest. Second group is no less biologically based than hunger and thirst, but it involves motives that transcend the individual alone and focus on his/her relations with other persons, such as sex, filial love, and aggression. Third group concerns social desires that are acquired through learning, such as the need to achieve, to attain prestige, or to amass possessions. Lifeline services may be deeply concerned with the satisfaction of the first two groups of biologically based human motives.[3)]

The organism including human exist in an internal environment as well as an external one. This internal environment is kept remarkably constant despite considerable fluctuations of the outside environment. The striking consistency is shown by the salt and water balance of the body, its oxygen concentration, its pH, its temperature, and so forth. In healthy organisms, all of these oscillate within very narrow limits and these limits define the organism's conditions for health and survival. This stable internal equilibrium is termed as homeostasis.

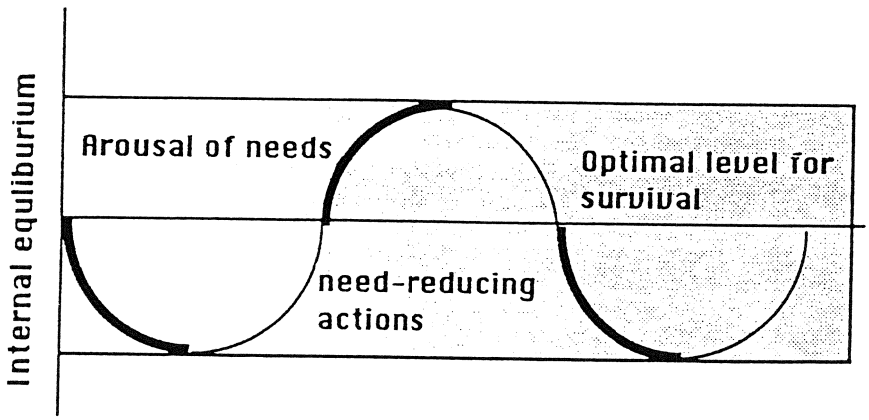

Fig. 2 Conceptual Model of Human Seeking the Internal Equilibrium

Taking human temperature regulation as an example, let us look at how the homeostasis mechanisms work. If our internal temperature is too high, various reflexive reactions such as vasodilation and sweating produce heat loss. An opposite pattern is called into play such as vasoconstriction when the internal temperature is too. These reflexive reactions are called into play when temperature deviated too far from some internal temperature setpoint. The homeostasis mechanisms are essentially involuntary. But there is no question that when the need arises, these reflexive mechanisms are supplemented by voluntary actions. Now the organism actively changes its external environment so

that its internal environment can stay the same. This negative feedback system is the biological basis of human motivational actions which regulate most of human behavior, including social behavior.

After major earthquakes, people experience turmoil and losses in many respects. They include the threat to their safety and possessions, the amenity of their living, and their psychological well-being. In other words, the stable internal equilibrium existed before the earthquake is disturbed so that the organism is motivated to restore the equilibrium or to establish a new balance. The suspension of lifeline services following earthquake causes a threat to the amenity of people's living which is mainly based on the satisfaction of human homeostatic needs. If it takes long time to restore lifeline services, it is expected that people may suffer inconvenience related with such biologically based needs.

The Fig. 2 indicates the basis of how we conceptualize the inconvenience people would have to suffer due to the suspension of lifeline services after the earthquake. Because of the unavailability of lifeline services, people are unable to start the action that people usually take when the need arises as their "routine behavior". Under these circumstances, people have to come up with some new measures to restore the pre-existing equilibrium or to establish new balance. There are at least three different measures: (1) Suspending the need itself; (2) Trying new actions; and (3) Displacing themselves from the scene.

A LIFELINE EARTHQUAKE MANAGEMENT MODEL

Fig. 3 shows how lifeline earthquake management approach conceptualize the post-earthquake response and recovery stages. In this figure, temporal sequence is presented by the configuration of boxes from the top to the bottom: pre-event, co-event, and post-event. Lifeline sector is represented on the left side of this figure, and people relying on lifeline systems on the right side. The key concept of this model is the "crisis" that people may experience due to the suspension of lifeline services after the earthquake. The nature and the severity of the post-earthquake crisis may be determined by a number of factors related with the lifeline earthquake engineering approach such as the lifeline dependence, the lifeline damages, and the lifeline recovery operations, which are represented by those boxes with bold line. It also may be determined by the efforts taken by the people as in the forms of the household preparedness and the coping responses adopted by them. It is obvious from the figure that the traditional lifeline engineering approach can be subsumed as a part of the lifeline earthquake management approach.

The lifeline dependence is determined as a joint function of the availability of lifeline services and appliances in use. People would not experience any inconvenience due to lifeline functional failure unless their daily living relies on lifeline systems and/or their appliances are vulnerable to earthquake. For example, such powers distributed through lines can be supplemented by other power source stored on the spot. If the damages due to earthquake is small in quantity and limited in space, and If they are followed by quick and efective response and recovery operations, little crisis would be observed.

Household preparedness has at least two aspects: Appliances in use and other preparations for disasters. A good combination of appliances can reduce the inconvenience due to lifeline functional failure. Since it usually takes fewer days for electricity to recover than gas, electric powered appliances can be used as the alternatives for the gas appliances. Preparing necessary goods for emergency situations may be helpful to reduce the severity of the crisis. As mentioned in the previous section, people begin to take such coping responses other than their routine behavior as suppressing needs, trying new actions, and displacing themselves from the disaster scene (or evacuation).

The crisis also can be affected by the availability of social services. For example, let us look at the "island of civilization" found in Hiroshima city in Japan after Typhoon 9119.[4] This typhoon caused a large scale electric power failure for at most five days. It is designated as the island of civilization those areas which cover the center of social activities of Hiroshima city, where the underground power distributing system has been implemented so that no blackouts were observed due to salt damage which lasted for the last three days of five days blackouts. As a result, there found little social disorder among the people in Hiroshima city because of the availability of social services provided on the island of civilization even in the middle of a prolonged blackouts.

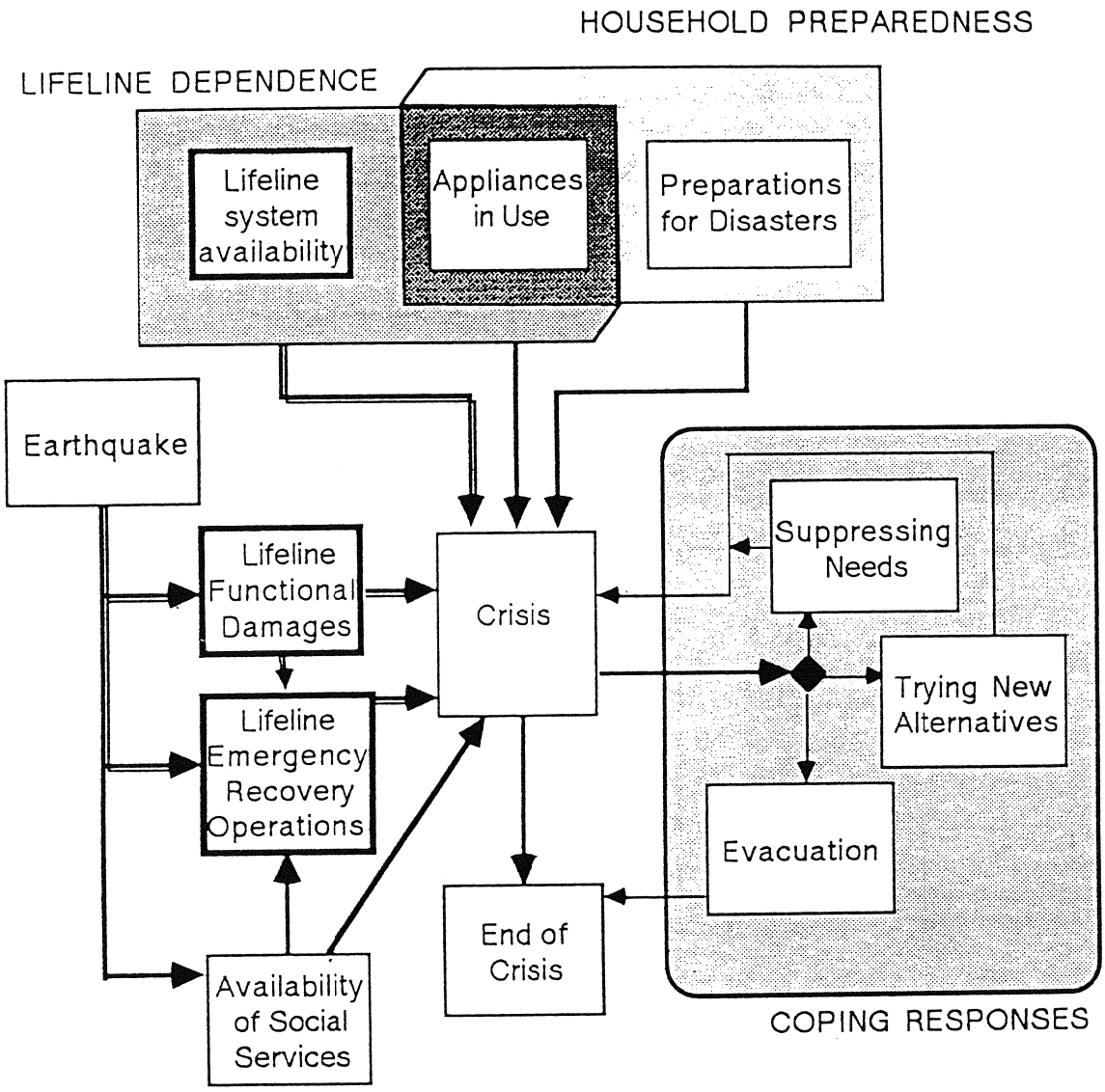

Fig. 3 A Lifeline Earthquake Management Model

THE NATURE AND EXTENT OF CRISIS EXPERIENCED BY THE PEOPLE LIVING IN NOSHIRO CITY AFTER 1983 NIHONKAI- CHUBU EARTHQUAKE

In order to test the validity of our lifeline earthquake management model, we have conducted a questionnaire study with a sample of 1,508 people who lived in Noshiro city at the time of 1983 Nihonkai-chubu earthquake, where a severe lifeline functional failure was occurred after the earthquake. In this paper, we would like to examine quantitatively the nature and the extent of the crisis experienced by the people in Noshiro city after the earthquake. It was assessed by the self report as to the severity of 39 inconveniences and troubles they might experienced. As listed in Table 1, these 39 items were the summary of the facts found in the reconnaissance reports published after various earthquakes.

A factor analysis was conducted to identify the types of crisis people may experience. Based on the scree test, we decided to retain five factors extracted by the principal component method. The total variance explained by these five factors amounts to 0.5700. Table 1 summarizes the factor loadings of five factors rotated by Varimax rotation method.

The first factor can be interpreted as "Water-related activities" because all the activities with high factor loadings on this factor can not be performed without water supply. Some activities rely only on water-supply such as drinking water and flushing water, others need or prefer to have some kinds of heat source. This factor is directly related with the suspension of lifeline services. The second factor can be interpreted as the factor concerning the "Social stability after earthquake". This factor reflects the anxieties held by the people as to the stability of the social services available to them before the earthquake. Thus, this factor is related with the availability of social services. The third factor again is directly related with the suspension of lifeline services. All the items with high factor loadings on this factor would be in trouble directly or indirectly as the results of the electric power supply, or "{Electricity-related activity". Another common feature of this factor is the fact that relatively small proportion of people had suffered on those activities with high factor loadings on this factor. The fourth factor reflects the "Informational needs" held by the people after the earthquake. With the earthquake, lots of information should be acquired before people understand exactly what happened to them as well as to their community to restore their internal equilibrium. Since telecommunication systems and transportation systems provide the basis for acquiring such information, this factor reflects indirectly the suspension of lifeline services. The last factor is concerned with "the property losses" caused by the earthquake. Since houses and real estate comprises of an important part of personal assets for many people, there would be no question people would be deeply concerned with the property losses.

CONCLUSION

The results of factor analysis of inconveniences and troubles experienced by the people in Noshiro indicated that there are five different kinds of inconveniences: (1) Water-related household activities, (2) Anxieties as to the social stability after earthquake, (3) Electricity-related household activities, (4) Informational needs held by the people after the earthquake, and (5) The property losses caused by the earthquake. In relation to lifeline earthquake management, three of these factors turned out to be concerned with the suspension of lifeline services directly and indirectly. It found that electricity and water are the two basic supply systems which results in the inconveniences for many household activities. The suspension of services by both telecommunication systems and transportation systems affects the informational needs held by people after the earthquake. In the next step, we would like to clarify the relationships between these three types of inconveniences and the coping strategies taken by the people after the earthquake.

REFERENCES

[1] Nojima, N., Kameda, H.,& Shinozuka, M. (1990) Fundamental structure of earthquake disaster countermeasures in lifelines., Journal of Natural Disaster Science, vol.12, No.1, pp.29-47.

[2] Kameda, H, & Nojima, N. (1992) Developments of lifeline earthquake engineering., The Proceedings of IDNDR International Symposium on Earthquake Disaster Reduction Technology - 30th Anniversary of IISEE, pp.111-128.

[3] Gleitman, H. (1991) Psychology, 3rd Ed., W.W.Norton & Co., New York.

[4] Hayashi, H. (1993) "Island of civilization-A lesson for large scale lifeline functional failure. The Proceedings of IDNDR Aichi/Nagoya Conference, UNCRD.

Table 1 A Factor Analysis of Incontinences and Troubles Experienced by the People Living in Noshiro city at the time of 1983 Nihonkai-Chubu earthquake

INCONVENIENCES AND TROUBLES	FACTOR1	FACTOR2	FACTOR3	FACTOR4	FACTOR5
Doing dishes	0.86584	0.17753	0.06806	0.09941	0.07736
Washing faces	0.86309	0.16889	0.02811	0.03491	0.11819
Doing laundry	0.86012	0.17821	-0.02825	0.03785	0.14984
No drinking water	0.83905	0.16515	0.00806	0.05487	0.13812
Cooking	0.82733	0.14109	0.17603	0.11977	0.00897
Taking a bath	0.81836	0.16672	-0.03388	0.02906	0.20423
Boiling water	0.77551	0.13829	0.23652	0.11684	0.02278
Cooking rice	0.73027	0.11554	0.28622	0.19596	0.00749
Flushing toilet	0.49723	0.01150	0.26798	-0.00135	0.09512
Social Disorder	0.04628	0.74643	0.37002	0.08061	0.10072
Disease	0.26725	0.72174	0.22129	0.13249	0.17003
No merchandize to sale	0.30858	0.70529	0.19265	0.19779	0.08382
Fire	0.02465	0.69957	0.24025	0.12614	0.12336
Inflation	0.05642	0.69550	0.32499	0.08450	0.11260
Sanitation	0.40827	0.67203	0.12509	0.11219	0.16958
Tsunami	0.21962	0.53543	-0.10383	0.28913	0.12831
Child fearing earthquake	0.14903	0.48986	0.04510	0.26226	0.09651
Aftershock	0.30539	0.48041	-0.18941	0.35801	0.18437
No cooling	0.11179	0.16041	0.71388	0.00632	0.10242
No heating	0.14748	0.22234	0.67593	0.01145	0.18495
No radio	0.25105	0.17487	0.65273	0.18705	-0.01007
No television	0.29815	0.14972	0.60280	0.28223	0.01561
No refrigerator	0.47575	0.09224	0.53094	0.22461	0.03648
No cleaning a house	0.47726	0.20973	0.52530	0.09743	0.10206
No lights	0.22810	0.06491	0.49815	0.37432	0.17097
No injuries (personal)	-0.03186	0.07666	0.45030	0.05394	0.12897
No injuries (family)	-0.04454	0.05296	0.38816	0.07650	0.17280
No contact with friends and relatives	0.09854	0.17591	-0.02375	0.76541	0.02520
No contact with family	0.06776	0.18203	0.01150	0.71275	0.04088
No information regarding disasters	0.09625	0.19936	0.12334	0.70885	0.07609
No commuting	0.04609	0.15833	0.33028	0.59112	0.17350
No business communications	0.03775	0.12632	0.31085	0.58641	0.08452
No business	0.07646	0.07430	0.28168	0.53030	0.23384
Repairing the house	0.11779	0.12762	0.04345	0.08046	0.79193
Cleaning up outside the house	0.09496	0.09326	0.15328	0.05285	0.77992
Repairing gates and walls	0.07460	0.12004	0.17020	0.04437	0.73142
Cleaning up mess inside the house	0.20304	0.13875	0.01539	0.15805	0.64999
Repairing furniture	0.15752	0.18348	0.15091	0.11670	0.57538
Troubles in relation to real estate	-0.01641	0.06568	0.32175	0.10172	0.53690
EIGENVALUE	7.00055	4.39759	4.09598	3.41680	3.32015
PROPORTION	0.1795	0.1128	0.1050	0.0876	0.0851

GUIDE TO DOCUMENTING EARTHQUAKE DAMAGE TO POWER SYSTEMS

Anshel J. Schiff

Consulting Professor, Civil Engineering, Stanford University
Principal, Precision Measurement Instruments

ABSTRACT

Recent earthquakes have identified new issues about and elevated the importance of older issues that need more scrutiny so that they can be better understood. Guidance is provided to aid investigators in identifying these areas of concern. New methods of documenting damage are also presented through the use of prepared substation schematic diagrams. Guidance is provided for identifying damage when investigating substations. It is recommended that the electric power industry establish and implement a procedure for an inter-utility group to conduct post-earthquake investigations. It is recommended that a follow up investigation be made several months after the earthquake to identify additional damage and to get a better understanding of the causes of damage. It is recommended that strong motion seismographs be placed at major power facilities so that equipment performance can be quantitatively evaluated.

INTRODUCTION

Role and History of Post-Earthquake Investigations of Power Systems

Information gained from post-earthquake investigations is the major source of data for improving earthquake design, practice, standards and codes. Observations from the 1925 Santa Barbara and 1933 Long Bear earthquakes were the main impetus for adding earthquake provisions in building codes. After 1933 some power companies in Southern California started to anchor bulk power transformers and to use flexible bus rather than rigid bus in the construction of substations. A group of engineers and seismologists, which would eventually become the Earthquake Engineering Research Institute (EERI), were active in "chasing" earthquakes, although their primary interest was construction based on civil engineering, such as buildings and bridges. Early lifeline investigations of power systems were directed primarily at identifying items that were damaged, such as circuit breakers, transformers, etc. Even after the 1971 San Fernando earthquake, very little effort was devoted to formally identifying failure modes and factors that may have contributed to the failures, although observations were used to improve designs and installation practices. In 1974 the Technical Council on Lifeline Earthquake Engineering (TCLEE) was established in the American Society of Civil Engineers. Under TCLEE the Earthquake Investigations Committee was formed and has been active in investigating earthquakes, often in conjunction with EERI. In the mid 1980's the Electric Power Research Institute (EPRI) became active in investigating earthquake damage and it has gathered more detailed information defining the equipment. Their emphasis has been on equipment that is found in nuclear generating plants, particularly safe shutdown equipment, although other power facilities are investigated. EERI and TCLEE earthquake investigation efforts are primarily professional volunteer activities with partial support for travel expenses. EPRI funds its investigators to gather the detailed data they need for their program.

In 1985 the TCLEE Earthquake Investigation Committee began to develop a guide for the post-earthquake investigation of lifelines. This Guide was developed to address a situation that is unique to lifeline investigations. Most lifelines are complicated systems made up of many facilities (nodes), that are usually linked to form a network. These systems are often designed with a high degree of redundancy to enhance system reliability. Redundancy is incorporated not only into the links that

form the lifeline network, but also at the system nodes. To properly investigate a lifeline, equipment and structural damage must be identified. The impact of equipment damage on each facility and the resulting effect on system performance should be evaluated. Each of these evaluations should identify failure modes and design features and installation practices that contributed to the damage or failure. The Guide reviews the elements in the lifeline, their function within the facility and their performance in past earthquakes. The role of various facilities in system operations is also reviewed.

This paper provides additional information on how to find and evaluate power system earthquake damage. The paper is organized into the following sections as follows: objectives of post-earthquake investigations, review key of issues discussed in Guide, items requiring special attention that were not emphasized in the Guide, new methods of documentation, finding damage and factors contributing to it, and recommendations and conclusions.

OBJECTIVES OF POST-EARTHQUAKE INVESTIGATIONS

The objectives of a post-earthquake investigation are to identify equipment that was damaged or that failed to operate and identify equipment that performed well when subjected to significant seismic exposure. The investigator should attempt to identify in quantitative terms the seismic exposure by searching out strong motion records. In addition to identifying equipment performance, factors that could influence its performance should be documented. Information about site conditions, installation practices including details of anchorage, support structures and electrical connections should be recorded. The investigator is in the best position to make engineering estimates about the failure modes and the factors that contributed to the failures, as the local setting can be observed. In addition to damage, other factors, such as system configuration and operating procedures, that may have influenced the performance of the system in a post-earthquake environment should be noted. Where the cause of a failure is not clear, tests and analysis should be suggested that could resolve the issue. Changes in design and practice should be put forward for consideration to improve seismic performance. Also, changes in procedure and methods to improve post-earthquake investigations

should be identified. Finally, the observations of the investigation should be communicated to the professional community.

REVIEW KEY ISSUES DISCUSSED IN THE GUIDE

The "Guide to Post-Earthquake Investigation of Lifelines," TCLEE, Monograph No. 3, August 1991 provides general information on conducting an investigation and specific information on power systems. Information on pre-departure preparation, personal and investigation equipment needs, gaining access to facilities, interviewing techniques, and general information that should be gathered at most sites that are investigated is given. Packing lists and check lists of information that should be gathered in the field for each lifeline are provided. In addition, an overview of the configurations, facilities, equipment operation, and functions and seismic performance of equipment and facilities are reviewed for each lifeline. These topics will not be reviewed here. It is recommended that the Guide be studied to gain insight into these aspects of earthquake investigation of power systems.

ITEMS REQUIRING SPECIAL ATTENTION NOT EMPHASIZED IN THE GUIDE

Damage in recent earthquakes indicates that several items not emphasized or discussed in the Guide should be given more attention so that they can be better understood. Some of the damage has been observed previously, but the perception of its prevalence or significance has changed. It is emphasized that the following topics are to be investigated in addition to those identified in the Guide.

Transformer Bushings

Transformers are one of the few items in a power system whose function cannot be eliminated or substituted. Bushings can crack and must be replaced. There can also be slipping or oil leaks at the interface between the porcelain and the metal flange that make up the bushing. Figure 1 illustrates an extreme example of bushing offset. This interface should be carefully observed for signs of oil leaks, small offsets, or gaskets protruding from the interface. Epoxy is often placed on the outside of the bushing - flange interface in an attempt to stop oil leaks.

Surge Arresters

Surge or lightening arresters are one of the more vulnerable items in a switchyard. Within a substation they are typically connected to each conductor on each side of power transformers and are often supported on a boom mounted on the transformer. The surge arrester is frequently supported on small porcelain standoffs with a ground path through a strike counter. Surge arresters can be connected directly to the bushing or they may have their own drops from an overhead conductor. In the former case, if the surge arrester fails and falls, it can put a direct load on the transformer bushing and damage it. Additional information is needed on the performance of surge arresters, their standoffs, the method in which they are connected into the circuit, and their impact of transformer bushings.

Leaking Transformer Radiators

Prior to the development of the Guide, it was known that large, manifold-mounted radiators are vulnerable to leaks. New data shows that "large" individual radiator elements that are connected directly to the transformer are also vulnerable. Additional information is needed to better define what constitutes a "large" radiator.

Disconnect Switches

Two failure modes have been observed in disconnect switches. The first is the failure of post insulators used to fabricate disconnect switched. The second is the misalignment of the switch so that the contacts do not engage properly. An indication that this problem has occured is the use of rope to hold the misaoligned disconnect switches together so that circuits can be quickly and temporarily put back into service before final repairs are made, as indicated in Fig. 2. The misalignment can be caused by several effects that should be checked. Differential settlement of the disconnect switch footings may distort the disconnect switch support structure, the metal platform to which the post insulator is bolted or the bearing just below it may deform, the channels at locations that support the lower disconnect switch bearing housing may deform, or the operating leakage may slip or be deformed. This information can best be obtained from service personnel at the site.

Emergency Power

Emergency power in the form of station batteries and engine-generators has performed poorly. The diverse causes of emergency power failures and the impacts of the loss of emergency power need to be more fully documented.

Interactions with Suspended Wave Traps or Current-Voltage Transformer s

Wave traps and current-voltage transformers are occasionally suspended from conductor support structures. They are restrained from below by column supported post insulators or insulator strings, which are anchored to a pedestal, a ground anchor, or some other support structure. Earthquake induced lateral motion of the suspended item may interact with adjacent equipment if adequate slack in conductors is not provided. Information on the seismic performance of the various configurations of this equipment is needed.

Rigid Bus

There have been several failures associated with loads transferred by rigid bus or by connections to rigid bus that has fallen from its supports. In some cases, the falling bus has damaged equipment. The performance of various configurations needs to be documented.

Communications Equipment

Most substations have communication equipment associated with protective relay systems and other control and monitoring functions. This equipment is typically installed in communication racks that are anchored to large aluminum angles that are bolted to the control room floor. These racks tend to be very flexible and equipment in the rack may be inadequately anchored. The performance of various configurations needs to be documented.

Quality Assurance of Anchorage Details

One of the better methods of anchoring heavy equipment, such as power transformers, is to weld the case of the equipment to steel plates embedded in the

concrete foundation pad. This method has failed due to inadequate design capacity of welds, welds smaller than called for in designs, poor weld penetration and poor design associated with the anchorage load path. The performance of various configurations needs to be documented.

Black Start Capability

The performance of black start capability has been very poor. It is important to get a detailed evaluation of the diverse causes that disrupt black start systems.

METHODS OF DOCUMENTATION

Since the Guide was originally written, small, light-weight moderately priced video cameras have become available. The use of video has some advantages over photographic slides or prints. While a video does not have as large a dynamic range as film, it can get pictures in poorer lighting conditions. The video also has an audio channel so that the pictures can be documented with voice descriptions as it is being shot, one of the main advantages of using a video recorder. It is often difficult to document slides, even if a small tape recorder is used. When taking pictures of substation damage, it is often difficult to identify the location of the picture when the film is evaluated later, because substation equipment looks very similar. For example, a large 230 KV rack may have 20 breaker-and-a-half positions (a common configuration used in substations). With a video recorder, the sound track can be used to identify the position, or the video recorder can be panned from the position identification number to the item of interest. The large zoom available on newer recorders allows both wide angle and telephoto shots to be made without changing lenses. Low cost audio-visual computer equipment is becoming more common and it can be used for analyzing video data and generating hard copy that can be directly incorporated into reports.

Video does have some disadvantages. It is another item that must be carried, a burden when getting in and out of vehicles and in climbing around facilities. There is also a need to have an adequate supply of power, which may require that several extra battery packs be used. In cold weather and when power is disrupted, power for the camera may be a severe problem. In analyzing data, it is not convenient to

compare different shots or find a specific shot using video. For publication purposes and general preservation, pictures have much better quality. It is necessary to be able to stop the video to analyzed picture contents. When this is done using a VCR and a television monitor, the quality of the picture may not be preserved with some equipment. The resolution of video is much poorer than that of film and in some situations the large zoom of the video may not be able to compensate for the poor resolution. For example, things in the background frequently provide valuable information. This is often not observed at the time so that a close-up picture was not obtained. The need to take both video and photographic pictures requires additional time. Like any tool, it may take some practice to become familiar with all of its advantages and disadvantage.

While a broad range of items have been damaged in power system facilities, damage is concentrated in high-voltage substation. Damage must be documented in such a way that the data can be analyzed later to identify potential failure modes and factors that may have contributed to the failures. For example, if a wave trap fails, its method of support and the locations of the damage should be documented. The use of a standard preprinted form can speed data collection and provide a more accurate and complete record of the damage. Most substations take one of a few standard configurations. Two configurations are considered here, a breaker-and-a-half configuration and a double-bus-double-breaker configuration. Copies of these forms can be used in the field to document damage. The configurations shown in the schematic diagrams have been fully "stuffed", that is, the maximum number of auxiliary items is shown. For example, in Figure 3, each of the three phases for a breaker-and-a-half position has a wave trap and current-voltage-transformer. In practice, many of the wave traps and current-voltage-transformers will not be used. A standard procedure for indicating that some items are not present and the exact location of damaged items allows damage to be quickly documented. At the bottom of the figure several common configurations of equipment are illustrated. These can be used to document items at a given site. The collection of the diagrams for a switchyard allows damage patterns to be observed, which can help in identifying failure modes.

FINDING DAMAGE AND FACTORS CONTRIBUTING TO IT

Finding and documenting damage is complicated by the fact that utility personnel start to clean up and restoration damage within an hour or two after the earthquake, even when there is major damage. If only one or two sites are slightly or moderately damaged, clean up and restoration starts almost immediately. As a result, restoration will almost always be in progress or may be completed before the investigator arrives at the site. The procedures given in the Guide should be followed, that is, start where the high voltage lines enter the site and work though the system. It can be useful to go to the "grave yard" and "bone pile" before inspecting the equipment. The "grave yard" is usually located along the boundary fence on one side of the switchyard and contains the remains of damaged equipment, such as circuit breakers and current-voltage transformers. The "bone pile" is usually a collection of damaged post insulators that were used to support equipment, such as wave traps or bus or were part of damaged disconnect switches (disconnect switches are fabricated using post insulators). This will give an indication of the types and amount of damage at the site, if the damaged equipment has not already been removed from the site. When restoration work has started, it may be difficult to identify damage.

When broken porcelain is still in place at the time of the investigation it is clear what equipment has been damaged. This is also the best situation for identifying failure modes and factors contributing to them. This is why it is important to investigate sites as soon after an earthquake as possible. If porcelain items are missing, in general it is reasonable to infer that the item was damaged and removed. However, undamaged items are frequently cannibalized to reconstruct other circuits. Porcelain shards on the ground under the missing item is a good indication that it was damaged.

Some equipment may be reconstructed at the time of the investigation, so that it may be necessary to infer damage by some tell-tale signs. Broken porcelain on the ground has already been mentioned. Mismatched porcelain on an item is also an indication that equipment has been restored with spares that were available or by cannibalizing damaged equipment. For example, one type of disconnect switch contains six porcelain post insulator stacks, two for each phase. It is very rare to find stacks that are mismatched, that is, different colors or different shed (small fins to

shed water) patterns. Figure 4 shows a conductor near a circuit breaker bushing that has had its aluminum rope lay opened when the post insulator on an adjacent disconnect switch failed, fell, and pulled on the conductor. Figure 5 shows a series of chipped paint marks on a circuit breaker case caused by a falling post insulator that failed and fell from the adjacent disconnect switch. Porcelain chard at the base of the circuit breaker is also a sign that the adjacent disconnect switch failed. Chipped sheds on post insulators or bushings is an indication of secondary damage, so that the failure that caused this damage should be sought out. Exposed surfaces of chipped porcelain that is still usable are often given a protective coating to prevent moisture absorption. The typically barn-red color of this coating makes the repair obvious. Many equipment items, such as transformers, current-voltage transformers, and current transformers contain oil, so that signs of a recent oil spill is an indication of damage. Indications of an oil leak are a sheen on equipment surfaces or their support structures, discoloration of paint on support structure, as indicated in Fig. 6, oil absorbing material below the item, or discoloration of the gravel below the item. Transformer bushings that have developed leaks at the porcelain-flange interface may have an epoxy coating to stop the leak. New looking conductor connecting hardware or unoxidized conductor may indicate that the connections had to be reworked to accommodate different sized replacement equipment. On rigid-type conductor, shiny conductor near a weld indicates recent repairs. Distress at anchor bolts will be a sign of large loads and possible equipment failure. A stretched bolt is indicated if nuts on studs or anchor bolts are loose. Frequently nuts are staked with a center punch, painted over, corroded, or jammed so that they can not turn, but a loose washer below the nut indicates the stud has stretched. Also look for chipped or cracked paint or deformations near gussets or anchor points. Temporary repairs made with rope or wire to hold conductors or other items are an indication of failed connecting hardware, as indicated in Fig. 7. Freshly poured footing suggests that a pad for new equipment has been installed.

One of the major problems in identifying failure modes is to distinguish between interaction problems due to inadequate slack and inertial loads. Two features of the fracture surface of porcelain can be used to identify the location where the failure started. If this point is not lined up with the orientation of the conductor, interaction is probably not the cause of the failure. When observing one of the fractured surfaces, there may be a large hump or depression on the side opposite the point where the failure started. This is referred to as the hinge. Another feature

that may be present is referred to as waves. These waves have the appearance of waves at a beach that have broken and have then been flattened. These waves are directed towards to point where the failure started.

After completing an initial inspection of the site, try to do a quick walkdown of the site with the foreman who is in charge of work at the site. It is best to set this up when arriving at the site so that he or she can work it into their schedule. Damage that has been missed or repaired and cannibalized items can be identified.

CONCLUSIONS AND RECOMMENDATIONS

Observations on the actual performance of power system equipment and facilities are one of the best ways to improve equipment design and installation practices. Careful observations using all clues are needed to identify damaged equipment and their failure modes.

When there is major power system damage, the affected utility will often be overwhelmed in attempting to restore service and there may not be adequate resources available to document damage. While informal arrangements between major California power companies exist to facilitate post earthquake inspections, there is a need to develop this capability in other regions of the county and to assure that it will work in California if there is a catastrophic earthquake.

There is a need to get power equipment manufacturer engineers in the field after an earthquake so that they better understand the performance of their equipment under seismic loads. In the long run this may improve the design and seismic performance of equipment.

There is a need for strong motion instruments to be located at important sites so that data will be available to evaluate and better understand the performance of the equipment.

There should be a follow up investigation several months after the earthquake, as additional damage may have been identified and the utility may have a better understanding of the failures.

ACKNOWLEDGMENTS

The cooperation of utilities are gratefully acknowledge for providing access to facilities so that damage could be documented.

FIGURES

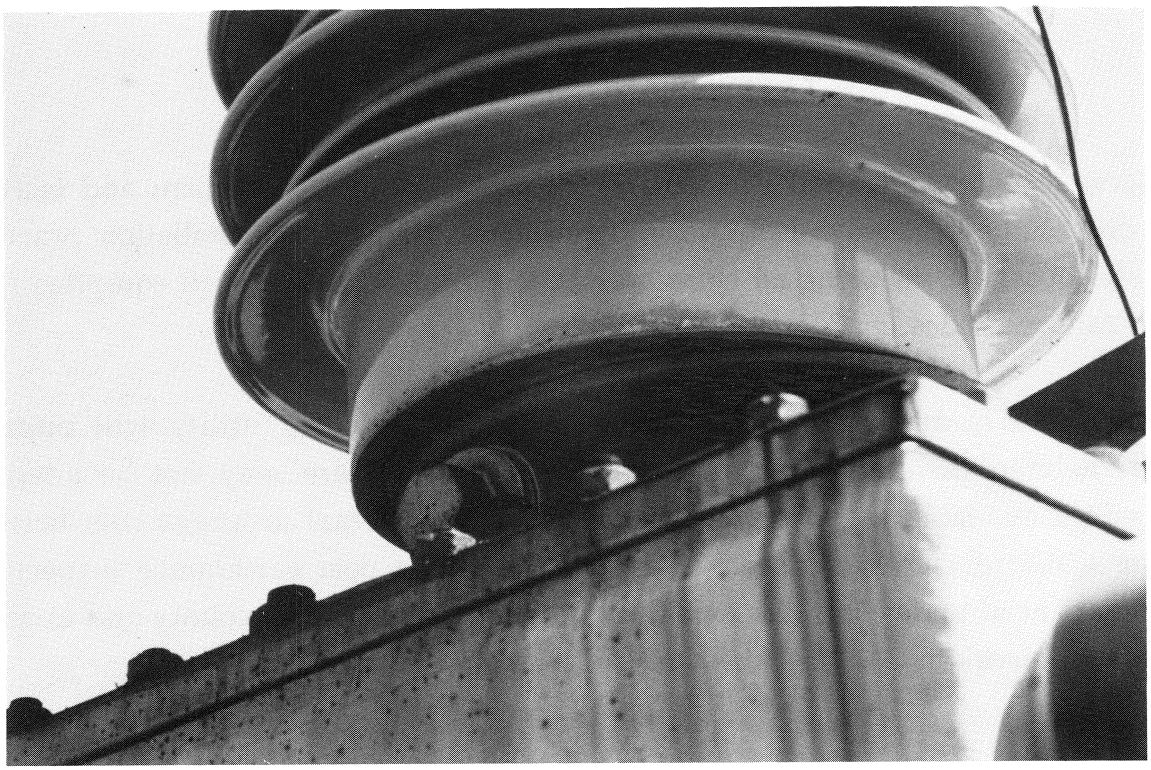

Fig. 1 Shifted Transformer Bushing

Fig. 2 Rope Used To Temporarily Place A Disconnect Switch Back Into Service.

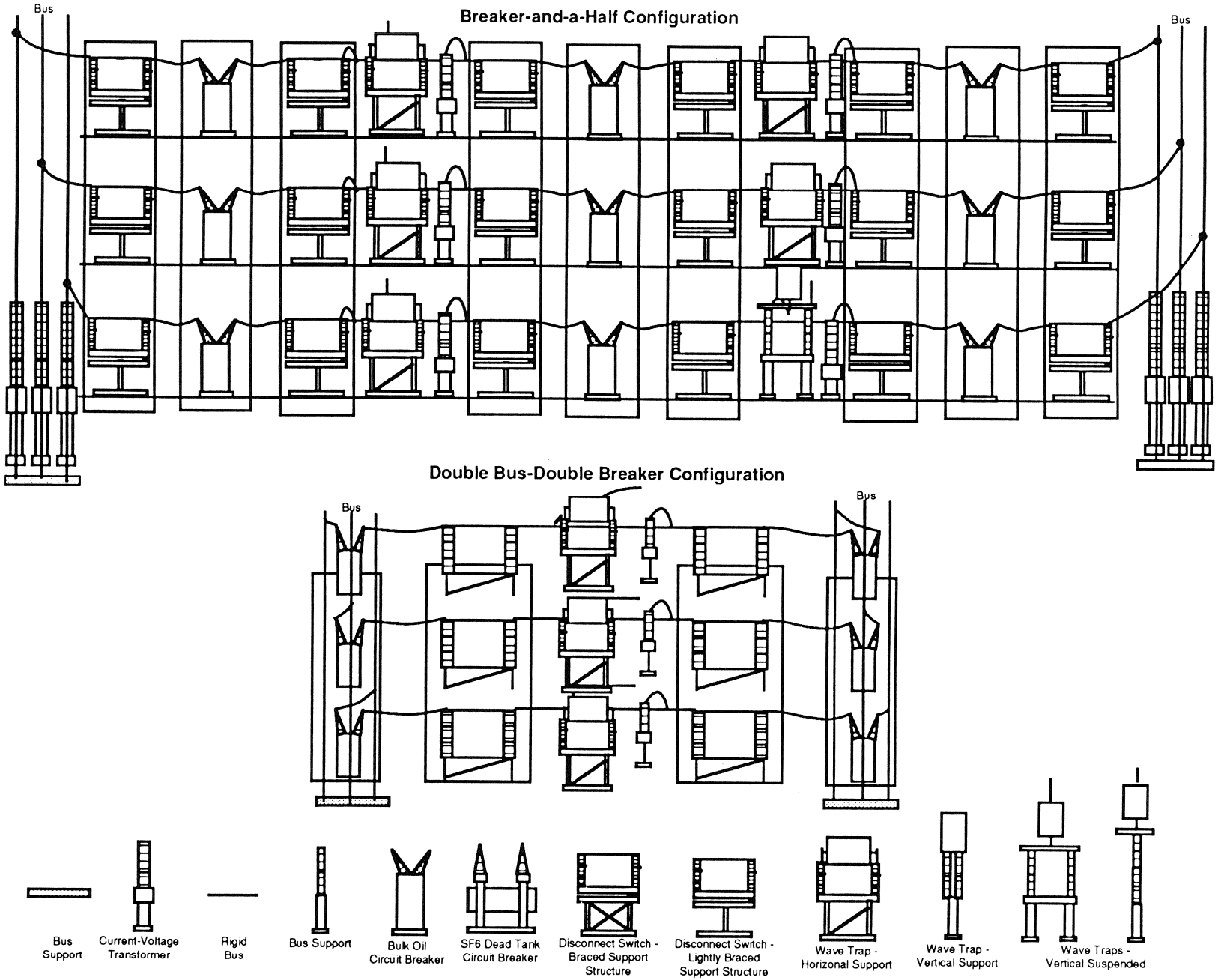

Fig. 3 Schematic Diagrams of Common Switchyard Equipment Configurations.

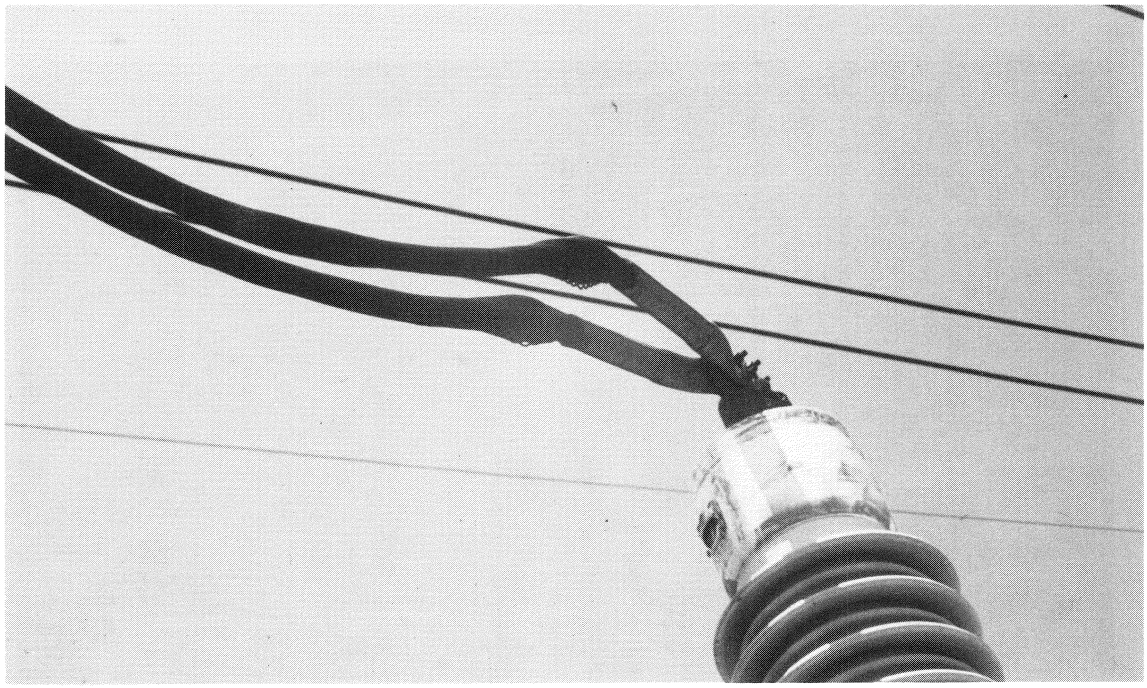

Fig. 4 Deformed Conductor Indicates Equipment Has Been Damaged and Repaired

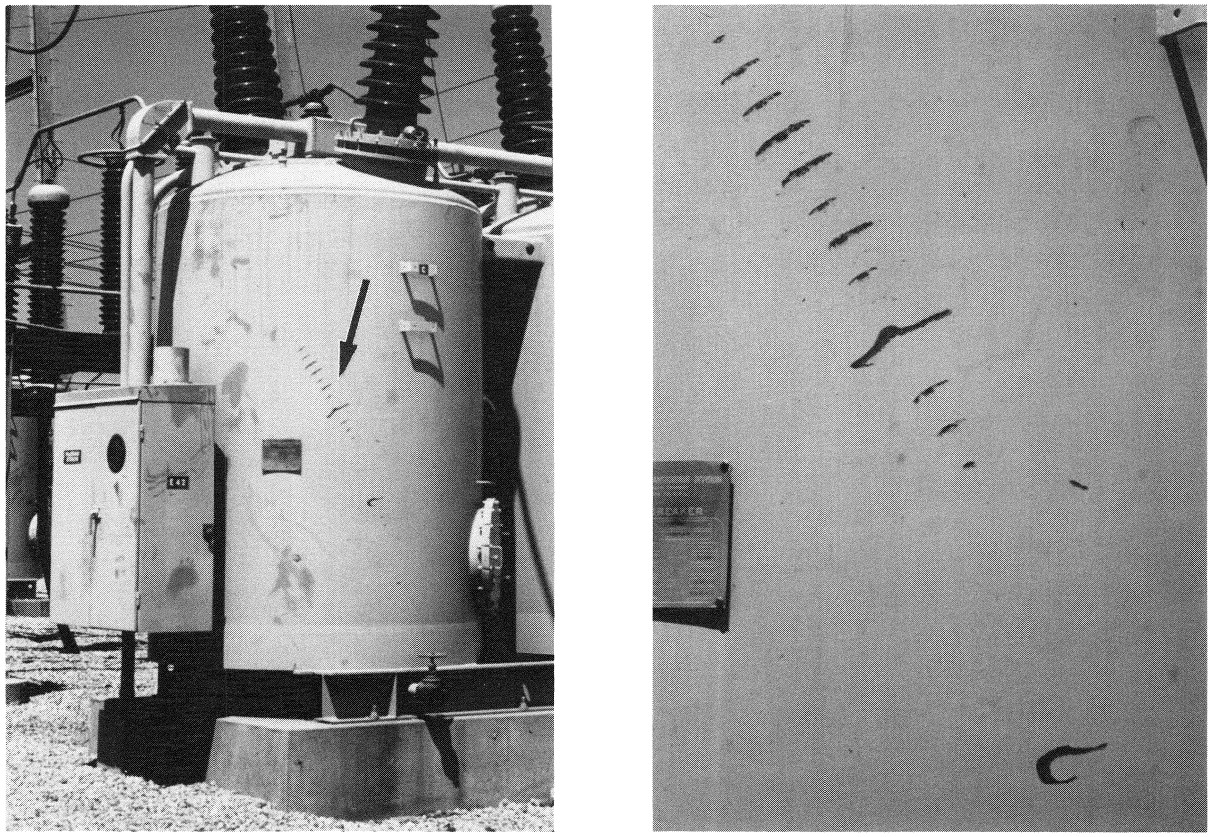

Fig. 5 Chipped Paint Indicates That Adjacent Equipment Has Been Damaged.

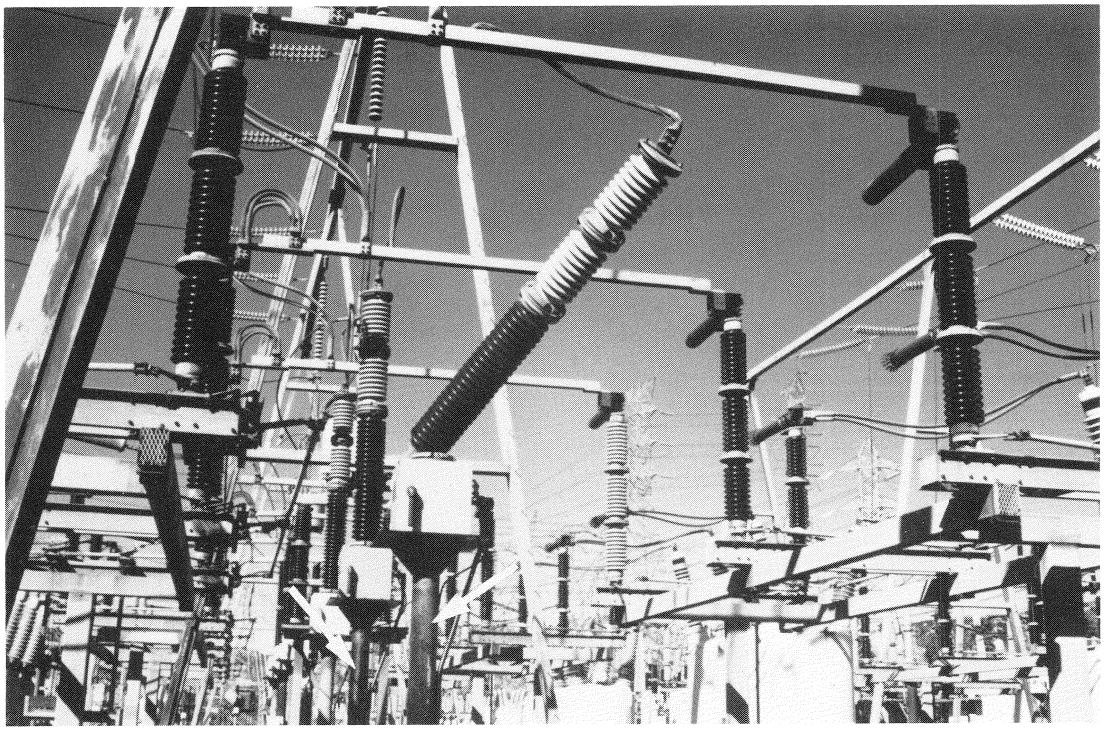

Fig. 6 Discoloration of Support Columns Indicates That Two CVTs Have Failed.

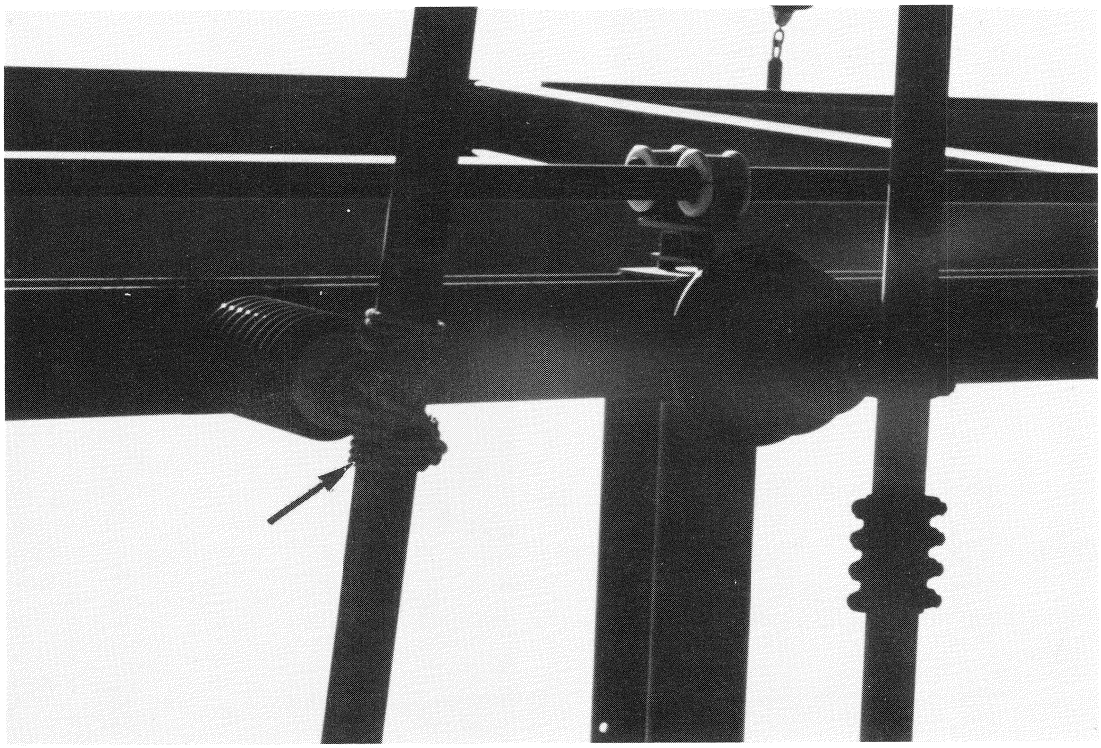

Fig. 7 Rope Used As Temporary Replacement for Damage Hardware.

Probabilistic Evaluation of Liquefaction Spread for Lifeline Structures

Ikuo Katayama[1], J. A. Pires[2] and A. H.-S. Ang[2]

ABSTRACT

Using Monte Carlo simulation, the probability of liquefaction in a soil layer spreading over a finite area is calculated. Vertical propagation of seismic wave and horizontally layered soil are assumed for random vibration analysis. Statistical spatial correlation of the undrained shear strength of sand against liquefaction is considered with perfectly correlated input ground motion excitation characterized by power spectrum and peak factor. The fragility curves against liquefaction spread of finite strips extending along lifelines with specified levels of base input ground motions for typical sand layers of Metropolitan Tokyo are presented.

1. Introduction

The authors have been developing a probabilistic analysis method of liquefaction of layered soil under random seismic loads[1].

The method has been applied to evaluate the seismic reliability of the connectivity of electric power transmission network of a small area of Metropolitan Tokyo. The reliability of the connectivity of an example low voltage power network was found to be strongly degraded by the presence of liquefaction of the sand layers within which the pipes were buried at shallow depth[2].

It was assumed that an area of 500 m x 500 m would totally liquefy when the soil profile representing the soil properties of the above unit area showed the possibility of liquefaction against a given ground acceleration, that the hume-pipes for power transmission buried within the area would be damaged somewhere within the area and that when damage of the pipes due to liquefaction should occur the power cables installed therein would be cut off without exception causing electrical disconnection.

This assumption was adopted, because there is no information about the behavior of buried hume-pipes under liquefaction; however, the assumption

---

1) Tokyo Electric Power Services Co., Ltd., Tokyo, Japan

2) Department of Civil Engineering, University of California, Irvine, U.S.A.

seems reasonable for discussing electrical disconnectivity. The authors have extended their work in two areas: one is to estimate the strength of soil after liquefaction and its interaction with buried pipes[3]; the other is to probabilistically estimate the lateral liquefaction spread within an area which has liquefied[4].

The last work is comprehensively discussed in J.A. Pires et al[5]; however, there we discussed only the case where a finite area will liquefy and contiguously spread with decreasing probability in all directions.

When we apply our results to a practical case of liquefaction of soil surrounding buried power cable ducts of low voltage, lifelines that are closest to demands, we should consider the practical situation of these pipes: due to installation of a pipe underground, the surrounding soil might have been disturbed, and with the work and the existence of the pipe underground water will collect along the pipe that may extend several hundred meters for various configurations. Therefore, the liquefied area of the surrounding soil may collectively spread along the pipe more than in the other directions; such damages as uplift of manholes and heaving-up of the buried pipes along the path of pipes due to liquefaction have been observed in recent past earthquakes.

In this paper, not only to estimate the proximity of liquefaction along the buried structure but also to estimate the magnitude of the area along the buried structures where restoration work may be necessary after liquefaction, the probability of contiguous soil liquefaction spread along a finite longitudinal strip is discussed.

2. Liquefaction Analysis Model

2.1 Cyclic Resistance Curves against Liquefaction

The resistance of sand against liquefaction is defined by the number of cycles, $N_l(\bar{\tau})$, of constant amplitude shear stress ratio, $\bar{\tau}$, necessary to induce liquefaction known as "cyclic resistance curve". The load term, the shear stress ratio, is defined as τ/σ'_{v0}, where τ is the working stress in the soil and σ'_{v0} is the effective overburden stress. Based on the occurrence of liquefaction during past earthquakes, the cyclic stress ratios have been correlated with Standard Penetration Test Blowcount normalized to an effective overburden stress of 1.0 ton/ft^2 and an energy ratio of 60%, $(N_l)_{60}$-SPT[6].

Based on the above observed correlation between $(N_l)_{60}$-SPT and the stress ratio, τ/σ'_{v0}, the authors derived such "cyclic resistance curves against liquefaction" as is shown in Fig. 1 with different fine contents for Magnitude 7.5 earthquake. The detail of the process to obtain the curves is given in J.A. Pires

et al[1].

2.2 Random Seismic Loading

Any of the "cyclic resistance curves" can be interpreted by

$$N_l(\bar{\tau})[E_c(\bar{\tau})\,h(\bar{\tau})] = W_u \tag{1}$$

where W_u is an arbitrary constant, $E_c(\bar{\tau})$ is the energy dissipated through hysteresis in one cycle of shear stress amplitude $\bar{\tau}$, and $h(\bar{\tau})$ is a weighing function. The concept of the number of equivalent uniform loading cycles implies that under **N** loading cycles with different shear stress, $\bar{\tau}_l$, liquefaction will occur when

$$W = \sum_{l=1}^{N} E_c(\bar{\tau}_l)\,h(\bar{\tau}_l) \tag{2}$$

reaches W_u.

The probability that liquefaction will occur at any point in the critical layer of a layered soil, independently of liquefaction occurring anywhere else in the layer, is given by

$$P[E_0] = \int_0^{\infty} F_{W_u}(q)\,f_{W(a,t)}(q)\,dq \tag{3}$$

where F_{W_u} denotes the PDF of W_u and $f_{W(a,t)}$ is the probability density function of $W(a,t)$.

For an earthquake with a given intensity $A=a$, and a strong motion duration $T_E=t$, liquefaction occurs when

$$Z = W_u - W(a,t) < 0.0 \tag{4}$$

where W_u denotes the hysteretic energy dissipation capacity of the soil layer and if this capacity is exhausted the liquefaction will set up. The quantity $W(a,t)$ is given by

$$W(a,t) = \int_0^{t} X(r)\,\dot{\varepsilon}_T(r)\,dr \tag{5}$$

where $\dot{\varepsilon}_T(\tau)$ is the rate of hysteretic energy dissipated at time r and $X(r)$ is an equivalent weighing function to include the effect of random stress

amplitude[7],

$$X(r) = [\int_0^{\overline{\tau_m}} h(\bar{\tau}) E_c(\bar{\tau}) f_T(\bar{\tau}, r) d\bar{\tau}] \; / \; [\int_0^{\overline{\tau_m}} E_c(\bar{\tau}) f_T(\bar{\tau}, r) d\bar{\tau}] \tag{6}$$

where $\overline{\tau_m}$ is the normalized maximum of the hysteretic component of the shear stress for the sand and $f_T(\bar{\tau}, r)$ is the probability density function of the peaks of $\bar{\tau}$ at time r.

The mean and variance of $W(a, t)$ are obtained from random vibration analysis [7,8].

On the other hand, the statistics of W_u are obtained from the uncertainty analysis of the cyclic resistance against liquefaction and the "cyclic resistance curves" in Figs. 1(a) to 1(c), are regarded as the mean resistance curves and the coefficient of variation(c.o.v.) was found to be 0.57 for a given ***N-SPT blowcount*** by assuming independence of the stress ratio to cause liquefaction[1]. When the uncertainties in the ***N-SPT blowcount*** are considered, the c.o.v. of the ***N-SPT blowcount*** will increase. Considering the c.o.v. of 0.15 for the ***N-SPT blowcount***, the c.o.v. of approximately 0.8 for the number of uniform loading cycles till liquefaction is used in our study.

2.3 Response Analysis of the Layered Soil

The total shear strain at each layer of the liquefiable layer defined by $\dot{\gamma}_i = (x_{i+1} - x_i) / \Delta h_i$ is calculated by idealizing the soil layer as a multi-degree of freedom lumped mass model with viscous damper at the bottom with the outcrop input ground motion defined at the top of the base layer; where x_i and Δh_i denote the total response displacement of the mass i and the thickness of the i-th layer, respectively. A hysteretic model and an analytical procedure[7,9,10] are used here to represent the soil hysteresis and calculate the necessary component of the shear stress by a first-order differential equation. Statistical linearlization is used in the solution of the nonlinear equation.

The hysteretic component, z, of the shear strain is expressed by

$$\frac{\partial z}{\partial \gamma} = A - \beta \frac{|\dot{\gamma}|}{\dot{\gamma}} |z|^{r-1} - \delta |z|^r \tag{7}$$

where γ is the total shear strain, A, β, δ and r are parameters that describe the shape of the hysteresis loop. Then the shear stress is given by

$$\tau = \alpha G_m \gamma + (1-\alpha) G_m z \tag{8}$$

where G_m is the initial shear modulus and αG_m is the residual stiffness. The maximum hysteretic shear stress is then given by

$$\tau_m = (1-\alpha) G_m [A/(\beta+\delta)]^{1/r} \tag{9}$$

In this study, the following values are used for the smooth hysteretic model:

Assuming $r=0.5$ in Eq.(7) and the Hardin-Drnevich type strain-dependency curve is assumed with the reference strain $\gamma_r = 4.0 \times 10^{-4}$, respectively. Also the following parameters are used:

$$A = 1.0, \quad \delta = \beta, \quad \alpha = 0.05$$

with β and γ calculated from Eq.(9) for a specified value of τ_m.

2.4 Input Ground Motion Statistics

In the analysis, the stochastic input ground motion is characterized by a stationary Gaussian random process; power spectral density function defined by Clough-Penzien[11].

$$S(\omega) = S_0 \frac{1+4\zeta_B^2(\omega/\omega_B)}{[1-(\omega/\omega_B)^2+4\zeta_B^2(\omega/\omega_B)^2} \frac{(\omega/\omega_G)^4}{[1-(\omega/\omega_G)]^2+4\zeta_G^2(\omega/\omega_G)^2} \tag{10}$$

where the parameters $\omega_B = 16.9$ *rad/s*, $\zeta_B = 0.94$, $\zeta_G = 0.7$, and $\omega_G = 1.25$ *rad/s* were chosen. This ground motion is applied at the hypothetical outcrop surface of the base layer.

2.5 Calibration of the method

In order to assess the reliability of the above method, the probabilities of liquefaction were computed for some past case histories of occurrence or non-occurrence of liquefaction. The case histories investigated are summarized in Table 1. Cases 1, 3, 4, 6, 9B, 9T, 10 and 11 were investigated. The results of the investigation are shown in Fig. 2. The line shown in Fig. 2 separates the data for which liquefaction has occurred from those data for which liquefaction has not occurred for Magnitude 7.5 earthquakes. The probability of the onset of liquefaction computed with the methodology appear to be consistent with the

observed data.

3. Lateral Extent of Liquefaction Spread

3.1 Methodology

The probability that liquefaction will occur at any point in the critical layer of a particular layered soil has been given by the previous Eq.(3). The soil resistance capacity and the load terms, respectively W_u and $W(a, t)$, are replaced by S and Q here, to simplify the description.

The soil resistance in a finite area, BxL, of concern is described by a two-dimensional homogeneous lognormal random process with mean $\overline{S}$, variance σ_s^2 and auto-correlation function of resistance capacity $R_{SS}(r_{ij})$, where r_{ij} is the horizontal distance between any two points in the layer. The area is divided into elementary squares with side D numbered $i=1,2,....,N$, as shown in Fig. 3.

The soil resistance against liquefaction at the center of the elementary squares are random variables denoted by S_i, $i=1,2,....,N$. Here, within the elementary square, the probability of liquefaction is assumed to be kept unchanged from the value given to the layer. Then the random variables S_i are identically distributed but are not statistically independent. The coefficient of correlation for a pair of random variables (S_i, S_j) is

$$\rho_{SS}(r_{ij}) = \frac{R_{SS}(r_{ij})}{\sigma_{S_i}\sigma_{S_j}} \tag{11}$$

where $\sigma_{S_i} = \sigma_{S_j} = \sigma_S$.

The probability that liquefaction will extend over the entire area BxL is the probability that all elements within that area will liquefy. Therefore,

$$P_L(B, L) = [(S_1 < Q) \cap (S_2 < Q) \cap ... \cap (S_N < Q)] \tag{12}$$

which can be written as

$$P_L(B, L) = \int_0^\infty F_{S_1....S_n}(q,....,q) f_Q(q)\, dq, \tag{13}$$

where

$$F_{S_1...S_N}(q,....,q) = \int_0^q \bullet\bullet\bullet \int_0^q f_{(S_1...S_N}(S_1,....,S_N)\, dS_1...dS_N \tag{14}$$

The integral in Eq.(13) for each value of q is evaluated using Monte Carlo

simulation. Here, it is assumed that the input ground motion defined at the base layer is perfectly correlated within the area BxL. The practical computation is performed after transforming both the variables S_j and Q(see [5]).

3.2 Contiguous Lateral Spread in All Direction

The examples of liquefaction fragilities at any point within the area of concern for soil deposits B and F, the soil profiles of which are shown in Fig. 4, are shown in Fig. 5[5]. For these deposits, the correlation function

$$\rho_{S,S}(r) = \exp[-(r/b)^2] \tag{15}$$

is applied for generating two-dimensional homogeneous horizontally correlated random field. In the equation, b is a positive parameter called correlation coefficient and r is the horizontal distance between any two points in the layer.

Various methods have been proposed to estimate the parameter b for the correlation function of soil properties[12,13]. The correlation length defines a distance such that the average number of uncorrelated observations of the soil property within it is 1.0. The value b in Eq.(15) is converted from the correlation length δ_u as $b = \delta_u/\sqrt{\pi}$ and ranges from about 30 m to 40 m. The actual values of b should be evaluated for a particular case as the adverse consequences of liquefaction will depend on the size of contiguous liquefaction relative to the diameter of the buried pipes and manholes. In this paper, however, the liquefaction fragilities for soil deposit F with was computed by making the size of squared-area B=L as parameter; e.g., let B from 1.94 to 5.81 times b. Therefore, if we assume b=40 m, then B=L becomes about 80 m to 230 m.

The results are shown in Fig. 6; the probability of liquefaction contiguously spreading over a given area decreases very rapidly as the area increases. Fig.7 shows another expression of the probability of contiguous liquefaction with the size of squared-areas.

Using the proposed method it is also possible to compute the probabilities that a specified fraction of the area B x L will liquefy[14]. The method is also possible to be directly applied to estimate the probability of liquefaction spread along a finite strip where long pipes are assumed to be buried in shallow depth.

3.3 Contiguous Longitudinal Spread in a Strip

The proposed method was applied assuming rectangular-area as shown in Fig. 8. The soil deposits selected are the previous F and B, and further E of which soil profile is shown in Fig. 9. These soil deposits are very popular in

Metropolitan Tokyo.

First, the liquefaction fragilities for soil deposits F, E and B are shown in Fig. 11. Among them the results for soil deposits F and B are the same with those given in the previous Fig. 5 even if they were separately computed and the results for soil deposit E is newly added.

Taking width B and Length L of a rectangular-area in Fig. 8 as 40 and 500 m, respectively, the proposed method was directly applied to the above three types of deposits to estimate the probability of liquefaction spread along a finite strip where long pipes or ducts are assumed to be buried in shallow depth. The results are shown in Fig. 11. The size of element area was chosen as 20 m x 62.5 m and the correlation coefficient as b=62.4 m which may give more adverse consequences in spreading the liquefaction along the area of concern than the case using the reported values of b ranging from 30 m to 40 m.

The probability of liquefaction contiguously spreading over a given strip also decreases as the area increases.

For comparison, if we take the previous results for soil deposit F from the case with the base peak acceleration, PGA=0.095 g and lateral extent of liquefaction L=6(actual squared-area has L=B= 62.4 m x 5.81 = 363 m), the probability of contiguous liquefaction spread in the squared-area becomes about 0.35, whereas the corresponding result of this time, the probability of contiguous liquefaction spread along the strip, becomes 0.5 by taking Ls/L=363 m/500 m = 0.725 and the interpolated result at PGA=0.95 from those of PGAs 0.090 and 0.098 in Fig. 11. It seems reasonable to obtain more adverse result from the case of spread along a finite strip than the previous case of squared-area.

4. Discussion

As we already pointed out, when we consider the practical situation of soil surrounding buried pipes, due to installation of a pipe underground, the surrounding soil might have been disturbed and, with the work and the existence of the pipe, underground water will collect along the pipe that may extend several hundred meters for various configurations. Therefore, the liquefied area of the surrounding soil may collectively spread along the pipe more than in the other directions; such damages as uplift of manholes and heaving-up of the buried pipes along the path of pipes due to liquefaction have been observed in recent past earthquakes. The proposed method to evaluate lateral liquefaction spread of layered soil deposits has given reasonable results numerically as already shown in the preceding part of this paper.

Based upon the results above obtained, the proposed method seems to give us more useful and practical information in the evaluation of seismic reliability of power transmission network as follows:

Fig. 12 shows a model electric network located in Metropolitan Tokyo and the probability of black-out at the demand nodes of 66 kv in 25 years[2]. The location of the area of concern is plotted in Fig. 13(a) denoted as "C" and the Annual Probability of Exceedance of PGA at the location is given in Fig. 13(b). The higher values of probability of black-out(electrical disconnectivity just after an earthquake) for demand nodes are distributing within and near the hatched meshes which have been evaluated as the meshes very vulnerable to liquefaction. This is considered reasonable because these meshes are lying on old river bed or terrace.

It was assumed that an area(a mesh) of 500 m x 500 m would totally liquefy when the soil profile representing soil properties of the above unit area showed the possibility of liquefaction against a given ground acceleration, that the hume-pipes for power transmission buried within the area would be damaged somewhere within the area and that when damage of the pipes due to liquefaction should occur the power cables installed therein would be cut off without exception causing electrical disconnection.

This assumption was adopted, because there is no information about the behavior of buried hume-pipes under liquefaction and the assumption seems reasonable for discussing electrical disconnectivity; however, as already shown in the previous Figs. 7 and 11, the probability of liquefaction contiguously spreading over a given area decreases very rapidly as the area or the length of strip increases.

The hatched meshes in Fig. 12 consist of soil deposits 3, 4 and 6 shown in Fig. 14. Among them, soil-3 and soil-4 respectively corresponds to soil F and E in this study. The probabilities of liquefaction for these soil deposits are given in Table 2. Although it is not clear how the structural consequences due to liquefaction will be affected by the size of liquefaction spread along the structures, however, it may be reasonable to estimate severer damage for larger liquefaction spread but with less probability.

From the demand node distribution of the model network, hume-pipes for power transmission have around 250 m unit-length.

The expected PGA for 25 year-return period is 0.18 g at the ground surface evaluated as 0.12 g at the base layer[2], and the annual probability of exceedance of PGA at the location C is 0.25 from Figs. 13(a) and 13(b). The probabilities of liquefaction for soils F and E are 0.99 and 0.38 from Fig. 11. Therefore, the probability of liquefaction spreading contiguously over this length for each soil deposit will become $1-2.6\times10^{-3}$ and 9.1×10^{-1}, respectively; as similar to the results shown in Table 3. However, if we take the full length of the pipes within a mesh, it becomes $1-5.2\times10^{-3}$ and 0.08, respectively for soils F and E; in this case the decrease of the contiguous liquefaction probability is remarkable for soil deposit E(soil-6).

The above information obtained here may be helpful in planning the

restoration work and formation of work force for local power supply network after damaging earthquakes.

From the above results, it should be emphasized that since larger the value b becomes, the probability of contiguous liquefaction extending over a particular area or finite strip will become larger, the value b should be evaluated for a particular project; the adverse consequences of liquefaction will depend on the lateral extent of contiguous liquefaction relative to the diameter of the buried pipes and manholes. Also in this regards, the relation between the lateral extent of liquefaction and the practical consequences of buried structures should be extensively investigated.

5. Conclusion

A method to calculate the probability of the onset of liquefaction in horizontally layered soil deposits as a function of the expected maximum ground acceleration is presented. The method are practically consistent with past observed case histories of on-occurrence or non-occurrence of liquefaction.

The method was extended to compute the probability that liquefaction will spread over a given squared-area and a finite strip where lifelines are buried. It was observed that the probability of liquefaction spreading over a given area decreases as the contiguous lateral extent of liquefaction increases.

The method was applied to re-evaluate the vulnerability of a model power transmission network of Metropolitan Tokyo to liquefaction. The results may help future study on not only the seismic assessment of buried lifelines but also on the restoration planning by relevant organizations.

References

[1] J.A. Pires, A.H.-S. Ang, and I. Katayama, Probabilistic analysis of liquefaction, in : Structural Dynamics and Soil Structure Interaction, eds. A.S. Cakmak and I Herrera(Computational Mechanics Publications, England, 1989), pp.155-168.

[2] Ikuo Katayama, Ikumasa Yoshida, and Hitoshi Nakase, Reliability of electric power transmission systems in seismically active Metropolitan Tokyo, in Parts.1 to 3, Proceedings, ICOSSAR '89, pp.693-716.

[3] J.A. Pires, H.-S. Ang, I. Katayama and M. Satoh, Post-liquefaction soil-structure interaction for buried structures: Sensitivity studies, Proc., SMiRT-12, MK02/4(K. Kusmaul(Editor), 1993 Elsevier Science Publishers), pp.225-230.

[4] J.A. Pires, A.H.-S. Ang, and I. Katayama, Probabilistic evaluation of lateral

liquefaction spread under earthquake loading, Proc., ICOSSAR'93 (Structural Safety & Reliability, Shueller, Shinozuka & Yao(eds), 1994 Balkema), pp.2009-2015.

[5] J.A. Pires, A.H-S. Ang, and I. Katayama, Probabilistic evaluation of lateral extent of soil liquefaction under earthquake loading, Nuclear Engineering and Design 147, 1994, pp.157-170.

[6] H.B. Seed et al, The influence of SPT procedures in soil liquefaction evaluation, Report No. UCB/EERC-84/15, University of California, Berkeley, California (Oct., 1984)

[7] J.A. Pires, Y.K. Wen, and A.H.-S. Ang, Stochastic analysis of liquefaction under earthquake loading, Struct. Res. Series, 504, University of Illinois, Urbana, Illinois(April, 1983).

[8] J.A. Pires and M. Tang, Statistics of hysteretic energy dissipated under random dynamic loading, J. Engrg. Mech., ASCE, 116(8) (1990) pp.1706-1722.

[9] Y.K. Wen, Equivalent linealization for hysteretic systems under random excitation, J.Appl.Mech., Transactions, ASME, 47(1)(1980), pp.150-154.

[10] T.T. Baber and Y.K. Wen, Random vibration of hysteretic degrading multistory structures, J. Engrn. Mech., ASCE, 107(6)(1981), pp. 1069-1087.

[11] Ray W. Clough and Joseph Penzien, Dynamics of structures (McGraw-Hill, New York, 1975), pp.613-615.

[12] N.M. Fardis and D. Veneziano, Estimation of SPT-N and relative density, J.Geotech. Engrg., ASCE, 107(10) (1981) pp.1345-1359.

[13] E.H. Vanmarcke, Probabilistic modeling of soil profiles, J. Geotech. Engrg., ASCE, 103(11) (1977) pp.1227-1246.

[14] M. Hoshiya, Probability of liquefaction spread, in:Stochastic Structural Dynamics 2 - New Practical Applications, eds. I. Elishakoff, Y.K. Lin(Springer-Verlag, Heidelberg, 1991) pp.45-54.

Table 1 Pertinent Data for the Case Histories Analyzed (Cases 1,3,5,6,9_B,9_T and 11)

Case History	Data	Site	M	Distance (Miles)	T_E (sec)	a_{max}	Depth of Water Table (ft)	D (ft)	σ'_{vo} (paf)	N-SPT	N_1	$\frac{\tau_{ave}}{\sigma'_{vo}}$	Field Behavior	Reference
1	1964	Niigata	7.5	32	8	0.17	3	20	1200	7	10	0.195	Liq.	Seed and Idriss (1967)
2	1964	Niigata	7.5	32	8	0.17	3	25	1500	15	18	0.195	Liq.	Kishida (1966)
3	1964	Niigata	7.5	32	8	0.17	3	20	1200	9	14	0.195	No.Liq.	Seed and Idriss (1967)
4	1964	Niigata	7.5	32	8	0.17	12	25	2000	6	6	0.12	No.Liq.	Seed and Idriss (1967)
5	1968	Hachinohe	7.8	45-100	15	0.21	3	12	800	14	22	0.23	No.Liq.	Ohsaki (1970)
6	1968	Hachinohe	7.8	45-100	15	0.21	3	12	800	4	6	0.23	Liq.	Ohsaki (1970)
7	1968	Hachinohe	7.8	45-100	15	0.21	5	10	800	15	23	0.185	No.Liq.	Ohsaki (1970)
8	1968	Hakodate	7.8	100	15	0.21	3	15	1000	6	9	0.205	Liq.	Kishida (1970)
9_B	1968	Hachinohe	7.8	45-100	15	0.21	7	47	2900	25	18	0.19	No-Liq.	Ohsaki (1970)
9_T	1968	Hachinohe	7.8	45-100	15	0.21	7	9	850	16	23	0.16	No-Liq.	Ohsaki (1970)
10	1802	Niigata	6.6	24	8	0.12	3	20	1200	12	14	0.135	No-Liq.	Seed and Idriss (1967)
11	1887	Niigata	6.1	29	8	0.08	3	20	1200	9	14	0.09	No-Liq.	Seed and Idriss (1967)

Table 2 Parameters of Equivalent Lognormal Distribution for the Fragility Curves for Liquefaction

(cm/s²)

Soil Profile	1	2	3	4	5	6
Median	297.0	1240.0	72.1	102.0	418.0	105.0
Log Std. Dev.	0.24	0.44	0.20	0.22	0.38	0.18

Table 3 Probabilities of Liquefaction for Six Soil Profiles

Probability \ Soil Profile	1	2	3	4	5	6
Annual	1.6×10^{-3}	3.4×10^{-6}	2.5×10^{-1}	1.1×10^{-1}	7.9×10^{-4}	9.6×10^{-2}
25 years	3.9×10^{-2}	8.5×10^{-5}	$1\text{-}7.6 \times 10^{-4}$	9.4×10^{-1}	2.0×10^{-2}	9.2×10^{-1}
50 years	7.7×10^{-2}	1.7×10^{-4}	$1\text{-}5.6 \times 10^{-7}$	$1\text{-}3.4 \times 10^{-3}$	3.9×10^{-2}	$1\text{-}6.5 \times 10^{-3}$

$$P_{fn} = 1 - (1 - P_{f_1})^n$$

where : P_{fn} = probability in n years

P_{f_1} = annual probability

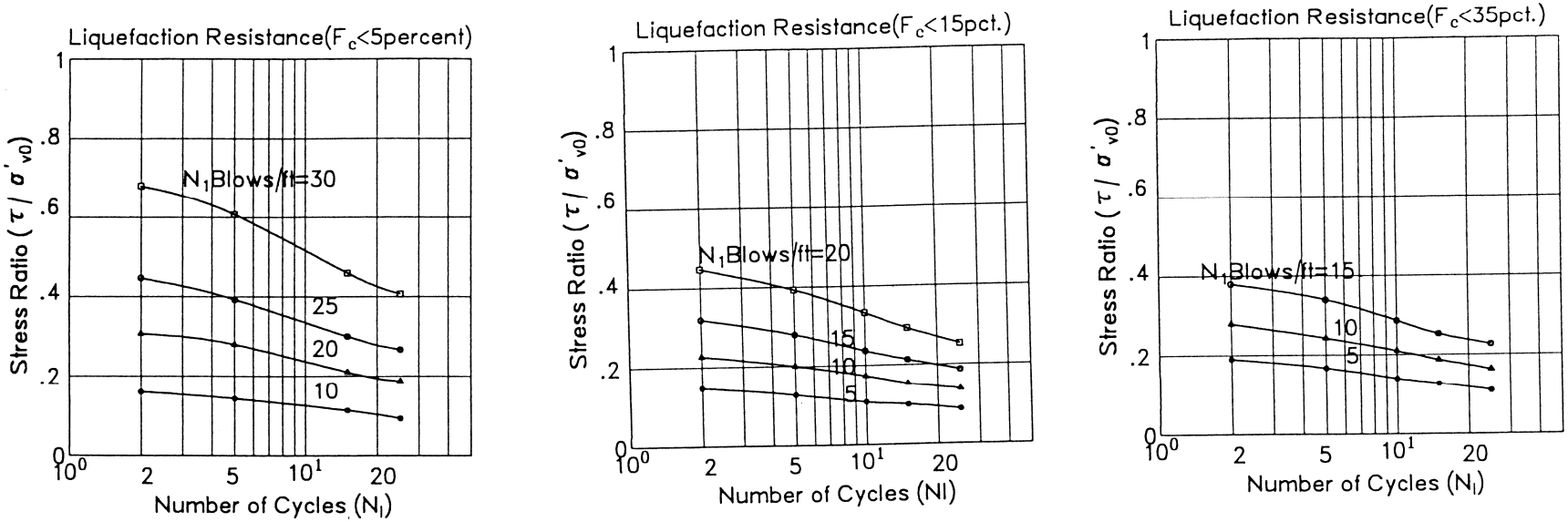

Fig. 1 Cyclic resistance curves against liquefaction for different Fine contents

CALCULATED PROBABILITIES

CASE HISTORY	PROBABILITY	CASE HISTORY	PROBABILITY
1	1.000	9_B	0.233
3	0.954	9_T	0.000026
5	0.460	10	0.142
6	1.000	1	0.000058

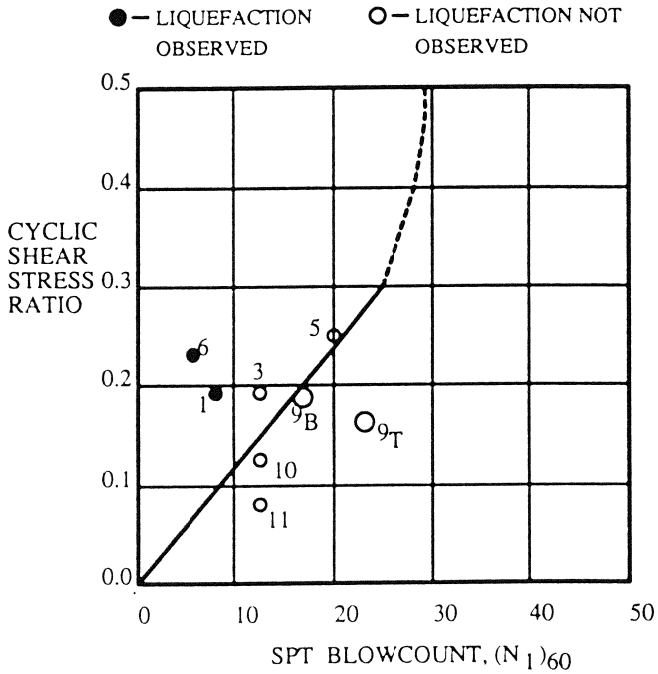

Fig. 2 Probabilities of liquefaction for selected case-histories.

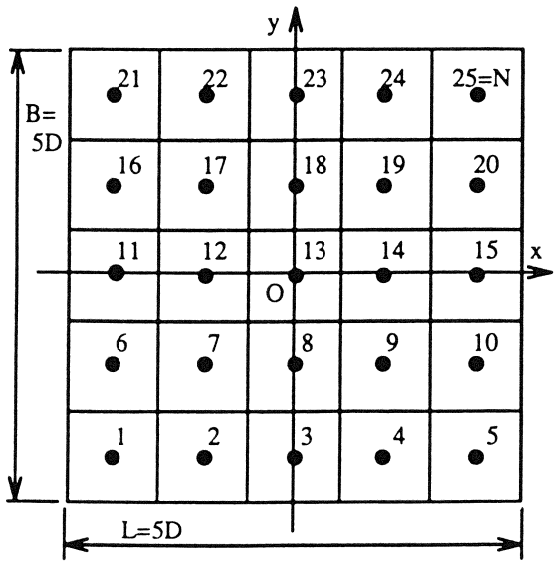

Fig. 3 Discretization of area $B \times L$ into elementary squared-areas.

Ⓐ

DEPTH (m)	SOIL TYPE	N-SPT Uncorrected	SHEAR WAVE VELOCITY(m/sec)	PERCENT FINES
Water Table 3.0				
7.0	LOAM	4	160	—
12.0	LOAM with CLAY	5	173	—
17.0	CLAYED SAND	22	225	32
23.0	SILT	18	263	—
		>50	>450	

(a)

Ⓑ

(m) G L	Name of Layer	N - SPT	Shear Wave Velocity (m/sec)	Fc (%)
0.5m				
6.0	Upper Yurakucho Formation (sand)	10	175	21
11.0	Lower Yurakucho Formation (clayed-sand)	3	119	44
		>50	> 450 m/sec	

(b)

Fig. 4 Soil deposits analyzed:(a) soil B; (b) soil F

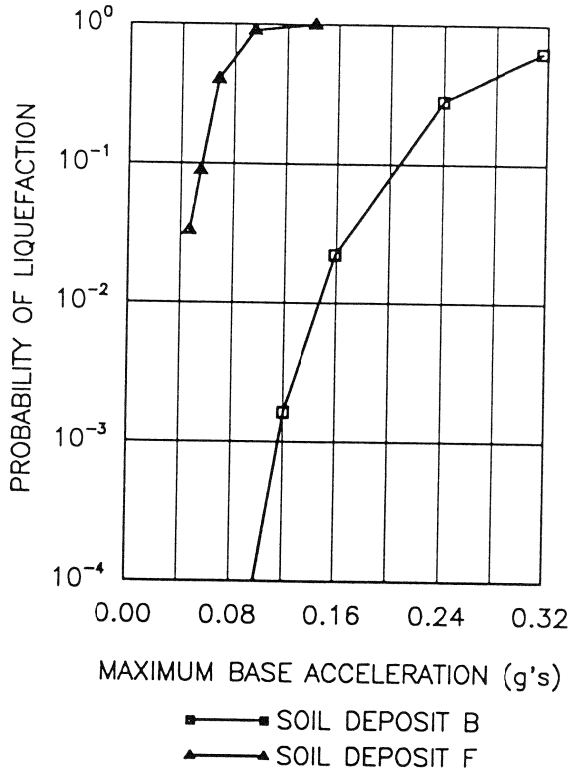

Fig. 5 Liquefaction fragilities for soil deposits B and F.

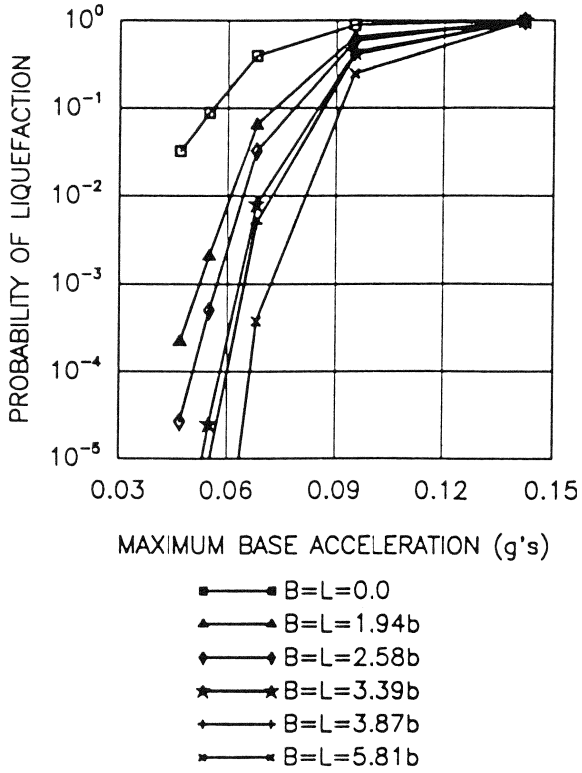

Fig. 6 Liquefaction fragilities soil deposits F

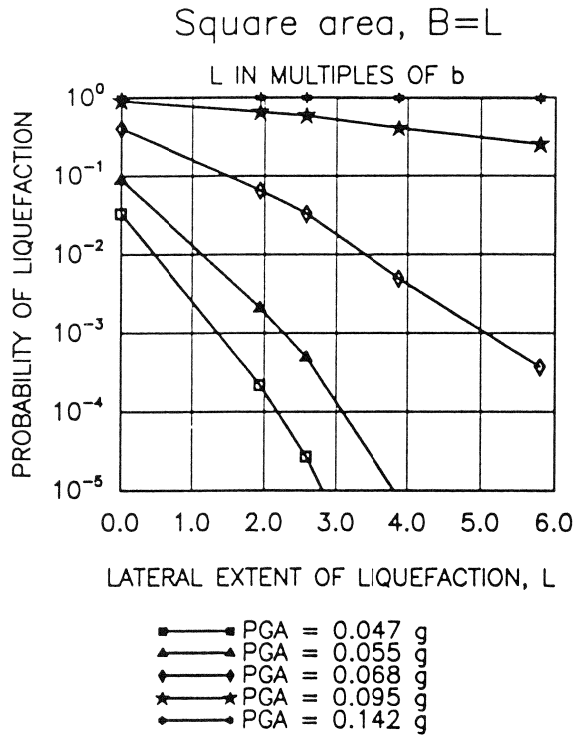

Fig. 7 Probability of liquefaction spreading in the layer (soil deposit F).

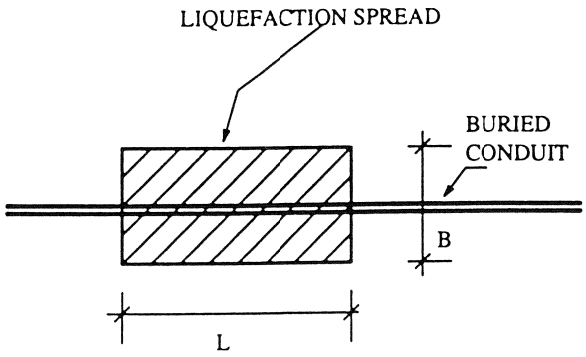

Fig. 8 Liquefaction spread along buried conduit.

Depth (m)	Name of Layer	N SPT *	Shear Wave Velocity (m/sec)	Percent Fines
0.5 5.0	Upper Yurakucho (SAND)	10	175	21
*UNCORRECTED		>50	>450	--

Fig. 9 Soil profile of soil deposit E

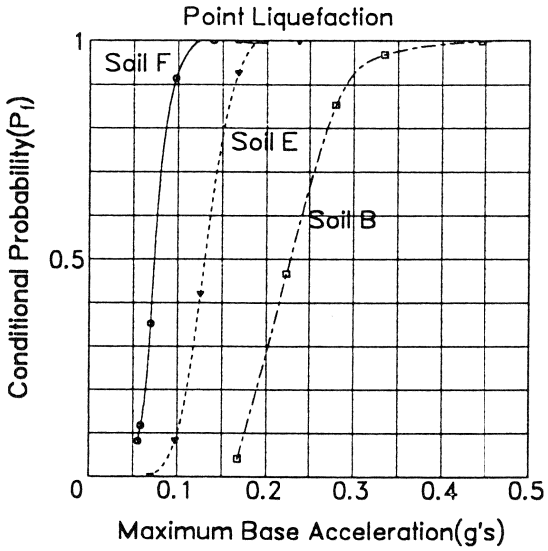

Fig.10 Probabilities of liquefaction for soil deposits analyzed

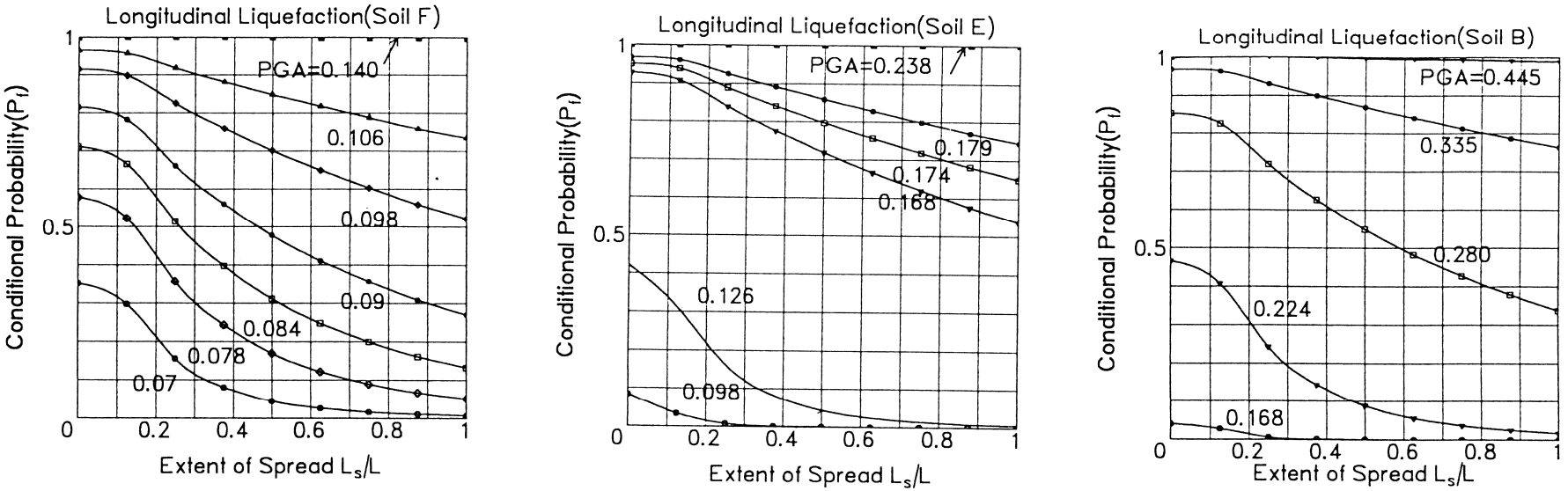

Fig.11 Probabilities of liquefaction for soil deposits analyzed

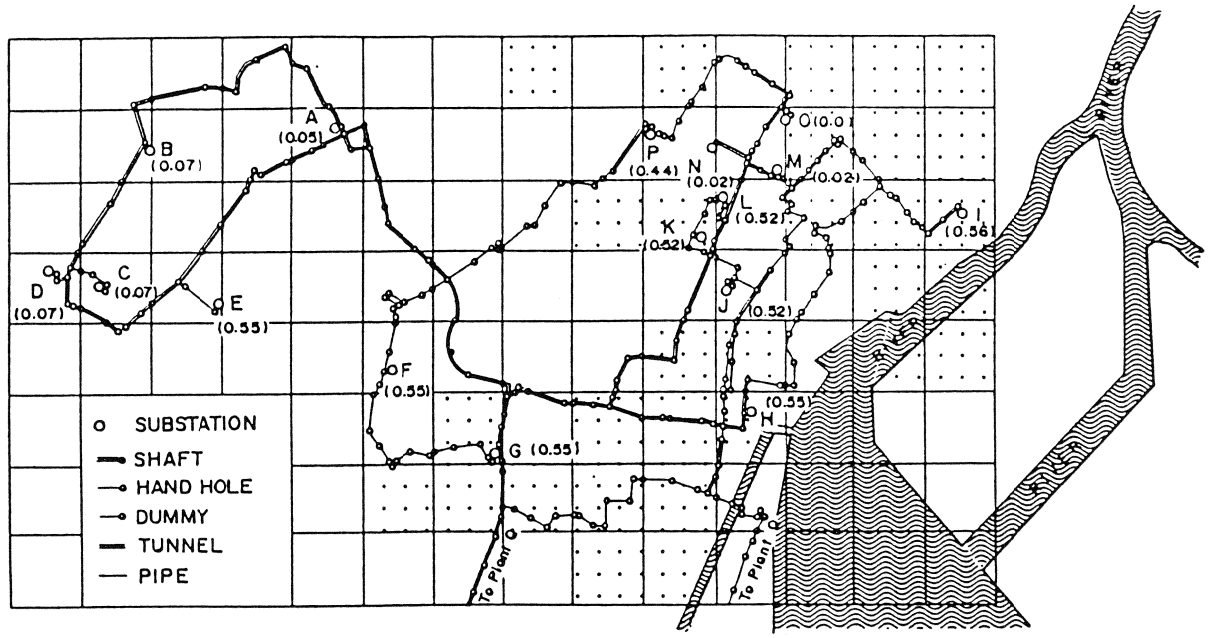

: Hatched meshes correspond to soil profiles 3, 4 and 6 which are easy to liquefy.

Fig.12 Model Electric Network and Probabilities of Black-Out at the Demand Nodes of 66 kv in 25 Years

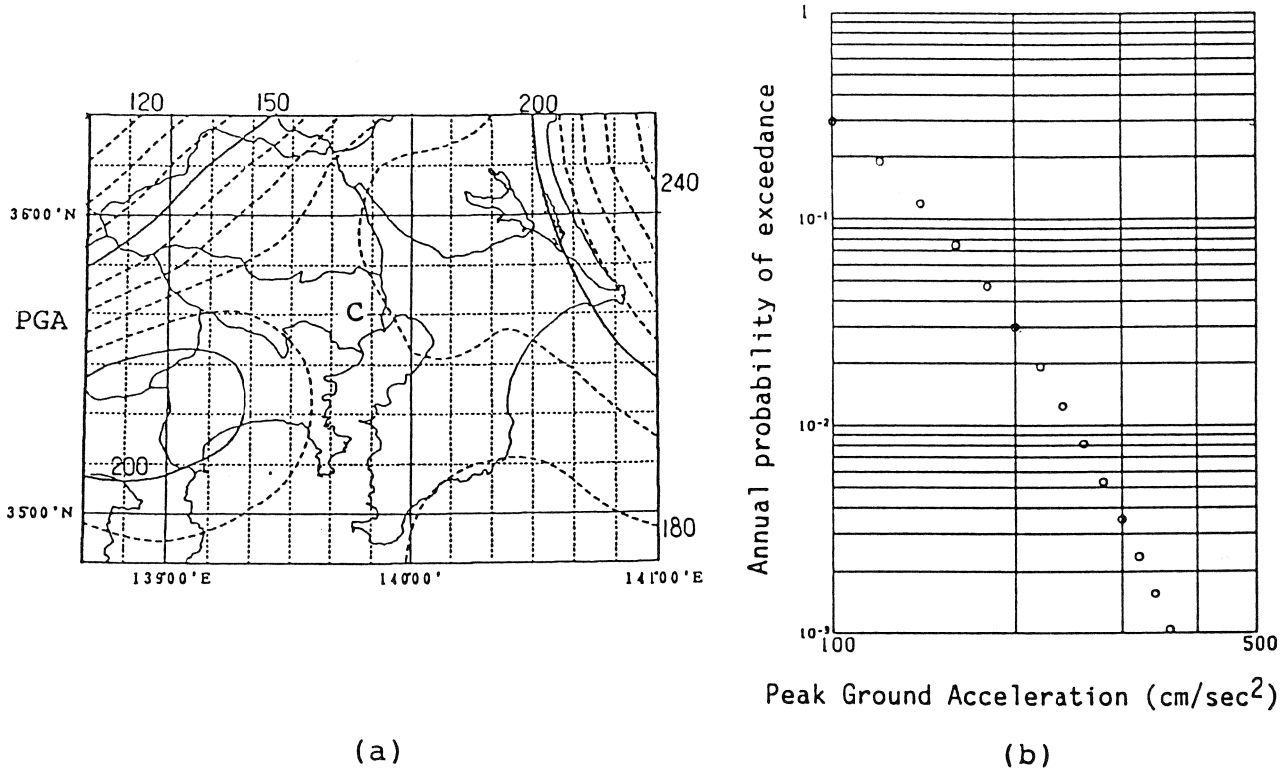

(a) (b)

Fig.13 Expected acceleration for 25 year return period(a) and annual probability of exceedance of PGA at C(b)

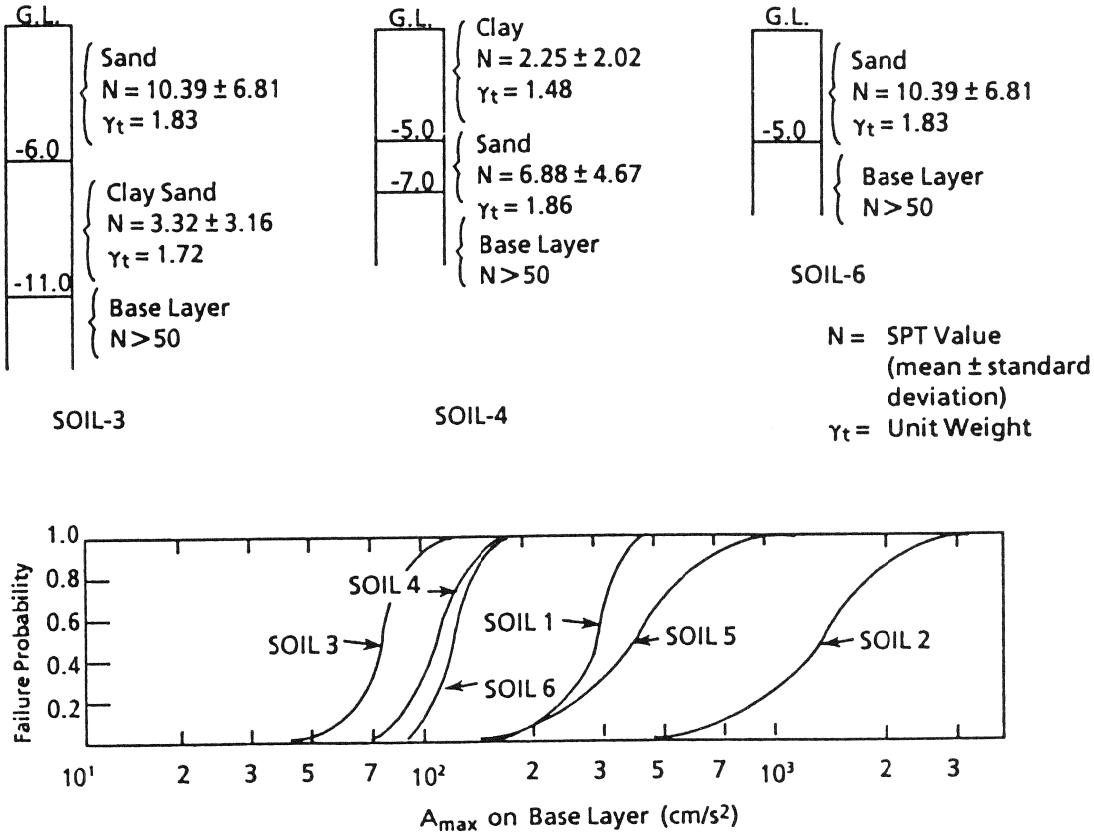

Fig.14 Fragility Curves of Liquefaction for the Soil Profiles in the Selected Area

FAILURE CRITERION FOR BURIED PIPE SUBJECT TO LONGITUDINAL PGD: BENCHMARK CASE HISTORY

Michael J. O'Rourke [1] and Xuejie Liu [2]

(1) Professor, (2) Ph.D. Candidate
Dept of Civil & Environmental Engineering
Rensselaer Polytechnic Institute, Troy, NY 12180-3590

ABSTRACT

The effects of longitudinal Permanent Ground Deformation (PGD) on a buried continuous steel pipeline is considered. Longitudinal PGD, (ground movement parallel to the pipe's axis) is characterized by the amount of movement, δ and its spatial extent, L. Local compressional buckling of the pipe wall and tensile failure of pipeline are taken as the failure modes of interest. Critical values for the amount of ground movement and the spatial extent, which lead to compressive failure, δ_{cr} and L_{cr}, are determined for five grades of steel, various R/t ratios and burial conditions.

Three buried pipelines which were subject to longitudinal PGD during the 1994 Northridge California event are used to benchmark the proposed failure criterion. The proposed analytical procedure suggests that two of the three pipes, the Los Angeles Dept of Water and Power Granada Trunk Line and the So. Cal. Gas (SCG) Line 120; both located along Balboa Blvd. at the Northern end of the San Fernando valley would suffer damage. The observed behavior matches the predicted behavior. The third line, the newer SCG line along McLennan Ave., is also considered. For the third line, we postulate as to why it was not damaged. There are two other lines along Balboa which were undamaged by the PGD. These two lines are excluded from consideration because of a lack of information on certain parameters.

Finally the effects of an expansion joint which was installed in the LADWP line after the 1971 San Fernando earthquake are discussed in detail.

INTRODUCTION

Permanent ground deformation refers to non-recoverable soil movement due to landslides, sur-

face faulting or liquefaction induced lateral spreading. In general a pipeline would be exposed to some combination of transverse PGD (ground movement perpendicular to the pipe's axis) and longitudinal PGD. The longitudinal PGD leads to axial tension and compression in a pipe whereas transverse PGD leads to flexural. O'Rourke and Nordberg (1992) conclude that longitudinal PGD is more likely to result in failure in continues pipeline. Herein we restrict our attention to longitudinal PGD due to lateral spreading induced by liquefaction of a subsurface layer.

Based on observed patterns of longitudinal PGD from Japan, we use an idealized Block pattern (uniform movement δ of a mass of soil having length L) to evaluate pipe strain. Assuming constant friction force per unit length at the soil pipe interface, the stress and strain in a pipeline are investigated using a Ramberg-Osgood model for the steel pipe material. Critical values for δ and L which result in wrinkling of the pipe wall in compression are determined for five grades of steel, various R/t ratios and various burial conditions.

The analysis method is applied to pipelines along Balboa Blvd., which were subjected to longitudinal PGD during 1994 Northridge event.

ANALYSIS PROCEDURE FOR LONGITUDINAL PGD

There are two cases to be considered for a buried pipeline subject to a Block pattern of longitudinal PGD. In Case I, the amount of ground movement δ is large and the pipe strain is controlled by the length, L, of the PGD zone. In Case II, L is large and the pipe strain is controlled by δ.

The distribution of pipe axial displacement, force and strain are shown in Figure 1 for Case I and in Figure 2 for Case II, where f_m is the friction force per unit length at the pipe-soil interface and L_e is the effective length over which f_m acts. The friction force can be expressed by:

$$f_m = (c + \mu \Upsilon H)\,\pi D \tag{1}$$

where c is the soil cohesion or the undrained shear strength, μ is the coefficient of friction at the soil-pipe interface, Υ is the effective unit weight of soil, H is the depth to centerline of the pipeline and D is the diameter of pipe.

Over the segment AB, the force in the pipe is linearly proportional to the distance from Point A. Using a Ramberg Osgood model for the pipe material, the pipe strain and displacement can be expressed as follows:

$$\varepsilon_{max} = \frac{\beta_p L_e}{2E}\left\{1 + \frac{n}{1+r}\left(\frac{\beta_p L_e}{2\sigma_y}\right)^r\right\} \tag{2}$$

$$\delta_{max} = \frac{\beta_p L_e^{\,2}}{E}\left\{1 + \frac{2}{2+r}\cdot\frac{n}{1+r}\cdot\left(\frac{\beta_p L_e}{\sigma_y}\right)^r\right\} \tag{3}$$

where n and r are Ramberg-Osgood parameter, E is the modulus of elasticity of the steel pipe, σ_y is the effective yield stress, β_p is the pipe burial parameter and Le is the distance from point A to point B in Figure 1 and Figure 2.

For sandy soil (c=0), the pipe burial parameter β_p and the frictional coefficient μ can be computed by:

$$\beta_p = \frac{\mu \Upsilon H}{t} \tag{4}$$

$$\mu = k\tan\phi \tag{5}$$

where ϕ is the angle of shear resistance of sand and k is a coefficient which depends upon the condition at soil pipe interface.

Hall and Newmark (1977) suggest that compressional wrinkling in a pipe normally begins at a strain of 1/3 to 1/4 of the theoretical value of ε_{theory}=0.6 t/R, where t is the pipe wall thickness and R is the pipe radius. Herein we assume that the onset of wrinkling occurs at the midpoint of the range established by Hall and Newmark, that is:

$$\varepsilon_{cr} = 0.175\frac{t}{R} \tag{6}$$

The strain associated with tensile rupture is on the order of 3% to 5% (Newmark and Hall, 1975). In this study we use an ultimate tensile value of 4%, beyond which the pipeline is considered to have failed in tension.

The critical length L_{cr} is established from Equation 2. Setting the peak strain equal to the critical strain, we solve for the corresponding effective length. The critical length, the length of the PGD zone leading to failure, is then twice this effective length The critical displacement δ_{cr} is established from Equation 3 by setting the effective length L_e equal to half the critical length L_{cr}.

The critical values, δ_{cr} and L_{cr}, which result in wrinkling of the pipe wall in compression are

given in Figure 3 for grade-B steel and in Figure 4 for X-60 steel for various combination of the pipe burial parameter β_p and the pipe radius over thickness ratio R/t. The analysis procedure suggests that the pipeline will be damaged if both L and δ are larger than their critical values (that is if the actual L and δ are above and to the right of the δ_{cr}, L_{cr} point).

Note that the potential for damage decreases (δ_{cr} and L_{cr} become larger) as the pipe burial parameter decreases. Also for a given value of the pipe burial parameter, the potential for damage decreases as the R/t ratio decreases. Finally the beneficial effects of higher grade steel are most noticeable at small R/t ratios.

For the pipes considered herein, the R/t values are large enough that the wrinkling strain from Equation 1 is in all cases smaller than the strain associated with tensile rupture. Hence the wrinkling occurs first in the straight pipeline crossing the longitudinal PGD zone considered here. Once wrinkling occurs, a determination of wether an additional tension failure would occur at the head of the PGD zone is complicated, and will not be discussed in detail here. That is, once a failure (in our cases when wrinkling occurs) we do not attempt to determine if additional failure occur in the line.

BALBOA BLVD. CASE HISTORY

The Northridge earthquake occurred on January 17, 1994 in the San Fernando Valley. The epicenter was about 1 mile south-southwest of Northridge or 20 miles west-northwest of Los Angeles at a focal depth of 12 miles (15 km). The surface wave magnitude assigned by the National Earthquake Information Center was Ms=6.7. The maximum horizontal and vertical ground acceleration recorded closest to the Balboa Blvd. site were 0.98g and 0.52g, respectively (Hall, 1994).

Figure 5 shows the map of major pipelines, ground deformation zones and locations of pipeline damage on Balboa Blvd. An area between the two shadowed belts in Figure 5 moved to the south due to Northridge event. The ground movement (essentially directly south or downslope) was parallel to Balboa which is a North/South street. According to O'Rourke and Palmer (1994), the pattern of ground deformation suggests that lateral spreading of the alluvial fan sediments took place. Nearby boreholes show loose silty sands at depths of 30 to 40 feet (9 to 12 m).

A total length of the PGD zone was about 500 yards (457 m). At the southern end of the zone, sidewalk overlapping and sidewalk buckling as shown in Figure 6 suggest an abrupt compressive ground movement of roughly 21 inches (0.53 m, O'Rourke, 1994). At the northern end of the zone, gaps in sidewalks and ground cracks as well as gaps in curbs as shown in Figure 7 suggest a tensile ground movement of at least 18 inches (0.46 m). Hence for the purpose of analysis we use L=457 m and δ=0.50 m.

Three out of five gas and water main pipelines along Balboa Blvd. were damaged by the Northridge earthquake. There were compressive and tensile failures in the 49 inch (1240mm) diameter Granada Trunk Line, the 68 inch (1730 mm) diameter Rinaldi Trunk Line and the 22 inch (550 mm) diameter gas line (old Line 120) in the compressive and tensile zones of ground deformation, respectively. The other lines are a 30 inch (750 mm)-diameter gas transmission line and 16 inch (400 mm)-diameter petroleum pipeline, which survived in the Northridge earthquake. In addition there is a new 24 inch (600 mm) gas line (new Line 120) located along McLennan Ave. which was subject to similar PGD as along Balboa but was apparently undamaged. Herein we consider only the Granada Trunk Line and both the old and new Line 120 because of a lack of information for the other lines.

Granada Trunk Line

As shown in Figure 5, the Granada Trunk Line installed in 1956 is 49 inch (1240 mm) in diameter and has 5/16 inch (7.9 mm) wall thickness with butt welded joints. Based on field observations by the first author, the pipe was buried with 5 feet (1.5 m) of cover over its top and had 1/2 inch (13 mm) inside and 1 inch (25 mm) outside mortar coatings. After the 1971 San Fernando earthquake, a 10 inch (254 mm) Dresser Coupling with 2 to 3 inches (51 to 76 mm) allowable movement was installed at a location a "couple hundred" feet north of Lorillard St. The grade of steel for this pipe is unknown.

As summarized in Table 1 herein we assume Grade B steel with σ_y=33 ksi, n=10, r=100, burial depth to top of pipe =5.0 feet (H=7 feet) and unit weight of soil Υ =105 lb/ft^3, angle of shearing resistant ϕ=35°. Based on Elhmadi and O'Rourke (1989), we take k=1.0 for concrete mortar/soil interface, which results in a friction coefficient μ=0.7 and a pipe burial parameter β_p=11.5 psi for the Granada Trunk Line.

Using β_p=11.5 psi and R/t=78 for the Granada Trunk Line, the critical length of the PGD zone is about 150m and the critical amount of the PGD is about 0.1 m from Figure 3 for a compressive failure strain of 0.0022. Both of the length of the PGD zone L=1500 feet (457 m) and amount of the PGD δ =20 inch (0.5 m) are larger than the critical values. Hence the analysis procedure indicates that, at least, the Granada Truck Line fails in compression. This computation for the Granada Trunk Line is shown in Table 2.

As noted above, the state of strain and stress in the line after a wrinkling failure is complex, and a detailed discussion is not attempted here. However it can be noted that if the lines were locally reinforced in the abrupt ground compression zone such that wrinkling would not occur, the analysis procedure suggests that the Granada Trunk line would suffer tensile failure since the actual values of L=457 m and δ=0.5 m are larger than δ_{cr} and L_{cr} for tensile failure in Table 2. In addition once wrinkling occurs, the tensile strain at the tension zone tends to increase since the

wrinkled zone can no longer take its full share of the applied load ($f_m L/2$).

Line 120

Old Line 120 (transmission gas pipeline) is 22 inch (550 mm) in diameter, 0.281 inches (7.2 mm) in wall thickness and was constructed in 1930 with unshielded electric arc girth welds. It was made of Grade B steel. The line was operated at about 175 psi (1.2 MPa) at the time of the earthquake. Line 120 had been scheduled for replacement in the Granada Hills area before the 1994 Northridge earthquake. Old Line 120 had a compressive shortening at the ground compression zone, and a separation between the failed ends at the ground tension zone of approximately 10 inch (250 mm). The compressive shortening and tensile failure occurred at welded joints. The new 24 inch (600 mm)-diameter pipeline (new Line 120), with electric arc girth welds, X-60 steel, and 0.25 inch (6.4 mm)-thick wall, had been constructed parallel to the older 22 inch-diameter line (old Line 120) along McLennan Avenue as shown in Figure 5. It had not been opened for gas flow at the time of the earthquake. It crossed similar zones of tensile and compressive PGD, however it was not damaged.

The properties of both old Line 120 along Balboa Blvd. and new Line 120 along McLennan Ave. are shown in Table 1. The buried depth of 4 feet (1.2 m, ground surface to top of pipe) for the old Line 120 was measured by the first author. That same value is assumed to the new Line 120. Assuming k=0.9 for gas pipeline without concrete/mortar coating, computations for both old and new of Line 120 (following the same procedure as that for Granada Trunk Line) are shown in Table 2.

The actual length of PGD zone and the amount of PGD are 457 m and 0.5 m which are larger than failure criteria for old Line 120. Hence the analysis procedure suggests that old Line 120 would likely be damaged in both the compressive and tensile zones of PGD. For new Line 120, the critical length and displacement for compressive failure are 331 m and 0.38 m respectively. Hence the analysis procedure indicates that this line should have failed by wrinkling. Apparently the line did not fail. This discrepancy could be due to a combination of effects. First the actual buried depth may be less than 4 feet (1.2 m) assumed herein. Secondly the length and amount of PGD movements along McLennan Ave. may have been less than that along Balboa Blvd. Finally and somewhat more likely, the pipe may well have followed under the street, that is a 90° elbow installed south of the ground compression zone. The presence of such an elbow or bent would reduce the compression axial stress and strain in that leg. Note that the possible presence of an elbow is not currently included in the analysis procedure. In addition because the actual displacement of the tensile PGD zone (0.5 m) is less than the critical value of 1.68 m, the analysis procedure suggests that no tensile failure for new Line 120 occur, which matches the observed behavior.

DISSCUSSION

The calculation for the Granada Trunk Line presented above does not take into consideration the presence of an expansion joint, which according to LADWP personnel, is located "a couple of hundred" feet north of Lorillard St.(possibly 140 m away from the location of tensile failure). The expansion joint was a Dresser type with an allowable relative movement of 2 to 3 inches (51 to 76 mm). Based on the calculation shown above, the critical length of PGD zone for Granada Trunk line is 150 m. Hence an expansion joint located about 140 m to the North of the ground tension zone would have no influence on the response of the pipeline because the expansion joint would be located outside the interaction region (140 m > 150 /2 =75 m). Even if the expansion joint is installed in the tensile zone of PGD, it would not greatly improve the performance of the pipeline because the allowable movement of the joint is too small relative to the amount of PGD.

If a single unlimited movement expansion joint is installed in a location near the margin of PGD zone, one can see from the distribution of pipe axial forces, shown in Figure 8 for case I, that the expansion joint actually make the situation worse.That is, if the single expansion joint is located just North of the PGD zone, the pipe strain at the compression zone increase since the total load, $f_m L$, is no longer shared equally at both the compression and tension zones.

Installation of two expansion joints, one to the North of the ground tension zone and another to the South of the ground compression zone, would reduce stress and strain in the pipe. However such an approach would require a prior knowledge of the actual location of the PGD zone as well as reasonable estimates of both L and δ. Hence, the use of high grade steel with modern welding technique, shallower burial depths, reduced friction at the soil pipe interface and/or decreased R/t ratios are probably somewhat better methods to reduce pipeline damage.

CONCLUSION

In this paper, an analysis procedure for pipeline subject to longitudinal PGD is reviewed. The failure criteria are used to predict damage in the Los Angeles DWP Granada Trunk Line and gas pipeline (Line 120) along Balboa Blvd. The analysis shows that the failures of DWP Granada Trunk Line and old Line 120 in 1994 Northridge earthquake are predicted by the analysis procedure.

REFERENCE

Elhmadi,K. and O'Rourke,M.J.(1989), Seismic Wave Effects on Straight Jointed Buried Pipeline, NCEER-89-0022

Hall,J.F., 1994, Northridge Earthquake January 17, 1994, Preliminary Reconnaissance Report, EERI 94-01.

Hall,W., Newmark,N.(1977), Seismic Design Criteria for Pipelines and Facilities, Current State of Knowledge of Lifeline Earthquake Engineering, Proc. ASCE Specialty Conf., Los Angeles, CA, pp18-34.

Newmark,N.M., Hall,W.J.(1975), Pipeline Design to Resist Large Fault Displacements, Proc. of U.S. National Conference on Earthquake Engineering, Ann Arbor, MI, June, 1975.

O'Rourke, M.J.(1994), Earthquake Performance of Water Pipeline During the Northridge Earthquake, NCEER Bulletin, Volume 8, Number 2, April 1994, pp6 - 8.

O'Rourke,M. and Nordberg,G(1990), Analysis Procedures for Buried Pipelines Subject to Longitudinal and Transverse Permanent Ground Deformation, Proc. Third Japan-U.S. Workshop on Earthquake Resistant Design of Lifeline Facilities and Counter-measures for Soil Liquefaction, San Francisco, CA, pp439-453; Tech. Rept. NCEER-91-0001, December.

O'Rourke,T.D., Palmer M.C.(1994), Earthquake Performance of Gas Transmission Pipelines During the Northridge Earthquake, NCEER, Volume 8, Number 2, April 1994, pp1 - 5.

Table 1 Properties of Three of the Pipeline in Balboa Lateral Spread Zone

Item	D (inch)	t (inch)	Material	Location	Installed Data	Performance
Granada Trunk Line	49	0.313	Grade-B	Balboa Blvd.	1956	Damaged
Old Line-120	22	0.281	Grade-B	Balboa Blvd.	1930s	Damaged
New Line-120	24	0.250	X-60	McLennan	After 1971	Survived

Table 2 Computation of Pipe Parameters

Item	Frictional Coeff. μ	R / t	β_p	Compression		Tension	
			(pci)	L_{cr}	δ_{cr}	L_{cr}	δ_{cr}
Granada Trunk Line	0.70	78	11.5	149 m	0.09 m	154 m	0.15 m
Old Line-120	0.63	39	8.2	211 m	0.13 m	217 m	0.21 m
New Line-120	0.63	48	9.2	331 m	0.38 m	422 m	1.68 m

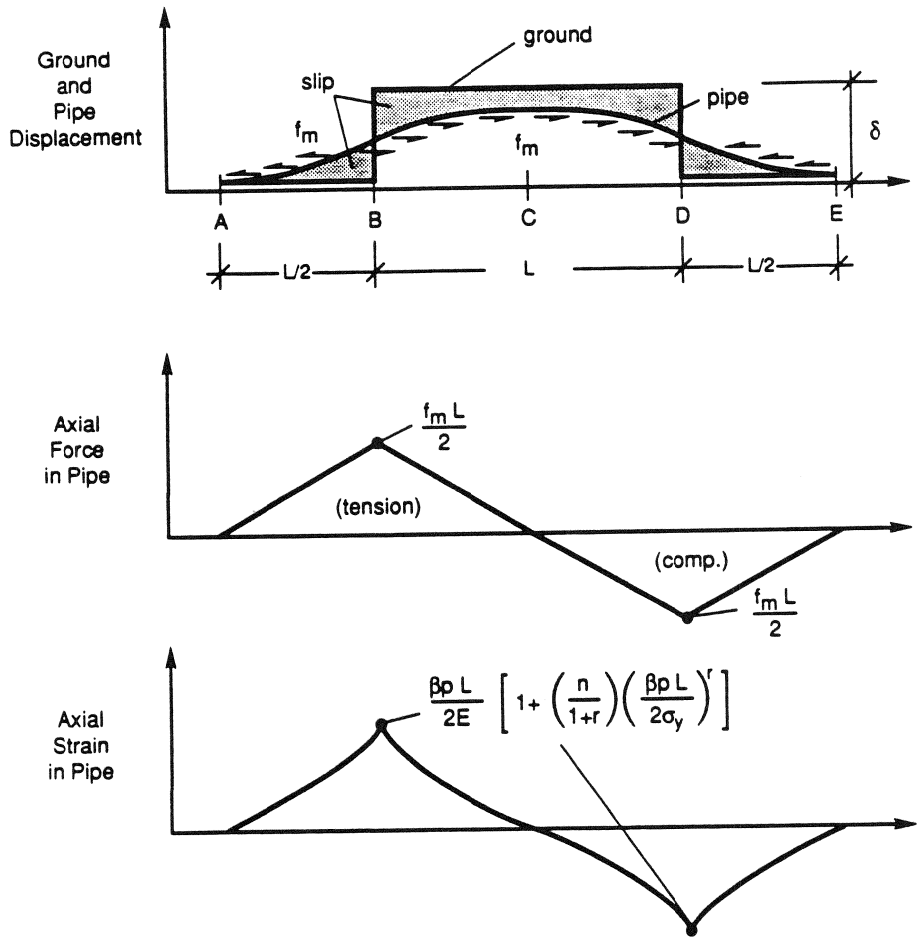

Figure 1 Pipe Axial Displacement, Force and Strain Due to Longitudinal PGD for Case I

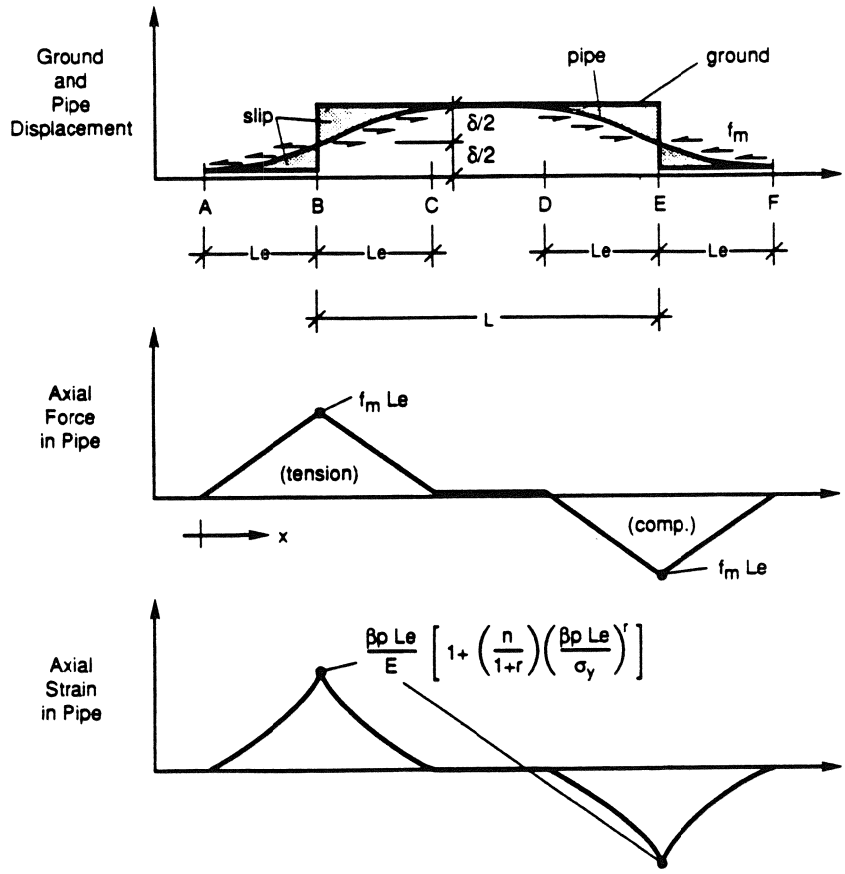

Figure 2 Pipe Axial Displacement, Force and Strain Due to Longitudinal PGD for Case II

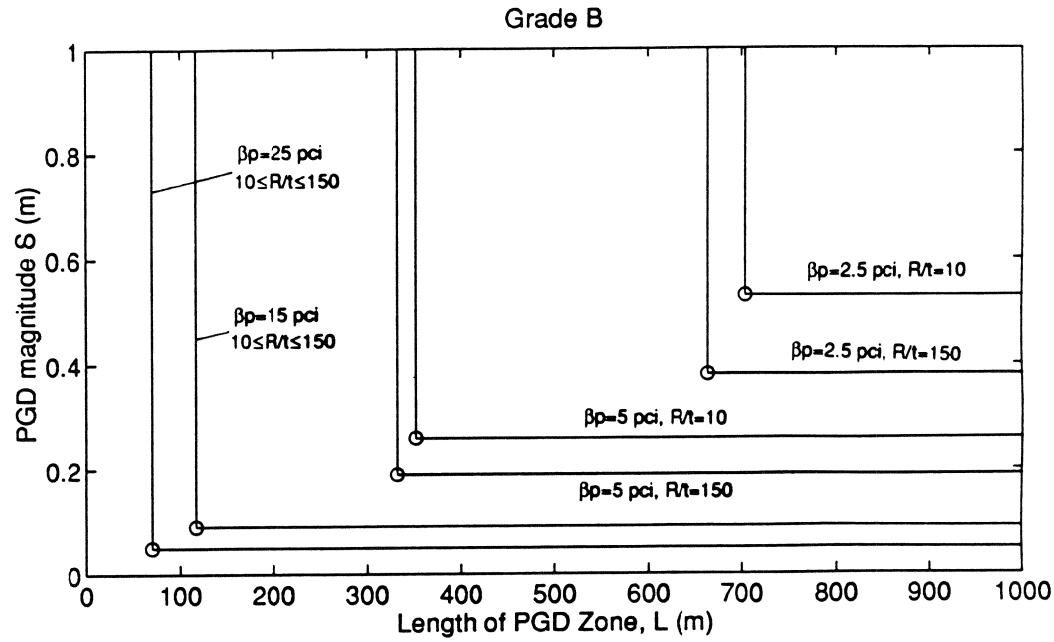

Figure 3 Critical Length L_{cr} and Displacement δ_{cr} for Grade-B steel in Compression

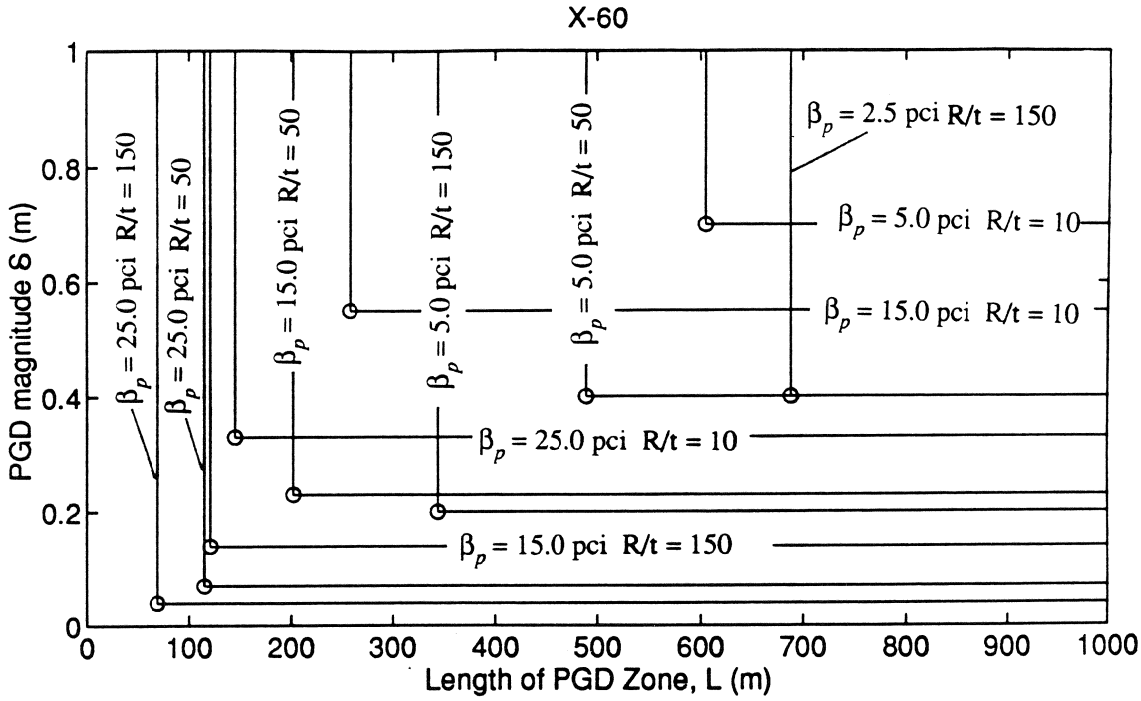

Figure 4 Critical Length L_{cr} and Displacement δ_{cr} for X-60 Steel in Compression

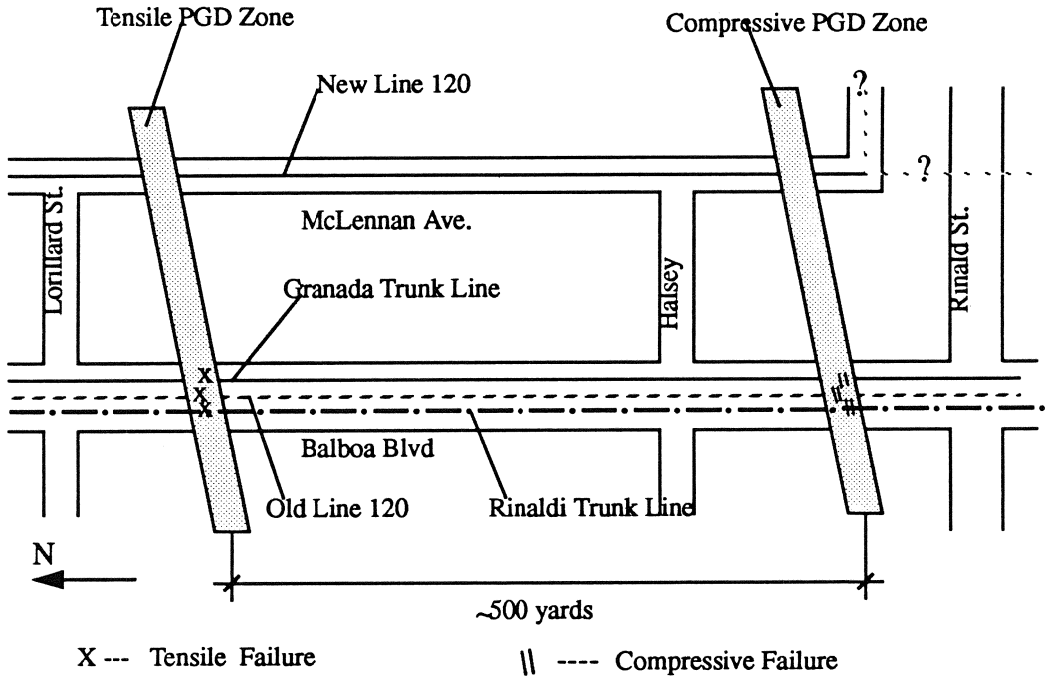

Figure 5 Map of Major Pipelines, Ground Deformation Zones and Locations of Pipeline Damage on Balboa Blvd.

Figure 6 Sidewalk Overlap on West Side of Balboa Blvd., Southern End of PGD Zone

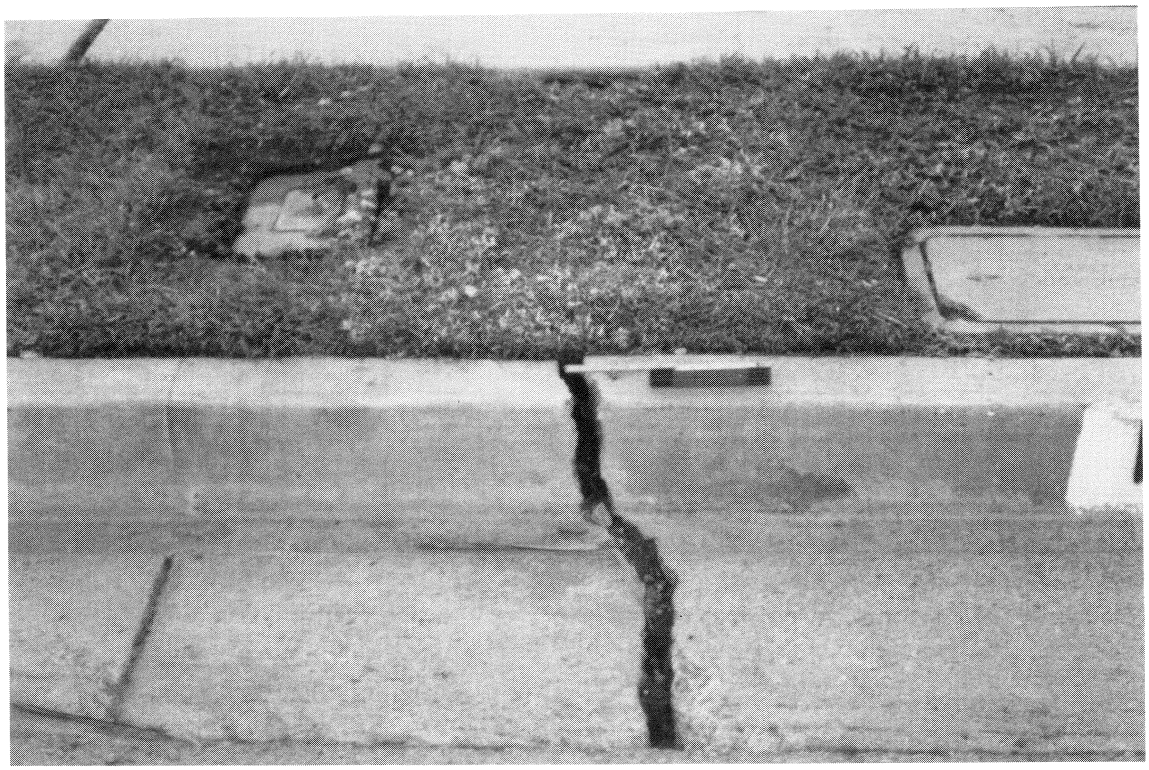

Figure 7 Gap in Curb on West Side of Balboa Blvd., Northern End of PGD Zone

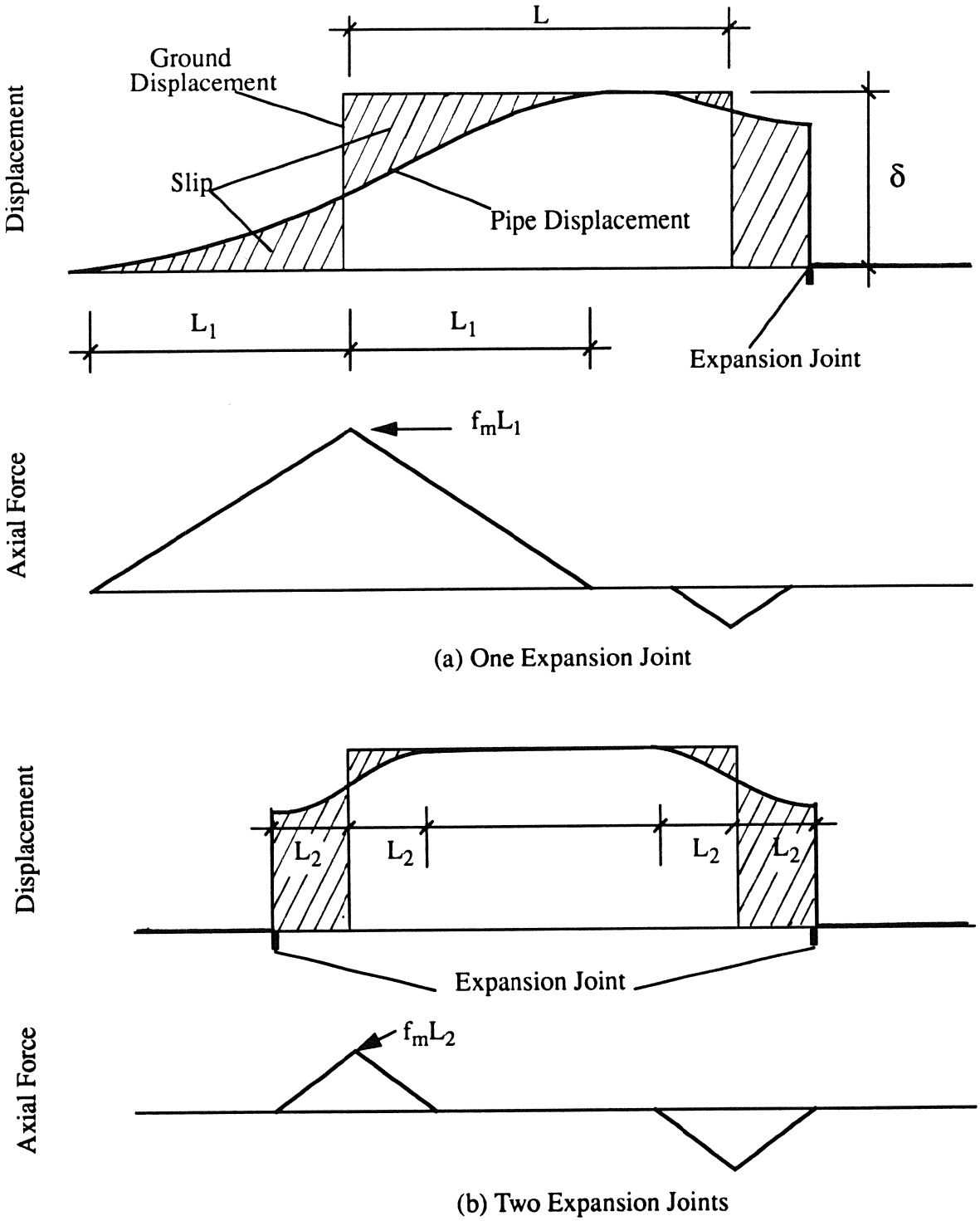

Figure 8 Distribution of Pipe Displacement and Axial Force with Expansion Joint

CHANGING NEEDS FOR HAZARD INFORMATION FOR PIPELINE LOSS ESTIMATION

Donald Ballantyne, P.E.

Associate
Dames & Moore, Seattle, Washington 98121

ABSTRACT

Continued development of pipeline loss estimation methods requires different types of permanent ground deformation, PGD, hazard information. This paper briefly summarizes methods for pipe loss models used over the past 20 years considering wave passage and liquefaction susceptibility. Current trends in loss modeling are explored such as:

- PGD net displacement for segmented pipelines (Harding Lawson, 1991)
- Soil block dimension influence on vulnerability (M. O'Rourke, 1992)
- Methodology to define areal extent of PGD

The need for PGD information associated with non-lateral spread and non-tectonic related ground movement is explored as evidenced by an estimated 1500 pipeline failures in the Northridge earthquake with almost no liquefaction and no surficial fault expression.

INTRODUCTION

Continued development of pipeline earthquake loss estimation methodologies is important; loss estimation is a useful tool in assessing the risk of pipeline system failure in earthquakes, developing earthquake mitigation programs, and developing emergency response programs.

This paper briefly reviews pipeline earthquake loss estimating methods used over the past 20 years. It then presents a proposal for a methodology for earthquake pipeline loss estimation associated with liquefaction induced lateral spreading. Finally, the proposed methodology is discussed, and the future direction of pipeline earthquake loss modeling is posed.

One of the objectives of having such a methodology available is for use in regional loss studies. With that in mind, it is important to minimize the required number of parameters required to achieve a meaningful result. The methodology proposed herein tries to limit the number of those variables.

This proposed methodology has been developed working with the Fragility Task Committee of the American Society of Civil Engineers Technical Council on Lifeline Earthquake Engineering. The objective of the committee is to establish a methodology for earthquake loss modeling of lifelines. Once an approach is established, it will provide a format for acquisition of earthquake damage data from future earthquakes. The methodology is designed to upgrade its components as new information is developed. Comments on the methodology from participants of this workshop are welcome.

OVERVIEW OF PIPELINE LOSS ESTIMATION

This section discusses the development of pipeline earthquake loss estimation as well as methods used to estimate PGD in support of pipeline loss estimation. Empirically based water pipeline damage algorithms reviewed in this paper were initiated in Japan and refined in both the United States and Japan as described below.

Katayama

A pipeline earthquake loss estimation methodology was introduced by Professor Katayama in the mid-1970s. He developed pipeline damage algorithms relating pipe failures and earthquake peak ground acceleration. His damage algorithm included an envelope of loss estimates depending on the soil response characteristics, including liquefaction (Katayama, 1975).

Eguchi

Pipeline damage from wave passage, fault rupture, and liquefaction was segregated by Eguchi in the early 1980s. He gathered empirical damage data from over 20 earthquakes worldwide, but was able

to develop the most significant relationships based on damage data from the 1971 Sylmar Earthquake (Eguchi, 1982). For that earthquake, he related earthquake intensity to cast iron pipeline failures from wave passage for a range of Modified Mercalli Intensities. He then related damage rates for other pipe materials to cast iron for one intensity, establishing a family of damage algorithms. For that same earthquake, he also developed pipeline damage rates for liquefaction conditions for a family of pipe materials, but did not relate them to permanent ground deformation from liquefaction.. Finally, he developed damage rates based on proximity-to/displacement-of the fault offset.

Ballantyne

In the late 1980s, Ballantyne segregated pipeline damage into pipeline breaks and pipeline leaks (Ballantyne, 1990). This information became valuable for use in deterministic post-earthquake water system hydraulic modeling. As part of the same study, the question of areal extent of liquefaction along a pipeline corridor or in a microzone had a very significant effect on loss estimation results. It became clear to this author in that study that permanent ground deformation pipeline damage would often control the overall system performance, and that pipeline unit damage rates for liquefaction/permanent ground deformation were an order of magnitude greater than for wave passage.

Youd, Perkins, and Bartlett; LSI and MLR

In 1987, Youd and Perkins published the Liquefaction Severity Index, LSI, approach to estimate the maximum permanent ground deformation at a given site for a particular earthquake scenario. Initially, this information was not applied as a pipeline damage estimation tool (Youd, 1987). More recently, Bartlett and Youd have refined the LSI method with the Multiple Linear Regression analysis method, MLR, for estimating maximum permanent ground deformation from liquefaction related lateral spreading (Bartlett, 1992).

M. O'Rourke

In 1992, M. O'Rourke identified the significance of lateral spread block geometry on the extent of continuous (welded steel) pipeline vulnerability (O'Rourke, 1992). A major problem related to this approach was being able to estimate the block size/ground breakup pattern.

San Francisco Liquefaction Study

Following the 1989 Loma Prieta Earthquake, the City and County of San Francisco selected a project team to estimate utility losses that might occur in liquefiable soil areas around the periphery of the city for a magnitude 8.3 San Andreas Earthquake (Harding Lawson, 1992). The project team developed damage algorithms relating pipeline damage to permanent ground deformation using

empirical damage data from the 1971 Sylmar Earthquake, the 1989 Loma Prieta Earthquake (including the San Francisco Marina District and the City of Santa Cruz data), and the 1983 Nihonkai Chubu, Japan Earthquake. It was found to be very difficult to find damage data that included a record of permanent ground deformation.

The San Francisco project team geotechnical engineers used Tohata's (1990) method to estimate the extent of lateral permanent ground deformation. The assumption was made that the entire soft soil area would liquefy considering the soil properties, large peak ground accelerations, and long duration. This permanent ground deformation displacement and areal extent information was then passed along to the earthquake lifeline pipeline project team members for use in estimating pipeline damage.

Further Loss Studies

The San Francisco project had an extensive geologic data set available, and a significant budget for analysis. Pipeline earthquake loss estimation projects for the Greater Vancouver Regional District in Vancouver, British Columbia (Kennedy/Jenks Consultants, 1993), and the Portland Bureau of Environmental Services, Portland Oregon, (Dames & Moore, 1994) made pipeline loss estimates using the LSI to estimate permanent ground deformation. In both cases the project team geotechnical engineers were asked to make estimates on the areal extent of liquefaction and a mean permanent ground deformation. In this author's opinion there was a significant level of uncertainty associated with those estimates because of the lack of available methods. The areal extent of liquefaction estimate is directly related to the damage estimate, so the degree of certainty is very important.

LIQUEFACTION AREAL EXTENT METHODOLOGY

Introduction

This section presents a methodology for estimating pipeline losses from permanent ground deformation. It includes consideration for estimating liquefaction susceptibility, probability, and areal extent, and applies that information to pipeline loss estimation.

Liquefaction Susceptibility

This reduced set of variables has been selected so that the methodology is applicable to conduct regional loss studies. First, establish three levels of liquefaction susceptibility: none/low, medium, and high. From a loss estimation perspective, none/low can be ignored, and medium usually ignored as it typically only represents less than 1 percent of estimated losses. In general, liquefaction susceptibility would take into account (criteria in parenthesis for high susceptibility) groundwater table depth (< 12 feet below grade), blow count N_1 (< 12), and depth to liquefiable deposit (< 25 feet below grade).

Liquefaction Probability and Magnitude Scaling Factor

The curves shown in Figure 1 define the probability of liquefaction, P_L, as a function of peak ground acceleration, PGA. These curves are defined as the probability of liquefaction occurring at a point in a soil mass in controlled field test conditions.

A family of curves are proposed for a range of earthquake magnitudes. Ultimately, separate curves would be required for a range of soils such as clean sands, silty sands, etc.. These curves could likely be developed from existing information such as Liao (1986). The PGA scale has been purposely not provided. These curves show the form expected in a finalized methodology. Additional curves can be added for earthquakes of other magnitudes. These curves are included to address the magnitude scaling factor, to compensate for the duration/number of earthquake cycles for earthquakes of varying magnitude.

Liquefaction Areal Extent

Apply a factor to estimate areal extent of liquefaction, P_{AE}, from probability of liquefaction (above) as defined in equation 2, below. P_{AE} is the conditional probability that an arbitrary surface location will exhibit liquefaction below grade.

$$P_{AE} = A_L / A_T \qquad (1)$$

where:

A_L = Area of liquefaction where it is evident that liquefaction has occurred by field observation such as where sand boils appear, or ground has subsided or moved laterally as evidenced by cracking.

A_T = Total area with same susceptibility to liquefaction (low, moderate, or high as defined above), subjected to the same approximate PGA.

It is the intent that this correction takes the probability of liquefaction developed for a volume of soil in a controlled condition and corrects it to estimate the areal extent of liquefaction occurring in an earthquake. The occurrence of liquefaction is defined as identified by field observation, as that is the basis on which most pipeline damage data has been generated. Field identification can include evidence of sand being ejected from below the surface and/or ground cracking from vertical and/or horizontal permanent ground deformation. The person making the field observations is expected to understand the liquefaction phenomena, and be aware of local ground water conditions.

The curve is expected to take the general form shown in Figure 2. Surface expression of liquefaction is expected to be influenced by the thickness of the layer of liquefiable (and liquefied) material. Other conditions may also have an effect such as variability of the liquefiable deposit. The final curve should reflect as many variables as applicable.

Maximum Permanent Ground Deformation

Apply the Liquefaction Severity Index methodology, LSI, to estimate the maximum PGDs within the study area. Correct the LSI for slope or proximity to a free face. If there is adequate information, apply the Multiple Linear Regression, MLR, analysis technique to estimate the maximum permanent ground deformation, PGD. (note that it is suggested only to correct LSI for slope/free face proximity, and not subsurface data because slope/free face proximity information is more readily available in GIS format).

Map the mean permanent ground deformation, PGD_m (one-half times the maximum PGD as a starting point) based on the LSI or the MLR.

Pipe Parameters and Permanent Ground Deformation Pipe Exposure

Measure the pipe length, L_P, of each pipe type category (defined by material and joint type) within each area with a defined range of PGD_m (such as 0-1 inch; 1-5 inches, etc.). Note that pipe type category may include more than one type of pipe, but they would all be expected to respond similarly in an earthquake.

Pipeline Damage Algorithms

Read the failure rate for the average of the range of PGD_m for each pipe type using the appropriate pipe damage algorithm, presented in terms of percent of length requiring replacement P_R(as a function of PGD), or failures per km F_K(as a function of PGD). Typical pipe damage algorithms are shown in Figures 3 and 4.

Pipeline Repair / Replacement

Calculate the pipe length to be replaced:

$$P_{AE} \times L_P \times P_R = \text{Pipe Length to be Replaced} \qquad (2)$$

for each PGD_m range/pipe type category for each range of PGD. Alternatively, calculate the total number of expected pipe failures:

$$P_{AE} \times L_P \times F_K = \text{Expected Pipe Failures} \quad (3)$$

for each PGD_m/pipe type category.

Further Corrections

Provide further corrections for: 1) pattern of liquefaction deformation, 2) pipe orientation to PGD, 3) corrosion condition/maintenance history, 4) number of connections/unit length, and 5) for welded steel pipe, wall thickness/pipe radius.

DISCUSSION AND UNRESOLVED ISSUES

This proposed methodology identifies two concepts that will have to be developed with time, areal extent of liquefaction, and mean PGD (PGD_m). As it is defined, areal extent of liquefaction would have to be developed using empirical field data gathered following earthquakes, in conjunction with liquefaction hazard maps for the same area that have defined liquefaction susceptibility relationships.

PGD_m is selected as being representative of the PGD which is seen by pipelines in the immediate area. Trying to develop a density function for the distribution of PGD, using the LSI as a maximum, was not thought to be useful due to the uncertainties associated with the density function as well as the pipeline damage algorithm itself. Using one-half the PGD is considered only a starting point.

It is apparent that pipeline damage associated with liquefaction is not only related to PGD, but to the breakage pattern and size of soil blocks that develop when lateral spreading occurs. Methods are needed to enable lifeline earthquake engineers to estimate soil block patterns, and then to relate pipeline damage to those patterns. Other parameters will also affect pipe strain as it is related to soil block patterns and movement including the coefficient of friction between the soil and pipe.

Ultimately, we may have to revert back to the generalized damage pipeline damage estimation approach originally proposed by Katayama. It is very difficult to be able to clearly define soil parameters/sources of permanent ground deformation along every length of pipeline. We currently have techniques to quantify liquefaction/lateral spread, landslide, and fault displacement-associated PGDs. There are two examples where mapping of these hazards have failed. First, in the study of the Seattle water system (Ballantyne, 1990), there were a number of clusters of pipeline failures following the 1949 and 1965 Seattle earthquakes in areas that today are mapped as competent glacial deposits. Based on evaluation of leak repair records, it is likely that there was localized liquefaction in those areas resulting in some PGD and pipeline failure. There was no reported indication of liquefaction on the surface.

Second, the Northridge Earthquake. There was significant surface cracking throughout the San Fernando Valley. There were in the order of 700 transmission and distribution pipeline failures in the valley (as well as an equal number of service failures). However there was only limited liquefaction

reported, and not widely distributed. While there has not been a decisive report, there have been discussions that the cracking is of tectonic origin. As a lifeline earthquake engineer, it will be very difficult to estimate the extent of surface cracking for any given earthquake scenario.

POST-EARTHQUAKE SOIL FAILURE/DAMAGE DATA NEEDS

In order to make the proposed methodology a reality, specific soil failure and pipeline damage data will be required such as the following:

- Inventory of areas where liquefaction has occurred
- Liquefaction susceptibility maps
- Definitive mapping of PGD
- Pipeline locations relative to PGD
- Pipeline damage mechanisms, and damage descriptions (leak, break, leakage rate)

Post-earthquake investigators are urged to gather this type of data. Some of this information currently exists such as from the Loma Prieta and Nihonkai Chubu earthquakes. The Japanese lifeline community has been more aggressive that their U.S. counterparts in gathering this type of data.

CONCLUSIONS

Pipeline earthquake loss estimation has developed from simple damage algorithms incorporating damage from "all" earthquake hazards, to more sophisticated algorithms that segregate damage mechanisms.

We have proposed a methodology to enable the lifeline community to better estimate pipeline damage from PGD in future earthquakes as a damage data base is developed using the proposed parameters.

ACKNOWLEDGEMENTS

We thank the National Center for Earthquake Engineering Research for support of expenses associated with meetings of the ASCE TCLEE Fragility Task Committee.

Members of the ASCE TCLEE Fragility Task Committee are acknowledged, listed alphabetically after the chair include: Professor Anshel Schiff, Chair, Mr. Donald Ballantyne, Mr. James Clark, Dr. C.B. Crouse, Mr. John Eidinger, Professor Anne Kiremidjian, Professor Michael O'Rourke, Dr. Douglas Nyman, Mr. Alex Tang, and Dr. Craig Taylor.

REFERENCES

Ballantyne, D.B.; April 4, 1994; *Development of Liquefaction Areal Extent Evaluation Methodology*; Memorandum to the ASCE TCLEE Fragility Task Committee.

Ballantyne, D.B.; Taylor, C.; 1990; *Earthquake Loss Estimation Modeling of the Seattle Water System*, USGS Grant Award 14-08-0001-G1526, Kennedy/Jenks/Chilton Report No.886005.00.

Bartlett, S.F.; and T.L. Youd; 1992; "Empirical Prediction of Lateral Spread Displacement"; *Proceedings of the Fourth Japan-U.S. Workshop on Earthquake Resistant Design of Lifeline Facilities and Countermeasures for Soil Liquefaction*, Hawaii, Report No. NCEER-92-0019.

Dames & Moore; 1994; *Seismic Vulnerability Assessment of the Portland Bureau of Environmental Services Sewer System*; being prepared for Brown & Caldwell and the Portland Bureau of Environmental Services; Project currently underway.

Eguchi, R. T.; *1982; Earthquake Performance of Water Supply Components During the 1971 San Fernando Earthquake*; Prepared for the NSF, Redondo Beach, CA: J. H. Wiggins Company.

Harding Lawson Associates, Dames & Moore, Kennedy/Jenks Consultants, EQE Engineering, 1991, *Liquefaction Study, San Francisco, California*, prepared for the City and County of San Francisco, Department of Public Works, San Francisco, California.

Katayama, T.; Kuho, K.; Sato, N.; 1975; "Earthquake Damage to Water and Gas Distribution Systems," *Proceedings of the 1st U.S. National Conference on Earthquake Engineering*. Berkeley, CA: Earthquake Engineering Research Institute.

Kennedy/Jenks Consultants in association with EQE Engineering and Design; 1993; *A Lifeline Study of the Regional Water Distribution System*; Prepared for the Greater Vancouver Regional District, Vancouver, British Columbia; K/J Project Number 936016.00.

Liao, S.S.C.; 1986; *Statistical Modeling of Earthquake-Induced Liquefaction*; Ph.D. Thesis, Massachusetts Institute of Technology, Department of Civil Engineering.

O'Rourke, M. J.; C. Nordberg; 1992, *Longitudinal Permanent Ground Deformation Effects on Buried Continuous Pipelines*, NCEER-92-0014, Buffalo, N.Y..

Towhata, I., K. Tokida, Y. Tamari, H. Matsumoto, and K. Yamada.; 1990; "Prediction of Permanent Lateral Displacement of Liquefied Ground by Means of Variational Principle", *Proceedings of the Third Japan-U.S. Workshop on Earthquake Resistant Design of Lifeline Facilities and Countermeasures for Soil Liquefaction;* San Francisco, California, December 1990.

Youd, T. L., D. M. Perkins, 1987, "Mapping of Liquefaction Severity Index" *Journal of Geotechnical Engineering, Vol. 113, No. 11*, pp. 1374-1392.

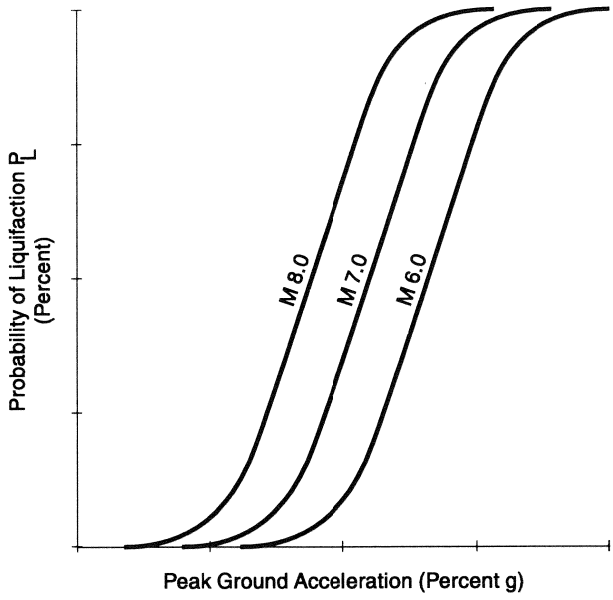

Figure 1
Liquefaction Probability Versus PGA for a Range of Earthquake Magnitudes

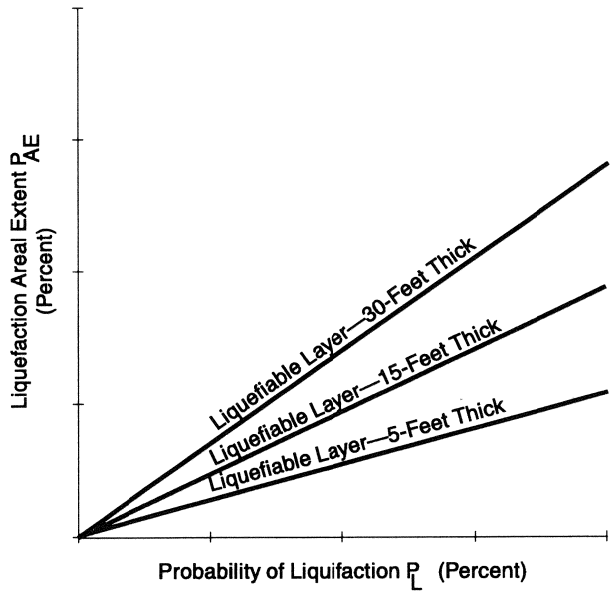

Figure 2
Liquefaction Areal Extent Versus Liquefaction Probability for a Range of Liquefiable Layer Thicknesses

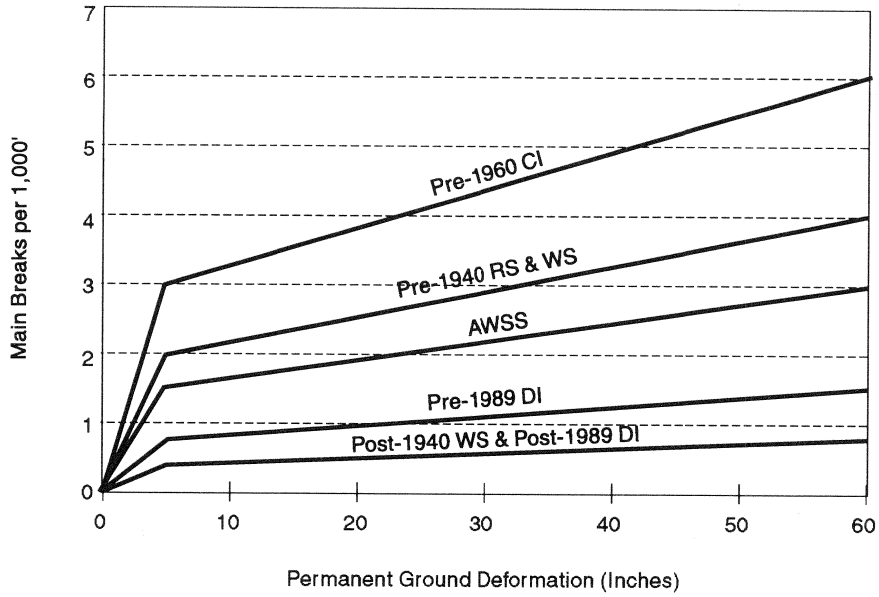

Figure 3
Main Breaks Versus Permanent Ground Deformation for Welded Steel, Cast Iron and Ductile Iron Water Pipelines (Harding-Lawson, 1990)

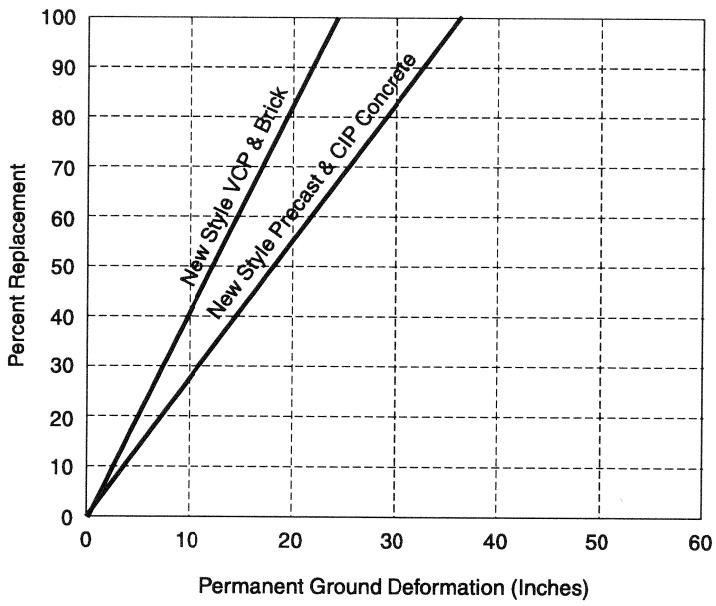

Figure 4
Percent Replacement Versus Permanent Ground Deformation for Gravity Sewer Pipelines (Harding-Lawson, 1990)

SHAKING TABLE TESTS ON FLOATATION OF BURIED PIPES DUE TO LIQUEFACTION OF BACKFILL SANDS

Susumu Yasuda[1], Hideo Nagase[2], Shigeru Itafuji[3],
Hisashi Sawada[4], and Keiichiro Mine[3]

1) Professor, Dept. of Civil Engineering, Tokyo Denki University, Saitama, JAPAN
2) Associate Professor, Dept. of Civil Engineering, Kyushu Institute of Technology, JAPAN
3) Graduate Student, ditto.
4) Engineer, West Japan Engineering Consultants Co., Ltd., Fukuoka, JAPAN

ABSTRACT

Many manholes and sewage pipes were floated due to liquefaction during the 1993 Kushiro-oki earthquake in Japan. To study the mechanism of the floatation, several shaking table tests were carried out under several conditions of soil densities, specific gravities of pipes, water levels and diameters of pipes. Tests were also conducted on the model grounds in which a trench was excavated and then backfilled with loose sands. Test results show that the speed and the height of floatation are affected by soil density, the specific gravity of the pipe or manhole, water level, and width and depth of the trench.

INTRODUCTION

Many manholes and buried pipes were elevated in the ground during the 1993 Kushiro-oki earthquake in Japan. Soil investigations and seismic response analyses revealed that this floatation was due to the liquefaction of backfill soils and alluvial sands. To study the mechanism of the floatation, shaking table test were carried out under several conditions.

FLOATATION OF MANHOLES AND PIPES DURING THE 1993 KUSHIRO-OKI EARTHQUAKE

On January 15, 1993, the Kushiro-oki earthquake of magnitude 7.8 occurred near Kushiro City in the northern Japan. The earthquake caused severe damage to sewage facilities, gas pipelines, road embankments, houses, harbor facilities, etc. In the sewage facilities, many sewage pipes, manholes, sewage disposal plants and pump stations were damaged in and around Kushiro City. In the city, 7,744m of sewage pipes were damaged and in the adjacent town, 10,838m of sewage pipes were damaged. The main patterns of pipe damage were meander, bends and joint failure. Moreover, about 20 manholes were raised in the Kiba and Katsuragi districts of Kushiro Town. The maximum amount of the floatation was 1.3m.

The Ministry of Construction's PWRI (Public Works Research Institute) and Kushiro Town officials inspected the floated manholes by excavating them and carried out soil investigations, including borings and laboratory tests. According to the boring data, an artificially filled layer with a thickness of about 2m and a peat layer with a thickness of 1 to 2m were deposited from the ground surface, as shown in Fig.1. Alluvial sand layers underlay them. As the bottom of the floated manholes was almost 4m below the ground surface, sand had been back filled to this depth around the manholes in excavated trenches during construction. The alluvial sands and the backfill sand were silty fine sands with SPT N-values of less than 10 and clean sand with SPT N-values of 0 to 11, respectively. Based on analyses of liquefaction, it is estimated that the backfill sand liquefied during the Kushiro-oki earthquake. Though it is difficult to judge whether the alluvial layers were liquefied or not, the authors

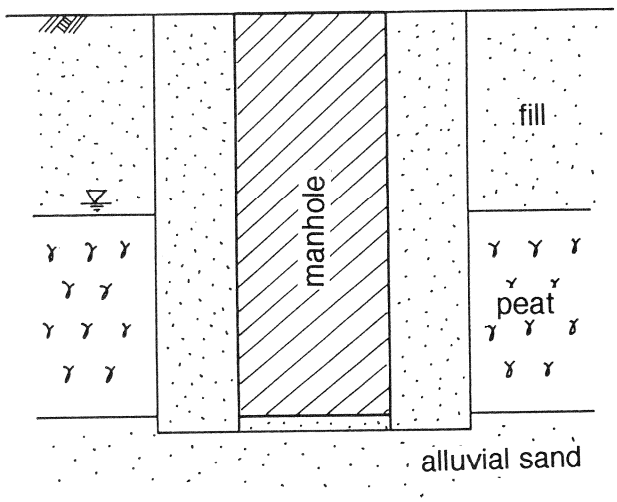

Fig.1 Schematic diagram of soil conditions

estimated that the alluvial sand layers did not liquefy during the earthquake.

Figure 2 shows the locations of damaged sewage pipes in Kushiro City and Kushiro Town. In geomorphological condition, Kushiro City and Kushiro Town are separated into four areas: (1) several artificially reclaimed lands are formed along the Pacific Ocean, (2) a sand dune runs along the Pacific Ocean, (3) peat ground extends widely behind the sand dune, and (4) hills exist in the east. As shown in Fig.2, most of the damaged sewage pipes were in the third and fourth areas. In the fourth area, damage probably occurred due to the sliding of slopes. In the third area, pipe damage was most likely induced by liquefaction, because many pipes were raised, as shown in Fig.2. The soil conditions to a depth of about 10m seemed to be similar to the soil conditions at the Kiba and Katsuragi district, as described before. Therefore, the authors concluded that the damage to pipes in the fourth area was also caused by the liquefaction of backfill sand.

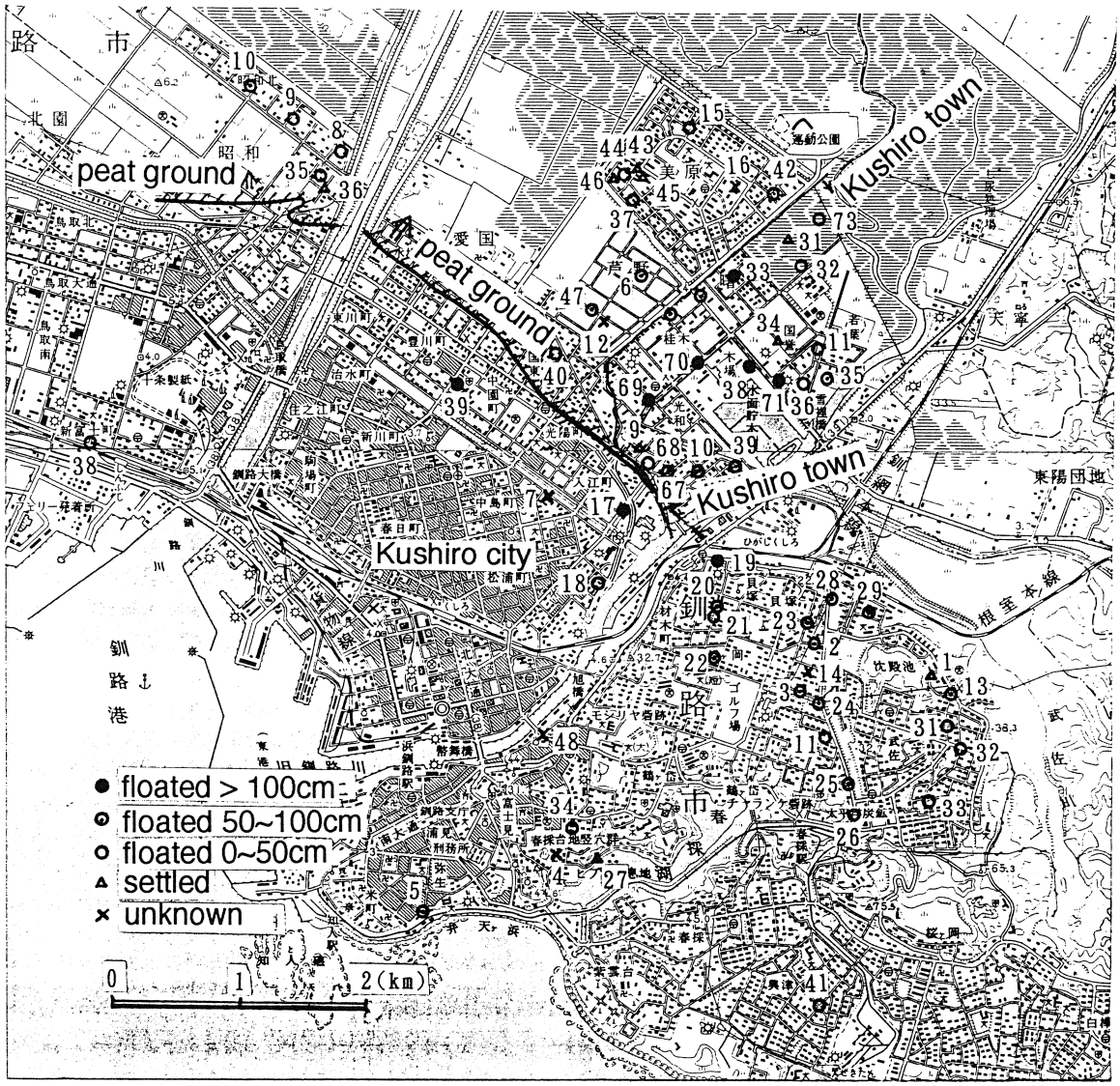

Fig.2 Locations of damaged sewage pipes

The possibility of floatation of buried pipes or manholes due to the liquefaction of backfill sand only had not been studied. Therefore, several shaking table tests were conducted to prove it. Fundamental tests to ascertain the mechanism of floatation of buried pipes and some factors which affect floatation were carried out before the tests on the possibility of floatation due to the liquefaction of backfill sands.

SHAKING TABLE TESTS ON THE MECHANISM OF FLOATATION

The shaking table used was 1m in length and 1m in width in plane. The soil container used was 100cm in length, 70cm in depth and 60cm in width, as show in Fig.3. A form rubber of 5cm in thickness was inserted inside both walls to induce uniform cyclic shear strain in a soil model during shaking. Very clean Toyoura sand with a mean diameter of 0.175mm was used. The soil was arranged in four grades: very loose, loose, medium dense and dense. The relative densities of these grades were about 0%, 30%, 50% and 70%. Two scales of model pipes: (1) 11.4cm in diameter and 55cm in length and (2) 6cm in diameter and 55cm in length, were buried in the soil to a depth of 30cm, as shown in Fig.3. The pipes were filled with clay to achieve five specific gravities, ρ_p, : 0.5, 1.5, 1.7, 1.8 and 1.9. One pair of rings was attached to both ends of the pipes, and two strings stretched in the vertical direction were passed inside the rings to float the buried pipes horizontally.

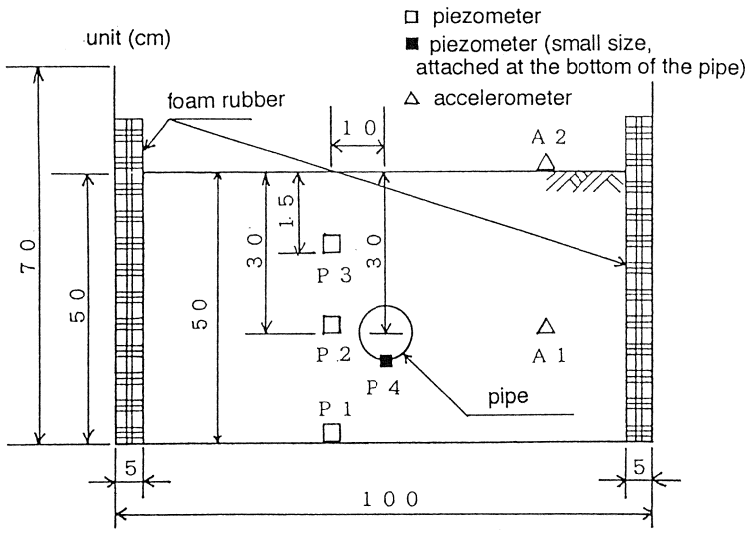

Fig.3 Diagram of apparatus for shaking table test

Four piezometers and two accelerographs were installed in the model ground, as shown in Fig.3. The floatation of the pipe was measured by the displacement of a string which was connected to the pipe. The water level was adjusted to a depth of 0cm or 15cm from the ground surface. Shaking motion was applied in one direction parallel to horizontal axis in Fig.3, at a frequency of 3 Hz and with an acceleration of 250 gals, until the floatation of the pipe is terminated. Moreover one series of tests were conducted under the higher acceleration of 400 gals, to know the effect of severity of liquefaction on the speed of floatation.

Figures 4 and 5 show relationships between the duration of shaking and the floatation of pipes with a specific gravity of 0.5 and 1.7, respectively, under different densities of soils. The speed of floatation decreased with soil density, the specific gravity of the pipe and water level in the case of $\rho_p = 0.5$. However, the effect of the specific gravity of the pipe is not clear in the case of $\rho_p = 1.7$. This may be due to the small difference between ρ_p and soil density. In dense sand, the pipes did not rise to the ground surface. Figures 6 and 7 compare the excess pore pressure ratio measured at the bottom of the pipe in loose sand with the ratio measured in dense sand, each pipe having a specific gravity of 1.7. As shown in these figures the excess pore pressure ratios increased to almost 1.0 due to shaking in both densities. Therefore, it may be said that some amount of resistance to floatation remained in the dense soil, even though the soil was liquefied.

Figures 8 and 9 show relationships between the

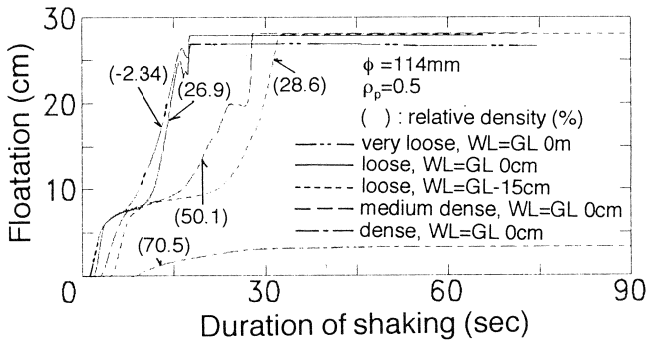

ρ_p: specific gravity of a pipe

Fig.4 Relationships between duration of shaking and floatation of a pipe with a specific gravity of 0.5

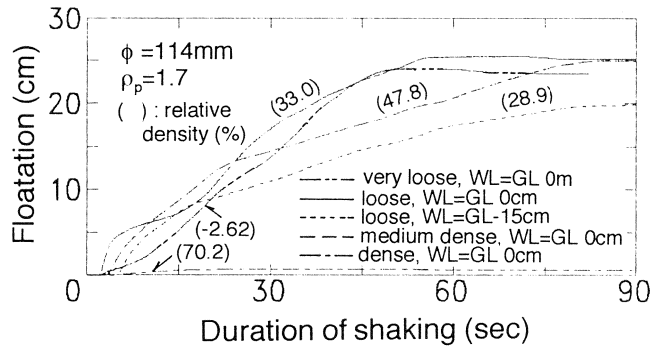

ρ_p: specific gravity of a pipe

Fig.5 Relationships between duration of shaking and floatation of a pipe with a specific gravity of 1.7

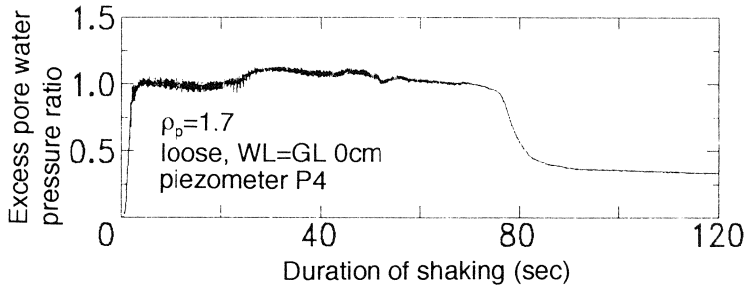

ρ_p: specific gravity of a pipe

Fig.6 Excess pore water pressure ratio in loose sand

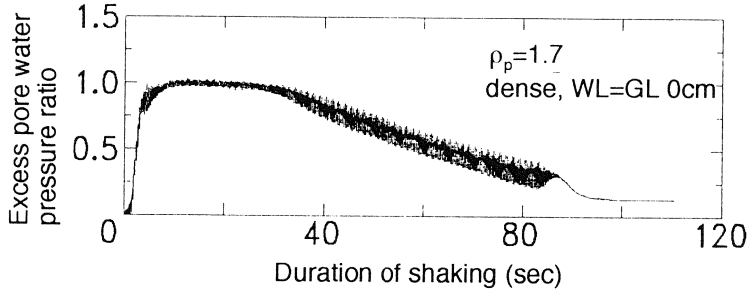

ρ_p: specific gravity of a pipe

Fig.7 Excess pore water pressure ratio in dense sand

duration of shaking and the floatation of pipes with diameters of 6cm and 11.4cm, respectively. It is clear again that the speed of floatation deceased with the specific gravity of the pipe. Moreover, the speed of floatation decreased slightly with the diameter of the pipe. As the unit weight of the soil in loose sand was about 1.88 tf/m^3, the pipe with the specific gravity of 1.9 was not floated to the ground surface.

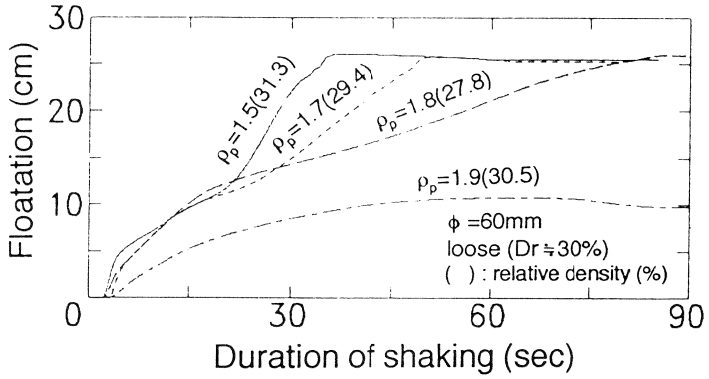

Fig.8 Comparison of the speed of floatation among different ρ_p for a small pipe

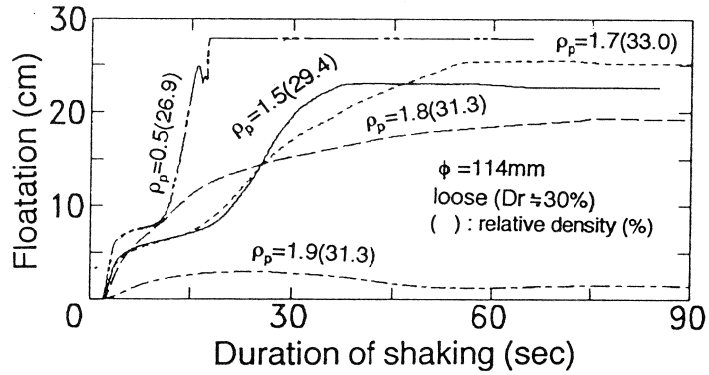

Fig.9 Comparison of the speed of floatation among different ρ_p for a large pipe

Figure 10 shows test results for severe shaking with the acceleration of 400 gals on the shaking table. By comparing Fig.10 and Fig.5, which are the same test conditions except the acceleration, the speeds of floatation in Fig.10 were higher than those in Fig.5. As shown in Fig.6 and Fig.7, fully liquefaction had already occurred when the floatation began. Therefore, the difference of the speed must be attributed to the difference of the severity of liquefaction. This means that the friction between pipe and liquefied soil or the stress-strain relationships of liquefied soil is affected by the severity of liquefaction, as same as the torsional test results on post liquefaction behavior (Yasuda et al. 1994c). And, it implies the necessity of consideration of the severity of liquefaction into the design of floatation or settlement of structures due to liquefaction.

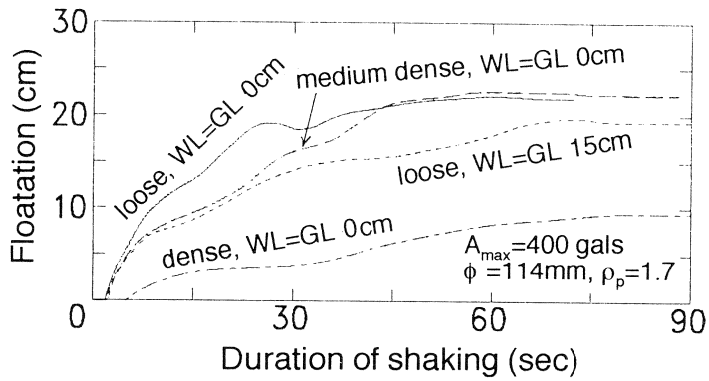

Fig.10 Test results for severe shaking with an acceleration of 400 gals

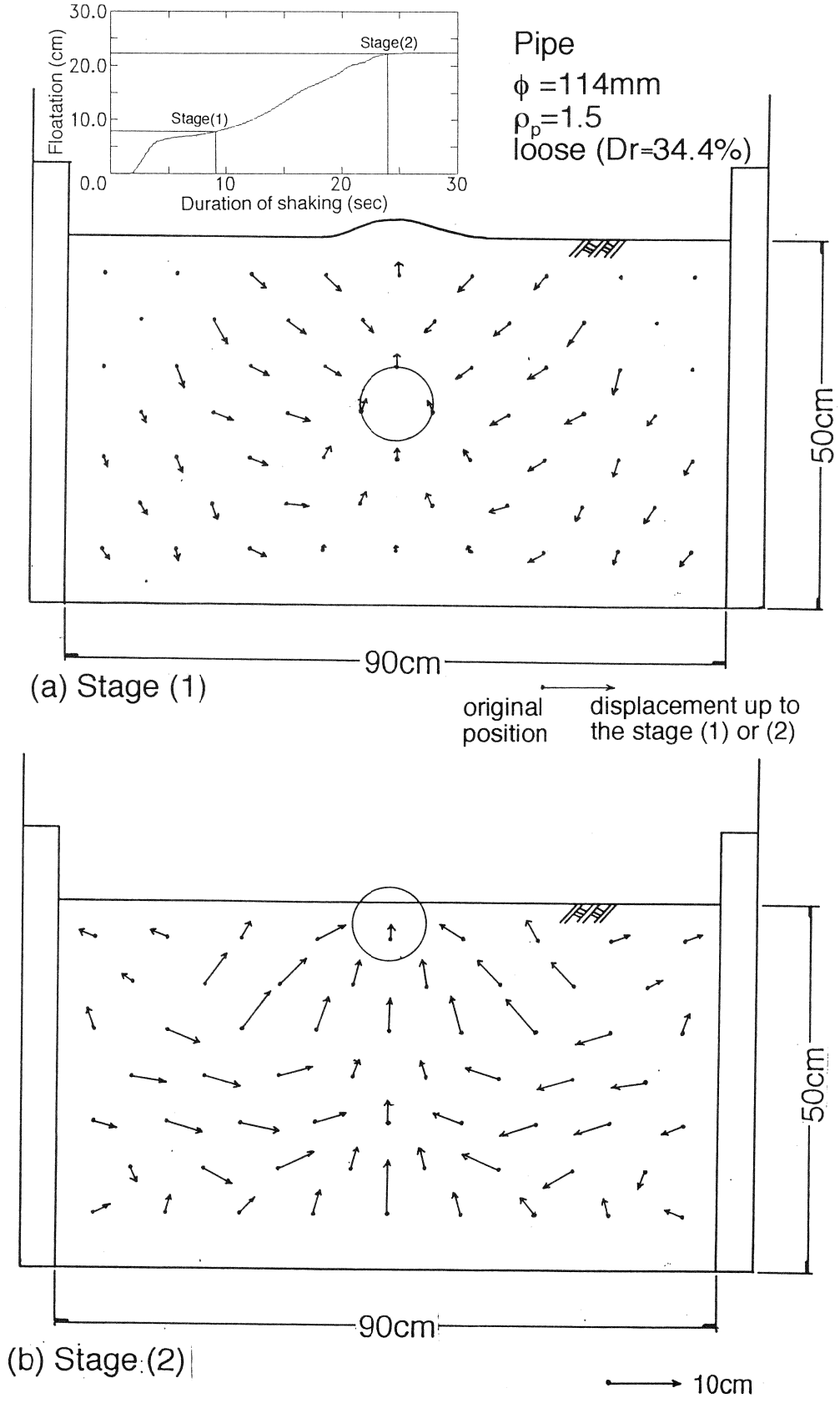

Fig.11 Observation of the movement of soil grains during the floatation of a buried pipe (ϕ=114mm, ρ_p=1.5)

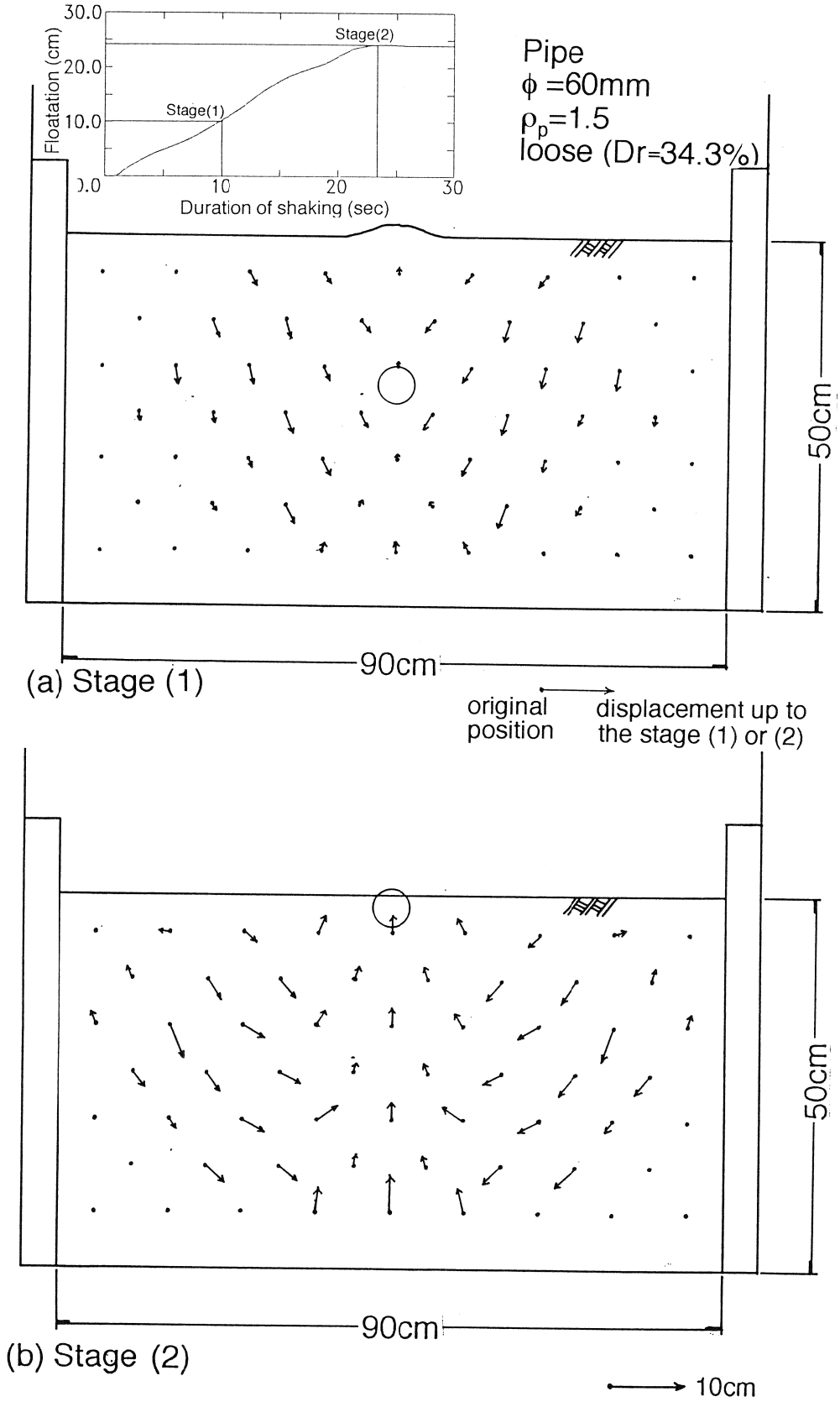

Fig.12 Observation of the movement of soil grains during the floatation of a buried pipe (ϕ=60mm, ρ_p=1.5)

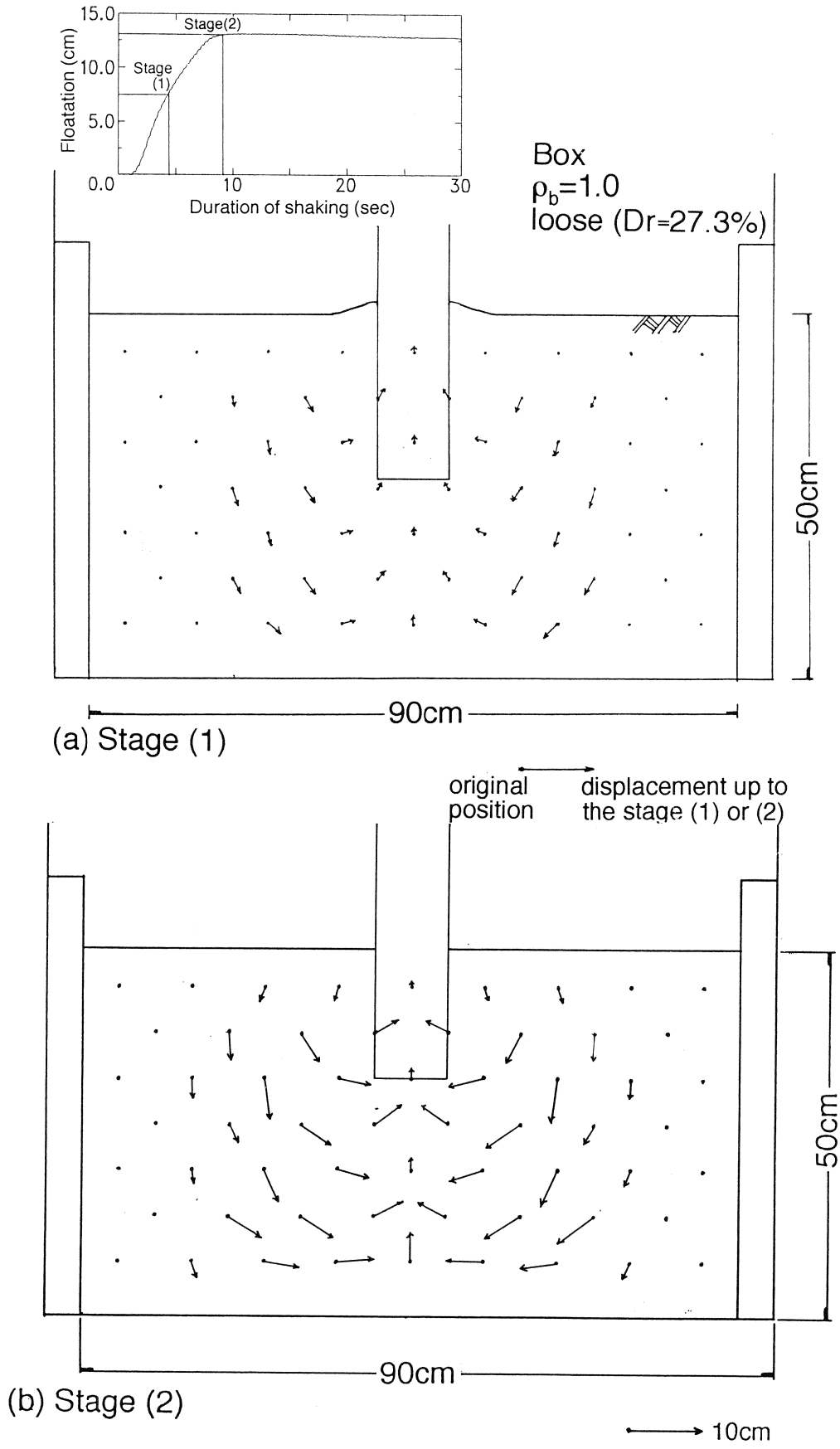

Fig.13 Observation of the movement of soil grains during the floatation of a buried box (width of the box is 35cm, ρ_b=1.0)

As shown in Fig.4, the speed of floatation was not constant in low-density soil and with pipes of low specific gravity. The speed slowed when the floatation reached almost 6 to 7cm., and after several seconds, the speed accelerated again. In the pipe of small diameter, though this phenomenon was also observed, it was not as clear. It was observed during shaking that a small mound appeared on the ground surface when the speed of floatation slowed. It is not clear why the floatation slowed, because the movement of the soil grains around the pipe was not measured. However, it is surmised that several minutes were required to move the upper or lateral soil toward the bottom of the pipe.

Then, the detailed observation of the movement of soil grains during the floatation was carried out by using a video camera, for better understanding. The movement was estimated by measuring the displacement of chips of noodles which were installed between soil and front glass with an interval of 10cm in horizontal and 6.25cm in vertical. Figure 11, Fig.12 and Fig.13 show the measured displacements during the floatation of the large pipe (ϕ =114mm), the small pipe (ϕ = 60mm) and a box, describes later, respectively, from the beginning of shaking to the two stages (1) and (2). Stage (1) and (2) are corresponded to the times when the speed of the pipe or the box was accelerated again and when the pipe or the box was elevated up to the ground surface. As shown in Fig.11 and Fig.12, soil upper and below the pipe moved to up during the floatation. Soils right and left sides of the pipe moved toward the bottom of the pipe. It is noted that the soil grain 30 cm far from the pipe moved also toward the bottom of the pipe. In the case of the box also, soils below and both sides of the box moved to up and toward the bottom of the box, respectively, as shown in Fig.13.

SHAKING TABLE TESTS ON THE EFFECT OF BACKFILL SOIL

In the tests to determine the effect of backfill soil on the floatation of buried pipes, the same shaking table, soil container and sand as mentioned above was used. Figure 14 shows the model tested. After filling the soil, the ground was densified to 90% relative density, so it would not liquefy during shaking. Then a trench with a depth Z and a width B was excavated, and while suspending a pipe or a box, the trench was backfilled with sand. The relative density of the backfilled sand was fixed at 30%, which is easy to liquefy due to shaking. A vinyl sheet was placed at the boundary between the trench and the surrounding ground to prevent the dissipation of excess pore water pressure induced in the backfill soil during shaking. However, a test without the vinyl sheet was also conducted to know the effect of permeability. The diameter and the specific gravity of the pipe was 11.4cm and 0.75, respectively. The width and the specific gravity of the box, which is the model of a manhole, was 11.4cm and 1.0, respectively. The depth of the

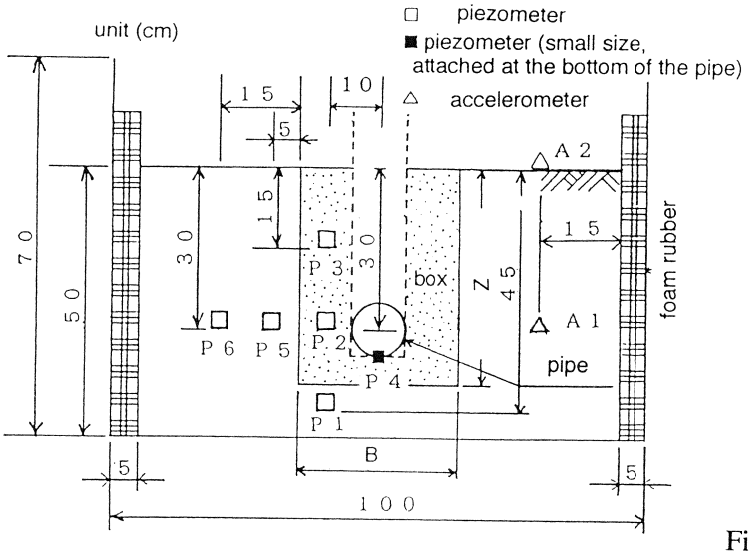

Fig.14 Diagram of apparatus for tests on the effect of backfill soil

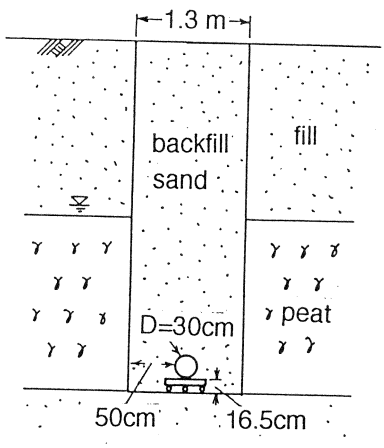

Fig.15 Diagram of a trench to bury a pipe

bottom of the pipe or the box was GL-35.7cm.

Figure 15 shows an example of a trench due to bury a sewage pipe in Kushiro Town. As shown in the figure, backfill sand with a thickness of 16.5cm and a width of 50cm existed below and around the pipe, respectively. As it was expected that the thickness and the width affect the floatation of the pipe due to liquefaction of the backfill sand, tests were conducted under several depths and widths of the trench in the model.

Figure 16 compares the relationships between the duration of shaking and the

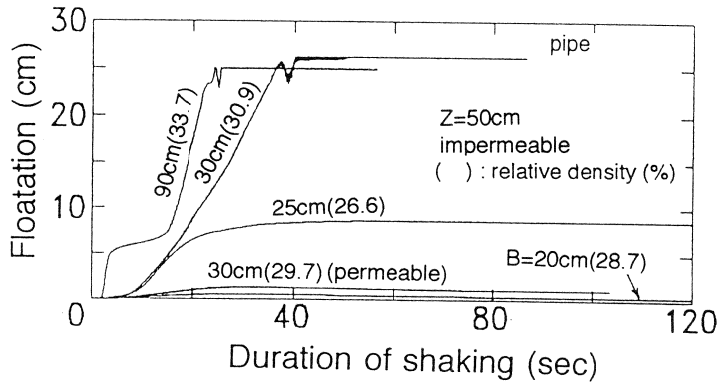

Fig.16 Effect of the width of a trench on the floatation of a pipe

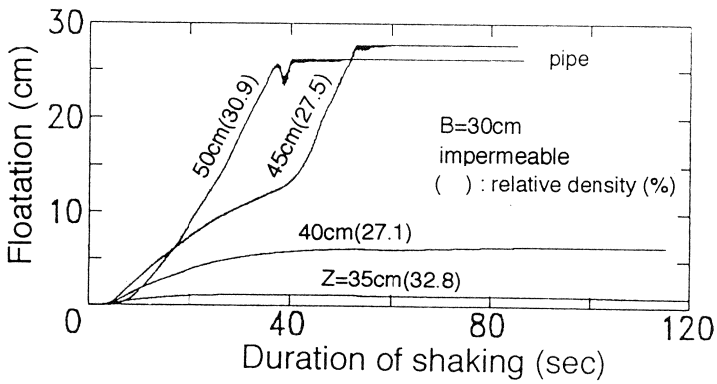

Fig.17 Effect of the depth of a trench on the floatation of a pipe

floatation of the pipe among different widths at a depth of 50cm. The speed and the maximum height of floatation increased with width. The pipe no longer rose when the width was limited to 20cm. Figure 17 compares the relationships between the duration of shaking and the floatation of the pipe at different depths when the width was kept at 30cm. It is clear that the speed and the maximum height of floatation increased with depth. When the pipe was placed on the bottom of the trench, at a depth of 35cm, the pipe did not rise. These two figures imply that a buried pipe can be floated even if liquefaction occurs only in backfill soil, and the floatation is affected by the width and depth of a trench.

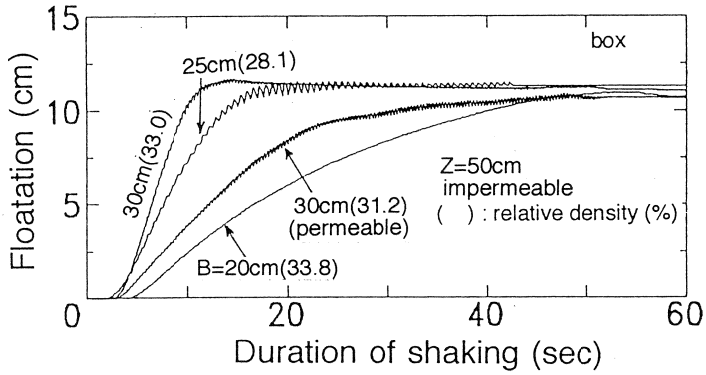

Fig.18 Effect of the width of a trench on the floatation of a box

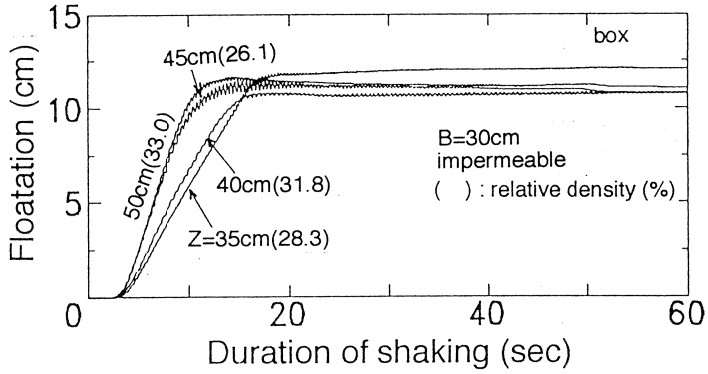

Fig.19 Effect of the depth of a trench on the floatation of a box

The effect of permeability at the boundary between the trench and the surrounding ground on floatation is also shown in Fig.16. Without the vinyl sheet at the boundary, the pipe was not floated because the excess pore water pressure induced in the backfill sand dissipated into the surrounding ground.

Figure 18 and 19 show relationships between the duration of shaking and the floatation of the box. Floating speed increased also with the width and depth of the trench. By comparing these results with the results of tests on the pipe, shown in Figs. 16 and 17, it can be seen that the box was floated more rapidly than the pipe.

CONCLUSIONS

By conducting shaking table tests on the floatation of a buried pipe or box due to liquefaction, the following conclusions were reached:

1. A pipe and a box can be floated due to the liquefaction of a backfill sand only.
2. The speed and the height of floatation are affected by soil density, the specific gravity of the pipe or box, water level, severity of liquefaction and width and depth of a trench. Grain size of the soil and shape of the pipe also must be affected to the floatation.

ACKNOWLEDGEMENTS

The tests were carried out by committees of the Association for the Development of Earthquake Prediction in Japan. The authors would like to express their thanks to the members of the committees. The data of the floatation of sewage pipes during Kushiro-oki earthquake and soil conditions were provided by PWRI, Kushiro City and Kushiro Town.

REFERENCES

1. Yasuda,S., Iwata,T., Nagase,H. and Itafuji, S.: Shaking Table Tests on Uplift of Buried Pipes due to Liquefaction , Proc. of the 29th Annual Conf., JSSMFE, pp.919~920, 1994a(in Japanese)
2. Itafuji,S., Yasuda,S., Masuda,T., Nagase,H, and Sawada,H.: Shaking Table Tests on Uplift of Underground Structures due to Liquefaction of Backfill Sands, Proc. of the 49th annual Conf. on Civil Engineering, JSCE, 1994b (in press, in Japanese)
3. Yasuda,S.,Masuda,T., Yoshida,N., Nagase,H., Kiku,H., Itafuji,S., Mine,K. and Sato,K.: Torsional Shear and Triaxial Compression Tests on Deformation Characters of Sands Before and After Liquefaction, This Workshop, 1994c.(in press)

EARTHQUAKE PERFORMANCE OF GAS TRANSMISSION PIPELINES

by

T.D. O'Rourke[1]
M.C. Palmer[2]

ABSTRACT

Over 61 years of earthquake performance of steel transmission pipelines operated by the Southern California Gas Company are reviewed. The seismic record includes 11 major earthquakes with $M_L \geq 5.8$ and epicenters within the transmission system. An evaluation is made of the most vulnerable types of piping, failure mechanisms, break statistics, threshold seismic intensity to cause failure, and damage induced by permanent ground displacement. The database assembled represents one of the most comprehensive and detailed records of seismic response in a large, complex gas transmission system.

[1]Professor, School of Civil & Environmental Engineering, Cornell University, Ithaca, NY
[2] Engineer, Mueser Rutledge Consulting Engineers, New York, NY

INTRODUCTION

Table I summarizes information about 11 of the most severe earthquakes which have occurred in southern California. The table provides data on the earthquake magnitude and maximum intensity, epicentral location, portion of pipeline network subjected to strongest shaking, and general observations about gas transmission and supply line response. The 1940 Imperial Valley earthquake is not included in the table because this area was not serviced with natural gas pipelines at the time of the earthquake.

No damage or disruption of transmission and supply lines was experienced in six of the earthquakes. In some of these cases, the earthquake epicenter and location of surface faulting were relatively close to transmission pipelines. For example, the epicenter of the 1986 North Palm Springs earthquake was approximately 5 km (3 mi.) from Lines 2000, 2001, and 5000, which are post-WWII lines of 750 to 900 mm (30 to 36 in.) diameter. In addition, surface faulting caused by the 1992 Landers earthquake has been traced to within tens of meters of a 150-mm- (6-in.)-diameter line conveying gas to Yucca Valley and Joshua Tree and a similar distance from Line 4000, a post-WWII 900-mm- (36-in.)-diameter pipeline.

Four earthquakes resulted in significant damage to the gas pipeline system. They are the 1933 Long Beach, 1952 and 1954 Kern County, 1971 San Fernando, and 1994 Northridge earthquakes. Although the 1979 Imperial Valley earthquake did not damage any gas transmission lines, three lines were crossed by surface ruptures along the Imperial fault and excavated for observation and stress relief. Case histories of the four earthquakes, which caused the most extensive damage, and associated pipeline response are provided in the next several sections.

This paper draws on previous work of O'Rourke and Palmer [1994a; b], and reference should be made to these publications for additional information. Transmission and distribution pipelines are defined in accordance with the Federal Code of Regulations [Office of the Federal Register, 1990] and General Order No. 112-D pertaining to the State of California [Public Utilities Commission (PUC) of the State of California, 1988]. In essence, a transmission line transports gas from a gathering line or storage facility to a distribution center or storage facility, and operates at a hoop stress of 20% or more of the specified minimum yield stress (SMYS) of the pipe steel. The Southern California Gas Company (SoCalGas) identifies an additional category of pipeline, referred to as distribution supply line, which is predominantly 50 to 300 mm (2 to 12 in.) in diameter and is operated typically in the range from 0.7 to 2.8 MPa (100 to 400 psi).

1933 LONG BEACH EARTHQUAKE

Figure 1 shows the locations of main line breaks of water, gas, and oil lines caused by the 1933 Long Beach earthquake as plotted by Hoff [1934] and superimposed on a map of liquefaction susceptibility prepared by Tinsley, et al. [1985]. Shaded areas are those Tinsley, et al. designate as having "very high" and "high" susceptibility to liquefaction on the basis of geologic age, type of sedimentary

TABLE I. Summary of Major Earthquakes in the Area of the Southern California Gas System

Earthquake	Magnitude[1]/ Intensity[2]	Location of Epicenter	Area Most Severely Affected	Gas Pipeline Performance	Selected References
1933 Long Beach	M_L = 6.3 MM VIII - IX	5.6 km (3.5 mi.) southwest of Newport Beach	Long Beach, Compton, and shore areas from Manhattan to Laguna Beach	Extensive damage to pipelines of Long Beach Municipal Gas Department, particularly areas of liquefaction	Wood [1933] Bryant [1934] Hoff [1934]
1952; 1954 Kern County	M_S = 7.7 MM VIII - X	40 km (25 mi.) south of Bakersfield near Wheeler Ridge	Area of approximately 10,000 km (4000 $mi.^2$) south of Bakersfield	Damage to several transmission lines within 10 to 25 km (6 to 16 mi.) of Wheeler Ridge	Newby [1954] Steinbrugge and Moran [1954]
1971 San Fernando	M_L = 6.4 MM VIII - X	13 km (8 mi.) northeast of San Fernando	Area of approximately 520 km^2 (204 $mi.^2$) around San Fernando	Serious damage to transmission and supply lines and disruption of service in San Fernando and Sylmar	Southern California Gas Co. [1973] O'Rourke, et al. [1992]
1979 Imperial Valley	M_S = 6.6 MM VI - VII	3 km (1.9 mi.) south of U.S.-Mexico border and 10 km (6.2 mi.) from Mexicali	Imperial Valley from Brawley to Calexico and Holtville	No damage to transmission lines, although three transmission lines were crossed by surface ruptures along the Imperial fault. The lines were excavated for inspection and stress relief	Dobry, et al. [1992] McNorgan [1989]
1986 North Palm Springs	M_L = 5.9 MM VII	16 km (10 mi.) northwest of North Palm Springs	Area of approximately 250 km^2 (9.6 $mi.^2$) centered on epicenter	No damage or disruption reported. Epicenter was 8 km (5 mi.) from three 750- to 900-mm (30- to 36-in.) transmission lines	EERI [1986]
1987 Whittier Narrows	M_L = 5.9 MM VIII	5 km (3 mi.) east of Rosemead	Crescent-shape area of approximately 500 km^2 with MM VII - VIII centered on Monterey Park	No damage to transmission and supply lines	Schiff [1988]

TABLE I. Summary of Major Earthquakes in the Area of the Southern California Gas System (completed)

Earthquake	Magnitude[1]/ Intensity[2]	Location of Epicenter	Area Most Severely Affected	Gas Pipeline Performance	Selected References
1991 Sierra Madre	M_L = 5.8 MM VII	20 km (12 mi.) northeast of Pasadena between Cogswell Reservoir and Mt. Wilson	Area including Pasadena, Sierra Madre, Monrovia, and Arcadia	No damage to transmission and supply lines	EERI [1991]
1992 Landers and 1992 Big Bear	M_S = 7.5 MM VIII - IX and M_S = 6.5 MM VII	Centered between Landers and Yucca Valley	Area including Landers, Joshua Tree, Yucca Valley, and Big Bear Lake	No damage to transmission lines; 900-mm (36-in.) and 150-mm (6-in.) transmission lines were located just north and south, respectively, of the main surface faulting	EERI [1992]
1994 Northridge	M_S = 6.8 MM VIII - IX	North central portion of San Fernando Valley	San Fernando Valley, Sylmar, Santa Monica, and Fillmore	Damage to transmission pipelines and widespread disruption of distribution system	O'Rourke and Palmer [1994a,b]

[1]Earthquake magnitudes are reported herein on the basis of published information in terms of local or surface wave magnitudes (M_L or M_S, respectively), with surface wave values given for magnitudes exceeding 6.5

[2]Maximum Modified Mercalli Intensity or range in intensities as reported or inferred from descriptions of damage

deposits, and groundwater depth. Youngest Holocene deposits of fluvial origin are most susceptible. The areas with the greatest number of breaks were the mouth of the San Gabriel River (Naples and North Seal Beach) and the North Long Beach/Compton/Clearwater area. About 85% of all plotted breaks fall within areas of high and very high liquefaction susceptibility.

Pipeline damage caused by the 1933 Long Beach earthquake has been described by Bryant [1934] and Hoff [1934]. There were more than 500 main line breaks of water, gas, and oil lines in the areas of maximum seismic intensity [Hoff, 1934]. Within the City of Long Beach gas distribution system, there were a total of 119 main breaks, 91 of which were in the high pressure feeder mains [Bryant, 1934]. Every failure discovered in the high pressure distribution system occurred at a welded joint, and more than 50 of the 91 breaks were in artificially-filled areas. Forty-six breaks were discovered in the large diameter mains [460 to 510 mm (18 to 20 in.)] that supplied the Harbor District of Long Beach, which was an area where artificial fills were predominant [Bryant, 1934]. Repair crews reported that the original welds lacked proper penetration and proper bond with the pipe body [Bryant, 1934].

Line 765, which is shown in the figure, was constructed in 1931. It was 650 mm (26 in.) in diameter, with 6.4 mm (0.25 in.) wall thickness. It was composed of Grade A and B steel, and had a maximum allowable operating pressure (MAOP) of 1.0 MPa (150 psi) just before it was removed from service in 1992. The pipeline was constructed with electric arc welds. The welding process differed from modern procedures for butt welded transmission pipe in that the weld was applied by unshielded electric arc techniques at opposing belled pipe ends, which were positioned on an underlying steel ring. Although the pipeline was located in the region of maximum seismic intensity, including locations of known liquefaction adjacent to the Los Angeles River, there are no records of pipeline damage or repair to this line dating from the time of the 1933 earthquake.

1952 AND 1954 KERN COUNTY EARTHQUAKES

Gas pipeline damage caused by the 1952 and 1954 Kern County earthquakes has been described by Newby [1954] and Lind [1954]. As a result of this earthquake and a subsequent smaller Kern County earthquake in January, 1954, there were ten incidents of damage at welded transmission line joints and two incidents of leaks at locations of external pipeline corrosion. Nine of the damaged welds were oxy-acetylene, and one was at an electric-welded band positioned at the location of an original oxy-acetylene weld. Figure 2 shows the locations of the damage relative to the epicenters of the main shock and the January 12, 1954 earthquake, which had a local magnitude of 5.9. Newby [1954] described the damage with reference to the figure as follows:

> "It developed that the 12-inch acetylene welded line installed in 1921 had broken welds at the three locations marked 1 on Figure No. 1 (Figure 2). The ends of the pipe were from 1/2 to 2 inches apart at the different breaks. The 12-inch line that had been reconditioned in 1932, and electric-welded using chill rings, failed at location marked 2. This weld evidently failed from compression and then from tension...

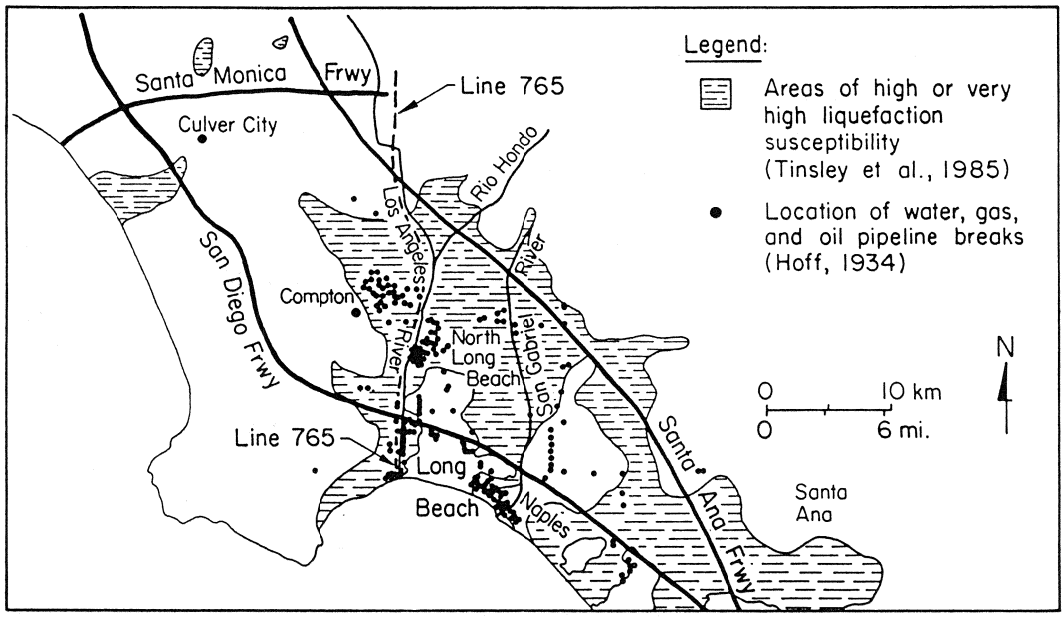

FIGURE 1. Pipeline Damage Caused by the 1933 Long Beach Earthquake [adapted from Hoff, 1934]

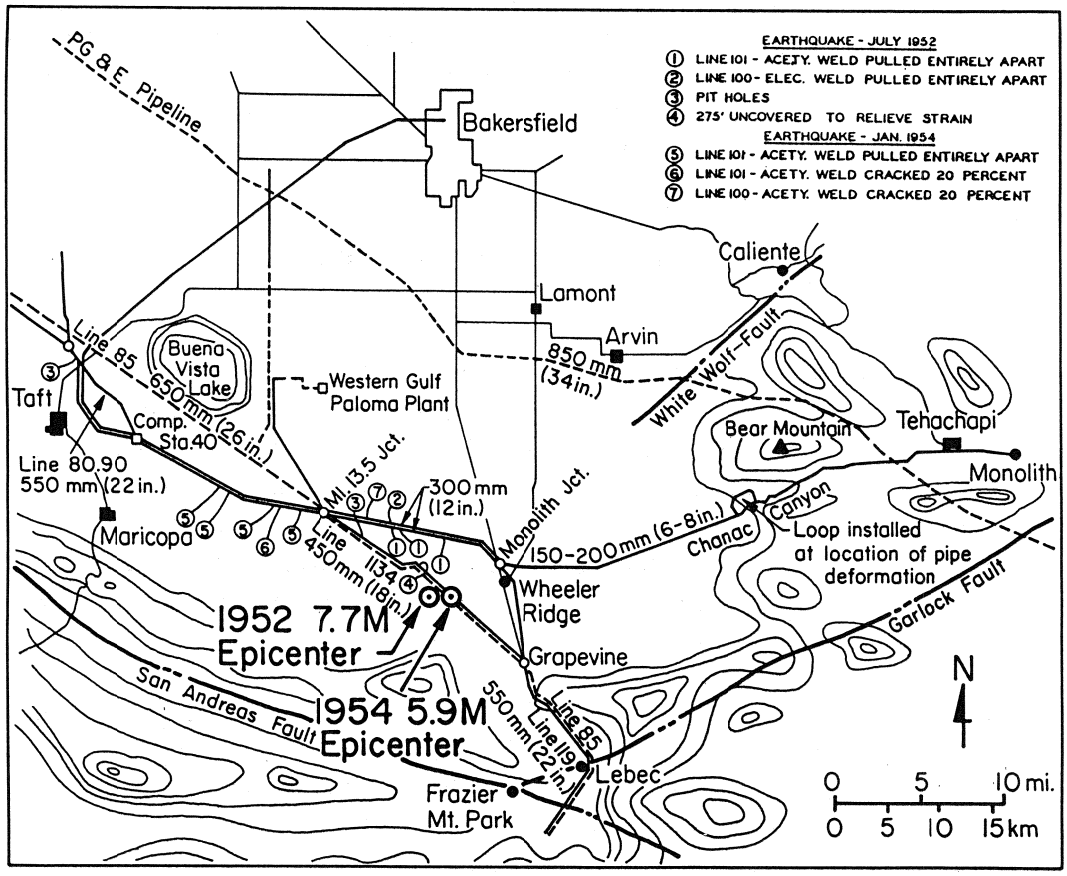

FIGURE 2. Gas Pipeline Damage Caused by the 1952 and 1954 Kern County Earthquakes [adapted from Newby, 1954]

Pit hole leaks popped out on a 22-inch line near Taft and on an 18-inch line at Wheeler Ridge, locations 3 (Figure 2). These leaks were from external corrosion. Location 4 shows where 275 feet of 18-inch line was uncovered to relieve strain from the 1952 quake.

We experienced another of our many quakes on January 12, 1954 that was not considered serious. However, it evidently centered near our two 12-inch lines in the Maricopa Flat area.

As shown on Figure 2, this quake parted the acetylene-welded line at four welds at locations marked 5, and cracked an acetylene weld 20% at location marked 6, and on the electric-welded line, a lone acetylene weld cracked 20% at location 7."

Newby also reported that the 150-mm- (6-in.)-diameter line providing gas to Tehachapi was deformed upward from the ground at two locations along a steep hillside where ground ruptures were observed. The line was intact. The line had been installed in 1926 with oxy-acetylene welds. A supplemental pipeline (referred to as a loop in Figure 2) was installed to provide a parallel emergency path. The original was kept in service without any repairs.

1971 SAN FERNANDO EARTHQUAKE

Gas transmission and supply line damage as a result of the San Fernando earthquake has been described by the Southern California Gas Company [1973] and O'Rourke, et al. [1992]. Figure 3 shows a map adapted from the Southern California Gas Company [1973] on which are plotted the gas transmission and supply lines most significantly affected by the earthquake, locations of damage between San Fernando and just north of Clampitt Junction, and the approximate zones of permanent ground deformation associated with liquefaction adjacent to the Upper Van Norman Reservoir, as well as surface faulting along the Sylmar and Mission Wells segments of the San Fernando fault.

Substantial damage was sustained by Lines 1001 and 115. Line 1001 was a 300-mm-(12-in.)-diameter steel pipeline, constructed in 1925 with oxy-acetylene welds and operated at MAOP of 2.4 MPa (345 psi). Because of numerous breaks, predominantly at welds, approximately 9.3 km (5.8 mi.) of the line were abandoned. Line 115 was a 400-mm- (16-in.)-diameter steel pipeline of unknown grade, constructed in 1926 with oxy-acetylene welds. In the approximate 9.7-km- (6-mi.)-length of pipeline between Clampitt Junction and San Fernando, there were 52 breaks. Shell buckling of the pipeline occurred in the vicinity of its crossing of the Sylmar segment of the San Fernando fault [Southern California Gas Company, 1973].

Line 85 was a 650-mm- (26-in.)-diameter pipeline, with Grade A steel pipe wall 6.4 mm (0.25 in.) thick, operated at MAOP of 1.7 MPa (250 psi). In Figure 3, the location marking the division between the electric arc and oxy-acetylene welded segments of Line 85 is shown. North of the division, the line was constructed originally with oxy-acetylene welds. In 1932, roughly 30% of the oxy-acetylene welds in this section were reconditioned with electric arc welded reinforcements. South of the division,

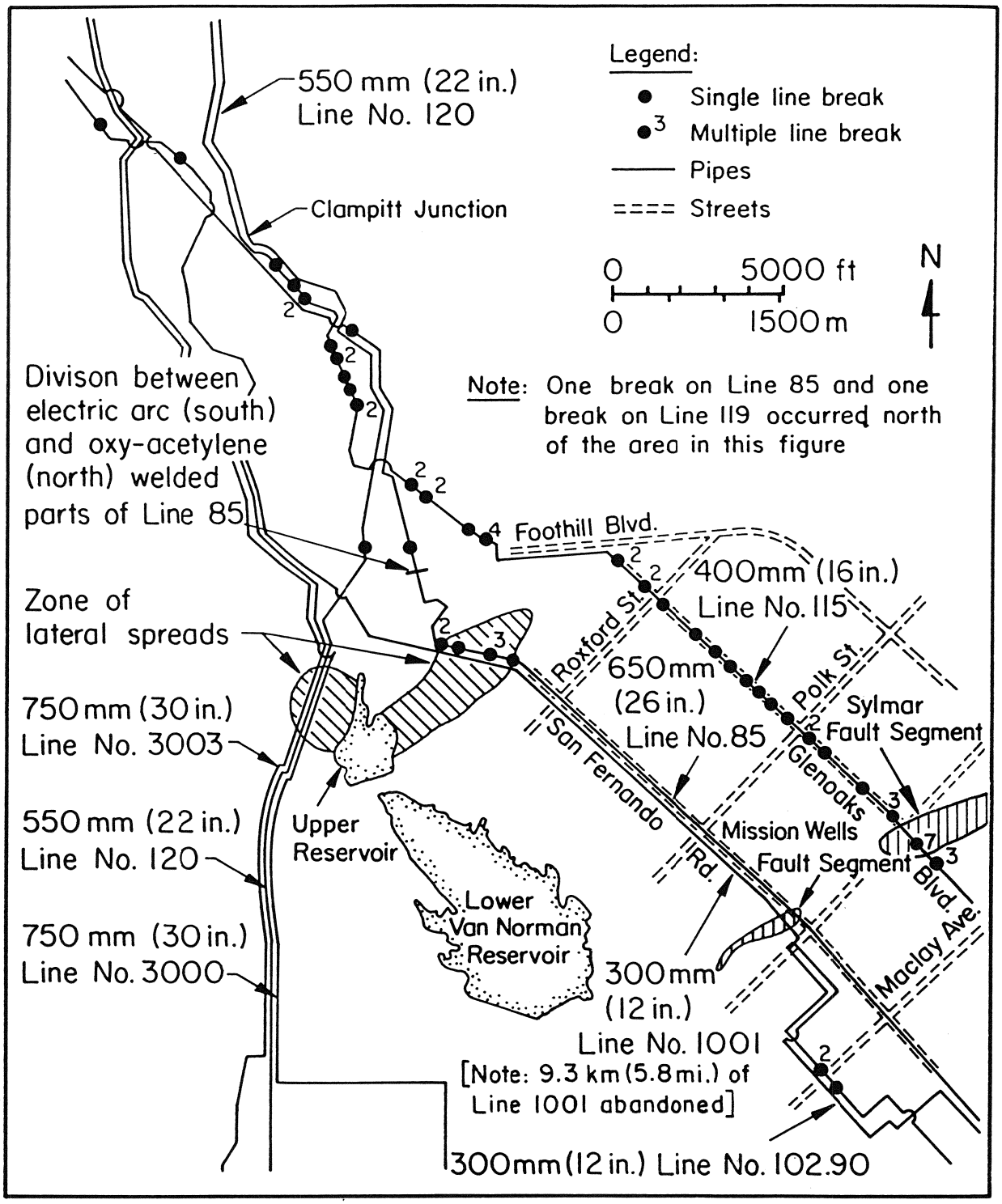

FIGURE 3. Locations of Gas Pipeline Damage, Lateral Spreads, and Fault Segments Associated with the 1971 San Fernando Earthquake [adapted from Southern California Gas Company, 1973]

the line was constructed with unshielded electric arc welded belled pipe in a manner similar to that for Line 765, which was affected by the 1933 Long Beach earthquake.

The electric arc welded portion of Line 85 was damaged at seven locations within the zone of lateral spread along the east side of the Upper Van Norman Reservoir. The partially reconditioned oxy-acetylene welded portion of the line was damaged at three locations north of the division, of which only two are shown in the figure.

The utility corridor on the western side of the Upper Van Norman Reservoir was subjected to as much as 3 m (9 ft) of lateral deformation caused by liquefaction; soil movements were distributed primarily across a 400- to 500-m- (1,300- to 1,640-ft)-length of the corridor. Pipelines at this location were of modern construction. One 560-mm- (22-in.)-diameter (Line 120) and two 760-mm- (30-in.)-diameter (Lines 3000 and 3003) gas pipelines, each constructed in 1966 of X-52 steel, were not damaged.

Figure 4 shows the locations of damage to Lines 115, 1001, 85, and 102.90 in the San Fernando area at an expanded scale. Damage locations were determined from repair records summarized by Southern California Gas personnel [Johnson, 1982]. The preponderant form of damage was rupture or leakage at oxy-acetylene welds. Also shown on the map are locations of ground failures and surface soil cracks as mapped by the U.S. Geological Survey and the California Division of Mines and Geology [U.S. Geological Survey Staff, 1971; Steinbrugge, et al., 1971].

Near the Sylmar segment of the San Fernando fault, there were approximately three compression and ten tensile ruptures of Line 115. One break occurred in Line 1001 at its crossing of the Mission Wells segment of the San Fernando fault, and three breaks were reported in this line in the vicinity of the Juvenile Hall lateral spread on San Fernando Road. With the exception of Line 85 damage at the lateral spread, all other breaks in Figure 4 do not appear to be associated with permanent ground movement.

1994 NORTHRIDGE EARTHQUAKE

There were 35 non-corrosion related repairs in the transmission system, of which 27 were at cracked or ruptured oxy-acetylene girth welds in pre-1932 pipelines. Figure 5 shows a plan view of selected transmission pipelines in the area of most severe ground shaking. Locations of damage in the form of pipeline breaks and leaking flanges are shown in the figure.

Figure 6 is a map of the area just north of the earthquake epicenter, showing the Aliso Canyon Gas Storage Field and the locations of two gas transmission line breaks on Balboa Blvd. The Aliso Canyon facility, which covers some 14.7 km^2 (3,600 acres) and 56 km (35 mi.) of access road, is used to store gas in an underground reservoir that once was used for oil production. Gas is injected during low demand summer months and withdrawn during high demand winter months. Earthquake effects in the facility included deformation of aboveground pipe supports, displacements of runs of injection and withdrawal lines, and structural damage to a fin fan unit used to cool compressed gas before its injection in storage wells. The supply of gas from Aliso Canyon was interrupted for five days.

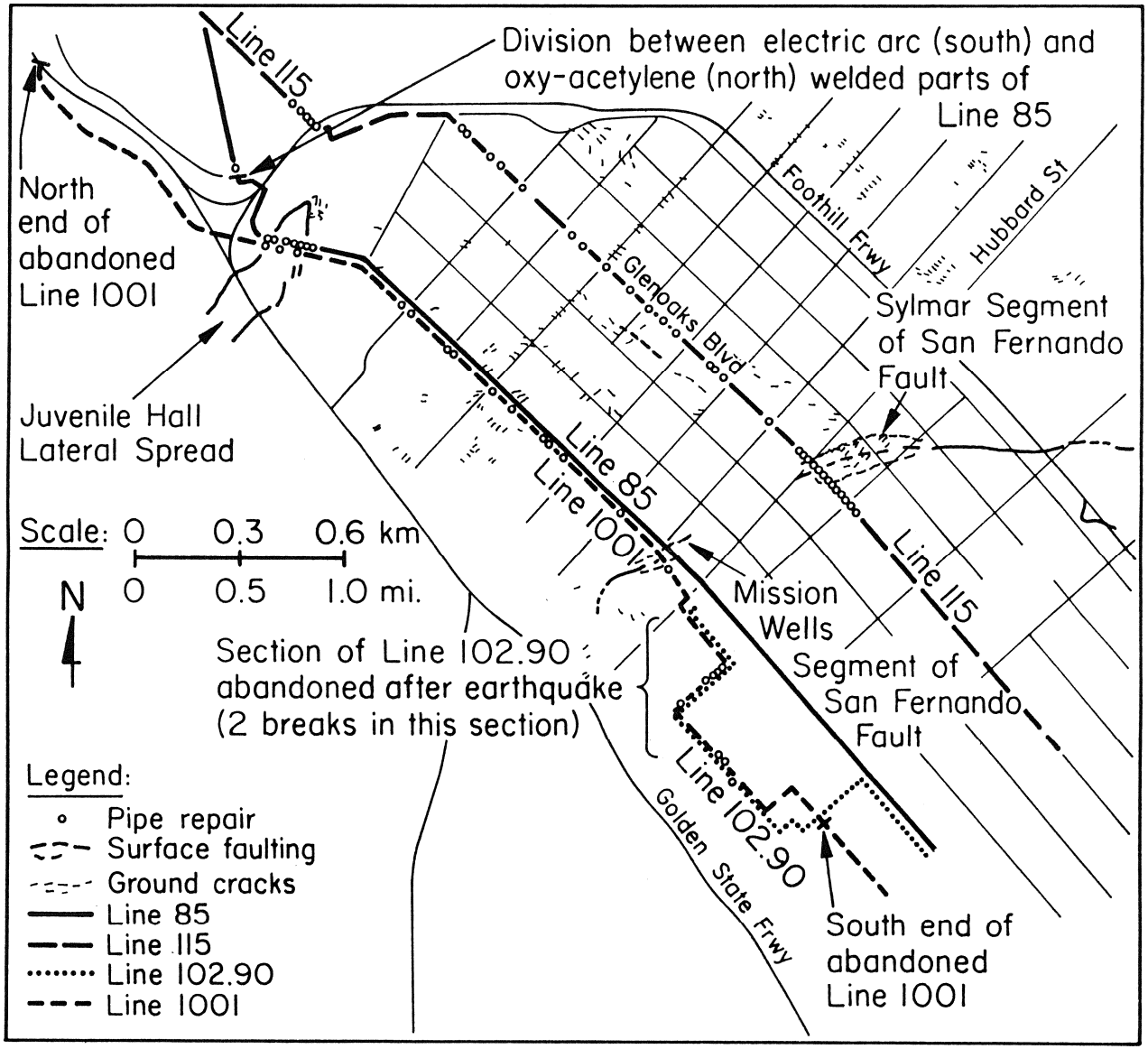

FIGURE 4. Locations of Damage to Lines 115, 1001, 85, and 102.90 in the San Fernando Area as a Result of the 1971 Earthquake

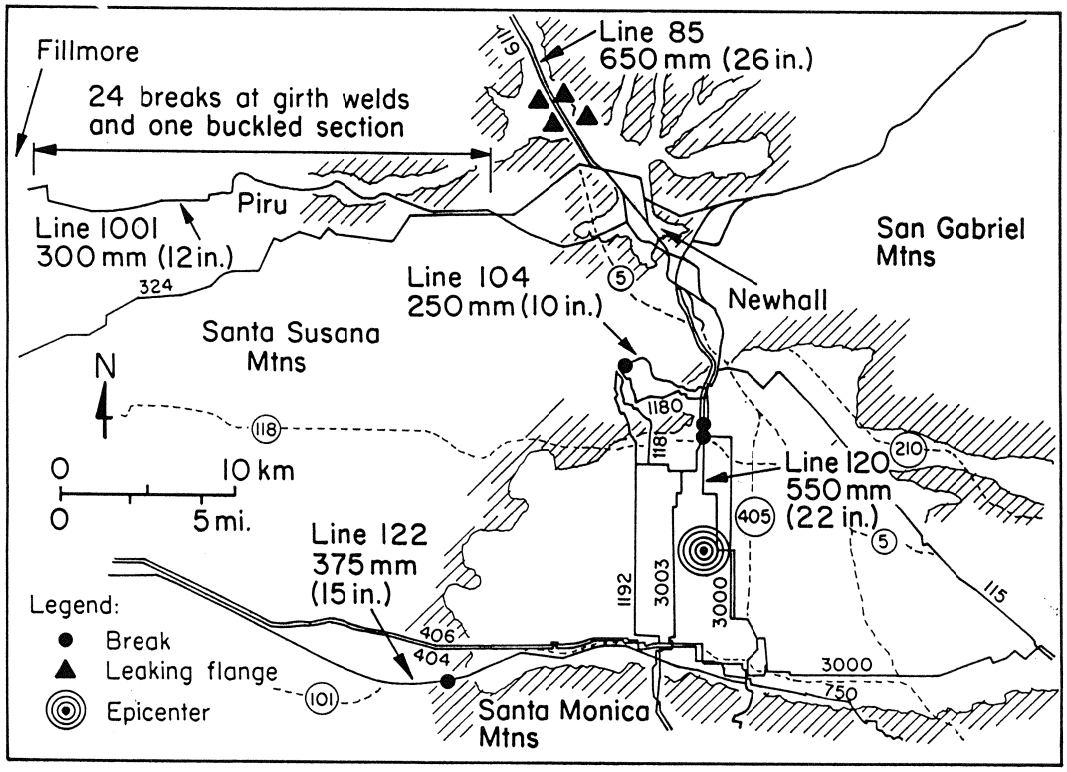

FIGURE 5. Map of Gas Transmission Pipelines in the Area of Strong Ground Shaking

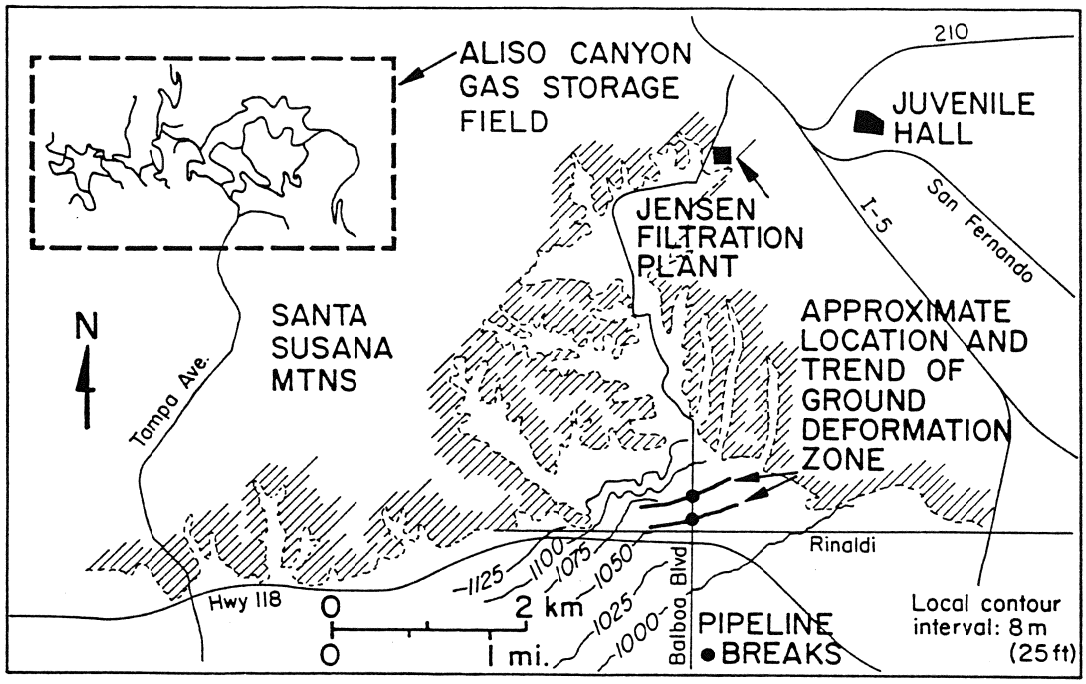

FIGURE 6. Map of the Area North of the Northridge Earthquake Epicenter

As shown in Figure 5, there were 24 breaks at oxy-acetylene girth welds and one location of buckled pipe in Line 1001, which conveys gas between Newhall and Fillmore, many of which were in Potrero Canyon. Line 1001 was constructed in 1925, and was operated at the time of the earthquake at 1.7 MPa (245 psi) internal pressure. The pipeline is 300 mm (12 in.) in diameter, with 5.6-mm- (0.22-in.)-thick wall of unknown grade steel.

Of the 25 repairs in Line 1001, 18 were in Potrero Canyon. Six breaks in oxy-acetylene welds were located in areas adjacent to the Santa Clara River east of Piru and west of Potrero Canyon. One oxy-acetylene weld ruptured at the eastern city limits of Fillmore, leaving a crater approximately 2.7 m (9 ft) deep and 4.5 m (15 ft) by 6 m (20 ft) in area. Gas escaping at the location of this break under Highway 126 was ignited by a downed power line.

Significant permanent ground deformation was reported in Potrero Canyon [Stewart, et al., 1994]. The canyon is filled with alluvial and colluvial deposits to a maximum depth of 80 m (260 ft). Sand boils were observed at several locations along the canyon, and prominent ground ruptures were plotted [Stewart, et al., 1994]. Along the southern margin of the canyon, ground cracks were both compressional and extensional, with minor left lateral offsets. Multiple ground fractures within zones 2 to 18 m (5 to 50 ft) wide accommodated as much as 600 mm (2 ft) of vertical movement. Preliminary evaluation of repairs to Line 1001 in the canyon suggest that about one half to two-thirds of the pipeline ruptures coincide with locations of mapped ground cracks. Other locations of pipe damage appear to have occurred in areas lacking significant differential ground displacement. A nearby strong motion station on soil recorded a peak horizontal ground acceleration of 0.46 g [Stewart, et al., 1994].

Flange leaks occurred at the four locations shown in Figure 5 at sections of aboveground piping. There was also a break in an oxy-acetylene weld in Line 85 at a location approximately 39 km (24 mi.) northwest of Newhall, which is not shown in the figure. Damage was mainly in the form of flange separation and leaking gaskets. One of the flanges was fractured. At the damaged locations, Line 85 is a 650-mm- (26-in.)-diameter pipeline with a pipe wall 6.4 mm (0.25 in.) thick, of Grade A steel, operated at MAOP of 2.2 MPa (317 psi). The ruptured oxy-acetylene weld and four leaking flanges occurred in a partially reconditioned portion of Line 85. The weld failure was at an original oxy-acetylene weld.

There was a break at a weld in Line 85 near Taft, approximately 120 km (75 mi.) north of the epicenter. This section of the pipeline was constructed in 1931 with electric arc welds. The line had an MAOP of 2.5 MPa (360 psi). There was a leaking flange at an aboveground section of Line 119 north of the area shown in Figure 4. This section of the 550-mm- (22-in.)-diameter pipeline was constructed in 1931 with a wall thickness of 7.9 mm (0.312 in.). There is no clear record of weld type. The SMYS of the steel and MAOP were 208 MPa (30,000 psi) and 2.5 MPa (360 psi), respectively.

A fractured oxy-acetylene girth weld was repaired in Line 122 at the location shown in Figure 5. Although this pipeline is not operated as a transmission line, it nevertheless is described in this paper because of its relatively high operating pressure of 1 MPa (150 psi). The pipeline was

installed in 1927 with oxy-acetylene girth welds, 6.4-mm- (0.25-in.)-thick wall, and steel of unknown grade.

As shown in Figure 5, there was a break in Line 104 inside the Aliso Canyon Gas Storage Field. The pipeline is 250 mm (10 in.) in diameter and has an MAOP of 1.6 MPa (228 psi), but it is operated at 1.4 MPa (200 psi). It was constructed with electric arc girth welds in 1941. The pipe has a 5.2-mm- (0.203-in.)-thick wall of unknown grade steel.

Gas pipeline damage on Balboa Blvd. occurred in Line 120, a 550-mm- (22-in.)-diameter steel pipeline constructed in 1930 with unshielded electric arc girth welds. At the time of the earthquake, the line was operated at about 1.2 MPa (175 psi). The pipe had a wall thickness of 7.2 mm (0.281 in.) and was composed of Grade B steel. The pipeline failed in tension in a zone of tensile ground deformation about 300 m (900 ft) north of a zone of compressive ground deformation where the pipe failed by compressive wrinkling. As shown in Figure 6, the ground rupture zones occurred in the toe area of an alluvial fan and are oriented subparallel to the surface elevation contour lines. The pattern of ground deformation suggests that lateral spreading of the alluvial fan sediments took place. Nearby boreholes show loose silty sands at depths of 9 to 12 m (30 to 40 ft), although water levels are indicated at considerably greater depths in dense materials.

Line 120 had been scheduled for replacement in the Granada Hills area. A new 600-mm- (24-in.)-diameter pipeline, with electric arc girth welds, X-60 steel, and 6.4-mm- (0.25-in.)-thick wall, had been constructed parallel to the older 550-mm- (22-in.)-diameter line along McLennan Ave. It had not been opened for gas flow at the time of the earthquake. Even though it crossed similar zones of tensile and compressive ground deformation, it was not damaged.

Figures 7 and 8 show maps of the pipelines in Balboa Blvd. near the zones of permanent ground deformation. In addition to numerous distribution mains, there were six transmission and water trunk lines at this site. There were two 750-mm- (30-in.)-diameter gas transmission lines constructed of X-52 steel in the 1950s which were not damaged. There was a 400-mm- (16-in.)-diameter petroleum pipeline, operated by the Mobil Oil Corporation, which was not damaged. The pipeline was composed of X-52 steel and installed in 1991. Two water trunk lines, the 1,240-mm- (49-in.)-diameter Granada and the 1,730-mm- (68-in.)-diameter Rinaldi Trunk Lines, failed in tension and compression in the tensile and compressive zones of ground deformation, respectively.

Gas escaping from Line 120 was ignited by sparks from the ignition system of a pickup truck that had stalled in the area of tensile ground deformation flooded by the ruptured trunk lines. The gas fire spread to adjacent properties, destroying five houses and partially damaging an additional structure.

A 150-mm- (6-in.)-diameter gas distribution pipeline along the eastern side of Balboa Blvd. was ruptured in tension and compression in the tensile and compressive ground deformation zones, respectively. This pipeline was operated at a pressure of approximately 0.3 MPa (45 psi). Gas escaping from the tensile rupture caught fire.

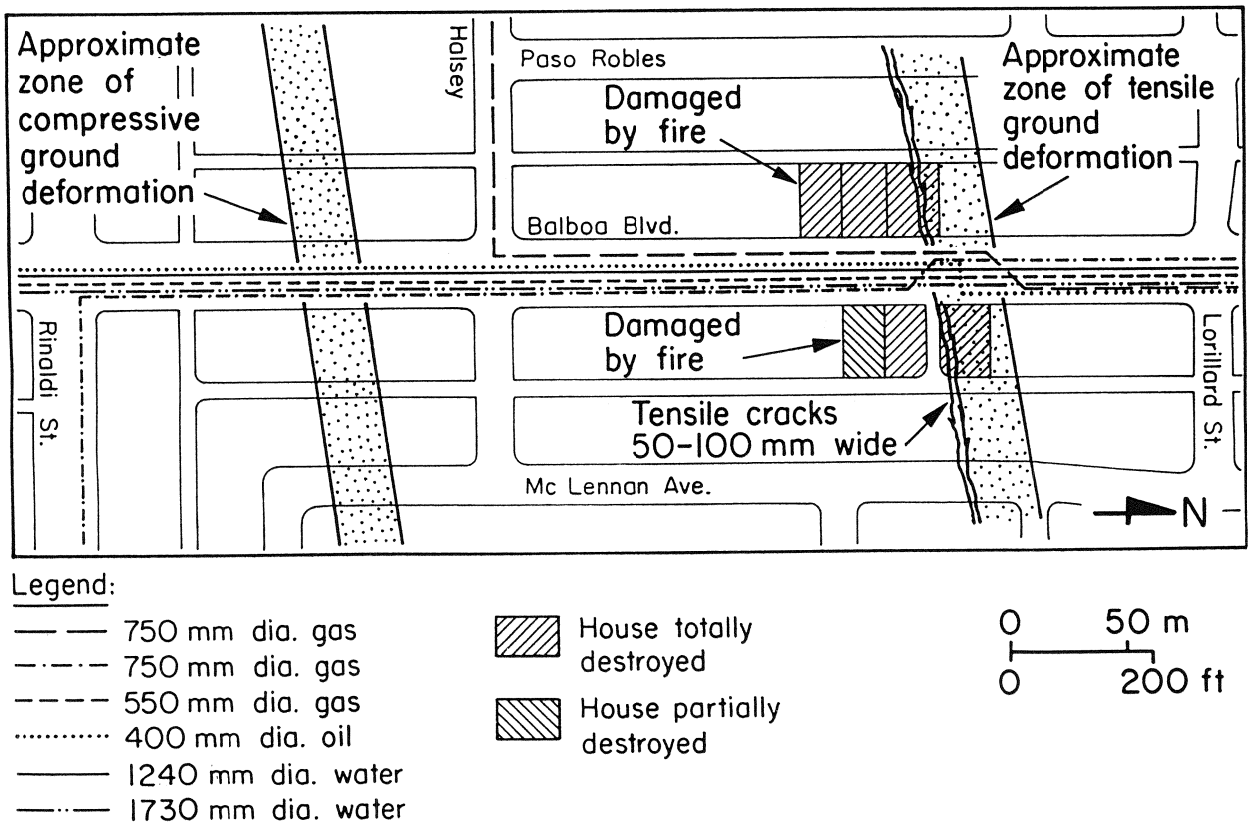

FIGURE 7. Map of Major Pipelines, Fire Damage, and Ground Deformation on Balboa Boulevard

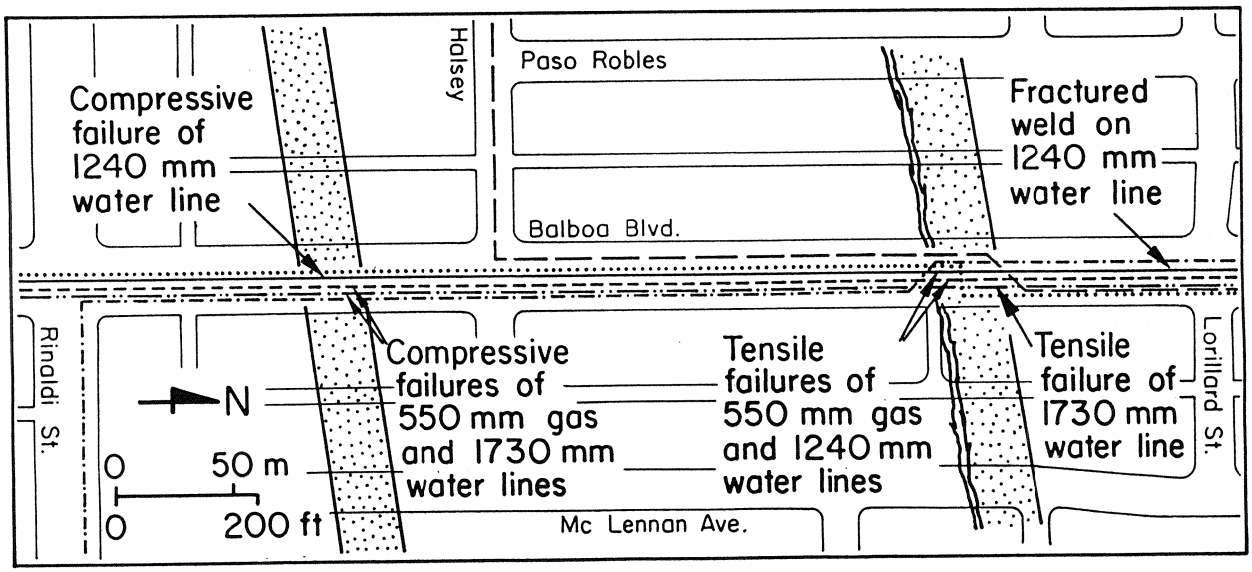

FIGURE 8. Map of Major Pipelines, Ground Deformation Zones, and Locations of Pipeline Damage on Balboa Boulevard

PIPELINE PERFORMANCE STATISTICS

Table II provides a summary of pre-WWII transmission and supply line response in areas where no permanent ground deformation was recorded during the 1933 Long Beach, 1952 and 1954 Kern County, 1971 San Fernando, and 1994 Northridge earthquakes. Failures in Lines 1001 and 85 at the Mission Wells segment of the San Fernando fault and the Juvenile Hall lateral spread are not included in the data set. Moreover, failures in Line 115 at the Sylmar segment of the San Fernando fault are included in the data set. As discussed in the previous section, significant permanent ground deformation was recorded in Potrero Canyon after the 1994 Northridge earthquake. The 18 repairs on Line 1001 in Potrero Canyon have been excluded from the table, and only the repairs and distance of pipeline from Fillmore to the Santa Clara River are listed.

The information is organized according to pipeline installation date, starting with the oldest lines. Damage rates, expressed as repairs per km and mi., were evaluated by dividing the line repairs by the total distance of a given line within the area of highest seismic intensity. The review of gas transmission and supply pipeline performance for 11 southern California earthquakes presented in this section shows that pipelines have ruptured predominantly in areas affected by MM VIII or larger. Hence, MM VIII or larger was used to establish the approximate limits of most intense shaking. The preponderance of damage to pre-WWII pipelines occurred as ruptures at oxy-acetylene welds. Damage not associated with pipeline rupture, in the form of leaks at corrosion pits, is not listed in the table.

The information in the table can be used to point out some interesting trends, as illustrated in Figure 9. In this figure, the repair rates for the 1952 and 1954 Kern County and 1971 San Fernando earthquakes are plotted according to age of installation. Both earthquakes show similar trends, in that the damage rate for pipelines constructed before 1930 are approximately an order of magnitude higher than those constructed during or after 1930.

A review of the repair records, and discussions with welders, who repaired lines after the 1971 San Fernando and 1994 Northridge earthquakes, indicate that the damage listed in Table II was predominantly at oxy-acetylene welds. This observation does not mean that oxy-acetylene welds are intrinsically weak. On the contrary, the metallurgical quality of an oxy-acetylene weld is not significantly different from that of an electric arc weld, provided the work is performed by qualified welders according to proven procedures. Well-made oxy-acetylene and electric arc welds are about equal in strength, although the heat-affected zone adjacent to an oxy-acetylene weld is somewhat larger and the joint ductility somewhat less than those associated with an electric arc weld. The reason for the higher incidence of weld damage is associated with poor weld quality. As described by O'Rourke and McCaffrey [1984], repair personnel reported that many of the welds on Line 115 had characteristics such as poor root penetration, undercutting and overlapping at the toe, and lack of good fusion between the pipe and the weld. These types of features result in a flawed weld, and are not representative of the welds achieved under the quality control standards currently in effect.

TABLE II. Summary of Pre-WWII Transmission and Supply Line Damage in Areas with No Reported Permanent Ground Deformation

Installation Date	Line No.	Nominal Diameter mm (in.)	Wall Thickness mm (in.)	SMYS[h] MPa (ksi)	Welds	Earthquake	Distance Affected[a] km (mi.)	No. of Repairs	Repairs/km (Repairs/mi.)
1913	100	300 (12)	6.4 (0.25)	unknown	partially reconditioned[b]	1952 and 1954 Kern County	50.4 (31.3)	2[c]	0.04 (0.06)
1920-21	102.90	300 (12)	6.4 (0.25)	unknown	oxy-acetylene	1971 San Fernando	2.9 (1.8)	3	1.03 (1.65)
1921	101	300 (12)	6.4 (0.25)	unknown	oxy-acetylene	1952 and 1954 Kern County	48.3 (30)	8[c]	0.17 (0.27)
1925	1001	300 (12)	5.6 (0.22)	unknown	oxy-acetylene	1971 San Fernando	19.3 (12)	25[d,f]	1.30 (2.08)[d,f]
1925	1001	300 (12)	5.6 (0.22)	172 (25)	oxy-acetylene	1994 Northridge	25.8 (16.0)[k]	7[k]	0.27 (0.44)
1926	115	400 (16)	7.9 (0.312)	unknown	oxy-acetylene	1971 San Fernando	24.5 (15.2)	39[d]	1.59 (2.56)[d,e]
1927	122	380 (15)	6.4 (0.25)	NR[c]	oxy-acetylene	1994 Northridge	19.3 (12.0)	1	0.05 (0.08)
1930	80.90	550 (22)	6.4 (0.25)	240 (35)	not recorded	1952 and 1954 Kern County	10.8 (6.7)	0	0
1930	120	550 (22)	7.9 (0.312)	240 (35)	electric arc[g]	1971 San Fernando	11.3 (7.0)	1	0.09 (0.14)
1930	119	550 (22)	7.9 (0.312)	208 (30)	electric arc[g]	1952 and 1954 Kern County	47.6 (29.5)	0	0
1930	119	550 (22)	7.9 (0.312)	207 (30)	electric arc[g]	1994 Northridge	3.2 (2.0)	0[l]	0[l]
1930	120	550 (22)	7.1 (0.281)	241 (35)	electric arc[g]	1994 Northridge	29.6 (18.4)	0	0
1930	121	650 (26)	6.4 (0.25)	241 (35)	oxy-acetylene	1994 Northridge	1.1 (0.7)	0	0
1931	85	650 (26)	6.4 to 7.9 (0.25 to 0.312)	228 (33)	electric arc[g]	1952 and 1954 Kern County	58 (36)	0	0
1931	85	650 (26)	6.4 to 7.9 (0.25 to 0.312)	228 (33)	partially reconditioned[b]	1952 and 1954 Kern County	36.7 (22.8)	0	0
1931	85	650 (26)	6.4 (0.25)	228 (33)	electric arc[g]	1971 San Fernando	8.7 (5.4)	0[f]	0[f]

TABLE II. Summary of Pre-WWII Transmission and Supply Line Damage in Areas with No Reported Permanent Ground Deformation (completed)

Installation Date	Line No.	Nominal Diameter mm (in.)	Wall Thickness mm (in.)	SMYS[h] MPa (ksi)	Welds	Earthquake	Distance Affected[a] km (mi.)	No. of Repairs	Repairs/km (Repairs/mi.)
1931	85	650 (26)	6.4 (0.25)	228 (33)	partially reconditioned[b]	1971 San Fernando	14.5 (9.0)	3	0.21 (0.33)
1931	85	650 (26)	6.4 (0.25)	228 (33)	partially reconditioned[b]	1994 Northridge	3.2 (2.0)	4[l,i]	1.56 (2.5)[l,i]
1931	85	650 (26)	6.4 (0.25)	228 (33)	electric arc[g]	1994 Northridge	NA[j]	NA[j,i]	NA[j,i]
1931	765	650 (26)	6.4 to 7.9 (0.25 to 0.312)	207 and 228 (30 and 33)	electric arc[g]	1933 Long Beach	16 (10)	0	0
1937	119	550 (22)	7.9 (0.312)	240 (35)	electric arc[g]	1971 San Fernando	6.5 (4.0)	1	0.15 (0.25)
1941	1134	450 to 500 (18 to 20)	6.4 (0.25)	240 (35)	electric arc	1952 and 1954 Kern County	24.3 (15.1)	0	0
1941	104	250 (10)	5.2 (0.203)	not reported	electric arc	1994 Northridge	3.7 (2.3)	0	0

[a]Based on area of greatest seismic intensity, MM VIII or greater
[b]Originally oxy-acetylene; many welds reinforced in 1932 with electric arc welds and electric arc welded bands and plates
[c]Cumulative breaks at welds for 1952 and 1954 earthquakes
[d]Pipe failures at fault crossing not included
[e]Break rate was locally as high as 6.04 breaks/km (9.72 breaks/mi.) on Glenoaks Blvd. between McClay and Foothill Blvd.
[f]Pipe failures at location of lateral spread on San Fernando Rd. not included
[g]Unshielded electric arc using belled end pipe with underlying steel ring (NOTE: further studies of Line 119 constructed in 1930 are being conducted to establish weld characteristics)
[h]Specified Minimum Yield Stress
[i]One pipeline break recorded in area where MMI $\leq$ VII
[j]Not applicable because entire section of pipeline outside MMI $\geq$ VIII area
[k]Based on pipeline repairs and distance between Fillmore and Potrero Canyon
[l] Four leaking flanges in Line 85 and one leaking flange in Line 119 in area where MMI $\leq$ VII

TABLE III. Summary of Pre-WWII Transmission and Supply Line Damage in Areas with Permanent Ground Deformation

Installation Date	Line No.	Nominal Diameter mm (in.)	Wall Thickness mm (in.)	SMYS[b] MPa (ksi)	Welds	Earthquake and Pipeline Response and Ground Deformation
1925	1001	300 (12)	5.6 (0.22)	unknown	oxy-acetylene	**1971 San Fernando**: 1 break at fault crossing; approx. 200 mm (8 in.) thrust and 30 mm (1.2 in.) lateral offset. Three breaks at lateral spread on San Fernando Rd.; approx. 2 m (6.5 ft) lateral displacement perpendicular to the line.
1925	1001	300 (12)	5.6 (0.22)	unknown	oxy-acetylene	**1994 Northridge**: 18 breaks in Potrero Canyon in area affected by dynamic consolidation of alluvial sediments, liquefaction, and compressive deformation at the toe of slopes along south side of canyon.
1926	115	400 (16)	6.4 (0.25)	unknown	oxy-acetylene	**1971 San Fernando**: Approx. 3 compression and 10 tension failures at fault crossing; 600 mm (24 in.) thrust and 1.9 m (6.2 ft) lateral offset
1930	120	550 (22)	7.9 (0.312)	240 (35)	electric arc	**1994 Northridge**: One compression and one tension failure at ground deformation on Balboa Blvd. in Granada Hills.
1931	85	650 (26)	6.4 (0.25)	228 (33)	electric arc[a]	**1971 San Fernando**: 7 breaks at lateral spread on San Fernando Rd.; displacement same as above.
1941	104	250 (10)	5.1 (0.203)	unknown	electric arc	**1994 Northridge**: One break consisting of buckle and split at weld at an overbend in Aliso Canyon Gas Storage Field.
1948	6000	200 (8)	7.1 (0.281)	240 (35)	electric arc	**1979 Imperial Valley**: No damage; approx. 400 mm (16 in.) of cumulative lateral movement at fault crossing.
1966	120	550 (22)	7.1 (0.281)	360 (52)	electric arc	**1971 San Fernando**: No damage; approx. 2 to 3 m (6 to 10 ft) of ground movement at lateral spread along utility corridor on west side of Upper Van Norman Reservoir.
1966	3000	750 (30)	9.5 (0.375)	360 (52)	electric arc	**1971 San Fernando**: Same.
1966	3003	750 (30)	9.5 (0.375)	360 (52)	electric arc	**1971 San Fernando**: Same
1966	6001	250 (10)	4.8 (0.188)	290 (42)	electric arc	**1979 Imperial Valley**: No damage; approx. 315 mm (12.4 in.) of cumulative lateral movement at fault crossing.

[a] Unshielded electric arc using belled end pipe with underlying steel ring; [b] Specified Minimum Yield Stress

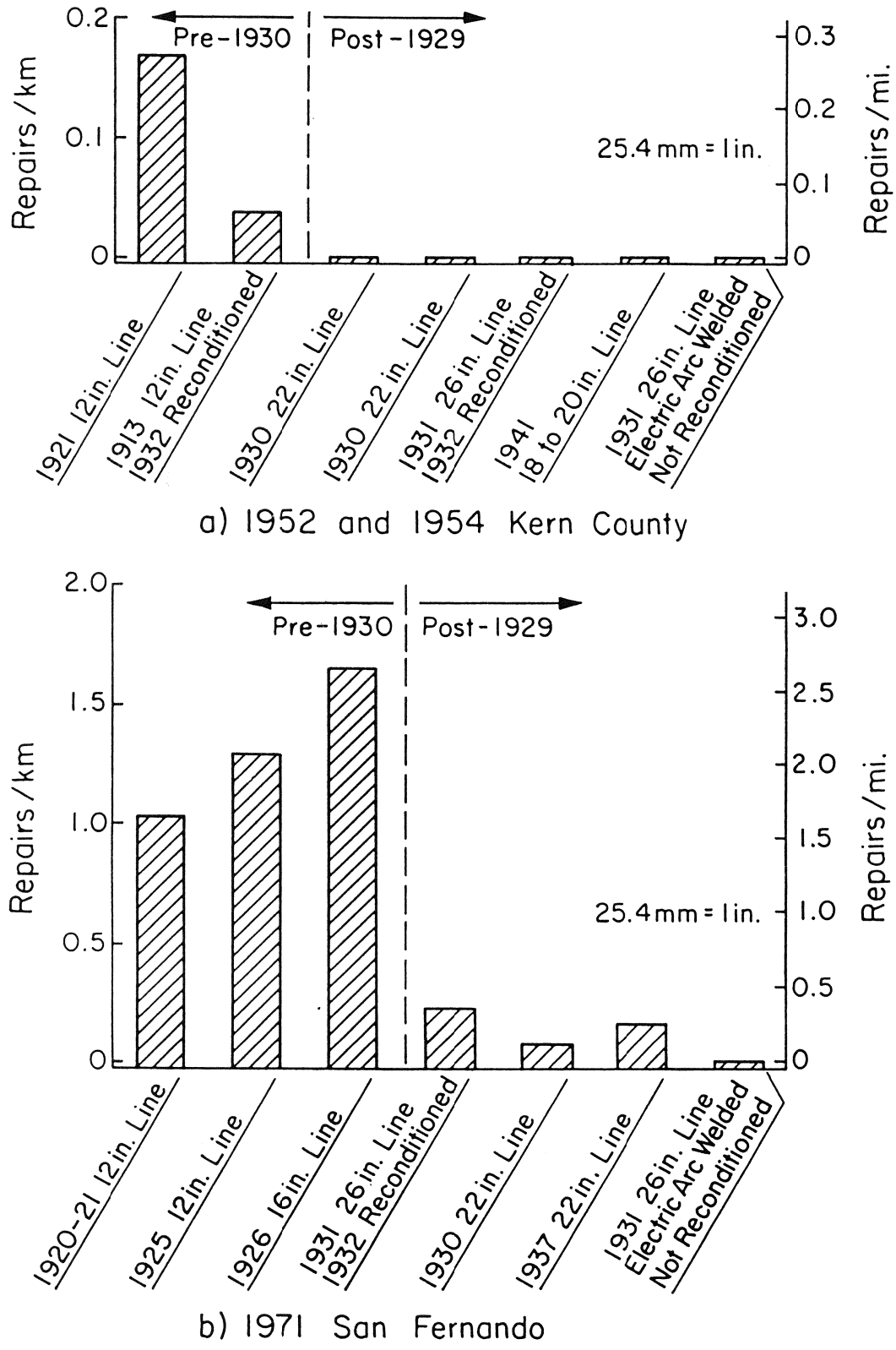

FIGURE 9. Damage Rates for Gas Transmission and Supply Lines in Areas with No Reported Permanent Ground Deformation

Table III provides a summary of transmission and supply line response to permanent ground deformation generated by surface faulting, liquefaction, dynamic consolidation, and slope movement. Only pipelines with nominal diameters equal to or larger than 300 mm (12 in.) are listed in the table. All damage occurred in pre-WWII oxy-acetylene welded and electric arc welded pipelines. No breaks nor disruption of supply has been experienced in gas pipelines constructed with quality welds administered by modern electric arc techniques. The table indicates that breaks were not sustained in modern, electric arc welded pipelines at locations of surface faulting and lateral spreads, even though the severity of ground deformation in these instances generally was consistent with that causing rupture in pre-WWII oxy-acetylene and electric arc welded pipelines.

SUMMARY

A review of the seismic performance of gas transmission and supply lines reported in this work shows that nearly all pipeline repairs occurred in areas with MMI $\geq$ VIII. The earthquake-related damage occurred primarily in the form of ruptures at oxy-acetylene girth welds.

Table IV and Figure 10 summarize all gas transmission and supply line repairs. The formats of the table and figure are similar to those presented by O'Rourke and Palmer (1994a,b) with several notable exceptions. The repair statistics are grouped under categories in which damage occurred in areas either with or without reported permanent ground deformation. Previous treatment of the statistics grouped repairs according to damage by either traveling ground waves or permanent ground deformation. Grouping the data according to the absence or presence of permanent ground deformation is more consistent with the evidence. The absence of reported ground displacements does not eliminate the possibility of movement which escaped observation. However, a careful check of damage locations, which had been inspected and/or mapped for ground movements, does show that many locations of damage to oxy-acetylene welded lines are in areas which lack significant permanent differential ground movement and thus were likely affected by traveling ground waves.

The evaluation of repair statistics in this work benefits from observations published after O'Rourke and Palmer (1994a,b) reported their findings. Specifically, the observations of permanent ground deformation in Potrero Canyon (Stewart, et al., 1994) has been used to identify 18 breaks in Line 1001 inside an area of significant permanent soil displacements. In this work, mapping the location of reported repairs to Lines 115 and 1001 at the Sylmar segment of the San Fernando fault and Juvenile Hall lateral spread, respectively, has resulted in a small number of additional damage locations being associated with areas of permanent ground deformation. Further study of repair statistics (Johnson, 1982) has resulted in a total count of 52 breaks in Line 115, one less than the number previously used by O'Rourke and Palmer.

Pipelines with the highest incidence of damage are those constructed before 1930 with oxy-acetylene welds, some of which have experienced damage at a relatively high rate of over 1 repair/km (1.61 repairs/mi). Oxy-acetylene welding for major transmission lines appears to have been discontinued by SoCalGas after 1931.

TABLE IV. Summary of Earthquake-Related Gas Pipeline Repairs

Type of Damage	Damage at Locations Where No Permanent Ground Deformation Recorded: Number of Repairs	Damage at Locations of Permanent Ground Deformation: Number of Repairs
Break in pre-WWII oxy-acetylene girth welded pipeline	88[a]	35[e]
Break in pre-WWII electric arc girth welded pipeline	4[b]	10[e]
Leakage at locations of corrosion	2[c]	---
Leaking flanges	5[d]	---

a Refer to Table I. Note that repairs to partially reconditioned Line 85 during the 1971 San Fernando earthquake were at oxy-acetylene welds and one of the repairs in Line 100 was at an oxy-acetylene weld. Repairs include damage to Line 122 during the 1994 Northridge earthquake
b Refer to Table II
c Includes leaks detected in Lines 80.90 and 1134 during the main 1952 Kern County earthquake
d Refer to Table I
e Refer to Table II

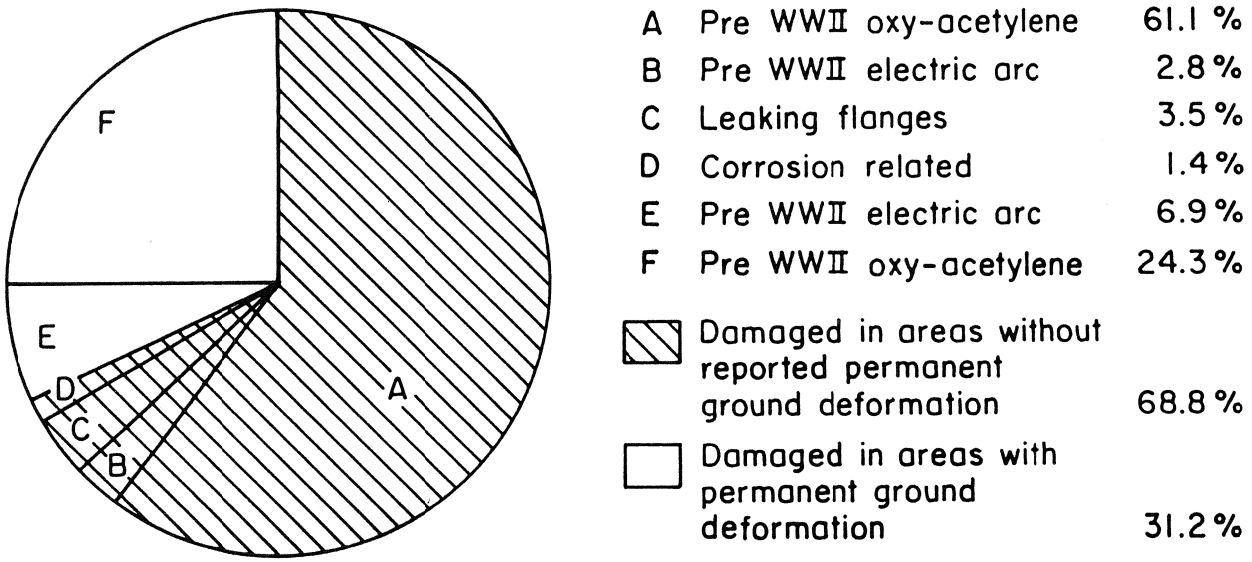

FIGURE 10. Pie Chart Showing Relative Proportions of Earthquake-Related Repairs Associated with Various Categories of Damage

In contrast to oxy-acetylene welded piping, pre-WWII pipelines with unshielded electric arc welds have fared much better in areas where permanent ground deformation has not been reported. Damage under these conditions accounts for only 2.8% of the total repairs, which is over 20 times less than the damage in similar areas to oxy-acetylene welded lines.

Damage from permanent ground deformation associated with surface faulting, liquefaction-induced lateral spread, dynamic consolidation, and slope movement represents 31.2% of the total repairs. This relatively low portion is associated with the relatively small percentage of surface area influenced by ground failure during an earthquake. Damage from permanent ground deformation can nonetheless be severe, resulting in some of the most conspicuous damage during a seismic event. Pipeline ruptures on Balboa Blvd. during the 1994 Northridge earthquake, and along Glenoaks Blvd. during the 1971 San Fernando earthquake, are examples. Permanent ground deformation damage during previous earthquakes has been confined entirely to oxy-acetylene and pre-WWII electric arc welded pipelines.

Post-WWII electric arc welded transmission pipelines in good repair have never experienced a break or leak during a southern California earthquake. A very small amount of damage can be attributed to leaks at pipe walls thinned by corrosion, such as the corrosion-related leakage detected after the 1952 Kern County main earthquake. Modern electric arc welded pipelines have been subjected to severe permanent ground displacement which has damaged adjacent welded water trunk lines, such as those subjected to 2.7 m (9 ft) of lateral spread next to the Jensen Filtration Plant during the 1971 San Fernando earthquake. Likewise, ground movement on Balboa Blvd. during the 1994 Northridge earthquake ruptured the pre-WWII electric arc welded Line 120, but did not damage two adjacent post-WWII electric arc welded transmission lines.

The lack of damage to post-WWII electric arc welded pipelines does not mean they are immune to permanent ground deformation. On the contrary, there is substantial experience with modern pipeline failures in areas of severe landslides. Nevertheless, the repair record shows that modern electric arc welded gas transmission lines in good repair are the most resistant type of piping, vulnerable only to very large and abrupt ground displacement, and generally highly resistant to traveling ground wave effects and moderate amounts of permanent deformation.

ACKNOWLEDGMENTS

The research summarized in this paper was supported by the National Center for Earthquake Engineering Research and by the Southern California Gas Company. The assistance of the gas company, including Mssrs. R. Gailing, J. Haynes, and J. McNorgan, is gratefully acknowledged. This work was performed in conjunction with research on the gas distribution network by EQE Engineering, for which R. Eguchi and H. Seligson were the principal investigators. The manuscript was prepared by K.J. Stewart and L. McCall, and the figures were drafted by A. Avcisoy.

REFERENCES

Bryant, E.S., "The Long Beach Earthquake of March 10, 1933," Proceedings, 41st Annual Convention of the Pacific Coast Gas Association, Oct. 1934, pp. 73-74.

Dobry, R., M.H. Baziar, T.D. O'Rourke, B.L. Roth, and T.L. Youd, "Liquefaction and Ground Failure in the Imperial Valley, Southern California During the 1979, 1981, and 1987 Earthquakes," Technical Report NCEER-92-0002, Vol. 2, National Center for Earthquake Engineering Research, Buffalo, NY, Feb. 1992.

Earthquake Engineering Research Institute, "Report on the North Palm Springs, California Earthquake - July 8, 1986," EERI Special Report, EERI Newsletter, Vol. 20, No. 9, Sept. 1986.

Earthquake Engineering Research Institute, "Sierra Madre Earthquake of June 28, 1991," EERI Special Earthquake Report, EERI Newsletter, Vol. 25, No. 8, Aug. 1991.

Earthquake Engineering Research Institute, "Landers and Big Bear Earthquakes of June 28 and 29, 1992," EERI Special Earthquake Report, EERI Newsletter, Aug. 1992, 12 p.

Johnson, W.T. - personal communication of repair statistics associated with 1971 San Fernando earthquake, Aug. 1982.

Hoff, N.L., "Earthquakes as a Cause of Major Interruptions to Gas Service," Proceedings, 41st Annual Convention of the Pacific Coast Gas Association, Oct. 1934, pp. 63-69.

Lind, R.J., "Earthquake Effect on a Gas Pipeline," Proceedings, Pacific Coast Gas Association 45, May 1954, pp. 103-105.

McNorgan, J.D., "Relieving Seismic Stresses Locked in Gas Pipeline," Technical Report NCEER-89-0032, National Center for Earthquake Engineering Research, Buffalo, NY, Sept. 1989, pp. 363-369.

Newby, A.B., "Pipelines Ride the Shock Waves," Proceedings, Pacific Coast Gas Association 45, May 1954, pp. 105-109.

Office of the Federal Register, "Transportation of Natural and Other Gas by Pipeline: Minimum Federal Safety Standards," Code of Federal Regulations, Title 49, Parts 191 and 192, Washington, D.C., Nov. 1990, pp. 575-633.

O'Rourke, T.D. and M.A. McCaffrey, "Buried Pipeline Response to Permanent Earthquake Ground Movements," Proceedings, 8th World Conference on Earthquake Engineering 7, July 1984, pp. 215-222.

O'Rourke, T.D., B.L. Roth, and M. Hamada, "Large Ground Deformations and Their Effects on Lifeline Facilities: 1971 San Fernando Earthquake," Technical Report NCEER-92-002, Vol. 2, National Center for Earthquake Engineering Research, Buffalo, NY, 1992.

O'Rourke, T.D. and M.C. Palmer, "The Northridge, California Earthquake of January 17, 1994: Performance of Gas Transmission Pipelines," Technical Report NCEER-94-0011, National Center for Earthquake Engineering Research, Buffalo, NY, May 1994a.

O'Rourke, T.D. and M.C. Palmer, "Feasibility Study of Replacement Procedures and Earthquake Performance Related to Gas Transmission Pipelines," Technical Report NCEER-94-0012, National Center for Earthquake Engineering Research, Buffalo, NY, May 1994b.

Public Utilities Commission of the State of California, "Rules Governing Design, Construction, Testing, Maintenance, and Operation of Utility Gas Gathering, Transmission, and Distribution Piping Systems," General Order No. 112-D, PUC of the State of California, San Francisco, CA, Nov. 1988.

Systems," General Order No. 112-D, PUC of the State of California, San Francisco, CA, Nov. 1988.

Schiff, A.J., "The Whittier Narrows, California Earthquake of October 1, 1987 - Response of Lifelines and Their Effect on Emergency Response," The Whittier Narrows Earthquake of October 1, 1987, Earthquake Spectra, Vol. 4, No. 1, Feb. 1988, pp. 339-366.

Southern California Gas Company, "Earthquake Effects on Southern California Gas Company Facilities," San Fernando, California Earthquake of February 9, 1971, Vol. 2, U.S. Department of Commerce, Washington, D.C., 1973, pp. 59-66.

Steinbrugge, K.V. and D.F. Moran, "An Engineering Study of the Southern California Earthquake of July 21, 1952 and Its Aftershocks," Bulletin of the Seismological Society of America, Vol. 44, No. 23, Apr. 1954, pp. 201-337.

Steinbrugge, K.V., E.E. Schader, H.C. Bigglestone, and C.A. Weirs, "San Fernando Earthquake February 9, 1971," Pacific Fire Rating Bureau, San Francisco, CA, 1971.

Stewart, J.P., J.D. Bray, R.B. Seed, and N. Sitar, "Preliminary Report on the Principal Geotechnical Aspects of the January 17, 1994 Northridge Earthquake," Report No. UCB/EERC-94/08, University of California, Berkeley, CA, June 1994.

Tinsley, J.C., T.L. Youd, D.M. Perkins, and A.T.F. Chen, "Evaluating Liquefaction Potential," U.S. Geological Survey Professional Paper 1360, Washington, D.C., 1985, pp. 263-316.

U.S. Geological Survey Staff, "Surface Faulting in the San Fernando, California Earthquake of February 9, 1971," The San Fernando, California Earthquake of February 9, 1971, U.S. Geological Survey Professional Paper 733, U.S. Department of the Interior and U.S. Department of Commerce, Washington, D.C., 1971, pp. 55-76.

Wood, H.O., "Preliminary Report on the Long Beach Earthquake," Bulletin of the Seismological Society of America, Vol. 23, No. 2, Apr. 1933, pp. 43-56.

MAGNITUDE SCALING FACTORS FOR ANALYSIS OF LIQUEFACTION

Tonya W. Loertscher
Graduate Student
Brigham Young University
Provo, Utah 84602

and

T. Leslie Youd
Professor of Civil Engineering
Brigham Young University
Provo, Utah 84602

ABSTRACT

The "simplified procedure" developed by Seed and Idriss is widely used in the United States to evaluate liquefaction hazard. Empirical evidence suggests that magnitude scaling factors (MSF) required in this procedure are very conservative for moderate-sized earthquakes. We compiled soil and site data for several earthquakes and localities where surface effects of liquefaction did or did not occur. We statistically analyzed these data using logistic regression to develop MSF that have about the same conservatism as other factors in the simplified procedure. Regressed MSF values for magnitude 5.5, 6, and 6.75 earthquakes are 4.5, 2.8, and 1.6, respectively, compared to values of 1.43, 1.32 and 1.13, respectively, as listed by Seed and Idriss. Use of the regressed MSF values may safely reduce calculated liquefaction hazard for moderate-sized earthquakes.

INTRODUCTION

Liquefaction is a phenomenon in which soil, usually sands or silty sands, are transformed from solid state into a liquid state due to shaking from an earthquake. Liquefaction is a major cause of damage during earthquakes and is a necessary consideration in seismic hazard investigations for buildings, pipelines, land use planning, railway and highway bridges, etc. The primary method for analyzing liquefaction hazard used in the United States and many other countries is the simplified procedure developed by Seed and Idriss (1971).

In order to evaluate the liquefaction hazard at a site, the simplified procedure requires several correction factors to account for conditions that differ from those directly analyzed in deriving the technique. The magnitude scaling factor (MSF) corrects the analysis for earthquake magnitudes other than 7.5; the standard used at the time of derivation.

The reliability of magnitude scaling factors developed by Seed and Idriss (1982) has never been confirmed, nor has a statistical analysis been made of the degree of uncertainty or conservatism in the numbers. Empirical evidence suggests that the MSF derived by Seed and Idriss are very conservative, that is, they appear to greatly overestimate the liquefaction hazard for small to moderate size earthquakes (M = 5 to 7).

The purpose of this study is to analyze statistically the reliability of the MSF proposed by Seed and Idriss and to develop a more appropriate set of factors if warranted. Case histories of field performance data were collected for a variety of earthquake magnitudes and soil conditions. Liquefaction hazard was calculated using the Seed and Idriss (1971; 1982) simplified procedure and, these predictions were compared against field performance data. From a statistical analysis of the results, we evaluated the reliability of the Seed and Idriss magnitude scaling factors and develop a statistically derived set of MSF values.

COLLECTION AND CATEGORIZATIONOF THE DATA

In order to test the validity of the magnitude scaling factors proposed by Seed and Idriss (1982), we applied the simplified procedure to 412 sites from 42 earthquakes where surface effects of liquefaction were or were not observed. To assure that these sites were accurately analyzed, we re-evaluated many variables which affect soil liquefaction and the best estimates of soil properties and seismic factors were determined for use in the site analyses. A liquefaction analysis program developed at Brigham Young University that applies the Seed and Idriss simplified procedure to borehole logs was used to calculate a prediction of liquefaction occurrence or nonoccurrence. The results from the predicted field performance were then compared with the observed performance.

In order to apply, the Seed and Idriss simplified procedure a compilation of case history data is required. The case history database in this study was developed from several earthquake catalogs: Seed and others (1985), Liao (1986), Ambraseys (1988), and Bartlett and Youd (1992). Case history sites unavailable in these earthquake logs were also added to the database (Loertscher, 1994). Original sources which provided site borehole logs were examined where available to verify the data in the earthquake catalogs.

Goodness-of-fit Statistics

Goodness-of-fit statistics are used in a logistic regression analysis to determine whether the proposed model is statistically significant. The Percent Correctly Predicted (PCP) was the primary method of goodness-of-fit used in this study to determine the adequacy of the logistic regression model. The response for the ith data point is correctly predicted if $Y_i = 1$ and $p_i > 0.5$ or if $Y_i = 0$ and $p_i < 0.5$. The probability, p_i, is calculated after equation (2) has been evaluated for the independent variables and their parameters. Other goodness-of-fit statistics could also be used to determine statistical significance.

LOGISTIC REGRESSION OF LIQUEFACTION DATABASE

With the database of case histories compiled for this study, we performed a regression analysis using the logistic method. The purpose of this logistic analysis to obtain a statistical analysis of the reliability of the MSF proposed by Seed and Idriss. In order to do this a set of scaling factors derived from the logistic analysis will be compared with those published by Seed and Idriss (1982).

The dependent variable, Y_i, used in this study is liquefaction occurrence or nonoccurrence denoted by a 1 or 0 respectively. Independent variables are physical properties of the soil or the earthquake which could affect the occurrence or nonoccurrence of liquefaction. The independent variables used in this study are those used in the Seed and Idriss simplified procedure because these variables are so widely accepted by the geotechnical profession. In the Seed and Idriss simplified procedure, corrected blowcount, $(N_1)_{60}$, and cyclic stress ratio, CSR, are specifically used to determine if liquefaction will or will not occur. In order to calculate a magnitude scaling factor from the logistic analysis, the independent variable of M_w must be used in addition to the other two independent variables.

Because a restricted number of independent variables, $(N_1)_{60}$ and CSR, are used in the Seed and Idriss simplified procedure, different combinations of these variables were used to increase the initial set of candidate variables in the logistic regression, for example, ln(CSR), $M_w(N_1)_{60}$, M_wCSR, etc. Only a limited number of variables and combinations can be made available in the logistic analysis. It is possible that variables other than those used in the Seed and Idriss procedure could be significant but, were not considered in this study.

A logistic regression analysis was performed on the liquefaction database developed for this study using the stepwise regression method. This procedure includes the most significant of the candidate independent variables in the regression model and provides an optimum model for the given set of variables. In the logistic regression analysis on this study's database, the stepwise regression procedure selected the following model:

$$\text{logit}(p) = -13.42 + 3.04M_w - 0.035M_w(N_1)_{60} + 0.41M_w\ln(CSR) \qquad (3)$$

where

logit(p)	=	the log-odds transform, equation (1)
p	=	the probability of liquefaction occurrence

M_w	=	the earthquake moment magnitude
$(N_1)_{60}$	=	the corrected SPT blowcount
CSR	=	the cyclic stress ratio.

Equation (3) allows prediction of the probability of liquefaction occurrence or nonoccurrence due to shaking from a specific earthquake based on the properties of a given site. The derivation of magnitude scaling factors from this logistic regression model is given in a later section.

The Percent Correctly Predicted (PCP) for the resultant model given in equation (3) indicates whether the model is statistically significant. For sites where liquefaction occurred ($Y_i=1$), those with a $p_i > 0.5$ are considered correctly predicted by the model and comprise approximately 92% of the results. For sites where liquefaction did not occur ($Y_i=0$), those with a $p_i < 0.5$ are considered correctly by the model and comprise approximately 85% of the results. The PCP clearly shows that the logistic regression model [equation (3)] correctly predicts a high percentage of the actual empirical data. Other goodness-of-fit statistics also give high values for the logistic regression model.

Probability in the Regression Model

In Seed and Idriss' plot of CSR versus $(N_1)_{60}$, a critical boundary separates liquefaction and no liquefaction sites (see Figure 1). In the simplified procedure for liquefaction hazard analysis, this boundary curve is used to calculate the cyclic stress ratio required to induce liquefaction. Because the Seed and Idriss bounding curve was fit by hand and not as a result of any mathematical or statistical procedure, the curve does not have any unique associated probability of liquefaction occurrence. Due to this fact, the actual probability that liquefaction will occur is unknown for cases when the Seed and Idriss simplified procedure predicts occurrence.

This study uses the concept of having a probability associated with prediction of liquefaction occurrence or nonoccurrence. The logistic regression model [equation (3)] relates the probability of liquefaction occurrence or nonoccurrence to magnitude, blowcount, and cyclic stress ratio. Several curves with different probabilities of liquefaction occurrence can be developed for a specified earthquake magnitude. Figure 2 shows an example of these contours of equal probabilities for magnitude 7.5. If the $(N_1)_{60}$ and CSR for a site give a point on one of these curves, the probability that liquefaction occurs ($Y_i=1$) for that site equals the probability associated with the curve.

Because probability is used in the regression model, several different estimates of scaling factor can be derived for each magnitude. The actual magnitude scaling factor to be used depends upon the degree of certainty desired in the prediction of liquefaction occurrence or nonoccurrence. If a high probability (e.g. $p = 95\%$) is used in a prediction, the user can be 95% certain that a prediction of liquefaction occurrence ($Y_i=1$) is correct. Sites where marginal liquefaction occurs will not be predicted using a magnitude scaling factor with a high probability value. Therefore, the probability of liquefaction occurrence associated with a magnitude scaling factor should be determined according to the degree of conservatism

Values for site variables (see Table 1) used to determine the occurrence or nonoccurrence of liquefaction were compiled for each site. To develop the greatest possible confidence in the predicted results, the values for each variable were examined and evaluated to give the best possible estimate.

LOGISTIC REGRESSION ANALYSIS

The method of logistic analysis is a type of statistical regression analysis. As with all regression analyses, logistic analysis assumes that changes in independent variables, X_i, create corresponding changes in a dependent variable, Y_i. Data with a binary dependent variable use the logistic method for analysis because typical linear or nonlinear regression analyses do not give a statistically sound answer for a noncontinuous variable.

Generalized Procedure

Logistic regression analysis on binary variables is performed in a manner similar to multiple regression with two main exceptions: (a) the response variable is the logit term derived from the dependent variable, Y_i, using equation (1), and (b) parameters, ß's, are interpreted according to effects on the logit term rather than on the dependent variable (Freeman, 1987).

For a given dependent variable, in this case liquefaction occurrence or nonoccurrence, p is the probability that liquefaction will occur ($Y_i=1$) for a set of independent variables, X_i. The probability of no liquefaction occurrence ($Y_i=0$) given the same set of independent variables is 1-p. To use a logistic regression analysis, Y_i must be transformed into a logit term, logit(p), that will be used as the new response variable. The logit term is given by the odds of liquefaction to no liquefaction:

$$\text{logit}(p) = \ln[(p)/(1-p)] \qquad (1)$$

With logit(p) as the response variable, a regression line is fit to the data set with the form given in equation (2).

$$\text{logit}(p) = ß_0 + ß_1X_1 + ß_2X_2 + \ldots + ß_nX_n \qquad (2)$$

The terms of $ß_i$ are parameters determined by the regression analysis. The X_i terms are the independent variables used to determine the probability of the liquefaction occurrence. These independent variables are properties used in the analysis which may or may not affect the dependent variable, for example, physical parameters of the soil or of the earthquake.

The independent variables are entered into the regression model using a stepwise procedure. Given an initial set of candidate independent variables, a stepwise regression analysis performs an automated search for the optimal combination of independent variables, that is, the combination which best explains changes in the dependent variable.

desired.

Another consideration also affects the determination of the probability used in deriving the MSF. If the MSF is to be used to scale the original Seed and Idriss M=7.5 curve, the probability associated with that original curve would be appropriate for use in the derivation of the scaling factors. Unfortunately, the Seed and Idriss bounding curve does not have a unique associated probability.

Thus, there are two factors to consider in determining an appropriate probability for the calculation of the magnitude scaling factors. (a) Use of a probability with enough conservatism to enable sites of marginal liquefaction to be predicted. (b) A probability which is somewhat consistent with the original Seed and Idriss curve for M = 7.5. Comparisons were made between the Seed and Idriss curve and curves with different probabilities of liquefaction occurrence developed from the logistic regression model. The p=32% logistic model curve has some consistency with the mid to upper portion of the Seed and Idriss curve and is also conservative. Points at this curve have a 32% probability that liquefaction will occur (Y_i=1). The probability, p=32%, meets the criteria we established and will be used in the derivation of magnitude scaling factors.

MAGNITUDE SCALING FACTORS

To simplify the logistic regression model, equation (3), the logit term is evaluated for p=32%. This simplification leads to an equation for cyclic stress ratio, CSR, in terms of magnitude, M_w, and corrected SPT blowcount, $(N_1)_{60}$.

$$CSR = \exp[-7.400 + 30.826/M_w + 0.0851(N_1)_{60}] \quad (4)$$

Magnitude scaling factor is defined as the ratio of the CSR for a given earthquake magnitude and the CSR for M_w=7.5 (Seed and Idriss, 1982), as illustrated by equation (5).

$$MSF = (CSR_M / CSR_{7.5}) \quad (5)$$

By evaluating equation (4) for $M_w = M$ and $M_w = 7.5$, respectively, and substituting into equation (5), an equation for magnitude scaling factor is generated. The final equation for MSF at a probability, p=32%, is as follows:

$$MSF = \exp\{30.826[(1/M_w) - (1/7.5)]\} \quad (6)$$

A comparison of the magnitude scaling factors from the logistic analysis for p=32% and those evaluated for two other probabilities with MSF published in the Seed and Idriss procedure (1982) is given in Table 2.

Recommended uses of the MSF

Magnitude scaling factors developed from the logistic analysis are used in the simplified procedure for liquefaction hazard analysis in the same manner as those developed by Seed

and Idriss. Analyses were performed to determine if the use of logistic MSF gives correct prediction of liquefaction occurrence or nonoccurrence for the case history sites in this study's database. The percent of site responses correctly predicted was determined for both the logistic MSF calculated in this study and the MSF published by Seed and Idriss (1982). For all magnitudes, the logistic MSF in this study correctly predicted 91% of the site responses and, the MSF proposed by Seed and Idriss correctly predicted 78% of the site responses. For magnitudes less than 7.5, the logistic MSF in this study correctly predicted 92% of the site responses and, the MSF proposed by Seed and Idriss correctly predicted 63% of the site responses. The MSF proposed by Seed and Idriss gave poor predictions for sites which did not liquefy. The results indicated:

(1) Use of the original Seed and Idriss M=7.5 curve as seen in Figure 1, with the logistic MSF gives good results.

(2) Use of a logistic curve calculated from equation (3) using the appropriate magnitude and probability, p= 32%, also gives good results.

(3) Use of the original MSF with the Seed and Idriss M=7.5 curve is very conservative.

Figure 3 shows an example of these three results. The case history data for magnitude 6.4 earthquakes show sites of liquefaction or no liquefaction. Also shown are three curves. (1) One of these curves is the original Seed and Idriss bounding curve scaled by the logistic MSF generated in this study. This curve gives good results for separating the liquefaction sites from no liquefaction sites. (2) The next curve is a logistic curve calculated from equation (3) for M_w = 6.4 and p = 32%. This curve also gives good results with one nonliquefied site falling on the liquefaction occurrence boundary. (3) The final curve is the original Seed and Idriss bounding curve scaled by the MSF proposed by Seed and Idriss (1982). This curve is conservative and includes four nonliquefied sites within the liquefaction occurrence boundary.

The good fit of the logistic regression model on the empirical case history data suggests that a new set of magnitude scaling factors are warranted. The scaling factors derived from this model predict liquefaction occurrence or nonoccurrence well and should be considered in future analyses.

CONCLUSIONS

The simplified procedure developed by Seed and Idriss (1971; 1982) is the most commonly used method to evaluate a site for liquefaction hazard as a result of earthquake ground motions. The simplified procedure requires several correction factors to account for conditions different from those directly analyzed in deriving the technique. One of these correction factors, the magnitude scaling factor (MSF) adjusts the analysis for earthquake magnitudes other than 7.5, the base value used by Seed and Idriss. In this study, we developed an extensive database from several earthquake catalogs of sites where surface effects of liquefaction did or did not occur. This database was used to analyze statistically the reliability of MSF values published by Seed and Idriss (1982). Regression analyses were

performed on this database to determine if a re-evaluation of the Seed and Idriss magnitude scaling factors was warranted. Logistic regression analysis proved to be the most appropriate analysis for the binary data in the case history database.

The variables used in the simplified procedure include cyclic stress ratio, CSR, and corrected SPT blowcount, $(N_1)_{60}$. These same variables were also used in this study to develop magnitude scaling factors that are compatible with the Seed and Idriss procedure. These variables proved to be significant in the final logistic regression model. From that model, we generated a set of magnitude scaling factors (Table 2). Because the analyses were performed on case history data, rather than laboratory test data, as was used by Seed and Idriss, the predicted results more closely match the field occurrence or nonoccurrence of liquefaction.

The goodness-of-fit for the logistic regression model on the empirical case history database suggests that use of this new set of magnitude scaling factors is warranted. The magnitude scaling factors generated from the logistic regression analysis (Table 3) predict liquefaction occurrence and nonoccurrence well and are recommended for use with the Seed and Idriss simplified procedure for liquefaction hazard analysis.

ACKNOWLEDGEMENTS

This study on Magnitude Scaling Factors for Analysis of Liquefaction Hazard was funded by the National Science Foundation (NSF). We are grateful to the NSF for their financial support and interest in forwarding research in hazard analysis for earthquake-induced liquefaction.

We also wish to express appreciation to the many people who contributed to this study. We wish to thank C.B. Crouse, Dames and Moore, for his review of the accelerations and magnitudes in the case history database. Likewise, we are grateful to Craig Taylor, Dames and Moore, for helping to develop statistical models for the study. Greg Snow, Morgan Wise and Dr. G. Rex Bryce of the BYU Statistical Research Center were invaluable in assisting with the statistical analyses. We also wish to thank Dr. John Tinsley of the U.S. Geological Survey and several geotechnical firms in the San Francisco area for help in compiling borehole logs. Finally, we wish to thank Dr. Steven F. Bartlett for the use of his liquefaction analysis program and for providing several borehole logs.

REFERENCES

Ambraseys, N. N., 1988, Engineering seismology, Earthquake Engineering and Structural Dynamics, Vol. 17, pp. 1-105.

Bartlett, S. F., and Youd, T. L., 1992, Empirical Analysis of Horizontal Ground Displacement Generated by Liquefaction-Induced Lateral Spreads, Technical Report NCEER-92-0021.

Freeman, Jr., D. H., 1987, Applied Categorical Data Analysis, Statistics: textbooks and monographs, Vol. 79, Marcel Dekker, Inc.: New York, 318 p.

Liao, S. S., 1986, Statistical Modelling of Earthquake-Induced Liquefaction, Doctoral Dissertation: Massachusetts Institute of Technology, 470 p.

Loertscher, T. W., 1994, Magnitude Scaling Factors for Analysis of Liquefaction Hazard, Doctoral Dissertation: Brigham Young University, 136 p.

Seed, H. B., and Idriss, I. M., 1971, Simplified procedure for evaluating soil liquefaction potential, Journal of Geotechnical Engineering, ASCE, Vol. 97, No. SM9, p. 1249 -1273.

Seed, H. B., and Idriss, I. M., 1982, Ground Motions and Soil Liquefaction During Earthquakes: EERI Monograph, 134 p.

Seed, H. B., Tokimatsu, K., Harder, L. F., and Chung, R. M., 1985, Influence of SPT procedures in soil liquefaction resistance evaluations, Journal of Geotechnical Engineering, ASCE, Vol. 111, No. 12, p. 1425-1445.

TABLE 1. Site Condition Variables

Y_i	Liquefaction occurrence (yes=1/no=0)
M	Earthquake magnitude; in this study moment magnitude, M_w
a_{max}	Peak horizontal ground acceleration (g)
σ_o	Total overburden pressure (kg/cm^2)
σ'_o	Effective overburden pressure (kg/cm^2)
r_d	Stress reduction coefficient
$(N_1)_{60}$	Standard penetration test blowcount
FC	Fines content (<0.075 mm) (%)
D_{50}	Median grain size (mm)

TABLE 2. Comparison of Magnitude Scaling Factors from Logistic Analysis and Seed and Idriss (1982)

Magnitude	MSF p=32%	MSF p=50%	MSF p=68%	Seed & Idriss
8.50	0.62	0.60	0.58	0.89
8.00	0.77	0.76	0.75	0.94
7.50	1.00	1.00	1.00	1.00
7.00	1.34	1.36	1.39	1.08
6.75	1.58	1.62	1.67	1.13
6.50	1.88	1.95	2.03	1.19
6.00	2.79	2.97	3.16	1.32
5.50	4.46	4.87	5.32	1.43

TABLE 3. Recommended Magnitude Scaling Factors for use with the Seed and Idriss Simplified Procedure

Magnitude	MSF
8.50	0.62
8.00	0.77
7.50	1.00
7.00	1.34
6.75	1.58
6.50	1.88
6.00	2.79
5.50	4.46

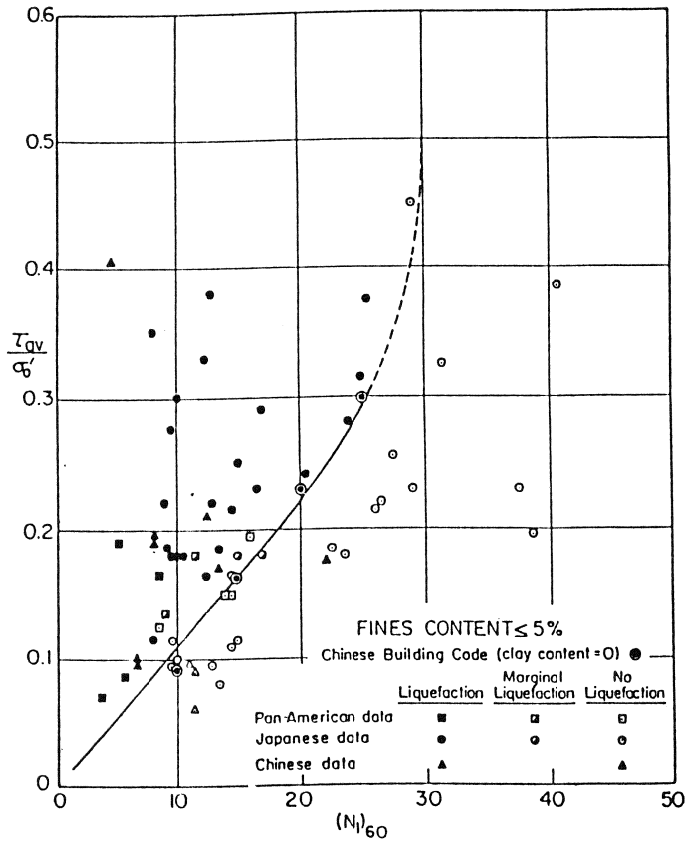

FIGURE 1. Relationship between cyclic stress ratio and $(N_1)_{60}$ for a magnitude 7.5 earthquake (Seed and others, 1985)

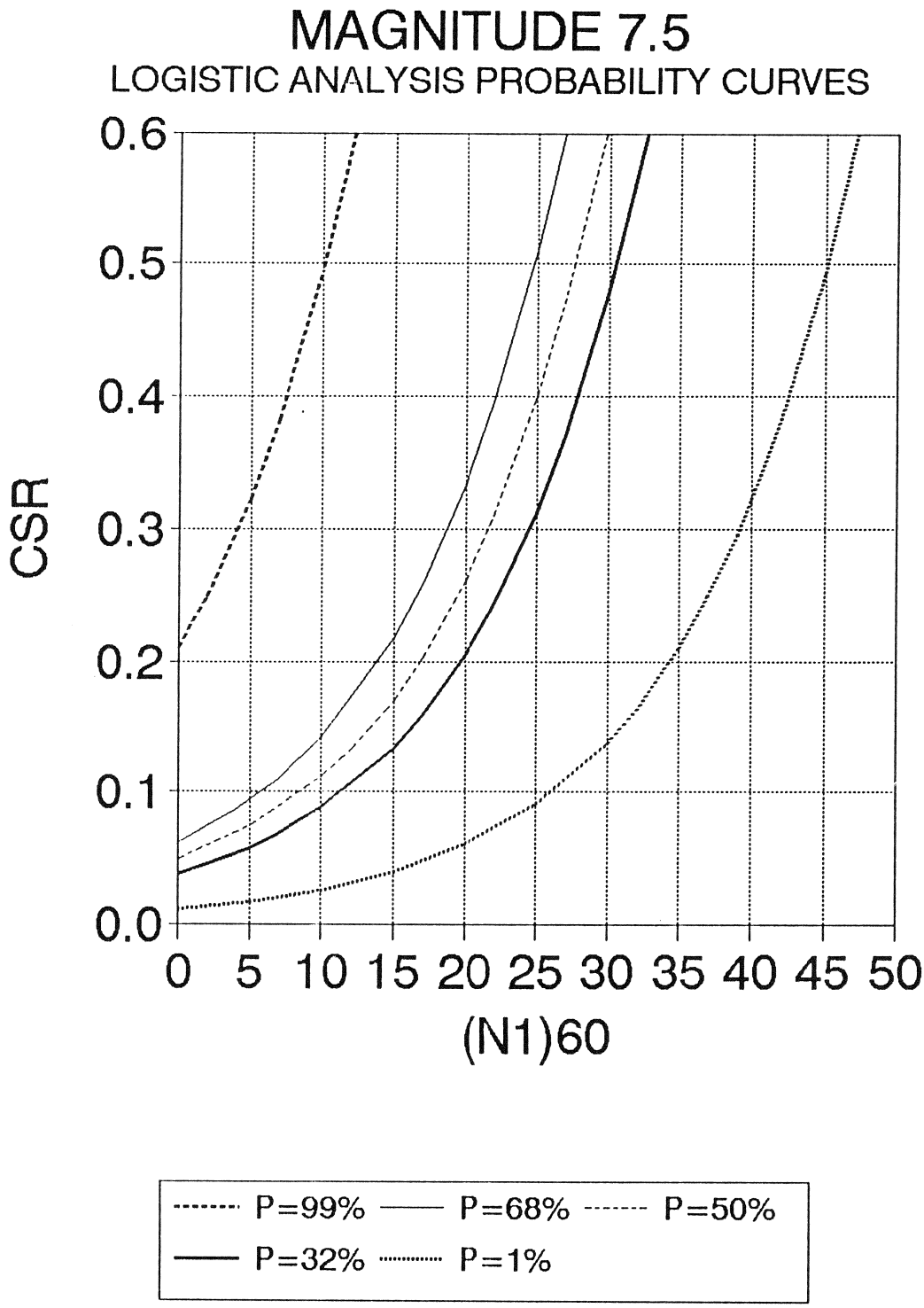

FIGURE 2. Contours of equal probabilities of liquefaction occurrence for M_w=7.5

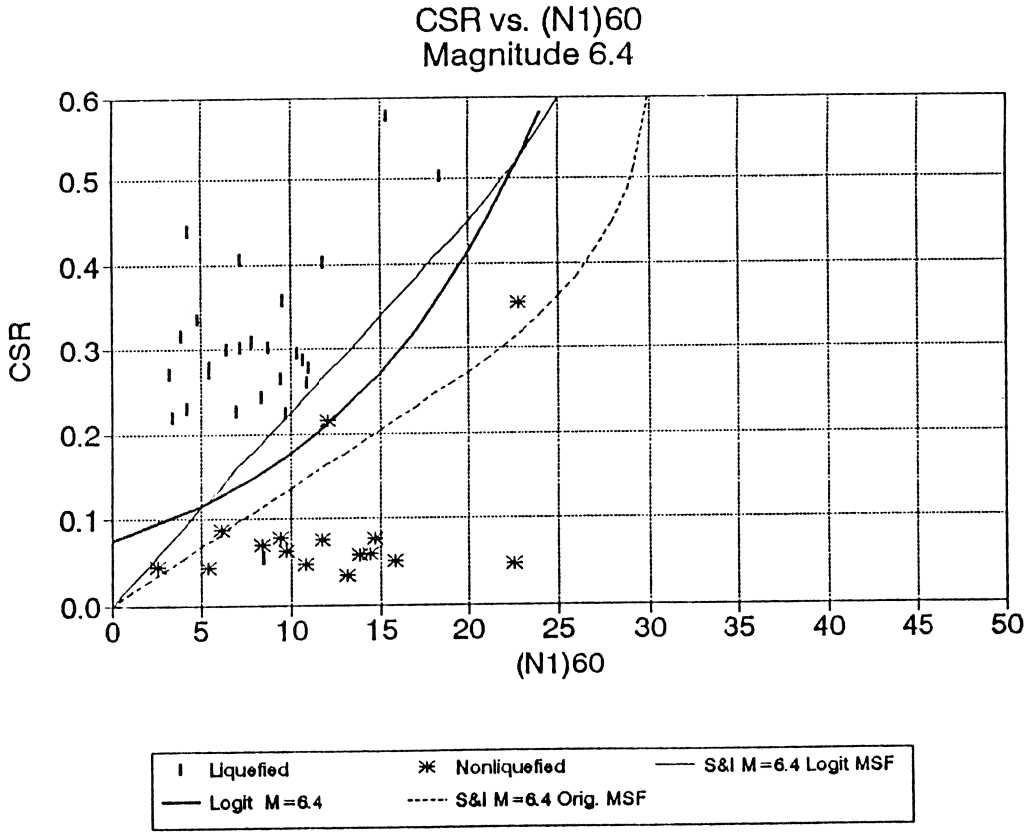

FIGURE 3. A comparison between Logistic curve and Seed and Idriss curve with recommended MSF for M_w = 6.4 case sites

Damage to Water Pipes During the 1994 Northridge Earthquake

Masanori Hamada
Professor of Civil Engineering, Waseda University

Takashi Tazoh
Senior Research Engineer, Shimizu Corporation

Toshiyuki Iwamoto
Senior Research Engineer, Kubota Corporation

Nobuhisa Suzuki
Senior Research Engineer, NKK Corporation

Jyohji Ejiri
Senior Research Engineer, Ohbayashi-Gumi Corporation

and

Keizo Ohtomo
Senior Research Engineer, Central Research Institute of Electric Power Industry

ABSTRACT

This paper presents damage to pipes of a water supply network system under the control of the Department of Water and Power of City of Los Angels (LADWP). Site investigation was conducted at San Fernando Valley where the damage to trunk lines, distribution pipes and service pipes were concentrated.

Sixteen breaks of large diameter trunk lines and approximately 1,670 breaks of small diameter distribution pipes and service pipes were damaged during the earthquake. The damage to the trunk lines contains breaks of joints and pipes of an old riveted trunk line buried along Roscoe Street, which breaks were occurred just over or very close to the epicenter. Other typical damage to the trunk lines were telescopic crashes and failures in tension of welded bell joints due to slight permanent ground movement at Balboa Boulevard.

Most of the breaks of small diameter distribution pipes were caused to old and weak gray cast iron pipes connected with sockets and spigot joints, whose flexibility or strength against dynamic and permanent ground movement could not be expected. And the breaks include those of the service pipes were concentrated in Northridge district including Granada hills, San Fernando district and Sherman Oaks district.

INTRODUCTION

Water supply system of City of Los Angels were affected by the 1994 Northridge earthquake, which magnitude was Ms=6.8. The epicenter was located at Northridge district of San Fernando valley and the depth was 18 km. Peak accelerations more than 1.0 g were measured at several observation points near the epicenter [1].

The epicenter area is adjacent to that of the 1971 San Fernando earthquake. As the earthquake occurred beneath an urbanized and populated area, there were also a lot of localized damage to other lifeline structures such as a gas supply system, a power supply system, a telecommunication system and a traffic system.

One of the most serious result occurred by the earthquake was a fire and flooded water on Balboa Blvd. It has been pointed out that an interaction between lifelines during an earthquake would become the most important subject. The chaos happened at Balboa Blvd. might be different from the interaction pointed out, however, it implied that we have to consider possible occurrences of similar confusion and scenarios how to cope with the unexpected confusion.

Sixteen breaks of large diameter trunk lines and approximately 1,670 breaks of small diameter distribution pipes and service pipes were occurred. The damage to the trunk lines contains breaks of joints and pipes of an old riveted trunk line buried along Roscoe Street which passes over the epicenter. Other typical damage to the trunk lines were telescopic crashes and failures in tension of welded bell joints due to slight permanent ground movement at Balboa Boulevard.

Most of the breaks of small diameter pipes, distribution pipes, were caused to old and weak gray cast iron pipes connected with sockets and spigot joints, whose flexibility and strength against seismic excitation could not be expected. And the breaks were concentrated in Northridge district including Granada hills, San Fernando district and Sherman Oaks district.

This investigation had been carried out for ten days from March 16 as a part of a study of the research group on 'Seismic Design and Mitigation of Structures at Water Front Area' organized in ADEP. As the investigation team was sent to the interested areas about two months after the earthquake, most of restoration works for the damaged water pipes had been completed. So most of the information described in this paper were offered by engineers of the headquarter and the West and East Valley District Office of LADWP.

WATER SUPPLY SYSTEM OF CITY OF LOS ANGELES

Distribution System

LADWP distributes 2,600,000 m^3 per day to 660,000 meters which are approximately equivalent to 3,600,000 customers [2]. The amount of water has been supplied from three sources which are the Los Angeles Aqueduct derived from Sierra Nevada mountains, ground water of San Fernando

Valley and purchase from the MWD (Metropolitan Water District). Percentage of the sources are 75 %, 15 % and 10 %, respectively.

The location of the aqueducts and reservoirs of LADWP are shown in Fig.1. Total length of distribution pipes is as long as 7,000 miles and their diameters range from 4 to 12 inches. The water gathered from the sources is saved in 107 reservoirs and is distributed by gravity flow or via 85 pump stations to 102 subdivided distribution blocks. The maximum reservoir is the San Fernando Lake, which locates in the north of San Fernando Valley.

The distribution area is subdivided into five districts as shown in Fig.2, which districts are the West Valley, the East Valley, the Western, the Central and the Harbor districts.

Damage to Pipes

Approximately 65 % of 1,670 breaks of the pipes were occurred in the West Valley district and 35 % of that in the East Valley district [3][4]. And most of the damage were concentrated in three areas as shown in Fig.3. About 800 breaks were reported within area A, and 60 in area B, and 360 in area C. The number of the damage to the trunk lines were accumulated to 16 including damage to Granada trunk line at Balboa Blvd.

WEST VALLEY DISTRICT

Distribution System

Figure 4 shows the network of trunk lines of the West Valley district of LADWP. Some of the trunk lines are riveted steel pipe constructed in the 1910's. Some of them are steel pipes with one end of the pipe is flared (bell joint) and the joints are connected with fillet-weld.

The bell joints with fillet weld have been used to reduce construction works and minimize the set-up time of the pipes in the U.S., on the contrary, butt-welded joints have been used for the construction to utilize the strength of steel pipes and survive against various seismic effects in Japan. The distribution pipes are gray cast iron pipes, ductile iron pipes, steel pipes and asbestos cement pipes and percentage of total length are 70-80 %, 15-20 %, 2-3 % and 2-3 %, respectively.

Damage to Pipes

The number of damage to the trunk lines was 16, the distribution pipes 800, and the service pipes 230. Ninety percent of the damage to the distribution pipes were occurred to the gray cast iron pipes having lead or cement caulked joints. There was no damage to the gray cast iron pipes having the joint sealed with a rubber ring because it generates enough bending flexibility of the joint against the ground motion.

The damage to the gray cast iron pipes were reported as breaks of the pipes and slip-out of the joints. The breaks of the pipes were mainly cracks in the circumferential direction and occurred at tapping sleeves for fire hydrants. The damage to the asbestos cement pipes were breaks of pipes

and joints because of their fragility and low strength. The damage to the steel pipes were cracks of welded joints of 45 degree bends. The ductile iron pipes could survive during the earthquake.

Six breaks were occurred to Roscoe trunk line as shown in Fig.4, which was constructed in 1918 and the diameter ranges from 35 to 42 in. The pipes of Roscoe trunk line were connected with rivets both in the circumferential and the longitudinal seams. Some of the damage can be considered as effects of ground deformation as Fig.5 shows cracks near the points on Roscoe St. where the damage were occurred.

Granada and Rinaldi trunk lines were broken in compression and tension at Balboa Blvd. The different kinds of failures of the two trunk lines were occurred at points whose distance was from 80 to 100 ft as shown in Fig.5. Photo 1 shows a compressed welded bell joint taken from Granada trunk line and the length of compression is estimated approximately 1 ft. The distance of the pipes failured in tension was about from 12 to 15 ft apart from each other. Another compressive collapse was reported at a point close to the intersection of Balboa Blvd. and Rinaldi St.

Table 1 shows observed changes of surface along Roscoe St. and related changes of sidewalks near damaged points. The numbers in the table correspond the damage to the pipe from the east to the west. And the street inclines toward the east as shown in the table. We can find obvious relationship between damage to pipes and cracks on the street at four of seven points of the table. We can also observe the cracks at 1/3 of flat point and 3/4 of inclined point. And widths of the opening cracks are from 0.2 to 0.4 in.

Ring supports of another 60 in. diameter trunk line was collapsed to the south of Lower Van Norman lake, which trunk line was constructed in the 1920's. This failure was affected by the link of concrete supports, however, the pipe and the joint themselves were undamaged as shown in Photo 2. It seems to be the most preferable failure mode under the effects of earthquakes.

EAST VALLEY DISTRICT

Distribution System

Steel pipes having diameters ranging from 16 to 60 in. are mainly used for the trunk lines of the East Valley District. The gray cast iron pipes are used for a very small percentage of the trunk lines. Also gray cast iron pipes are used for more than 90 percent of the distribution pipes and their diameters are smaller than 12 in.

The joints of the distribution pipes are lead or cement caulked or sealed with rubber rings. Ductile iron pipes have been used since 1980 instead of the gray cast iron pipes. Copper pipes are used for service pipes.

Damage to Pipes

Damage to the trunk lines were concentrated to the joints of the gray cast iron pipes whose diameter is 24 in. The number of reported damage was five, however, riveted steel pipes buried at the

same area survived and undamaged. Approximately 420 failures of the joints of the gray cast iron pipes were restored. There were no damage to the ductile iron pipes having been laid alongside the damaged gray cast iron pipes. More than 200 failures of the service pipes were reported.

CONCLUDING REMARKS

The damages to the distribution pipes, which diameters are comparatively small, were concentrated to the weak and old gray cast iron pipes having joints with less flexibility and strength. The damage were also concentrated at three areas in San Fernando Valley, where the foundation is soft or the boundary region of hard and soft foundations.

And the damage to Roscoe trunk line were comparatively small although the trunk line is buried just over the epicenter and the strength of the pipes could not have been expected against seismic excitation. On the other hand, the pipes of Granada trunk line and Rinaldi trunk line are connected with welded bell joints, however, there were some failures in compression and tension related to permanent ground deformations. Analytical and experimental studies should be required to estimate the strength of the joint and find out some countermeasures.

The maximum acceleration of ranging from 0.5 to 1.8 g were recorded, however, the damage to pipes or failure rate (number of failures per unit length) were smaller than those reported during past earthquakes. The failure rate of the pipes are equivalent to that have occurred by an earthquake with the magnitude of 0.30 g. Similar tendency of the damage was observed due to the 1993 Kushiro-oki earthquake. These facts may yield a consensus comment on that the seismic design of underground lifeline structures based on ground acceleration should be implemented or revised.

REFERENCES

[1] UCB, "Preliminary Report on the Seismological and Engineering Aspects of the January 17, 1994, Northridge Earthquake," UCB/ERRC-94/01, Jan. 1994.
[2] LADWP, 'Department of Water and Power, City of Los Angeles.'
[3] Lund, L.V., "Northridge Earthquake, January 17, 1994, Lifeline Performance," ASCE Technical Council on Lifeline Earthquake Engineering, 1994.
[4] Edited by Goltz J.D., "The Northridge, California Earthquake of January 17, 1994," Technical Report NCEER-94-0005, Preliminary, March 1994.

ACKNOWLEDGMENT

Most of the data used in this paper have been offered by engineers of LADWP. The authors would like to express their appreciation to Mr. R.L.Simmons and Mr. C.T.Horner of the Head Office of LADWP, Mr. J.A.Castruita and Mr. S.Malinoski of the West Valley District Office, and Mr. M.Lopez and Mr. R.Togazzini of the East Valley District Office.

The authors also wish to express appreciation to Prof. T.D.O'Rourke and Dr. Y.Shiba of Cornell University, Dr. R.T.Eguchi and Dr. J.D.Goltz of EQE International and Mr. J.Ikeda of ADEP for their invaluable advice and comments.

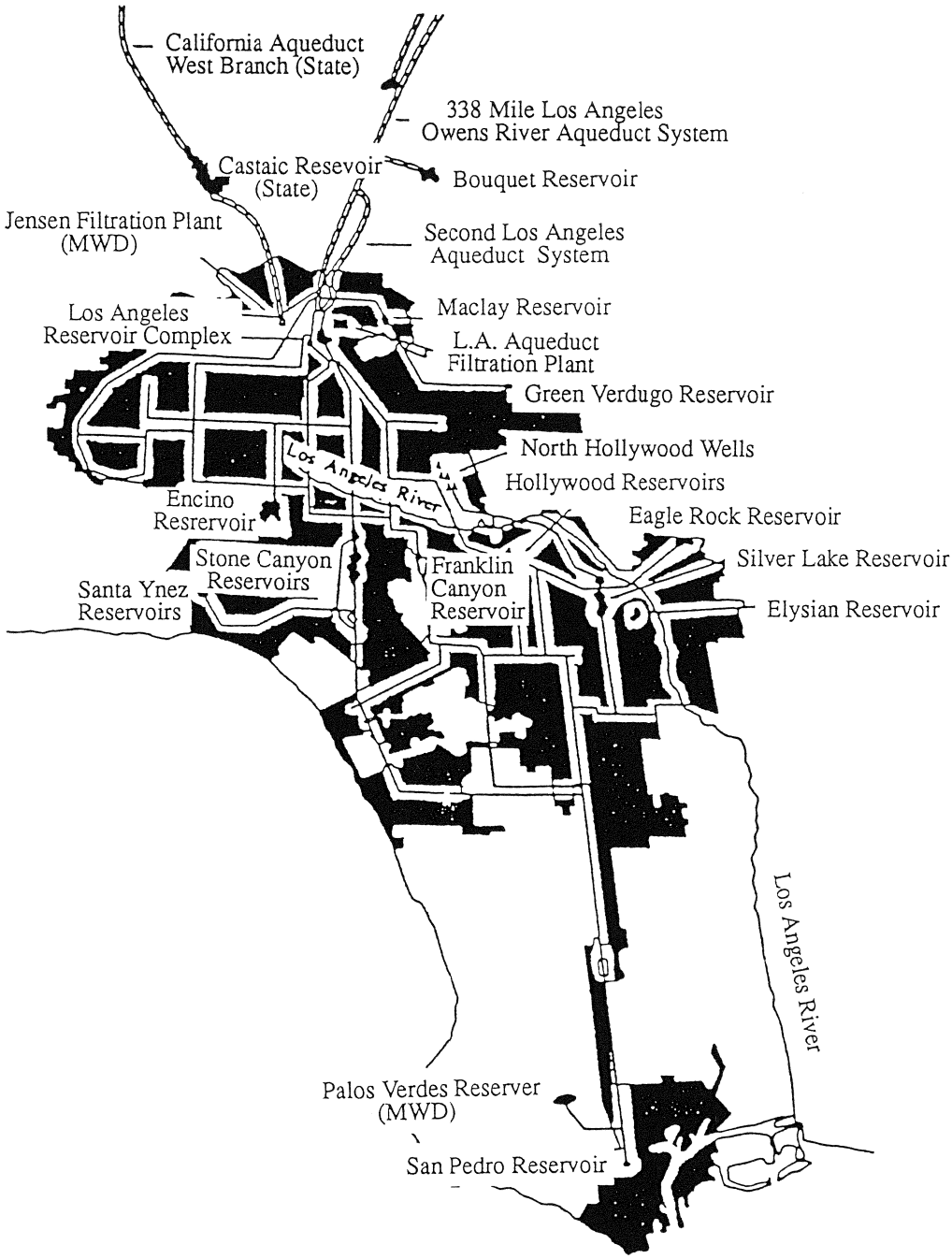

Figure 1 Aqueducts and Reservoirs of LADWP

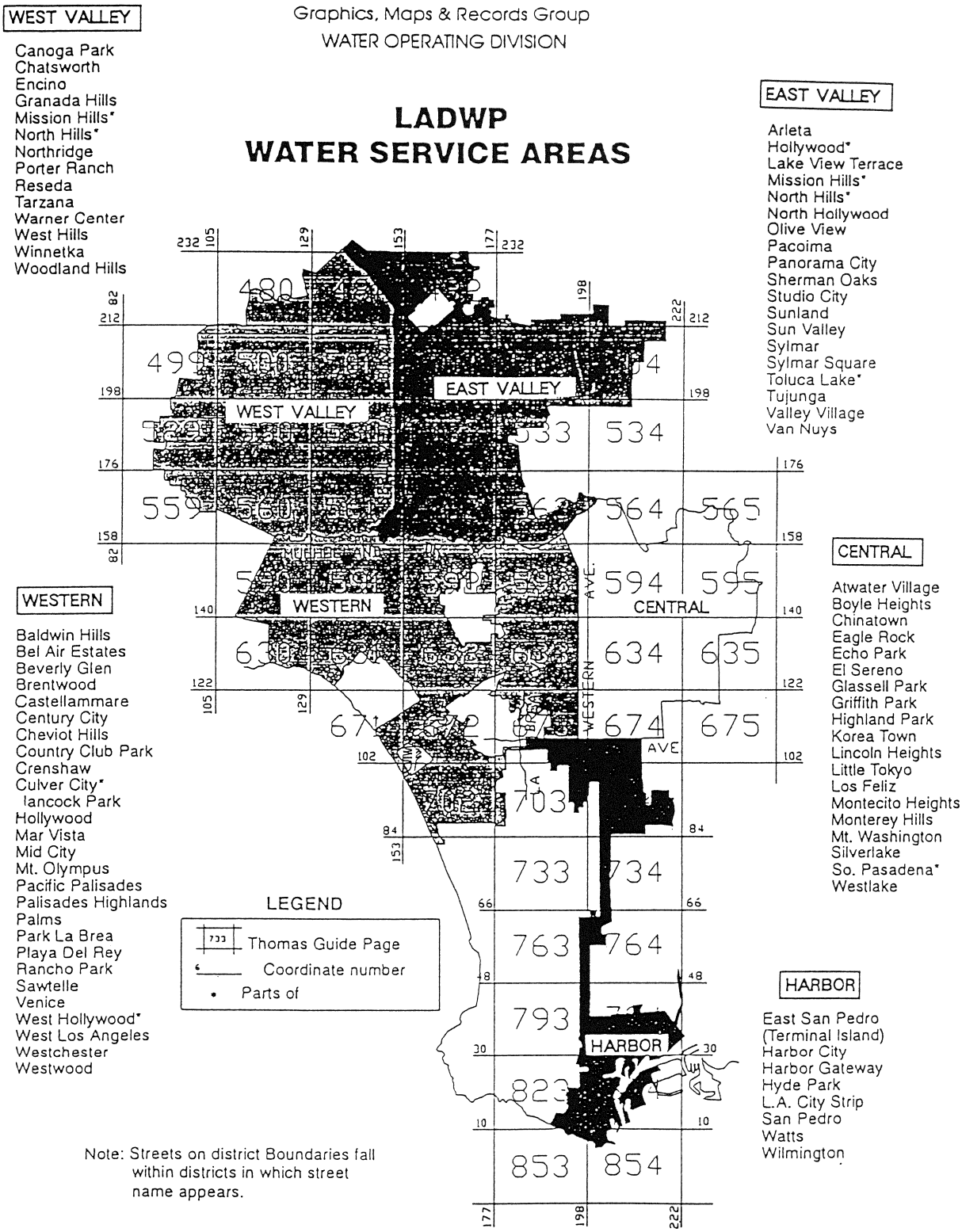

Figure 2 Water Distribution District of LADWP

Figure 3 Concentrated Areas of Damage to Distribution and Service Pipes

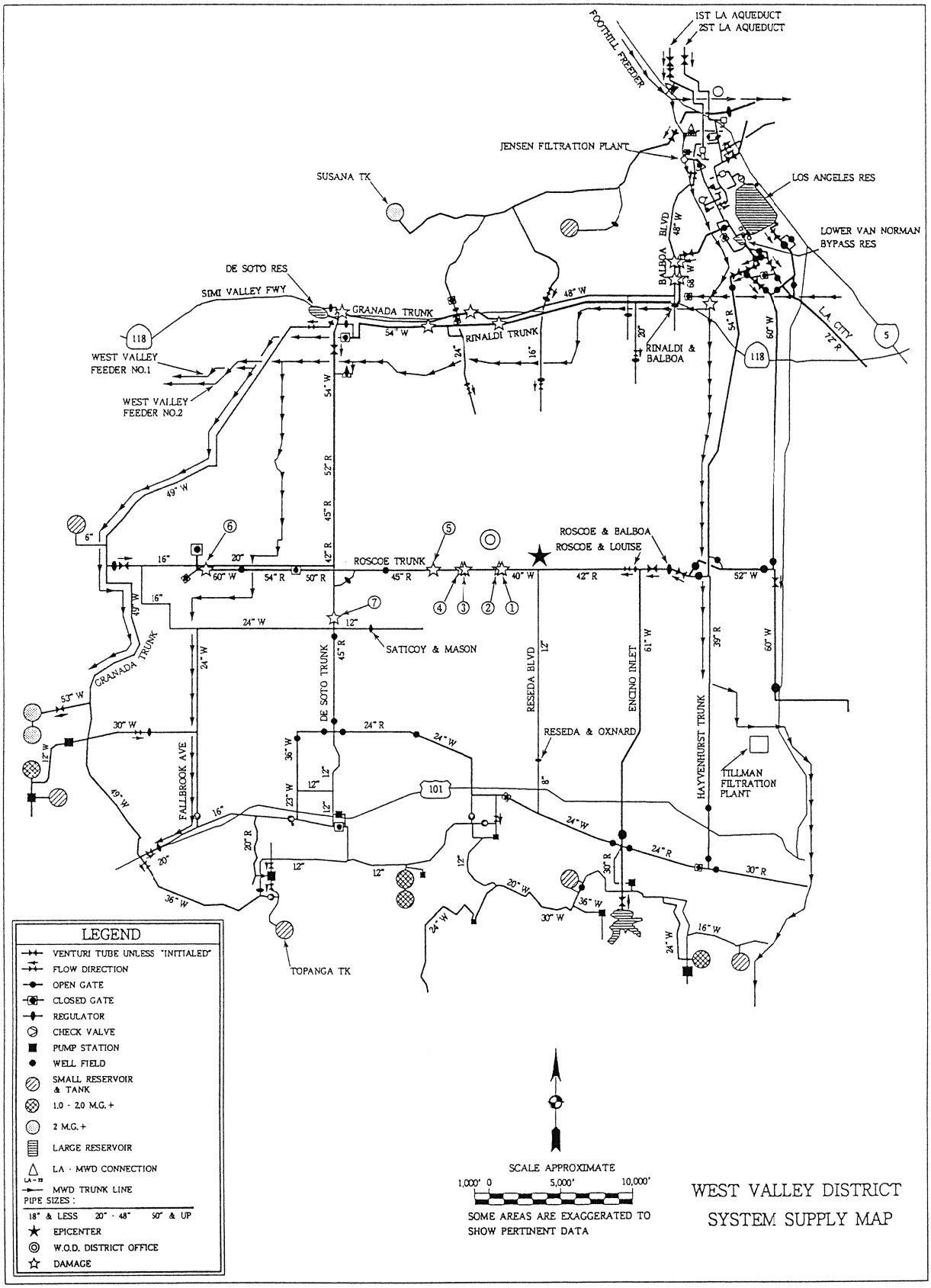

Figure 4 Damage to Trunk Lines at West Valley District

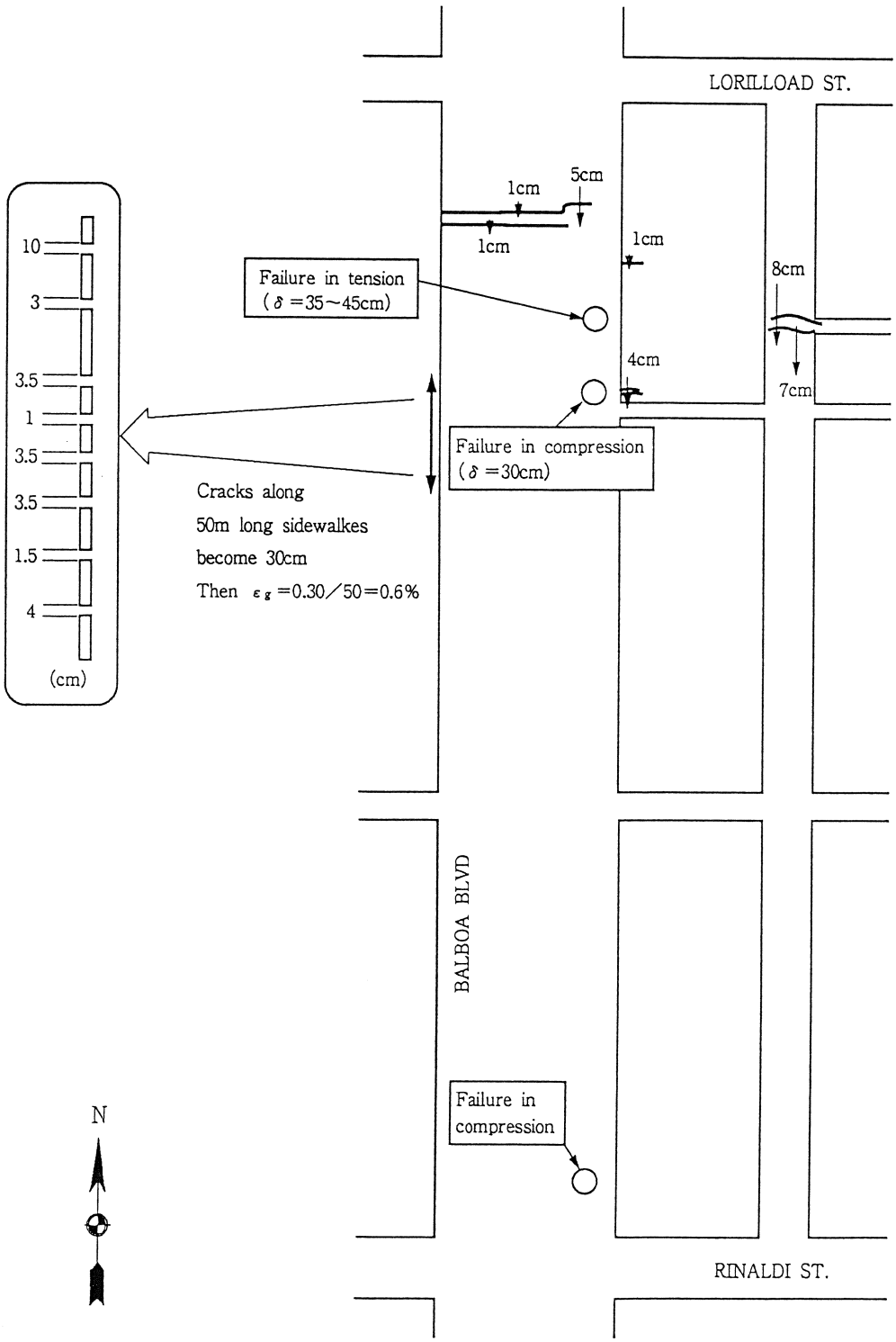

Figure 5 Damage to Trunk Lines at Balboa Blvd. and Permanent Ground displacements

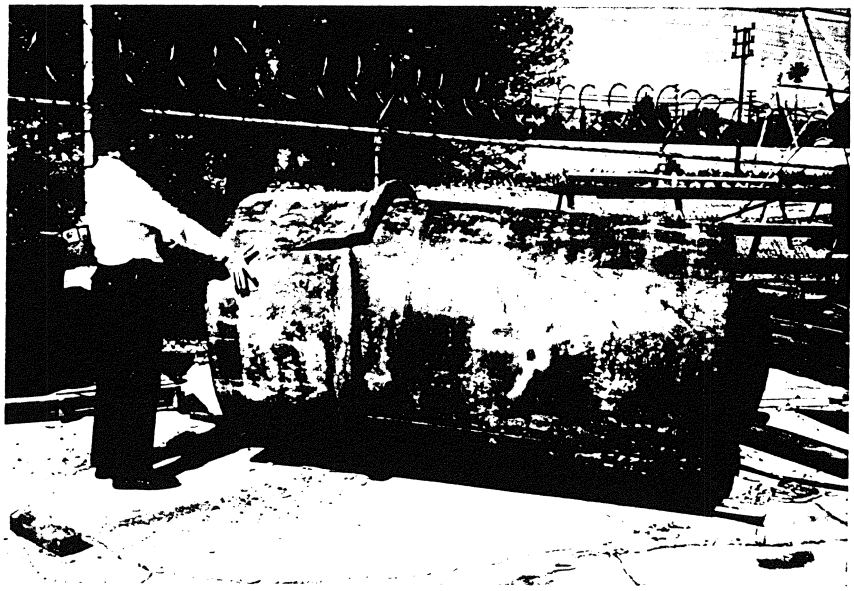

Photo 1 Damage to Granada Trunk Line

Table 1 Fissures Observed Near Damaged Points Along Roscoe Trunk Line

No.	Surface	Changes on Surface	Avenue
1	Flat	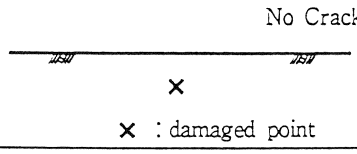	Fallbrook Ave.
2	Flat	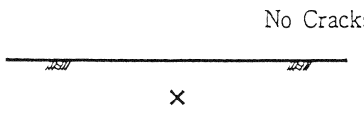	Oakdale Ave.
3	Flat	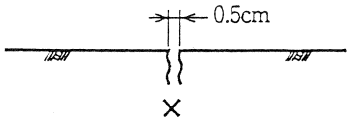	Oakdale Ave.
4	Inclined	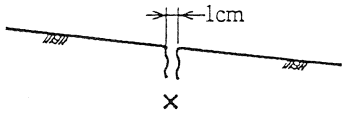	Shirely Ave.
5	Inclined	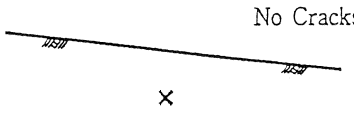	Shirely Ave.
6	Inclined	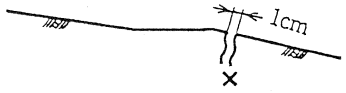	Wilbur Ave.
7	Inclined	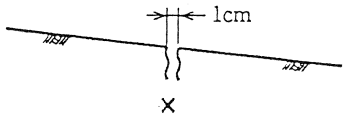	Desoto & Ingomar

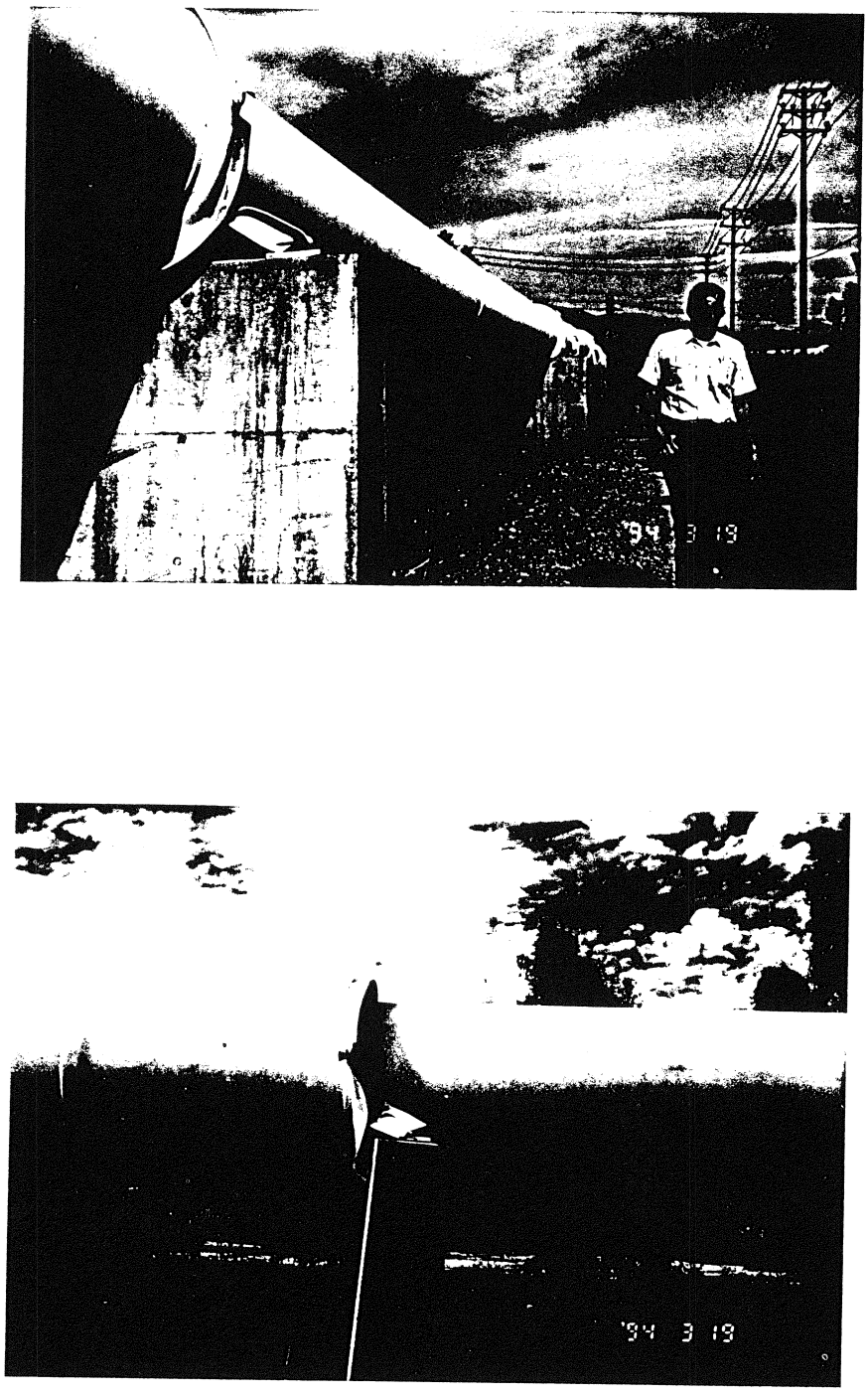

Photo 2 Damage to Trunk Line to the South of Lower Van Norman Lake

VI WORKING GROUP SESSIONS

Report From Working Group No. 1, Modeling Liquefaction and Its Related Ground Deformation
Report From Working Group No. 2, Ground Deformation Response of Lifelines and Underground Structures
Report From Working Group No. 3, Damage Assessment and Hazard Mitigation of Lifeline Networks
Report From Working Group No. 4, Countermeasures and Earthquake Resistant Design

REPORT FROM WORKING GROUP 1

MODELING LIQUEFACTION AND ITS RELATED GROUND DEFORMATION

Group Leaders: Dr. N. Yoshida, Prof. H.E. Stewart, and Prof. T.L. Youd

From Japan:	From United States:		Other International
T. Katada	K. Arulandan	Raman Pichumani	Kay Ahlfield
T. Kawakami	J.P. Bardet	Jean H. Prevost	W.D. Liam Finn
N. Suematsu	Steve Bartlett	Adel (Tony) Saada	Peter K. Robertson
F. Toyota	Steve Dickenson	Sukamnder Singh	
N. Yoshida	Thomas Holzer	Harry E. Stewart	
	Robert Kayen	John C. Tinsley	
	Matthew Mabey	T. Leslie Youd	

SUMMARY

The meeting opened with a presentation of the main results of recent Japanese research. Key areas where their thinking has changed were presented during the workshop. Past thinking was that sloped ground became level following liquefaction, but more recent experimental results indicate that initially sloped ground may retain some degree of sloping following liquefaction. Perhaps previous shaking table experiments involved too much shaking, which was not representative of real conditions. Current thought is that small, unstable regions develop during cyclic loading, which causes lateral spreading, but during continuous shear the strains cause stiffening which limits its deformations preventing the slopes from becoming fully level. The main findings were discussed of the following several groups:

Yasuda and Yoshida have developed experiments and analytical models for soil behavior following liquefaction. These models incorporate large static strain. Low stiffness zones were identified. These zones are affected by the amount of cyclic load, relative density, and perhaps seepage forces.

Kawakami et al. performed experiments in which 1-g models were shaken then tilted. These experiments showed that limited deformation occurred after tilting, but the final surfaces were not level.

Hamada et al. developed a model in which zones of zero stiffness transformed into zones of high stiffness during lateral movement. This model predicts non-level slopes following liquefaction and lateral spreading.

Toyota and Towhata performed 1-g shake-table experiments with impulse and cyclic loadings to study further final surface configurations. Impulse loading resulted in non-level ground and cyclic shaking experiments resulted in level ground.

The recent Japanese findings have emphasized the nature of low stiffness regions and transformation states when large strains are imposed on liquefied soil. These new concepts are very different from the ideas of residual strength.

General Discussion - The primary contributions to the discussion topics are paraphrased below.

Discussion Topic 1: What Do We Know and What Don't We Know About Mechanisms of Liquefaction and Pore Pressure Generation?

We have the least experience with what happens after liquefaction. This is the highest priority topic. Most recent experiments suggest that we should use the new data with existing predictive models. We should concentrate on what we know about liquefaction and how we can get a better handle on it. We have a reasonable handle on the potential for liquefaction, and should focus now on the consequences. It would be good to understand the new material about low stiffness regions and transitional states.

We have poor ability to predict pore pressures for collapse susceptible soils.

What do we know about the mechanisms? We understand the mechanism of pore pressure generation, i.e., disturbance to the ground, related to stresses, strains, energy , leads to a tendency for compaction or compression that leads to development of pore pressures under undrained conditions. We have techniques for predicting pore pressure generation up to near 60 to 80% for material that is not extremely loose. For very loose sands we have a collapse mechanism that is not well understood. We can predict pore pressures for cyclic loading, but our predictions are not so good for sloped ground and flow slides.

Field predictions are limited by heterogeneity.

If the soil is contractive in sloped ground, there can be flow. If the soil is dilative then there will be limited deformation. The ability to predict pore pressure for contractive sands with a single triggering event is uncertain.

This is a question of triggering or non-triggering of a collapsible structure from a single event, which is different than pore pressure buildup resulting from cyclic loading.

For clean sands under known conditions we're OK. Three-dimensional effects and variability in nature are major issues. Analytical models at present cannot represent this complexity.

Soil characterization is complex. We may need to rely on probabilistic modeling of soil properties.

Maybe we just get gross stiffness properties and global characterizations. Until we can understand fundamental mechanisms better we won't make totally accurate field predictions.

We deal with pore pressure as a local condition but we might need to consider it as a bifurcation problem.

Summary of Topic 1 Discussion.

We "know" that we can predict pore pressures reasonably for cyclic loading in a laboratory environment. Field difficulties may be related to site characterizations. Very unstable, structured soils are in a different category, and pore pressure predictions for these soils are difficult. Triggering

mechanisms differ and response may be catastrophic. We "don't know" how to handle unstable structure effects and sudden collapse, or how to deal with nonhomogeneity and proper extrapolation of lab results to more complex field conditions.

Discussion Topic 2: What Do We Know and What Don't We Know About Mechanisms and Prediction of Ground Deformation?

The mechanism for granular soil deformation has been treated as a solid that strain softens during loading to a point where the stress reaches a yield surface. If the soil is contractive, flow deformation will occur. If the material is dilative then after some limiting strain, pore pressures will decrease and motion will stop. Continued deformation occurs as a complex sequence of cycles of softening and stiffening driven by a combination of gravity and inertial forces. How much yielding occurs is a function of density and dilatancy. The Wildlife site provides a good model for understanding how ground motions and pore pressures interact and how deformations accumulate.

The amplitude of motion should be small after shaking stops.

We know that horizontal deformations occur during and after the earthquake.

Do we know how to include rate effects? How do we include diffusion and distribution of pore pressure with time because deformations occur, in some cases, long after the earthquake? During large shear strains there is dilation, and in the field water will be sucked toward the dilating zone. For large field strains how do we use lab results? Granular soils in the field are not truly undrained, so how do undrained lab tests apply?

Summary of Topic 2 Discussion.

We "know" that horizontal deformations occur during and after the earthquake. Also, lab tests seem consistent with respect to dilatancy stiffening at large strains. We "don't know" the point at which the material softens sufficiently to initiate motion, perhaps a pore pressure ratio of 70%, as suggested previously. What is the role of pore pressure diffusion in time dependency? How do we include strain dilatancy and locking into simplified predictive methods like Newmark analyses? How do we evaluate volumetric strain in the field? Post-liquefaction compressibilities are very different. How do we reconcile lab data? For example, how do we relate laboratory tests, that are usually fully undrained, to field behavior, that may respond to a variety of drainage possibilities?

Discussion Topic 3: What New Research Tasks Are Needed to Improve Our Knowledge to be Able to Answer the Questions Listed Above?

What about properties of liquefied soil? What do we know about residual strength?

Almost nothing. It has such a wide range and has very different definitions.

Are embankment residual strengths the same as those that might develop in lightly sloping ground? The stress conditions are very different for these cases.

Two important issues are how to characterize the sites, and how to predict deformations that occur during and after earthquakes.

We need to develop indices to quantify the severity of liquefaction, since properties can be influenced by post-liquefaction conditions. This is particularly evident in terms of continued straining after soil has become liquefied, and the transition from low to higher stiffness zones as a result of large deformations.

We need to develop a common code for practitioners to use.

The best route is to know whatever code you have, that is select one and stick to it. One can get consistent answers with many codes, as long as you know how to select the properties for that program.

Water velocities are important. Seepage and drainage patterns can affect the buildup and dissipation of pore pressures, and may effect the magnitude of lateral movements.

Post-liquefaction studies in the lab should be continued, but should include varying levels of static shear. They should include large strain. We need detailed analytical studies of lateral spread to see if we can predict what happened. We need to continue fundamental analytical studies.

We need more investment in characterizing lateral spreads. This would be a good area for continued U.S.-Japan cooperation.

We need more information on the influences of silt content on soil behavior, and the nature of the silt, including plasticity and varying grain size distribution. The influence of texture needs to be extended to include gravely soils as well.

Is maximum acceleration a meaningful parameter? Maybe a more useful index is energy input. How do we apply lab data to field conditions? Present numerical models seem OK for certain problems, but new ways are needed to handle the complexities of liquefaction. For example, two-phase instabilities cannot be modeled presently. Do we understand microscopic effects? What do we mean by "undrained" problems?

Residual strengths are uncertain. Back-calculated values have high uncertainty. We need to separate gravity and inertial components of motion. We may need to consider statistical characterization of sites.

Comparisons between measured response at instrumented sites and analytical predictions are important.

Summary of Topic 3 Discussion.

Residual strength concept in terms of actual soil behavior may be applied incorrectly for shallow slopes. Very flat ground and more steeply sloping ground (i.e., embankments) have very different stress conditions, which lead to different mobilized strengths. We need to develop reasonable engineering methods and appropriate "strengths" for predicting deformations, as they are used in practice now.

REPORT FROM WORKING GROUP 2
GROUND DEFORMATION RESPONSE OF LIFELINES AND UNDERGROUND STRUCTURES

Group Leaders: Dr. G. Martin and Dr. F. Miura

From the U.S.	From Japan	Other International
P. Constantine	T. Iwatate	R. Flores
R. Gailing	S. Sakhai	
D. Honegger	Y. Shiba	
D. Lau	K. Wakamatsu	
C.H. Lee		
J. McNorgan		
S. Musser		
M. O'Rourke		

SUMMARY

The charge to the Working Group was as follows: "Evaluate what we currently know, what we currently do not know, and what we should know".

The working group activity began with brief presentations on the current state-of-the-art with respect to pipelines, piles and tunnels. These presentations and observations by the working group members led to the following summaries for pipelines and piles.

Pipelines

It was the group view that "what we currently know" regarding pipeline response to permanent ground deformation (PGD) could be summarized as follows:

- Soil structure interaction for pipelines in non-liquefied ground (i.e., pipeline located in competent soil above a layer which liquefied) is well established. There has been recent progress in determining appropriate load deformation relations for pipelines in liquefied ground. However, the procedures are not, as yet, well established.

- Analytical procedures utilizing computer models for pipeline response to PGD are commonly used in practice. Analytical procedures utilizing closed form solutions (i.e., hand calculations) are available for many situations. However, for some, particularly involving segmented pipe, closed form solutions are currently not available. At present, there is a lack of verification of these procedures, either computer or closed form, using case history benchmarks or full scale laboratory tests.

- Failure criteria for modern welded steel pipe are fairly well established. Appropriate failure criterion for segmented pipe is not as well established and may be characterized as "spotty".

Based on what the group felt is currently known, a list in priority order of what is needed (i.e., "what we currently do not know and should know") was developed as follows:

- Verify existing analytical relations and failure criteria with benchmark case histories and/or full scale laboratory tests.

- Establish failure criteria for old steel pipe welds in tension and quantify variability of weld quality.

- For steel pipe which has wrinkled due to longitudinal compression, quantify the additional strain or deformation along the wrinkling zone which results in tearing of the pipe wall.

- For large diameter concrete pipe, established failure criteria for crushing at the joints due to longitudinal compression.

- Establish the force-deformation and moment-rotation characteristics for segmented pipe joints.

- Establish failure criteria for plastic gas distribution pipe.

Piles

The working group felt that the state-of-knowledge (i.e., "what we currently know") for the seismic behavior and design of piles is well established for everything except piles subject to PGD.

The following lists in priority order "what we currently do not know and should know.

- Quantify the reduction factor (i.e., load deformation relation at the liquefied soil/pile interface) in terms of realistic design parameters.

- Quantify through laboratory or numerical studies "group" or "pile cap" effects for piles subject to PGD.

- Evaluate through full scale testing the effectiveness of flexible pile joints, and determine pile moment-curvature relations where this information is unknown.

Geotechnical Inputs

The group felt that certain characteristics of permanent ground deformation were currently ill defined. Listed below are the types of information needed for analysis, evaluation, and design of buried facilities.

- Given a map of expected PGD (in feet or meters), what is the likely number of separate isolated PGD zones.

- Given a map of expected PGD (in feet or meters), what is the expected spatial extent (i.e., length and width) of separated, isolated PGD zones.

- For a given zone of PGD as shown in Fig. A, what is the relative likelihood of abrupt offsets at the margin (see. Fig. B) versus distributed ground movements across the zone (see Fig. C).

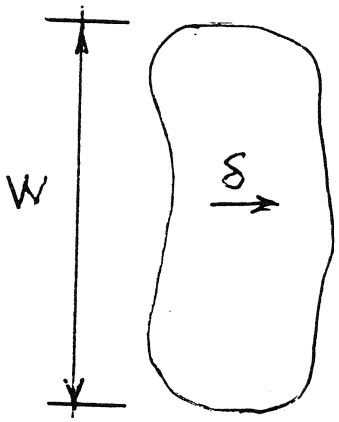

Fig. A
Isolated PGD zone with width W & maximum ground movement δ

Fig. B
Uniform PGD of amount δ across width (i.e. abrupt offset at margin)

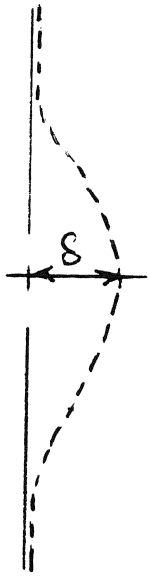

Fig. C
Non uniform PGD across zone

REPORT FROM WORKING GROUP 3
DAMAGE ASSESSMENT AND HAZARD MITIGATION OF LIFELINE NETWORKS

Group Leaders: Dr. R. Eguchi and Dr. I. Katayama

From the U.S.	From Japan	Other International
D. Ballantyne	K. Kubo	J. Murria
W. Savage		D. Lau
T. Kano		
A. Schiff		
S. Glaser		
L. Lund		
H. Hwang		
E. Keane		
C. Scawthorn		

SUMMARY

The Group reviewed the three questions presented in the guidelines for group activities: 1) What do we know?; 2) What don't we know?; and 3) What activities should we be engaged in for the next several years to enhance mitigation of earthquake hazards for lifeline networks? Following an extended discussion, the Group concluded:

1. What do we know?

a. Recent past earthquakes have permitted collection of valuable data and experience on performance. These events have included the Kushiro-oki, Hokkaido-nansei-oki and Northridge earthquakes. However, information about the system response and restoration are generally not available. Electric power, gas, sewage, etc. agencies are separated in exchanging their experiences. Little effort has been made to collect and develop databases of experiences in Japan. In the U.S., more effort has been made, notably by TCLEE for underground pipe in the Loma Prieta earthquake, but more could be done.

b. The primary modes of damage for buried facilities have been identified as associated with permanent ground deformations (PGD). We have general knowledge regarding liquefaction hazard, modes, and areas for western U.S. and Japanese cities. Quantification of PGD is still difficult.

c. While much remains to be done in quantifying hazards and lifeline network analysis methods, a spectrum of mitigation techniques is available, including strengthening of facilities, reduction in liquefaction potential via soil improvement or other techniques, and development of enhanced network performance via redundant links and nodes, emergency, response and recovery planning, etc.

2. What don't we know?

a. The primary need is for consistent and complete quantified mapping of PGD hazards. Specifics include (i) areal extent, (ii) distribution of PGD (quantified fields), (iii) lurching probability, and (iv) ridge shattering. Techniques to accomplish this are data intensive, and methods for efficient collection and analysis of requisite data are needed. GIS technology offers some assistance in this area, but geotechnical engineering needs to develop better methods.

b. Researchers need more interaction and information from system operators. Communications and involvement of system operators in lifeline earthquake engineering is sparse. This includes system response and restoration data.

3. What activities should we be engaged in for the next several years, to enhance mitigation of earthquake hazards for lifeline networks?

a. Encourage GIS (Geographic Information Systems) methods for data collection and analysis. Additionally, explore applications of GPS (Geographic Positioning Systems) for mapping of ground deformations.

b. Increase involvement of lifeline operators, and institutionalize damage assessment, ground characteristics, and failure mapping program within lifeline organizations. This should include involvement of utility owner associations and development of standardized data protocols.

c. Engage in technology transfer, in usable formats, to lifeline organizations. This needs substantial interaction between researchers and lifeline organizations to determine their needs, appropriate formats for effective communications, etc.

d. Address methods for extending the life of buried pipelines. This need is associated with the finding that most damage to buried pipe is associated with older pipe, often poorly welded. Rather than a major replacement program, ways of repairing welds in-situ, lining pipes in-situ, or other technologies should be explored, since similar techniques are presently being employed for re-lining of water pipe, etc.

Lastly, the Group suggested that the organizers of the workshop focus on:

a. Encouraging attendance and participation of lifeline operators and organizations.

b. Several sessions be devoted to lifeline end-user applications.

c. Several sessions be devoted to data collection and mapping, particularly applications of GIS and GPS technologies.

REPORT FROM WORKING GROUP 4
COUNTERMEASURES AND EARTHQUAKE RESISTANT DESIGN

Group Leaders: Dr. G. Martin and Mr. S. Yasuda

From the U.S.

David Baska
Peter Byrne
Shah Vahdani
Kyle Rollins
Carlos Braccros
Darin Sjoblom
James Golden
Ahmed Elgamal
Stephen Dickenson
Abbas Abghari

From Japan

Hiroshi Sato
Susumu Okada
Ryoji Isoyama
Ikuo Towhata

SUMMARY

Following introductions by the Group Leaders, the workshop session commenced with brief presentations by several participants on various aspects of the countermeasure problem.

A description was given of remediation options for stabilizing a new construction site at the Port of Seattle. Because of the high fines content and to minimize costs, a timber pile reinforcement scheme at the toe of a wharf slope was adopted. No densification was assumed and reinforcement was used to minimize lateral spread potential.

A retrofit remediation plan was discussed for approach spans of a bridge over the Fraser River in Vancouver. Analyses indicated as much as two meters of liquefaction induced horizontal displacement of pile supported piers during the design earthquake. The proposed remediation plan entailed the construction of a densified "donut" around each pier using vibroreplacement. Design concerns included the potential migration of high pore water pressure from adjacent liquefied zones into the densified zone, and the extent of protection the densified donut provided to prevent liquefaction beneath pile tips.

A case history was presented about soil performance at Treasure Island during the Loma Prieta earthquake. It was observed that an area treated with vibroreplacement performed well in comparison to nearby non-treated areas.

A discussion ensued on bridge sites in Costa Rica during the 1992 earthquake, where in some cases, several meters of lateral spread of approach embankments occurred. However, only limited movement of piers supporting abutments occurred. The question

was posed, "can computer codes match observed performance"? The need for good soil data at such sites for analysis purposes was noted and also the difficulties and expense of obtaining such data. With respect to dynamic compaction, needs were emphasized for improved methods for estimating increases in density utilizing deep dynamic compaction and the possible use of deacceleration measurements for this purpose.

Problems were discussed associated with potential liquefaction of oil tanks constructed in Japan before 1985. Tanks built after 1985 required ground remediation before construction, whereas many tanks before 1985 were sited on potentially liquefiable soils. Details of ongoing research on a variety of retrofit options were presented. Research included centrifuge model tests, where it had been observed that liquefaction was not induced directly below tanks but occurred outside the perimeter of the tank, leading to lateral spread. Retrofit criteria included the avoidance of oil leakage and the desire to keep post liquefaction settlement less than 1% of the tank diameter. The pros and cons of retrofit options, including gravel drains, sheet pile rings, underpinning, grouting, and dewatering were presented and discussed.

The mitigation of liquefaction hazards at California bridge sites was discussed. In particular, the need for improved soil-struction interaction analyses for the case of foundations supported by ductile piles, where the piles extended through liquefiable sand layers into denser sands. The question of post liquefaction stiffness and residual strength as related to p-y curves for liquefied soils has yet to be finally resolved. Proposals for centrifuge tests at UC-Davis and analytical methodologies to address these problems were described.

The increasing levels of peak acceleration being observed in recent earthquakes and the effect on liquefaction evaluations utilizing the Seed simplified approach was discussed. It was noted that a new text on "Remedial Treatment of Liquefiable Soils" was published in 1993 by the Japanese Society of Soils Mechanics and Foundation Engineering. An English version is scheduled to be published in 1995.

Following the above presentations, discussion ensued on what we know, what we do not know, and how do we improve our knowledge with respect to countermeasures. It was observed that in past U.S./Japan Workshops the emphasis was primarily on site remediation methods and countermeasure case histories. Whereas site remediation methods are generally well established and countermeasure case histories are increasing as a result of recent earthquakes, it is clear that more concern and interest is now being directed toward the problem of retrofit of existing structures where liquefaction problems are present. Because of the difficulties of retrofit involving ground remediation and the need to optimize cost, increasing attention is being paid to performance criteria, i.e., how much deformation can a structure tolerate from a lateral spread. In addition, there is increasing interest in structural design of foundation systems as a countermeasure technique, such as the design of ductile piles and the use of large diameter piles to resist deformation. With respect to the latter problems and the retrofit of existing structures, the following research needs were summarized by the working group:

1) The development of an improved mechanistic understanding of the performance of various countermeasure methods, such as the use of densification "donuts".

2) The development of improved analytical methods to assess lateral spread deformations and soil structure interaction with liquefied soil for existing structures, with an emphasis on simplifications related to design needs.

3) The need for validation of design methods through either/or instrumented sites and centrifuge model tests.

4) The need for improved understanding of the behavior of very silty sands or sandy silts with respect to liquefaction potential and the development of improved ground remediation techniques.

5) Further, detailed case histories of structures which have successfully or unsuccessfully resisted earthquake loading.

6) Further studies of the potential applications and design approaches utilizing compaction grouting and blasting techniques.

7) Continued research on improving in-situ testing techniques for evaluation of ground densification.

VII WORKSHOP PARTICIPANTS

LIST OF PARTICIPANTS

A. Abghari
California Department of
Transportation
Office of Geotechnical Engineering
5900 Folsom Blvd.
Sacramento, CA 95819
Tel. 916-227-7165
Fax. 916-227-7244

K. Ahlfield
BC Hydro
Hydroelectric Engineering Division
6911 Southpoint Drive, Podium A02
Burnaby, BC V3N 4X8
CANADA
Tel. 604-528-2403
Fax. 604-528-1940

K. Arulanandan
Department of Civil Engineering
University of California
Bainer Hall
Davis, CA 95616
Tel. 916-752-0895
Fax. 916-752-8924

D. Ballantyne
Associate
Dames & Moore
2025 1st Avenue, Suite 500
Seattle, WA 98121
Tel. 206-728-0744
Fax. 206-727-3350

J. Bardet
Department of Civil Engineering
University of Southern California
Los Angeles, CA 90089-2531
Tel. 213-740-0608
Fax. 213-744-1426

S. Bartlett
Westinghouse Savannah River Co.
Environmental Restoration
1995 So. Centennial Blvd.
Aiken, SC 29802
Tel. 803-644-6774
Fax. 803-644-6922

D. Baska
Hart Crowser, Inc.
1910 Fairview Avenue East
Seattle, WA 98102-3699
Tel. 206-324-9530
Fax. 206-328-5581

J. Bischoff
State of Utah
Department of Transportation
Research & Development
Geotechnical Division
4501 South 2700 West
Salt Lake City, UT 84119-5998
Tel. 801-965-4568
Fax. 801-965-4796

C. Braceras
Value Engineer, Manager
Engineering Services
State of Utah
Department of Transportation
4501 South 2700 West
Salt Lake City, UT 84119-5998
Tel. 801-965-4234
Fax. 801-965-4564

P. Byrne
Professor
Department of Civil Engineering
2324 Main Mall
Vancouver, B.C. V6T 1Z4
CANADA
Tel. 604-822-2637
Fax. 604-822-6901

D. Chaudhuri
School of Civil and
Environmental Engineering
Cornell University
Hollister Hall
Ithaca, NY 14853-3501
Tel. 607-255-3365
Fax. 607-255-9004

M. Christenson
Kleinfelder
2749 East Parley's Way
Suite 100
Salt Lake City, UT 84109
Tel. 801-466-6769
Fax. 801-466-6788

D. Christenson
State of Utah
Department of Transportation
Structures Division
4501 South 2700 West
Salt Lake City, UT 84119-5998
Tel. 801-965-4000
Fax. 801-965-4338

P. Constantine
Southern California Gas Company
555 West Fifth Street
Los Angeles, CA 90013-1011
Tel. 213-244-5414
Fax. 213-244-8202

R. Cook
State of Utah
Department of Transportation
4501 South 2700 West
Salt Lake City, UT 84119-5998
Tel. 801-965-4000
Fax. 801-965-4338

A. Dargush
Assistant Director for Research
and Education
National Center for Earthquake
Engineering Research
State University of New York
at Buffalo
Red Jacket Quadrangle
Box 610025
Buffalo, NY 14261-0025
Tel. 716-645-3391
Fax. 716-645-3399

S. Davis
Senior Engineer
Kleinfelder
2749 East Parley's Way
Suite 100
Salt Lake City, UT 84109
Tel. 801-466-6769
Fax. 801-466-6788

S. Dickenson
Department of Civil Engineering
Oregon State University
Apperson Hall, Room 202
Corvallis, OR 97331
Tel. 503-737-3111
Fax. 503-737-3052

J. Egan
Geomatrix Consultants
100 Pine Street, 10th Floor
San Francisco, CA 94111
Tel. 415-434-9400
Fax. 415-434-1365

R. Eguchi
Vice President
EQE International
18101 Von Karman Ave, St. 400
Irvine, CA 92715
Tel. 714-833-3303
Fax. 714-833-3391

A. Elgamal
Associate Professor
Department of Civil and
Environmental Engineering
Rensselaer Polytechnic Institute
Troy, NY 12180-3590
Tel. 518-276-2836
Fax. 518-276-4833

J. Figueroa
Department of Civil Engineering
Case Western Reserve University
10900 Euclid Avenue
Cleveland, OH 44106-7201
Tel. 216-368-6247
Fax. 216-368-5229

L. Finn
Department of Civil Engineering
The University of British Columbia
2324 Main Mall Room 2010
Vancouver, B.C.
V6T 1Z4 CANADA
Tel. 604-822-2637
Fax. 604-822-6901

R. Flores-Berrones
Mexican Institute of Water Technology
Bahia de Ballenas #49
Col. Veronica Anzures
Mexico, D.F. 11300
Tel. 73-208-671 ext. 760
Fax. 73-194-341

R. Gailing
Southern California Gas Company
555 W. Fifth Street
Los Angeles, CA 90013-1011
Tel. 213-244-5404
Fax. 213-244-8202

C. Garris
Woodward-Clyde Consultants
8925 Union Park Center
Suite 110
Midvale, UT 84047
Tel. 801-561-0447

S. Glaser
Colorado School of Mines
Division of Engineering
Golden, CO 80401
Tel. 303-273-3961
Fax. 303-273-3602

J. Golden
Assistant Chief Structural Engineer
State of Utah
Department of Transportation
Structures Division
4501 South 2700 West
Salt Lake City, UT 84119-5998
Tel. 801-965-4191
Fax. 801-965-4796

M. Grigoriu, Professor
School of Civil and
Environmental Engineering
367 Hollister Hall
Cornell University
Ithaca, NY 14853-3501
Tel. 607-255-3334
Fax. 607-255-9004

M. Hamada
Department of Civil Engineering
Waseda University
3-4-1- Ohkubo
Shinjiuki-Ku
Tokyo, JAPAN 101
Tel. 03-3203-4141 ext. 73-3522
Fax. 03-3208-0349

D. Hawks
State of Utah
Department of Transportation
Research Division
4501 South 2700 West
Salt Lake City, UT 84119-5998
Tel. 801-965-4000
Fax. 801-965-4338

H. Hayashi
Disaster Prevention Research Institute
Kyoto University
Gokasho, Uji, Kyoto, 611
JAPAN
Tel. 0774-32-3111 ext. 3251
Fax. 0774-31-8294

T. Holzer
United States Geological Survey
345 Middlefield Rd., MS 977
Menlo Park, CA 94025
Tel. 415-329-5637
Fax. 413-329-5143

D. Honegger
EQE Engineering
18191 Von Karman, St. 400
Irvine, CA 92715
Tel. 714-833-3303
Fax. 714-833-3392

D. Horns
Kleinfelder
2749 East Parley's Way
Suite 100
Salt Lake City, UT 84109
Tel. 801-466-6769
Fax. 801-466-6788

H. Hwang
Professor
Center for Earthquake Research
and Information
University of Memphis
3890 Central Avenue
Memphis, TN 38152
Phone: 901-678-4830
Fax: 901-678-4734

M. Hylland
Utah Geological Survey
2303 South Foothill Drive
Salt Lake City, UT 84109
Tel. 801-467-7970

S. Iai
Port & Harbor Research Institute
3-1-1 Nagase,
Yokosuka, Kanagawa 239
JAPAN
Tel. 0468-44-5028
Fax. 0468-44-4095

R. Isoyama
Japan Engineering Consultants Co., Ltd.
5-33-11 Hon-cho
Nakano-Ku, Tokyo
JAPAN
Tel. 03-5385-5111
Fax. 03-5385-8520

T. Iwatate
Professor
Department of Civil Engineering
Tokyo Metropolitan University
Minami-Osawa 1-1
Hachioji City, Tokyo, 192-03
JAPAN
Tel. 0426-77-2946
Fax. 0426-77-2772

K. Jackura
Senior Engineer
California Department of Transportation
Office of Geotechnical Engineering
5900 Folsom Boulevard
Sacramento, CA 95819
Tel. 916-227-7165
Fax. 916-227-7244

T. Jensen
State of Utah
Department of Transportation
Maintenance Division
4501 South 2700 West
Salt Lake City, UT 84119-5998
Tel. 801-965-4000
Fax. 801-965-4338

W. Juszack
Division of Facilities
Construction & Management
Department of Administrative Services
4110 State Office Building
Salt Lake City, UT 84114
Tel. 801-538-3292
Fax. 801-538-3378

T. Kano
Salt Lake County Public Works
Operations Division
7125 South 600 West
PO Box 308
Midvale, UT 84047
Tel. 801-562-6490
Fax. 801-562-6470

T. Katada
Department of Civil Engineering
Musashi Kogyo University
1-28-1 Tamazutsumi
Setagaya-Ku, Tokyo 158
JAPAN
Tel. 03-3703-3111 ext. 3244
Fax. 03-5707-2202

I. Katayama
Advanced Engineering Operation Center
Tokyo Electric Power Service Co.
TEPSCO Ueno-center
3-3 Higashi-Ueno, Taito-Ku,
Tokyo, 110 JAPAN
Tel. 03-5818-7790
Fax. 03-5818-7608

T. Kawakami
Department of Civil Engineering
Tokai University
3-20 Orido, Shimizu, Shizuoka, 424
JAPAN
Tel. 0543-34-0411
Fax. 0543-34-5095

R. Kayen
United States Geological Survey
345 Middlefield Road, MS 999
Menlo Park, CA 94025
Tel. 415-354-3036
Fax. 415-354-3191

E. Keane
State of Utah
Department of Transportation
Geotechnical Division
4501 South 2700 West
Salt Lake City, UT 84119-5998
Tel. 801-965-4000
Fax. 801-965-4338

H. Kirkham
State of Utah
Department of Transportation
Construction Division
4501 South 2700 West
Salt Lake City, UT 84119-5998
Tel. 801-965-4000
Fax. 801-965-4338

D. Krueger
Centennial Engineering, Inc.
310 East 4500 South
Suite 200
Salt Lake City, UT 84107
Tel. 801-268-9805
Fax. 801-268-2736

K. Kubo
Association for the Development
of Earthquake Prediction
3 Kanda Mitoshiro-cho
Chiyoda-Ku, Tokyo 101
JAPAN
Tel. 03-3295-1966
Fax. 03-3295-1996

F. Kulhawy
School of Civil and Environmental
Engineering
Cornell University
263 Hollister Hall
Ithaca, NY 14853-3501
Tel. 607-255-4820
Fax. 607-255-9004

D. Lau
Department of Civil and
Environmental Engineering
Carleton University
3432 C.J. Mackenzie Bldg.
1125 Col. By Drive
Ottawa, K1S 5B6, Ontario
CANADA
Tel. 613-788-5784
Fax. 613-788-3951

C. Lee
Pacific Gas and Electric Co.
123 Mission Street, Room 1165
Mail Code H11A, PO Box 770000
San Francisco, CA 94177
Tel. 415-973-5179
Fax. 415-973-4463

L. Lund
Civil Engineer
3245 Lowry Road
Los Angeles, CA 90027
Tel. 213-664-4432

M. Mabey
Geotechnical Earthquake Specialist
Oregon Dept. of Geology and Mineral Industries
Suite 965
800 NE Oregon St. Box #28
Portland, OR 97232
Tel. 503-731-4100
Fax. 503-731-4066

D. Marble
Utah Division of Water Rights
1636 West North Temple, Suite 220
Salt Lake City, UT 84116-3156
Tel. 801-538-7376
Fax. 801-538-7467

G. Martin
Research Professor
University of Southern California
Department of Civil Engineering
3620 South Vermont Avenue, KAP-210
Los Angeles, CA 90089-2531
Tel. 213-740-9124
Fax. 213-744-1426

L. McCall
School of Civil and Environmental Engineering
265 Hollister Hall
Cornell University
Ithaca, NY 14853-3501
Phone: 607-255-7511
Fax: 607-255-9004

P. McDonough
Mountain Fuel Supply Co.
180 East First South
P.O. Box 11368
Salt Lake City, UT 84139
Tel. 801-539-3499
Fax. 801-539-3345

J. McNorgan
Staff Supervisor Pipeline Design
Engineering and Operations Support
Southern California Gas Company
Box 3249 ML2OEO
Los Angeles, CA 90051-1249
Tel. 213-244-5540
Fax. 213-244-8201

R. Miller
State of Utah
Department of Transportation
Construction Division
4501 South 2700 West
Salt Lake City, UT 84119-5998
Tel. 801-965-4000
Fax. 801-965-4338

F. Miura
Professor
Department of Computer Science
and Systems Engineering
Faculty of Engineering
Yamaguchi University
Tokiwadai, UBE, Yamaguchi, 755
JAPAN
Tel. 0836-35-9483
Fax. 0836-35-9483

M. Miyajima
Department of Civil Engineering
Kanazawa University
2-40-20 Kodatsuno, Kanazawa 920
JAPAN
Tel. 0762-34-4656
Fax. 0762-34-4644

J. Moffat
State of Utah
Department of Transportation
Construction Division
4501 South 2700 West
Salt Lake City, UT 84119-5998
Tel. 801-965-4000
Fax. 801-965-4338

P. Mohanty
State of Utah
Department of Transportation
Roadway Design Division
4501 South 2700 West
Salt Lake City, UT 84119-5998
Tel. 801-965-4000
Fax. 801-965-4338

J. Murria
MARAVEN
Apartado Postal 173
Lagunillas, Edo.Zulia 4016-A
VENEZUELA
Tel. 58-61-203582
Fax. 58-61-205608

S. Musser
State of Utah
Department of Transportation
Research Division
4501 South 2700 West
Salt Lake City, UT 84119-5998
Tel. 801-965-4000
Fax. 801-965-4338

D. Nazare
State of Utah
Department of Transportation
Research Division
4501 South 2700 West
Salt Lake City, UT 84119-5998
Tel. 801-965-4000
Fax. 801-965-4338

B. Nooranbakht
U.S. Army Corps. of Engineers
Emergency Management Branch
300 N. Los Angeles St. Room 6050
Los Angeles, CA 90012
Tel. 213-894-3440
Fax. 213-894-5364

S. Okada
Kiso-Jiban Consultants
AXIS Touyou-cho Bldg.
3-22-6- Touyou, Koutou-Ku
Tokyo, JAPAN
Tel. 03-5632-6800
Fax. 03-5632-6815

D. O'Brien
Project Coordinator
Earthquake Education Office
University of Utah Seismograph Stations
705 William Browning Building
University of Utah
Salt Lake City, UT 84112
Tel. 801-581-6201
Fax. 801-581-7065

D. O'Rourke
Program Specialist
National Center for Earthquake
Engineering Research
State University of New York
at Buffalo
Red Jacket Quadrangle
Box 610025
Buffalo, NY 14261-0025
Tel. 716-645-3391
Fax. 716-645-3399

M. O'Rourke
Professor
Department of Civil
and Environmental Engineering
Rensselaer Polytechnic Institute
Troy, NY 12180-3590
Tel. 518-276-6933
Fax. 518-276-4833

T. O'Rourke
Professor
School of Civil and Environmental
Engineering
265 Hollister Hall
Cornell University
Ithaca, NY 14853-3501
Phone: 607-255-6470
Fax: 607-255-9004

R. Owens
Dames and Moore
127 South 500 E. Suite 300
Salt Lake City, UT 84111
Tel. 801-521-9255

J. Pease
School of Civil and
Environmental Engineering
Cornell University
Hollister Hall
Ithaca, NY 14853-3501
Tel. 607-255-4292
Fax. 607-255-9004

R. Pichumani
Geotechnical Engineer
Mail Stop 0-7H15
U.S. Nuclear Regulatory Commission
Washington, DC 20555
Tel. 301-504-2734
Fax. 301-504-2260

R. Popescu
Department of Civil Engineering
School of Engineering and
Applied Science
Princeton University
Princeton, NJ 08544
Tel. 609-258-5424
Fax. 609-258-1270

J. Prevost
Chairman
Department of Civil Engineering
and Operations Research
School of Engineering and Applied Science
Princeton University
Princeton, NJ 08544
Tel. 609-258-5424
Fax. 609-258-1270

A. Rauch
Virginia Polytechnic and State University
Department of Civil Engineering
104 Patton Hall
Blacksburg, VA 24062-0105
Tel. 703-231-5103
Fax. 703-231-7532

L. Rausher
State of Utah
Department of Transportation
Geotechnical Division
4501 South 2700 West
Salt Lake City, UT 84119-5998
Tel. 801-965-4000
Fax. 801-965-4338

P. Robertson
Department of Civil Engineering
University of Alberta
393 Civil/Elec. Engineering Building
Edmonton T6G2G7
CANADA
Tel. 403-492-5106
Fax. 403-492-8198

K. Rollins
Department of Civil Engineering
Brigham Young University
368 CB
Provo, UT 84602
Tel. 801-376-6327
Fax. 801-378-4429

A. Saada
Department of Civil Engineering
Case Western Reserve University
10900 Euclid Avenue
Cleveland, OH 44106-7201
Tel. 216-368-2427
Fax. 216-368-5229

S. Sakhai
State of Utah
Department of Transportation
Geotechnical Division
4501 South 2700 West
Salt Lake City, UT 84119-5998
Tel. 801-965-4000
Fax. 801-965-4338

H. Sato
Researcher
Civil Engineering
and Architecture Dept.
Power Engineering Research &
Development Center
Tokyo Electric Power Company
4-1 Egasaki-cho Tsurumi-Ku
Yokohama 230 JAPAN
Tel. 81-45-585-8605
Fax. 81-45-585-8631

K. Sato
Central Research Institute
of Electric Power Industry
1646 Abiko, Abiko-City,
Chiba, 270-11 JAPAN
Tel. 0471-82-1811
Fax. 0471-83-2962

W. Savage
Pacific Gas and Electric
123 Mission Street, Room 1165
Mail Code H11A, PO Box 770000
San Francisco, CA 94177
Tel. 415-973-3116
Fax. 415-973-8147

C. Scawthorn
Vice President
EQE International
44 Montgomery Street
Suite 3200
San Francisco, CA 94104
Tel. 415-989-2000
Fax. 415-397-5209

A. Schiff
Precision Measurement
Instruments
27750 Edgerton Rd.
Los Altos Hills, CA 94022
Tel. 415-941-9233
Fax. same as phone

Y. Shiba
Senior Research Engineer
Earthquake Engineering Team
Earthquake & Wind Engineering
Research Group
Taisei Corporation
Technology Research Center
344-1 Nasemachi, Totsuka-ku
Yokohama, 245 JAPAN
Tel. 045-812-1211
Fax. 045-813-2747

B. Siel
Federal Highway Administration
555 Zang Street, No. 400
Lakewood, CO 80228
Tel. 303-969-5772 ext. 352
Fax. 303-969-6727

S. Singh
Department of Civil Engineering
Santa Clara University
Santa Clara, CA 95053
Tel. 408-554-4061
Fax. 408-554-5474

P. Sizemore
Geologist-Engineering
State of Utah
Utah Department of Transportation
Geotechnical Unit
Calvin L. Rampton Complex
4501 South 2700 West
Salt Lake City, UT 84119-5998
Tel. 801-965-4304
Fax. 801-965-4338

B. Solomon
Utah Geological Survey
2363 South Foothill Drive
Salt Lake City, UT 84109
Tel. 801-467-7970

D. Sjoblom
State of Utah
Department of Transportation
Geotechnical Division
4501 South 2700 West
Salt Lake City, UT 84119-5998
Tel. 801-965-4000
Fax. 801-965-4338

H. Stewart
Associate Professor
School of Civil and Environmental Engineering
Hollister Hall
Cornell University
Ithaca, NY 14853-3501
Tel. 607-255-4734
Fax. 607-255-9004

N. Suemasa
Department of Civil Engineering
Musashi Kogyo University
1-28-1 Tamazutsumi
Setagaya-Ku, Tokyo, JAPAN 158
Tel. 03-3703-3111 ext. 3244
Fax. 03-5707-2202

J. Tinsley
United States Geological Survey
Branch of Western Regional Geology
345 Middlefield Road, MS 975
Menlo Park, CA 94025
Tel. 415-329-4928
Fax. 415-329-4936

S. Toprak
School of Civil and Environmental Engineering
Cornell University
Hollister Hall
Ithaca, NY 14853-3501
Tel. 607-255-3365
Fax. 607-255-9004

I. Towhata
Department of Civil Engineering
University of Tokyo
7-3-1 Hongo, Bunkyo-Ku,
Tokyo, 113 JAPAN
Tel. 03-3812-2111 ext. 6121
Fax. 03-3818-5692

H. Toyota
Department of Civil Engineering
University of Tokyo
7-3-1 Hongo, Bunkyo-Ku,
Tokyo, 113 JAPAN
Tel. 03-3812-2111 ext. 6122
Fax. 03-3818-5692

W. Turner
Geotechnical Engineer
Terracon Consultants Western, Inc.
92 W. 3900 South, Suite 100
Salt Lake City, UT 84107
Tel. 801-266-2100
Fax. 801-266-2191

S. Vahdani
Associate
Treadwell & Rollo
555 Montgomery Street, Suite 1300
San Francisco, CA 94111
Tel. 415-955-9040
Fax. 415-955-9041

K. Wakamatsu
Advanced Research Center for
Science & Engineering
Waseda University
17 Kikui-cho,
Shinjuku-Ku
Tokyo, 162 JAPAN
Tel. 03-3203-4141
Fax. 03-3203-4339

S. Yasuda
Department of Civil Engineering
Tokyo Denki University
Ishizaka, Hatoyama-cho
Hiki-Gun
Saitama JAPAN
Tel. 0492-96-2911
Fax. 0492-96-6501

N. Yoshida
Engineering Research Institute
Sato Kogyo Co., Ltd.
47-3 Mita, Atsugi,
Kanagawa, 243-02 JAPAN
Tel. 0462-41-2171
Fax. 0462-41-4784

T. Youd
Professor
Department of Civil Engineering
Brigham Young University
368 CB
Provo, UT 84602
Tel. 801-378-6327
Fax. 801-378-4449

M. Zeghal
Department of Civil and
Environmental Engineering
Rensselaer Polytechnic University
Troy, NY 12180
Tel. 518-376-2836
Fax. 518-276-4833

NATIONAL CENTER FOR EARTHQUAKE ENGINEERING RESEARCH
LIST OF TECHNICAL REPORTS

The National Center for Earthquake Engineering Research (NCEER) publishes technical reports on a variety of subjects related to earthquake engineering written by authors funded through NCEER. These reports are available from both NCEER's Publications Department and the National Technical Information Service (NTIS). Requests for reports should be directed to the Publications Department, National Center for Earthquake Engineering Research, State University of New York at Buffalo, Red Jacket Quadrangle, Buffalo, New York 14261. Reports can also be requested through NTIS, 5285 Port Royal Road, Springfield, Virginia 22161. NTIS accession numbers are shown in parenthesis, if available.

NCEER-87-0001 "First-Year Program in Research, Education and Technology Transfer," 3/5/87, (PB88-134275).

NCEER-87-0002 "Experimental Evaluation of Instantaneous Optimal Algorithms for Structural Control," by R.C. Lin, T.T. Soong and A.M. Reinhorn, 4/20/87, (PB88-134341).

NCEER-87-0003 "Experimentation Using the Earthquake Simulation Facilities at University at Buffalo," by A.M. Reinhorn and R.L. Ketter, to be published.

NCEER-87-0004 "The System Characteristics and Performance of a Shaking Table," by J.S. Hwang, K.C. Chang and G.C. Lee, 6/1/87, (PB88-134259). This report is available only through NTIS (see address given above).

NCEER-87-0005 "A Finite Element Formulation for Nonlinear Viscoplastic Material Using a Q Model," by O. Gyebi and G. Dasgupta, 11/2/87, (PB88-213764).

NCEER-87-0006 "Symbolic Manipulation Program (SMP) - Algebraic Codes for Two and Three Dimensional Finite Element Formulations," by X. Lee and G. Dasgupta, 11/9/87, (PB88-218522).

NCEER-87-0007 "Instantaneous Optimal Control Laws for Tall Buildings Under Seismic Excitations," by J.N. Yang, A. Akbarpour and P. Ghaemmaghami, 6/10/87, (PB88-134333). This report is only available through NTIS (see address given above).

NCEER-87-0008 "IDARC: Inelastic Damage Analysis of Reinforced Concrete Frame - Shear-Wall Structures," by Y.J. Park, A.M. Reinhorn and S.K. Kunnath, 7/20/87, (PB88-134325).

NCEER-87-0009 "Liquefaction Potential for New York State: A Preliminary Report on Sites in Manhattan and Buffalo," by M. Budhu, V. Vijayakumar, R.F. Giese and L. Baumgras, 8/31/87, (PB88-163704). This report is available only through NTIS (see address given above).

NCEER-87-0010 "Vertical and Torsional Vibration of Foundations in Inhomogeneous Media," by A.S. Veletsos and K.W. Dotson, 6/1/87, (PB88-134291).

NCEER-87-0011 "Seismic Probabilistic Risk Assessment and Seismic Margins Studies for Nuclear Power Plants," by Howard H.M. Hwang, 6/15/87, (PB88-134267).

NCEER-87-0012 "Parametric Studies of Frequency Response of Secondary Systems Under Ground-Acceleration Excitations," by Y. Yong and Y.K. Lin, 6/10/87, (PB88-134309).

NCEER-87-0013 "Frequency Response of Secondary Systems Under Seismic Excitation," by J.A. HoLung, J. Cai and Y.K. Lin, 7/31/87, (PB88-134317).

NCEER-87-0014 "Modelling Earthquake Ground Motions in Seismically Active Regions Using Parametric Time Series Methods," by G.W. Ellis and A.S. Cakmak, 8/25/87, (PB88-134283).

NCEER-87-0015 "Detection and Assessment of Seismic Structural Damage," by E. DiPasquale and A.S. Cakmak, 8/25/87, (PB88-163712).

NCEER-87-0016 "Pipeline Experiment at Parkfield, California," by J. Isenberg and E. Richardson, 9/15/87, (PB88-163720). This report is available only through NTIS (see address given above).

NCEER-87-0017 "Digital Simulation of Seismic Ground Motion," by M. Shinozuka, G. Deodatis and T. Harada, 8/31/87, (PB88-155197). This report is available only through NTIS (see address given above).

NCEER-87-0018 "Practical Considerations for Structural Control: System Uncertainty, System Time Delay and Truncation of Small Control Forces," J.N. Yang and A. Akbarpour, 8/10/87, (PB88-163738).

NCEER-87-0019 "Modal Analysis of Nonclassically Damped Structural Systems Using Canonical Transformation," by J.N. Yang, S. Sarkani and F.X. Long, 9/27/87, (PB88-187851).

NCEER-87-0020 "A Nonstationary Solution in Random Vibration Theory," by J.R. Red-Horse and P.D. Spanos, 11/3/87, (PB88-163746).

NCEER-87-0021 "Horizontal Impedances for Radially Inhomogeneous Viscoelastic Soil Layers," by A.S. Veletsos and K.W. Dotson, 10/15/87, (PB88-150859).

NCEER-87-0022 "Seismic Damage Assessment of Reinforced Concrete Members," by Y.S. Chung, C. Meyer and M. Shinozuka, 10/9/87, (PB88-150867). This report is available only through NTIS (see address given above).

NCEER-87-0023 "Active Structural Control in Civil Engineering," by T.T. Soong, 11/11/87, (PB88-187778).

NCEER-87-0024 "Vertical and Torsional Impedances for Radially Inhomogeneous Viscoelastic Soil Layers," by K.W. Dotson and A.S. Veletsos, 12/87, (PB88-187786).

NCEER-87-0025 "Proceedings from the Symposium on Seismic Hazards, Ground Motions, Soil-Liquefaction and Engineering Practice in Eastern North America," October 20-22, 1987, edited by K.H. Jacob, 12/87, (PB88-188115).

NCEER-87-0026 "Report on the Whittier-Narrows, California, Earthquake of October 1, 1987," by J. Pantelic and A. Reinhorn, 11/87, (PB88-187752). This report is available only through NTIS (see address given above).

NCEER-87-0027 "Design of a Modular Program for Transient Nonlinear Analysis of Large 3-D Building Structures," by S. Srivastav and J.F. Abel, 12/30/87, (PB88-187950).

NCEER-87-0028 "Second-Year Program in Research, Education and Technology Transfer," 3/8/88, (PB88-219480).

NCEER-88-0001 "Workshop on Seismic Computer Analysis and Design of Buildings With Interactive Graphics," by W. McGuire, J.F. Abel and C.H. Conley, 1/18/88, (PB88-187760).

NCEER-88-0002 "Optimal Control of Nonlinear Flexible Structures," by J.N. Yang, F.X. Long and D. Wong, 1/22/88, (PB88-213772).

NCEER-88-0003 "Substructuring Techniques in the Time Domain for Primary-Secondary Structural Systems," by G.D. Manolis and G. Juhn, 2/10/88, (PB88-213780).

NCEER-88-0004 "Iterative Seismic Analysis of Primary-Secondary Systems," by A. Singhal, L.D. Lutes and P.D. Spanos, 2/23/88, (PB88-213798).

NCEER-88-0005 "Stochastic Finite Element Expansion for Random Media," by P.D. Spanos and R. Ghanem, 3/14/88, (PB88-213806).

NCEER-88-0006 "Combining Structural Optimization and Structural Control," by F.Y. Cheng and C.P. Pantelides, 1/10/88, (PB88-213814).

NCEER-88-0007 "Seismic Performance Assessment of Code-Designed Structures," by H.H-M. Hwang, J-W. Jaw and H-J. Shau, 3/20/88, (PB88-219423).

NCEER-88-0008 "Reliability Analysis of Code-Designed Structures Under Natural Hazards," by H.H-M. Hwang, H. Ushiba and M. Shinozuka, 2/29/88, (PB88-229471).

NCEER-88-0009 "Seismic Fragility Analysis of Shear Wall Structures," by J-W Jaw and H.H-M. Hwang, 4/30/88, (PB89-102867).

NCEER-88-0010 "Base Isolation of a Multi-Story Building Under a Harmonic Ground Motion - A Comparison of Performances of Various Systems," by F-G Fan, G. Ahmadi and I.G. Tadjbakhsh, 5/18/88, (PB89-122238).

NCEER-88-0011 "Seismic Floor Response Spectra for a Combined System by Green's Functions," by F.M. Lavelle, L.A. Bergman and P.D. Spanos, 5/1/88, (PB89-102875).

NCEER-88-0012 "A New Solution Technique for Randomly Excited Hysteretic Structures," by G.Q. Cai and Y.K. Lin, 5/16/88, (PB89-102883).

NCEER-88-0013 "A Study of Radiation Damping and Soil-Structure Interaction Effects in the Centrifuge," by K. Weissman, supervised by J.H. Prevost, 5/24/88, (PB89-144703).

NCEER-88-0014 "Parameter Identification and Implementation of a Kinematic Plasticity Model for Frictional Soils," by J.H. Prevost and D.V. Griffiths, to be published.

NCEER-88-0015 "Two- and Three- Dimensional Dynamic Finite Element Analyses of the Long Valley Dam," by D.V. Griffiths and J.H. Prevost, 6/17/88, (PB89-144711).

NCEER-88-0016 "Damage Assessment of Reinforced Concrete Structures in Eastern United States," by A.M. Reinhorn, M.J. Seidel, S.K. Kunnath and Y.J. Park, 6/15/88, (PB89-122220).

NCEER-88-0017 "Dynamic Compliance of Vertically Loaded Strip Foundations in Multilayered Viscoelastic Soils," by S. Ahmad and A.S.M. Israil, 6/17/88, (PB89-102891).

NCEER-88-0018 "An Experimental Study of Seismic Structural Response With Added Viscoelastic Dampers," by R.C. Lin, Z. Liang, T.T. Soong and R.H. Zhang, 6/30/88, (PB89-122212). This report is available only through NTIS (see address given above).

NCEER-88-0019 "Experimental Investigation of Primary - Secondary System Interaction," by G.D. Manolis, G. Juhn and A.M. Reinhorn, 5/27/88, (PB89-122204).

NCEER-88-0020 "A Response Spectrum Approach For Analysis of Nonclassically Damped Structures," by J.N. Yang, S. Sarkani and F.X. Long, 4/22/88, (PB89-102909).

NCEER-88-0021 "Seismic Interaction of Structures and Soils: Stochastic Approach," by A.S. Veletsos and A.M. Prasad, 7/21/88, (PB89-122196).

NCEER-88-0022 "Identification of the Serviceability Limit State and Detection of Seismic Structural Damage," by E. DiPasquale and A.S. Cakmak, 6/15/88, (PB89-122188). This report is available only through NTIS (see address given above).

NCEER-88-0023 "Multi-Hazard Risk Analysis: Case of a Simple Offshore Structure," by B.K. Bhartia and E.H. Vanmarcke, 7/21/88, (PB89-145213).

NCEER-88-0024 "Automated Seismic Design of Reinforced Concrete Buildings," by Y.S. Chung, C. Meyer and M. Shinozuka, 7/5/88, (PB89-122170). This report is available only through NTIS (see address given above).

NCEER-88-0025 "Experimental Study of Active Control of MDOF Structures Under Seismic Excitations," by L.L. Chung, R.C. Lin, T.T. Soong and A.M. Reinhorn, 7/10/88, (PB89-122600).

NCEER-88-0026 "Earthquake Simulation Tests of a Low-Rise Metal Structure," by J.S. Hwang, K.C. Chang, G.C. Lee and R.L. Ketter, 8/1/88, (PB89-102917).

NCEER-88-0027 "Systems Study of Urban Response and Reconstruction Due to Catastrophic Earthquakes," by F. Kozin and H.K. Zhou, 9/22/88, (PB90-162348).

NCEER-88-0028 "Seismic Fragility Analysis of Plane Frame Structures," by H.H-M. Hwang and Y.K. Low, 7/31/88, (PB89-131445).

NCEER-88-0029 "Response Analysis of Stochastic Structures," by A. Kardara, C. Bucher and M. Shinozuka, 9/22/88, (PB89-174429).

NCEER-88-0030 "Nonnormal Accelerations Due to Yielding in a Primary Structure," by D.C.K. Chen and L.D. Lutes, 9/19/88, (PB89-131437).

NCEER-88-0031 "Design Approaches for Soil-Structure Interaction," by A.S. Veletsos, A.M. Prasad and Y. Tang, 12/30/88, (PB89-174437). This report is available only through NTIS (see address given above).

NCEER-88-0032 "A Re-evaluation of Design Spectra for Seismic Damage Control," by C.J. Turkstra and A.G. Tallin, 11/7/88, (PB89-145221).

NCEER-88-0033 "The Behavior and Design of Noncontact Lap Splices Subjected to Repeated Inelastic Tensile Loading," by V.E. Sagan, P. Gergely and R.N. White, 12/8/88, (PB89-163737).

NCEER-88-0034 "Seismic Response of Pile Foundations," by S.M. Mamoon, P.K. Banerjee and S. Ahmad, 11/1/88, (PB89-145239).

NCEER-88-0035 "Modeling of R/C Building Structures With Flexible Floor Diaphragms (IDARC2)," by A.M. Reinhorn, S.K. Kunnath and N. Panahshahi, 9/7/88, (PB89-207153).

NCEER-88-0036 "Solution of the Dam-Reservoir Interaction Problem Using a Combination of FEM, BEM with Particular Integrals, Modal Analysis, and Substructuring," by C-S. Tsai, G.C. Lee and R.L. Ketter, 12/31/88, (PB89-207146).

NCEER-88-0037 "Optimal Placement of Actuators for Structural Control," by F.Y. Cheng and C.P. Pantelides, 8/15/88, (PB89-162846).

NCEER-88-0038 "Teflon Bearings in Aseismic Base Isolation: Experimental Studies and Mathematical Modeling," by A. Mokha, M.C. Constantinou and A.M. Reinhorn, 12/5/88, (PB89-218457). This report is available only through NTIS (see address given above).

NCEER-88-0039 "Seismic Behavior of Flat Slab High-Rise Buildings in the New York City Area," by P. Weidlinger and M. Ettouney, 10/15/88, (PB90-145681).

NCEER-88-0040 "Evaluation of the Earthquake Resistance of Existing Buildings in New York City," by P. Weidlinger and M. Ettouney, 10/15/88, to be published.

NCEER-88-0041 "Small-Scale Modeling Techniques for Reinforced Concrete Structures Subjected to Seismic Loads," by W. Kim, A. El-Attar and R.N. White, 11/22/88, (PB89-189625).

NCEER-88-0042 "Modeling Strong Ground Motion from Multiple Event Earthquakes," by G.W. Ellis and A.S. Cakmak, 10/15/88, (PB89-174445).

NCEER-88-0043 "Nonstationary Models of Seismic Ground Acceleration," by M. Grigoriu, S.E. Ruiz and E. Rosenblueth, 7/15/88, (PB89-189617).

NCEER-88-0044 "SARCF User's Guide: Seismic Analysis of Reinforced Concrete Frames," by Y.S. Chung, C. Meyer and M. Shinozuka, 11/9/88, (PB89-174452).

NCEER-88-0045 "First Expert Panel Meeting on Disaster Research and Planning," edited by J. Pantelic and J. Stoyle, 9/15/88, (PB89-174460).

NCEER-88-0046 "Preliminary Studies of the Effect of Degrading Infill Walls on the Nonlinear Seismic Response of Steel Frames," by C.Z. Chrysostomou, P. Gergely and J.F. Abel, 12/19/88, (PB89-208383).

NCEER-88-0047 "Reinforced Concrete Frame Component Testing Facility - Design, Construction, Instrumentation and Operation," by S.P. Pessiki, C. Conley, T. Bond, P. Gergely and R.N. White, 12/16/88, (PB89-174478).

NCEER-89-0001 "Effects of Protective Cushion and Soil Compliancy on the Response of Equipment Within a Seismically Excited Building," by J.A. HoLung, 2/16/89, (PB89-207179).

NCEER-89-0002 "Statistical Evaluation of Response Modification Factors for Reinforced Concrete Structures," by H.H-M. Hwang and J-W. Jaw, 2/17/89, (PB89-207187).

NCEER-89-0003 "Hysteretic Columns Under Random Excitation," by G-Q. Cai and Y.K. Lin, 1/9/89, (PB89-196513).

NCEER-89-0004 "Experimental Study of `Elephant Foot Bulge' Instability of Thin-Walled Metal Tanks," by Z-H. Jia and R.L. Ketter, 2/22/89, (PB89-207195).

NCEER-89-0005 "Experiment on Performance of Buried Pipelines Across San Andreas Fault," by J. Isenberg, E. Richardson and T.D. O'Rourke, 3/10/89, (PB89-218440). This report is available only through NTIS (see address given above).

NCEER-89-0006 "A Knowledge-Based Approach to Structural Design of Earthquake-Resistant Buildings," by M. Subramani, P. Gergely, C.H. Conley, J.F. Abel and A.H. Zaghw, 1/15/89, (PB89-218465).

NCEER-89-0007 "Liquefaction Hazards and Their Effects on Buried Pipelines," by T.D. O'Rourke and P.A. Lane, 2/1/89, (PB89-218481).

NCEER-89-0008 "Fundamentals of System Identification in Structural Dynamics," by H. Imai, C-B. Yun, O. Maruyama and M. Shinozuka, 1/26/89, (PB89-207211).

NCEER-89-0009 "Effects of the 1985 Michoacan Earthquake on Water Systems and Other Buried Lifelines in Mexico," by A.G. Ayala and M.J. O'Rourke, 3/8/89, (PB89-207229).

NCEER-89-R010 "NCEER Bibliography of Earthquake Education Materials," by K.E.K. Ross, Second Revision, 9/1/89, (PB90-125352).

NCEER-89-0011 "Inelastic Three-Dimensional Response Analysis of Reinforced Concrete Building Structures (IDARC-3D), Part I - Modeling," by S.K. Kunnath and A.M. Reinhorn, 4/17/89, (PB90-114612).

NCEER-89-0012 "Recommended Modifications to ATC-14," by C.D. Poland and J.O. Malley, 4/12/89, (PB90-108648).

NCEER-89-0013 "Repair and Strengthening of Beam-to-Column Connections Subjected to Earthquake Loading," by M. Corazao and A.J. Durrani, 2/28/89, (PB90-109885).

NCEER-89-0014 "Program EXKAL2 for Identification of Structural Dynamic Systems," by O. Maruyama, C-B. Yun, M. Hoshiya and M. Shinozuka, 5/19/89, (PB90-109877).

NCEER-89-0015 "Response of Frames With Bolted Semi-Rigid Connections, Part I - Experimental Study and Analytical Predictions," by P.J. DiCorso, A.M. Reinhorn, J.R. Dickerson, J.B. Radziminski and W.L. Harper, 6/1/89, to be published.

NCEER-89-0016 "ARMA Monte Carlo Simulation in Probabilistic Structural Analysis," by P.D. Spanos and M.P. Mignolet, 7/10/89, (PB90-109893).

NCEER-89-P017 "Preliminary Proceedings from the Conference on Disaster Preparedness - The Place of Earthquake Education in Our Schools," Edited by K.E.K. Ross, 6/23/89, (PB90-108606).

NCEER-89-0017 "Proceedings from the Conference on Disaster Preparedness - The Place of Earthquake Education in Our Schools," Edited by K.E.K. Ross, 12/31/89, (PB90-207895). This report is available only through NTIS (see address given above).

NCEER-89-0018 "Multidimensional Models of Hysteretic Material Behavior for Vibration Analysis of Shape Memory Energy Absorbing Devices, by E.J. Graesser and F.A. Cozzarelli, 6/7/89, (PB90-164146).

NCEER-89-0019 "Nonlinear Dynamic Analysis of Three-Dimensional Base Isolated Structures (3D-BASIS)," by S. Nagarajaiah, A.M. Reinhorn and M.C. Constantinou, 8/3/89, (PB90-161936). This report is available only through NTIS (see address given above).

NCEER-89-0020 "Structural Control Considering Time-Rate of Control Forces and Control Rate Constraints," by F.Y. Cheng and C.P. Pantelides, 8/3/89, (PB90-120445).

NCEER-89-0021 "Subsurface Conditions of Memphis and Shelby County," by K.W. Ng, T-S. Chang and H-H.M. Hwang, 7/26/89, (PB90-120437).

NCEER-89-0022 "Seismic Wave Propagation Effects on Straight Jointed Buried Pipelines," by K. Elhmadi and M.J. O'Rourke, 8/24/89, (PB90-162322).

NCEER-89-0023 "Workshop on Serviceability Analysis of Water Delivery Systems," edited by M. Grigoriu, 3/6/89, (PB90-127424).

NCEER-89-0024 "Shaking Table Study of a 1/5 Scale Steel Frame Composed of Tapered Members," by K.C. Chang, J.S. Hwang and G.C. Lee, 9/18/89, (PB90-160169).

NCEER-89-0025 "DYNA1D: A Computer Program for Nonlinear Seismic Site Response Analysis - Technical Documentation," by Jean H. Prevost, 9/14/89, (PB90-161944). This report is available only through NTIS (see address given above).

NCEER-89-0026 "1:4 Scale Model Studies of Active Tendon Systems and Active Mass Dampers for Aseismic Protection," by A.M. Reinhorn, T.T. Soong, R.C. Lin, Y.P. Yang, Y. Fukao, H. Abe and M. Nakai, 9/15/89, (PB90-173246).

NCEER-89-0027 "Scattering of Waves by Inclusions in a Nonhomogeneous Elastic Half Space Solved by Boundary Element Methods," by P.K. Hadley, A. Askar and A.S. Cakmak, 6/15/89, (PB90-145699).

NCEER-89-0028 "Statistical Evaluation of Deflection Amplification Factors for Reinforced Concrete Structures," by H.H.M. Hwang, J-W. Jaw and A.L. Ch'ng, 8/31/89, (PB90-164633).

NCEER-89-0029 "Bedrock Accelerations in Memphis Area Due to Large New Madrid Earthquakes," by H.H.M. Hwang, C.H.S. Chen and G. Yu, 11/7/89, (PB90-162330).

NCEER-89-0030 "Seismic Behavior and Response Sensitivity of Secondary Structural Systems," by Y.Q. Chen and T.T. Soong, 10/23/89, (PB90-164658).

NCEER-89-0031 "Random Vibration and Reliability Analysis of Primary-Secondary Structural Systems," by Y. Ibrahim, M. Grigoriu and T.T. Soong, 11/10/89, (PB90-161951).

NCEER-89-0032 "Proceedings from the Second U.S. - Japan Workshop on Liquefaction, Large Ground Deformation and Their Effects on Lifelines, September 26-29, 1989," Edited by T.D. O'Rourke and M. Hamada, 12/1/89, (PB90-209388).

NCEER-89-0033 "Deterministic Model for Seismic Damage Evaluation of Reinforced Concrete Structures," by J.M. Bracci, A.M. Reinhorn, J.B. Mander and S.K. Kunnath, 9/27/89.

NCEER-89-0034 "On the Relation Between Local and Global Damage Indices," by E. DiPasquale and A.S. Cakmak, 8/15/89, (PB90-173865).

NCEER-89-0035 "Cyclic Undrained Behavior of Nonplastic and Low Plasticity Silts," by A.J. Walker and H.E. Stewart, 7/26/89, (PB90-183518).

NCEER-89-0036 "Liquefaction Potential of Surficial Deposits in the City of Buffalo, New York," by M. Budhu, R. Giese and L. Baumgrass, 1/17/89, (PB90-208455).

NCEER-89-0037 "A Deterministic Assessment of Effects of Ground Motion Incoherence," by A.S. Veletsos and Y. Tang, 7/15/89, (PB90-164294).

NCEER-89-0038 "Workshop on Ground Motion Parameters for Seismic Hazard Mapping," July 17-18, 1989, edited by R.V. Whitman, 12/1/89, (PB90-173923).

NCEER-89-0039 "Seismic Effects on Elevated Transit Lines of the New York City Transit Authority," by C.J. Costantino, C.A. Miller and E. Heymsfield, 12/26/89, (PB90-207887).

NCEER-89-0040 "Centrifugal Modeling of Dynamic Soil-Structure Interaction," by K. Weissman, Supervised by J.H. Prevost, 5/10/89, (PB90-207879).

NCEER-89-0041 "Linearized Identification of Buildings With Cores for Seismic Vulnerability Assessment," by I-K. Ho and A.E. Aktan, 11/1/89, (PB90-251943).

NCEER-90-0001 "Geotechnical and Lifeline Aspects of the October 17, 1989 Loma Prieta Earthquake in San Francisco," by T.D. O'Rourke, H.E. Stewart, F.T. Blackburn and T.S. Dickerman, 1/90, (PB90-208596).

NCEER-90-0002 "Nonnormal Secondary Response Due to Yielding in a Primary Structure," by D.C.K. Chen and L.D. Lutes, 2/28/90, (PB90-251976).

NCEER-90-0003 "Earthquake Education Materials for Grades K-12," by K.E.K. Ross, 4/16/90, (PB91-251984).

NCEER-90-0004 "Catalog of Strong Motion Stations in Eastern North America," by R.W. Busby, 4/3/90, (PB90-251984).

NCEER-90-0005 "NCEER Strong-Motion Data Base: A User Manual for the GeoBase Release (Version 1.0 for the Sun3)," by P. Friberg and K. Jacob, 3/31/90 (PB90-258062).

NCEER-90-0006 "Seismic Hazard Along a Crude Oil Pipeline in the Event of an 1811-1812 Type New Madrid Earthquake," by H.H.M. Hwang and C-H.S. Chen, 4/16/90(PB90-258054).

NCEER-90-0007 "Site-Specific Response Spectra for Memphis Sheahan Pumping Station," by H.H.M. Hwang and C.S. Lee, 5/15/90, (PB91-108811).

NCEER-90-0008 "Pilot Study on Seismic Vulnerability of Crude Oil Transmission Systems," by T. Ariman, R. Dobry, M. Grigoriu, F. Kozin, M. O'Rourke, T. O'Rourke and M. Shinozuka, 5/25/90, (PB91-108837).

NCEER-90-0009 "A Program to Generate Site Dependent Time Histories: EQGEN," by G.W. Ellis, M. Srinivasan and A.S. Cakmak, 1/30/90, (PB91-108829).

NCEER-90-0010 "Active Isolation for Seismic Protection of Operating Rooms," by M.E. Talbott, Supervised by M. Shinozuka, 6/8/9, (PB91-110205).

NCEER-90-0011 "Program LINEARID for Identification of Linear Structural Dynamic Systems," by C-B. Yun and M. Shinozuka, 6/25/90, (PB91-110312).

NCEER-90-0012 "Two-Dimensional Two-Phase Elasto-Plastic Seismic Response of Earth Dams," by A.N. Yiagos, Supervised by J.H. Prevost, 6/20/90, (PB91-110197).

NCEER-90-0013 "Secondary Systems in Base-Isolated Structures: Experimental Investigation, Stochastic Response and Stochastic Sensitivity," by G.D. Manolis, G. Juhn, M.C. Constantinou and A.M. Reinhorn, 7/1/90, (PB91-110320).

NCEER-90-0014 "Seismic Behavior of Lightly-Reinforced Concrete Column and Beam-Column Joint Details," by S.P. Pessiki, C.H. Conley, P. Gergely and R.N. White, 8/22/90, (PB91-108795).

NCEER-90-0015 "Two Hybrid Control Systems for Building Structures Under Strong Earthquakes," by J.N. Yang and A. Danielians, 6/29/90, (PB91-125393).

NCEER-90-0016 "Instantaneous Optimal Control with Acceleration and Velocity Feedback," by J.N. Yang and Z. Li, 6/29/90, (PB91-125401).

NCEER-90-0017 "Reconnaissance Report on the Northern Iran Earthquake of June 21, 1990," by M. Mehrain, 10/4/90, (PB91-125377).

NCEER-90-0018 "Evaluation of Liquefaction Potential in Memphis and Shelby County," by T.S. Chang, P.S. Tang, C.S. Lee and H. Hwang, 8/10/90, (PB91-125427).

NCEER-90-0019 "Experimental and Analytical Study of a Combined Sliding Disc Bearing and Helical Steel Spring Isolation System," by M.C. Constantinou, A.S. Mokha and A.M. Reinhorn, 10/4/90, (PB91-125385).

NCEER-90-0020 "Experimental Study and Analytical Prediction of Earthquake Response of a Sliding Isolation System with a Spherical Surface," by A.S. Mokha, M.C. Constantinou and A.M. Reinhorn, 10/11/90, (PB91-125419).

NCEER-90-0021 "Dynamic Interaction Factors for Floating Pile Groups," by G. Gazetas, K. Fan, A. Kaynia and E. Kausel, 9/10/90, (PB91-170381).

NCEER-90-0022 "Evaluation of Seismic Damage Indices for Reinforced Concrete Structures," by S. Rodriguez-Gomez and A.S. Cakmak, 9/30/90, PB91-171322).

NCEER-90-0023 "Study of Site Response at a Selected Memphis Site," by H. Desai, S. Ahmad, E.S. Gazetas and M.R. Oh, 10/11/90, (PB91-196857).

NCEER-90-0024 "A User's Guide to Strongmo: Version 1.0 of NCEER's Strong-Motion Data Access Tool for PCs and Terminals," by P.A. Friberg and C.A.T. Susch, 11/15/90, (PB91-171272).

NCEER-90-0025 "A Three-Dimensional Analytical Study of Spatial Variability of Seismic Ground Motions," by L-L. Hong and A.H.-S. Ang, 10/30/90, (PB91-170399).

NCEER-90-0026 "MUMOID User's Guide - A Program for the Identification of Modal Parameters," by S. Rodriguez-Gomez and E. DiPasquale, 9/30/90, (PB91-171298).

NCEER-90-0027 "SARCF-II User's Guide - Seismic Analysis of Reinforced Concrete Frames," by S. Rodriguez-Gomez, Y.S. Chung and C. Meyer, 9/30/90, (PB91-171280).

NCEER-90-0028 "Viscous Dampers: Testing, Modeling and Application in Vibration and Seismic Isolation," by N. Makris and M.C. Constantinou, 12/20/90 (PB91-190561).

NCEER-90-0029 "Soil Effects on Earthquake Ground Motions in the Memphis Area," by H. Hwang, C.S. Lee, K.W. Ng and T.S. Chang, 8/2/90, (PB91-190751).

NCEER-91-0001 "Proceedings from the Third Japan-U.S. Workshop on Earthquake Resistant Design of Lifeline Facilities and Countermeasures for Soil Liquefaction, December 17-19, 1990," edited by T.D. O'Rourke and M. Hamada, 2/1/91, (PB91-179259).

NCEER-91-0002 "Physical Space Solutions of Non-Proportionally Damped Systems," by M. Tong, Z. Liang and G.C. Lee, 1/15/91, (PB91-179242).

NCEER-91-0003 "Seismic Response of Single Piles and Pile Groups," by K. Fan and G. Gazetas, 1/10/91, (PB92-174994).

NCEER-91-0004 "Damping of Structures: Part 1 - Theory of Complex Damping," by Z. Liang and G. Lee, 10/10/91, (PB92-197235).

NCEER-91-0005 "3D-BASIS - Nonlinear Dynamic Analysis of Three Dimensional Base Isolated Structures: Part II," by S. Nagarajaiah, A.M. Reinhorn and M.C. Constantinou, 2/28/91, (PB91-190553).

NCEER-91-0006 "A Multidimensional Hysteretic Model for Plasticity Deforming Metals in Energy Absorbing Devices," by E.J. Graesser and F.A. Cozzarelli, 4/9/91, (PB92-108364).

NCEER-91-0007 "A Framework for Customizable Knowledge-Based Expert Systems with an Application to a KBES for Evaluating the Seismic Resistance of Existing Buildings," by E.G. Ibarra-Anaya and S.J. Fenves, 4/9/91, (PB91-210930).

NCEER-91-0008 "Nonlinear Analysis of Steel Frames with Semi-Rigid Connections Using the Capacity Spectrum Method," by G.G. Deierlein, S-H. Hsieh, Y-J. Shen and J.F. Abel, 7/2/91, (PB92-113828).

NCEER-91-0009 "Earthquake Education Materials for Grades K-12," by K.E.K. Ross, 4/30/91, (PB91-212142).

NCEER-91-0010 "Phase Wave Velocities and Displacement Phase Differences in a Harmonically Oscillating Pile," by N. Makris and G. Gazetas, 7/8/91, (PB92-108356).

NCEER-91-0011 "Dynamic Characteristics of a Full-Size Five-Story Steel Structure and a 2/5 Scale Model," by K.C. Chang, G.C. Yao, G.C. Lee, D.S. Hao and Y.C. Yeh," 7/2/91, (PB93-116648).

NCEER-91-0012 "Seismic Response of a 2/5 Scale Steel Structure with Added Viscoelastic Dampers," by K.C. Chang, T.T. Soong, S-T. Oh and M.L. Lai, 5/17/91, (PB92-110816).

NCEER-91-0013 "Earthquake Response of Retaining Walls; Full-Scale Testing and Computational Modeling," by S. Alampalli and A-W.M. Elgamal, 6/20/91, to be published.

NCEER-91-0014 "3D-BASIS-M: Nonlinear Dynamic Analysis of Multiple Building Base Isolated Structures," by P.C. Tsopelas, S. Nagarajaiah, M.C. Constantinou and A.M. Reinhorn, 5/28/91, (PB92-113885).

NCEER-91-0015 "Evaluation of SEAOC Design Requirements for Sliding Isolated Structures," by D. Theodossiou and M.C. Constantinou, 6/10/91, (PB92-114602).

NCEER-91-0016 "Closed-Loop Modal Testing of a 27-Story Reinforced Concrete Flat Plate-Core Building," by H.R. Somaprasad, T. Toksoy, H. Yoshiyuki and A.E. Aktan, 7/15/91, (PB92-129980).

NCEER-91-0017 "Shake Table Test of a 1/6 Scale Two-Story Lightly Reinforced Concrete Building," by A.G. El-Attar, R.N. White and P. Gergely, 2/28/91, (PB92-222447).

NCEER-91-0018 "Shake Table Test of a 1/8 Scale Three-Story Lightly Reinforced Concrete Building," by A.G. El-Attar, R.N. White and P. Gergely, 2/28/91, (PB93-116630).

NCEER-91-0019 "Transfer Functions for Rigid Rectangular Foundations," by A.S. Veletsos, A.M. Prasad and W.H. Wu, 7/31/91.

NCEER-91-0020 "Hybrid Control of Seismic-Excited Nonlinear and Inelastic Structural Systems," by J.N. Yang, Z. Li and A. Danielians, 8/1/91, (PB92-143171).

NCEER-91-0021 "The NCEER-91 Earthquake Catalog: Improved Intensity-Based Magnitudes and Recurrence Relations for U.S. Earthquakes East of New Madrid," by L. Seeber and J.G. Armbruster, 8/28/91, (PB92-176742).

NCEER-91-0022 "Proceedings from the Implementation of Earthquake Planning and Education in Schools: The Need for Change - The Roles of the Changemakers," by K.E.K. Ross and F. Winslow, 7/23/91, (PB92-129998).

NCEER-91-0023 "A Study of Reliability-Based Criteria for Seismic Design of Reinforced Concrete Frame Buildings," by H.H.M. Hwang and H-M. Hsu, 8/10/91, (PB92-140235).

NCEER-91-0024 "Experimental Verification of a Number of Structural System Identification Algorithms," by R.G. Ghanem, H. Gavin and M. Shinozuka, 9/18/91, (PB92-176577).

NCEER-91-0025 "Probabilistic Evaluation of Liquefaction Potential," by H.H.M. Hwang and C.S. Lee," 11/25/91, (PB92-143429).

NCEER-91-0026 "Instantaneous Optimal Control for Linear, Nonlinear and Hysteretic Structures - Stable Controllers," by J.N. Yang and Z. Li, 11/15/91, (PB92-163807).

NCEER-91-0027 "Experimental and Theoretical Study of a Sliding Isolation System for Bridges," by M.C. Constantinou, A. Kartoum, A.M. Reinhorn and P. Bradford, 11/15/91, (PB92-176973).

NCEER-92-0001 "Case Studies of Liquefaction and Lifeline Performance During Past Earthquakes, Volume 1: Japanese Case Studies," Edited by M. Hamada and T. O'Rourke, 2/17/92, (PB92-197243).

NCEER-92-0002 "Case Studies of Liquefaction and Lifeline Performance During Past Earthquakes, Volume 2: United States Case Studies," Edited by T. O'Rourke and M. Hamada, 2/17/92, (PB92-197250).

NCEER-92-0003 "Issues in Earthquake Education," Edited by K. Ross, 2/3/92, (PB92-222389).

NCEER-92-0004 "Proceedings from the First U.S. - Japan Workshop on Earthquake Protective Systems for Bridges," Edited by I.G. Buckle, 2/4/92, (PB94-142239, A99, MF-A06).

NCEER-92-0005 "Seismic Ground Motion from a Haskell-Type Source in a Multiple-Layered Half-Space," A.P. Theoharis, G. Deodatis and M. Shinozuka, 1/2/92, to be published.

NCEER-92-0006 "Proceedings from the Site Effects Workshop," Edited by R. Whitman, 2/29/92, (PB92-197201).

NCEER-92-0007 "Engineering Evaluation of Permanent Ground Deformations Due to Seismically-Induced Liquefaction," by M.H. Baziar, R. Dobry and A-W.M. Elgamal, 3/24/92, (PB92-222421).

NCEER-92-0008 "A Procedure for the Seismic Evaluation of Buildings in the Central and Eastern United States," by C.D. Poland and J.O. Malley, 4/2/92, (PB92-222439).

NCEER-92-0009 "Experimental and Analytical Study of a Hybrid Isolation System Using Friction Controllable Sliding Bearings," by M.Q. Feng, S. Fujii and M. Shinozuka, 5/15/92, (PB93-150282).

NCEER-92-0010 "Seismic Resistance of Slab-Column Connections in Existing Non-Ductile Flat-Plate Buildings," by A.J. Durrani and Y. Du, 5/18/92.

NCEER-92-0011 "The Hysteretic and Dynamic Behavior of Brick Masonry Walls Upgraded by Ferrocement Coatings Under Cyclic Loading and Strong Simulated Ground Motion," by H. Lee and S.P. Prawel, 5/11/92, to be published.

NCEER-92-0012 "Study of Wire Rope Systems for Seismic Protection of Equipment in Buildings," by G.F. Demetriades, M.C. Constantinou and A.M. Reinhorn, 5/20/92.

NCEER-92-0013 "Shape Memory Structural Dampers: Material Properties, Design and Seismic Testing," by P.R. Witting and F.A. Cozzarelli, 5/26/92.

NCEER-92-0014 "Longitudinal Permanent Ground Deformation Effects on Buried Continuous Pipelines," by M.J. O'Rourke, and C. Nordberg, 6/15/92.

NCEER-92-0015 "A Simulation Method for Stationary Gaussian Random Functions Based on the Sampling Theorem," by M. Grigoriu and S. Balopoulou, 6/11/92, (PB93-127496).

NCEER-92-0016 "Gravity-Load-Designed Reinforced Concrete Buildings: Seismic Evaluation of Existing Construction and Detailing Strategies for Improved Seismic Resistance," by G.W. Hoffmann, S.K. Kunnath, A.M. Reinhorn and J.B. Mander, 7/15/92, (PB94-142007, A08, MF-A02).

NCEER-92-0017 "Observations on Water System and Pipeline Performance in the Limón Area of Costa Rica Due to the April 22, 1991 Earthquake," by M. O'Rourke and D. Ballantyne, 6/30/92, (PB93-126811).

NCEER-92-0018 "Fourth Edition of Earthquake Education Materials for Grades K-12," Edited by K.E.K. Ross, 8/10/92.

NCEER-92-0019 "Proceedings from the Fourth Japan-U.S. Workshop on Earthquake Resistant Design of Lifeline Facilities and Countermeasures for Soil Liquefaction," Edited by M. Hamada and T.D. O'Rourke, 8/12/92, (PB93-163939).

NCEER-92-0020 "Active Bracing System: A Full Scale Implementation of Active Control," by A.M. Reinhorn, T.T. Soong, R.C. Lin, M.A. Riley, Y.P. Wang, S. Aizawa and M. Higashino, 8/14/92, (PB93-127512).

NCEER-92-0021 "Empirical Analysis of Horizontal Ground Displacement Generated by Liquefaction-Induced Lateral Spreads," by S.F. Bartlett and T.L. Youd, 8/17/92, (PB93-188241).

NCEER-92-0022 "IDARC Version 3.0: Inelastic Damage Analysis of Reinforced Concrete Structures," by S.K. Kunnath, A.M. Reinhorn and R.F. Lobo, 8/31/92, (PB93-227502, A07, MF-A02).

NCEER-92-0023 "A Semi-Empirical Analysis of Strong-Motion Peaks in Terms of Seismic Source, Propagation Path and Local Site Conditions, by M. Kamiyama, M.J. O'Rourke and R. Flores-Berrones, 9/9/92, (PB93-150266).

NCEER-92-0024 "Seismic Behavior of Reinforced Concrete Frame Structures with Nonductile Details, Part I: Summary of Experimental Findings of Full Scale Beam-Column Joint Tests," by A. Beres, R.N. White and P. Gergely, 9/30/92, (PB93-227783, A05, MF-A01).

NCEER-92-0025 "Experimental Results of Repaired and Retrofitted Beam-Column Joint Tests in Lightly Reinforced Concrete Frame Buildings," by A. Beres, S. El-Borgi, R.N. White and P. Gergely, 10/29/92, (PB93-227791, A05, MF-A01).

NCEER-92-0026 "A Generalization of Optimal Control Theory: Linear and Nonlinear Structures," by J.N. Yang, Z. Li and S. Vongchavalitkul, 11/2/92, (PB93-188621).

NCEER-92-0027 "Seismic Resistance of Reinforced Concrete Frame Structures Designed Only for Gravity Loads: Part I - Design and Properties of a One-Third Scale Model Structure," by J.M. Bracci, A.M. Reinhorn and J.B. Mander, 12/1/92, (PB94-104502, A08, MF-A02).

NCEER-92-0028 "Seismic Resistance of Reinforced Concrete Frame Structures Designed Only for Gravity Loads: Part II - Experimental Performance of Subassemblages," by L.E. Aycardi, J.B. Mander and A.M. Reinhorn, 12/1/92, (PB94-104510, A08, MF-A02).

NCEER-92-0029 "Seismic Resistance of Reinforced Concrete Frame Structures Designed Only for Gravity Loads: Part III - Experimental Performance and Analytical Study of a Structural Model," by J.M. Bracci, A.M. Reinhorn and J.B. Mander, 12/1/92, (PB93-227528, A09, MF-A01).

NCEER-92-0030 "Evaluation of Seismic Retrofit of Reinforced Concrete Frame Structures: Part I - Experimental Performance of Retrofitted Subassemblages," by D. Choudhuri, J.B. Mander and A.M. Reinhorn, 12/8/92, (PB93-198307, A07, MF-A02).

NCEER-92-0031 "Evaluation of Seismic Retrofit of Reinforced Concrete Frame Structures: Part II - Experimental Performance and Analytical Study of a Retrofitted Structural Model," by J.M. Bracci, A.M. Reinhorn and J.B. Mander, 12/8/92, (PB93-198315, A09, MF-A03).

NCEER-92-0032 "Experimental and Analytical Investigation of Seismic Response of Structures with Supplemental Fluid Viscous Dampers," by M.C. Constantinou and M.D. Symans, 12/21/92, (PB93-191435).

NCEER-92-0033 "Reconnaissance Report on the Cairo, Egypt Earthquake of October 12, 1992," by M. Khater, 12/23/92, (PB93-188621).

NCEER-92-0034 "Low-Level Dynamic Characteristics of Four Tall Flat-Plate Buildings in New York City," by H. Gavin, S. Yuan, J. Grossman, E. Pekelis and K. Jacob, 12/28/92, (PB93-188217).

NCEER-93-0001 "An Experimental Study on the Seismic Performance of Brick-Infilled Steel Frames With and Without Retrofit," by J.B. Mander, B. Nair, K. Wojtkowski and J. Ma, 1/29/93, (PB93-227510, A07, MF-A02).

NCEER-93-0002 "Social Accounting for Disaster Preparedness and Recovery Planning," by S. Cole, E. Pantoja and V. Razak, 2/22/93, (PB94-142114, A12, MF-A03).

NCEER-93-0003 "Assessment of 1991 NEHRP Provisions for Nonstructural Components and Recommended Revisions," by T.T. Soong, G. Chen, Z. Wu, R-H. Zhang and M. Grigoriu, 3/1/93, (PB93-188639).

NCEER-93-0004 "Evaluation of Static and Response Spectrum Analysis Procedures of SEAOC/UBC for Seismic Isolated Structures," by C.W. Winters and M.C. Constantinou, 3/23/93, (PB93-198299).

NCEER-93-0005 "Earthquakes in the Northeast - Are We Ignoring the Hazard? A Workshop on Earthquake Science and Safety for Educators," edited by K.E.K. Ross, 4/2/93, (PB94-103066, A09, MF-A02).

NCEER-93-0006 "Inelastic Response of Reinforced Concrete Structures with Viscoelastic Braces," by R.F. Lobo, J.M. Bracci, K.L. Shen, A.M. Reinhorn and T.T. Soong, 4/5/93, (PB93-227486, A05, MF-A02).

NCEER-93-0007 "Seismic Testing of Installation Methods for Computers and Data Processing Equipment," by K. Kosar, T.T. Soong, K.L. Shen, J.A. HoLung and Y.K. Lin, 4/12/93, (PB93-198299).

NCEER-93-0008 "Retrofit of Reinforced Concrete Frames Using Added Dampers," by A. Reinhorn, M. Constantinou and C. Li, to be published.

NCEER-93-0009 "Seismic Behavior and Design Guidelines for Steel Frame Structures with Added Viscoelastic Dampers," by K.C. Chang, M.L. Lai, T.T. Soong, D.S. Hao and Y.C. Yeh, 5/1/93, (PB94-141959, A07, MF-A02).

NCEER-93-0010 "Seismic Performance of Shear-Critical Reinforced Concrete Bridge Piers," by J.B. Mander, S.M. Waheed, M.T.A. Chaudhary and S.S. Chen, 5/12/93, (PB93-227494, A08, MF-A02).

NCEER-93-0011 "3D-BASIS-TABS: Computer Program for Nonlinear Dynamic Analysis of Three Dimensional Base Isolated Structures," by S. Nagarajaiah, C. Li, A.M. Reinhorn and M.C. Constantinou, 8/2/93, (PB94-141819, A09, MF-A02).

NCEER-93-0012 "Effects of Hydrocarbon Spills from an Oil Pipeline Break on Ground Water," by O.J. Helweg and H.H.M. Hwang, 8/3/93, (PB94-141942, A06, MF-A02).

NCEER-93-0013 "Simplified Procedures for Seismic Design of Nonstructural Components and Assessment of Current Code Provisions," by M.P. Singh, L.E. Suarez, E.E. Matheu and G.O. Maldonado, 8/4/93, (PB94-141827, A09, MF-A02).

NCEER-93-0014 "An Energy Approach to Seismic Analysis and Design of Secondary Systems," by G. Chen and T.T. Soong, 8/6/93, (PB94-142767, A11, MF-A03).

NCEER-93-0015 "Proceedings from School Sites: Becoming Prepared for Earthquakes - Commemorating the Third Anniversary of the Loma Prieta Earthquake," Edited by F.E. Winslow and K.E.K. Ross, 8/16/93.

NCEER-93-0016 "Reconnaissance Report of Damage to Historic Monuments in Cairo, Egypt Following the October 12, 1992 Dahshur Earthquake," by D. Sykora, D. Look, G. Croci, E. Karaesmen and E. Karaesmen, 8/19/93, (PB94-142221, A08, MF-A02).

NCEER-93-0017 "The Island of Guam Earthquake of August 8, 1993," by S.W. Swan and S.K. Harris, 9/30/93, (PB94-141843, A04, MF-A01).

NCEER-93-0018 "Engineering Aspects of the October 12, 1992 Egyptian Earthquake," by A.W. Elgamal, M. Amer, K. Adalier and A. Abul-Fadl, 10/7/93, (PB94-141983, A05, MF-A01).

NCEER-93-0019 "Development of an Earthquake Motion Simulator and its Application in Dynamic Centrifuge Testing," by I. Krstelj, Supervised by J.H. Prevost, 10/23/93, (PB94-181773, A-10, MF-A03).

NCEER-93-0020 "NCEER-Taisei Corporation Research Program on Sliding Seismic Isolation Systems for Bridges: Experimental and Analytical Study of a Friction Pendulum System (FPS)," by M.C. Constantinou, P. Tsopelas, Y-S. Kim and S. Okamoto, 11/1/93, (PB94-142775, A08, MF-A02).

NCEER-93-0021 "Finite Element Modeling of Elastomeric Seismic Isolation Bearings," by L.J. Billings, Supervised by R. Shepherd, 11/8/93, to be published.

NCEER-93-0022 "Seismic Vulnerability of Equipment in Critical Facilities: Life-Safety and Operational Consequences," by K. Porter, G.S. Johnson, M.M. Zadeh, C. Scawthorn and S. Eder, 11/24/93, (PB94-181765, A16, MF-A03).

NCEER-93-0023 "Hokkaido Nansei-oki, Japan Earthquake of July 12, 1993, by P.I. Yanev and C.R. Scawthorn, 12/23/93, (PB94-181500, A07, MF-A01).

NCEER-94-0001 "An Evaluation of Seismic Serviceability of Water Supply Networks with Application to the San Francisco Auxiliary Water Supply System," by I. Markov, Supervised by M. Grigoriu and T. O'Rourke, 1/21/94.

NCEER-94-0002 "NCEER-Taisei Corporation Research Program on Sliding Seismic Isolation Systems for Bridges: Experimental and Analytical Study of Systems Consisting of Sliding Bearings, Rubber Restoring Force Devices and Fluid Dampers," Volumes I and II, by P. Tsopelas, S. Okamoto, M.C. Constantinou, D. Ozaki and S. Fujii, 2/4/94, (PB94-181740, A09, MF-A02 and PB94-181757, A12, MF-A03).

NCEER-94-0003 "A Markov Model for Local and Global Damage Indices in Seismic Analysis," by S. Rahman and M. Grigoriu, 2/18/94.

NCEER-94-0004 "Proceedings from the NCEER Workshop on Seismic Response of Masonry Infills," edited by D.P. Abrams, 3/1/94, (PB94-180783, A07, MF-A02).

NCEER-94-0005 "The Northridge, California Earthquake of January 17, 1994: General Reconnaissance Report," edited by J.D. Goltz, 3/11/94, (PB193943, A10, MF-A03).

NCEER-94-0006 "Seismic Energy Based Fatigue Damage Analysis of Bridge Columns: Part I - Evaluation of Seismic Capacity," by G.A. Chang and J.B. Mander, 3/14/94, (PB94-219185, A11, MF-A03).

NCEER-94-0007 "Seismic Isolation of Multi-Story Frame Structures Using Spherical Sliding Isolation Systems," by T.M. Al-Hussaini, V.A. Zayas and M.C. Constantinou, 3/17/94, (PB193745, A09, MF-A02).

NCEER-94-0008 "The Northridge, California Earthquake of January 17, 1994: Performance of Highway Bridges," edited by I.G. Buckle, 3/24/94, (PB94-193851, A06, MF-A02).

NCEER-94-0009 "Proceedings of the Third U.S.-Japan Workshop on Earthquake Protective Systems for Bridges," edited by I.G. Buckle and I. Friedland, 3/31/94, (PB94-195815, A99, MF-MF).

NCEER-94-0010 "3D-BASIS-ME: Computer Program for Nonlinear Dynamic Analysis of Seismically Isolated Single and Multiple Structures and Liquid Storage Tanks," by P.C. Tsopelas, M.C. Constantinou and A.M. Reinhorn, 4/12/94.

NCEER-94-0011 "The Northridge, California Earthquake of January 17, 1994: Performance of Gas Transmission Pipelines," by T.D. O'Rourke and M.C. Palmer, 5/16/94.

NCEER-94-0012 "Feasibility Study of Replacement Procedures and Earthquake Performance Related to Gas Transmission Pipelines," by T.D. O'Rourke and M.C. Palmer, 5/25/94.

NCEER-94-0013 "Seismic Energy Based Fatigue Damage Analysis of Bridge Columns: Part II - Evaluation of Seismic Demand," by G.A. Chang and J.B. Mander, 6/1/94, to be published.

NCEER-94-0014 "NCEER-Taisei Corporation Research Program on Sliding Seismic Isolation Systems for Bridges: Experimental and Analytical Study of a System Consisting of Sliding Bearings and Fluid Restoring Force/Damping Devices," by P. Tsopelas and M.C. Constantinou, 6/13/94, (PB94-219144, A10, MF-A03).

NCEER-94-0015 "Generation of Hazard-Consistent Fragility Curves for Seismic Loss Estimation Studies," by H. Hwang and J-R. Huo, 6/14/94.

NCEER-94-0016 "Seismic Study of Building Frames with Added Energy-Absorbing Devices," by W.S. Pong, C.S. Tsai and G.C. Lee, 6/20/94, (PB94-219136, A10, A03).

NCEER-94-0017 "Sliding Mode Control for Seismic-Excited Linear and Nonlinear Civil Engineering Structures," by J. Yang, J. Wu, A. Agrawal and Z. Li, 6/21/94.

NCEER-94-0018 "3D-BASIS-TABS Version 2.0: Computer Program for Nonlinear Dynamic Analysis of Three Dimensional Base Isolated Structures," by A.M. Reinhorn, S. Nagarajaiah, M.C. Constantinou, P. Tsopelas and R. Li, 6/22/94.

NCEER-94-0019 "Proceedings of the International Workshop on Civil Infrastructure Systems: Application of Intelligent Systems and Advanced Materials on Bridge Systems," Edited by G.C. Lee and K.C. Chang, 7/18/94, to be published.

NCEER-94-0020 "Study of Seismic Isolation Systems for Computer Floors," by V. Lambrou and M.C. Constantinou, 7/19/94.

NCEER-94-0021 "Proceedings of the U.S.-Italian Workshop on Guidelines for Seismic Evaluation and Rehabilitation of Unreinforced Masonry Buildings," Edited by D.P. Abrams and G.M. Calvi, 7/20/94.

NCEER-94-0022 "NCEER-Taisei Corporation Research Program on Sliding Seismic Isolation Systems for Bridges: Experimental and Analytical Study of a System Consisting of Lubricated PTFE Sliding Bearings and Mild Steel Dampers," by P. Tsopelas and M.C. Constantinou, 7/22/94.

NCEER-94-0023 "Development of Reliability-Based Design Criteria for Buildings Under Seismic Load," by Y.K. Wen, H. Hwang and M. Shinozuka, 8/1/94, to be published.

NCEER-94-0024 "Experimental Verification of Acceleration Feedback Control Strategies for an Active Tendon System," by S.J. Dyke, B.F. Spencer, Jr., P. Quast, M.K. Sain, D.C. Kaspari, Jr. and T.T. Soong, 8/29/94.

NCEER-94-0025 "Seismic Retrofitting Manual for Highway Bridges," Edited by I.G. Buckle and I.F. Friedland, to be published.

NCEER-94-0026 "Proceedings from the Fifth U.S.-Japan Workshop on Earthquake Resistant Design of Lifeline Facilities and Countermeasures Against Soil Liquefaction," Edited by T.D. O'Rourke and M. Hamada, 11/7/94.

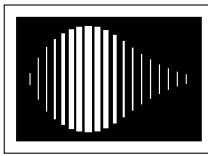

NATIONAL CENTER FOR EARTHQUAKE ENGINEERING RESEARCH

Headquartered at the State University of New York at Buffalo

State University of New York at Buffalo
Red Jacket Quadrangle
Buffalo, New York 14261
Telephone: 716/645-3391
FAX: 716/645-3399

ISSN 1088-3800